
Understanding the evolutionary modes of disks with resolved $H\alpha$ maps of 390 galaxies in local groups

Sandesh Kulkarni



München 2015

Understanding the evolutionary modes of disks with resolved $H\alpha$ maps of 390 galaxies in local groups

Sandesh Kulkarni

Dissertation
an der Faculty of Astrophysics
der Ludwig-Maximilians-Universität
München

vorgelegt von
Sandesh Kulkarni
aus Thane, India

München, den October 2015

Erstgutachter: Priv.-Doz. Dr. Roberto Saglia

Zweitgutachter: Prof. Hans Böhringer

Tag der mündlichen Prüfung: 22nd October 2015

Zusammenfassung

Die Verteilung von sternbildendem Gas in Galaxien, die sich in Galaxienhaufen wie dem Virgohaufen befinden, unterscheidet sich von derjenigen in vergleichbaren Feldgalaxien. Räumlich aufgelöste Beobachtungen von sternbildendem Gas helfen dabei zu bestimmen, welche physikalischen Prozesse für das Unterdrücken (engl. quenching) der Sternentstehung verantwortlich sind. Doch nur ein kleiner Teil der lokalen Galaxienpopulation ($< 10\%$) ist in Haufen zu finden. Für das Verständnis der physikalischen Mechanismen, die die Sternentstehung in den meisten passiven Galaxien unterdrücken, das sind Galaxien, die keine neuen Sterne mehr bilden, benötigen wir daher räumlich aufgelöste Beobachtungen von Galaxien in Gruppen.

In dieser Arbeit präsentiere ich Ergebnisse der “ $H\alpha$ Galaxy Groups Imaging Survey” (HAGGIS), einer schmalbandigen Durchmusterung im lokalen Universum bei Rotverschiebungen von $0.01 < z < 0.055$. Es wurden gezielt 100 Galaxiengruppen mit einer großen Bandbreite an Massen des Gruppenhalos ($M_{\text{halo}} = 10^{12} - 10^{14} M_{\odot}$) beobachtet, diese wurden aus einem Gruppenkatalog ausgewählt, der wiederum aus der “Sloan Digital Sky Survey” (SDSS) abgeleitet wurde. Zusätzlich finden sich im Gesichtsfeld der Beobachtungen noch 20 weitere Gruppen. Es wurden Paare von Schmalbandfiltern benutzt, um von den Galaxien kontinuumssubtrahierte Aufnahmen guter Qualität in einem Wellenlängenbereich zu erhalten, der im Ruhesystem dem Bereich um die $H\alpha$ -Linie entspricht. Auf diesen Bildern kann die Verteilung des sternbildenden Gases in Gruppengalaxien nachverfolgt werden. Diese Arbeit baut auf der Analyse von 390 HAGGIS-Galaxien in 107 der beobachteten Gruppen auf.

Das Gas in den äußeren Regionen von Galaxien ist schwach gebunden und kann daher einfach durch den Staudruck (engl. ram pressure) entfernt werden, der durch das Medium innerhalb der Gruppe (engl. intra-group medium, IGM) ausgeübt wird. Galaxien in Gruppen erfahren auch gravitative Wechselwirkungen, die ebenfalls die Verteilung des sternbildenden Gases stören können, aber diese haben im Gegensatz zum Staudruck auch Auswirkungen auf die Verteilung der Sterne.

HAGGIS liefert nun zum ersten Mal den Beweis, dass sowohl das Abstreifen des Gases durch den Staudruck als auch die Gezeiteneffekte aktive, häufige und wichtige Prozesse in Gruppen darstellen. In Satellitengalaxien, also Galaxien, die sich im Gravitationspotential einer größeren Galaxie bewegen und die in unserer Stichprobe typische stellare Massen von bis zu $10^{10.3} M_{\odot}$ haben, sind die Scheiben aus H α -Gas üblicherweise kleiner als die stellaren Scheiben. Dies deutet darauf hin, dass das Unterdrücken der Sternentstehung von außen nach innen durch das Abstreifen von Gas geschieht. Besonders in massiveren Halos kann dies zu einer erheblich kompakteren H α -Morphologie führen, mit deutlich abgeschwächter Sternentstehung. Dies sind die Übergangsgalaxien, nach denen seit langem in Studien zur Unterdrückung der Sternentstehung gesucht wird.

Wir haben auch beobachtet, dass bei Galaxien, in denen die Sternentstehung teilweise oder vollständig unterdrückt ist, besonders bei denjenigen niedriger Masse, die Größe des stellaren Anteils kompakt ist und das Flächenhelligkeitsprofil die Form einer nach oben gebogenen, anti-trunkierten geknickten Exponentialfunktion (engl. broken exponential) besitzt. Über die Ursache für solche Profile wird debattiert, wobei Verschmelzungen von zwei Galaxien mit einem großen Massenunterschied (engl. minor mergers) das wahrscheinlichste Szenario darstellen. Nichtsdestotrotz weisen die Änderungen im stellaren Helligkeitsprofil darauf hin, dass zusätzlich zu den abstreifenden Prozessen auch gravitative Prozesse ablaufen müssen, da nur letztere auch die stellare Morphologie beeinflussen.

Es wurde vorhergesagt, dass schnelles Abstreifen von äußerem Gas in Abwesenheit von anderen physikalischen Wechselwirkungen zu einer eindeutigen Form des azimuthal gemittelten radialen H α -Flächenhelligkeitsprofils in Galaxien führen würde, nämlich einer geknickten Exponentialfunktion, wobei diese im Virgohaufen nachgewiesen werden könnte. Für viele HAGGIS-Galaxien, besonders bei niedrigen Massen, wird tatsächlich ein solches Profil beobachtet. Jedoch besitzen diese Galaxien auch Sternentstehungsraten, die mit denen von gewöhnlichen Galaxien bei derselben stellaren Masse vergleichbar sind, und treten häufiger in Halos mit geringer Masse auf. Dies weist darauf hin, dass diese Form der Trunkierung der H α -Scheibe für die Mehrzahl dieser Galaxien nichts mit den Wechselwirkungen mit ihrem Umfeld zu tun hat. Der Großteil der Galaxien mit in Relation zu ihrer Masse niedriger Sternentstehung zeigt stattdessen einfache exponentielle H α -Profile, die stärker radial abfallen als die stellaren Profile. Unter Berücksichtigung aller Indizien ziehe ich den Schluss, dass eine Kombination von gravitativen und abstreifenden Mechanismen notwendig ist, um die beobachtete, von außen nach innen verlaufende Unterdrückung der Sternentstehung in Gruppengalaxien zu erklären.

Abstract

The distribution of star-forming gas is observed to be different in galaxies living in clusters of galaxies such as Virgo compared to similar galaxies in the field. Spatially resolved observations of star-forming gas helps to constrain the physical processes that drive the quenching of star-formation. But only a small fraction of the local galaxy population ($< 10\%$) lives in clusters. To understand the physical mechanisms involved in the quenching process for the majority of passive galaxies (i.e. galaxies that are not forming new stars), we require spatially resolved observations of galaxies in groups.

In this thesis, I present results from the “H α Galaxy Groups Imaging Survey” (HAGGIS) a narrow-band imaging survey in the local universe (in the redshift range of $0.01 < z < 0.055$). We have observed 100 galaxy groups over a wide range of group halo mass ($M_{\text{halo}} = 10^{12} - 10^{14} M_{\odot}$), selected from a group catalogue derived from the “Sloan Digital Sky Survey” (SDSS). Additionally, 20 serendipitous groups are found in the images. We have used pairs of narrow-band filters to obtain good quality continuum-subtracted rest-frame H α images of these galaxies, tracing the distribution of star-forming gas in group galaxies. This thesis is based on the analysis of 390 HAGGIS galaxies in 107 of the observed groups.

Gas in the outer regions of galaxies is loosely bound and hence can be removed easily under the ram-pressure exerted by the intra-group medium (IGM). Galaxies in groups also experience frequent tidal interactions or mergers which can also disturb the distribution of star-forming gas, but, unlike ram-pressure, also influences the distribution of stars.

HAGGIS provides evidence, for the first time, that ram-pressure stripping and tidal effects are active, common, and important in the group environment. In satellite galaxies i.e. galaxies orbiting within the potential well of a larger galaxy, which in our sample typically have stellar masses $\leq 10^{10.3} M_{\odot}$, H α disks are usually smaller than their stellar disks, suggestive of the outside-in quenching of star formation

by the stripping of gas. Especially in more massive halos, this can lead to much more compact $H\alpha$ morphology, with suppressed global star formation: These are the transition galaxies long sought after in studies of quenching.

We have also observed that galaxies with partially or totally quenched star formation, especially those at lower mass, typically have compact stellar sizes, and an up-bending (anti-truncated) broken-exponential stellar surface brightness profile. The origin of such profiles is debated although minor mergers are a primary candidate. Regardless, the changes to the stellar profile tell us that gas-stripping processes must be supplemented by gravitational processes which affect the stellar morphology.

It has been claimed that the rapid stripping of outer gas, in the absence of any other physical interactions, leads to a distinct broken-exponential (truncated) $H\alpha$ azimuthally averaged radial surface brightness profile in galaxies, demonstrable in the Virgo cluster. Many HAGGIS galaxies, especially at low mass, are observed to have such profiles. But these galaxies are found to have star forming activity comparable to normal galaxies of their stellar mass and are more common in low mass haloes which suggests that this form of truncation in $H\alpha$ disks is not associated with environmental interactions for majority of these galaxies. The majority of galaxies with low levels of star formation for their stellar mass have, instead, single-exponential $H\alpha$ profiles that show a steeper radial decline compared to their stellar profiles. Combining all the evidence, I conclude that a combination of gravitational and stripping mechanisms is required to explain the observed outside-in quenching of star formation in group galaxies.

Contents

List of Figures	xiii
-----------------	------

List of Tables	xxi
----------------	-----

1	Introduction	1
1.1	Galaxy evolution	2
1.1.1	Hierarchical build up	3
1.1.2	Clusters vs field	4
1.1.3	Secular evolution: Nature vs Nurture	5
1.2	Era of large surveys	6
1.2.1	Definition of groups and environment	7
1.2.2	Galaxy sizes	8
1.2.3	Color distribution	9
1.2.4	Passive fraction	9
1.2.5	SFR-density relation	10
1.2.6	Physical mechanisms	12
1.3	Resolved properties	14
1.3.1	Stellar surface brightness profiles	15
1.3.2	H α surface brightness profiles	17
1.4	Motivation for a narrow-band imaging survey	19
1.5	Thesis overview	21
2	The HAGGIS survey	23
2.1	Sample Selection	23
2.2	Observations	27
3	Data reduction pipeline	29
3.1	HAGGIS data processing	29
3.1.1	Basic processing	29
3.1.2	Astrometry	33
3.1.3	Regridding	35
3.1.4	Sky subtraction	37
3.1.5	PSF matching	38

3.1.6	Flux Scaling and flux calibration	41
3.1.6.1	H α in Absorption	44
4	Surface brightness profile generation and classification	47
4.1	Continuum and H α profile generation	48
4.2	Profile classification	51
4.2.1	Continuum profile classification	53
4.2.2	H α profile types	53
4.2.3	Comparison of stellar and H α profile types	57
4.3	Computation of derived parameters	58
4.3.1	Fitting radii	59
4.3.2	Galaxy sizes	59
4.3.3	Central excess / deficit	61
4.3.4	Break radii	61
4.3.5	Integrated fluxes	63
4.3.6	H α luminosity	63
4.3.7	Star-formation rate	64
4.4	SDSS comparison	65
5	Relation of stellar and Hα sizes to stellar mass and profile types	71
5.1	Stellar and H α Size-mass relation	72
5.2	Stellar continuum profile types	80
5.2.1	Stellar and H α size-mass relations	80
5.2.2	Offset from the size-mass relations	82
5.3	H α profile types	84
5.3.1	Stellar and H α size-mass relations	84
5.3.2	Offset from the size-mass relations	84
5.4	Comparison of H α and stellar sizes	87
5.5	Conclusions	90
6	Relation between star formation rate, stellar mass and $\text{Re}_{\text{H}\alpha}/\text{Re}_{\text{c}}$	93
6.1	SDSS and HAGGIS fiber SF MS comparison	94
6.2	SDSS and HAGGIS global SF MS comparison	97
6.3	H α 3 and HAGGIS global SF MS comparison	100
6.4	SF MS for different H α profile types	101
6.5	Differences in SDSS and HAGGIS SFRs as a function of $\text{Re}_{\text{H}\alpha}/\text{Re}_{\text{c}}$	103
6.6	$\Delta(\log\text{SFR})_{\text{M}_*}$ as a function of $\text{Re}_{\text{H}\alpha}/\text{Re}_{\text{c}}$	104
6.7	Conclusion	106
7	Stellar mass and galaxy environment	109
7.1	Effects of stellar mass	110
7.2	Group halo mass	112
7.3	Centrals vs Satellites	115
7.3.1	Sizes	116
7.3.2	SF MS	120

7.4	Conclusions	122
8	Conclusions and future work	127
8.1	Summary	128
8.1.1	Size-mass relations	128
8.1.2	SFR-mass relations	129
8.1.3	Stellar mass and galaxy environment	130
8.2	Discussion	132
8.3	Future prospects	134
8.3.1	Prospects of HAGGIS	135
8.3.2	Other surveys	135
	Bibliography	143
	A Profile plots	145
	B SDSS derived parameters	537
	C HAGGIS derived parameters	545
	Acknowledgements	559

List of Figures

1.1	Hubble sequence. Image credits - http://skyserver.sdss.org/dr1/en/proj/advanced/galaxies/tuningfork.asp	3
1.2	Showing the morphology-density relation obtained by Dressler (1980) using observations of 55 clusters. The fraction of spirals decrease in high density regions while the fractions of S0 and elliptical galaxies increase.	5
1.3	Showing the distributions of H α equivalent width (EW) for star-forming (SF) galaxies in low density (dotted line) and high density (solid line) regions obtained by Balogh et al. (2004a). H α EW traces star-formation rate per unit luminosity. The similar distribution of H α EW in two environments suggest that the star-formation rate in star-forming galaxies is not affected by galaxy environment. . . .	11
1.4	Comparison of the specific SFR distributions of cluster (red histograms) and field (blue dashed histograms) galaxies for low redshift universe obtained by Haines et al. (2013) using Spitzer/MIPS 24 μ m observations. Vertical red/blue dot-dashed lines indicate the mean of each distribution.	12
1.5	The cartoon made by George et al. (2013) to explain the effects of physical processes on galaxy morphologies and color. The gas stripping mechanisms like ram pressure stripping, starvation and quasar feedback typically change the galaxy color while having minimal effect on galaxy morphology. Tidal interactions, minor mergers and disk instabilities (which can lead to formation of bars and bulges in galaxies) can change the galaxy morphology very effectively but may have limited effect on galaxy color while major mergers can affect both color and morphology of the galaxy.	15
1.6	Median H α profiles for different classes of Virgo and isolated galaxies obtained by Koopmann & Kenney (2004). <i>Top left</i> : Median H α profiles of isolated galaxies divided into two bins in concentration index. Median H α profiles are not affected by the differences of concentration index in R-band. <i>Top middle</i> : The median Virgo cluster H α profile is truncated in the outer region compared to median isolated H α profile. <i>Other panels</i> : Median H α profiles for various other classes of galaxies in the Virgo cluster compared with the same for normal Virgo spiral galaxies. The H α profiles for these different classes are significantly different than the median H α profile of normal Virgo galaxies.	18

2.1	(a) Shows the distribution in halo mass of observed groups in HAGGIS (blue) and the distribution of groups used in this thesis (red) with halo mass. (b) Shows the distribution of observed galaxies in HAGGIS (blue) and the distribution of galaxies used in this thesis (red).	25
2.2	Filter response functions of (a) the Wide Field Image (WFI) on the MPG/ESO 2.2 m telescope and (b) the Wide Field Camera (WFC) on the Isaac Newton Telescope (INT) used for the HAGGIS observations.	28
3.1	The layouts for (a) the 8 chips of the Wide Field Imager and (b) the 4 chips of the Wide Field Camera.	30
3.2	Flow chart showing the steps taken in data reduction.	31
3.3	The fringe pattern obtained for observations with different narrow-band filters using the WFI camera (the filter numbers are labelled on each panel). Fringing was largely absent except for one WFI filter — #847.	33
3.4	Example plot showing the accuracy of astrometric calibration. Upper panels show the astrometric accuracy obtained for WFI galaxies using SDSS DR5 data as a reference catalog while the lower panels show the same after relative astrometry was performed using a few selected stars. An astrometric accuracy of at least a tenth of a pixel was achieved.	34
3.5	Weight maps in (a) LANCZOS interpolation and (b) bilinear interpolation. More pixels are flagged as bad using LANCZOS interpolation.	36
3.6	(a) Moiré pattern observed after bilinear interpolation. (b) The RMS background map obtained for the image. It completely recovers the Moiré pattern observed in the image. (c) Shows that the Moiré is largely reduced when oversampling was performed during the interpolation.	37
3.7	Shows an example of sky subtraction for a WFI image. (a) Shows a median smoothed image before the sky subtraction and (b) the same image after the sky subtraction. The sky gradient is reduced considerably.	39
3.8	Shows how the flux ratio of simulated stars (green; triangle = main sequence, circle = giants) and galaxies (red) for the #847 and #858 narrow-band WFI filter pair depends on the (a) $r-i$ and (b) $g-r$ color of the object. The flux ratio depend upon the response function of the two filters and on the spectral shape of the object. This is problematic for the PSF matching algorithm.	42

3.9	Full SDSS spectrum of galaxy 112723-1 is shown in lower panel. The upper panel is zoomed in at around the $H\alpha$ wavelength. The ON band (red) and OFF band (blue) filter response functions are over-plotted. The green line is the median smoothed version of the spectrum while the red line denotes the polynomial fit to this smoothed spectrum which is used to obtain the continuum level for the ON band.	43
3.10	Left hand panels show the narrow-band continuum image while the right hand panels show continuum subtracted $H\alpha$ image. Fig. 3.10(a) shows an example galaxy (31811-1) for which $H\alpha$ is detected in absorption at intermediate radii while fig. 3.10(b) shows the galaxy (1228-12) showing absorption in the outermost region.	45
4.1	Continuum (upper left) and $H\alpha$ (upper right) image cutouts of the galaxy 3071-1 and best-fit values of ellipticity and position angle as a function of semi-major axis to the continuum image (lower panels) obtained using the IRAF <i>ellipse</i> task. The plot shows how position angle and ellipticity varies for different components of the galaxy. Except for the bar region (\sim between $5''$ - $25''$), the ellipticity increases and position angle decreases monotonically until they converge at larger radii ($\geq 70''$) where the disk dominates. These convergent values (shown by the dashed horizontal lines) are then fixed for the second iteration of the <i>ellipse</i> task to obtain the surface brightness profiles.	50
4.2	The continuum (blue) and $H\alpha$ (red) surface brightness profiles for the same galaxy (3071-1) as shown in fig. 4.1. The gray line denotes the approximate noise level in $H\alpha$ obtained using 100 black sky regions around the galaxy.	52
4.3	Different types of continuum profiles (blue). The solid gray line denotes the approximate noise level. Linear fits to different regions are marked with dashed gray lines, where fits are made between the open diamonds. The break radius — the radius at which the disk profile changes its slope — is marked by an open circle.	54
4.4	Different types of $H\alpha$ profile (emission in red and absorption in green). The continuum profiles (blue) are shown for reference. The solid gray line denotes approximate noise level. The fitting radii for a linear fitting of different regions are marked with open diamonds and the linear fits are marked with dashed gray lines.	56
4.5	The distribution of stellar continuum profile types among different classes of galaxies based on their $H\alpha$ surface brightness profiles. $H\alpha$ profile types are arranged such that they form a sequence of decreasing fraction of type II galaxies and increasing fraction of type III and non-exponential galaxies (left to right). Type I fraction is generally unrelated with the $H\alpha$ profile type (along this sequence) although they are somewhat more common in exponential and steep exponential galaxies ($> 40\%$) and less common in truncated and flat-truncated galaxies (~ 25 - 30%).	58

4.6	Comparison of HAGGIS and SDSS $H\alpha$ flux measurements within the aperture of $3''$ diameter (SDSS fiber size) for HAGGIS galaxies color-coded with $H\alpha$ profile types. AGNs identified in SDSS DR7 are marked on the plot with open circles. The two flux measurements match quite well except for few cases.	65
4.7	(a) Comparison of HAGGIS and SDSS fiber SFRs for HAGGIS galaxies color-coded with $H\alpha$ profile types. (b) Comparison of HAGGIS global SFR measurements with SDSS aperture corrected SFR measurements for HAGGIS galaxies color-coded with $H\alpha$ profile types. AGNs identified in SDSS DR7 are not shown on both plots. The fiber SFR measurements agrees well for the two datasets while the SDSS aperture corrected measurements and HAGGIS global SFR measurements show larger discrepancies.	67
4.8	Difference between HAGGIS total SFR and SDSS aperture corrected SFRs (a) against HAGGIS total SFR (b) against stellar mass. Both plots are color-coded with $H\alpha$ profile types. AGNs identified in SDSS DR7 are not shown on these plots. SDSS overestimates SFRs for many low mass and low SFR HAGGIS galaxies which includes most of the steep exponentials and many galaxies with truncated $H\alpha$ disks while it underestimates the SFRs for galaxies having larger SFR activity which includes many sawtooth galaxies. The high mass galaxies show larger discrepancies between the two SFR measurements (> 1 dex).	70
5.1	Size-mass relations of stellar disks using measurements of half light radii (Re_c) in 5.1(a) and main disk scale lengths (Rd_c) in 5.1(b). Both plots are color-coded by global specific star-formation rate (sSFR). This shows that the sSFR is correlated with size at fixed stellar mass such that the galaxies with low sSFR at fixed stellar mass (and galaxies detected with absorption in the HAGGIS observations) exhibit compact stellar disks.	73
5.2	Plots showing the correlation of the deviation from the fitted stellar size-mass relations with global sSFR using the stellar continuum (a) half light radius and (b) disk scale length measurements. Pure absorption galaxies are excluded. The black dashed line denotes the best fit relation obtained using all the data points with equal weights.	76
5.3	Size-mass relations of $H\alpha$ disks using the measurements of (a) half light radii ($Re_{H\alpha}$) and (b) main disk scale lengths ($Rd_{H\alpha}$). The $H\alpha$ sizes of galaxies which have $H\alpha$ emission line profile consistent with the PSF profile (obtained for a similar observing condition) are marked by upper limits. Both plots are color-coded by the global specific star-formation rates (sSFR) which shows that the galaxies with low sSFR have compact $H\alpha$ disks. Size of the $H\alpha$ disks is seen to correlate positively with stellar mass with a power law relation.	78

5.4	Plots showing the correlation of the deviation from the fitted size-mass relations for $H\alpha$ disks with global sSFR using (a) $H\alpha$ half light radius and (b) $H\alpha$ disk scale length measurements. Galaxies which have the $H\alpha$ emission line profile consistent with the PSF profile (obtained for a similar observing condition) are marked by upper limits. The black dashed line denotes the best fit relation obtained by using all the data points with equal weights.	79
5.5	The size-mass relations for stellar and $H\alpha$ disks color-coded by stellar continuum profile types. Type III and non-exponential galaxies are observed to populate the stellar size-mass relation observed for the quenched galaxies and form a dominant population of galaxies that deviate from $\log(R_{H\alpha}) - \log(M_*)$ relation.	81
5.6	Distribution of the offsets from stellar continuum and $H\alpha$ half light sizes-mass relations among different stellar continuum profile types.	83
5.7	Size-mass relations for stellar and star-forming disks color-coded by $H\alpha$ profile types. Only SF galaxies in HAGGIS sample are shown here ($\log(R_{H\alpha}) - \log(M_*)$ for the passive galaxies can be seen in fig. 5.5(a)). Steep exponential galaxies dominate the population having compact $H\alpha$ and stellar sizes. Truncated and flat-truncated galaxies are found on the fitted relations i.e. their half light sizes are relatively large.	85
5.8	Distribution of the offsets from stellar and $H\alpha$ size-mass relations for different $H\alpha$ profile types.	86
5.9	$H\alpha$ half light radius vs continuum half light radius for HAGGIS galaxies color-coded by $H\alpha$ profile types. AGNs identified in the SDSS DR7 catalog are shown with open circles. The majority of HAGGIS galaxies have compact $H\alpha$ disks compared to their stellar disks.	88
5.10	Upper panel (5.10(a)) shows the logarithmic ratio of $H\alpha$ half light size to stellar continuum half light size vs galaxy stellar mass while the lower panel (5.10(b)) shows the distribution of the size ratio for two mass bins. Most of the low mass galaxies have smaller $H\alpha$ sizes compared to their stellar sizes while high mass galaxies show a dichotomy in size ratios with some galaxies exhibiting similar or larger $H\alpha$ sizes and others exhibiting very compact $H\alpha$ sizes compared to their stellar sizes.	89
6.1	Fiber SFR - M_* (SFR integrated over central 3" SDSS fiber diameter). The contour levels correspond to the whole SDSS dataset in the redshift range of HAGGIS survey while the purple and gray points represent the HAGGIS and SDSS measurements respectively for the HAGGIS SF galaxies. The MS fit (black line) is derived by identifying the peak of the SFR distribution in narrow M_* bins (large triangles).	95

6.2	Distributions of $\Delta(\log(\text{SFR}_{\text{Fiber}}))_{M_*}$ for the whole SDSS dataset for $0.01 < z < 0.055$ (grey), for SDSS measurements for all galaxies in HAGGIS survey (dashed-red) and for SDSS measurements (red) and for the HAGGIS measurements (blue) just for the HAGGIS SF galaxies.	97
6.3	Global SFR- M_* plane for HAGGIS galaxies: HAGGIS SFR (purple) and SDSS aperture corrected SFR (grey). The contour levels correspond to the MS measurements for the whole SDSS dataset for $0.01 < z < 0.055$. The MS fit (black line) is derived by identifying the peak of the SFR distribution (large triangles).	98
6.4	Distributions of $\Delta(\log(\text{SFR}_{\text{Total}}))_{M_*}$ for whole SDSS dataset in the redshift range of HAGGIS survey (grey); for SDSS measurements for all HAGGIS galaxies (dashed-red), and for SDSS measurements (solid-red) and for the HAGGIS measurements (solid-blue) just for the HAGGIS SF galaxies.	99
6.5	SFR MS derived for HAGGIS SF galaxies using HAGGIS global SFR measurements (red) and SDSS aperture corrected measurements (blue). SFR of galaxies in the H α 3 survey Gavazzi et al. (2015) are shown by gray points for comparison. The MS fit (equation 6.3) derived using SDSS aperture corrected SFR measurements for the galaxies with $0.01 < z < 0.055$ is shown in black while the magenta and blue dashed lines denote the SFR 1 dex above and below the MS respectively.	100
6.6	(a) Galaxy integrated star-formation rate (SFR) vs stellar mass and (b) SDSS aperture-corrected SFR vs stellar mass for HAGGIS galaxies color-coded with H α profile types. The black line is the MS fit derived using SDSS aperture corrected SFR measurements for the galaxies in the redshift range of HAGGIS survey while magenta and blue dashed lines represent the SFR levels 1 dex above and below the MS respectively.	102
6.7	Difference between SDSS aperture corrected SFR and HAGGIS total SFR against $\text{Re}_{\text{H}\alpha}/\text{Re}_c$ color-coded with H α profile types. SDSS overestimates the SFR for galaxies having compact H α disks compared to its stellar disks while it underestimates the SFRs for galaxies having larger H α disks compared to their stellar disks.	103
6.8	Deviation from the MS ($\Delta(\log(\text{SFR}))_{M_*}$) vs $\log \text{Re}_{\text{H}\alpha}/\text{Re}_c$ color-coded with H α profile types (a) for HAGGIS narrow-band SFR and (b) for the SDSS aperture-corrected SFRs. The deviation from the MS correlates with the size ratios especially for galaxies with compact H α disks which is indicative of outside-in quenching. SDSS aperture-corrected SFRs also produce a similar trend for region III, albeit with smaller deviation compared to HAGGIS SFRs.	105

- 7.1 (a) The frequency of stellar profile types as a function of stellar mass among star-forming (solid lines) and quenched (dashed lines) galaxies. Quenched galaxies are dominated by type III at low mass and non-exponentials at high mass. Star-forming galaxies have a higher fraction of type II galaxies, a lower fraction of type III and non-exponentials, and a similar fraction of type I galaxies compared to quenched systems. (b) The frequency of $H\alpha$ profile types as a function of stellar mass. The frequency of truncated, flat-truncated and exponentials decrease with stellar mass, compensated by an increase in the frequency of sawtooth, absorption (plus non-detections) and steep exponentials. Anti-truncated are not shown on the plot due to their low fractions. 111
- 7.2 (a) The frequency of continuum profile types as a function of group halo mass for SF (solid lines) and quenched (dashed lines) galaxies. Among SF galaxies, type I (II) are more (less) common in high mass haloes than at low mass, while type III have no halo mass dependence. Quenched galaxies are dominated by type III (I) galaxies in low (high) mass groups with a significant contribution of non-exponentials but few type IIs. (b) The frequency of $H\alpha$ profile types as a function of halo mass. Truncated, exponential and sawtooth galaxies are relatively rare while the steep exponentials (both including and excluding AGNs) and absorption (including non-detections) galaxies are more common in high mass haloes. Flat-truncated show a flat trend with halo mass. 113
- 7.3 Log $H\alpha$ half light radius vs log continuum half light radius color-coded with $H\alpha$ profile types (a) for centrals and (b) for satellites. AGNs identified in the SDSS DR7 catalog are marked by an open circle. Galaxies having an $H\alpha$ emission line profile consistent with the PSF profile (obtained for a similar observing condition) are marked by upper limits. Most centrals have similar or even larger $H\alpha$ disks than their stellar disks while most satellites have smaller $H\alpha$ disks compared to their stellar disks suggesting that they may be affected by their environment. A small fraction (19^{+5}_{-4} %) of central galaxies have very compact $H\alpha$ disks ($Re_{H\alpha}/Re_c < 0.4$) out of which 69^{+14}_{-11} % are AGN. 117
- 7.4 Ratio of $Re_{H\alpha}$ to Re_c vs stellar mass color-coded with sSFR for (a) centrals and (b) for satellites. AGNs identified in SDSS DR7 are marked on both plots by an open circle. Galaxies which have $H\alpha$ emission line profile consistent with the PSF profile (obtained for a similar observing condition) are marked by upperlimits. The majority of satellites are seen to have ratios below one while many centrals are seen to have ratios close to or larger than one. 118
- 7.5 Distribution of $Re_{H\alpha}/Re_c$ for centrals (blue) and satellites (red) split into low and high mass bins. AGNs identified in SDSS DR7 are excluded from these. 119

- 7.6 Deviation from MS vs $\log(\text{Re}_{\text{H}\alpha}/\text{Re}_c)$ color-coded with $\text{H}\alpha$ profile types (a) for centrals and (b) for satellites. Galaxies which have an $\text{H}\alpha$ emission profile consistent with the PSF profile (obtained for a similar observing condition) are marked by upper limits. The deviation from the MS correlates steeply with size ratios below 0.45 ($\log(\text{Re}_{\text{H}\alpha}/\text{Re}_c) < -0.35$) for satellites while only few centrals show a deviation below the MS. A larger scatter for galaxies with disk ratios close to one is evident in satellites indicating that SFR is suppressed or enhanced in some galaxies, maintaining the average size and shape of the star-forming disks. 121

List of Tables

2.1	This is a sample table containing the SDSS derived parameters. The full table containing all the galaxies can be found in Appendix (B).	26
4.1	Table of derived parameters for continuum and $H\alpha$ profiles. Full table can be found in Appendix (C).	62
5.1	Fit coefficients, Spearman rank coefficients, and corresponding p-values for the stellar size-mass relations in log-log space and for the respective residual relations with log sSFR.	75
5.2	Fit coefficients and Spearman rank coefficient with its corresponding p-values for the $H\alpha$ size-mass relations in log-log space and for the respective residual relations with sSFR.	80
5.3	Showing median values of the ratio of $Re_{H\alpha}$ to Re_c for different $H\alpha$ profile types.	90
B.1	Table of derived parameters from SDSS photometric and spectroscopic data.	538
C.1	Table of derived parameters for continuum and $H\alpha$ profiles.	546

Dedicated to my

Grandmother

(Late Smt. Prabhavati Kulkarni)

Chapter 1

Introduction

Astronomers as early as in the 18th century discovered that some objects in the night sky look fuzzier than point-like stars which they termed as ‘nebulae’. In 1771, French astronomer and comet hunter Charles Messier compiled a list of ~ 100 such fuzzy looking objects, that are not comets, which is now famously known as the *Messier list*. After Messier, contemporary astronomers like William and Caroline Herschel, their son John Herschel and Dreyer published similar lists of an increasing number of such objects.

The *New General Catalogue of Nebulae and Clusters of Stars (NGC)* and its supplementary catalogues called *Index Catalogues (IC)* published by Dreyer in the late nineteenth century contained more than 13000 such objects. The nature of these nebular objects was controversial; one group argued that these objects are part of our Milky way galaxy while the other group argued that these objects are individual “island universes” similar to our Milky way.

The two groups gave competing ideas that kept the controversy alive until 1925 when [Hubble \(1925\)](#) used the measurements of Cepheid variable stars ¹ to nail down the distances to two of these so called ‘spiral nebulae’ in Messier’s list, M31 and M33. He estimated that they are ~ 300 kpc ² away which was well outside any known object in our Galaxy.

¹These stars pulsate radially which varies temperature and radius inducing periodic changes in the surface brightness. The period of variation is related to the star’s luminosity. Hence, the distance of the star can be measured by measuring the period of variation and its observed flux.

²Kilo-parsec (kpc) is a distance measure in astronomy. A parsec is a distance at which the parallax in the position of the object equals 1” as measured from two diametrically opposite positions of Earth’s orbit around the Sun. One parsec is equivalent to 3.085×10^{16} meters.

With the availability of large telescopes and improving quality of photographic plates, Hubble made detailed observations of these extra-galactic objects which helped him to group them into particular classes based on their appearance ([Hubble \(1926\)](#)). Hubble found that some galaxies have regular shapes while some others are irregulars. He divided the regular galaxies into following classes -

- **Ellipticals (E):** These galaxies have smooth ellipsoidal morphology with very little internal structure. These galaxies are further classified based on their ellipticity from spheroidal (E_0) to highly flattened elliptical shapes (E_6 , E_7).
- **Lenticulars (S0):** These galaxies form a transitional class having a central spheroidal bulge and flattened outer disk with no visible spiral arms.
- **Spirals (S/SB):** These are galaxies having an outer disk structure with visible spiral arms and can contain a central spheroidal structure called a bulge. They are subdivided into two parallel sequences, normal spirals (S) and barred spirals (SB), based on whether they contain a visible elongated bar-like structure or not. Each of these are further divided into subclasses Sa/SBa — Sb/SBb — Sc/SBc of decreasing prominence of their central bulge and simultaneous opening of their spiral arm structure.

This classification scheme is known as the “Hubble sequence” (see figure 1.1) and it is still widely used today to assess the morphological differences between galaxies. These morphological differences indicate that they most likely have different formation mechanisms and hence a different formation history. Indeed Hubble termed the ellipticals and lenticulars as ‘early-types’ and spirals as ‘late-types’ suggesting that he had an impression for their evolutionary connection although he mentions in his paper that the nomenclature is used only to describe their position on the sequence and does not represent any temporal connection. The two parallel sequences formed by the normal spirals and barred spirals along with ellipticals give a characteristic ‘tuning fork’ shape to the Hubble sequence.

1.1 Galaxy evolution

It is very difficult to answer the questions like ‘*How have galaxies formed and how have they evolved into various different types we see today?*’. The study of galaxy

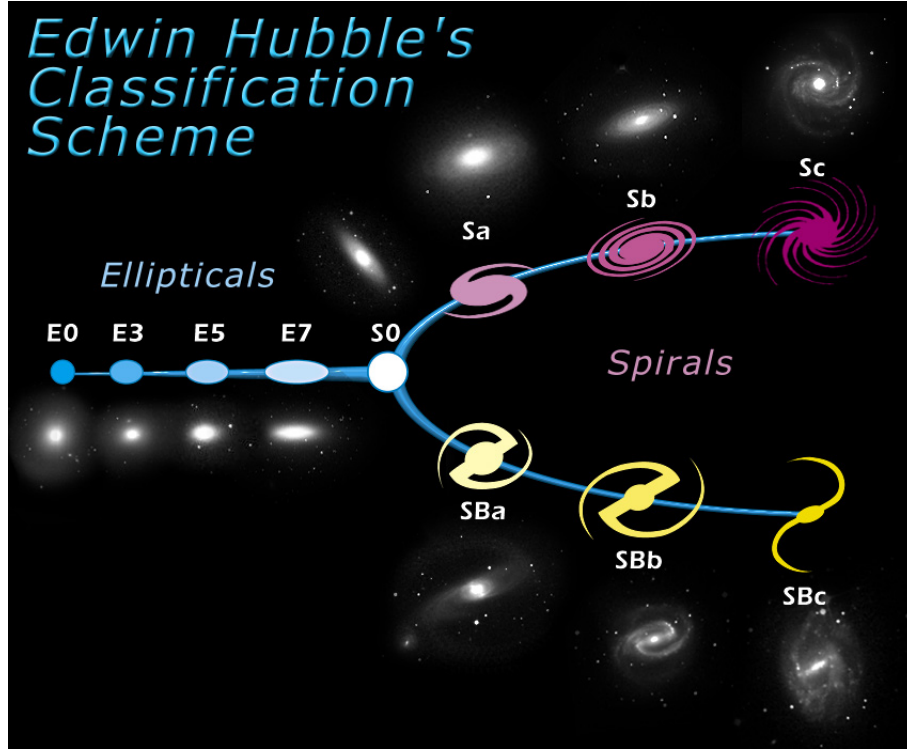


FIGURE 1.1: Hubble sequence. Image credits - <http://skyserver.sdss.org/drl/en/proj/advanced/galaxies/tuningfork.asp>.

evolution involves understanding complex physical mechanisms on timescales varying in length by at least 3-4 orders of magnitude – from the time required for the evolution of massive stars ($\sim 10^7$ years) to the age of the universe ($\sim 10^{10}$ years) – and on physical scales of at least 10 orders of magnitude – from size of individual star-forming regions called HII regions (few tens of parsecs) to the size of the visible universe itself ($\sim \text{few } 10^{10}$ parsecs). Due to this enormous complexity, many questions in the understanding of galaxy evolution remain unsolved. Nevertheless, we have made a vast amount of progress in the last century since Hubble discovered the extra-galactic nature of the so called ‘nebulae’.

1.1.1 Hierarchical build up

The notion of the expansion of the universe came to life when Hubble (1929) discovered that galaxies are receding from each other and their recession velocities are proportional to their distances, now known as Hubble’s law. The discovery has opened many avenues in the evolutionary studies of galaxies. Because of this expansion, the spectral distribution of galaxies in the distant universe appear to be shifted towards the redder end due to the Doppler effect. This ‘redshift’ of the

spectral distribution thus provides a measure of distance as well as look-back time³ for the distant universe.

The observations of galaxies in clusters and the motion of satellite galaxies around the Milky way lead to the proposition that there is more matter in the universe than is visible to us (e.g. Zwicky (1933), Zwicky (1937), Ostriker et al. (1974), Einasto et al. (1974)). It is now widely accepted that a large fraction of galaxy mass ($\sim 90\%$) is made up of weakly interacting non-baryonic ‘dark matter’ (see Bennett et al. (2013) for current measurements). With current theories, the large scale structures in the universe are formed from initial small-amplitude density fluctuations in the early universe. The high density regions collapsed first to form small dark matter haloes which over time fell towards each other under gravity and merged together to form larger haloes (see e.g. Lacey & Cole (1993)). Gas which accreted on to these dark matter haloes formed the first stars and galaxies. This model of structure formation is known as ‘hierarchical assembly’. This model suggests that groups and clusters are formed by merging of two or more dark matter haloes that are hosting their own galaxies.

1.1.2 Clusters vs field

Observers in the early twentieth century knew the differences in the population of galaxies between clusters and isolated fields (Hubble & Humason (1931)). But, the quantification of the correlation between morphology and environmental density (known as T- Σ relation) was first provided by Dressler (1980) using observations of 55 galaxy clusters (see figure 1.2). He showed that the fraction of spiral galaxies decreases from $\sim 60\%$ in the lowest density regions to less than 10% in the highest density regions while the fraction of S0 and elliptical galaxies show an opposite trend. He also observed a similar relation with cluster centric radius (T-R relation) but found that it was not as pronounced as the T- Σ relation. Latter studies have confirmed the existence of a T-R relation when the cluster-centric distance is normalized by the characteristic radius of the cluster (Whitmore et al. (1993); also see Fasano et al. (2015) for a detailed account).

Apart from morphology, various other galaxy properties are also observed to be affected by the cluster environment. 21 cm radio observations revealed that the

³Due to the finite speed of light, it takes more time for the light from the distant galaxies to reach us compared to nearby galaxies and hence the ‘redshift’ is also a measure of the look back time. Observations of galaxies at high redshift thus provides us with an opportunity to understand the early evolution of present day galaxies.

galaxies in high density regions contain a smaller fraction of atomic hydrogen (HI) compared to field galaxies (e.g. [Davies & Lewis \(1973\)](#), [Chincarini \(1984\)](#), [Giovanelli & Haynes \(1985\)](#)). This has led to the reclassification of the Hubble sequence for cluster galaxies to include a population of anemic spirals ([van den Bergh \(1976\)](#)). Similarly, galaxy color is also observed to correlate with environment such that the redder galaxies are observed more frequently in high density regions while field galaxies are observed to have bluer colors (e.g. [Kodama et al. \(2001\)](#)).

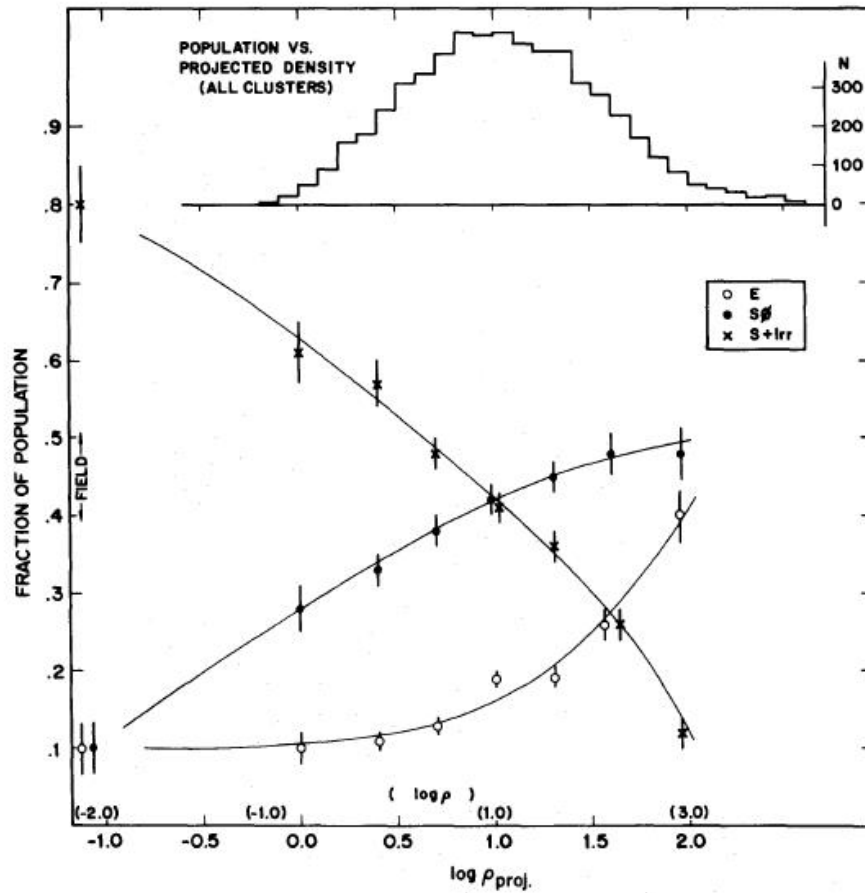


FIGURE 1.2: Showing the morphology-density relation obtained by [Dressler \(1980\)](#) using observations of 55 clusters. The fraction of spirals decrease in high density regions while the fractions of S0 and elliptical galaxies increase.

1.1.3 Secular evolution: Nature vs Nurture

Galaxy properties like morphology, color, luminosity, etc are observed to be strongly correlated with each other in both cluster and isolated field environments. For example, the early type galaxies are typically more luminous and redder in color while late-types are typically bluer and less luminous (e.g. [Roberts & Haynes \(1994\)](#)).

This suggests that apart from environment, galaxy properties are also regulated by internal mechanisms. Since, high density regions are most likely formed from the highest density peaks in the primordial field of density fluctuations, cluster galaxies are expected to have undergone an accelerated evolution with respect to regions of average density (e.g. see discussion in [De Lucia et al. \(2006\)](#)). Thus a question arises ‘*Are the differences between the cluster and field populations due to environmental interactions, or due to the internal mechanisms that happen more rapidly for galaxies in clusters?*’. The role of secular processes in the environmental correlations we see today is yet to be fully understood but there are some indications that they can be disentangled from direct environmental processes (see section [1.2.4](#)).

1.2 Era of large surveys

We cannot watch the evolution of individual galaxies due to very large timescales involved in the process of evolution. Thus, we need to rely on understanding the properties of various different types of galaxies in a statistical sense at different epochs of time, and try to form a temporal link between them. For this, we require observations of large number of galaxies covering a wide range in their spectral energy distribution as well as covering a wide range in redshift. Knowing all of these requirements, astronomers by the end of the 20th century devised large galaxy redshift surveys like the *2 Degree Field Galaxy Redshift Survey* (2dFGRS; [Colless \(1999\)](#)), the *Sloan Digital Sky Survey* (SDSS; [York et al. \(2000\)](#)) and more recent the *Galaxy and Mass Assembly* (GAMA; [Driver et al. \(2011\)](#)) and somewhat more focused, higher redshift surveys like *zCOSMOS* ([Lilly et al. \(2007\)](#)) which is based on the original *Cosmological Evolution Survey* (COSMOS, [Scoville et al. \(2007\)](#)).

The SDSS survey is the largest optical photometric and spectroscopic survey which covers a field of ~ 14500 square degrees. The latest data release has provided photometry for ~ 933 million objects over 5 broad bands u, g, r, i, z as well as optical spectra of ~ 1.5 million objects covering a wavelength range of 3800-9200 Å. With this dataset, many essential measurements of galaxy observables and structural parameters like galaxy broad-band magnitudes and colors, half light sizes, absorption line indices, etc and some derivable quantities like stellar masses and star-formation rates along with accurate astrometry and redshift information are now publicly available for a vast number of galaxies which has improved our

understanding about galaxies many fold. Some of the important findings are discussed here briefly.

1.2.1 Definition of groups and environment

The initial efforts in understanding the environmental effects on galaxy properties have been focused primarily on very dense cluster environments as clusters and their members are relatively easier to select. But clusters account for a very small fraction of galaxies in the local universe ($< 10\%$) and hence they are not representative of a general population of galaxies. A significant fraction of galaxies in the local universe ($> 60\%$) are living in groups (Eke et al. (2004)). Also, it is likely that some cluster galaxies were pre-processed in their group environment before they were accreted onto their current host. Clusters are indeed expected to have accreted a significant fraction of their final galaxy populations via galaxy groups (e.g. McGee et al. (2009)).

It is thus important to study environmental relations in these less dense regions where the bulk of the population live. But, it is difficult to assess the environmental correlations in galaxy groups, as defining a group of galaxies and its member galaxies itself is a hard task. The difficulty arises because groups have fewer members and lower contrast with the background and foreground objects in the sky than clusters, and so group definitions are affected to a larger extent by projection effects ⁴.

With the availability of accurate redshift information from large spectroscopic surveys like 2dFGRS and SDSS, clever algorithms have been developed to define groups in the survey area minimizing the population of interlopers (see e.g. Yang et al. (2005) which uses an iterative halo-based algorithm to define groups). The environment then can be quantified in various different ways, from local density to large scale structures, and which environment matters the most is an open debate (see e.g. Berlind et al. (2005), Tinker et al. (2012)). We have briefly summarized below some of the widely used definitions of environment.

- **Centrals vs satellites:** The most simple definition of environment based on dichotomous classification of galaxies into centrals i.e. galaxies that live near to the center of their group potential and satellites which are all remaining

⁴Galaxies can look close in the sky if they are in the same line of sight from us even if they are well separated in space (different redshift).

galaxies in the group. This definition, although simpler, has been found to be quite useful as it shows very strong correlations with galaxy properties (e.g. [Weinmann et al. \(2006\)](#), [van den Bosch et al. \(2008\)](#)). The central galaxy generally tend to be the most massive galaxy in the group and hence many authors use a criteria based on stellar mass to define the two populations.

- **Local density (Σ):** This is generally quantified by measuring the local surface density of neighbors within some distance of the galaxy. This also shows a good correlation with galaxy properties.
- **Group centric radius:** The measurement of group centric distance normalized by a characteristic radius generally provides a useful measurement of projected environment. Some environmental correlations are observed using this definition (e.g. [George et al. \(2013\)](#)).
- **Group Halo mass:** This is more general, larger scale definition of environment. Group halo mass is observed to correlate strongly with morphological fractions (e.g. [Wilman & Erwin \(2012\)](#)) similar to the morphology-density relation observed in clusters. This suggests that the cluster morphology-density relation might be explained, at least partially, by the already well established relation at low density environments suggesting that the pre-processing contributes significantly.

1.2.2 Galaxy sizes

The size of a galaxy is observed to correlate with its stellar mass such that bigger galaxies contain more stellar material than smaller galaxies (e.g. [Shen et al. \(2003\)](#), [Lange et al. \(2015\)](#)) although there is a large scatter in this relation. This size-mass relation, evolves naturally in hydrodynamical simulations under the assumption that the specific angular momentum is conserved and the fraction of baryons that form stars is similar to that in standard feedback models based on galactic winds. [Dutton et al. \(2007\)](#) claim that the models in which galaxies have ~ 30 per cent lower specific angular momentum than their DM haloes are in good agreement with the local size-mass relation. The existence of a size-mass relation thus provides an important constraint for galaxy formation models.

Quenched galaxies (galaxies where the star-formation has been shut down) are found to be more compact than normal star-forming galaxies ([Williams et al. \(2010\)](#)) suggesting that quenching mechanism affects the overall size of the galaxy

(and thereby its specific angular momentum). Galaxies are found to be slightly larger in field environments compared to dense regions especially for late-type morphologies and low stellar masses ($M_* < \text{few } 10^{10} M_\odot$; [Maltby et al. \(2010\)](#), [Poggianti et al. \(2013\)](#), [Cebrián & Trujillo \(2014\)](#); also see [Kelkar et al. \(2015\)](#) who claim no environmental dependence on the size-mass relation).

1.2.3 Color distribution

The color of the galaxy is a good first order approximation for its current rate of star-formation. Galaxies that are forming new stars have a larger fraction of giant OB stars which are hot, short-lived, blue in color and overwhelm the total galaxy UV or blue luminosity. When the star-formation in galaxies is quenched, these stars die within a few million years leaving behind older stars some of which evolve into red giants. For this reason, star-forming galaxies appear quite blue in color while quenched systems have redder optical colors.

The SDSS dataset has showed that the galaxy colors follow a bimodal distribution formed by blue star-forming galaxies also known as the ‘blue cloud’ and passively evolving red galaxies known as the ‘red sequence’ (e.g. [Strateva et al. \(2001\)](#), [Balogh et al. \(2004b\)](#)). The existence of a local minimum in the color distribution puts limits on the number of transitional galaxies undergoing a transformation from blue star-forming to passively evolving red population.

Using classification of a subsample of galaxies, [Strateva et al. \(2001\)](#) showed that the two peaks of the distribution broadly represent early and late-type morphologies in galaxies confirming the well known color-morphology relation ([Roberts & Haynes \(1994\)](#)). In particular, they found that almost all early type galaxies belong to the red sequence while the late-types have a much broader distribution of colors indicating that the red sequence contains some galaxies with late-type morphology and low star-formation rates and/or highly reddened colors due to dust extinction (see e.g. [Wolf et al. \(2009\)](#) for a discussion about dusty red spirals).

1.2.4 Passive fraction

[Baldry et al. \(2006\)](#) showed that the fraction of red galaxies f_r is a function of stellar mass and environmental density such that a unified relation $f_r = F(\Sigma, M)$ can be defined. [Peng et al. \(2010\)](#) later confirmed this and noted that the red

fraction becomes dominant at progressively lower stellar masses in more dense environments, while almost all the massive galaxies are found to be quenched irrespective of environment. They suggested that the two modes of quenching mechanism — one based on environment called ‘environmental quenching’ and other based on mass called ‘mass quenching’ — operate independently of each other.

The environmental quenching is found to be driven mainly by the satellite population while the passive fraction of central galaxies is observed to be largely independent of the environmental density (e.g. [van den Bosch et al. \(2008\)](#), [Peng et al. \(2012\)](#), [Kovač et al. \(2014\)](#)) although there are indications that some present-day central galaxies may have been satellites in the past and therefore, they could have experienced the environmental effects for some fraction of their lifespan ([Hirschmann et al. \(2014\)](#)). Several authors have argued that the galaxy color is a much better indicator of environmental effects as other indicators such as morphology or concentration show a very weak trend with environment at fixed color (e.g. [Ball et al. \(2008\)](#), [Skibba et al. \(2009\)](#), [Deng & Zou \(2009\)](#)).

1.2.5 SFR-density relation

Although the fraction of red galaxies is seen to be correlated strongly with environment, the mean colors in both the red and the blue sequence are observed to be only weakly dependent on environment (e.g. [Baldry et al. \(2004\)](#), [Wilman et al. \(2010\)](#)) at fixed luminosity. Using SDSS fiber based spectroscopic observations, [Balogh et al. \(2004a\)](#) have also shown that the distribution of $H\alpha$ equivalent width (EW)⁵ in star-forming galaxies is similar in different environments (see figure 1.3) suggesting that the environment does not have a strong effect on the star-formation activity in SF galaxies, even though it is observed to play a role in the quenching of star-formation. These results imply that the environmental quenching mechanisms must act in a quick fashion leaving a low and insignificant fraction of transient galaxies undergoing transformation. This leaves us in a difficult position, as it is hard to understand the physical mechanisms involved in the environmental quenching of these galaxies and to understand the timescales over which they operate.

⁵ $H\alpha$ EW traces SFR per unit luminosity. The detailed account of $H\alpha$ luminosity as a tracer of SFR is given in section 1.3.2.

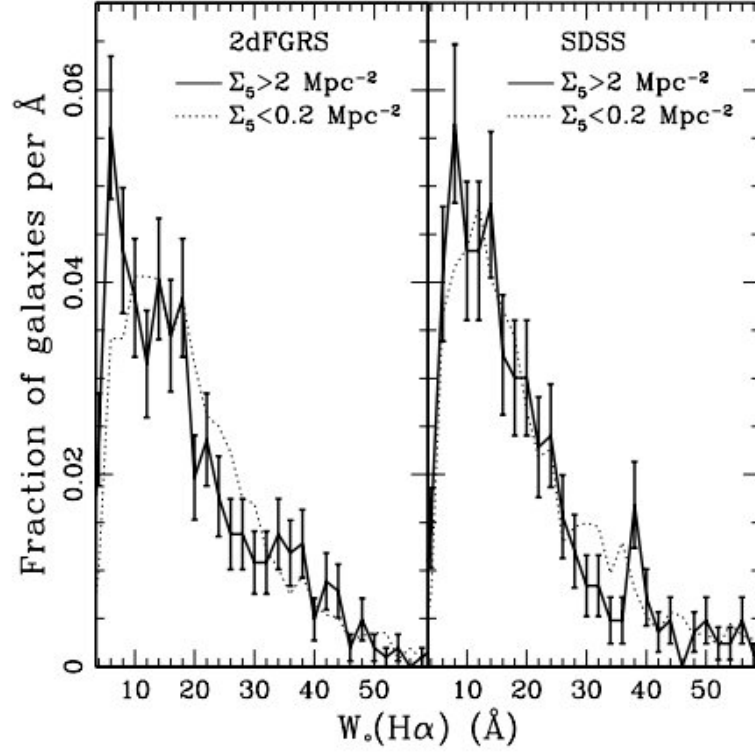


FIGURE 1.3: Showing the distributions of $H\alpha$ equivalent width (EW) for star-forming (SF) galaxies in low density (dotted line) and high density (solid line) regions obtained by [Balogh et al. \(2004a\)](#). $H\alpha$ EW traces star-formation rate per unit luminosity. The similar distribution of $H\alpha$ EW in two environments suggest that the star-formation rate in star-forming galaxies is not affected by galaxy environment.

There is still an ongoing debate about whether the SFR in SF galaxies show any connection with galaxy environment. Some authors find that the distribution of SFR per unit stellar mass known as specific SFR (sSFR) is similar in all environments (e.g. [Wetzel et al. \(2012\)](#), [Lin et al. \(2014\)](#)) with no excess of the 'green valley' galaxies implying a rapid quenching of SF possibly with a delay in the onset of quenching (e.g. [Tal et al. \(2014\)](#)) while some authors argue that the environmental effects are mostly seen in dwarf SF galaxies suggesting that the use of unbiased tracers of SF activity and sensitivity to dwarf galaxies are required to separate the mass-driven effects from the environmental correlations (e.g. [Gavazzi et al. \(2010\)](#), [Cybulski et al. \(2014\)](#)). However, the distribution of sSFR in clusters is observed to be slightly offset towards smaller sSFR values compared to the distribution in field galaxies ([Haines et al. \(2013\)](#); see figure 1.4) indicating that the environment does affect SFR in SF galaxies in very dense regions.

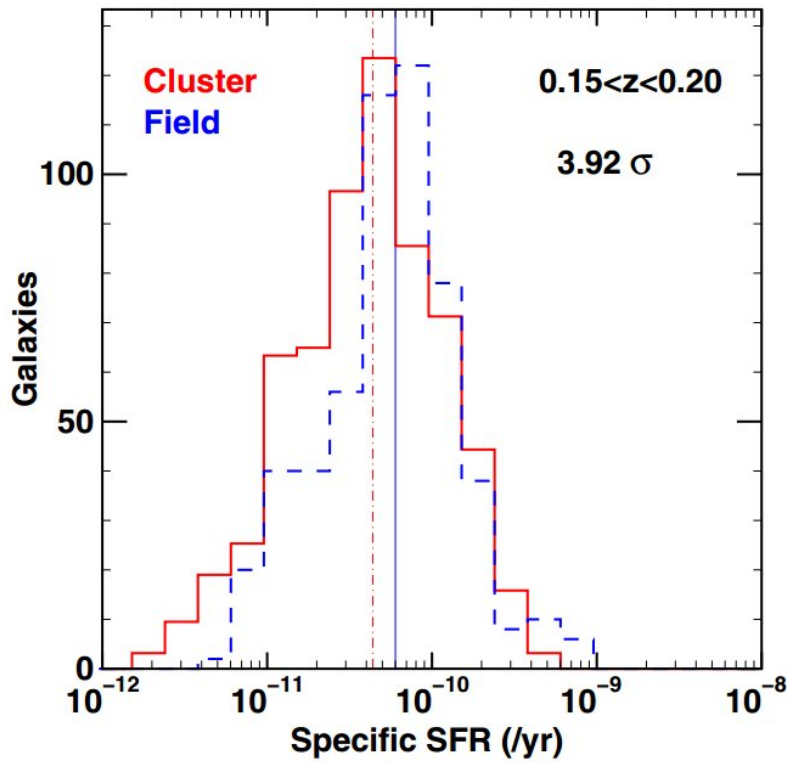


FIGURE 1.4: Comparison of the specific SFR distributions of cluster (red histograms) and field (blue dashed histograms) galaxies for low redshift universe obtained by [Haines et al. \(2013\)](#) using Spitzer/MIPS 24 μm observations. Vertical red/blue dot-dashed lines indicate the mean of each distribution.

1.2.6 Physical mechanisms

Several physical mechanisms have been proposed to explain the observed environmental correlations with various galaxy properties. However the exact mechanisms responsible for these observed correlations is yet unclear. These physical processes can be broadly classified into gas stripping mechanisms, gravitational tidal interactions and minor & major mergers. These processes are discussed briefly below while figure 1.5 summarizes the effects of different processes on galaxy morphology and color.

1. Gas stripping

- **Viscous stripping:** Turbulence and various other transport processes in the intra-cluster medium (ICM) can lead to stripping of gas from a cluster galaxy ([Nulsen \(1982\)](#)).

- **Thermal evaporation:** Gas can evaporate from a galaxy's outer region where the cold galactic gas interacts with a hot ICM (Cowie & McKee (1977)).
- **ICM pressure:** The pressure exerted by the ICM can compress galactic gas triggering star-formation (Dressler & Gunn (1983)). This can lead to faster depletion of star-forming gas in galaxies.
- **Ram pressure stripping:** This more extreme mechanism is proposed especially for dense clusters where the galaxies have large velocities relative to the ICM. This exerts a strong pressure on the gas component, enough to remove even the relatively tightly bound cold gas from the galaxy, which has immediate effects on the star-formation rate (e.g. Gunn & Gott (1972)). Recent simulations suggest that this effect coupled with tidal interactions can remove up to 90 % of gas in the galaxy within ~ 2.4 Gyrs (Vijayaraghavan & Ricker (2015)). More loosely bound cold gas at larger radii is expected to get stripped first (outside-in quenching) in the ram pressure stripping scenario (Boselli et al. (2006)).
- **Strangulation:** The hot halo gas in a galaxy is least tightly bound and hence it gets stripped very easily. The stripping of hot halo gas can exhaust the supply of cold gas to the galaxy and the galaxy would eventually run out of its cold gas and the star-formation ceases due to this. Simulations show that this process takes approximately 3 Gyrs to transform a star-forming galaxy into a quenched one.
- **AGN (quasar) feedback**
Radiation, winds, and jets from active galactic nuclei (AGN) in massive galaxies can interact with their interstellar medium. This can lead to heating or ejection of the galactic gas which in turn can terminate the star formation in the galaxy (e.g. Fabian (2012)).

2. Tidal effects

- **Low speed tidal interactions:** The low speed encounters of galaxies in clusters or groups can tidally disturb their star-forming gas triggering star-formation. This can cause occasional bursts of star-formation which depletes the star-forming gas faster. Also, it can lead to 'tidal stripping' of stars and gas during the interaction of galaxies having unequal mass. These interactions require low speed flybys, and thus happen more often in groups and the outer regions of clusters.

- **High speed tidal interactions (Harassment):** The high speed encounters of galaxies can induce violent disruptions in star-forming and stellar disks in galaxies especially when the two interacting galaxies are of very unequal mass (Moore et al. (1996)).

3. Mergers

- **Major merger:** The merger of similar mass galaxies can violently disrupt the morphologies of two galaxies and induce a burst of star-formation. Eventually the merged system becomes an elliptical via violent relaxation.
- **Minor merger:** The merger of two galaxies of very unequal mass does not lead to a violent phase similar to the major merger. The smaller galaxy smoothly dissolves into the larger system leaving some signatures like a stellar halo or low surface brightness tidal streams, and possibly contributing to the bulge and/or thick disk of the remnant galaxy.

1.3 Resolved properties

The vast amount of data coming from large redshift surveys have enabled us to understand how the global properties of galaxies such as morphology, concentration, color, SFR, etc vary among galaxy populations and how they depend on galaxy's stellar mass and its local and global environment. The effects of environment are particularly hard to quantify as it is difficult to disentangle the effects of secular evolution from the environmental ones. Moreover, many proposed physical mechanisms responsible for environmental interactions, such as gas stripping mechanisms, are expected to be more effective in the outer regions of galaxies where the gas is less tightly bound and could thus leave little impact on its global properties for a long period of time. Thus, to understand the effects of environment it is crucial to obtain resolved observations of galaxies. In this section, we summarize the findings of various resolved studies based on galaxy stellar continuum light and $H\alpha$ emission line observations.

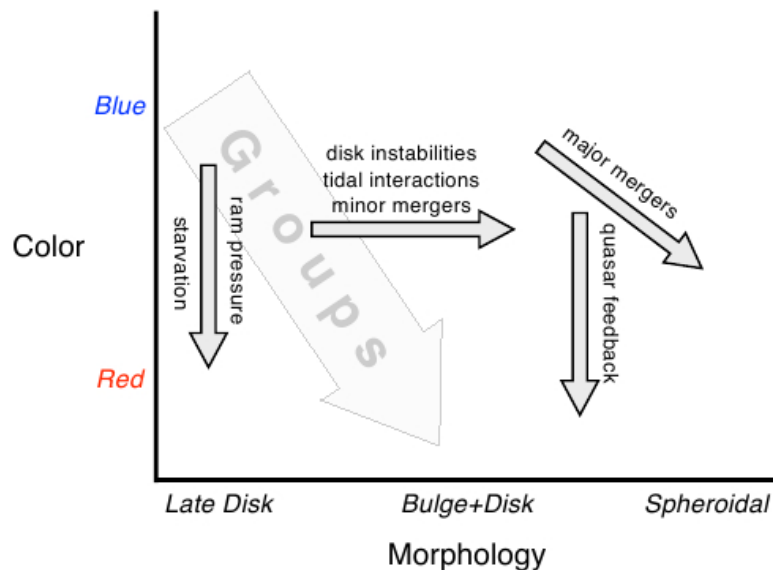


FIGURE 1.5: The cartoon made by [George et al. \(2013\)](#) to explain the effects of physical processes on galaxy morphologies and color. The gas stripping mechanisms like ram pressure stripping, starvation and quasar feedback typically change the galaxy color while having minimal effect on galaxy morphology. Tidal interactions, minor mergers and disk instabilities (which can lead to formation of bars and bulges in galaxies) can change the galaxy morphology very effectively but may have limited effect on galaxy color while major mergers can affect both color and morphology of the galaxy.

1.3.1 Stellar surface brightness profiles

Many disk galaxies show two distinct components in their one-dimensional stellar surface brightness profiles: an inner component — dominated by a spheroidal bulge — having a steeper radial dependence than the outer disk component which follows a somewhat exponentially declining radial surface brightness profile. Apart from this, some disk galaxies show a truncation in their stellar disks at around 3-5 times their exponential scale length ([van der Kruit \(2001\)](#)) beyond which the galaxy light follows a steeper exponential surface brightness profile ([Pohlen et al. \(2004\)](#)) while some disk galaxies show an anti-truncation at larger radii beyond which the galaxy light follows a shallower radial decline ([Erwin et al. \(2005\)](#)). A comprehensive classification scheme for disk galaxies has now emerged based on the break in the stellar surface brightness profiles ([Pohlen & Trujillo \(2006\)](#), [Erwin et al. \(2008a\)](#)) by extending the classification scheme first described by [Freeman](#)

(1970). The disk galaxies can be classified into three main classes (also known as profile types) —

- **Type I (*no break*):** These galaxies have a single-component exponentially declining radial disk surface brightness profile out to very large radii, covering several scale lengths of the disk (e.g. [Bland-Hawthorn et al. \(2005\)](#) found an exponential disk out to a radius covering 10 scale lengths).
- **Type II (*down-bending break; truncation*):** These galaxies have a broken-exponential surface brightness profile such that the outer disk follows a steeper exponential compared to the inner disk profile.
- **Type III (*up-bending break; anti-truncation*):** These galaxies have a broken-exponential surface brightness profile such that the outer disk follows a shallower exponential compared to inner disk profile.

Apart from these three main classes, some galaxies are also observed to have a composite three-component profile such that the galaxy surface brightness has a down-bending profile at intermediate radii which is followed by an un-bending profile in the outermost region. These galaxies are called type II + III ([Erwin et al. \(2008a\)](#)), but they are found to be very rare, forming less than 10 % of disk galaxies.

Different studies have found that the frequency of type II galaxies is somewhat higher than type I and type III galaxies (e.g. [Pohlen & Trujillo \(2006\)](#), [Erwin et al. \(2008a\)](#), [Gutiérrez et al. \(2011\)](#), [Laine et al. \(2014\)](#), etc). Type I and type III profiles are found to be more common in early-type galaxies while type II profiles are common among late-types ([Erwin et al. \(2008b\)](#), [Gutiérrez et al. \(2011\)](#)). These profile types are also found to be correlated with galaxy environment with the frequency of type I S0 galaxies observed to increase in rich clusters like Virgo while type II S0s become almost non-existent (e.g. [Erwin et al. \(2012\)](#)).

A variety of physical mechanisms from major & minor mergers and radial migration to SF thresholds are proposed to explain the origin of individual profile types (e.g. [Schaye \(2004\)](#), [Younger et al. \(2007\)](#), [Roškar et al. \(2008\)](#), [Martínez-Serrano et al. \(2009\)](#), [Comerón et al. \(2012\)](#), [Minchev et al. \(2012\)](#), [Borlaff et al. \(2014\)](#), etc). The recent hydrodynamical simulations performed by [Herpich et al. \(2015\)](#) show that the type of a galaxy's mass density profile depends on the halo spin parameter; haloes with $\lambda > 0.035$ host type II galaxies, haloes with $\lambda < 0.035$

host type III galaxies while haloes with $\lambda \sim 0.035$ host type I systems. This means that type III galaxies have smaller angular momentum than type I or type II galaxies. It is important here to note that the classification of galaxies based on the stellar surface mass density profile is not always consistent with the classification based on a galaxy's surface brightness profile, although [Bakos et al. \(2008\)](#) have showed that both these measurements provide a consistent classification for type III galaxies.

1.3.2 $H\alpha$ surface brightness profiles

The giant O stars formed in the star-forming regions of galaxies can ionize the surrounding atomic gas by UV radiation. The ionized atomic hydrogen atoms recombine with the free electron giving many characteristic emission lines. The strongest emission is seen at 6563 Å which is known as Hydrogen Balmer α or simply $H\alpha$ emission. The strength of the ionization and thereby the strength of the $H\alpha$ emission is proportional to number of O stars formed and thus the rate of star-formation in that region. Since O stars have a short lifespan of few million years, the $H\alpha$ emission in galaxies gives a near-instantaneous measurement of the star-formation rate (see [Kennicutt \(1998\)](#) for a detailed account).

Many surveys have been devised based on observations of the $H\alpha$ emission line for galaxies in the local universe using narrow-band filters (e.g. [Cohen \(1976\)](#), [Kennicutt & Kent \(1983\)](#), [Moss & Whittle \(2000\)](#), [Balogh & Morris \(2000\)](#), etc). Galaxies having compact star-forming disks compared to their stellar disks have been observed in dense cluster environments using resolved observations (e.g. [Koopmann & Kenney \(2004\)](#), [Vogt et al. \(2004\)](#), [Koopmann et al. \(2006\)](#)) suggesting that gas has been stripped from the outer regions of these galaxies. A good candidate for ram pressure stripping of a galaxy in the Virgo cluster ([Boselli et al. \(2006\)](#)) has a broken exponential $H\alpha$ surface brightness profile with an outer exponential much steeper than the inner exponential, similar to the truncation in stellar type II profiles.

[Koopmann & Kenney \(2004\)](#) attempted to classify $H\alpha$ surface brightness profiles of Virgo disk galaxies based on the the ratio of $H\alpha$ flux to R-band flux in the same aperture for the five radial bins viz. $r < 0.1r_{24}$, $0.1r_{24} < r < 0.3r_{24}$, $0.3r_{24} < r < 0.5r_{24}$, $0.5r_{24} < r < 0.7r_{24}$ and $0.7r_{24} < r < 1.0r_{24}$ where r_{24} is the radius at which the R-band flux drops to 24 magnitude arcsec⁻². The flux ratio of $H\alpha$ to R-band, also called the “normalized massive star formation rate” (NMSFR) is proportional

to $\text{EW}[\text{H}\alpha]$. They defined different classes by comparing the values of NMSFR of a galaxy in these 5 radial bins with the median values obtained from normal isolated galaxies.

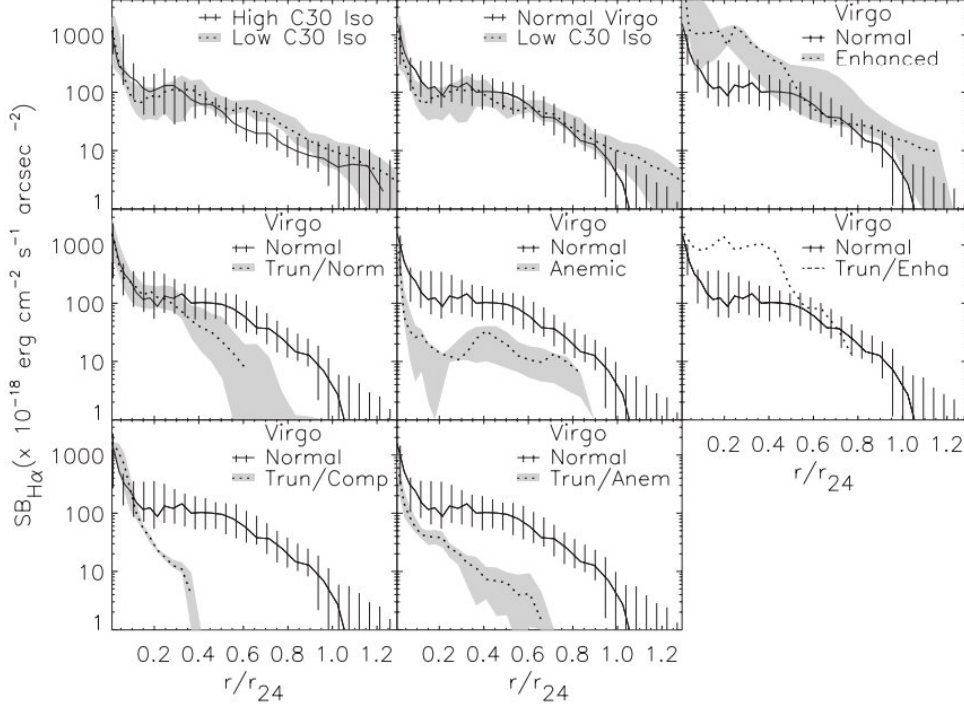


FIGURE 1.6: Median $\text{H}\alpha$ profiles for different classes of Virgo and isolated galaxies obtained by [Koopmann & Kenney \(2004\)](#). *Top left*: Median $\text{H}\alpha$ profiles of isolated galaxies divided into two bins in concentration index. Median $\text{H}\alpha$ profiles are not affected by the differences of concentration index in R-band. *Top middle*: The median Virgo cluster $\text{H}\alpha$ profile is truncated in the outer region compared to median isolated $\text{H}\alpha$ profile. *Other panels*: Median $\text{H}\alpha$ profiles for various other classes of galaxies in the Virgo cluster compared with the same for normal Virgo spiral galaxies. The $\text{H}\alpha$ profiles for these different classes are significantly different than the median $\text{H}\alpha$ profile of normal Virgo galaxies.

The Virgo galaxies are classified into 4 broad classes — *normal*, *anemic*, *enhanced* and *truncated*⁶ — based on this classification scheme. Truncated galaxies are further classified as *truncated-normal*, *truncated-anemic*, *truncated-enhanced* and *truncated-compact* based on the inner $\text{H}\alpha$ profile. They found that the frequency of truncated galaxies (52 %) is much larger in Virgo compared to other classes (normal - 37 %, anemic - 6 %, enhanced - 6 %). Figure 1.6 shows the median profiles of all of these different galaxy classes, along with median profiles of isolated galaxies.

⁶We would like to note that “truncated” galaxies do not always have broken-exponential $\text{H}\alpha$ surface brightness profile as the classification is based on a different criteria.

1.4 Motivation for a narrow-band imaging survey

Galaxies live in different environments; some are isolated and some live in groups and clusters. While galaxy environment has been observed to play a role in shaping various galaxy properties like morphology and color, its influence on the rate of star-formation in the star-forming galaxies is not completely understood in spite of the availability of SFR measurements for vast numbers of galaxies in large spectroscopic surveys like SDSS (see e.g. section 1.2.5).

These SFR measurements, though, have been derived using fiber-based spectroscopic observations which cover just a few arcseconds on the sky and hence a very small central region for galaxies in the local universe. These central measurements, even with sophisticated bayesian techniques used for the correction of aperture effects, may not be very useful in understanding environmental effects on the SF gas in galaxies as many of the proposed physical mechanisms are expected to be more effective in the outer regions of galaxies, producing outside-in quenching (see e.g. section 1.2.6). Hence, one must obtain spatially resolved information, especially of SFR, for a large and diverse sample of galaxies in order to understand the environmental influence on galaxy properties.

Differences in star-formation activity between cluster and field galaxies have been reported in some resolved studies (e.g. [Koopmann & Kenney \(2004\)](#), [Vogt et al. \(2004\)](#), [Haines et al. \(2013\)](#), etc). For example, galaxies in the Virgo cluster are observed to have, on average, 20 % smaller star-forming disks compared to their stellar disks ([Koopmann et al. \(2006\)](#)) which suggests that the star-formation in star-forming galaxies is affected at least in the dense environments. Although these studies have been successful in establishing a relation between the star-formation rate and galaxy environment, they have been focused mainly in very dense cluster environments and completely ignore the bulk of the galaxy population that live in small groups which comprise ~ 60 % of the local volume ([Eke et al. \(2004\)](#)). Moreover, the individual studies are based on just one or at best a few clusters and hence lack the statistical power of large datasets like SDSS for understanding the general galaxy population.

We were thus motivated to undertake a survey of a large number of galaxies in a range of environments aimed at obtaining the spatially resolved star-formation maps which will help in quantifying the environmental effects on star-forming

disks and in identifying the physical mechanisms associated with them. Different observable quantities like UV or far infra-red luminosity, and emission lines such as the Hydrogen Balmer α ($H\alpha$) at λ 6563 Å and the Oxygen II doublet at $\lambda\lambda$ 3726, 3729 Å corrected for dust extinction are known to correlate with the galaxy star-formation rates and hence can be used as a proxy for measuring the SFR in galaxies (see Kennicutt (1998)).

A fairly direct and reliable indicator for the SF has been the $H\alpha$ emission line as it provides near instantaneous measurement of SF. The emission line luminosity can be easily converted into SFR once it is corrected for the galactic dust extinction (see Kennicutt (1998)). To obtain spatially resolved $H\alpha$ maps, one can use either narrow-band imaging or perform spatially resolved spectroscopic observations using either a long slit or an integral field unit (IFU). Since spectroscopy requires a large amount of telescope time compared to imaging observations, narrow-band imaging has been a preferred choice for large surveys, and can provide better spatial resolution and coverage.

One caveat of narrow-band observations is that observations of $H\alpha$ emission can be made for galaxies over only a very narrow range of redshift with a given narrow-band filter, and hence multiple specially designed filters are required to carry out observations over a broader redshift range. Also, the stellar continuum emission of the galaxy at the position of the $H\alpha$ line needs to be estimated and subtracted from the total flux to obtain pure emission line maps. In the past, this has been done using continuum broad band observations (mainly r-band), or using adjacent narrow-bands which gives a better continuum estimation.

The other drawbacks of narrow-band imaging are the contamination of the neighboring emission lines [NII] $\lambda\lambda$ 6548 and 6584 Å, and the possible contribution to the line emission by a central active galactic nucleus (AGN). Since we are more interested in knowing the distribution of star-formation within galaxies than the actual level of star-formation, the NII contamination can be neglected. Nevertheless, an average correction for the contamination of NII emission can be applied to the star-forming galaxies. Galaxies with AGN can be identified using emission line ratios (“BPT diagrams”⁷) if the spectroscopic data are available and such galaxies can then be excluded from the final analysis.

⁷“Baldwin, Phillips and Terlevich” (BPT) diagrams are used to distinguish the star-forming regions in galaxies from AGNs or low-ionization nuclear emission-line regions (LINERs) based on [O III] λ 5007 / $H\beta$, [N II] λ 6583 / $H\alpha$, and [S II] $\lambda\lambda$ 6716, 6731 / $H\alpha$ flux ratios.

As the merits of the narrow-band imaging far outweighs the few caveats (many of which could be either be ignored or corrected), we have undertaken a large narrow-band imaging survey named: “**H**alpha **G**alaxy **G**roups **I**maging **S**urvey” (HAGGIS) to observe galaxies in a range of different environments.

1.5 Thesis overview

Within this thesis, we aim to understand the role of galaxy’s stellar mass and its environment in shaping various galaxy observables. The analysis will be based on a sample of galaxies that live in a moderately dense group environment which is representative of the bulk of the galaxy population in the local universe.

The sample selection and observational details for the HAGGIS resolved $H\alpha$ observations are described in Chapter 2. We have described the data reduction techniques employed for reduction of this dataset in Chapter 3. Chapter 4 describes the techniques used for the generation of surface brightness profiles, the classification scheme based on these profiles and the computation of various derivable properties like galaxy half light size, scale lengths, break radius, integrated fluxes in different regions and for whole galaxy, etc along with the comparison of some of these measurements with similar measurements performed on the SDSS dataset.

The galaxy stellar and $H\alpha$ size-mass relations for different $H\alpha$ and stellar profile types and the comparison of $H\alpha$ sizes of galaxies with their stellar sizes are described in chapter 5. The relation of a galaxy’s global SFR with its stellar mass for the HAGGIS galaxies is shown in Chapter 6. We then describe the correlation between the offset from this SFR-stellar mass relation with the ratio of $H\alpha$ size to stellar continuum size. The frequency of different $H\alpha$ and stellar profile types as a function of stellar mass and group halo mass is then studied in chapter 7. The $H\alpha$ sizes are compared with their stellar sizes separately for central and satellite galaxies in our sample.

Finally we conclude the thesis work in chapter 8 by tying together the key findings of this thesis. We describe the future prospects of the large dataset provided by the HAGGIS survey and its potential contributions in the scientific explorations of other ongoing surveys thereafter. Throughout this thesis, we adopt a cosmology based on WMAP 9 measurements ($H_0 = 69.3 \text{ km Mpc}^{-1} \text{ sec}^{-1}$, $\Omega_\Lambda = 0.714$, $\Omega_m = 0.286$; see [Bennett et al. \(2013\)](#)).

Chapter 2

The HAGGIS survey

2.1 Sample Selection

Surveys based on resolved $H\alpha$ observations have been mainly focused on comparing the spatial distribution of SF in cluster galaxies with that in field galaxies. Thus we wanted to bridge the gap between the two extremes with our HAGGIS survey by observing galaxies living in a wide range of environments spanning low to quite high environmental densities. To select groups for HAGGIS observations, we have used the [Yang et al. \(2007\)](#) group catalog which is based on SDSS DR4 spectroscopic data. They use an iterative halo-based group finder algorithm to identify the groups in the SDSS footprint (see [Yang et al. \(2005\)](#) for details).

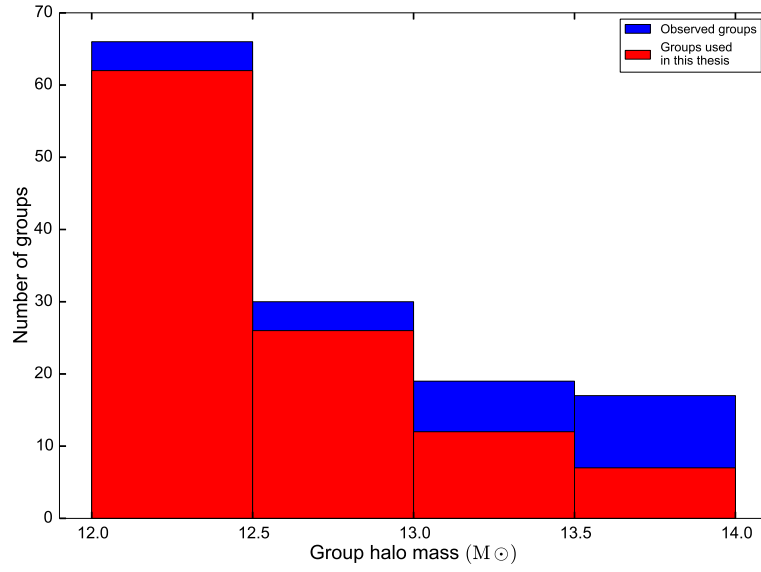
In the first iteration they identify the centers and members of the potential groups using a traditional friends of friends (FOF) algorithm. The remaining unassigned galaxies are considered as tentative centers of additional potential groups. Group halo masses are assigned to each of these potential groups using halo abundance matching techniques in which they match the ranking of the groups based on total stellar mass for all group members with $M_r - 5 \log h \leq 19.5$ with the ranking of halo masses obtained from the dark matter only simulations at fixed number density. Estimates of group size and velocity dispersion are then computed based on these halo masses for each potential group. Group memberships are re-defined based on these measurements. The halo masses are then re-estimated using abundance matching. The procedure continues in this loop until the group definitions converge.

With this procedure, halo masses are assigned even to single isolated galaxies. In this way, the [Yang et al. \(2007\)](#) catalog exhibits a wider dynamic range in halo mass compared to dynamical mass estimates. The inclusion of isolated field galaxies in their catalog was especially useful for the HAGGIS sample selection, as with the isolated galaxies we can disentangle the effects of secular processes on the distribution of star-formation from the environmental ones given that the isolated galaxies are generally considered to have undergone fewer environmental interactions compared to the galaxies in groups or clusters.

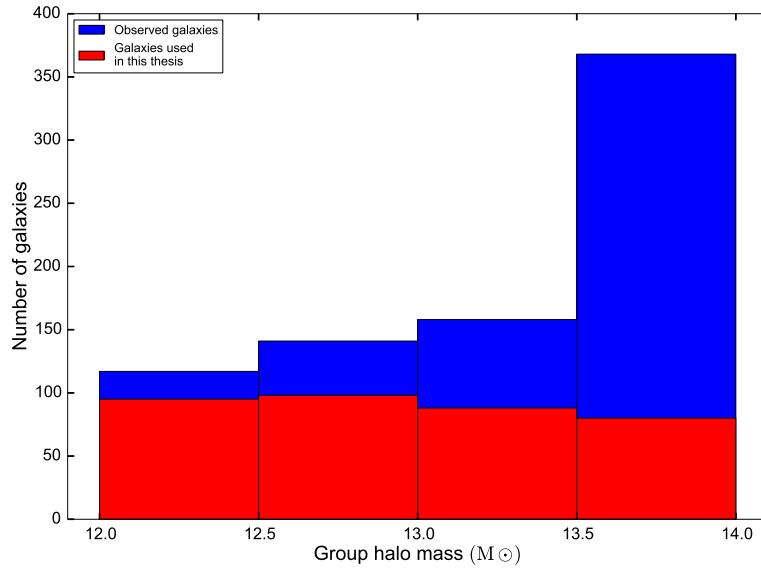
We have selected 100 galaxy groups from the [Yang et al. \(2007\)](#) catalog in the range of $M_{\text{halo}} = 10^{12} - 10^{14} M_{\odot}$ for HAGGIS observations. This range in M_{halo} corresponds to Milky-way like haloes at the lower end to poor clusters at the upper end. This will allow us to understand the environmental trends from field to cluster-like populations. We have deliberately avoided clusters as they cover a much larger area on the sky compared to the field of view of the wide field cameras available. Their high velocity dispersions also shift the $\text{H}\alpha$ wavelength out of the transmission band of the selected narrow-band filters for some of the member galaxies. We chose wide field cameras mounted on 2 m class telescopes — the Wide Field Imager (WFI) on the 2.2 m MPG/ESO telescope at La Silla, Chile and the Wide Field Camera (WFC) on the Isaac Newton Telescope (INT) at La Palma, Spain — which offer multiple narrow-band filters.

For the selection of target groups, we have first identified the groups that have a suitable redshift to observe the red-shifted $\text{H}\alpha$ emission using the available narrow-band filters at these facilities and are visible from the selected observatories during the observing runs. Then the target groups for the observations are selected semi-randomly. Massive groups typically have large number of galaxies compared to low mass groups. Hence, the selection algorithm is optimized to obtain a balance between the number of target groups and number of target galaxies at all group halo masses such that both represent a statistically representable sample. This selection method gives the distribution seen in [fig. 2.1](#) i.e. decrease in number of groups but increase in number of galaxies with halo mass. In addition to the targeted groups, we have found 20 serendipitous groups (typically at low group halo mass). The results in this thesis are obtained by analyzing the sub-sample of 390 HAGGIS galaxies in 107 groups (including the 20 serendipitous low mass groups).

Table [2.1](#) list basic properties including group and galaxy identification number, positional coordinate and redshift along with some derived quantities like stellar



(a)



(b)

FIGURE 2.1: (a) Shows the distribution in halo mass of observed groups in HAGGIS (blue) and the distribution of groups used in this thesis (red) with halo mass. (b) Shows the distribution of observed galaxies in HAGGIS (blue) and the distribution of galaxies used in this thesis (red).

and halo mass of the observed galaxies. The details of each column of the tables are as follows -

- **Group id** : Group id from the [Yang et al. \(2007\)](#) catalog based on SDSS DR7 data.
- **Gal id** : Galaxy id assigned for the observed galaxy in the HAGGIS survey.

TABLE 2.1: This is a sample table containing the SDSS derived parameters. The full table containing all the galaxies can be found in Appendix (B).

Group id (1)	Galaxy id (2)	NYU VAGC (3)	Galaxy RA (4)	Galaxy DEC (5)	Group RA (6)	Group DEC (7)	SDSS redshift (8)	$\log_{10}(M_*)$ (M_\odot) (9)	$\log_{10}(M_{\text{halo}})$ (M_\odot) (10)	Central/ Satellite (11)
13	13-1	1734937	13.84570	-1.21122	14.22688	-0.66597	0.0418	10.47	14.52	2
13	13-2	1734938	13.86252	-1.22312	14.22688	-0.66597	0.0435	9.77	14.52	2
13	13-3	1734939	13.87968	-1.22345	14.22688	-0.66597	0.0430	10.25	14.52	2
13	13-4	1734940	13.88462	-1.21108	14.22688	-0.66597	0.0459	10.27	14.52	2
13	13-8	1734957	13.93995	-1.05483	14.22688	-0.66597	0.0440	10.02	14.52	2
13	13-9	1734958	13.94026	-1.08428	14.22688	-0.66597	0.0423	9.88	14.52	2
13	13-11	1734960	13.95665	-1.08169	14.22688	-0.66597	0.0446	10.56	14.52	2
13	13-12	1734961	13.96307	-1.16473	14.22688	-0.66597	0.0477	11.14	14.52	2
13	13-13	1734963	13.97218	-1.11654	14.22688	-0.66597	0.0455	9.82	14.52	2
13	13-14	1734965	13.99140	-1.23990	14.22688	-0.66597	0.0446	10.22	14.52	2
13	13-15	1734966	13.99661	-1.16351	14.22688	-0.66597	0.0459	10.11	14.52	2
13	13-16	1734968	14.01688	-1.21748	14.22688	-0.66597	0.0437	9.70	14.52	2
13	13-17	1734969	14.02069	-1.13594	14.22688	-0.66597	0.0450	10.07	14.52	2
13	13-18	1734970	14.02506	-1.05712	14.22688	-0.66597	0.0432	10.29	14.52	2
13	13-19	1734978	14.05973	-1.14435	14.22688	-0.66597	0.0450	10.41	14.52	2
13	13-20	1734990	14.12800	-1.17288	14.22688	-0.66597	0.0422	10.71	14.52	2

- **NYU VAGC** : Galaxy id from New York University Value-Added Galaxy Catalog (NYU VAGC) catalog based on SDSS DR7 data. This can be used in cross-matching HAGGIS galaxies with SDSS and other surveys.
- **Galaxy RA, Galaxy DEC** : Positional coordinates of the galaxy in world coordinate (WCS) system in decimal degrees (J2000).
- **Group RA, Group DEC** : Weighted average of the positional coordinates in world coordinate (WCS) system in decimal degrees (J2000) of all galaxies in the respective groups derived for this work.
- **SDSS redshift** : SDSS spectroscopic redshift of the galaxy.
- **$\log_{10}(M_*)$** : The logarithmic stellar mass of the galaxy in units of M_\odot computed using *i*-band luminosity derived from SDSS photometric observations and *i*-band mass to light ratio computed from SDSS derived *g-i* color based on the prescriptions given in [Zibetti et al. \(2009\)](#) which assume a Chabrier IMF.
- **$\log_{10}(M_{\text{halo}})$** : The estimated logarithmic halo mass of the group in units of M_\odot described in [Yang et al. \(2007\)](#). It is derived as described in section 2.1.
- **Central/Satellite** : The classification of a galaxy into central (1) or satellite (2) based on a ranking in stellar mass.

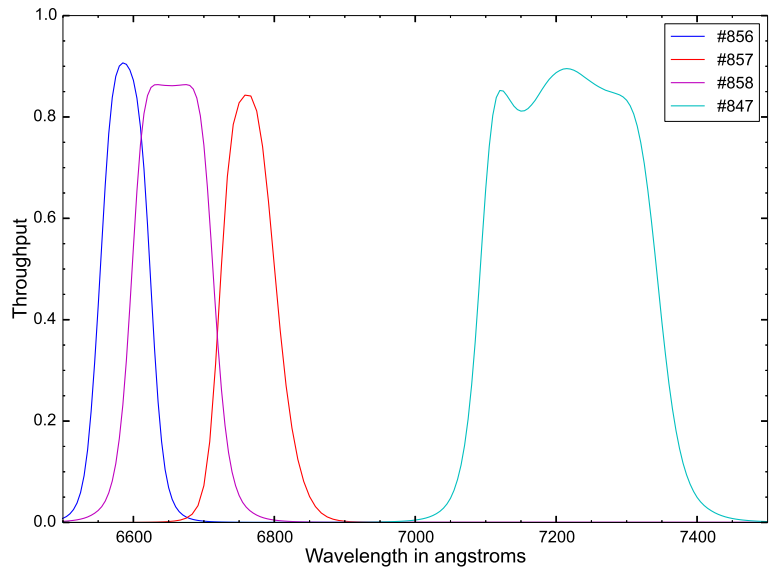
2.2 Observations

The observations were carried out using the Wide Field Camera (WFC) on the Isaac Newton Telescope (INT) at La Palma, Spain during 15-17 December 2011 and the Wide Field Imager (WFI) on the 2.2 m MPG/ESO telescope at La Silla, Chile from 26 January 2012 to 2 February 2012. These wide field imagers (WFI & WFC) give $\sim 30'$ of field of view which allowed us to target whole groups (or sometimes even 2-3 adjacent groups) with one pointing with exception of very massive groups which were targeted with a mosaic of pointings.

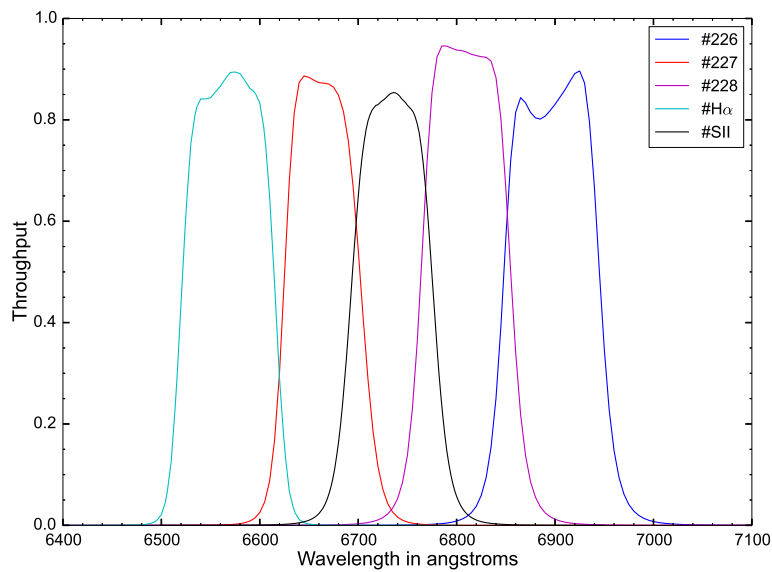
We have used pairs of narrow-band filters for each group such that the redshifted $H\alpha$ emission (or absorption) for each galaxy in the group would fall in one of the filters (ON-band) while the other filter, close in wavelength, would then be used to estimate the continuum underlying the $H\alpha$ emission (OFF-band). The filters for the continuum observations are chosen to avoid contamination from any prominent emission lines. The filter response functions of the narrow-band filters used for these observations are given in fig. 2.2.

Each group is observed for 3×5 minutes of dithered exposures in each filter in order to reach the desired S/N in $H\alpha$ surface brightness. Calibration frames were also taken each night. This includes bias, dark and flat fields. For flat-fielding, both dome flat frames and sky flat frames are observed to characterize both small and large scale variations.

We were allotted 7 nights to observe with the Wide Field Imager (WFI) on the ESO/MPG 2.2 m telescope and 3 nights to observe with the Wide Field Camera (WFC) on the Isaac Newton Telescope (INT). About ten groups were observed per night on average, so that we could reach the total sample of ~ 100 groups.



(a)



(b)

FIGURE 2.2: Filter response functions of (a) the Wide Field Image (WFI) on the MPG/ESO 2.2 m telescope and (b) the Wide Field Camera (WFC) on the Isaac Newton Telescope (INT) used for the HAGGIS observations.

Chapter 3

Data reduction pipeline

The wide field cameras used for the HAGGIS observations are made up of multiple charged coupled device (CCD) chips; the Wide Field Imager (WFI) is a mosaic of 8 chips while the Wide Field Camera (WFC) is made up of 4 chips (see figure 3.1). The observation strategy, described in the last chapter, yielded 3 ON-band and 3 OFF-band frames per pointing, generating 48 science frames per group for WFI and 24 science frames per group for WFC.

Together with calibration frames, this means ~ 5000 raw files for ~ 75 groups observed with the WFI instrument and ~ 1000 raw files for ~ 25 groups observed with the WFC instrument. Hence, together with automation, a good quality control at each step of the data reduction was a pre-requisite in order to maintain the quality of final products. The data reduction pipeline for the 7 nights of WFI data was developed by myself and is described in this chapter while the same for WFC was developed by our collaborator Leonel Gutiérrez in Mexico and is also briefly discussed here. The flow chart (fig. 3.2) illustrates the huge task of reducing this massive amount of data.

3.1 HAGGIS data processing

3.1.1 Basic processing

We used the ASTROWISE environment (Valentijn et al. (2007)) to do the basic processing of Wide Field Imager (WFI) data while the *Image reduction and analysis facility*, commonly known as *IRAF* (see Tody (1986) and Tody (1993))

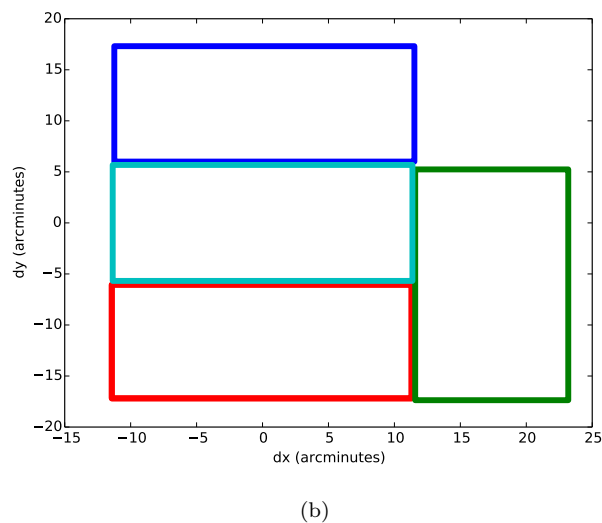
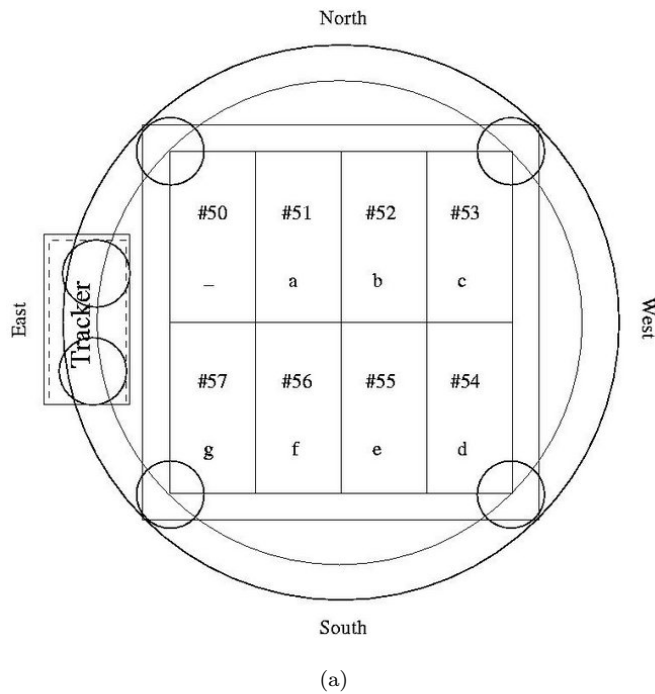


FIGURE 3.1: The layouts for (a) the 8 chips of the Wide Field Imager and (b) the 4 chips of the Wide Field Camera.

and some other tools were used for the Wide Field Camera (WFC) data. The ASTROWISE environment is a database management system developed for the processing of large amounts of astronomical data and its algorithms are especially fine-tuned for wide-field cameras such as WFI. The use of the ASTROWISE environment and its well established recipes made the basic processing quite easy and quick, given the level of automation. The environment also allowed us to process the data using a local computer cluster, reducing the processing time considerably.

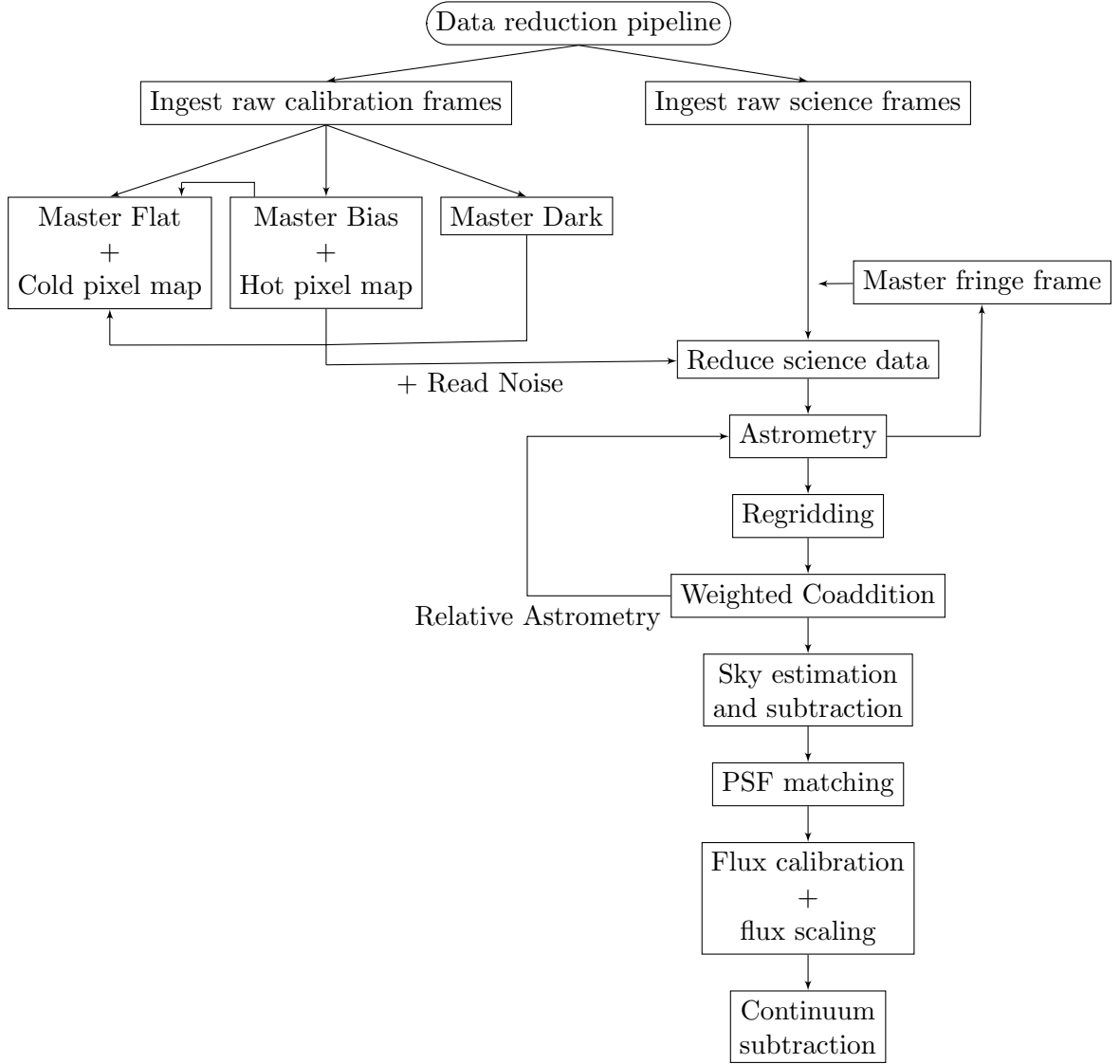


FIGURE 3.2: Flow chart showing the steps taken in data reduction.

The raw data were first ingested into the ASTROWISE data base. ASTROWISE generates meta-data for each raw frame, saving information about the instrument, filter, observational conditions, etc. This meta-data was then passed to all the intermediate and final frames produced at different stages of data reduction, which makes it easy to back-trace the files that went into the process and to correct the process at any stage if required. Unfortunately, data from Wide Field Camera (WFC) mounted on the INT is not recognized by the ASTROWISE environment and hence Leonel Gutiérrez decided to use IRAF routines for their reduction. The steps taken in the data reduction were identical except for some small details which are explained below at each step.

The first steps in the basic data reduction were to generate the master flat, master

dark and master bias frames. The dome flat frames and sky flat frames were debiased and combined together to generate a master flat frame whenever they were available and were clean, without any artifacts. Cold pixels, i.e. pixels which record small number of counts — generally unrelated to the amount of signal that falls onto it, were identified for each chip using flat frames.

Hot pixels, which similarly record values close to the saturation level irrespective of the amount of signal available at their position, were identified using bias frames. Since bad pixels affect all the neighboring pixels in the readout column, the whole column was flagged whenever there is a cold or hot pixel in the readout column. Maps of cold and hot pixels were generated, taking this into consideration. Raw science frames were also used to detect saturated pixels, cosmic rays and satellite tracks. A combined bad pixel map was generated using all of these individual maps during the science reduction pipeline.

After generating basic calibration frames, the bias was subtracted from raw science frames and then the frames were flat-fielded. Error maps were generated during the reduction pipeline using debiased raw science frames considering the contributions of photon and read noise. They were then converted into weight maps. Separate weight maps were generated using the master flat-frame and combined bad pixel maps. These two weight maps were then combined forming a master weight map, with all bad pixels given zero weight. These weight maps were then propagated through ASTROWISE in all subsequent steps and were also applied when coadding individual frames.

Fringing was observed in a subset of filters viz. #847 for WFI, and #226 and #228 for WFC (see fig. 3.3) and was subsequently reduced by using a master fringe frame which was generated per night using all the reduced science frames of that filter on that night. The fringe pattern was quite stable and was largely removed using this method.

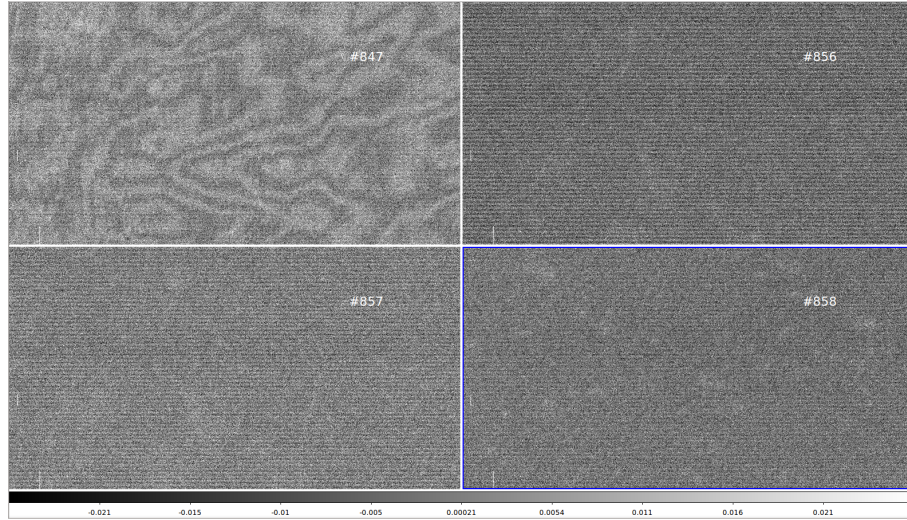


FIGURE 3.3: The fringe pattern obtained for observations with different narrow-band filters using the WFI camera (the filter numbers are labelled on each panel). Fringing was largely absent except for one WFI filter — #847.

3.1.2 Astrometry

After the basic reduction, the six dithered exposures per pointing (three in each filter) were astrometrically calibrated using the SDSS DR5 catalog as a reference (see upper panel of fig. 3.4). The astrometric calibration is performed in ASTROWISE using a set of LDAC routines (see <ftp://ftp.strw.leidenuniv.nl/pub/ldac/software/pipeline.pdf> for details) which compare the image pixel coordinates of various stars in the source catalog obtained from the observed images to the world coordinate system (WCS) coordinates of the same stars in the reference catalog to derive an astrometric calibration. This default astrometric calibration routine in ASTROWISE provides an astrometric accuracy of about 0.1".

Since we wanted to subtract the OFF band (narrow-band continuum) images from the ON band images at the final step, we needed a better relative astrometric accuracy than provided by the default ASTROWISE recipe. Hence, we decided to do a relative astrometric calibration of all the reduced frames using a reference catalog generated from the coadded OFF band frames. The coaddition of OFF band frames was done using SWarp (Bertin et al. (2002)).

SEXTRACTOR (Bertin & Arnouts (1996)) was then applied to the coadded image to generate a source catalog. SEXTRACTOR gives the centroid position of each detected object in both pixel coordinates and the world coordinate system (wcs) coordinates and hence it can be used as a reference catalog for the astrometric calibration of other frames with a similar field of view. SEXTRACTOR generates

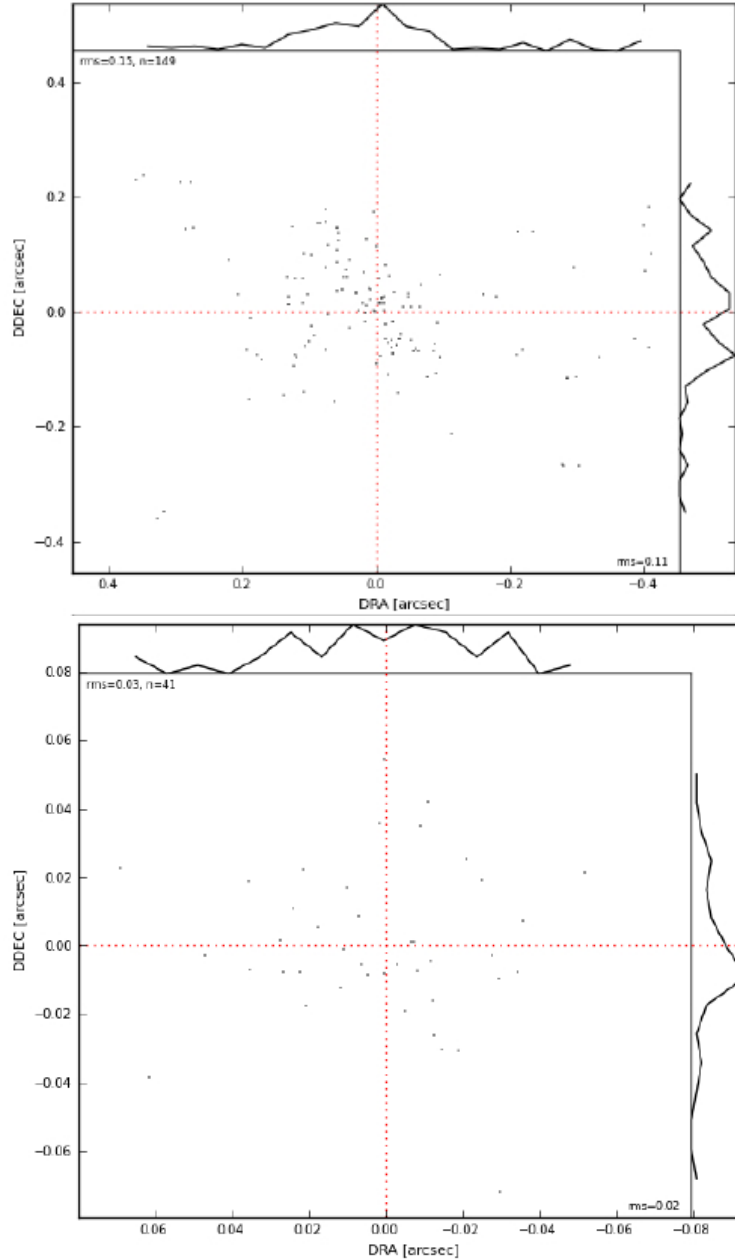


FIGURE 3.4: Example plot showing the accuracy of astrometric calibration. Upper panels show the astrometric accuracy obtained for WFI galaxies using SDSS DR5 data as a reference catalog while the lower panels show the same after relative astrometry was performed using a few selected stars. An astrometric accuracy of at least a tenth of a pixel was achieved.

a parameter called `class_star` which is useful in separating the star-like sources from extended galaxy-like objects. Also, it generates flags for each object designed to detect cases of artifacts, blended sources, saturated pixels, incomplete data, etc.

These flags are used along with a threshold in `class_star` to extract star-like unsaturated sources for each chip. These catalogs were then ingested into ASTROWISE and each reduced frame was again astrometrically calibrated this time using these

catalogs as reference. This step gives an astrometric accuracy of a tenth of a pixel or better across the full frame (see lower panel of fig. 3.4). All the frames were visually inspected for any errors in astrometric calibration and some occasional failures (mainly arising due to fewer number of stars detected in the observed images) were manually improved by increasing the number of sources in the reference catalog ingested in ASTROWISE or by adjusting some of the constraints in generating SEXTRACTOR catalogs and/or in the extraction of star-like sources from them.

3.1.3 Regridding

The wide field images generally have a large and complex distortion pattern due to a large field of view and hence they need to be corrected for distortion. The astrometric solution derived in ASTROWISE provides distortion parameters in the header file which can be used to correct it. Effectively this means regridding on a Cartesian, regular pixel grid. This is done using SWarp in ASTROWISE. SWarp uses an interpolation techniques to perform the regridding.

The default interpolation method is LANCZOS interpolation which uses a large interpolation kernel, helping to reduce any artifacts that arise in the interpolation compared to simpler interpolation techniques like bilinear interpolation. But the LANCZOS interpolation gets problematic if there are large numbers of bad pixels as in the case of WFI chips. This is because all the neighboring pixels within the interpolated region around the bad pixel get flagged as bad in the regridded weight image (see figure 3.5). This results in a significant data loss, especially where a target galaxy lies near a bad column. Thus, we decided to use a simpler bilinear interpolation method instead of the default LANCZOS interpolation.

The disadvantage of bilinear interpolation is that it creates some artifacts. The most prominent artifact we have noticed was the Moiré pattern, as shown in fig. 3.6(a). To investigate the pattern, we generated 10 X 10 pixel median-smoothed background images and were astonished to see that the background was quite smooth and the pattern did not exist in the background image at all (fig 3.6(b)). Instead, we recovered the pattern completely when we examined the RMS background for the same image. The amplitude of the pattern was about 1 or 2 counts above the background level. In other words, the observed pattern was entirely in the noise, not in the background level. We decided to oversample at the interpolation step to reduce this Moiré pattern. The oversampling has effectively reduced

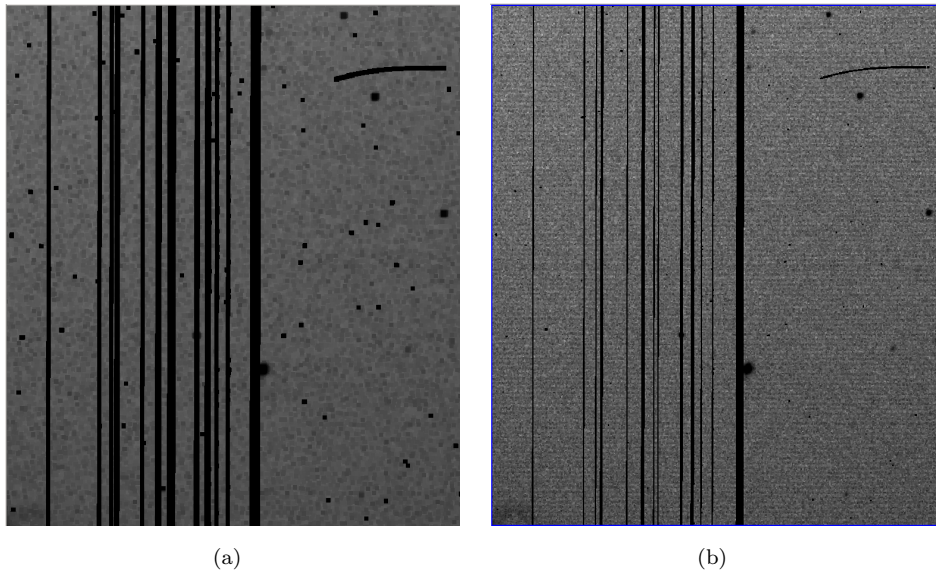


FIGURE 3.5: Weight maps in (a) LANCZOS interpolation and (b) bilinear interpolation. More pixels are flagged as bad using LANCZOS interpolation.

the amplitude of the pattern to about a tenth of a count (see fig. 3.6(c)), sufficient for our scientific goals.

After regridding the science frames, the three dithered exposures in each band need to be aligned to each other before coaddition. This was done using *wscut* - a utility developed by Johannes Koppenhöfer. *wscut* aligns the frames using the world coordinate system (wcs) information stored in the header of each frame that was obtained from astrometric calibration and then the frames are padded with zeros where there was no data. Similarly, the weight frames were also adjusted.

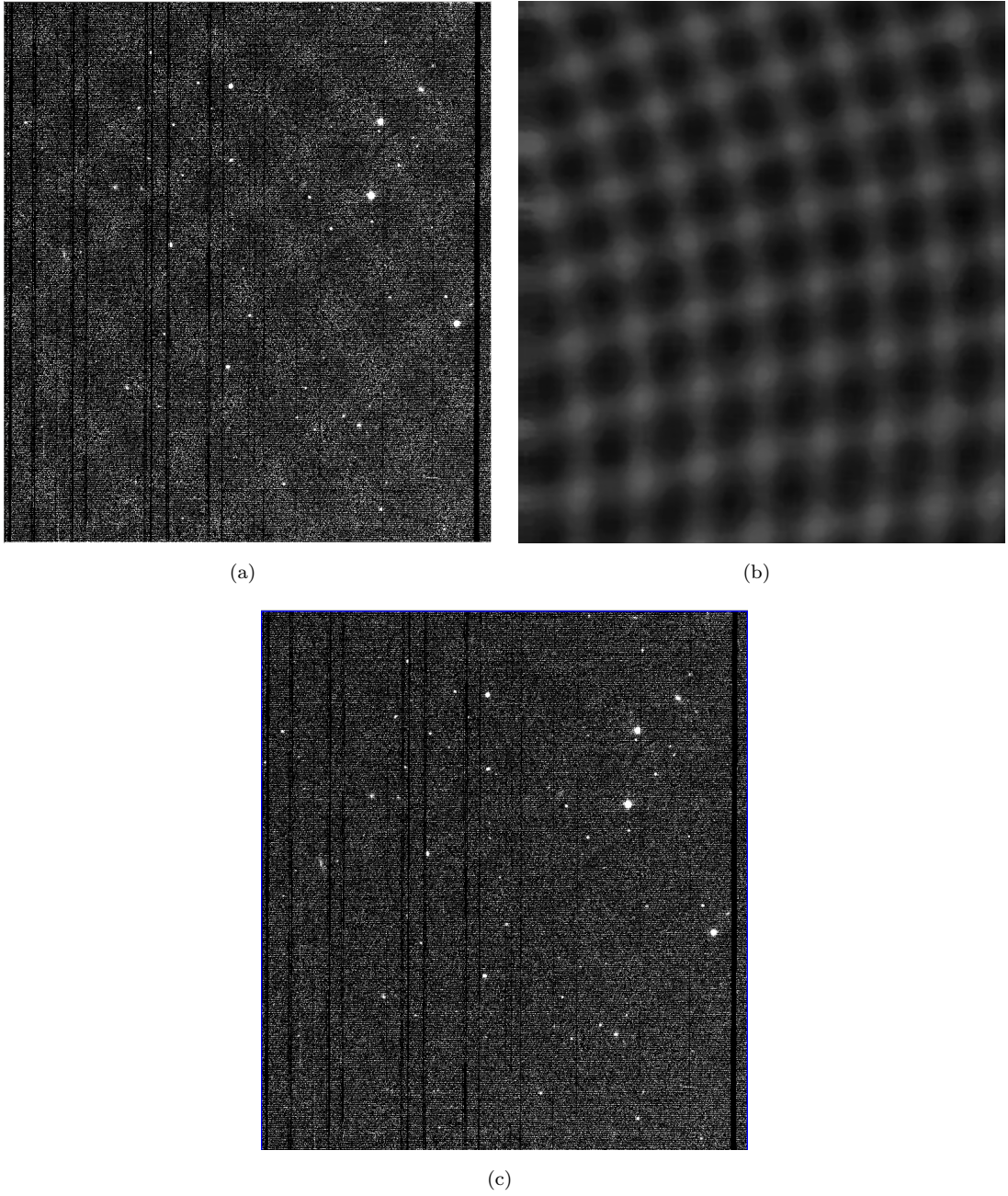


FIGURE 3.6: (a) Moiré pattern observed after bilinear interpolation. (b) The RMS background map obtained for the image. It completely recovers the Moiré pattern observed in the image. (c) Shows that the Moiré is largely reduced when oversampling was performed during the interpolation.

3.1.4 Sky subtraction

The sky background characterization for wide field images is a difficult and time consuming job. But we wanted to do this as accurately as possible since we hoped to detect $H\alpha$ emission down to very faint levels. To achieve this, all the objects need to be masked before estimating the sky background. In order to detect faint

objects, we coadded the wcs aligned, OFF band, regridded images using SWarp and a source catalog was generated using SEXTRACTOR. The detection threshold of SEXTRACTOR was kept very low at $2.5\text{-}\sigma$ above the noise level to detect faint sources in the images.

A SAOimage DS9 region file was then generated for each image using this catalog. These regions were then over-plotted on the coadded images using ds9 to inspect and edit them visually. The wide field images show large reflection images surrounding bright stars which have different patterns according to the telescope and filter combination. Since SEXTRACTOR is not developed to detect these artifacts, it generally assigns multiple sources to these patterns which is not ideal for masking the entire pattern. The visual analysis was hence very crucial to determine the masks for these artifacts. Moreover, since the shape and position of the artifact changes slightly with the filter combination, the regions were adjusted to encompass the artifacts on both ON and OFF band images.

The final set of region files were then fed to the IRAF task *makemask* written by Peter Erwin which uses these to generate a mask image. Pixels inside each region were assigned a value of 0 and all the remaining pixels were assigned a value of 1. All the 6 individual wcs-aligned frames (3 for each filter) were then multiplied by the mask image to generate the input files for the sky estimation routine.

Sky estimation was performed on these masked images using *getsky* (see fig. 3.7) — a tool developed by Johannes Koppenhöfer (for details visit <http://www.usm.uni-muenchen.de/people/arri/mupipe/>). It fits the unmasked region of the image with a two dimensional polynomial of specified degree. We found that a 3rd order polynomial gave good estimate of the sky background with small residuals for WFI images. This fitted sky was then subtracted from the respective science exposures. The sky-subtracted exposures for each filter were then coadded once more using SWarp.

3.1.5 PSF matching

The point spread function (PSF) for an optical instrument is the measure of how the light from a point source is distributed on the detector. The PSF for a diffraction-limited astronomical telescope is mainly defined by the atmospheric conditions and thus it varies with time with changes in atmospheric conditions. In addition, it can differ slightly for different instrumental setups. Since our observations were separated in time and were taken with two different narrow-band

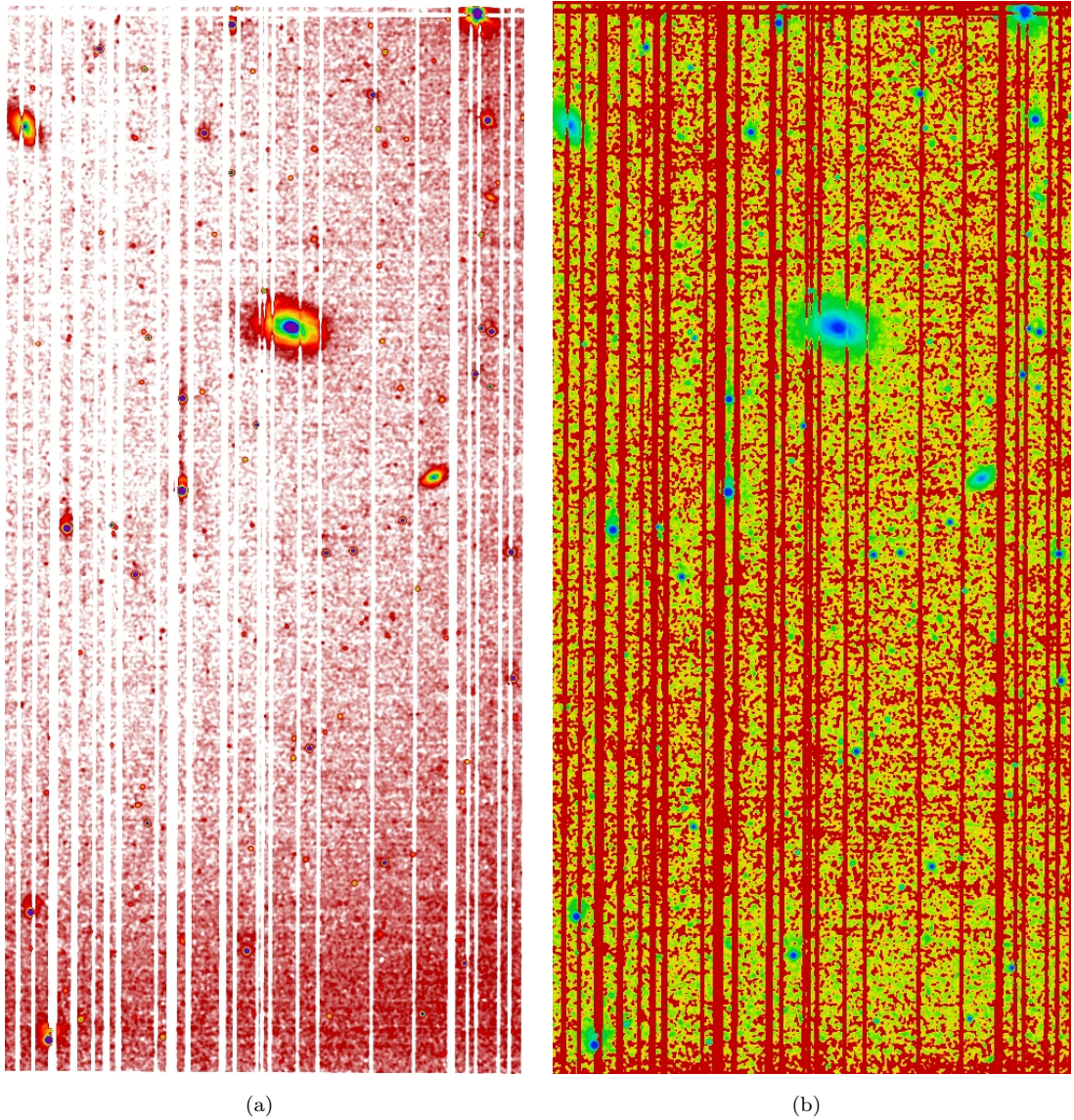


FIGURE 3.7: Shows an example of sky subtraction for a WFI image. (a) Shows a median smoothed image before the sky subtraction and (b) the same image after the sky subtraction. The sky gradient is reduced considerably.

filters, we can clearly see differences in the PSFs in our images. Also, the wide field images show some spatial variations in the shape of the PSF, which is also a function of instrumental setup. The differences in size and shape of the PSF between the two narrow-band images can create strong residuals in the difference image.

Since we need to subtract the OFF-band image from the ON-band as accurately as possible to obtain the H α emission line maps, we needed to match the PSFs of the two narrow-band images. We used specialized tools developed by Arno Riffeser and Johannes Koppenhöfer called *skycalc*, *diffima*, *select_stars* and *convolve_simple*

to perform this task as accurately as possible. Information about these routines can be found at <http://www.usm.uni-muenchen.de/people/arri/mupipe/>.

A difference imaging technique is used by *diffima* and *skycalc* to generate a convolution kernel using some selected stars for the two images. The difference image formed from any pair of images whose flux can be expressed as $A(x,y)$ and $B(x,y)$ is given by

$$d(x,y) = A(x,y) - k(x,y) * B(x,y) - s(x,y) \quad (3.1)$$

where $d(x,y)$ is the flux level in the difference image, $k(x,y)$ is the convolution kernel which is to be obtained by solving the equation and $s(x,y)$ is the differential sky background. Since we have subtracted the background in the two images in the previous steps as accurately as possible, we can drop the $s(x,y)$ term from the equation during the computation of the kernel.

The convolution kernel $k(x,y)$ can then be obtained by solving the simplified equation and minimizing $d^2(x,y)$. The kernel thus obtained will describe the variation of the PSF plus a photometric scaling of the two images. Since the observations of OFF and ON band images were close in time, we expect that the atmospheric conditions have little impact on the photometric scale factor. The scale factor depends instead upon the differences in the full width at half maximum (FWHM) band-width values of the two narrow-band filters used for the observations, as well as on the shape and level of the object spectra at the position of these filters (see fig. 3.8). Hence, in order to find the convolution kernel which simply corrects the difference in PSF of the two images, a photometric scale factor has to be applied to each individual object.

Since *diffima* was developed for the purpose of detecting transient objects in observations well separated in time but taken with the same instrumental setup, it only uses a single scale factor during the computation of kernel. We had selected some stars on our image using the *select_stars* tool which uses a SEXTRACTOR generated catalog to select good stars in order to obtain the convolution kernel. The criteria used for selection was to have the *class_star* parameter greater than 0.9, the total flux in the star between 0.6 to 0.95 times the saturation level and no bad pixel in the 7 pixel x 7 pixel matrix (i.e. the size of the kernel) around the star. Around 50 stars were selected for each chip in order to get the desired accuracy in determining the convolution kernel. To obtain a scale factor for each

star, we used *skycalc* which uses a difference imaging technique to obtain the scale factor for each selected star.

The region around each star is scaled appropriately in the image and a mask image was generated, with the unscaled pixels set to 0. *diffima* reads this mask and uses only unmasked regions for the computation of the kernel. In some cases the x-component of the PSF in one band was of poorer resolution while the y-component had a better resolution in the other band. This created problems for the difference imaging tool. For this reason, we degraded one of the coadded images by convolving a Gaussian with small full width half maximum (FWHM) of 1 pixel using the *convolve_simple* tool. This degraded image was then used as a reference image for *diffima* and the convolution kernel was obtained for the differentially scaled target coadded image. The PSF of the target image was then matched with that of reference image using the *convolve_simple* routine.

3.1.6 Flux Scaling and flux calibration

An appropriate scaling of the OFF band galaxy image was the next crucial step. Our goal was an accurate continuum subtraction to generate pure H α images from our narrow-band observations. Observations of standard stars are generally used for the flux calibration of narrow-band images. But the flux calibration of the OFF band was not sufficient to accurately estimate the continuum level at the wavelength of the ON band: One needs to scale the OFF band image with some spectrally dependent scaling factor before subtracting it from the ON band image. This scaling factor depends upon the differences in filter FWHM and transmission as well as the shape and level of the object spectrum at the wavelength of these narrow-bands as discussed in previous section (see for example fig. 3.8).

The scaling of the OFF band image needs to be done for each galaxy separately to account for these spectral differences. For this reason, we decided to use flux calibrated SDSS fiber spectra, available for almost all galaxies in the HAGGIS sample, to perform the flux calibration and to compute the scaling factors for our narrow-band images.

The SDSS spectra were retrieved for each galaxy in our sample using a Python routine called *fetchsdss* developed by Peter Erwin (for more details see <http://www.mpe.mpg.de/~erwin/code/>). The spectra were then convolved with the filter response functions of both ON and OFF band filters, deriving the flux in

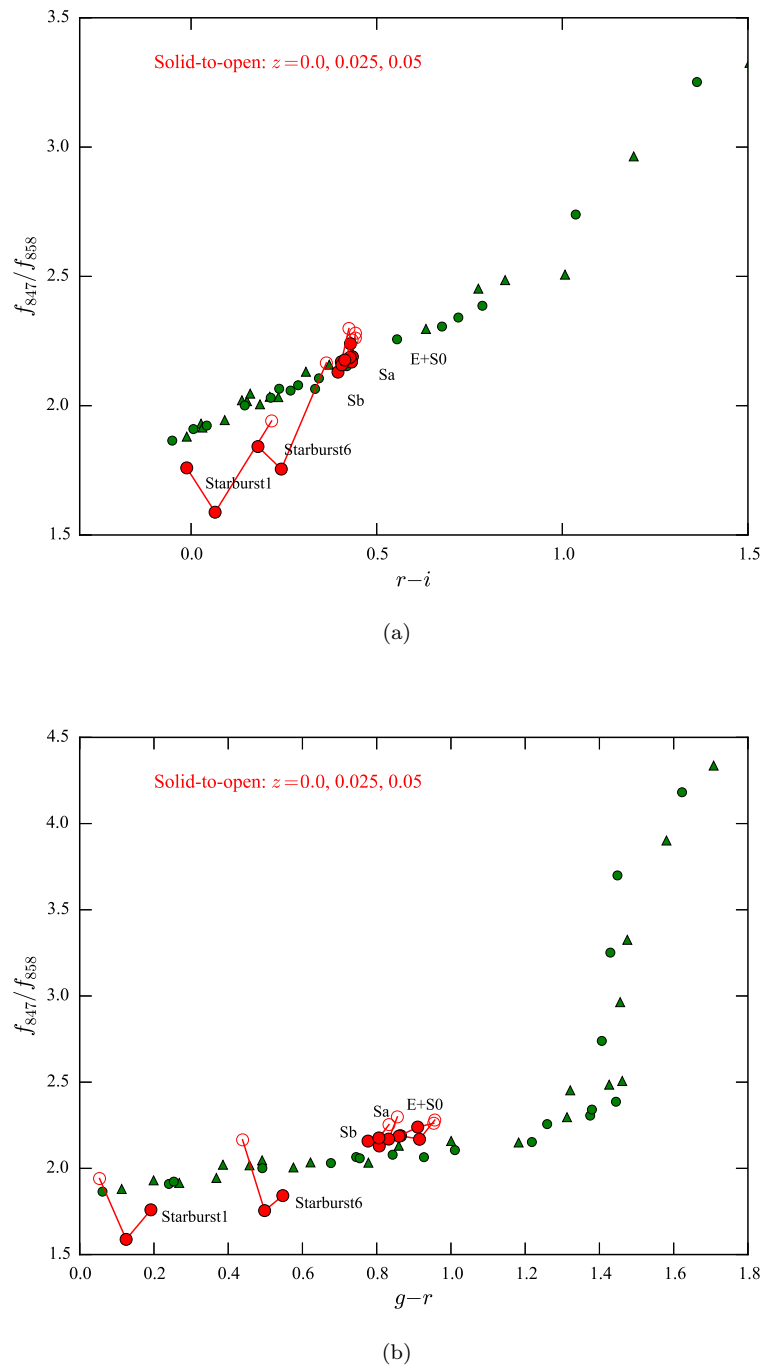


FIGURE 3.8: Shows how the flux ratio of simulated stars (green; triangle = main sequence, circle = giants) and galaxies (red) for the #847 and #858 narrow-band WFI filter pair depends on the (a) $r-i$ and (b) $g-r$ color of the object. The flux ratio depend upon the response function of the two filters and on the spectral shape of the object. This is problematic for the PSF matching algorithm.

each filter. To obtain the *continuum* level at the position of ON band, the galaxy spectra were smoothed using a moving median method with a large box size of

200 resolution elements to reduce the effects of emission and absorption lines on the continuum estimation.

A third order polynomial was fit to the smoothed spectrum to give a good representation of the continuum level at the position of the $H\alpha$ line (see fig. 3.9). This continuum fit was then convolved with the ON band filter response function to obtain the continuum level at the position of $H\alpha$ emission. In this way, we estimate the true flux levels in ON band and OFF band filters for the flux calibration, and an underlying continuum level in the ON band for the flux scaling. The flux scaling factor for the OFF band was computed by comparing this continuum level to the OFF band flux.

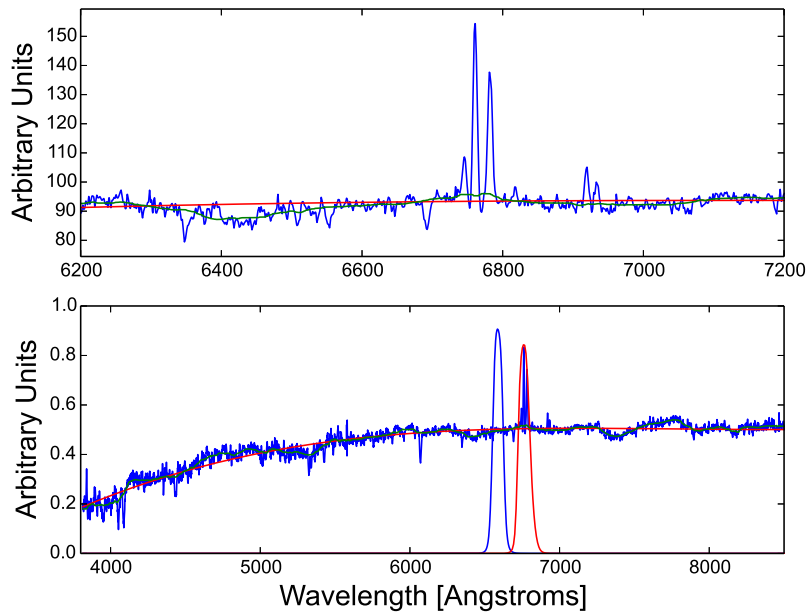


FIGURE 3.9: Full SDSS spectrum of galaxy 112723-1 is shown in lower panel. The upper panel is zoomed in at around the $H\alpha$ wavelength. The ON band (red) and OFF band (blue) filter response functions are over-plotted. The green line is the median smoothed version of the spectrum while the red line denotes the polynomial fit to this smoothed spectrum which is used to obtain the continuum level for the ON band.

The absolute flux calibration of the images was then performed by comparing the flux values obtained from spectra with the aperture photometry values obtained from the same region of the galaxy from our narrow-band images. To match the exact region of the galaxy from which the SDSS spectrum was obtained, we convolved our narrow-band images using the *convolve_simple* tool to match the average seeing of the SDSS spectroscopic observations, since our observations were generally taken under better seeing conditions. The FWHM of the Gaussian kernel

used for this convolution was computed based upon the difference in seeing between HAGGIS and SDSS observations.

Aperture photometry with a 3" diameter circular aperture, i.e. the size of the SDSS fiber, was then performed at the fiber position on both the narrow-band images convolved to SDSS seeing to obtain the flux levels in ADU counts in the region of SDSS fibers. The conversion factors from counts sec^{-1} to flux levels in units of $\text{ergs cm}^{-2} \text{sec}^{-1}$ were then computed by comparing the flux values obtained in the aperture photometry to the flux values obtained using SDSS spectra for OFF and ON bands as explained above. The OFF band calibration factor was multiplied with the flux scale factor computed from the smoothed spectrum to match the continuum level at the position of $\text{H}\alpha$ emission. The narrow-band images were then multiplied with their respective conversion factors.

Postage stamp size cutouts were obtained from the flux calibrated ON band image and the flux scaled continuum image for each galaxy in the group. The rest-frame $\text{H}\alpha$ image for each galaxy was then obtained by subtracting the scaled continuum image from the ON band image. The technique used for the HAGGIS galaxies gives a far more accurate flux scaling compared to the flux scaling performed using standard stars, as the latter assumes a single flux scale factor for all galaxies ignoring their spectral differences. Nonetheless, this novel technique has its limitations since it assumes that the galaxy has a constant color at all radii which is same as in the central 3", which is not always true.

3.1.6.1 $\text{H}\alpha$ in Absorption

With the novel flux scaling technique used for the HAGGIS observations, we were able to detect absorption in the regions of galaxies where the star-formation has ceased recently¹. In addition to detecting absorption in completely passive galaxies, we are able to detect absorption within some star-forming galaxies, with absorption typically seen either coincident with the position of the bar (possibly explained by bar driven gas flows) or at the outermost radii (possibly indicative of environmental gas stripping mechanisms). Figure 3.10 shows spectacular examples of each of these two cases. Fig. 3.10(a) shows a galaxy with absorption at intermediate radii, coincident with the position of a strong bar, while the galaxy in Fig. 3.10(b) shows absorption in the outer disk.

¹Galaxies that have ceased their star-formation recently ($\sim \text{Gyr}$) contain many 'A' stars which have strong $\text{H}\alpha$ absorption.

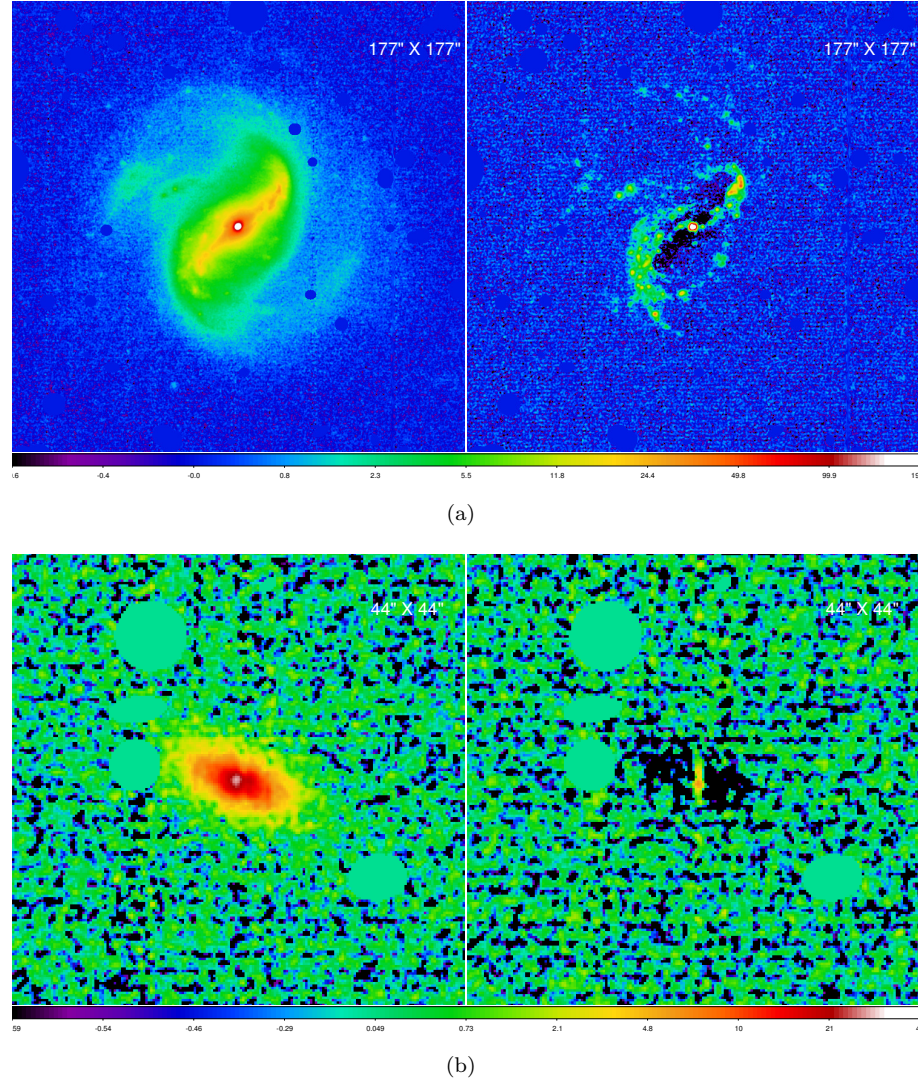


FIGURE 3.10: Left hand panels show the narrow-band continuum image while the right hand panels show continuum subtracted $H\alpha$ image. Fig. 3.10(a) shows an example galaxy (31811-1) for which $H\alpha$ is detected in absorption at intermediate radii while fig. 3.10(b) shows the galaxy (1228-12) showing absorption in the outermost region.

It has not usually been possible to detect absorption with narrow-band imaging in previous studies. This is because most studies used broad-band filters for the continuum estimation which reduces the accuracy, for example due to the contamination of emission and absorption lines in these broad-band filters. With the HAGGIS observations, we have deliberately chosen adjacent narrow-band filters that are selected to avoid strong emission lines. This, together with the novel flux scaling technique and a careful analysis, has increased the accuracy of the continuum estimation for the HAGGIS galaxies. We have not analyzed the $H\alpha$ absorption in HAGGIS galaxies in this thesis, but the quality of HAGGIS data makes it possible in the future.

Chapter 4

Surface brightness profile generation and classification

It has been observed, especially in dense clusters, that environmental processes can affect the star-formation activity in some galaxies via gas removal mechanisms such as ram pressure stripping. This is the mechanism through which the atomic and molecular gas in the galaxy is removed due to the pressure exerted by the relative motion of the galaxy in the intra-cluster medium as discussed in the introduction of this thesis. Galaxies exhibit compact star-forming disks compared to their stellar disks as the loosely bound outer gas is removed more efficiently compared to the gas in the inner regions. Galaxies with clear ram pressure effects have been identified in some clusters like Virgo (e.g. [Boselli et al. \(2006\)](#)) and they are often termed as (star-formation) “truncated” galaxies (see e.g. [Koopmann & Kenney \(2004\)](#)).

Such truncations in star-forming disks can be easily identified using azimuthally averaged one dimensional radial surface brightness profiles of the $H\alpha$ emission, which traces the star-forming gas in the galaxies. Moreover, using these one dimensional profiles one can easily measure the position and strength of the truncations, with the measurement of scale lengths and break radii, which can help us understand systematic differences between truncated star-forming disks in different environments. By generating similar one-dimensional profiles using stellar continuum images, we can also understand how these effects on star-forming gas correlate with the underlying stellar disk profiles. In addition to these intriguing questions, the one-dimensional stellar continuum and $H\alpha$ profiles can help

in understanding various different aspects of galaxies by answering some of the questions like -

- Do galaxies in groups show a variety of different $H\alpha$ and stellar continuum radial surface brightness profiles?
- Do we see removal of SF gas in some galaxies and how does the $H\alpha$ surface brightness profile look for such galaxies?
- Do galaxies in different environments show differences in their surface brightness profiles?

To answer these and many similar questions, it is necessary to obtain azimuthally averaged one-dimensional surface brightness profiles for HAGGIS galaxies using the stellar continuum and $H\alpha$ images. A classification scheme based on these profiles can then be used to understand the similarities and differences in the profiles of different galaxies and to understand whether the type of profile correlates with various galaxy properties like stellar mass, size of its stellar and $H\alpha$ disk, rate of star-formation, etc to understand the effects of environmental and secular processes on galaxies. In the following sections, we describe the generation of the narrow-band continuum and $H\alpha$ profiles in section 4.1, the classification schemes based on these profiles in section 4.2, the measurement of various different quantities using these profiles in section 4.3 and the comparisons between SDSS and HAGGIS measurements for $H\alpha$ fluxes and fiber and global SFRs in section 4.4.

4.1 Continuum and $H\alpha$ profile generation

The surface brightness profiles for each individual galaxy in both continuum and continuum subtracted $H\alpha$ are derived using the IRAF task *ellipse* which fits ellipses to galaxy isophotes. The *ellipse* task requires an initial guess for the centroid, ellipticity and position angle of the source. These input values can be allowed to vary with radius or can be kept fixed during the measurement of the azimuthally averaged intensity. Measurements with variable ellipticity and position angle have been often used to examine the effects of the bars and other internal structures on the shape of the overall surface brightness profile as these internal structures generally have different orientation and shape compared to that of the stellar disks.

But this is disadvantageous when we want to understand the shape and structure of the surface brightness profile of the underlying disk component. [Erwin et al. \(2008a\)](#) have shown that instead of using the free ellipses we can fix the shape and orientation of the ellipses to the values obtained for the projected galaxy disk, and then we recover the general exponential shape of the disk surface brightness profile even in the presence of a strong bar. This is similar, to the first approximation, to obtaining a radial surface brightness profile of a face-on galaxy using a circular aperture. For this reason we have opted to use the fixed ellipse method to obtain the surface brightness profiles for our galaxies.

Postage stamp size images of stellar continuum and $H\alpha$ emission were obtained for the profile generation for all the galaxies in HAGGIS sample as discussed in the previous chapter. We also included all serendipitous galaxies with measured redshifts which are similar to that of the target group, allowing us to obtain their $H\alpha$ emission. Before generating surface brightness profiles, all artifacts such as stellar reflections, and bad pixel columns as well as nearby objects were carefully masked, keeping only the target galaxy unmasked. This masking is similar to that which we used for the sky background estimation described in the last chapter (see section 3.1.4). The IRAF tool *imexam* was then used on the masked OFF band image of the target galaxy to obtain an initial guess for the galaxy centroid, ellipticity and position angle (PA). The *ellipse* task was then run on the masked OFF band image using the free ellipse method and our initial estimates. *ellipse* generates isophotal fits from which we examine the radial variation of ellipticity and position angle.

Figure 4.1 shows the variation of ellipticity and PA with semi-major axis for an example galaxy. The innermost region shows rounder isophotes due to the influence of the PSF and bulge and the intermediate region shows how the ellipticity and PA are influenced by the presence of strong bar. Both ellipticity and PA values then converge. Many galaxies show a similar pattern with values generally converging at larger galactic radii where the disk dominates. The *ellipse* task is then run again on OFF band and $H\alpha$ images, keeping the ellipticity and PA fixed at disk values and the centroid fixed to that determined from the OFF band (continuum centroid). In this way, we obtain the azimuthally averaged continuum and $H\alpha$ surface brightness profiles for the underlying stellar and star-forming disks, minimizing the effects of internal structures such as bars, spiral arms, nuclear rings on these profiles (see Fig. 4.2).

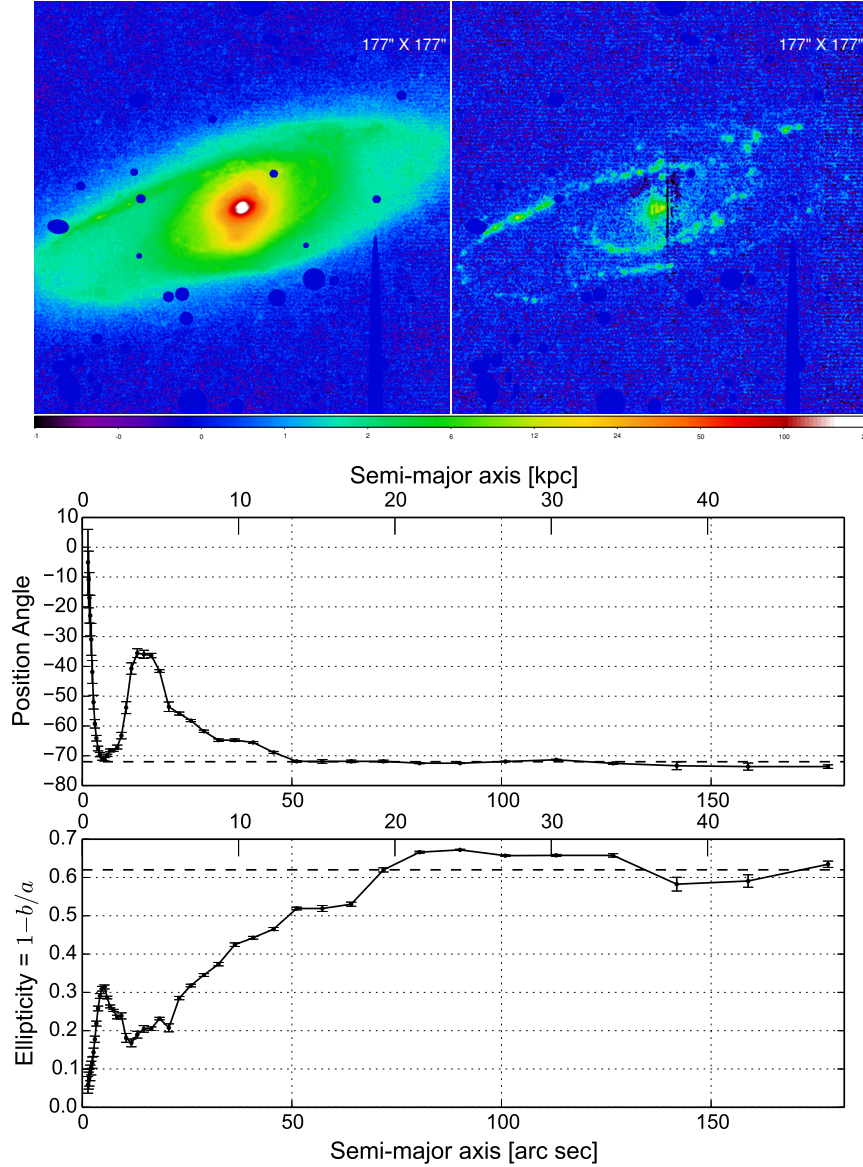


FIGURE 4.1: Continuum (upper left) and H α (upper right) image cutouts of the galaxy 3071-1 and best-fit values of ellipticity and position angle as a function of semi-major axis to the continuum image (lower panels) obtained using the IRAF *ellipse* task. The plot shows how position angle and ellipticity varies for different components of the galaxy. Except for the bar region (\sim between 5''-25''), the ellipticity increases and position angle decreases monotonically until they converge at larger radii ($\geq 70''$) where the disk dominates. These convergent values (shown by the dashed horizontal lines) are then fixed for the second iteration of the *ellipse* task to obtain the surface brightness profiles.

To estimate the noise level in our images, we have generated equivalent surface brightness radial profiles for 100 blank sky regions close to the galaxy in the H α image. For this, we generated another masked cutout for each galaxy where we masked all the objects and artifacts including the target galaxy similar to the one

used for generation of the profiles. We then measured the surface brightness profiles on these masked cutouts using the *ellipse* task with 100 randomly generated positions (avoiding the masked regions) and keeping the shape and orientation of the fixed ellipses the same as that used for the respective target galaxy. In this way, we have tried to estimate the noise fluctuation for each individual elliptical annulus to understand the significance of the measured surface brightness of the target galaxy at each radial bin. A radial noise profile is generated by obtaining the absolute value of the median and standard deviation for each annulus of all the 100 individual noise measurements. We use the noise profile to derive a threshold value for each radial bin. The noise profiles are over-plotted with a gray line in fig. 4.2 as well as in all the profile plots of the HAGGIS galaxies that can be found in the Appendix A. These noise profiles also provide (somewhat conservative) threshold for the HAGGIS continuum profiles.

We note that although with this technique we can determine the significance of each individual point of the object profile, it is not a measure of the uncertainty in the surface brightness measurement, as it does not include the contribution of the source flux, i.e. Poisson noise and other uncertainties that originate from the measurement of flux calibration and scaling, etc. We have found that, on average, our azimuthally averaged profiles reach a flux level of 10^{-18} ergs cm $^{-2}$ sec $^{-1}$ arcsec $^{-2}$ per radial bin which is similar to studies in cluster fields (viz. [Koopmann & Kenney \(2004\)](#)).

4.2 Profile classification

After the profile generation for all our target galaxies, we inspected the profiles visually in an iterative way to classify them based on their characteristics. For the classification of the stellar continuum profiles, we have adopted the disk classification scheme explained in [Erwin et al. \(2005\)](#) and [Erwin et al. \(2008a\)](#) which is based on the exponential regions of the disk profile. The classification of H α profiles was tricky as the classification scheme developed for stellar continuum profiles was observed to be insufficient to classify the H α profiles in HAGGIS galaxies and other existing classification schemes based on H α profiles have used a different criteria than the one used in stellar profile classification. For example, [Koopmann & Kenney \(2004\)](#) have classified the Virgo galaxies based on the comparison of the ratio of H α flux to R-band flux in 5 different radial bins for various Virgo galaxies with the similar ratios obtained for the isolated galaxies. Such classification

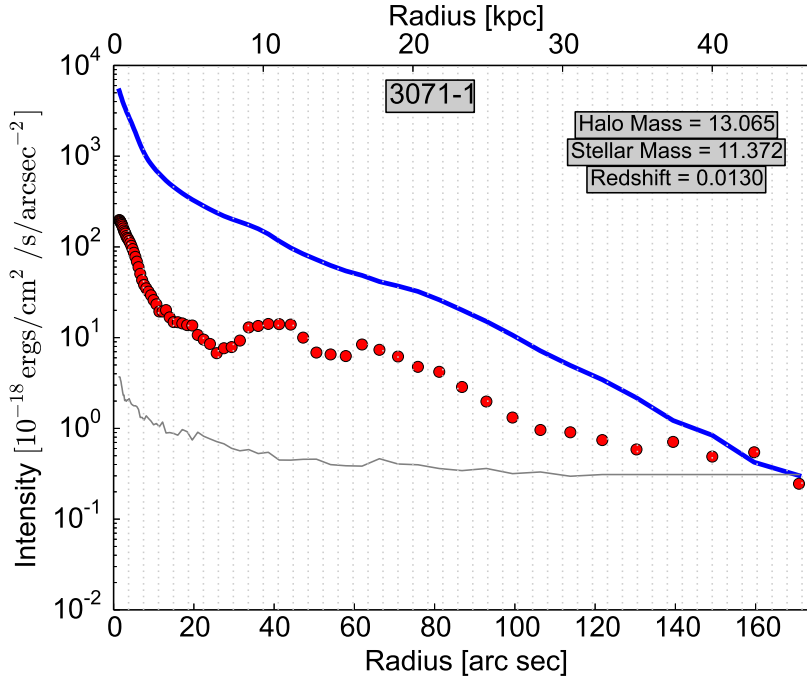


FIGURE 4.2: The continuum (blue) and H α (red) surface brightness profiles for the same galaxy (3071-1) as shown in fig. 4.1. The gray line denotes the approximate noise level in H α obtained using 100 black sky regions around the galaxy.

scheme is not universally applicable. To be sure, several authors have used the shape of the H α profile to identify galaxies with exponential and broken exponential H α disks (e.g. [Boselli et al. \(2006\)](#)), but a well defined classification scheme based on the shape of the profile similar to the one used for the stellar surface brightness profiles does not exist. Hence, we devised a new classification scheme for our H α profiles.

It is important to note that although the new H α classification scheme helps us quantify the role of environment and other internal dynamical processes in shaping the surface brightness profiles of the underlying star-forming disk, some of the analysis cannot be easily compared to existing literature as we are defining the classification scheme for H α profiles for the first time. Nevertheless, some global quantities independent of the profile shape, such as measurements of half light radii and global star-formation rates, etc. described in next section, can be used to understand whether the HAGGIS data provides a picture consistent with previous studies.

4.2.1 Continuum profile classification

Optical light of many spiral galaxies can be separated in two distinct components comprising an inner spheroidal bulge and an outer disk. Some galaxies can also contain an elongated bar-like structure in their central regions. [Freeman \(1970\)](#) observed that the disk surface brightness for spiral galaxies (neglecting the inner bulge and/or bar) exhibits two types of surface brightness profile — some galaxies have an exponential profile shape extending out to the faintest surface brightness levels while some others have a down-bending (or truncated) broken exponential profile. He called the former galaxies type I, and the latter ones type II.

Using deep datasets, [Erwin et al. \(2005\)](#) observed that in addition to these two types, some galaxies also show an up-bending (or anti-truncated) broken exponential surface brightness profile which they called type III, extending the classification scheme devised by Freeman. They also identified a minority of galaxies with a composite type II + III profile i.e. down-bending inner profile followed by an up-bending outer one. We have used this extended classification scheme for the profiles of disk galaxies in addition to the non-exponential profiles observed for the ellipticals and a few early-type galaxies to classify the continuum surface brightness profiles of the HAGGIS galaxies. Fig. 4.3 shows examples of all stellar continuum profile types in HAGGIS galaxies.

4.2.2 $H\alpha$ profile types

The $H\alpha$ emission line profiles obtained from continuum-subtracted $H\alpha$ images show various different forms and radial extents. We were able to broadly classify the emission line profiles into 6 different classes viz. “exponential”, “steep exponential”, “exponential-truncated”, “flat-truncated”, “sawtooth” and “anti-truncated”. Some galaxies are detected in $H\alpha$ absorption (negative flux values in our continuum subtracted images) throughout their radial extent. These are classified as “absorption galaxies”. A minority of galaxies exhibit ill-defined shapes of their $H\alpha$ profiles, mostly due to their low surface brightness. We label these as “non-detections/non-classifiables”. Apart from these broad classes, some galaxies show a central excess or deficit in their profiles irrespective of the broad profile type, except for the sawtooth profiles which by definition cannot have central deficits. The central excess in the profiles sometimes follows the photometric bulge seen in the stellar continuum profile. Figure 4.4 shows all the broad classes of $H\alpha$ profiles. More details about each of these profile types are given below.

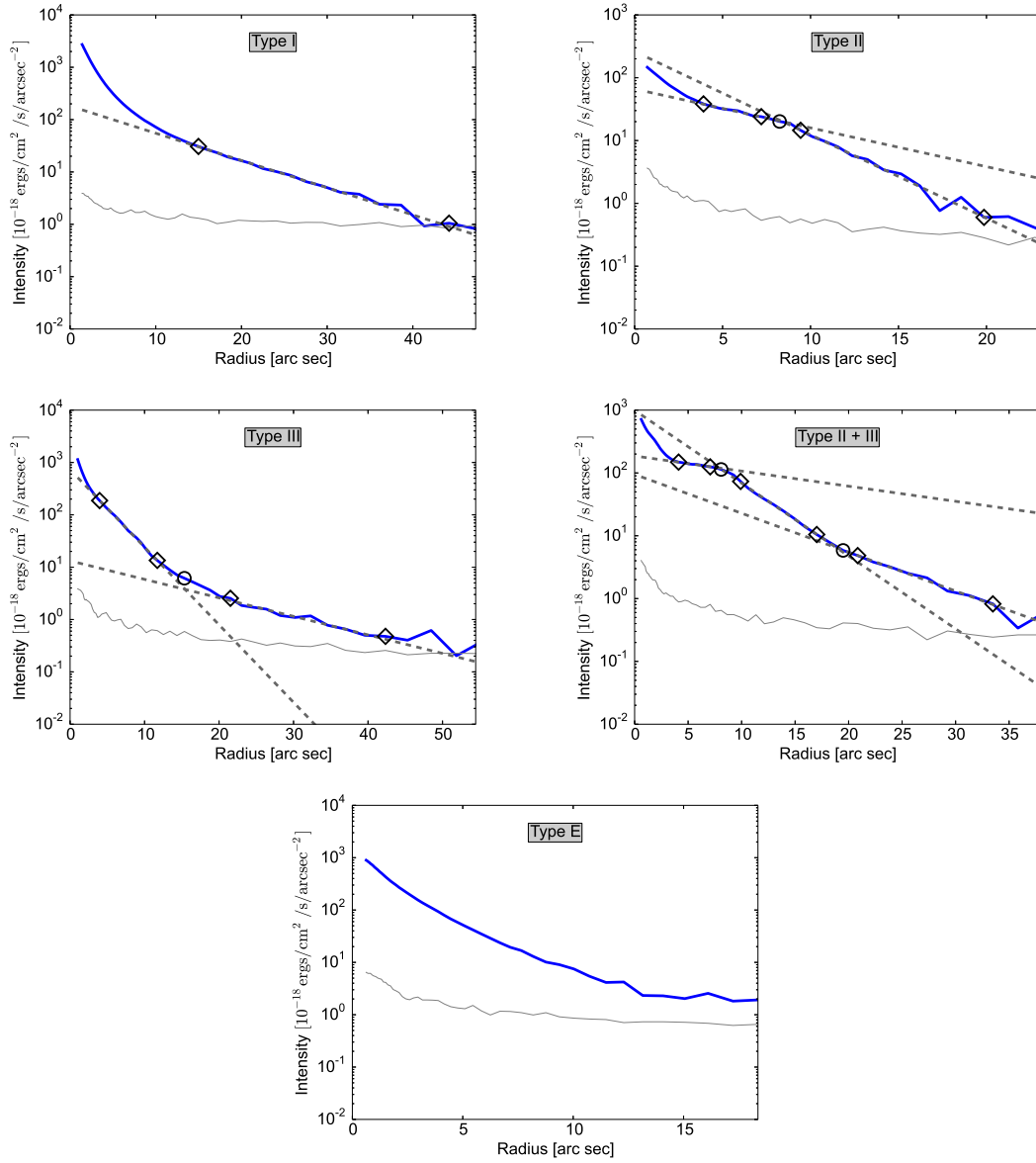


FIGURE 4.3: Different types of continuum profiles (blue). The solid gray line denotes the approximate noise level. Linear fits to different regions are marked with dashed gray lines, where fits are made between the open diamonds. The break radius — the radius at which the disk profile changes its slope — is marked by an open circle.

1. Exponentials (E)

The H α surface brightness for these galaxies can be approximated by a single exponential out to the noise limit. These H α profiles can sometimes show wiggles on top of a general exponential shape which arise mainly due to the patchy H α emission in the galaxy or due to internal structures such as spiral arms. The H α scale lengths of these galaxies are similar to the stellar continuum scale lengths in most cases (see chapter 5).

2. Steep exponentials (SE)

The $H\alpha$ profile for some galaxies have a single exponential profile that is significantly steeper than continuum profile. The steep $H\alpha$ profile makes the star-forming disks in these galaxies much more compact and centrally concentrated than the stellar disks. This type of compact $H\alpha$ disks have also been reported in cluster galaxies (for ex. see [Koopmann & Kenney \(2004\)](#) which classify these galaxies as truncated disks).

3. Sawtooths (ST)

Star-forming spiral galaxies with stronger spiral structure often exhibit a sawtooth profile with a central excess followed by a dip (or multiple dips similar to a sawtooth shape) and an outer exponential. A few sawtooth profiles are also truncated further out in the exponential region. In the intermediate dip region, some sawtooth profiles have no emission, or are seen in absorption. The intermediate dip or absorption in many cases is associated with a bar. Sawtooth-like $H\alpha$ profiles have been observed in a similar narrow-band field survey — the $H\alpha$ Galaxy Survey ($H\alpha$ GS): [James & Percival \(2015\)](#) give a detailed account of the properties of these galaxies. The low level $H\alpha$ emission in the intermediate dip region of their sawtooth galaxies has been identified as LINER-like.

4. Exponential-truncated (truncated; T)

The $H\alpha$ surface brightness profile for this type of galaxies is characterized by a broken exponential with the outer exponential steeper than the inner one, similar to the type II stellar continuum profiles. Exponential-truncated (or simply “Truncated”) profiles have been previously detected mainly in dense environments such as the Virgo cluster and in some compact groups (see e.g. [Boselli et al. \(2006\)](#)). Ram pressure stripping of outer gas has been identified by [Boselli et al. \(2006\)](#) as the cause of truncation for an exponential-truncated Virgo galaxy.

5. Flat-truncated (FT)

The $H\alpha$ emission of this type of galaxy has a flat or even outwardly increasing inner surface brightness profile towards the centre, followed by an exponentially declining surface brightness region beyond the break radius. Some authors (e.g. [Hunter et al. \(2011\)](#)) have observed similar $H\alpha$ and UV profiles in dwarf irregular galaxies. They can exhibit a central excess or deficit.

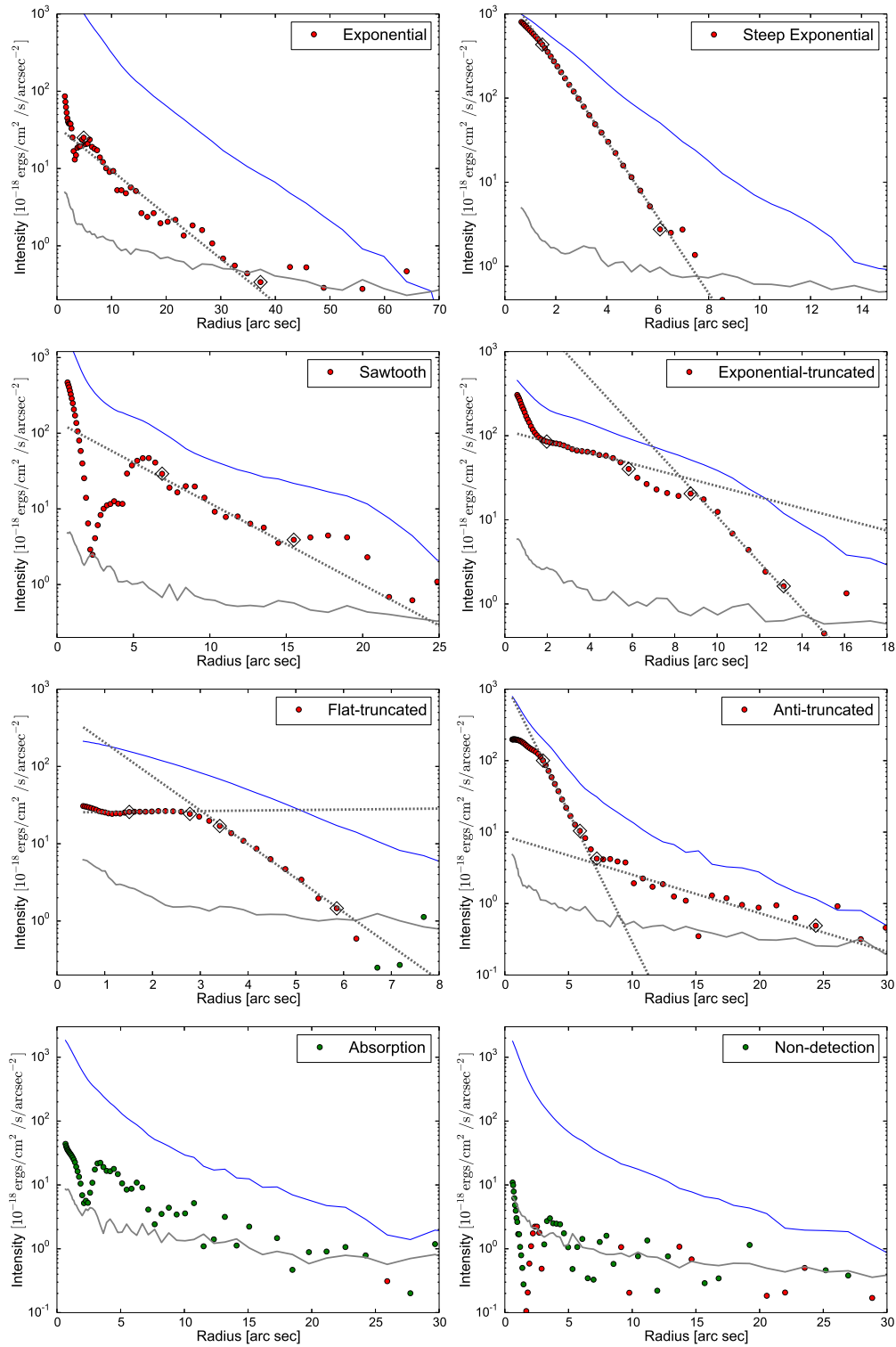


FIGURE 4.4: Different types of H α profile (emission in red and absorption in green). The continuum profiles (blue) are shown for reference. The solid gray line denotes approximate noise level. The fitting radii for a linear fitting of different regions are marked with open diamonds and the linear fits are marked with dashed gray lines.

6. Anti-truncated (AT)

Only 5 galaxies in the sample have been identified to have an anti-truncated $H\alpha$ profile that is similar to the type III stellar continuum profile. They have a broken exponential profile with the outer exponential shallower than the inner exponential. There is no example with central excess or dip among HAGGIS anti-truncated galaxies. To the best of our knowledge, this type of $H\alpha$ profile has not been reported in the literature.

7. Absorption galaxies (A)

Some galaxies are only detected in $H\alpha$ absorption throughout the full radial range (until the profile goes below noise levels). Only those galaxies which do not show any $H\alpha$ emission above the noise levels at any radial bin are classified as absorption galaxies. The detection of absorption in these galaxies means that the star-formation has ceased in these galaxies and they have been passively evolving ever since.

8. Non-detections and non-classifiables

The $H\alpha$ emission (or absorption) for some galaxies is very faint and hence we cannot detect it significantly in our observations; i.e. the profile of these galaxies is either consistent with or stays below the noise level at all radii. These galaxies are classified as non-detections. A few other galaxies where the shape of the profile cannot be explained within our broad classification scheme for various reasons are also included in this type. These profiles are often noisy detections which makes it difficult to identify the shape of the profile.

The cutout images and radial surface brightness profiles of all galaxies in both continuum and $H\alpha$ wavelengths along with their SDSS spectra and position angle and ellipticity plots from the free *ellipse* run are given in Appendix A.

4.2.3 Comparison of stellar and $H\alpha$ profile types

Figure 4.5 shows the distribution of different stellar continuum profile types among different classes of galaxies based on their $H\alpha$ surface brightness profiles. It shows that we can form a sequence of $H\alpha$ profile types viz., flat-truncated — sawtooth — truncated — exponential — steep exponential — absorption, based on the decreasing fraction of type II galaxies and simultaneous increase in fraction of type

III and non-exponential galaxies along this sequence. But, the fraction of type I galaxies is observed to be uncorrelated with the $H\alpha$ profile types in this sequence although their fraction is somewhat larger in exponential and steep exponential galaxies ($> 40\%$) and smaller in truncated and flat-truncated galaxies ($\sim 25\text{-}30\%$). The interdependence of the two profile types on one another suggests that the mechanisms that are responsible for the formation of a particular stellar profile type also have some effect on the galaxy's $H\alpha$ surface brightness profile and vice versa.

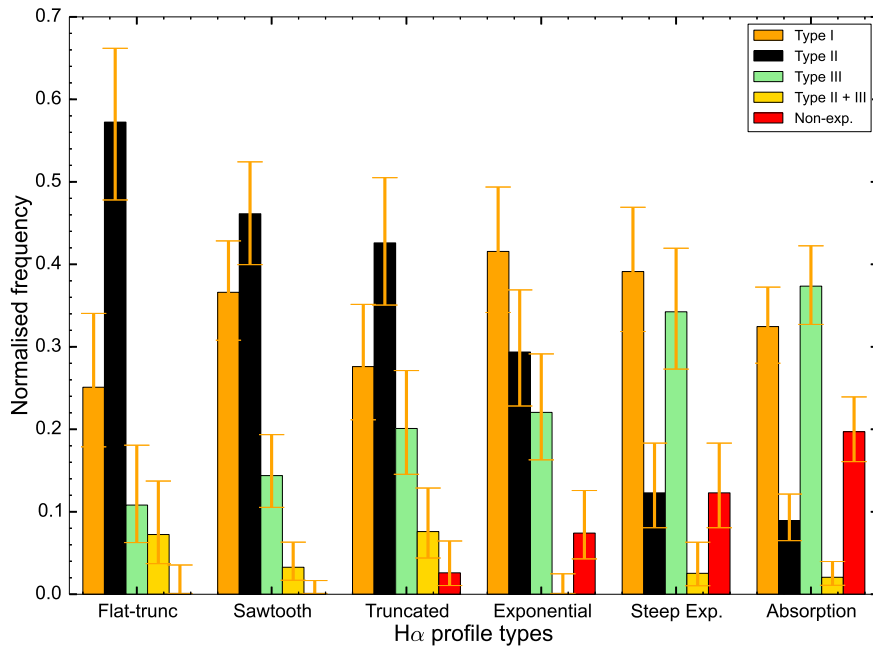


FIGURE 4.5: The distribution of stellar continuum profile types among different classes of galaxies based on their $H\alpha$ surface brightness profiles. $H\alpha$ profile types are arranged such that they form a sequence of decreasing fraction of type II galaxies and increasing fraction of type III and non-exponential galaxies (left to right). Type I fraction is generally unrelated with the $H\alpha$ profile type (along this sequence) although they are somewhat more common in exponential and steep exponential galaxies ($> 40\%$) and less common in truncated and flat-truncated galaxies ($\sim 25\text{-}30\%$).

4.3 Computation of derived parameters

Various observable properties of galaxies such as galaxy sizes, integrated fluxes, luminosities, star-formation rate, etc can be measured using the continuum and $H\alpha$ surface brightness profiles. These measurements are necessary to understand various scaling relations in galaxies and to quantify the differences with respect

to galaxy stellar mass and its environment. The following section describes these measurements in detail. The measured quantities used in this thesis for all the HAGGIS galaxies are given in a table in the Appendix C while a sample table is included here (see table 4.1).

4.3.1 Fitting radii

During the classification of profiles, the radial range of approximately exponential regions were identified for both stellar continuum and H α profiles. Fitting radii for each disk region were marked with open diamonds in figures 4.3 and 4.4, and in all profiles given in the Appendix A. These fitting radii were fed to a routine which performs an exponential fit to each region. The fitting is performed using equal weights for each radial bin. We have also defined an outer radius at which the profile drops below the noise limit (r_{noise}). This was used as an upper limit radius for all measurements.

4.3.2 Galaxy sizes

Galaxies don't exhibit a sharp edge in the distribution of their stellar material and hence their size cannot be defined in this way. Several indicators are developed to quantify the size of a galaxy and to facilitate a meaningful comparison between different galaxies. Widely used galaxy size measurements include -

- **Disk scale length (Rd):** Galaxy stellar disks often exhibit an exponentially declining radial surface brightness profile which can be expressed as -

$$\mu(r) = I_0 e^{-r/Rd} \quad (4.1)$$

where $\mu(r)$ is the surface brightness in an annulus between r and $r + dr$, I_0 is the central surface brightness and Rd is the scale length of the exponential profile i.e. the radius at which the surface brightness drops to $1/e \times I_0$.

In a log-linear space the equation becomes -

$$\log_{10}(\mu(r)) = \log_{10}(I_0) - \log_{10}(e) \times r/Rd \quad (4.2)$$

Hence, a scale length can be measured by measuring the slope of an exponential surface brightness profile in the log-linear space. The scale lengths

of each exponential regions for HAGGIS galaxies are obtained from the fits. They are measured in physical units (i.e. in kpc).

- **Half light radius (Re):** Galaxy size can also be expressed by measuring the radius containing half of the total galaxy light. This size measurement is known as half light radius. It can be measured using galaxy surface brightness profile by solving for equation 4.3.

$$\int_0^{Re} \mu(r) (1 - e) 2\pi r \, dr = 0.5 \times \int_0^{\infty} \mu(r) (1 - e) 2\pi r \, dr \quad (4.3)$$

where $\mu(r)$ is the surface brightness in an annulus between r and $r + dr$, $(1 - e) 2\pi r \, dr$ is the area of the elliptical annulus between r and $r + dr$ with e being ellipticity of the galaxy, and Re is the half light radius. The half light radius for each profile is computed using the curve of growth method to obtain the radius at which the integrated flux in the observed profile is half the total integrated flux in the profile. For calculating the half light radius for $H\alpha$ profiles, the contribution from absorption regions are excluded from the total flux which may affect the half light radius measurement, especially for galaxies with central or intermediate absorption regions or deficits observed mainly in sawtooth galaxies. For an exponentially declining surface brightness profile, the half light radius is related to the disk scale length via the equation -

$$Re = 1.67835 \, Rd \quad (4.4)$$

- **Petrosian radius (Rp):** Galaxy size can also be measured by calculating the radius at which the local surface brightness in an annulus at that radius equals some predefined fraction of the mean surface brightness within that radius as shown in equation 4.5.

$$\mu(Rp) = \eta \left(\frac{\int_0^{Rp} \mu(r) 2 \pi r \, dr}{\pi Rp^2} \right) \quad (4.5)$$

where $\mu(r)$ is the surface brightness between r and $r + dr$, Rp is the Petrosian radius, η is the predefined fraction used to compute the Petrosian radius and $\mu(Rp)$ is the surface brightness in a small annulus around Rp . The SDSS data reduction pipeline uses $\eta = 0.2$ for the measurement of the Petrosian radius.

All of these measurements have some advantages and disadvantages. For example, the scale length is a direct measurement for the size of the disk and it is least affected by contamination of e.g. bulge light, while both half light radius and Petrosian radius are affected by bulge contamination. On the other hand, scale lengths can only be measured where a disk can be identified and fit — for only those galaxies where the surface brightness profile can be approximated to an exponential — while the other size measurements can be made on any type of galaxy irrespective of the profile shape. Also, measurement uncertainties can have significant effects while comparing the sizes of different galaxies. The surface brightness threshold and estimation of sky background are the prominent source of uncertainties in the measurement of the half light radii. The substructures in galaxies like spiral arms, bars, rings, etc can deviate the surface brightness profile from an exponential shape which can impact the fitting of the exponential region affecting the scale length measurements. Noise, substructure, profile shape, etc can also cause complications in the measurement of the Petrosian radius; certain objects can have no Petrosian radius and some others can have more than one such radius. Taking this into consideration, we opted to measure only scale length and half light radius for HAGGIS galaxies.

4.3.3 Central excess / deficit

The central excess (or deficit) is computed by subtracting the extrapolated inner disk flux from the integrated observed flux in the region of inner disk (i.e. out to the first break radius or r_{noise} depending on profile type). The r_{excess} or the radius at which central excess light equals the (inner) disk light is computed for both continuum and $\text{H}\alpha$ profiles.

4.3.4 Break radii

When a galaxy has more than one exponential region in its surface brightness profile, a break radius (or radii) can be defined as the radius (radii) at which profile slope changes. The break radius (radii) is measured for HAGGIS galaxies as the intersection point of the linear fits of the two exponential regions. It is shown by an open circle in fig. 4.3 and in Appendix A.

TABLE 4.1: Table of derived parameters for continuum and H α profiles. Full table can be found in Appendix (C).

Galaxy ID	Continuum										H α					
	Profile Type	R _{break} (kpc)		Re (kpc)	Scale length (kpc)			Flux ($\times 10^{-17}$ ergs sec $^{-1}$ cm $^{-2}$)	Profile Type	R _{break} (kpc)	Re (kpc)	Scale length (kpc)		Flux ($\times 10^{-17}$ ergs sec $^{-1}$ cm $^{-2}$)	Log Luminosity (ergs sec $^{-1}$)	Log SFR (M_{\odot} yr $^{-1}$)
		1-2 (3)	2-3 (4)		1 (6)	2 (7)	3 (8)					1 (13)	2 (14)			
(1)	(2)	(3)	(4)	(5)	(6)	(7)	(8)	(9)	(10)	(11)	(12)	(13)	(14)	(15)	(16)	(17)
13-1	I	-	-	4.7	3.5	-	-	15062	SE	-	1.1	0.3	-	99	39.73	0.04
13-2	III	5.5	-	2.2	1.0	2.1	-	3293	A	-	8.5	-	-	2	38.11	0.00
13-3	I	-	-	3.9	2.5	-	-	6869	A	-	7.1	-	-	19	39.05	0.01
13-4	III	9.4	-	3.7	1.8	5.6	-	8598	A	-	11.9	-	-	113	39.85	0.06
13-8	II	-	-	0.6	1.5	-	-	3044	N	-	-	-	-	-	-	-
13-9	II	2.7	-	3.4	3.6	1.8	-	4925	SE	-	1.5	0.9	-	176	39.96	0.07
13-11	III	5.6	-	2.1	1.1	2.1	-	7480	A	-	9.0	-	-	18	39.03	0.01
13-12	I	-	-	4.1	3.1	-	-	18450	SE	-	1.1	0.6	-	62	39.68	0.04
13-13	I	-	-	2.6	1.4	-	-	2578	A	-	2.8	-	-	21	39.10	0.01
13-14	E	-	-	2.1	-	-	-	5210	A	-	-	-	-	0	-	-
13-15	III	6.6	-	3.0	1.5	2.6	-	4288	A	-	8.0	-	-	34	39.33	0.02
13-16	II	11.0	-	2.5	2.4	1.4	-	2706	A	-	6.7	-	-	14	38.88	0.01
13-17	III	5.3	-	3.4	1.6	2.5	-	3493	A	-	10.9	-	-	19	39.05	0.01
13-18	III	10.6	-	3.1	1.7	3.0	-	8180	A	-	12.7	-	-	10	38.79	0.00
13-19	E	-	-	3.9	-	-	-	10624	N	-	3.0	-	-	39	39.41	0.02
13-20	E	-	-	3.7	-	-	-	25213	A	-	30.0	-	-	299	40.26	0.14
13-21	I	-	-	3.4	4.1	-	-	18349	A	-	20.7	-	-	52	39.58	0.03
13-22	2+3	6.7	23.4	26.4	3.3	10.8	18.5	54407	SE	-	1.7	2.7	-	93	39.78	0.05
13-23	III	10.7	-	3.8	2.0	2.9	-	11660	A	-	-	-	-	-	-	-
13-24	III	4.2	-	2.2	1.0	1.6	-	2791	N	-	4.4	-	-	85	39.63	0.03
13-25	III	6.1	-	3.7	1.8	2.5	-	9948	A	-	15.5	-	-	22	39.16	0.01
13-32	I	-	-	9.0	8.9	-	-	84901	SE	-	2.6	1.6	-	469	40.58	0.30
13-34	E	-	-	-	-	-	-	-	A	-	-	-	-	-	-	-
13-35	II	5.0	-	2.3	1.4	0.7	-	3469	N	-	3.8	3.5	-	138	39.93	0.07
13-37	III	6.9	-	2.7	1.4	2.5	-	6857	A	-	8.4	-	-	107	39.85	0.06
13-38	E	-	-	-	-	-	-	-	A	-	-	-	-	-	-	-
13-40	III	5.7	-	2.8	1.4	2.7	-	5240	A	-	11.2	-	-	59	39.62	0.03
13-41	I	-	-	2.4	1.3	-	-	4232	A	-	8.7	-	-	29	39.27	0.01
13-43	E	-	-	-	-	-	-	-	N	-	-	-	-	-	-	-
183-1	I	-	-	2.6	1.6	-	-	3667	A	-	-	-	-	0	-	-

4.3.5 Integrated fluxes

The flux in each exponential region and the flux for the whole galaxy are computed by integrating the surface brightness using equation 4.6.

$$F = \int_{r_0}^{r_1} \mu(r) (1 - e) 2\pi r \, dr \quad (4.6)$$

where F is the integrated flux, $\mu(r)$ is the surface brightness between r and $r + dr$, $(1 - e) 2\pi r \, dr$ is the area of the elliptical annulus between r and $r + dr$ with e being ellipticity of the galaxy, while the limits r_0 and r_1 are determined for each disk region and for the whole galaxy separately as described below.

For type I profiles the integrations of the linear fits are performed from zero to infinity while for type II and type III profiles the fluxes in the inner and outer disk regions are computed by integrating the profile fits from zero to the break radius for the inner disk and from break radius to infinity for the outer disk. Similarly, for type II + III profiles, the fluxes in the 3 disk regions are computed by integrating from zero to the first break radius, from the first break radius to the second break radius and from the second break radius to infinity. The undetected flux for the galaxy is measured as the difference between the integration of the outer disk region to infinity and the same to r_{noise} . The total flux for the whole galaxy is obtained by integrating the observed flux from zero to r_{noise} . For $H\alpha$ profiles, two quantities of total flux are measured — one measuring only the $H\alpha$ emission in the galaxy neglecting any contribution coming from absorption regions and another which includes the absorption flux as negative intensity. It is important to note here that the former integration of $H\alpha$ flux may still contain some contribution from absorption within each radial bin, as the azimuthal integration is performed by the *ellipse* task.

4.3.6 $H\alpha$ luminosity

The $H\alpha$ luminosity for HAGGIS galaxies is computed using the emission line flux measurements using equation 4.7.

$$L_{H\alpha} = 4 \pi D_L^2 F_{H\alpha} \quad (4.7)$$

where $L_{H\alpha}$ is the $H\alpha$ luminosity, $F_{H\alpha}$ is the integrated $H\alpha$ flux and D_L is the luminosity distance of the galaxy which is computed using the redshift obtained from SDSS fiber spectroscopy. We use two measurements of $H\alpha$ luminosity for HAGGIS galaxies; one corrected for galactic and internal dust extinction and another an uncorrected raw measurement. The Galactic extinction correction is performed using the color excess $E(B - V)$ obtained from the far-IR dust map of [Schlegel et al. \(1998\)](#) and using the relation $A(H\alpha) = 2.6 \times E(B - V)$ for the estimation of extinction at $H\alpha$ wavelengths ([Gavazzi et al. \(2012\)](#)). The average internal dust extinction correction is applied to the $H\alpha$ luminosity based on prescriptions given in [Lee et al. \(2009\)](#) using a Johnson B-band absolute magnitude obtained by converting SDSS g magnitudes, adopting the relation: $B = g \times 0.983 + 0.692$ mag ([Gavazzi et al. \(2012\)](#)). The extinction law at the wavelength of $H\alpha$ can be expressed as $A(H\alpha) = 1.971 + 0.323 B + 0.0134 B^2$ for $B < -14$ and $A(H\alpha) = 0.1$ otherwise.

4.3.7 Star-formation rate

The extinction corrected $H\alpha$ luminosity is converted to star formation rate for the galaxy using a relation given in [Kennicutt & Evans \(2012\)](#) (see equation 4.8).

$$\text{Log } SFR (M_{\odot} \text{ yr}^{-1}) = \text{Log } L_{H\alpha} (\text{ergs s}^{-1}) - 41.27 \quad (4.8)$$

This transformation of $H\alpha$ Luminosity to SFR has been derived assuming solar abundances and a Kroupa initial mass function (IMF) over a range of stellar masses from $0.1 - 100 M_{\odot}$ and assuming that the $H\alpha$ luminosity is corrected for galactic and internal dust extinction.

The global star-formation rates for HAGGIS galaxies are derived using the extinction corrected $H\alpha$ luminosities that are computed from the integrated $H\alpha$ fluxes. We also derive SFRs for the central $3''$ diameter aperture of each galaxy, which corresponds to size of a SDSS fiber. This is used to understand the quality of our dataset by comparing with the SDSS derived fiber SFRs for HAGGIS galaxies.

4.4 SDSS comparison

It is important to assess the quality of our dataset and to understand the accuracy of our measurements before applying any analytical techniques to quantify the effects of environment and stellar mass on various derived properties of galaxies in the HAGGIS sample. As we have used SDSS flux calibrated fiber spectra for the flux calibration and continuum estimation for our dataset, the comparison between HAGGIS and SDSS $H\alpha$ flux measurements for the aperture of central 3'' that corresponds to SDSS fiber diameter provides a good check on the quality of the HAGGIS measurements.

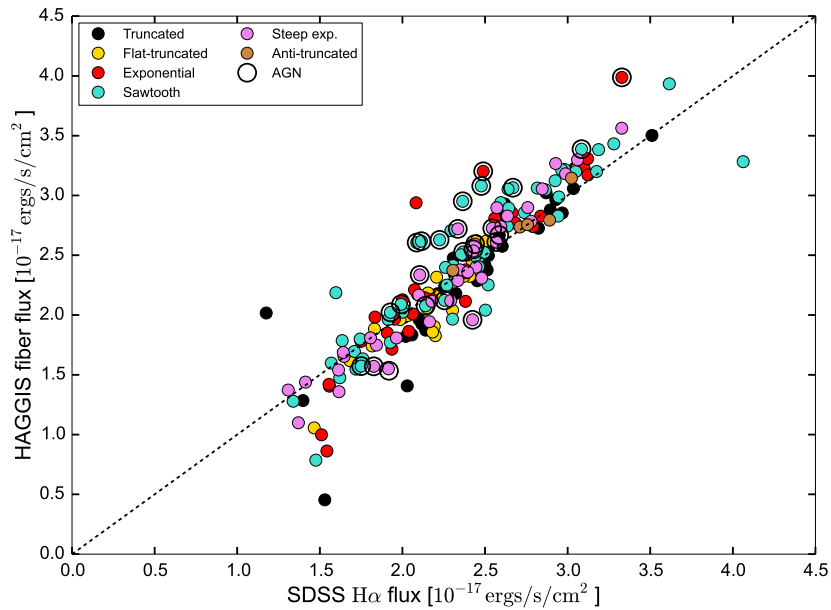


FIGURE 4.6: Comparison of HAGGIS and SDSS $H\alpha$ flux measurements within the aperture of 3'' diameter (SDSS fiber size) for HAGGIS galaxies color-coded with $H\alpha$ profile types. AGNs identified in SDSS DR7 are marked on the plot with open circles. The two flux measurements match quite well except for few cases.

Figure 4.6 shows the flux comparison for galaxies that are detected in emission in HAGGIS dataset. The plot is color-coded with the $H\alpha$ profile type defined for the galaxies using HAGGIS dataset. AGNs that are identified in SDSS DR7 are shown on the plot as open circles. SDSS fluxes are obtained from SDSS DR7 data release and are derived based on the precepts given in Brinchmann et al. (2004). The derivation of fluxes involves modeling of the SDSS spectra based on population synthesis models which gives accurate continuum subtraction and subtracts the contribution of stellar absorption underlying the emission lines to

obtain accurate emission line fluxes. SDSS and HAGGIS flux measurements are corrected for galactic extinction as well as for internal dust extinction. HAGGIS fluxes are also corrected for average NII contamination as described in the last section.

The two flux measurements match quite well with each other for various different types of galaxies classified based on their $H\alpha$ surface brightness profiles. But, $\sim 21_{-3}^{+3}$ % of galaxies show a discrepancy of > 10 % between the two flux measurements although 50_{-7}^{+7} % of this population comprises AGNs, composites, unclassifiables and low S/N liners as classified in the SDSS DR7 data release. We would like to note here that small discrepancies between two flux measurements are expected due to the differences in measurement techniques (e.g. we cannot employ the sophisticated techniques to estimate and correct for the underlying stellar absorption in our resolved observations). Also, we have used an average dust extinction correction in HAGGIS based on Johnson absolute B-band magnitudes which is less accurate, especially for the central regions where the amount of dust is typically higher, compared to the sophisticated dust extinction employed in SDSS measurements. Thus accounting all these differences, we conclude that with our method of flux calibration and continuum scaling and subtraction we can measure the $H\alpha$ fluxes with good enough accuracy for most of the normal star-forming galaxies.

This $H\alpha$ flux estimation accuracy translates into the accuracy with which we can derive the SFRs in the fiber region of these galaxies. But fiber SFRs derived by the MPA-JHU team for the SDSS DR7 data release (<http://wwwmpa.mpa-garching.mpg.de/SDSS/DR7/sfrs.html>) are derived using a full spectral modeling of the observed spectra which accounts for the differences in the metallicity, the ionization state of the gas and the diffuse emission in the galaxy along with the internal dust extinction. Although this method gives much better estimate of SFRs than using a fixed conversion factor, especially for the high mass galaxies, the spectral information required for such modeling is not available outside the SDSS fiber coverage for the HAGGIS galaxies. Because of this, the method cannot be used to compute the HAGGIS SFRs. Hence, for the purpose of assessing the data quality of the HAGGIS observations, we have re-derived the SDSS fiber SFRs using SDSS $H\alpha$ flux measurements.

Figure 4.7(a) shows a comparison of such fiber SFR measurements obtained using HAGGIS and SDSS datasets for different $H\alpha$ profile types. Both SFRs are derived using Kennicutt & Evans (2012) calibration which assumes a universal Kroupa

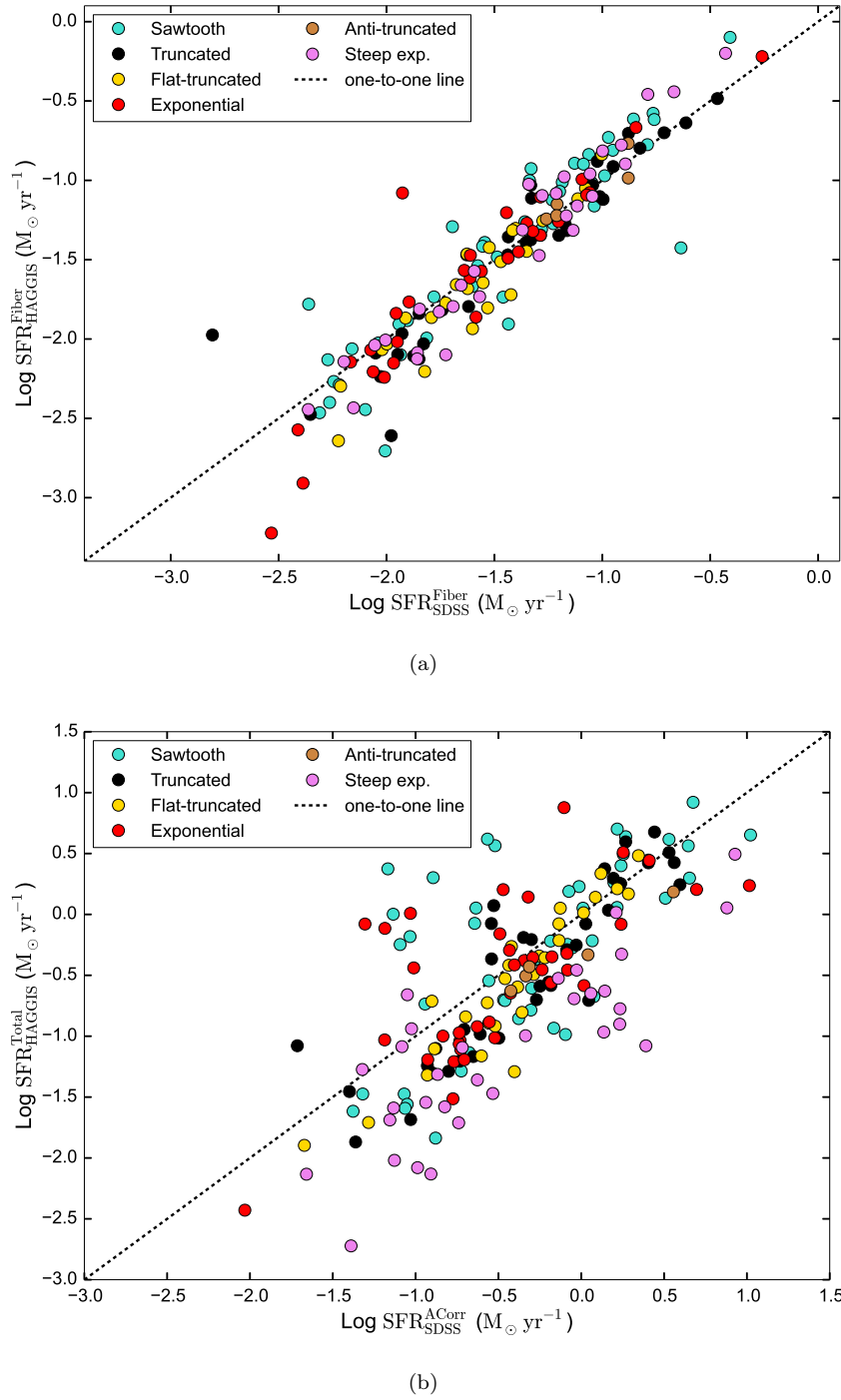


FIGURE 4.7: (a) Comparison of HAGGIS and SDSS fiber SFRs for HAGGIS galaxies color-coded with $H\alpha$ profile types. (b) Comparison of HAGGIS global SFR measurements with SDSS aperture corrected SFR measurements for HAGGIS galaxies color-coded with $H\alpha$ profile types. AGNs identified in SDSS DR7 are not shown on both plots. The fiber SFR measurements agrees well for the two datasets while the SDSS aperture corrected measurements and HAGGIS global SFR measurements show larger discrepancies.

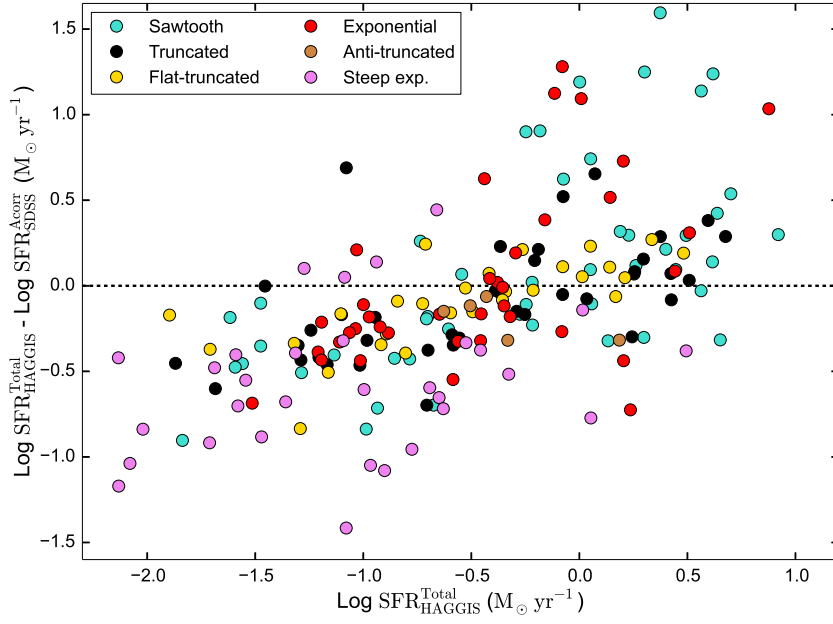
IMF. AGNs identified in SDSS DR7 are not shown on the plot as it is difficult to estimate their SFR in the HAGGIS dataset. The figure shows that the two SFR measurements agree very well with each other ($1\text{-}\sigma$ difference of 0.23) and no strong systematic offset as a function of galaxy's $\text{H}\alpha$ surface brightness profile is observed for any of these measurements.

The good quality spectral information available for the SDSS galaxies enables them to use the complex techniques for more accurate estimation of SFR in the fiber region of the galaxies. But, this accurate measurement of fiber SFR does not represent the global SFR for these galaxies as the fiber only covers a central $\sim 0.3 - 1.5$ kpc for the galaxies in the redshift range of the HAGGIS survey. The effects of aperture size on these measurements can be rectified to a large extent using the vast amount of ancillary photometric data available for these galaxies from the SDSS photometric survey. The aperture corrections from Brinchmann et al. (2004) are computed using the spatially resolved $g-r$ and $r-i$ color information for each galaxy (see <http://wwwmpa.mpa-garching.mpg.de/SDSS/DR7/sfrs.html> for more details of its application to SDSS DR7).

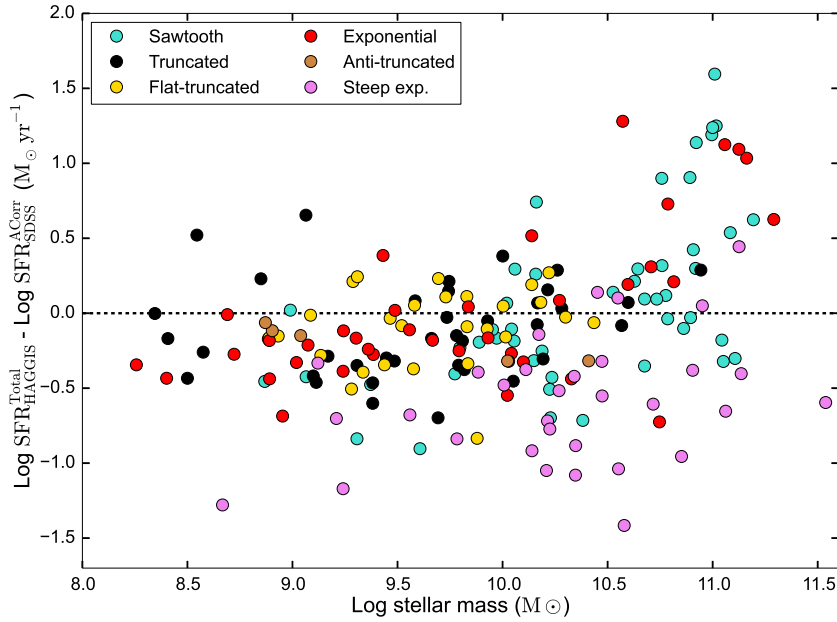
Figure 4.7(b) shows the comparison of the total integrated SFR measurements from HAGGIS narrow-band imaging with the SDSS aperture corrected SFRs. The plot is color-coded with $\text{H}\alpha$ profile types. Both SFRs are derived assuming a universal Kroupa IMF and AGNs are omitted from this comparison as their contamination in HAGGIS measurements is difficult to correct. The two SFR measurements show a rough agreement with each other ($1\text{-}\sigma$ difference of 0.55) although there is a larger scatter compared to the fiber based measurements.

SDSS SFRs are overestimated compared to HAGGIS measurements for the galaxies with low SFRs while they are slightly underestimated for the galaxies having larger SF activity. The difference between HAGGIS and SDSS measurements as a function of total SFR derived using HAGGIS narrow-band data is shown in figure 4.8(a), which illustrates this more clearly. The discrepancies between the SFRs are largest among steep exponentials and sawtooth galaxies reaching 1-1.5 dex in some of these galaxies. SDSS overestimate the SFR for almost all (barring 4) steep exponentials while they underestimate the SFRs for many sawtooths. On the other hand, the discrepancies are smaller among truncated and flat-truncated galaxies reaching ~ 0.5 dex in some of these galaxies. This indicates that there are some systematic biases in the aperture corrected SFR estimation which is a function of the shape of the $\text{H}\alpha$ profile.

Finally we compare the difference between HAGGIS and SDSS SFR measurements as a function of galaxy stellar mass in figure 4.8(b). The figure is also color-coded by H α profile types. It shows that the SFRs are underestimated for most of the low mass galaxies in SDSS measurements by about 0.2 – 0.5 dex while the discrepancies are ≥ 1 dex for high mass galaxies. SFRs for some high mass galaxies, especially those with a sawtooth H α profile, are underestimated in SDSS measurements while it is overestimated for steep exponentials. While we cannot be sure HAGGIS SFR measurements are not systematically wrong in some cases due to remaining issues with resolved dust and SFR calibrations, etc, these plots underline the limitations of fiber-based spectroscopic observations and thereby mark the importance of spatially resolved datasets especially in the context of understanding the effects of galaxy environment.



(a)



(b)

FIGURE 4.8: Difference between HAGGIS total SFR and SDSS aperture corrected SFRs (a) against HAGGIS total SFR (b) against stellar mass. Both plots are color-coded with H α profile types. AGNs identified in SDSS DR7 are not shown on these plots. SDSS overestimates SFRs for many low mass and low SFR HAGGIS galaxies which includes most of the steep exponentials and many galaxies with truncated H α disks while it underestimates the SFRs for galaxies having larger SFR activity which includes many sawtooth galaxies. The high mass galaxies show larger discrepancies between the two SFR measurements (> 1 dex).

Chapter 5

Relation of stellar and H α sizes to stellar mass and profile types

Galaxy disks are considered to grow via the accretion of gas within hierarchically growing cold dark matter (CDM) haloes. Rotationally supported stable disks are formed when the angular momentum of the accreted gas exerts an outward pressure which halts the gravitational collapse of further material. Using the vast amount of SDSS photometric data, [Shen et al. \(2003\)](#) showed that for galaxies in the local universe, the galaxy size correlates with its stellar mass ¹ (also see [Lange et al. \(2015\)](#)).

In this chapter, we discuss the stellar and H α size - mass relations for the HAGGIS galaxies in section 5.1. Sections 5.2 and 5.3 describe how these size - mass relations compare for different types of galaxies classified based on their stellar continuum and H α surface brightness profiles. In section 5.4, we describe how the H α disk sizes compare with the size of their stellar disks for different H α profile types. We note here that edge-on galaxies are not included in any of these analyses, as the surface brightness measurements and thus the size measurements in these galaxies can be affected due to projection effects ².

¹Here size is referred to R_{50} . It is the circular radius containing half of the total light in a Petrosian aperture (i.e. $2 \times$ Petrosian radius).

²For edge-on galaxies, the material at different physical radii can be located in the same line-of-sight due to projection effects. Thus the azimuthally averaged profiles for these galaxies are averaged over different physical extents within them.

5.1 Stellar and H α Size-mass relation

Figure 5.1 shows the size-mass plane for stellar disks of the half light radius (Re_c ; above) and scale length (Rd_c ; below) measurements (see 4.3) for the HAGGIS galaxies measured from narrow-band continuum profiles. Plots are color-coded with the galaxy-wide (global) specific star-formation rates (sSFR). The passive galaxies that are detected in absorption are assigned very low sSFR values (10^{-12} yr^{-1} which is a detection limit of the survey). We derive a power law relation between Re_c and galaxy stellar mass which can be expressed as a linear relation in a log-log space. The best fit linear $\log(Re_c) - \log(M_*)$ relation for the HAGGIS star-forming galaxies (i.e. all galaxies except absorption and non-detections) is -

$$\log(Re_c) = 0.1596^{(+0.0212)}_{(-0.0280)} \log(M_*) - 0.9401^{(+0.2944)}_{(-0.2180)} \quad (5.1)$$

This linear fit is derived in two iterations of linear regression using equal weights for all data points. In the first iteration, all star-forming galaxies i.e. the galaxies that show significant H α emission above the detection threshold (the noise level derived using 100 blank sky apertures) are used to derive the fit parameters. This fit is shown by a blue dashed line on the plot.

A linear relation, 0.1 dex below this line, is then used as a threshold for selecting galaxies in the second iteration which is shown by a green dashed line on the plot. A new relation is obtained by excluding all galaxies below this threshold line. This new relation, shown by a red dashed line on the plot, describes the overall trend very well for the normal star-forming galaxies. The errors for the fit coefficients of this relation are obtained at 95 % confidence level by a bootstrapping method using 10000 bootstrap samples. The Spearman rank coefficient ³ for the correlation has a value of 0.74 with negligibly small p-value ⁴ at 10^{-29} suggesting that the positive correlation is highly probable.

³A statistical measure of how two variables depend on each other, without assuming a linear relation. Coefficient values range between +1 and -1 which corresponds to a perfect positive and a perfect negative correlation while a value of 0 means no correlation.

⁴The probability of the null hypothesis that “the two variables are independent of each other”. The probability is computed by obtaining the distribution of standard error on the slope of the linear relation assuming a slope to be zero under the null hypothesis. The standard error for the slope of the linear regression follows a student t-distribution given by -

$$SE_{\hat{\beta}} = \frac{\sqrt{\frac{1}{n-2} \sum_{i=1}^n (y_i - \hat{y}_i)^2}}{\sqrt{\sum_{i=1}^n (x_i - \hat{x})^2}} \quad (5.2)$$

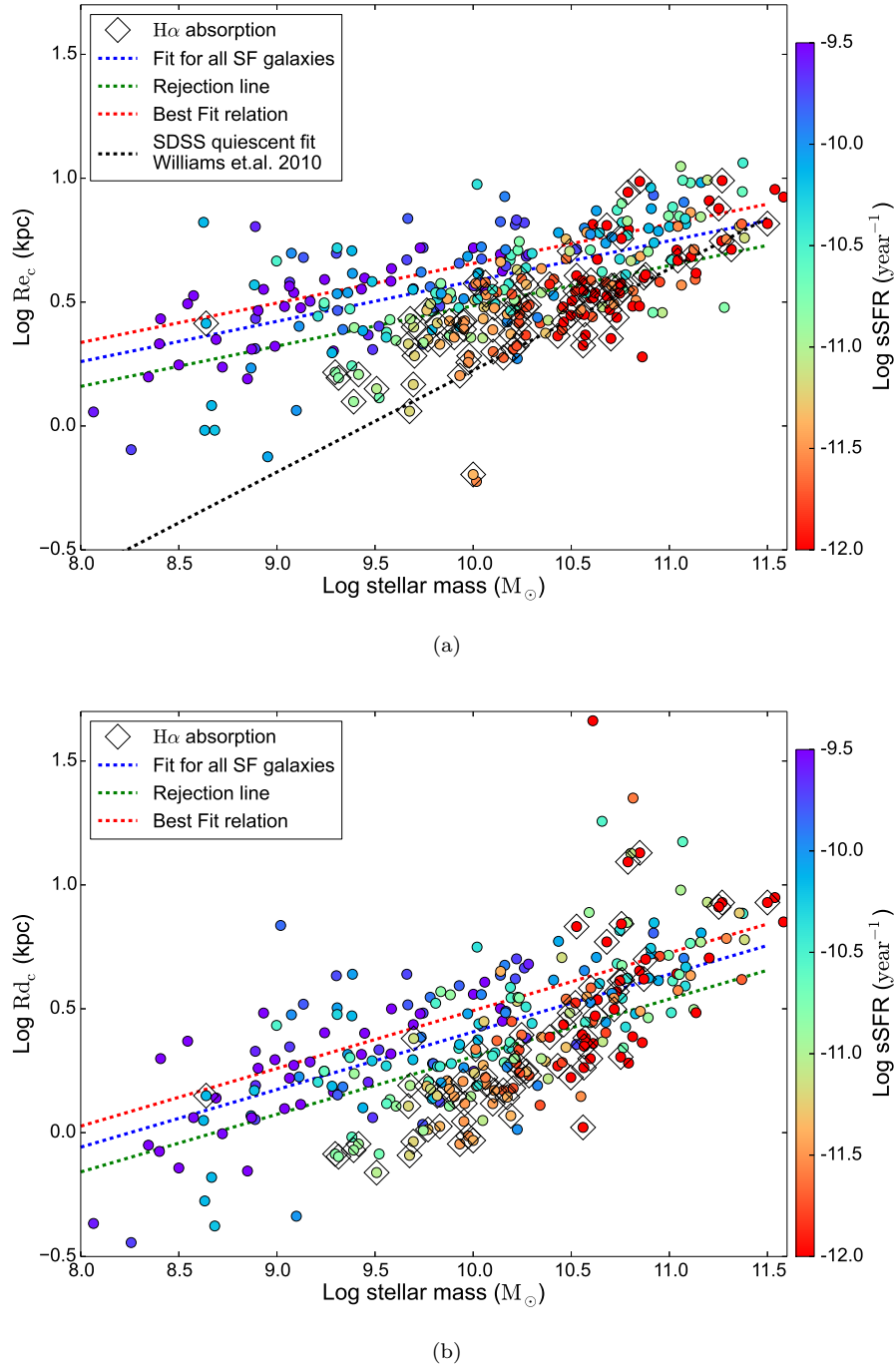


FIGURE 5.1: Size-mass relations of stellar disks using measurements of half light radii (Re_c) in 5.1(a) and main disk scale lengths (Rd_c) in 5.1(b). Both plots are color-coded by global specific star-formation rate (sSFR). This shows that the sSFR is correlated with size at fixed stellar mass such that the galaxies with low sSFR at fixed stellar mass (and galaxies detected with absorption in the HAGGIS observations) exhibit compact stellar disks.

where $SE_{\hat{\beta}}$ is the standard error on the slope ($\hat{\beta}$) of the linear relation obtained from the regression analysis, $y_i - \hat{y}_i$ is the y-residual, $x_i - \hat{x}$ is the x-residual from the fitted relation and n is the number of data points.

We observe a systematic residual correlation of galaxy size with its sSFR, such that the galaxies with low sSFR at fixed stellar mass exhibit compact stellar profiles. This is especially true for the passive galaxies which have very compact stellar sizes. This is in agreement with the relation for passive galaxies in the local universe derived using SDSS data (Williams et al. (2010)). The passive galaxies identified in the HAGGIS sample follow a similar, tight correlation which deviates notably from that of the SF galaxies towards the compact end as observed by Williams et al. (2010) for passive SDSS galaxies. The correlations of size with SFR indicates that either the mechanisms that shut down star-formation in galaxies lead to compactification of stellar disks, or that already compact galaxies are more prone to a reduction in SFR. There is an indication that these processes are more efficient at the low stellar mass end, as these galaxies show a larger deviation compared to galaxies at high mass. Figure 5.2(a) shows how the offset from the best fit $\log(\text{Re}_c) - \log(M_*)$ relation correlates with galaxy global sSFR measurements for the HAGGIS star-forming galaxies. The offset has a positive correlation with sSFR as indicated by a Spearman coefficient of 0.3 with very small p-value of 10^{-6} .

The apparent correlation of sSFR and galaxy size at fixed stellar mass could also result from the massive bulges which are seen in many quenched galaxies, as bulge light can bias the half light radius measurements towards smaller values. To disentangle the effects of bulges from the size measurements of the stellar disks, we use the continuum disk scale length which is least affected by bulge contamination. Figure 5.1(b) shows a similar size-mass relation using the disk scale length measurements obtained for the galaxies where exponential disks can be identified. The scale length for the main disk region defined during the visual classification is used, which is usually the innermost disk region of the galaxy (see 4.3). This figure is qualitatively similar to the $\log(\text{Re}_c) - \log(M_*)$ case, with the disk scale length also exhibiting a strong positive correlation with stellar mass as indicated by the Spearman rank coefficient of 0.82 with negligibly small p-value of 10^{-36} . The best fit linear relation in a log-log space obtained for the normal star-forming galaxies is given by -

$$\log(Rd_c) = 0.2331^{(+0.0243)}_{(-0.0293)} \log(M_*) - 1.8388^{(+0.3006)}_{(-0.2469)} \quad (5.3)$$

The fitting is performed in two iterations of linear regression analogous to the fitting of the $\log(\text{Re}_c) - \log(M_*)$ relation with some small differences in the selection of galaxies. Galaxies with non-exponential profiles are obviously excluded from

the plot and from the fit as they do not have scale length measurements. Galaxies with very large scale length measurements ($\log(R_d) > 1$) are also excluded from the fit as they are outliers from the general size-mass trend.

The slope of the linear fit at 0.23 ± 0.03 is quite different than the slope of $\log(R_{e,c}) - \log(M_*)$ relation (which is 0.16 ± 0.03) showing how the bulge contamination affects the size measurements especially for the galaxies at high mass end. Nevertheless, the residual correlation of galaxy sSFR with galaxy disk scale length at fixed stellar mass does exist (at least for galaxies at low to intermediate stellar masses). The trend is less clear at the high mass end. At low to intermediate stellar mass, galaxies with lower than normal star-formation rates have indeed systematically smaller disks and the larger bulges in quiescent galaxies cannot fully explain this apparent sSFR-size relation.

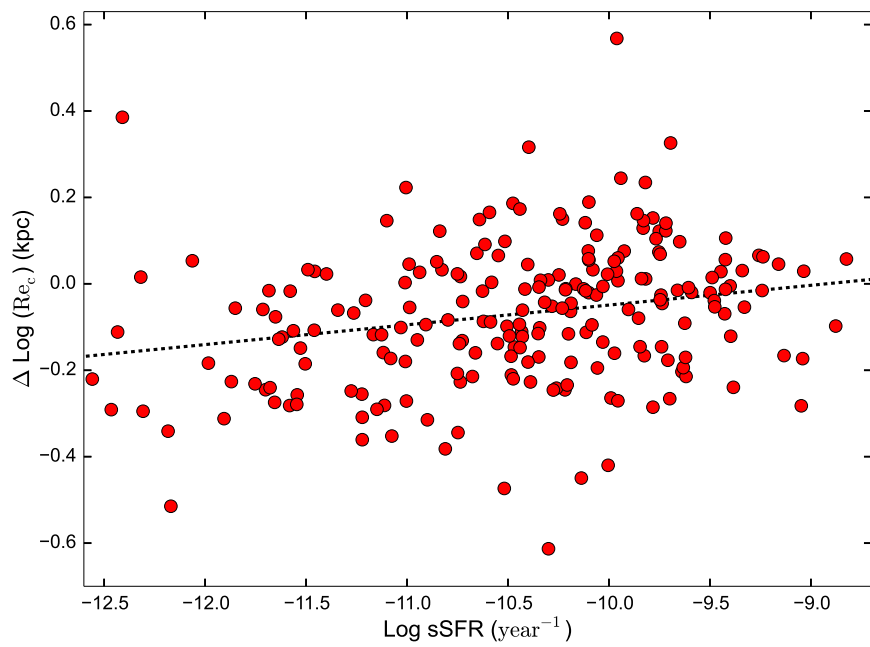
Figure 5.2(b) shows how the offset from the fitted $\log(R_{d,c}) - \log(M_*)$ relation correlates with galaxy global sSFR measurements for the star-forming galaxies. The offset has a weak positive correlation with sSFR as indicated by a Spearman coefficient of 0.19 with a p-value at 0.05.

Table 5.1 lists the coefficients of the fits along with the Spearman rank coefficient and its corresponding p-values for the $\log(R_{e,c}) - \log(M_*)$ and $\log(R_{d,c}) - \log(M_*)$ relations, as well as for the relations of the offsets from these fitted size-mass relations with global sSFRs.

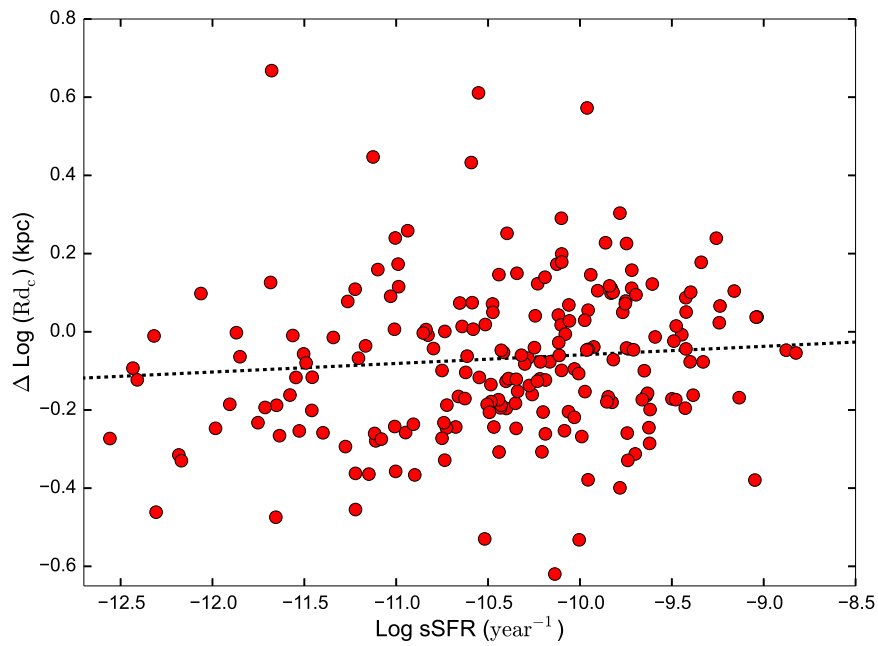
TABLE 5.1: Fit coefficients, Spearman rank coefficients, and corresponding p-values for the stellar size-mass relations in log-log space and for the respective residual relations with log sSFR.

Relation	slope	y-intercept	Spearman Coeff.	p-value
$\log(R_{e,c}) - \log(M_*)$	$0.1596^{+0.0212}_{-0.0280}$	$-0.9401^{+0.2944}_{-0.2180}$	0.74	1.22×10^{-29}
$\log(R_{d,c}) - \log(M_*)$	$0.2331^{+0.0243}_{-0.0293}$	$-1.8388^{+0.3006}_{-0.2469}$	0.82	7.08×10^{-36}
$\Delta(\log(R_{e,c}) - \log(M_*)) - \text{sSFR}$	$0.0457^{+0.0227}_{-0.0219}$	$0.4081^{+0.2358}_{-0.2310}$	0.30	4.92×10^{-6}
$\Delta(\log(R_{d,c}) - \log(M_*)) - \text{sSFR}$	$0.0152^{+0.0299}_{-0.0614}$	$0.1363^{+0.3086}_{-0.6239}$	0.19	5.01×10^{-2}

With the help of continuum-subtracted H α images, we can also study how the size of star-forming disks traced by H α emission scale with stellar mass for the HAGGIS galaxies. This is shown in fig. 5.3. Galaxies with no significant H α emission are not shown as they have no measurement of H α half light radius. Also, the H α sizes of some galaxies which have a H α emission line profile that is



(a)



(b)

FIGURE 5.2: Plots showing the correlation of the deviation from the fitted stellar size-mass relations with global sSFR using the stellar continuum (a) half light radius and (b) disk scale length measurements. Pure absorption galaxies are excluded. The black dashed line denotes the best fit relation obtained using all the data points with equal weights.

consistent with the PSF profile derived for their observations (obtained from the surrounding foreground stars) are marked by upper limits.

The H α half light size correlates positively with stellar mass as indicated by a Spearman rank coefficient of 0.77 with a negligibly small p-value at 10^{-31} . The linear fit to the $\text{Re}_{\text{H}\alpha} - M_*$ relation in a log-log space is given by the equation -

$$\log(\text{Re}_{\text{H}\alpha}) = 0.2376^{(+0.0375)}_{(-0.0345)} \log(M_*) - 1.7692^{(+0.3447)}_{(-0.3740)} \quad (5.4)$$

The fitting is performed in two iterations of linear regression analogous to the fitting of the $\log(\text{Re}_c) - \log(M_*)$ relation, with the second iteration performed by excluding the galaxies 0.1 dex below the fit obtained in first iteration. Most galaxies with low specific star-formation rates for their stellar mass are seen to lie below this tight relation. This means that the galaxies with compact H α disks are forming fewer new stars compared to the general star-forming population. This correlation is shown in figure 5.4(a) which shows that the galaxy global sSFR correlates with the deviation from the best fit $\log(\text{Re}_{\text{H}\alpha}) - \log(M_*)$ relation. The correlation is positive as indicated by Spearman rank coefficient of 0.52 with negligibly small p-value at 10^{-17} . This suggests that the size of the star-forming disks, as traced by H α emission, closely relates to the level of star-formation in the galaxy.

The H α disk scale length, on the other hand, shows a slightly weaker correlation with galaxy stellar mass, with larger scatter compared to the half light radius, as seen in fig. 5.3(b). The best linear fit for the $\log(\text{Rd}_{\text{H}\alpha}) - \log(M_*)$ relation for the normal star-forming galaxies is given by -

$$\log(\text{Rd}_{\text{H}\alpha}) = 0.1870^{(+0.0341)}_{(-0.0417)} \log(M_*) - 1.4244^{(+0.4349)}_{(-0.3423)} \quad (5.5)$$

The positive correlation is statistically significant with a Spearman rank coefficient of 0.50 at negligibly small p-value of 10^{-10} . The larger scatter in the relation can be attributed to large uncertainties in the measurement of the H α scale length due to internal structures in galaxies, the stochastic nature of the star-formation (the star-formation is often clumpy as it predominantly happens in individual HII regions), and the necessity to choose a single exponential region where galaxy H α disks are usually best described by more complex profiles. Nevertheless, the residuals show a good correlation with global sSFR which is qualitatively similar to the $\Delta(\log(\text{Re}_{\text{H}\alpha}) - \log(M_*)) - \text{sSFR}$ relation, evident from the figure 5.4(b).

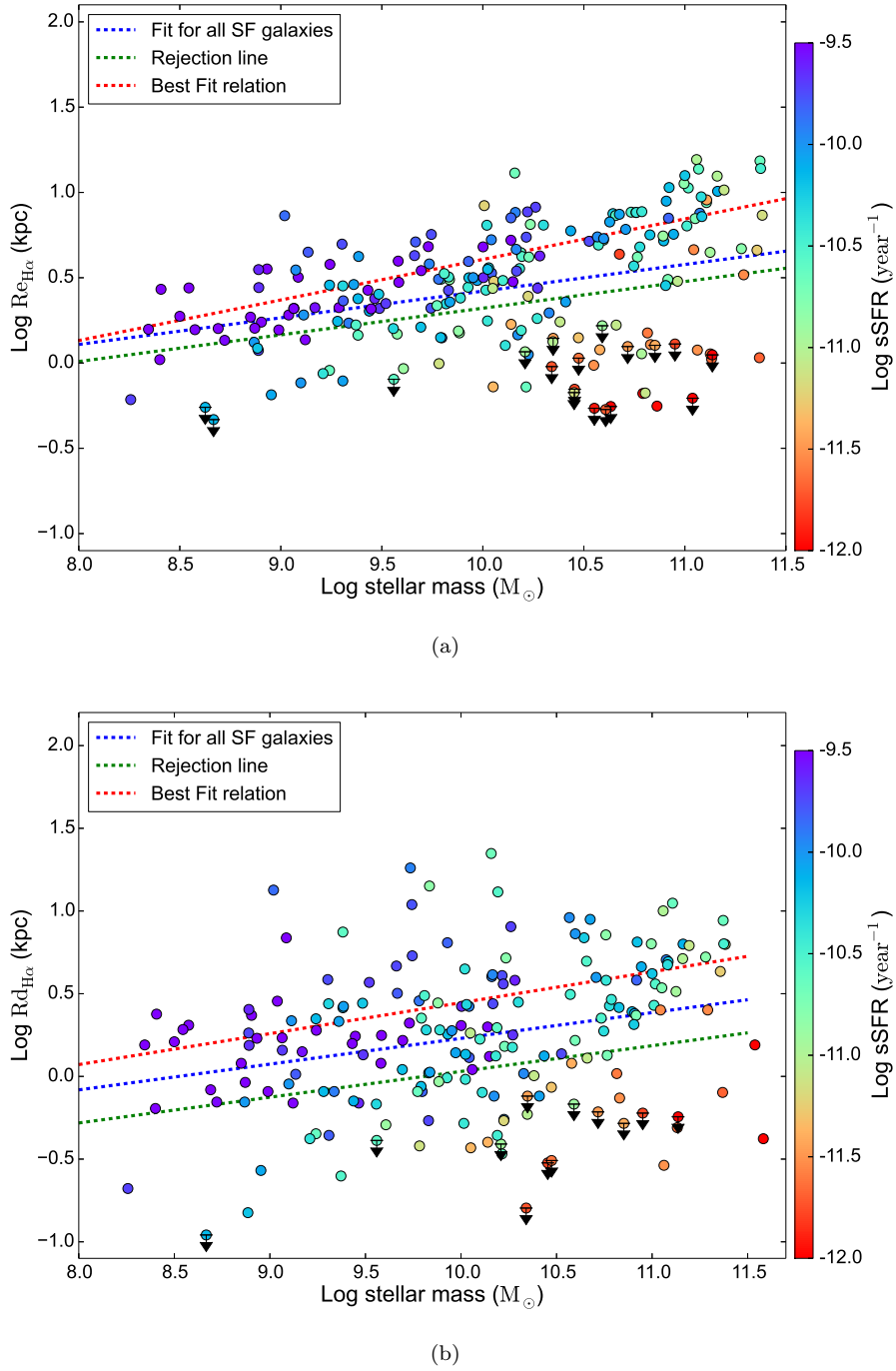
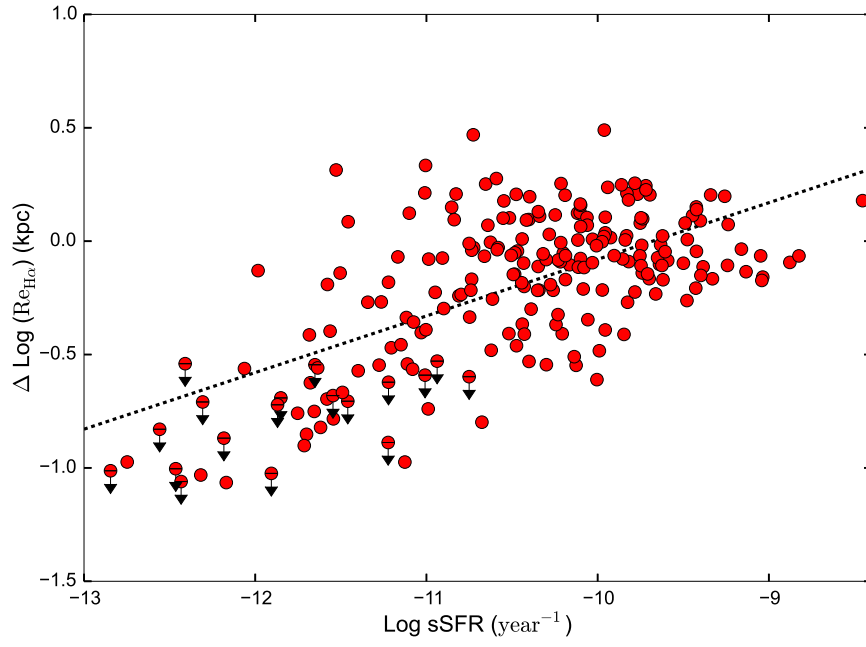
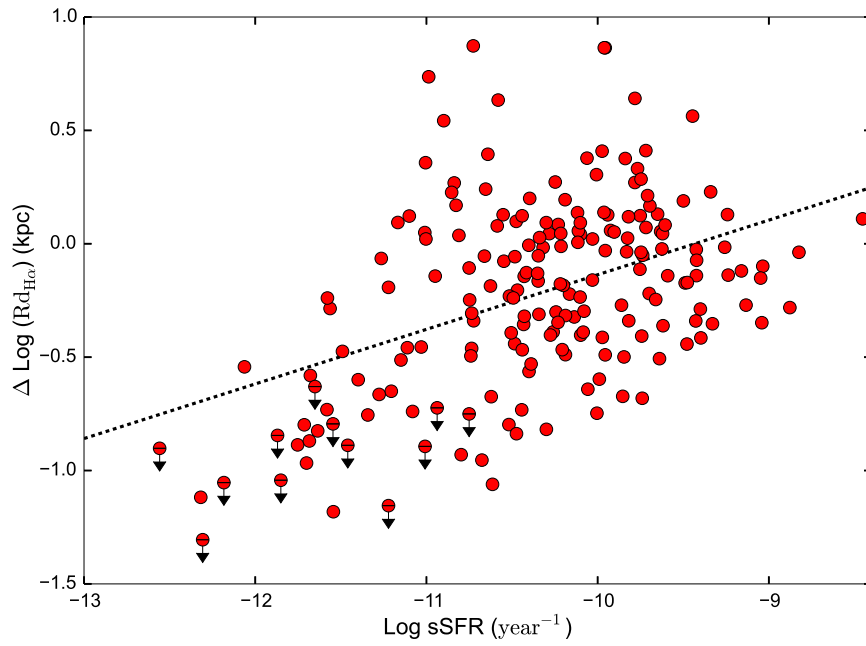


FIGURE 5.3: Size-mass relations of H α disks using the measurements of (a) half light radii ($Re_{H\alpha}$) and (b) main disk scale lengths ($Rd_{H\alpha}$). The H α sizes of galaxies which have H α emission line profile consistent with the PSF profile (obtained for a similar observing condition) are marked by upper limits. Both plots are color-coded by the global specific star-formation rates (sSFR) which shows that the galaxies with low sSFR have compact H α disks. Size of the H α disks is seen to correlate positively with stellar mass with a power law relation.

The deviation from the $\log(Rd_{H\alpha}) - \log(M_*)$ relation correlates with galaxy global



(a)



(b)

FIGURE 5.4: Plots showing the correlation of the deviation from the fitted size-mass relations for H α disks with global sSFR using (a) H α half light radius and (b) H α disk scale length measurements. Galaxies which have the H α emission line profile consistent with the PSF profile (obtained for a similar observing condition) are marked by upper limits. The black dashed line denotes the best fit relation obtained by using all the data points with equal weights.

sSFR with a Spearman coefficient for correlation at 0.39 with negligibly small p-value at 10^{-8} .

The table 5.2 lists the coefficients of linear fits along with the Spearman rank coefficient and corresponding p-values for the $\log(\text{Re}_{\text{H}\alpha}) - \log(M_*)$ and $\log(\text{Rd}_{\text{H}\alpha}) - \log(M_*)$ relations and residual relations versus global log sSFR.

TABLE 5.2: Fit coefficients and Spearman rank coefficient with its corresponding p-values for the H α size-mass relations in log-log space and for the respective residual relations with sSFR.

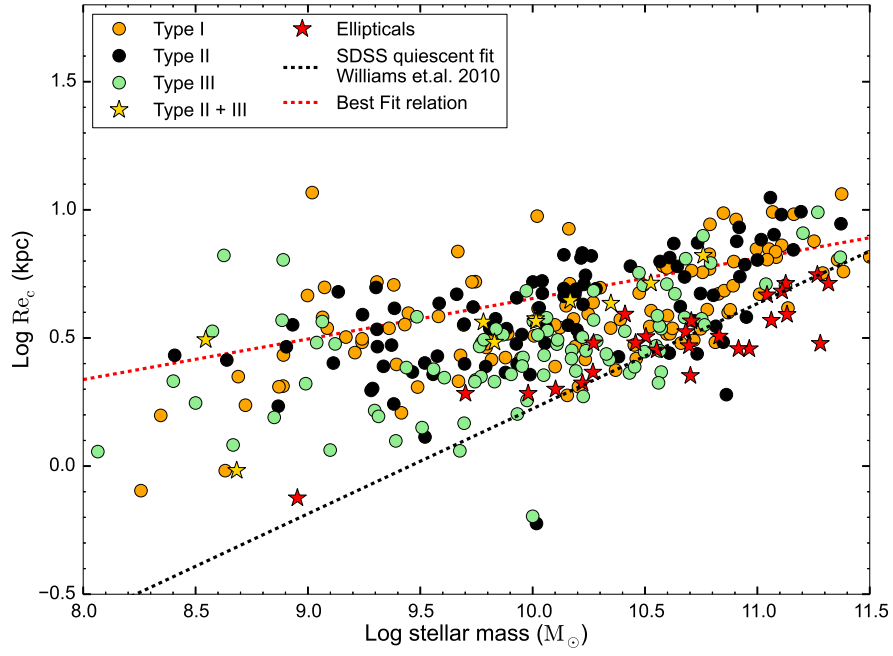
Relation	slope	y-intercept	Spearman Coeff.	p-value
$\log(\text{Re}_{\text{H}\alpha}) - \log(M_*)$	$0.2376^{+0.0375}_{-0.0345}$	$-1.7692^{+0.3447}_{-0.3740}$	0.77	9.42×10^{-31}
$\log(\text{Rd}_{\text{H}\alpha}) - \log(M_*)$	$0.1870^{+0.0341}_{-0.0417}$	$-1.4244^{+0.4349}_{-0.3423}$	0.50	6.62×10^{-10}
$\Delta(\log(\text{Re}_{\text{H}\alpha}) - \log(M_*)) - \text{sSFR}$	$0.2497^{+0.0399}_{-0.0429}$	$2.4168^{+0.4124}_{-0.4394}$	0.52	6.99×10^{-17}
$\Delta(\log(\text{Rd}_{\text{H}\alpha}) - \log(M_*)) - \text{sSFR}$	$0.2408^{+0.0557}_{-0.0646}$	$2.2717^{+0.5776}_{-0.6599}$	0.39	1.47×10^{-8}

5.2 Stellar continuum profile types

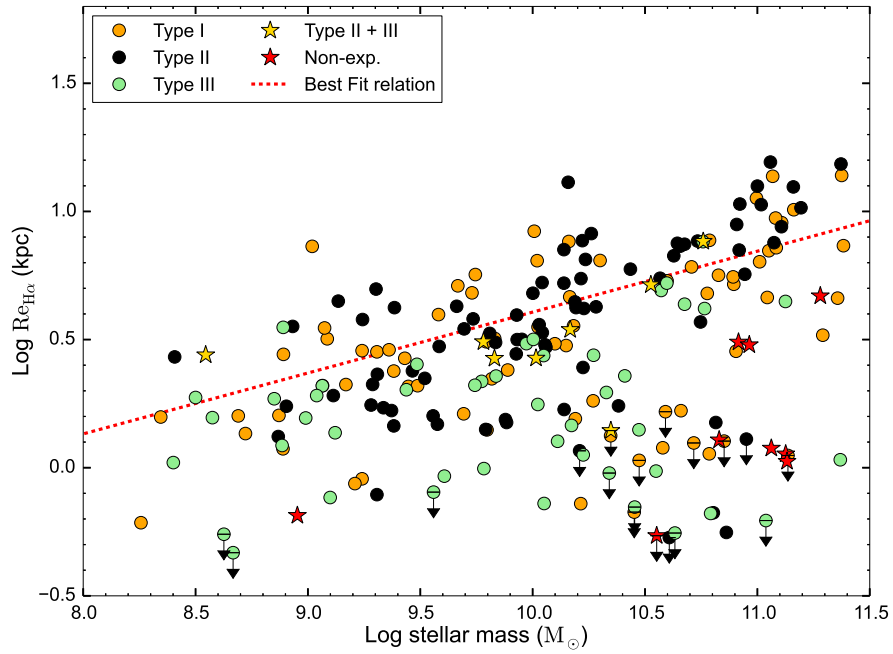
Galaxies show differences in their azimuthally averaged stellar continuum surface brightness distributions. This means that either different galaxies have assembled their stellar material in different ways or the distribution of stellar material gets altered due to some physical mechanisms. In any case, we would naively expect that the change in the distribution of stellar material would also change the distribution of star-forming gas. This argument leads to an obvious question — whether the systematic deviations seen in the galaxy stellar and H α size-mass planes relate to the differences observed in stellar surface brightness profiles. This can be tested using the classification scheme based on these profiles (see chapter 4 section 4.2).

5.2.1 Stellar and H α size-mass relations

Figure 5.5 shows stellar and H α half light size-mass relations color-coded with continuum profile type. The tight correlation seen for the passive galaxies between stellar size and mass (fig 5.1(a)) is seen to be populated mainly by type III galaxies at the low mass end and galaxies with non-exponential profiles towards the high mass end. This might suggest that when the star-forming disks



(a)



(b)

FIGURE 5.5: The size-mass relations for stellar and H α disks color-coded by stellar continuum profile types. Type III and non-exponential galaxies are observed to populate the stellar size-mass relation observed for the quenched galaxies and form a dominant population of galaxies that deviate from $\log(\text{Re}_{\text{H}\alpha}) - \log(M_*)$ relation.

are removed the underlying stellar profile is also transformed into either a non-exponential, typically elliptical type or a type III disk. Alternatively galaxies with these stellar profiles might just be more prone to quenching. It is also interesting to note that although type III galaxies show anti-truncations in their outer surface brightness profile, they have overall compact stellar half light sizes for their stellar mass. Apart from compact stellar sizes, the majority of type III galaxies also host compact H α disks for their stellar mass as seen in fig 5.5(b).

5.2.2 Offset from the size-mass relations

Figure 5.6(a) shows the distribution of the residual offsets from the best fit stellar half light size-mass relation for different continuum profile types. Type I and type II galaxies show a skewed distribution with $\sim 76 (\pm 4) \%$ of these galaxies having sizes either above or close to (within 0.2 dex) the best fit half light size-mass relation and the remaining fraction of galaxies having compact stellar sizes for their stellar mass. Type III galaxies, on the other hand, have a very different, double-peaked distribution with $\sim 49 (\pm 5) \%$ of galaxies having compact stellar sizes for their stellar mass (< 0.2 dex below the best fit relation) while galaxies with non-exponential profiles show a single peaked distribution with $\sim 77 (\pm 9) \%$ of galaxies having stellar sizes that are significantly offset from the best fit relation towards the compact end.

The K-S statistics yields 99.966 and 99.998 % confidence that type III galaxies have a different distribution for the offsets from the $\log(\text{Re}_c) - \log(M_*)$ relation than type I and type II galaxies respectively. Similarly, the differences in the distribution of offsets between non-exponentials and type I as well as between non-exponentials and type II are both confirmed at 99.999 % confidence using K-S test. On the other hand, the differences between non-exponentials and type III & between type I and type II are not significant. The latter indicates that the truncation in stellar disk does not have a significant effect on the half-light size of a galaxy.

Figure 5.6(b) illustrates the distribution of systematic offsets from the H α half light size-mass relation for different continuum profile types. All profile types except non-exponentials show a double peaked distribution with the larger peak being near to the zero offset and a secondary peak at large negative offsets corresponding to the galaxies having very compact H α disks for their stellar mass. Non-exponential galaxies show a single-peaked distribution that peaks at large

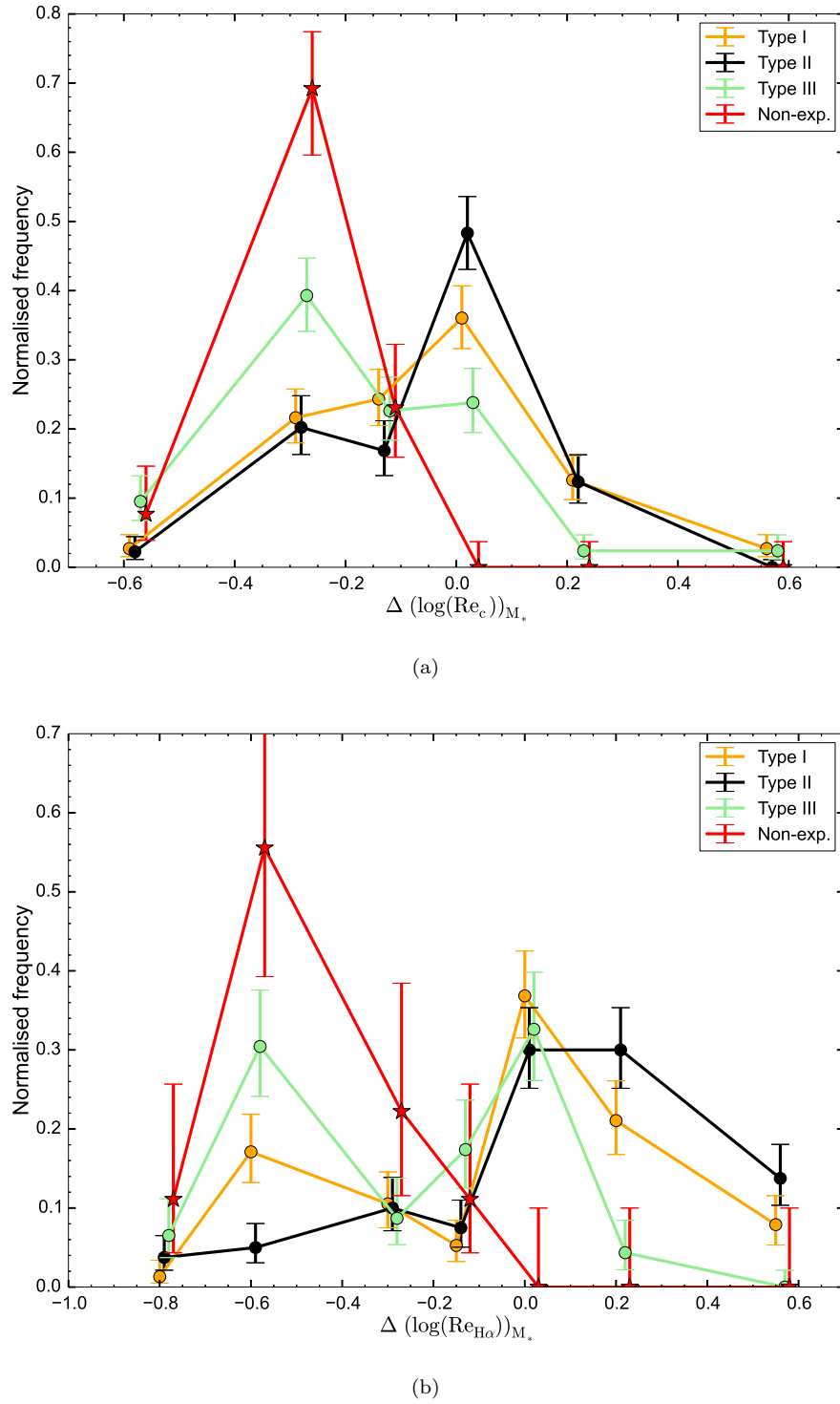


FIGURE 5.6: Distribution of the offsets from stellar continuum and H α half light sizes-mass relations among different stellar continuum profile types.

negative offsets. The differences in the distribution of offsets between type II and type III galaxies, between type II and non-exponential galaxies and between type I and non-exponential galaxies are confirmed at 99.63 %, 99.98 % and 98.15 % confidence respectively using K-S test.

5.3 H α profile types

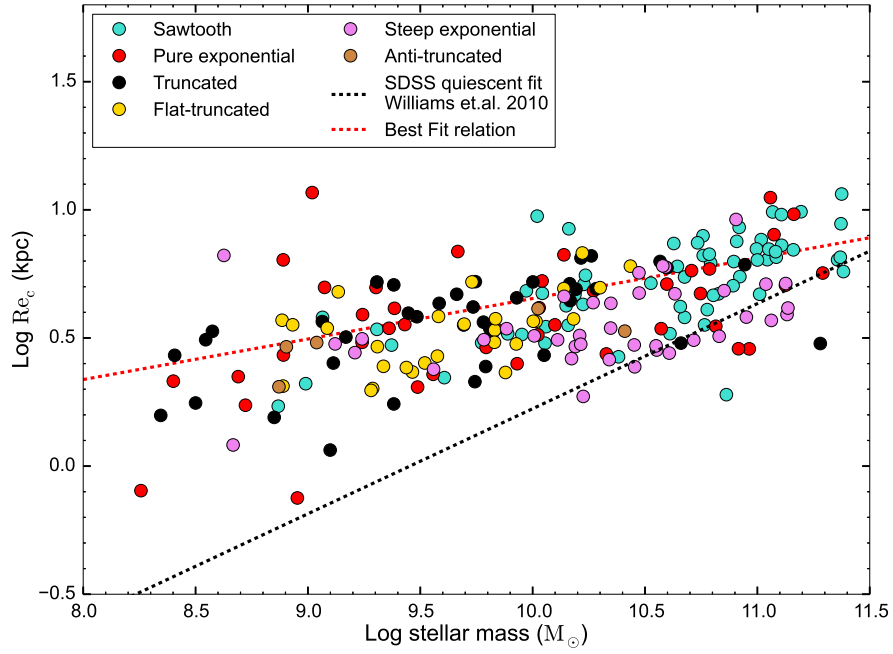
Galaxies also exhibit differences in the azimuthally averaged H α surface brightness distributions. We have classified the emission line galaxies in the HAGGIS survey into 6 types based on the shape of their H α surface brightness profiles (see section 4.2.2). The comparison of global size measurements for different H α profile types can help us understand whether the the distribution of star-forming gas affects the stellar and H α size-mass relations.

5.3.1 Stellar and H α size-mass relations

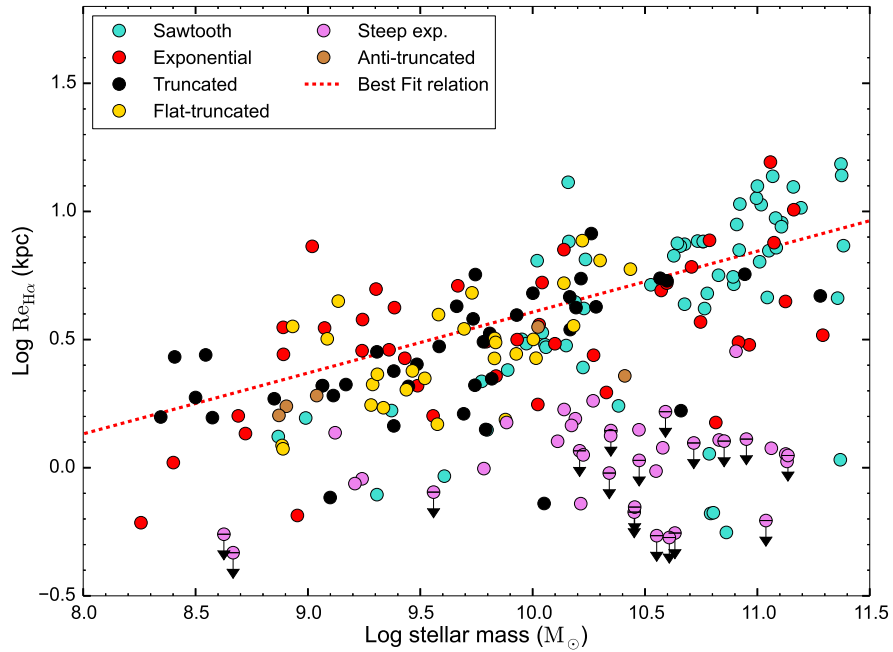
Figure 5.7 shows the stellar continuum and H α half light size-mass relations color-coded with H α profiles types for all star-forming galaxies, i.e. for galaxies that have some H α emission. The exponential-truncated and flat-truncated galaxies lie on the fitted relations in both of these plots, which is expected to be populated by normal star-forming galaxies. This indicates that the truncations in H α disks do not affect the overall half light sizes of stellar or H α disks. Also, these galaxies are predominantly seen at low stellar mass which indicates that the physical mechanisms causing H α disk truncations are less efficient at high mass. Sawtooth galaxies are seen to be the dominant population at high mass. Galaxies that deviate to more compact stellar sizes are mainly steep exponentials, with a few other H α profile types (apart from the absorption galaxies which are not shown on the plot). Similarly, galaxies that deviate to more compact H α sizes are mainly steep exponentials along with some sawtooth and other profile types.

5.3.2 Offset from the size-mass relations

Figure 5.8(a) illustrates the distribution of residual offsets from the stellar half light size-mass relation for different H α profile types. Galaxies with exponential, truncated and steep exponential profiles show a double peaked distribution similar to the one shown by type III galaxies while sawtooth and flat truncated galaxies show a single-peaked distribution that peaks near to the zero offset and absorption galaxies show a single-peaked distribution that peaks at large negative offset that corresponds to compact stellar sizes. 10 (± 4) % of sawtooth, 14 (± 6) % of flat-truncated, 20 (± 6) % of truncated, 27 (± 7) % of exponential, 44 (± 8) % of steep



(a)



(b)

FIGURE 5.7: Size-mass relations for stellar and star-forming disks color-coded by H α profile types. Only SF galaxies in HAGGIS sample are shown here ($\log(\text{Re}_c) - \log(M_*)$ for the passive galaxies can be seen in fig. 5.5(a)). Steep exponential galaxies dominate the population having compact H α and stellar sizes. Truncated and flat-truncated galaxies are found on the fitted relations i.e. their half light sizes are relatively large.

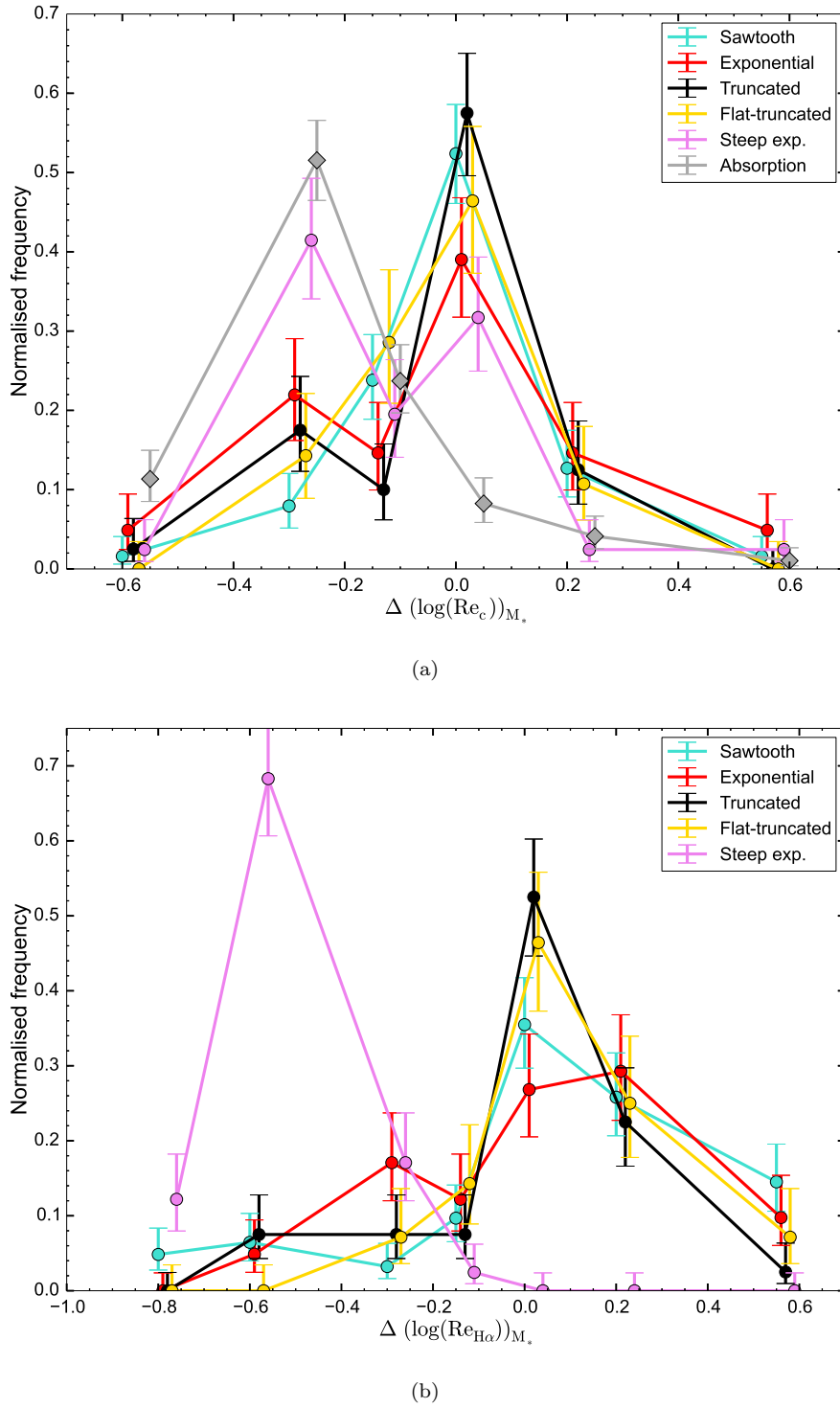


FIGURE 5.8: Distribution of the offsets from stellar and H α size-mass relations for different H α profile types.

exponential and 63 (± 5) % of absorption galaxies have compact stellar disks for their stellar mass (< 0.2 dex of the best fit relation).

The differences in the distribution of offsets are confirmed using the K-S test at

99.999 % confidence for absorption galaxies when compared with the individual distributions for the galaxies showing sawtooth, exponential, truncated and flat-truncated profiles. Similarly, the differences in the distribution of offsets between steep exponentials with other profile types are confirmed at 99.95 % with truncated galaxies, 99.78 % with sawtooths, 98.3 % with absorption galaxies, 97.98 % with flat-truncated galaxies and 96.09 % with exponentials using K-S test. The differences in the distribution of offsets between sawtooth, exponential, truncated and flat-truncated types are not statistically significant.

Figure 5.8(b) illustrates the distribution of residual offsets from the H α half light size-mass relation for different H α profile types. All galaxies except steep exponentials have very similar distributions. Steep exponentials almost by their definition have compact H α disks for their stellar mass and hence almost all of them have negative offsets from the relation. 0_{-0}^{+3} % of flat-truncated, 11_{-3}^{+5} % of sawtooth, 8_{-3}^{+5} % of truncated, 5_{-2}^{+5} % of exponential and 81_{-7}^{+5} % of steep exponential galaxies have compact H α disks for their stellar mass (< 0.2 dex of the best fit relation). The K-S test also yields 99.9999 % confidence that the distribution of offsets for steep exponentials is different when compared to the individual distributions for all other H α profile types. But the distribution of offsets for other types are not significantly different from one another.

5.4 Comparison of H α and stellar sizes

By comparing the spatial distribution of star-formation in galaxies with the distribution of already formed stars, we can infer whether galaxies are growing by adding new stars in the outer regions (an inside-out growth scenario). In a hierarchically growing universe, galaxies are considered to grow via accretion of gas (and also by occasional mergers). The galaxy environment is known to play a role in controlling the supply of cold gas in galaxies (e.g. Cortese et al. (2011)). Environmental interactions such as ram pressure stripping are more effective in the outer regions of galaxies as the gas is less tightly bound. This reduces the size of star-forming disks — i.e. outside-in suppression of SF (Bekki (2014)). Koopmann et al. (2006) found that galaxies in the Virgo cluster have, on average, 20 % smaller star-forming disks compared to their stellar disks while the field galaxies in their sample have on average larger star-forming disks than their stellar disks.

Figure 5.9 shows how the H α half light radius compares with the stellar continuum half light radius for different H α profile types. AGNs identified in SDSS DR7 data release using the precepts discussed in Brinchmann et al. (2004) are shown with open circles. The figure illustrates that the large majority of HAGGIS galaxies have star-forming disks smaller than their stellar disks. This agrees with the findings of Koopmann et al. (2006) in Virgo and implies that size growth in galaxies does not happen via extended star-forming disks in the local universe, at least for the bulk of population living in groups. To be sure, there are some exceptions which indeed have larger star-forming disks than their stellar disks. The majority of such galaxies have a sawtooth H α profile. Sawtooth galaxies have a central excess which is followed by an intermediate dip in surface brightness; indeed sometimes H α can be seen in absorption in that region. Gas in this region is probably redistributed to the center and/or outer disk, which affects the H α half light radius. Sawtooth galaxies are generally dominant at higher stellar mass and can be bulge dominated. This means that the continuum half light radius can be biased towards lower values due to bulge contamination. Both of these effects likely work together to drive larger H α half light sizes compared to stellar half light sizes.

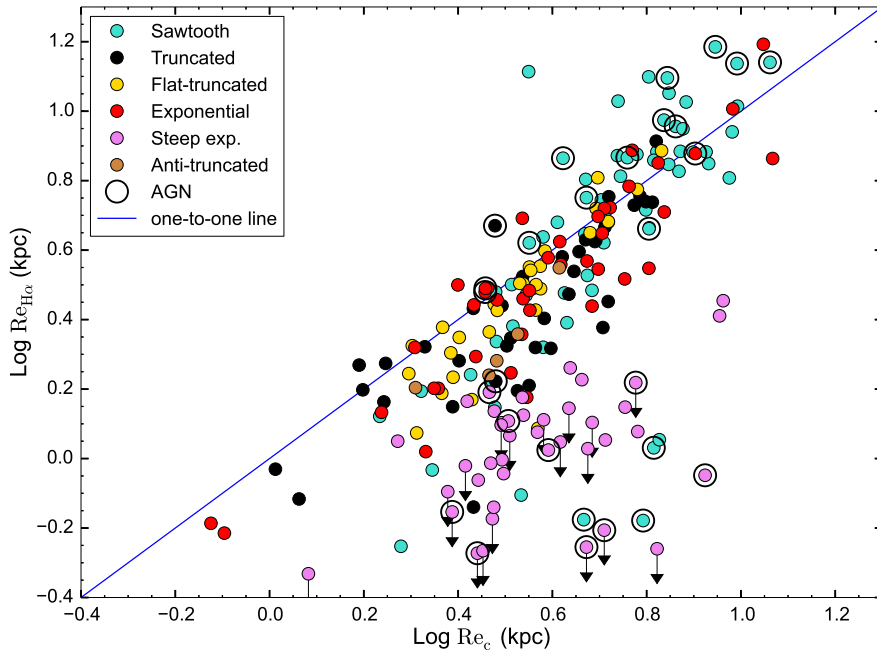


FIGURE 5.9: H α half light radius vs continuum half light radius for HAGGIS galaxies color-coded by H α profile types. AGNs identified in the SDSS DR7 catalog are shown with open circles. The majority of HAGGIS galaxies have compact H α disks compared to their stellar disks.

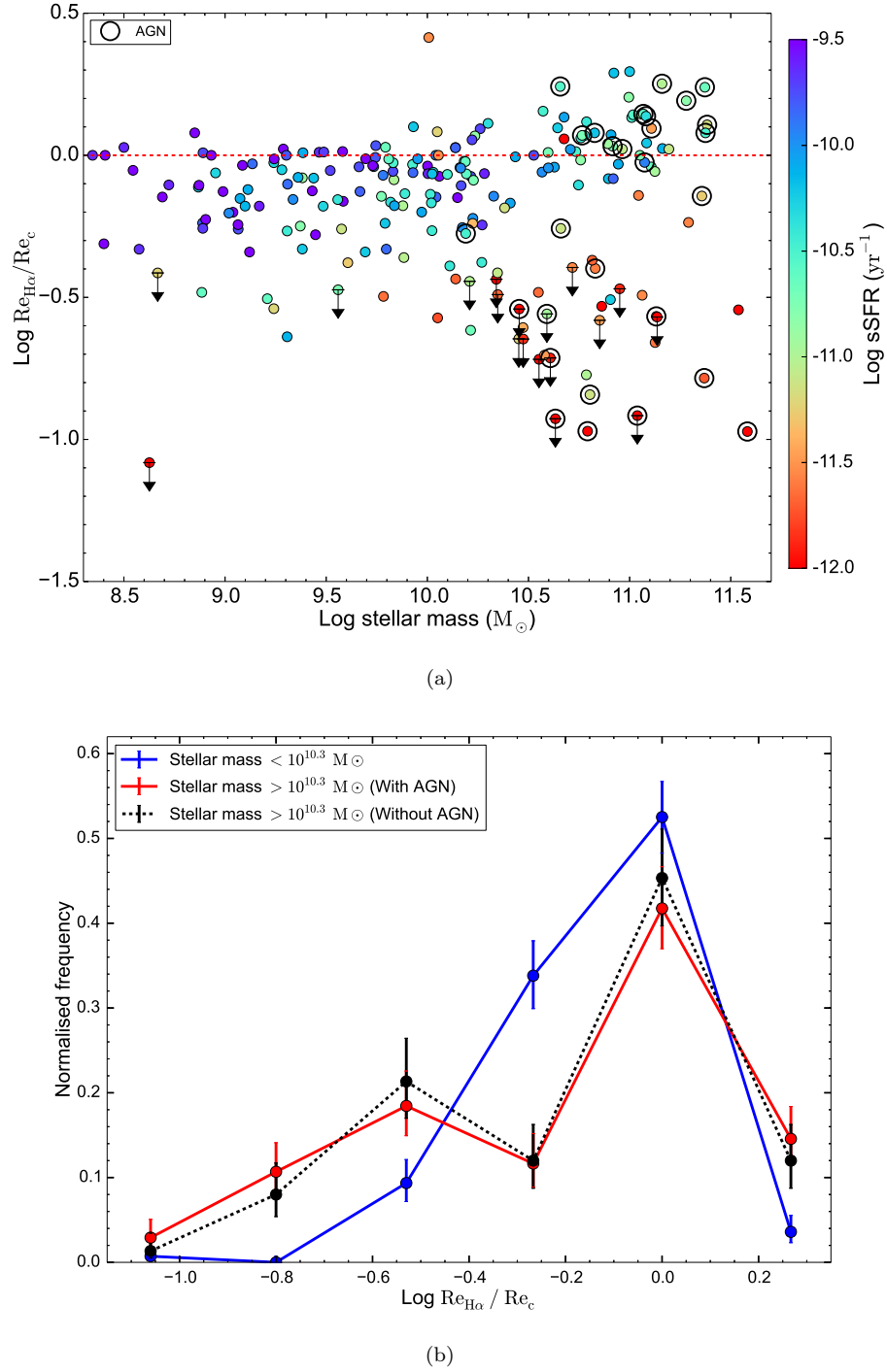


FIGURE 5.10: Upper panel (5.10(a)) shows the logarithmic ratio of H α half light size to stellar continuum half light size vs galaxy stellar mass while the lower panel (5.10(b)) shows the distribution of the size ratio for two mass bins. Most of the low mass galaxies have smaller H α sizes compared to their stellar sizes while high mass galaxies show a dichotomy in size ratios with some galaxies exhibiting similar or larger H α sizes and others exhibiting very compact H α sizes compared to their stellar sizes.

Galaxies which are relatively compact in their H α have a mix of H α profile types, dominated by steep exponential galaxies which show the largest deviation (as expected), while sawtooth galaxies form the largest minority of galaxies with the most compact H α disks compared to their stellar disks. Most of the galaxies identified with AGN have either steep exponential or sawtooth profiles with four exceptions. Table 5.3 lists the median for the ratio of $\text{Re}_{\text{H}\alpha}$ to Re_c for different profile types. It shows that the median sizes for all H α profile types lie slightly below the one-to-one ratio with steep exponentials showing the smallest ratios.

Fig. 5.10(a) shows the ratio of H α to stellar disk size vs stellar mass color coded by the global sSFR. The majority of low mass galaxies ($\log(M_*) < 10.3$) have smaller H α sizes than stellar sizes. Galaxies that deviate below the ratio of unity show a lower star-formation activity compared to galaxies having a ratio close to unity. The high mass galaxies show a distinct dichotomy in the size distribution with many galaxies showing either a larger H α size compared to their stellar size or else very compact H α disks as shown in figure 5.10(b). This dichotomy exists even when we exclude the galaxies identified with AGN. The low mass galaxies on the other hand shows a single peaked, skewed distribution of size ratios. The difference in the two distributions is confirmed by a K-S test at 99.66 % confidence when galaxies with AGNs are included in high mass bin and at 97.26 % confidence when they are excluded. This striking difference between the size ratio distributions in the two mass regimes might indicate either that different mechanisms operate, or that a mechanism reducing H α disk sizes operates at a much faster pace in high mass galaxies leaving very few intermittent objects.

TABLE 5.3: Showing median values of the ratio of $\text{Re}_{\text{H}\alpha}$ to Re_c for different H α profile types.

Profile types	Median ($\text{Re}_{\text{H}\alpha}/\text{Re}_c$)
Sawtooth	0.96
Exponential	0.87
Truncated	0.86
Flat-truncated	0.92
Steep Exponential	0.31

5.5 Conclusions

In this chapter, we have presented the stellar and H α size-mass relations and compared the sizes of H α disks with their respective stellar sizes for the galaxies in the HAGGIS sample. We have also used our classification schemes based on the

stellar and H α surface brightness profiles to understand the systematic differences in these relations.

It has been observed that sizes of stellar and H α disks, as measured by their half light radius as well as by the scale lengths of the main disk component, show a strong positive correlation with a galaxy’s stellar mass. All of these size measurements for the star-forming galaxies follow, on average, power law relations with galaxy’s stellar mass. These strong correlations suggest that the amount of stellar material in a galaxy is effective in regulating the stellar and H α disk sizes.

These relations agree well with the expectations from cosmological simulations and with other similar observations especially for the stellar size-mass relation (see e.g. [Shen et al. \(2003\)](#), [Williams et al. \(2010\)](#), [Dutton & van den Bosch \(2012\)](#), [Lange et al. \(2015\)](#), etc). Also, the existence of a H α size-mass relation can be inferred indirectly from some studies that compared the H α disk sizes with the size of their stellar disks in the local universe (e.g. [Koopmann et al. \(2006\)](#), [Fossati et al. \(2013\)](#)).

Although the size of the stellar and H α disks are observed to scale with the galaxy’s stellar mass, there is a large scatter in these relations. We have found that galaxies that are quenched or forming stars less rapidly than normal star-forming galaxies of a similar stellar mass have compact stellar sizes compared to the normally SF galaxies. This is consistent with the findings of [Williams et al. \(2010\)](#) who have also noted this ‘compactification’ of stellar disks in the SDSS dataset for the quenched galaxies. We extend this result by showing that the galaxies at fixed stellar mass, that have SF activity lower (but significant enough for HAGGIS measurements) than normal SF galaxies are also found to host relatively compact H α disks compared to the normal SF galaxies in our sample. These results suggest that the sizes of the stellar and H α disks are also governed by the rate of star-formation at fixed stellar mass and suggest that the quenching mechanisms that shut down the SF activity in galaxies totally, or even partially, make the stellar and H α disks more compact.

We have also made attempts to understand these correlations in the context of stellar and H α profile types in order to understand whether the effects of partial or total SF quenching are imprinted on the distribution of stellar and star-forming material. The majority of stellar type III galaxies are found to be more compact than type I and type II galaxies, and make up a large fraction of the compact galaxy population at lower mass. Galaxies with non-exponential profiles are more common in high mass compact galaxies.

This suggests that the quenching of star-formation and associated physical processes possibly play a significant role in establishing the diversity of disk surface brightness profiles, especially for the anti-truncated type III profiles. This will provide more constraints for the formation mechanisms for these anti-truncated profiles, as these mechanisms are still largely debated (e.g. [Younger et al. \(2007\)](#), [Minchev et al. \(2012\)](#), [Borlaff et al. \(2014\)](#), etc). The compact sizes of type III profiles observed here are in general agreement with the recent hydrodynamical simulations done by [Herpich et al. \(2015\)](#) which suggest that the type III profiles have the lowest angular momentum among all of the disk profile types.

Among the H α profile types, we have observed that the majority of HAGGIS galaxies that are detected with H α in absorption (passive galaxies) have compact stellar sizes and they follow the size-mass relation that is obtained for the quenched SDSS galaxies by [Williams et al. \(2010\)](#). Apart from this, galaxies having steep exponential H α profiles often show a compact stellar disk suggesting that these galaxies may be on their way to be fully quenched. It also indicates that the compactification of H α disks also affects the stellar disk size. On the other hand, galaxies with truncated and flat-truncated H α profiles are observed to lie close to the fitted stellar and H α size-mass relations which means that the truncation in the H α disk has minimal to no effect on the half light size of their stellar and H α disks (because the break is usually beyond this radius).

Many galaxies in the HAGGIS survey are observed to have smaller H α disks compared to their stellar disks. This is similar to what [Koopmann et al. \(2006\)](#) observed in Virgo cluster galaxies. As HAGGIS galaxies typically reside in less dense regions, this indicates that the environment has a significant effect on SF disks even in galaxies living in less dense groups. The majority of the low mass HAGGIS galaxies ($M_* < 10^{10.3} M_\odot$) have smaller H α disks than their stellar disks while the high mass galaxies ($M_* > 10^{10.3} M_\odot$) show a dichotomy in size ratios, with many high mass galaxies having larger H α disks than their stellar disks, while some show very compact H α disks. This suggests that either different quenching mechanisms operate in the two mass regimes, or that the mechanism operates at a much faster pace in high mass galaxies leaving very few intermittent objects.

These results suggest that quenching mechanisms have stronger effects not only on the galaxy SFR but also on the size and the distribution of galaxy stellar and star-forming material and while the effects are stronger in some galaxies (e.g. type III or steep exponentials), the majority of galaxies that live in the group environment have been affected to some extent.

Chapter 6

Relation between star formation rate, stellar mass and $Re_{H\alpha}/Re_c$

Normally star-forming galaxies are known to follow a well defined star-formation rate - stellar mass (SFR – M_*) relation known as the “star-forming main sequence” (SF MS) ([Brinchmann et al. \(2004\)](#), [Elbaz et al. \(2007\)](#), [Salim et al. \(2007\)](#), etc). This relation is generally expressed as

$$\text{Log } \Psi = \alpha \text{ Log } M_* + \beta \quad (6.1)$$

with α and β being free parameters. The values of α (slope of the MS) and β (MS normalization) are found by fitting the observed MS relation. Galaxies in local universe are observed to follow a relation with $\alpha \sim 0.7\text{-}1.0$ (e.g. [Elbaz et al. \(2007\)](#), [Elbaz et al. \(2011\)](#), [Zahid et al. \(2012\)](#), etc).

The differences in the local SFR MS can be attributed to the use of different star-formation rate indicators and their respective uncertainties in measuring the SFR as well as to the selection effects and differences in the selection of the star-forming population (see [Speagle et al. \(2014\)](#) for detailed description). This makes it difficult to compare the relations between two different studies, and to understand whether systematic differences exist in the relation with respect to other galaxy properties like morphology as well as with galaxy’s local and global environment. An accurate relative calibration is required to put SFR indicators from different observations on the same scale and to define the star-forming population in a similar way (e.g. [Speagle et al. \(2014\)](#)). Alternatively, one can use a larger survey

encompassing galaxies over a broad range in stellar mass and environment within which one can make an internal comparison (e.g. [Gavazzi et al. \(2015\)](#)).

With HAGGIS survey, we have resolved $H\alpha$ observations for a large sample of galaxies over a broad range in stellar and group halo mass. With these measurements, we can compare the distribution of SF in galaxies with different $H\alpha$ and stellar continuum profiles and which live in different environments. This is primarily interesting as it allows us to test the paradigm that galaxies are either forming stars at consistent rates with the SF MS, or are mostly passive. I.e. with spatially integrated SF, do we find many intermediate “green valley” objects, and how do they look? Chapter 5 suggests that compact $H\alpha$ disks are indeed found in objects with low SF so we shall explore this further.

In chapter 4, we have seen that the HAGGIS total integrated SFR measurements are systematically different than the SDSS aperture-corrected SFR measurements especially at high stellar mass (figure 4.8(b)). The origin of these systematic differences can be inferred by comparing the residual offsets from the SFR-stellar mass relation for the two measurements. A comparison with similar residual offsets obtained for the fiber SFR measurements in both surveys, would help us further in understanding the effects of the aperture on the SDSS SFR estimation.

We compare the SDSS and HAGGIS fiber SFR measurements in section 6.1, HAGGIS global (integrated) SFR and SDSS aperture corrected SFR measurements in section 6.2, and HAGGIS and $H\alpha 3$ global SFR measurements in section 6.3 using SFR - stellar mass diagrams and by obtaining the distributions of offset from the respective SF MS for these measurements. Section 6.4 describes the SF MS obtained using the HAGGIS global SFR and the SDSS aperture corrected SFR measurements in the context of $H\alpha$ profile types, the correlation between the difference in these two SFR measurements and $Re_{H\alpha}/Re_c$ is described in section 6.5, and finally the correlation of offset from SF MS and $Re_{H\alpha}/Re_c$ is discussed in the context of $H\alpha$ profile types in section 6.6.

6.1 SDSS and HAGGIS fiber SF MS comparison

Figure 6.1 shows the SFR - stellar mass plane using fiber SFR measurements for both HAGGIS and SDSS. The SDSS SFR is derived using $H\alpha$ fiber luminosities converted into SFRs using the [Kennicutt & Evans \(2012\)](#) calibration which

assumes a universal Kroupa IMF. $H\alpha$ fiber luminosities are computed using publicly available, extinction corrected fiber $H\alpha$ fluxes from SDSS DR7 (http://www.mpa-garching.mpg.de/SDSS/DR7/raw_data.html). Our calibration of SFR is applied identically for both HAGGIS and SDSS datasets. The SDSS calibration based on the techniques mentioned in Brinchmann et al. (2004) is not possible to apply self-consistently for the HAGGIS narrow-band data (see discussion in chapter 4 section 4.4).

The contours represent SDSS galaxies with $0.01 < z < 0.055$ (redshift range of HAGGIS survey) excluding the AGNs and composite galaxies for which the SFR measurements are unreliable. The contour levels reveal that the distribution of SFR at fixed stellar mass shows a dichotomy. The grey and purple points denote the measurements from the SDSS and HAGGIS dataset respectively for the “HAGGIS star-forming galaxies” including only galaxies that show significant $H\alpha$ emission somewhere in their HAGGIS profile and excluding the AGN and composite galaxies. The HAGGIS fiber SFR measurements for these SF galaxies agree with SDSS measurements which we have also seen in chapter 4 (figure 4.7(a)).

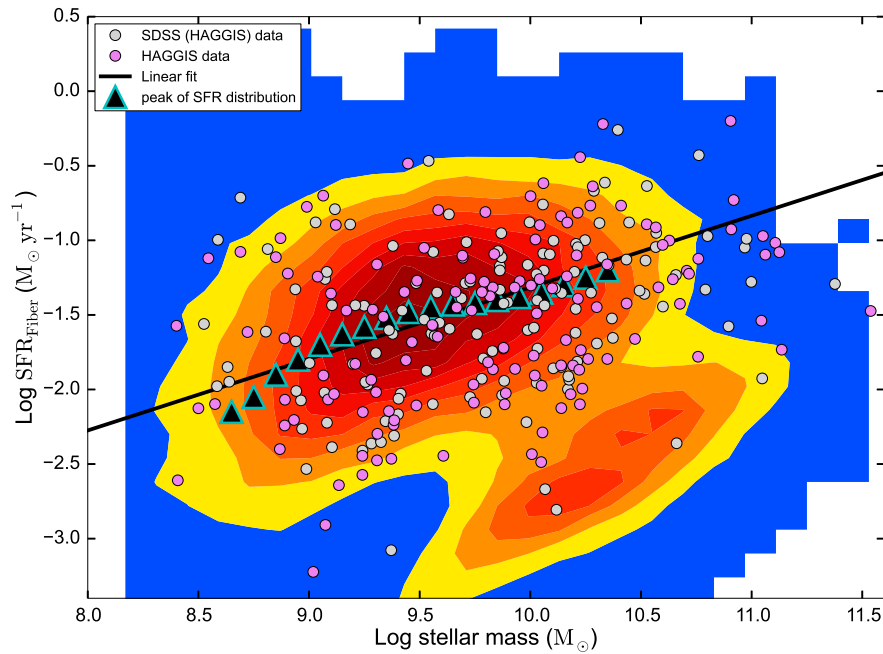


FIGURE 6.1: Fiber SFR - M_* (SFR integrated over central 3" SDSS fiber diameter). The contour levels correspond to the whole SDSS dataset in the redshift range of HAGGIS survey while the purple and gray points represent the HAGGIS and SDSS measurements respectively for the HAGGIS SF galaxies. The MS fit (black line) is derived by identifying the peak of the SFR distribution in narrow M_* bins (large triangles).

We have obtained a fit to the SF MS using the full SDSS dataset in the redshift range of HAGGIS survey ($0.01 < z < 0.055$) in order to use the better statistics provided by the larger dataset. To derive the fit, we have obtained the distributions of SFR in narrow stellar mass bins of bin size $0.1 M_{\odot}$ and visually identified the peak of the distribution which is shown by large triangles on the plot for each stellar mass bin. The linear fit to these individual measurements is shown by the black solid line and is given by -

$$\text{Log } \Psi = 0.48 \text{ Log } M_{*} - 6.11 \quad (6.2)$$

Figure 6.2 shows the normalized distributions of the deviation from this MS fit ($\Delta(\log(\text{SFR}))_{M_{*}}$). The grey distribution corresponds to all SDSS galaxies in the HAGGIS redshift range ($0.01 < z < 0.055$) excluding AGNs and composites while the dashed red distribution corresponds to the SDSS fiber measurements for all HAGGIS galaxies excluding AGNs and composites. The errors on the distribution are derived assuming that the fraction of galaxies in each bin of $\Delta(\log(\text{SFR}))_{M_{*}}$ compared to the total number of galaxies follows a binomial distribution. The distribution for the whole SDSS survey in the redshift range of HAGGIS galaxies shows the bi-modal distribution formed by SF and passive galaxies. The SDSS SFR distribution for overall HAGGIS galaxies (red) show much stronger bi-modality formed by two similar amplitude peaks compared to the distribution for the whole SDSS sample (grey) indicating that the HAGGIS survey contains a higher proportion of passive galaxies than the overall SDSS galaxies in the local universe. This difference is probably due to the selection: HAGGIS galaxies are selected to lie in groups which typically contain a larger fraction of passive galaxies.

The distribution of $\Delta(\log(\text{SFR}))_{M_{*}}$ shown by the solid red line corresponds to the SDSS fiber SFR measurements obtained for the ‘‘HAGGIS star-forming galaxies’’ while the distribution of $\Delta(\log(\text{SFR}))_{M_{*}}$ shown by the solid blue line corresponds to the HAGGIS fiber SFR measurements obtained for the same galaxies. The two distributions are very similar for star-forming galaxies indicating again that the measurements of fiber SFRs are consistent for the two datasets. Nevertheless, small differences are observed in the two distributions. This can possibly be explained by the differences in seeing, accuracy of continuum estimation and subtraction, correction for galactic dust and NII contamination (latter is only applicable to the HAGGIS dataset), etc.

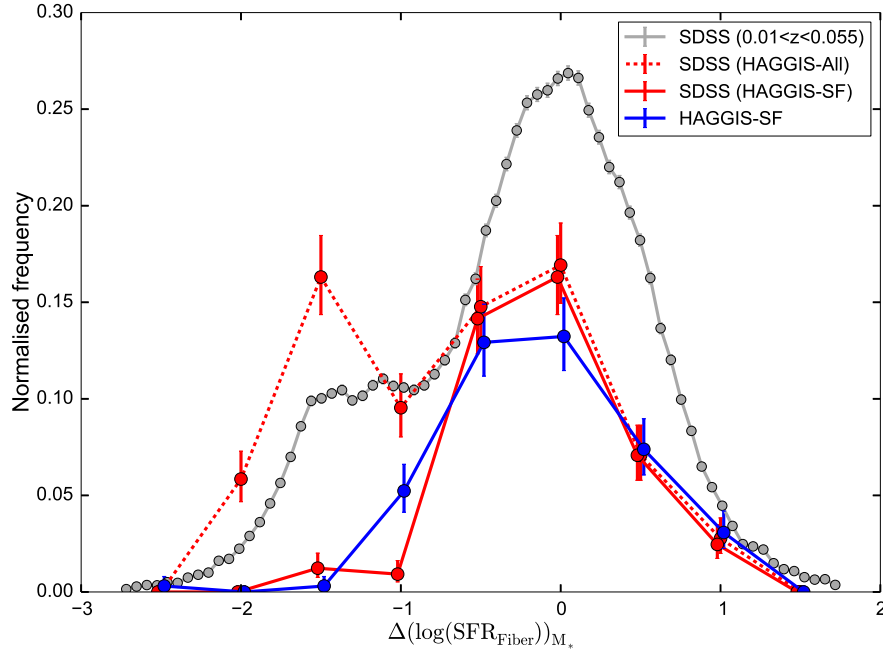


FIGURE 6.2: Distributions of $\Delta(\log(\text{SFR}_{\text{Fiber}}))_{M_*}$ for the whole SDSS dataset for $0.01 < z < 0.055$ (grey), for SDSS measurements for all galaxies in HAGGIS survey (dashed-red) and for SDSS measurements (red) and for the HAGGIS measurements (blue) just for the HAGGIS SF galaxies.

Also the bi-modality in the SFR distribution observed for the SDSS measurements for overall HAGGIS and SDSS galaxies is not visible for the “HAGGIS star-forming galaxies” for both HAGGIS and SDSS measurements. The faint $H\alpha$ emission in the galaxies with low SF activity remain possibly undetected in HAGGIS observations which might be the reason behind the non-existence of a bi-modality in “HAGGIS star-forming galaxies”.

6.2 SDSS and HAGGIS global SF MS comparison

Figure 6.3 shows how HAGGIS total (integrated) SFR measurements compare to the SDSS aperture corrected SFRs, via the SFR - M_* plane. The contour levels correspond to the measurements of aperture corrected SFR and stellar mass for all SDSS galaxies with $0.01 < z < 0.055$. The gray points represent the SDSS measurements, and the purple points represent the HAGGIS measurements, for the “HAGGIS star-forming galaxies”. The MS fit is derived by identifying the position of the peak in the SFR distributions for all the stellar mass bins of size

$0.1 M_{\odot}$ similar to the one derived for fiber SF MS described in last section. The large triangles represent peak value in the distribution of SFR for each stellar mass bin, and are used to derive the MS fit which is shown by the solid black line and is given by -

$$\text{Log } \Psi = 0.53 \text{ Log } M_* - 5.36 \quad (6.3)$$

The measurements of total SFR in HAGGIS and aperture corrected SFR in SDSS show larger discrepancies especially for very low mass and very high mass galaxies. The average correction for galactic dust and NII contamination in HAGGIS and the average correction for aperture effects based on galaxy color in SDSS might be the dominating sources for these discrepancies (see discussion in Chapter 4 section 4.4). Nevertheless, both HAGGIS and SDSS measurements of SFR for HAGGIS galaxies are consistent with the overall SF MS derived for all the SDSS galaxies with $0.01 < z < 0.055$ (HAGGIS redshift range). Thus equation 6.3 can be applied to HAGGIS galaxies as it is more robust given the vast number of galaxies used in deriving the fit which is certainly not possible with the smaller number in HAGGIS.

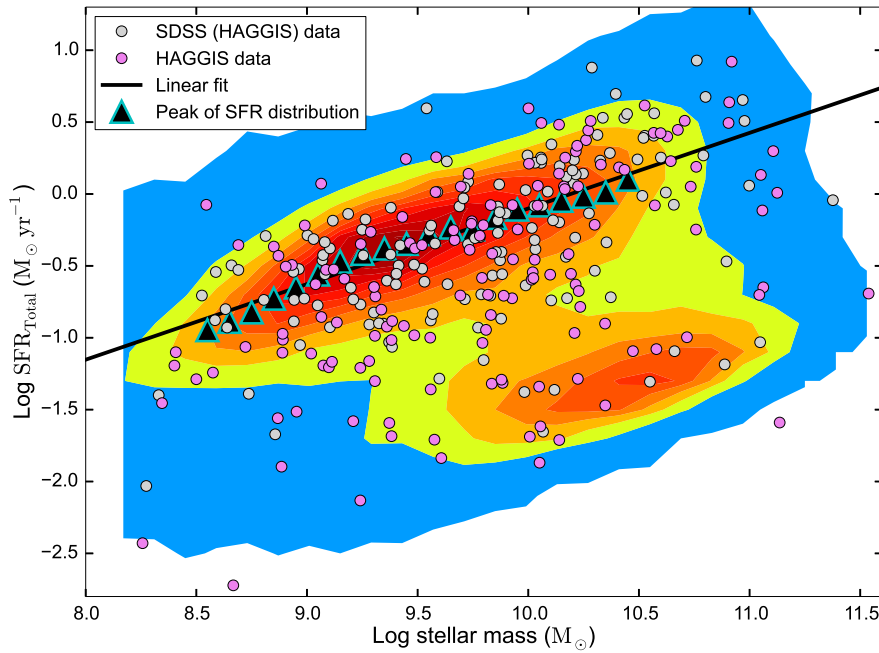


FIGURE 6.3: Global SFR- M_* plane for HAGGIS galaxies: HAGGIS SFR (purple) and SDSS aperture corrected SFR (grey). The contour levels correspond to the MS measurements for the whole SDSS dataset for $0.01 < z < 0.055$. The MS fit (black line) is derived by identifying the peak of the SFR distribution (large triangles).

Figure 6.4 shows the normalized distributions of deviation from this MS fit ($\Delta(\log(\text{SFR}))_{M_*}$). The errors on the distribution are derived assuming that the fraction of galaxies in each bin of $\Delta(\log(\text{SFR}))_{M_*}$ compared to total number of galaxies follows a binomial distribution. The distribution of $\Delta(\log(\text{SFR}))_{M_*}$ clearly shows a bi-modality for the overall SDSS galaxies with $0.01 < z < 0.055$ (grey line) as well as for the SDSS measurements of all HAGGIS galaxies (red-dashed line). The shape of these two distributions are quite similar except for the amplitude (a two-component Gaussian fit for these two distributions yield similar mean and σ for both Gaussian models). The distribution for SDSS galaxies has a larger peak at $\Delta(\log(\text{SFR}))_{M_*} \sim 0$ compared to the secondary peak at negative $\Delta(\log(\text{SFR}))_{M_*}$ while the two peaks are of approximately the same amplitude for the distribution of $\Delta(\log(\text{SFR}))_{M_*}$ obtained for the HAGGIS galaxies. The HAGGIS survey contains a larger fraction of passive galaxies compared to SDSS as the former contains more galaxies in fairly massive groups.

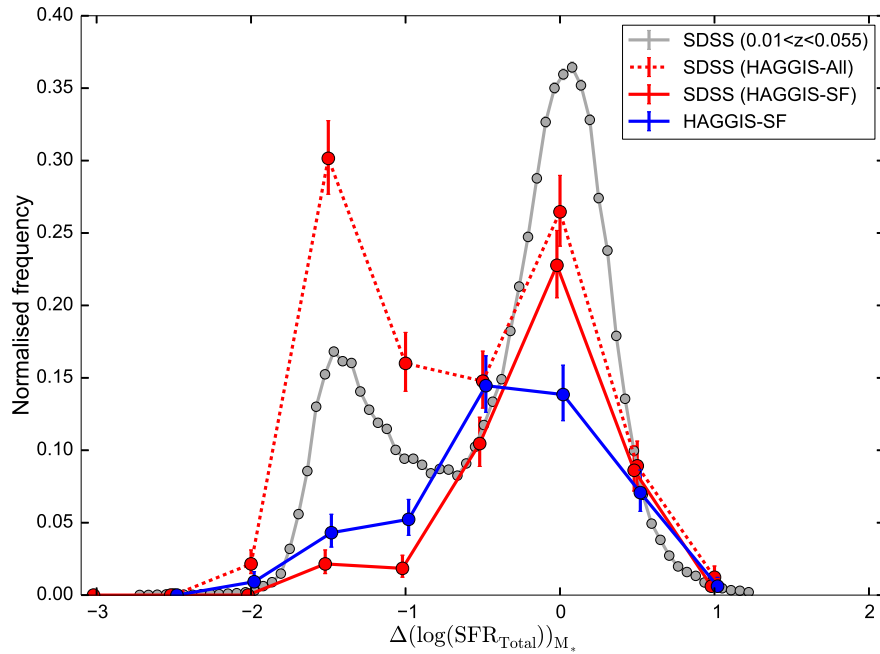


FIGURE 6.4: Distributions of $\Delta(\log(\text{SFR}_{\text{Total}}))_{M_*}$ for whole SDSS dataset in the redshift range of HAGGIS survey (grey); for SDSS measurements for all HAGGIS galaxies (dashed-red), and for SDSS measurements (solid-red) and for the HAGGIS measurements (solid-blue) just for the HAGGIS SF galaxies.

The distribution of $\Delta(\text{SFR})$ shown by the solid red line corresponds to the SDSS aperture corrected SFR measurements obtained for the “HAGGIS star-forming galaxies” while the distribution of $\Delta(\text{MS})$ shown by solid blue line corresponds to the HAGGIS total integrated SFR measurements obtained for the same galaxies. Both measurements show a non-Gaussian skewed distribution with a tail extending

well into the “passive galaxies” defined by the SFR distribution for the overall SDSS galaxies. This is confirmed by an Anderson-Darling (AD) test ¹ which yields the AD statistic at 5.1 and 1.5 for SDSS and HAGGIS distributions respectively. It is quite possible that galaxies in this asymmetric tail form a transitional class which are on their path to be quenched and hence terming these galaxies as “passive” is not useful especially in the context of environmental studies.

6.3 $H\alpha 3$ and HAGGIS global SF MS comparison

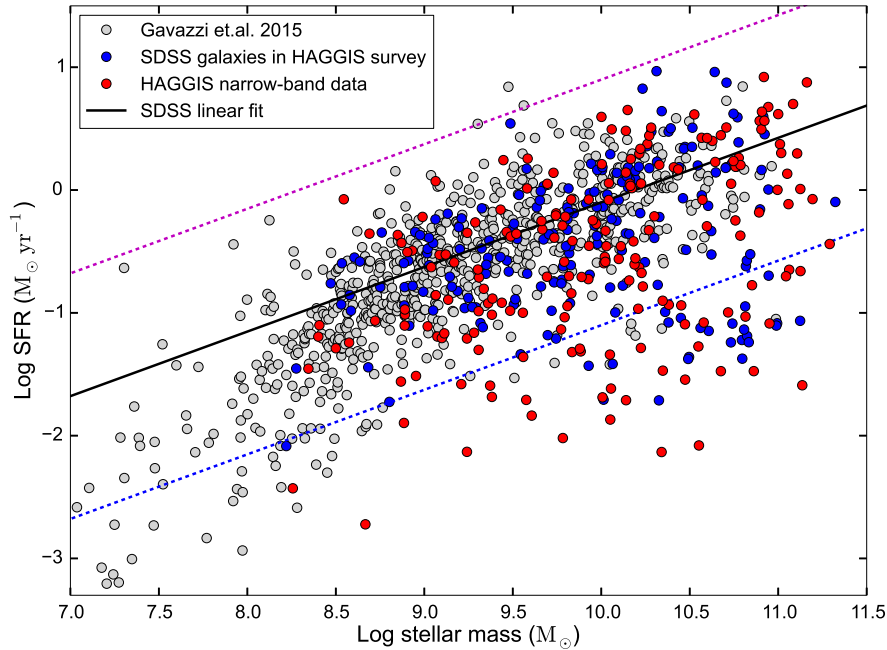


FIGURE 6.5: SFR MS derived for HAGGIS SF galaxies using HAGGIS global SFR measurements (red) and SDSS aperture corrected measurements (blue). SFR of galaxies in the $H\alpha 3$ survey Gavazzi et al. (2015) are shown by gray points for comparison. The MS fit (equation 6.3) derived using SDSS aperture corrected SFR measurements for the galaxies with $0.01 < z < 0.055$ is shown in black while the magenta and blue dashed lines denote the SFR 1 dex above and below the MS respectively.

Finally in figure 6.5 we compare the SFR MS derived for the HAGGIS galaxies using HAGGIS narrow-band measurements (red points) as well as using SDSS aperture corrected measurements (blue points) with the MS derived by Gavazzi

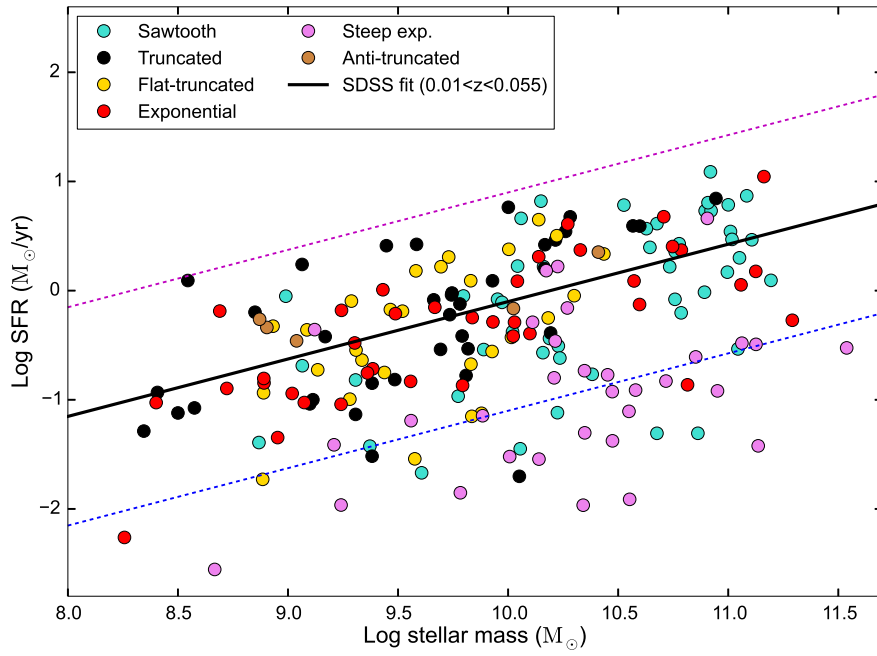
¹It is the modification of Kolmogorov-Smirnov (KS) test which tests the null hypothesis that a sample drawn from a population follows a particular distribution. The non-Gaussianity of the sample can be confirmed at 99 % significance if the AD test yields an AD statistic larger than 1.07 which is a critical value of the AD test to reject the null hypothesis

et al. (2015) (gray points) for the galaxies in H α 3 narrow-band imaging survey which uses a sample of HI selected galaxies from the ALFALFA survey. Both measurements of SFR for the HAGGIS galaxies — HAGGIS total integrated SFR measurements and SDSS aperture corrected SFR measurements — agree very well with these H α 3 measurements, and hence the MS fit derived using SDSS aperture-corrected measurements can be used to represent the MS for all of these datasets. The Gavazzi et al. (2015) SFR measurements provide a direct comparison for the HAGGIS SFR measurements as both of these measurements are based on narrow-band observations and use a same set of corrections for NII contamination and internal dust extinction. Thus, a general agreement between all of these measurements motivates further investigation of HAGGIS galaxies that deviate from the MS.

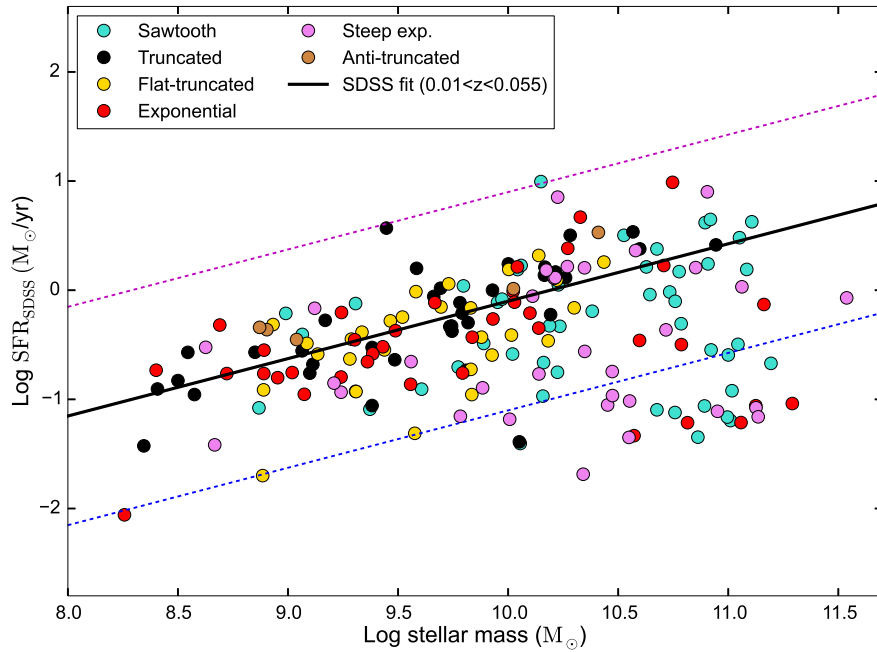
6.4 SF MS for different H α profile types

Fig. 6.6(a) shows the SF main sequence for the HAGGIS galaxies derived using HAGGIS narrow-band data. The plot is color-coded with H α profile types to understand whether differences in the H α surface brightness profiles lead to differences in SFRs. Galaxies identified to host AGN in SDSS DR7 are not shown on the plot. The linear fit of the MS derived using SDSS galaxies in the redshift range of HAGGIS survey is shown by a black line on the plot while the purple and blue dashed lines represent the SFR levels 1 dex above and below the MS respectively.

The MS relation is populated by truncated and flat-truncated profile types along with galaxies with exponential H α profiles at the low mass end. The high mass end of the MS is populated mainly by sawtooth and exponential profiles. The upper envelope of the relation is seen to be dominated by the truncated and flat-truncated galaxies which means that the truncation in H α disks does not affect the global SFRs in a significant way and in fact, on the contrary, it could lead to the enhancement of the global SFRs in some galaxies. To be sure, there are few cases of truncated H α disks that are below the MS relation but they constitute a minority of the population among the truncated and flat-truncated H α profile types. The galaxies that show a large deviation below the main sequence are mainly steep exponential galaxies along with few sawtooths and a minority of other profile types.



(a)



(b)

FIGURE 6.6: (a) Galaxy integrated star-formation rate (SFR) vs stellar mass and (b) SDSS aperture-corrected SFR vs stellar mass for HAGGIS galaxies color-coded with $H\alpha$ profile types. The black line is the MS fit derived using SDSS aperture corrected SFR measurements for the galaxies in the redshift range of HAGGIS survey while magenta and blue dashed lines represent the SFR levels 1 dex above and below the MS respectively.

Fig. 6.6(b) shows the SF main sequence for the HAGGIS galaxies using SDSS aperture-corrected SFR measurements. This plot is also color-coded with $H\alpha$ profile types and galaxies identified to host AGN in SDSS DR7 are not shown on the plot. The SDSS measurements can reproduce similar trends for different profile types as seen in fig. 6.6(a) except for the steep exponentials for which the SDSS on average overestimates the SFRs and sawtooths for which the SDSS on average underestimates the SFRs.

6.5 Differences in SDSS and HAGGIS SFRs as a function of $Re_{H\alpha}/Re_c$

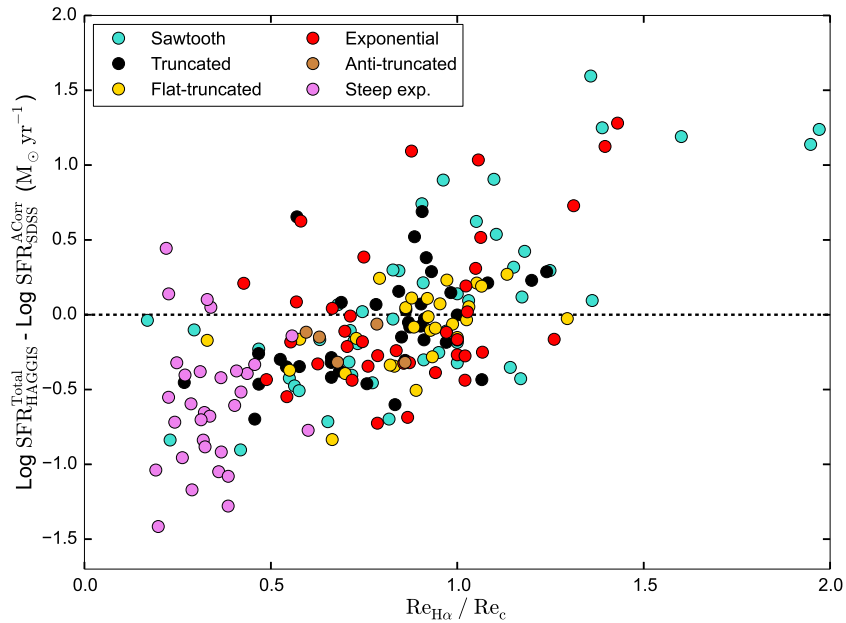


FIGURE 6.7: Difference between SDSS aperture corrected SFR and HAGGIS total SFR against $Re_{H\alpha}/Re_c$ color-coded with $H\alpha$ profile types. SDSS overestimates the SFR for galaxies having compact $H\alpha$ disks compared to its stellar disks while it underestimates the SFRs for galaxies having larger $H\alpha$ disks compared to their stellar disks.

Figure 6.7 shows how the systematic differences between the SDSS aperture-corrected SFR measurements and HAGGIS narrow-band measurements for the HAGGIS SF galaxies vary as a function of the ratio of the $H\alpha$ half light size to their stellar continuum half light size. SDSS SFR measurements are overestimated for galaxies having larger $H\alpha$ disks compared to their stellar disks while they are underestimated for the galaxies having smaller $H\alpha$ disks compared to their stellar disks.

The Spearman rank coefficient at 0.6 with negligibly small p-value at 10^{-20} confirms the correlation between the difference in two SFR measurements and $Re_{H\alpha}/Re_c$. This means that the aperture corrected SFR measurements do not provide an accurate measurement of global SFR for galaxies having compact $H\alpha$ disks as well as for galaxies having extended $H\alpha$ disks. This plot underlines the need for the resolved $H\alpha$ observations in understanding the effects of quenching processes on SF disks.

6.6 $\Delta(\log SFR)_{M_*}$ as a function of $Re_{H\alpha}/Re_c$

Figure 6.8(a) illustrates how the deviation from the star-formation rate main sequence correlates with $Re_{H\alpha}/Re_c$ for HAGGIS galaxies with HAGGIS total SFR measurements. Galaxies identified with central AGN in SDSS DR7 catalog are omitted from the plot as the HAGGIS SFR measurements for these galaxies are unreliable. Three regions can be defined for the plots as -

- **Region I:** $Re_{H\alpha}/Re_c > 0.7$ or $\log(Re_{H\alpha}/Re_c) > -0.15$
- **Region II:** $0.44 < Re_{H\alpha}/Re_c < 0.7$ or $-0.35 < \log(Re_{H\alpha}/Re_c) < -0.15$
- **Region III:** $Re_{H\alpha}/Re_c < 0.44$ or $\log(Re_{H\alpha}/Re_c) < -0.35$

These regions are marked by vertical lines on the plot while the dashed red horizontal line represents $\Delta(\log(SFR))_{M_*}=0$. The median values for the $\Delta(MS)$ for galaxies in each region are shown by larger red triangles while the error bars represent the one σ standard deviation of $\Delta(\log(SFR))_{M_*}$ for the galaxies in that region. Galaxies in region I are scattered around the MS and have median $\Delta(\log(SFR))_{M_*}$ close to zero while galaxies in region II have a median $\Delta(\log(SFR))_{M_*}$ slightly below zero and galaxies in region III have median $\Delta(\log(SFR))_{M_*}$ greater than 1 dex below zero.

This means that the global SFRs are not greatly affected for the galaxies in region II, although they have more compact $H\alpha$ disks than their stellar disks. Global SFR measurements are altered significantly only when the $H\alpha$ disks becomes very compact compared to their stellar disks. Almost all the galaxies with very compact $H\alpha$ disks compared to their stellar disks ($Re_{H\alpha}/Re_c < 0.44$) are below the MS relation with the majority of these galaxies being steep exponentials.

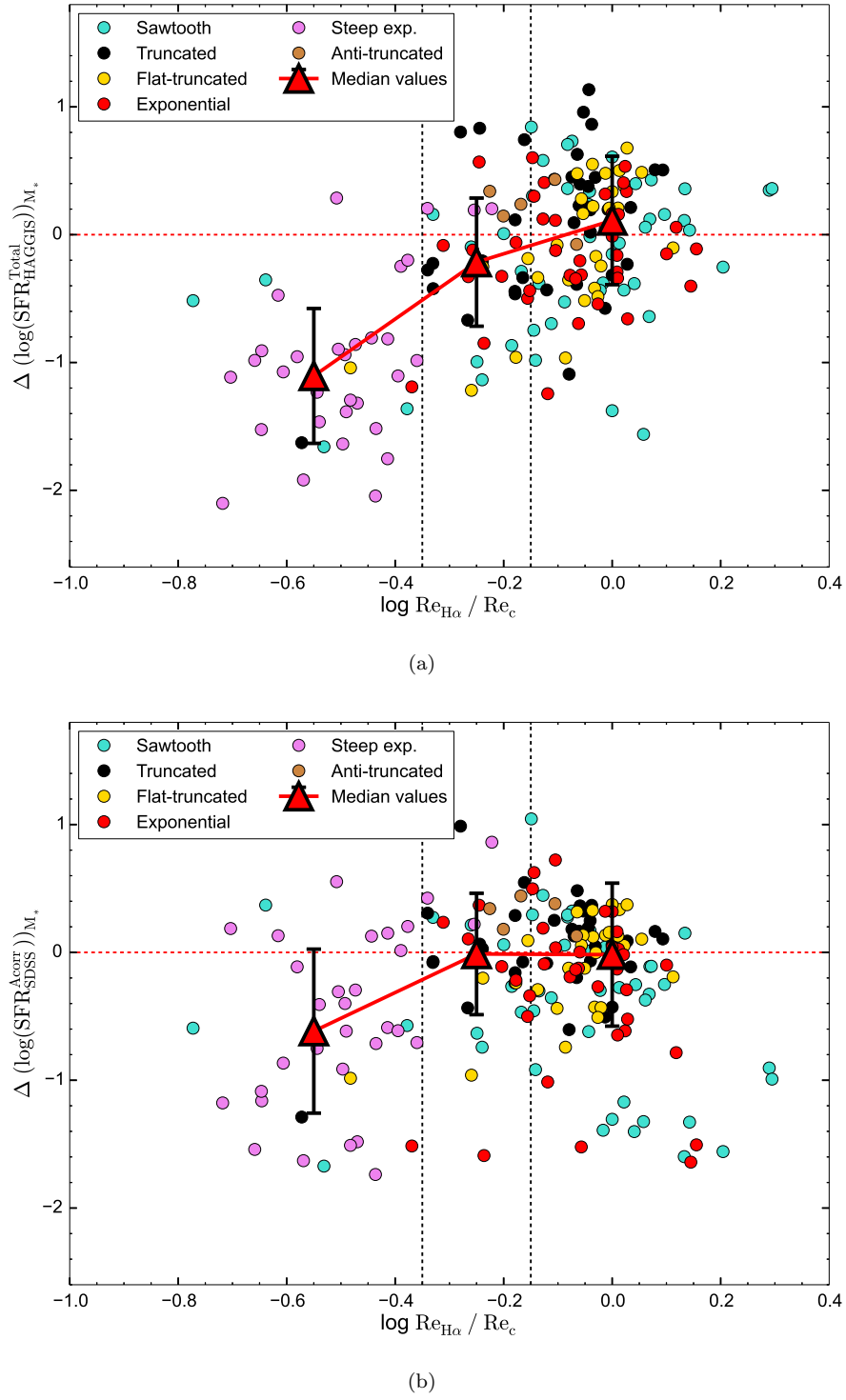


FIGURE 6.8: Deviation from the MS ($\Delta(\log(\text{SFR}))_{M_*}$) vs $\log Re_{H\alpha}/Re_c$ color-coded with H α profile types (a) for HAGGIS narrow-band SFR and (b) for the SDSS aperture-corrected SFRs. The deviation from the MS correlates with the size ratios especially for galaxies with compact H α disks which is indicative of outside-in quenching. SDSS aperture-corrected SFRs also produce a similar trend for region III, albeit with smaller deviation compared to HAGGIS SFRs.

Figure 6.8(b) shows a similar plot for the SDSS aperture corrected measurements. The SDSS measurements shows a similar trend for the galaxies in region III although the SDSS measurements on average overestimates the SFRs for these galaxies as we have seen in fig. 6.7. The SDSS SFR estimates also overestimate the SFRs for galaxies in region II with median $\Delta(\text{MS})$ close to zero. This explains differences in the distribution seen in fig. 6.4, and underlines the limitation of accuracy in estimating global SFRs using aperture corrected fiber measurements, and hence its use in understanding the effects of quenching mechanisms on SF disks.

6.7 Conclusion

In this chapter, we have used the star-formation rate – stellar mass diagrams (SF MS) to compare the SFRs derived using HAGGIS narrow-band images with the same obtained from SDSS and H α 3 datasets. We have also obtained the distributions of the SFR offsets from the respective main sequence fits to the SDSS data and we have analyzed whether the shape of the H α profile induces any systematic offsets in the SFR - M_* plane. In the last two sections we have described how the differences between HAGGIS global SFR measurements and SDSS aperture corrected measurements and the deviation of the galaxy’s star-formation rate from the SF MS correlates with the relative compactness of H α disk sizes to their stellar disk sizes.

We have found that the HAGGIS survey has a relatively large fraction of passive galaxies compared to SDSS. This apparent difference is mainly the result of survey selection as fairly massive groups (which typically contain a larger fraction of passive galaxies compared to the average field environment) are deliberately selected in the HAGGIS survey in order to study environmental effects. But, apart from this difference, the distribution of both HAGGIS and SDSS fiber SFR measurements derived for the “HAGGIS star-forming galaxies” agree very well with each other indicating that the two datasets provide similar measurements in the fiber region. There is also a rough agreement between the HAGGIS global SFR measurements and SDSS aperture corrected SFR measurements in the SFR - M_* plane.

Both HAGGIS and SDSS measurements obtained for the “HAGGIS star-forming galaxies” have a very skewed distribution towards the low SFR end which extends

well into the distribution of “passive galaxies” that is defined based on overall SDSS data. This suggests that the distinction between passive and SF galaxies based on SDSS measurements ignores this transitional class of galaxies which still exhibit weak emission, and are on their path to be quenched, and hence marks the limitation of the SDSS bi-modal distinction especially in the context of environmental studies.

The apparent absence of transitional galaxies in SDSS has been interpreted to mean a rapid quenching in galaxies (e.g. [Balogh et al. \(2004a\)](#), [Peng et al. \(2010\)](#), [Wetzel et al. \(2013\)](#)). The evidence of a relatively large number of transitional galaxies in HAGGIS groups thus suggests that the quenching in galaxies can be partial, and/or slow. This is consistent with results from clusters using IR-based SFR indicators which suffer less from systematics such as dust and aperture-effects (e.g. [Vulcani et al. \(2010\)](#), [Haines et al. \(2015\)](#)).

We have found that most of the HAGGIS SF galaxies are on the MS with some exceptions. It is remarkable in fact that galaxies having a variety of different $H\alpha$ profile shapes, including those having a truncation in their exponential disks, follow a similar SFR - M_* relation. This suggests that the shape of the $H\alpha$ profile is largely independent of the level of SF in the galaxy. The only exception are the steep exponentials, the majority of which are found significantly below the MS.

The SDSS aperture-corrected SFRs generally provide a consistent picture to the HAGGIS global SFR measurements except for the steep exponentials, for which the SDSS derived (aperture-corrected) SFRs are found to be overestimated, and for some sawtooths, for which the SDSS measurements are underestimated compared to HAGGIS measurements. A good correlation between the difference between the SDSS aperture-corrected SFRs and HAGGIS global SFR measurements, and the ratio of $H\alpha$ size to continuum size, also suggests that the SFRs derived in SDSS are systematically different for galaxies having compact as well as for galaxies having extended $H\alpha$ disks compared to their stellar disks. This marks limitations of the fiber-based spectroscopic data and underscores the need for the resolved $H\alpha$ observations, especially for understanding the environmental effects on galaxies.

Finally we have found that the deviation of a galaxy’s SFR from the MS correlates with the ratio of $H\alpha$ size to their stellar size, especially for galaxies having very compact $H\alpha$ disks compared to their stellar disks. We have defined three regions based on the ratio of disk sizes. Galaxies having size ratios above 0.7 are on average found to be on the MS, galaxies having size ratios between 0.44 and 0.7 are on average found to deviate modestly below the MS while almost all galaxies having

the size ratios below 0.45 are found to deviate significantly below the MS. This is suggestive that the outside-in quenching mechanisms are common in groups. This also suggests that some of the galaxies having compact $H\alpha$ disks and low level of SF for their stellar mass observed in Virgo cluster ([Koopmann & Kenney \(2004\)](#)), may have been pre-processed in their previous haloes.

Chapter 7

Stellar mass and galaxy environment

In last two chapters, we have seen that different classes of galaxy show systematic differences in the galaxy scaling relations viz. stellar and $H\alpha$ size-stellar mass relations and the star-formation rate - stellar mass (main sequence). Stellar type III and non-exponential galaxies are seen to be offset to both small $H\alpha$ and continuum size and low star-formation rate at fixed M_* indicating that the quenching of a galaxy's star-formation and establishment of stellar profile types are correlated somehow. Similarly, the galaxies with compact $H\alpha$ disks - often classified as steep exponentials based on the $H\alpha$ surface brightness profile - are below the star-forming main sequence suggestive of an outside-in quenching mechanism.

Galaxies statistically follow two different modes of quenching, one correlating with the galaxy stellar mass - called “Mass Quenching” and the other based on the galaxy environment - known as “Environmental Quenching” ([Peng et al. \(2010\)](#)). Although, we now know this broader picture, the exact processes that drive these two quenching modes is yet unclear. To understand the physical processes that lead to quenching of star-formation in galaxies, it is important to study correlations between stellar mass and galaxy environment and the resolved properties of the stellar and $H\alpha$ disks. Hence, we devote this chapter to understanding the correlations of stellar mass and environment with different galaxy properties. Section [7.1](#) describes how different stellar continuum and $H\alpha$ profile types depend on galaxy stellar mass while section [7.2](#) describes the same with respect to the group halo mass (derived by [Yang et al. \(2007\)](#)) which is one measure of galaxy environment. In section [7.3](#), we examine the correlations between stellar and $H\alpha$

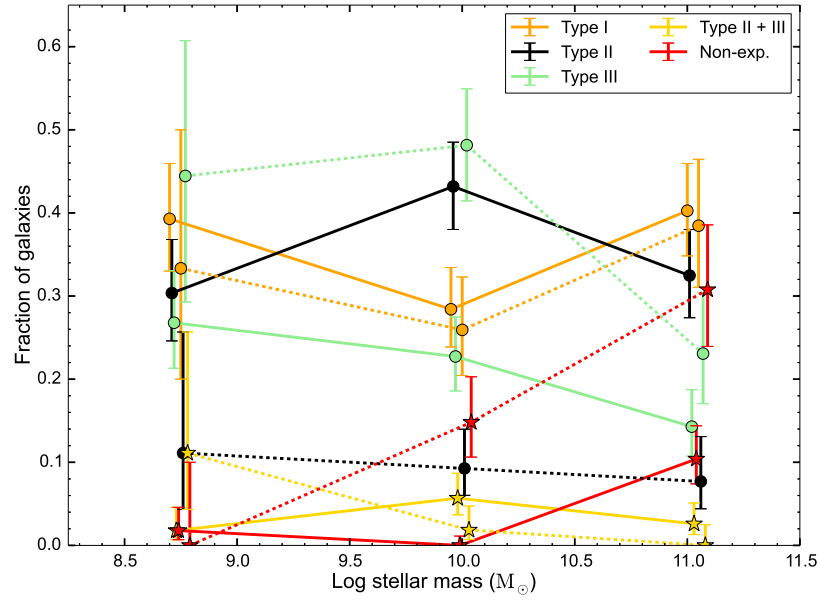
sizes with respect to galaxy's $H\alpha$ profile type, stellar mass and SFR (studied in chapters 5 and 6) with galaxies split into centrals and satellites.

7.1 Effects of stellar mass

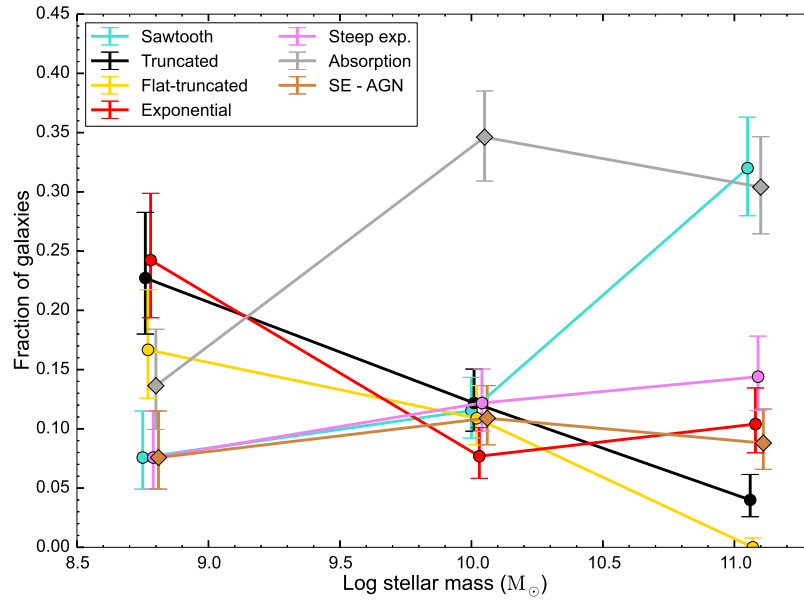
The figure 7.1(a) shows the frequencies of stellar continuum profile types with respect to galaxy stellar mass for the HAGGIS galaxies. The solid lines denote the fractions computed just for star-forming galaxies (excluding the galaxies with $H\alpha$ profiles classified as either absorption or non-detections) while the dashed lines denote the fractions computed just for quenched galaxies ($H\alpha$ profile types: absorption and non-detection). The errors on the fractions are the $1-\sigma$ confidence intervals derived using the Wilson (1927) approximation for a binomial distribution.

Type III is the most common type of quenched galaxy at low to intermediate mass ($\log(M_*) < 9.5 M_\odot$ and $9.5 M_\odot < \log(M_*) < 10.5 M_\odot$), comprising 45_{-15}^{+16} % and 48_{-7}^{+7} % of the quenched systems respectively which drops to 23_{-6}^{+7} % at high mass ($\log(M_*) > 10.5 M_\odot$). The frequency of non-exponentials increases with stellar mass in quenched galaxies from 0_{-0}^{+10} % in the low mass bin to 31_{-7}^{+8} % at high mass. As the non-exponential profile types mainly constitute ellipticals and few S0 galaxies, the increase in the fraction of these galaxies at higher stellar mass would be expected as these galaxies are generally found to be more massive than the star-forming late type galaxies (e.g. Wilman & Erwin (2012)). Type II galaxies are uncommon among the quenched population at all stellar masses (~ 10 %), type I galaxies do not show a well defined trend with stellar mass (comprising ~ 25 -40 %), while composite type II + III are rare at all stellar masses among quenched systems.

In contrast, type II galaxies are common (rare) among star-forming (quenched) galaxies forming ~ 30 -45 % (< 10 %) of the star-forming (quenched) population with no clear mass trend. The rare occurrence of type II profiles in quenched systems indicates that the truncations in stellar disks are not conserved during the quenching process. Type I galaxies, on the other hand, show similar frequencies in both star-forming and quenched systems at all stellar masses, comprising ~ 25 -40 %, suggesting that most pure exponential stellar disks are not destroyed during quenching. The fraction of type III star-forming galaxies decreases with stellar mass from 27_{-6}^{+6} and 23_{-5}^{+5} % at low and intermediate stellar masses to 14_{-4}^{+4} % at



(a)



(b)

FIGURE 7.1: (a) The frequency of stellar profile types as a function of stellar mass among star-forming (solid lines) and quenched (dashed lines) galaxies. Quenched galaxies are dominated by type III at low mass and non-exponentials at high mass. Star-forming galaxies have a higher fraction of type II galaxies, a lower fraction of type III and non-exponentials, and a similar fraction of type I galaxies compared to quenched systems. (b) The frequency of $H\alpha$ profile types as a function of stellar mass. The frequency of truncated, flat-truncated and exponentials decrease with stellar mass, compensated by an increase in the frequency of sawtooth, absorption (plus non-detections) and steep exponentials.

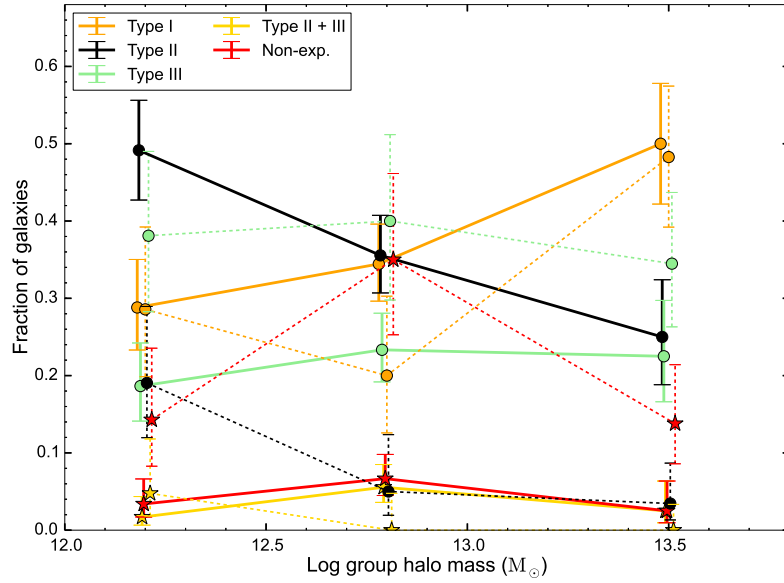
Anti-truncated are not shown on the plot due to their low fractions.

high mass. Type III galaxies show a similar trend with stellar mass in quenched systems suggesting that the anti-truncation is harder to form in high mass galaxies. However they are far more common in quenched galaxies compared to star-forming ones suggesting a connection between their formation and the quenching process. Star-forming non-exponentials show an increase in their frequencies in the high mass bin to 10^{+4}_{-3} % from the near zero frequencies in low and intermediate mass bins while frequencies of composite type II + III galaxies remain very low at all stellar masses.

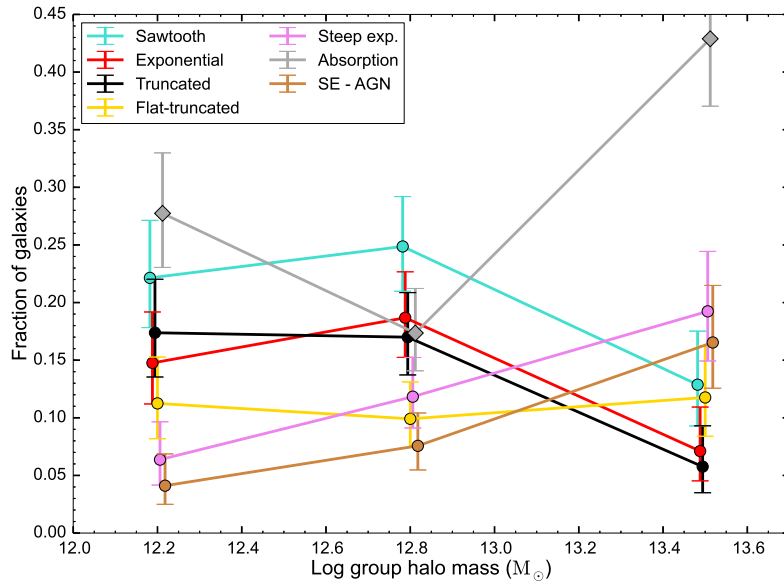
The $H\alpha$ profile types exhibit a strong correlation with stellar mass as seen in fig. 7.1(b). This suggests that the stellar mass is an important parameter in deciding the spatial distribution of star-formation in the disk. The plot shows that the galaxies with truncated $H\alpha$ disks i.e. exponential-truncated and flat-truncated galaxies are almost non-existent at high stellar mass – cumulatively comprising 4^{+2}_{-2} % – while cumulatively they account for 43^{+6}_{-6} % at low mass and 26^{+4}_{-4} % at intermediate mass. Galaxies with exponential $H\alpha$ profiles are also found to be more common in low mass galaxies comprising 26^{+6}_{-5} % of low mass systems going down to 9^{+3}_{-2} and 11^{+3}_{-3} % at intermediate and high masses respectively. Absorption (including non-detection) galaxies, sawtooths and steep exponentials on the other hand show an opposite trend of increasing frequencies with stellar mass. The fraction of absorption (plus non-detection) galaxies increases from 15^{+5}_{-4} % at low mass to 39^{+4}_{-4} and 33^{+5}_{-4} % at intermediate and high mass, the fraction of steep exponentials increases from 8^{+4}_{-3} % at low mass to 14^{+3}_{-3} and 16^{+4}_{-3} % at intermediate and high mass and the fraction of sawtooths increases from 8^{+4}_{-3} and 13^{+3}_{-3} % at low and intermediate mass to 35^{+5}_{-4} % at high mass. When AGN identified in SDSS DR7 are excluded from the steep exponentials, the stellar mass trend becomes almost flat, at ~ 10 %.

7.2 Group halo mass

Figure 7.2(a) shows the frequencies of stellar continuum profile types in different group halo mass as estimated by Yang et al. (2007) (see chapter 2). The solid lines denote the frequencies computed for the HAGGIS star-forming galaxies while dashed lines denote the frequencies computed for the quenched systems, similar to fig. 7.1(a). The errors on the fractions are also derived in a similar fashion by computing the $1\text{-}\sigma$ binomial confidence intervals.



(a)



(b)

FIGURE 7.2: (a) The frequency of continuum profile types as a function of group halo mass for SF (solid lines) and quenched (dashed lines) galaxies. Among SF galaxies, type I (II) are more (less) common in high mass haloes than at low mass, while type III have no halo mass dependence. Quenched galaxies are dominated by type III (I) galaxies in low (high) mass groups with a significant contribution of non-exponentials but few type IIs. (b) The frequency of $H\alpha$ profile types as a function of halo mass. Truncated, exponential and sawtooth galaxies are relatively rare while the steep exponentials (both including and excluding AGNs) and absorption (including non-detections) galaxies are more common in high mass haloes. Flat-truncated show a flat trend with halo mass.

The figure shows that the frequency of type II star-forming galaxies decreases monotonically with halo mass from 49_{-6}^{+6} % in low mass groups down to 25_{-6}^{+7} % in high mass groups. Type I star-forming galaxies show the exact opposite trend of monotonously increasing frequency with halo mass rising from 29_{-6}^{+6} % in low mass groups to 50_{-8}^{+8} % in high mass ones. This means that type II is the most common type of star-forming galaxy in low mass groups while in high mass haloes type I is most common. Type III star-forming galaxies, on the other hand, show a flattish trend with group halo mass comprising about ~ 20 % in all environments while non-exponentials and composite type II + III profiles are insignificant.

The frequencies of stellar types are very different in quenched galaxies. Type III galaxies dominate quenched systems in low mass groups comprising 38_{-10}^{+11} % which is significantly higher than their frequency in star-forming galaxies. In high mass groups, type I galaxies are the most common for quenched systems comprising 48_{-9}^{+9} %. Type III quenched galaxies show a flat trend with group halo mass while type I quenched galaxies show an increasing frequency with halo mass. Type II quenched galaxies are more common in low mass groups at 19_{-10}^{+7} % compared to 5_{-3}^{+7} % and 3_{-2}^{+5} % in intermediate to high mass groups. This is similar to the findings of [Erwin et al. \(2012\)](#) that Virgo cluster S0 galaxies show 0_{-0}^{+4} % type II fraction compared to 28_{-6}^{+7} % found in field environments. Consistent with the story told in [fig. 7.1\(a\)](#), the type II frequency in quenched systems is significantly lower than their frequencies in star-forming galaxies in all environments, the opposite situation to that of type IIIs and non-exponentials. The frequency of quenched non-exponentials is highest in intermediate mass groups at about 35_{-10}^{+11} % compared to about 14_{-6}^{+9} and 14_{-5}^{+8} % in low and high mass groups. Composite type II + III quenched galaxies are insignificant.

These strong trends with environment exist in the group regime. This suggests that “pre-processing” occurs in many galaxies in groups before they are accreted onto the cluster environment. Many established environmental correlations observed in the dense cluster environment can thus be explained, at least partially, by these galaxy pre-processing mechanisms that take place in moderately dense regions of the Universe.

H α profile types also show some interesting trends with group halo mass as shown in [fig. 7.2\(b\)](#). The frequency of steep exponential galaxies increases from 6_{-2}^{+3} % in low mass groups to 19_{-4}^{+5} % in high mass groups. Some of the steep exponentials can have significant contribution from the emission coming from a central AGN source. To disentangle the effects of AGNs on the classification, we also show

the trend of steep exponentials with halo mass excluding the AGNs identified in the SDSS DR7 catalogue. It shows that the increasing trend is retained even after exclusion of AGNs. Galaxies with exponential and exponential-truncated $H\alpha$ profiles show a decrease in frequencies from 15_{-4}^{+4} and 18_{-4}^{+5} % in low mass groups to 7_{-3}^{+4} and 6_{-2}^{+4} % in high mass groups respectively.

Sawtooth galaxies similarly show a decrease in frequency in high mass groups to 13_{-4}^{+5} % down from 23_{-4}^{+5} % in low mass groups. They are the most common type among star-forming galaxies in low to intermediate mass groups while steep exponentials are dominant among the star-forming galaxies in high mass groups even after the AGNs are excluded from the classification. Flat-truncated galaxies show a flat trend with halo mass with frequencies at about 11 % in all environments. The quenched systems (absorption plus non-detections) show an increase in frequency with halo mass from 28_{-5}^{+5} % in low mass groups to 43_{-6}^{+6} % in high mass ones. The intermediate mass groups show a (possibly surprising) decrease in frequency of quenched systems which stand at 17_{-3}^{+4} %.

The decrease in frequency of truncated galaxies in high mass groups indicates, contrary to our expectations, that truncations in $H\alpha$ surface brightness profiles are more common in less dense environments. This suggests that these truncations are not driven by environmental processes for most of the galaxies.

7.3 Centrals vs Satellites

The effects of environmental processes are known to be felt differently by galaxies that live in or near to the center of the group potential which are known as “Central Galaxies” than the galaxies that have fallen in and are orbiting within the potential well of a larger galaxy which are known as “Satellite Galaxies”. Since the central galaxies live near to the center of the group potential, we expect them to accrete gas from within the group potential, fueling star-formation. We can treat the most massive galaxy in the group as a central galaxy for all practical purposes. All the remaining galaxies are then termed as satellites. We have used this method of classification for HAGGIS galaxies to understand the differences between the two populations.

7.3.1 Sizes

Fig. 7.3 shows how $H\alpha$ half-light sizes compare with stellar continuum half light sizes in a log-log space (similar to fig. 5.9) for the HAGGIS centrals and satellites. The plot is color-coded by $H\alpha$ profile type to understand whether particular $H\alpha$ profile types have systematically different size ratios than the general population. Most satellite galaxies have smaller $H\alpha$ disks compared to their stellar disks. This is in stark contrast with central galaxies which have mostly similar or even larger $H\alpha$ disks compared to their stellar disks. This suggests that most satellite galaxies are affected by their environment to some extent and it is in agreement with the general consensus that the satellite galaxies are the main driver of the environmental effects (see e.g. section 1.2.1).

A small fraction (19^{+5}_{-4} %) of centrals show a very compact $H\alpha$ morphology ($Re_{H\alpha}/Re_c < 0.4$; we call these as compact $H\alpha$ disks hereafter). These are mainly steep exponentials and a few sawtooths. These central galaxies with compact $H\alpha$ disks show no correlation between $H\alpha$ size and stellar size which is confirmed by a Spearman test which yields a high p-value at 0.3 which means that there is a 30 % chance that the observed correlation can be explained if there is no correlation. Satellites with compact $H\alpha$ disks, on the other hand, show a very good correlation between the two sizes which is confirmed by a Spearman rank coefficient of 0.49 with negligible p-value at 0.006.

Central AGNs in galaxies can give rise to a point-source like compact $H\alpha$ emission as the AGN source can also ionize the surrounding atomic gas. Hence, it is important to understand what fraction of galaxies having compact $H\alpha$ disks host a central AGN and such galaxies need to be segregated from the general analysis. We use the catalog of AGN identifications given in SDSS DR7 data release based on the precepts given in Brinchmann et al. (2004) to understand the effects of AGNs in our analysis.

We find that 9 out of 13 or 69^{+14}_{-11} % of the central galaxies having compact $H\alpha$ disks host a central AGN where only 2 out of 28 or 7^{+6}_{-3} % of such satellites host a central AGN. This means that the origin of these compact $H\alpha$ disks in centrals and satellites might be different. 76^{+8}_{-7} % galaxies that are identified to host an AGN are centrals out of which 92^{+7}_{-4} % have either sawtooth or steep exponential $H\alpha$ surface brightness profile. This suggests that the central AGN source can affect the distribution of star-formation in galaxies giving rise to a very centrally concentrated emission region.

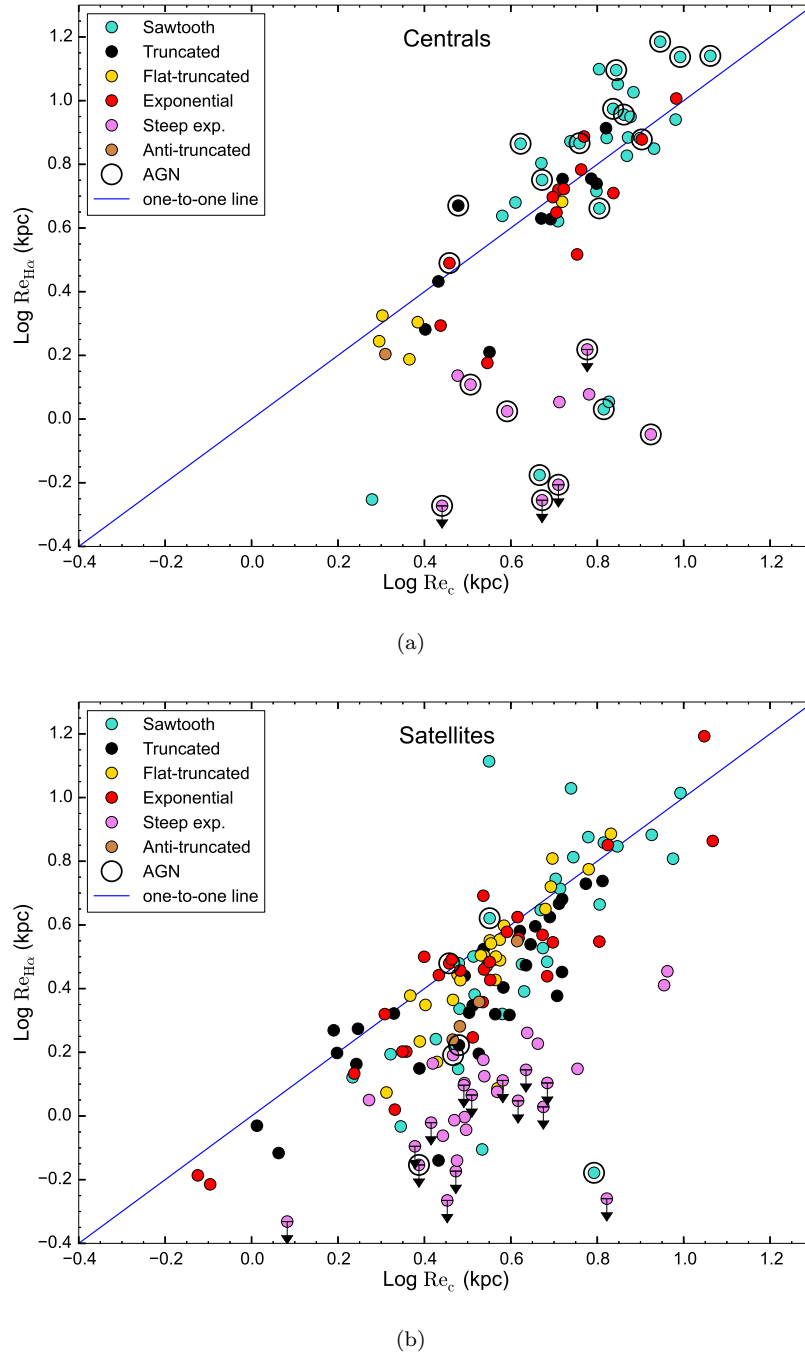


FIGURE 7.3: Log H α half light radius vs log continuum half light radius color-coded with H α profile types (a) for centrals and (b) for satellites. AGNs identified in the SDSS DR7 catalog are marked by an open circle. Galaxies having an H α emission line profile consistent with the PSF profile (obtained for a similar observing condition) are marked by upper limits. Most centrals have similar or even larger H α disks than their stellar disks while most satellites have smaller H α disks compared to their stellar disks suggesting that they may be affected by their environment. A small fraction (19^{+5}_{-4} %) of central galaxies have very compact H α disks ($\text{Re}_{\text{H}\alpha}/\text{Re}_c < 0.4$) out of which 69^{+14}_{-11} % are AGN.

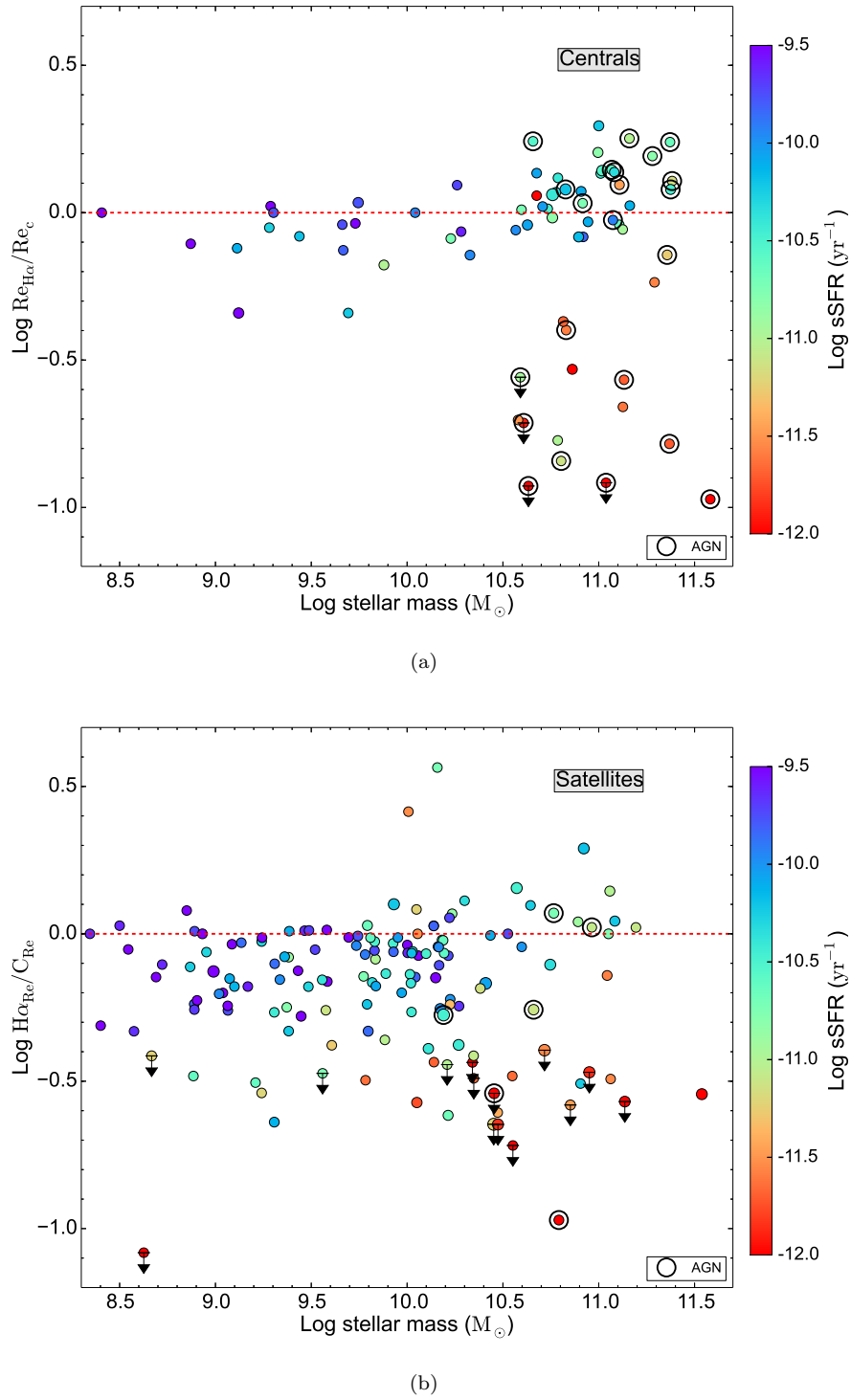


FIGURE 7.4: Ratio of $\text{Re}_{\text{H}\alpha}$ to Re_c vs stellar mass color-coded with sSFR for (a) centrals and (b) for satellites. AGNs identified in SDSS DR7 are marked on both plots by an open circle. Galaxies which have $\text{H}\alpha$ emission line profile consistent with the PSF profile (obtained for a similar observing condition) are marked by upperlimits. The majority of satellites are seen to have ratios below one while many centrals are seen to have ratios close to or larger than one.

Figure 7.4 shows how the logarithmic ratio of $\text{Re}_{\text{H}\alpha}$ to Re_c varies as a function of stellar mass for centrals and satellites. AGNs identified in the SDSS DR7 catalog are marked on both plots by an open circle. The plot shows that the majority of satellites have smaller $\text{H}\alpha$ half light sizes compared to their stellar half light sizes at all stellar mass, indicating that they may be affected by their environment. The majority of central galaxies, on the other hand, have larger $\text{H}\alpha$ half light sizes compared to their stellar half light sizes. As many HAGGIS central galaxies are more massive than satellites, these differences can be partially attributed to the mass trend we have observed in fig. 5.10(b); low mass galaxies ($\log(\frac{M_*}{M_\odot}) < 10.3$) have smaller $\text{H}\alpha$ sizes than their stellar sizes while high mass galaxies ($\log(\frac{M_*}{M_\odot}) > 10.3$) show a dichotomy of size ratios with most galaxies exhibiting larger $\text{H}\alpha$ sizes compared to their stellar sizes and some others exhibit very compact $\text{H}\alpha$ disks. It is important thus to compare the distribution of size ratios in two mass bins to understand the actual differences between the two population.

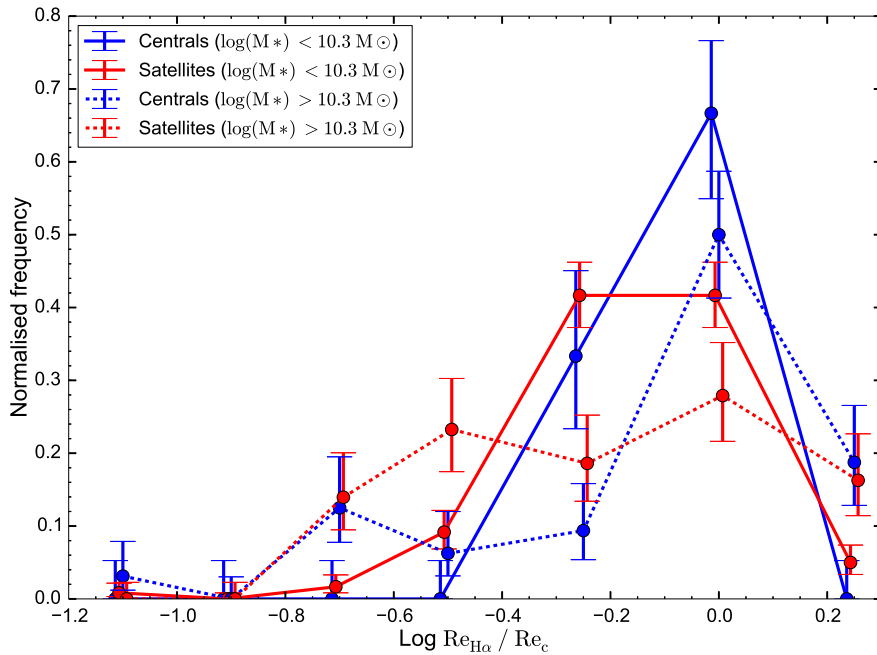


FIGURE 7.5: Distribution of $\text{Re}_{\text{H}\alpha}/\text{Re}_c$ for centrals (blue) and satellites (red) split into low and high mass bins. AGNs identified in SDSS DR7 are excluded from these.

Figure 7.5 shows the distribution of $\log(\text{Re}_{\text{H}\alpha}/\text{Re}_c)$ for the low and high mass centrals and satellites excluding all AGNs (split at $10^{10.3} M_\odot$). At low stellar mass, both centrals and satellites show a single peaked distribution which is skewed towards ratios below 1 ($\log \text{ratio} < 0$) while they show a double peaked distribution

or dichotomy of size ratios at high mass. The low mass centrals show a distribution of size ratios peaking near the ratio of unity with 67^{+10}_{-12} % of low mass centrals having $\text{Re}_{\text{H}\alpha}/\text{Re}_c$ larger than 0.8 ($\log(\text{Re}_{\text{H}\alpha} / \text{Re}_c) \geq -0.1$). In contrast, the satellites show a distribution that peaks at smaller ratios with only 47^{+5}_{-4} % of satellites having $\text{Re}_{\text{H}\alpha}/\text{Re}_c$ larger than 0.8. For the high mass galaxies, 69^{+9}_{-8} % of centrals have ratios larger than 0.8 ($\log(\text{Re}_{\text{H}\alpha} / \text{Re}_c) \geq -0.1$) compared to just 44^{+7}_{-7} % of satellites.

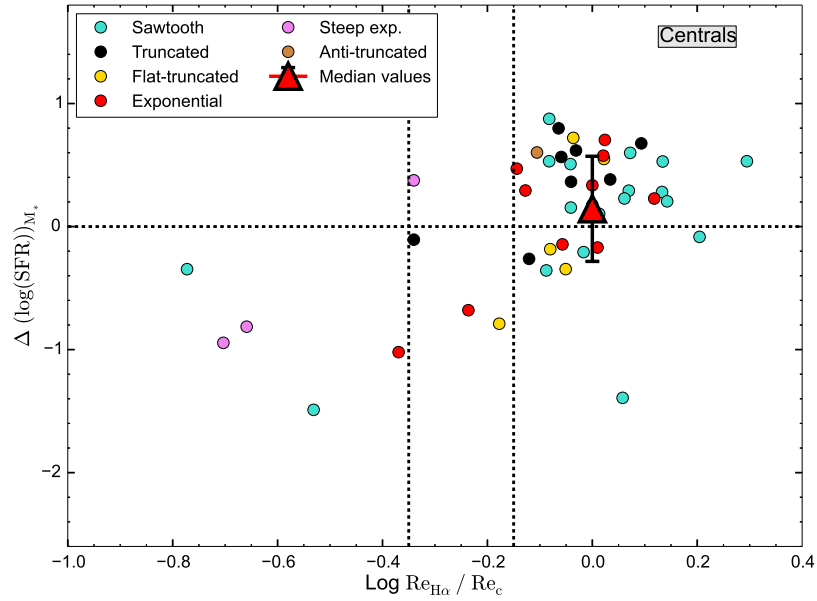
7.3.2 SF MS

Building on figure 6.8(a) in chapter 6, figure 7.6 illustrates how the deviation from the star-formation rate main sequence correlates with $\text{Re}_{\text{H}\alpha}/\text{Re}_c$ for the star-forming satellite and central galaxies. Galaxies identified with central AGN in the SDSS DR7 catalog are omitted from the plot as the star-formation rates (and possibly also the $\text{H}\alpha$ sizes) for these galaxies would possibly be affected due to the AGN contamination. Similar to figure 7.6, we define three regions of the plot as -

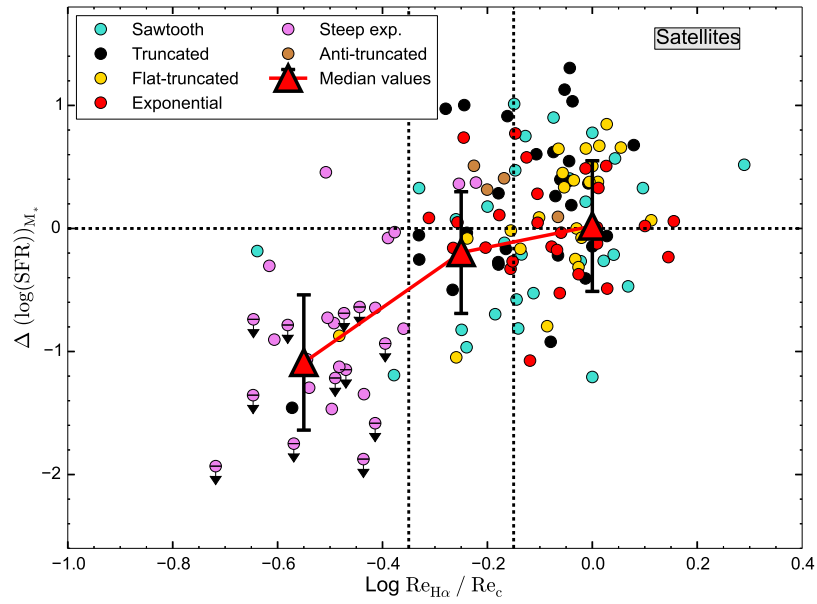
- **Region I:** $\text{Re}_{\text{H}\alpha}/\text{Re}_c > 0.8$ or $\log(\text{Re}_{\text{H}\alpha}/\text{Re}_c) > -0.1$
- **Region II:** $0.44 < \text{Re}_{\text{H}\alpha}/\text{Re}_c < 0.8$ or $-0.35 < \log(\text{Re}_{\text{H}\alpha}/\text{Re}_c) < -0.1$
- **Region III:** $\text{Re}_{\text{H}\alpha}/\text{Re}_c < 0.44$ or $\log(\text{Re}_{\text{H}\alpha}/\text{Re}_c) < -0.35$

For satellite galaxies, the median $\Delta (\log\text{SFR})_{\text{M}^*}$ is close to zero for the region I, slightly below zero for region II while the region III shows median $\Delta (\log\text{SFR})_{\text{M}^*}$ well below zero.

The majority of SF centrals lie in region I of the plot (81^{+5}_{-6} % of SF centrals compared to 55^{+4}_{-4} % of SF satellites) and have with median $\Delta (\log\text{SFR})_{\text{M}^*}$ slightly above zero (an outlier central galaxy in the region I is removed from the computation). We note here that the definition of centrals is somewhat vague with the assumption that the most massive galaxy is at the center of the potential which is not always true. Hence, we expect some centrals to be mis-classified satellites and vice versa.



(a)



(b)

FIGURE 7.6: Deviation from MS vs $\log(\text{Re}_{\text{H}\alpha}/\text{Re}_c)$ color-coded with H α profile types (a) for centrals and (b) for satellites. Galaxies which have an H α emission profile consistent with the PSF profile (obtained for a similar observing condition) are marked by upper limits. The deviation from the MS correlates steeply with size ratios below 0.45 ($\log(\text{Re}_{\text{H}\alpha}/\text{Re}_c) < -0.35$) for satellites while only few centrals show a deviation below the MS. A larger scatter for galaxies with disk ratios close to one is evident in satellites indicating that SFR is suppressed or enhanced in some galaxies, maintaining the average size and shape of the star-forming disks.

7.4 Conclusions

We have presented here the dependence of stellar continuum and H α profile type frequencies in both star-forming and quenched galaxies on a galaxy's stellar mass as well as on the halo mass of the group.

The relation between stellar and H α half light sizes with respect to a galaxy's stellar mass is then analyzed in the context of whether the galaxy is a central or a satellite. Similarly, the relation between the deviation of the galaxy's star-formation rate from the star-forming main sequence and the ratio of the galaxy's H α half light size to the stellar continuum half light size is analyzed separately for centrals and satellites.

We have found that the frequency of type III galaxies decreases and the frequency of galaxies with non-exponential profiles increases with galaxy stellar mass for both star-forming and quenched galaxies. The former indicates that the anti-truncations are possibly harder to form at higher stellar masses while the latter is the confirmation of the fact that elliptical galaxies which have such non-exponential profiles tend to be more massive than disk galaxies which have exponential (or broken-exponential) disks. The frequencies of other profile types do not show any clear dependence on galaxy stellar mass.

The frequency of type IIs is observed to be significantly larger ($> 30\%$) in star-forming galaxies compared to quenched galaxies ($< 10\%$), while type III and non-exponential galaxies are more common among quenched systems than star-forming ones. The significantly lower fraction of type II galaxies in quenched systems suggests that most of these galaxies are transformed into other profile types if their star-formation is shut down. Type I frequency, on the other hand, is largely independent of the star-formation activity in the galaxy, suggesting that they are largely unperturbed by the quenching mechanisms.

The frequency of both type I and type II galaxies shows a stronger trend with group halo mass while the frequency of type III galaxies is largely independent of environment, and the frequency of non-exponentials does not show any clear trend with halo mass for either star-forming or quenched populations. Type II galaxies are more common in low mass haloes while type I galaxies are more common in high mass haloes. Type II quenched galaxies are especially very rare in the highest mass haloes ($< 5\%$ in haloes above $\sim 10^{13}M_{\odot}$).

A similar trend is observed in cluster galaxies in comparison with field samples (Erwin et al. (2012)). This suggests that some of the environmental correlations observed in rich clusters can be, at least partially, explained by the pre-processing of galaxies in haloes $\geq 10^{13} M_{\odot}$, as clusters are expected to have accreted a significant fraction of their galaxies from groups (McGee et al. (2009)).

These results suggest that both stellar mass and environment are responsible for establishing the diversity of stellar profile types we see in the local universe. This provides an important constraint on the formation mechanisms of these diverse classes which is still largely debated (see e.g. Schaye (2004), Younger et al. (2007), Martínez-Serrano et al. (2009), Comerón et al. (2012), Minchev et al. (2012), Borlaff et al. (2014), etc).

Since recent simulations have suggested that type II galaxies have, on average, larger angular momentum compared to other profile types (Herpich et al. (2015)), these results now suggest that many galaxies lose angular momentum when they are accreted into high mass haloes and transform their type II stellar profile into type I. Many type IIs also have truncated $H\alpha$ disks (30^{+5}_{-5} %; also see fig 4.5) suggesting that the profile is continuously reinforced via new stars while star-forming which is in agreement with simulations (Roškar et al. (2008)).

Among the $H\alpha$ profile types, the truncated, flat-truncated and exponential galaxies are more common at lower stellar mass while sawtooth and absorption galaxies are more common towards the high mass end. After removing AGN, there is no significant trend for steep exponential galaxies with stellar mass.

The frequency of galaxies seen in $H\alpha$ emission (i.e. excluding absorption and non-detections) is observed to decrease to higher halo mass, in agreement with the general consensus that the fraction of passive galaxies increases in denser regions (see section 1.2.4).

Divided by $H\alpha$ profile type, galaxies with steep exponential profiles are the only exception: their frequency increases to high halo mass. This, along with the flatter mass trend observed for the steep exponentials (after exclusion of AGNs) suggests that the environment is largely responsible for forming these compact $H\alpha$ disks, and suggests they might be galaxies on the way to becoming completely quenched via an outside-in mechanism. Since HAGGIS galaxies live in groups of $10^{12} - 10^{14} M_{\odot}$, this suggests that the environment affects galaxies substantially in high mass haloes ($\geq 10^{12} M_{\odot}$).

We find that the galaxies with truncated $H\alpha$ disks are less common in massive haloes which is opposite to the findings in cluster galaxies (see e.g. [Koopmann & Kenney \(2004\)](#)) although many of these cluster galaxies would actually be classified as steep exponentials based on our classification scheme. These truncated $H\alpha$ disks typically belong to the normal SF MS population (see section 6.4), and are often found to have type II (truncated) stellar disks (49^{+6}_{-6} %; see figure 4.5), suggesting that these $H\alpha$ truncations are likely not a result of any environmental interaction.

Recent multi-wavelength observations suggest that similar truncations in the outer SF disks observed in nearby galaxies are the result of extremely inefficient SF with typical gas depletion timescales of $\sim 10^{11}$ yrs ([Bigiel et al. \(2010\)](#)) and the configuration remaining stable over a galaxy's lifetime ([Hunter et al. \(2011\)](#)).

The dichotomous distribution in the ratio of $H\alpha$ half light size to continuum half light size observed for high mass galaxies seen in chapter 5 (fig. 5.10(b)) is also seen for central galaxies in HAGGIS groups, while most HAGGIS satellites have much smaller size ratios (< 1), indicating that most satellites in HAGGIS groups are likely affected to some extent by their environment. This agrees with the general consensus that satellites are the main driver of the environmental interactions (see e.g. section 1.2.1).

Galaxies that have size ratios larger than one mainly exhibit sawtooth profiles which are typically found at high mass. Hence, the larger $H\alpha$ sizes compared to their stellar sizes can be the effect of somewhat biased measurements in both stellar continuum half light radius, which can be biased to smaller values due to the bulge contamination, and $H\alpha$ half light radius, which can be biased to larger values due to the presence of the intermediate dip region in the $H\alpha$ profiles.

Finally we also look at the relation between the deviation of the galaxy's SFR from the SF main sequence with the ratio of its $H\alpha$ and stellar continuum sizes in the context of centrals and satellites. We have found that the majority (81^{+5}_{-6} %) of SF centrals (excluding AGN) have $H\alpha$ half light sizes similar or even larger to their stellar continuum half light sizes and have SFRs that are slightly higher than the MS fit.

For the SF satellites, three regions can be defined with respect to the size ratios. Satellite galaxies having $Re_{H\alpha}/Re_c > 0.8$ are observed to have SFR on average close to the MS with some scatter, satellites having $0.45 < Re_{H\alpha}/Re_c < 0.8$ are observed to have slightly lower SFR on average than MS galaxies, while satellites having much smaller $Re_{H\alpha}/Re_c$ (< 0.44) are observed to have SFRs way below the

SF MS. This is indicative of outside-in quenching of satellite galaxies, probably due to stripping of their outer disks.

Chapter 8

Conclusions and future work

We began this thesis by noting that some of the questions in the theory of galaxy evolution like “whether the galaxy environment affects the SFR in SF galaxies?” and “where and how the quenching of SF activity happens in some galaxies?” would remain unanswered unless and until we explore the resolved properties of galaxies living in groups which are representative of the bulk of the galaxy population (e.g. [Eke et al. \(2004\)](#)). To address these questions, we have devised a narrow-band imaging survey called the “HAGGIS survey”. We have observed 100 (plus 20 serendipitously found) galaxy groups in the local universe ($0.01 < z < 0.055$) over a wide range of halo masses ($M_{\text{halo}} = 10^{12} - 10^{14} M_{\odot}$) using pairs of narrow-band filters with the aim to trace star-formation within galaxies using the resolved continuum-subtracted $H\alpha$ emission.

We have used accurate and novel data reduction techniques for HAGGIS data which includes accurate relative astrometric registration and point spread function (PSF) matching of two narrow-band observations, and accurate flux scaling of our continuum narrow-band images using SDSS flux-calibrated spectra. We have thus obtained good quality continuum-subtracted $H\alpha$ and narrow-band continuum images and derived azimuthally averaged radial surface brightness profiles. These profiles are used to classify HAGGIS galaxies using a pre-existing classification scheme for stellar continuum profiles and a newly devised classification scheme for $H\alpha$ profiles.

We have then explored the relations between various global galaxy properties like stellar and $H\alpha$ size, global SFR and stellar mass, and analyzed the systematic deviations in these relations with respect to other galaxy properties, with respect to the classifications based on stellar continuum and $H\alpha$ profiles, and with respect

to whether the galaxy is a ‘central’ (which lives in or near to the center of the group potential) or a ‘satellite’ (galaxies that orbit around the center of the group potential). We have also analyzed the role played by galaxy’s stellar mass and the mass of the group halo in which it resides, in shaping its stellar and $H\alpha$ profiles.

In section 8.1, we summarize the key results from chapters 5, 6 and 7 of this thesis. In section 8.2, we tie together the key findings of this thesis emphasizing their impact on our current understanding of galaxy evolution and compare them with the available literature. Finally, we consider the future prospects of the large dataset provided by the HAGGIS survey and its potential role in driving the scientific explorations of other ongoing surveys in section 8.3.

8.1 Summary

8.1.1 Size-mass relations

In chapter 5, we have derived power law relations of the galaxy’s stellar continuum and $H\alpha$ sizes with its stellar mass and observed that the residual relation correlates with galaxy SFR. We have also used our dual classification schemes to understand these relations with respect to galaxy’s continuum and $H\alpha$ surface brightness profiles. We have found that:

- Galaxies that are quenched or forming stars less rapidly than normal star-forming galaxies of the similar stellar mass have compact stellar sizes compared to the SF galaxies. This is in qualitative agreement with the findings for SDSS galaxies (Williams et al. (2010)). At fixed stellar mass, galaxies that have low star-forming activity compared to the normal star-forming population have more compact $H\alpha$ disks. This suggests that the quenching mechanisms compactify the stellar and $H\alpha$ disks in galaxies.
- At the low mass end, the majority of galaxies with compact stellar and $H\alpha$ disks compared to SF galaxies of similar mass have stellar type III profiles while galaxies with non-exponential profiles are more common at high mass. Type III galaxies are in general found to have more compact stellar and $H\alpha$ disks compared to other disk profile types. This suggests that the majority of these anti-truncated stellar disks are the result of, or relate to quenching mechanisms.

- The galaxies with compact stellar disks are typically detected with $H\alpha$ in absorption in HAGGIS observations. Many galaxies with exponentially declining $H\alpha$ profiles that are steeper compared to their stellar profile (which are thus classified as “steep exponentials”) also have compact stellar disks suggesting that these galaxies are possibly undergoing the transformation to become a passive galaxy. Broken-exponential $H\alpha$ profiles (“truncated”) or profiles starting flat and then truncated (“flat-truncated”), on the other hand, exhibit normal stellar and $H\alpha$ half light radii for their stellar mass.
- The majority of HAGGIS galaxies, especially at low mass ($M_* < 10^{10.3} M_\odot$), are found to have smaller $H\alpha$ disks compared to their stellar disks which is similar to findings for cluster galaxies (Koopmann et al. (2006)). The high mass HAGGIS galaxies ($M_* > 10^{10.3} M_\odot$) show a dichotomy in $\text{Log}(\text{Re}_{H\alpha}/\text{Re}_c)$ with many galaxies having larger $H\alpha$ disks and some having very compact $H\alpha$ disks compared to their stellar disks. The difference in the distribution of $\text{Log}(\text{Re}_{H\alpha}/\text{Re}_c)$ suggests that quenching mechanisms act differently in the two mass regimes.

8.1.2 SFR-mass relations

We have compared the SFR-stellar mass relations in chapter 6, using various SFR measurements from the HAGGIS, SDSS and $H\alpha 3$ datasets in order to assess the quality of our SFR measurements. By comparing the distribution of the SFR offset from the star-forming main sequence (SF MS; the SFR-stellar mass relation for normal SF galaxies) for the SDSS and HAGGIS galaxies, we have found that the HAGGIS survey has a larger fraction of passive galaxies compared to SDSS. This is possibly the result of the survey selection, as more massive groups, which typically contain a larger than average fraction of passive galaxies, are deliberately selected for the HAGGIS survey in order to study environmental effects. We have defined a class of galaxies called the “HAGGIS star-forming galaxies” in this chapter based on the detection of $H\alpha$ emission while excluding galaxies having Active Galactic Nuclei (AGN) and Low Ionization Nuclear Emission Region (LINER) from the sample using SDSS spectroscopic classifications to ensure that the emission is coming only from SF. The key results from this chapter are:

- “HAGGIS star-forming galaxies” have a very skewed distribution towards the low SFR end which extends well into the range of SFR defined by Brinchmann et al. (2004) in SDSS to be “passive” and dominated by galaxies for

which SFR estimates are based upon stellar spectral features and not on emission lines. This suggests that the SDSS definition of “passive galaxies” also include some galaxies with very low but significant SFR that may be undergoing a transformation to become a passive galaxy. Such galaxies form an important class to study the effects of quenching mechanisms, especially in the context of environmental interactions, but will have been missed by SDSS.

- Galaxies with most types of $H\alpha$ surface brightness profile, including those with a break or “truncation” in their $H\alpha$ profiles have similar SFRs for their stellar mass. This suggests that the shape of the $H\alpha$ profile is largely independent of the total level of SF in these galaxies.
- The only exception to this are the steep exponentials, which typically have very low SFRs for their stellar mass.
- Although these trends can also be reproduced by the SDSS aperture corrected SFRs, we have found that SDSS SFRs are systematically different compared to the HAGGIS measurements. The latter correlate very well with $\text{Log}(\text{Re}_{H\alpha}/\text{Re}_c)$, while SDSS SFRs are found to be overestimated for galaxies having compact $H\alpha$ disks and underestimated for galaxies having extended $H\alpha$ disks compared to their stellar disks.
- We have also found that the deviation of a galaxy’s SFR from the MS ($\Delta(\text{SFR})$) correlates with $\text{Log}(\text{Re}_{H\alpha}/\text{Re}_c)$, especially for galaxies having very compact $H\alpha$ disks compared to their stellar disks ($\text{Re}_{H\alpha}/\text{Re}_c < 0.45$).

8.1.3 Stellar mass and galaxy environment

We have compared the frequencies of different classes of galaxies as a function of the galaxy’s stellar mass and of the mass of the group halo in which they reside in chapter 7. Also, we have analyzed some of the relations shown in chapters 5 and 6 separately for the centrals and satellites of HAGGIS groups. The key findings are:

- Up-bending type III and non-exponential stellar continuum profiles are more common among passive galaxies than the SF ones while the majority of down-bending type II profiles are observed in SF galaxies. The frequency of pure exponential type I is similar for both the passive and the SF populations.

This suggests that the quenching mechanisms affect the shape of the stellar surface brightness profiles, or otherwise favors certain types of galaxy.

- Type III galaxies are more common at low stellar masses and non-exponentials are more common at high masses. The latter is the confirmation of the fact that elliptical galaxies, which have such non-exponential profiles, tend to be more massive than the disk profile types. The frequency of type I and type II profiles does not show any clear correlation with stellar mass.
- On the other hand, the frequency of type III and non-exponentials is independent of the group halo mass. The frequency of type I and type II shows stronger trends such that the type I galaxies are more common in high mass haloes and type IIs are more common in low mass ones. Type II quenched galaxies are almost non-existent in high mass haloes, mirroring the findings in the Virgo cluster ([Erwin et al. \(2012\)](#)).
- Galaxies with truncated, flat-truncated and exponential $H\alpha$ profiles are more common at lower stellar mass while galaxies with sawtooths and absorption (including non-detections) $H\alpha$ profiles are more common at high stellar mass.
- Most $H\alpha$ emission line profile types (i.e. excluding absorption and non-detections) are observed to be less common in high mass haloes. This is in agreement with the consensus that the fraction of SF galaxies decreases in massive groups (e.g. [Weinmann et al. \(2006\)](#), [van den Bosch et al. \(2008\)](#)).
- The steep exponentials are the only exception among the SF galaxies, and are increasingly more common in high mass haloes. This is strong evidence for an environmental formation mechanism, linked to outside-in quenching.
- The majority of HAGGIS SF satellites have $Re_{H\alpha}/Re_c < 1$ indicating that most satellites in HAGGIS groups are affected to some extent by their environment. The satellites having very compact $H\alpha$ disks compared to their stellar disks are observed to have very low SFRs compared to the SF MS galaxies of similar mass suggesting an outside-in quenching.
- HAGGIS SF centrals, being typically more massive than satellites, show a dichotomous distribution of $Re_{H\alpha}/Re_c$ as shown by high mass galaxies. The majority of SF centrals (81^{+5}_{-6} %) are on, or even slightly above the MS and the rest have very low $Re_{H\alpha}/Re_c$ (≤ 0.45) and very low SFRs compared to the SF MS galaxies of similar mass.

8.2 Discussion

Over a period of time, we have built a picture of how galaxies have evolved to their present form and what are the drivers of this evolution. Now, the general consensus is that the blue star-forming galaxies are transformed into passive red galaxies via quenching processes which are function of a galaxy’s stellar mass (“mass quenching”) and its environment (“environmental quenching”). The latter is driven mainly by the satellite population (see the discussion in the introduction of this thesis, especially Section 1.2) although the physical processes involved in this transformation and the timescale over which they operate on galaxies are yet unclear.

With the HAGGIS survey, we have observed that the galaxies show stark differences in two bins of stellar mass split at $10^{10.3} M_{\odot}$. Almost all galaxies in the low mass bin (most of which are satellites) have $H\alpha$ disks of the same, or usually smaller size than their stellar disks. The global SFR of these galaxies is a function of the ratio of $H\alpha$ to stellar sizes such that the galaxies with smaller $H\alpha$ disks are likely to have lower SF activity compared to the average SFR for their stellar mass (i.e. they are below the main sequence of star forming galaxies). However the SFR is only strongly affected for $H\alpha$ half light sizes < 0.44 of their stellar half light size.

On the other hand, star-forming galaxies at high mass (the majority of which are centrals) show a distinct dichotomy in the ratio of $H\alpha$ disk size to their stellar disk size with $\sim 60^{+5}_{-5} \%$ having $H\alpha$ disks of similar or even larger size and the remaining fraction have very compact $H\alpha$ disks compared to their stellar disks. This suggests that the evolutionary processes which drive the changes in the $H\alpha$ disk size and the global SFR, are either different in the two mass regimes or have different timescales.

In addition to this clear difference between these two stellar mass regimes, we have found that all galaxies which have very compact $H\alpha$ disks ($Re_{H\alpha}/Re_c < 0.45$) have SFRs that are below that of the SF MS galaxies of similar mass. Most of these galaxies have a steep exponential $H\alpha$ profile, and the majority are satellites (when AGNs are removed from the classification). This is suggestive of an outside-in quenching due to environmental interactions which is driven mainly by the satellite population.

Galaxies with steep exponential $H\alpha$ profiles are typically below the SF MS, and are found to be more common in high mass haloes with a frequency independent of stellar mass, especially when the AGNs (which are typically classified as steep exponential due to their centrally concentrated $H\alpha$ emission) are excluded from the classification. This suggests that these galaxies are likely the outcome of environmental interactions. Similar compact galaxies are also found in clusters like Virgo and are rare in isolated environments (Koopmann & Kenney (2004)). Our results now suggest that the frequency of these galaxies monotonously increases as a function of group halo mass over the range of HAGGIS groups ($10^{12} - 10^{14} M_{\odot}$). This suggests that some of the environmental trends observed in clusters can be explained, at least partially, by the ‘pre-processing’ of galaxies in their previous (group) environment before they are accreted onto their current haloes.

Galaxies with truncated (down-bending broken-exponential) $H\alpha$ disks, on the other hand, are typically found to be on the SF MS, and have similar half light sizes of $H\alpha$ disks compared to their stellar disks, and are rare at high mass and in massive haloes. This suggests that the environmental interactions do not cause these truncations in the $H\alpha$ profile for the majority of such galaxies. Although some clear cases of ram-pressure stripping have been identified in clusters to be associated with a truncation in $H\alpha$ profiles (e.g. Boselli et al. (2006)), our results suggest that these might be a minority of such galaxies, especially in group environments. We also would like to note that the increase in the fraction of truncated galaxies in the Virgo cluster compared to field galaxies reported by Koopmann & Kenney (2004) is the result of a different definition of truncation used in their work and many of so called ‘truncated galaxies’ in their sample have compact $H\alpha$ disks similar to the steep exponentials in our sample.

We have observed that the stellar disks are also affected by the quenching mechanisms. Galaxies which are already quenched or are forming fewer new stars than the SF galaxies of similar stellar mass, have been found to have relatively compact stellar disks for their stellar mass. The majority of these galaxies have type III (up-bending) stellar profiles at low mass and non-exponential profiles at high mass. The stellar and halo mass dependence of stellar profile types in the SF and quenched population suggest that the type II (down-bending) stellar disks are transformed into other disk profile types if they are quenched, or when they are accreted onto larger haloes. The recent hydrodynamic simulations performed by Herpich et al. (2015) suggest that type II (III) galaxies have on average larger

(smaller) angular momentum compared to other disk types. Our findings thus suggest that galaxies lose internal angular momentum during the quenching process and when they are accreted into larger haloes.

Taken together, our results suggest that the transformation of the galaxy’s stellar profile and compactification of $H\alpha$ and stellar disks are associated with the quenching of SF especially in satellites galaxies in high mass groups. This suggests that gas-stripping processes like ‘ram-pressure stripping’ which lead to compactification of $H\alpha$ disks must be supplemented by gravitational tidal interactions which affect the stellar morphology.

Compared to HAGGIS measurements, we have found that the SDSS aperture corrected SFR measurements over-(under-)estimate the SFR in galaxies with small (large) $H\alpha$ sizes relative to their continuum ones. We have found that the definition of ‘passive galaxies’ based on these SDSS measurements is not very useful to distinguish the star-forming galaxies from the passive ones as the [Brinchmann et al. \(2004\)](#) definition of ‘passive galaxies’ also includes some transitional galaxies having low but measurable SFRs compared to normal SF galaxies which are an important class especially to understand the quenching mechanisms. This marks the limitation of SDSS measurements and highlights the importance of resolved $H\alpha$ studies like HAGGIS.

8.3 Future prospects

The HAGGIS dataset with its vast amount of resolved $H\alpha$ and continuum narrow-band images can potentially be used to address many unsolved scientific questions about galaxy evolution. But there are inherent limitations in narrow-band imaging some of which are discussed in this thesis, especially in chapter 6. The next generation galaxy evolution surveys are now based on observations that are both spectrally and spatially resolved which means that they could apply the powerful spectroscopic techniques used in the SDSS survey to these spatially resolved galaxy spectra which would revolutionize our understanding of galaxy evolution. In this section, we describe some of the prospective scientific explorations we think one can undertake with HAGGIS and with the ongoing next generation IFU surveys.

8.3.1 Prospects of HAGGIS

The HAGGIS dataset provides 2-dimensional resolved images for stellar continuum and continuum subtracted $H\alpha$ which can be used effectively to classify galaxies based on the complete 2-dimensional information and to measure some of the quantities like concentration and asymmetry. This would provide a natural extension of the work we have done in this thesis. A more detailed study of each individual $H\alpha$ and stellar profile type could also help us to understand the origin of these different classes. For example, one can undertake a systematic study to compare the position and strength of the breaks in $H\alpha$ and stellar profiles which would help in understanding their origin and address some questions like “what mechanisms are involved in forming these breaks in the surface brightness profiles?”. Similarly, the galaxies with sawtooth $H\alpha$ profiles can be studied in detail to understand “what causes the intermediate dip in the $H\alpha$ profile of these galaxies?”; for example their relationship with bars.

The accurate continuum estimation in the HAGGIS dataset has enabled us to detect $H\alpha$ in absorption where there is no emission in the galaxy. This absorption information can be used to constrain the star-formation history in these galaxies and would help us understand “how, where and when these galaxies have quenched their SF activity?”. A stack of surface brightness profiles and/or the 2-dimensional images for HAGGIS galaxies would also help us understand how environmental mechanisms affect the galaxies living in groups in a statistical sense. It would also be useful to extend the mass range in the HAGGIS sample by searching for very low mass galaxies on our images which are detected in emission but do not have SDSS redshifts.

8.3.2 Other surveys

Our understanding of evolutionary processes would be incomplete if we do not have spatially resolved multi-wavelength observations for a very large sample of galaxies. The ongoing state of the art “integral field unit” (IFU) surveys like MaNGA, SAMI, CALIFA, etc that provide both spectrally and spatially resolved observations of large datasets are thus going to revolutionize our understanding of galaxy evolution. With this type of dataset, we can measure the stellar and gas phase kinematics, perform spatially resolved stellar population synthesis modeling analysis that can provide 2-dimensional maps of stellar age, star-formation history, metallicity, element abundance ratio, etc. Along with the measurements of current

SFR and galaxy's structural parameters, these measurements will help us understand the physical processes involved in galaxy evolution, especially in the context of quenching of SF. The better spatial coverage and spatial resolution of narrow-band imaging surveys like HAGGIS will provide an important complementary dataset to these state of the art surveys. I find that the results presented in this thesis can also provide a good starting point to devise targeted IFU observations. For example, to track the recent SF history using stellar population analysis of the outer disk of galaxies which host central SF to examine the outside-in quenching hypothesis.

Bibliography

- Bakos, J., Trujillo, I., & Pohlen, M. 2008, *ApJ*, 683, L103
- Baldry, I. K., Balogh, M. L., Bower, R., Glazebrook, K., & Nichol, R. C. 2004, in *American Institute of Physics Conference Series*, Vol. 743, *The New Cosmology: Conference on Strings and Cosmology*, ed. R. E. Allen, D. V. Nanopoulos, & C. N. Pope, 106–119
- Baldry, I. K., Balogh, M. L., Bower, R. G., et al. 2006, *MNRAS*, 373, 469
- Ball, N. M., Loveday, J., & Brunner, R. J. 2008, *MNRAS*, 383, 907
- Balogh, M., et al. 2004a, *MNRAS*, 348, 1355
- Balogh, M. L., Baldry, I. K., Nichol, R., et al. 2004b, *ApJ*, 615, L101
- Balogh, M. L., & Morris, S. L. 2000, *MNRAS*, 318, 703
- Bekki, K. 2014, *MNRAS*, 438, 444
- Bennett, C. L., Larson, D., Weiland, J. L., et al. 2013, *ApJS*, 208, 20
- Berlind, A. A., Blanton, M. R., Hogg, D. W., et al. 2005, *ApJ*, 629, 625
- Bertin, E., & Arnouts, S. 1996, *A&AS*, 117, 393
- Bertin, E., Mellier, Y., Radovich, M., et al. 2002, in *Astronomical Society of the Pacific Conference Series*, Vol. 281, *Astronomical Data Analysis Software and Systems XI*, ed. D. A. Bohlender, D. Durand, & T. H. Handley, 228
- Bigiel, F., Leroy, A., Walter, F., et al. 2010, *AJ*, 140, 1194
- Bland-Hawthorn, J., Vlažić, M., Freeman, K. C., & Draine, B. T. 2005, *ApJ*, 629, 239
- Borlaff, A., Eliche-Moral, M. C., Rodríguez-Pérez, C., et al. 2014, *A&A*, 570, A103

- Boselli, A., Boissier, S., Cortese, L., et al. 2006, *ApJ*, 651, 811
- Brinchmann, J., Charlot, S., White, S. D. M., et al. 2004, *MNRAS*, 351, 1151
- Cebrián, M., & Trujillo, I. 2014, *MNRAS*, 444, 682
- Chincarini, G. 1984, *Advances in Space Research*, 3, 393
- Cohen, J. G. 1976, *ApJ*, 203, 587
- Colless, M. 1999, *Royal Society of London Philosophical Transactions Series A*, 357, 105
- Comerón, S., Elmegreen, B. G., Salo, H., et al. 2012, *ApJ*, 759, 98
- Cortese, L., Catinella, B., Boissier, S., Boselli, A., & Heinis, S. 2011, *MNRAS*, 415, 1797
- Cowie, L. L., & McKee, C. F. 1977, *ApJ*, 211, 135
- Cybulski, R., Yun, M. S., Fazio, G. G., & Gutermuth, R. A. 2014, *MNRAS*, 439, 3564
- Davies, R. D., & Lewis, B. M. 1973, *MNRAS*, 165, 231
- De Lucia, G., Springel, V., White, S. D. M., Croton, D., & Kauffmann, G. 2006, *MNRAS*, 366, 499
- Deng, X.-F., & Zou, S.-Y. 2009, *Astroparticle Physics*, 32, 129
- Dressler, A. 1980, *ApJ*, 236, 351
- Dressler, A., & Gunn, J. E. 1983, *ApJ*, 270, 7
- Driver, S. P., Hill, D. T., Kelvin, L. S., et al. 2011, *MNRAS*, 413, 971
- Dutton, A. A., & van den Bosch, F. C. 2012, *MNRAS*, 421, 608
- Dutton, A. A., van den Bosch, F. C., Dekel, A., & Courteau, S. 2007, *ApJ*, 654, 27
- Einasto, J., Kaasik, A., & Saar, E. 1974, *Nature*, 250, 309
- Eke, V. R., Baugh, C. M., Cole, S., et al. 2004, *MNRAS*, 348, 866
- Elbaz, D., Daddi, E., Le Borgne, D., et al. 2007, *A&A*, 468, 33
- Elbaz, D., Dickinson, M., Hwang, H. S., et al. 2011, *A&A*, 533, A119

- Erwin, P., Beckman, J. E., & Pohlen, M. 2005, *ApJ*, 626, L81
- Erwin, P., Gutiérrez, L., & Beckman, J. E. 2012, *ApJ*, 744, L11
- Erwin, P., Pohlen, M., & Beckman, J. E. 2008a, *AJ*, 135, 20
- Erwin, P., Pohlen, M., Gutiérrez, L., & Beckman, J. E. 2008b, in *Astronomical Society of the Pacific Conference Series*, Vol. 396, *Formation and Evolution of Galaxy Disks*, ed. J. G. Funes & E. M. Corsini, 207
- Fabian, A. C. 2012, *ARA&A*, 50, 455
- Fasano, G., Poggianti, B. M., Bettoni, D., et al. 2015, *MNRAS*, 449, 3927
- Fossati, M., Gavazzi, G., Savorgnan, G., et al. 2013, *A&A*, 553, A91
- Freeman, K. C. 1970, *ApJ*, 160, 811
- Gavazzi, G., Fumagalli, M., Cucciati, O., & Boselli, A. 2010, *A&A*, 517, A73
- Gavazzi, G., Fumagalli, M., Galardo, V., et al. 2012, *A&A*, 545, A16
- Gavazzi, G., Consolandi, G., Viscardi, E., et al. 2015, *A&A*, 576, A16
- George, M. R., Ma, C.-P., Bundy, K., et al. 2013, *ApJ*, 770, 113
- Giovanelli, R., & Haynes, M. P. 1985, *ApJ*, 292, 404
- Gunn, J. E., & Gott, III, J. R. 1972, *ApJ*, 176, 1
- Gutiérrez, L., Erwin, P., Aladro, R., & Beckman, J. E. 2011, *AJ*, 142, 145
- Haines, C. P., Pereira, M. J., Smith, G. P., et al. 2013, *ApJ*, 775, 126
- . 2015, *ApJ*, 806, 101
- Herpich, J., Stinson, G. S., Dutton, A. A., et al. 2015, *MNRAS*, 448, L99
- Hirschmann, M., De Lucia, G., Wilman, D., et al. 2014, *MNRAS*, 444, 2938
- Hubble, E. 1929, *Proceedings of the National Academy of Science*, 15, 168
- Hubble, E., & Humason, M. L. 1931, *ApJ*, 74, 43
- Hubble, E. P. 1925, *Popular Astronomy*, 33, 252
- . 1926, *ApJ*, 64, 321

- Hunter, D. A., Elmegreen, B. G., Oh, S.-H., et al. 2011, *AJ*, 142, 121
- James, P. A., & Percival, S. M. 2015, ArXiv e-prints, arXiv:1504.04013
- Kelkar, K., Aragón-Salamanca, A., Gray, M. E., et al. 2015, ArXiv e-prints, arXiv:1503.08225
- Kennicutt, R. C., & Evans, N. J. 2012, *ARA&A*, 50, 531
- Kennicutt, Jr., R. C. 1998, *ApJ*, 498, 541
- Kennicutt, Jr., R. C., & Kent, S. M. 1983, *AJ*, 88, 1094
- Kodama, T., Smail, I., Nakata, F., Okamura, S., & Bower, R. G. 2001, *ApJ*, 562, L9
- Koopmann, R. A., Haynes, M. P., & Catinella, B. 2006, *AJ*, 131, 716
- Koopmann, R. A., & Kenney, J. D. P. 2004, *ApJ*, 613, 866
- Kovač, K., Lilly, S. J., Knobel, C., et al. 2014, *MNRAS*, 438, 717
- Lacey, C., & Cole, S. 1993, *MNRAS*, 262, 627
- Laine, J., Laurikainen, E., Salo, H., et al. 2014, *MNRAS*, 441, 1992
- Lange, R., Driver, S. P., Robotham, A. S. G., et al. 2015, *MNRAS*, 447, 2603
- Lee, J. C., Gil de Paz, A., Tremonti, C., et al. 2009, *ApJ*, 706, 599
- Lilly, S. J., Le Fèvre, O., Renzini, A., et al. 2007, *ApJS*, 172, 70
- Lin, L., Jian, H.-Y., Foucaud, S., et al. 2014, *ApJ*, 782, 33
- Maltby, D. T., Aragón-Salamanca, A., Gray, M. E., et al. 2010, *MNRAS*, 402, 282
- Martínez-Serrano, F. J., Serna, A., Doménech-Moral, M., & Domínguez-Tenreiro, R. 2009, *ApJ*, 705, L133
- McGee, S. L., Balogh, M. L., Bower, R. G., Font, A. S., & McCarthy, I. G. 2009, *MNRAS*, 400, 937
- Minchev, I., Famaey, B., Quillen, A. C., et al. 2012, *A&A*, 548, A126
- Moore, B., Katz, N., Lake, G., Dressler, A., & Oemler, A. 1996, *Nature*, 379, 613
- Moss, C., & Whittle, M. 2000, *MNRAS*, 317, 667

- Nulsen, P. E. J. 1982, MNRAS, 198, 1007
- Ostriker, J. P., Peebles, P. J. E., & Yahil, A. 1974, ApJ, 193, L1
- Peng, Y.-j., Lilly, S. J., Renzini, A., & Carollo, M. 2012, ApJ, 757, 4
- Peng, Y.-j., Lilly, S. J., Kovač, K., et al. 2010, ApJ, 721, 193
- Poggianti, B. M., Calvi, R., Bindoni, D., et al. 2013, ApJ, 762, 77
- Pohlen, M., Beckman, J. E., Hüttemeister, S., et al. 2004, in *Astrophysics and Space Science Library*, Vol. 319, *Penetrating Bars Through Masks of Cosmic Dust*, ed. D. L. Block, I. Puerari, K. C. Freeman, R. Groess, & E. K. Block, 713
- Pohlen, M., & Trujillo, I. 2006, A&A, 454, 759
- Roberts, M. S., & Haynes, M. P. 1994, ARA&A, 32, 115
- Roškar, R., Debattista, V. P., Stinson, G. S., et al. 2008, ApJ, 675, L65
- Salim, S., Rich, R. M., Charlot, S., et al. 2007, ApJS, 173, 267
- Schaye, J. 2004, ApJ, 609, 667
- Schlegel, D. J., Finkbeiner, D. P., & Davis, M. 1998, ApJ, 500, 525
- Scoville, N., Aussel, H., Brusa, M., et al. 2007, ApJS, 172, 1
- Shen, S., Mo, H. J., White, S. D. M., et al. 2003, MNRAS, 343, 978
- Skibba, R. A., Bamford, S. P., Nichol, R. C., et al. 2009, MNRAS, 399, 966
- Speagle, J. S., Steinhardt, C. L., Capak, P. L., & Silverman, J. D. 2014, ApJS, 214, 15
- Strateva, I., Ivezić, Ž., Knapp, G. R., et al. 2001, AJ, 122, 1861
- Tal, T., Dekel, A., Oesch, P., et al. 2014, ApJ, 789, 164
- Tinker, J. L., George, M. R., Leauthaud, A., et al. 2012, ApJ, 755, L5
- Tody, D. 1986, in *Society of Photo-Optical Instrumentation Engineers (SPIE) Conference Series*, Vol. 627, *Instrumentation in astronomy VI*, ed. D. L. Crawford, 733
- Tody, D. 1993, in *Astronomical Society of the Pacific Conference Series*, Vol. 52, *Astronomical Data Analysis Software and Systems II*, ed. R. J. Hanisch, R. J. V. Brissenden, & J. Barnes, 173

- Valentijn, E. A., et al. 2007, in *Astronomical Society of the Pacific Conference Series*, Vol. 376, *Astronomical Data Analysis Software and Systems XVI*, 491
- van den Bergh, S. 1976, *ApJ*, 206, 883
- van den Bosch, F. C., Aquino, D., Yang, X., et al. 2008, *MNRAS*, 387, 79
- van der Kruit, P. C. 2001, in *Astronomical Society of the Pacific Conference Series*, Vol. 230, *Galaxy Disks and Disk Galaxies*, ed. J. G. Funes & E. M. Corsini, 119–126
- Vijayaraghavan, R., & Ricker, P. M. 2015, *MNRAS*, 449, 2312
- Vogt, N. P., Haynes, M. P., Giovanelli, R., & Herter, T. 2004, *AJ*, 127, 3300
- Vulcani, B., Poggianti, B. M., Finn, R. A., et al. 2010, *ApJ*, 710, L1
- Weinmann, S. M., van den Bosch, F. C., Yang, X., & Mo, H. J. 2006, *MNRAS*, 366, 2
- Wetzel, A. R., Tinker, J. L., & Conroy, C. 2012, *MNRAS*, 424, 232
- Wetzel, A. R., Tinker, J. L., Conroy, C., & van den Bosch, F. C. 2013, *MNRAS*, 432, 336
- Whitmore, B. C., Gilmore, D. M., & Jones, C. 1993, *ApJ*, 407, 489
- Williams, R. J., Quadri, R. F., Franx, M., et al. 2010, *ApJ*, 713, 738
- Wilman, D. J., & Erwin, P. 2012, *ApJ*, 746, 160
- Wilman, D. J., Zibetti, S., & Budavári, T. 2010, *MNRAS*, 406, 1701
- Wilson, E. 1927, *Journal of the American Statistical Association*, 22, 209
- Wolf, C., Aragón-Salamanca, A., Balogh, M., et al. 2009, *MNRAS*, 393, 1302
- Yang, X., Mo, H. J., van den Bosch, F. C., & Jing, Y. P. 2005, *MNRAS*, 356, 1293
- Yang, X., et al. 2007, *ApJ*, 671, 153
- York, D. G., Adelman, J., Anderson, Jr., J. E., et al. 2000, *AJ*, 120, 1579
- Younger, J. D., Cox, T. J., Seth, A. C., & Hernquist, L. 2007, *ApJ*, 670, 269
- Zahid, H. J., Dima, G. I., Kewley, L. J., Erb, D. K., & Davé, R. 2012, *ApJ*, 757, 54

Zibetti, S., Charlot, S., & Rix, H.-W. 2009, MNRAS, 400, 1181

Zwicky, F. 1933, Helvetica Physica Acta, 6, 110

—. 1937, ApJ, 86, 217

Appendix A

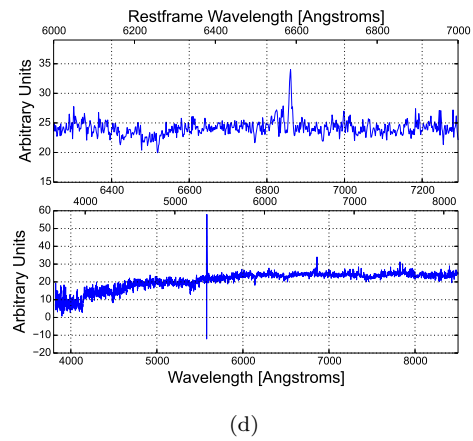
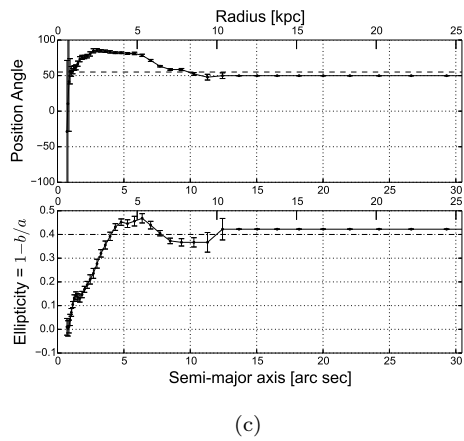
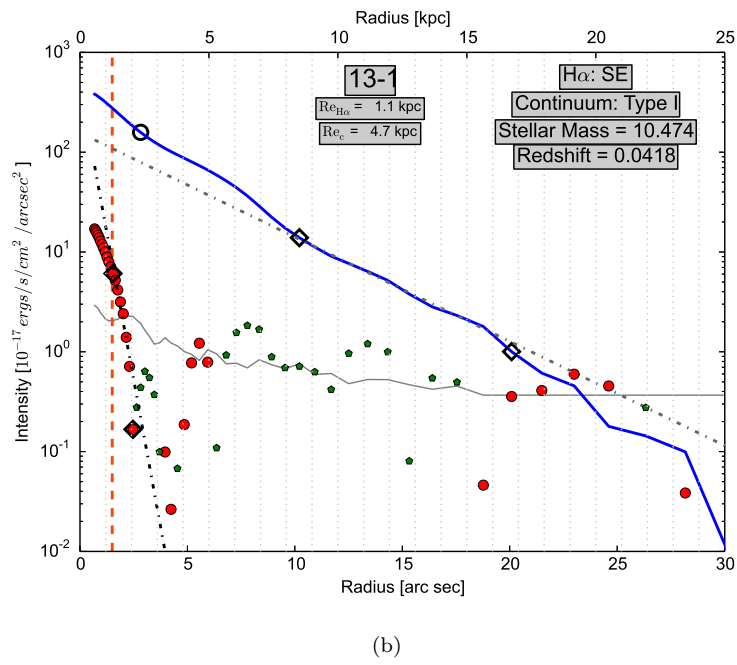
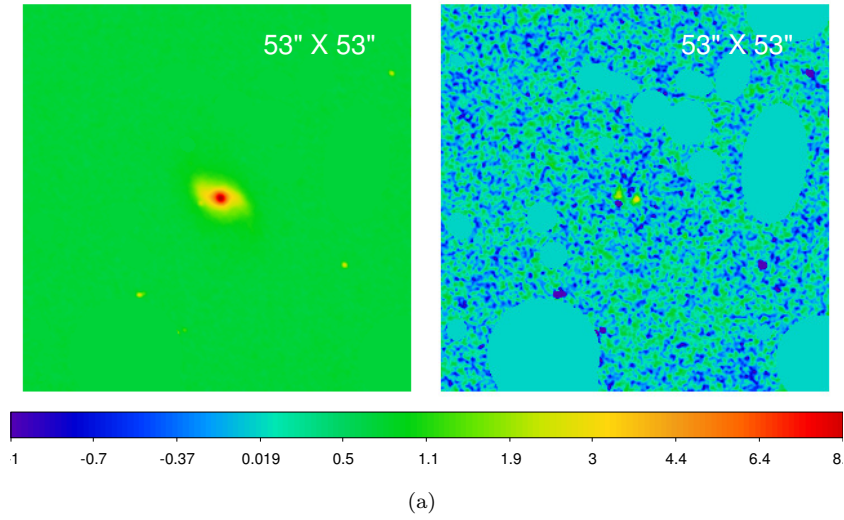
Profile plots

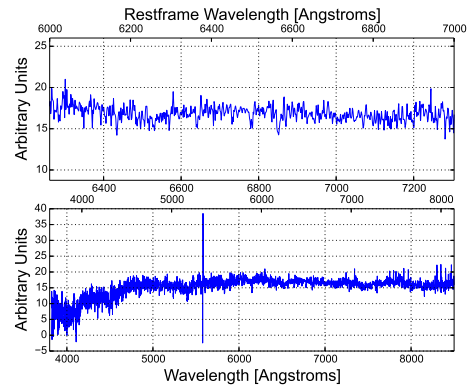
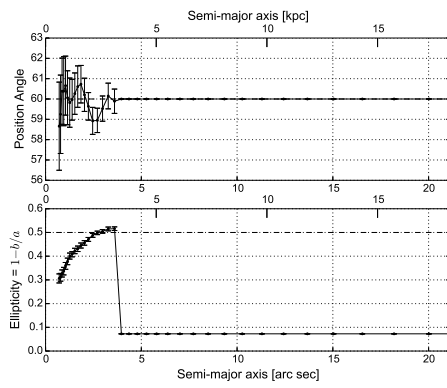
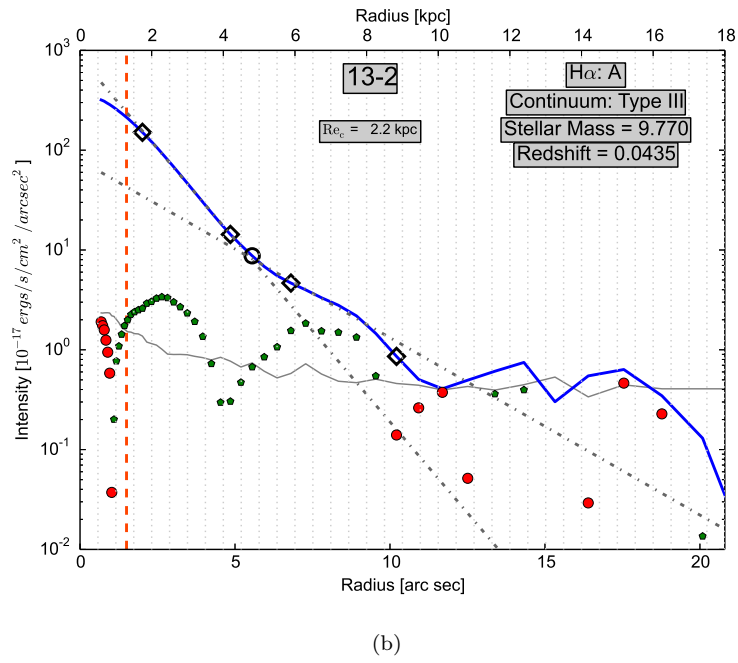
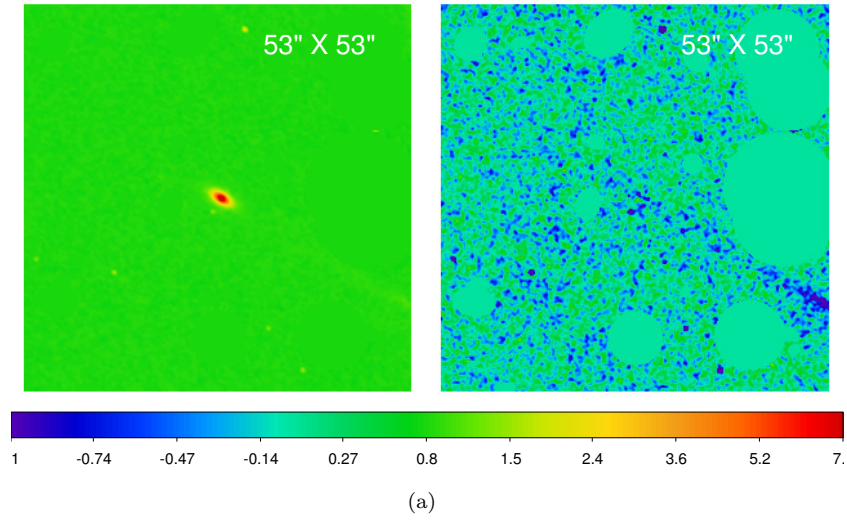
(a) Shows continuum (left) and continuum-subtracted $H\alpha$ (right) images. The physical scale of the cutout image in arc seconds is noted on both sub-panels. The color bar specifies the intensity level in units of $10^{-17} \text{ ergs sec}^{-1} \text{ cm}^{-2} \text{ pixel}^{-2}$.

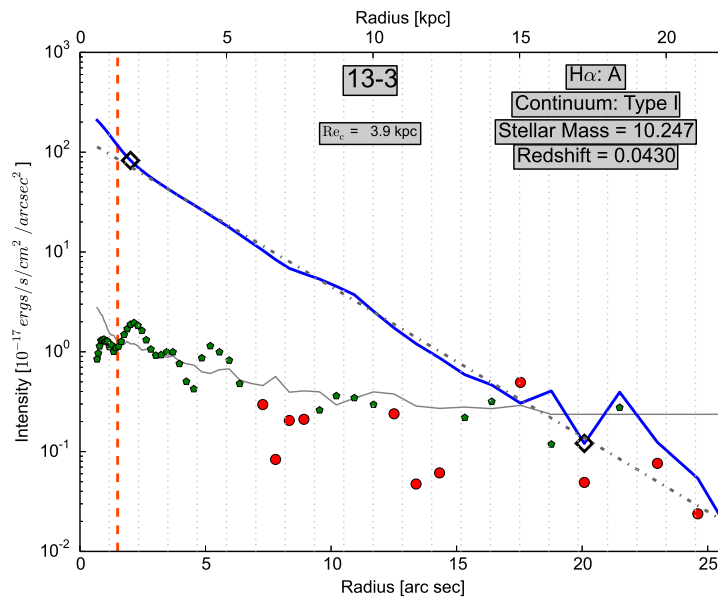
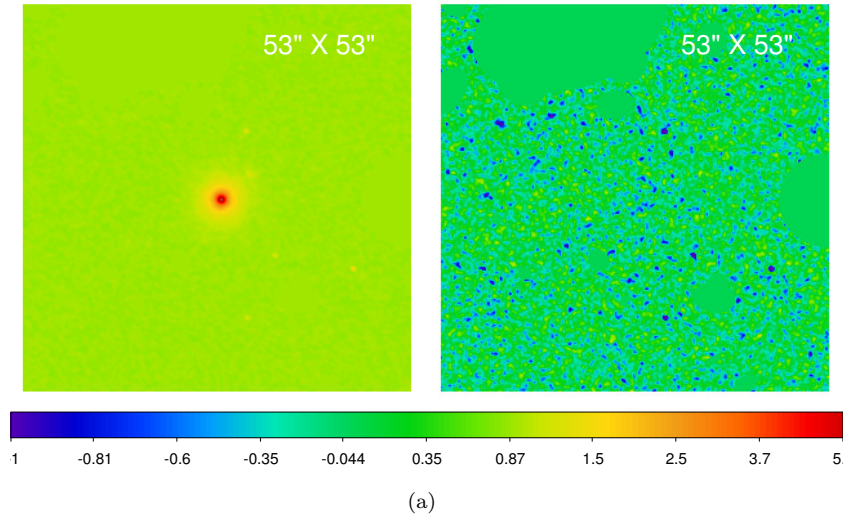
(b) Shows the continuum (blue) and $H\alpha$ (red in emission; green in absorption) surface brightness profiles from our narrow-band observations. The dashed orange vertical line specifies the size of the SDSS fiber. The grey line denotes the approximate rms noise level obtained for each radial bin from 100 blank sky regions. The linear fits to the continuum and $H\alpha$ profiles are over-plotted by dashed lines. The fitting radii are marked with open diamonds and the break radii are marked with open circles. Various text boxes on the plot specify the HAGGIS galaxy ID, the continuum and $H\alpha$ half light radii (R_{ec} and $R_{\text{H}\alpha}$), the type of the galaxy based on both of these profiles, the galaxy's stellar mass (as $\text{Log} \left(\frac{M_{\star}}{M_{\odot}} \right)$) and the redshift of the galaxy derived using SDSS spectroscopic data.

(c) Shows the ellipticity and position angle of the galaxy as a function of radius derived by the IRAF *ellipse* task using the narrow-band continuum image. The dashed lines on both of these plots denote the ellipticity and position angle values corresponding to the galaxy's outer disk which are used in deriving the surface brightness profiles.

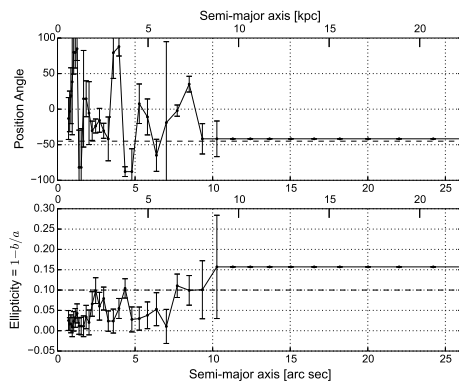
(d) Shows the SDSS spectrum of the galaxy for the whole wavelength range of SDSS observations (bottom panel) and zoomed in at around the $H\alpha$ wavelength (top panel).



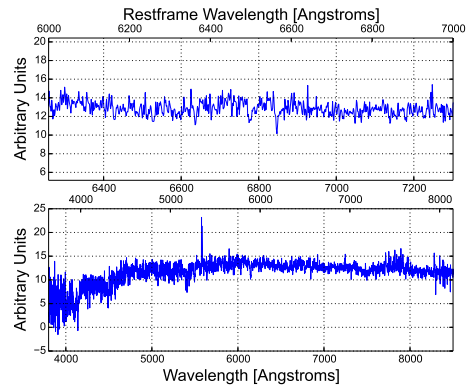




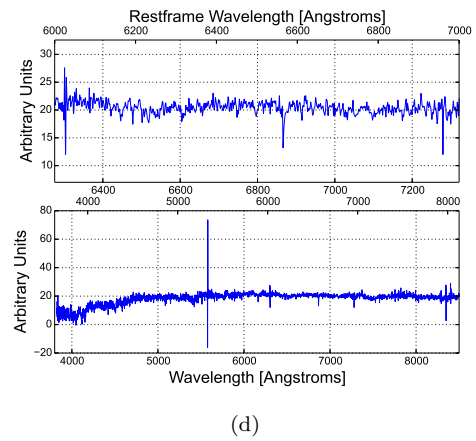
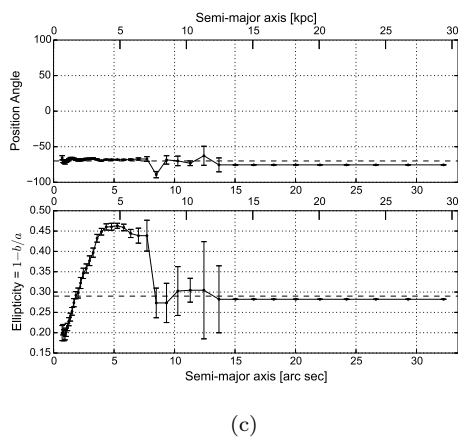
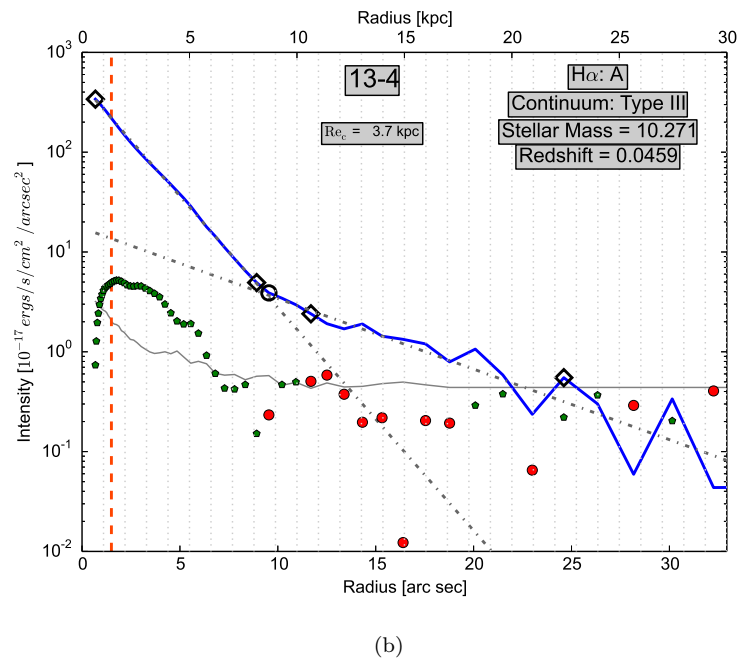
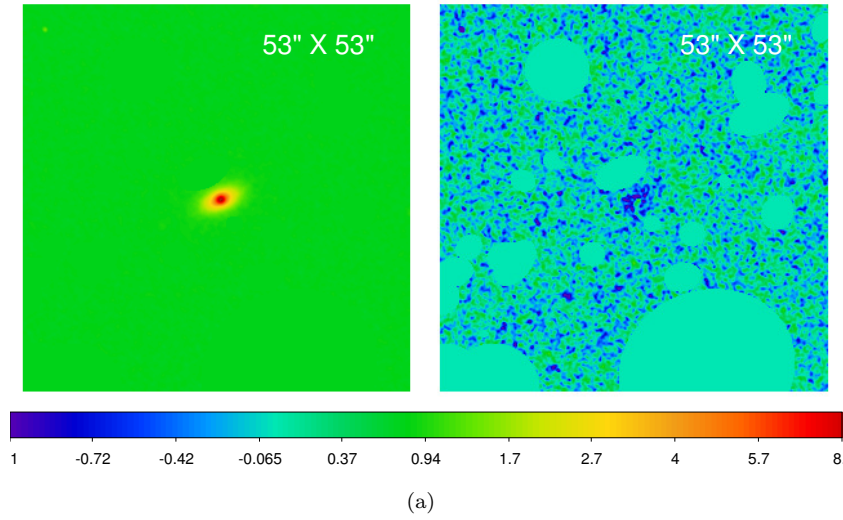
(b)

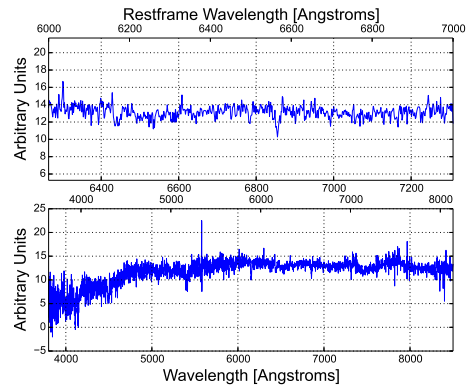
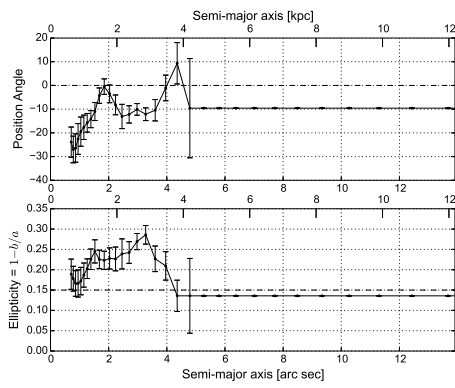
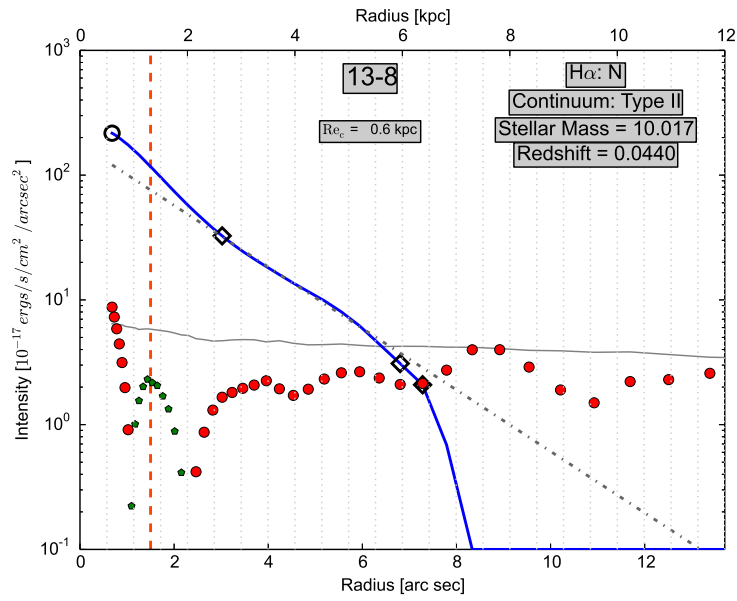
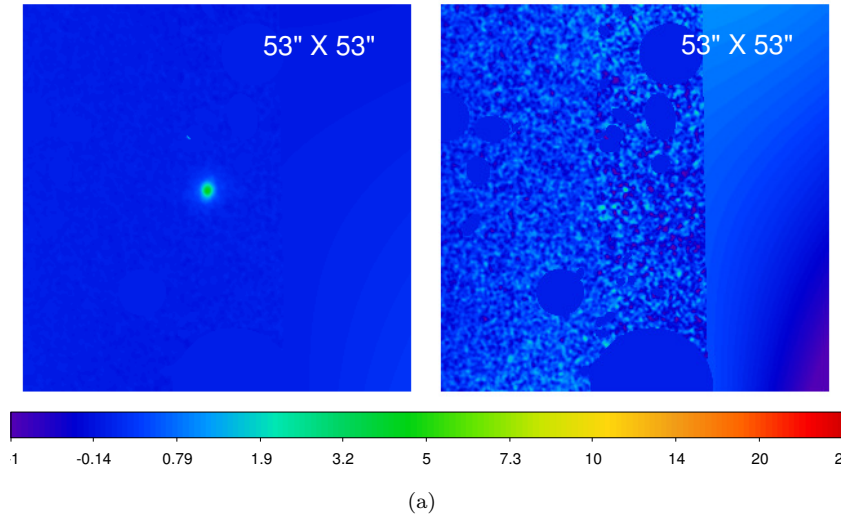


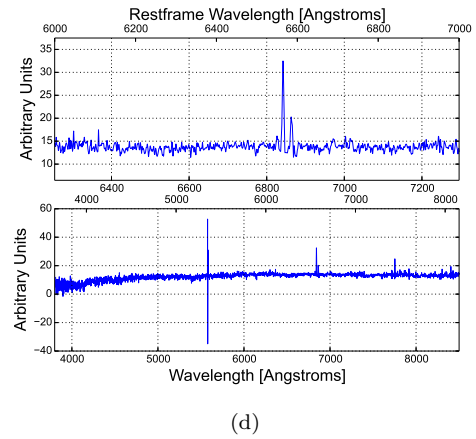
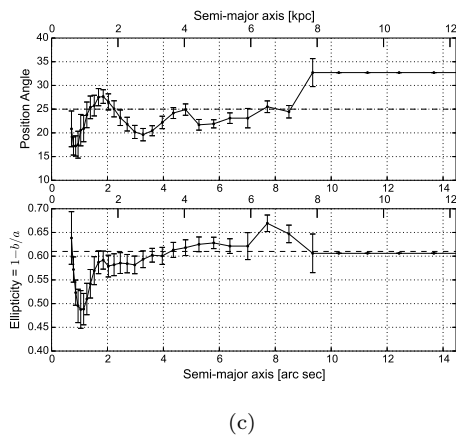
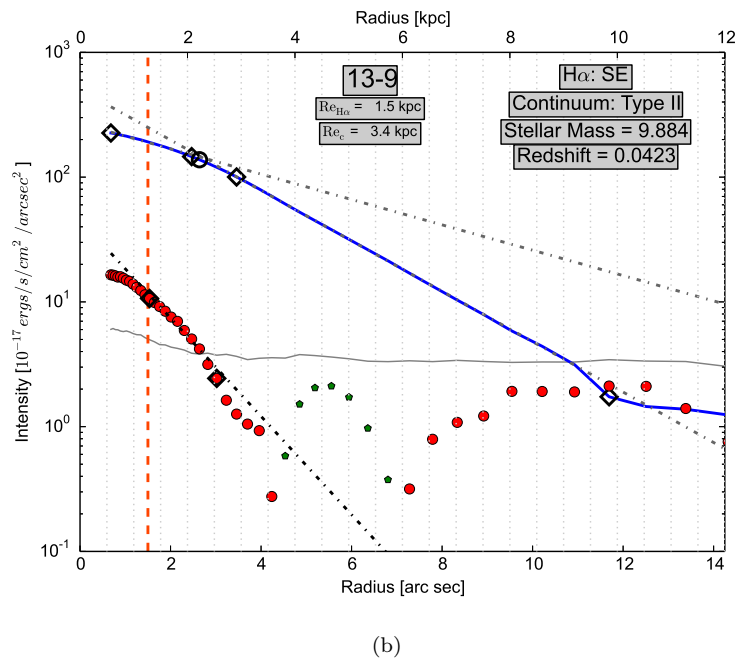
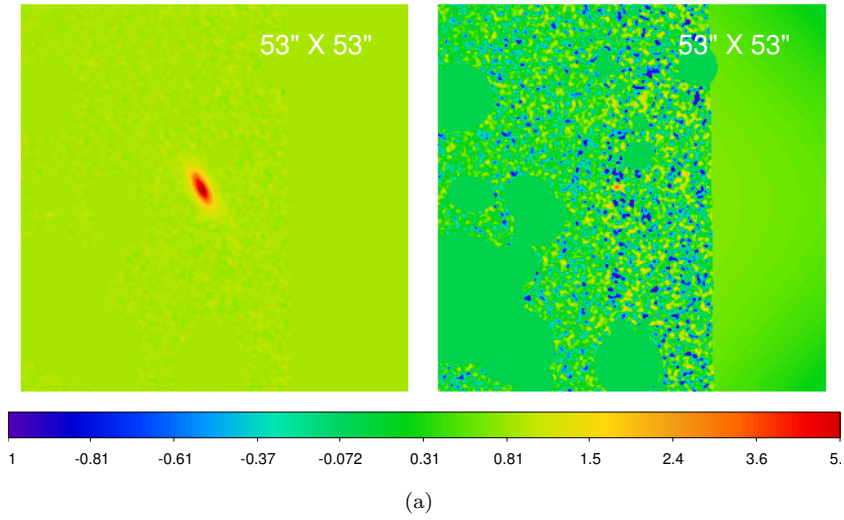
(c)

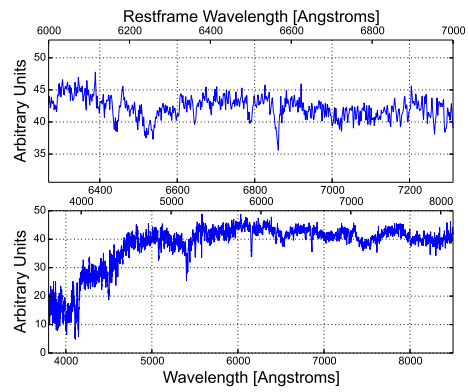
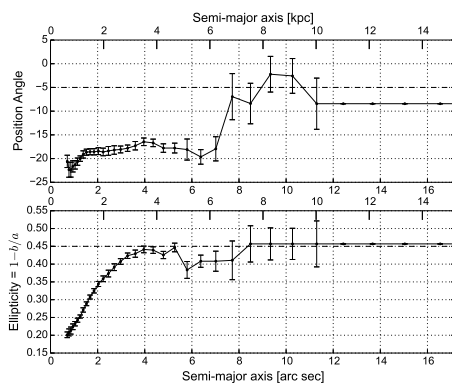
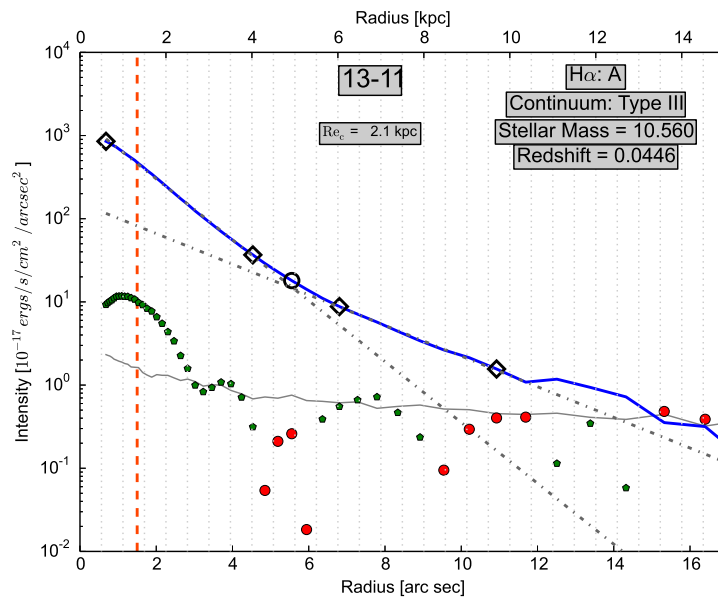
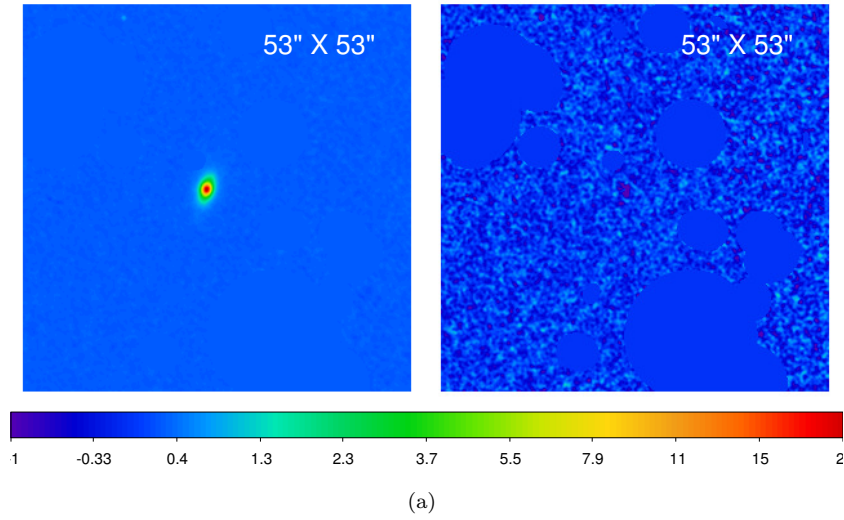


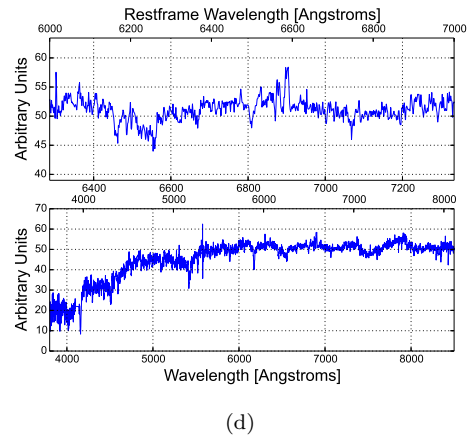
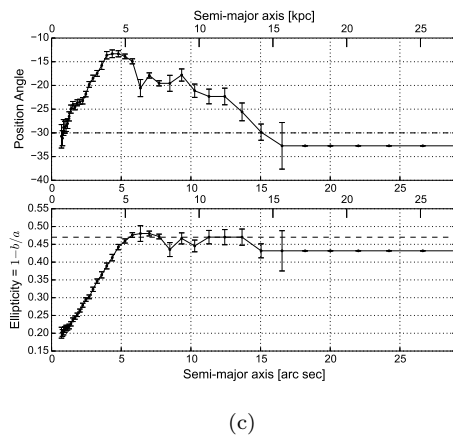
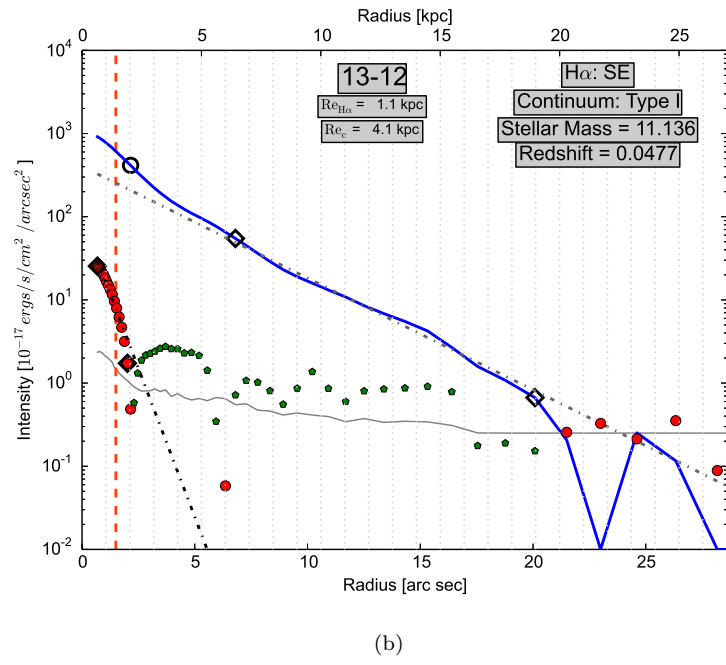
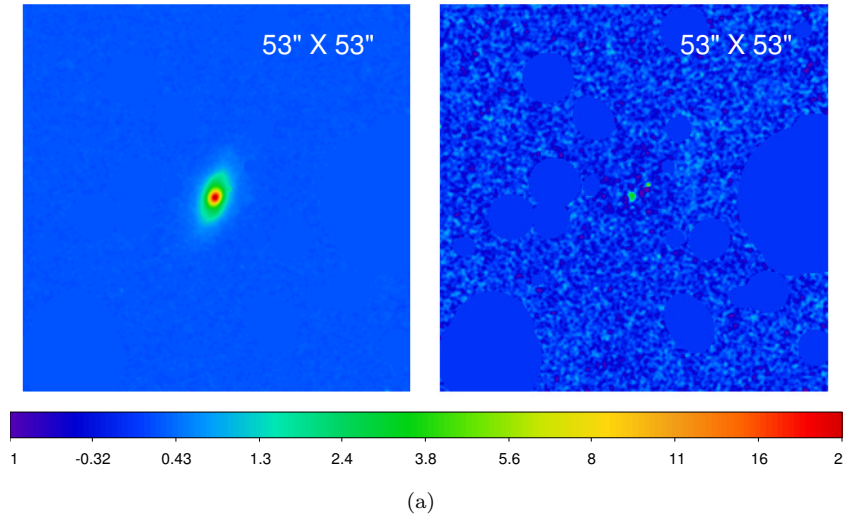
(d)

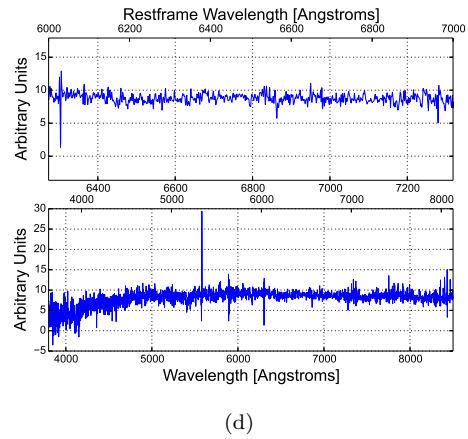
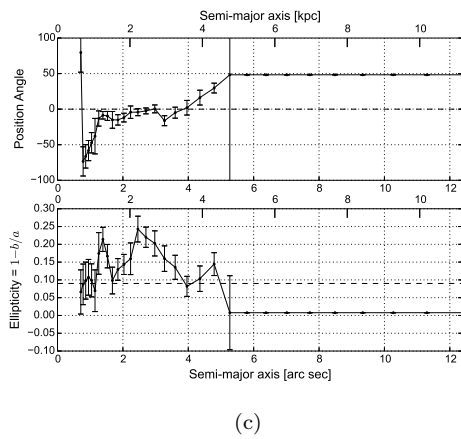
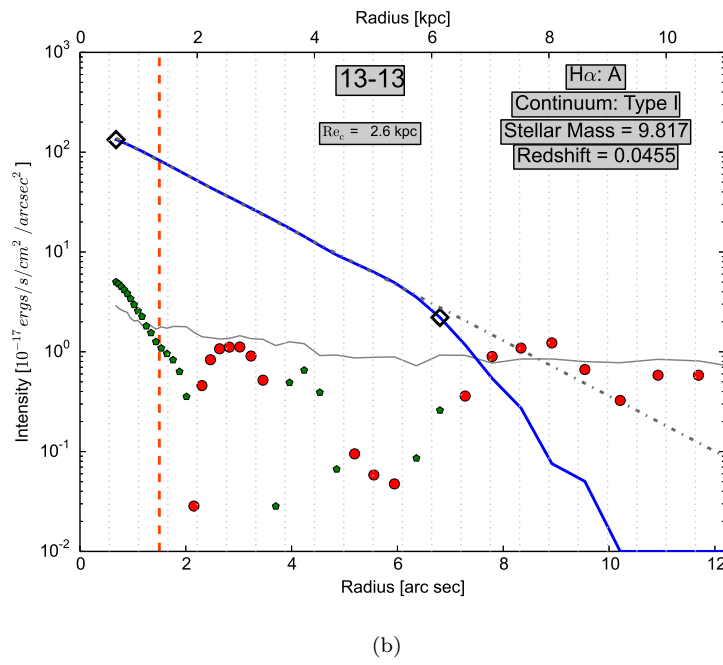
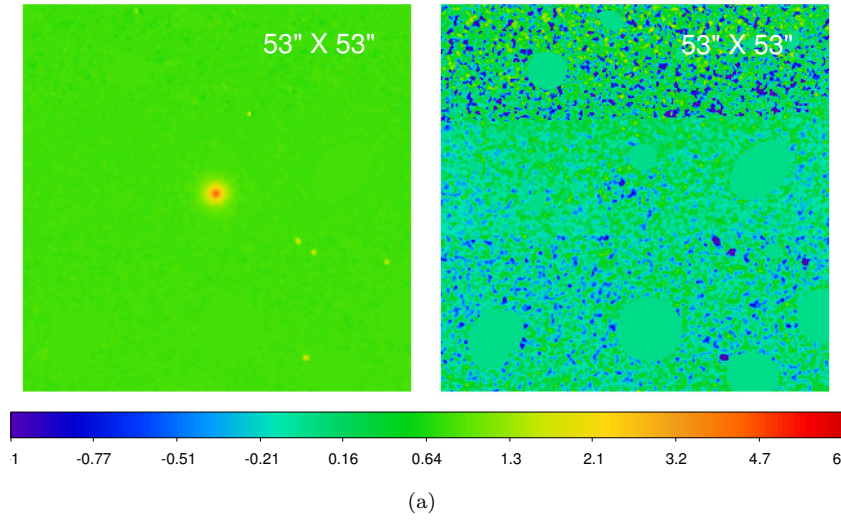


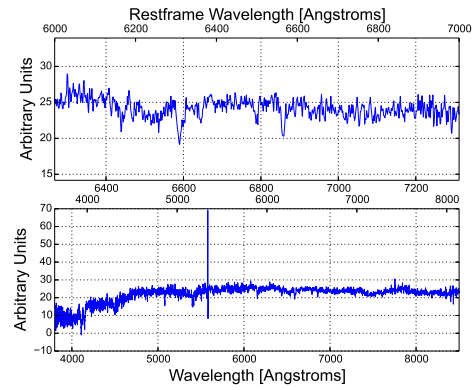
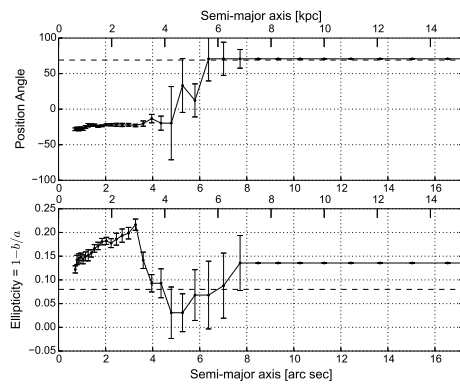
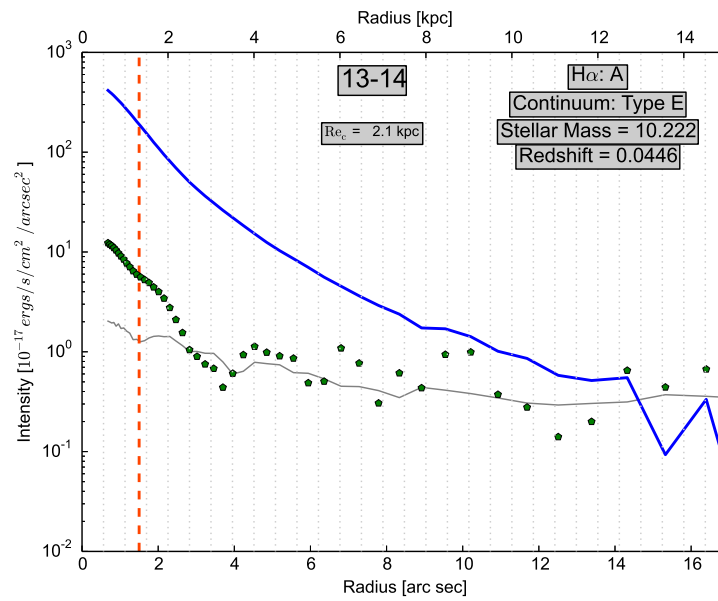
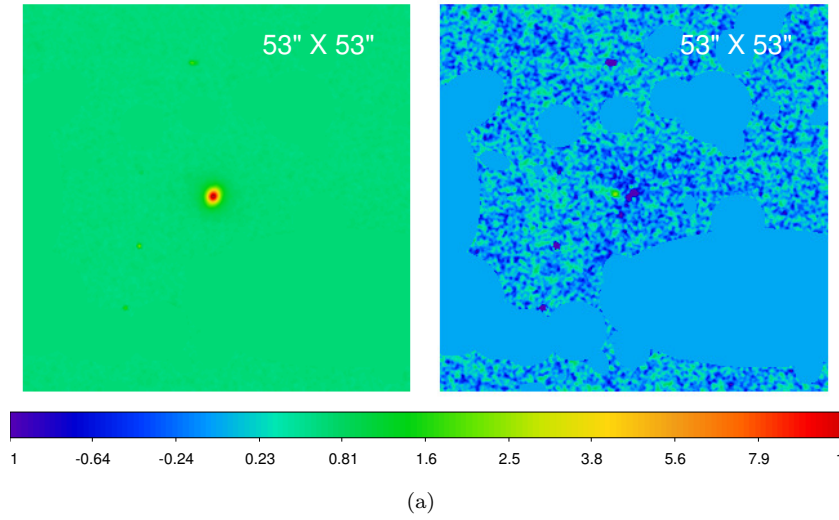


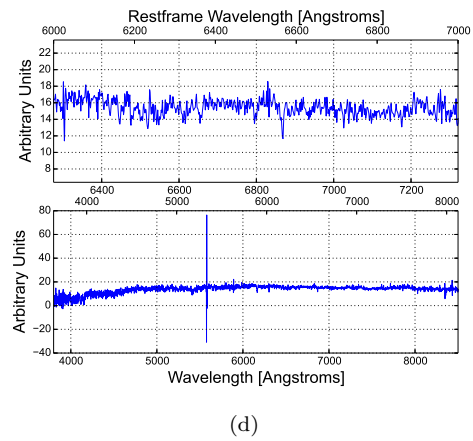
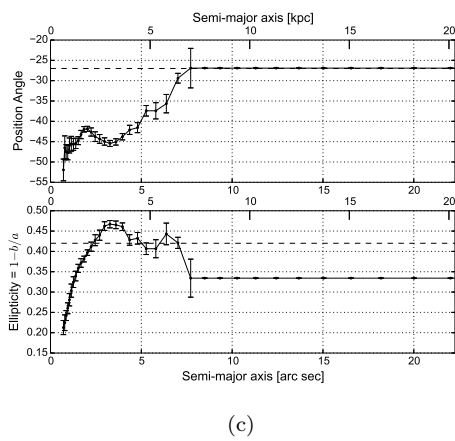
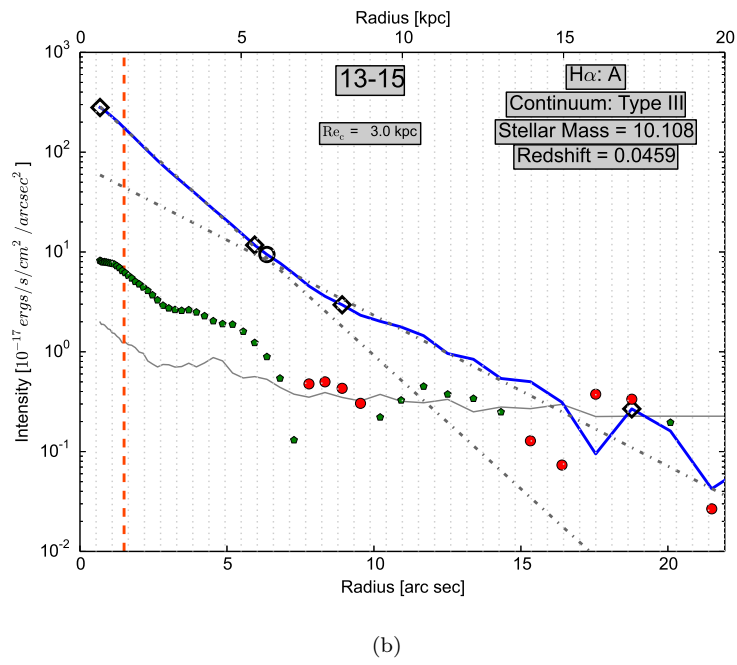
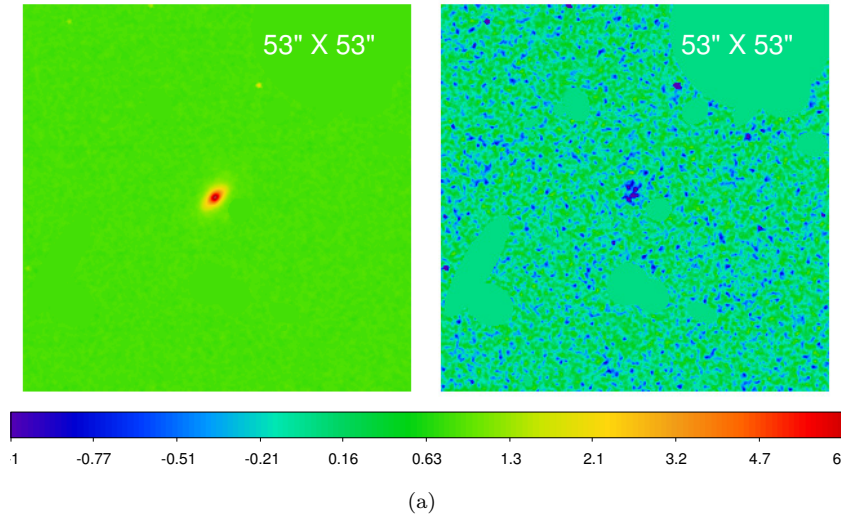


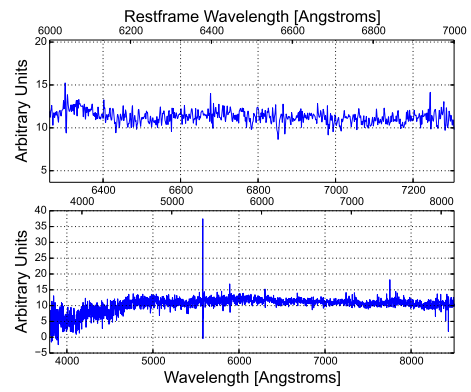
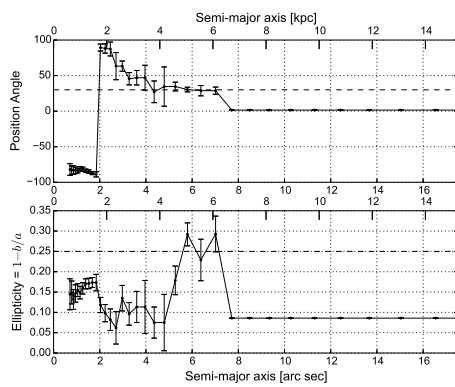
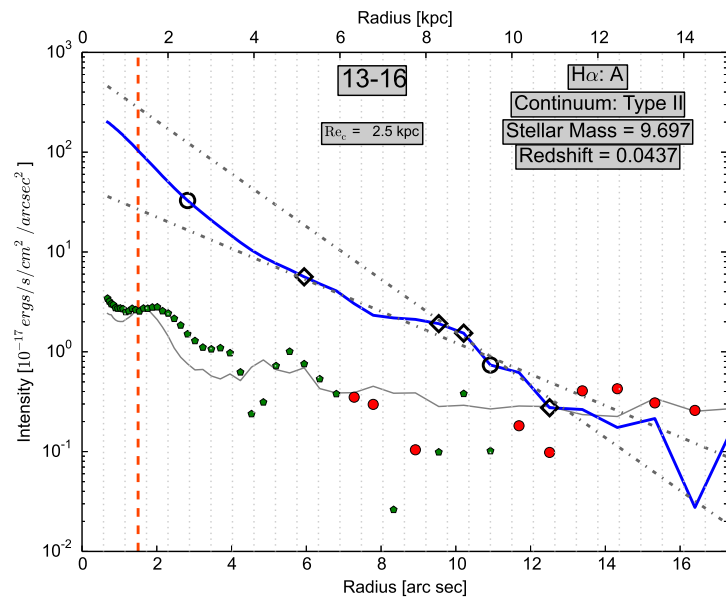
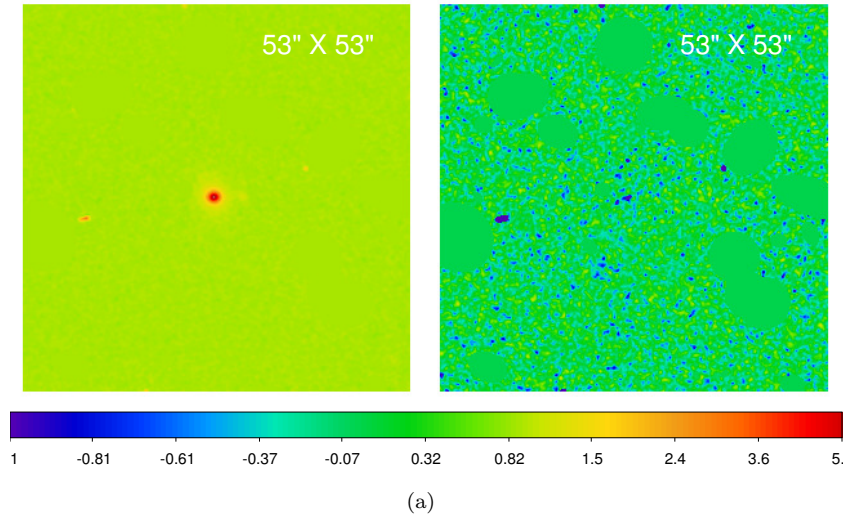


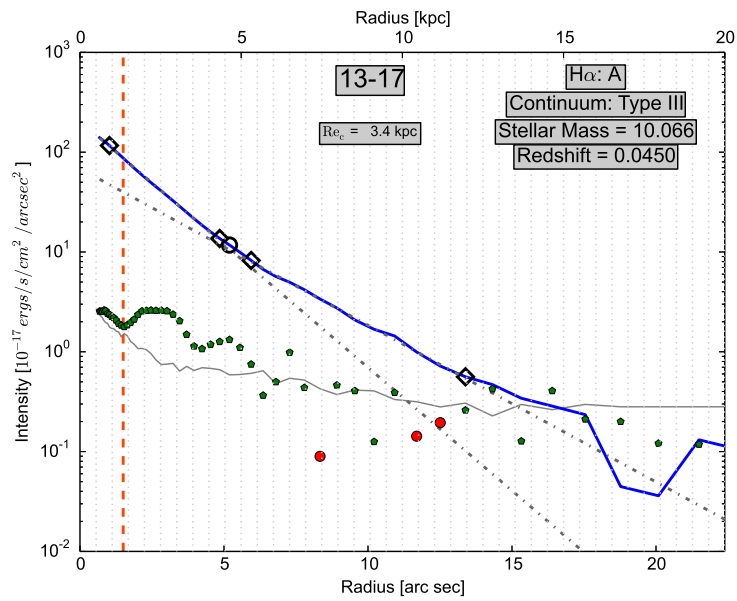
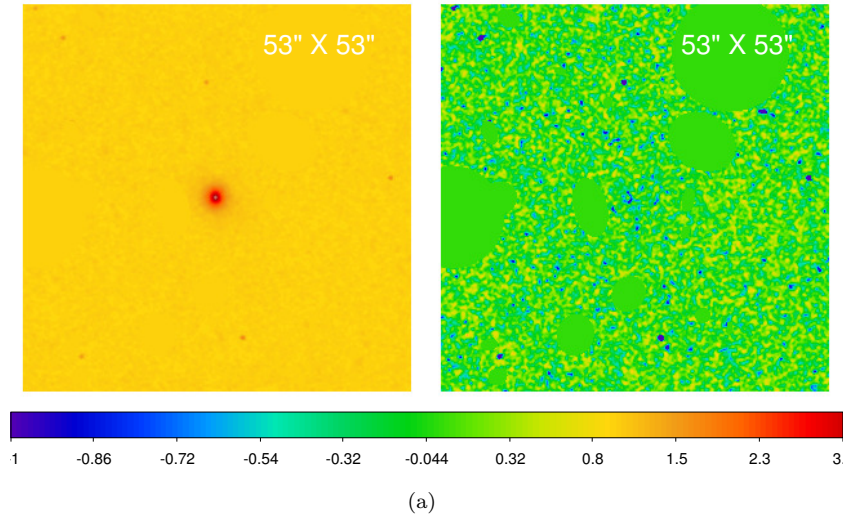




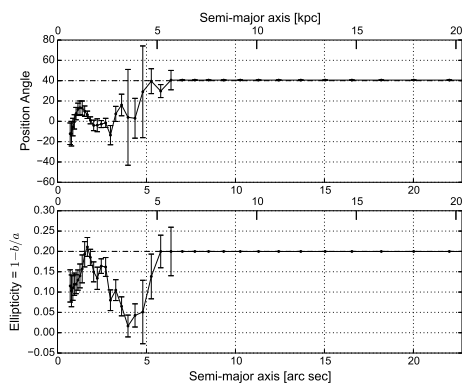




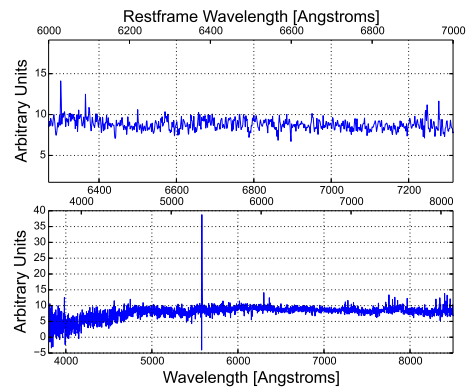




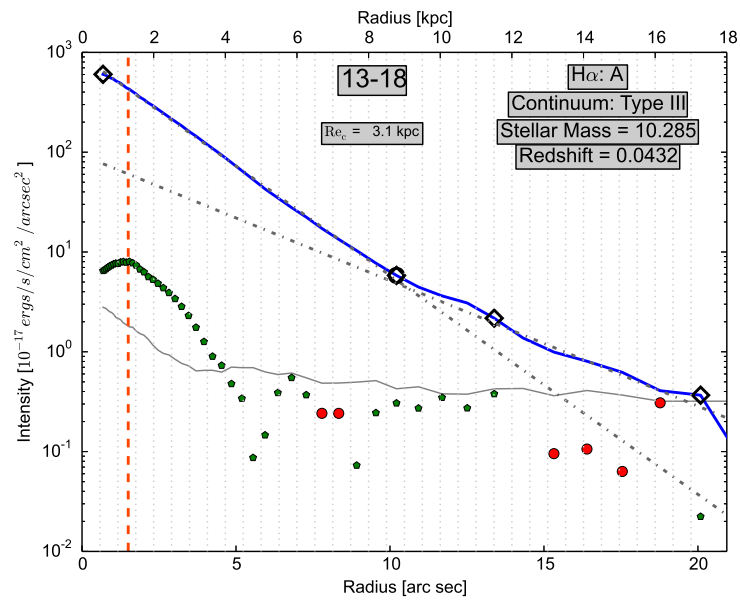
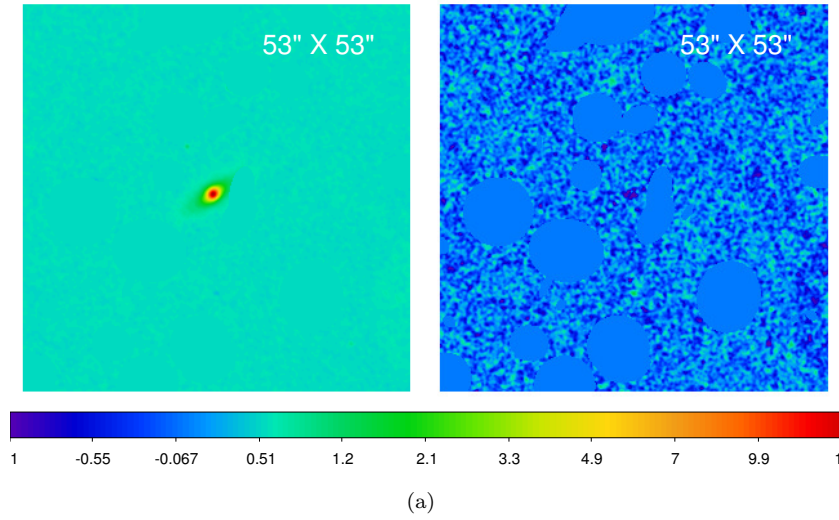
(b)



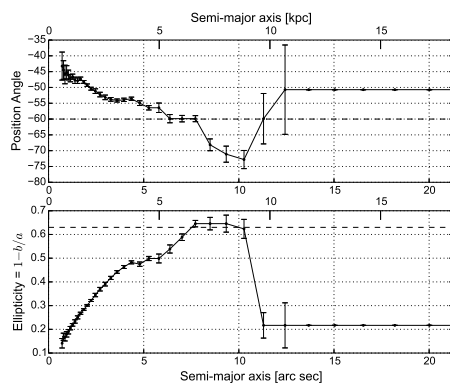
(c)



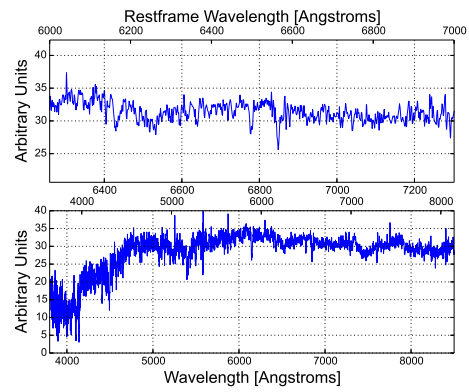
(d)



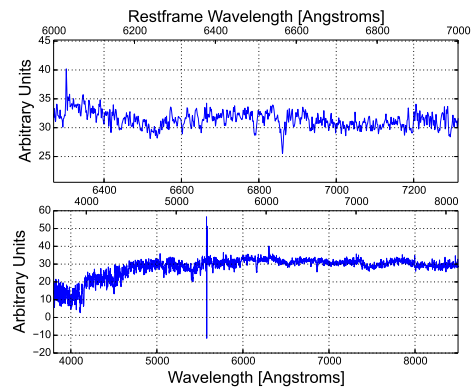
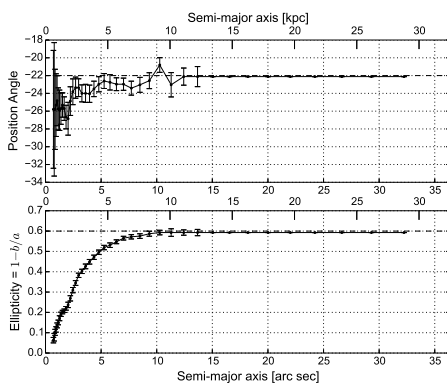
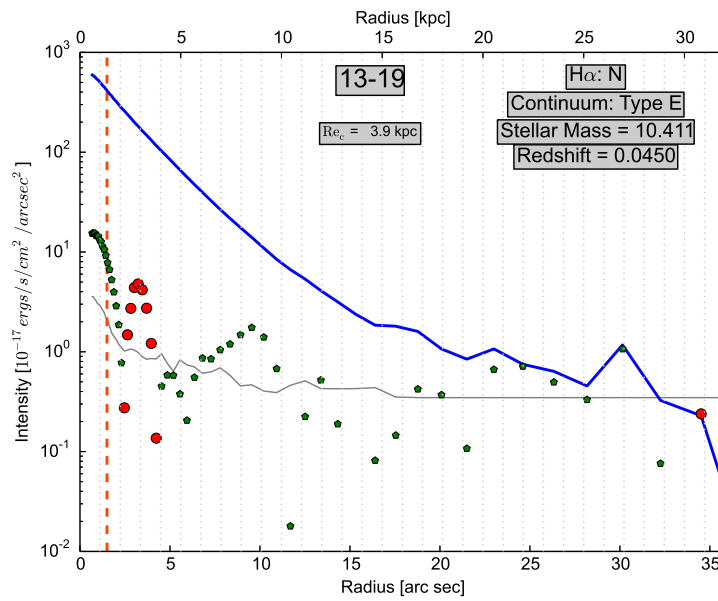
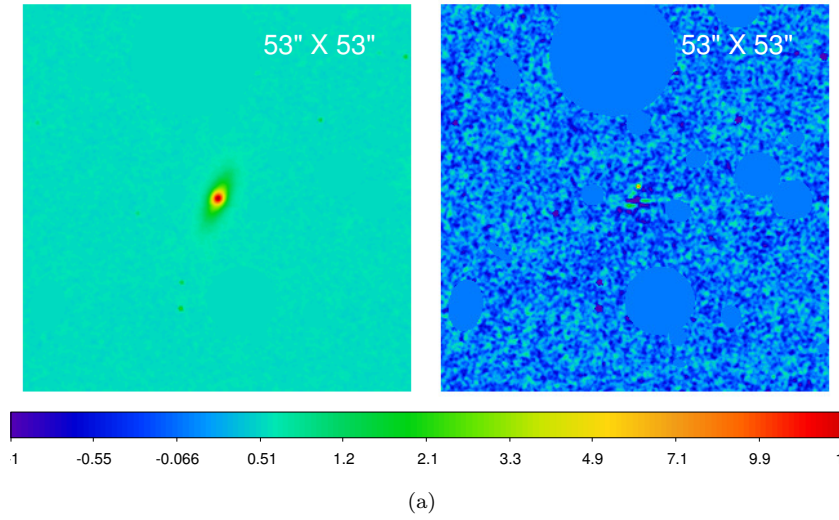
(b)

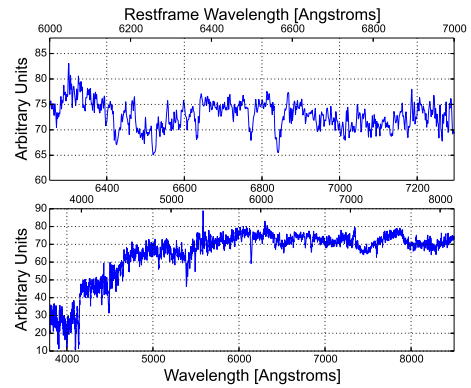
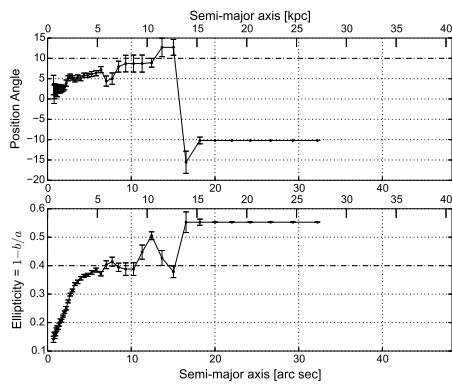
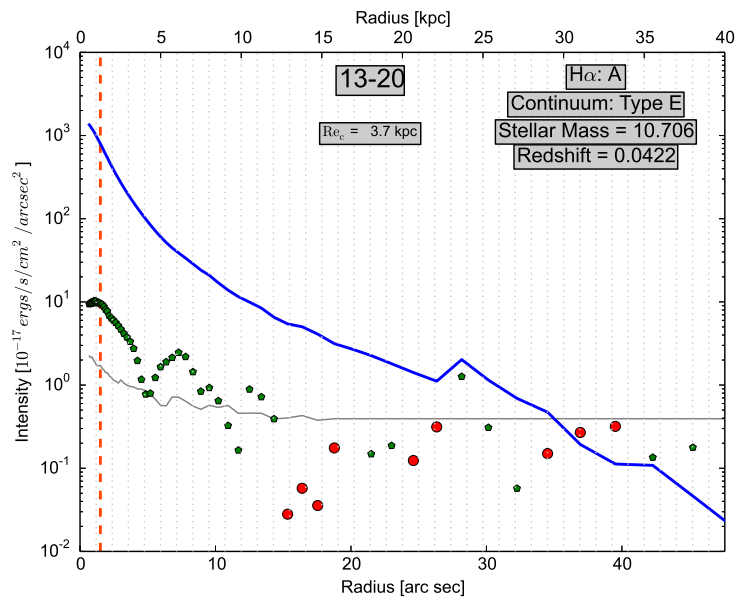
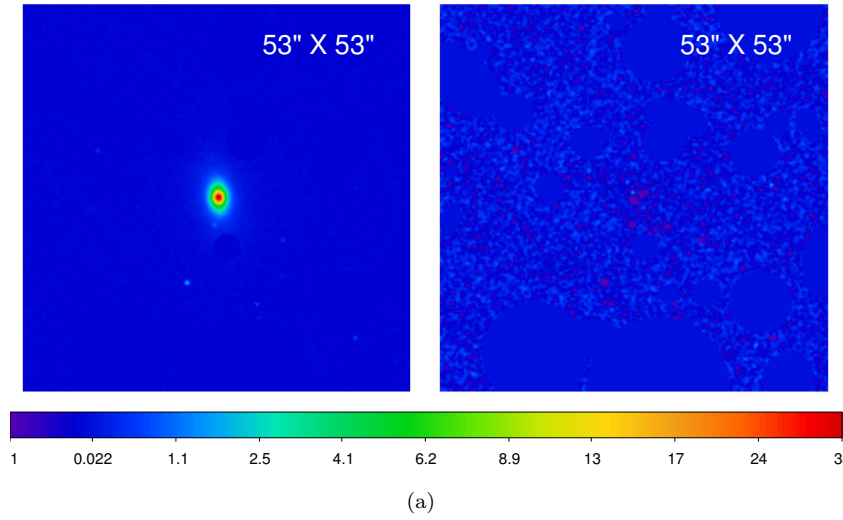


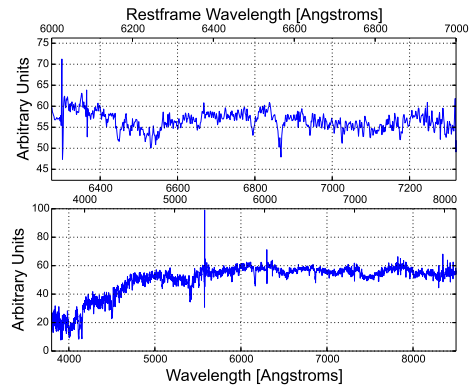
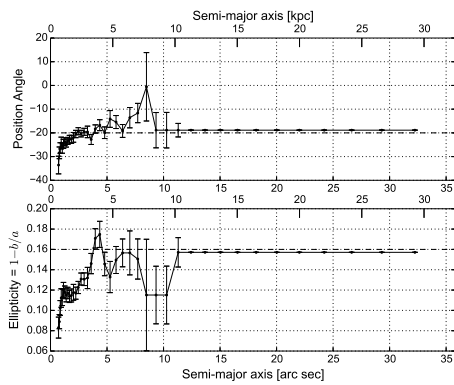
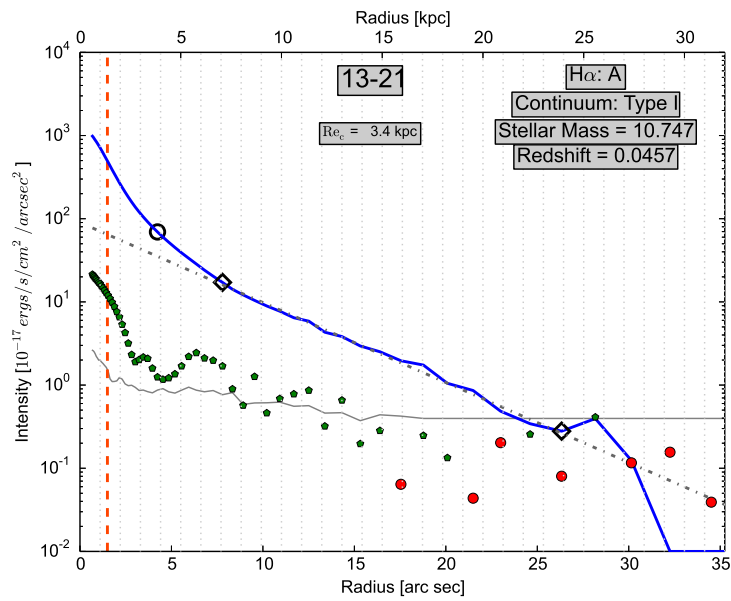
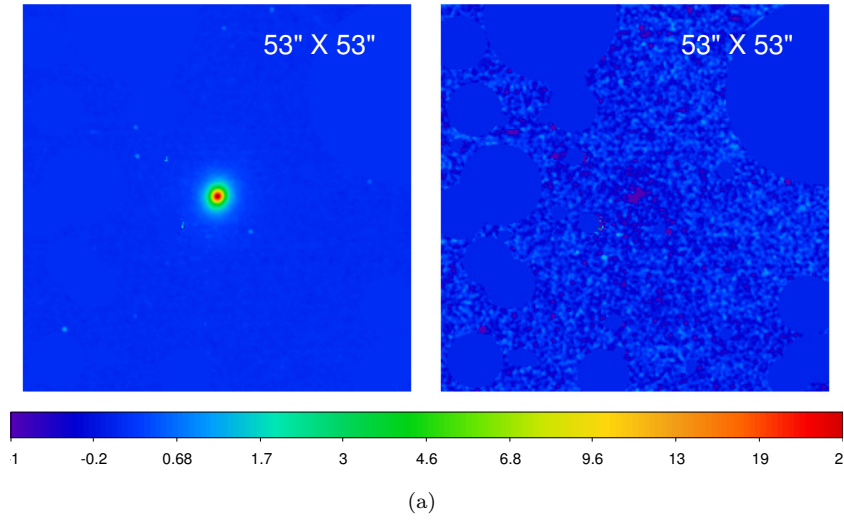
(c)

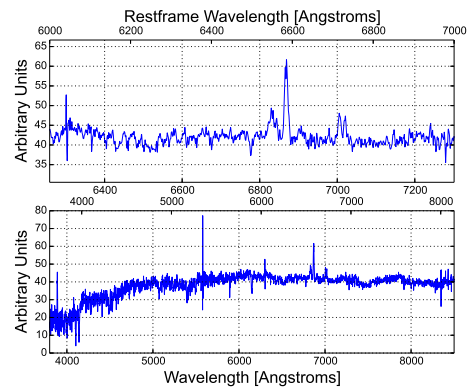
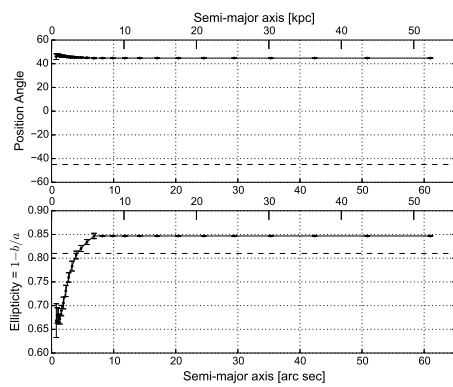
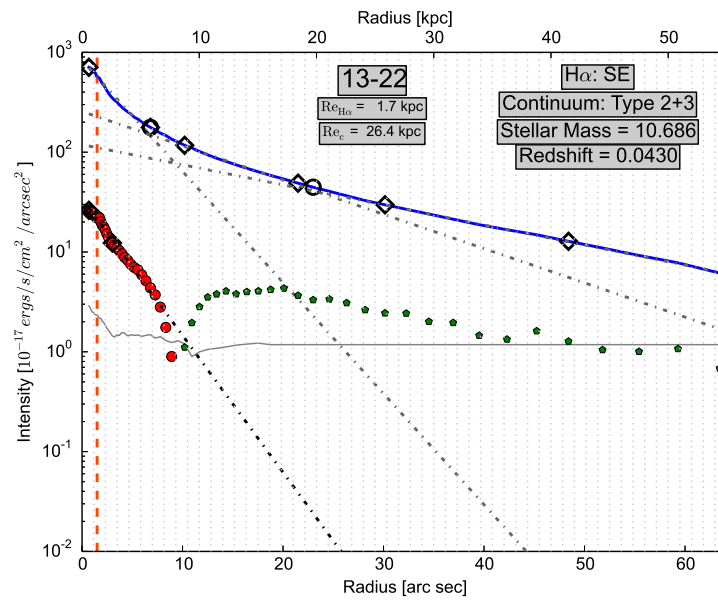
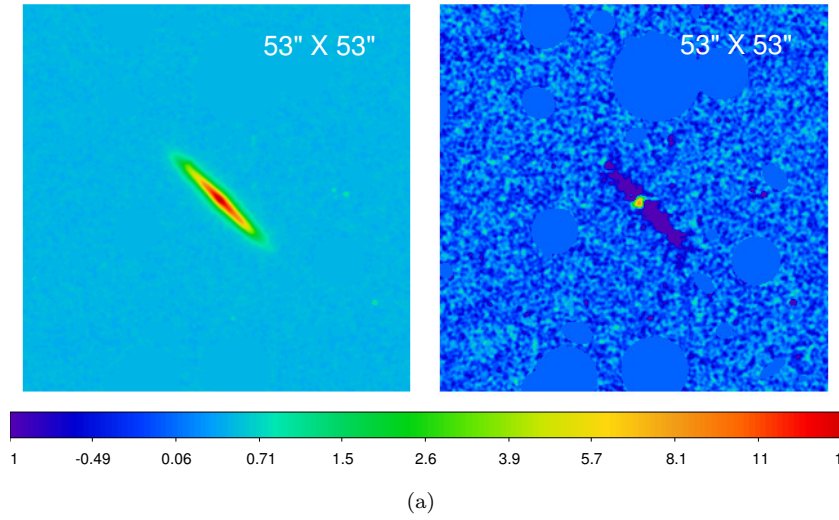


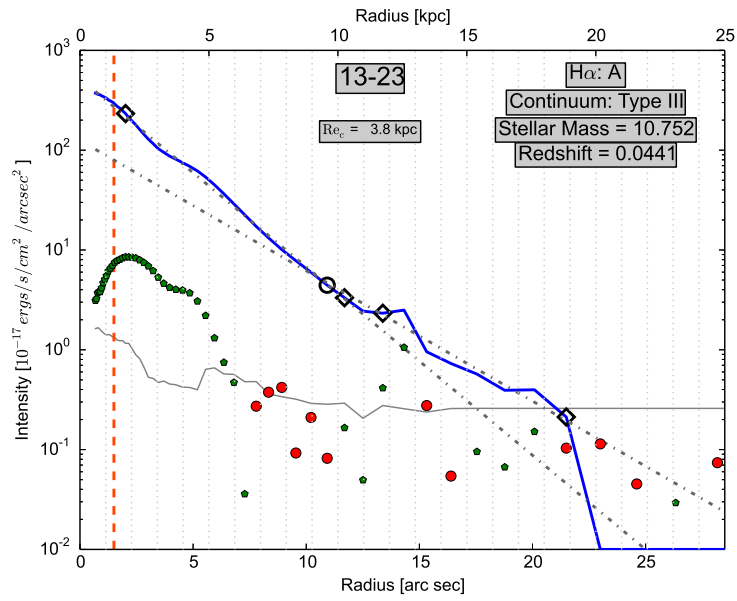
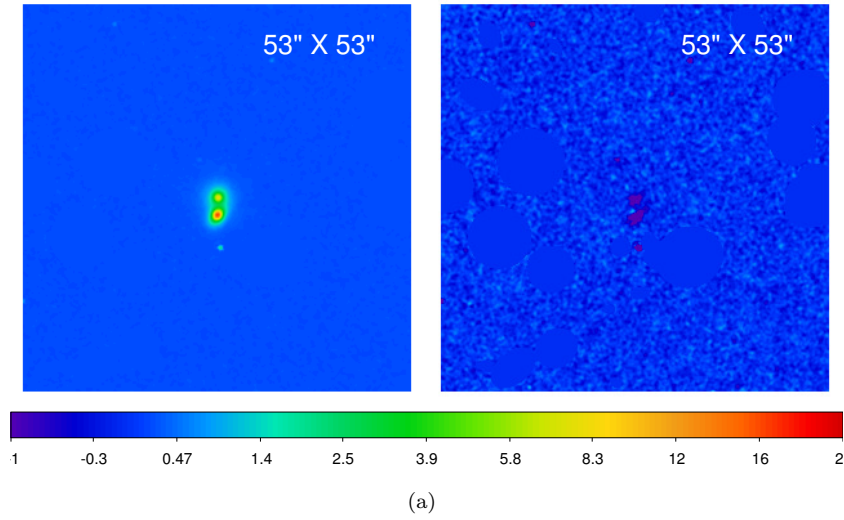
(d)



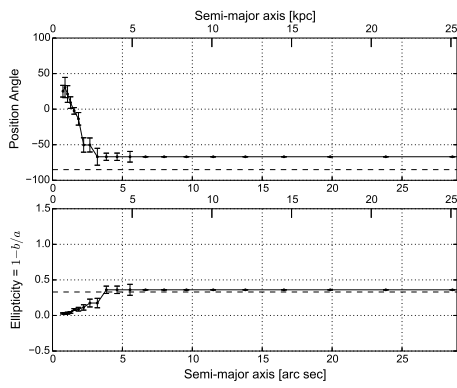




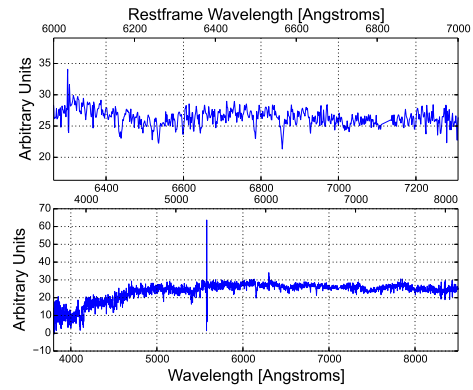




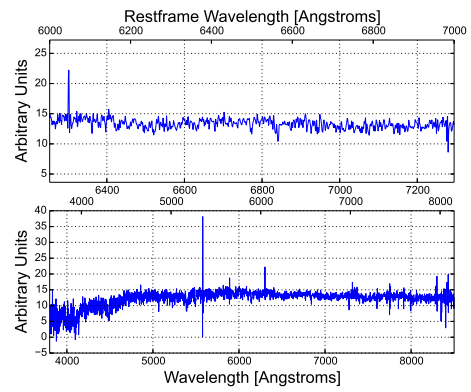
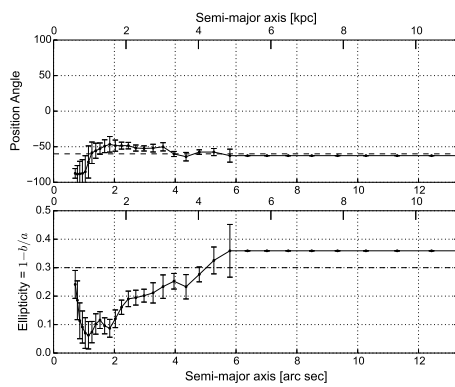
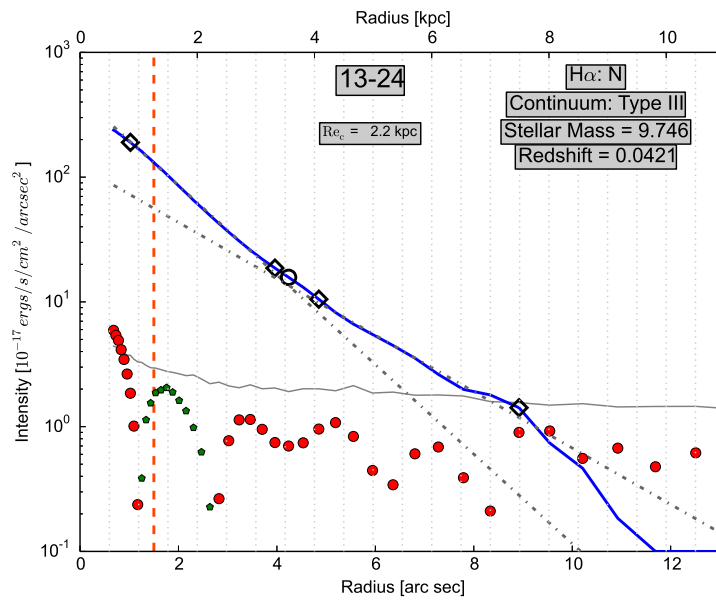
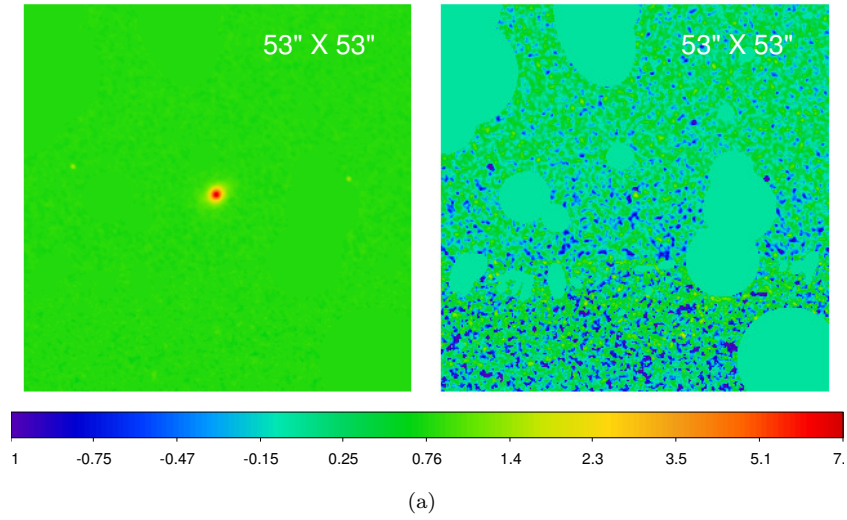
(b)

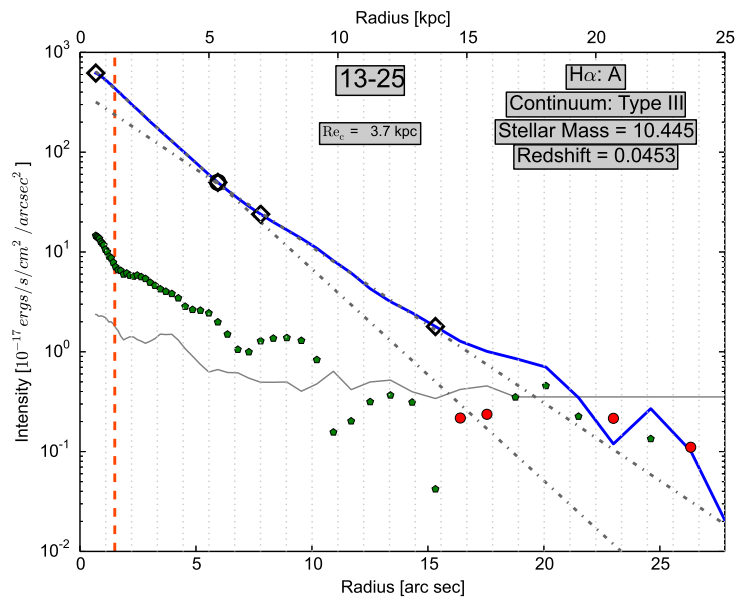
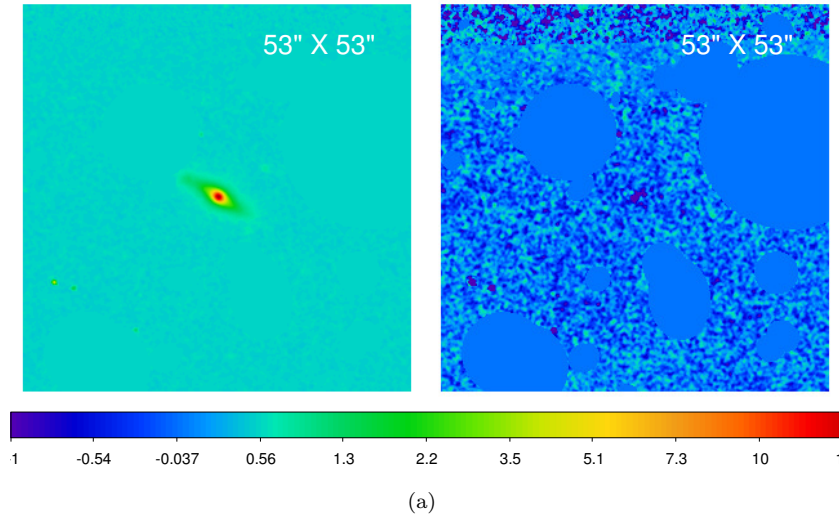


(c)

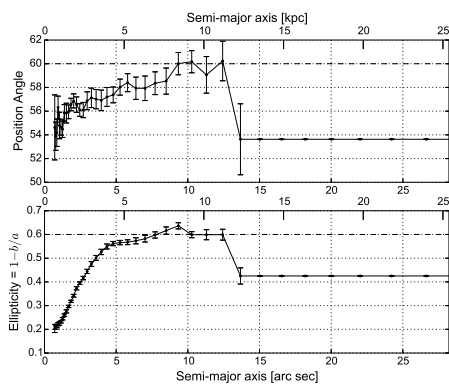


(d)

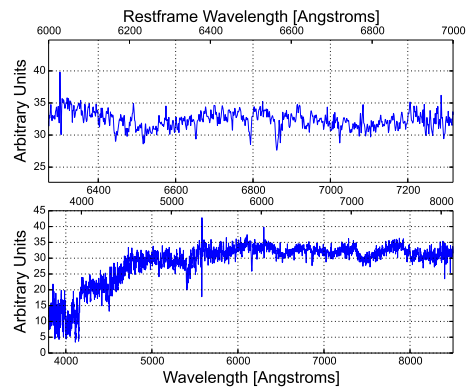




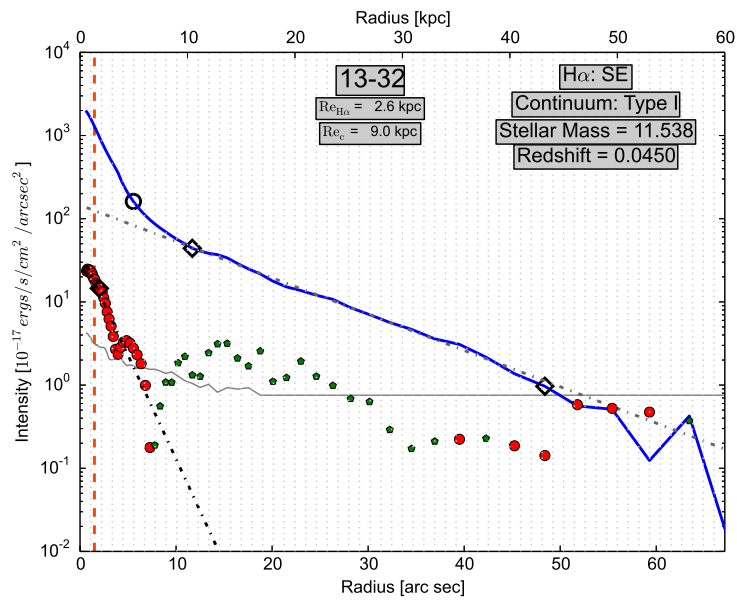
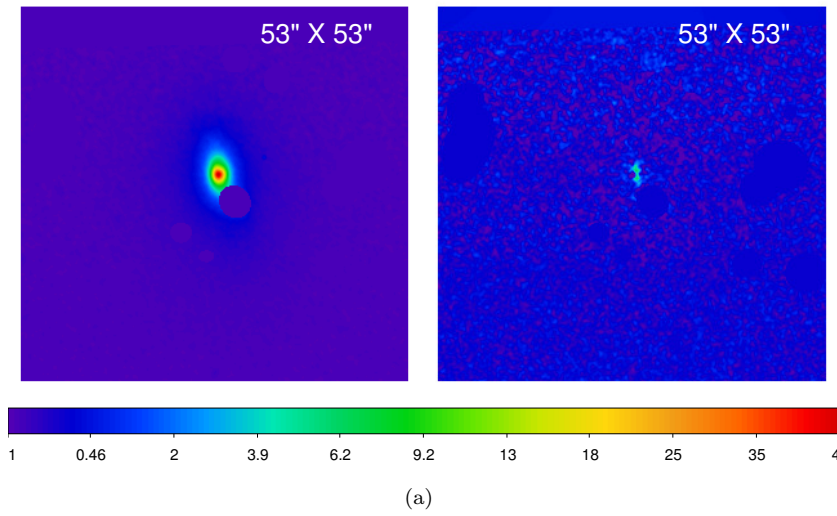
(b)



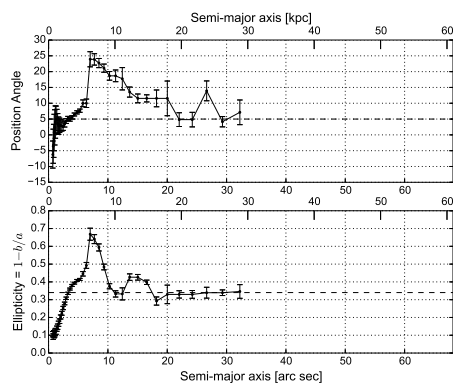
(c)



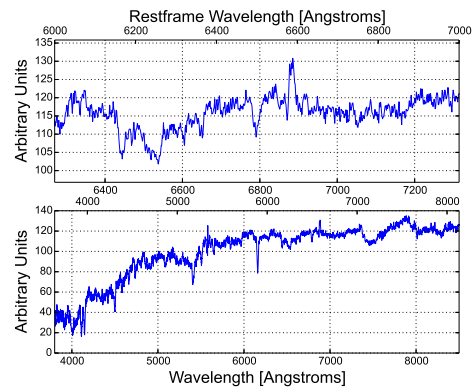
(d)



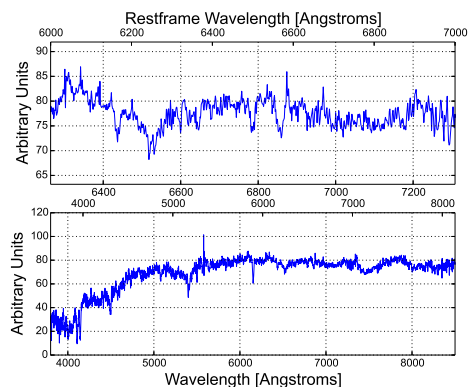
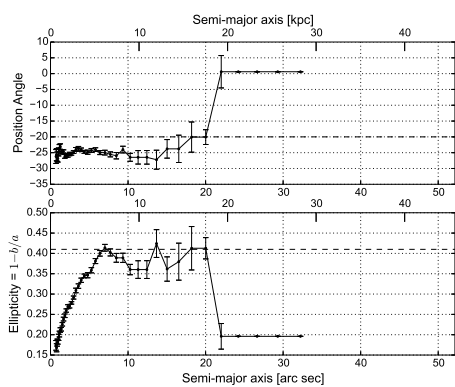
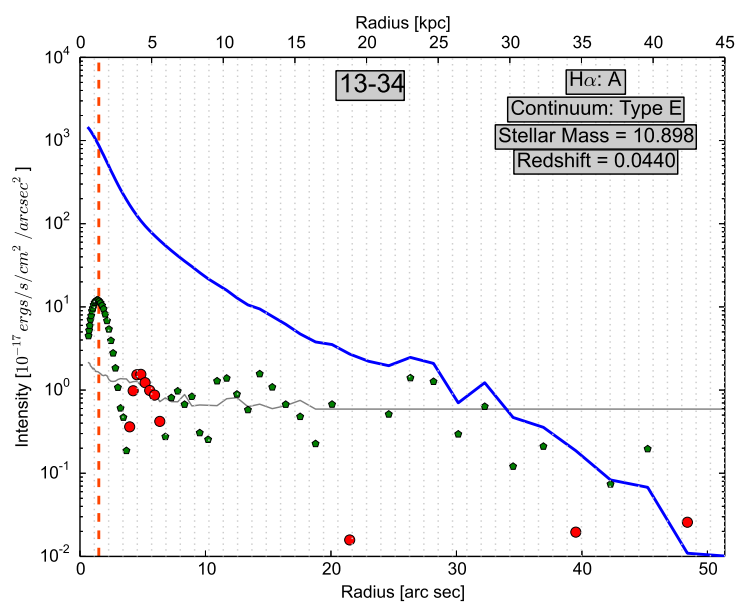
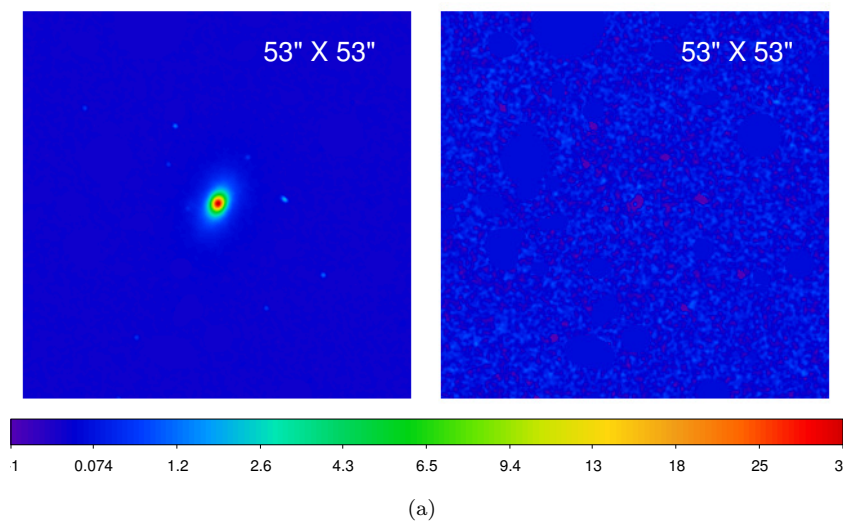
(b)

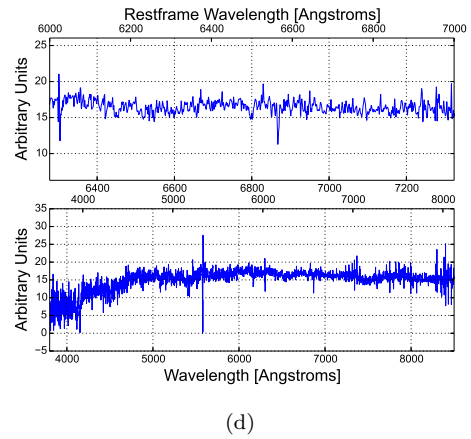
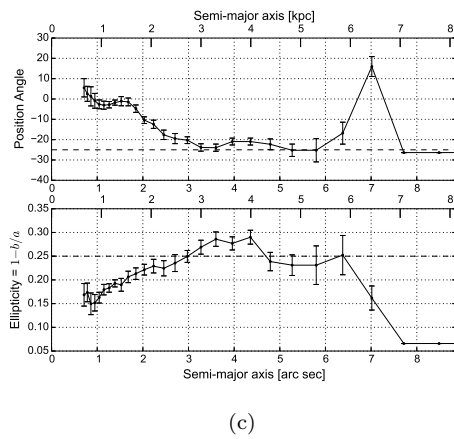
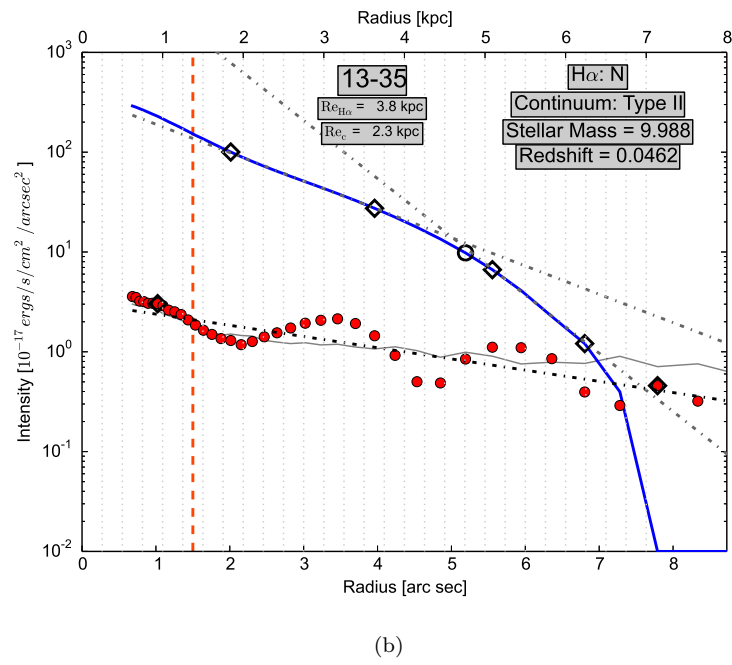
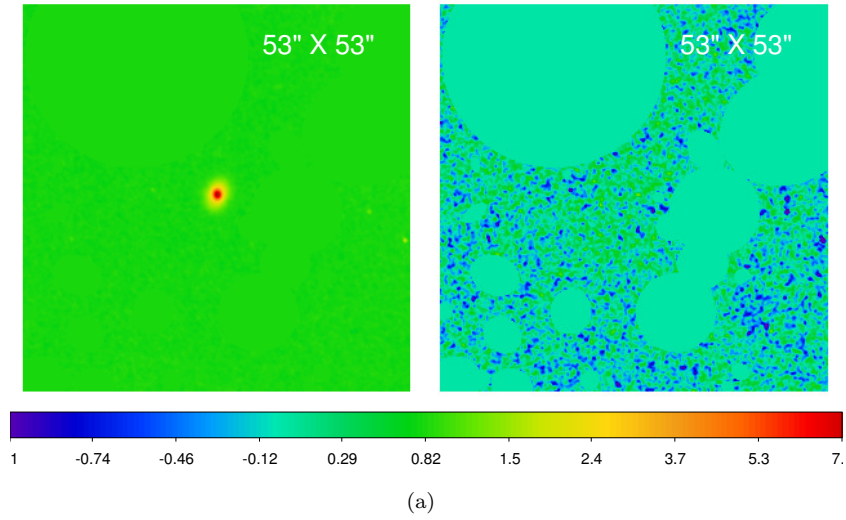


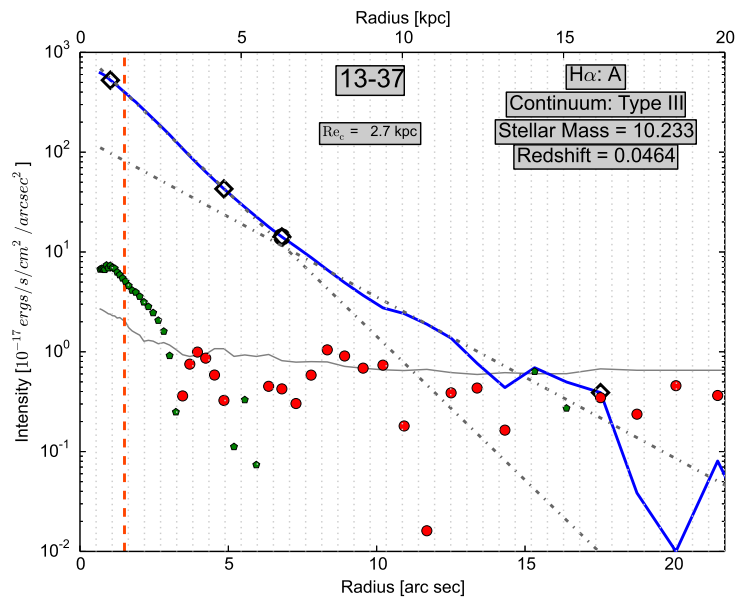
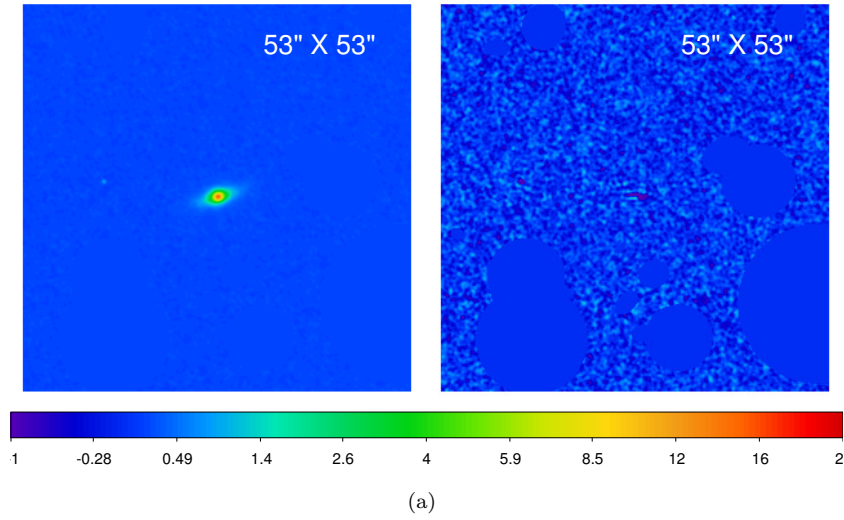
(c)



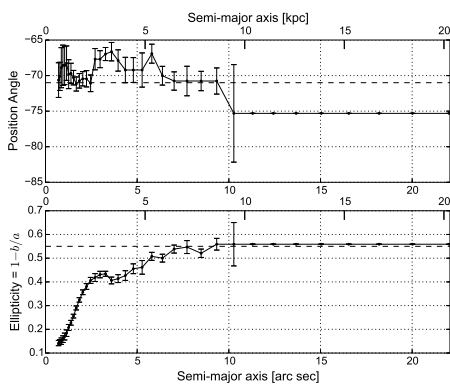
(d)



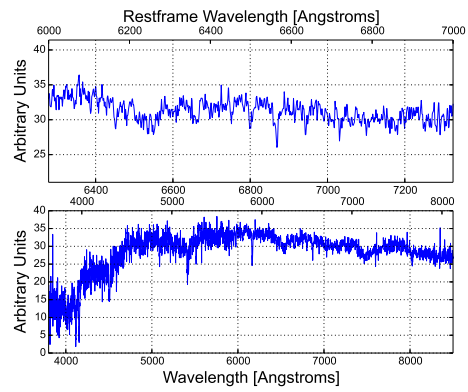




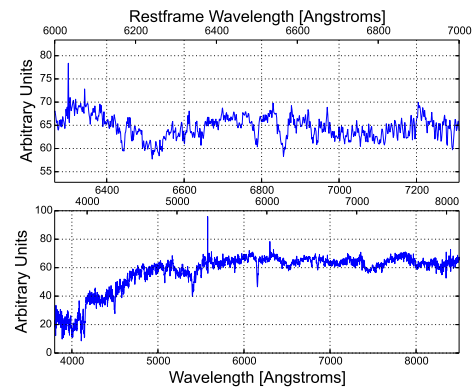
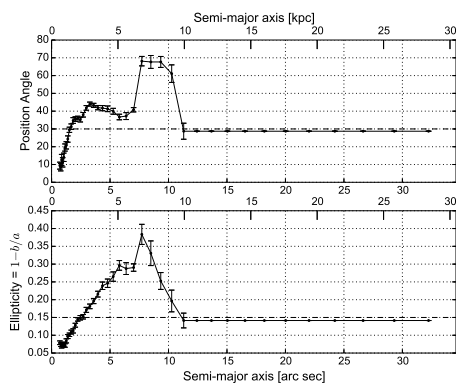
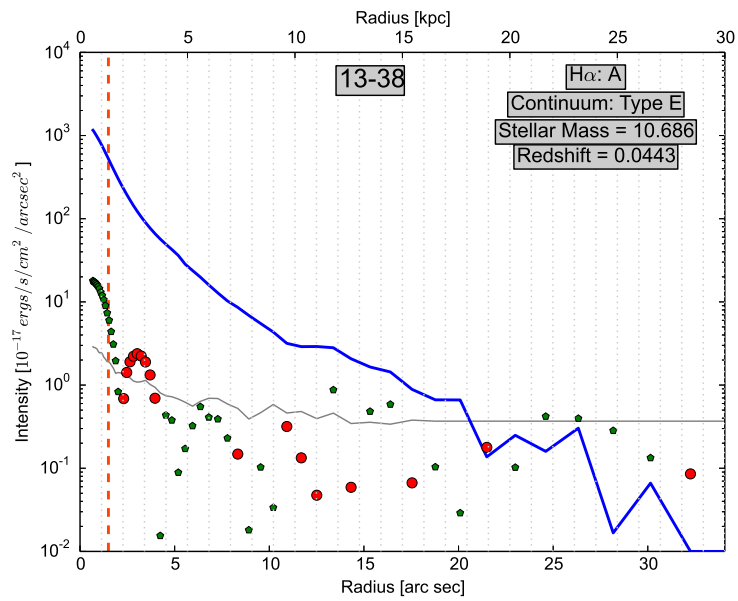
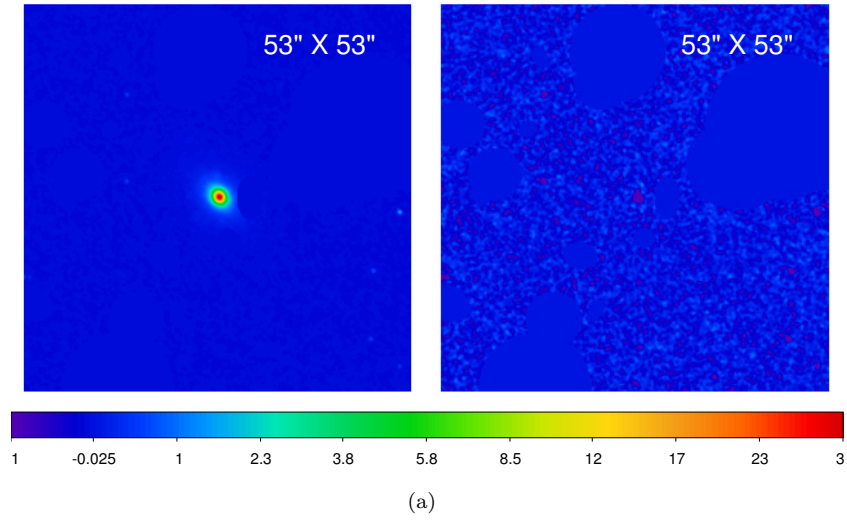
(b)

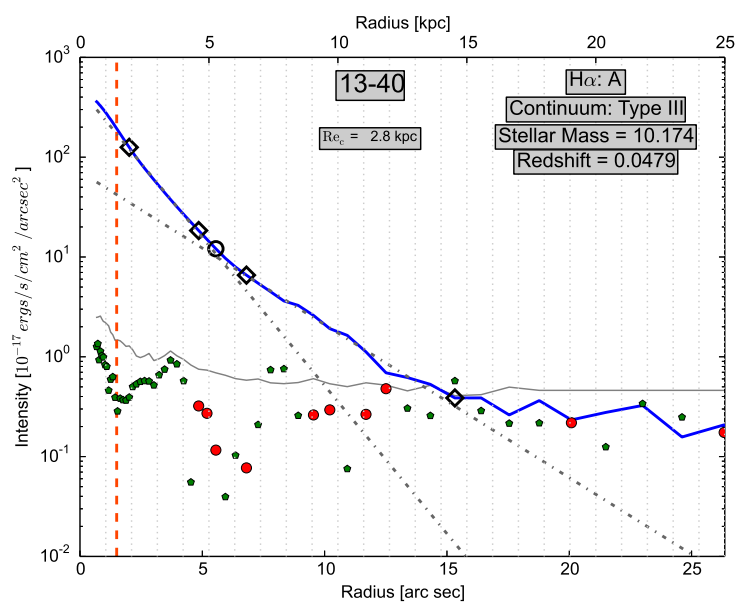
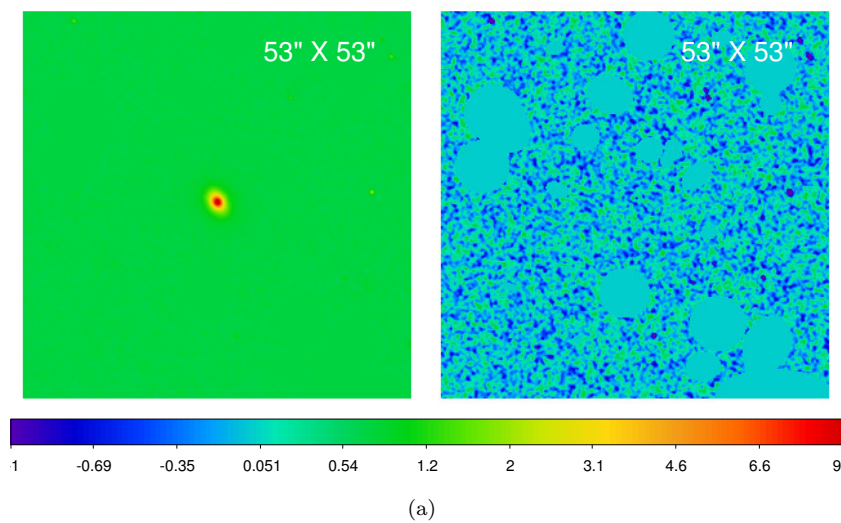


(c)

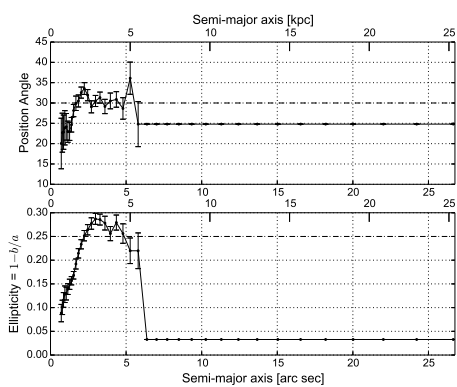


(d)

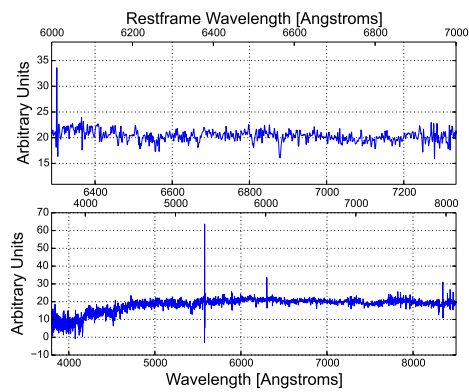




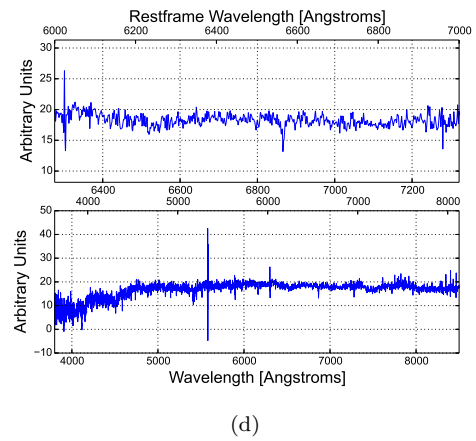
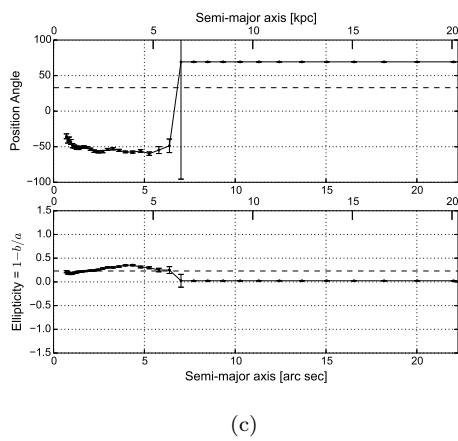
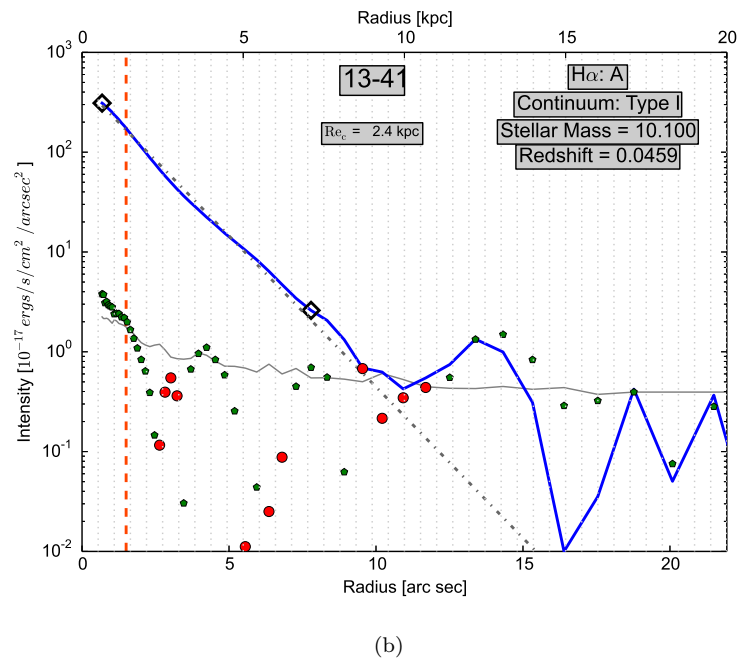
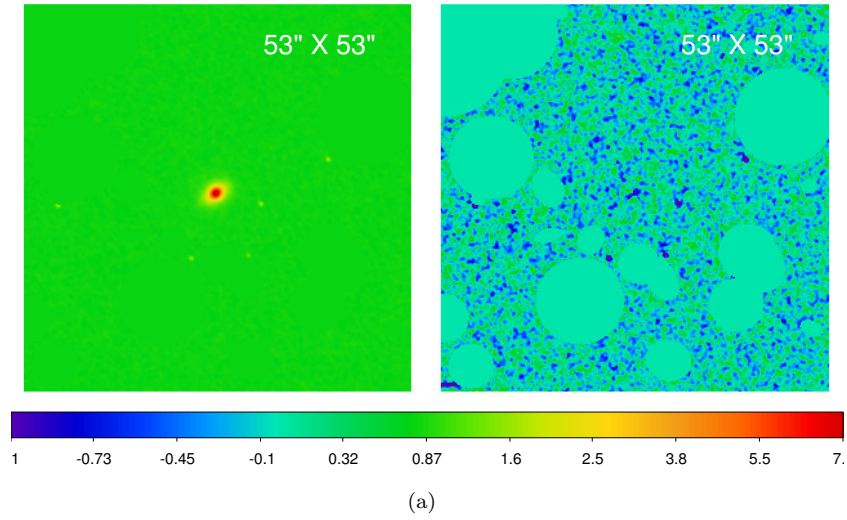
(b)

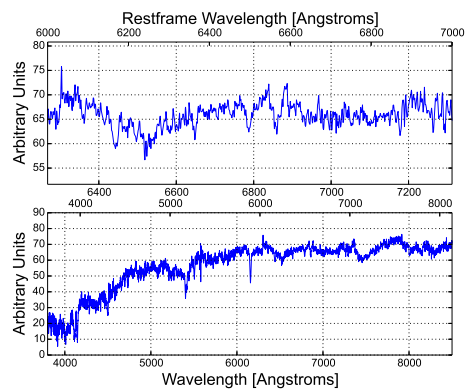
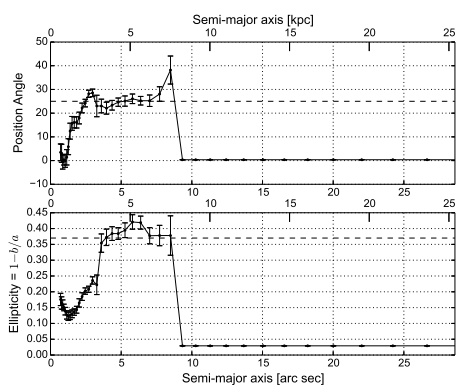
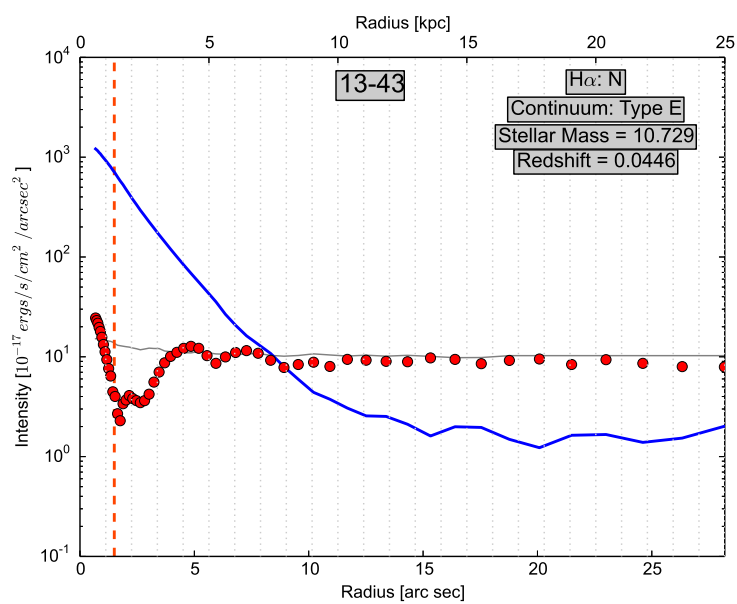
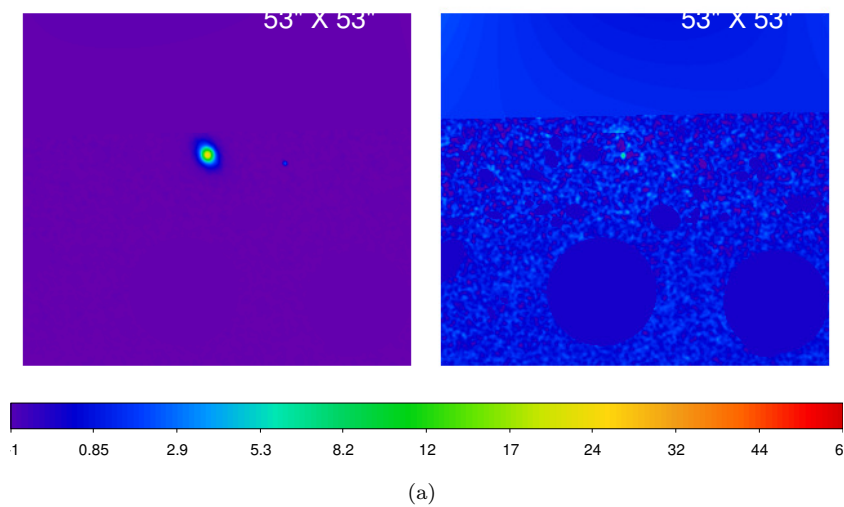


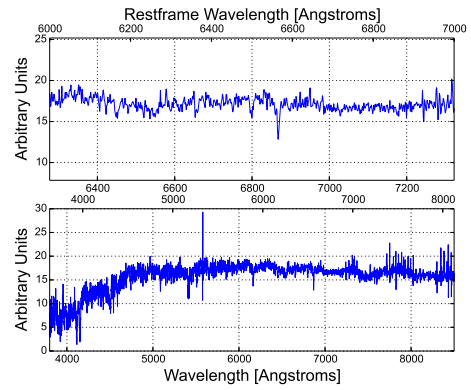
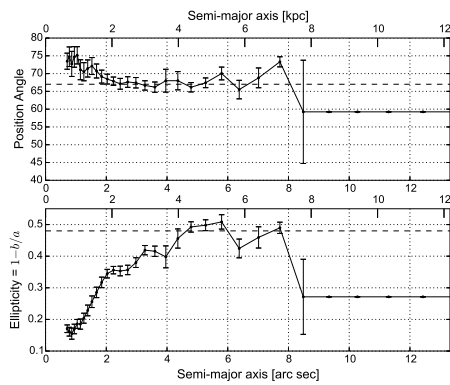
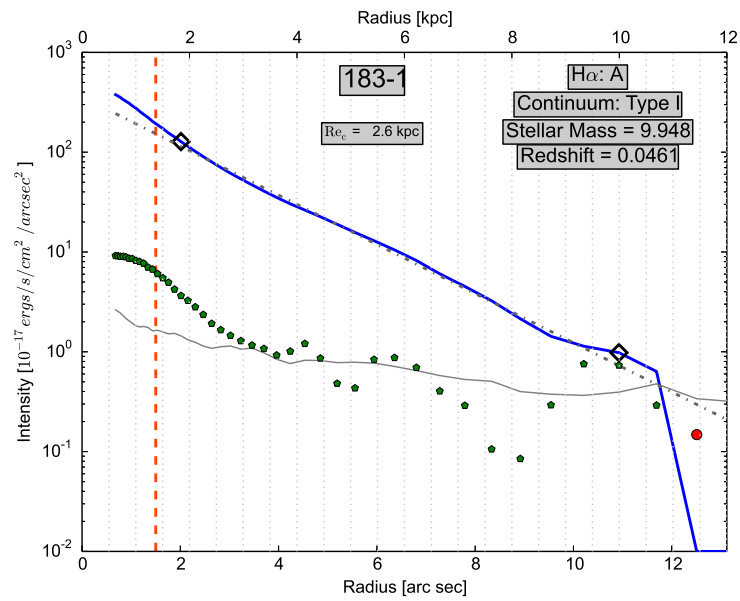
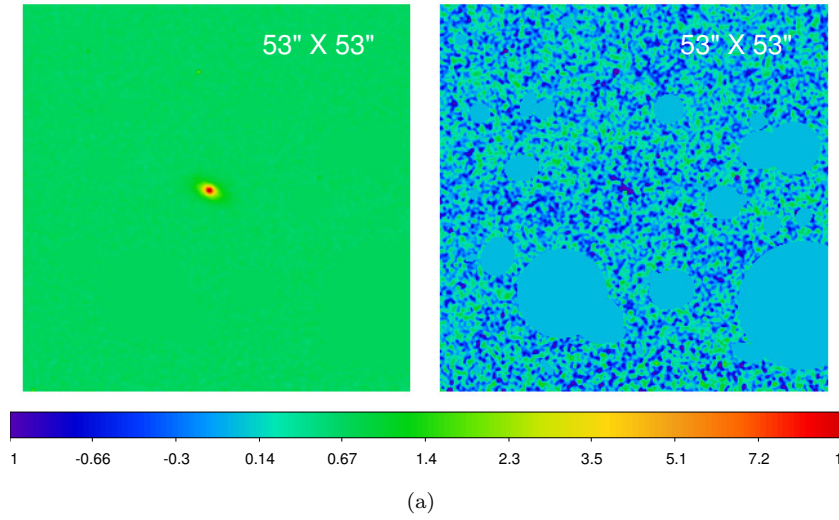
(c)

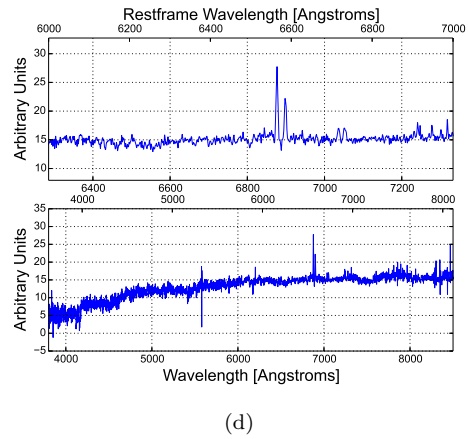
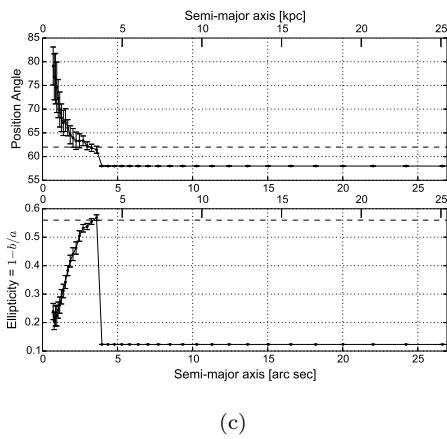
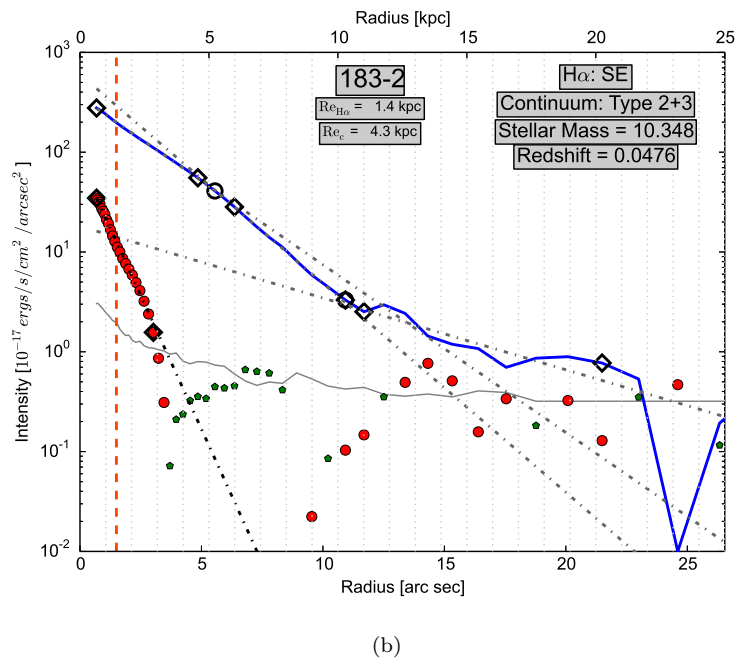
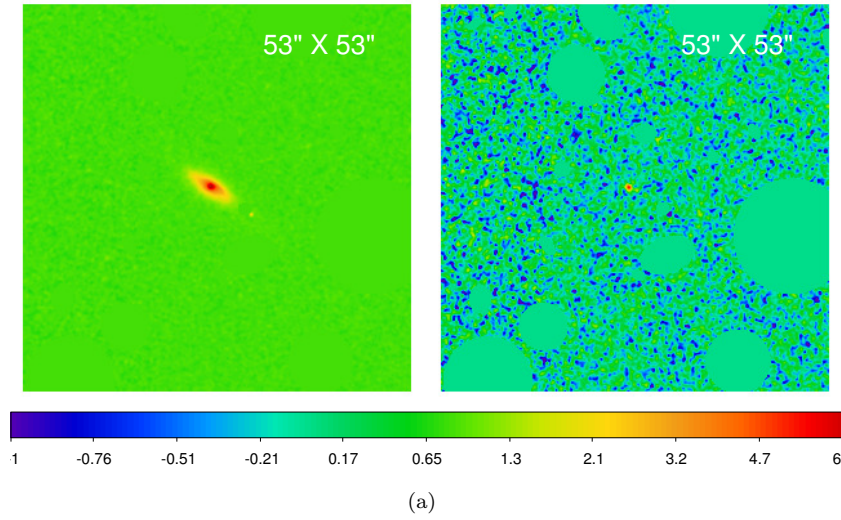


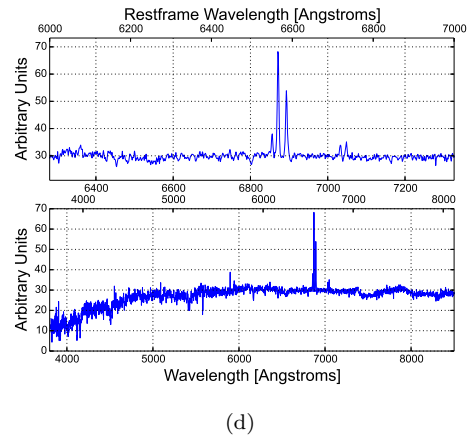
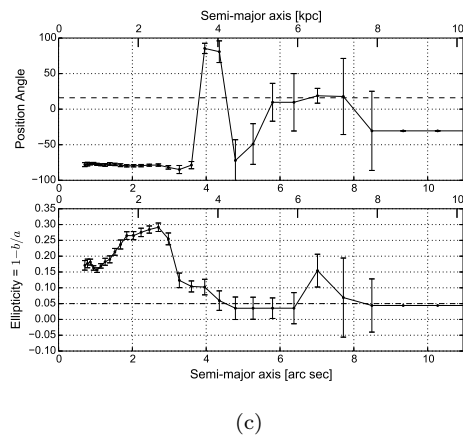
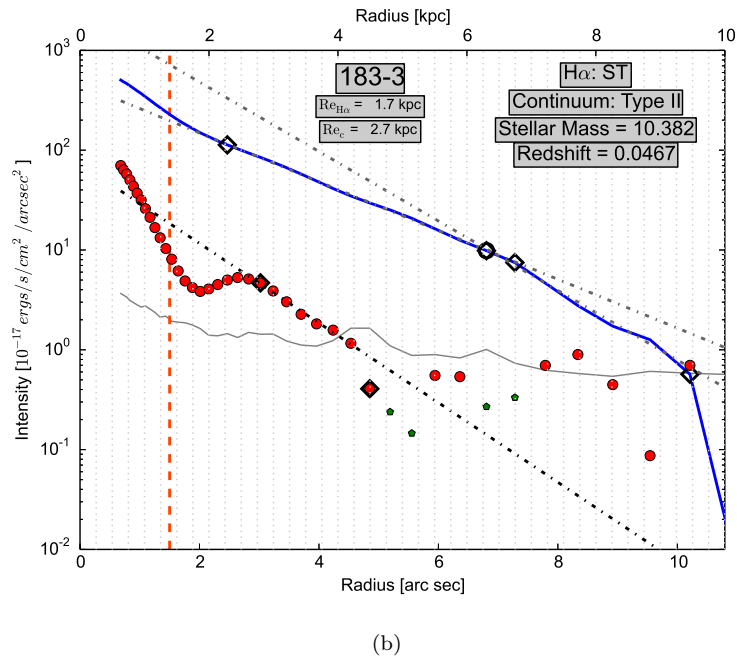
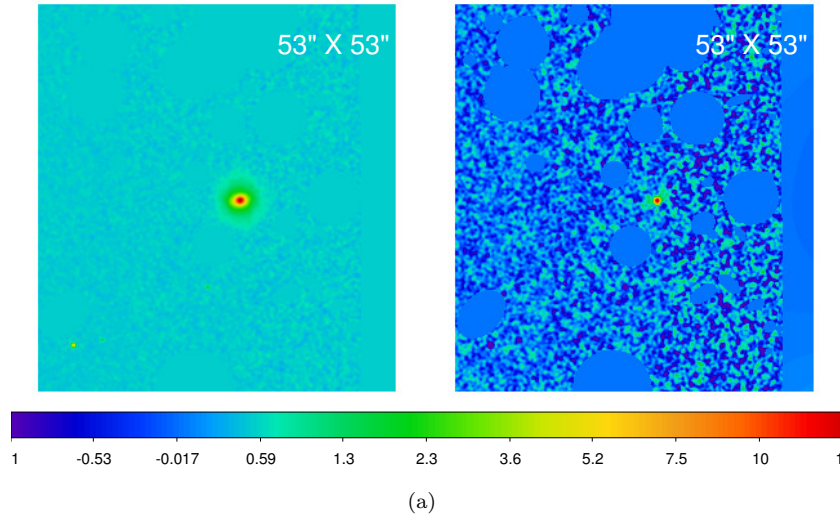
(d)

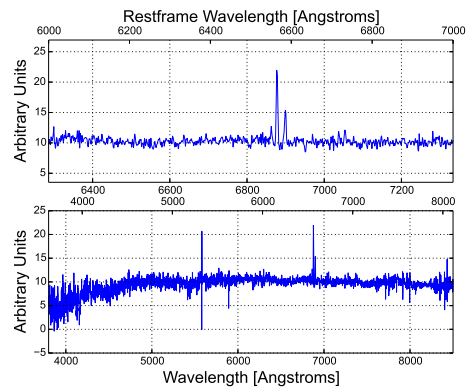
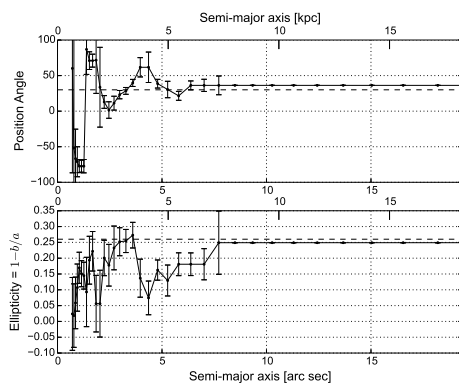
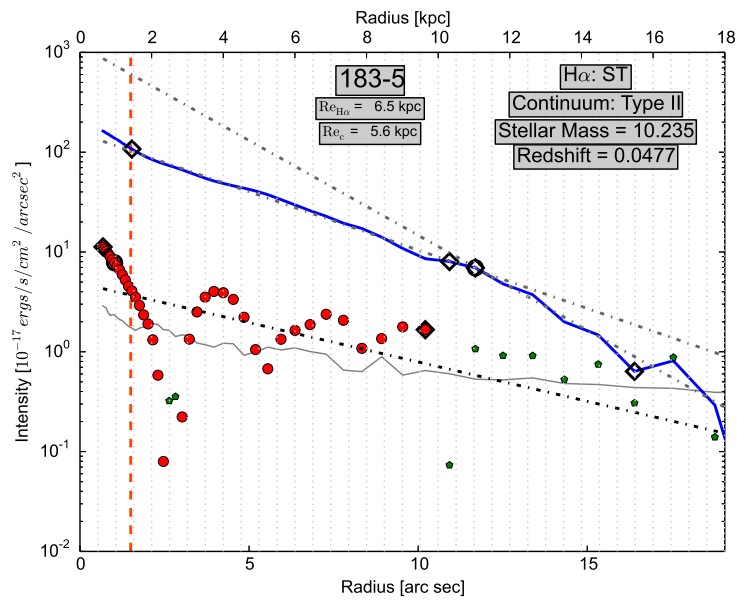
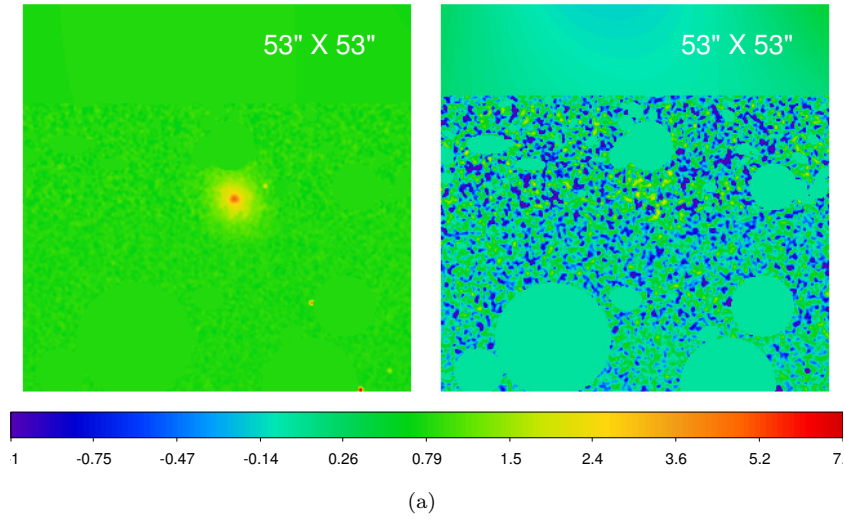


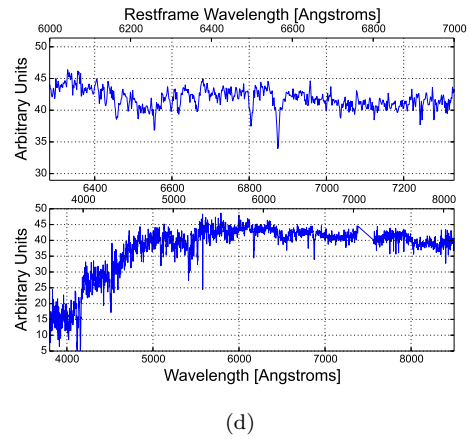
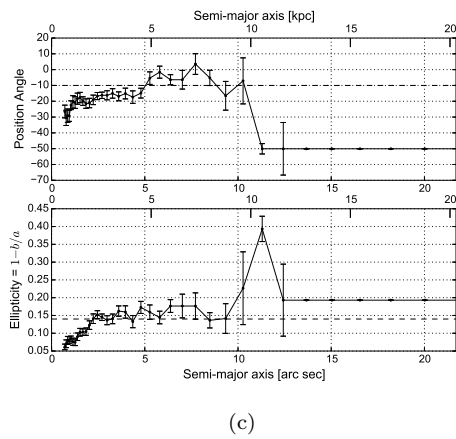
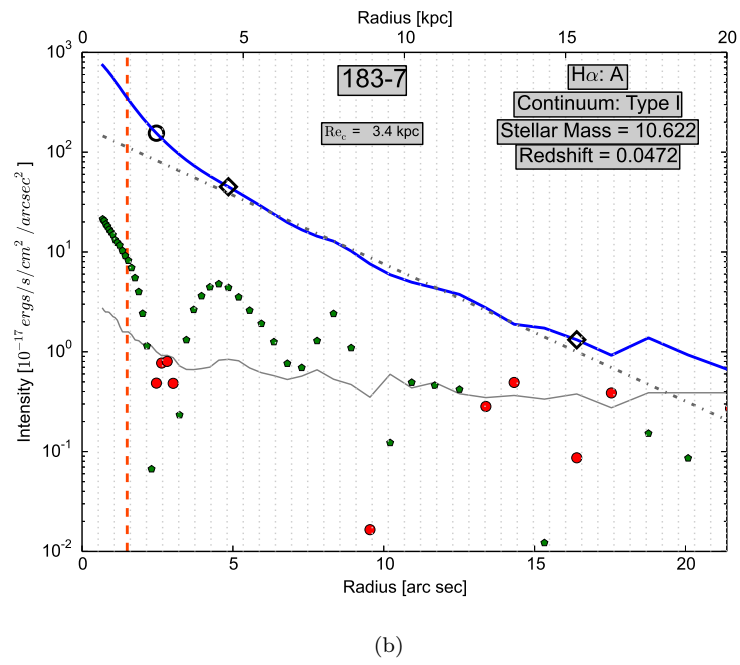
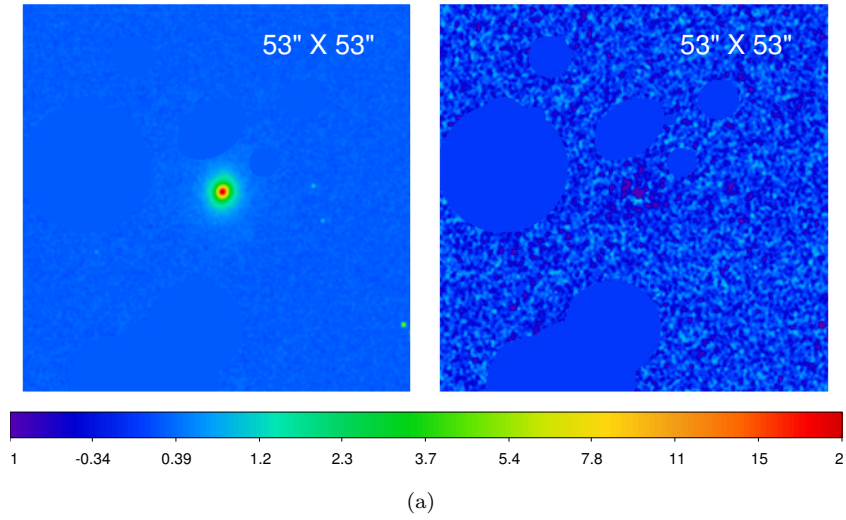


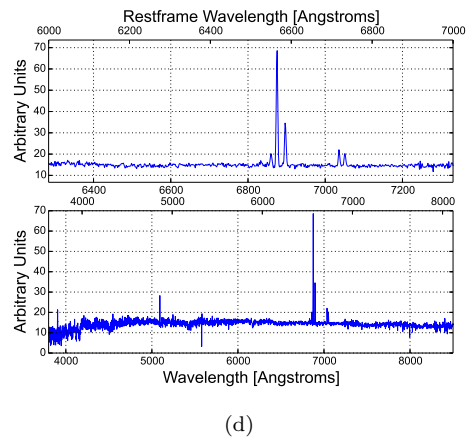
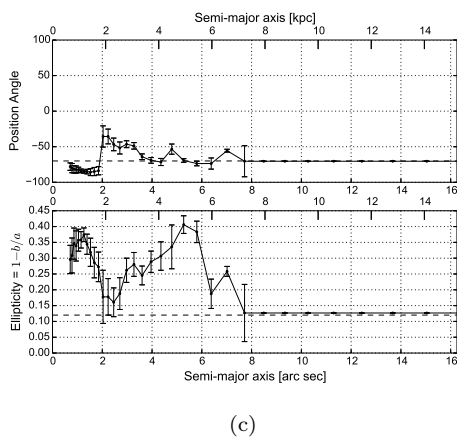
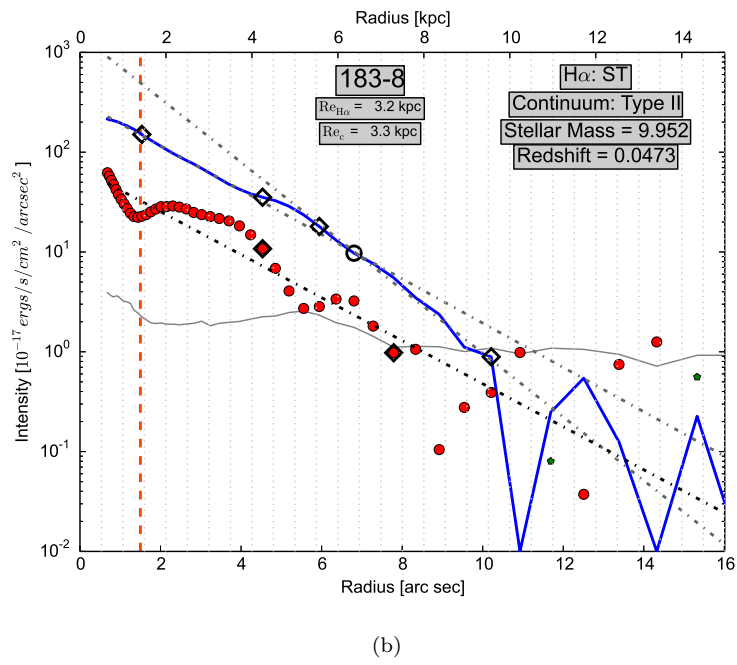
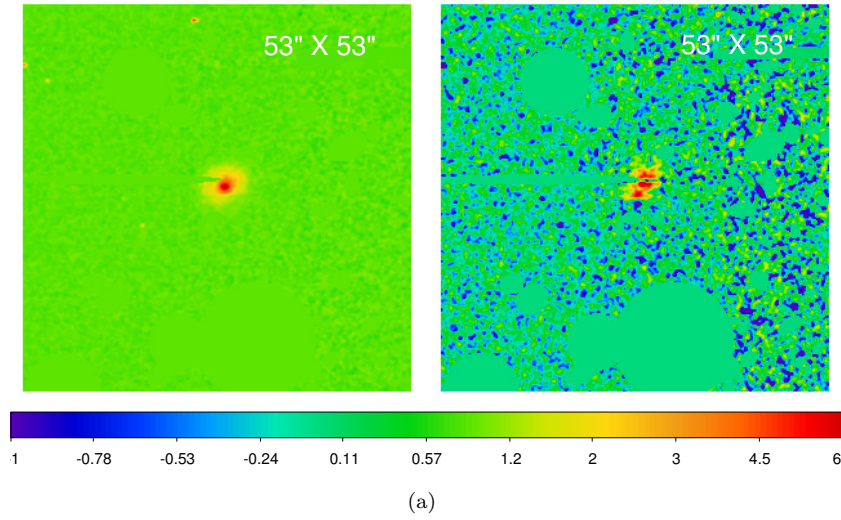


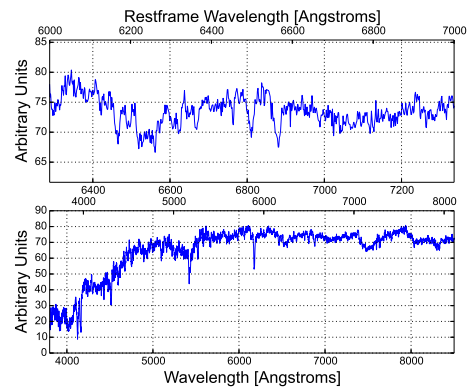
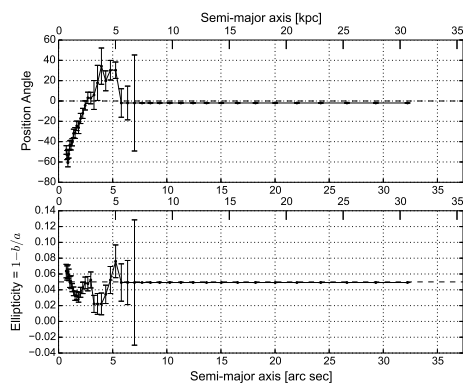
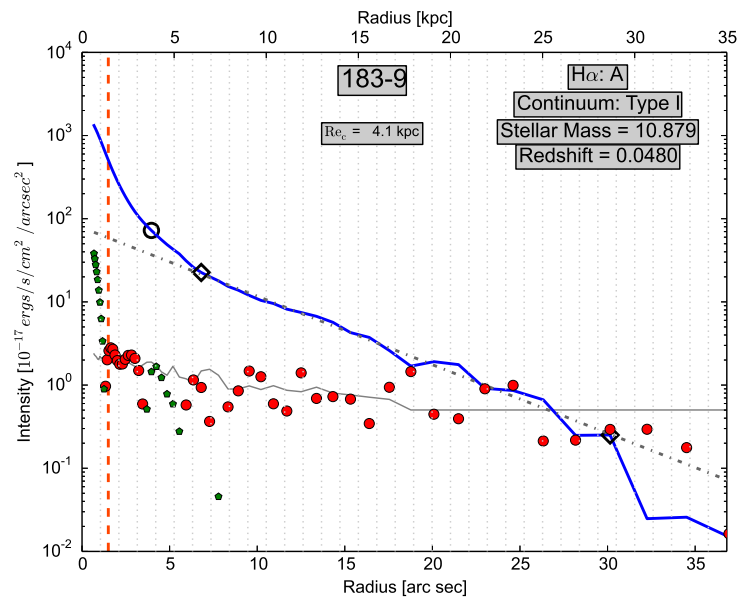
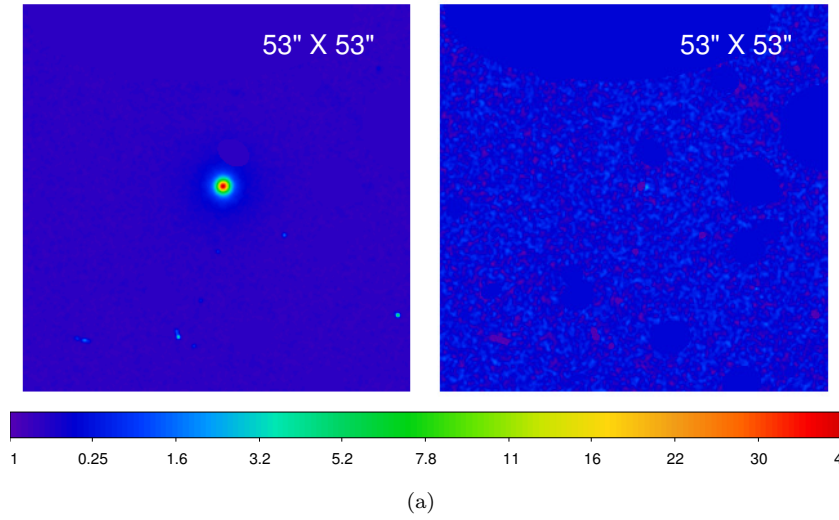


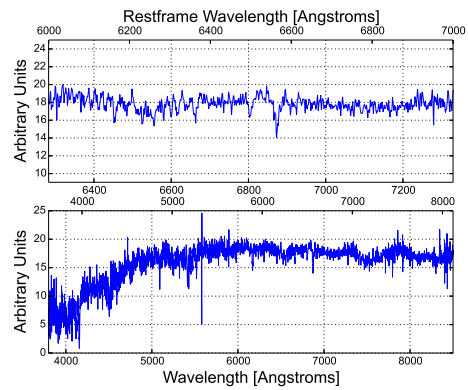
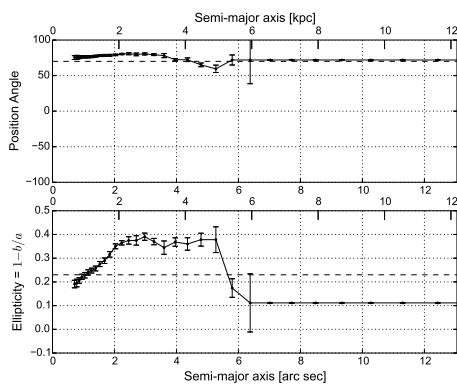
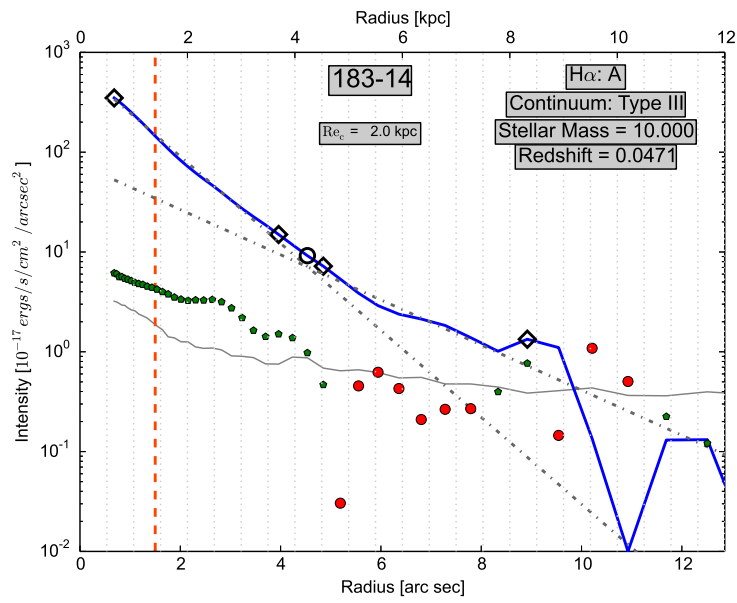
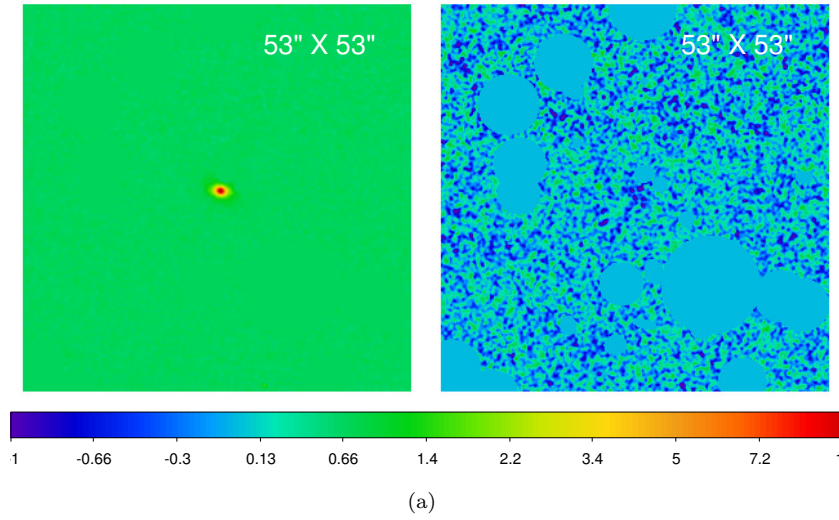


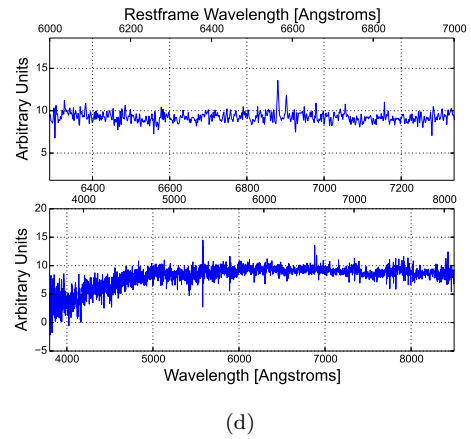
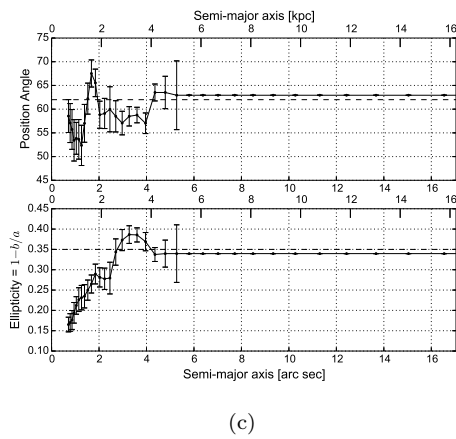
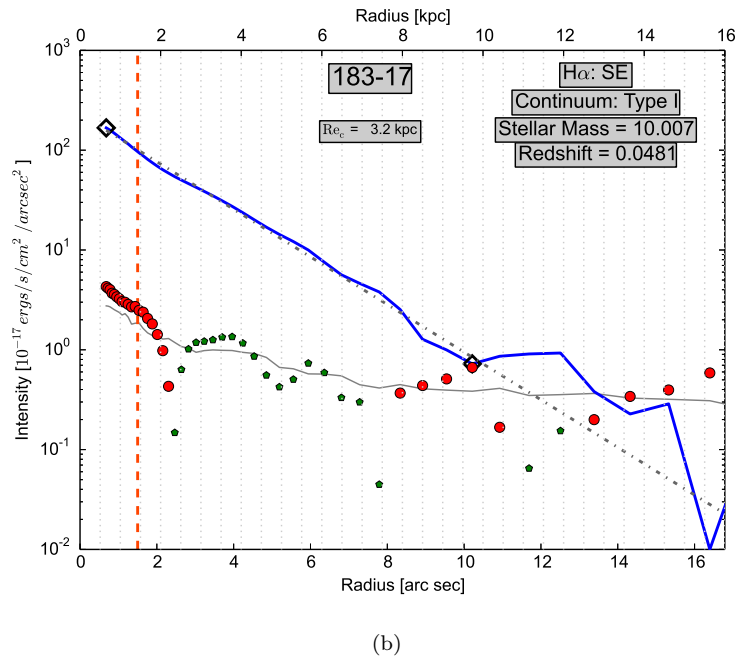
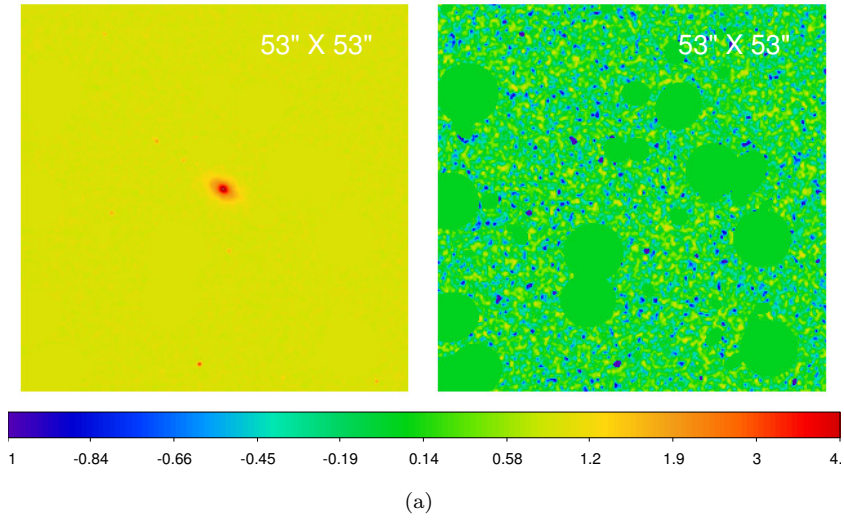


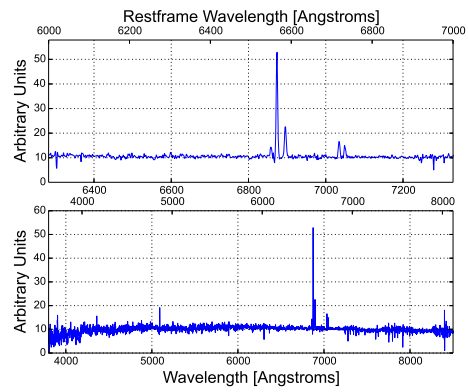
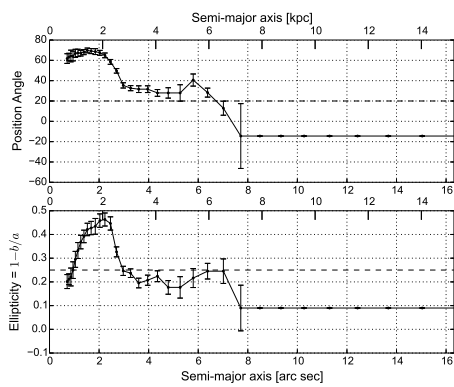
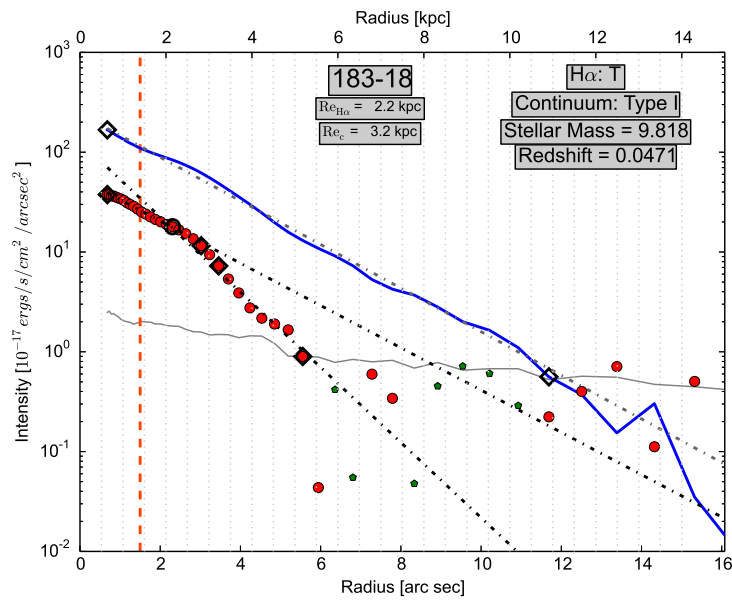
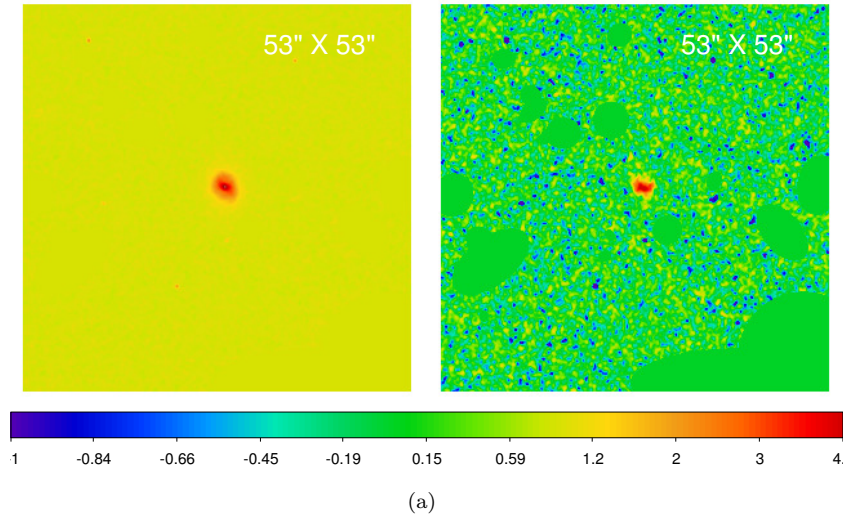


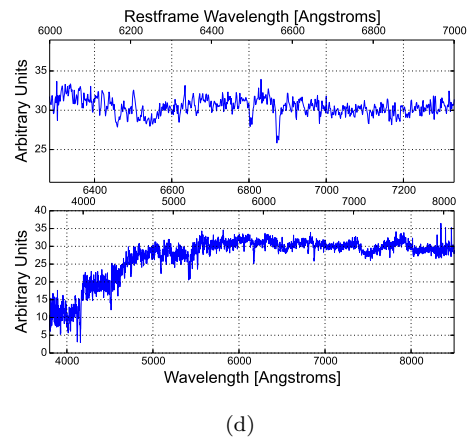
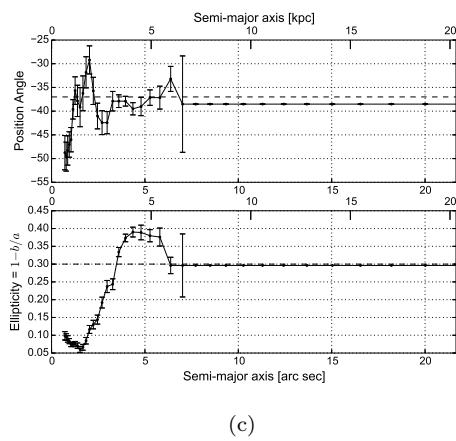
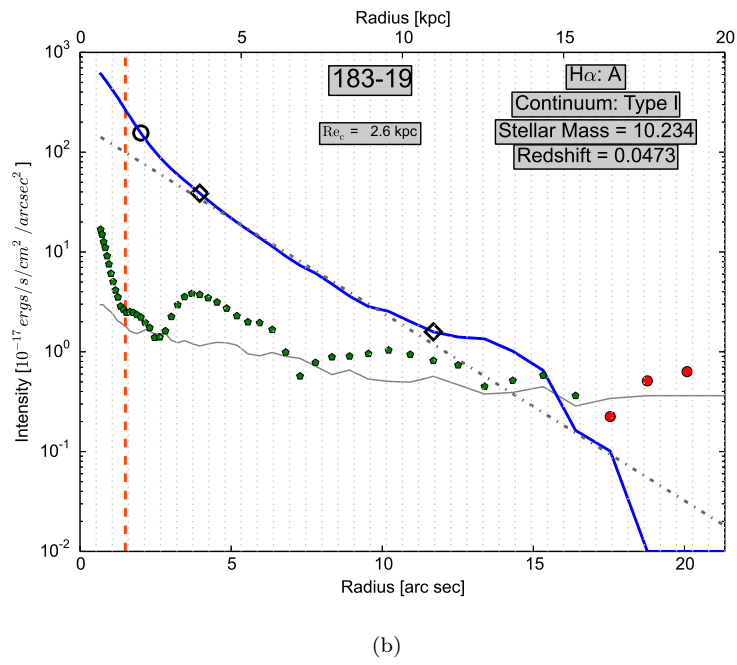
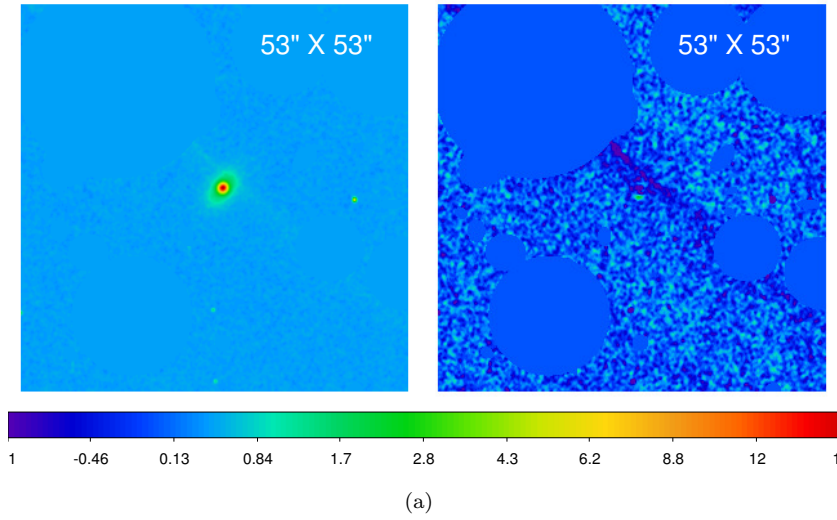


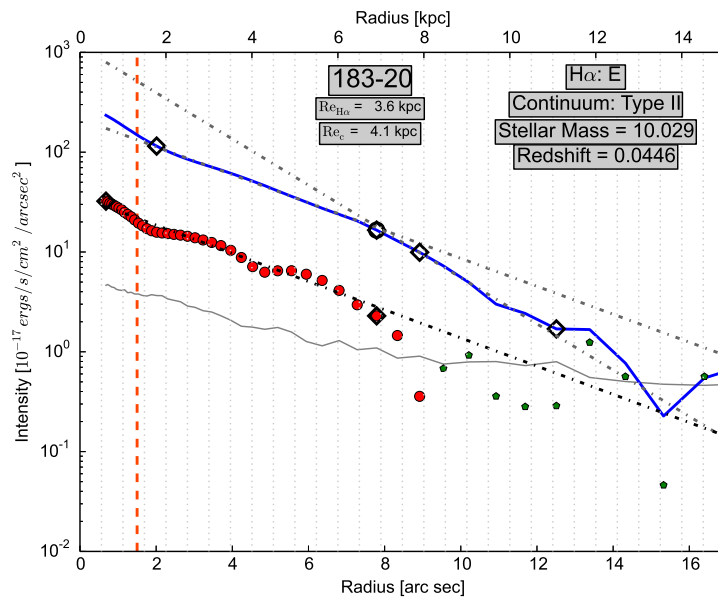
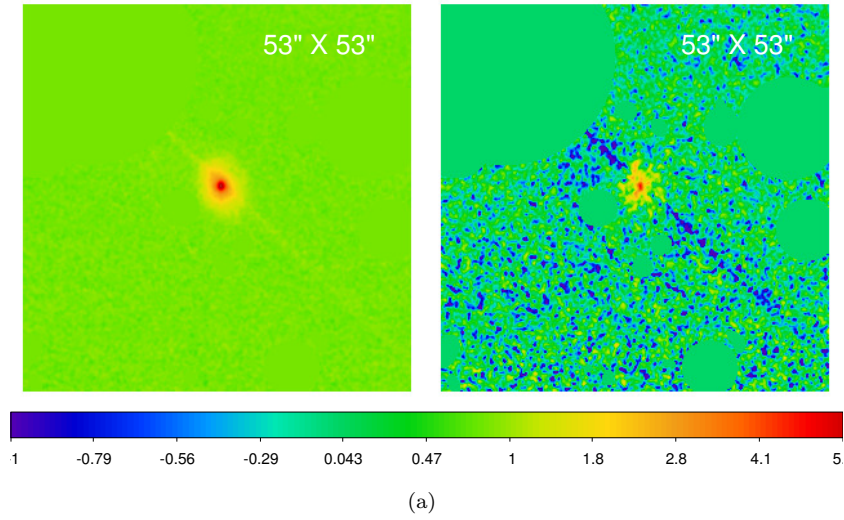




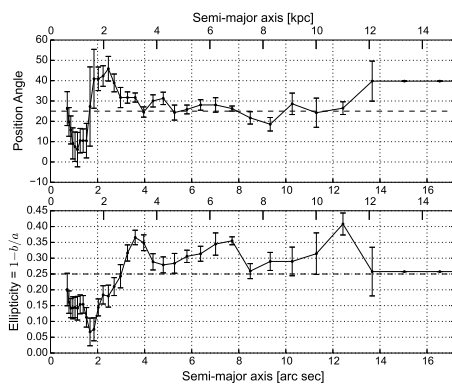




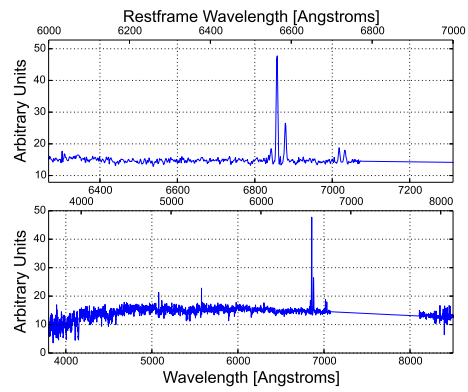




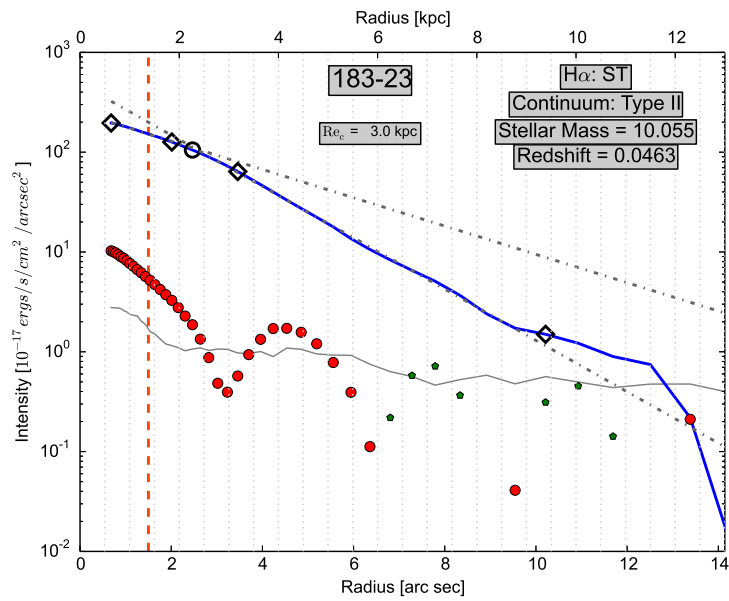
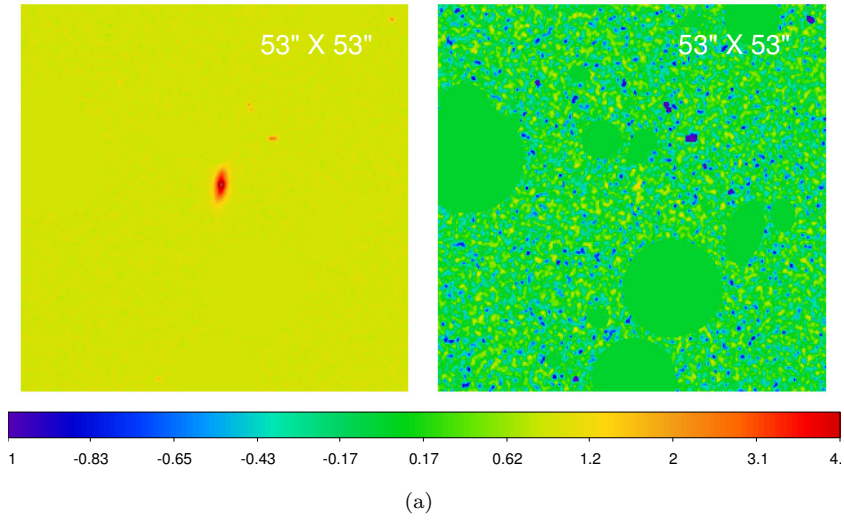
(b)



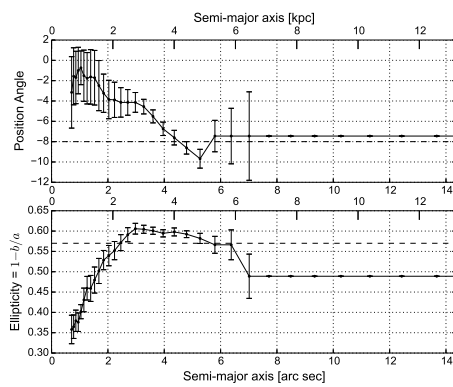
(c)



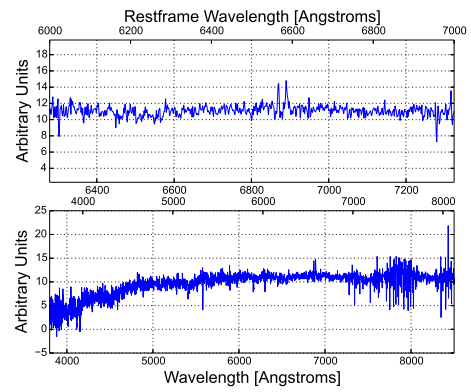
(d)



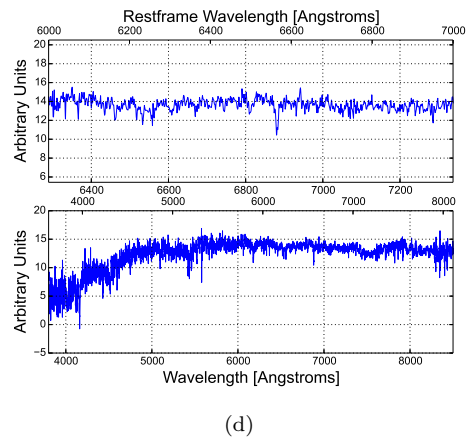
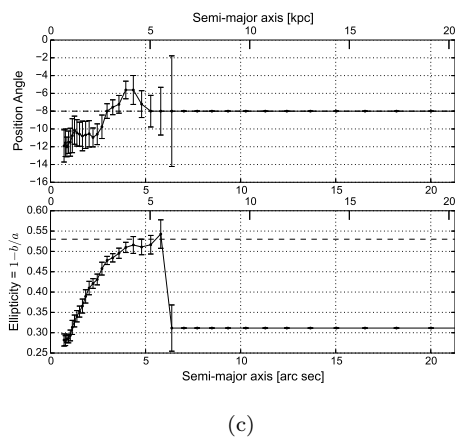
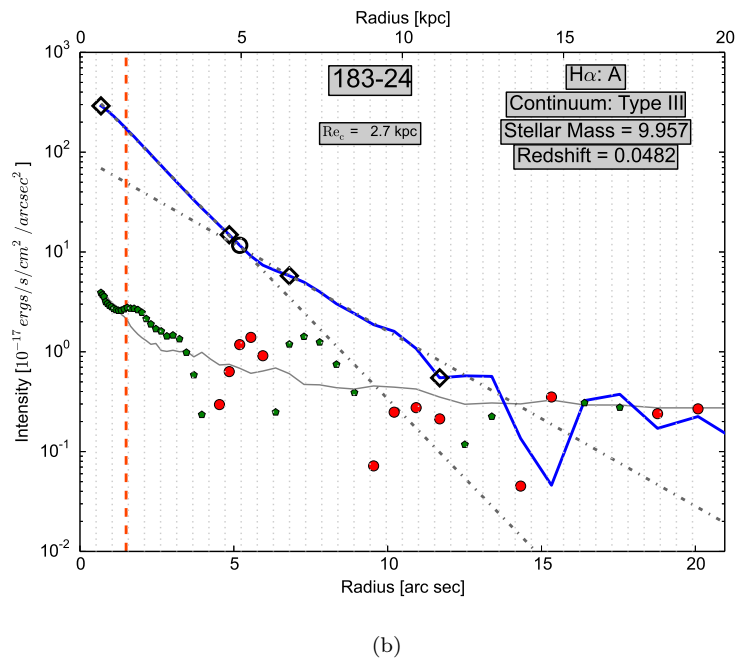
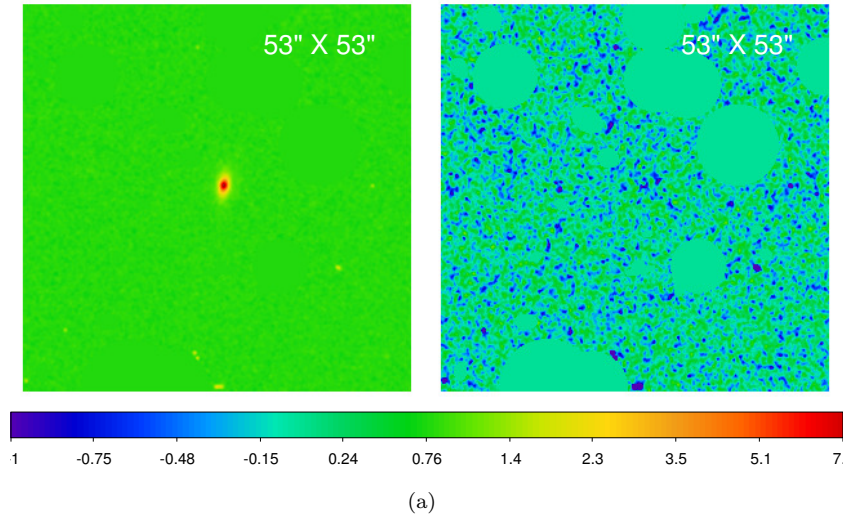
(b)

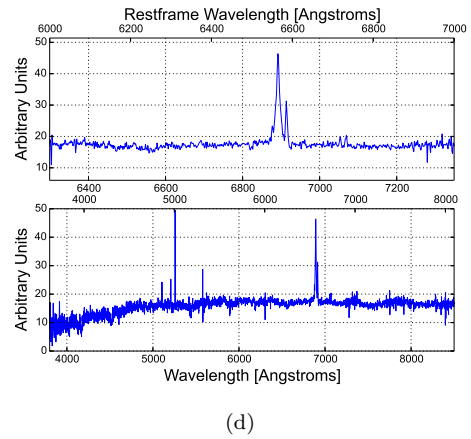
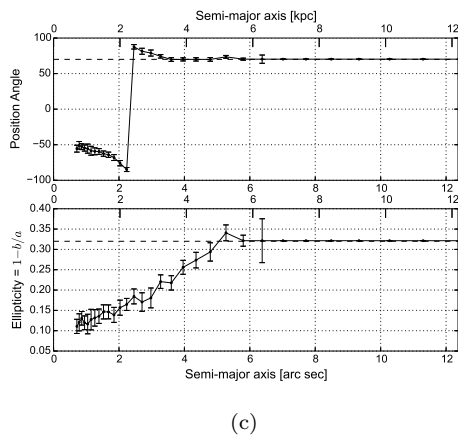
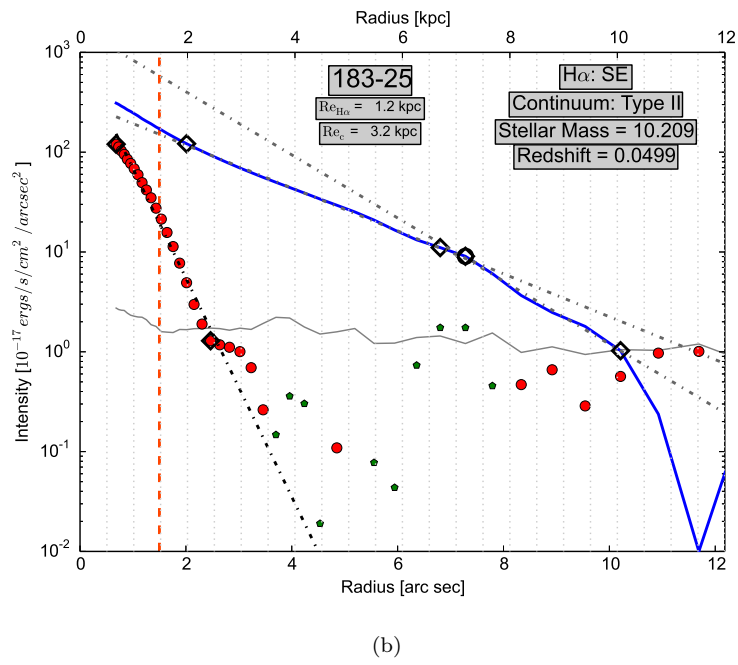
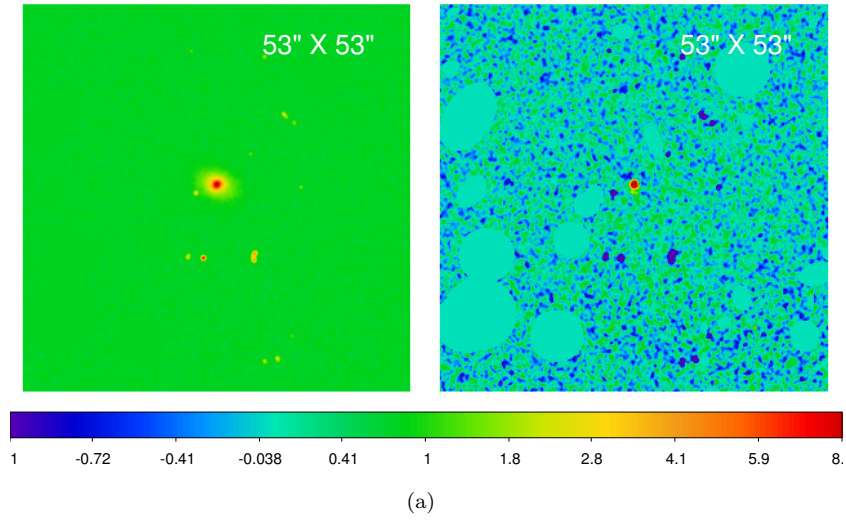


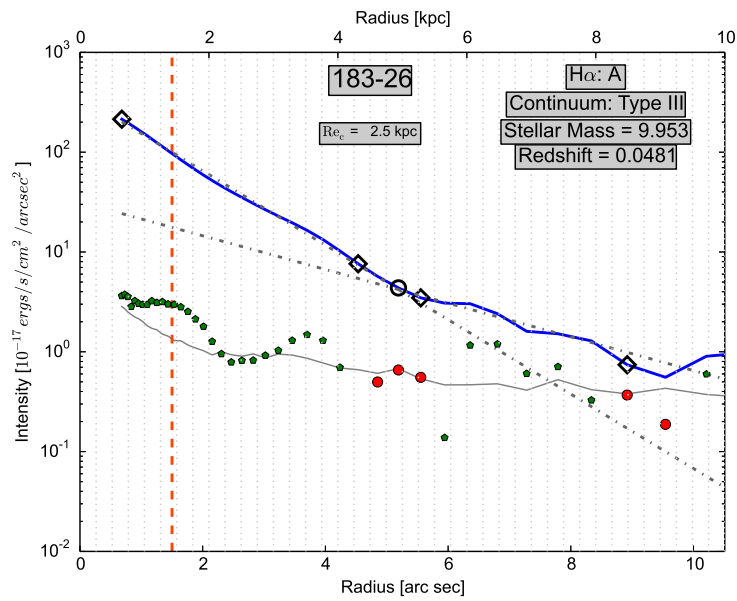
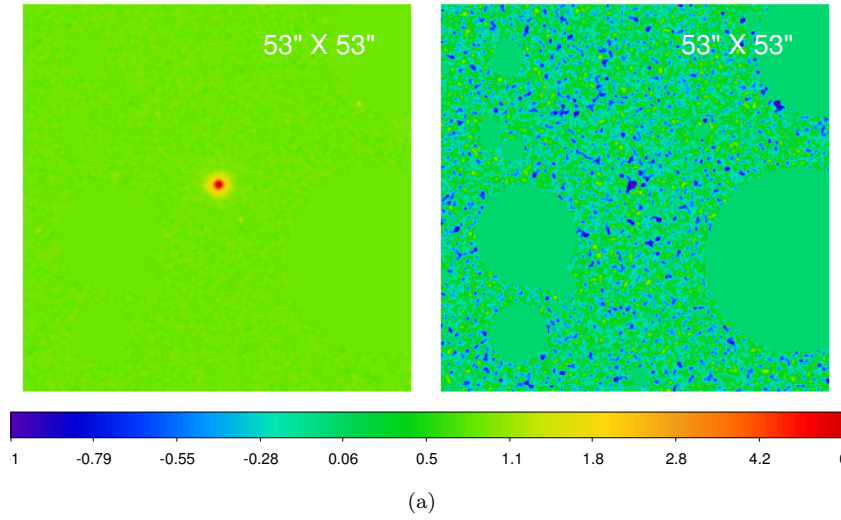
(c)



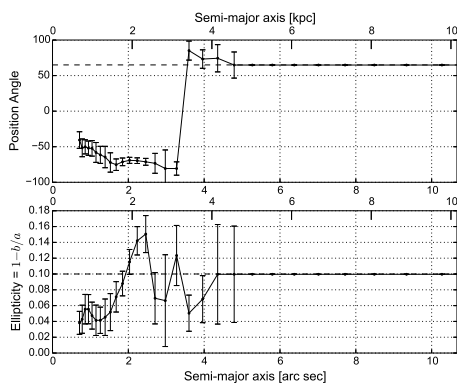
(d)



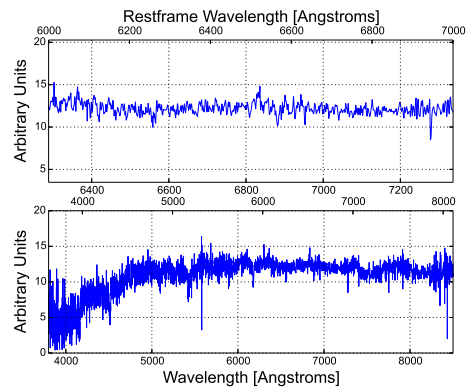




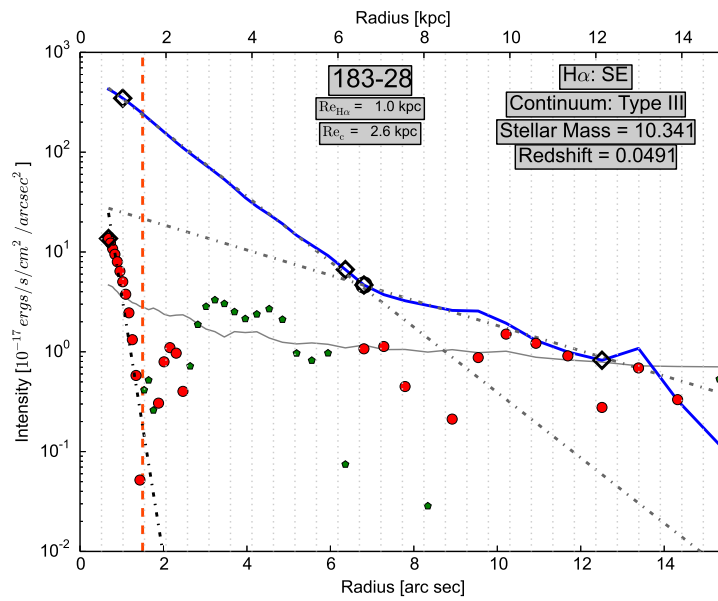
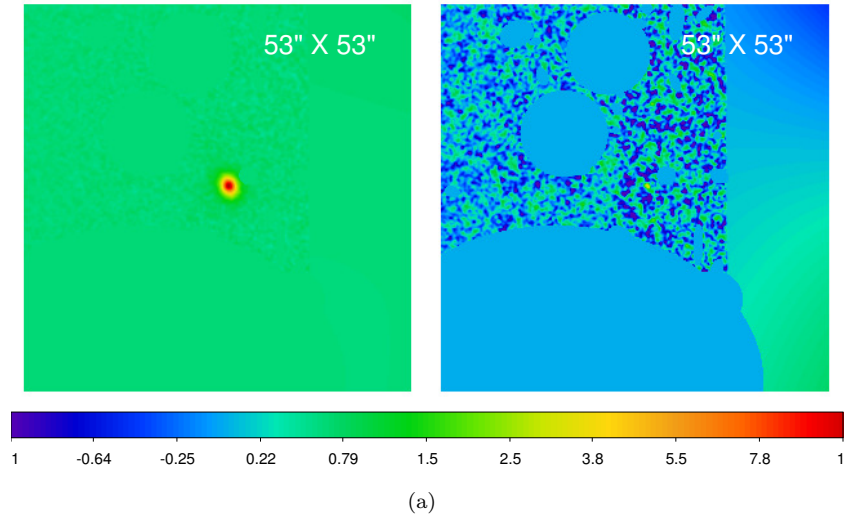
(b)



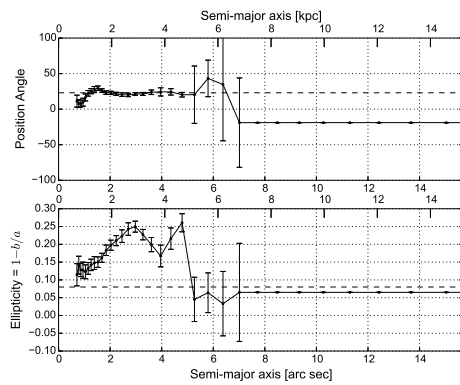
(c)



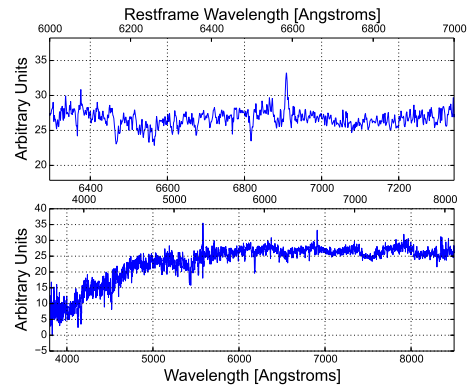
(d)



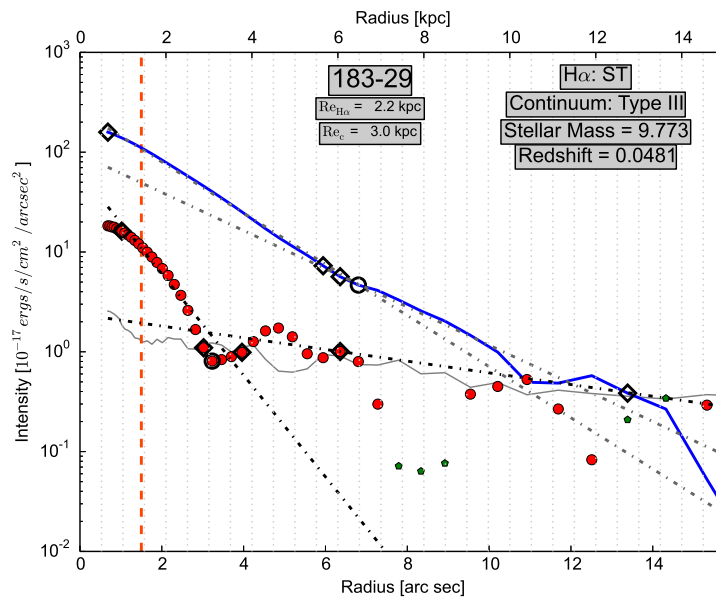
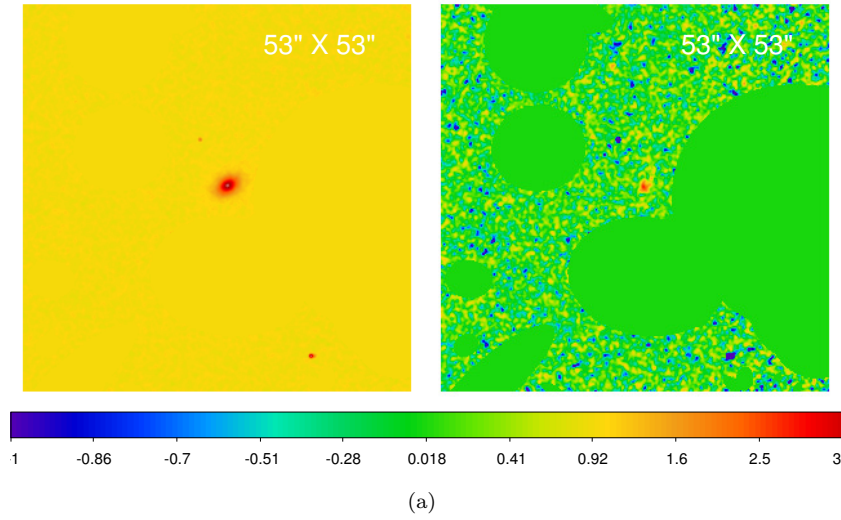
(b)



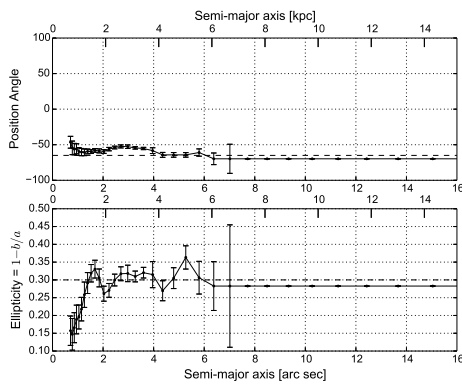
(c)



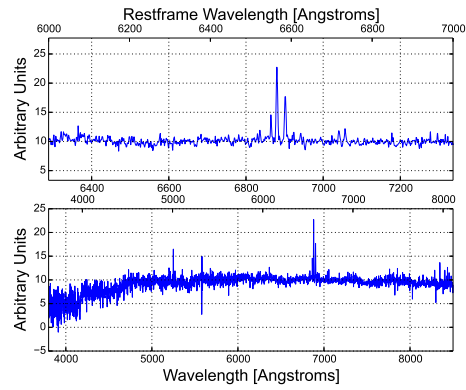
(d)



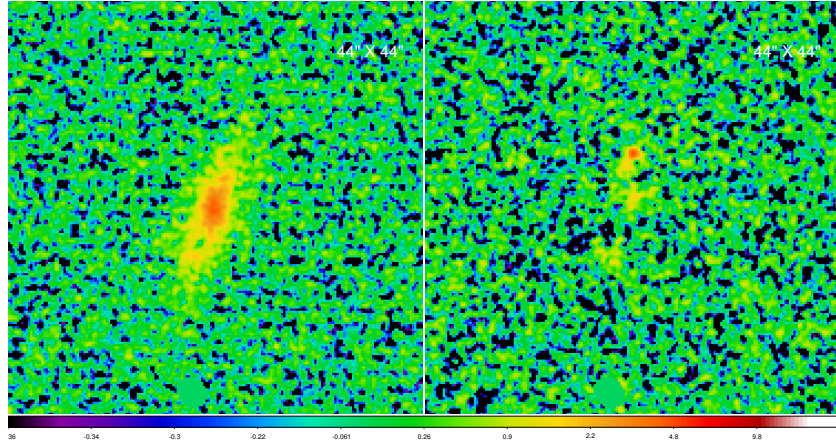
(b)



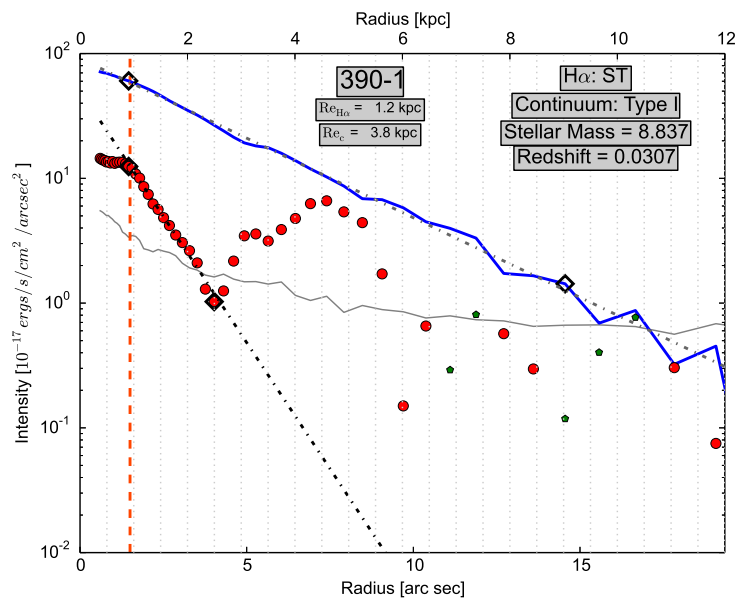
(c)



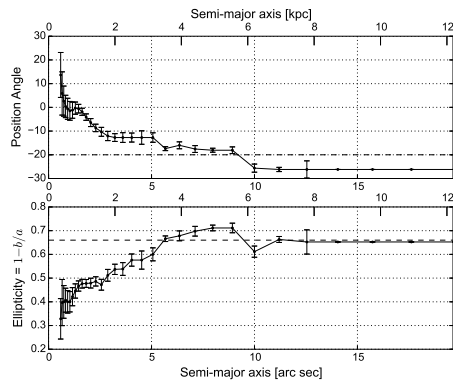
(d)



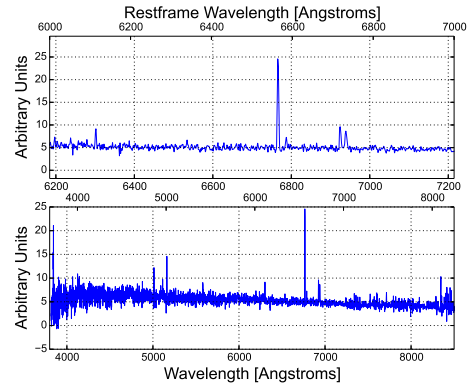
(a)



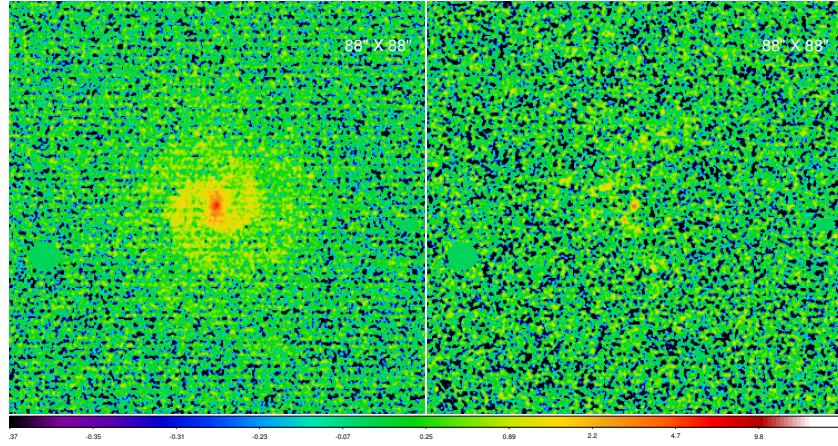
(b)



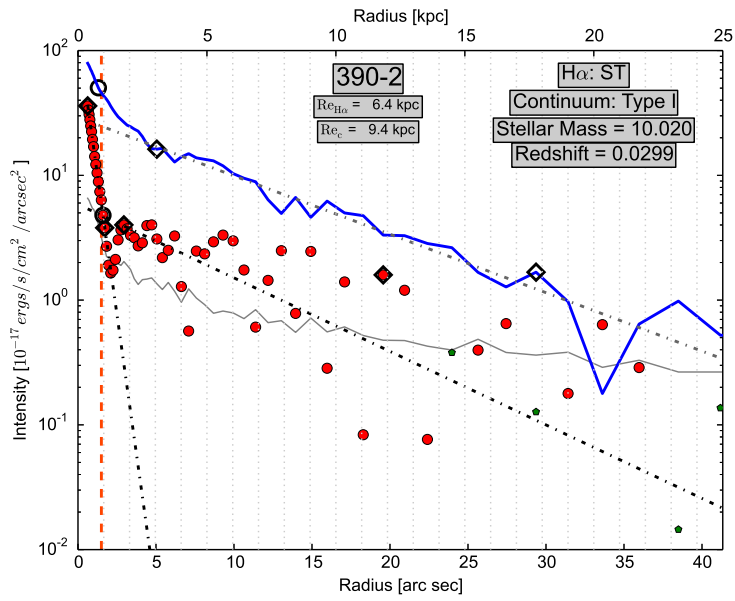
(c)



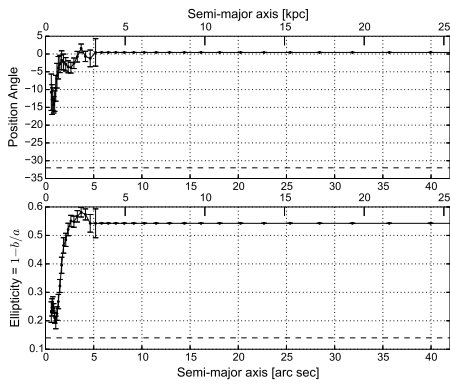
(d)



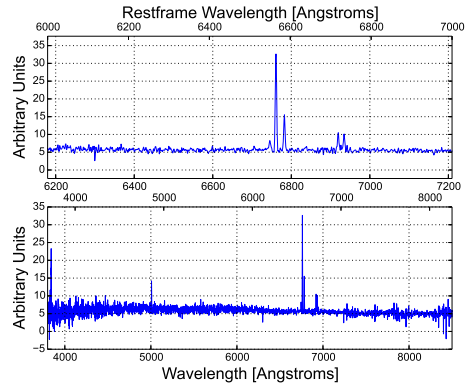
(a)



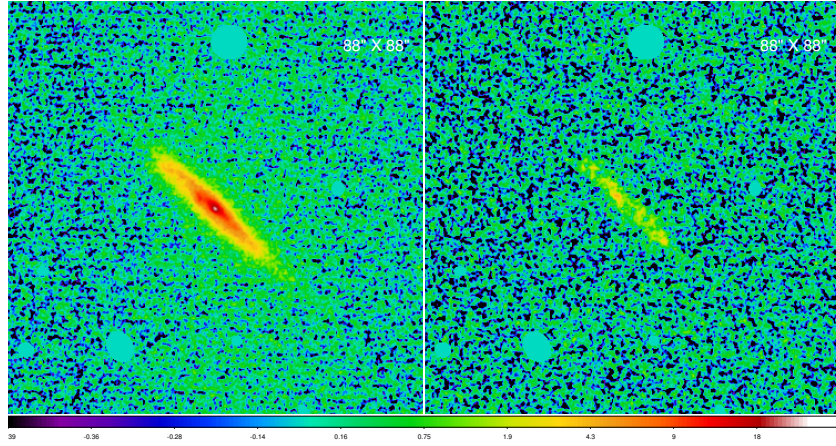
(b)



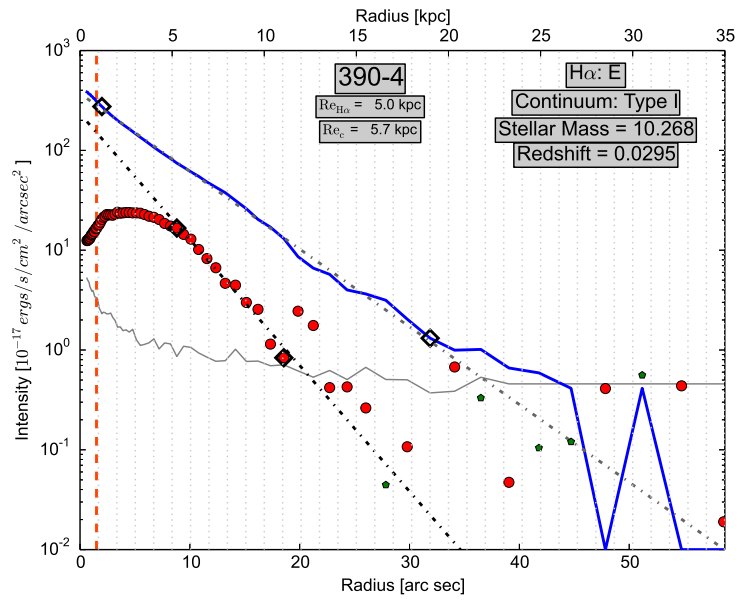
(c)



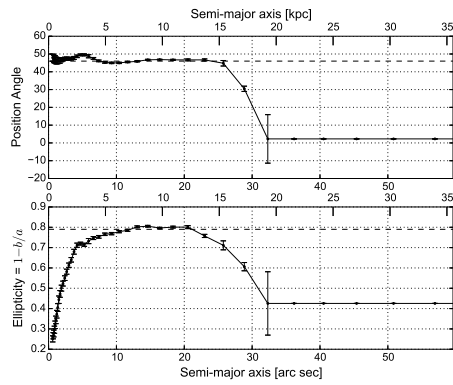
(d)



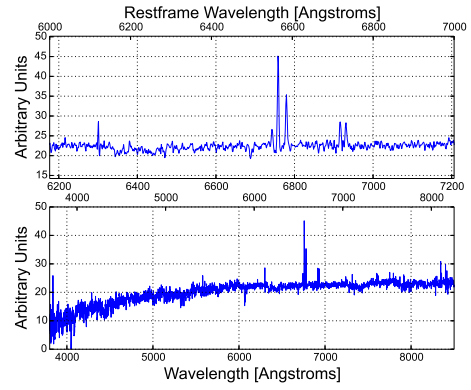
(a)



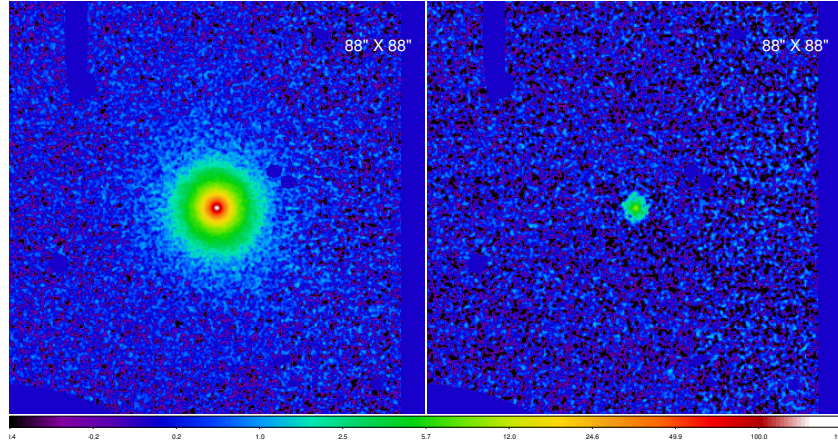
(b)



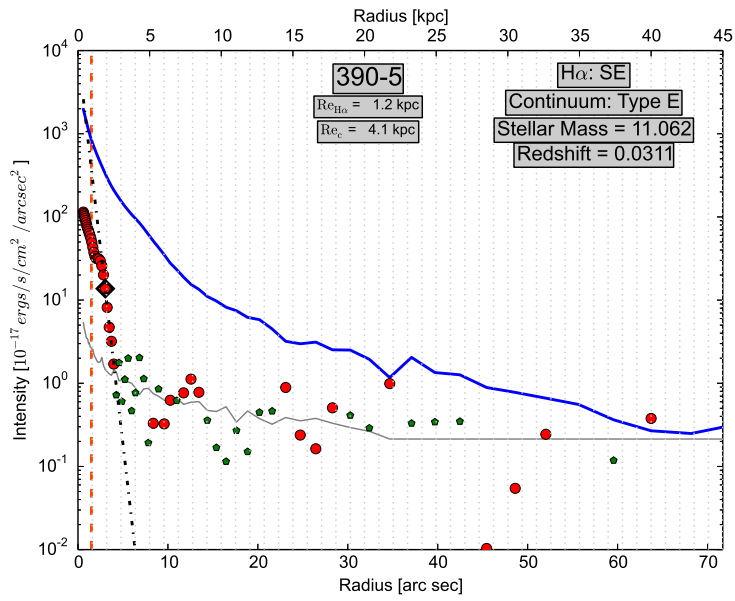
(c)



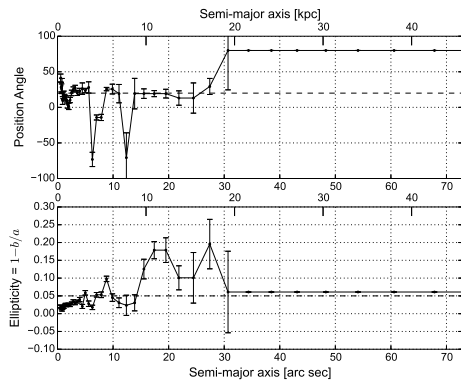
(d)



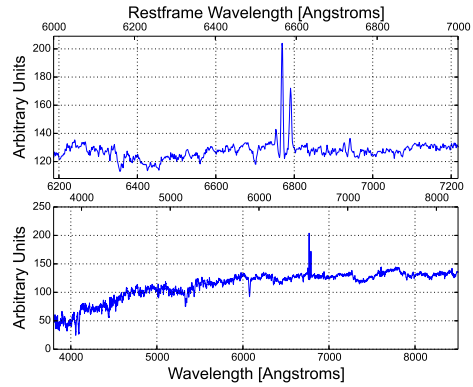
(a)



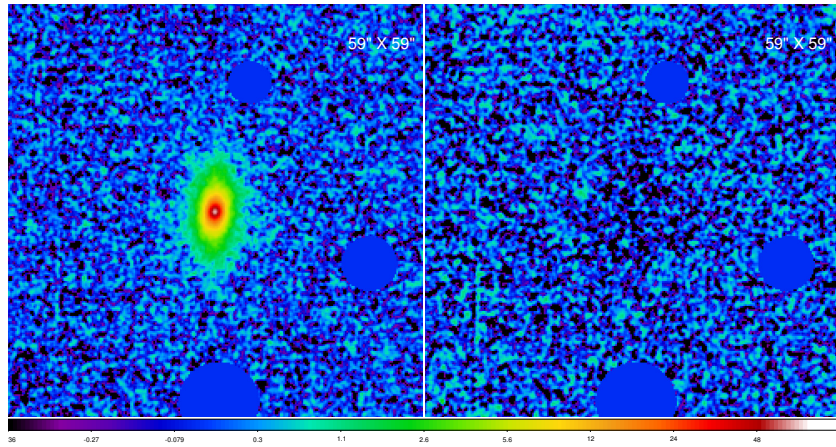
(b)



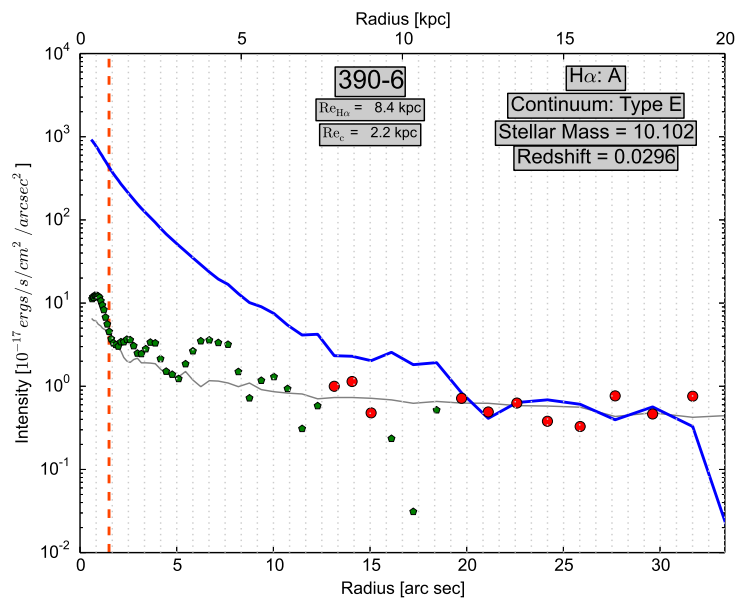
(c)



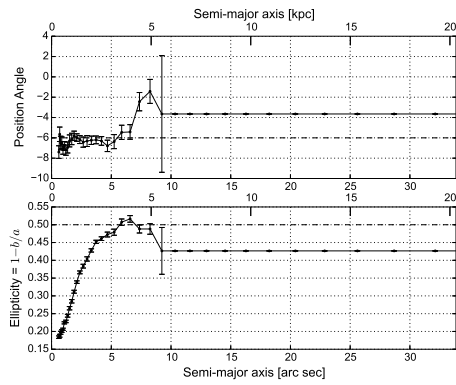
(d)



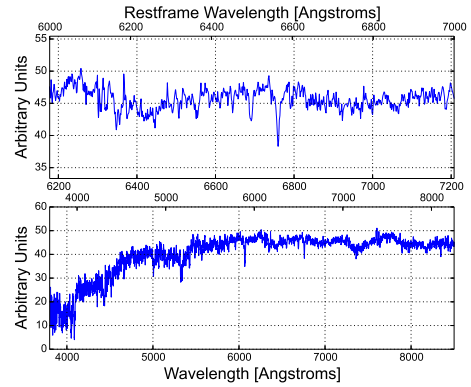
(a)



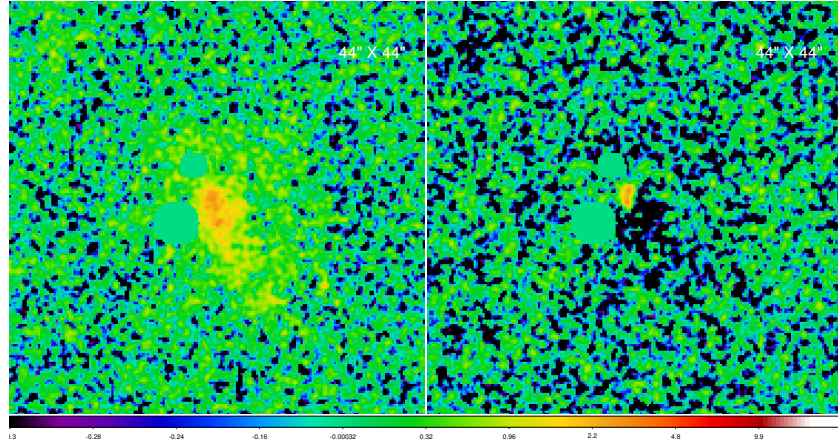
(b)



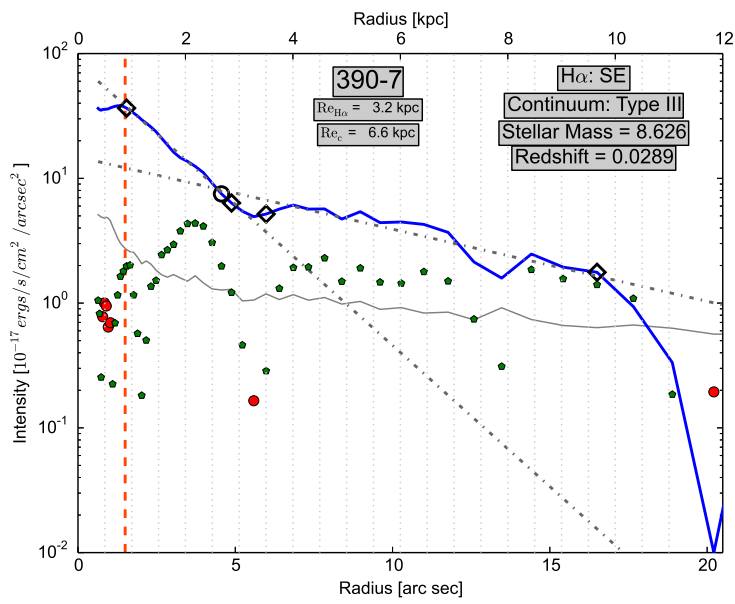
(c)



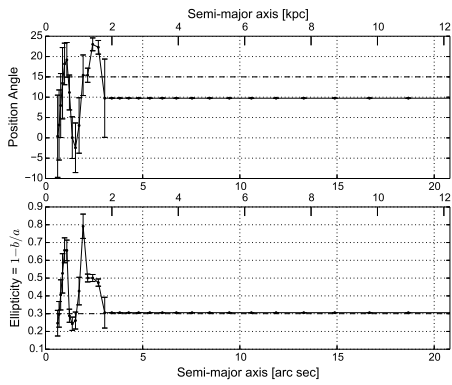
(d)



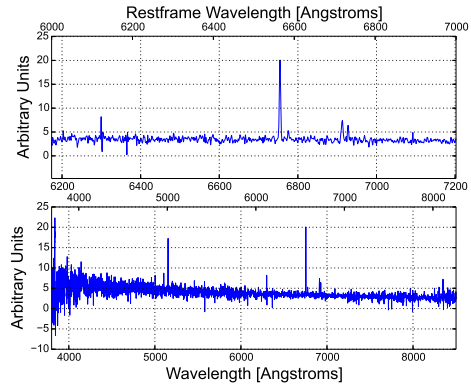
(a)



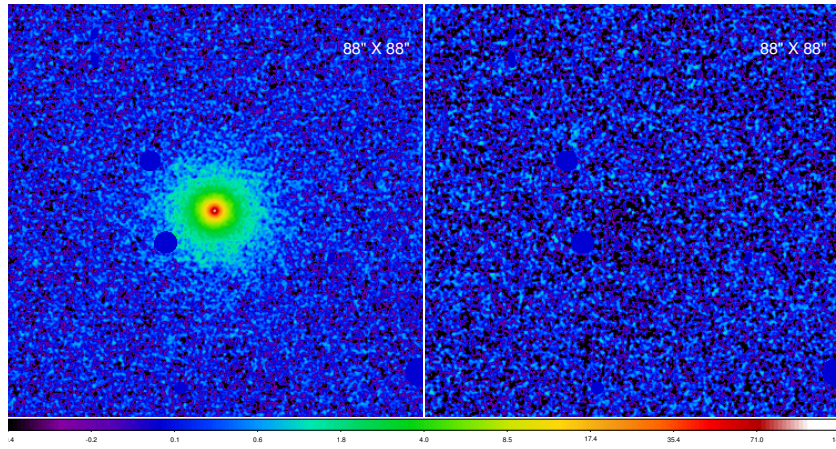
(b)



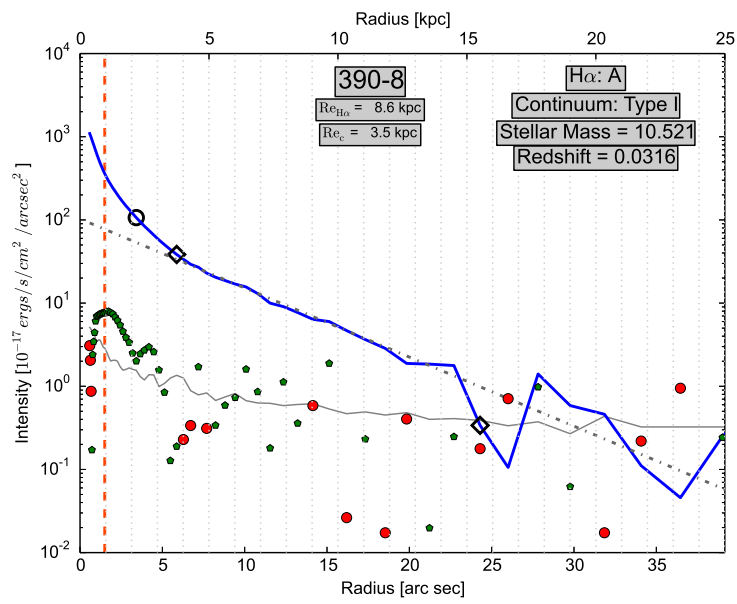
(c)



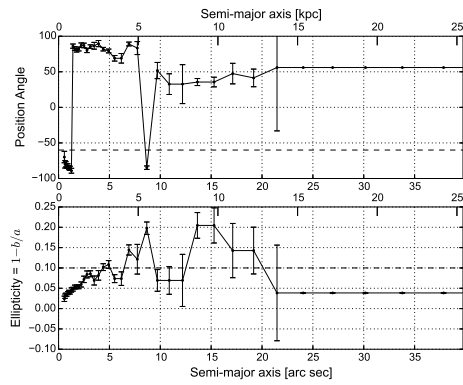
(d)



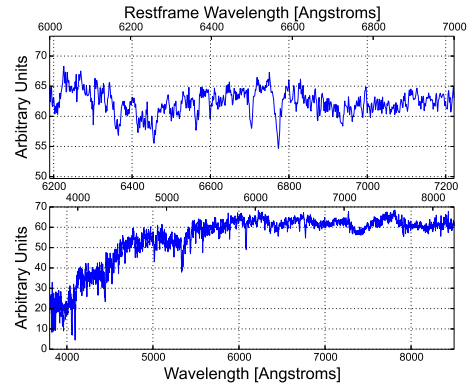
(a)



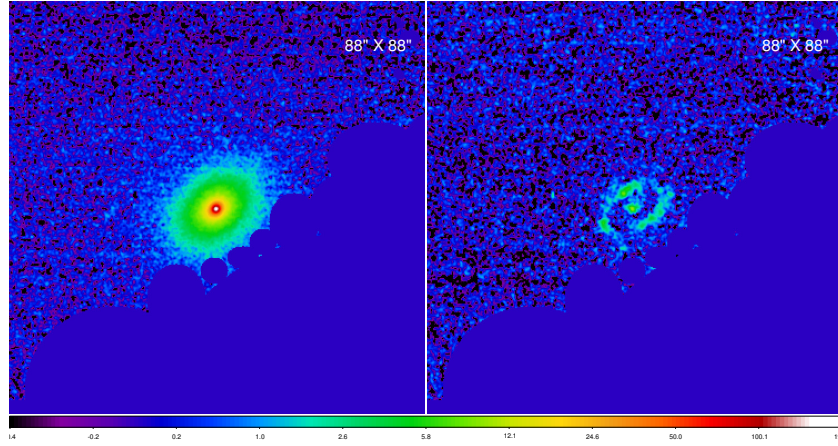
(b)



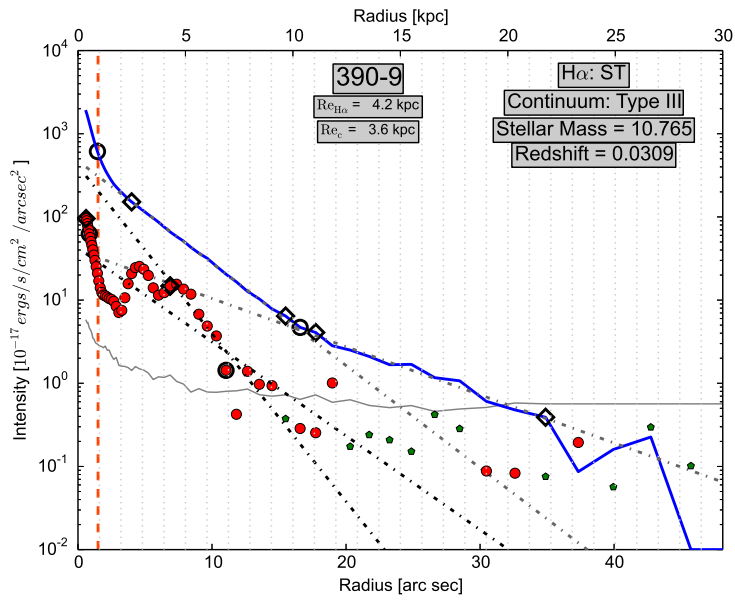
(c)



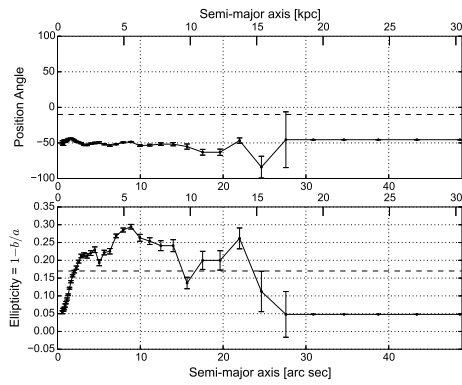
(d)



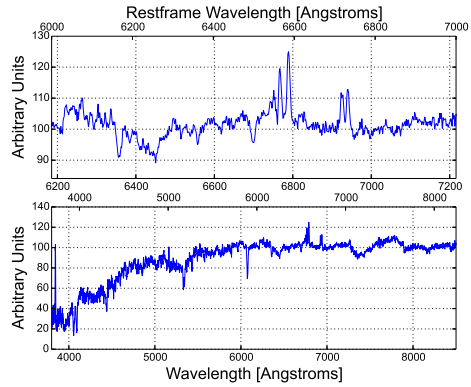
(a)



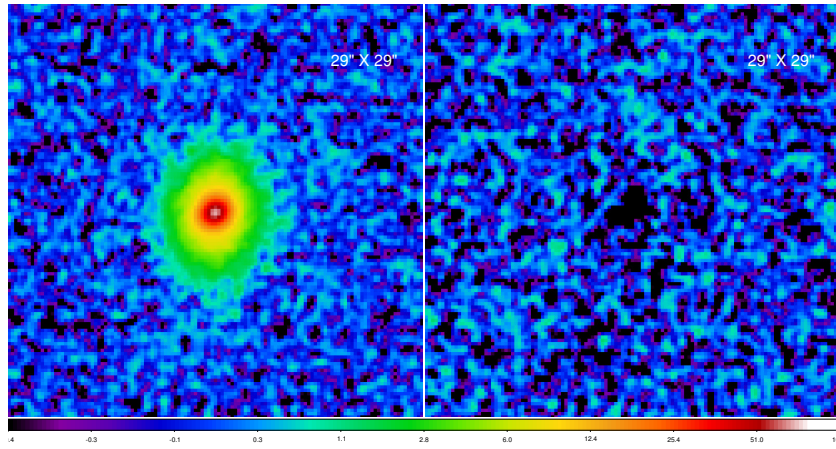
(b)



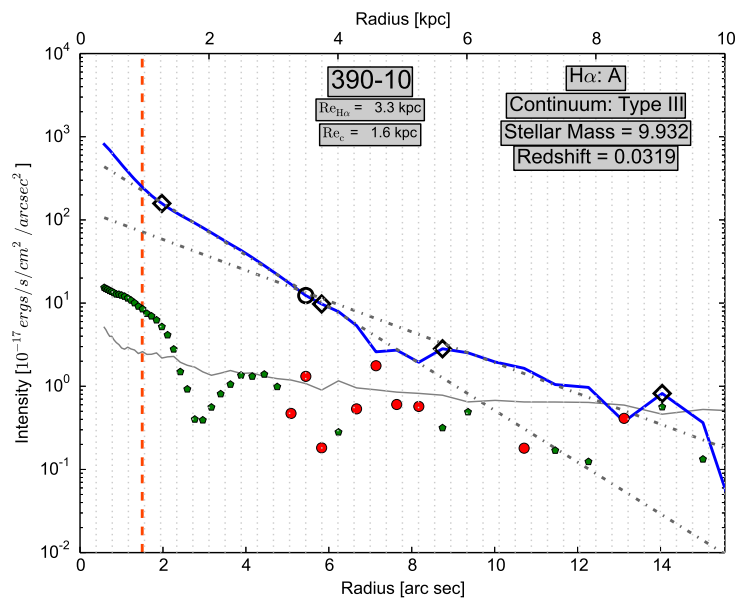
(c)



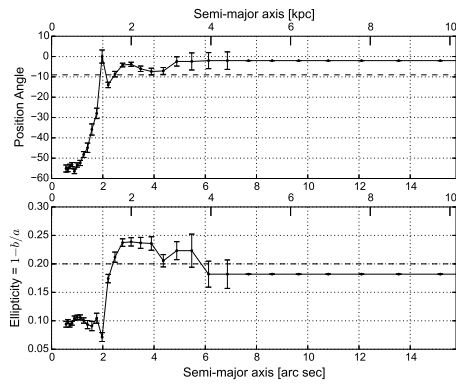
(d)



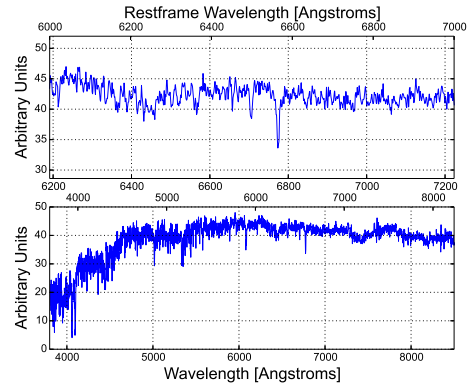
(a)



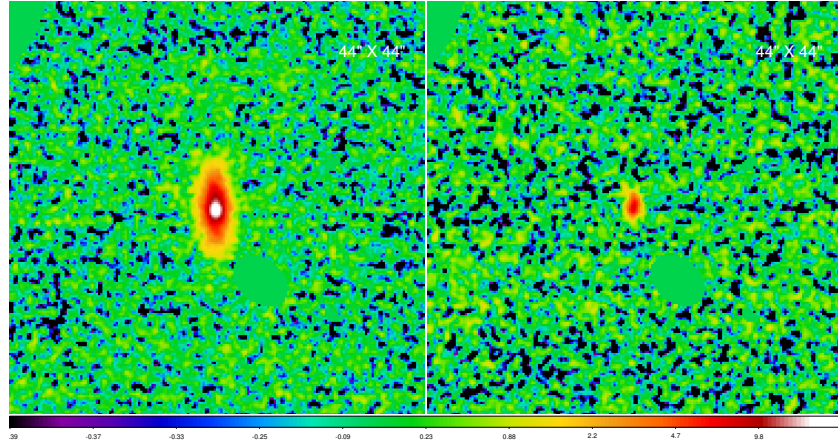
(b)



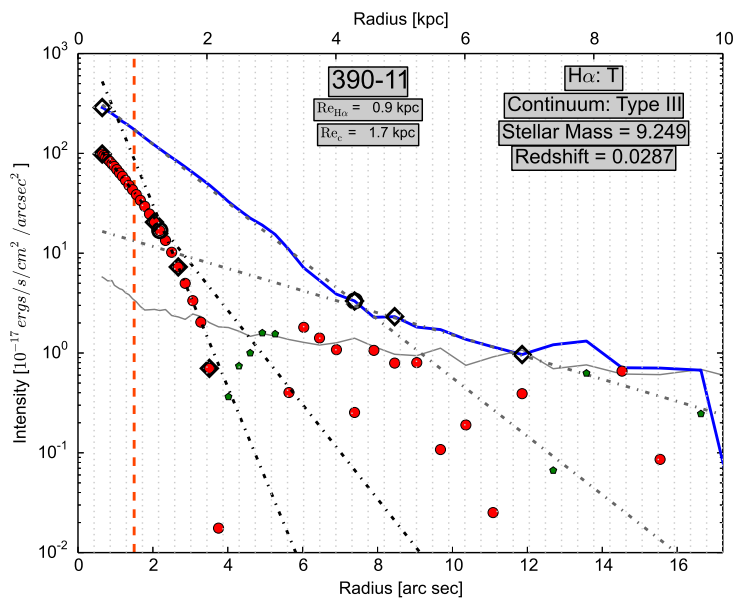
(c)



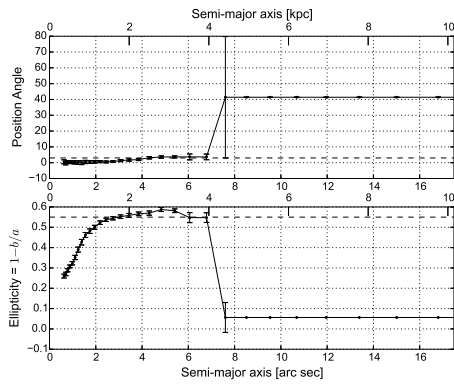
(d)



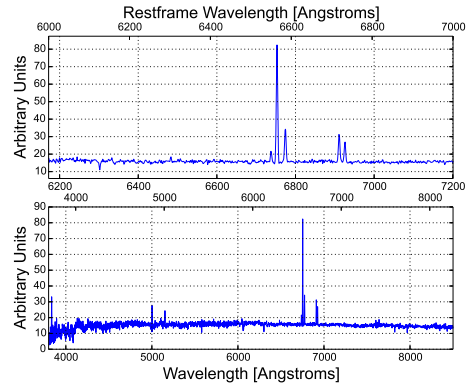
(a)



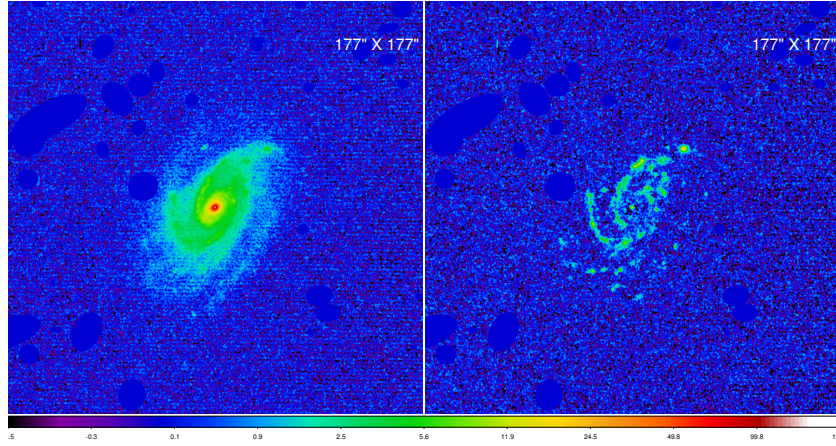
(b)



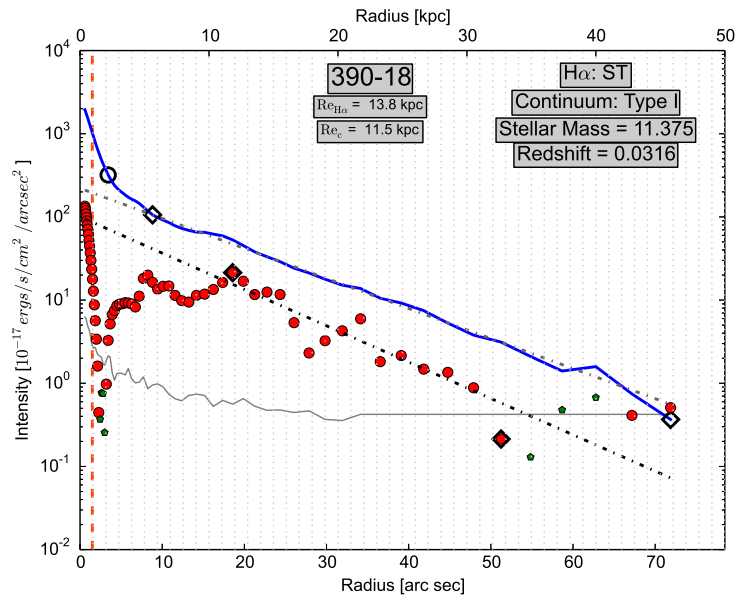
(c)



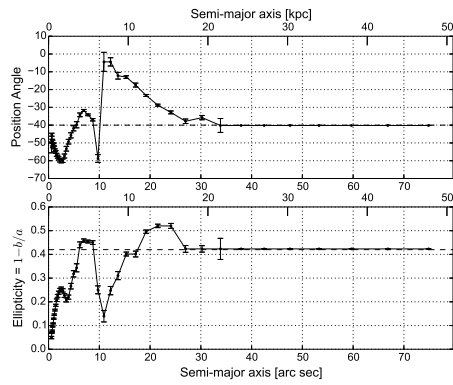
(d)



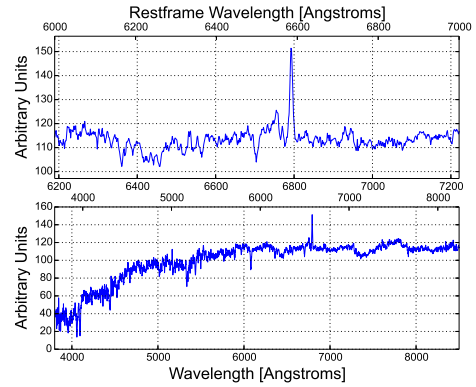
(a)



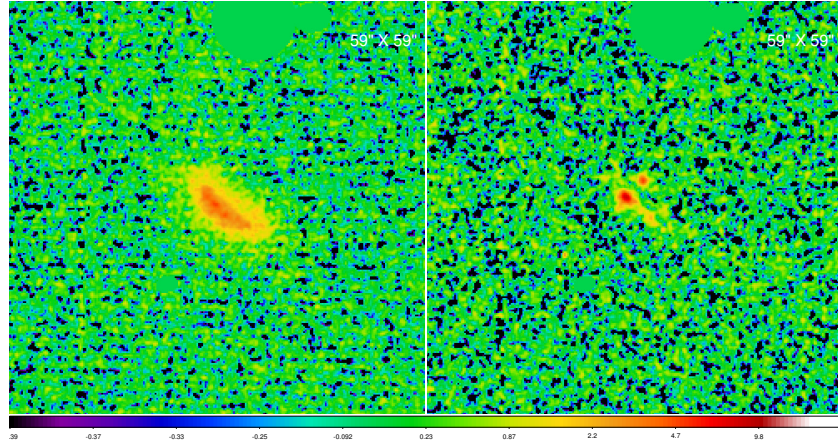
(b)



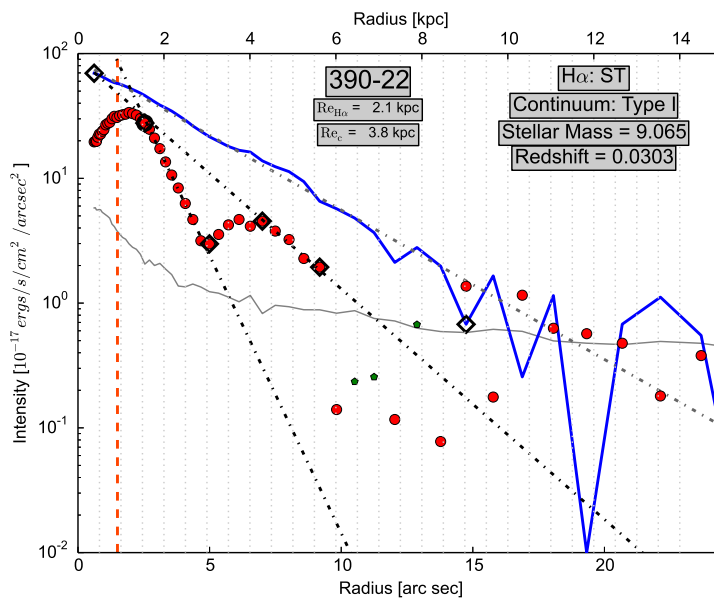
(c)



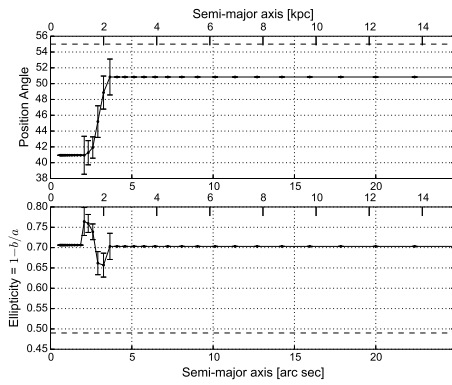
(d)



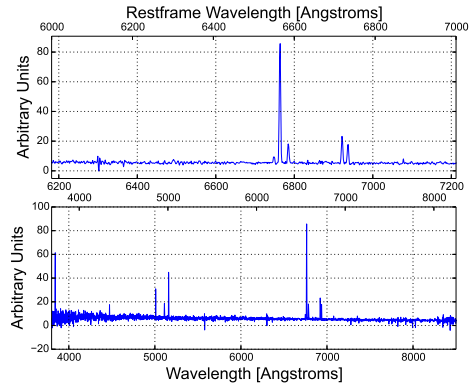
(a)



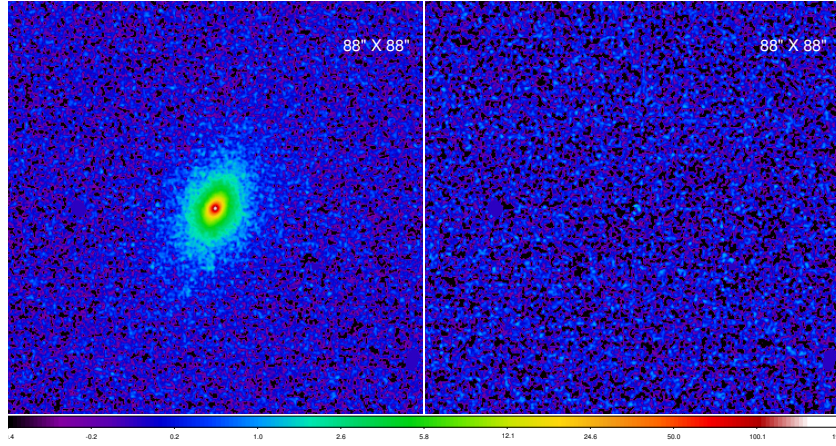
(b)



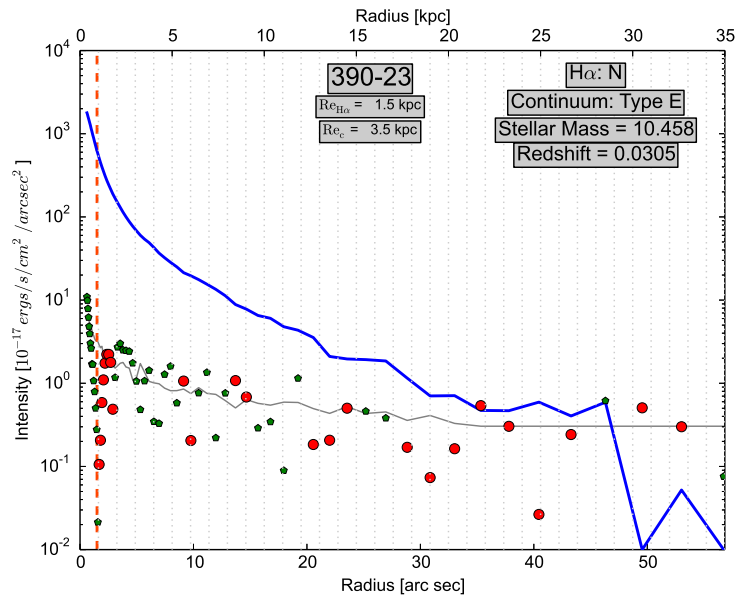
(c)



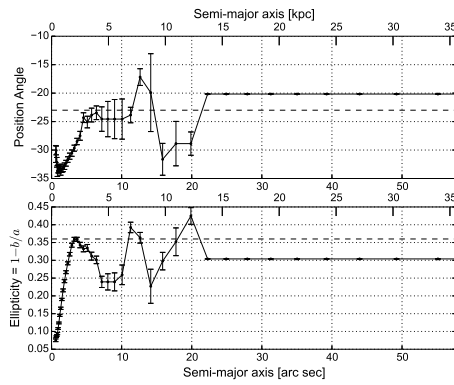
(d)



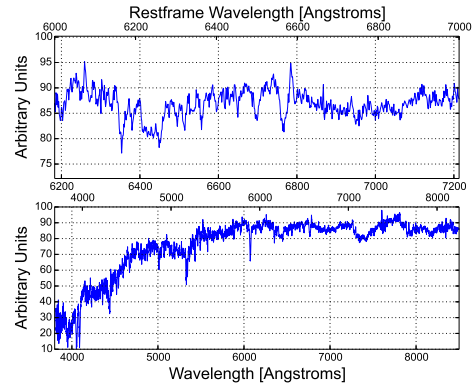
(a)



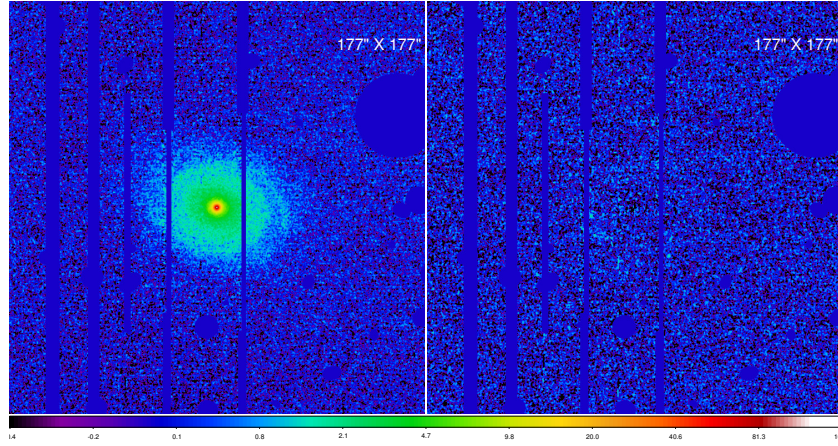
(b)



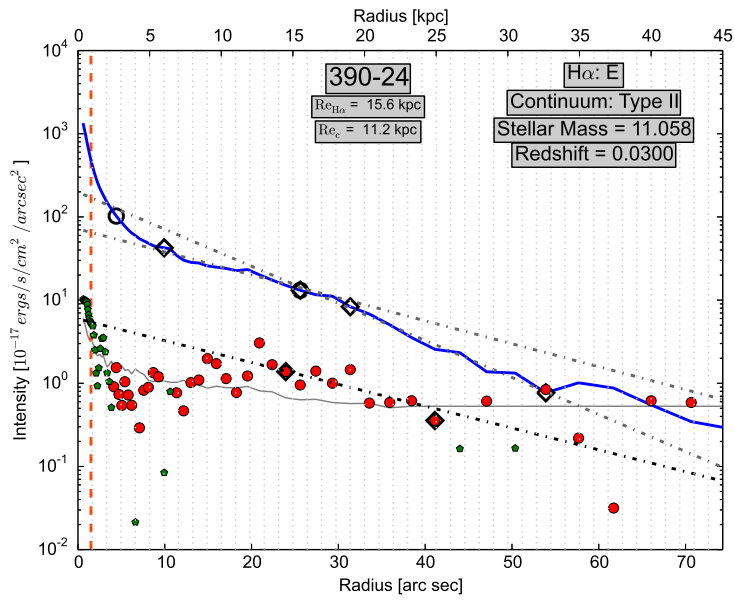
(c)



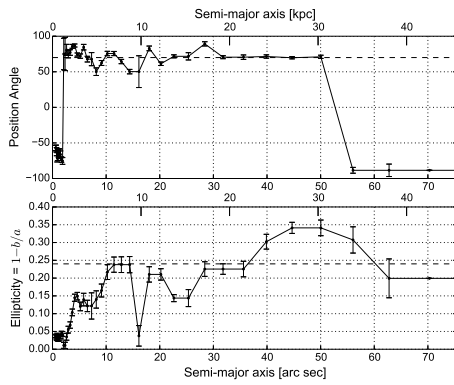
(d)



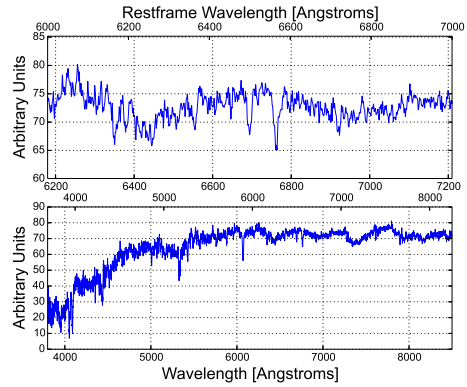
(a)



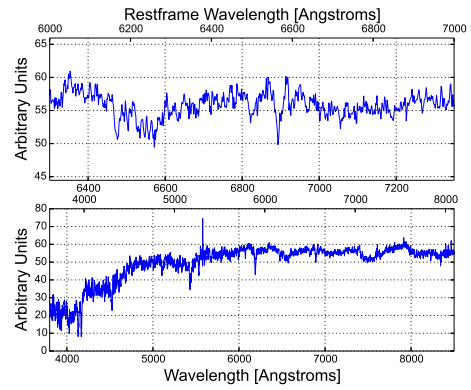
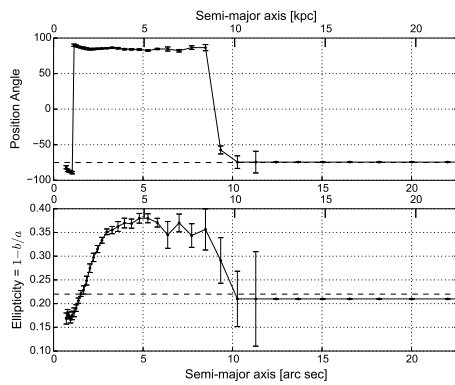
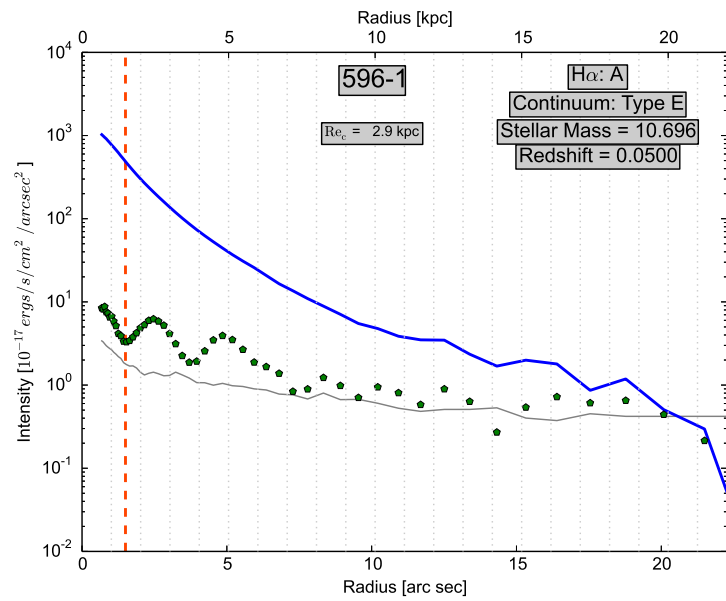
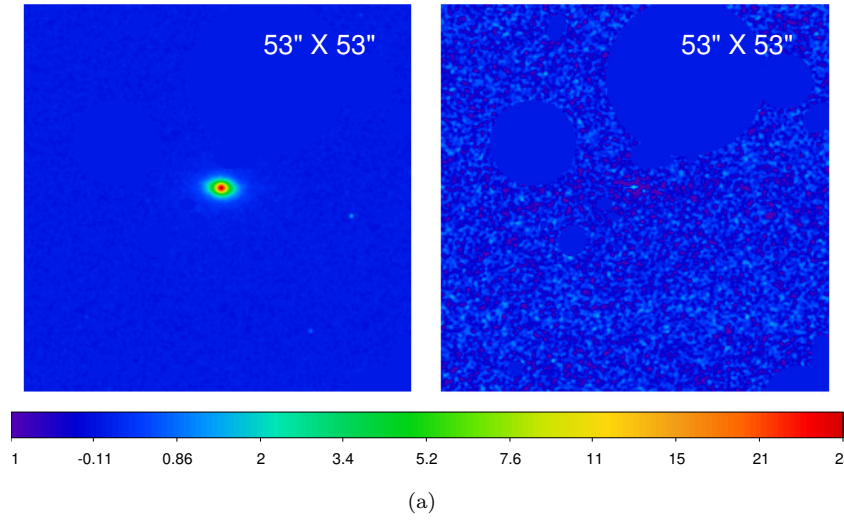
(b)

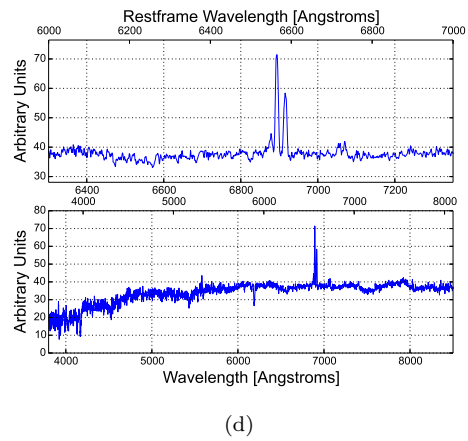
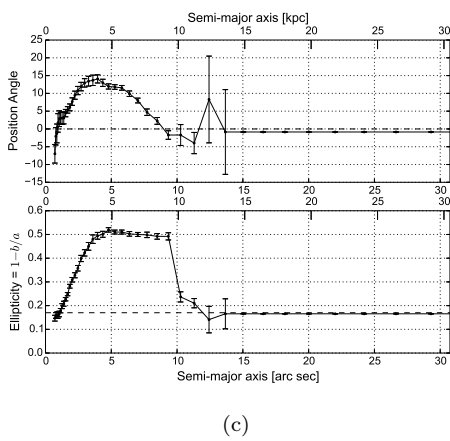
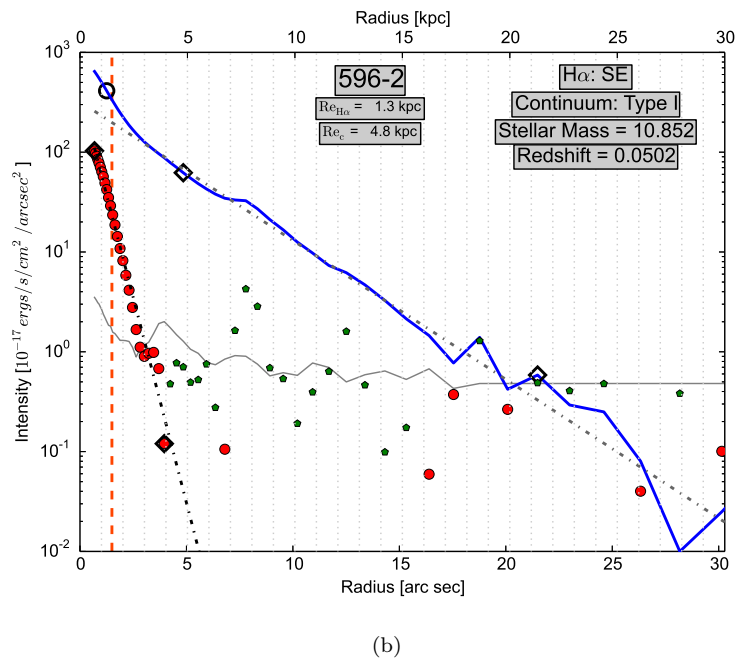
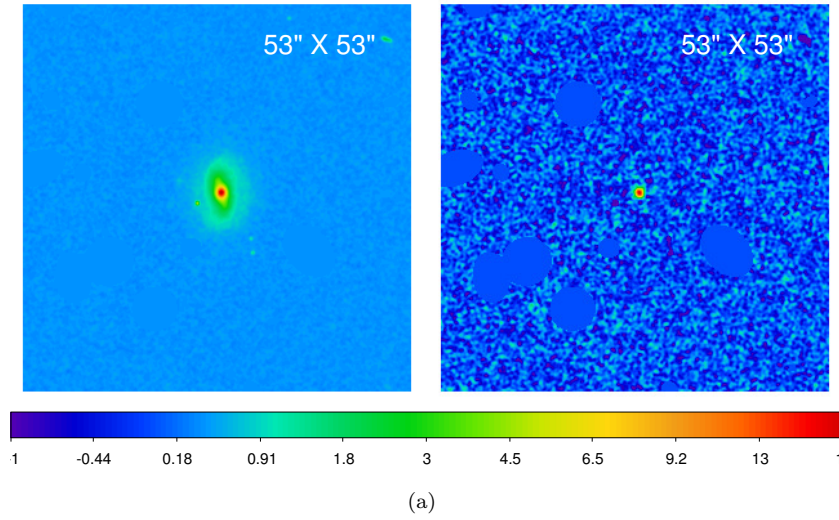


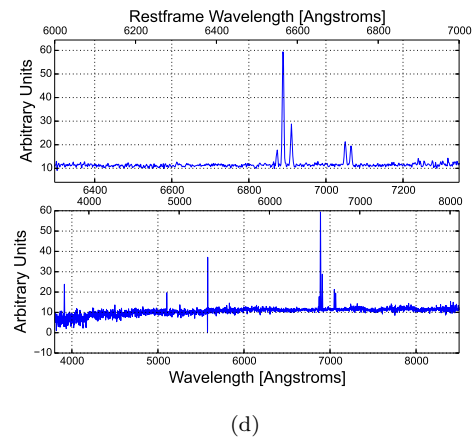
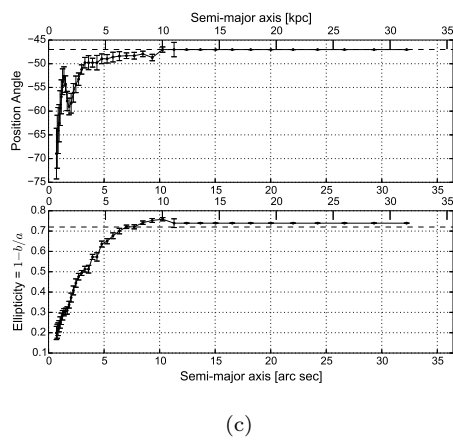
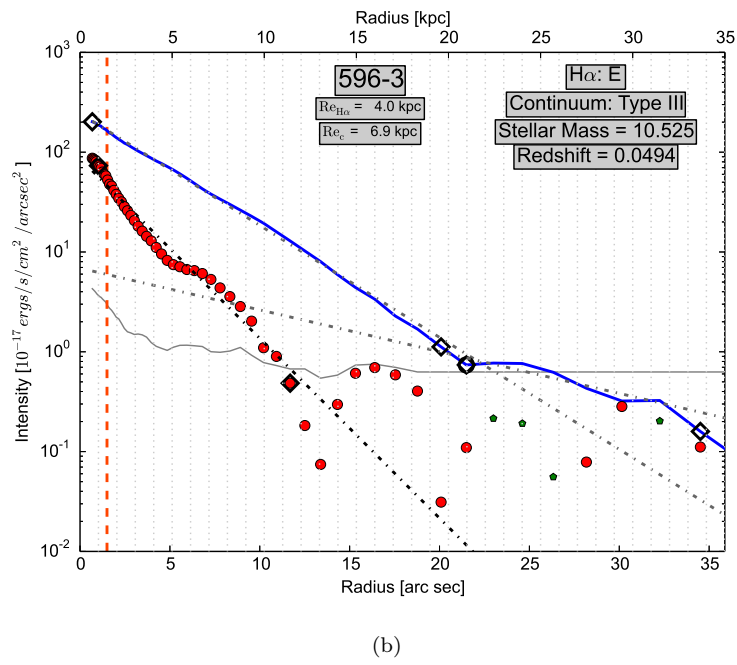
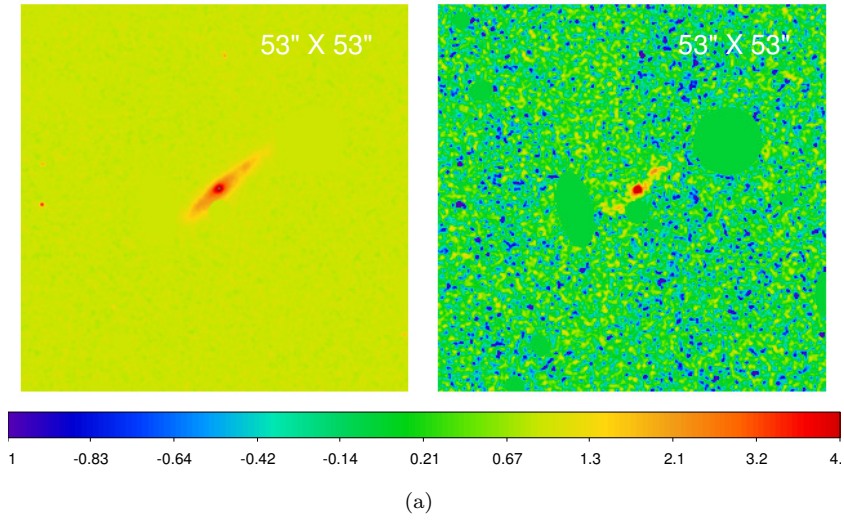
(c)

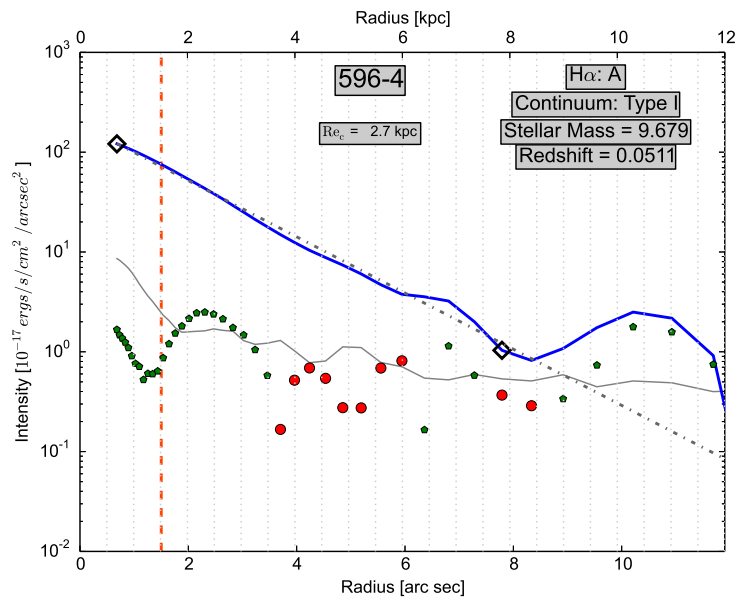
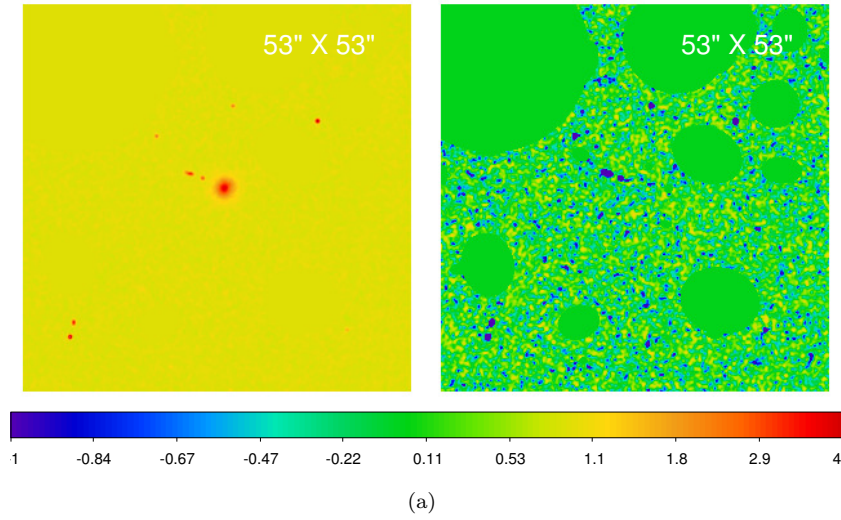


(d)

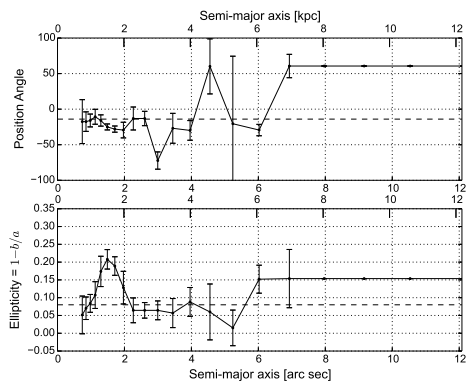




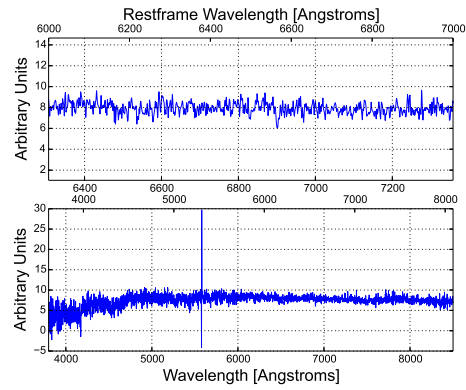




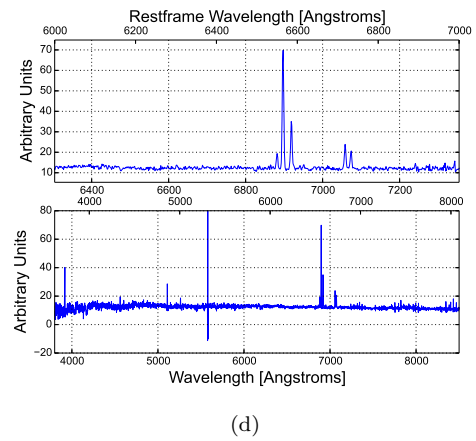
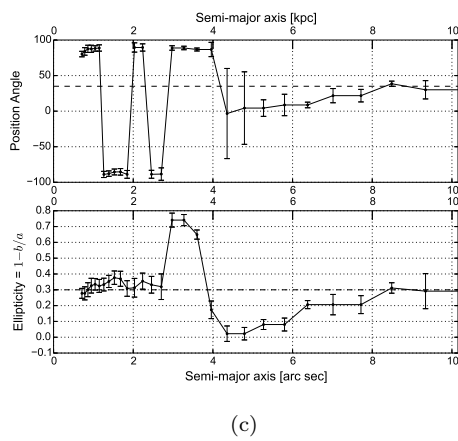
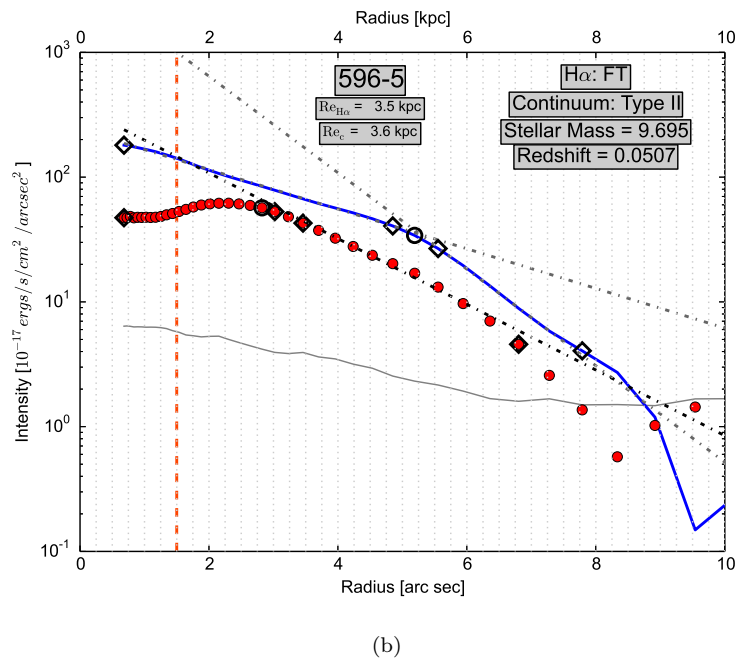
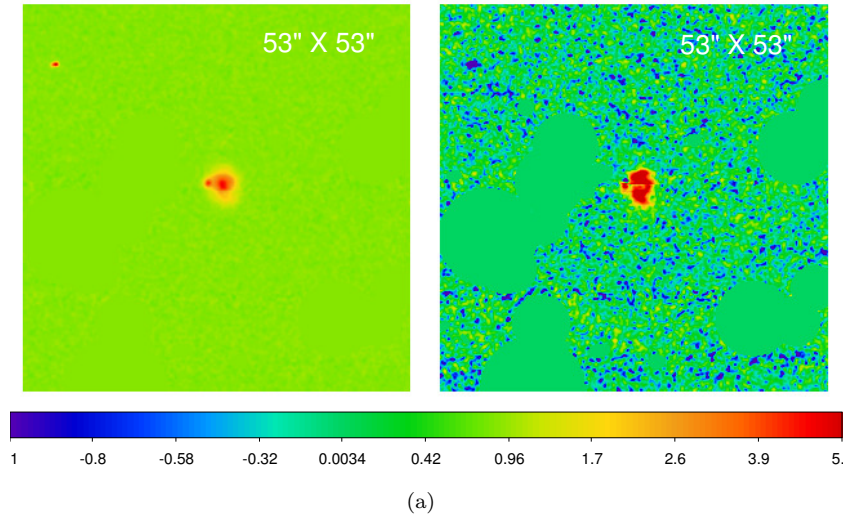
(b)

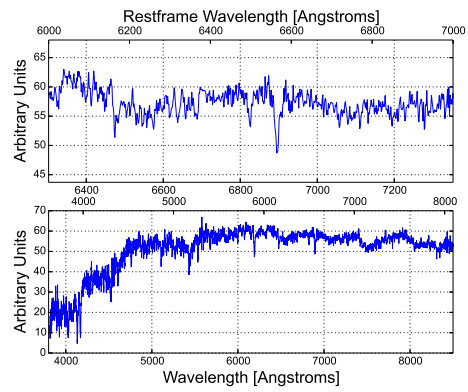
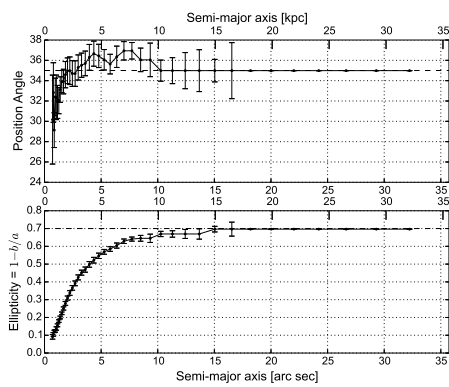
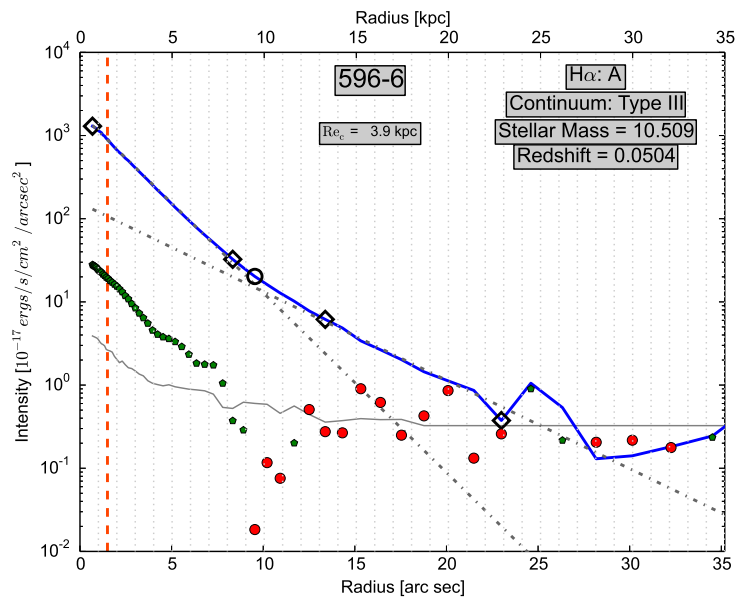
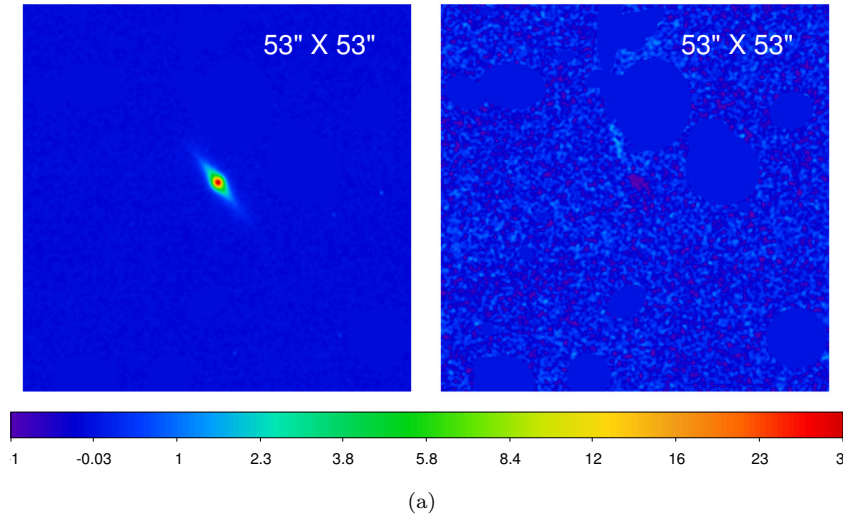


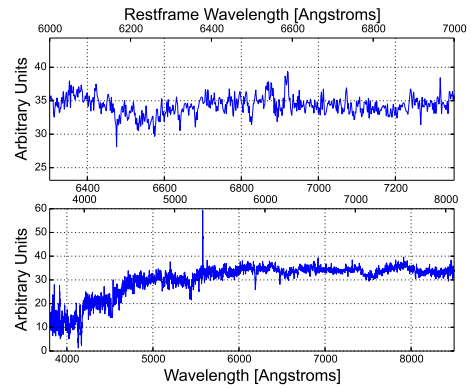
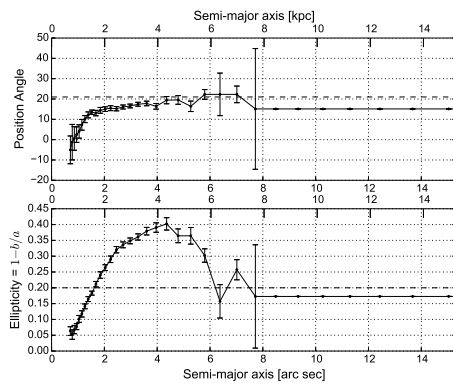
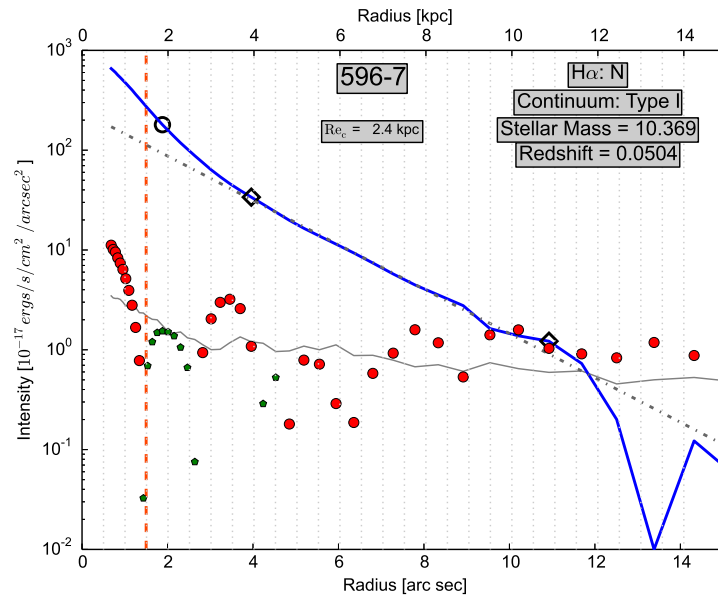
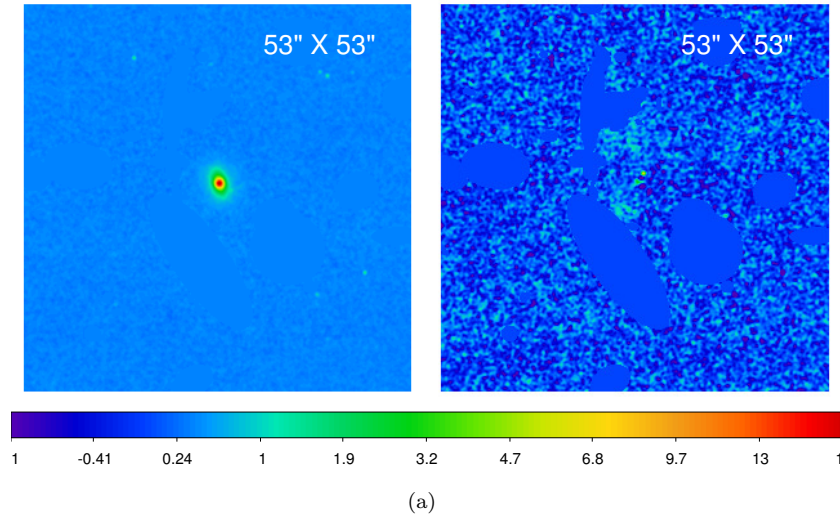
(c)

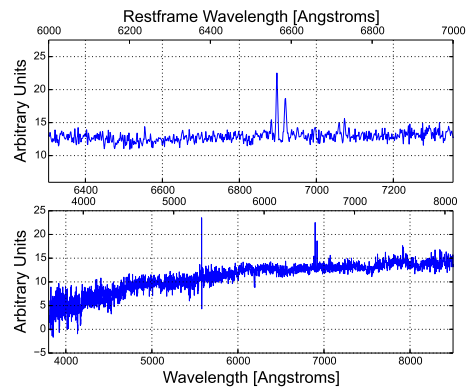
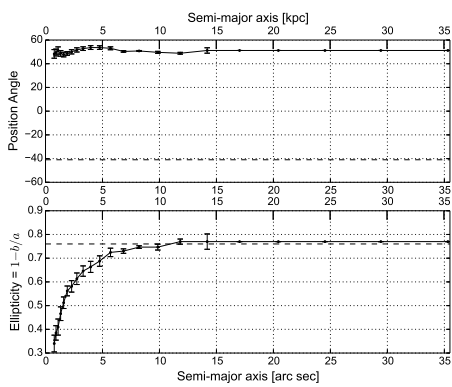
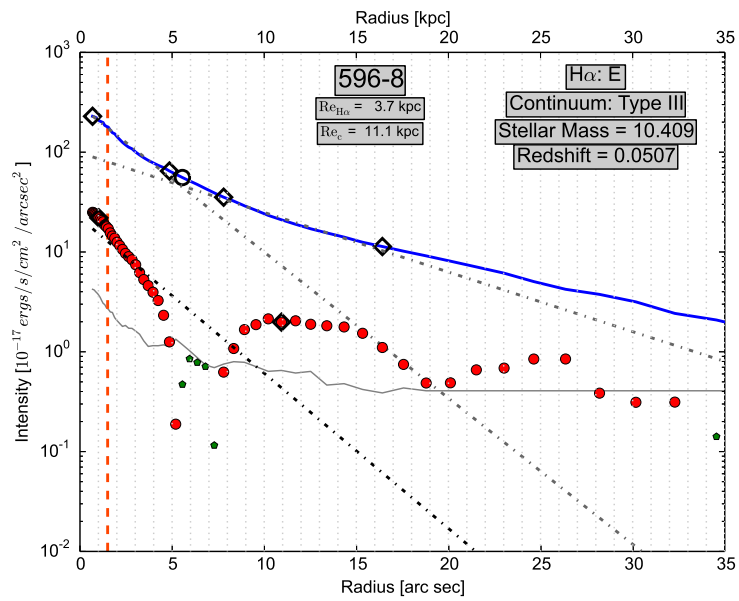
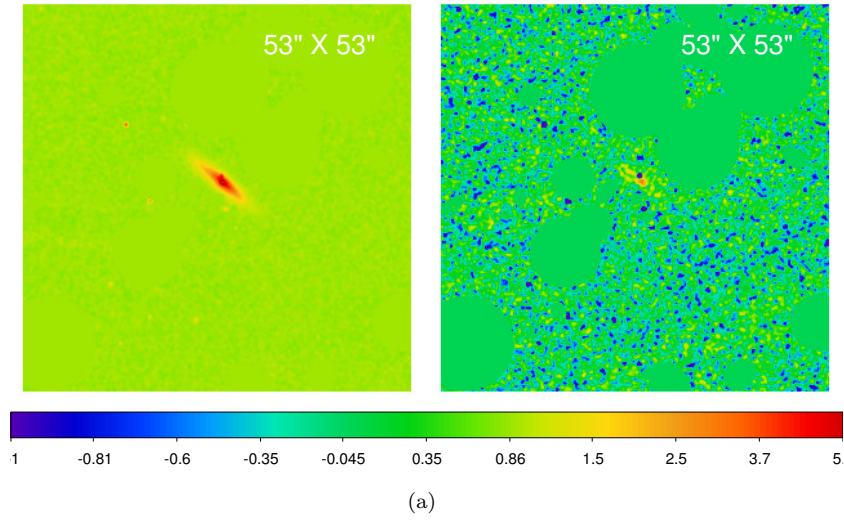


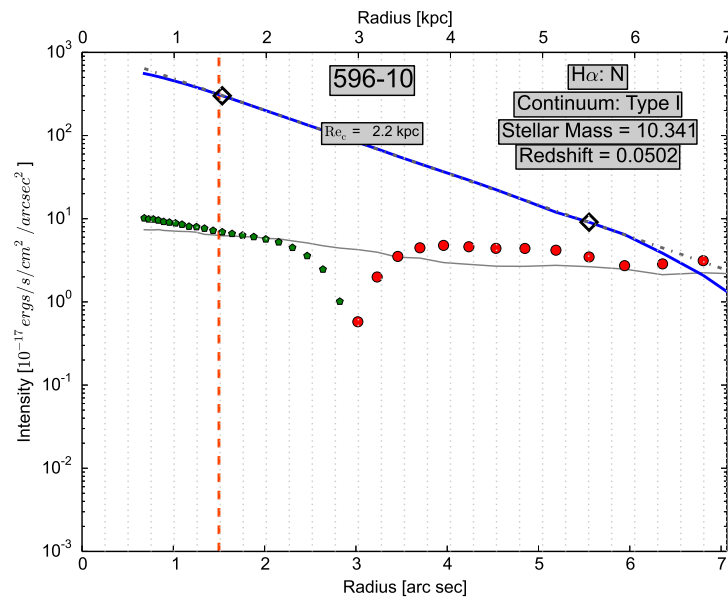
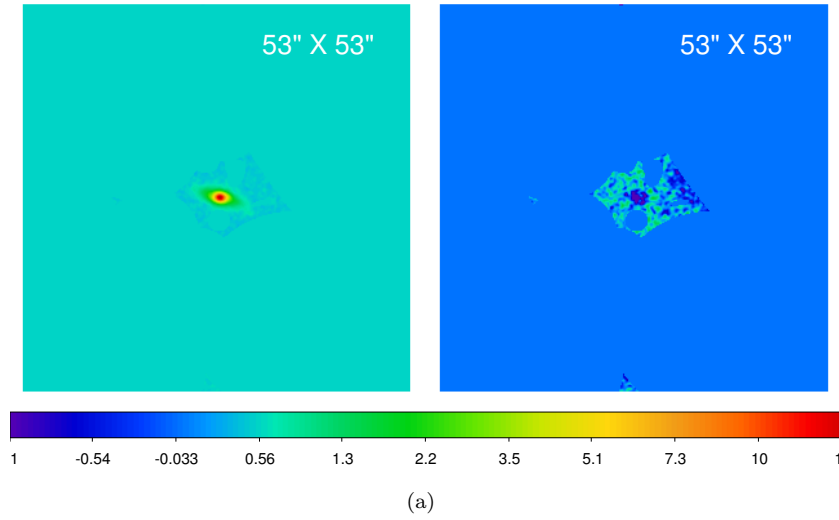
(d)



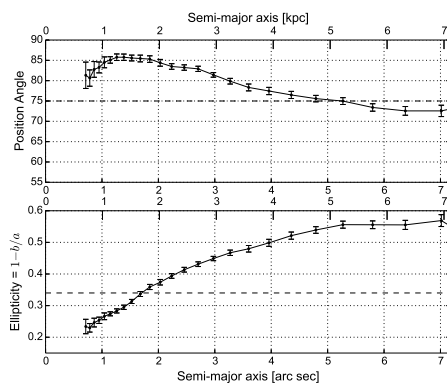




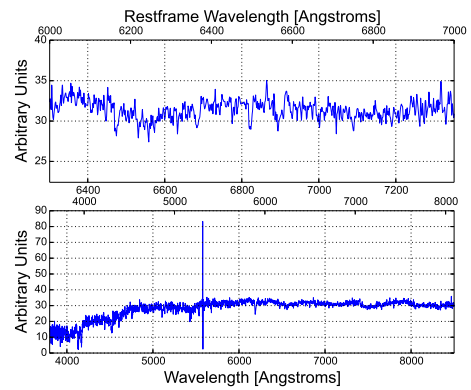




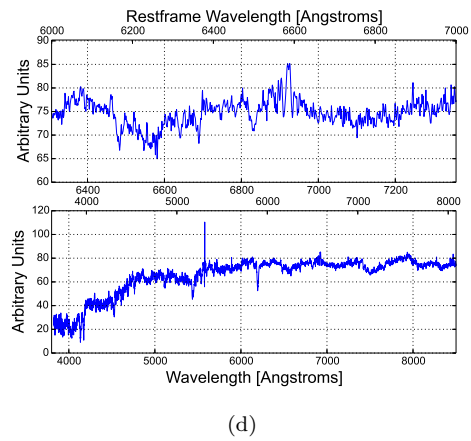
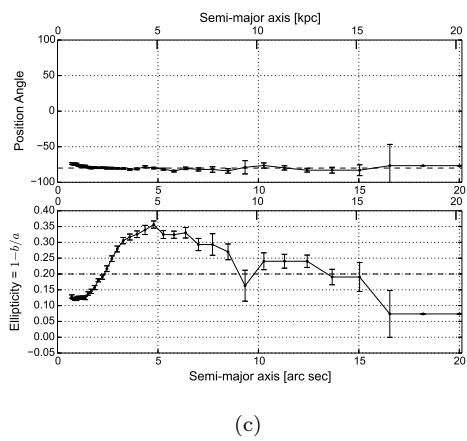
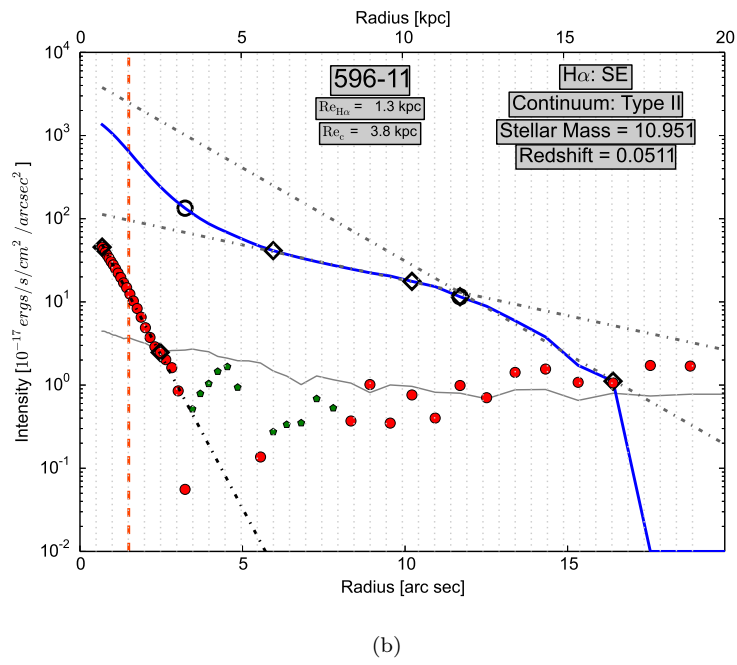
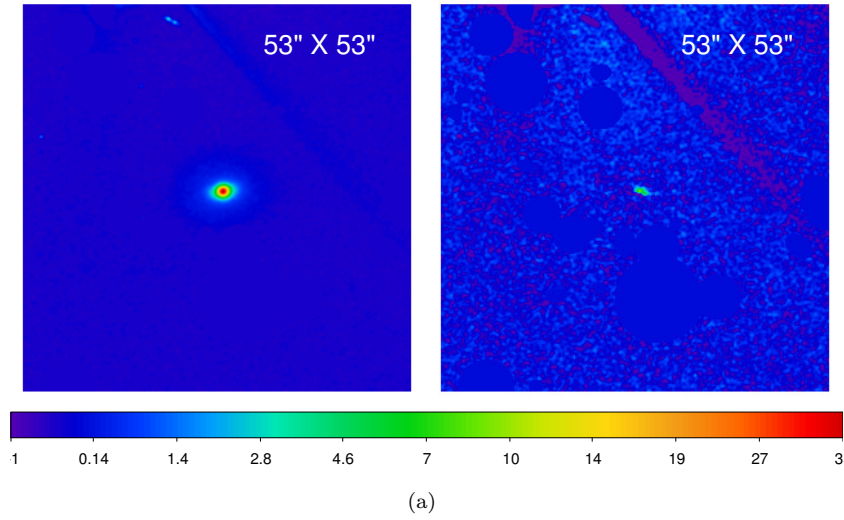
(b)

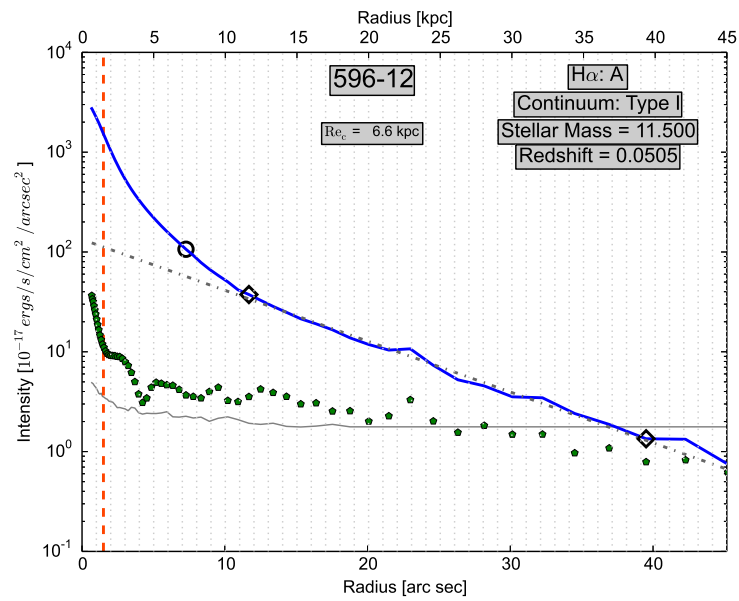
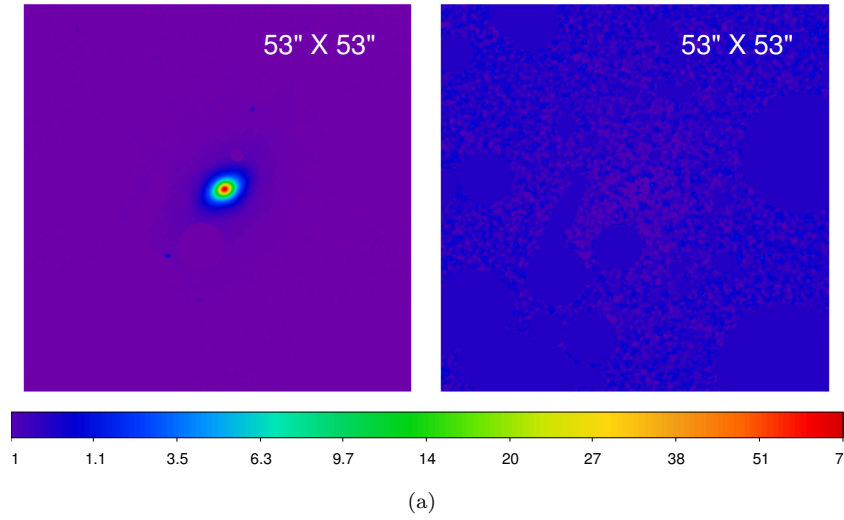


(c)

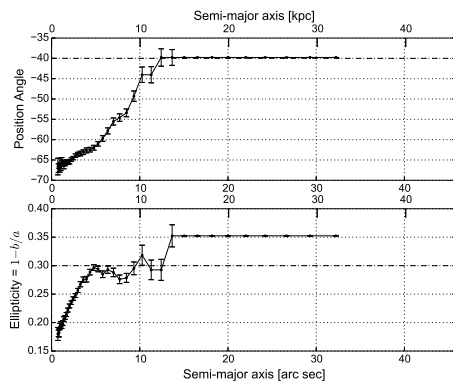


(d)

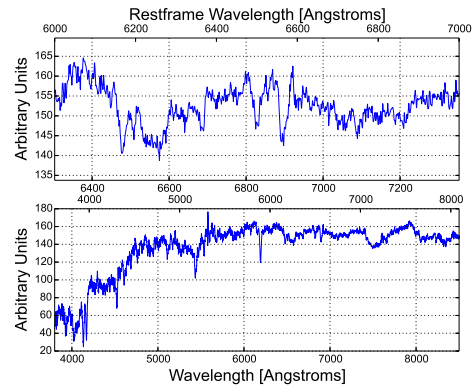




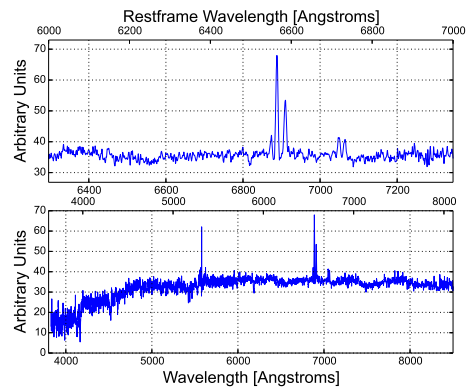
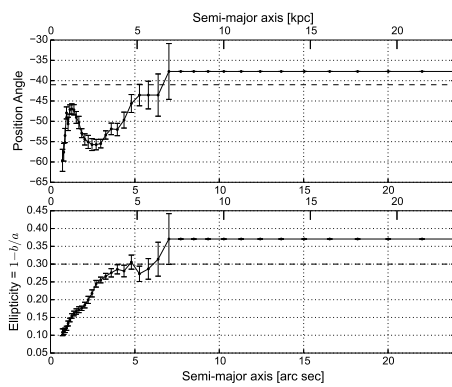
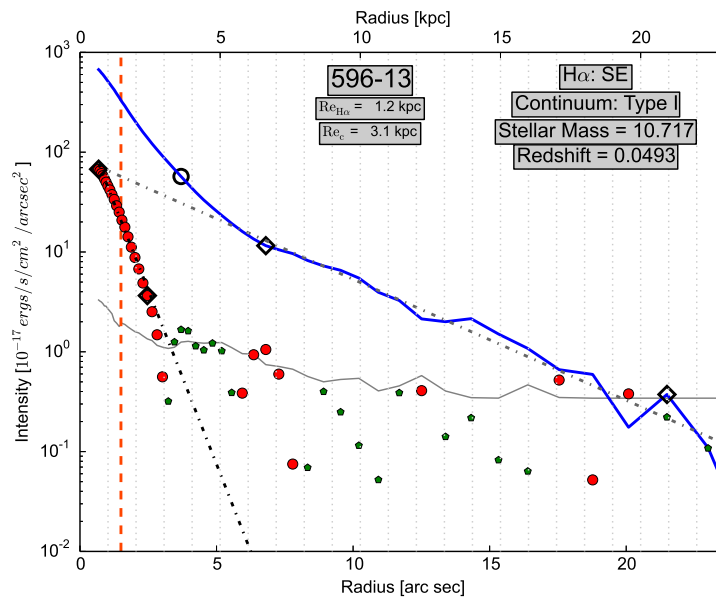
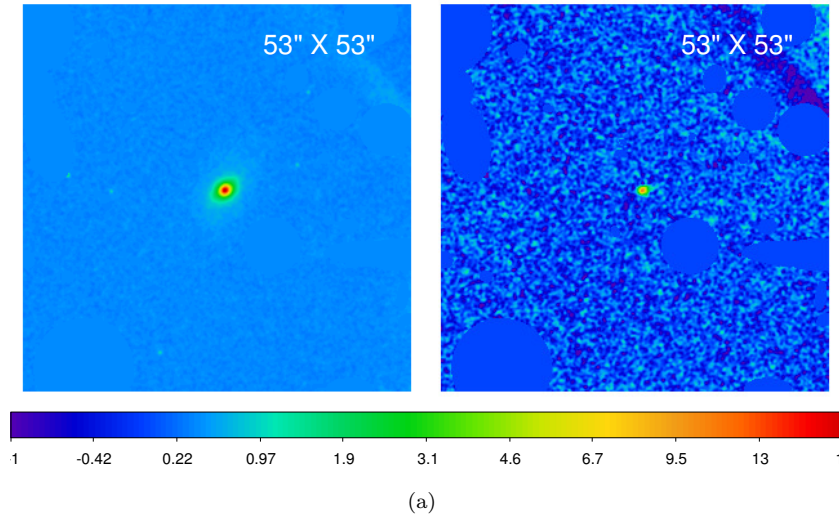
(b)

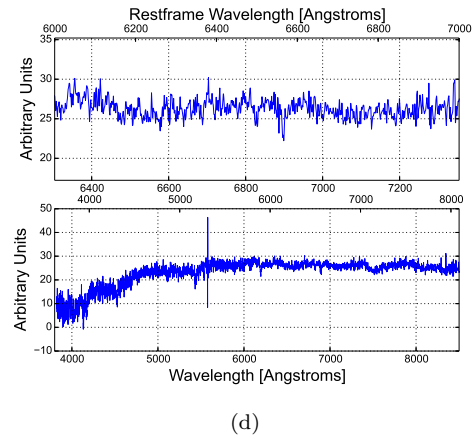
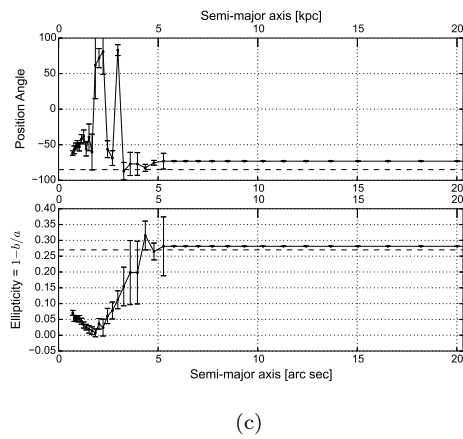
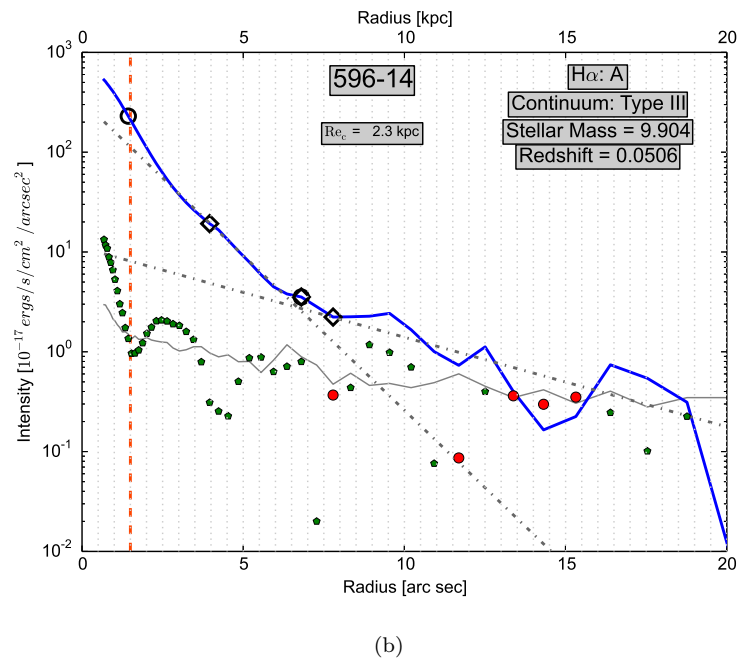
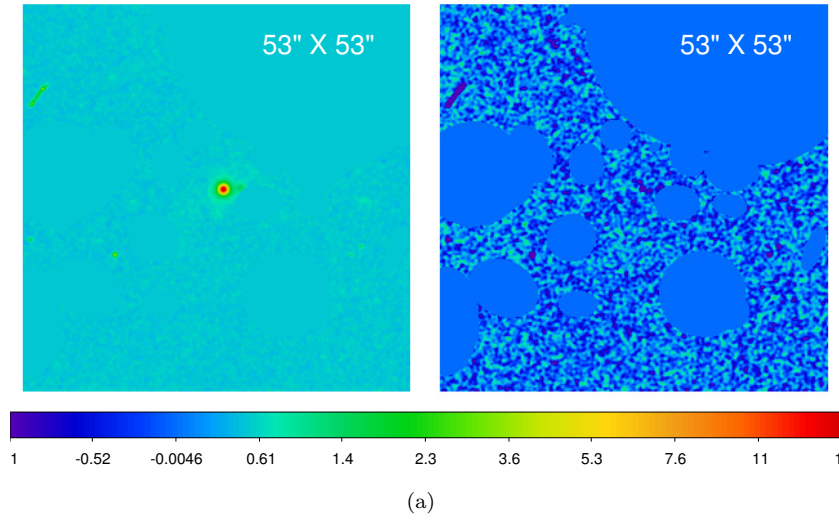


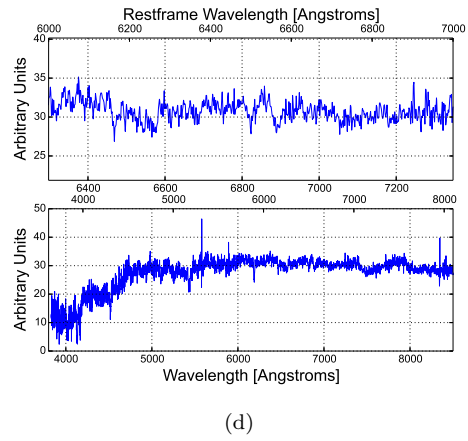
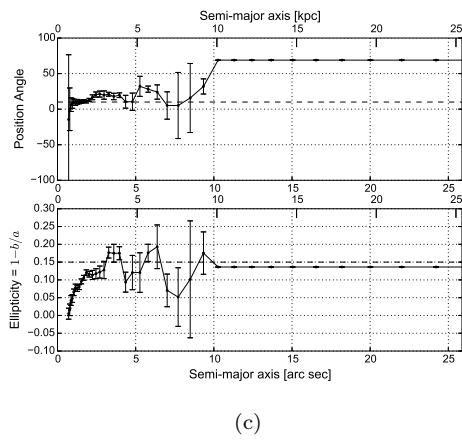
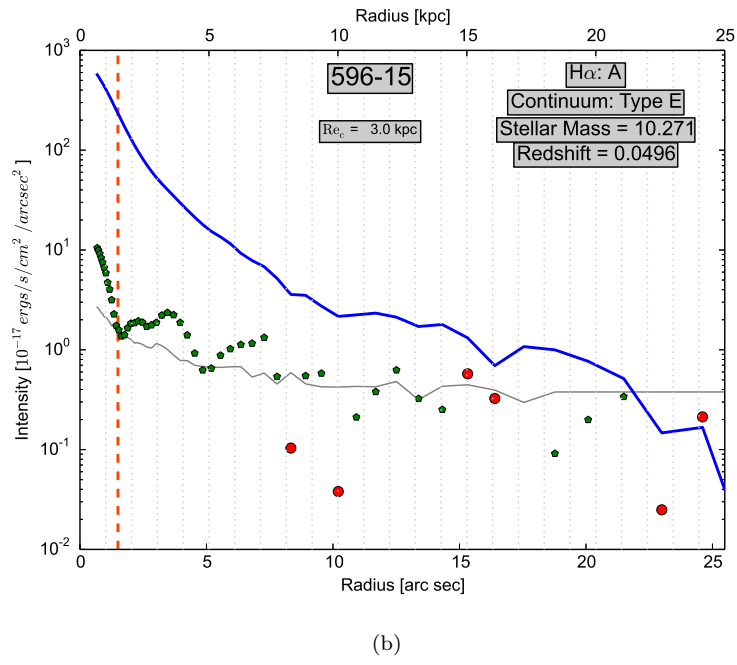
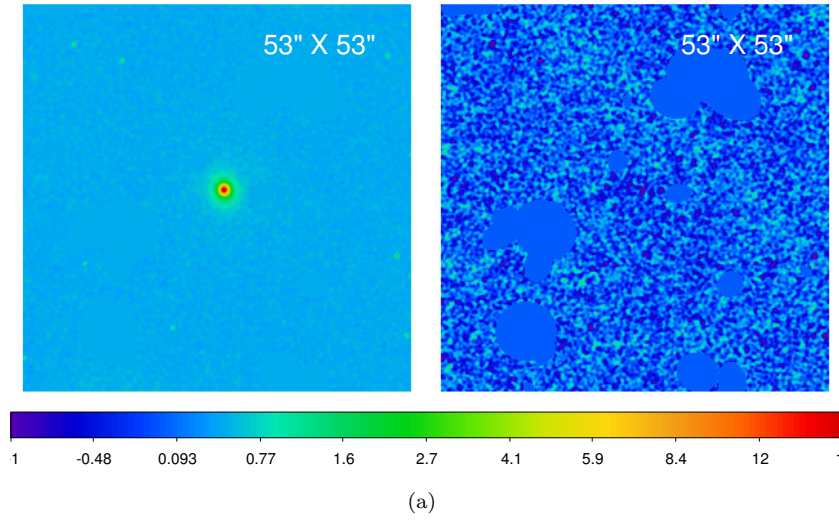
(c)

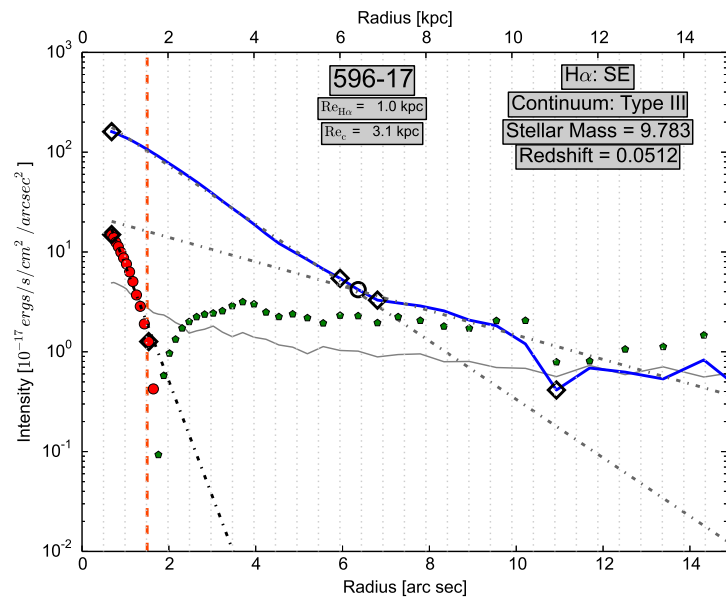
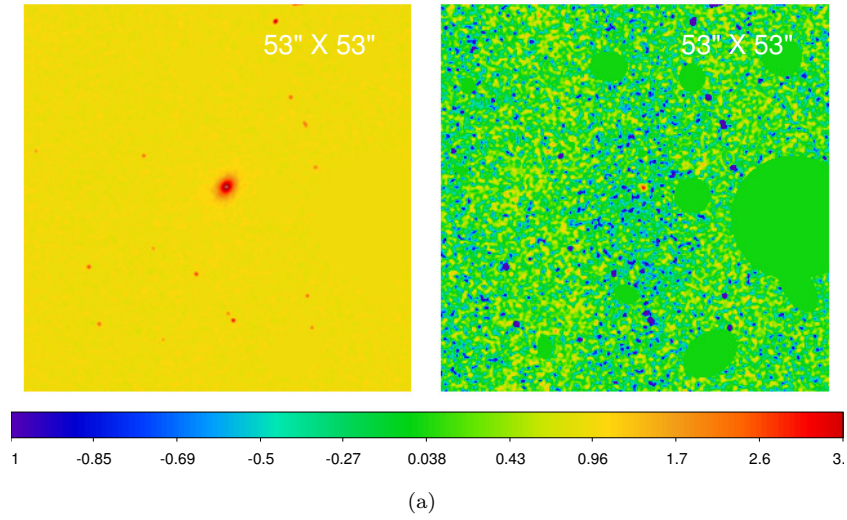


(d)

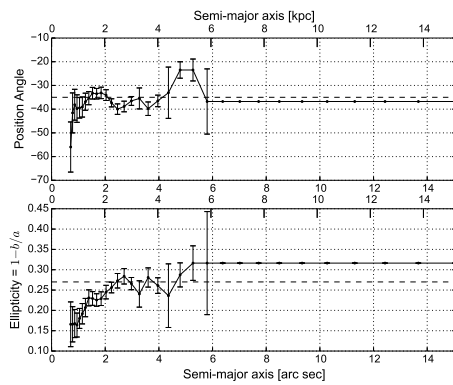




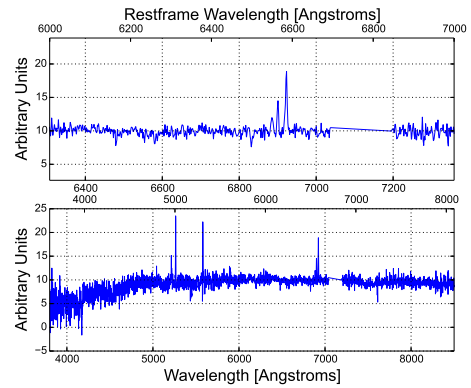




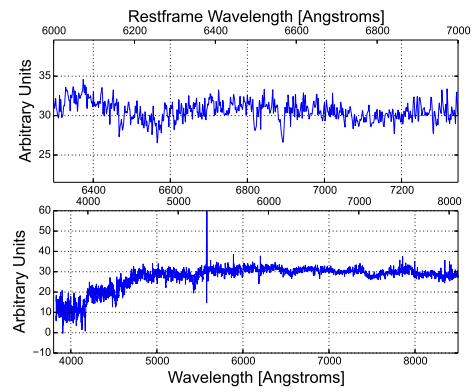
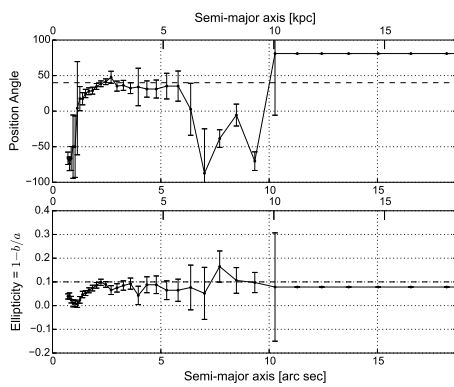
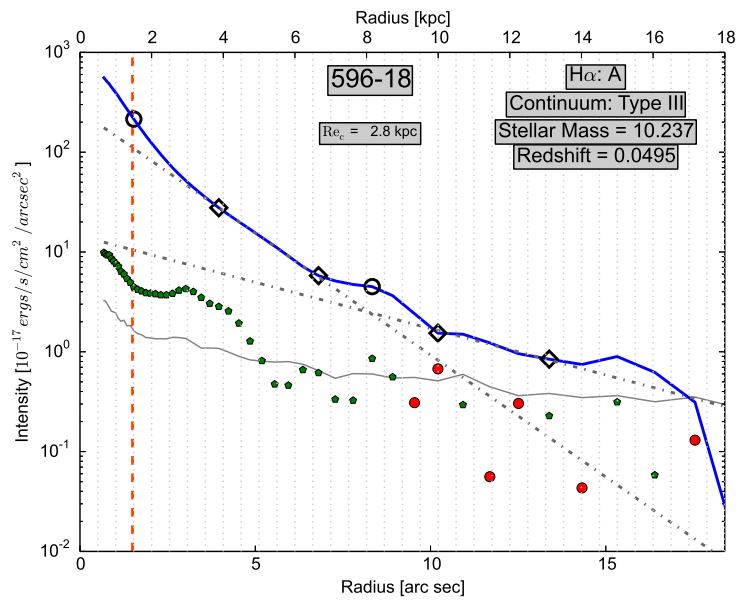
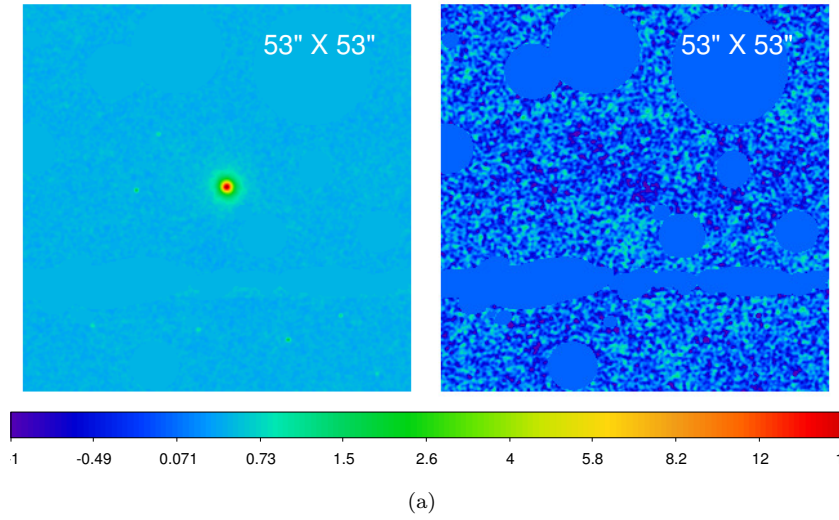
(b)

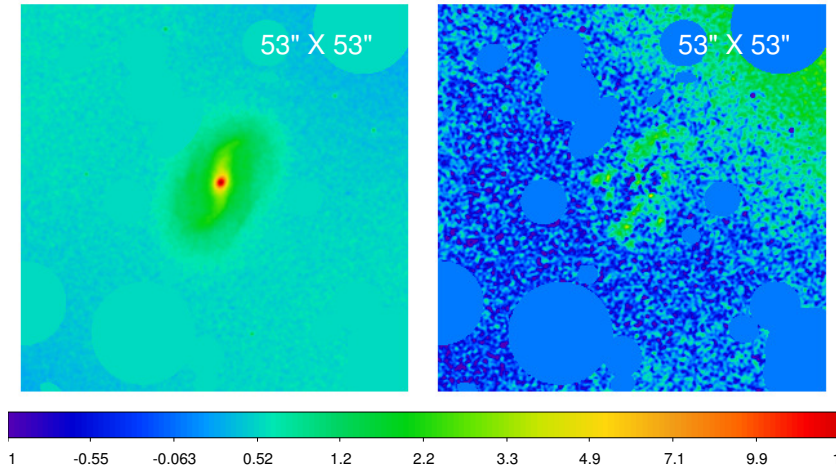


(c)

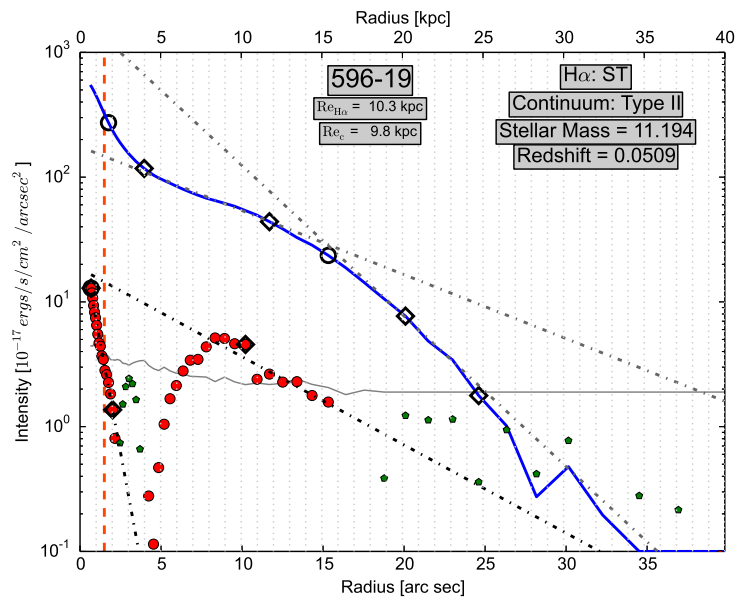


(d)

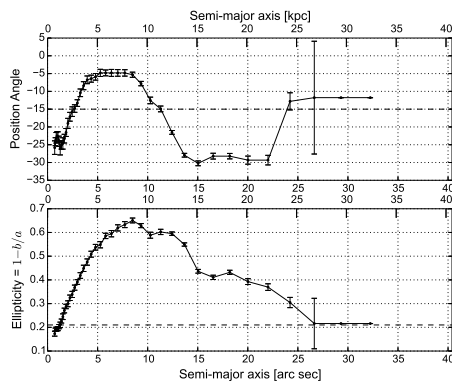




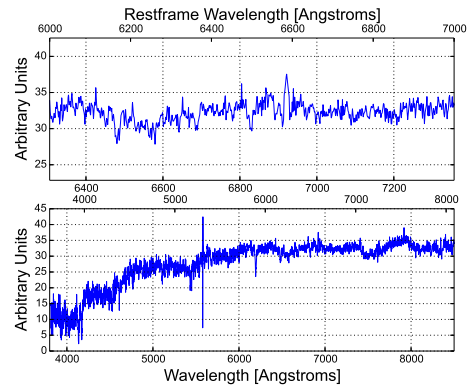
(a)



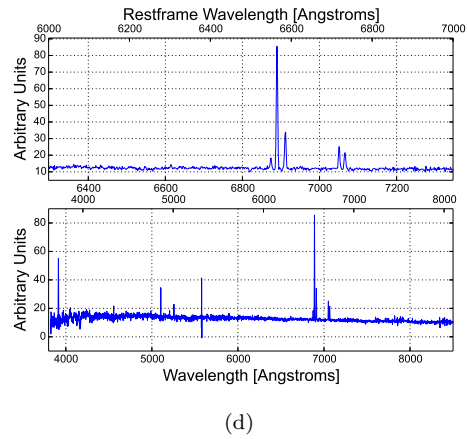
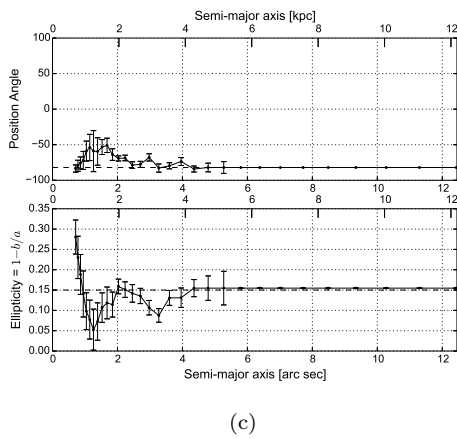
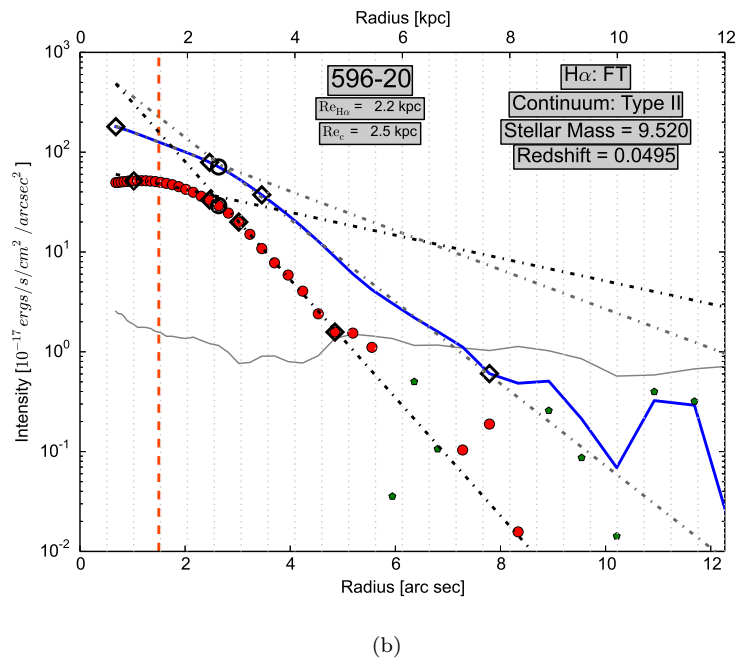
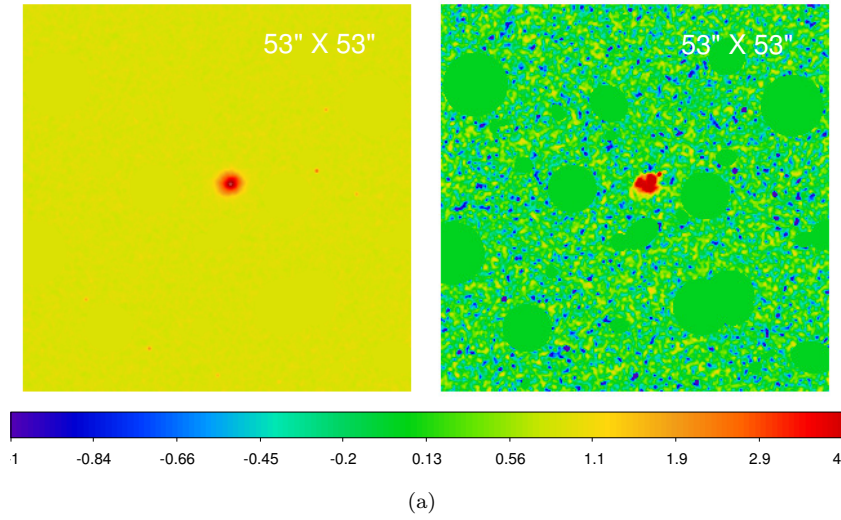
(b)

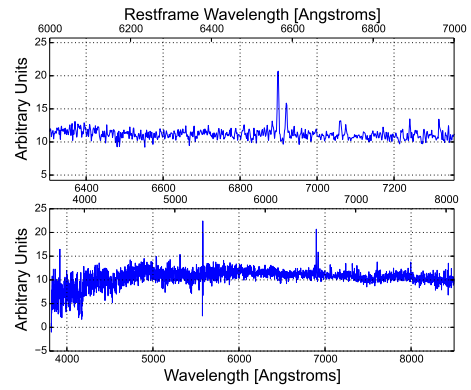
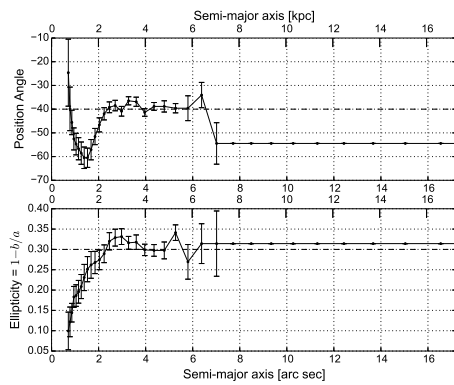
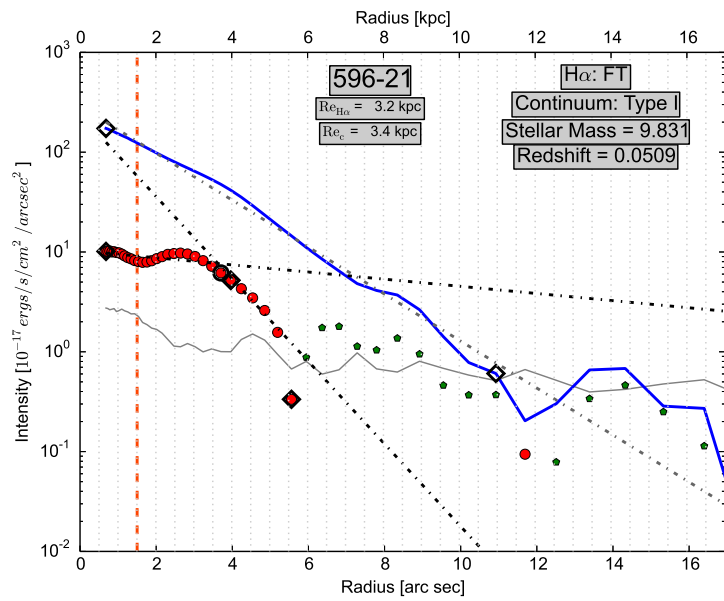
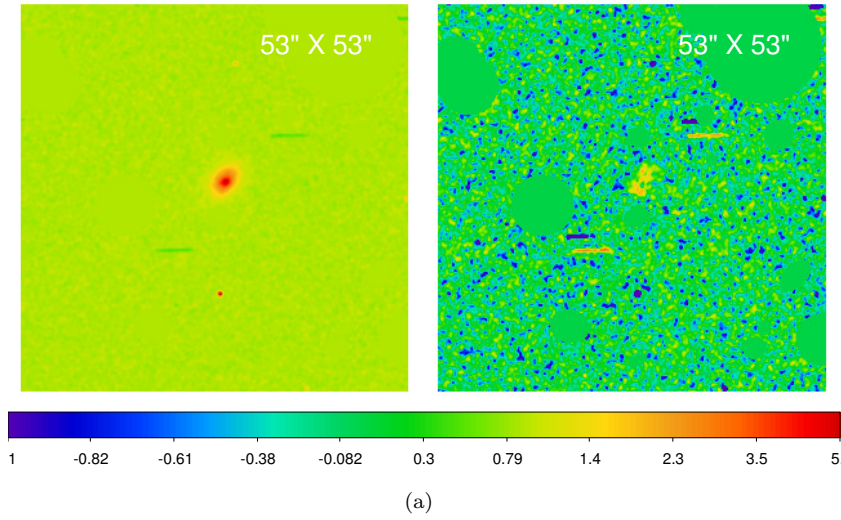


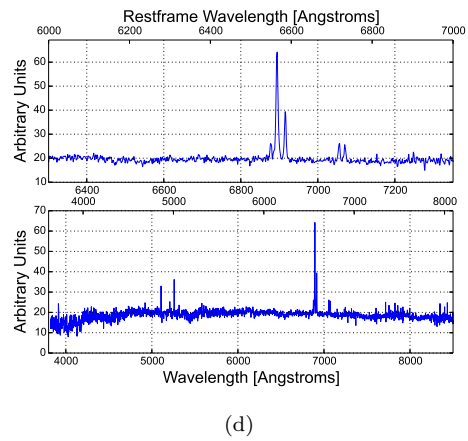
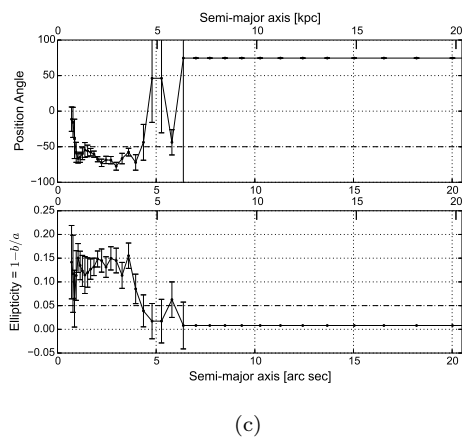
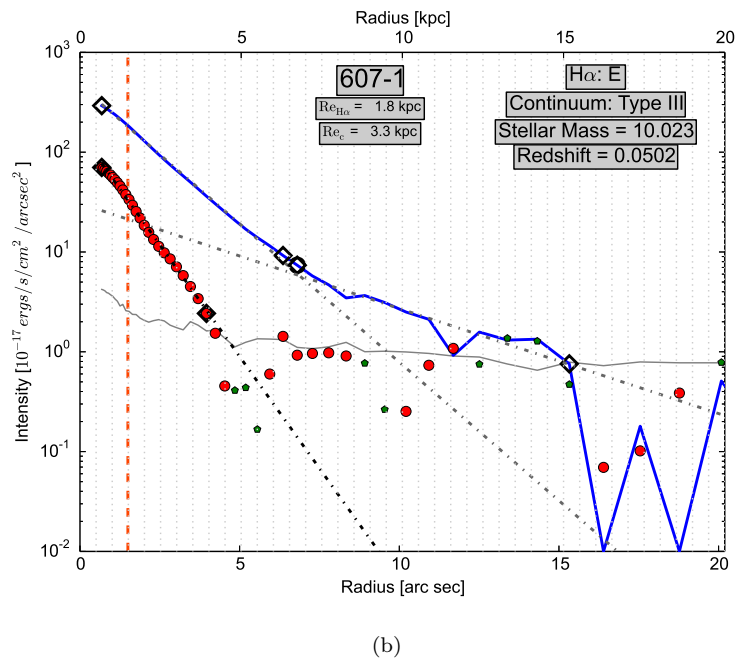
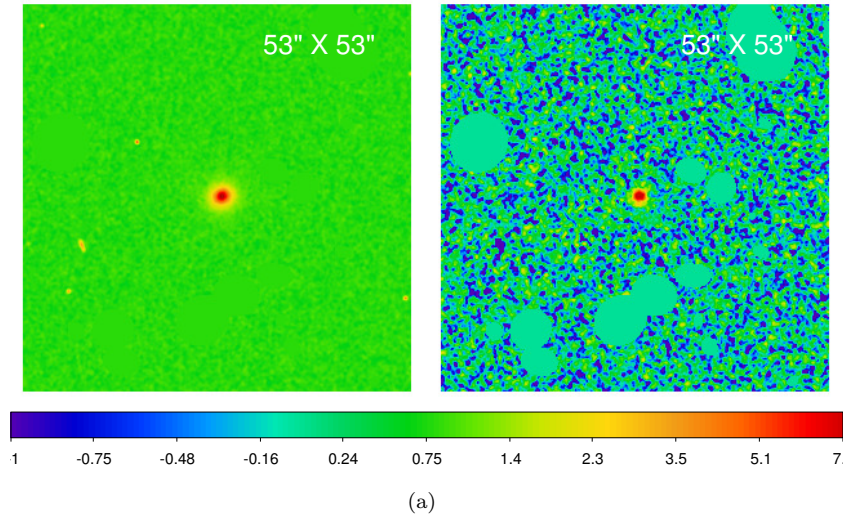
(c)

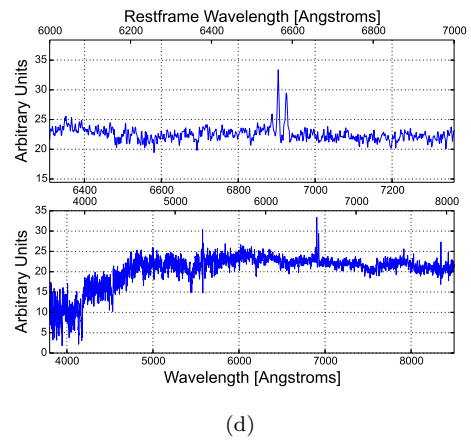
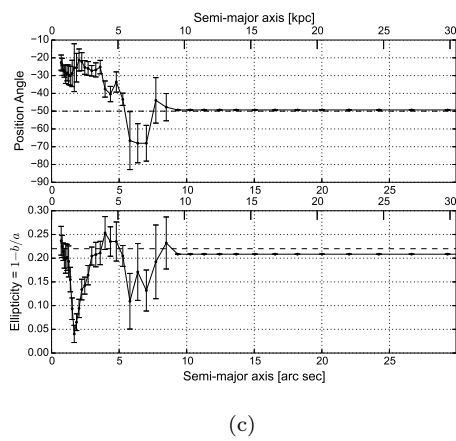
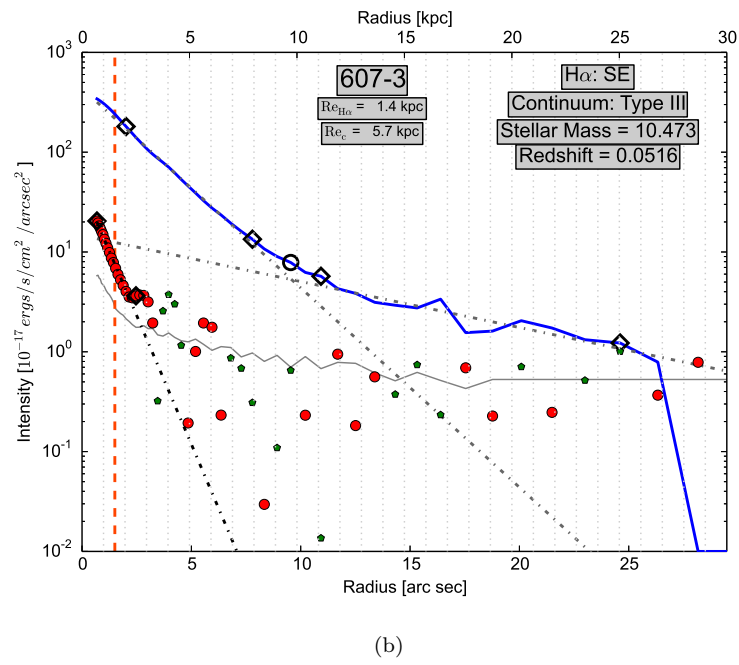
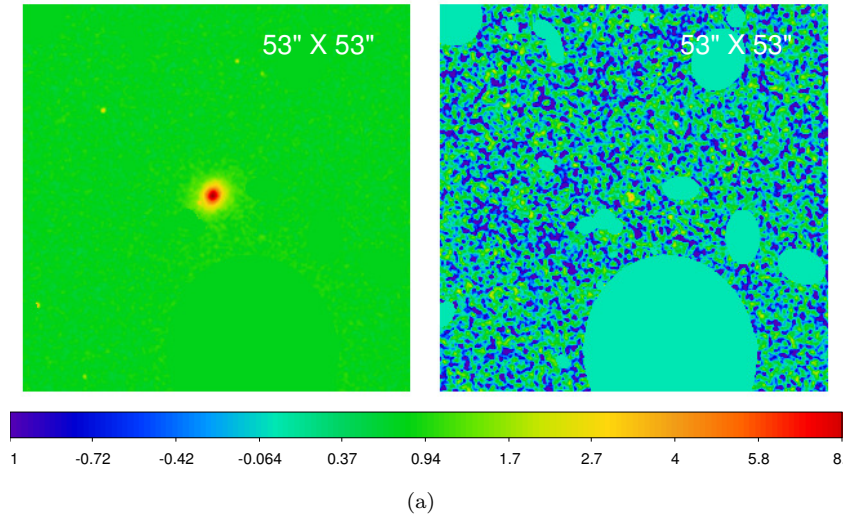


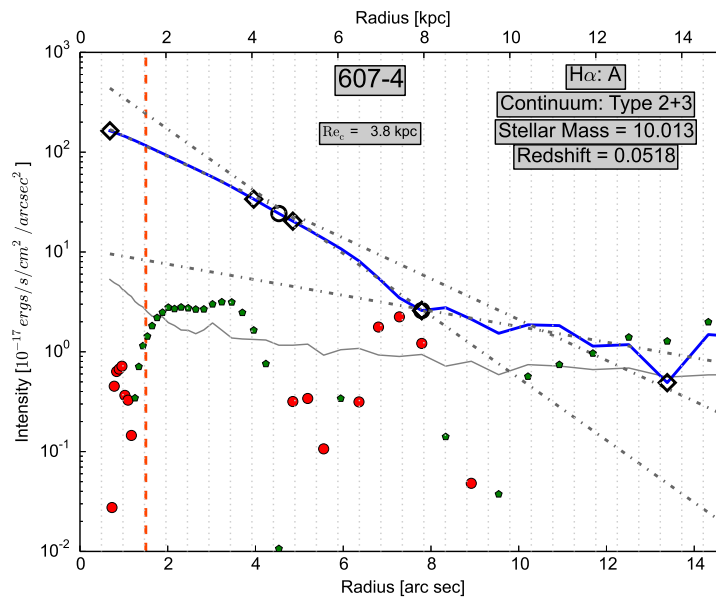
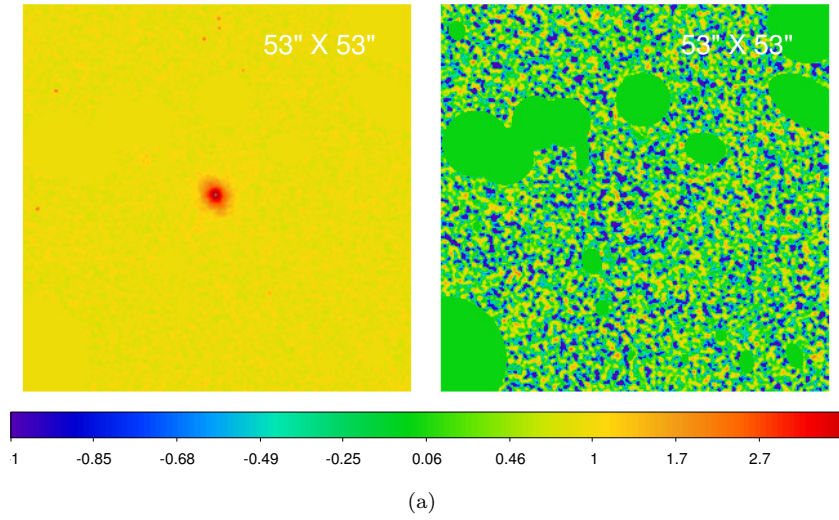
(d)



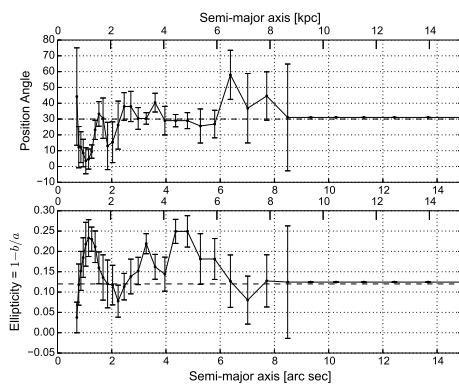




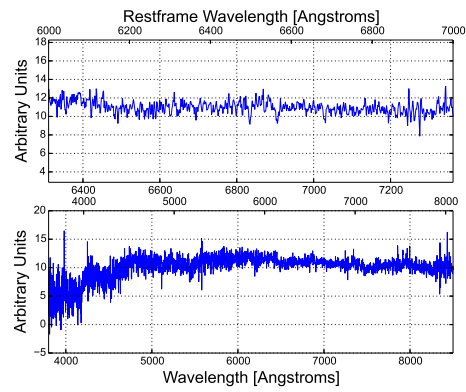




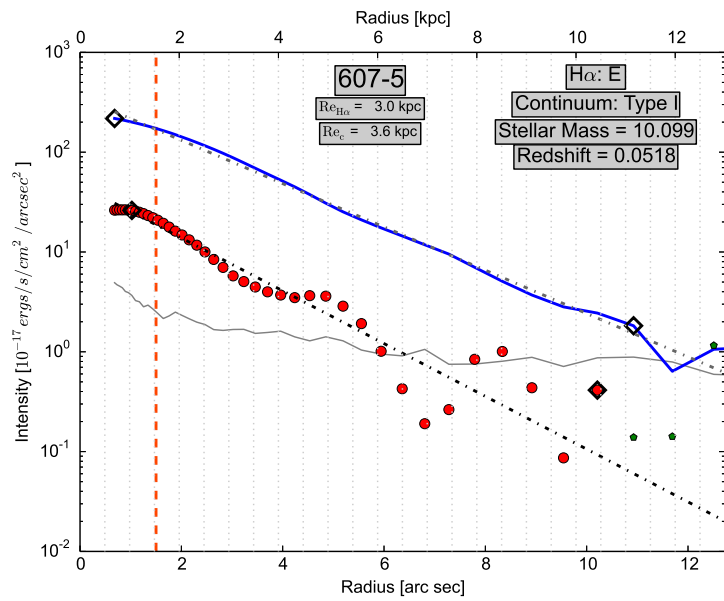
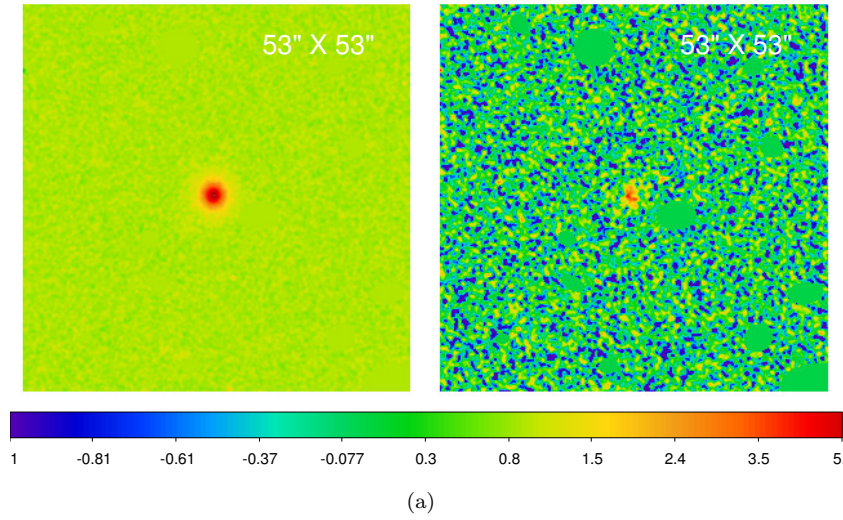
(b)



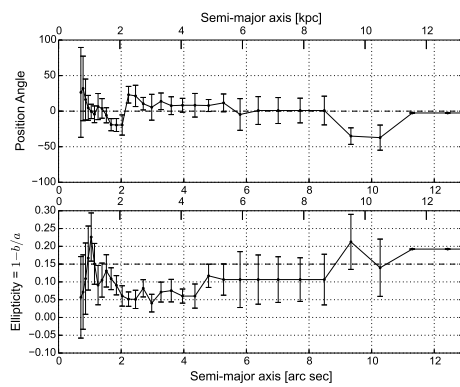
(c)



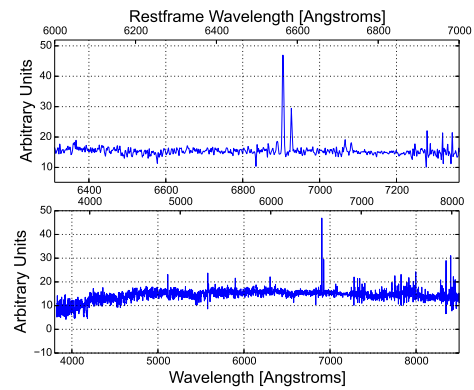
(d)



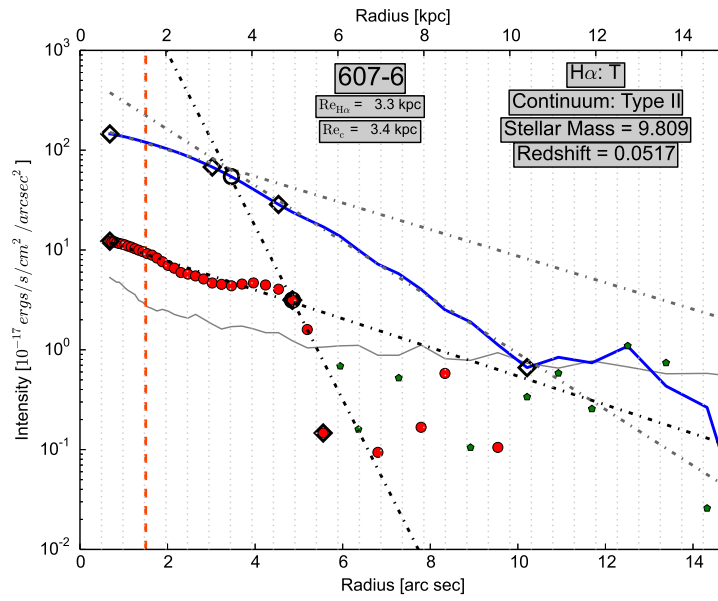
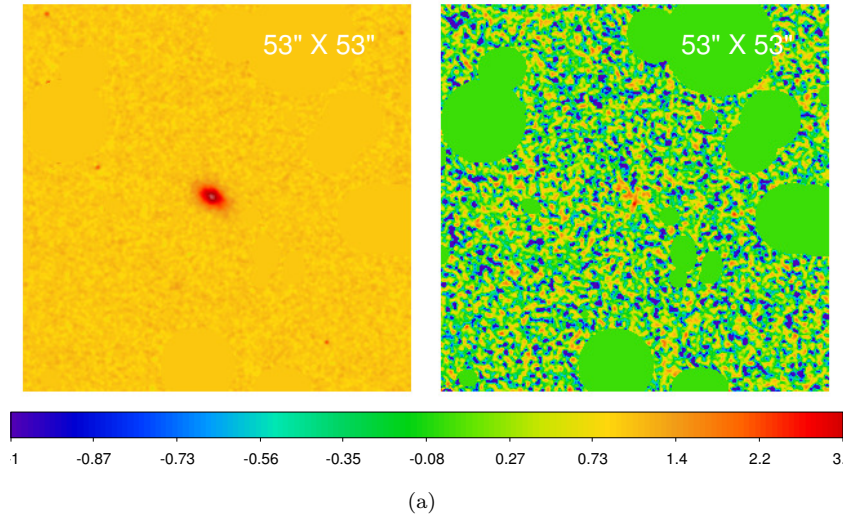
(b)



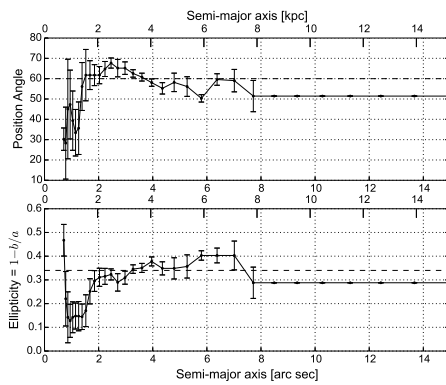
(c)



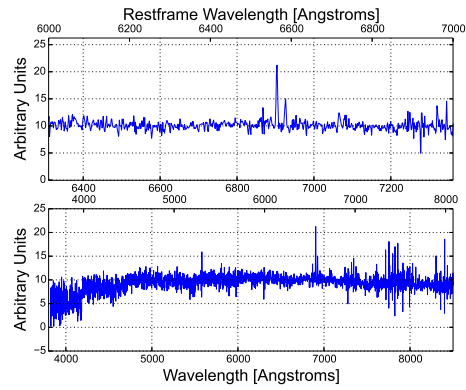
(d)



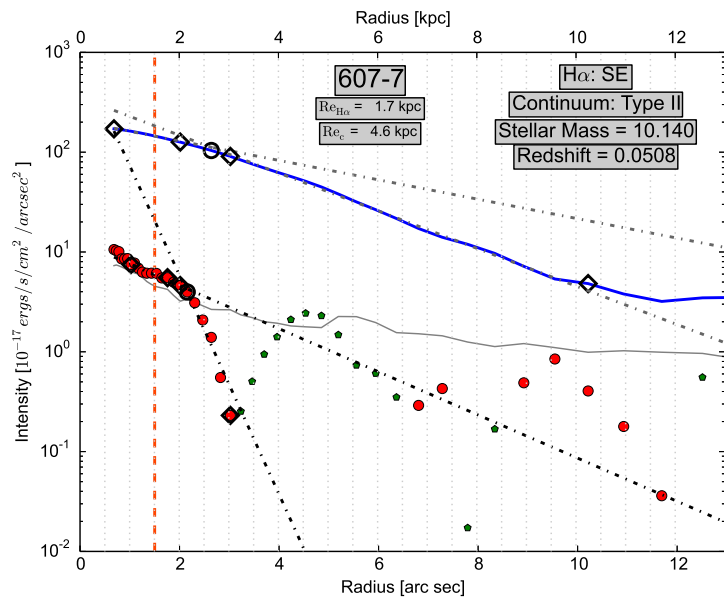
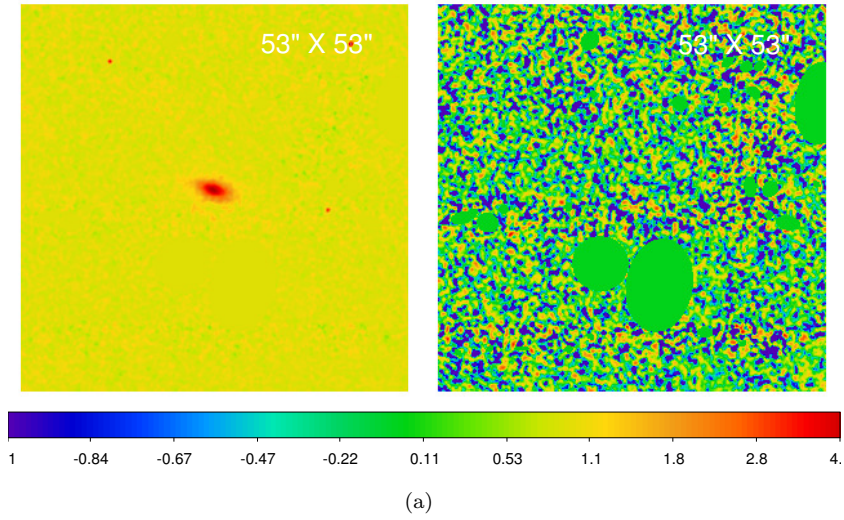
(b)



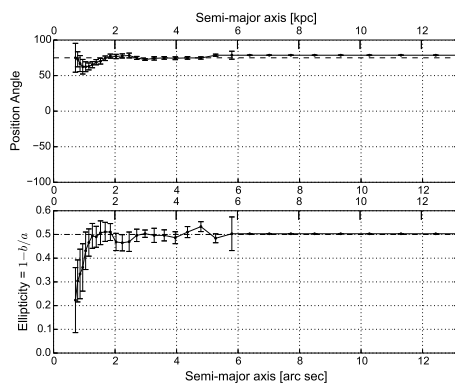
(c)



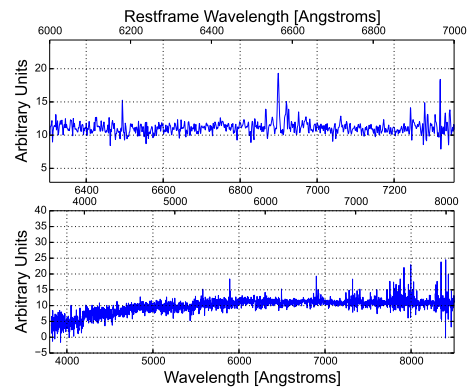
(d)



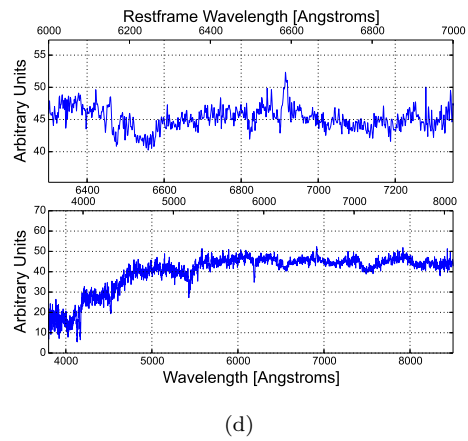
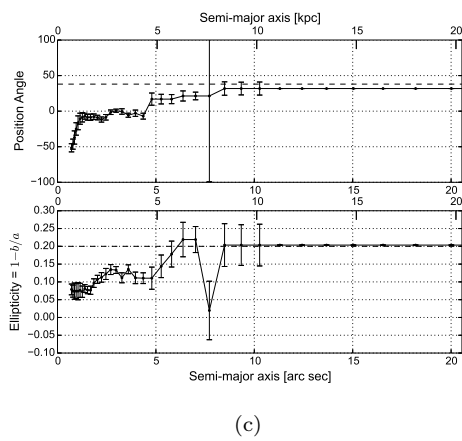
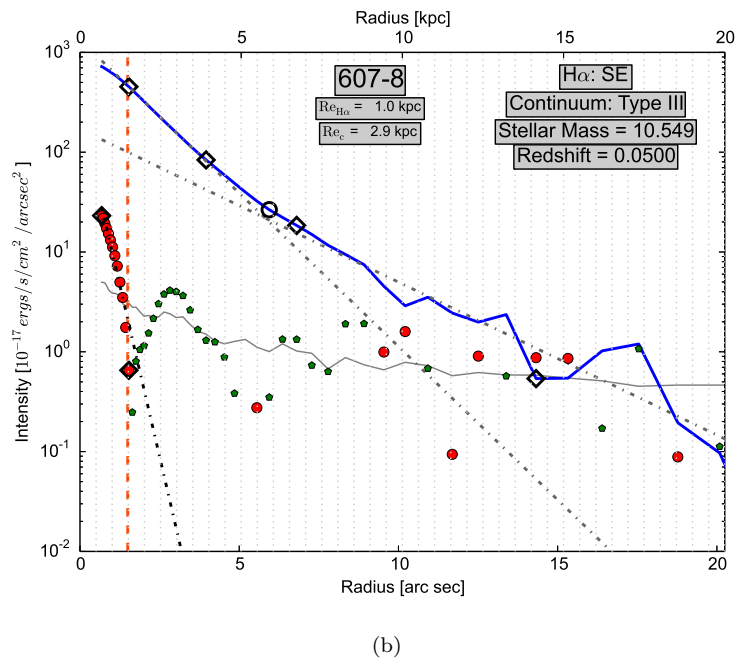
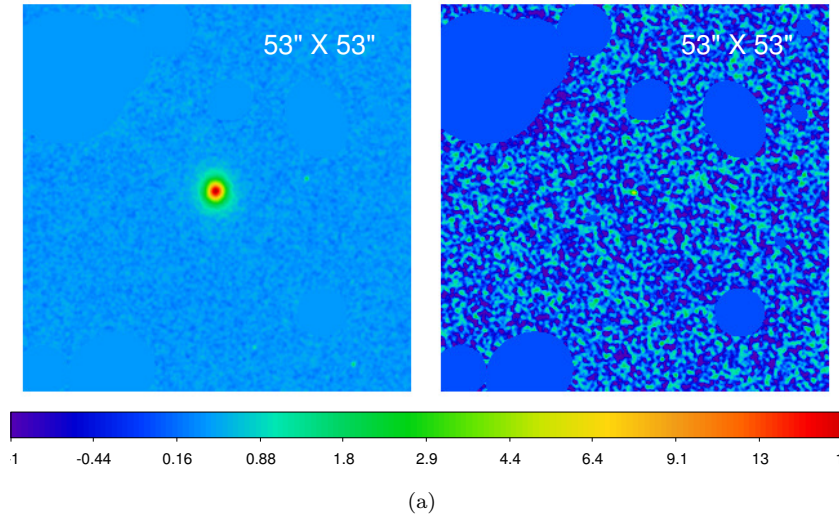
(b)

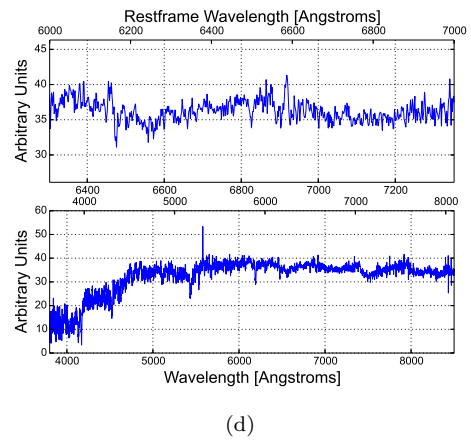
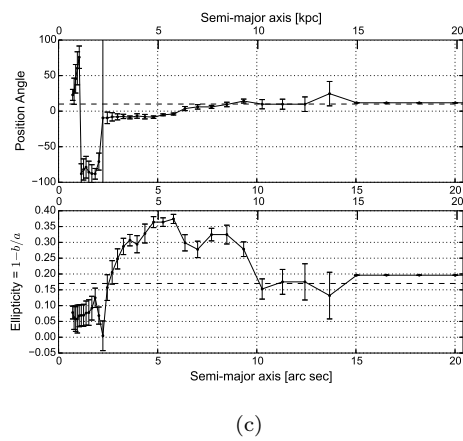
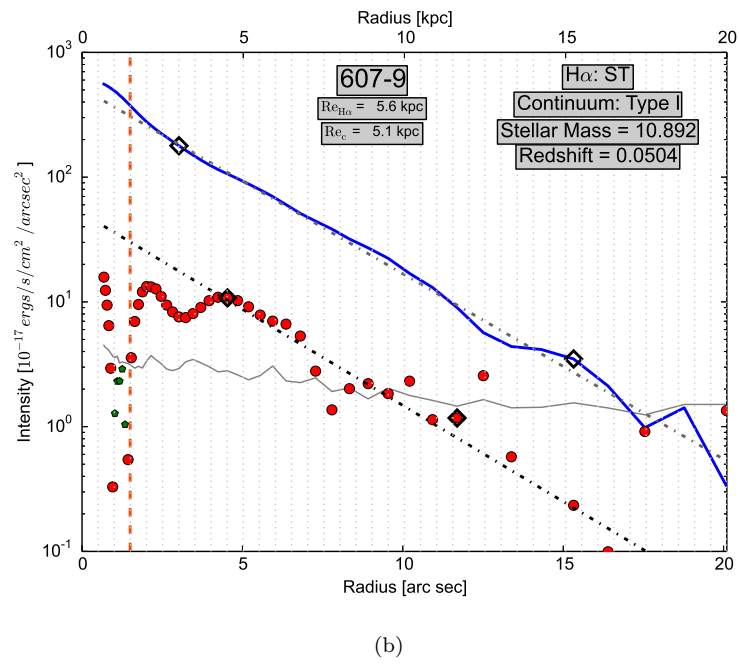
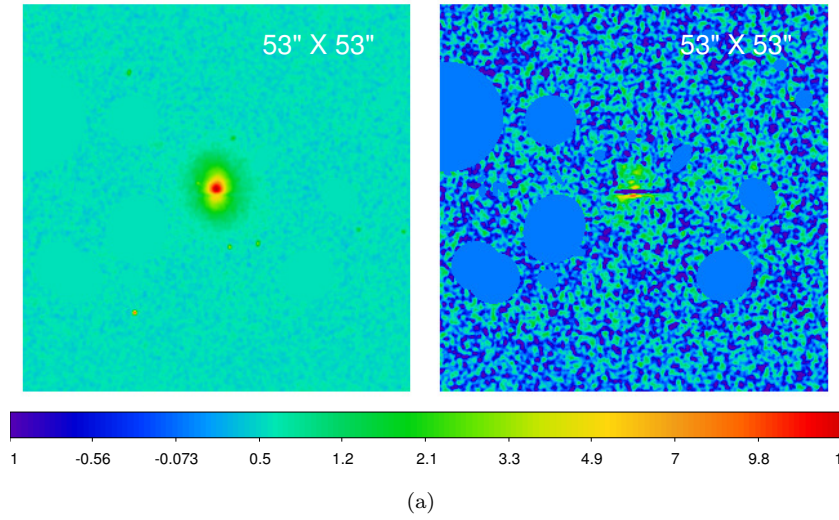


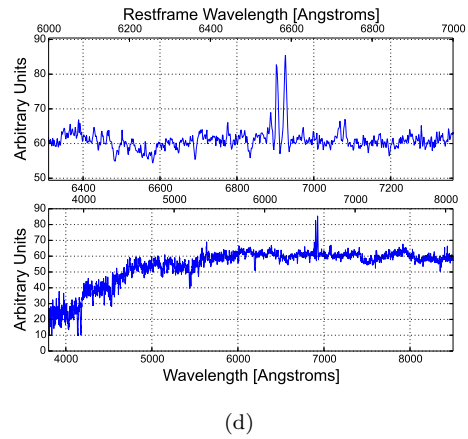
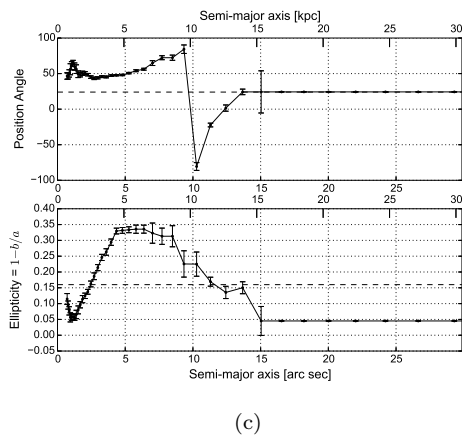
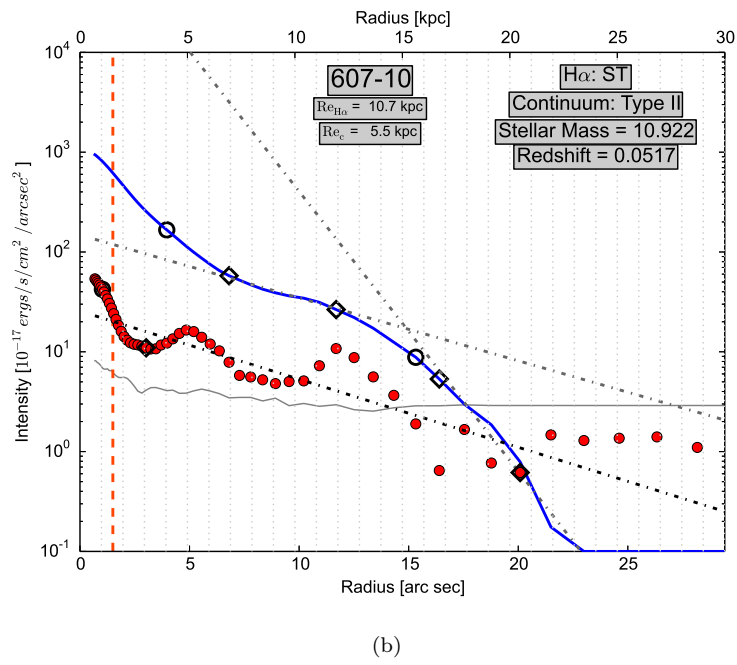
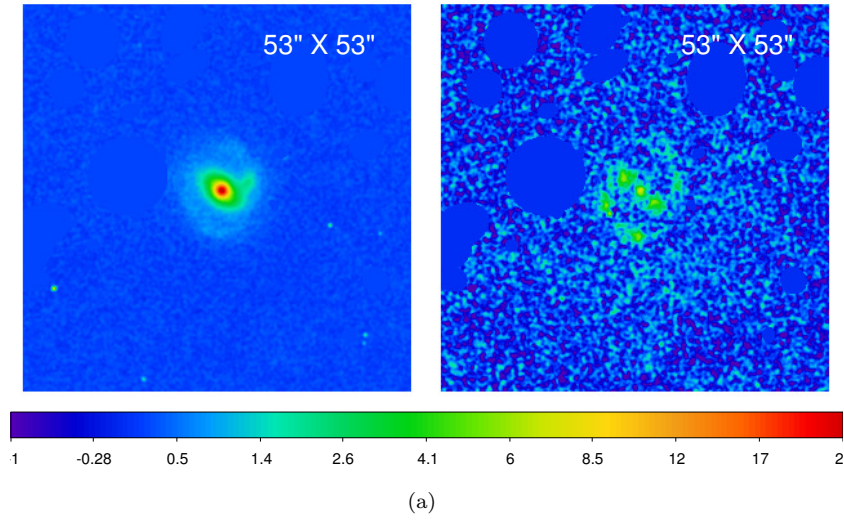
(c)

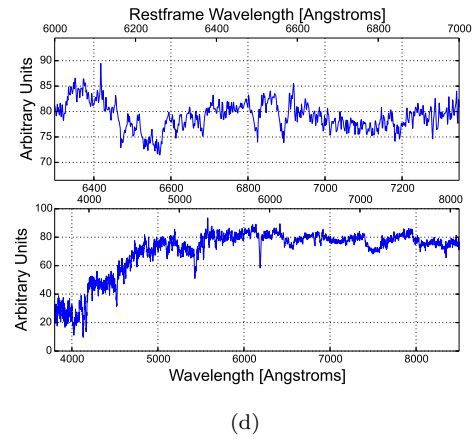
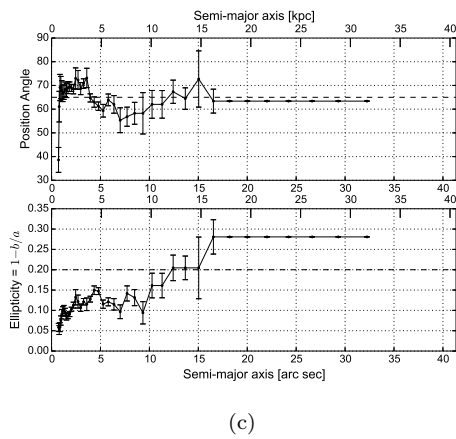
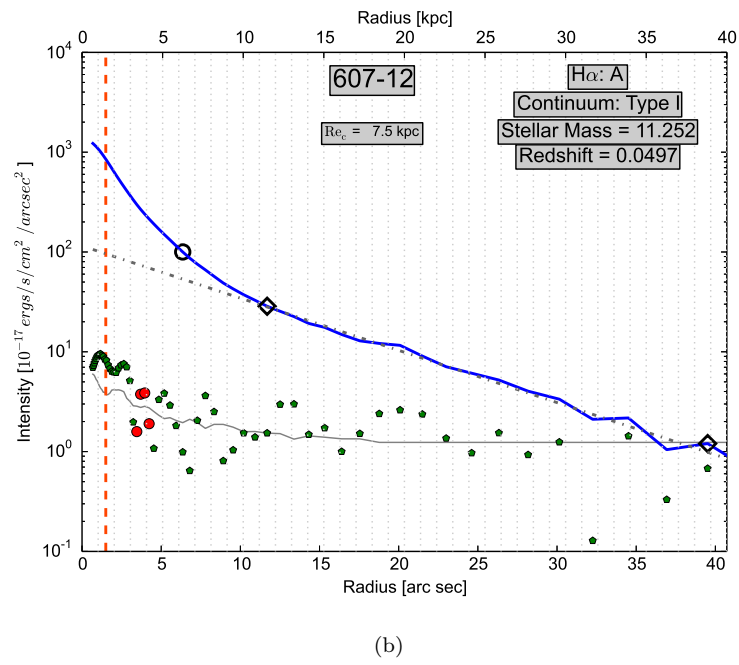
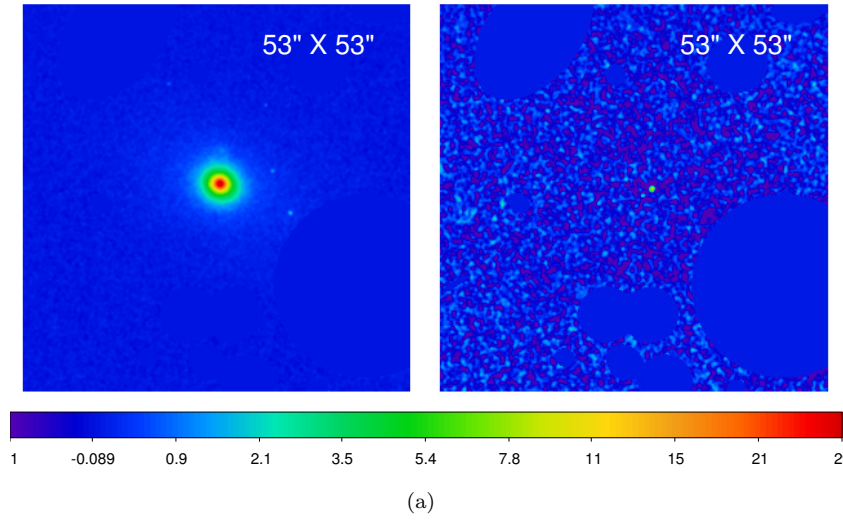


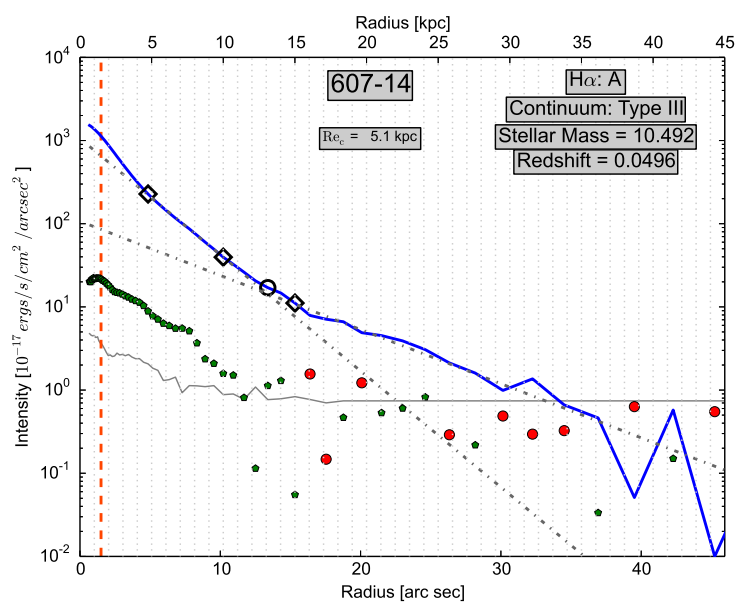
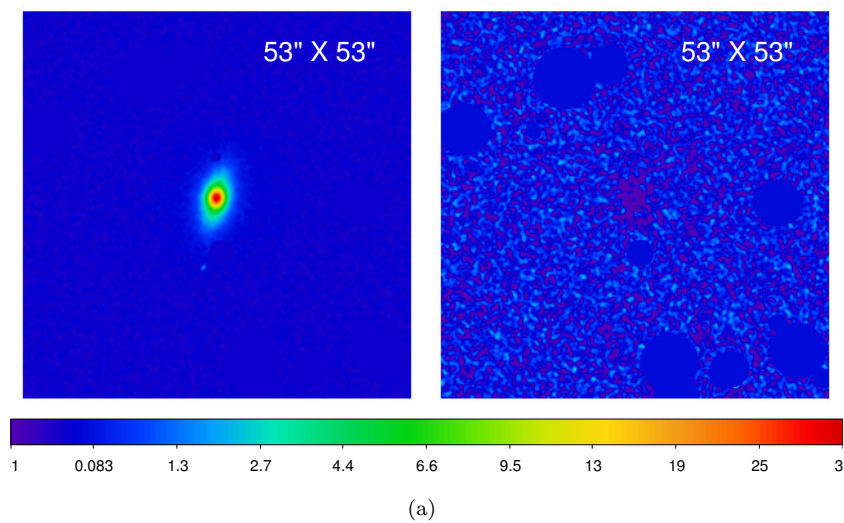
(d)



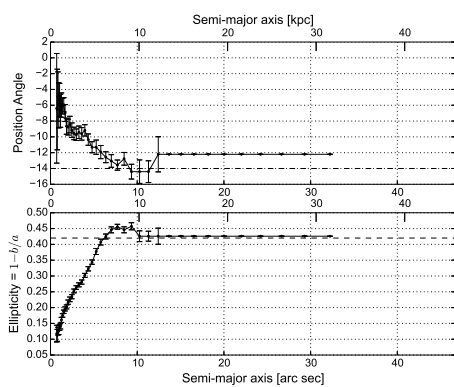




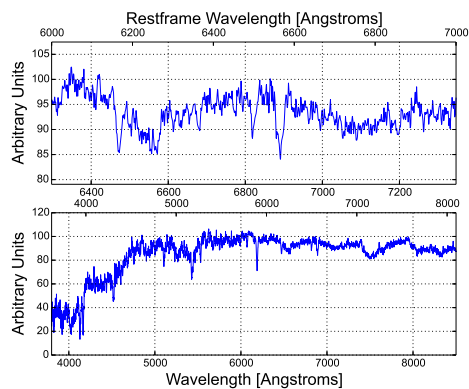




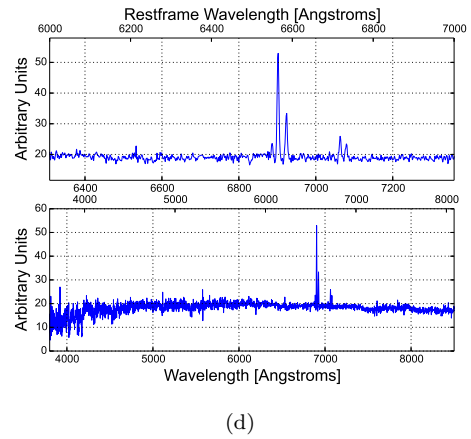
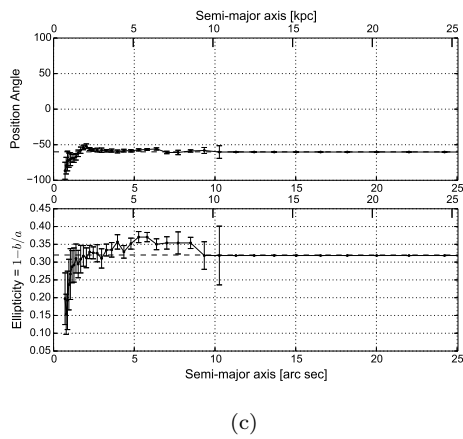
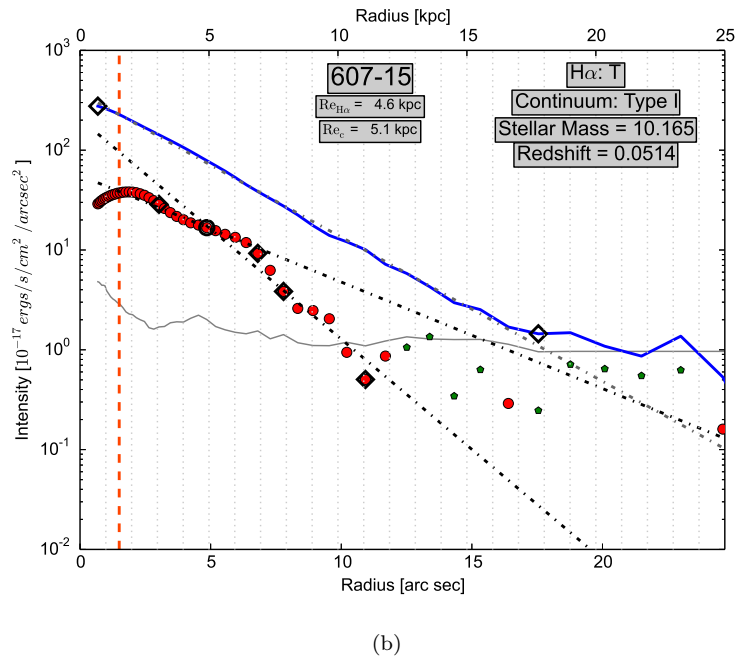
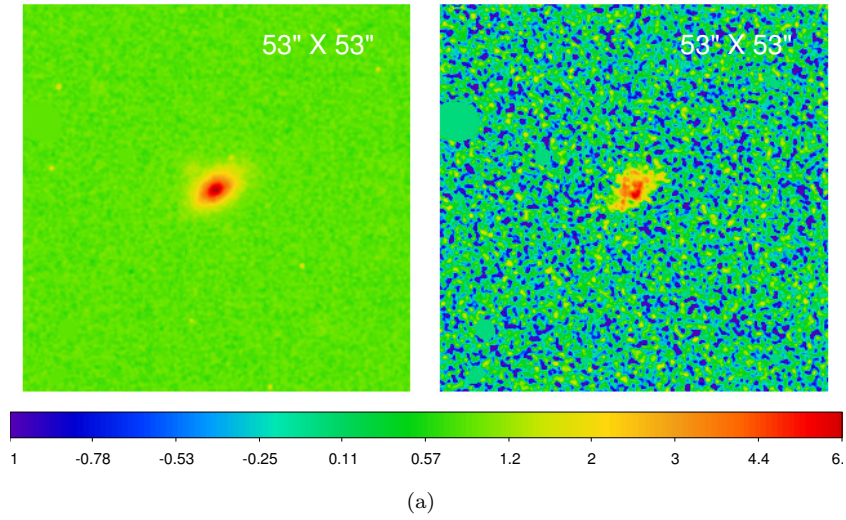
(b)

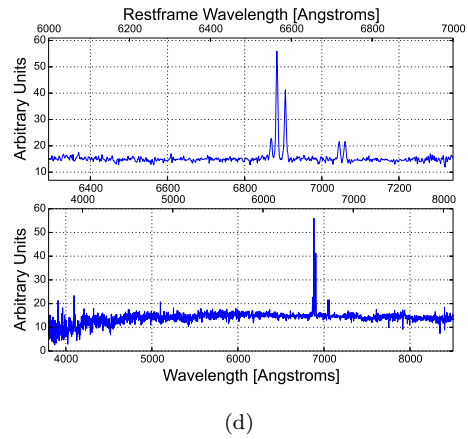
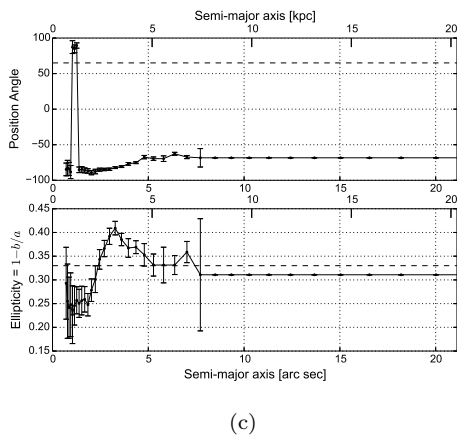
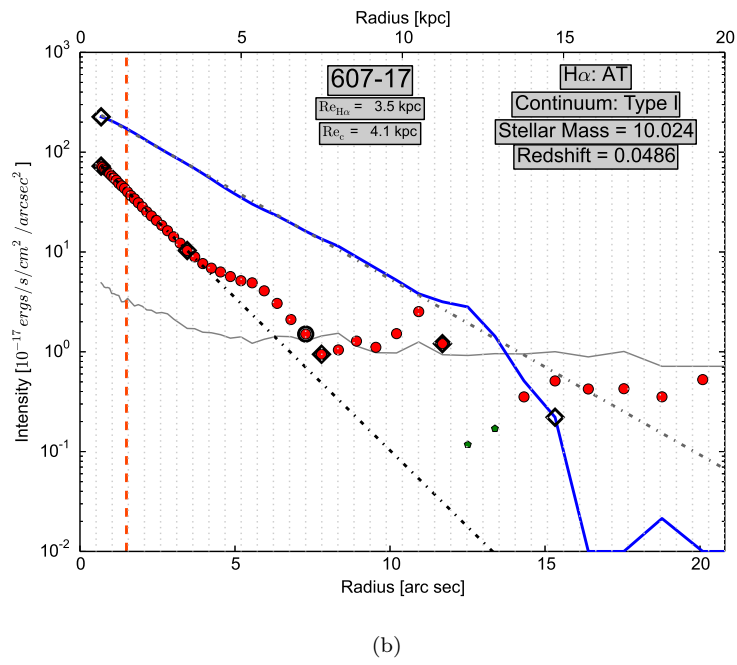
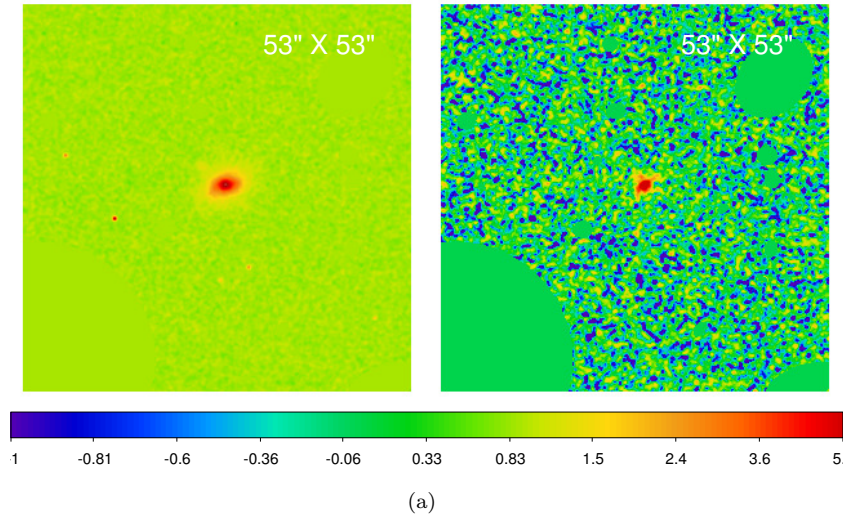


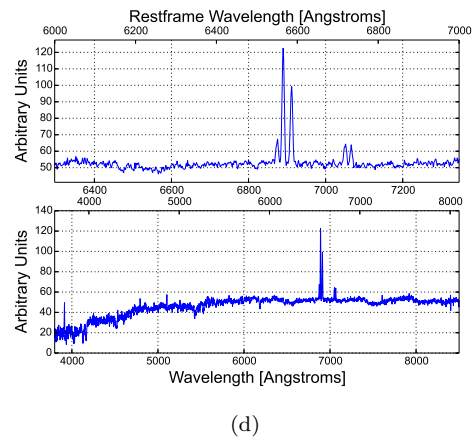
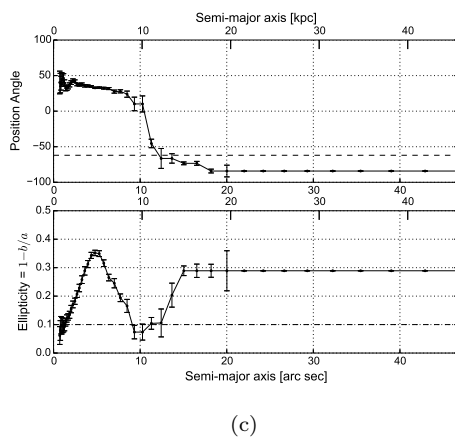
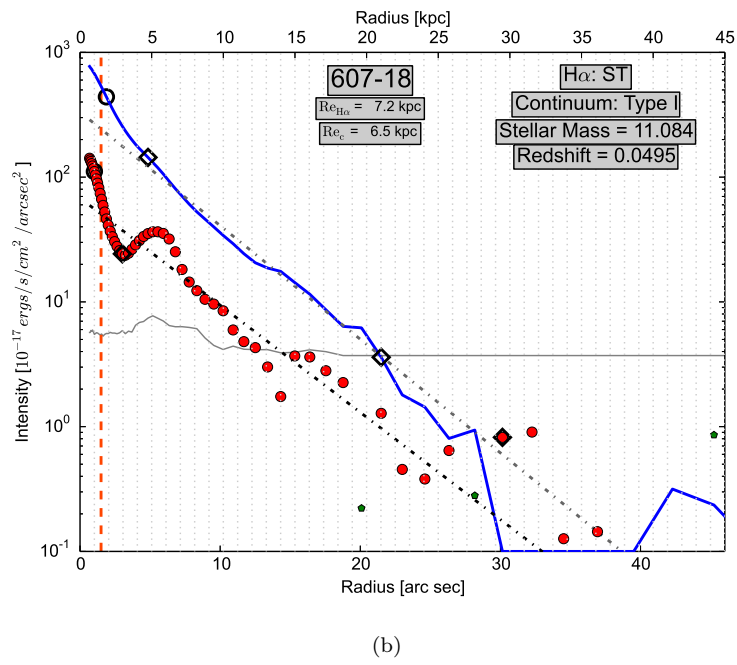
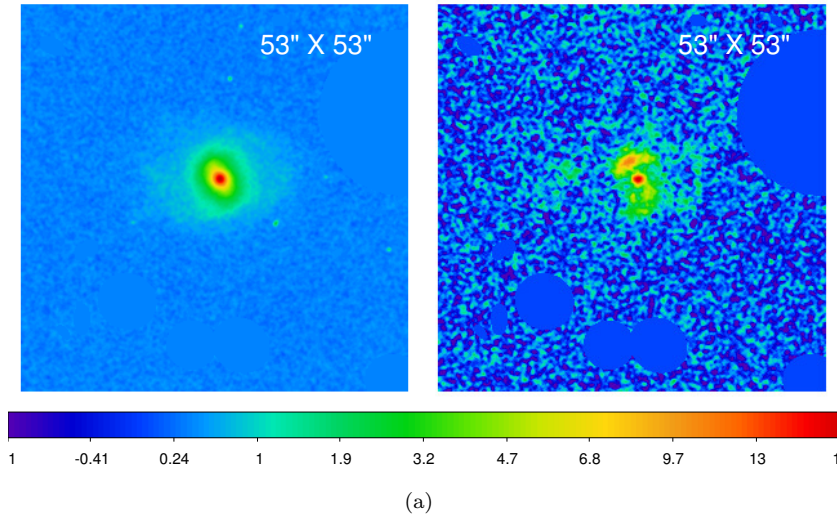
(c)

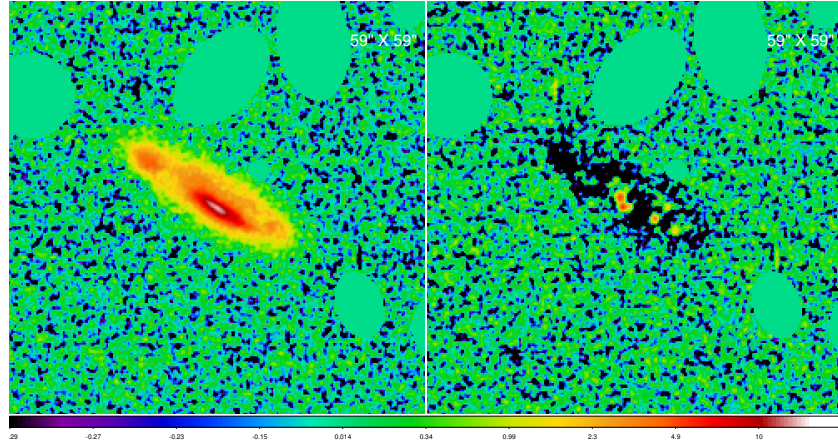


(d)

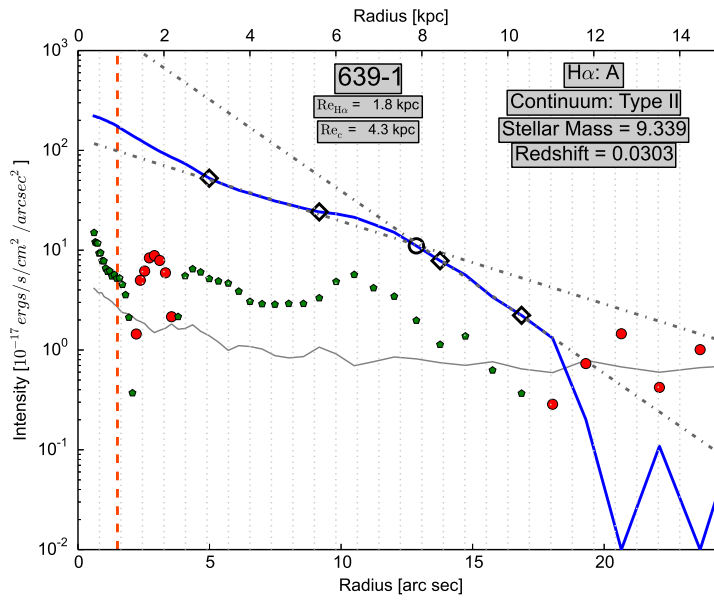




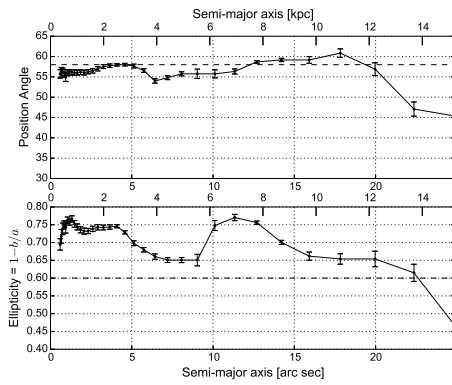




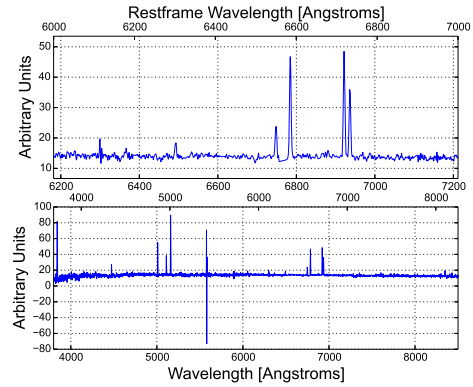
(a)



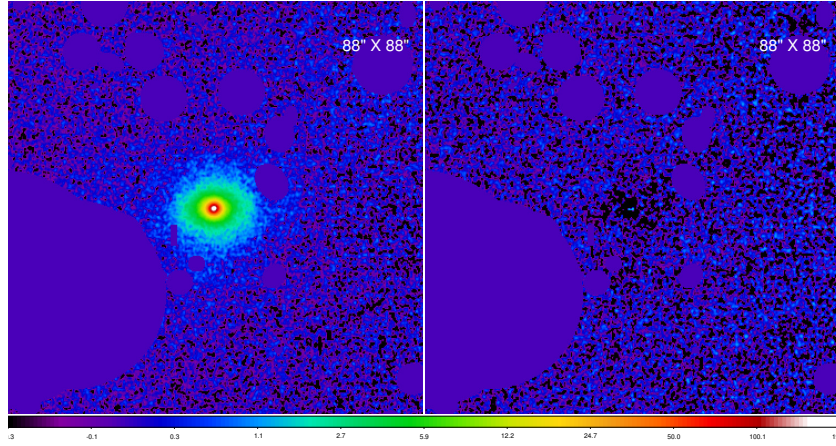
(b)



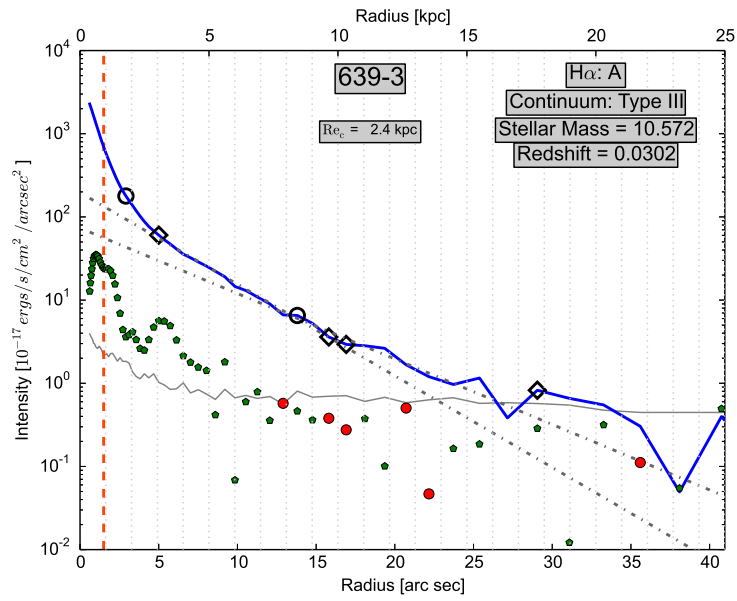
(c)



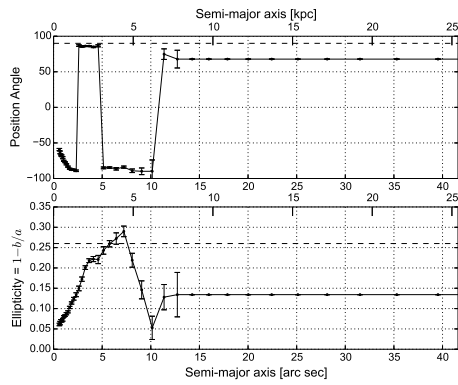
(d)



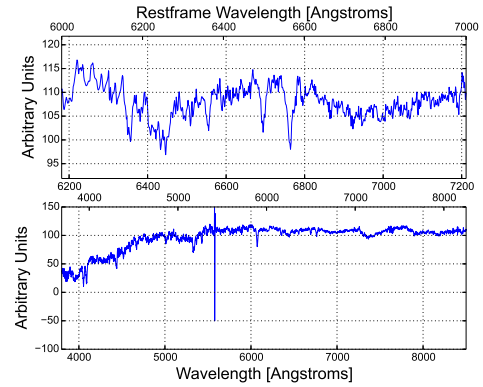
(a)



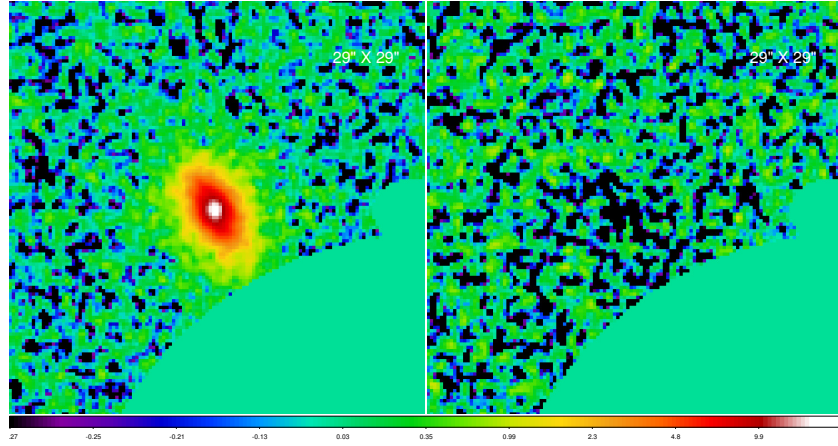
(b)



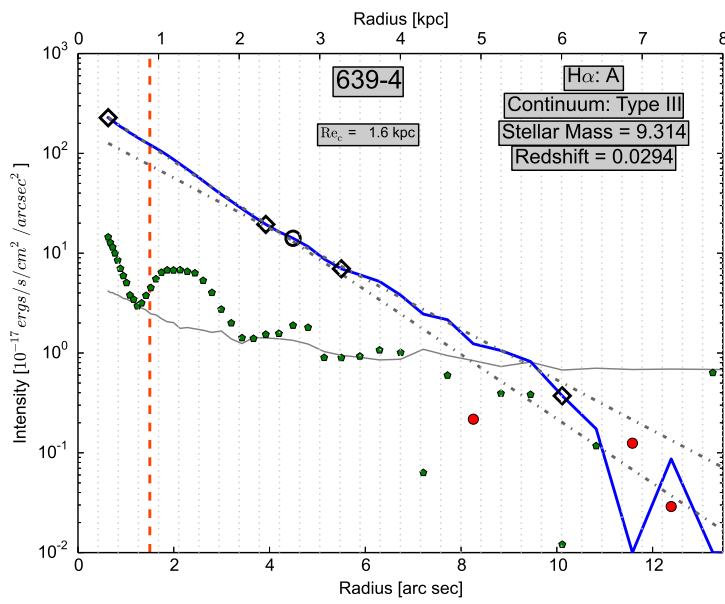
(c)



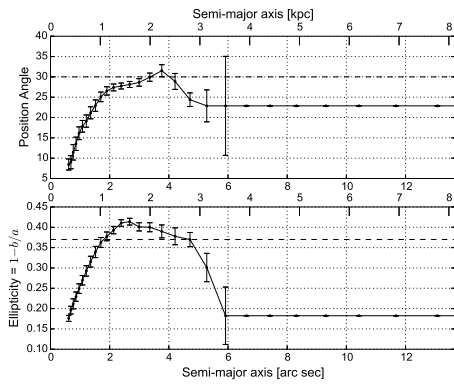
(d)



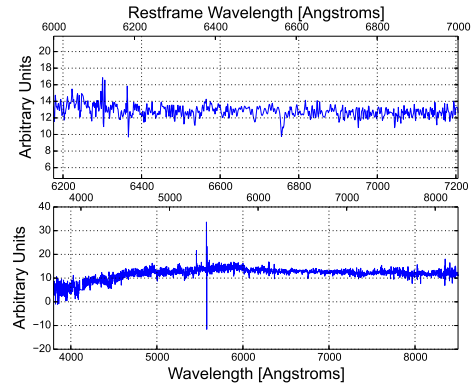
(a)



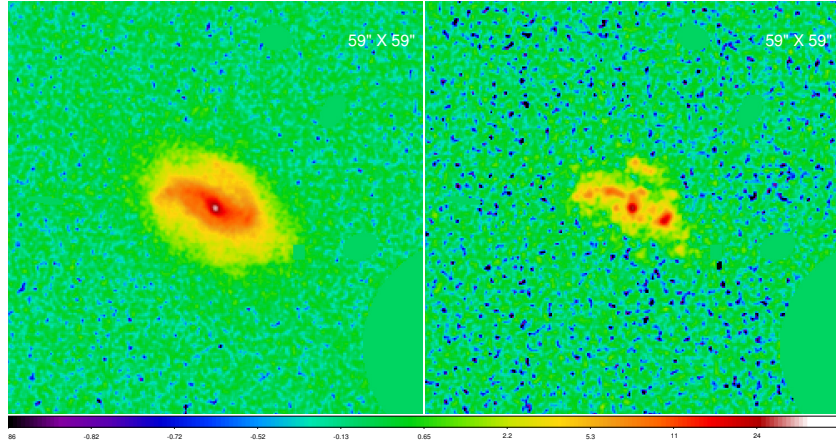
(b)



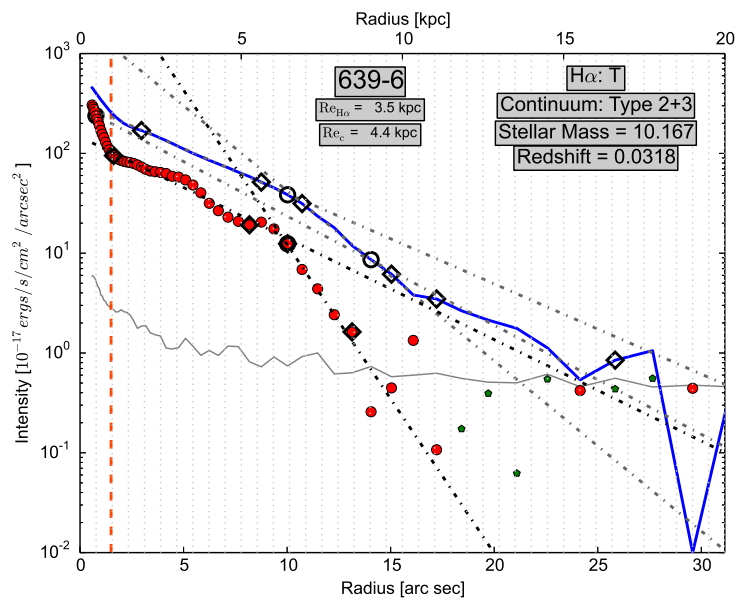
(c)



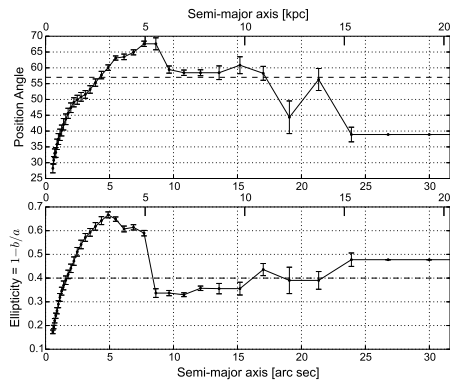
(d)



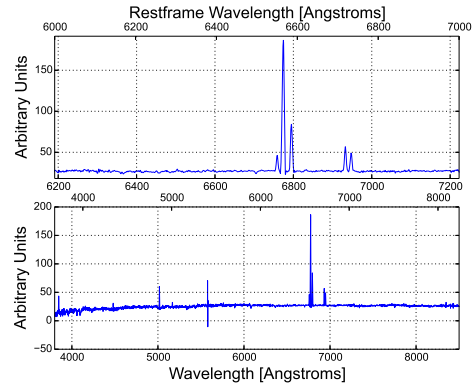
(a)



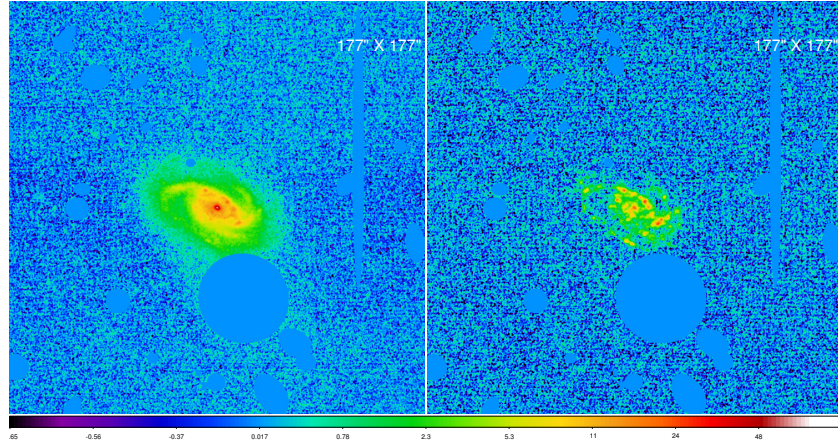
(b)



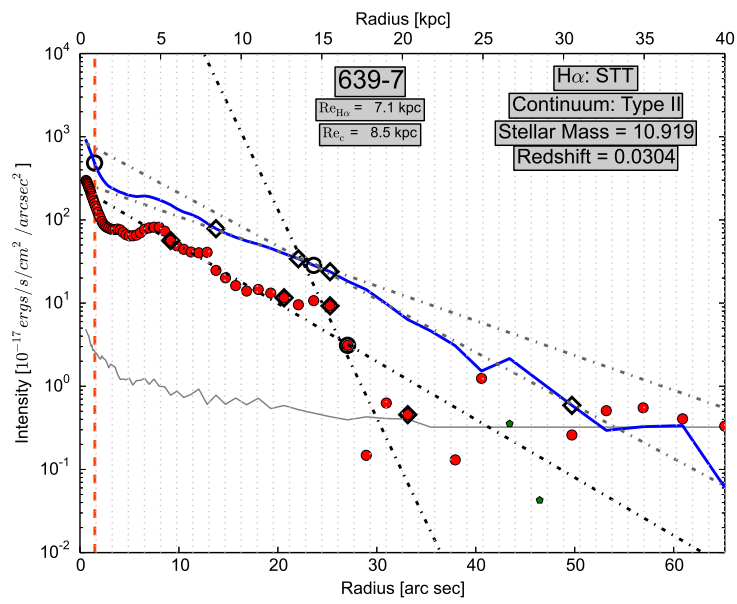
(c)



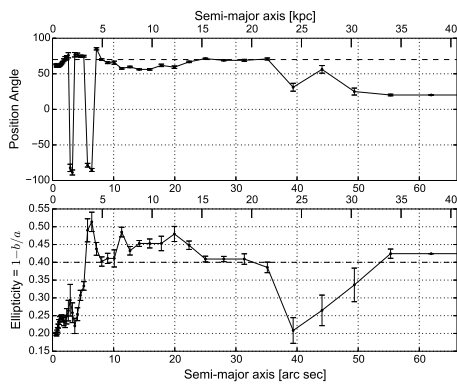
(d)



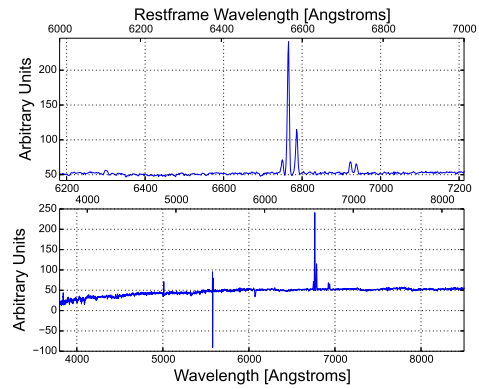
(a)



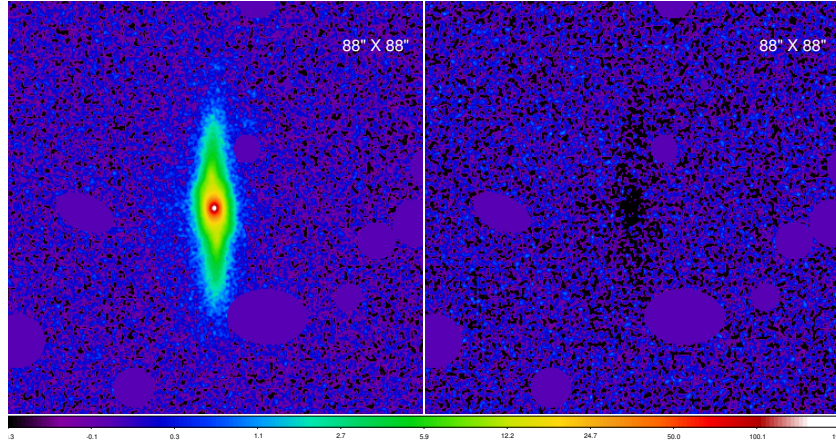
(b)



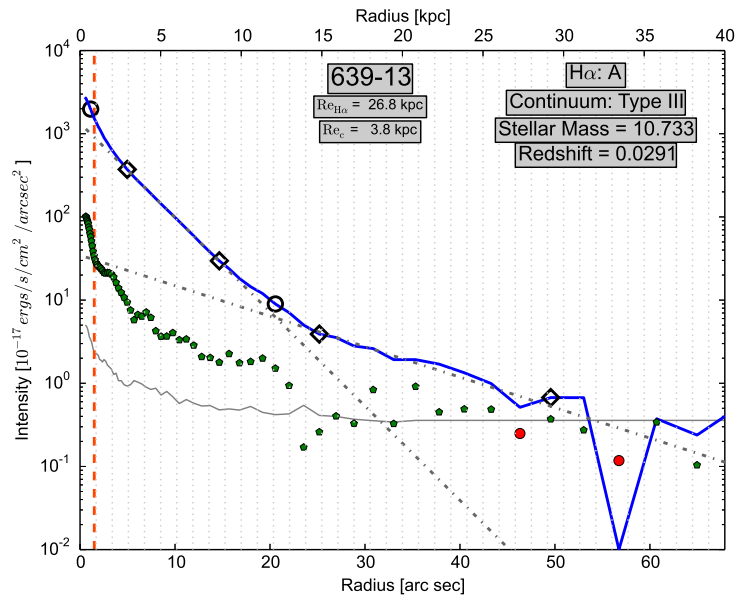
(c)



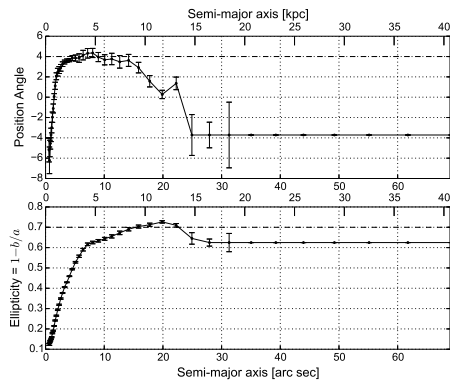
(d)



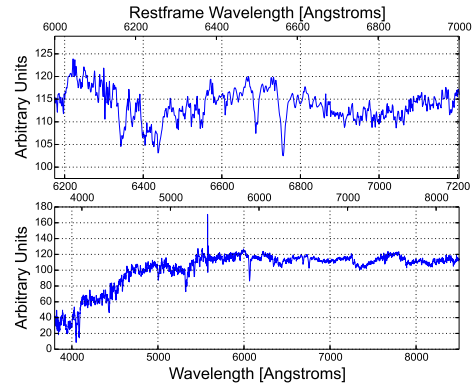
(a)



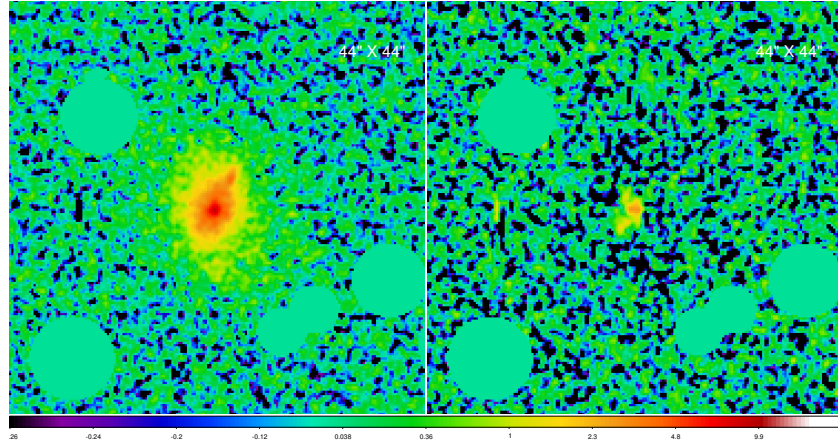
(b)



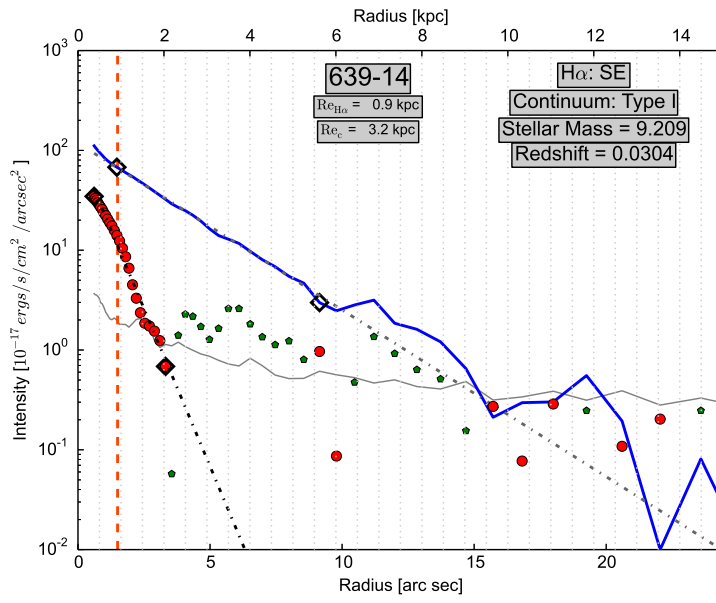
(c)



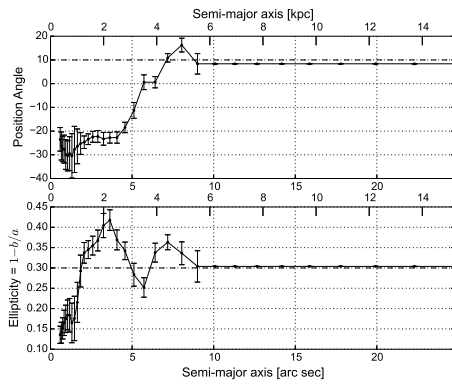
(d)



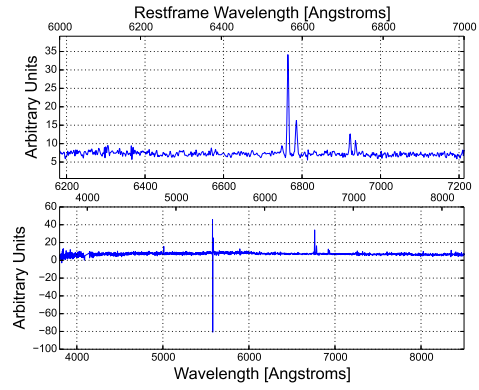
(a)



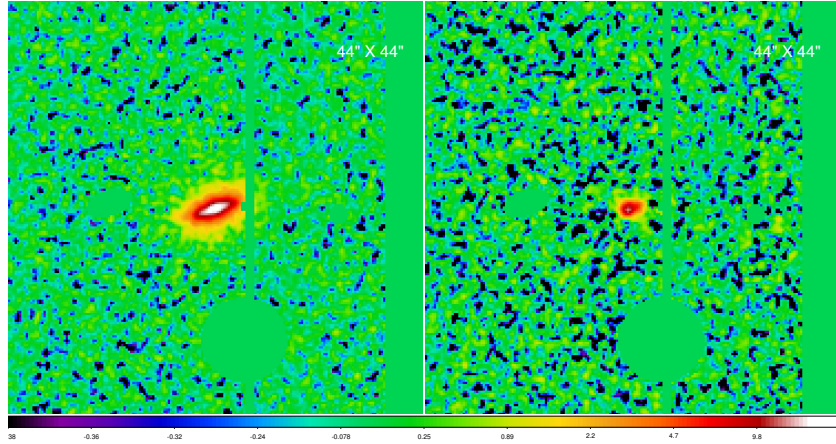
(b)



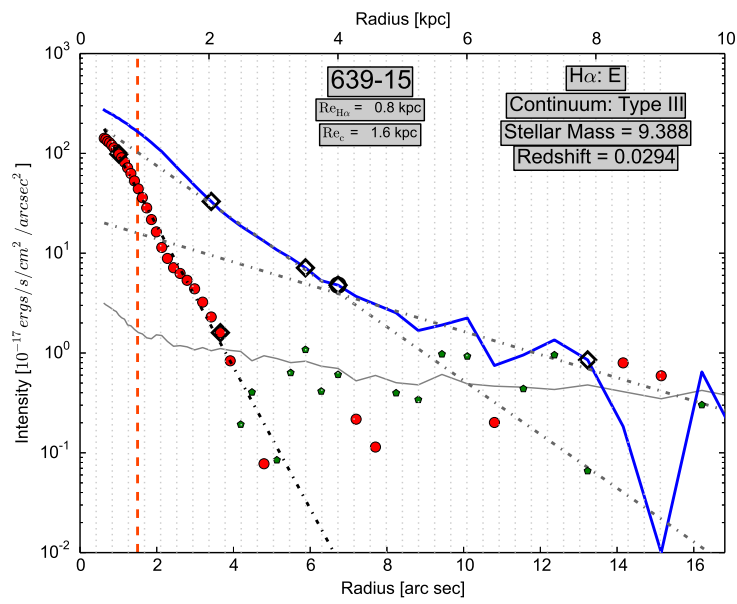
(c)



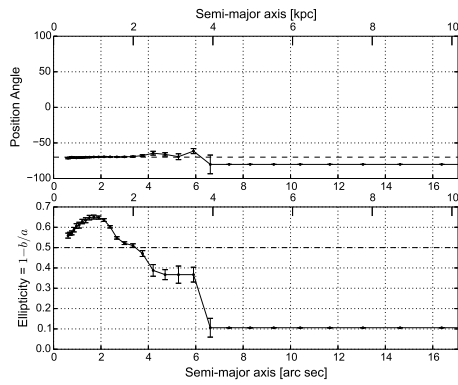
(d)



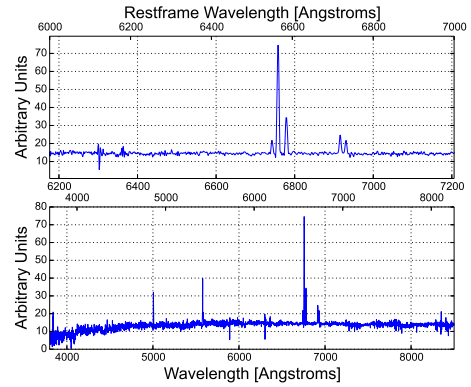
(a)



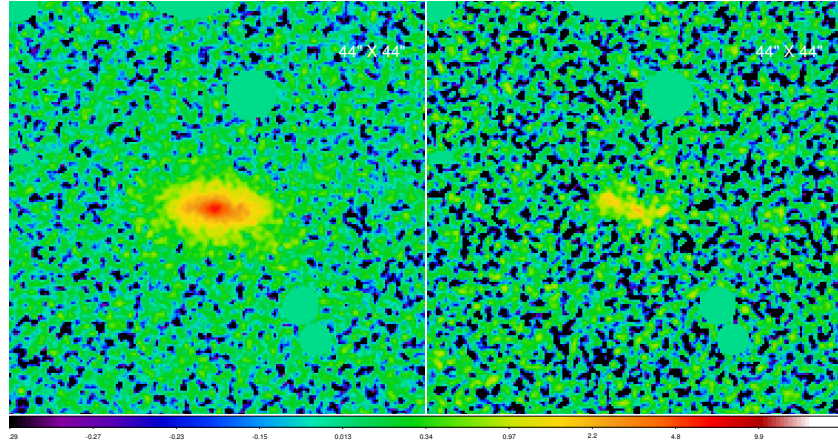
(b)



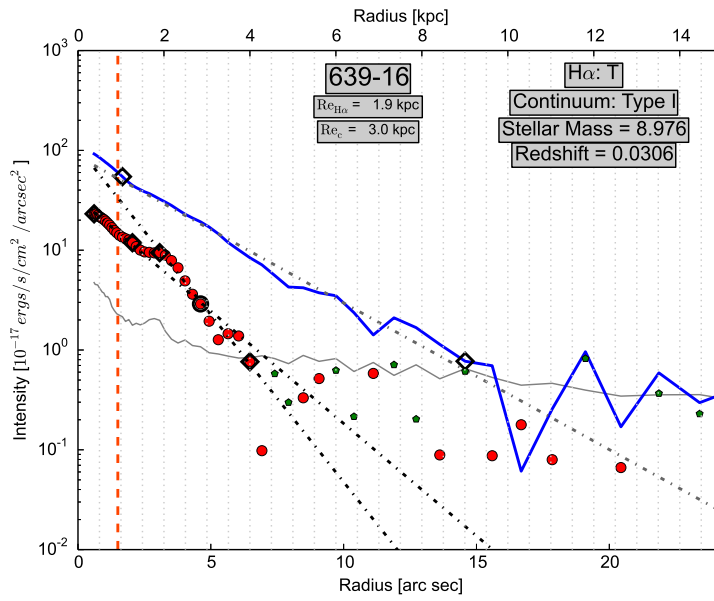
(c)



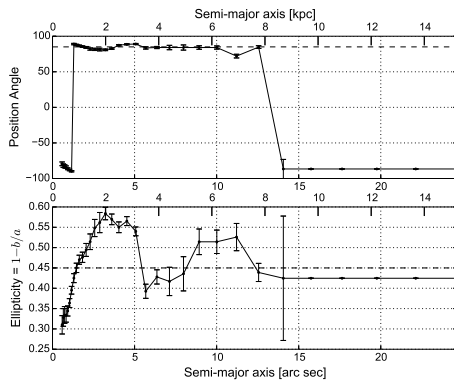
(d)



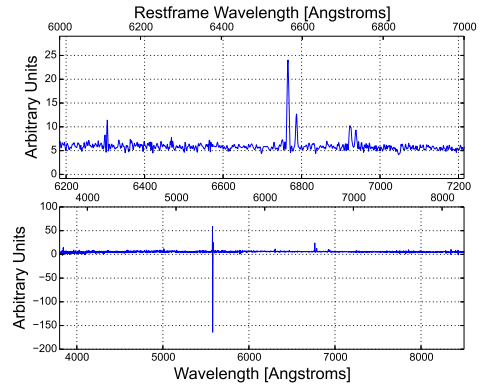
(a)



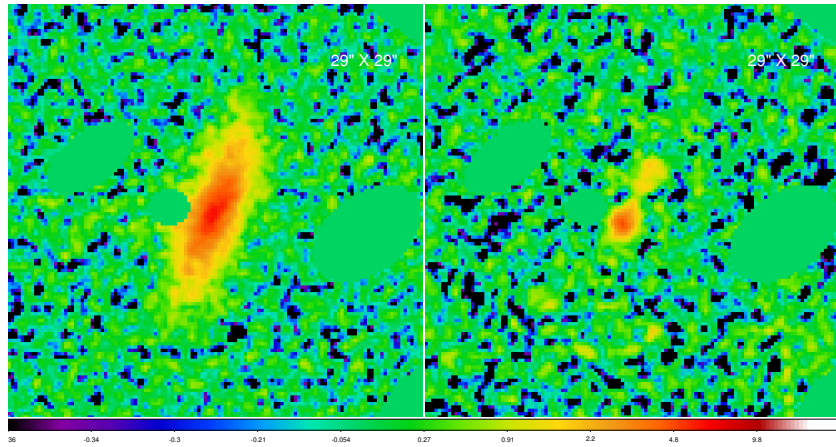
(b)



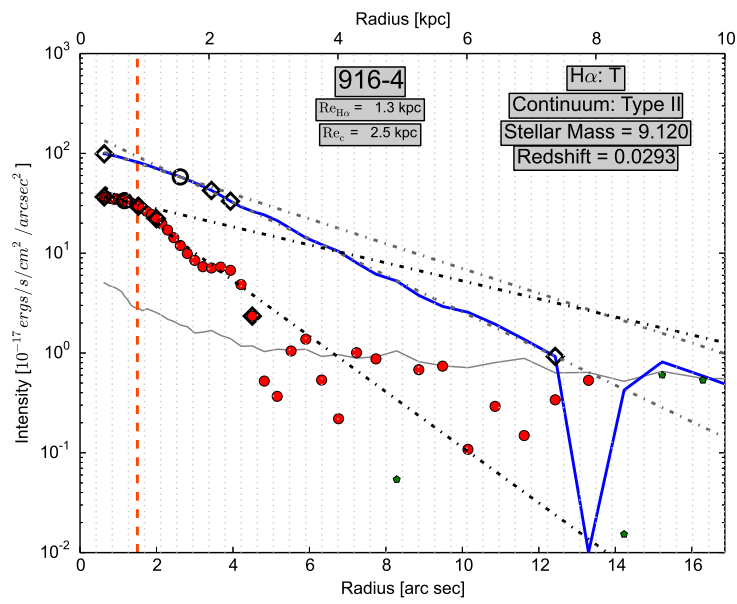
(c)



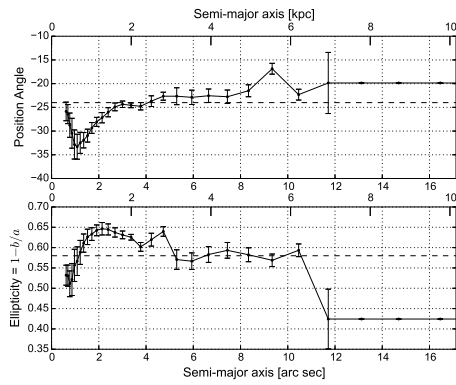
(d)



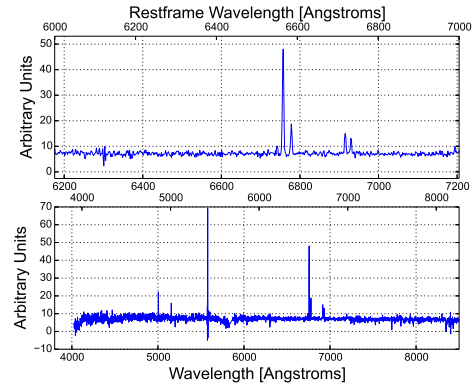
(a)



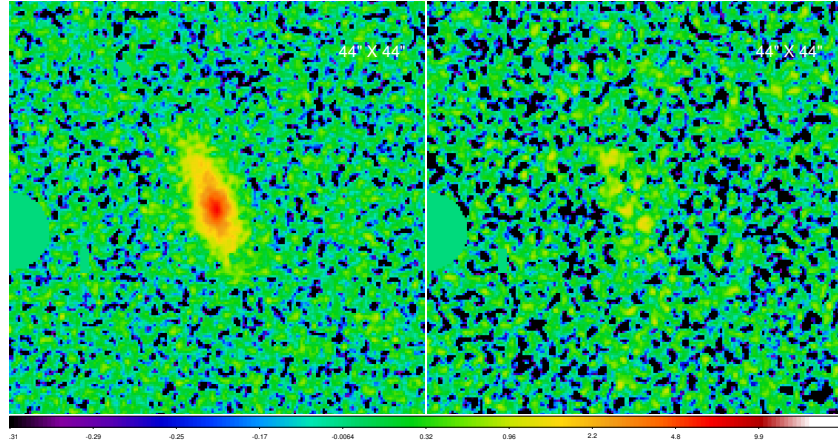
(b)



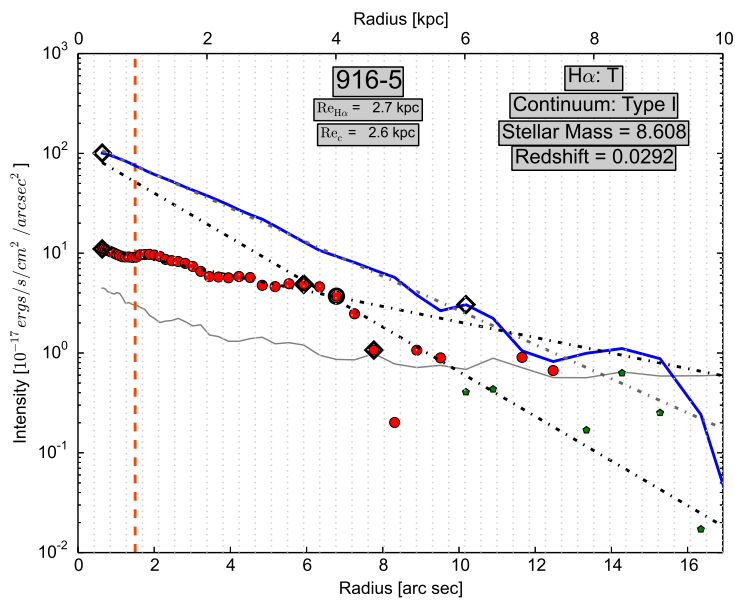
(c)



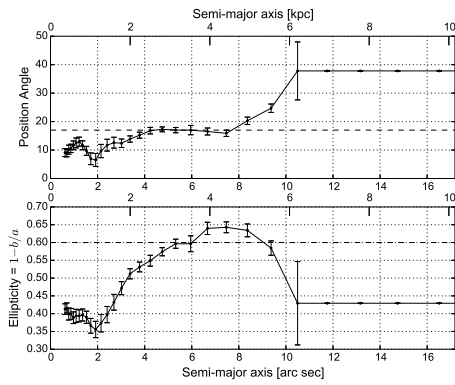
(d)



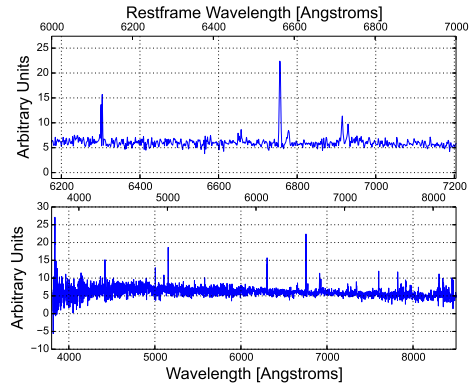
(a)



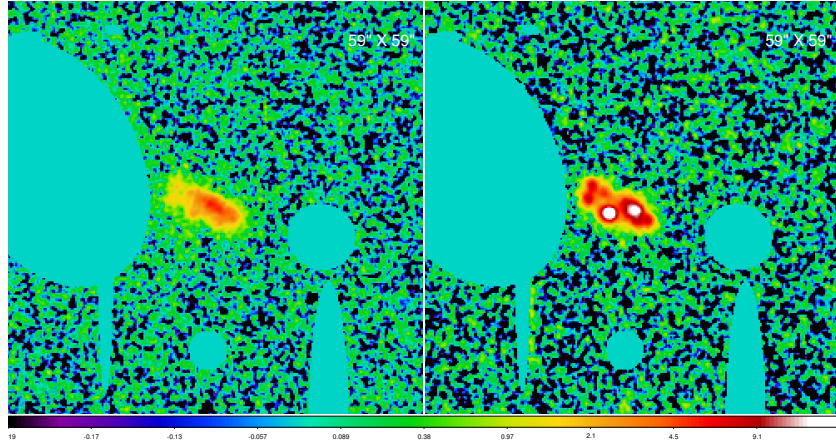
(b)



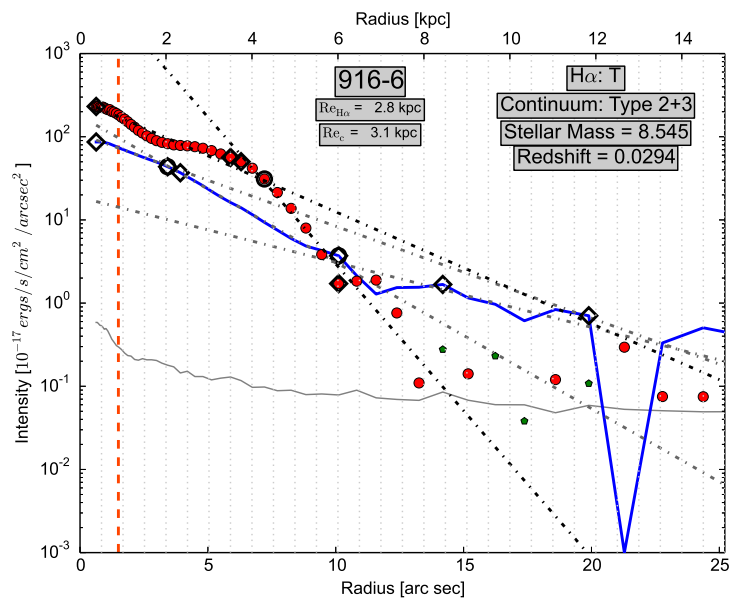
(c)



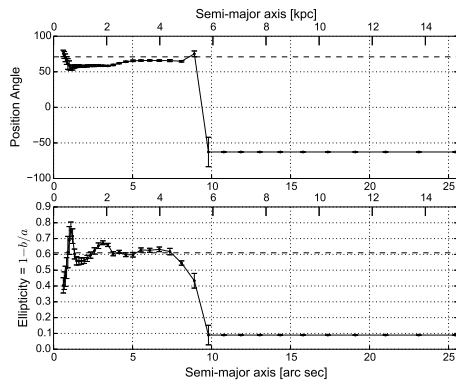
(d)



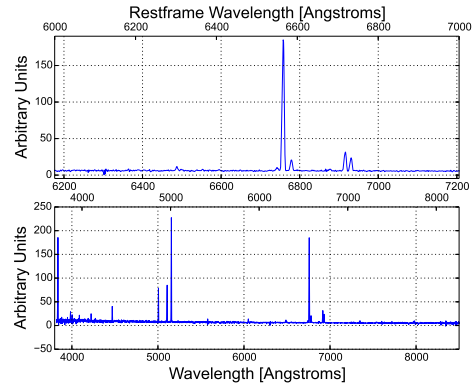
(a)



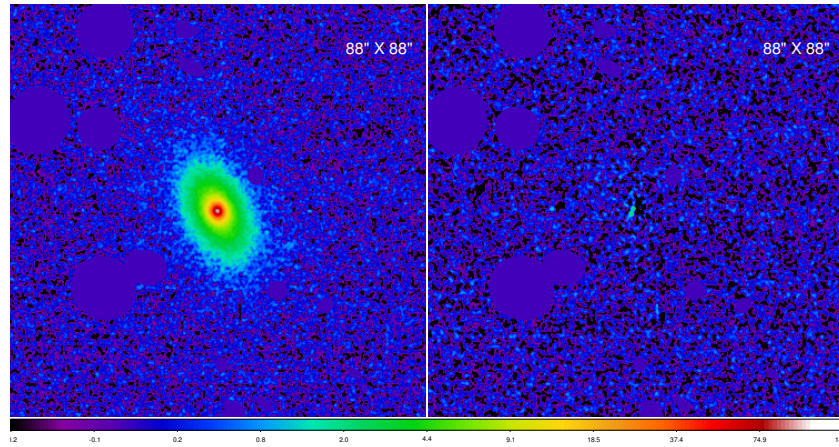
(b)



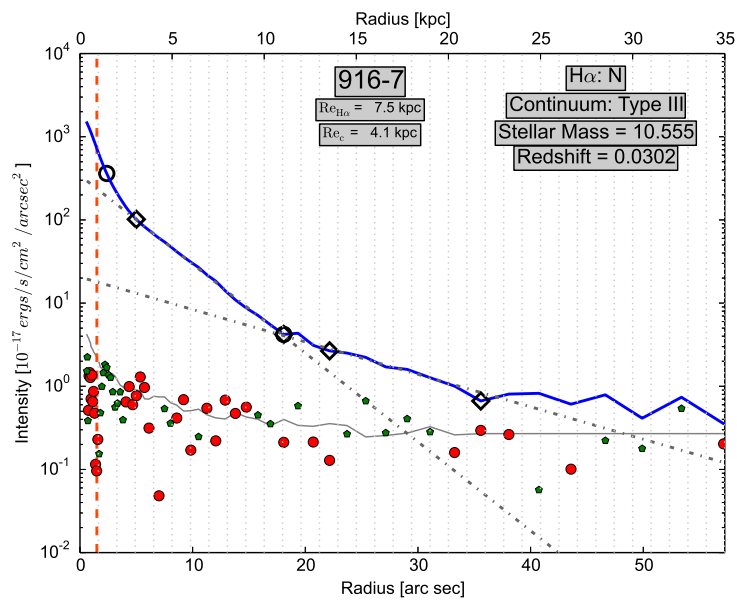
(c)



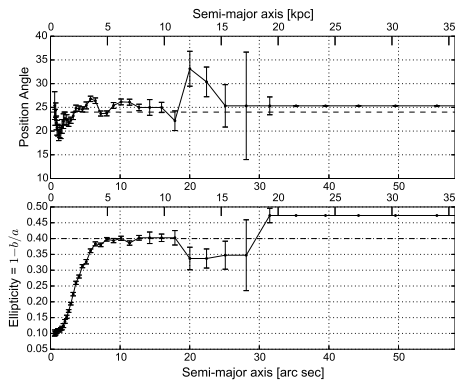
(d)



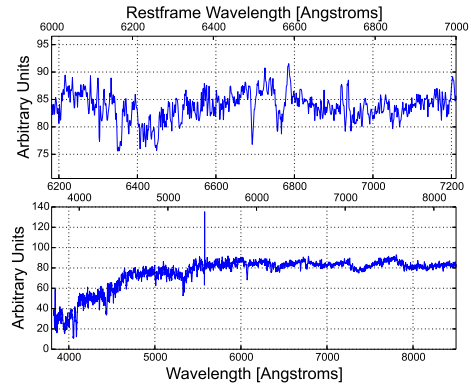
(a)



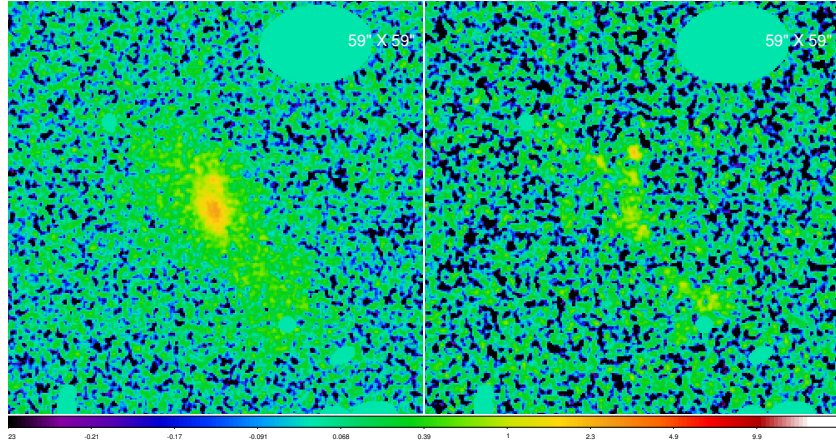
(b)



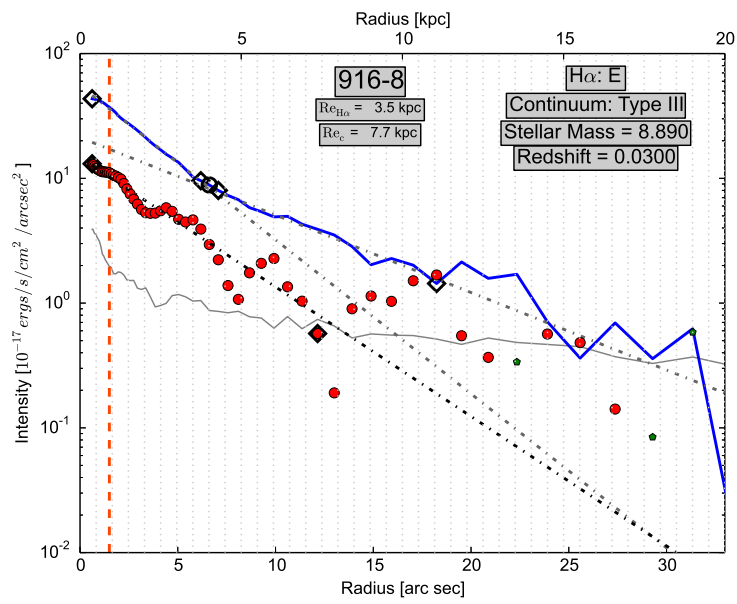
(c)



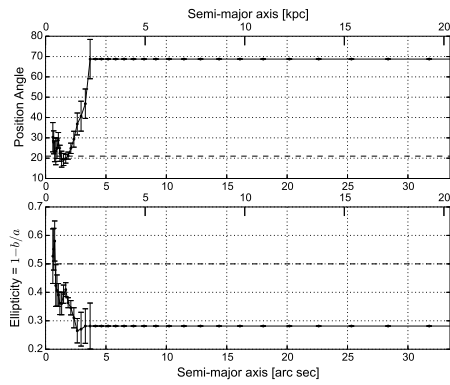
(d)



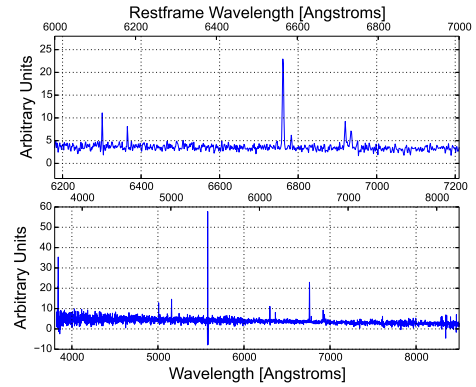
(a)



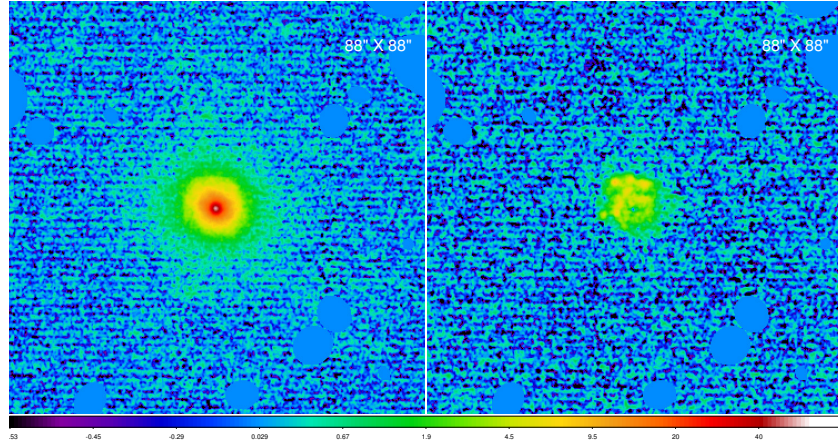
(b)



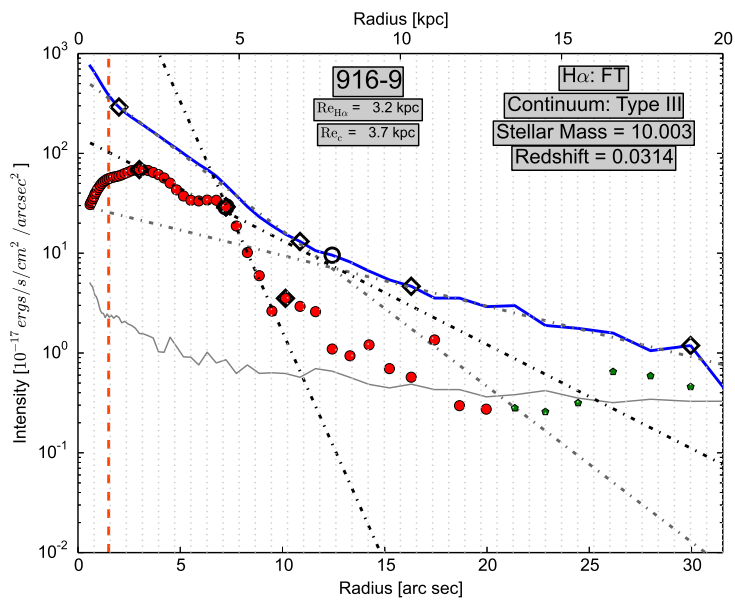
(c)



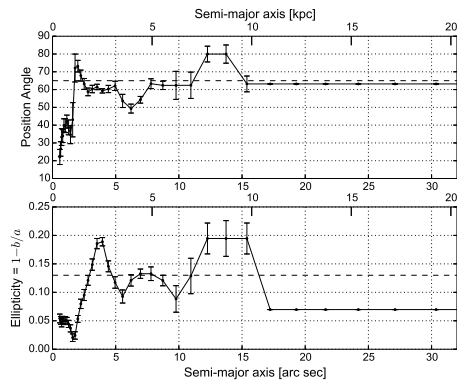
(d)



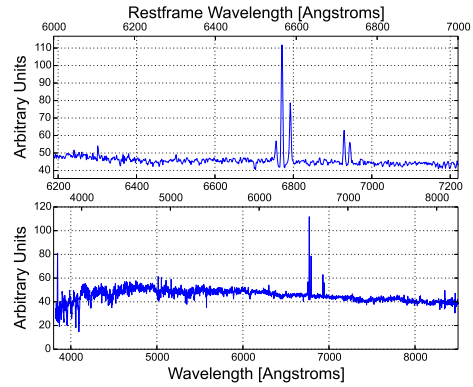
(a)



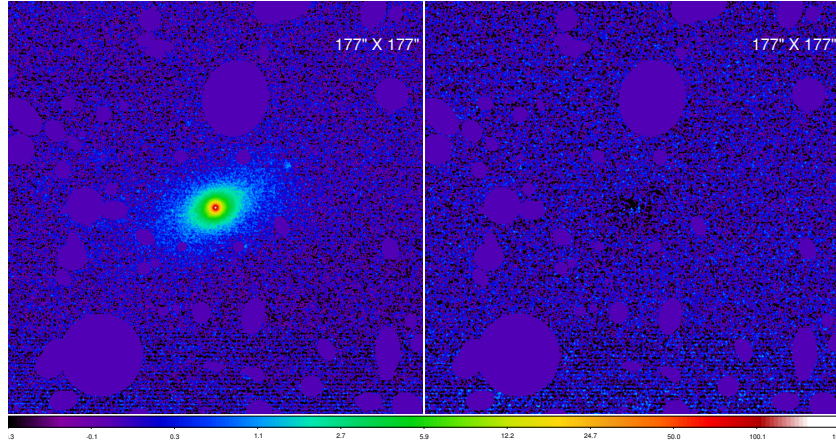
(b)



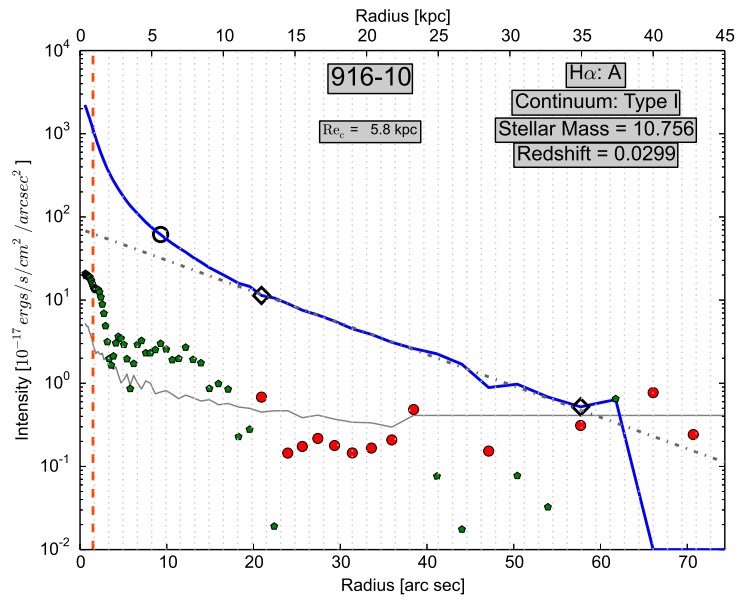
(c)



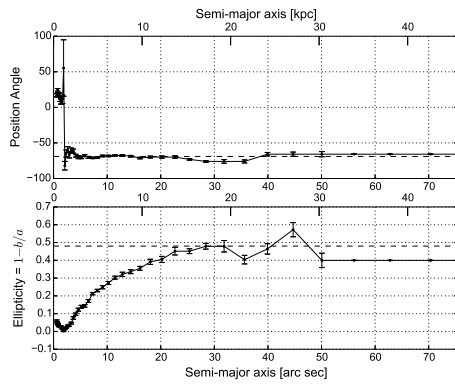
(d)



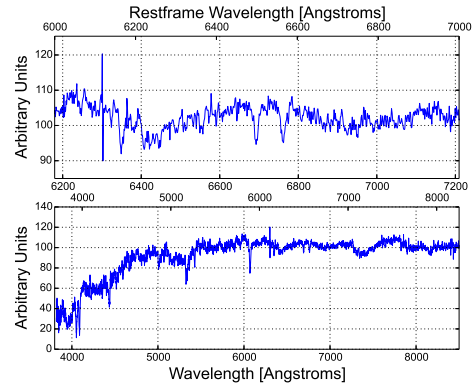
(a)



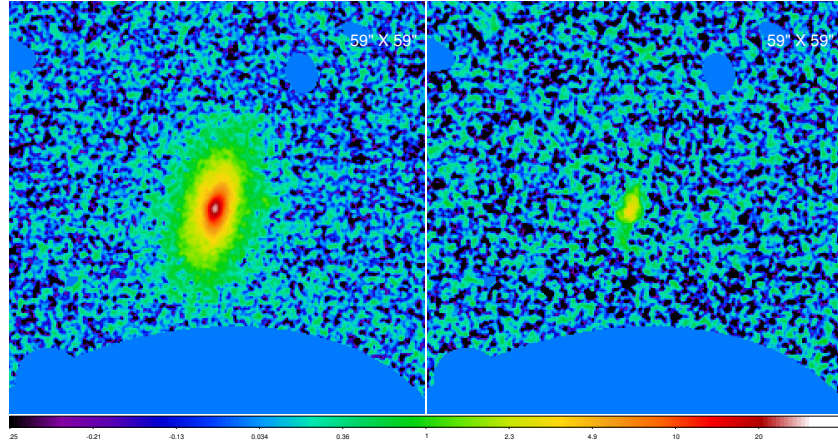
(b)



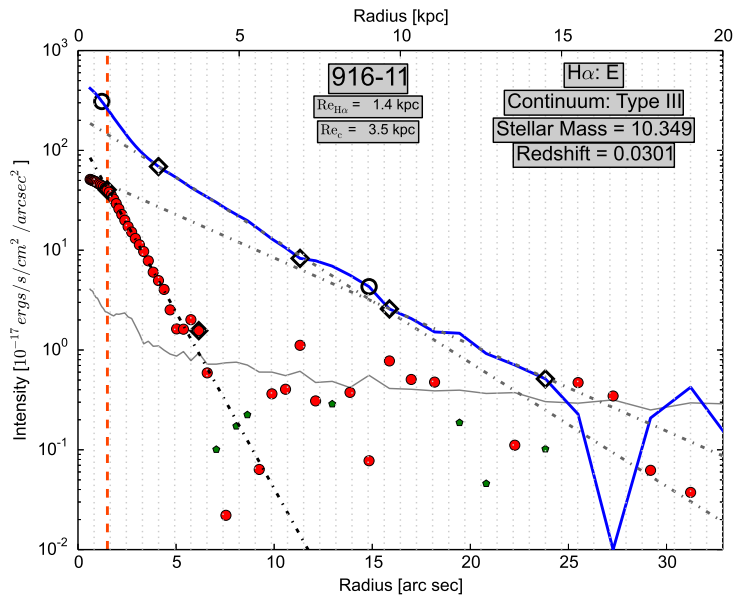
(c)



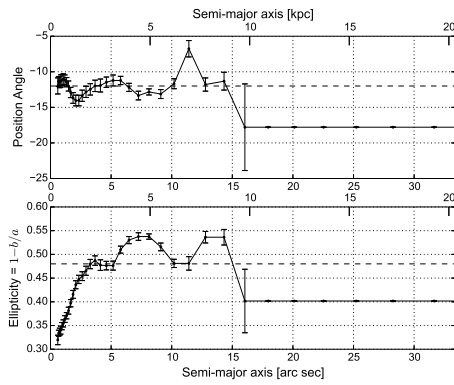
(d)



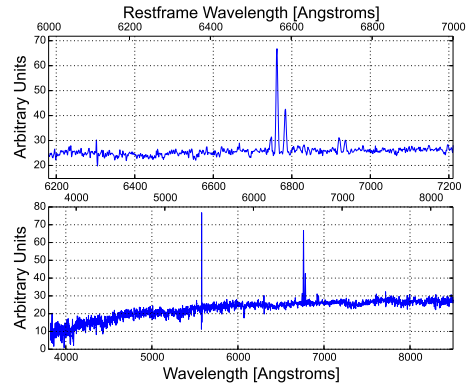
(a)



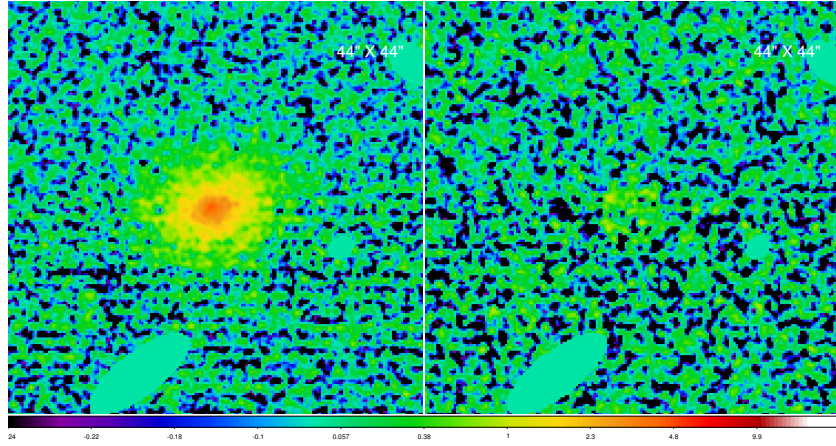
(b)



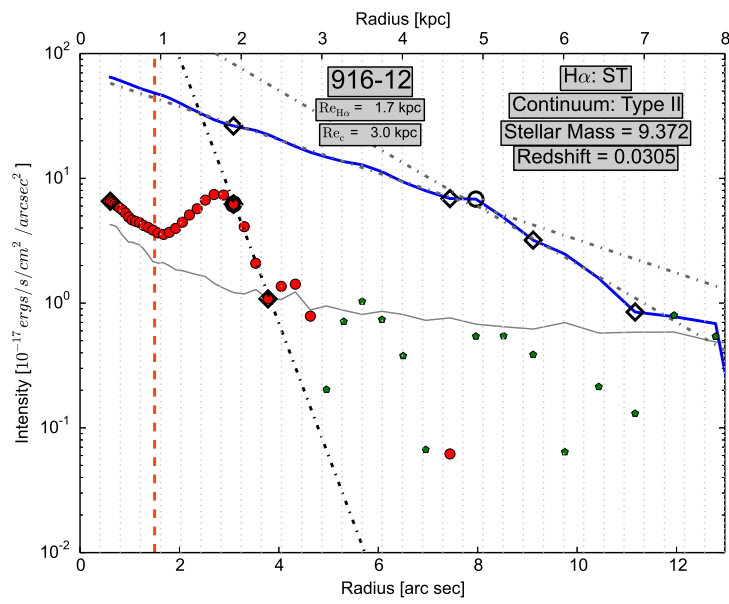
(c)



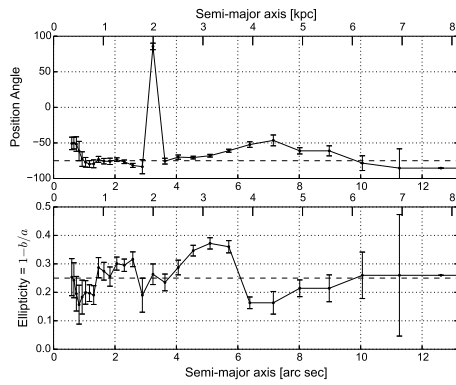
(d)



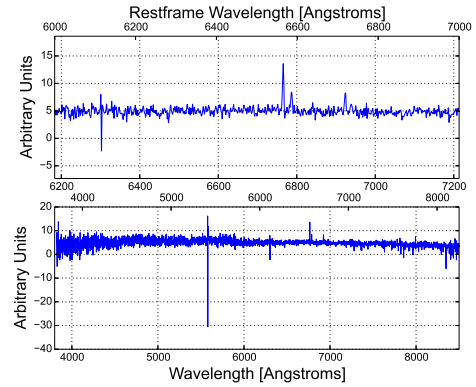
(a)



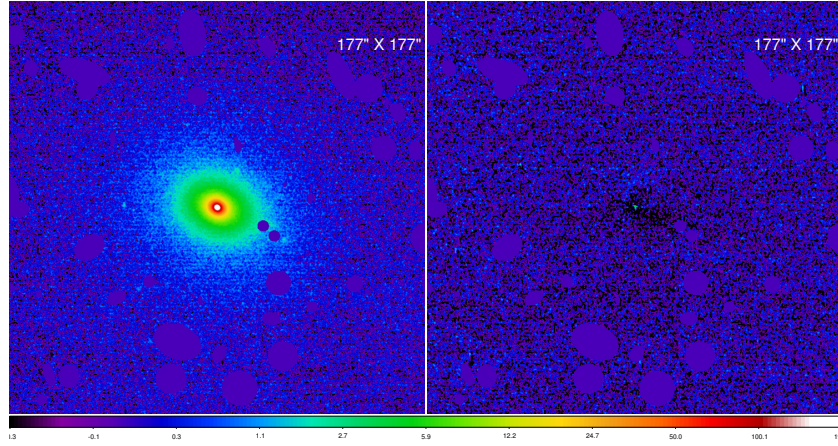
(b)



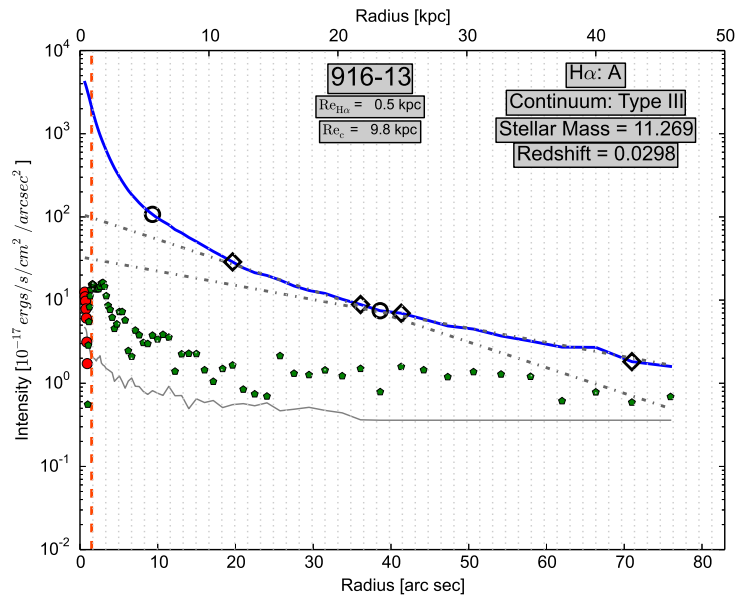
(c)



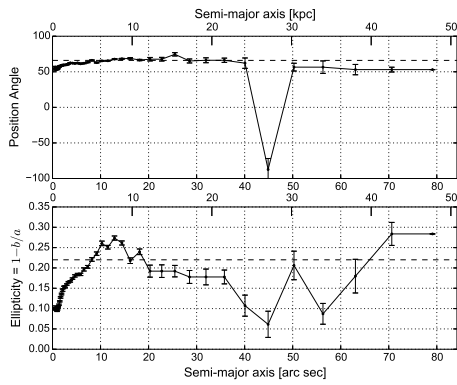
(d)



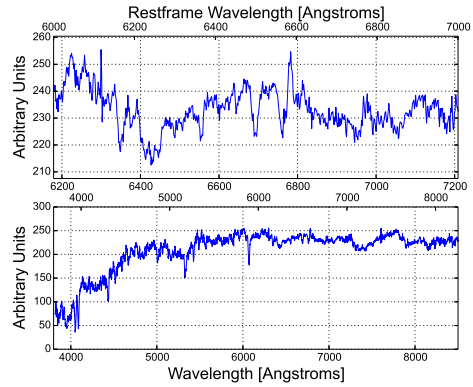
(a)



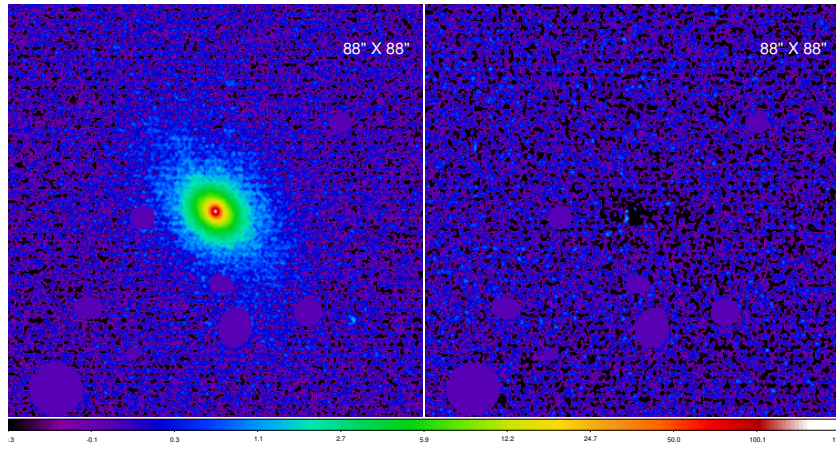
(b)



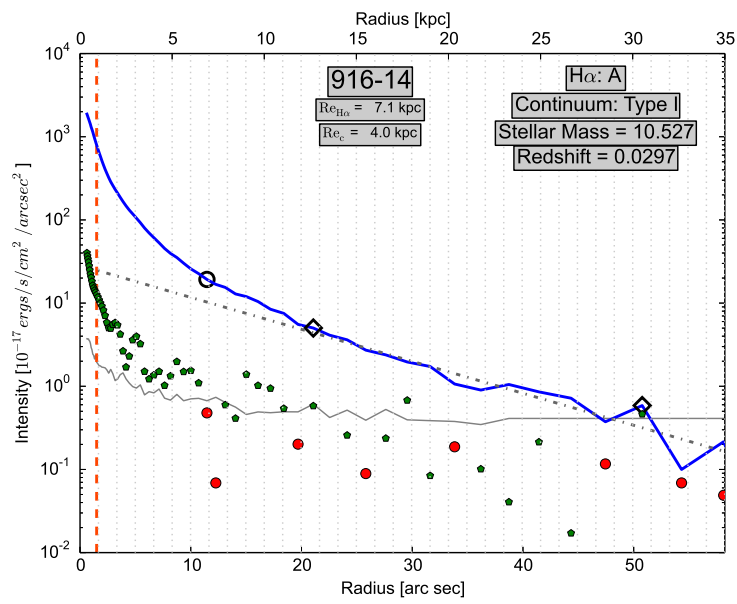
(c)



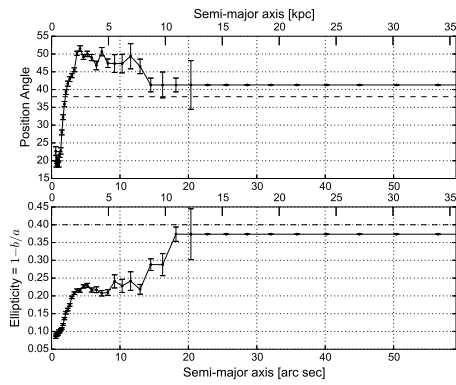
(d)



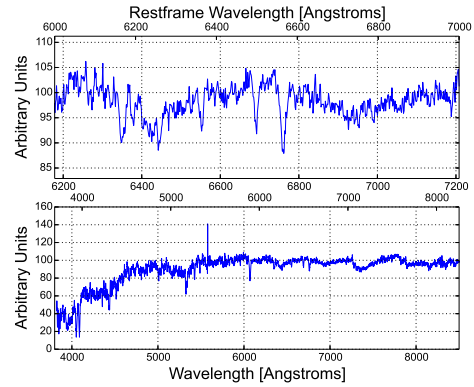
(a)



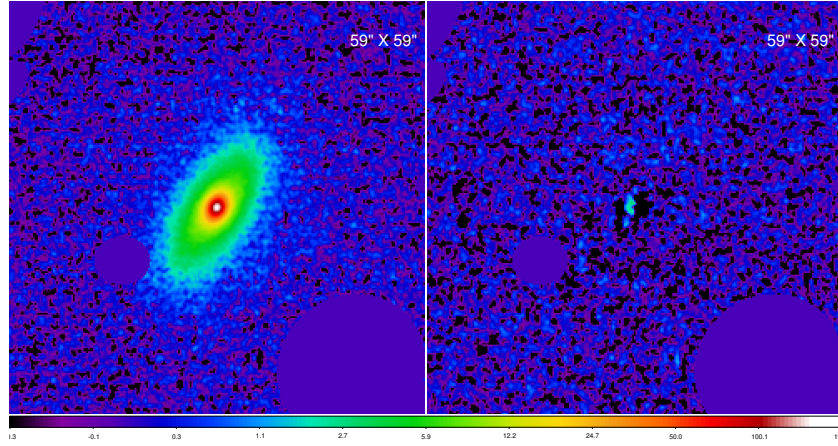
(b)



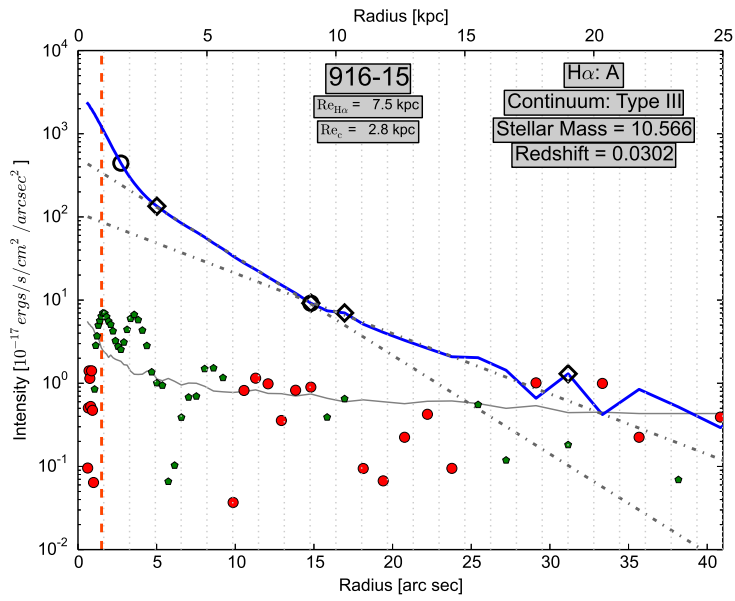
(c)



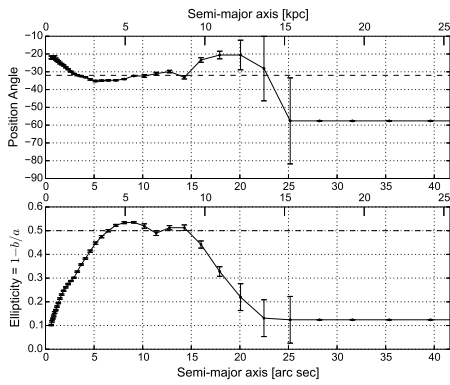
(d)



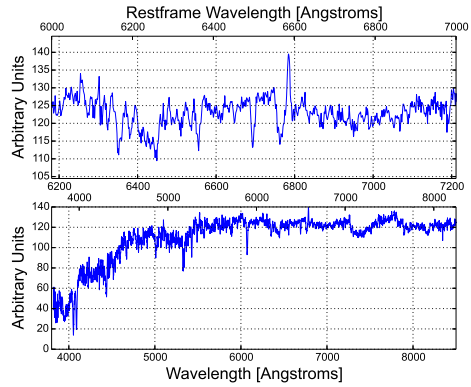
(a)



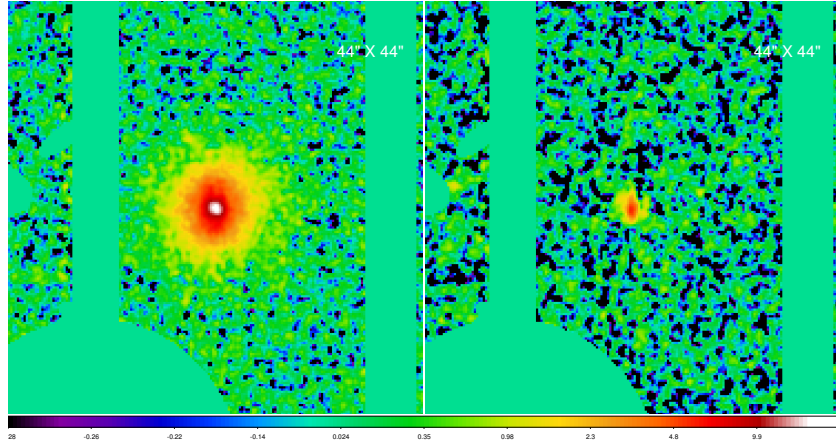
(b)



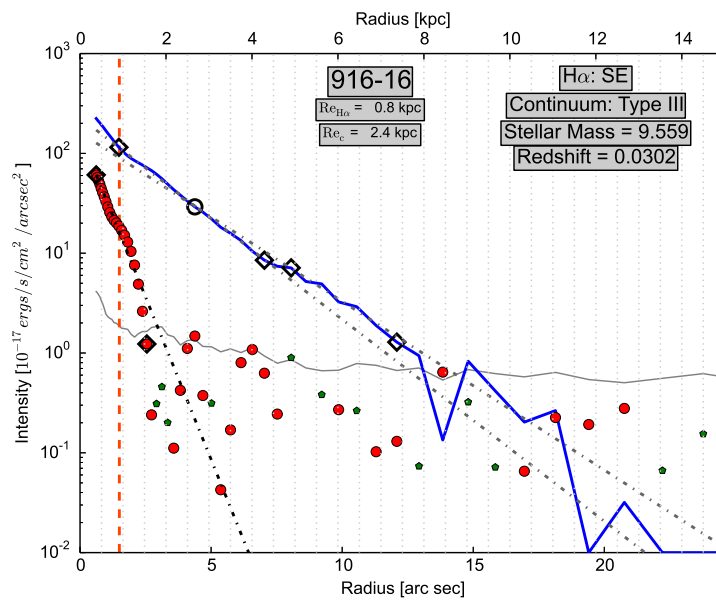
(c)



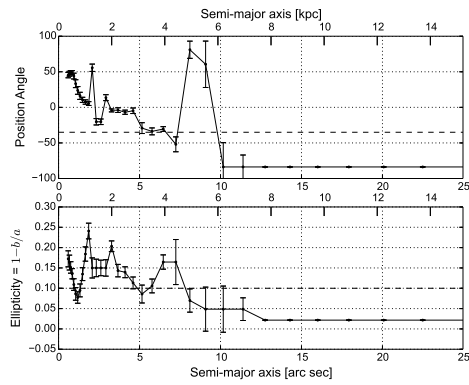
(d)



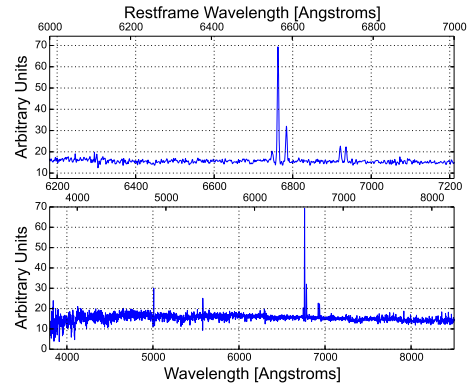
(a)



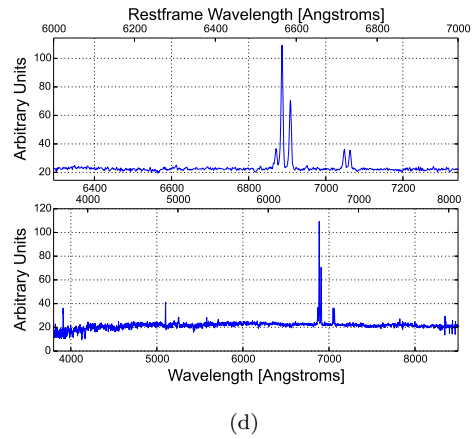
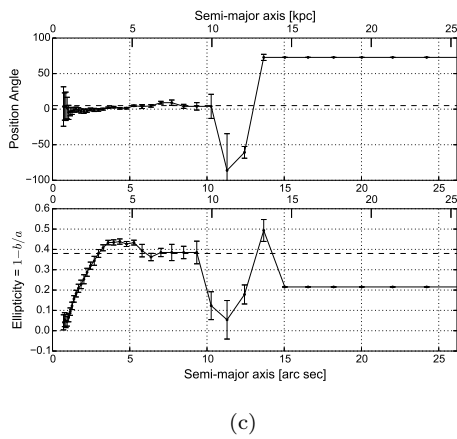
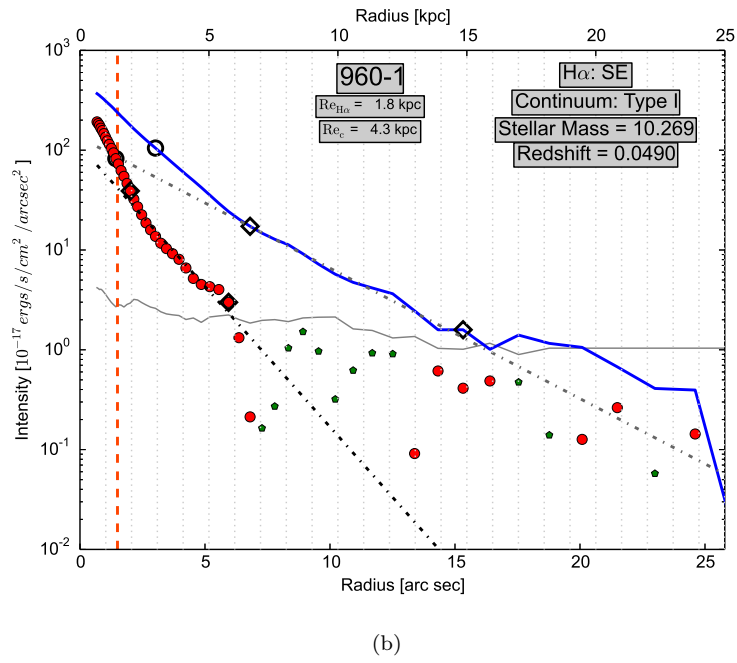
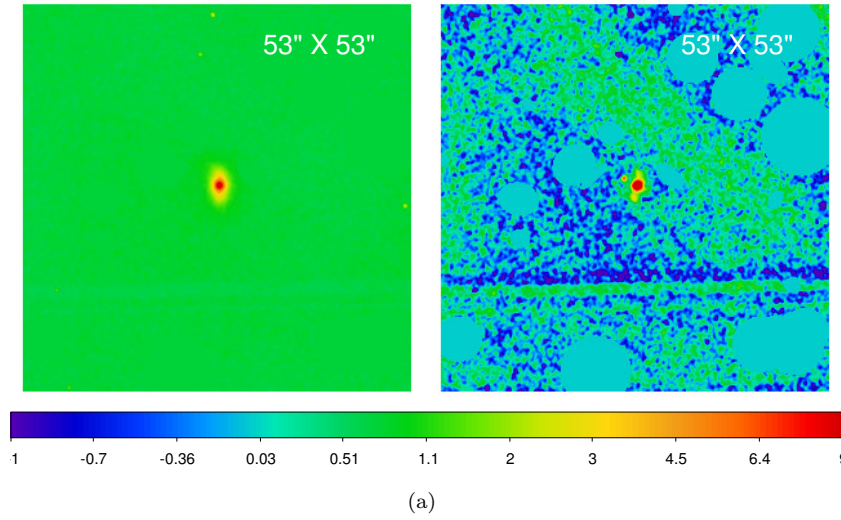
(b)

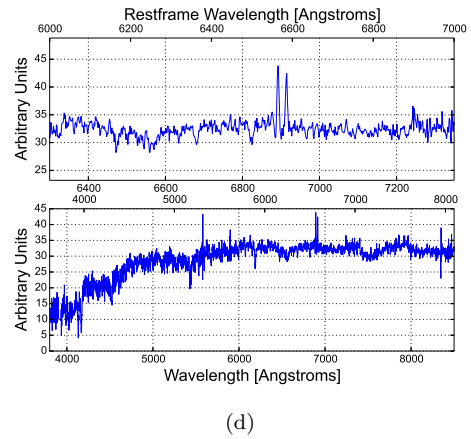
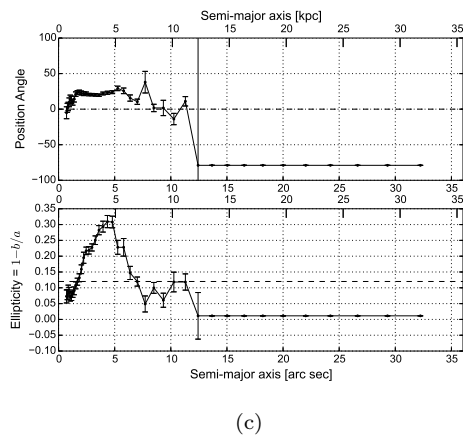
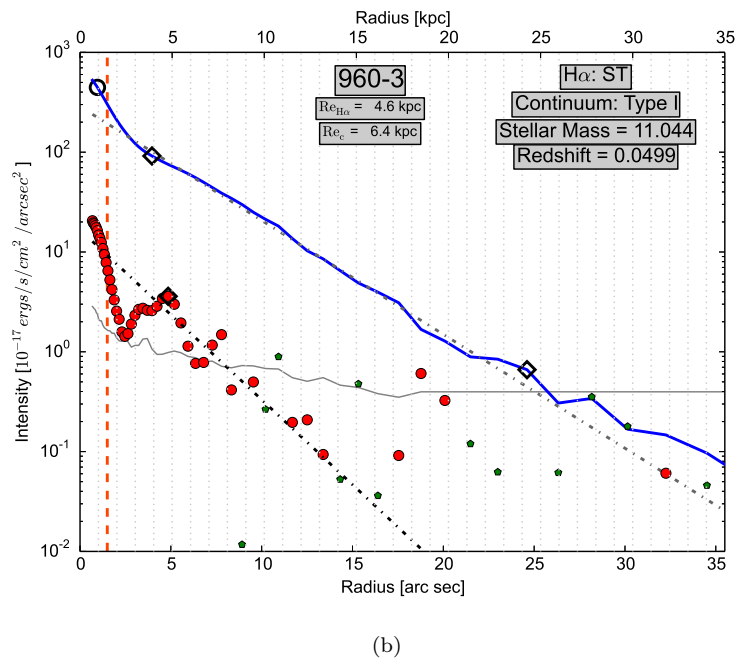
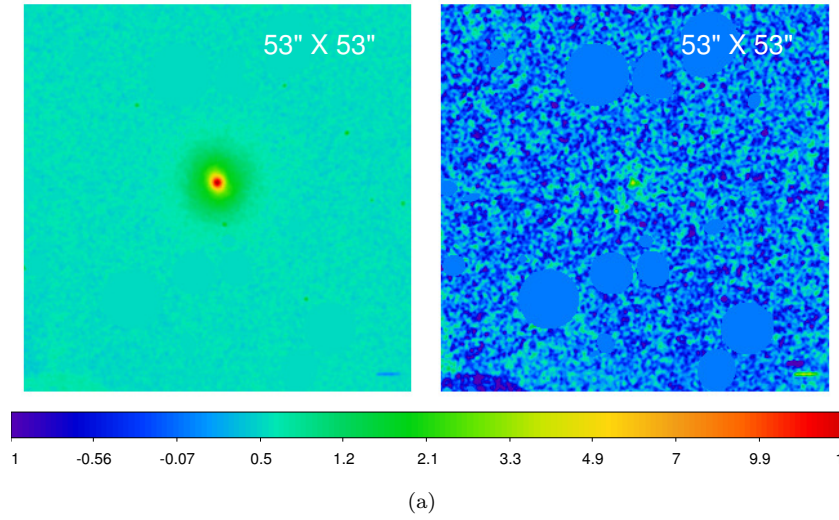


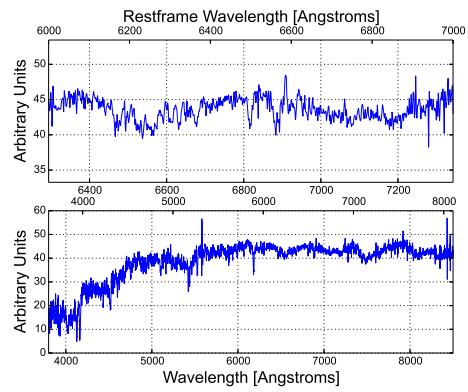
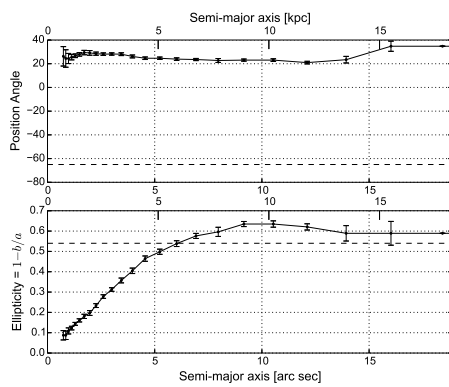
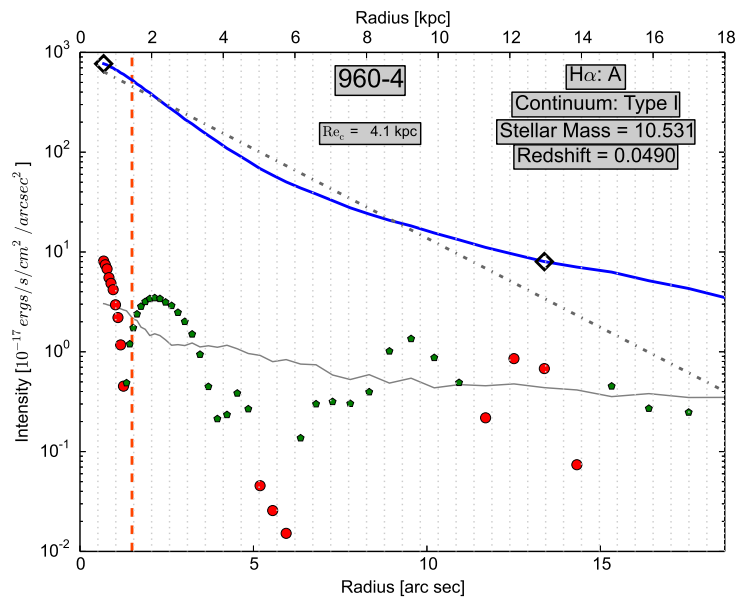
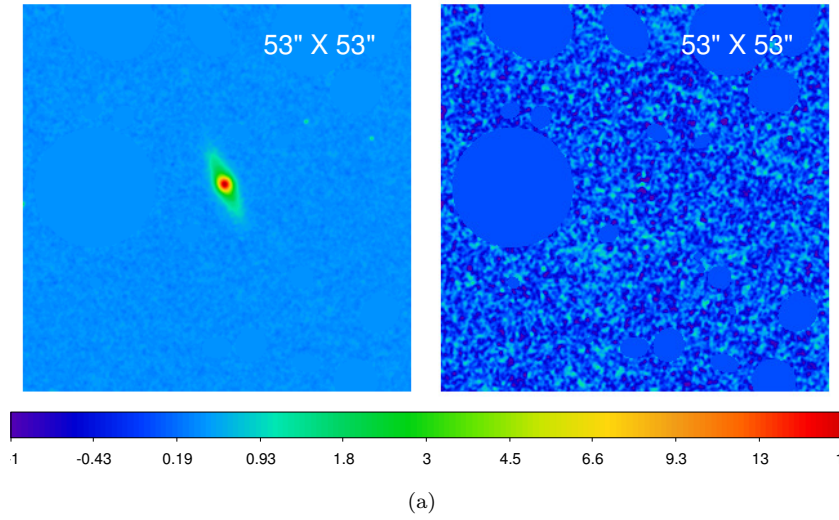
(c)

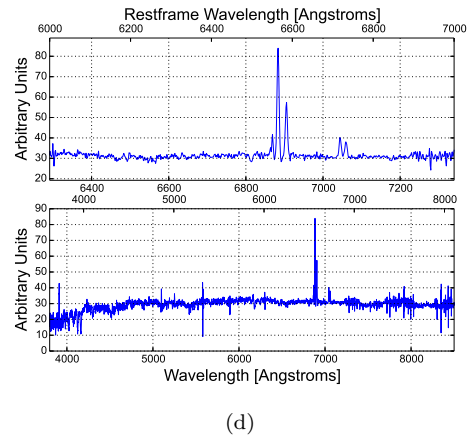
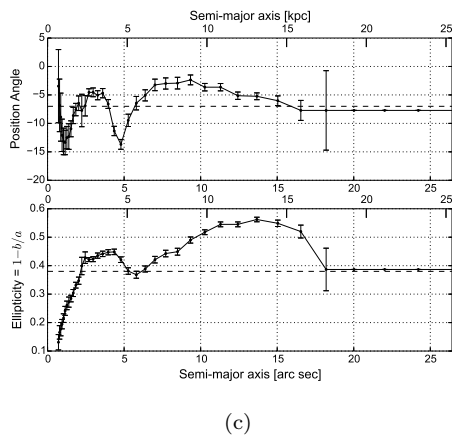
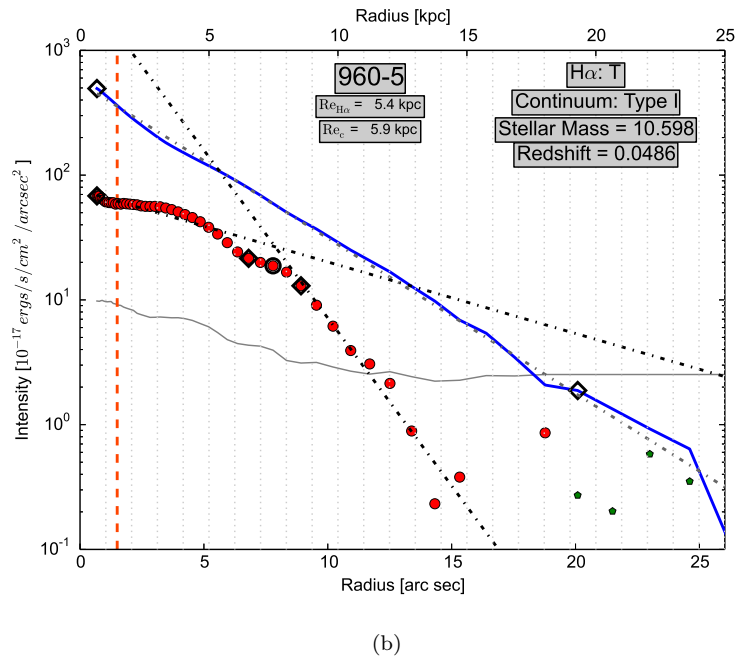
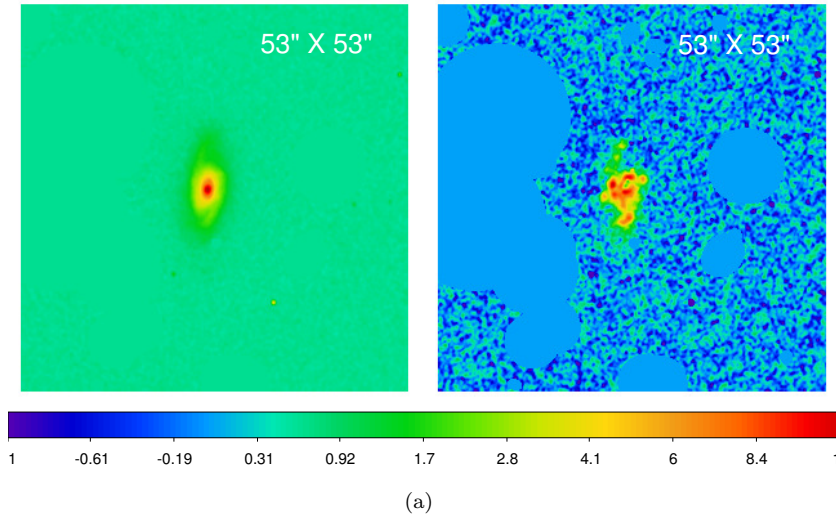


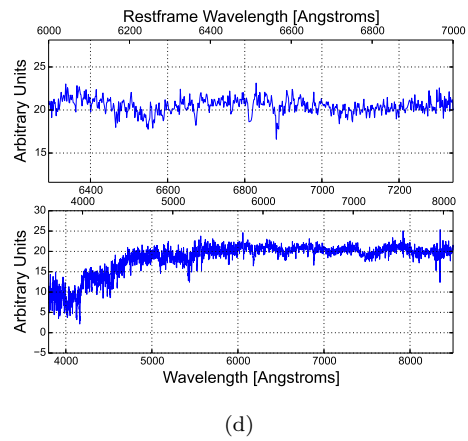
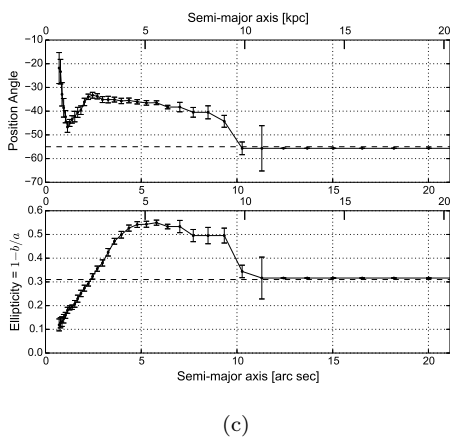
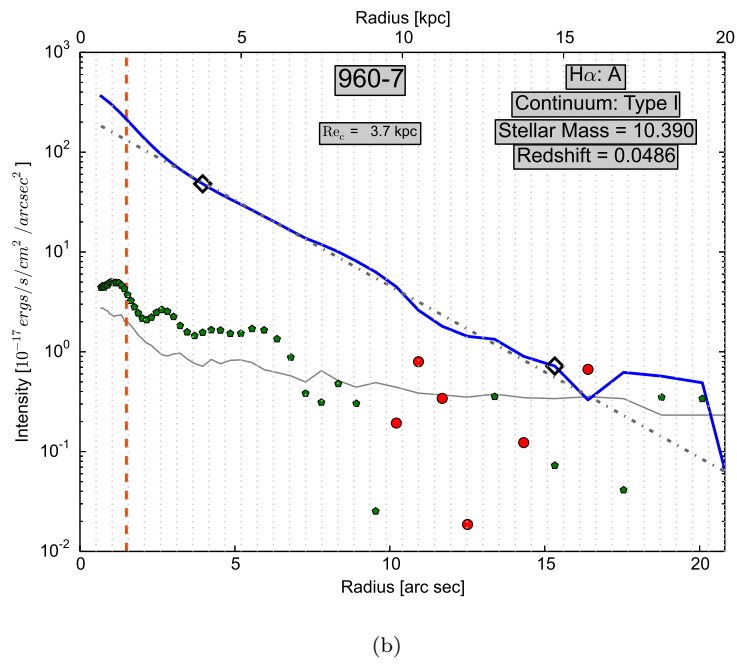
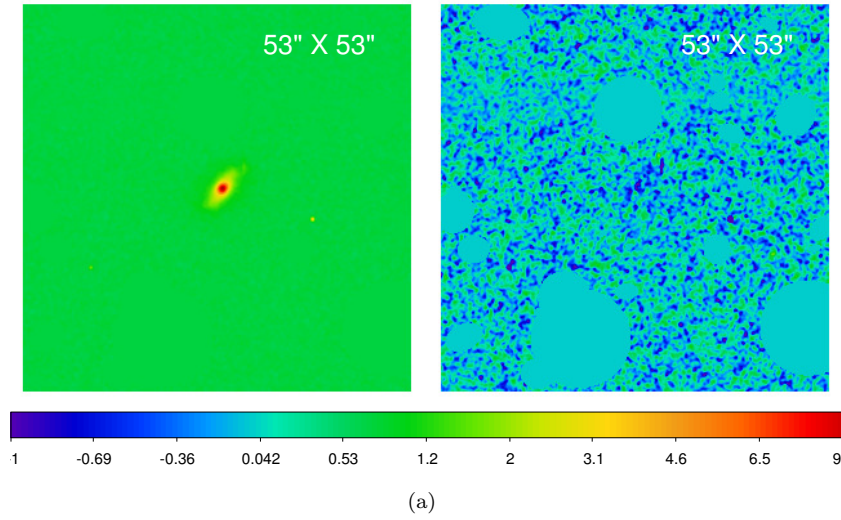
(d)

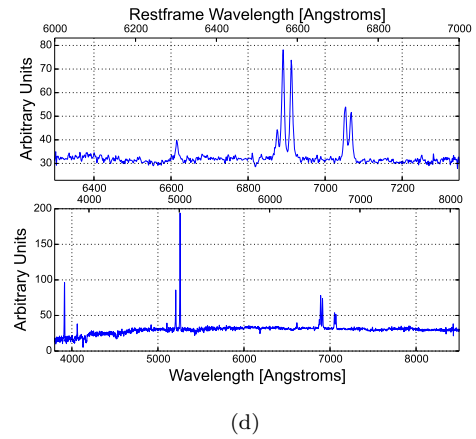
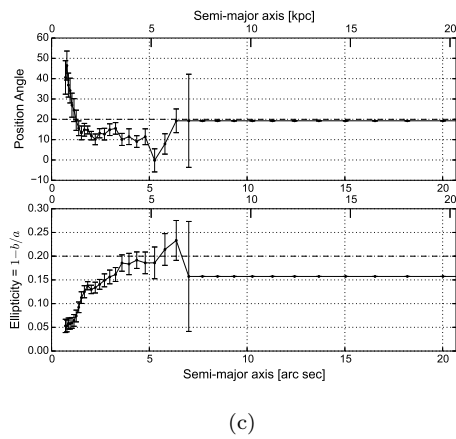
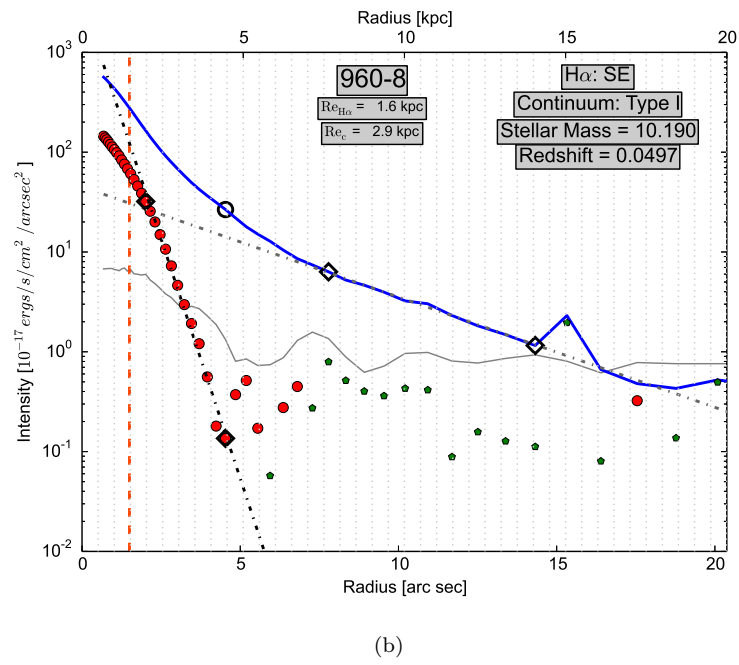
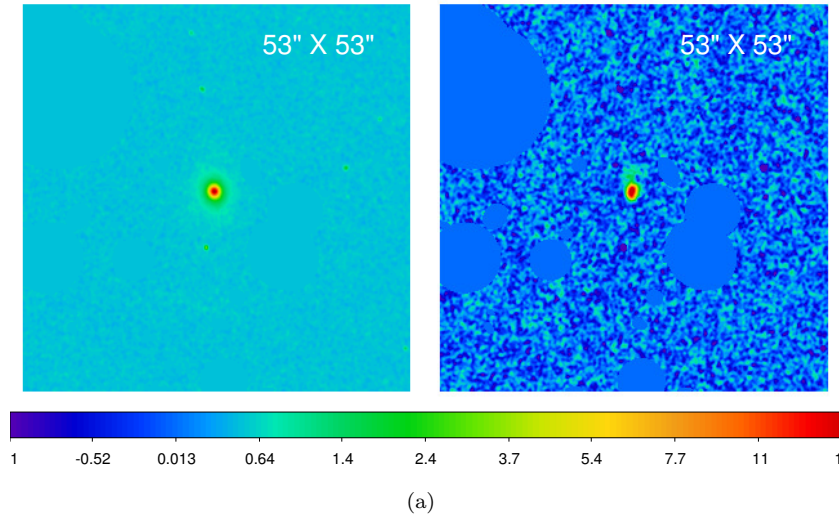


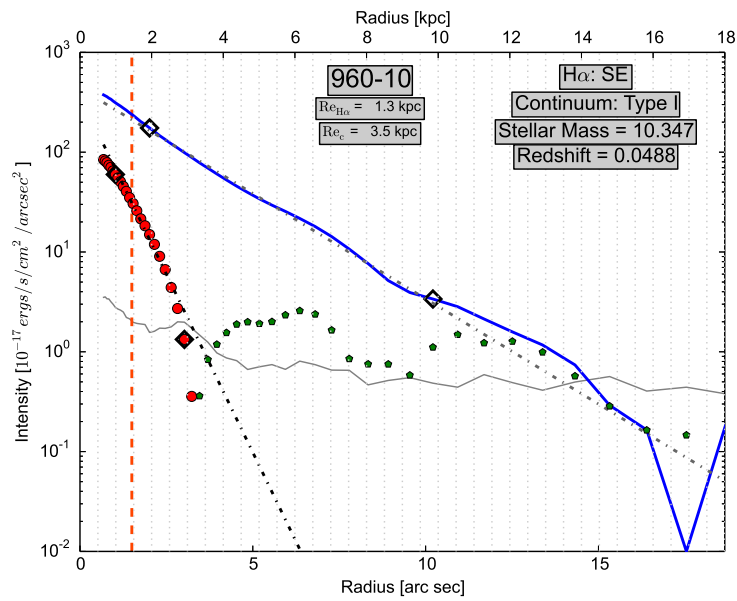
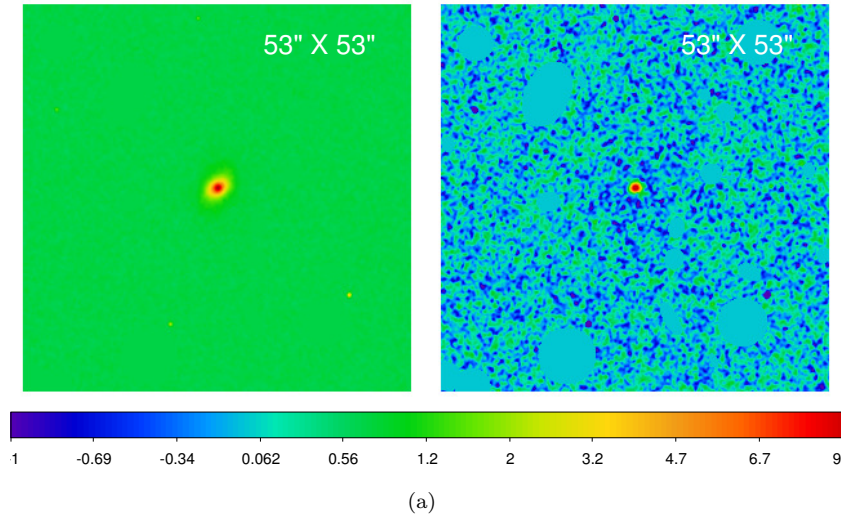




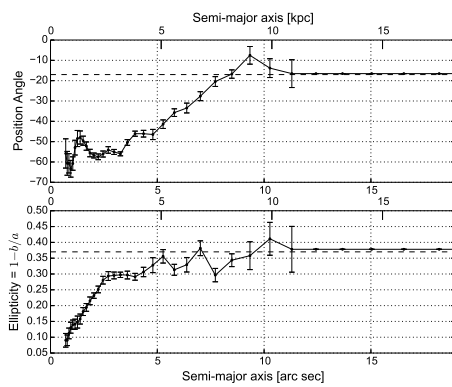




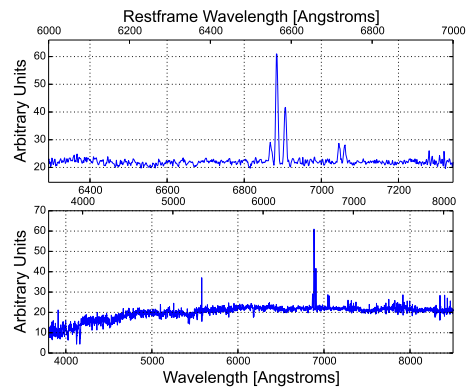




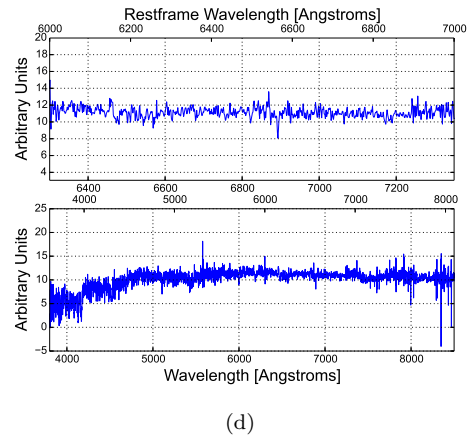
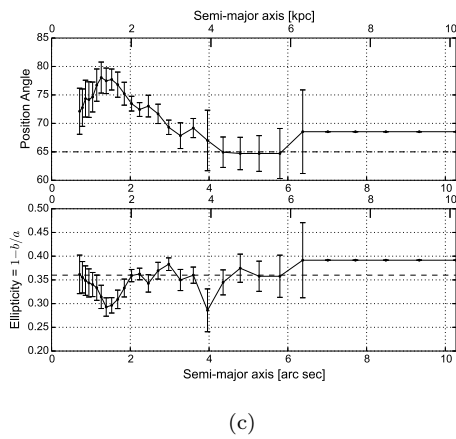
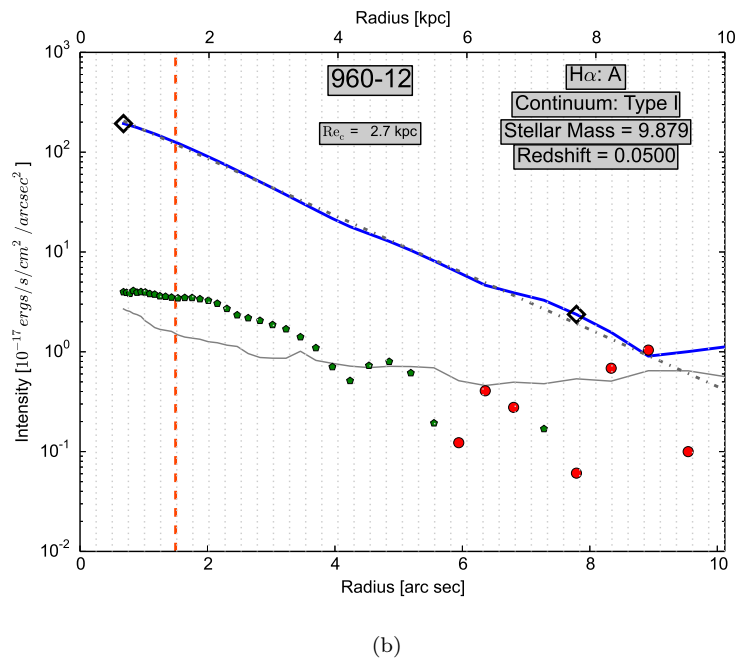
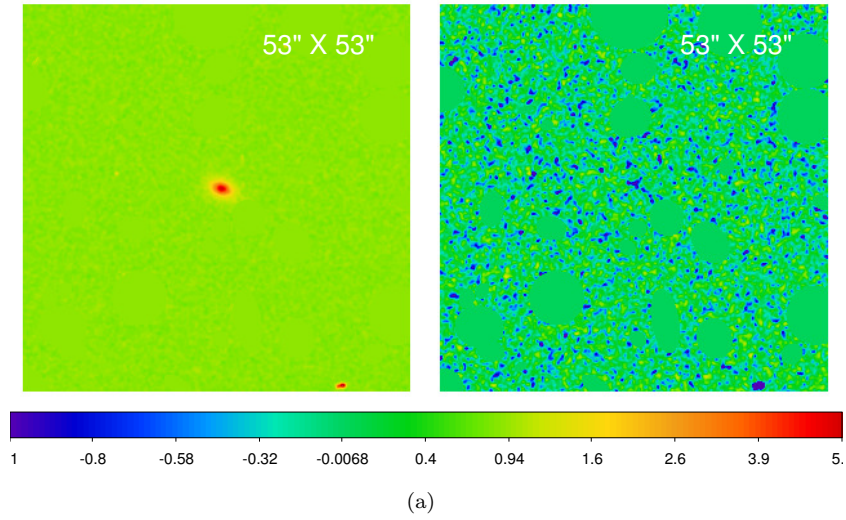
(b)

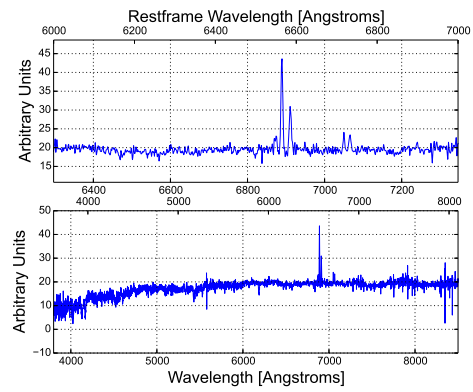
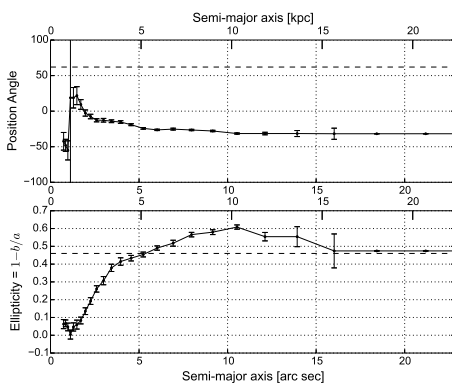
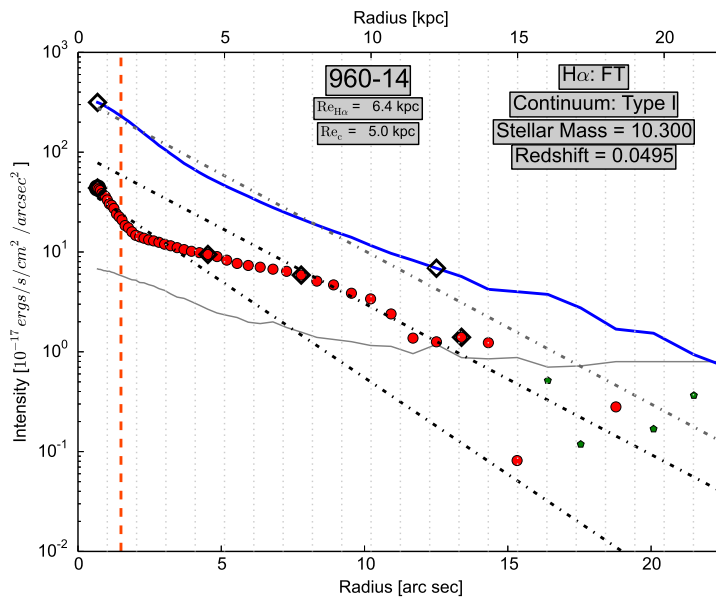
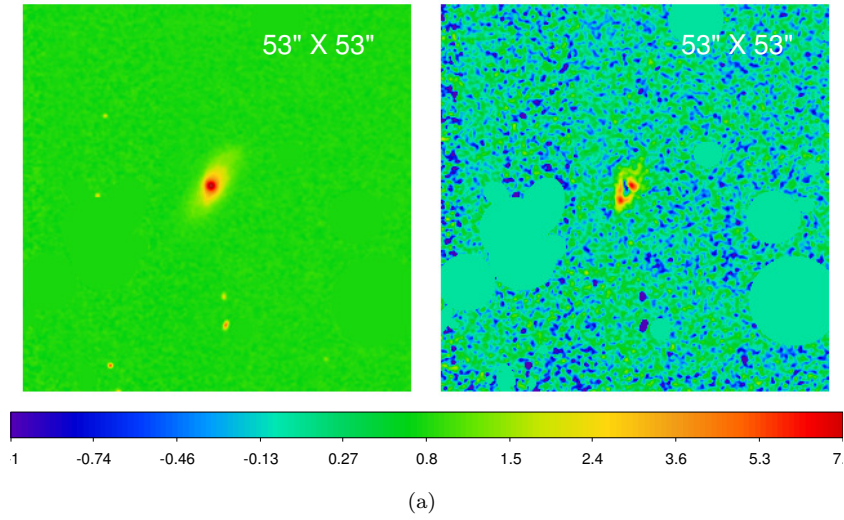


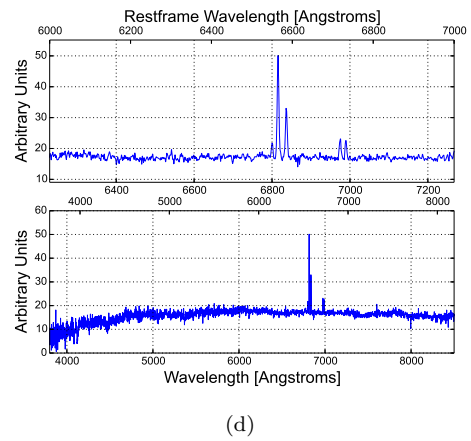
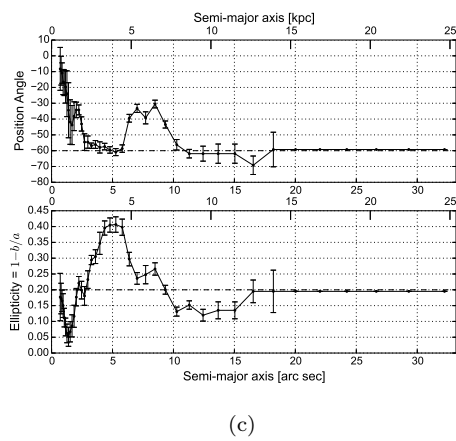
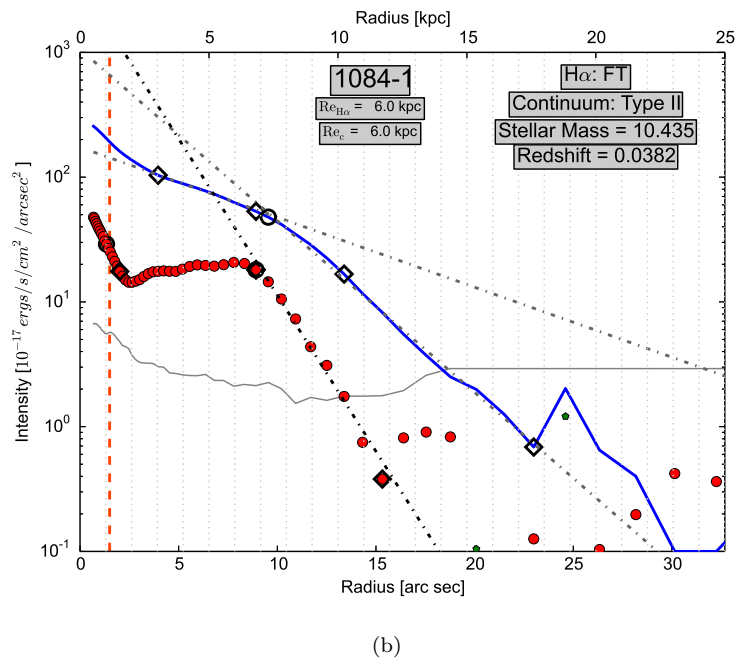
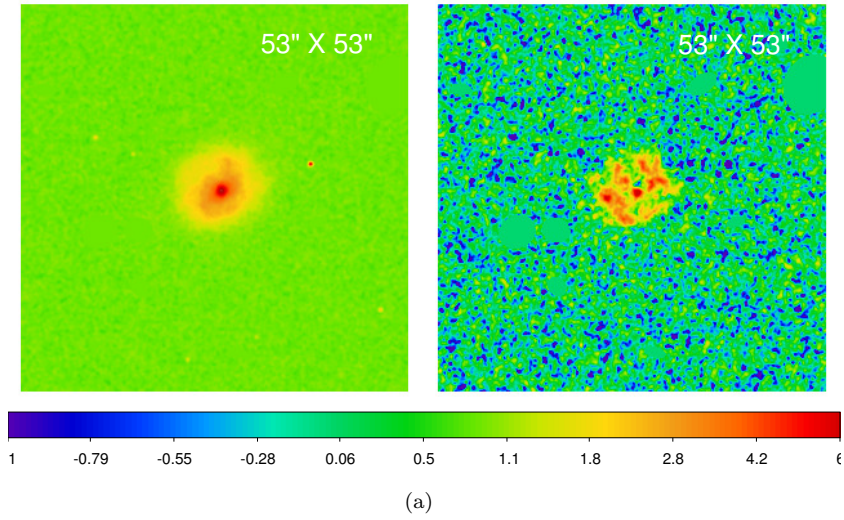
(c)

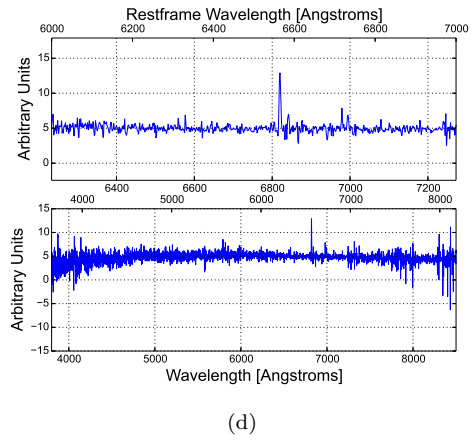
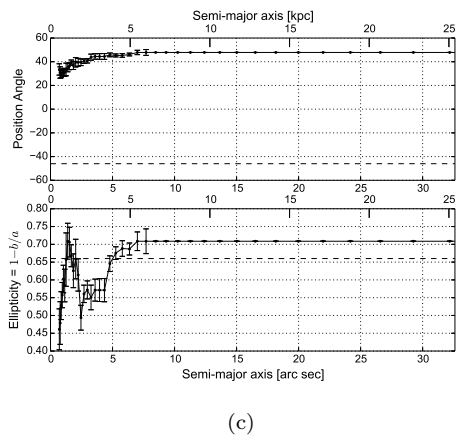
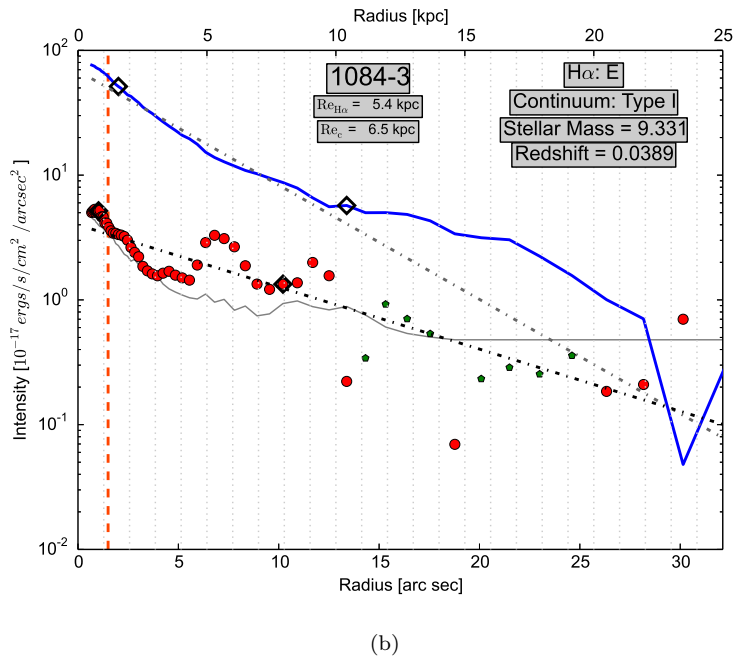
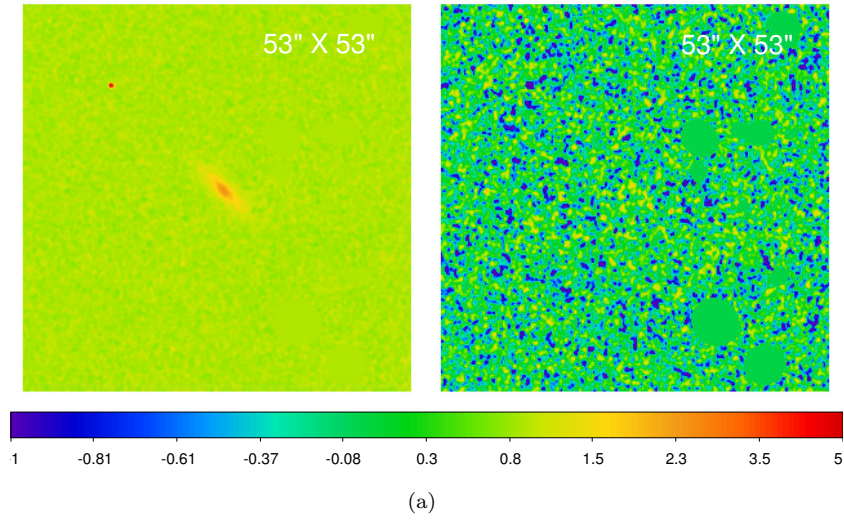


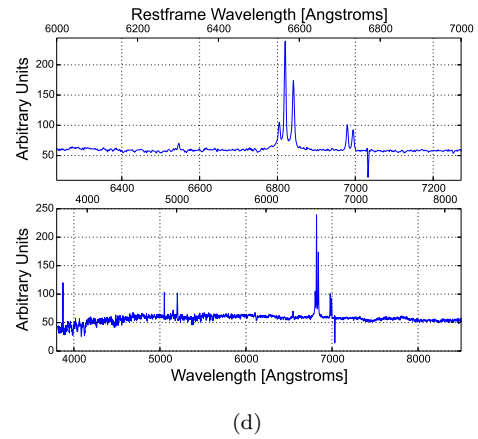
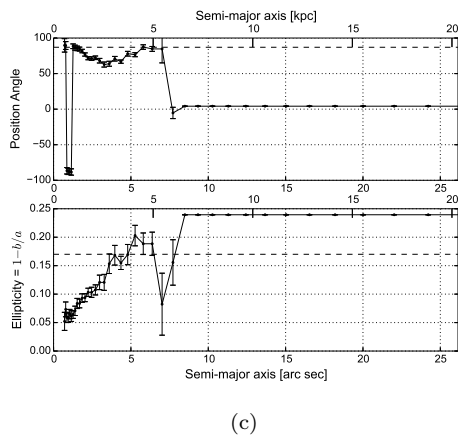
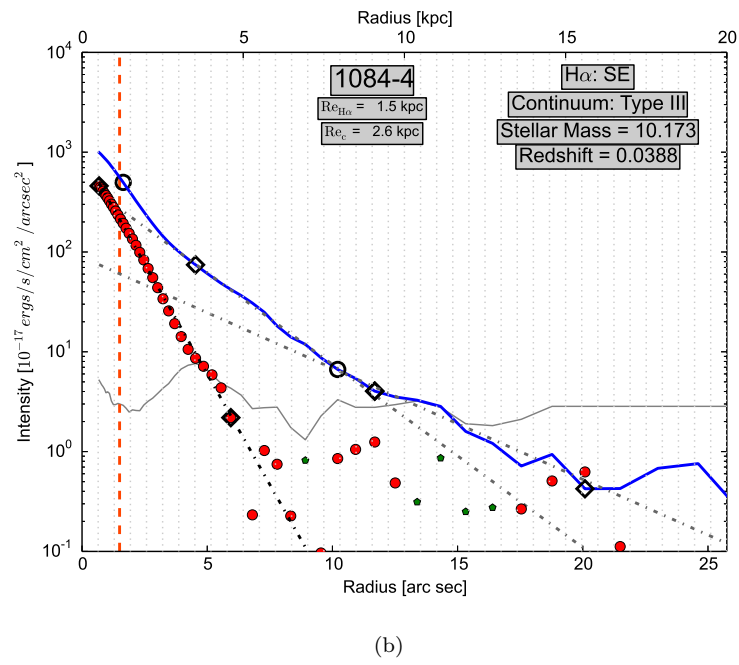
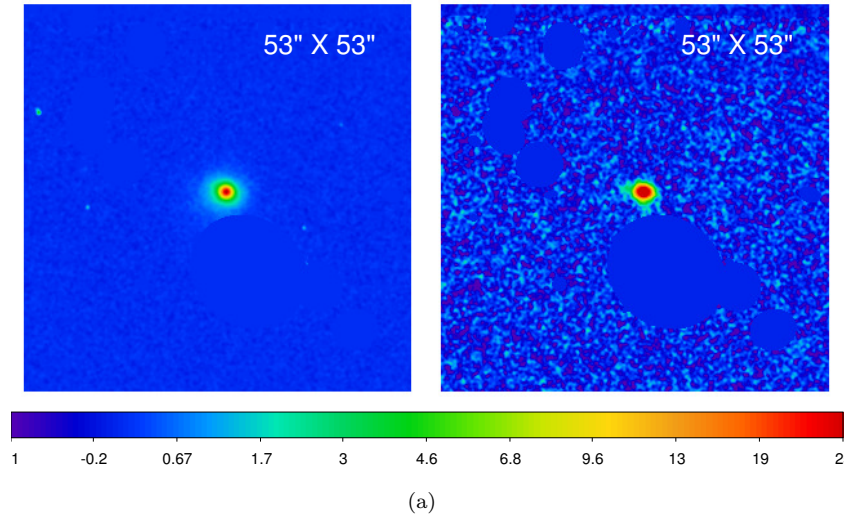
(d)

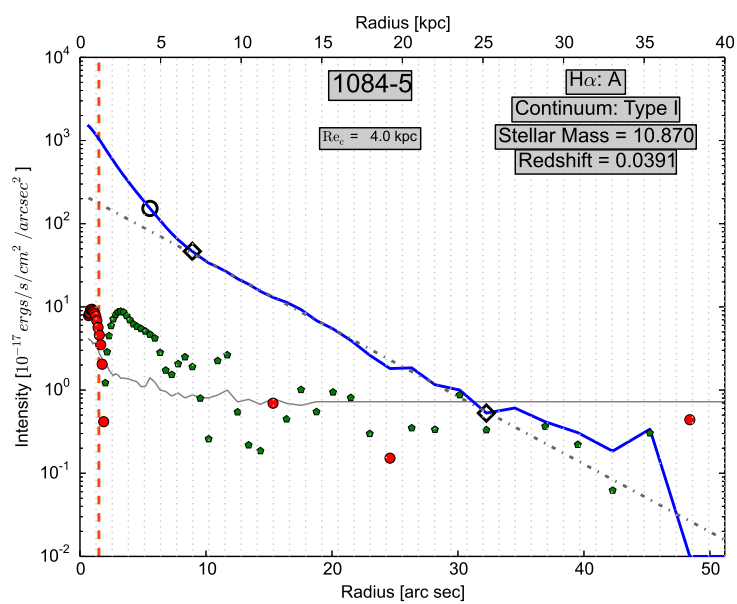
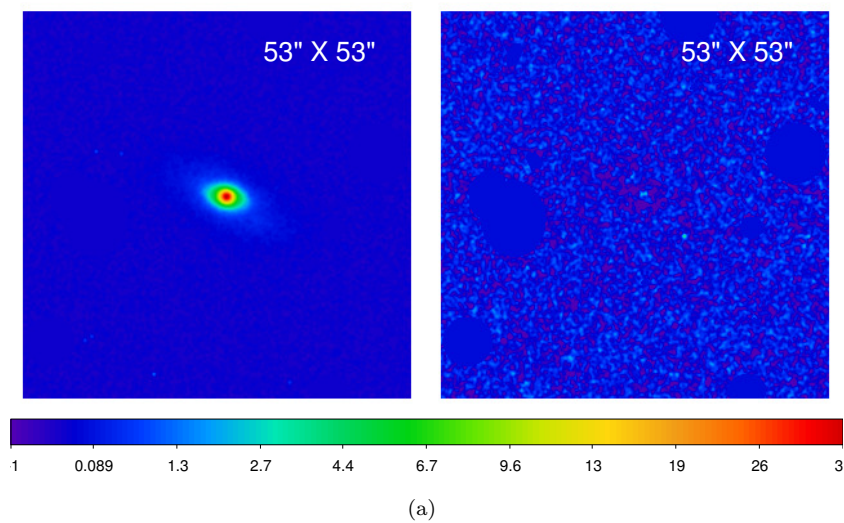




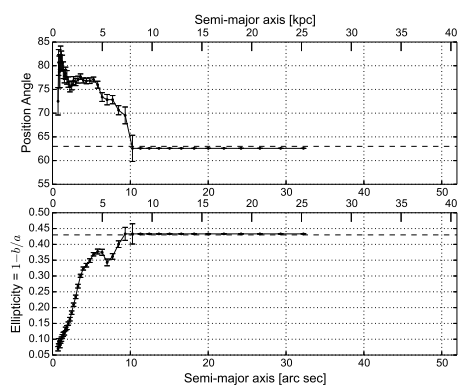




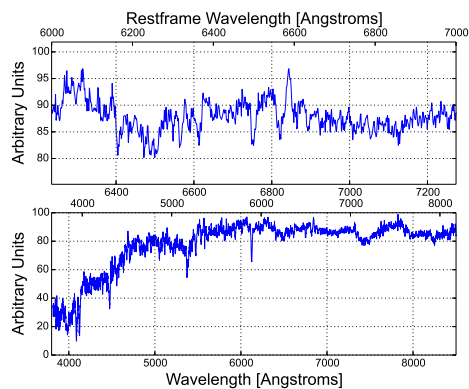




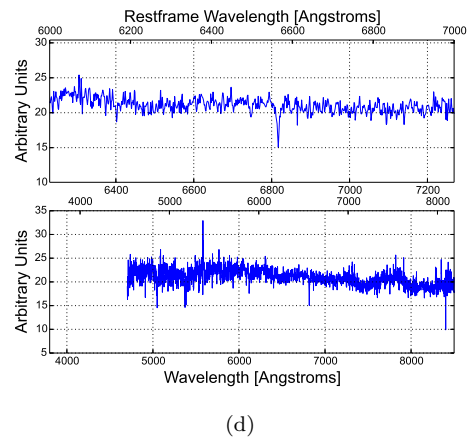
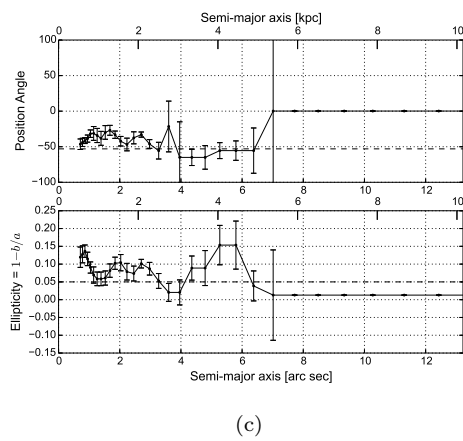
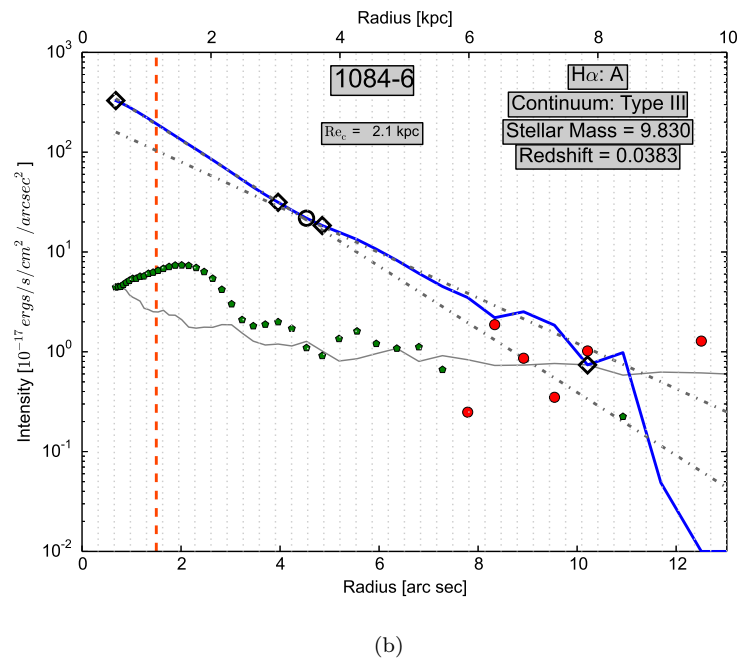
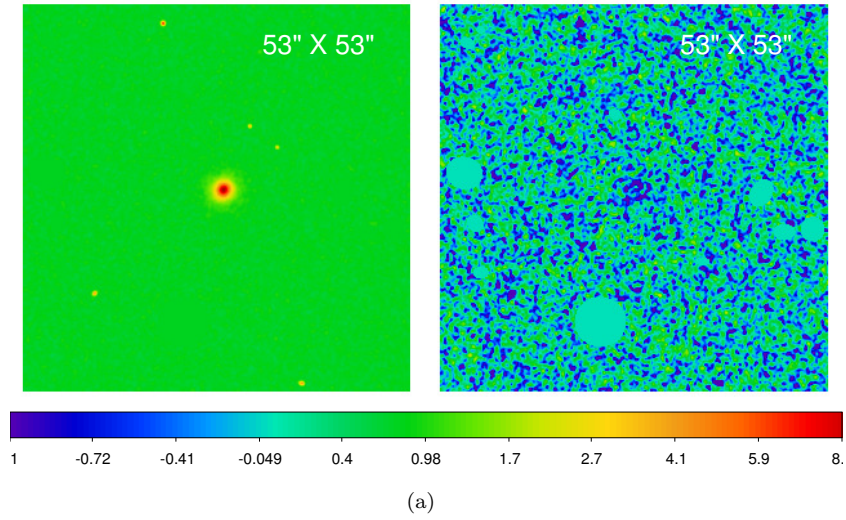
(b)

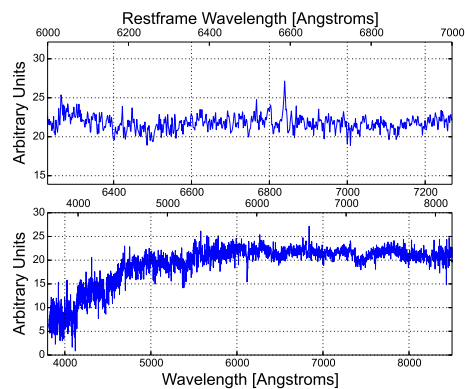
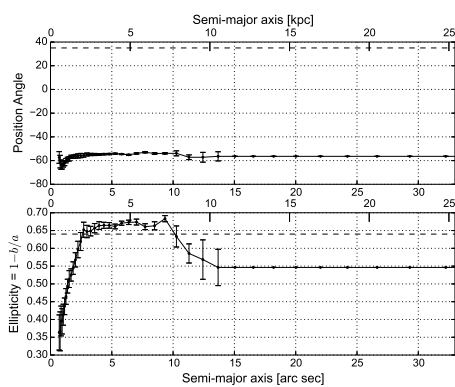
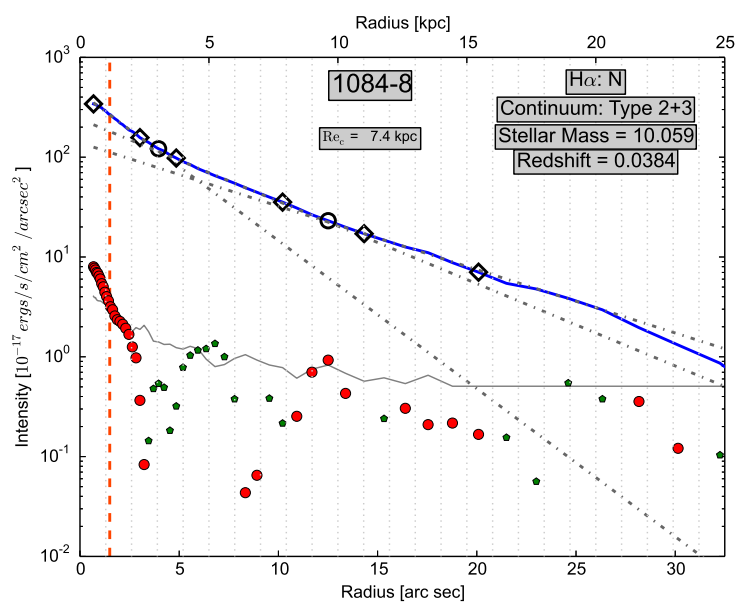
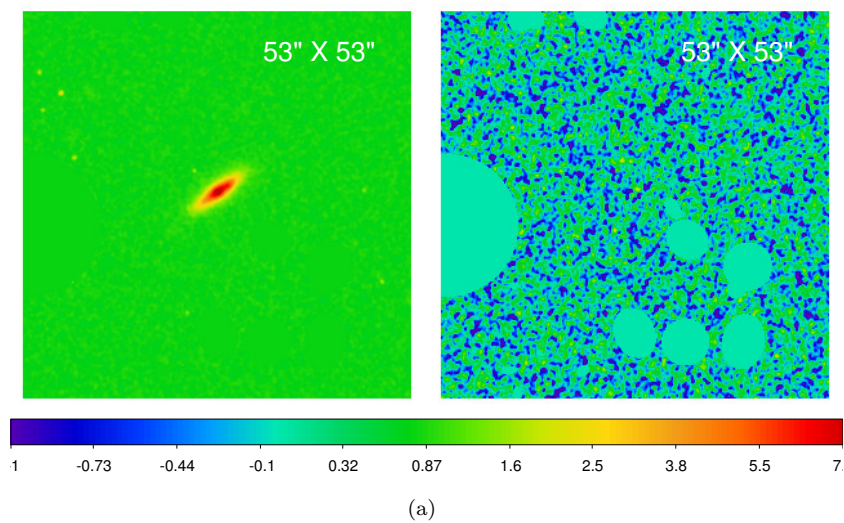


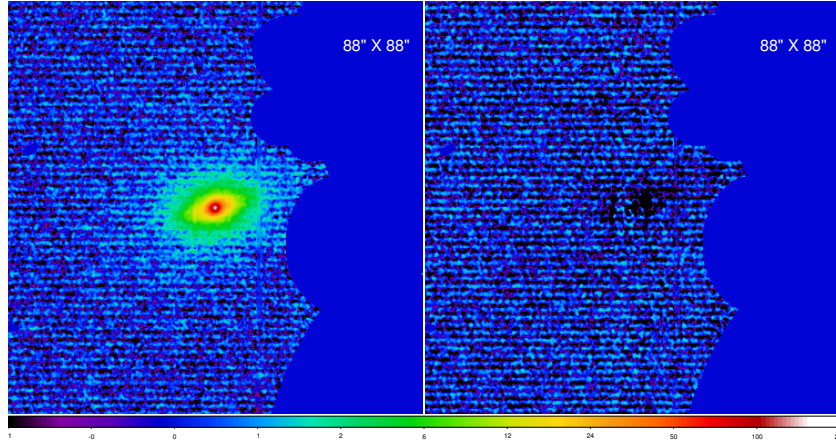
(c)



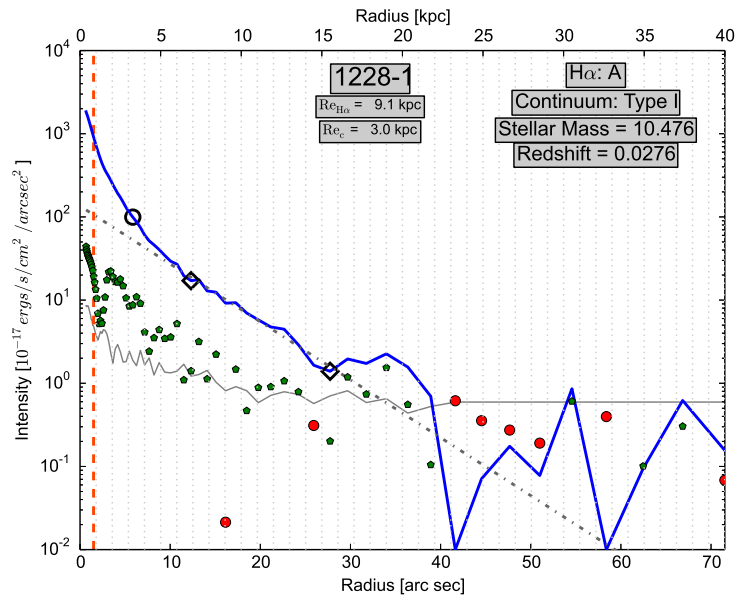
(d)



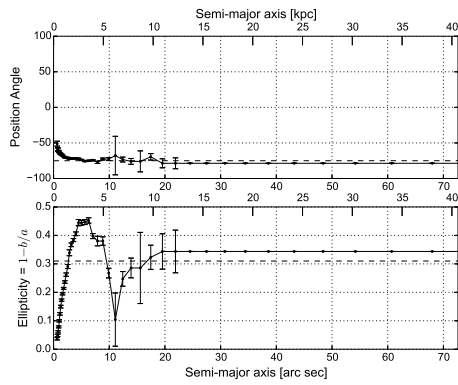




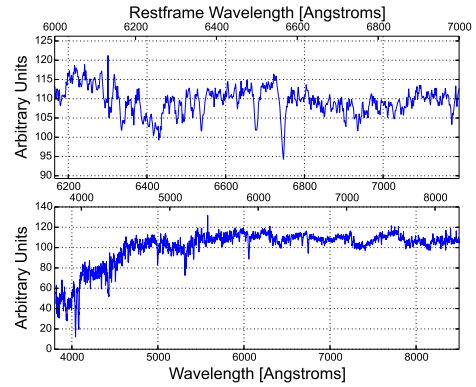
(a)



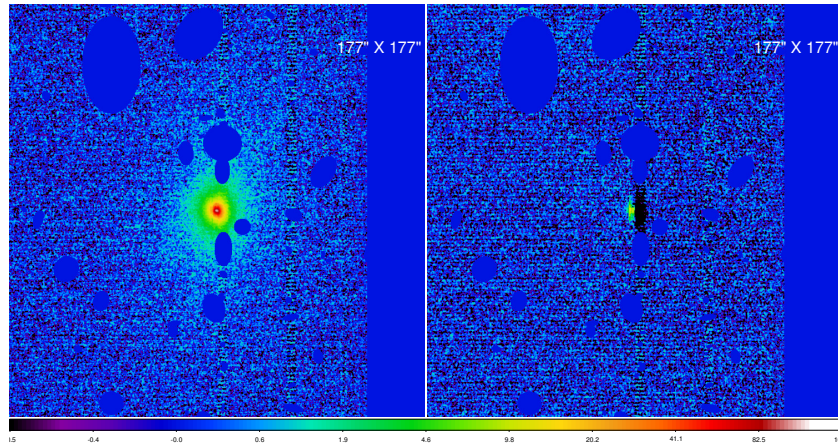
(b)



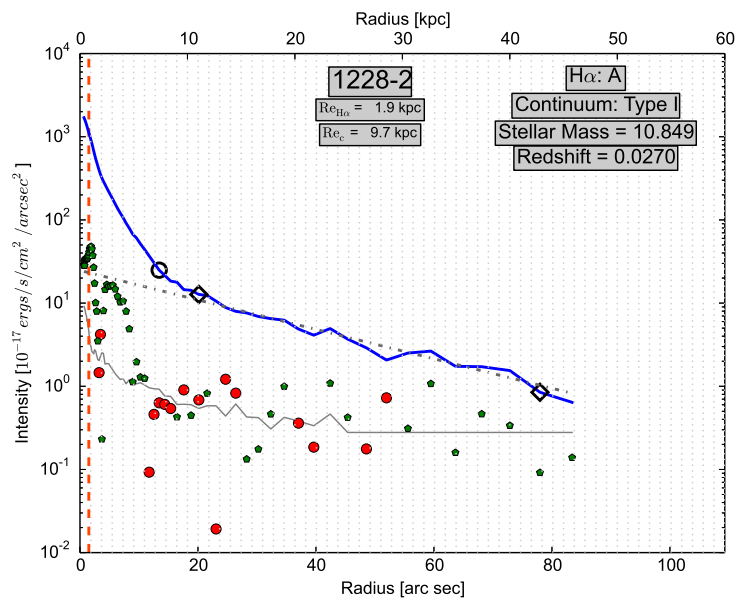
(c)



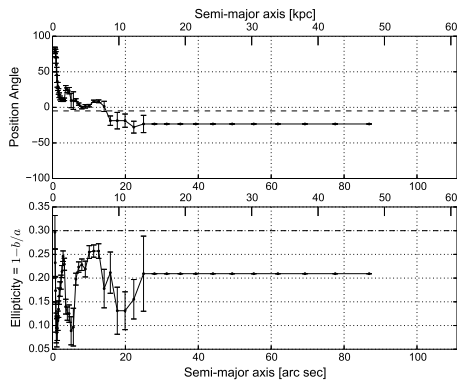
(d)



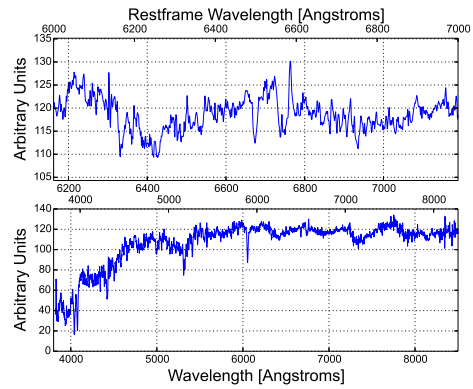
(a)



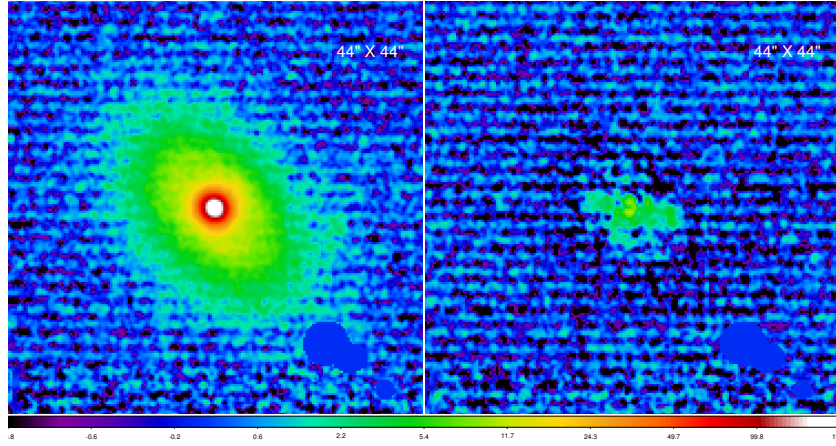
(b)



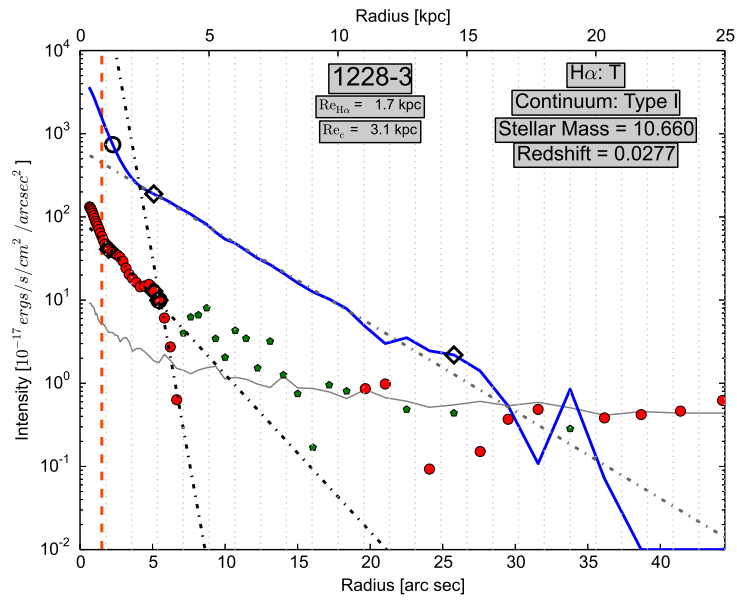
(c)



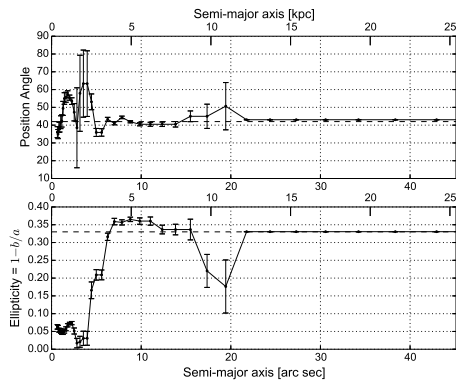
(d)



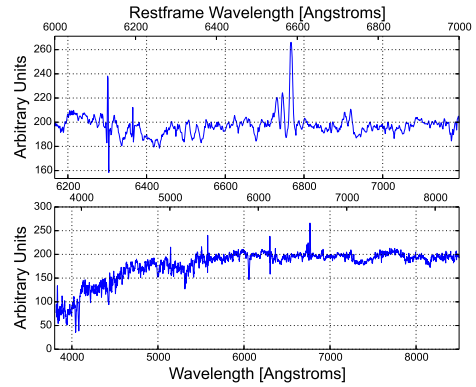
(a)



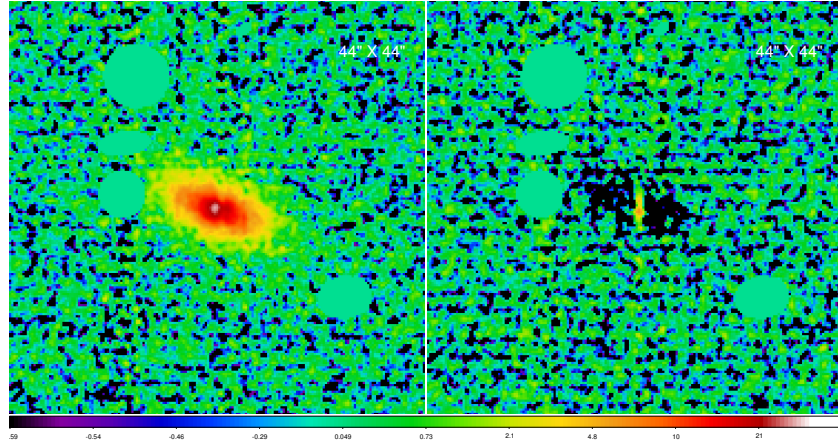
(b)



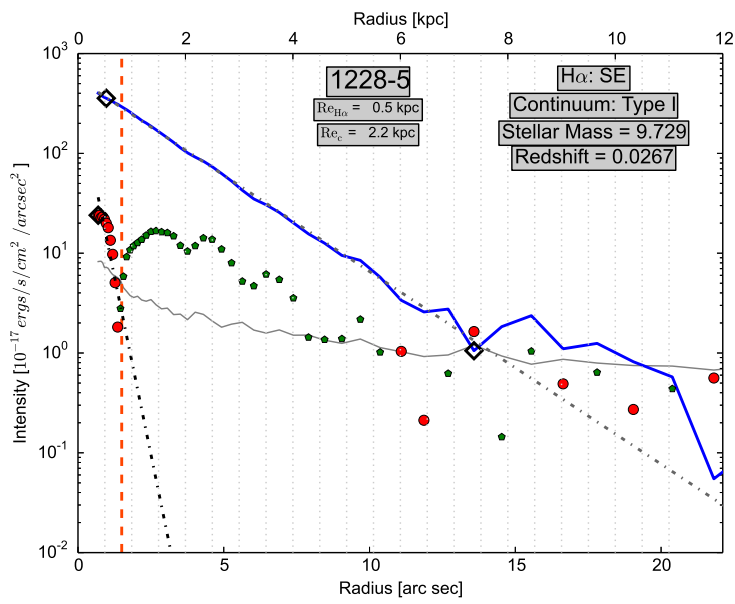
(c)



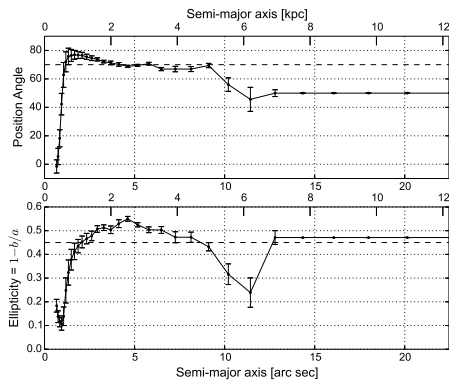
(d)



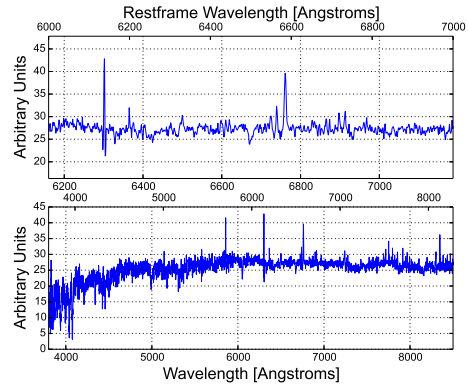
(a)



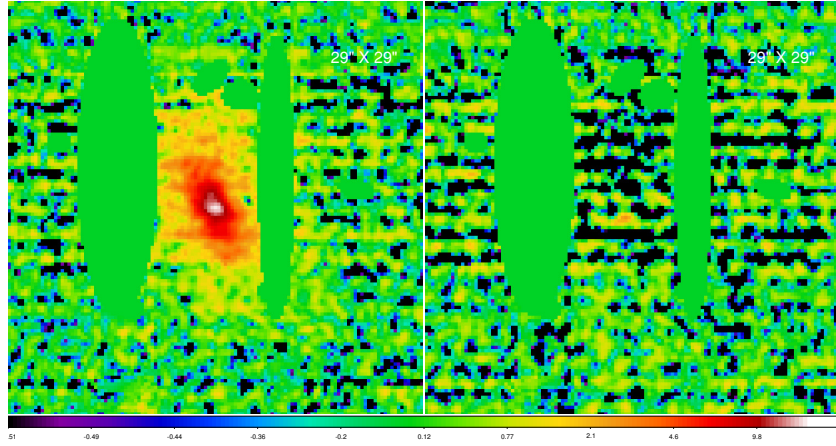
(b)



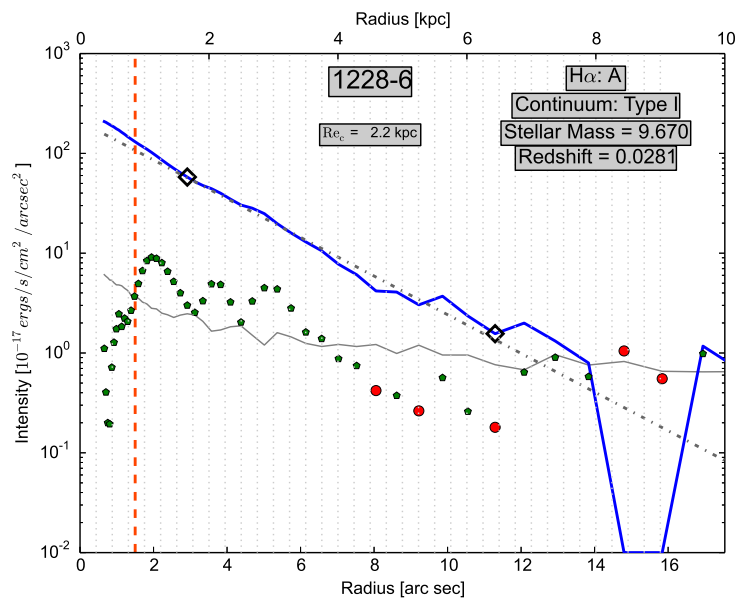
(c)



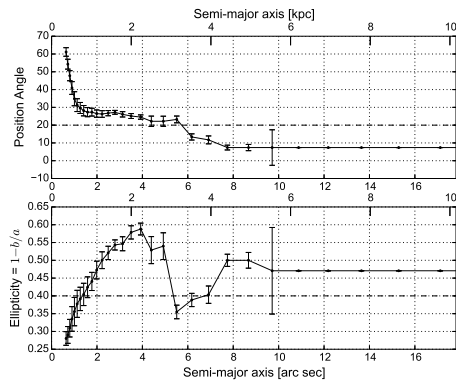
(d)



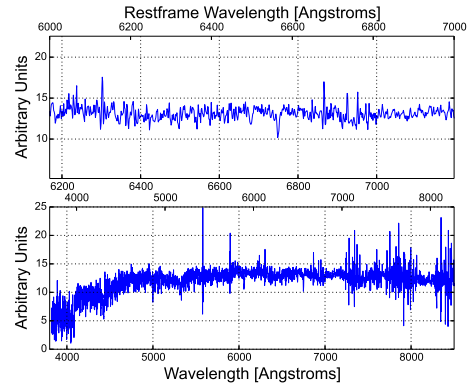
(a)



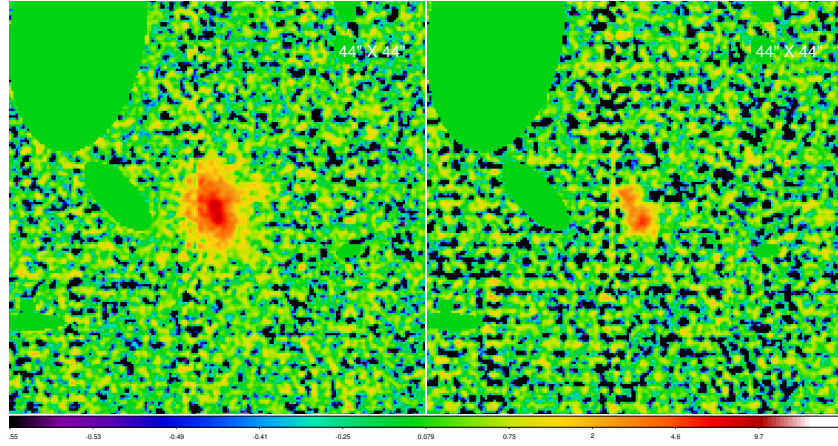
(b)



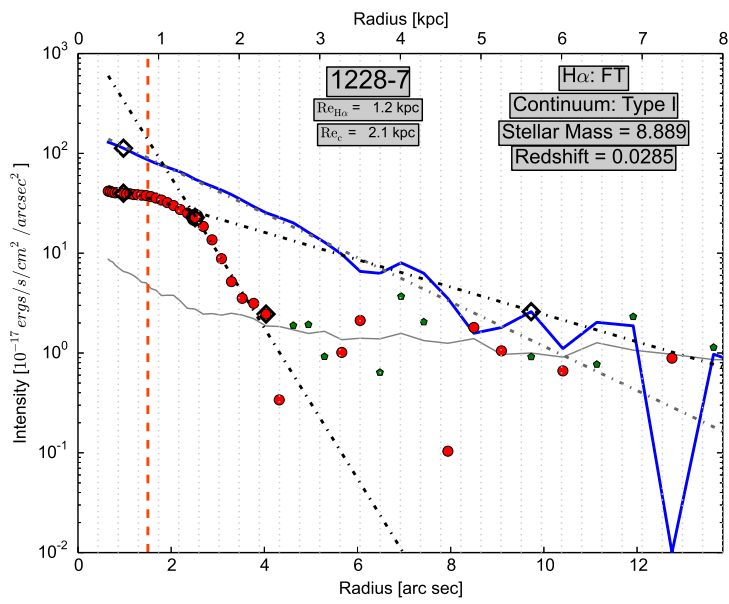
(c)



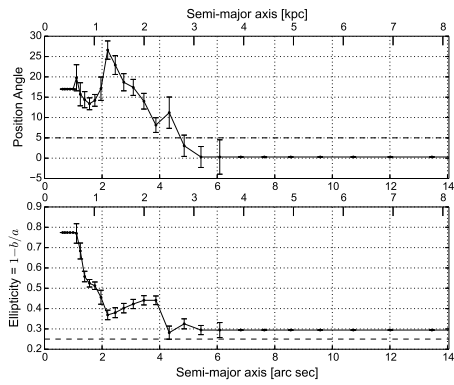
(d)



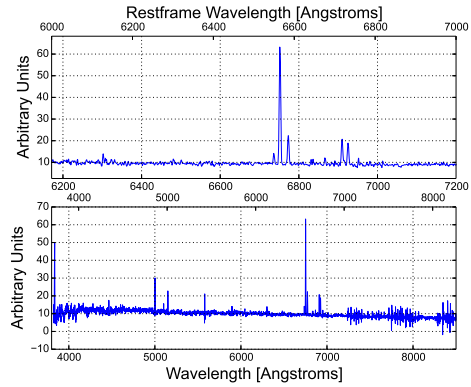
(a)



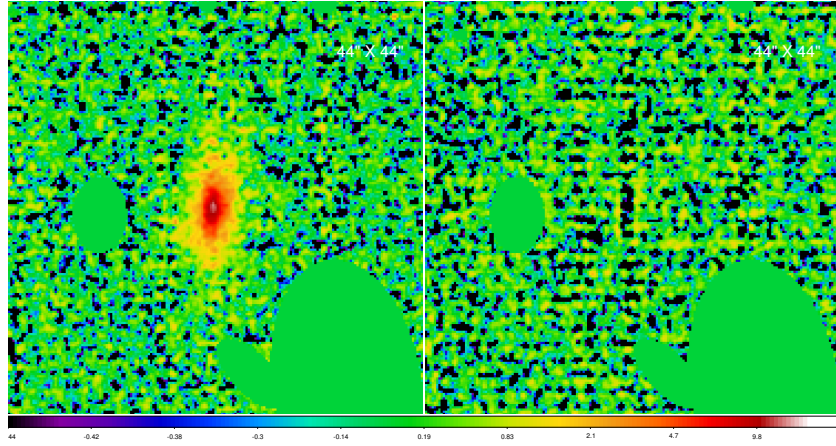
(b)



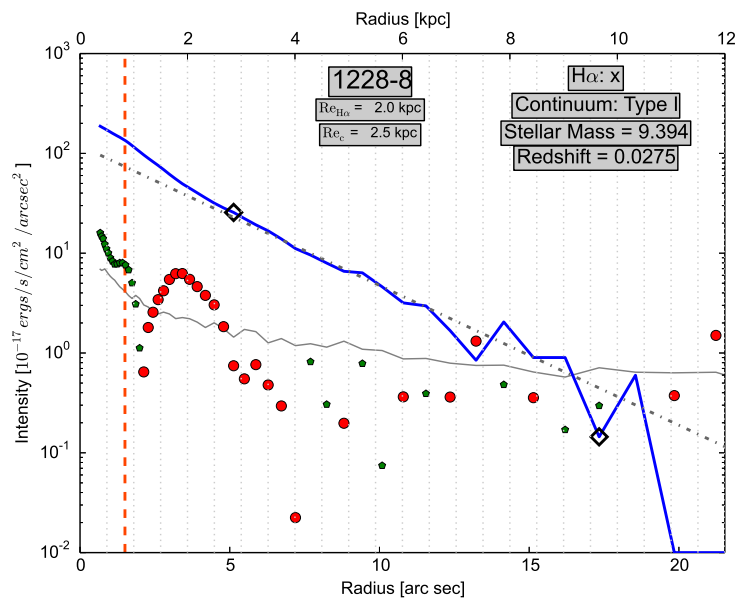
(c)



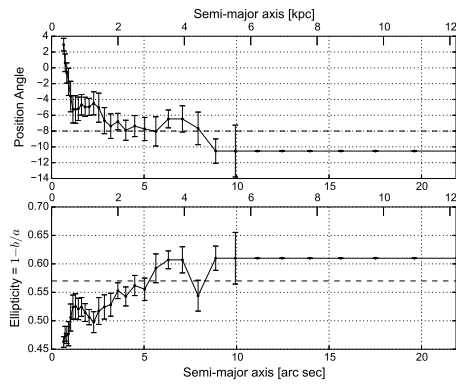
(d)



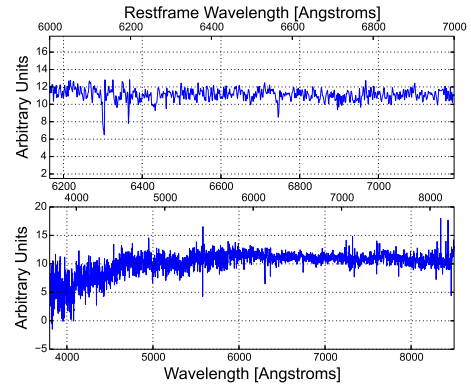
(a)



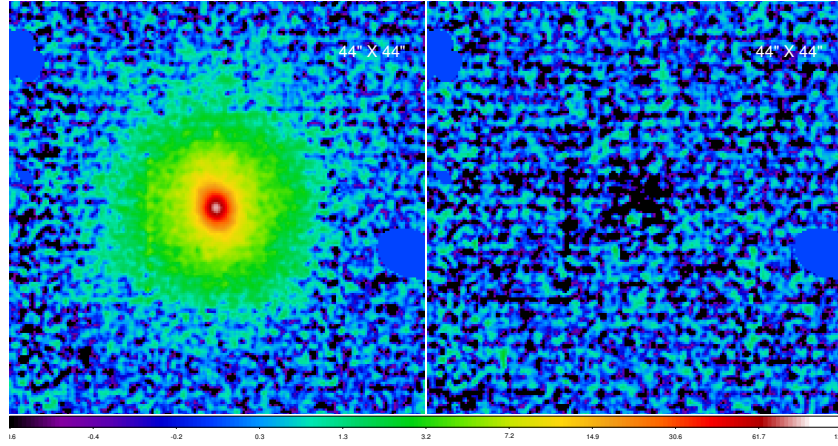
(b)



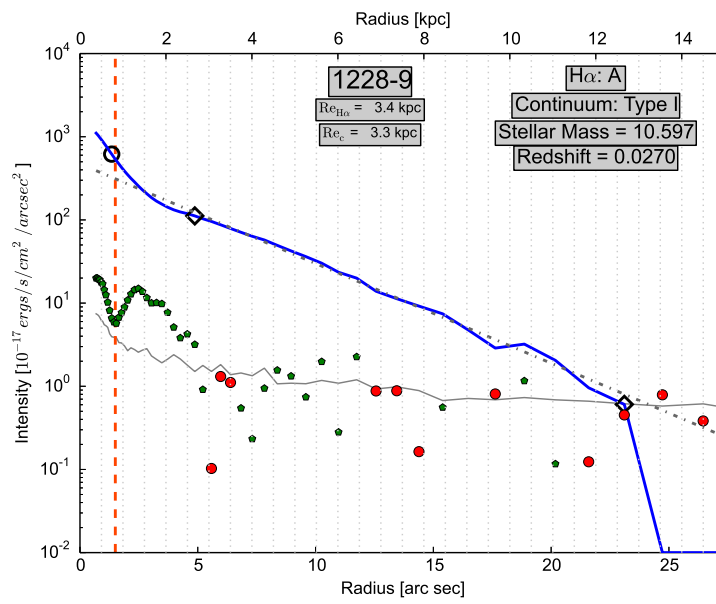
(c)



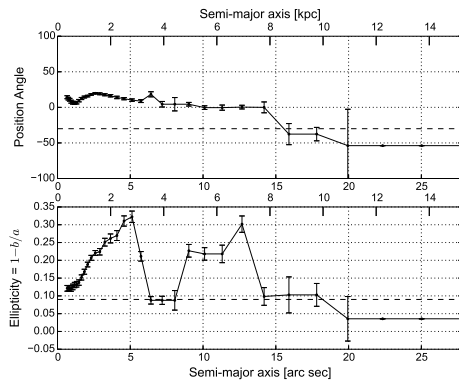
(d)



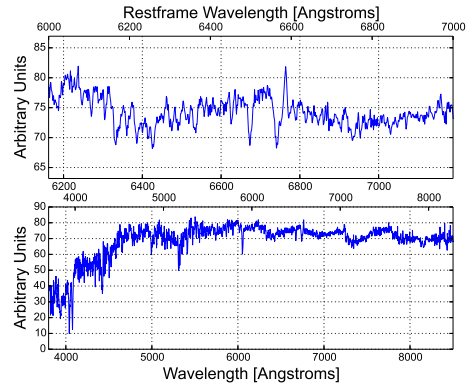
(a)



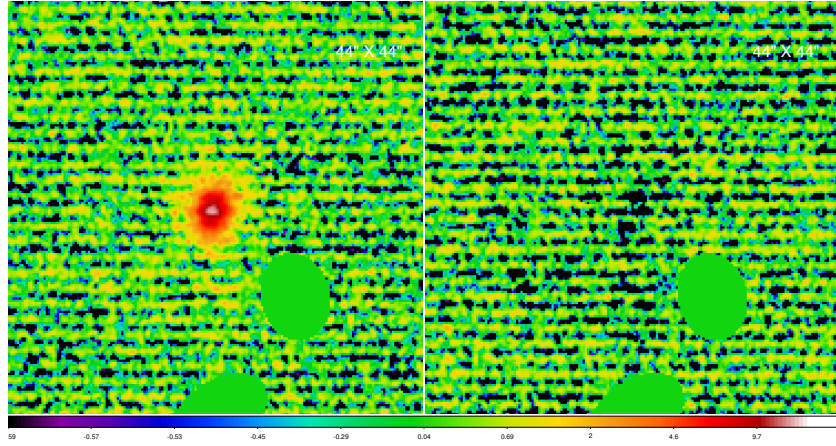
(b)



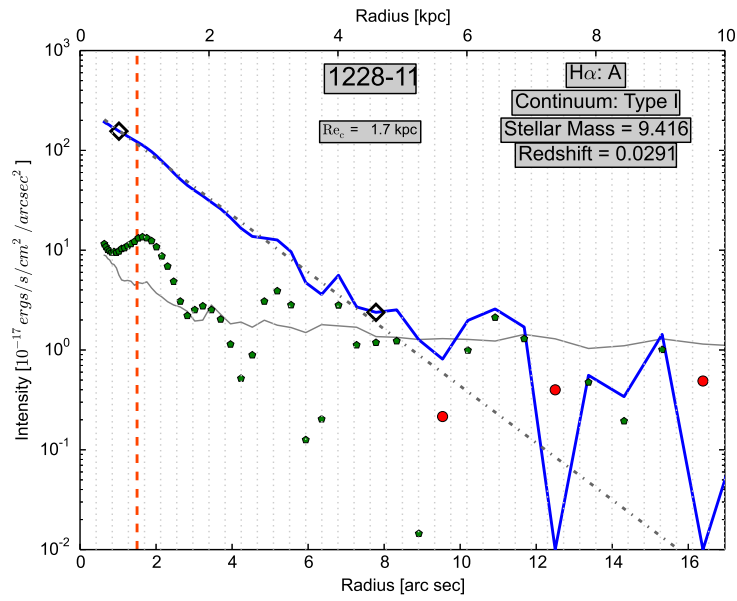
(c)



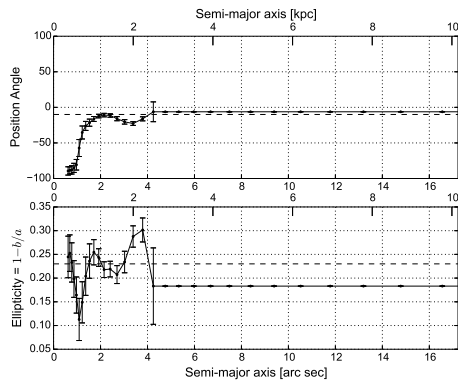
(d)



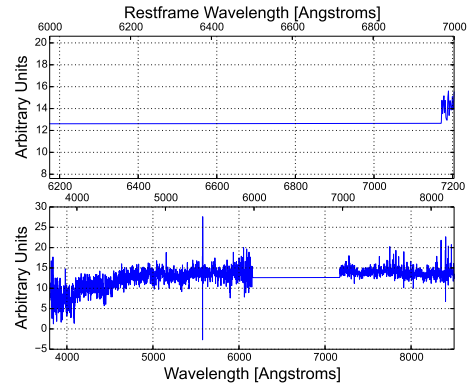
(a)



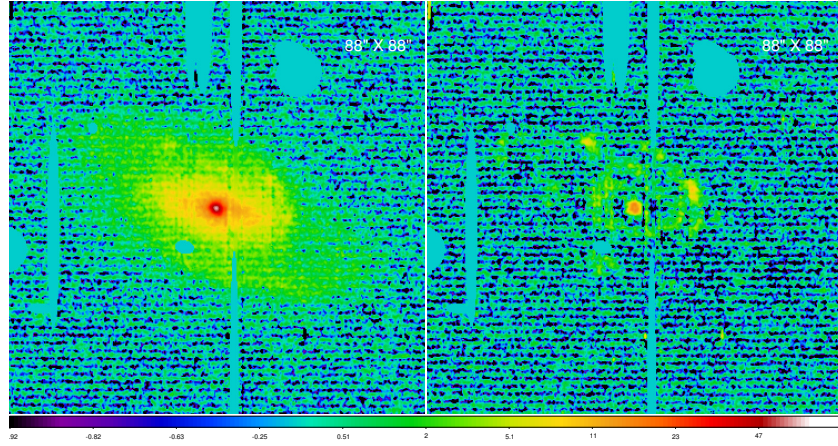
(b)



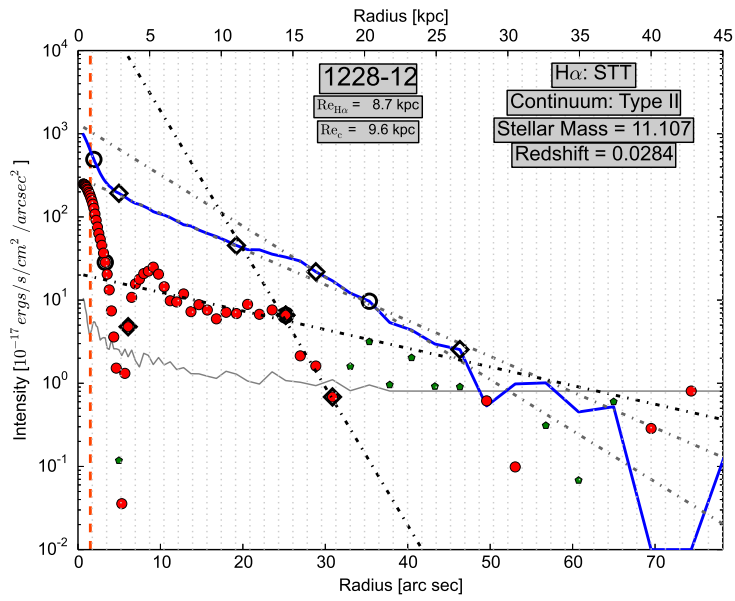
(c)



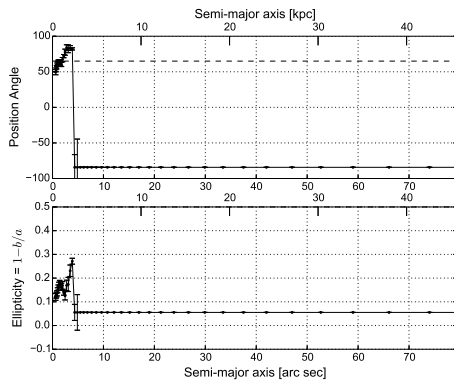
(d)



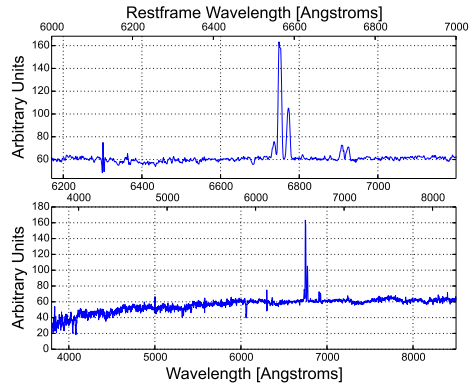
(a)



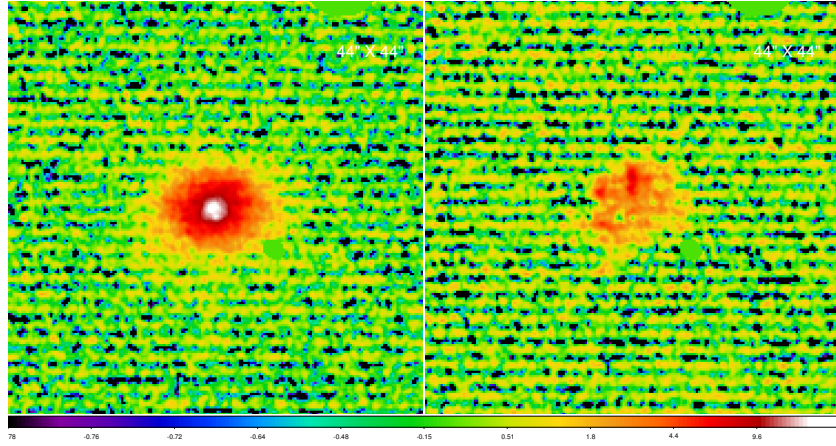
(b)



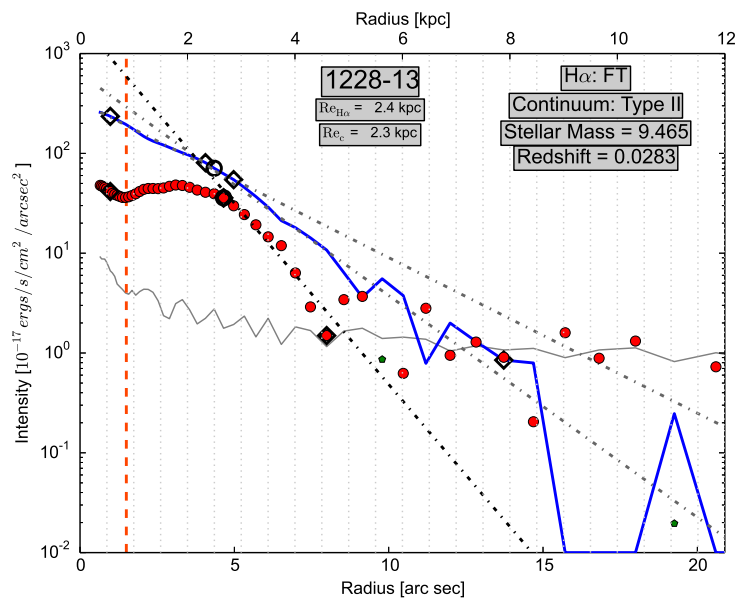
(c)



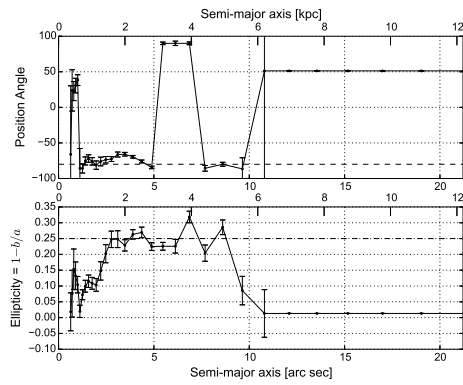
(d)



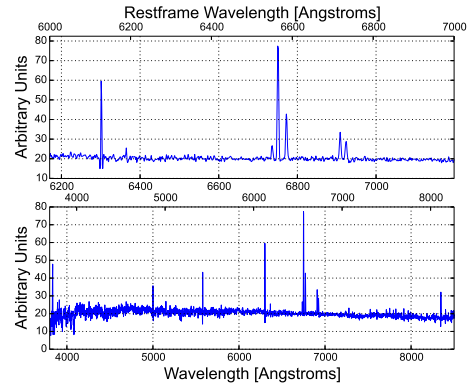
(a)



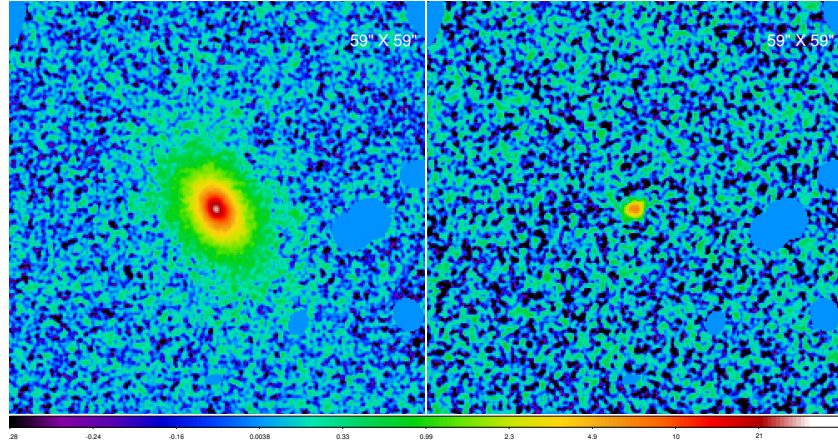
(b)



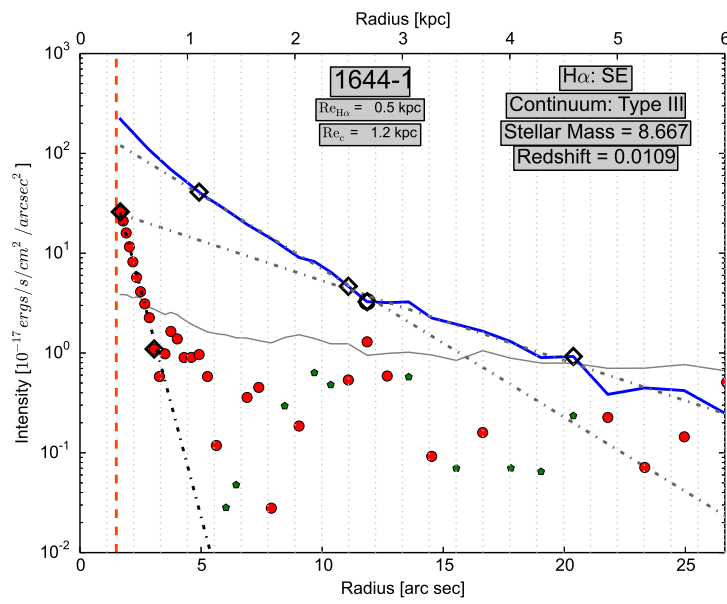
(c)



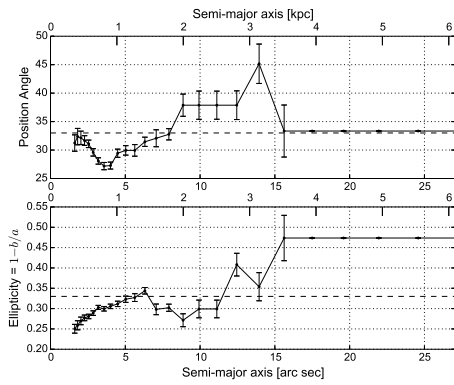
(d)



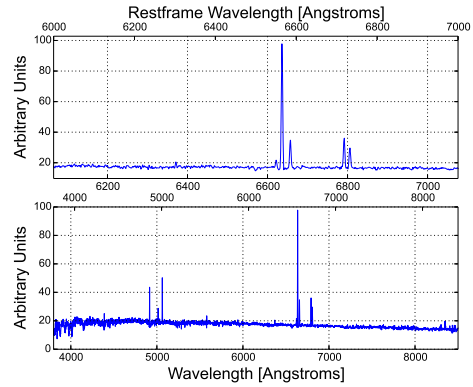
(a)



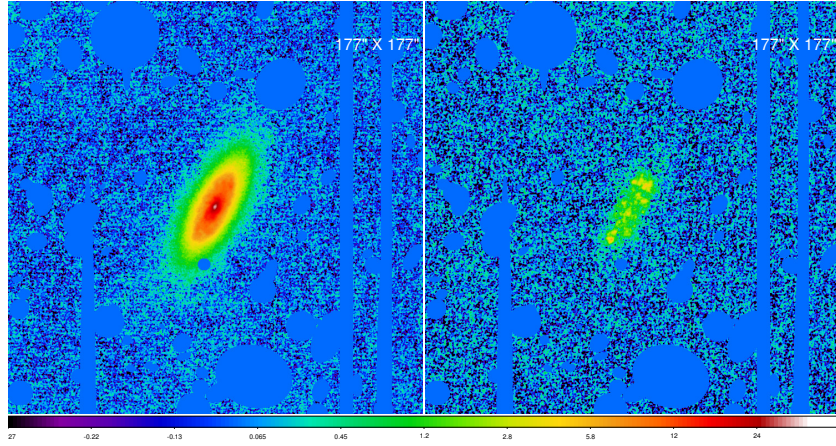
(b)



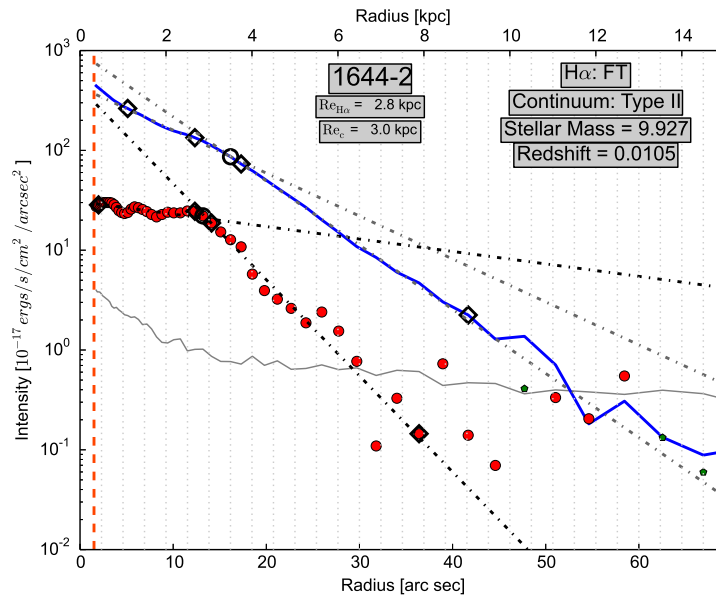
(c)



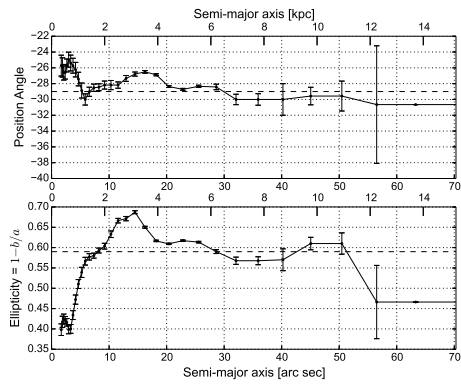
(d)



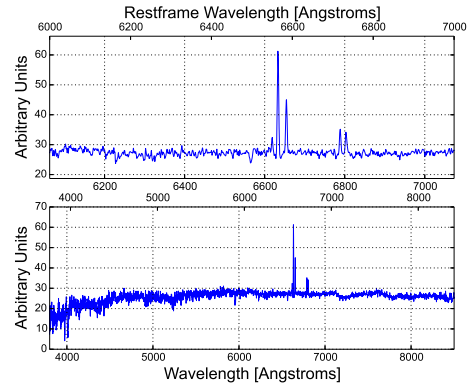
(a)



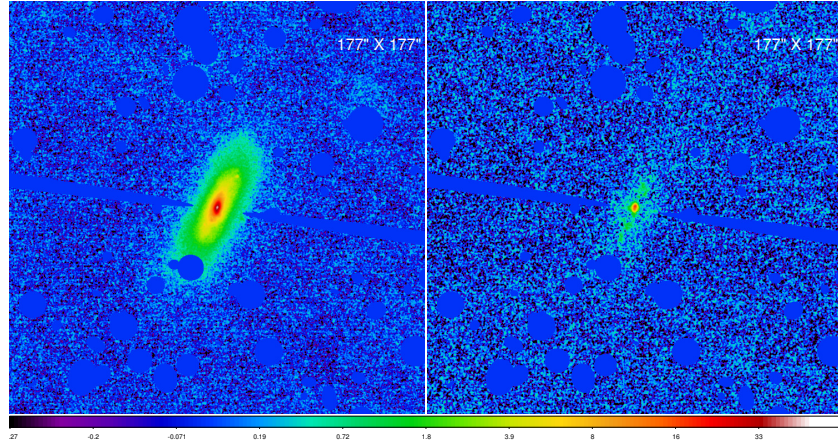
(b)



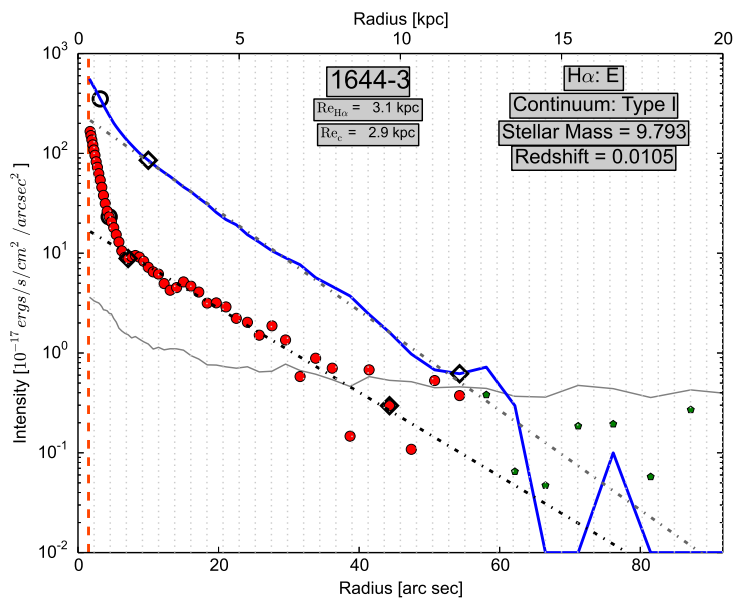
(c)



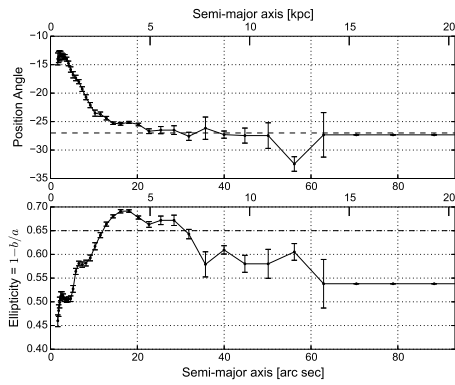
(d)



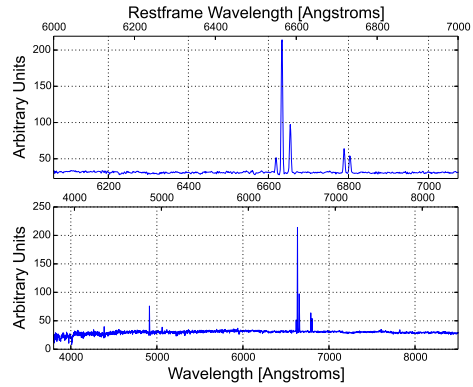
(a)



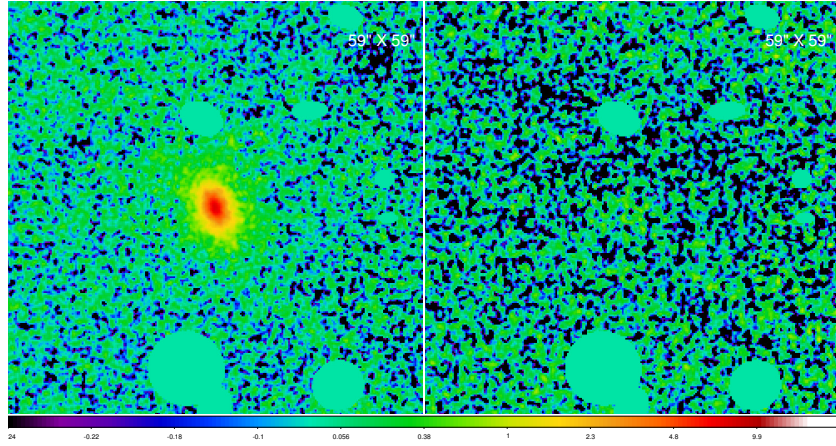
(b)



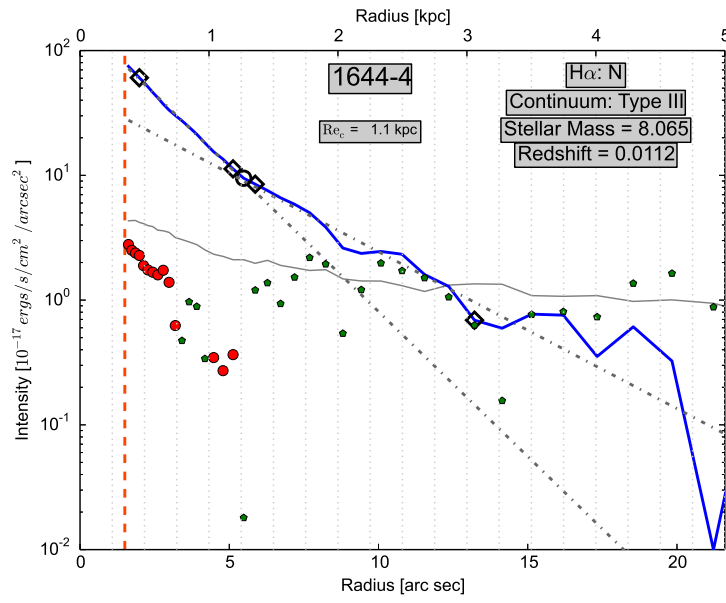
(c)



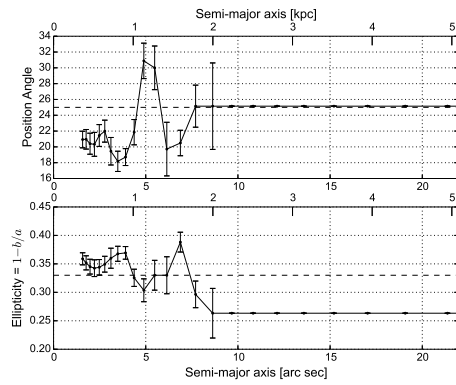
(d)



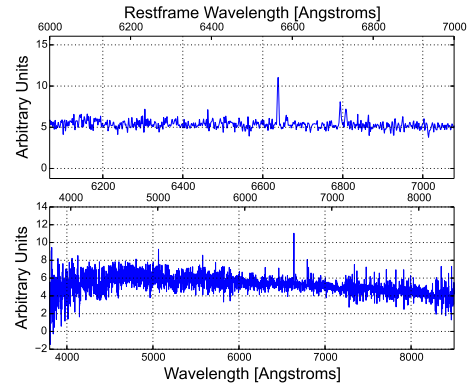
(a)



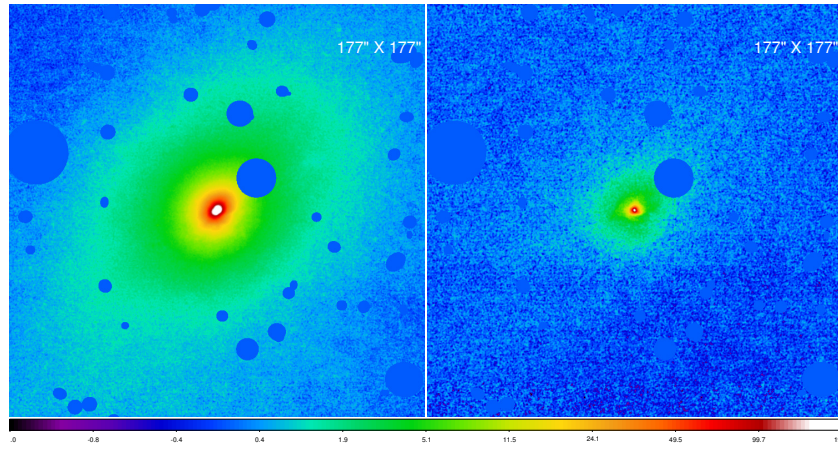
(b)



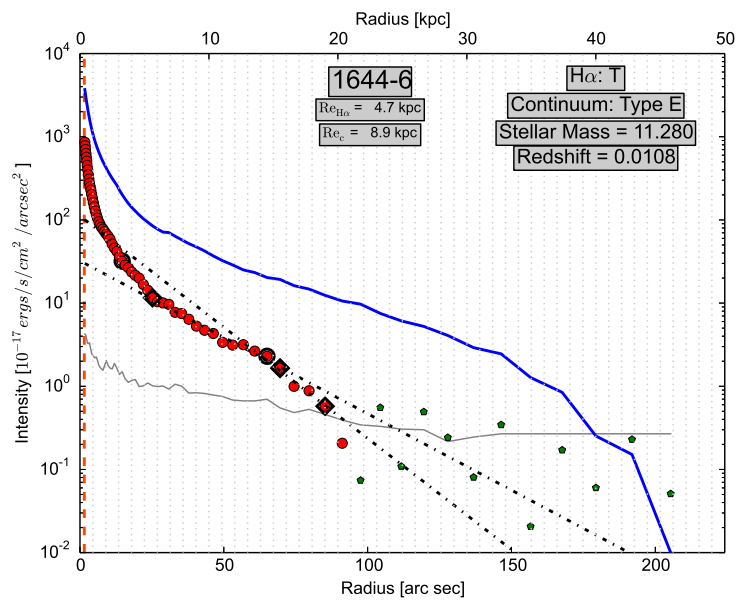
(c)



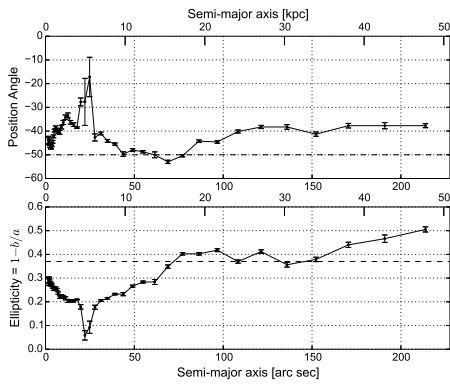
(d)



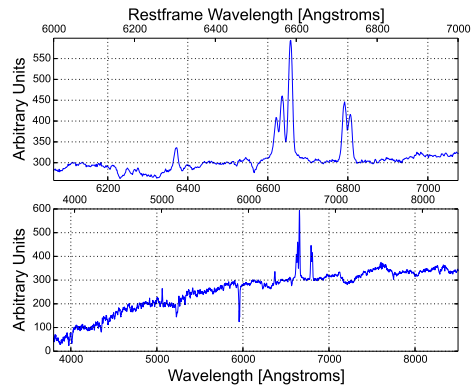
(a)



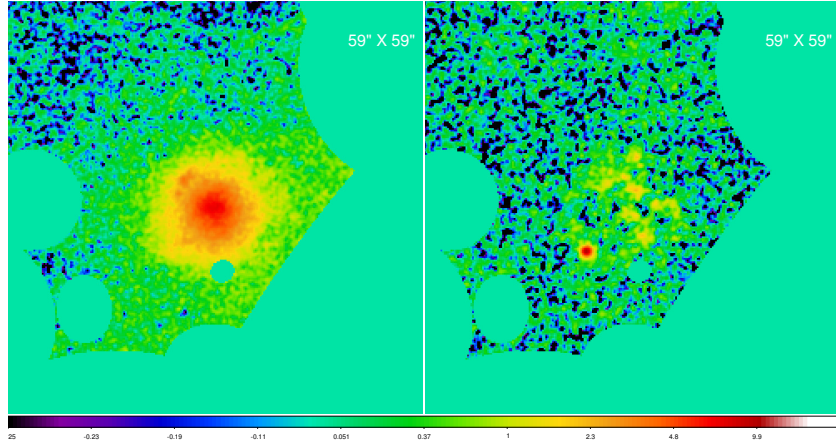
(b)



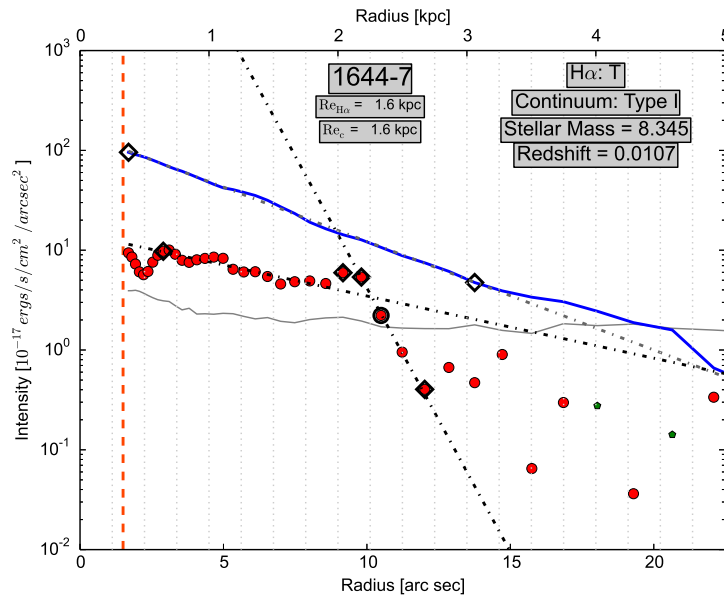
(c)



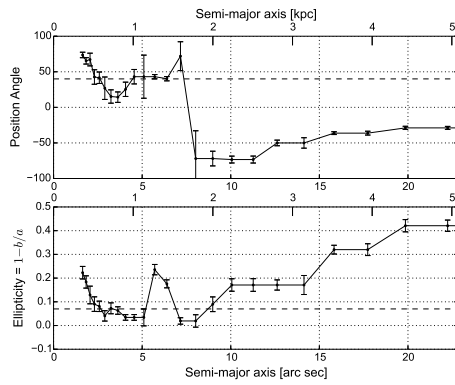
(d)



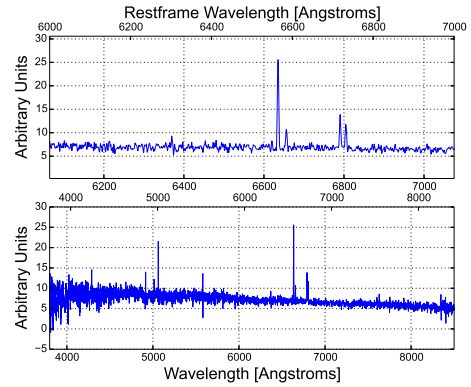
(a)



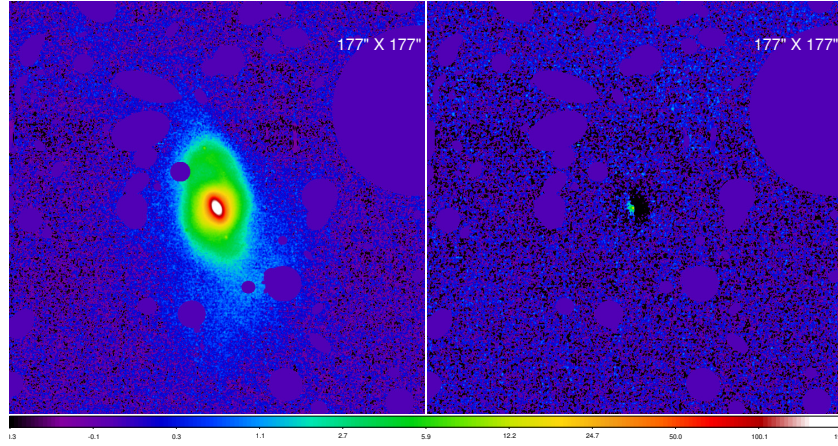
(b)



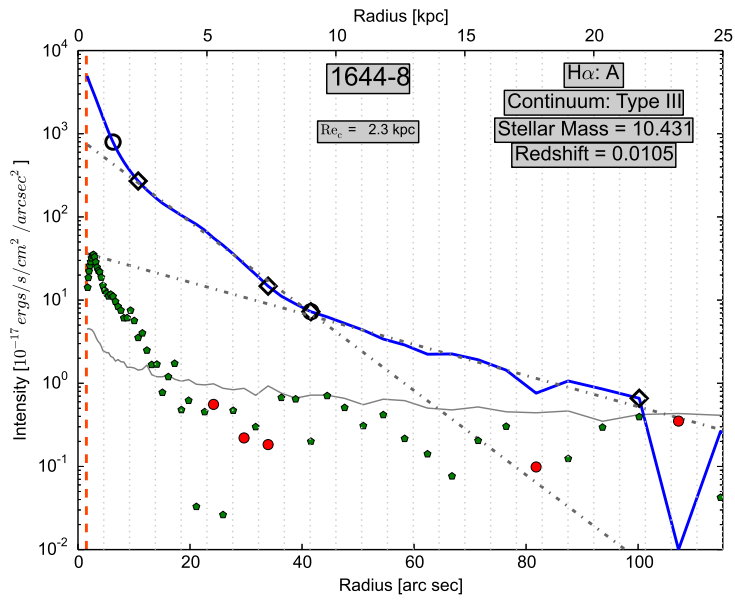
(c)



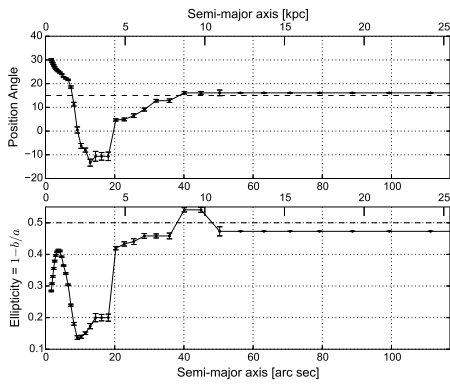
(d)



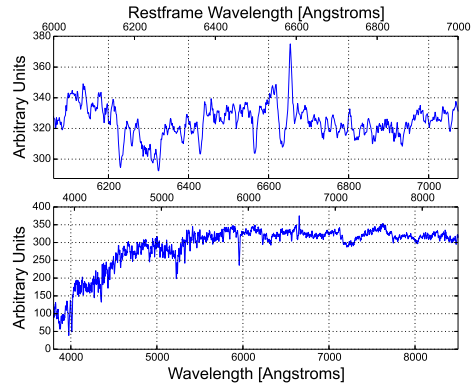
(a)



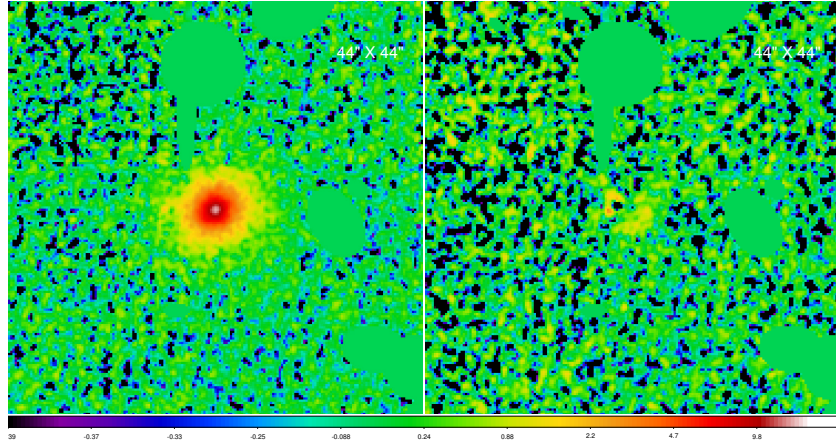
(b)



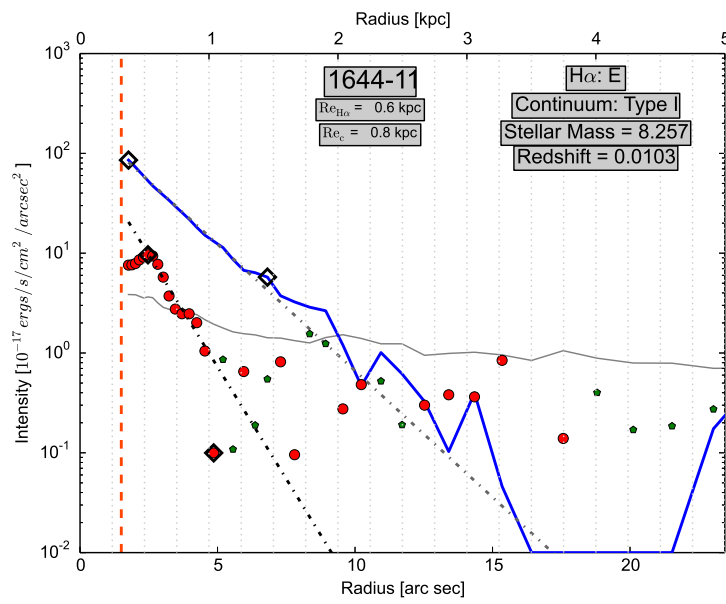
(c)



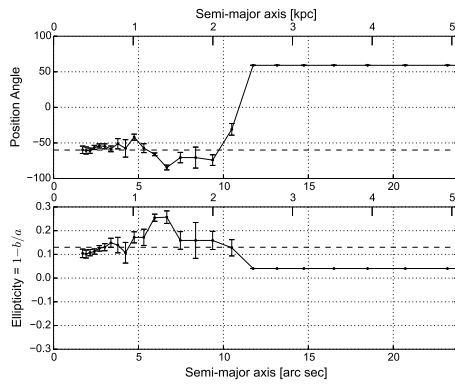
(d)



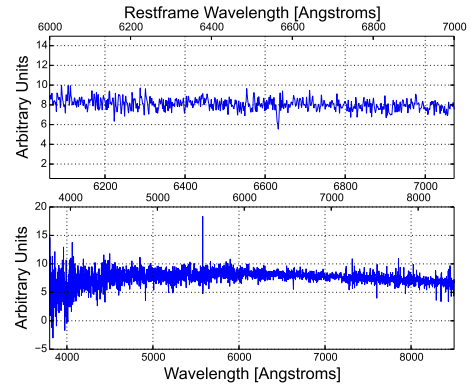
(a)



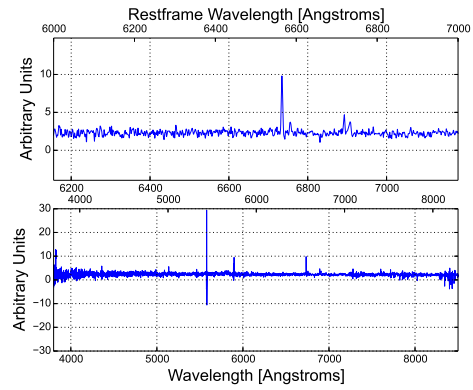
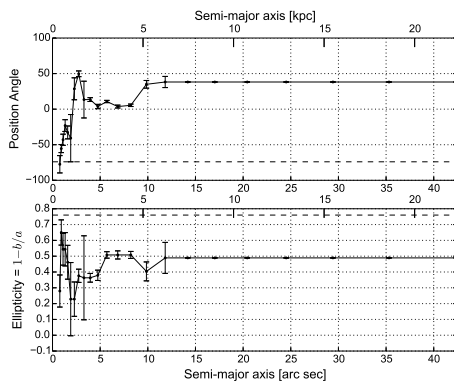
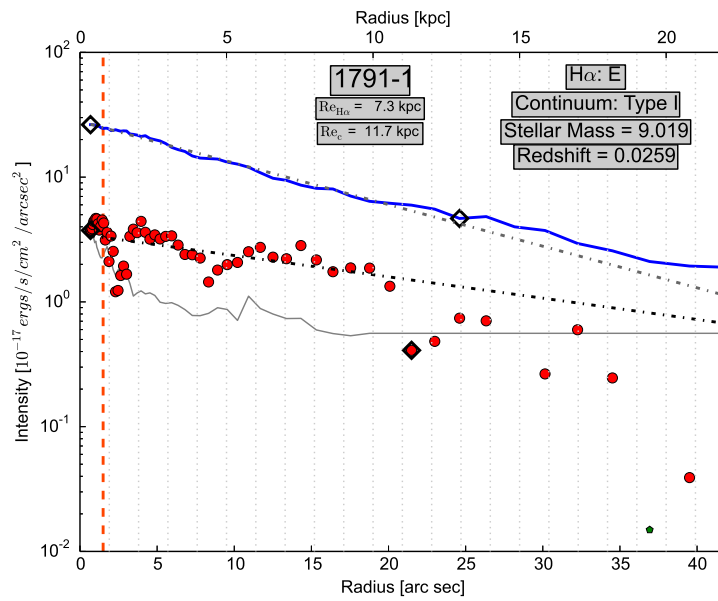
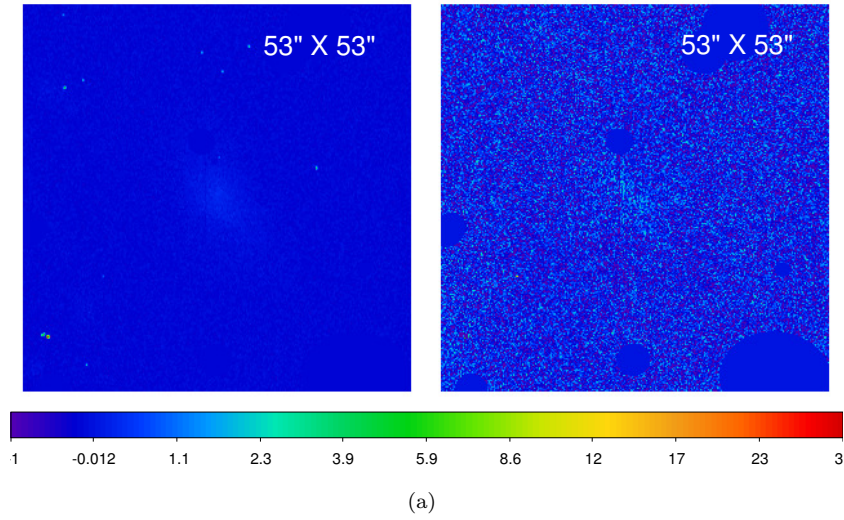
(b)

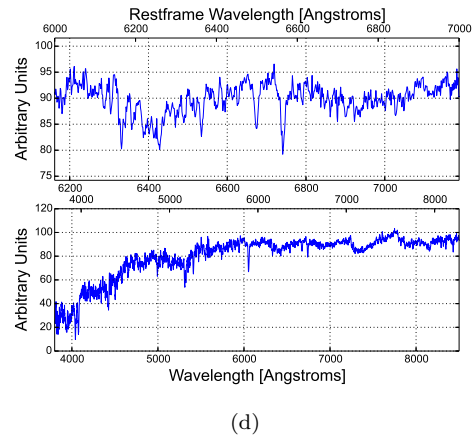
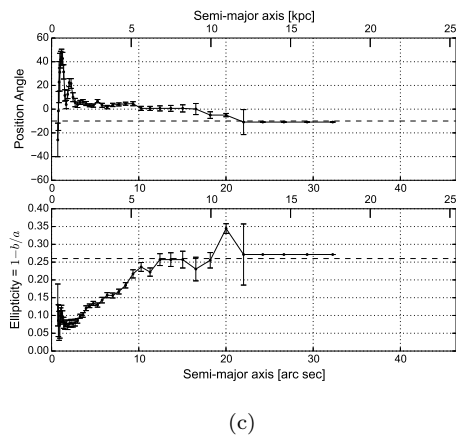
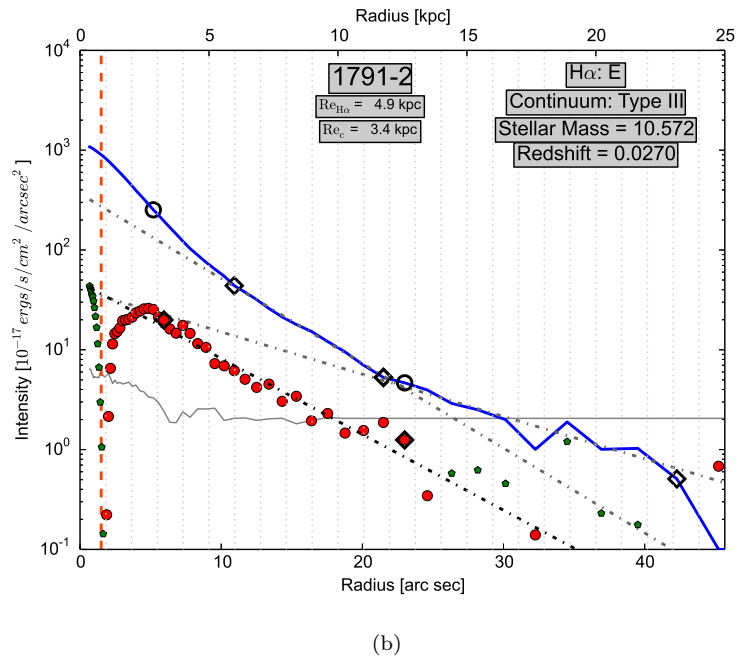
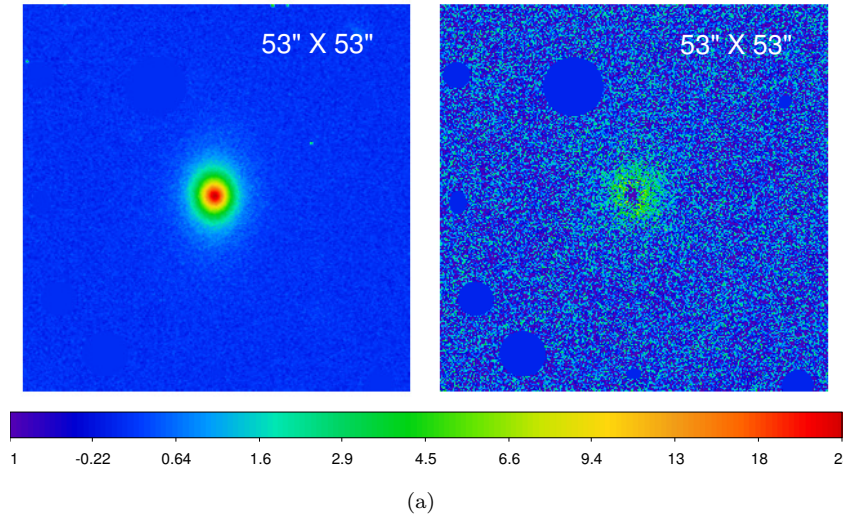


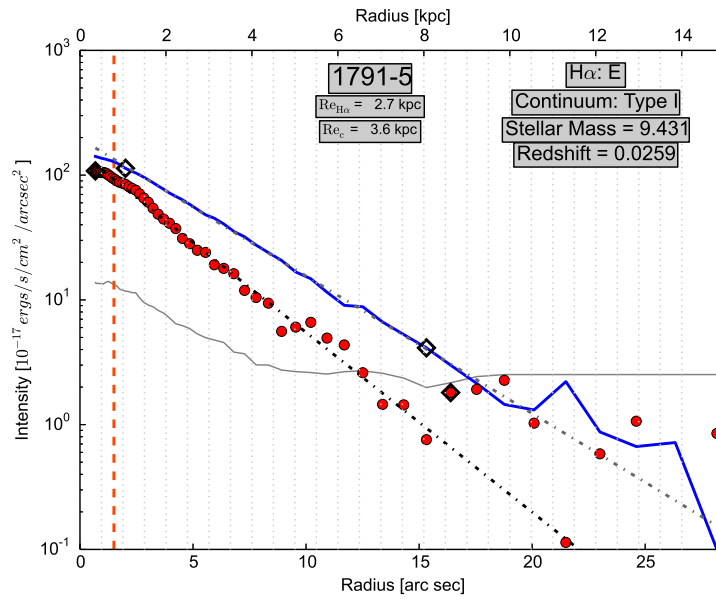
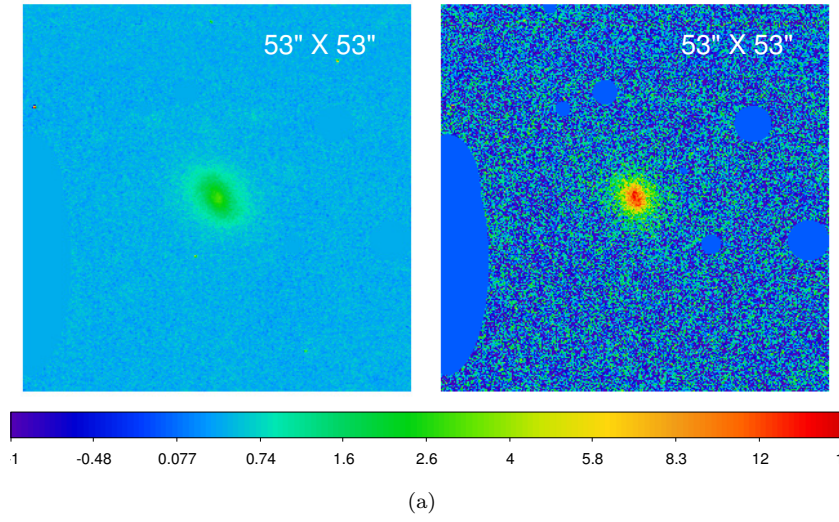
(c)



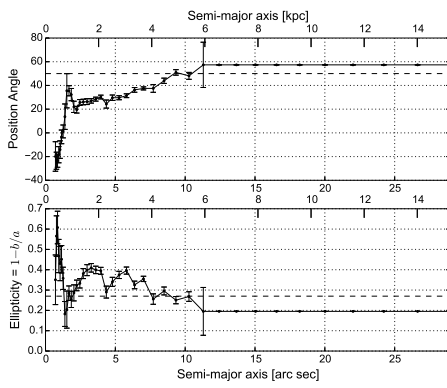
(d)



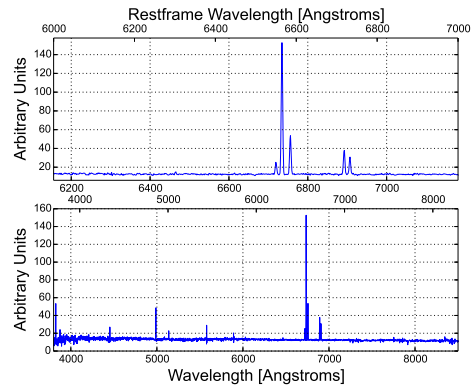




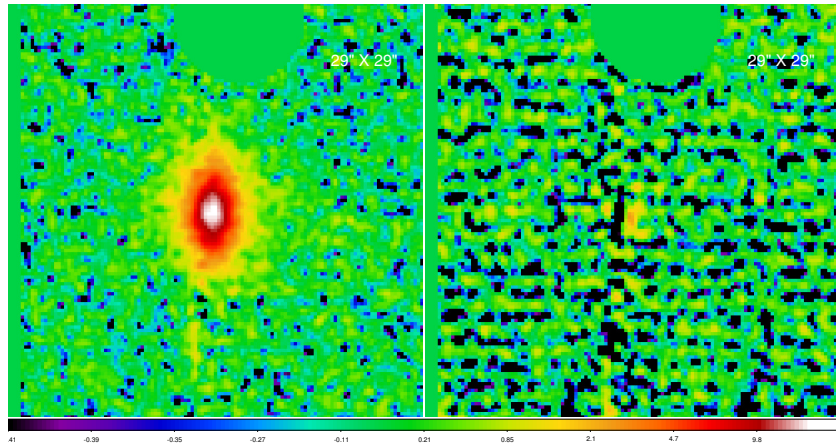
(b)



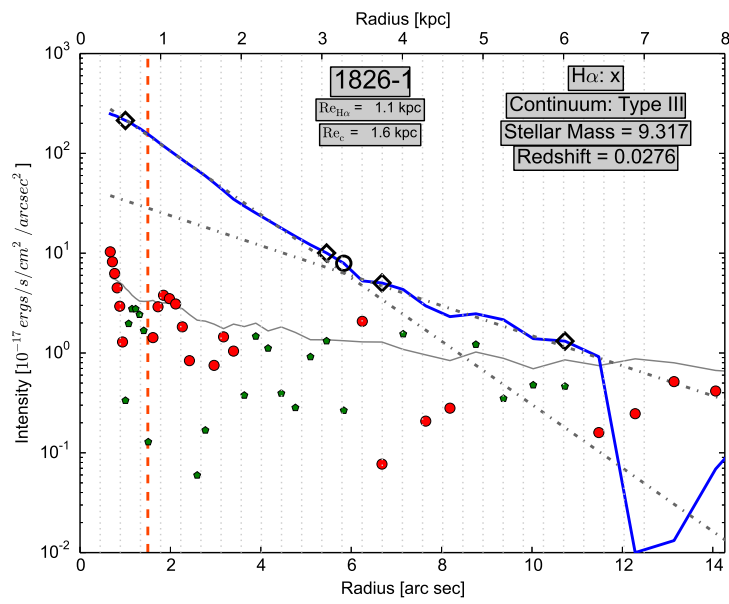
(c)



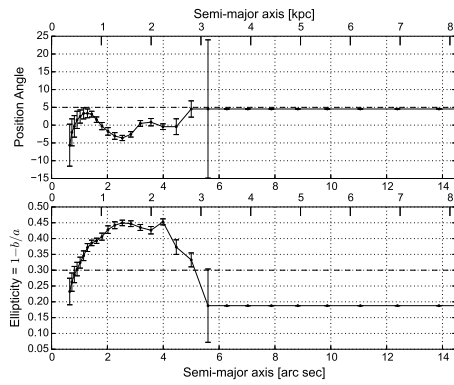
(d)



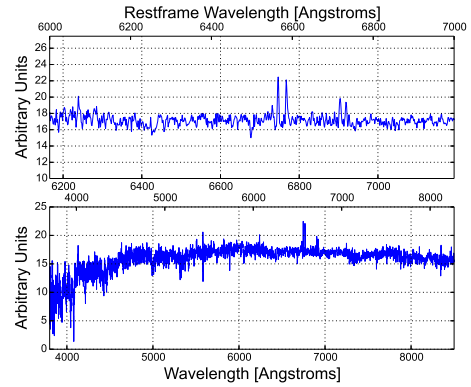
(a)



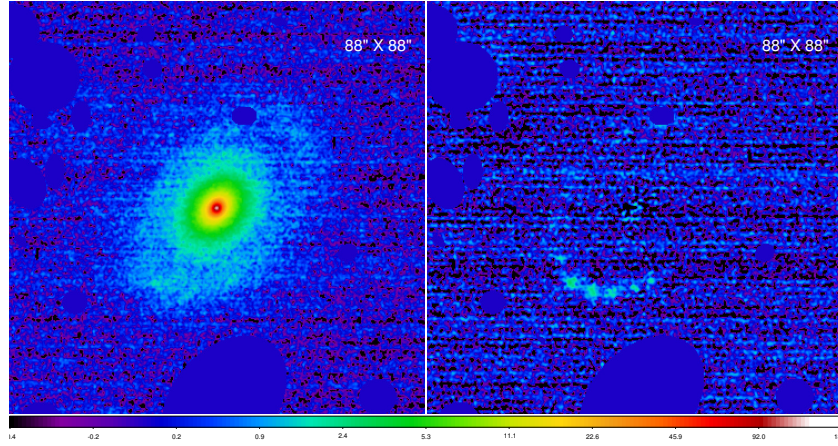
(b)



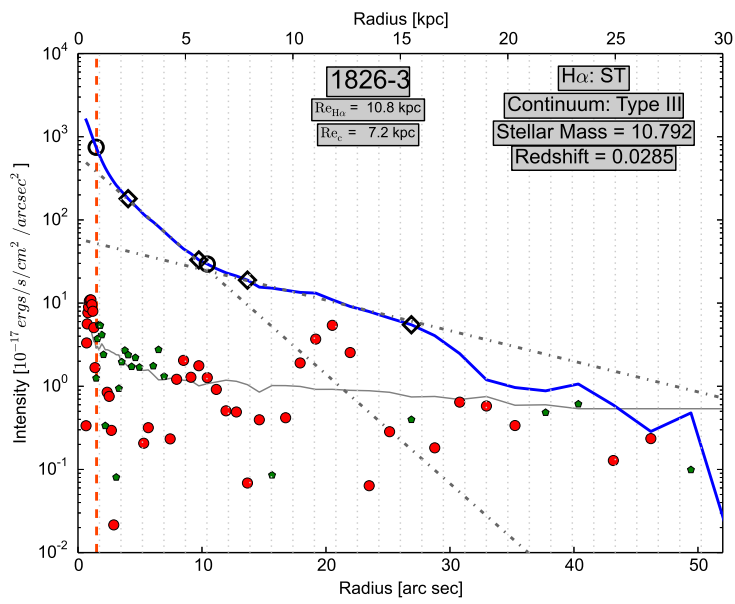
(c)



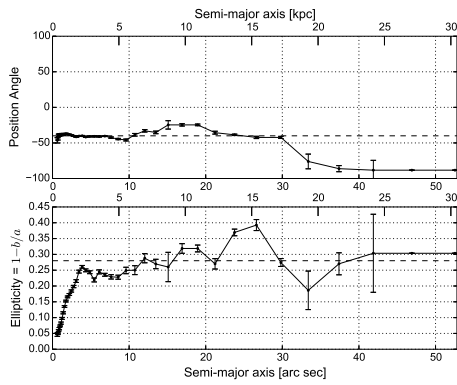
(d)



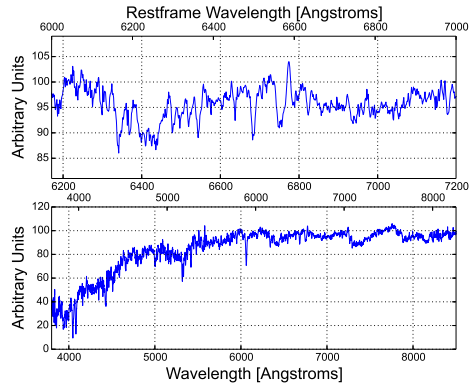
(a)



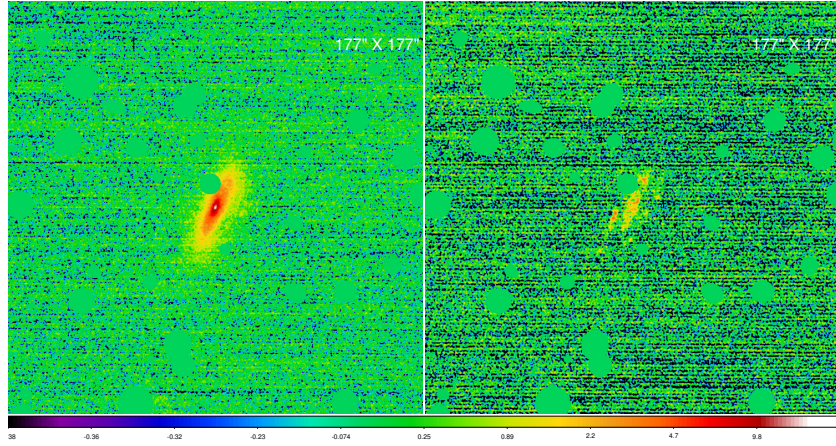
(b)



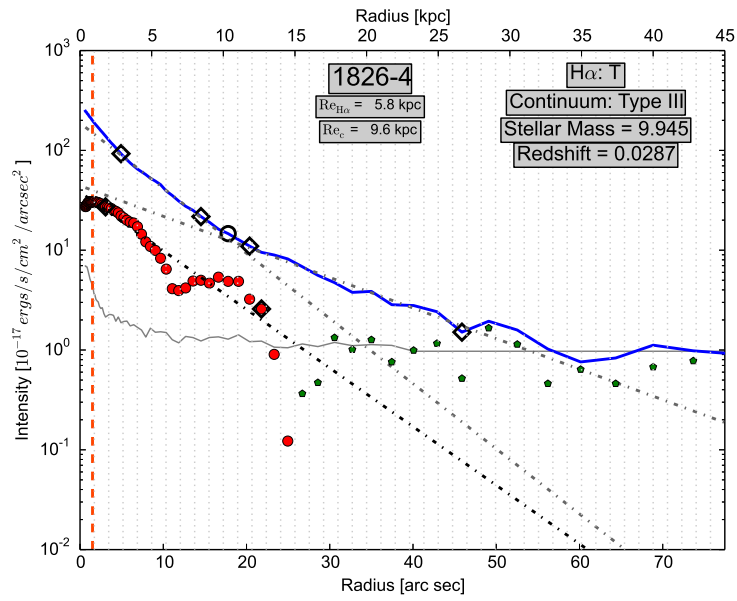
(c)



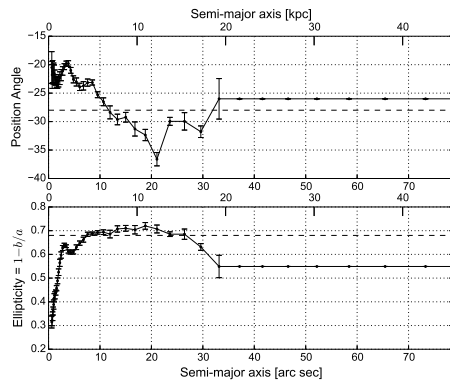
(d)



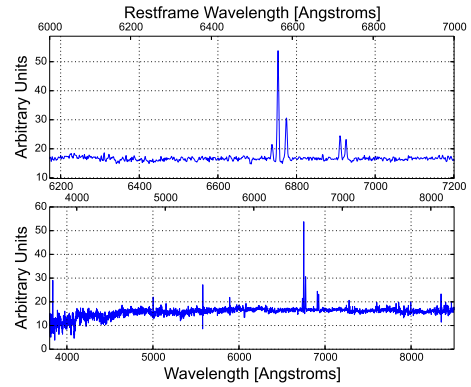
(a)



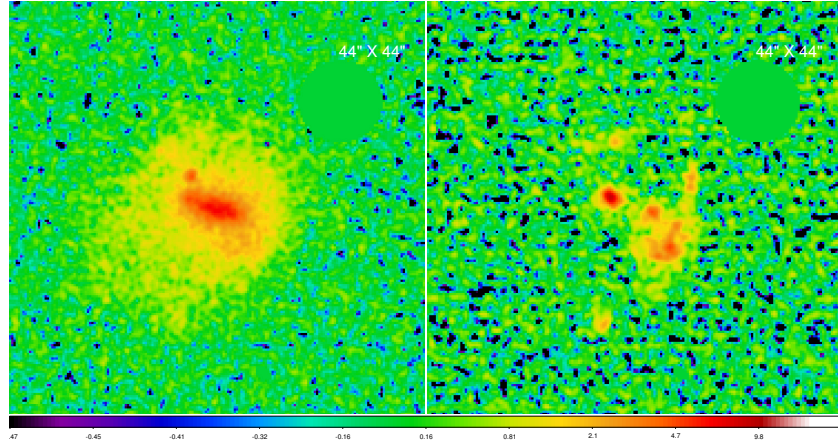
(b)



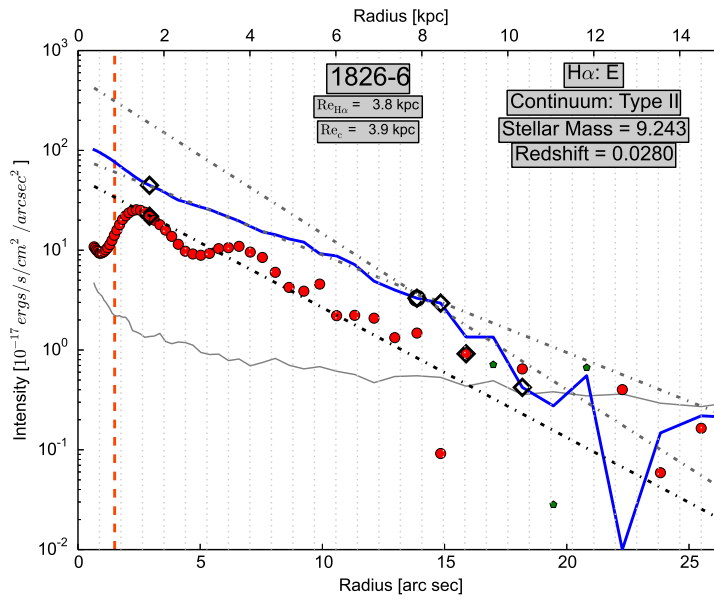
(c)



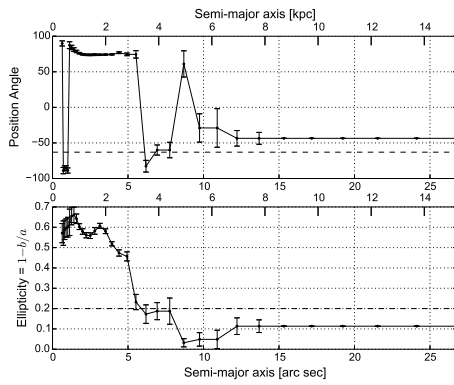
(d)



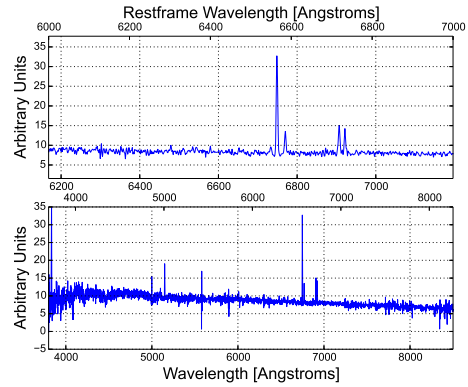
(a)



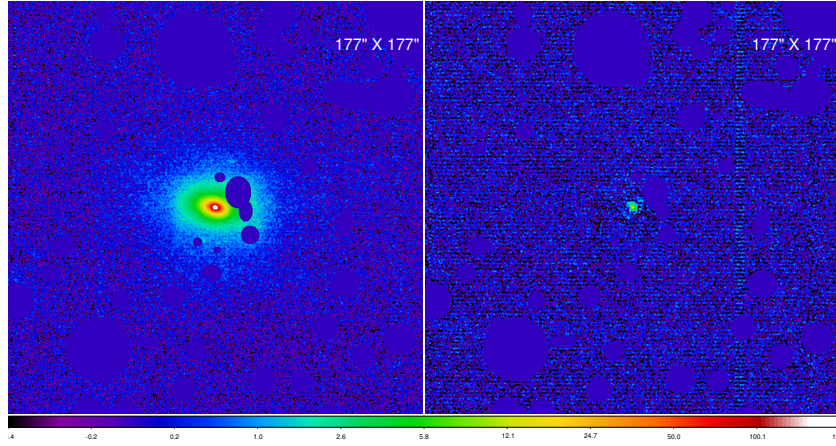
(b)



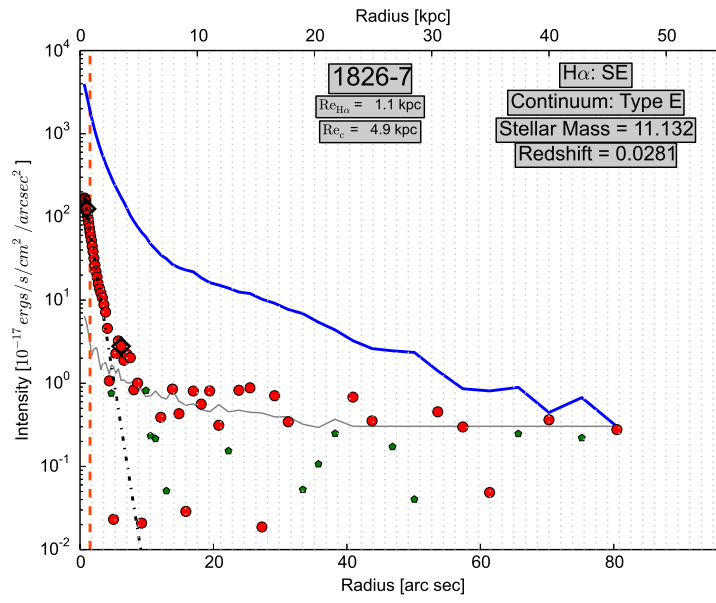
(c)



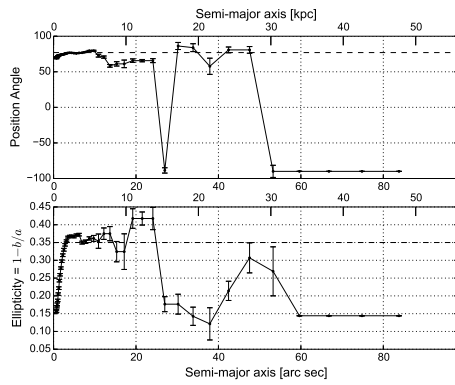
(d)



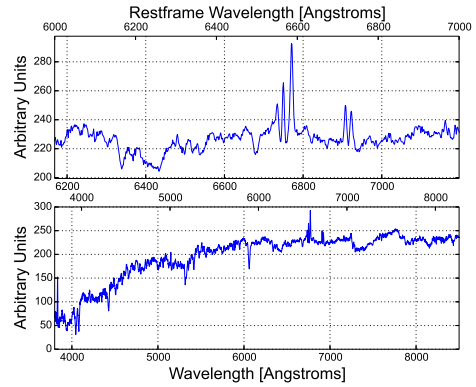
(a)



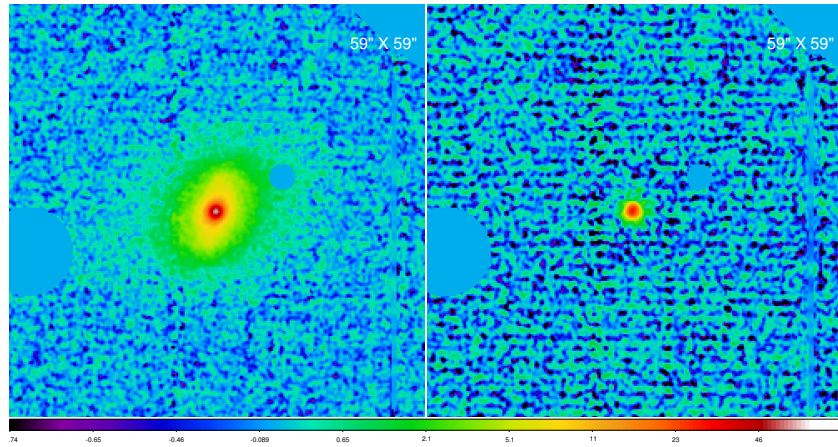
(b)



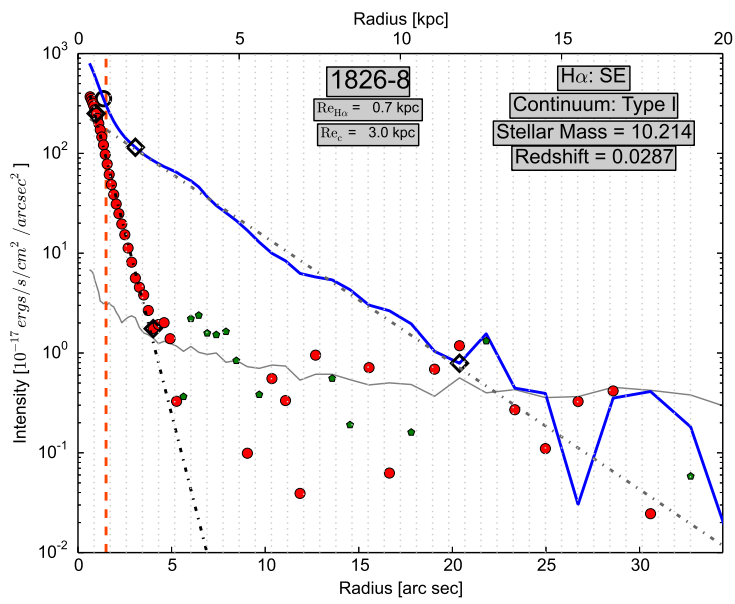
(c)



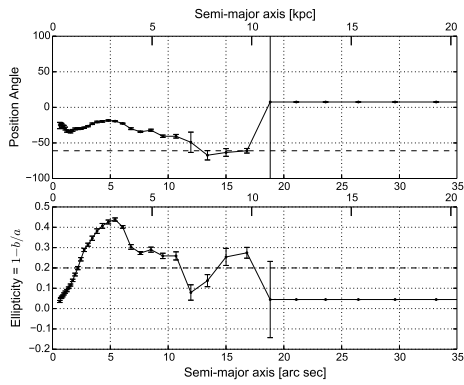
(d)



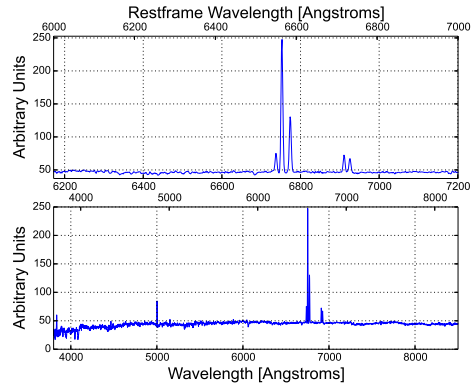
(a)



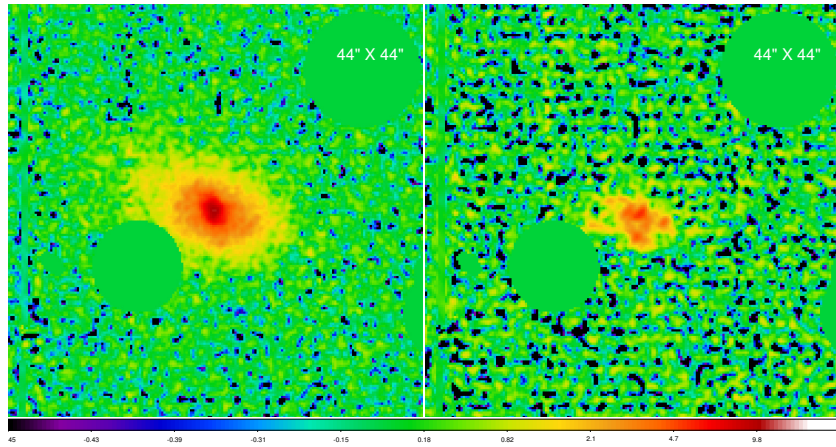
(b)



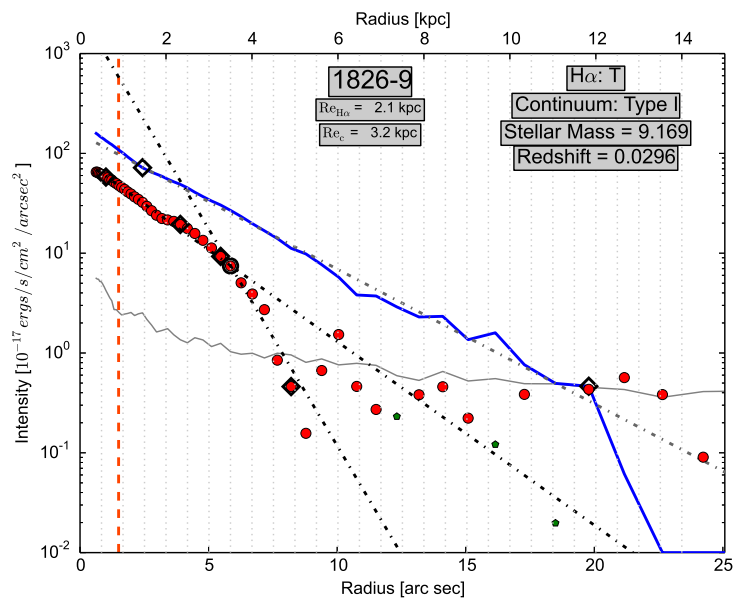
(c)



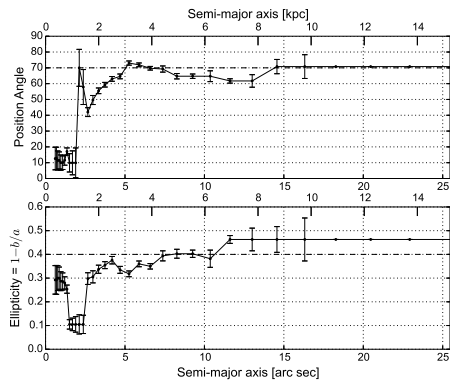
(d)



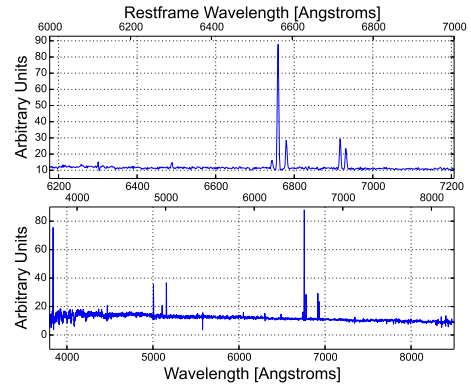
(a)



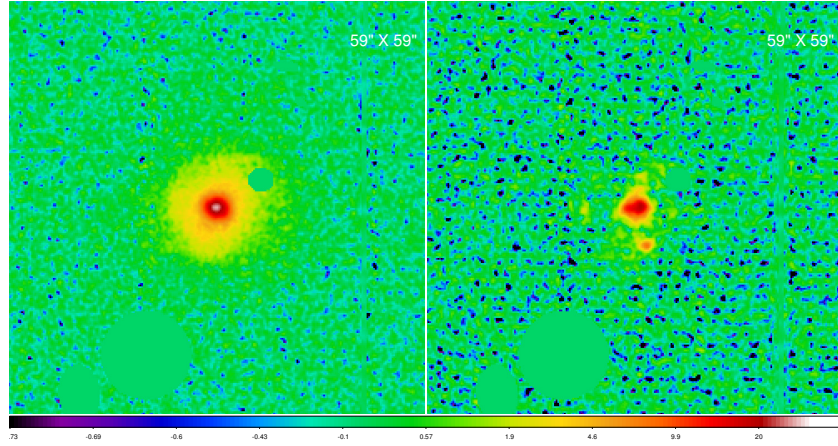
(b)



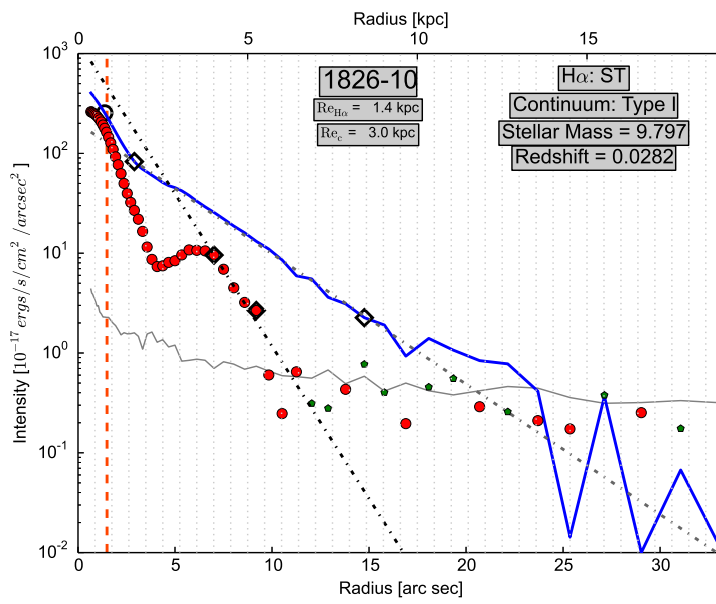
(c)



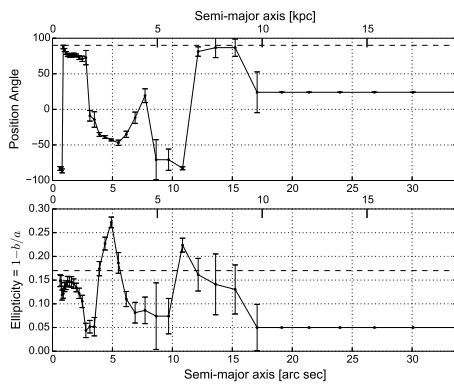
(d)



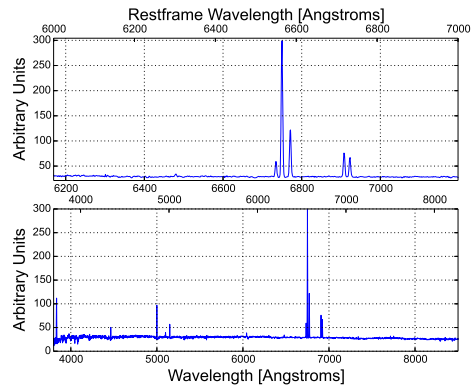
(a)



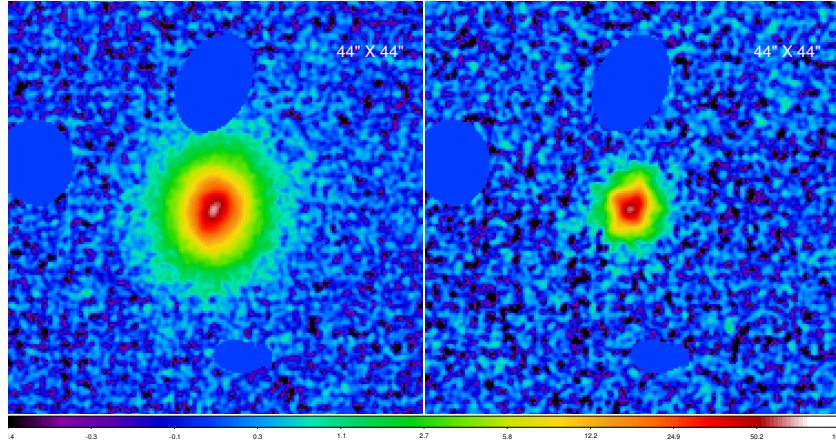
(b)



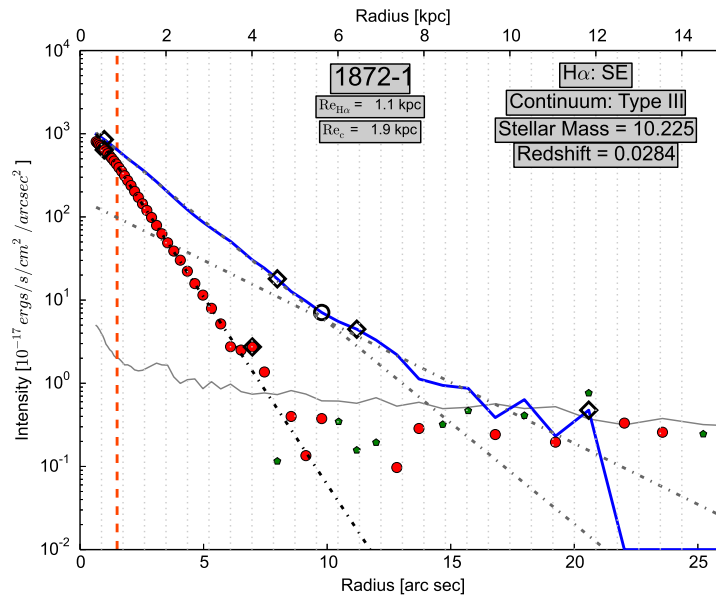
(c)



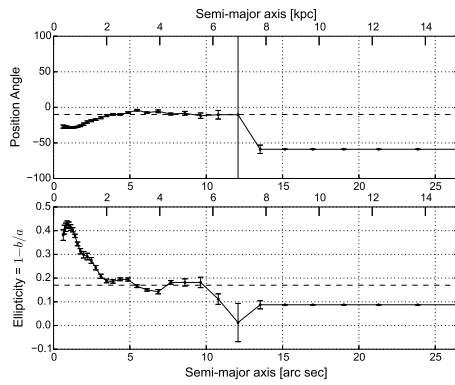
(d)



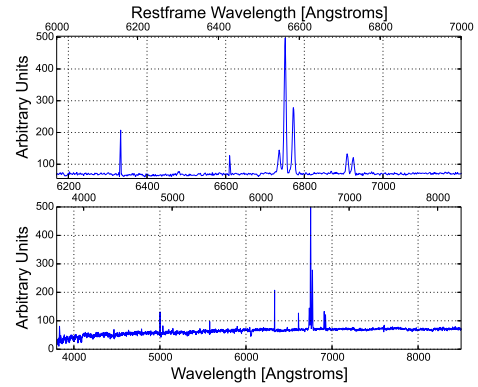
(a)



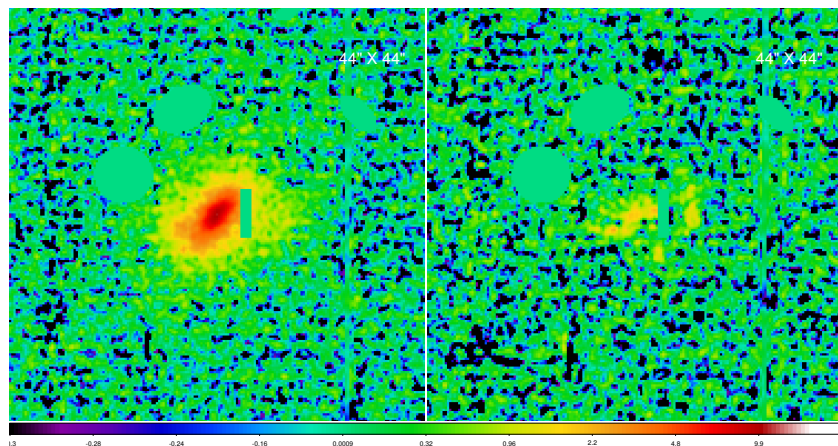
(b)



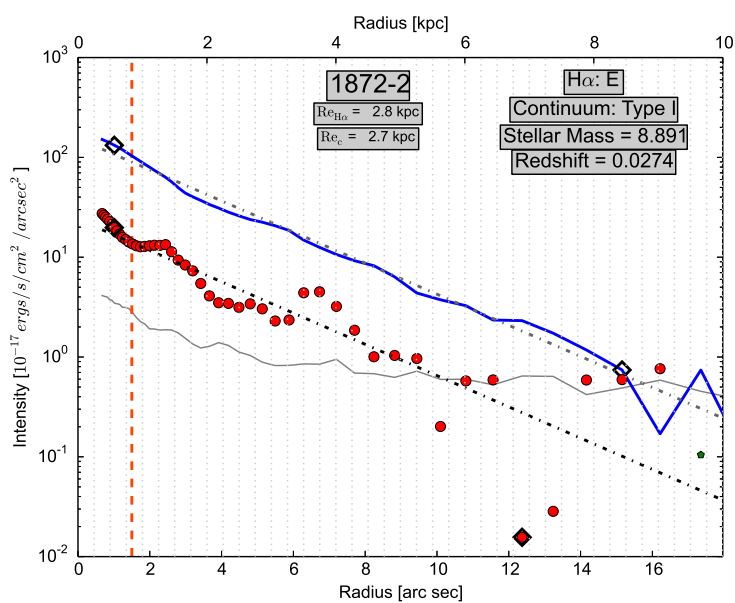
(c)



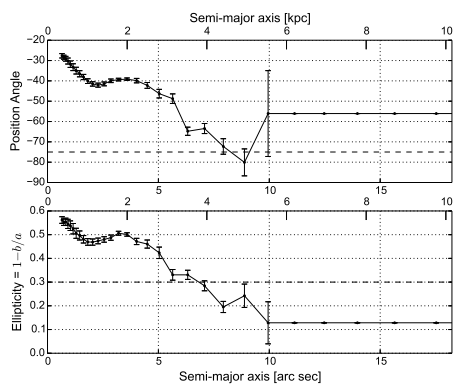
(d)



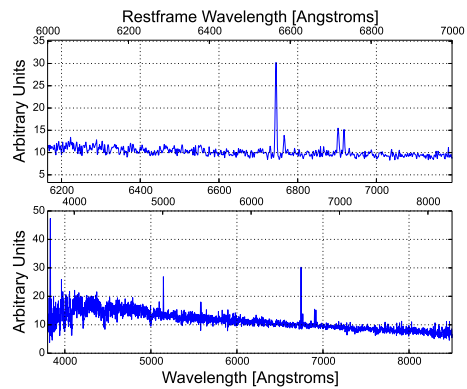
(a)



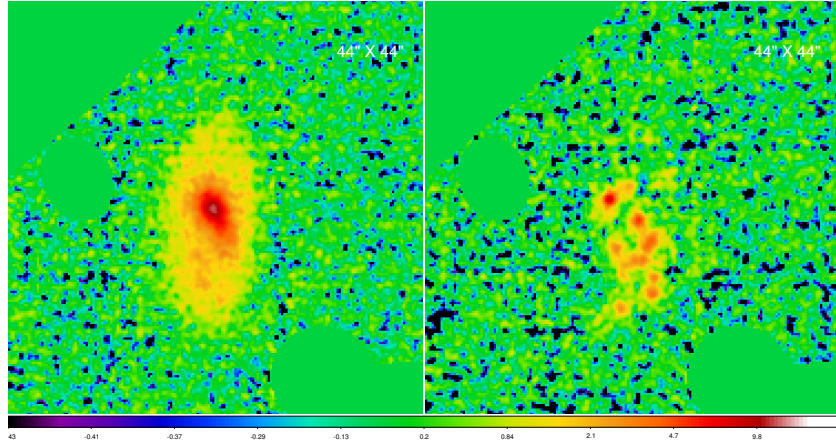
(b)



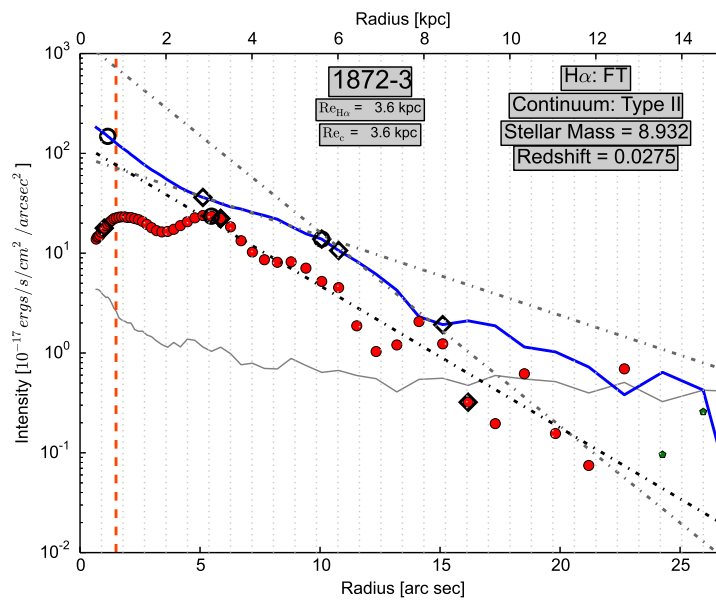
(c)



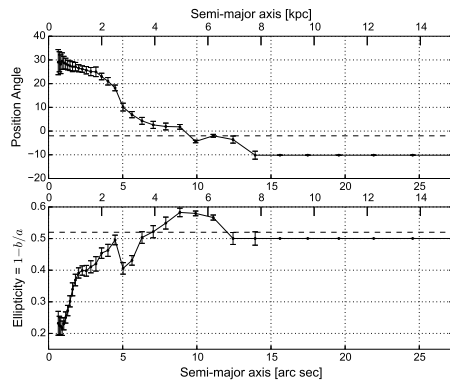
(d)



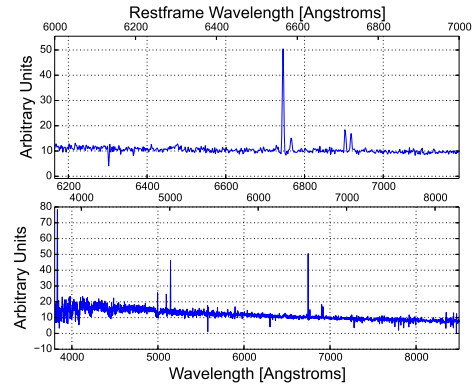
(a)



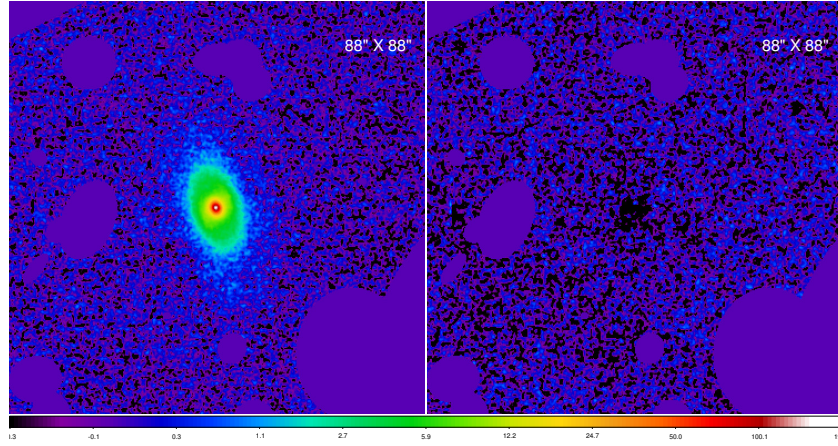
(b)



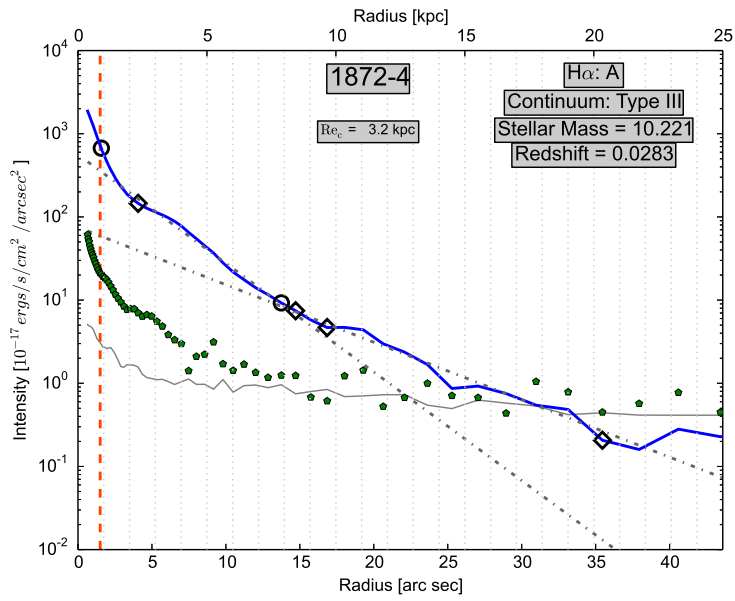
(c)



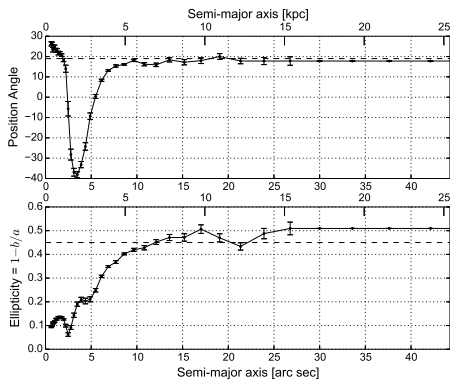
(d)



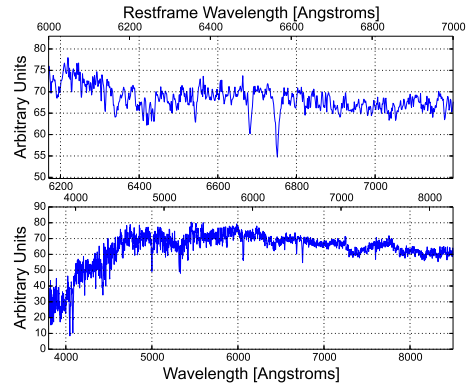
(a)



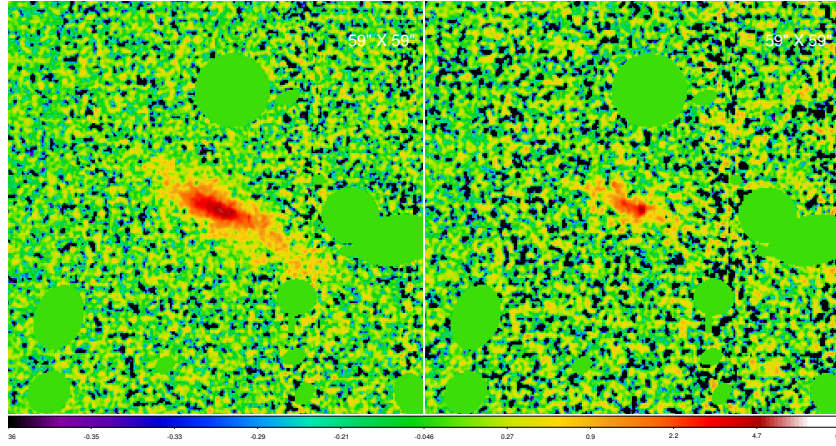
(b)



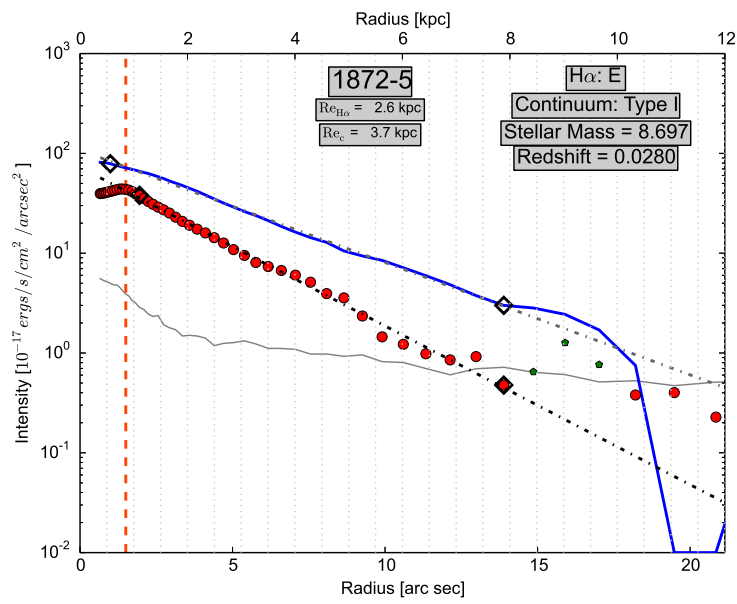
(c)



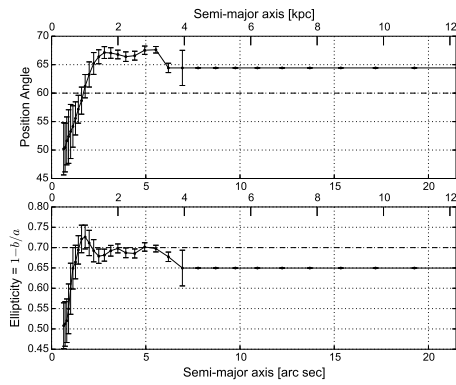
(d)



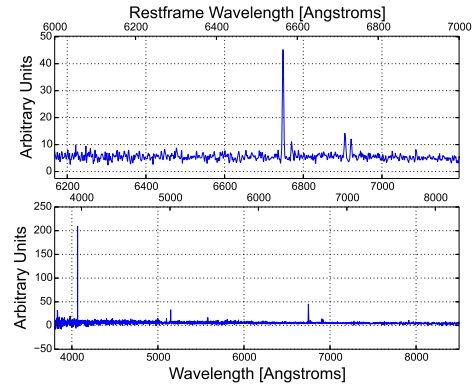
(a)



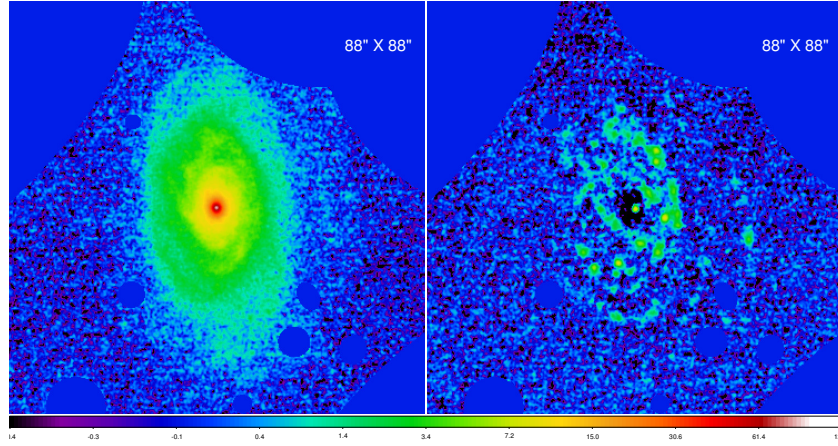
(b)



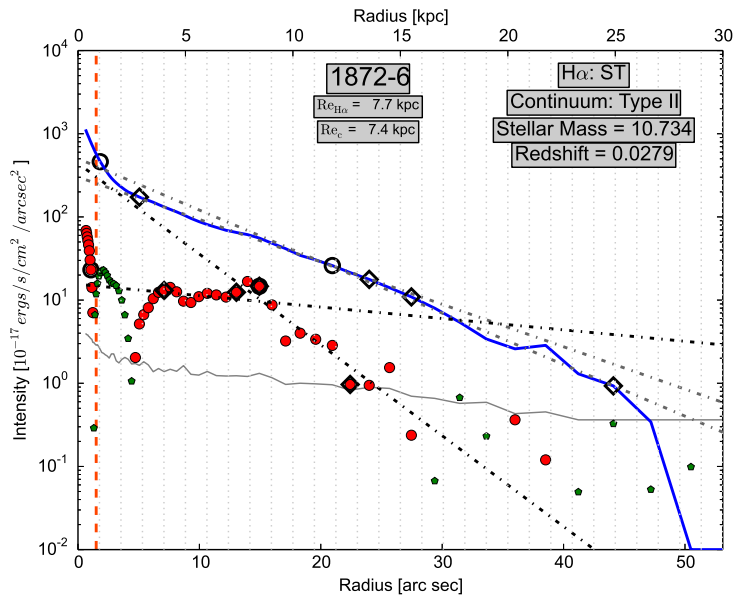
(c)



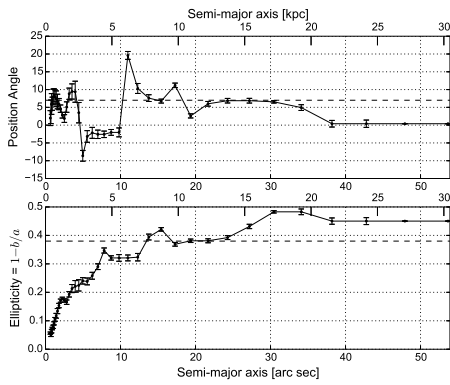
(d)



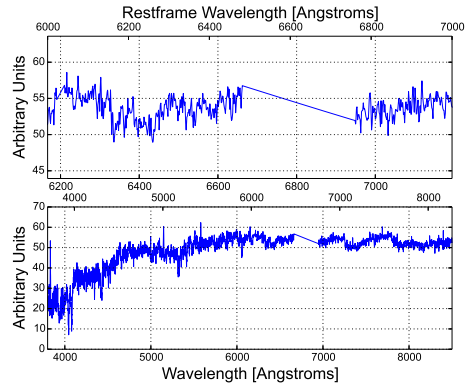
(a)



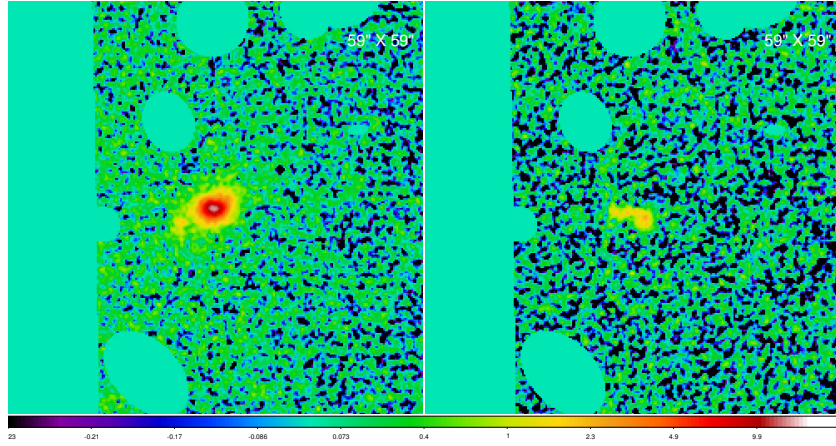
(b)



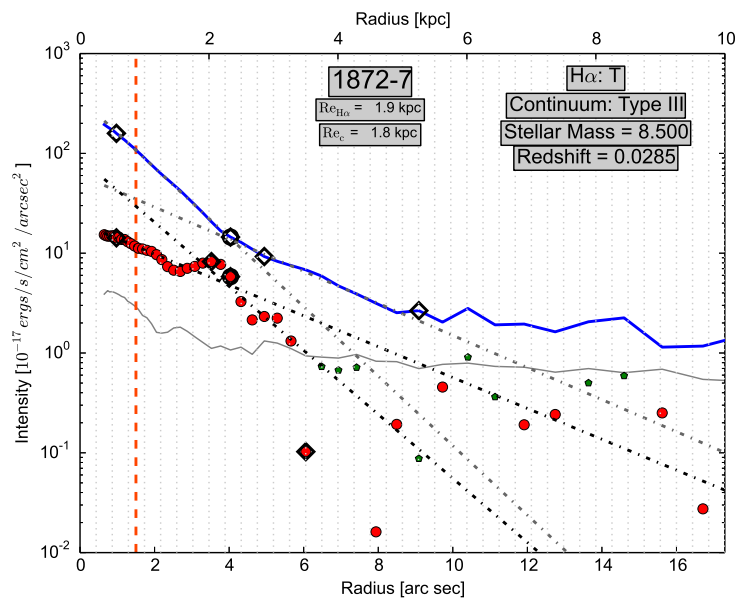
(c)



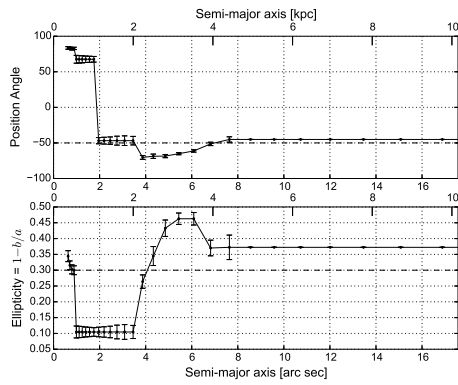
(d)



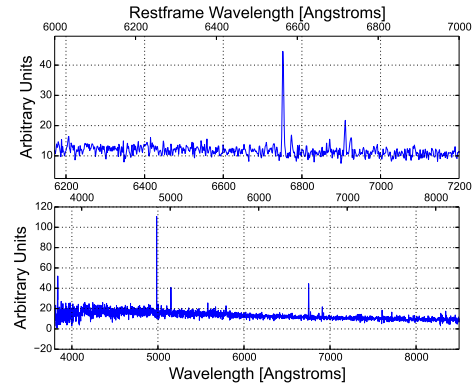
(a)



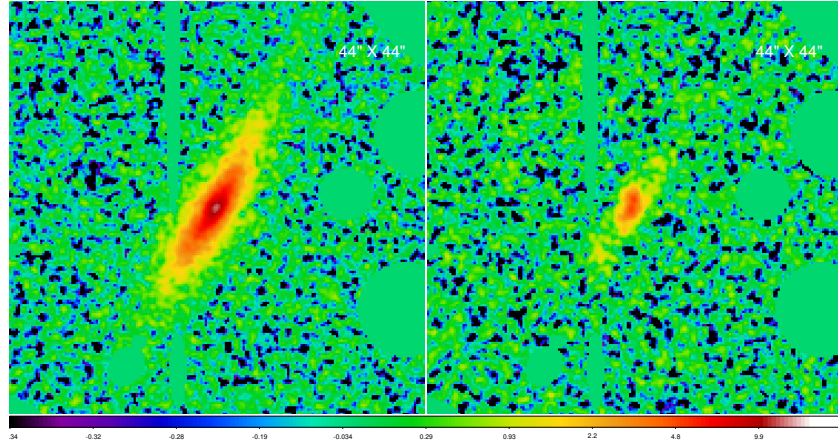
(b)



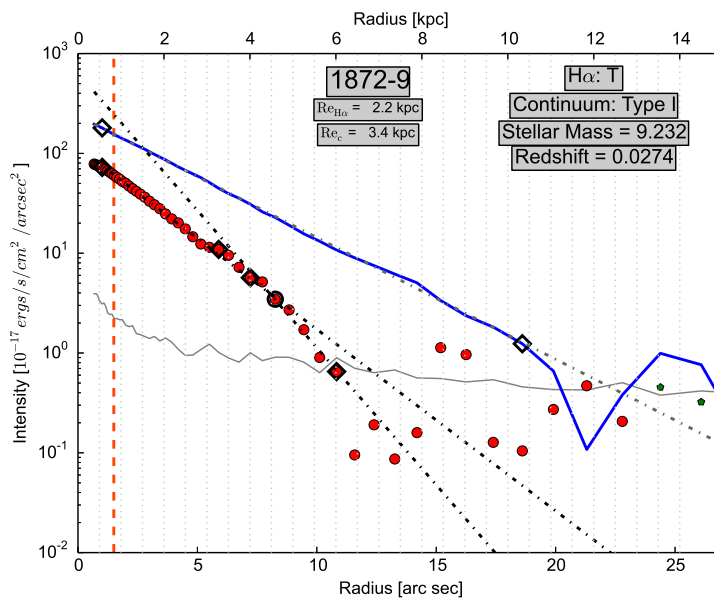
(c)



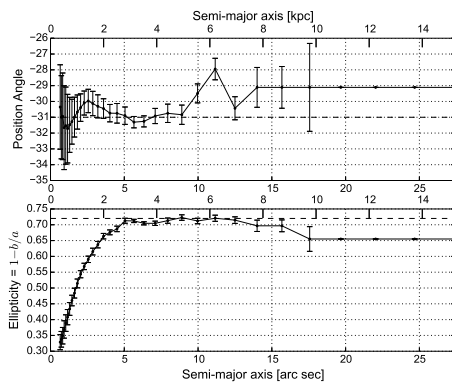
(d)



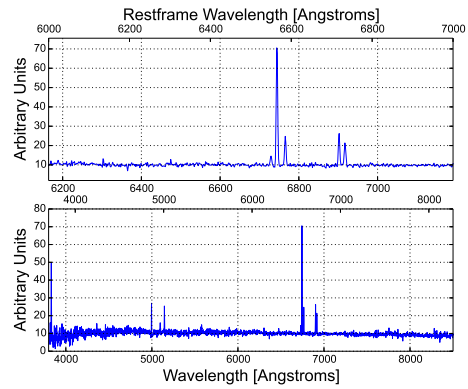
(a)



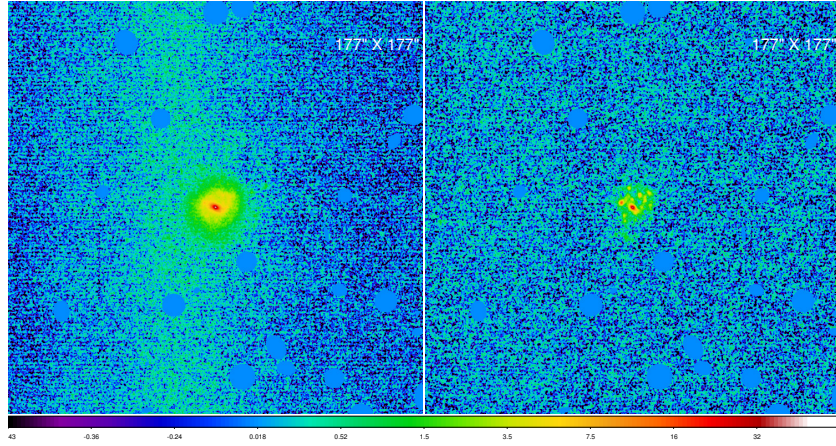
(b)



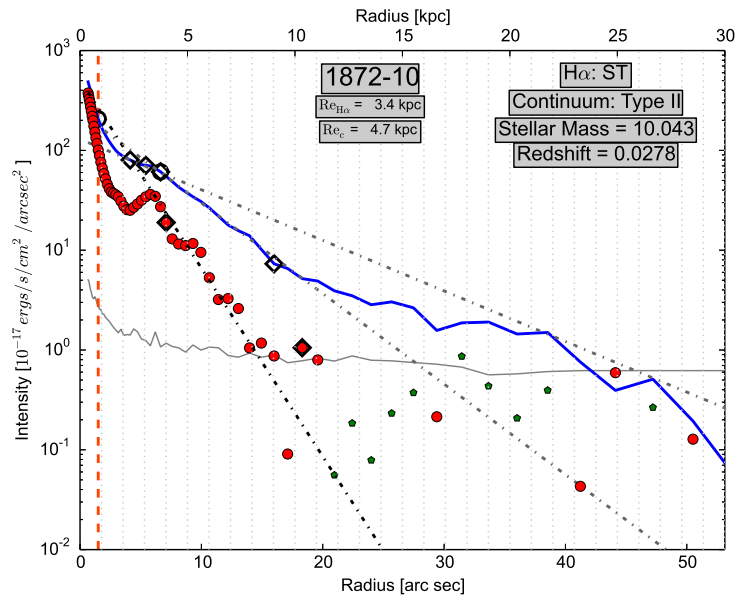
(c)



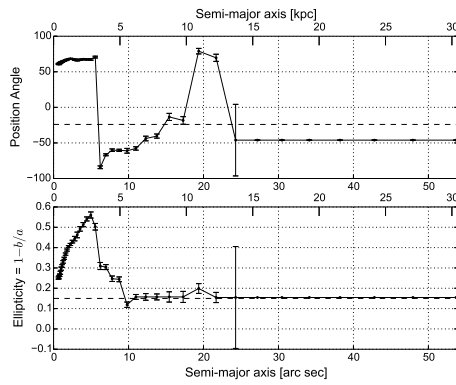
(d)



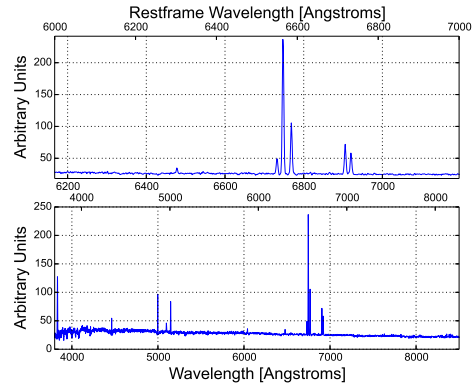
(a)



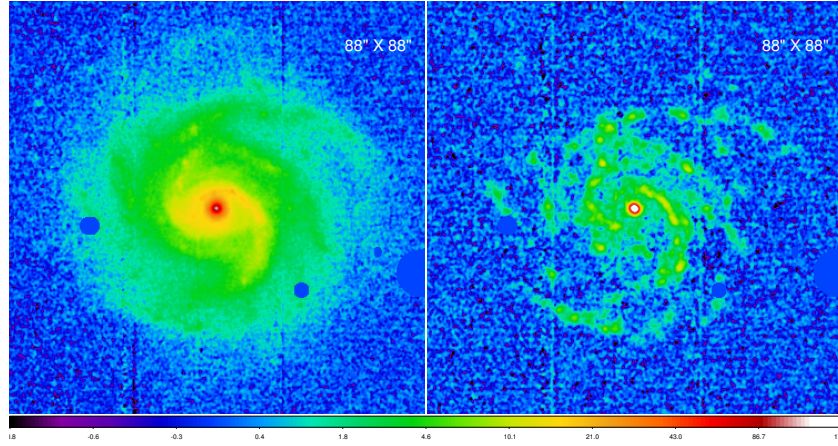
(b)



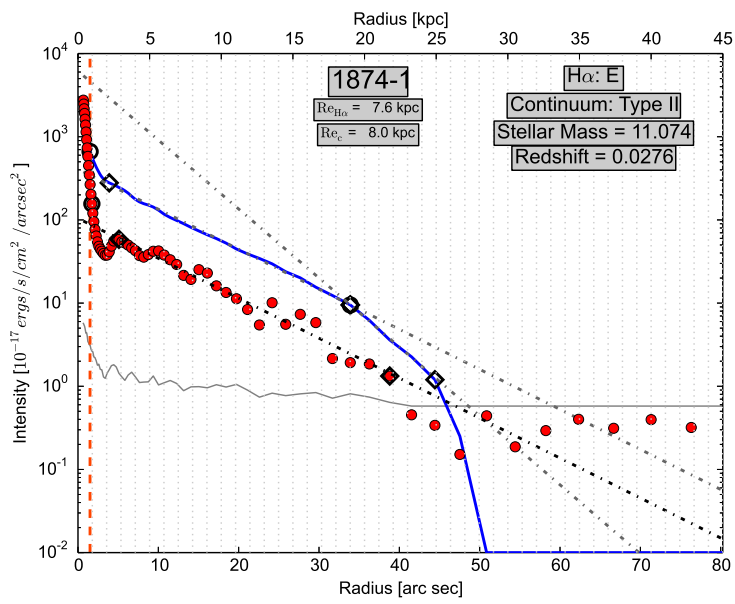
(c)



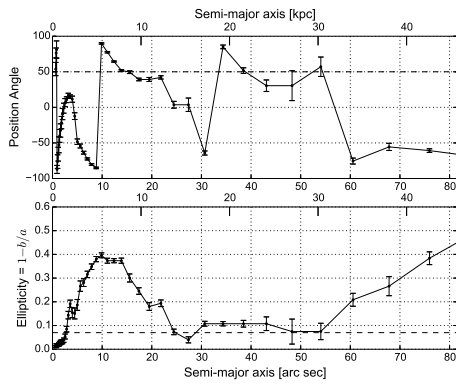
(d)



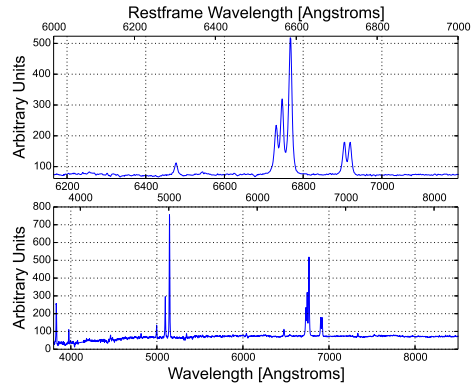
(a)



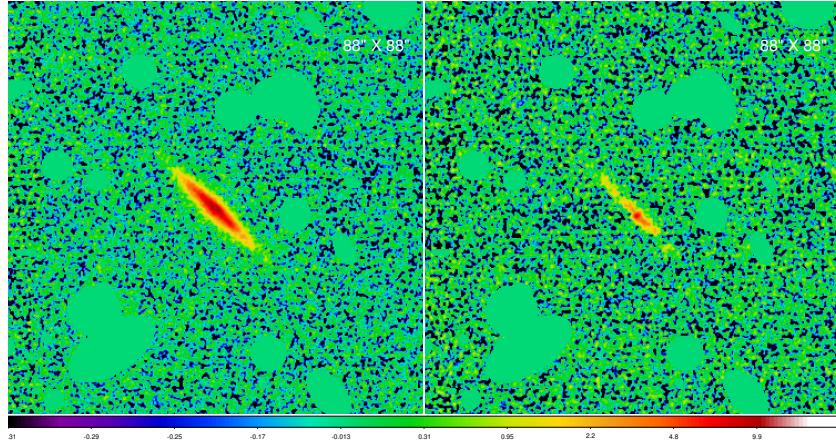
(b)



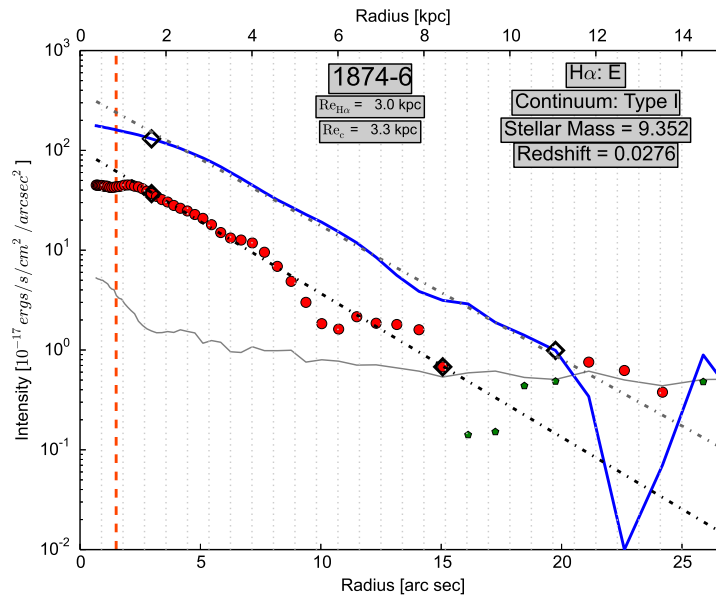
(c)



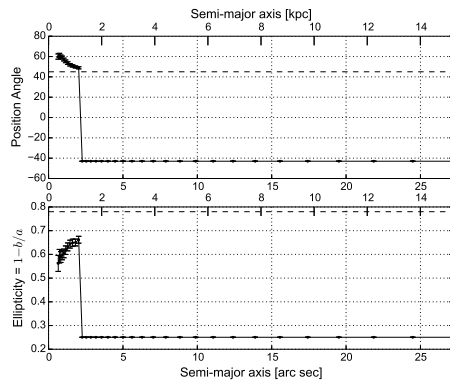
(d)



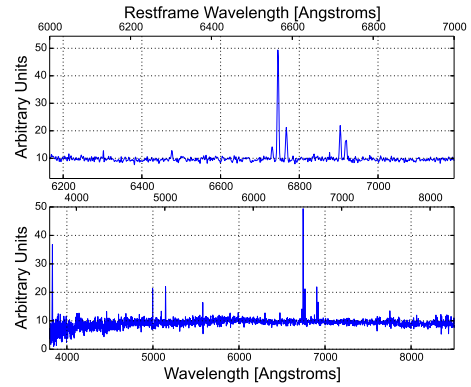
(a)



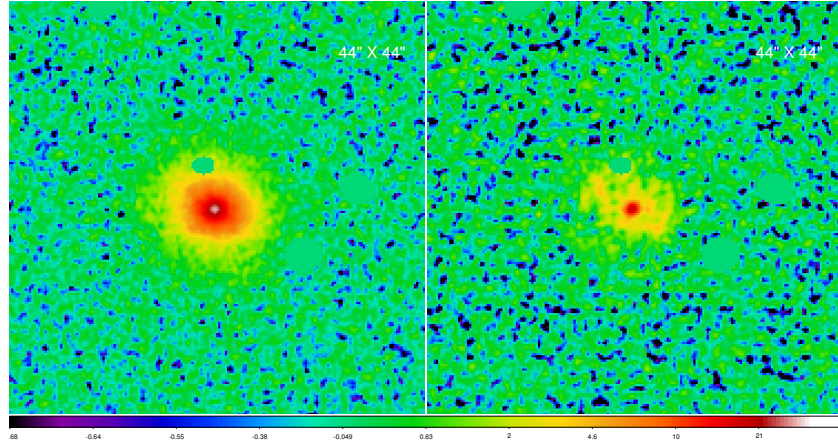
(b)



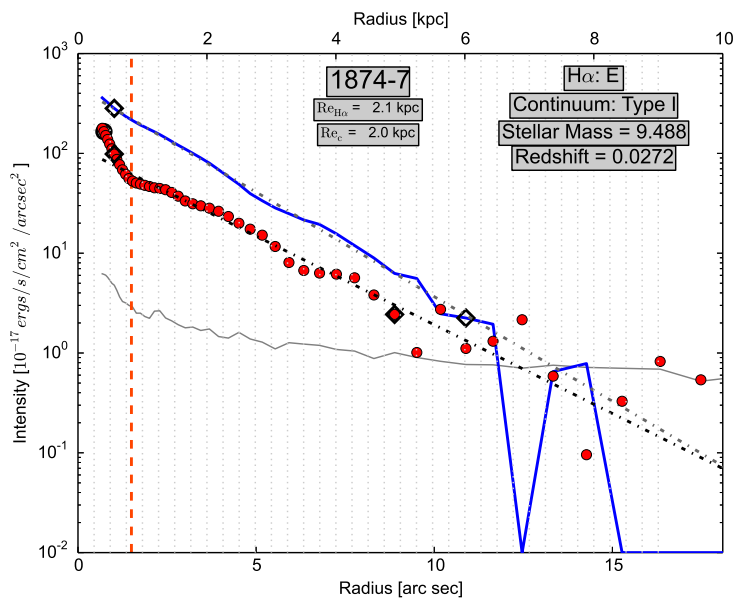
(c)



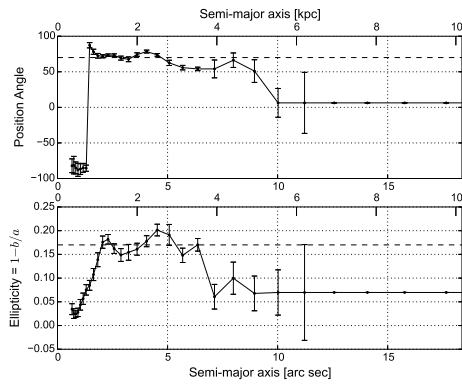
(d)



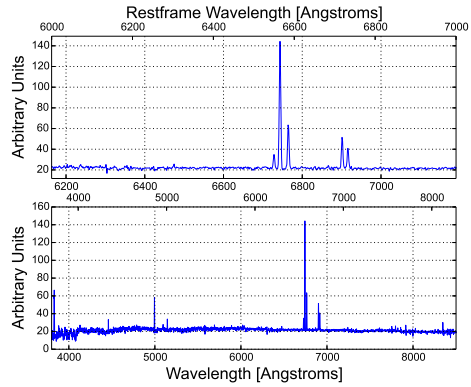
(a)



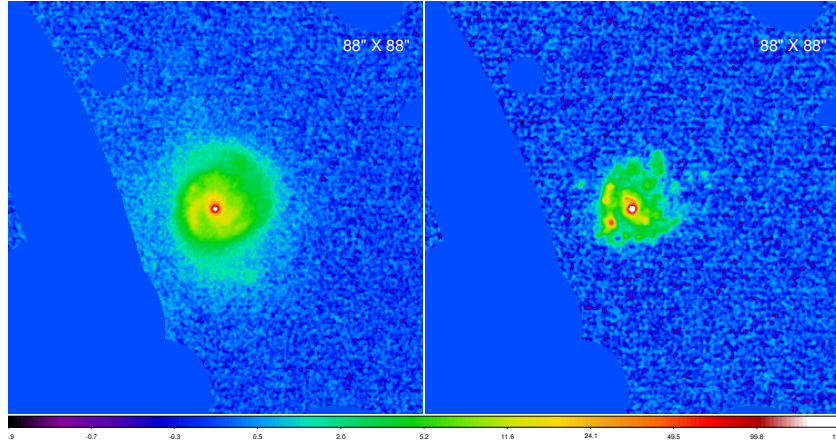
(b)



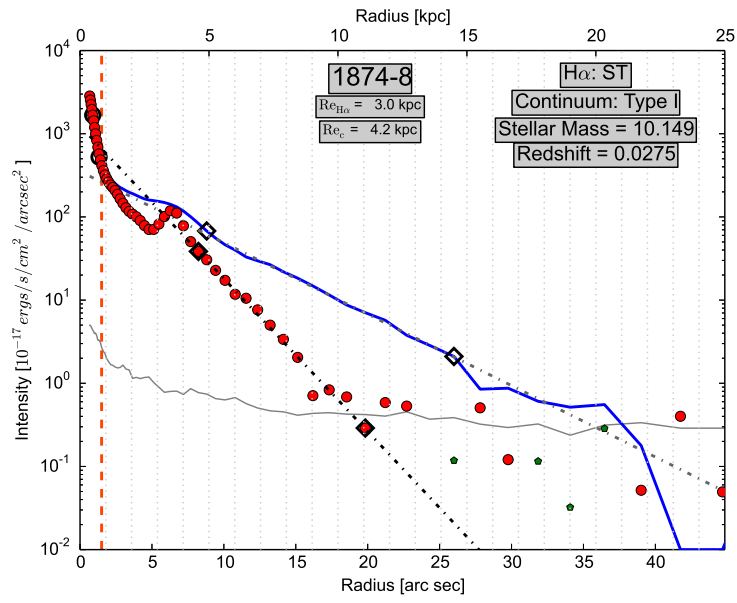
(c)



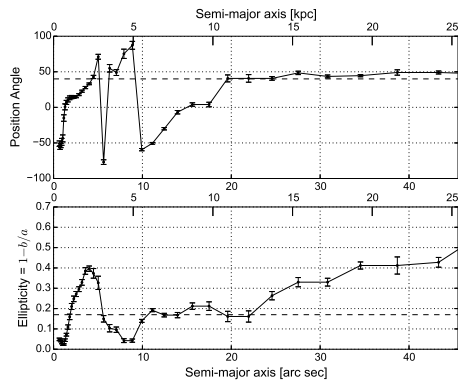
(d)



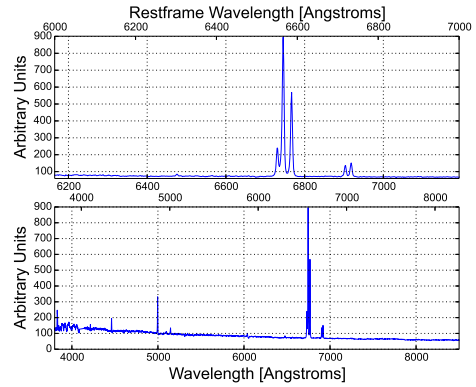
(a)



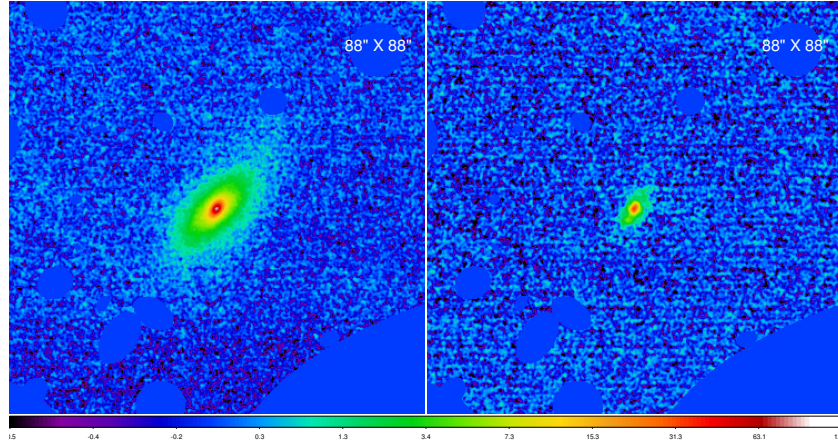
(b)



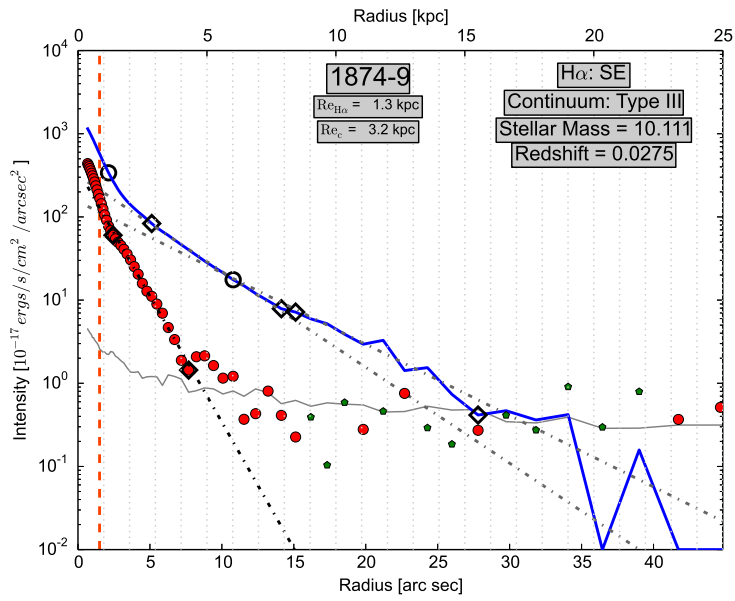
(c)



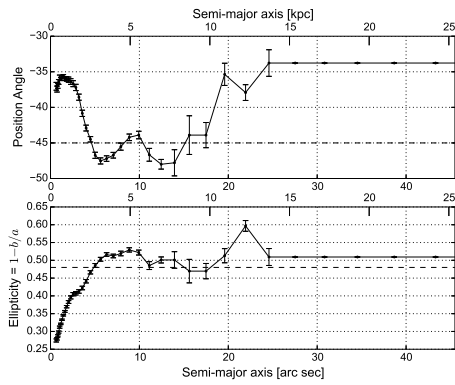
(d)



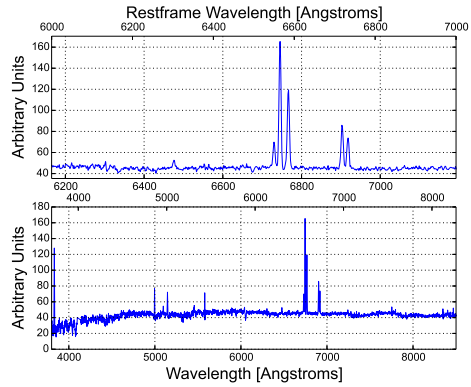
(a)



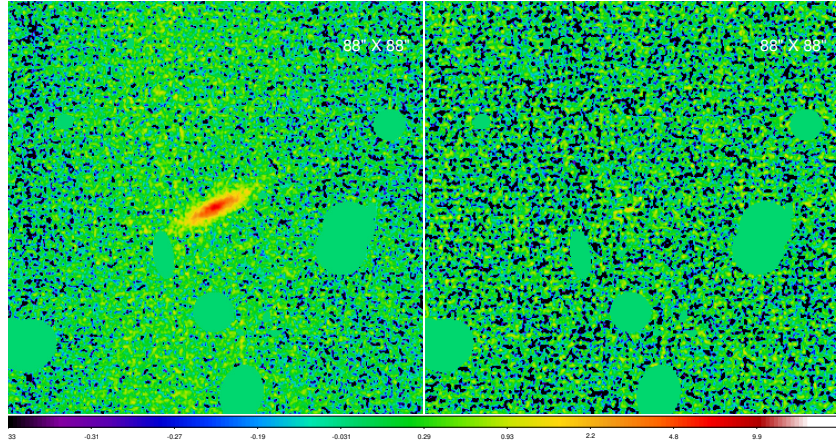
(b)



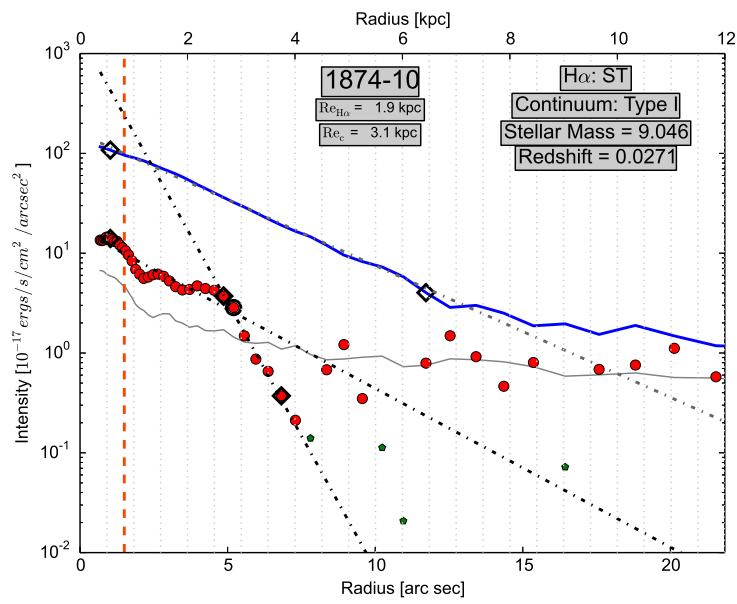
(c)



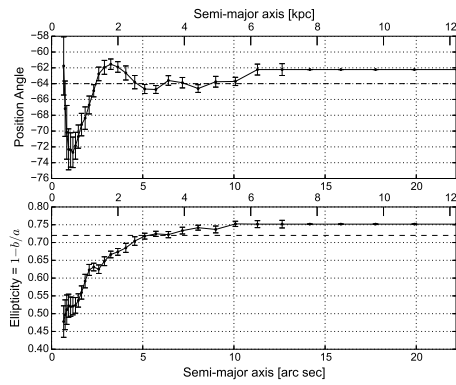
(d)



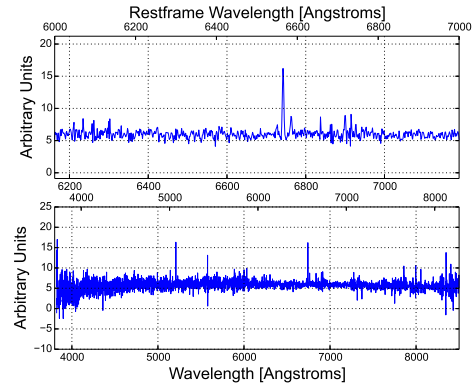
(a)



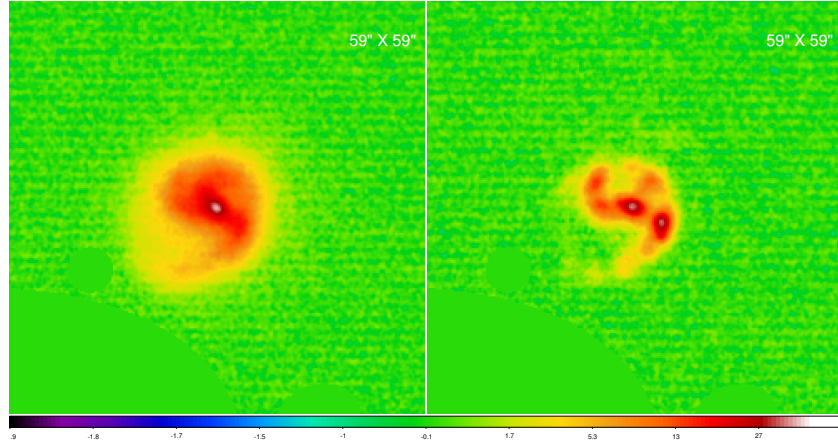
(b)



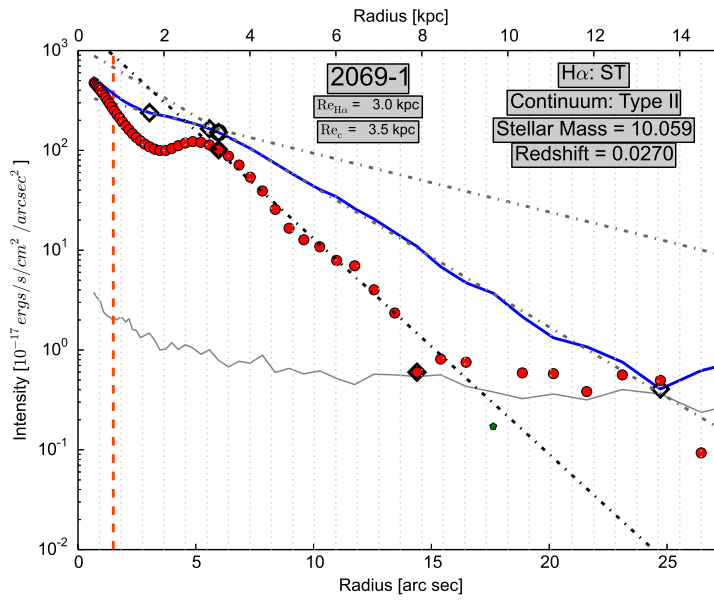
(c)



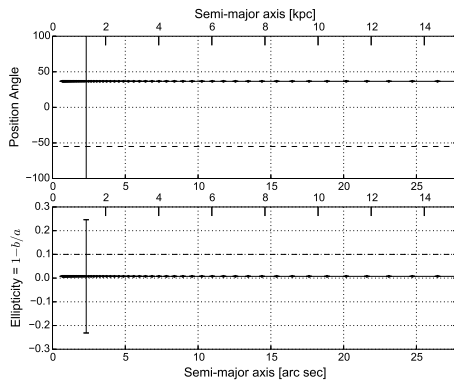
(d)



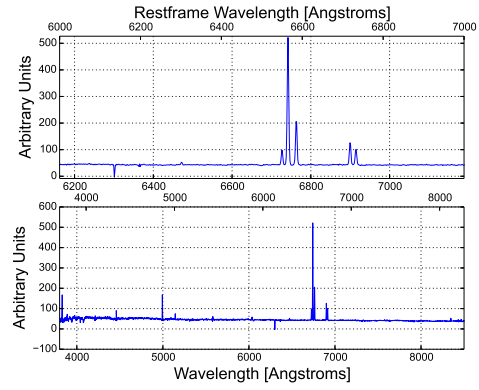
(a)



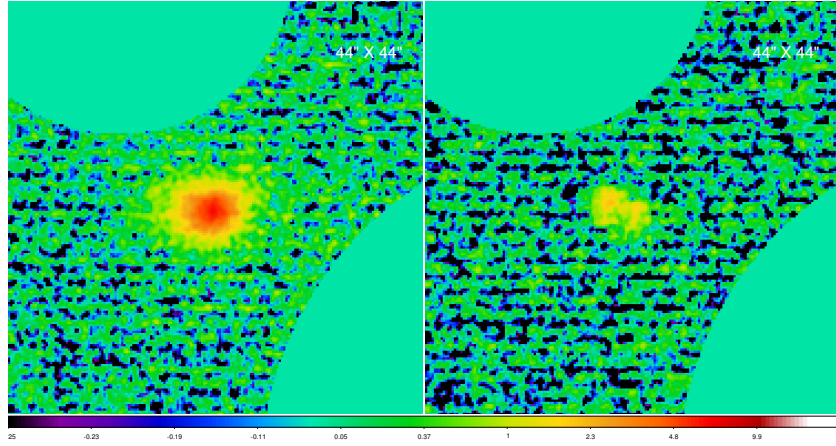
(b)



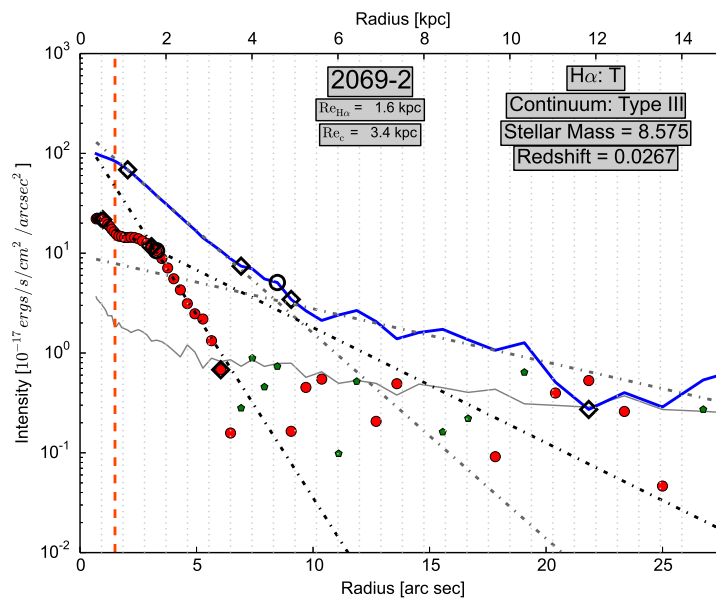
(c)



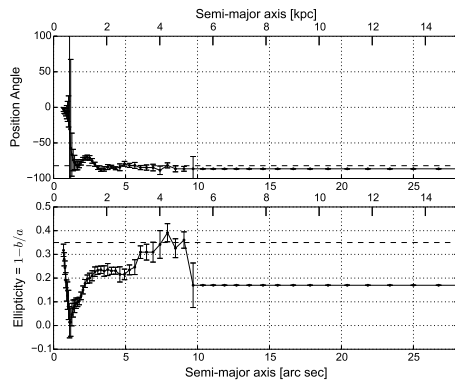
(d)



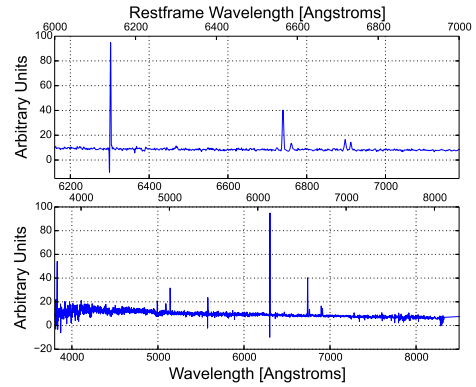
(a)



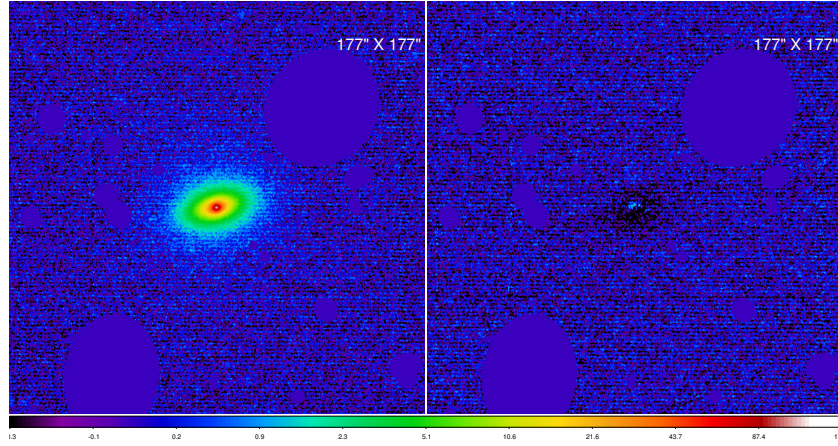
(b)



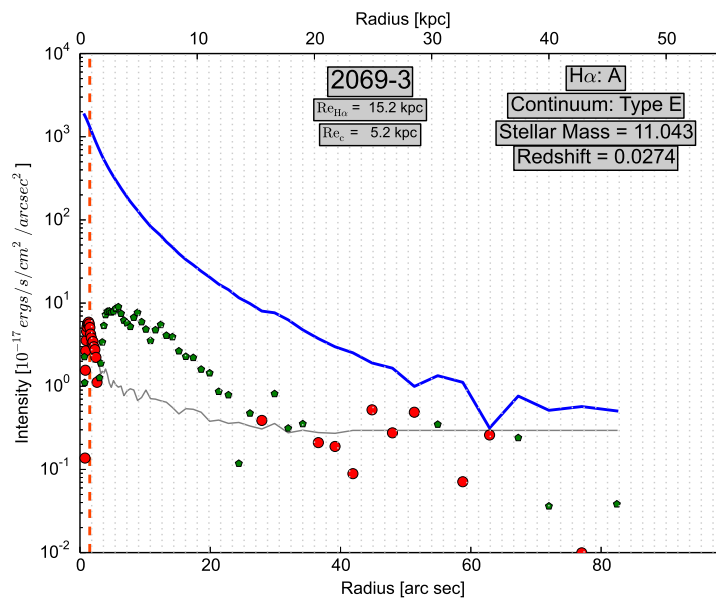
(c)



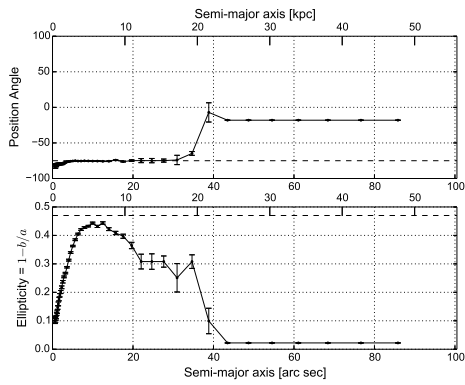
(d)



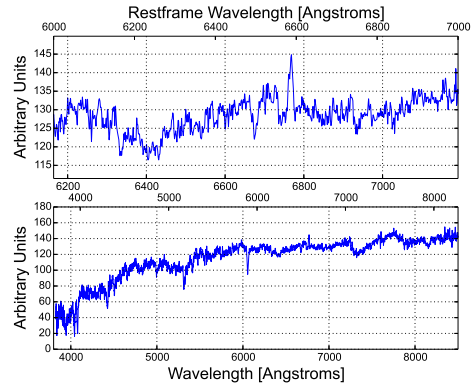
(a)



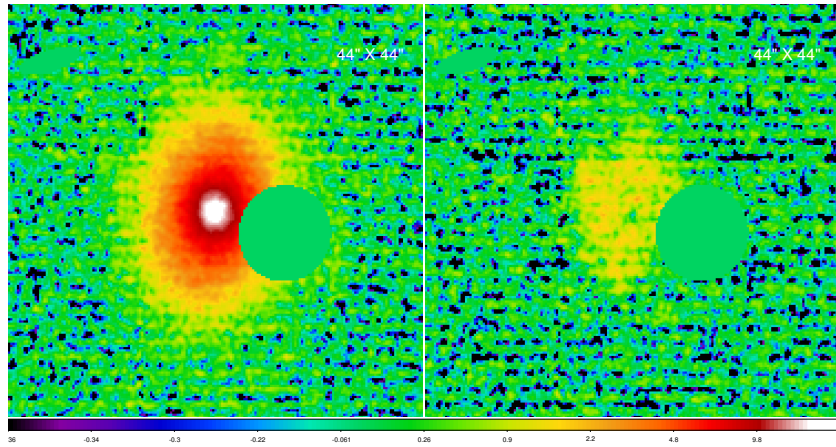
(b)



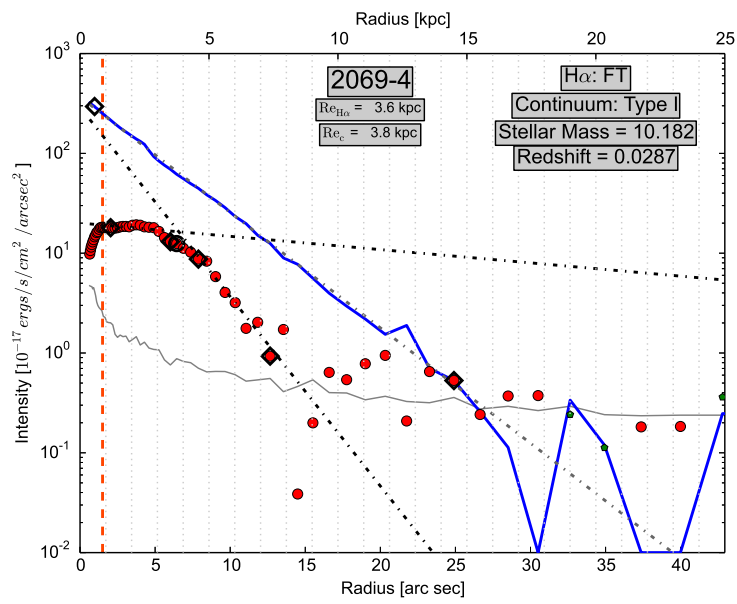
(c)



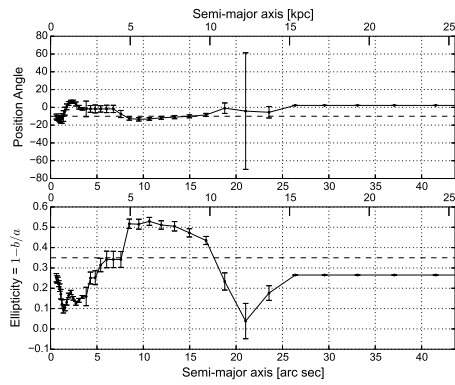
(d)



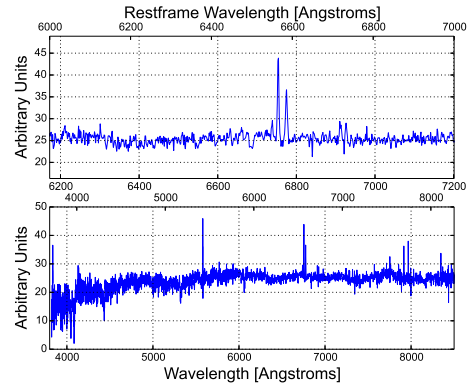
(a)



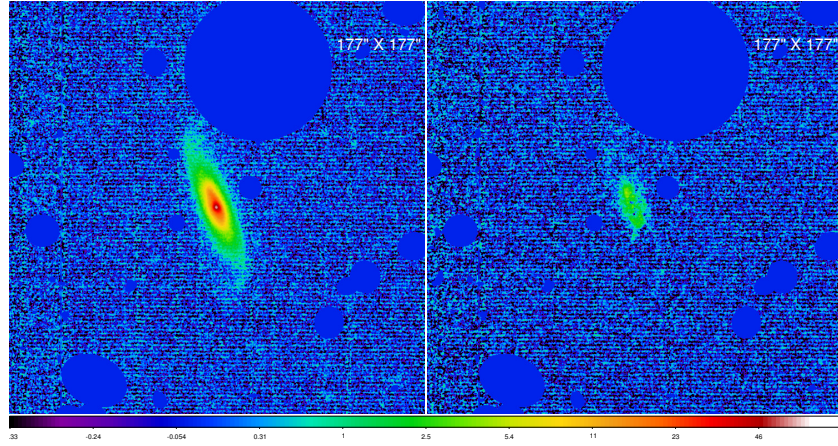
(b)



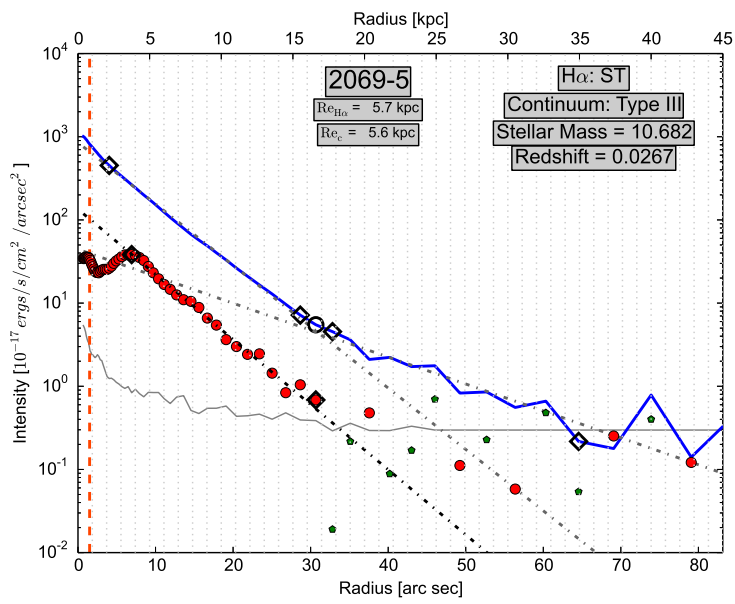
(c)



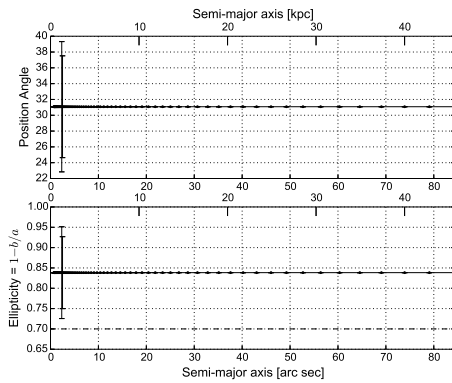
(d)



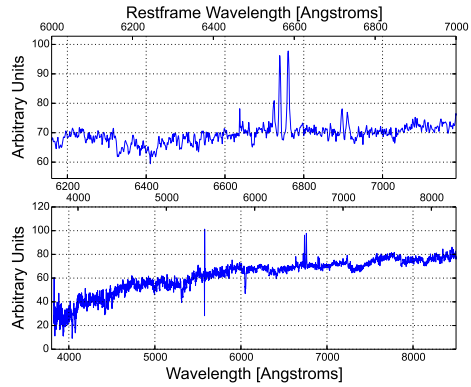
(a)



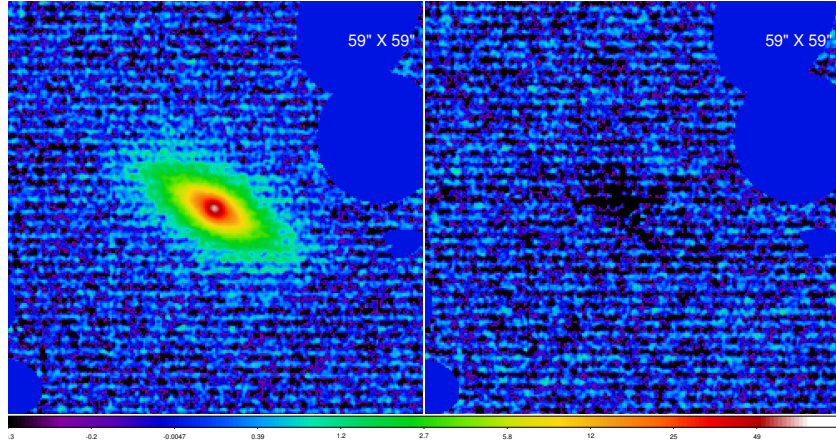
(b)



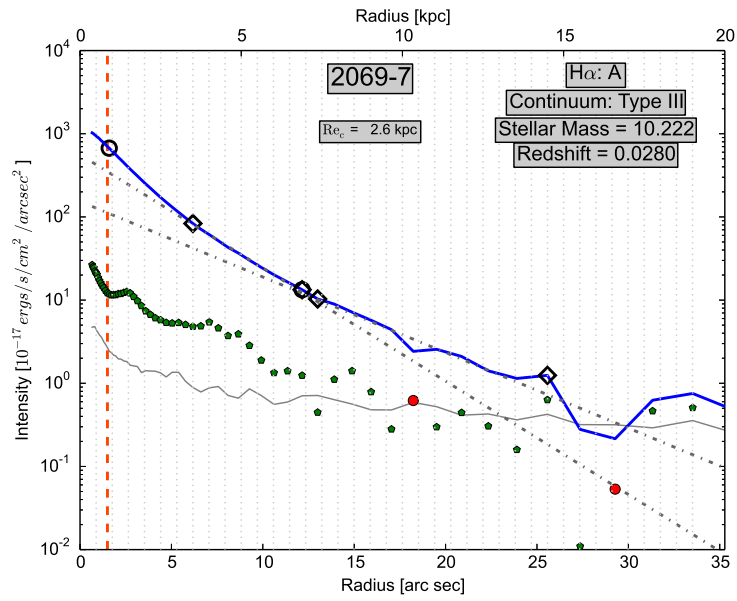
(c)



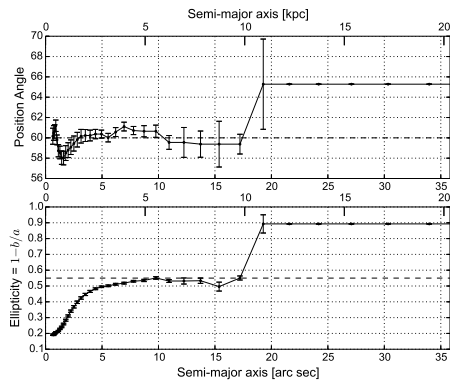
(d)



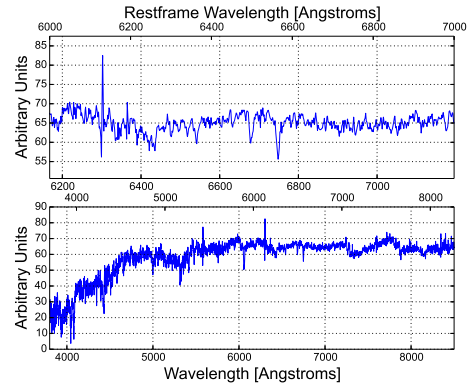
(a)



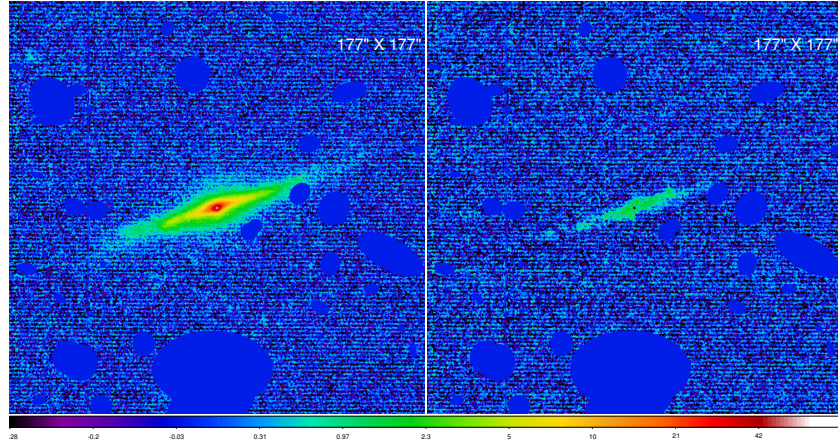
(b)



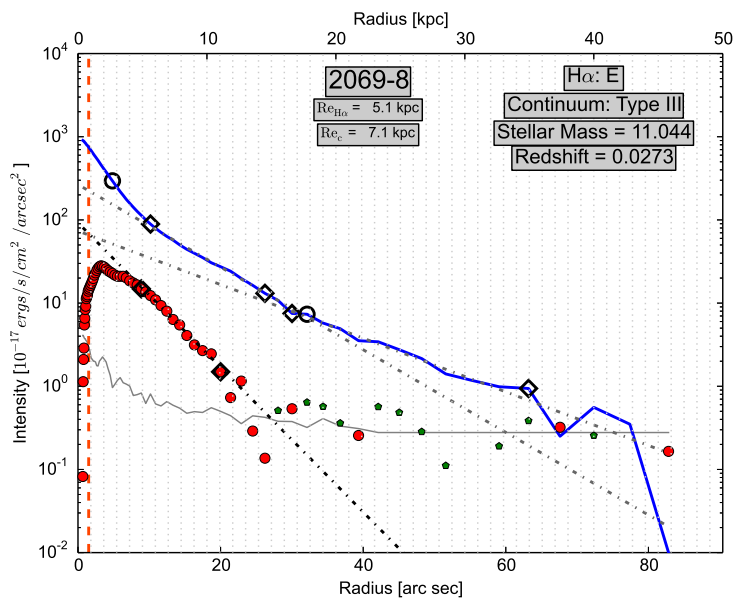
(c)



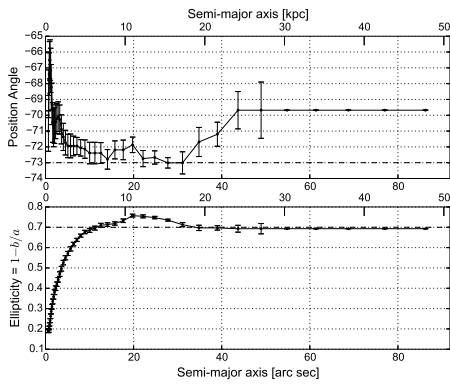
(d)



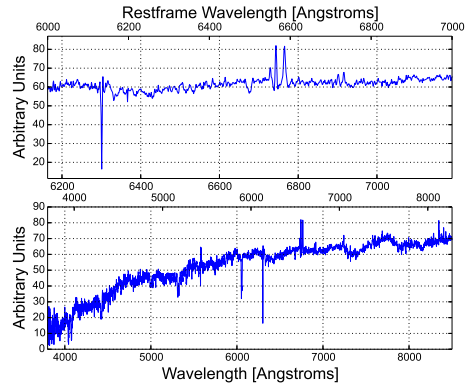
(a)



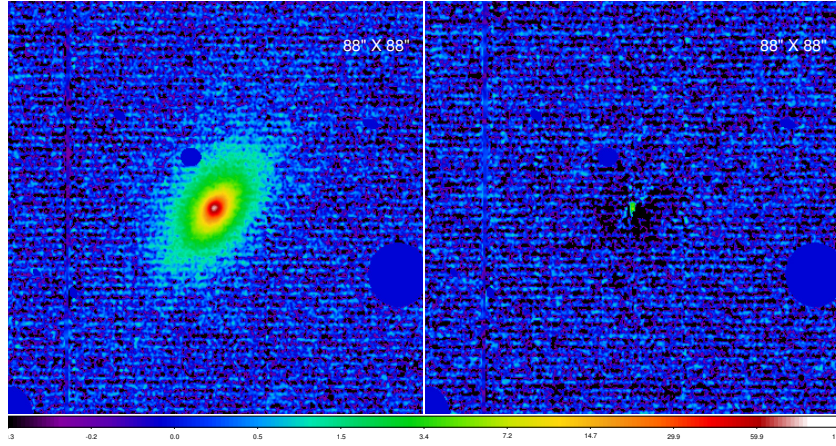
(b)



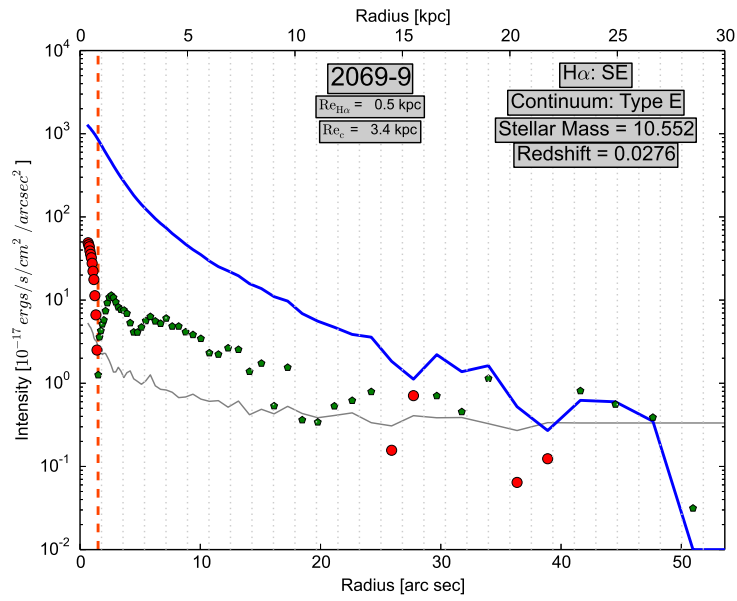
(c)



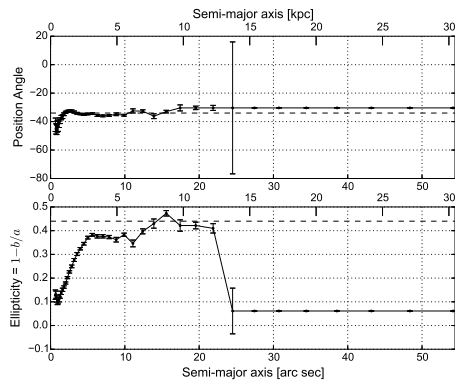
(d)



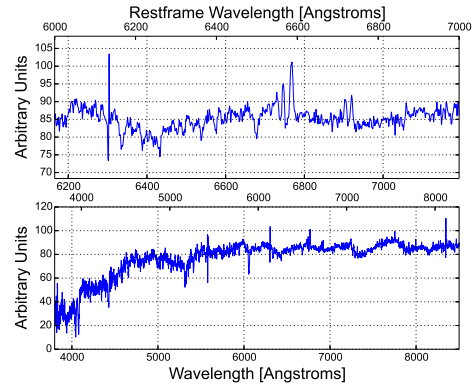
(a)



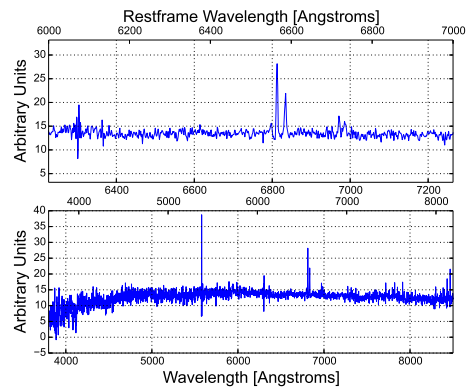
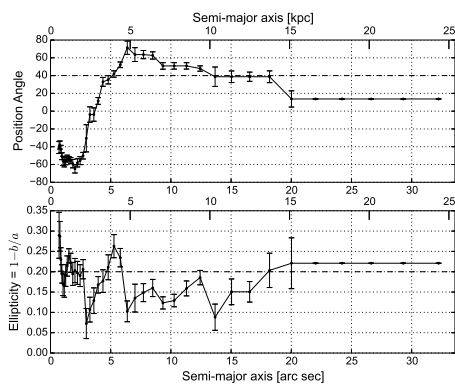
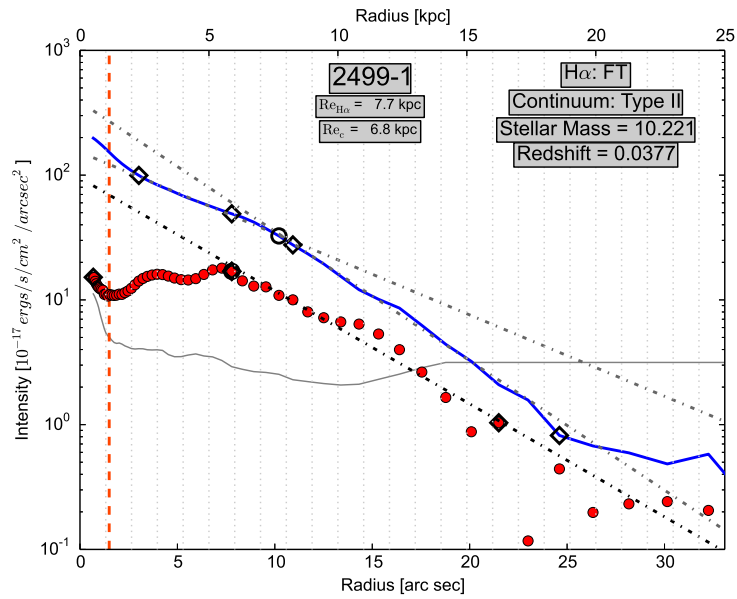
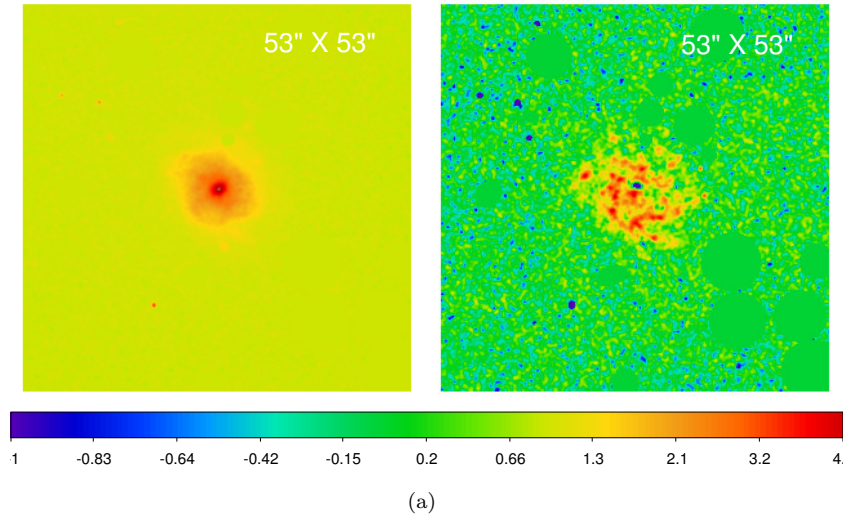
(b)

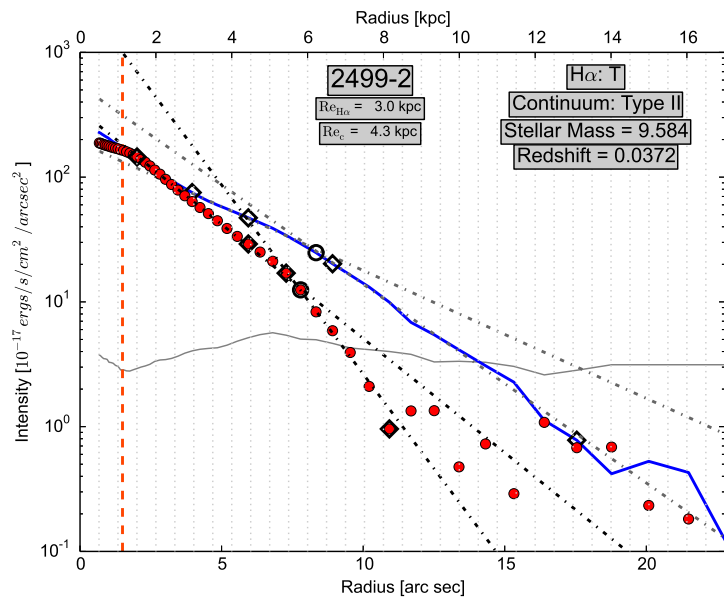
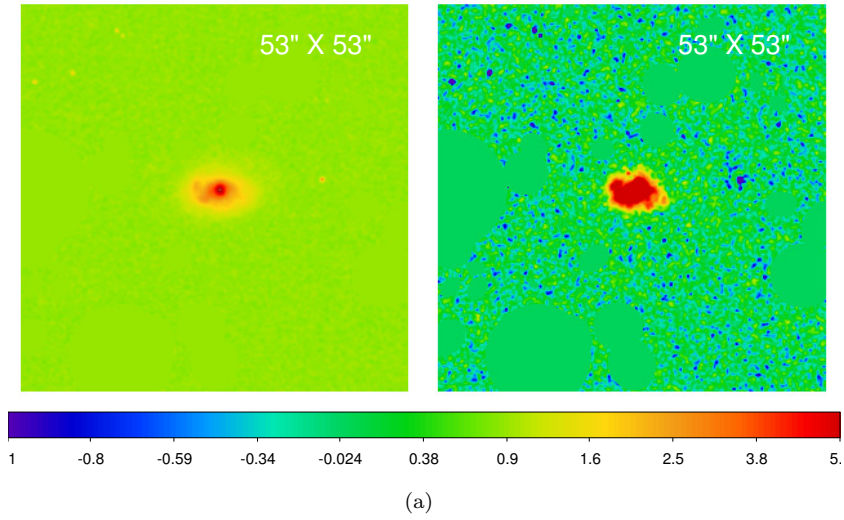


(c)

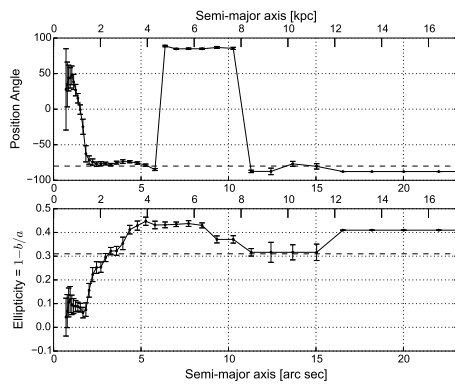


(d)

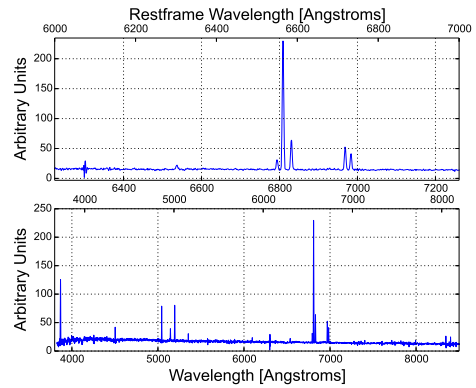




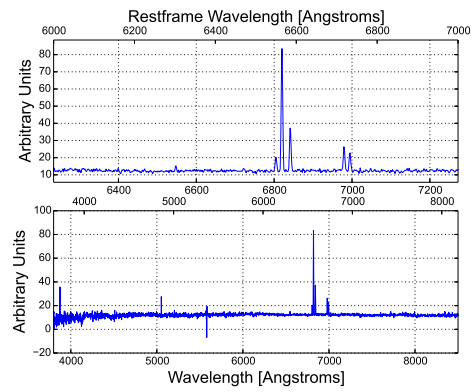
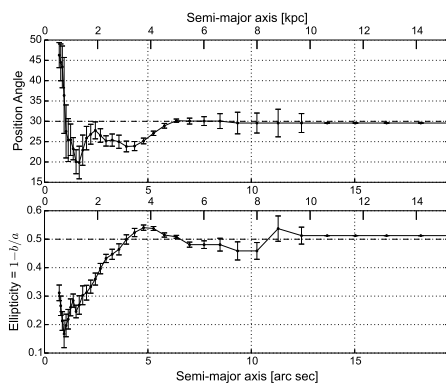
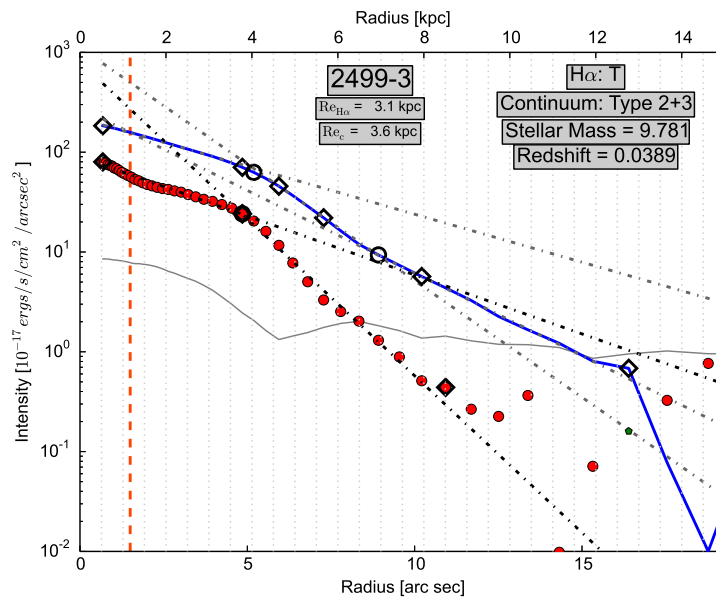
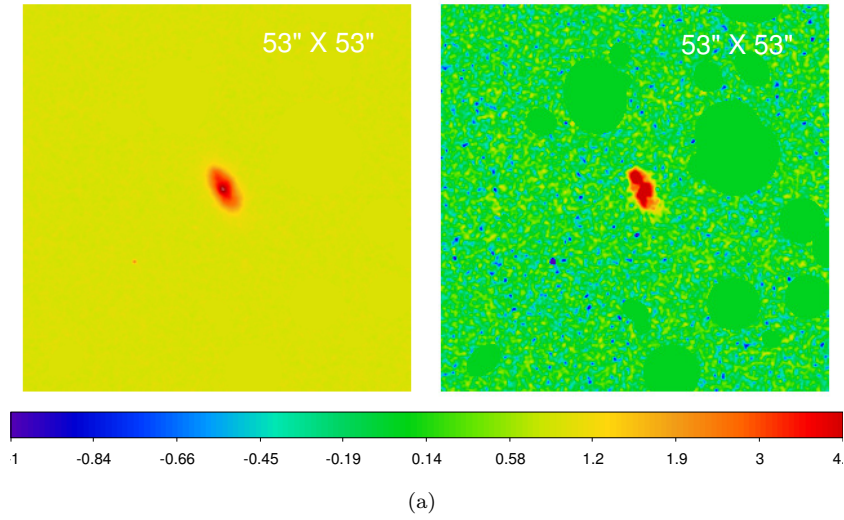
(b)

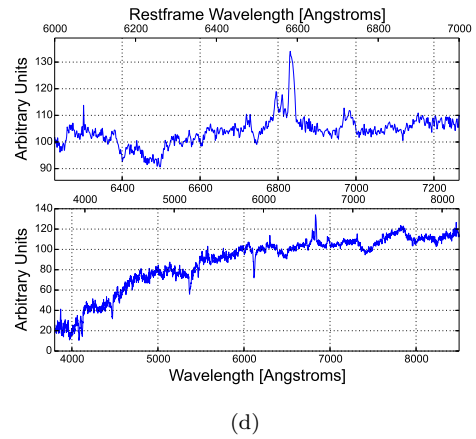
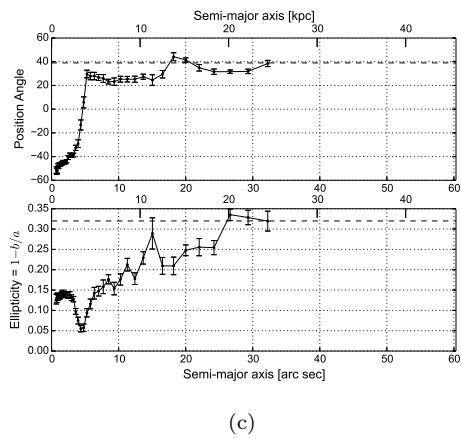
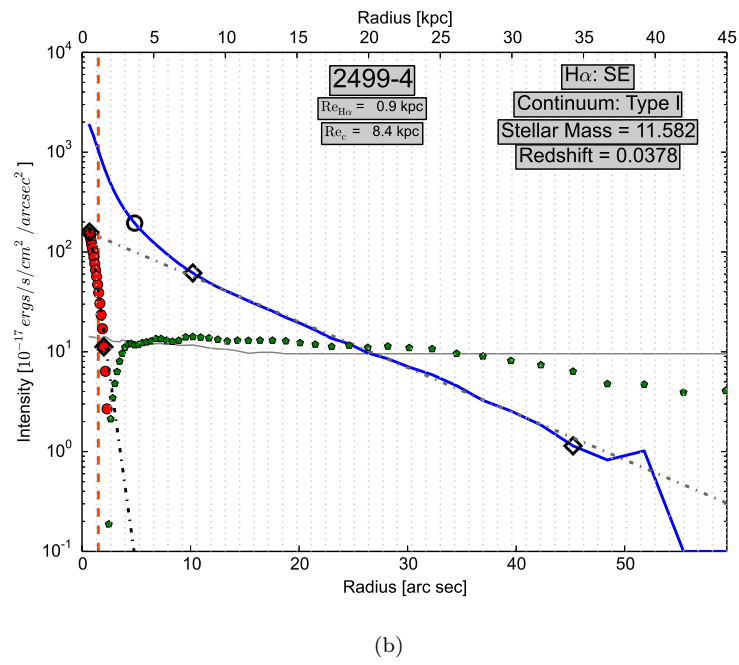
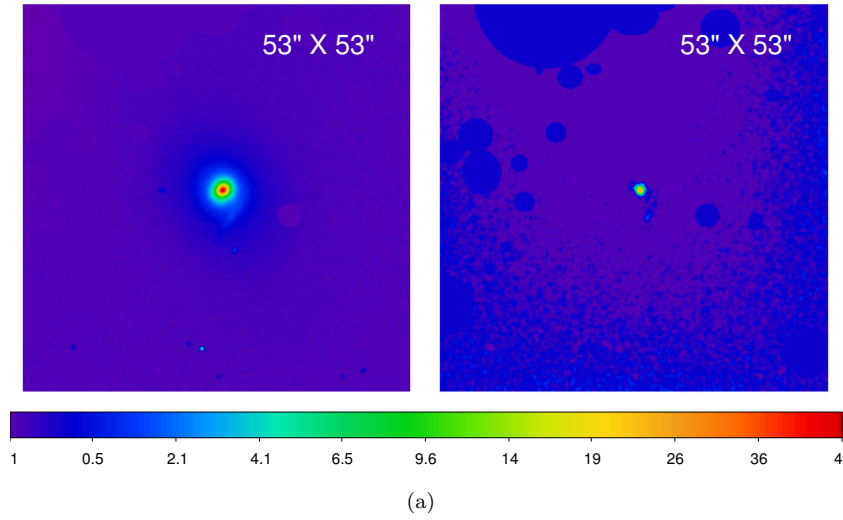


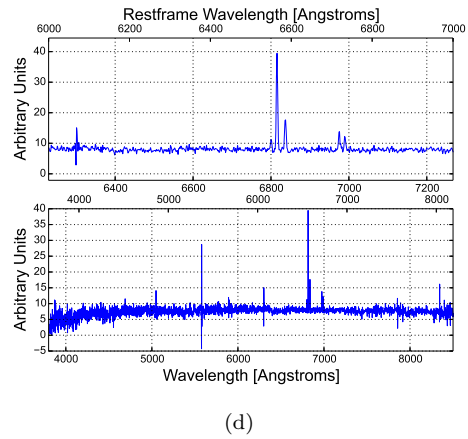
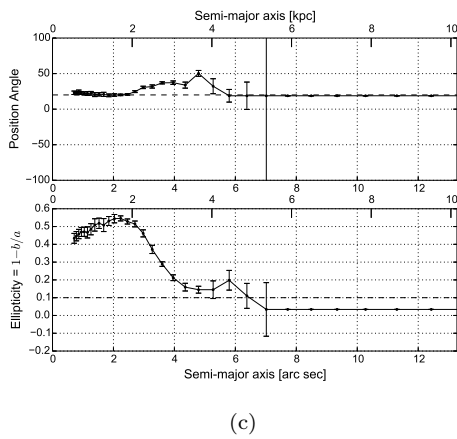
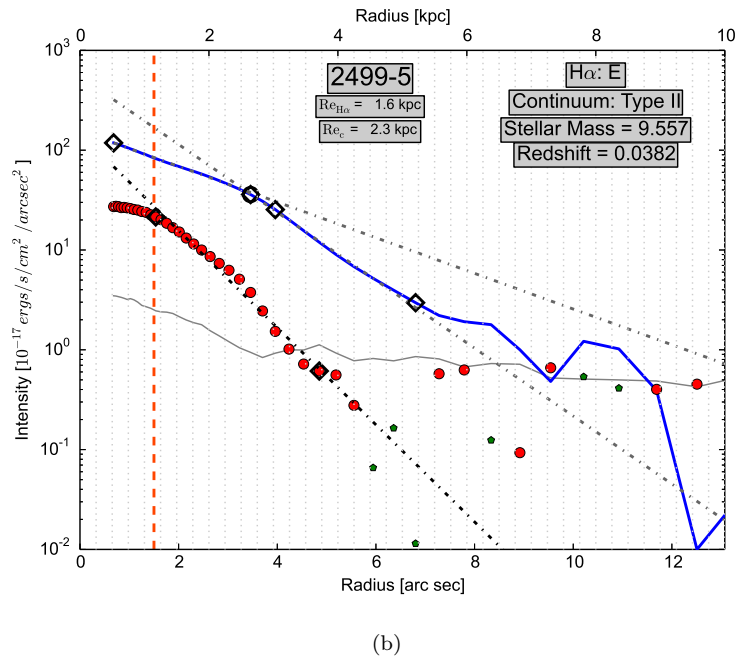
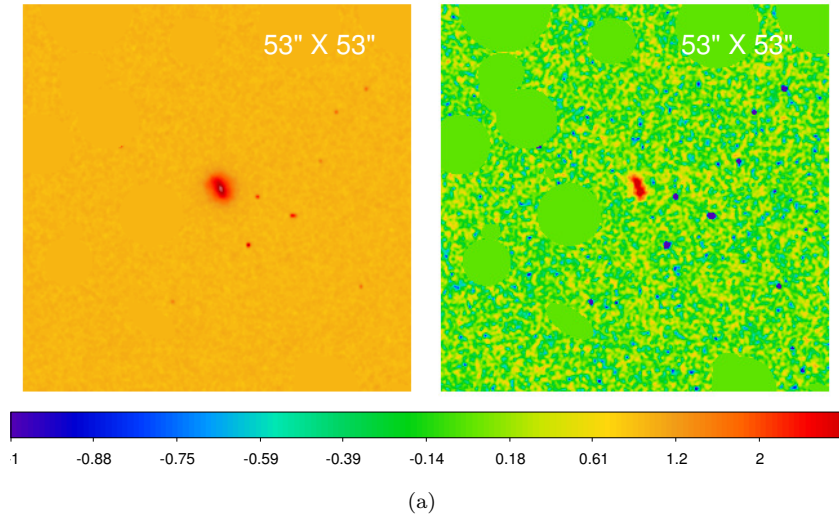
(c)

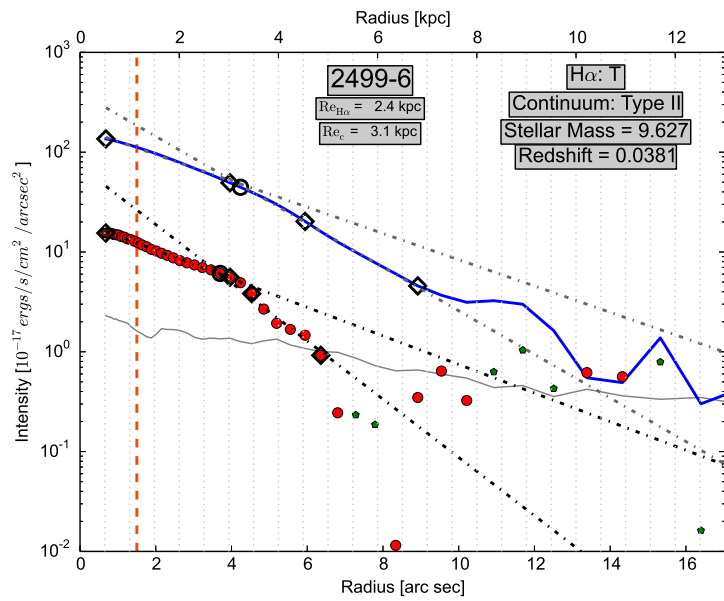
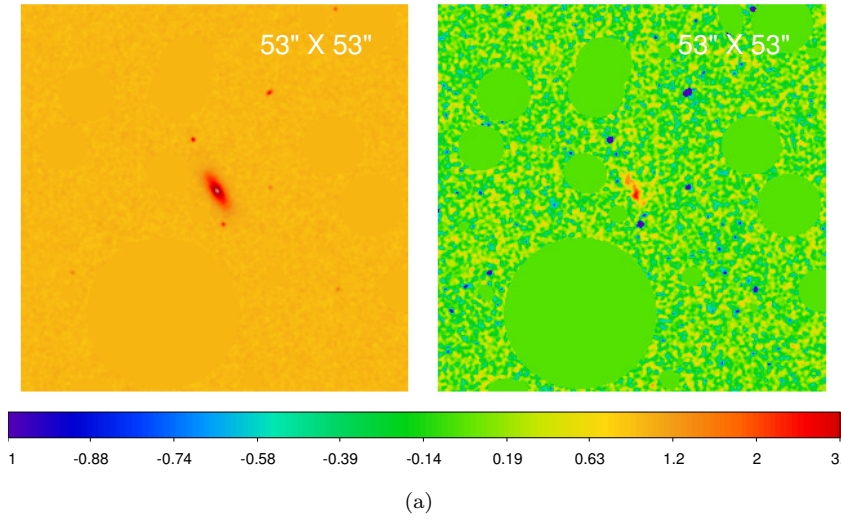


(d)

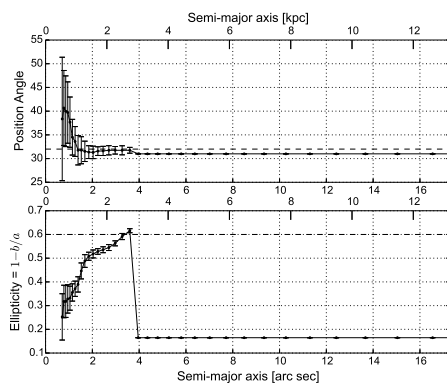




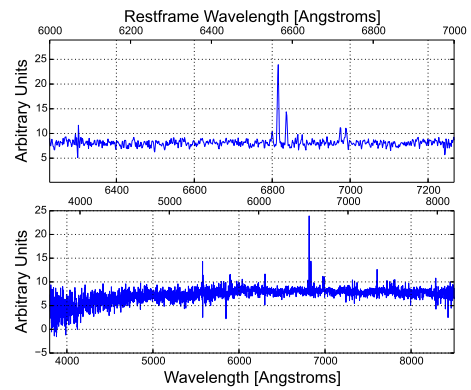




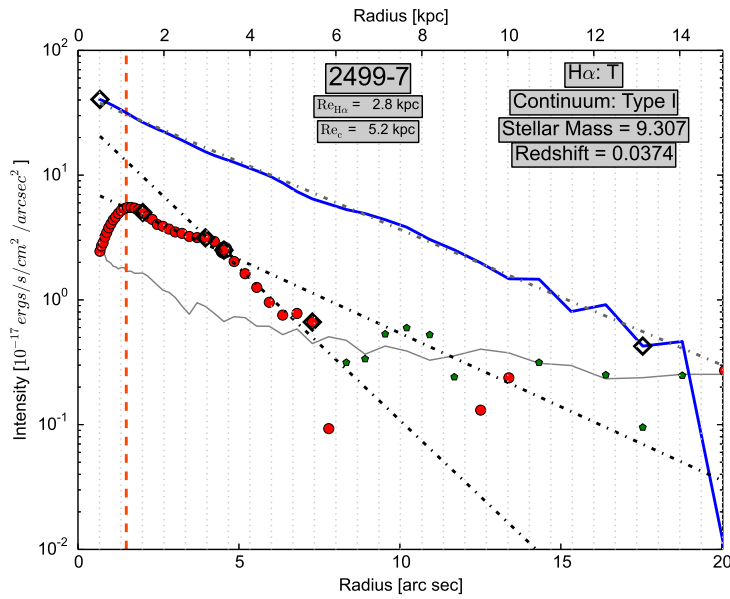
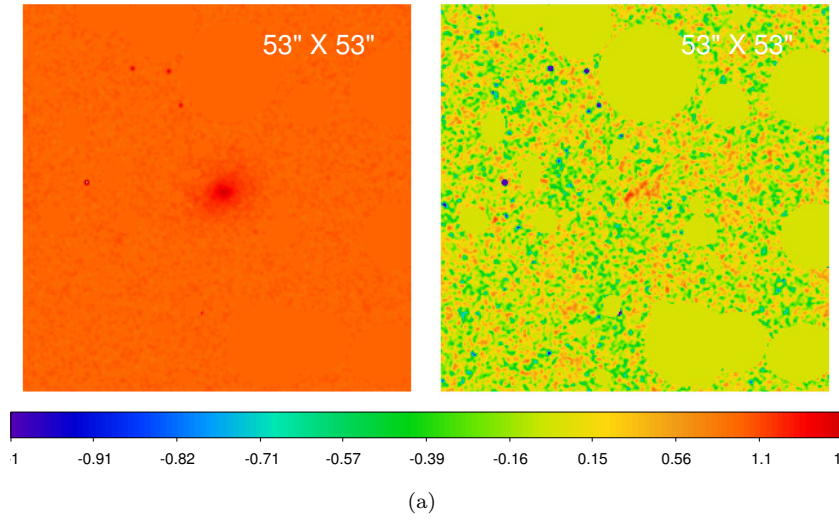
(b)



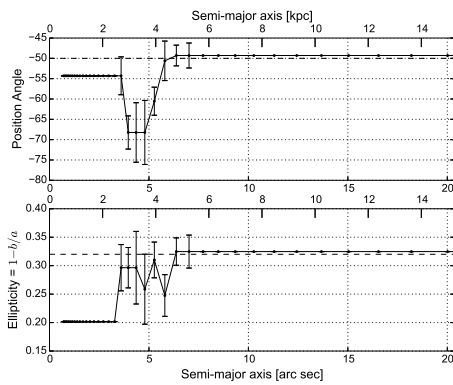
(c)



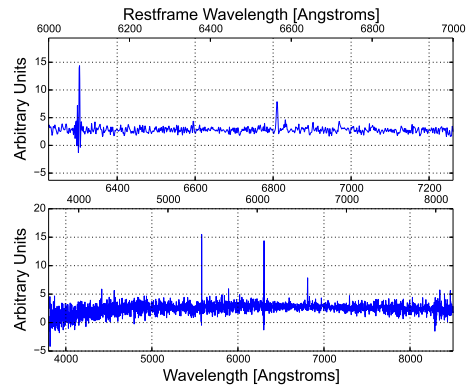
(d)



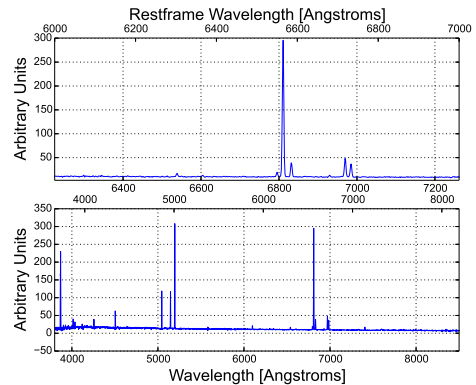
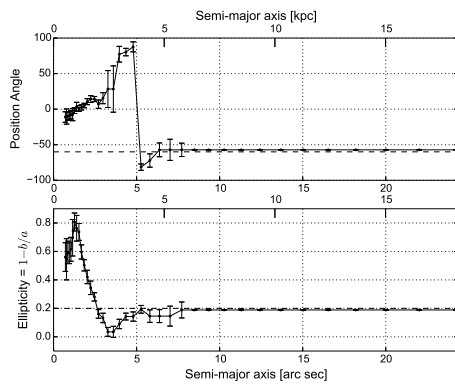
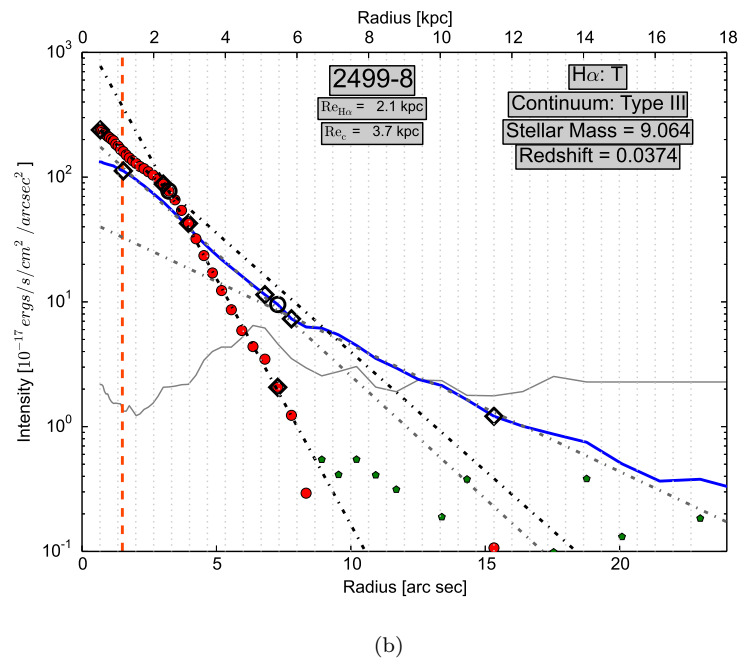
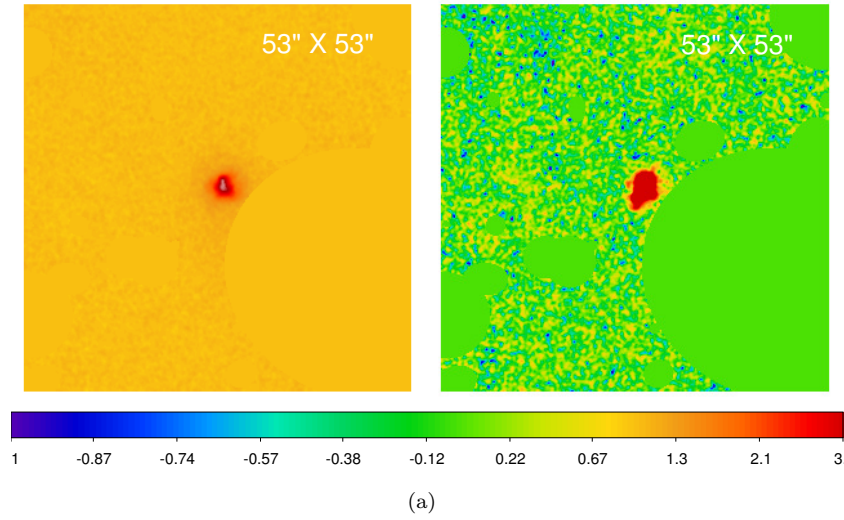
(b)

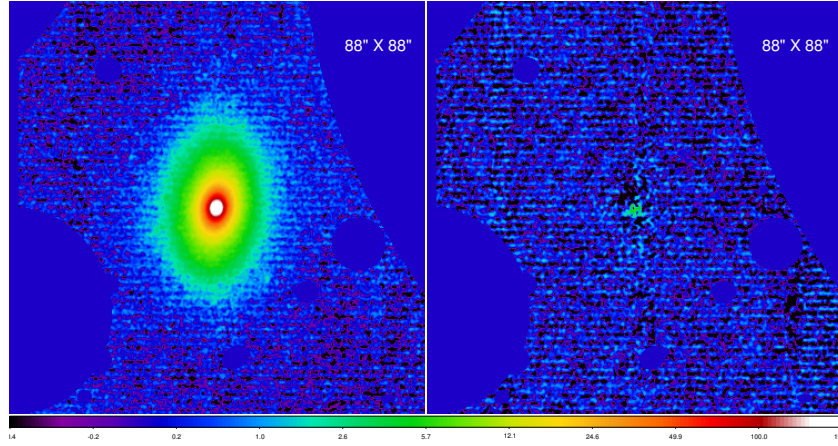


(c)

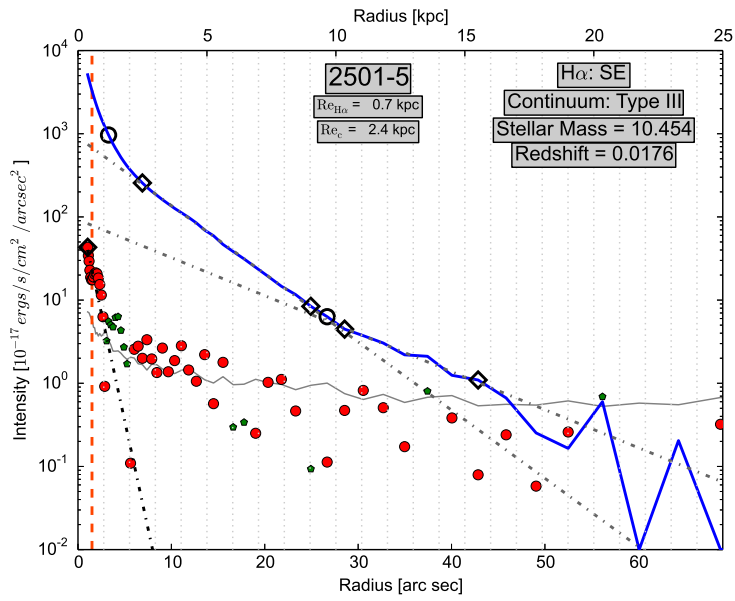


(d)

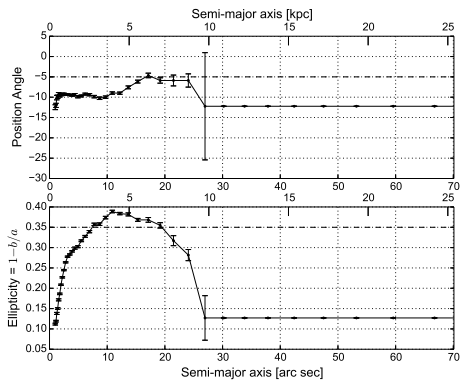




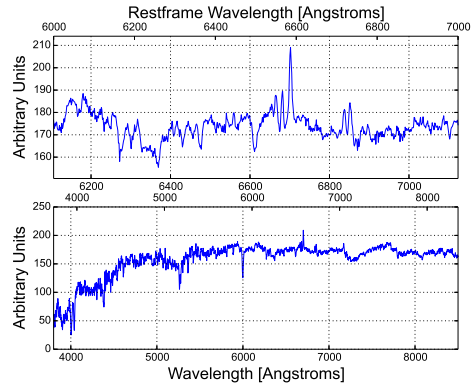
(a)



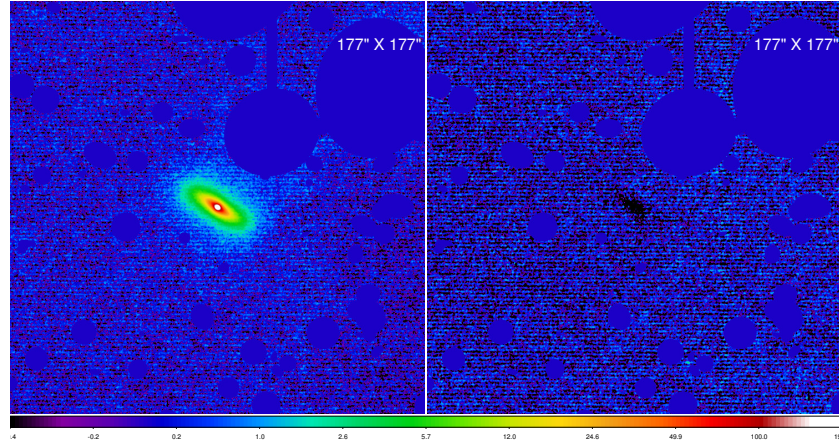
(b)



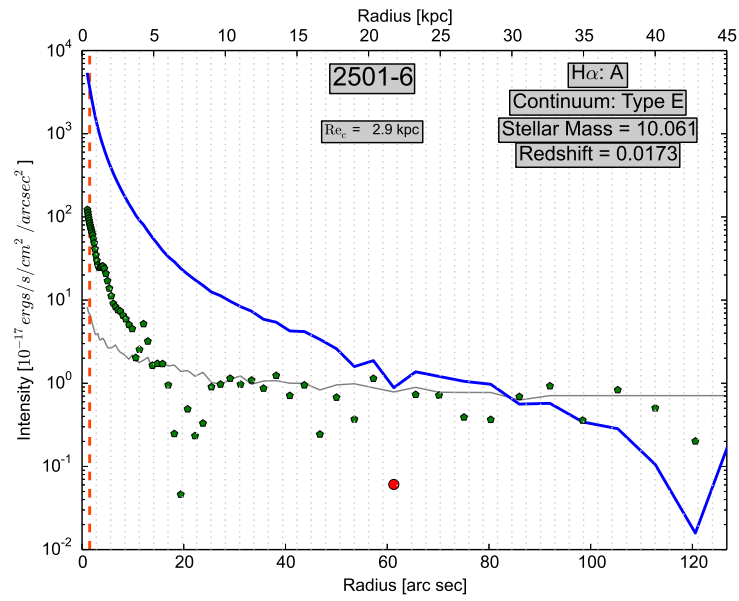
(c)



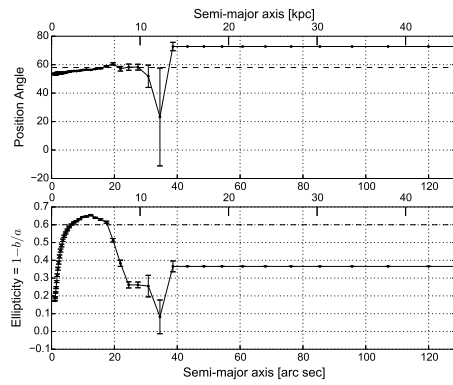
(d)



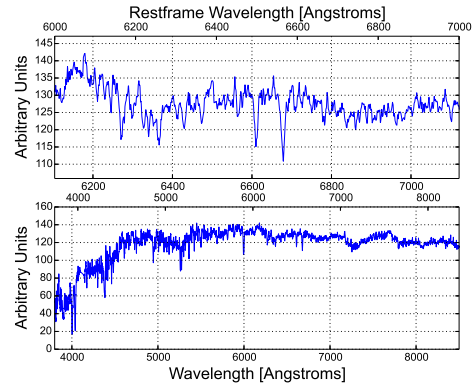
(a)



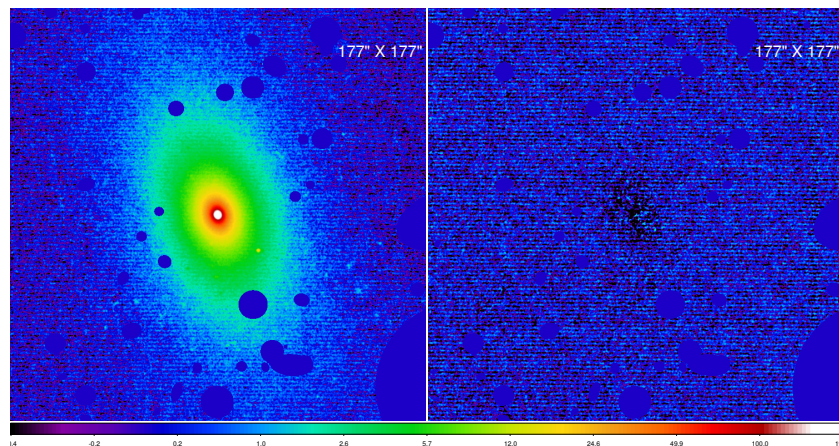
(b)



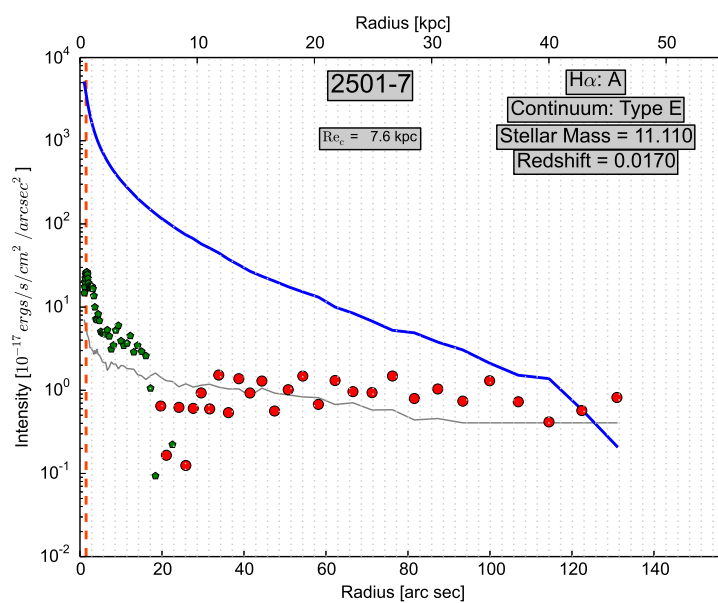
(c)



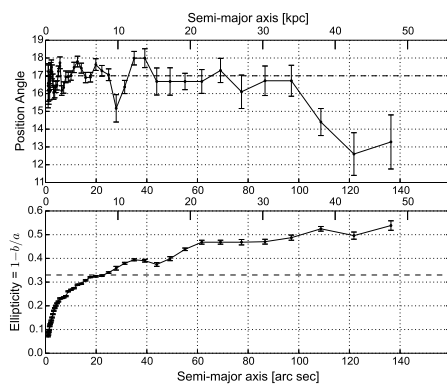
(d)



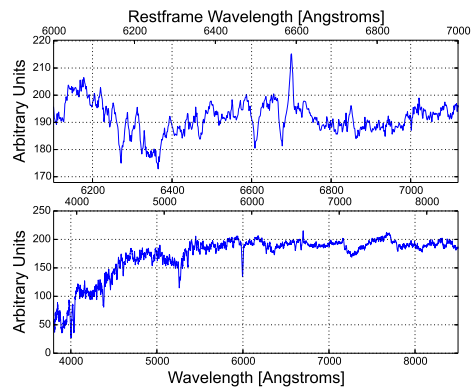
(a)



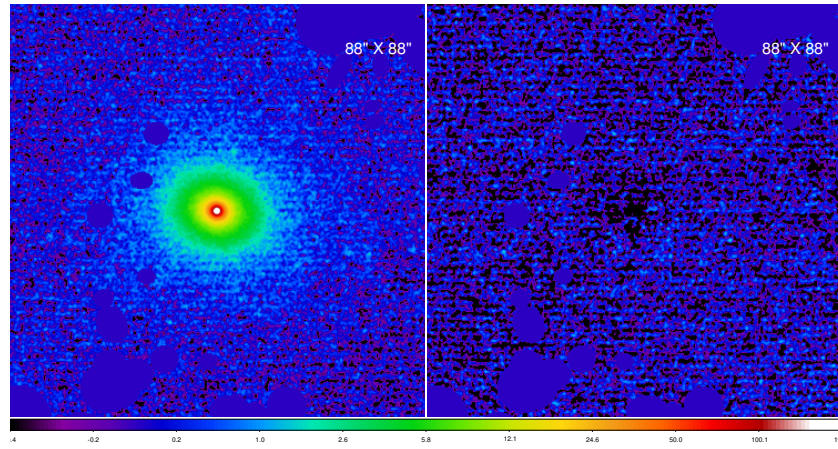
(b)



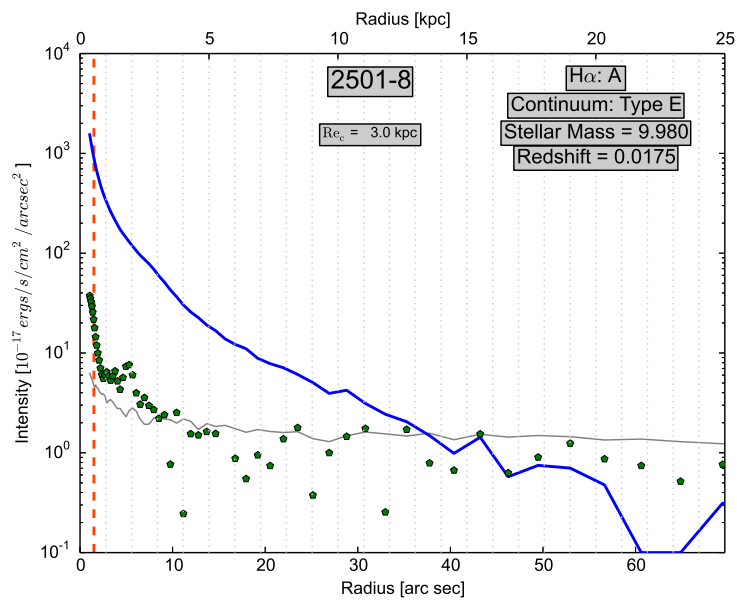
(c)



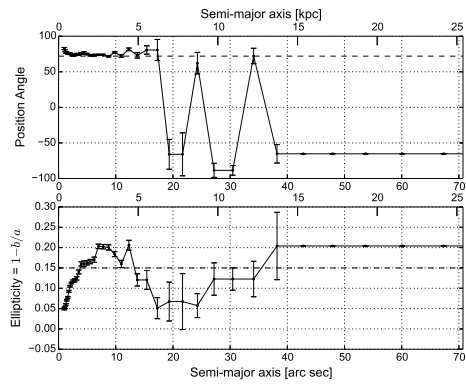
(d)



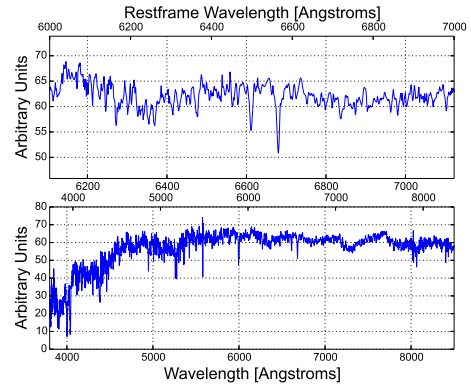
(a)



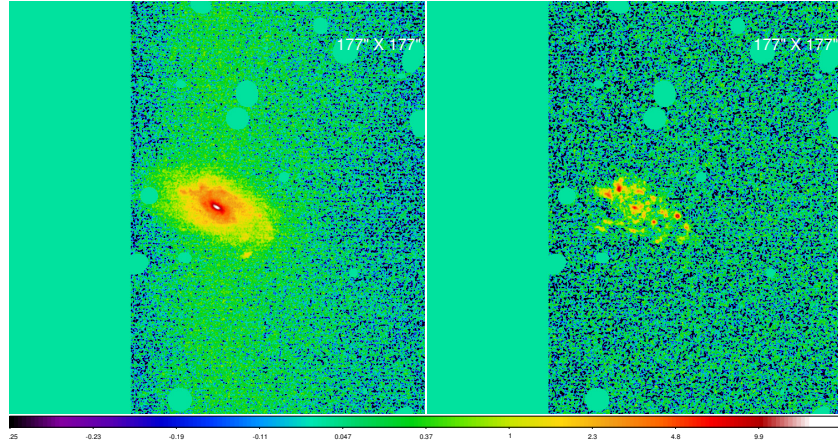
(b)



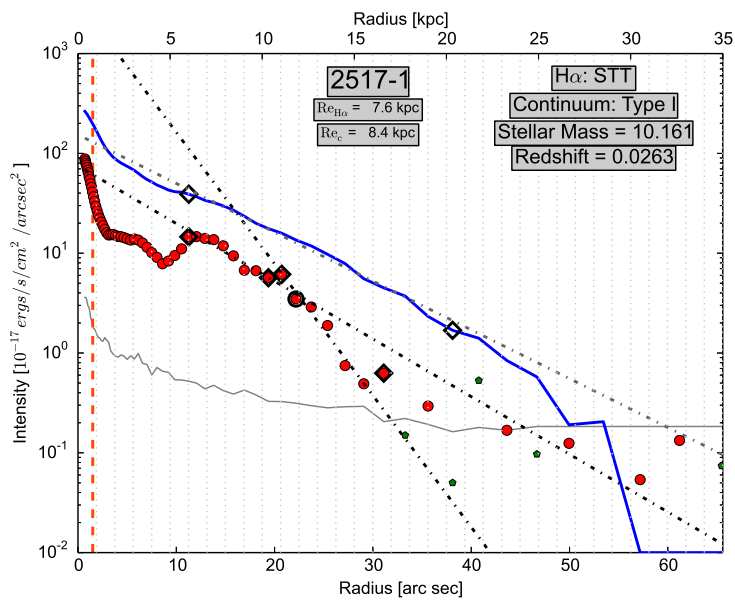
(c)



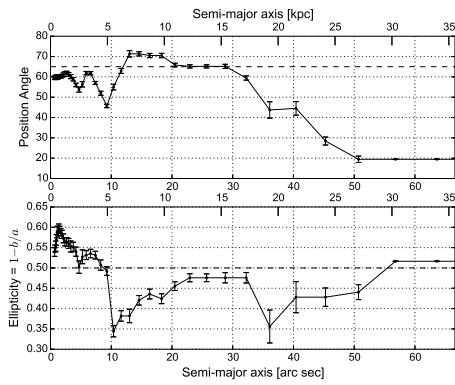
(d)



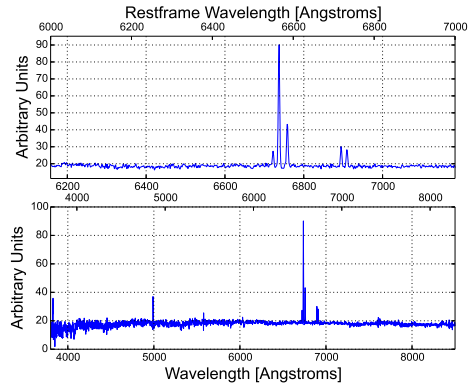
(a)



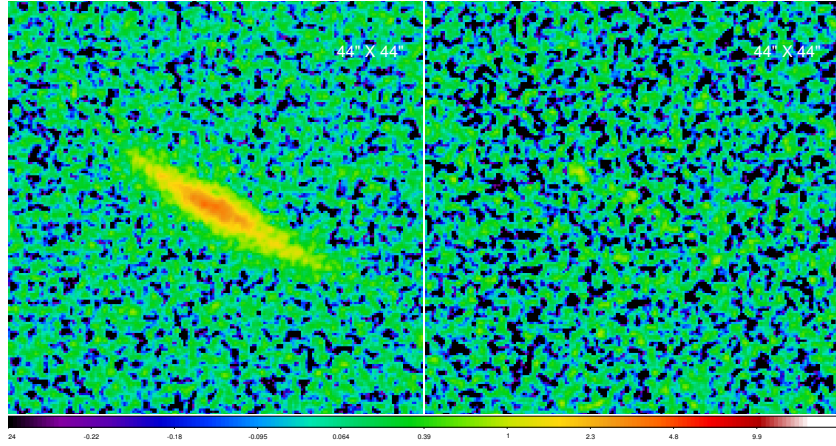
(b)



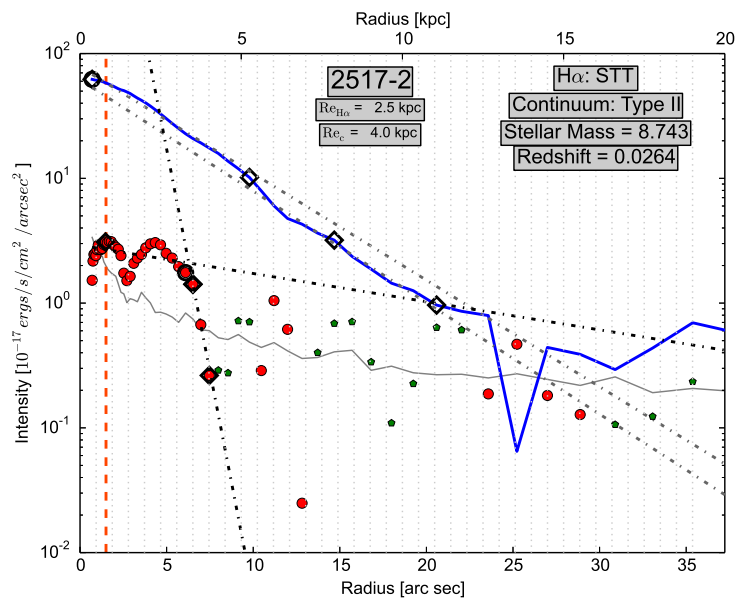
(c)



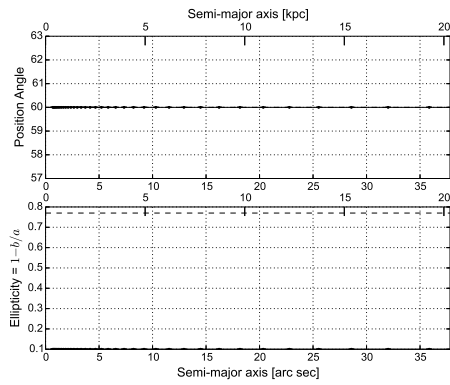
(d)



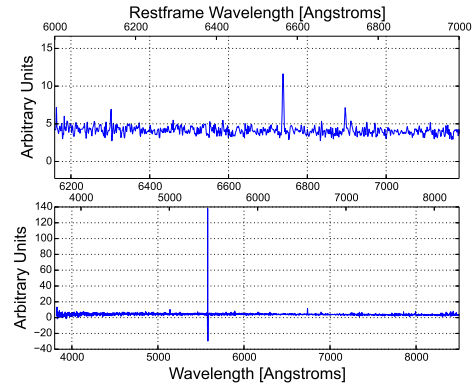
(a)



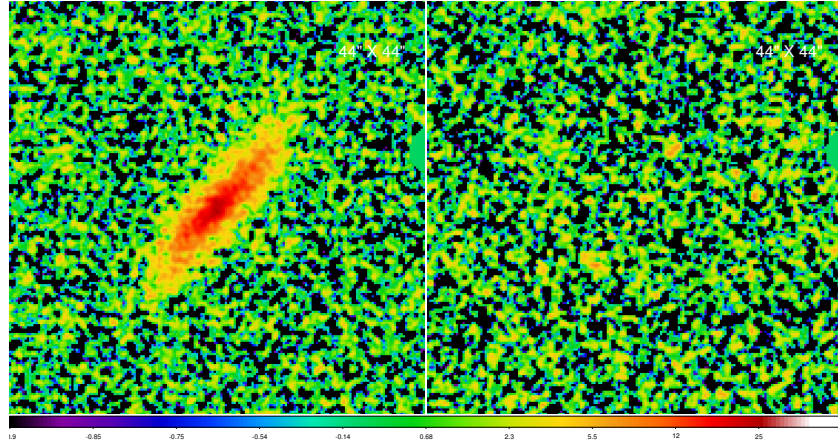
(b)



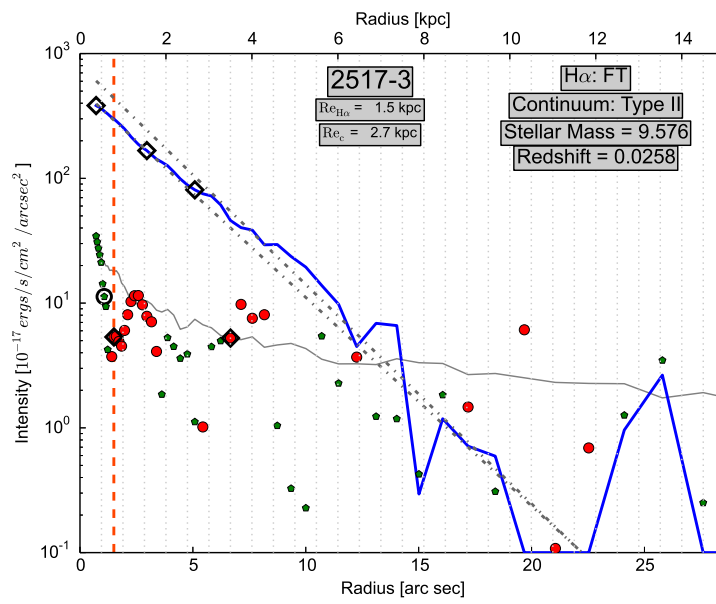
(c)



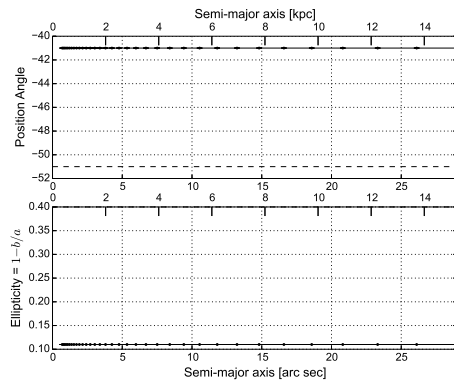
(d)



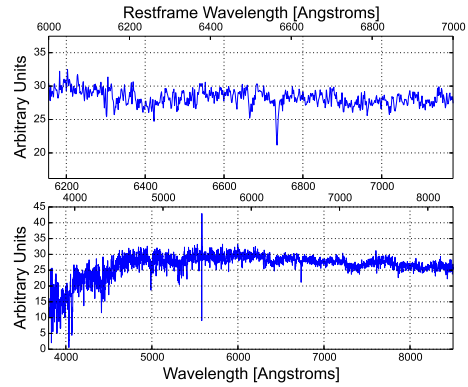
(a)



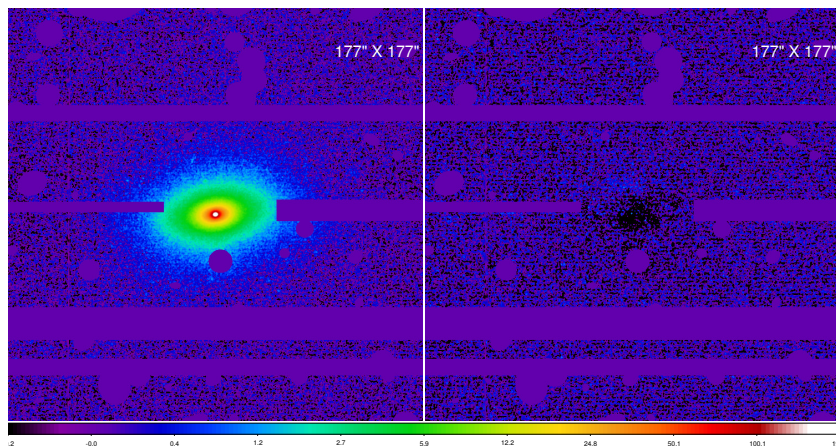
(b)



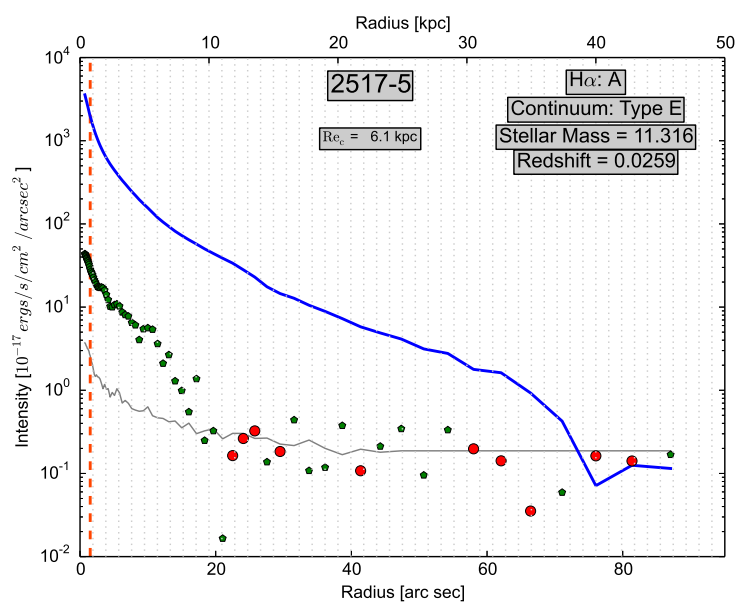
(c)



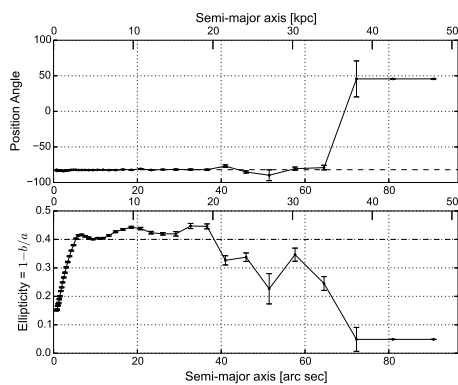
(d)



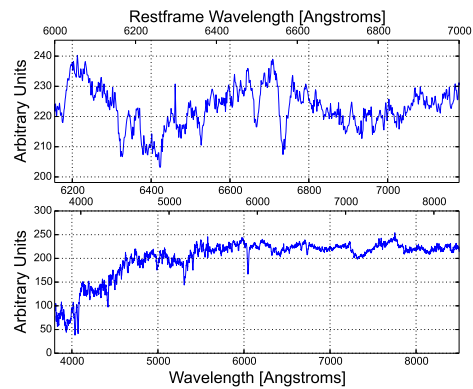
(a)



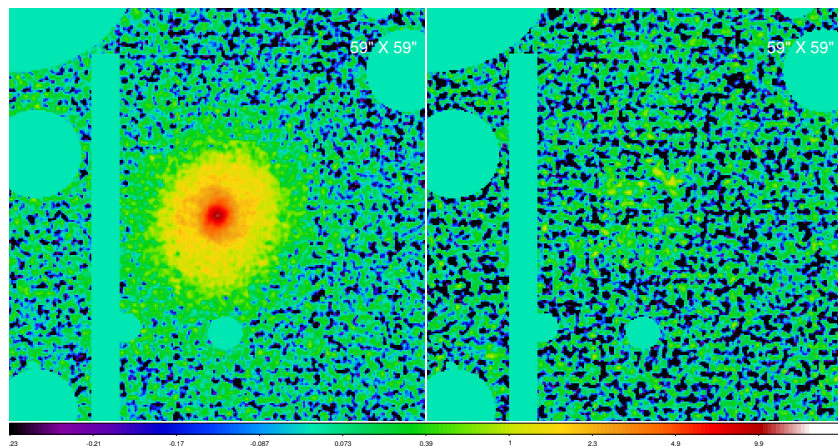
(b)



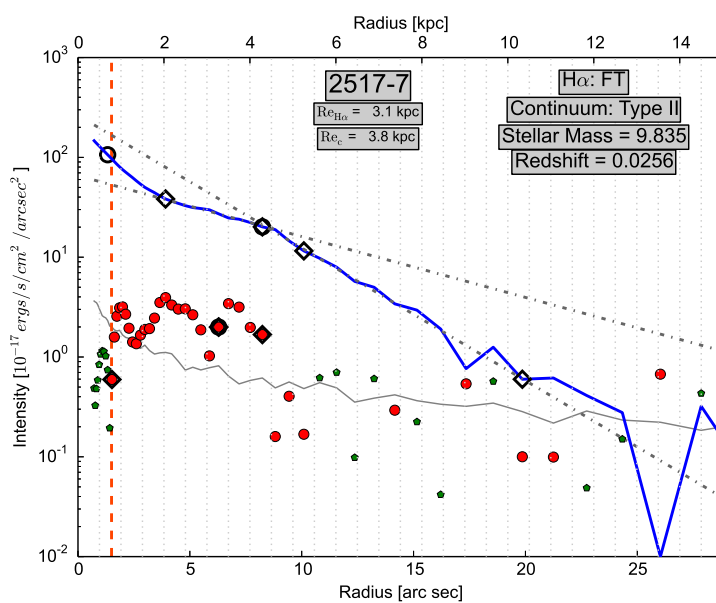
(c)



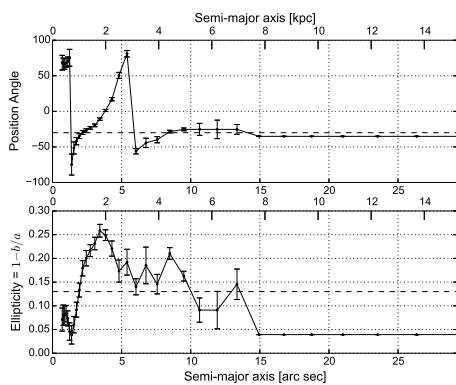
(d)



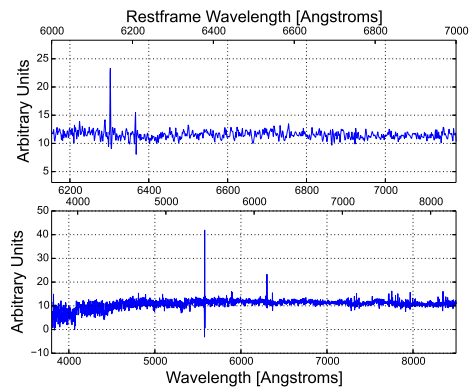
(a)



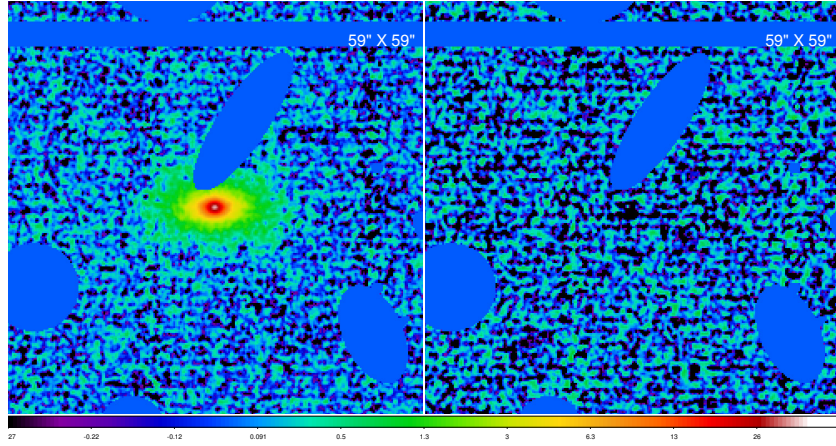
(b)



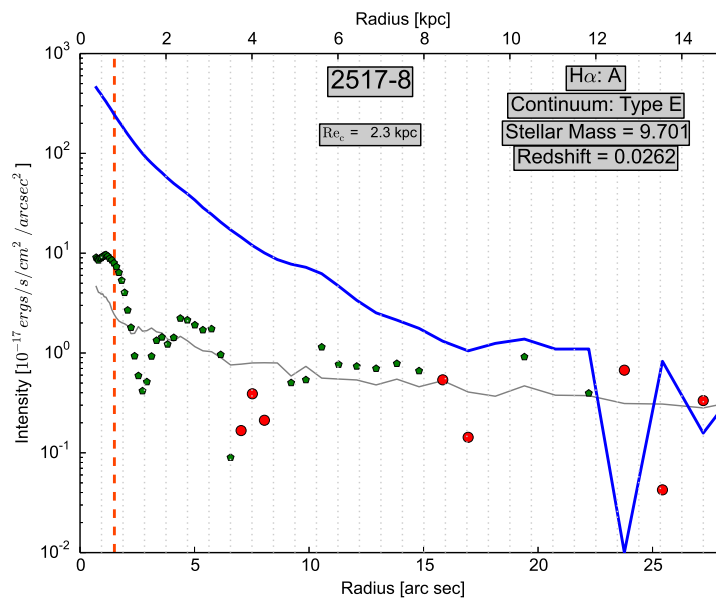
(c)



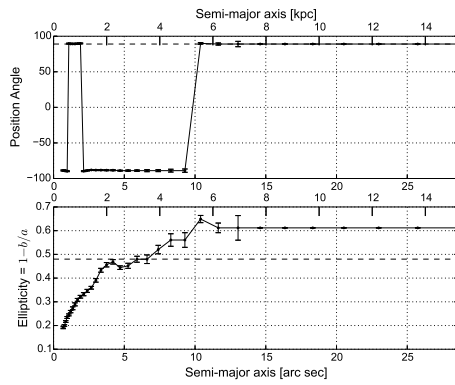
(d)



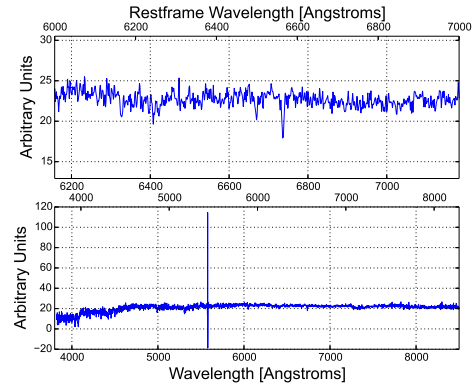
(a)



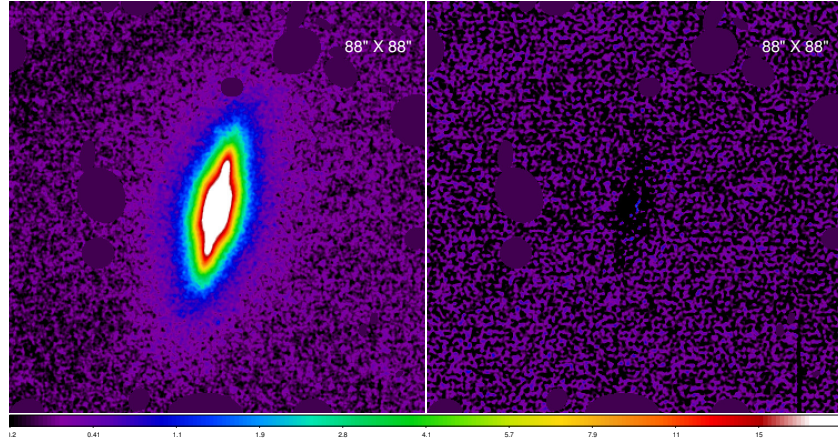
(b)



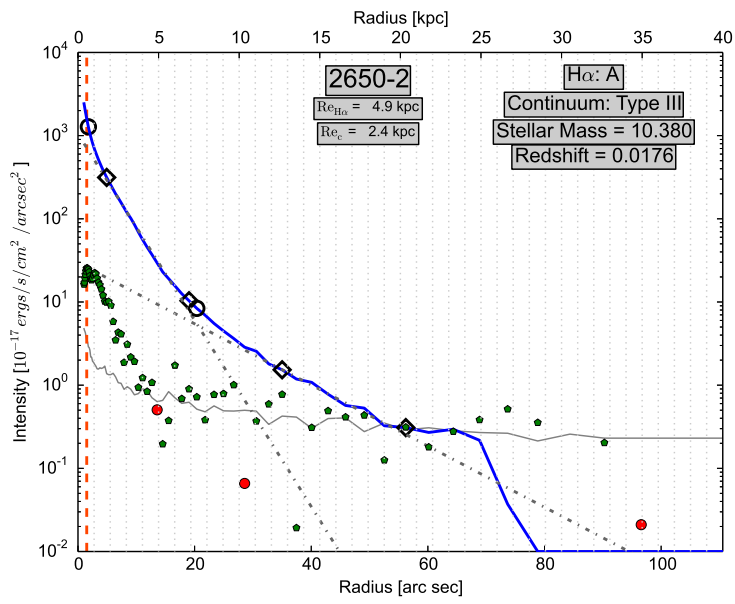
(c)



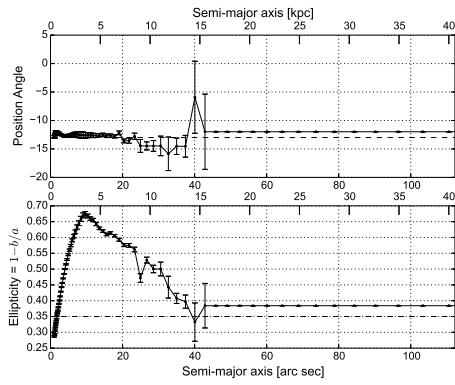
(d)



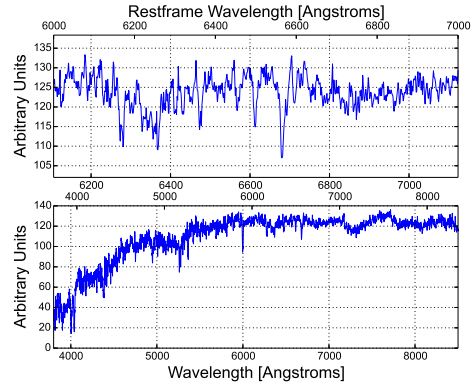
(a)



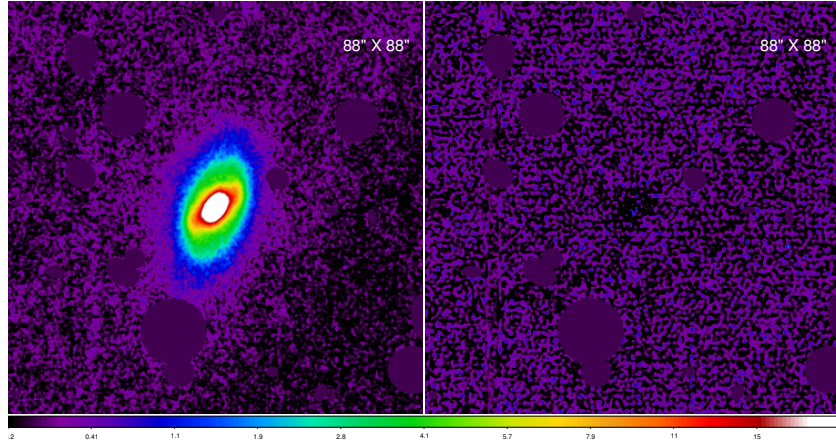
(b)



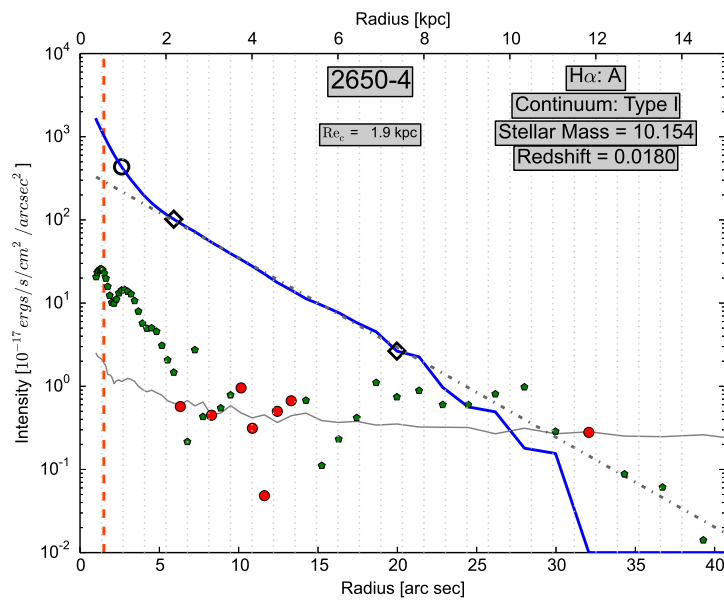
(c)



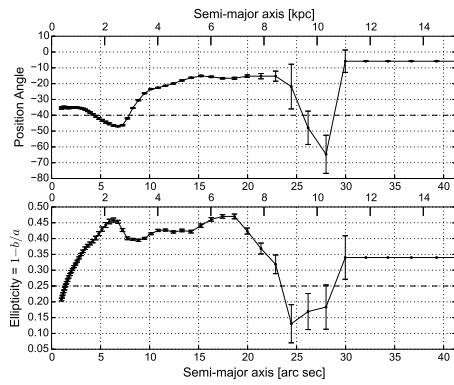
(d)



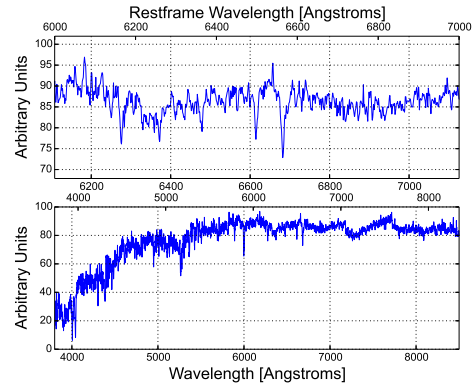
(a)



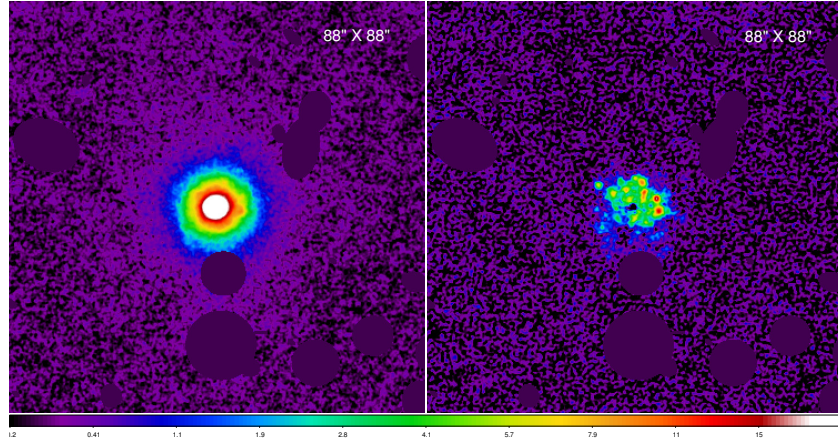
(b)



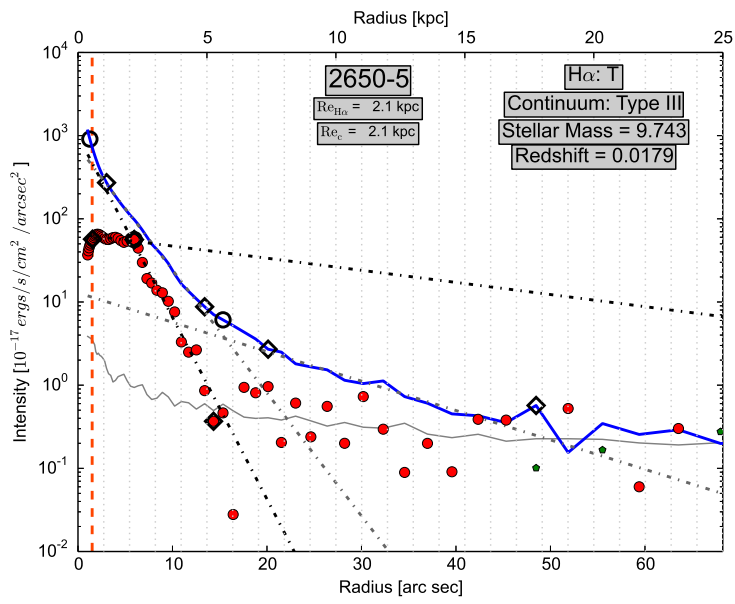
(c)



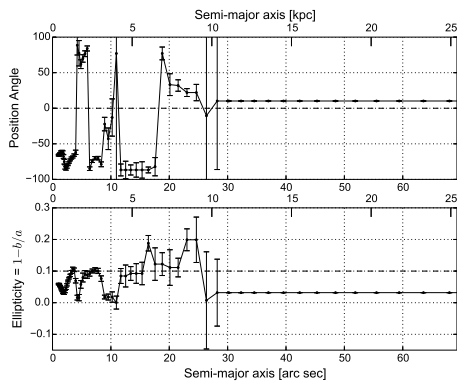
(d)



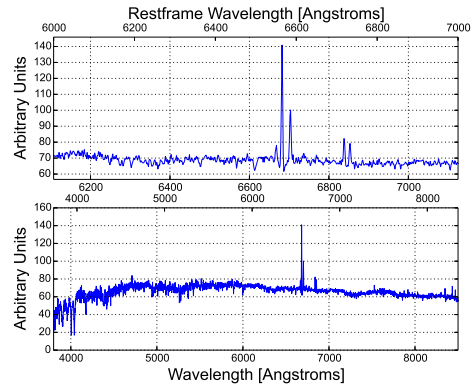
(a)



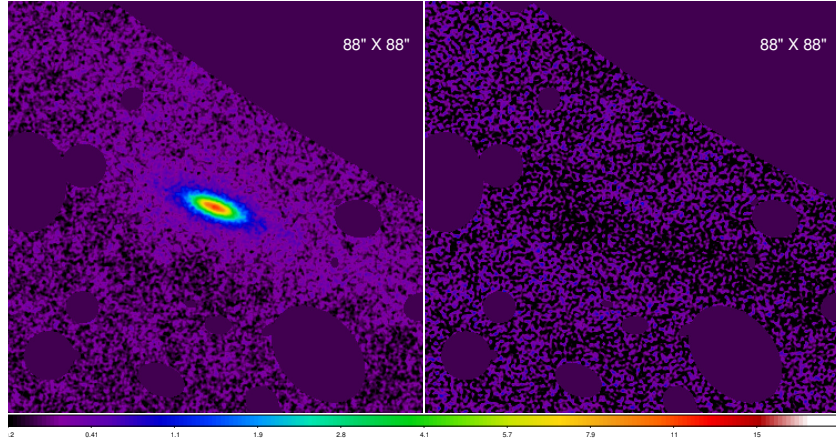
(b)



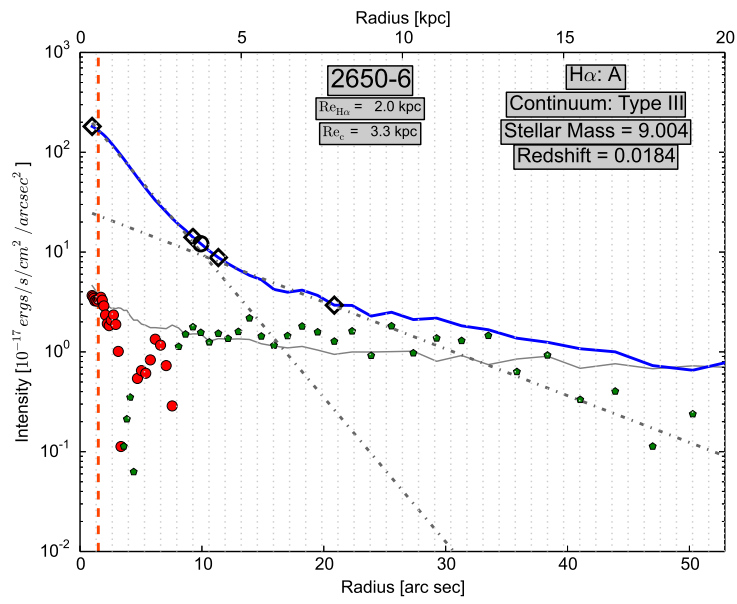
(c)



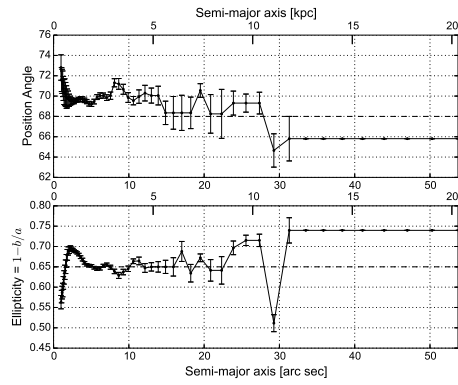
(d)



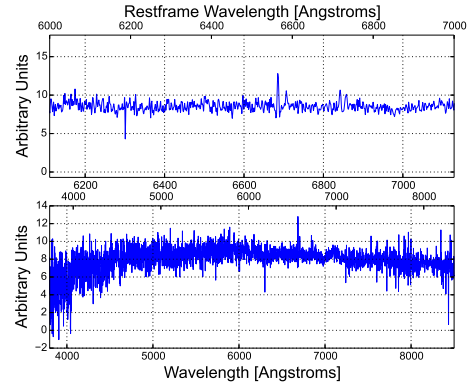
(a)



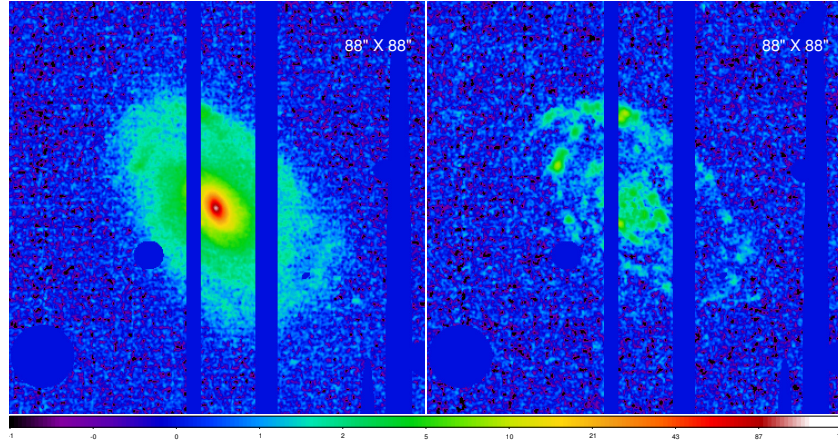
(b)



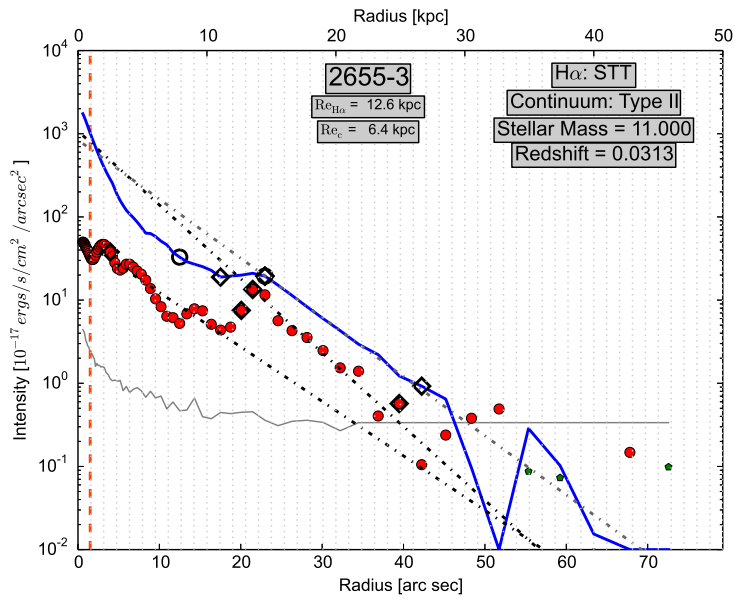
(c)



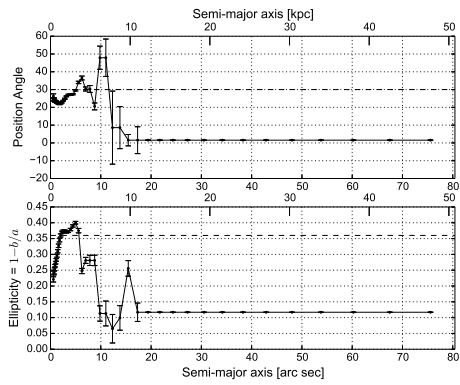
(d)



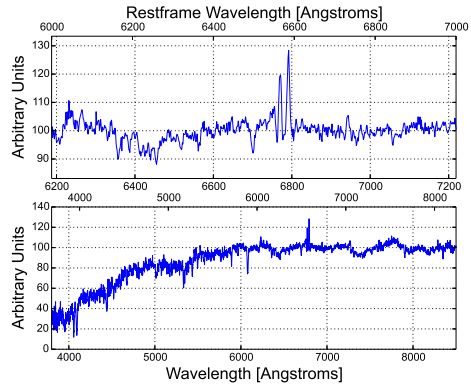
(a)



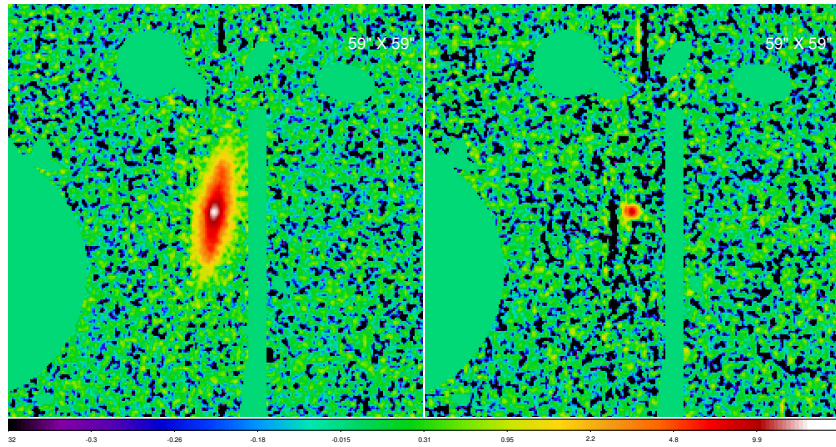
(b)



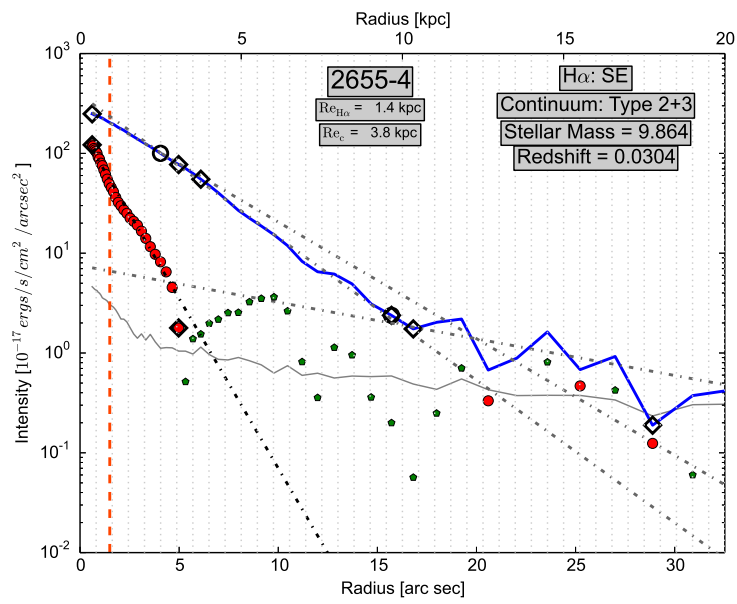
(c)



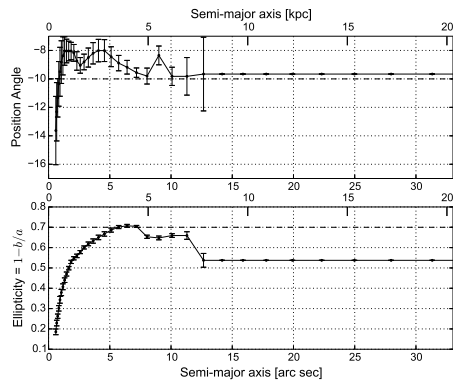
(d)



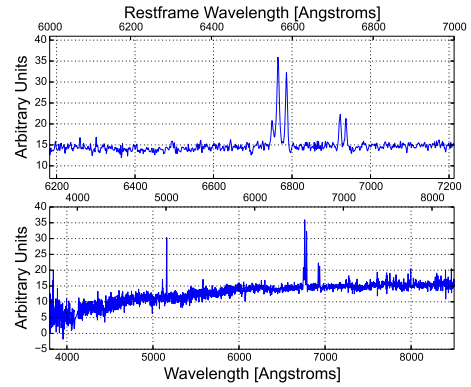
(a)



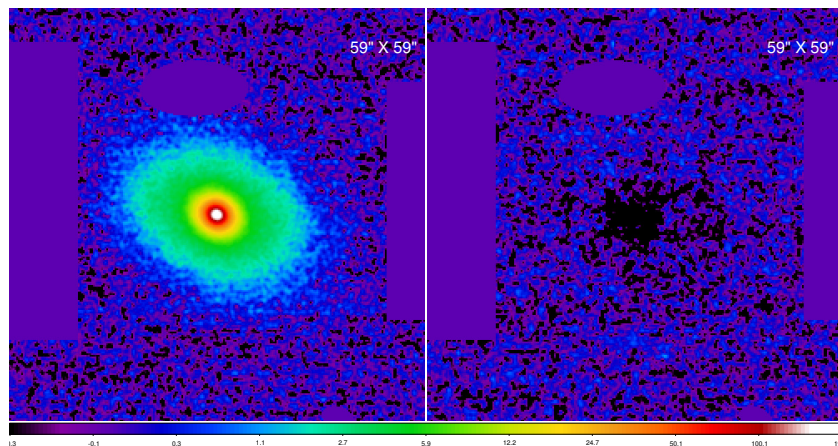
(b)



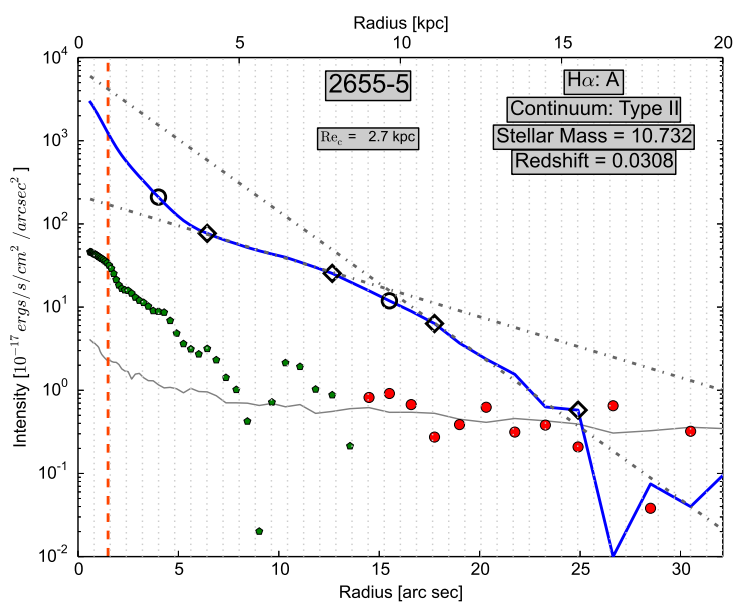
(c)



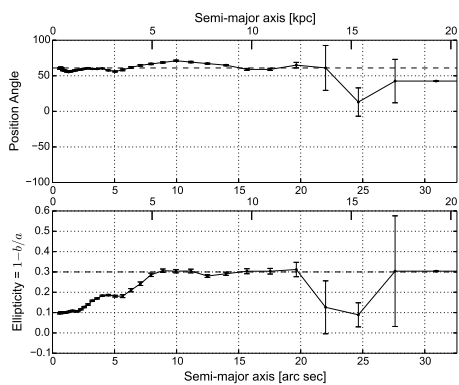
(d)



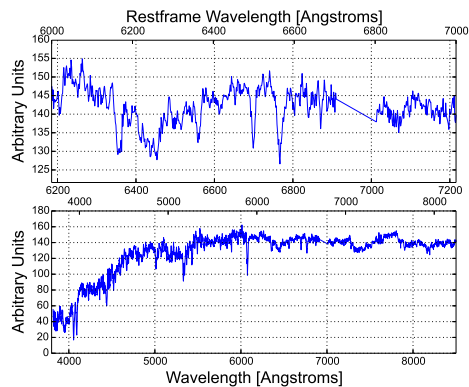
(a)



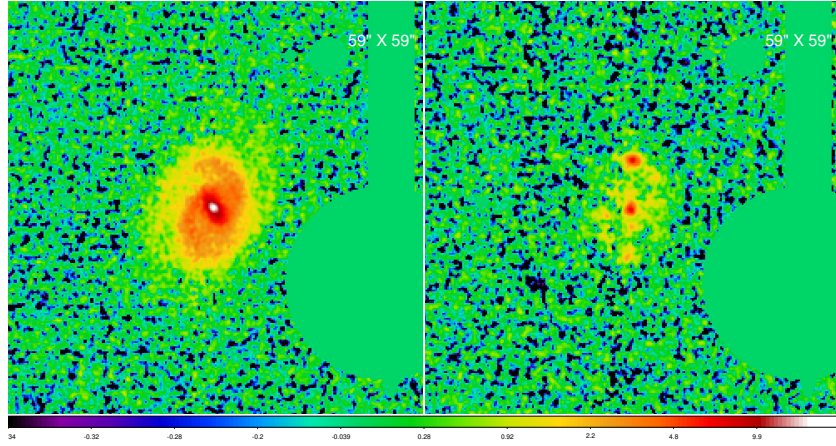
(b)



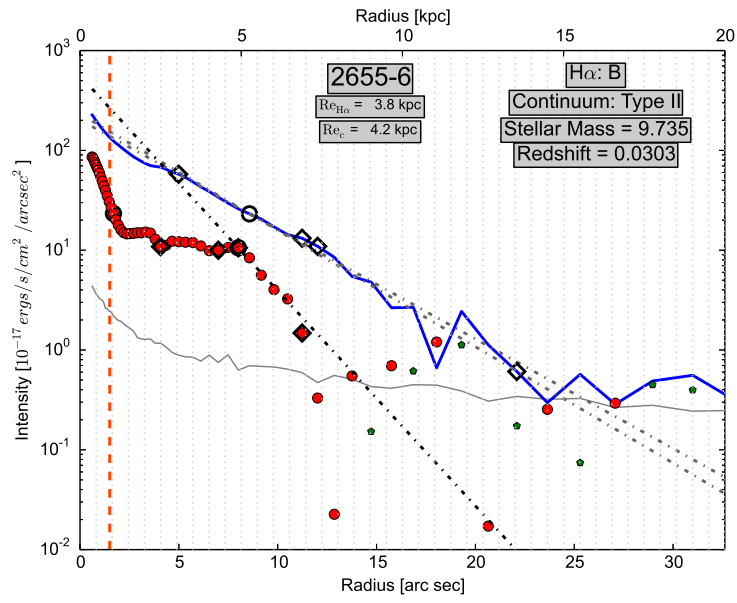
(c)



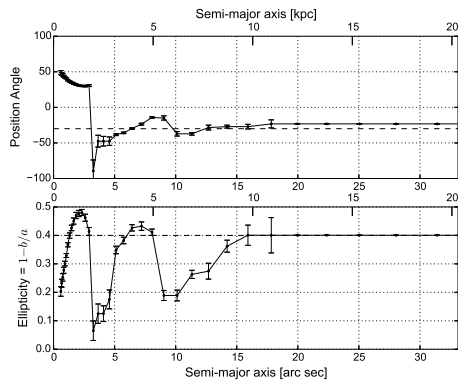
(d)



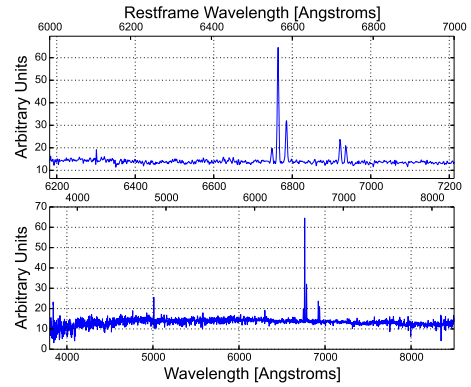
(a)



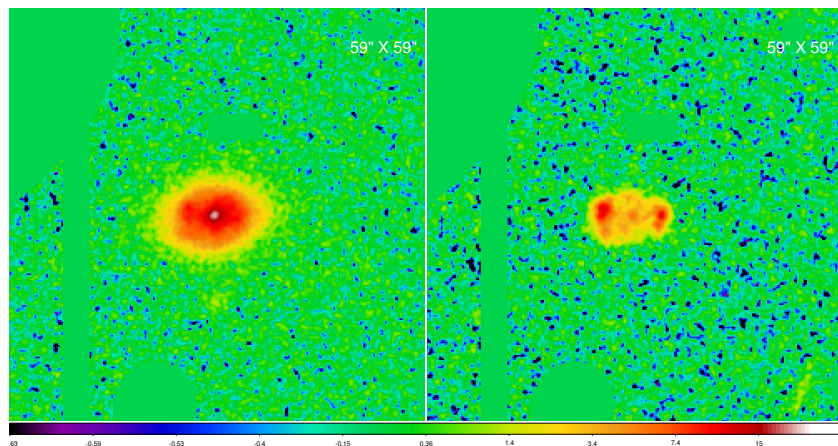
(b)



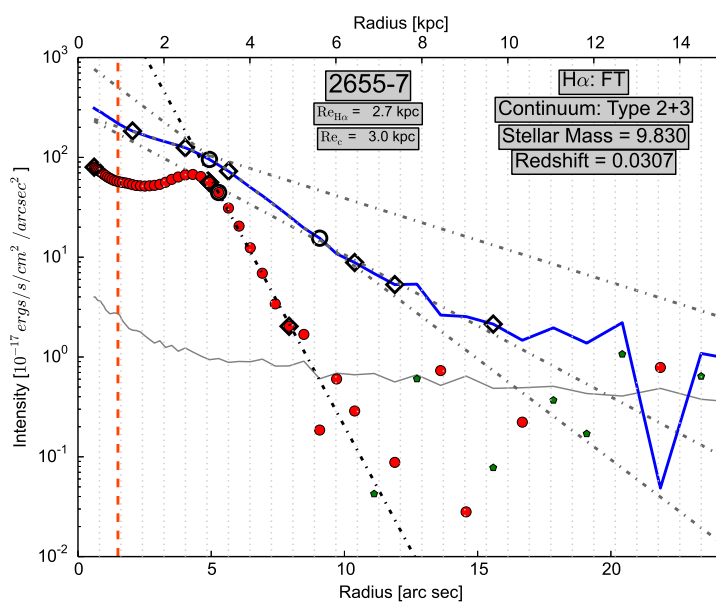
(c)



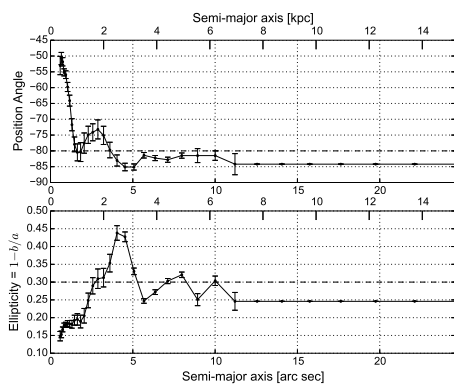
(d)



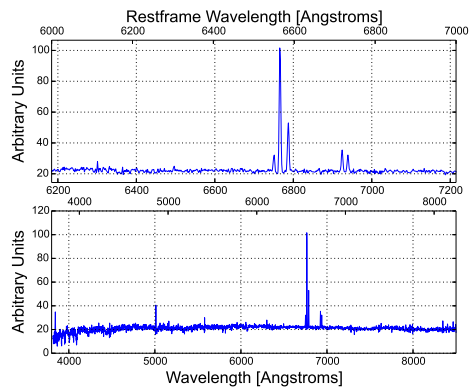
(a)



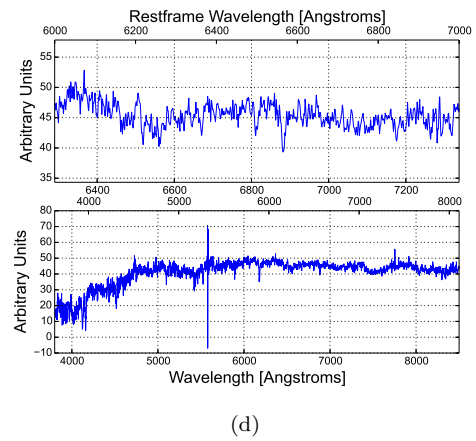
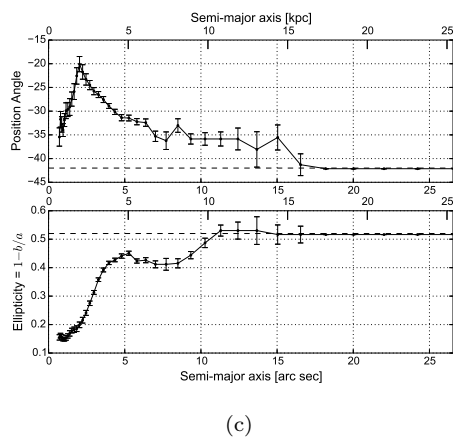
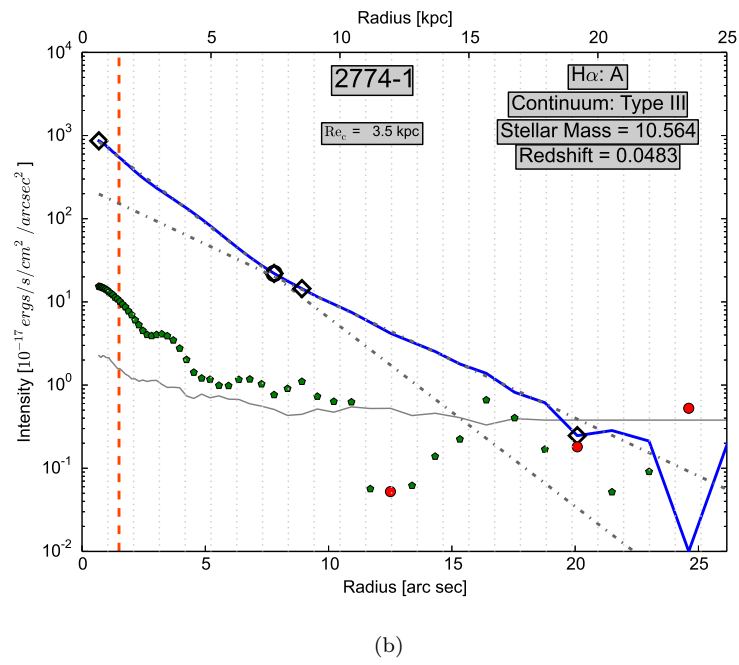
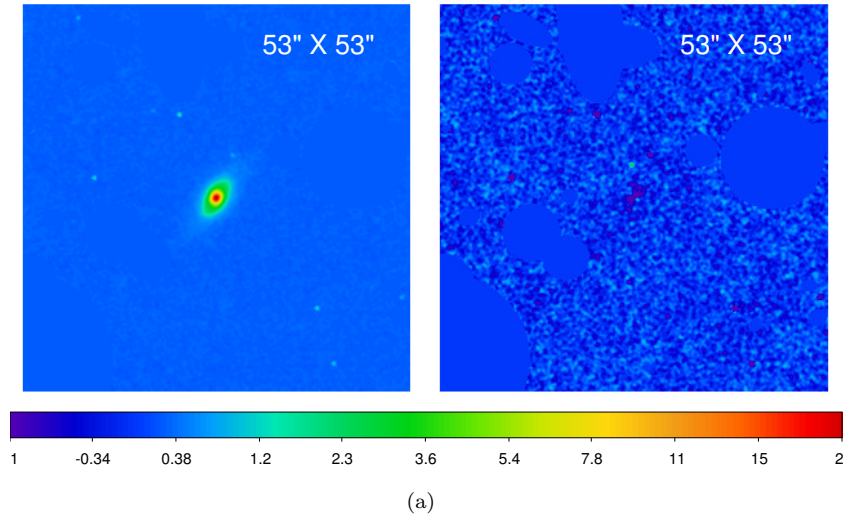
(b)

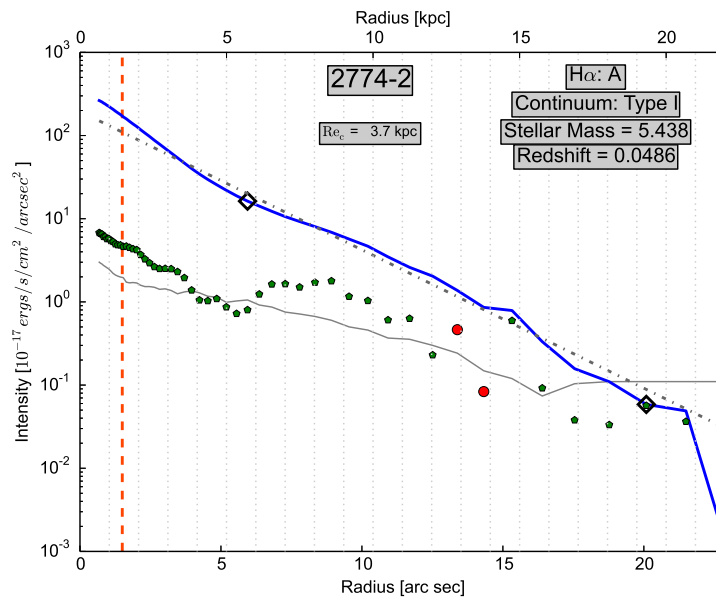
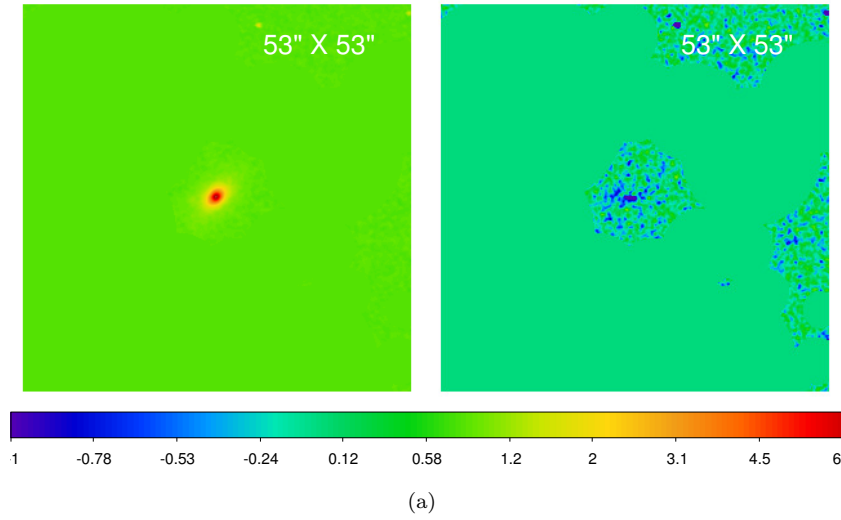


(c)

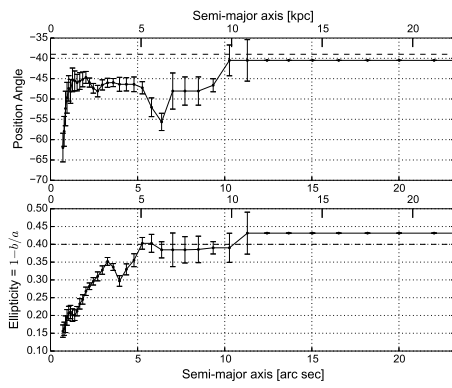


(d)

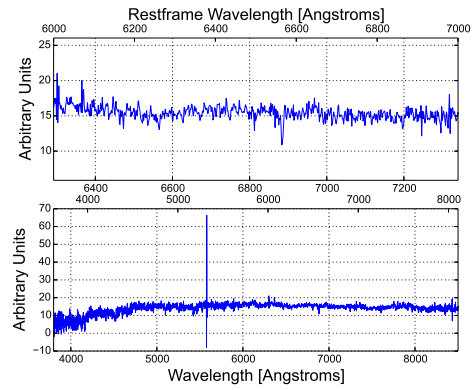




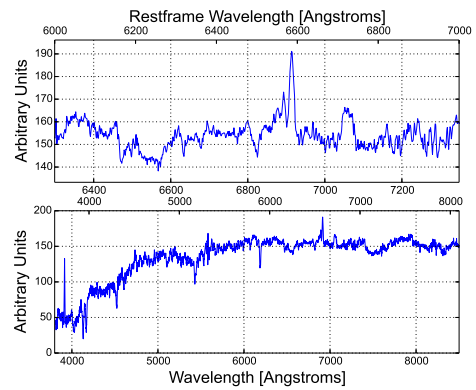
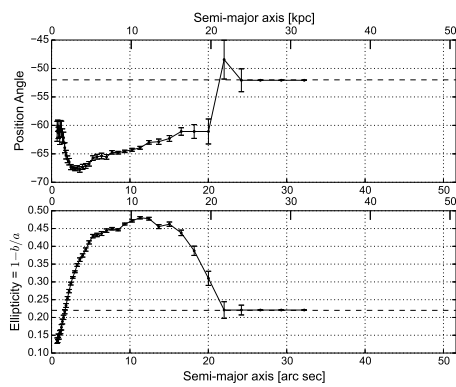
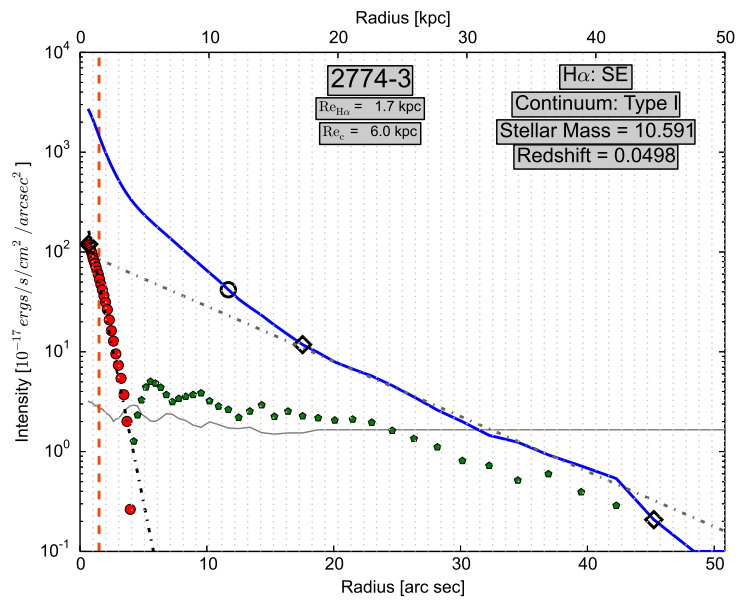
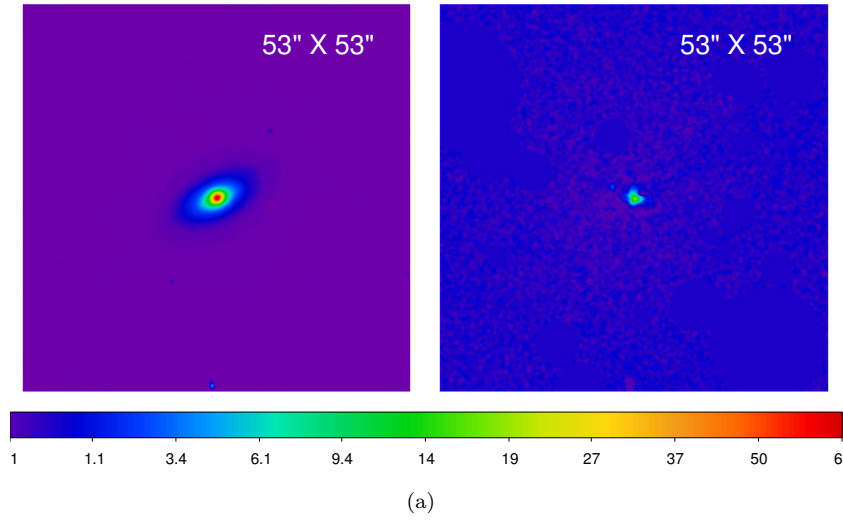
(b)

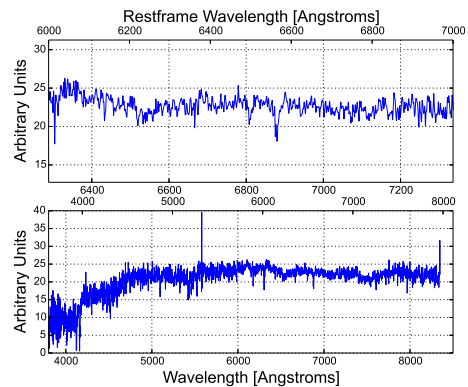
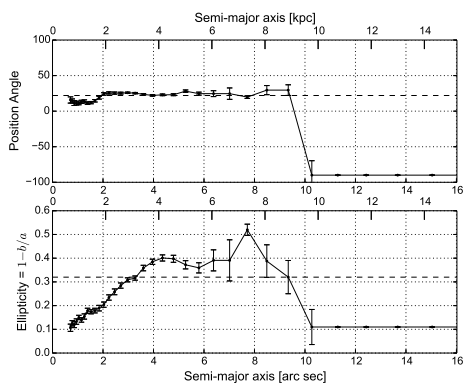
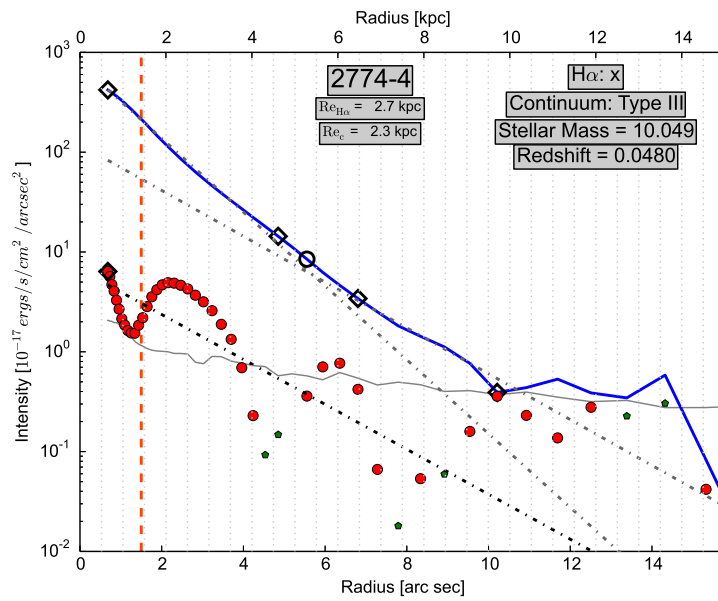
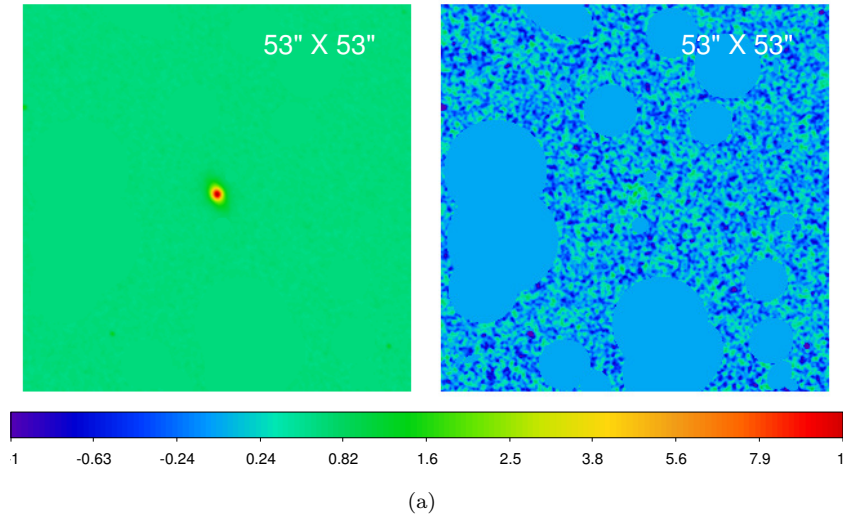


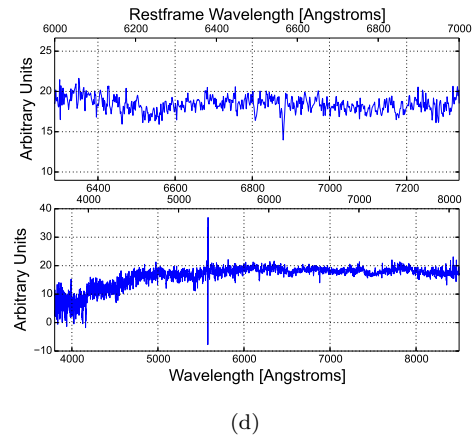
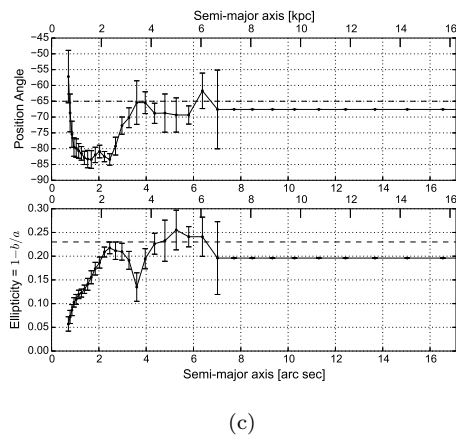
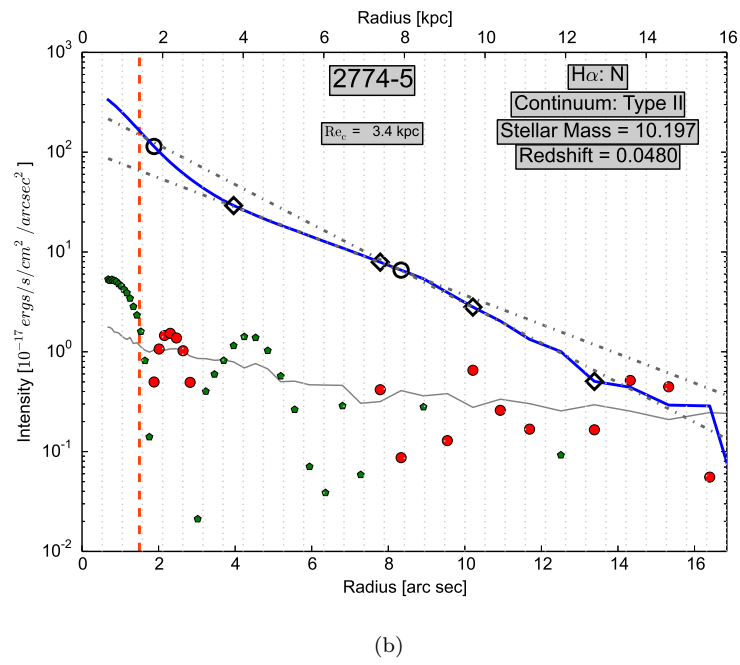
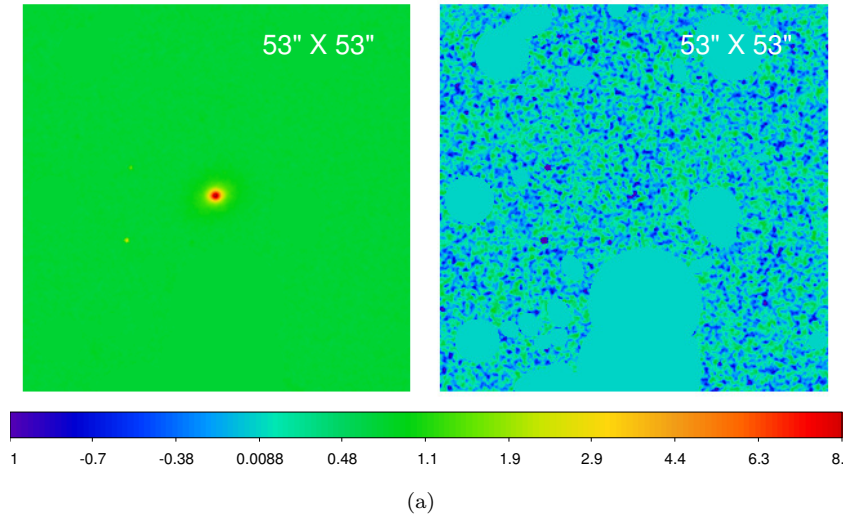
(c)

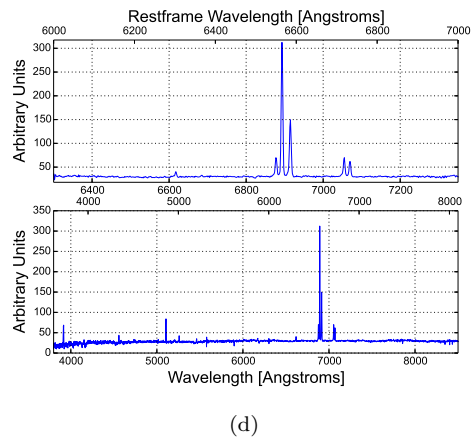
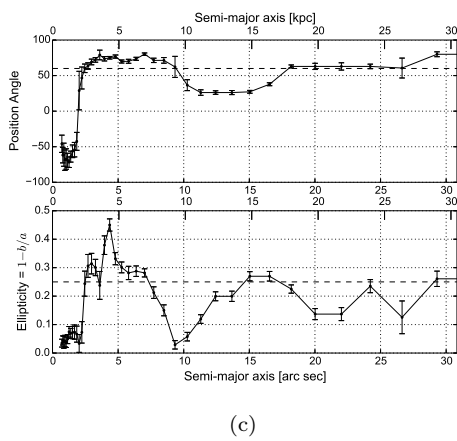
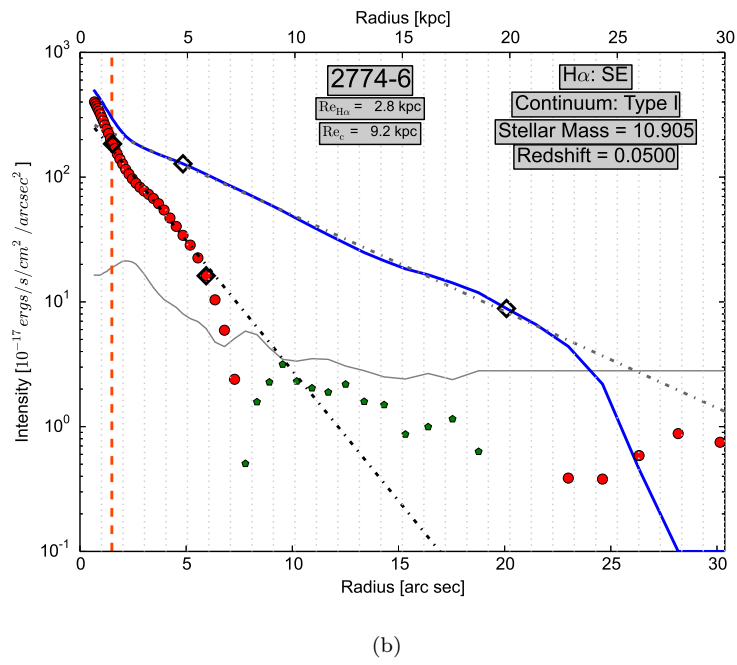
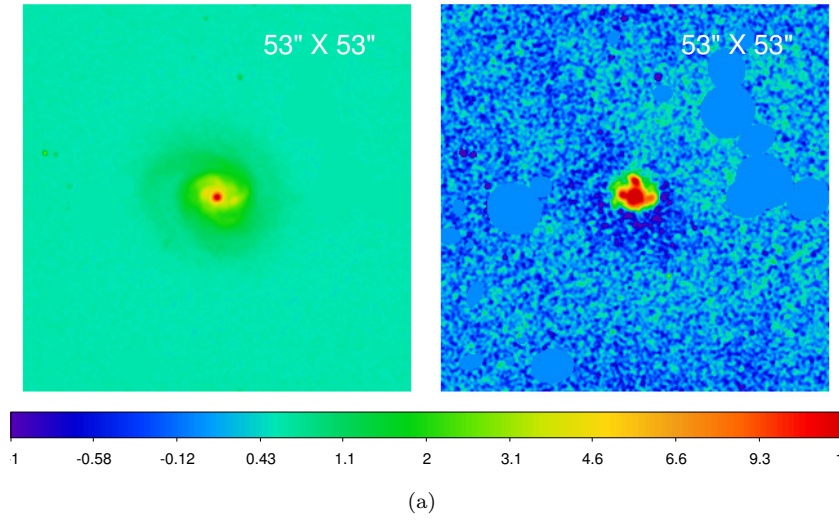


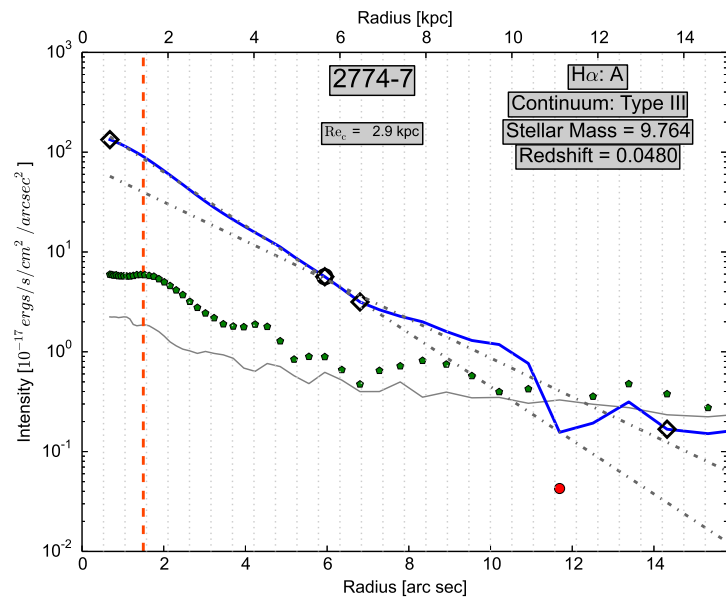
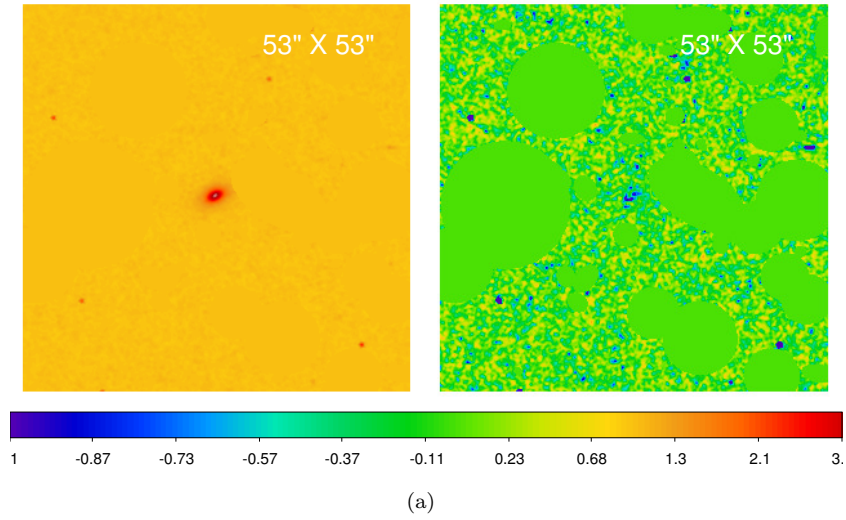
(d)



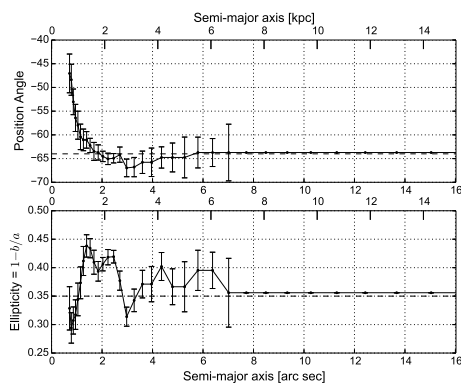




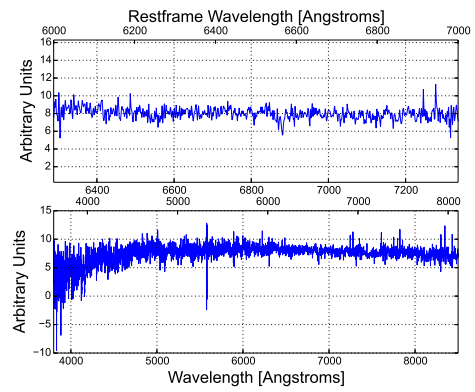




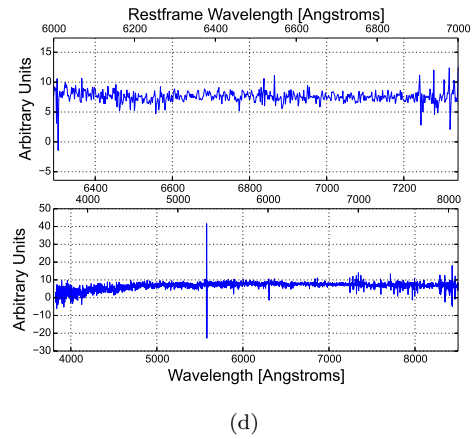
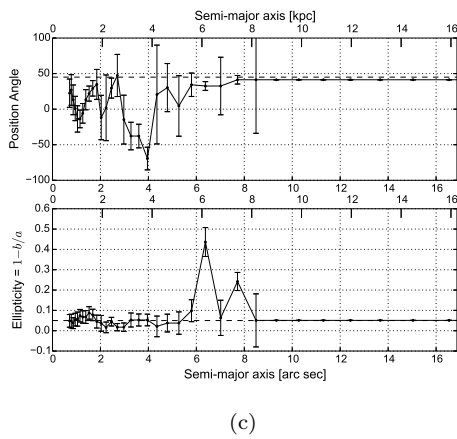
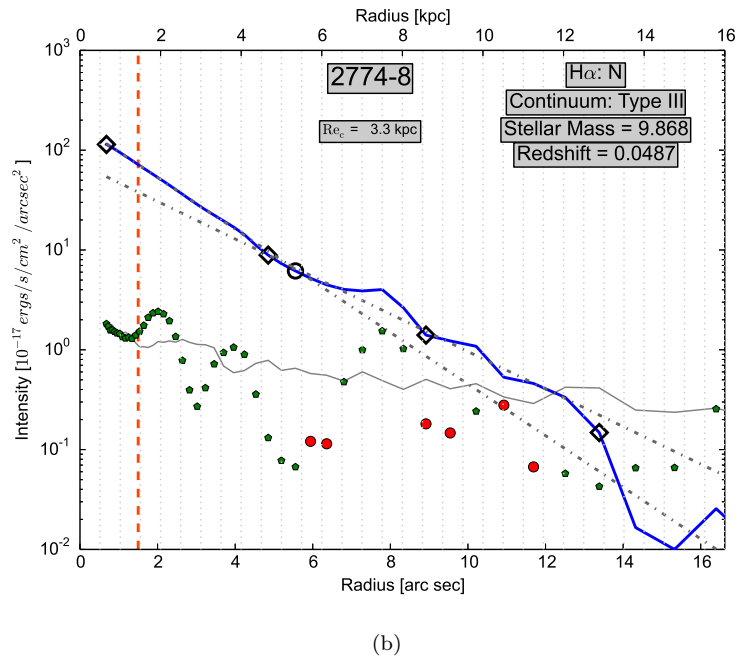
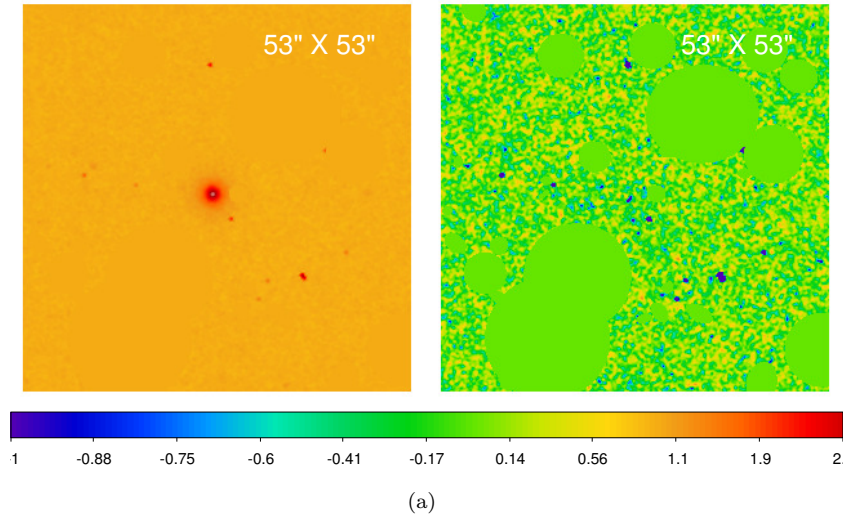
(b)

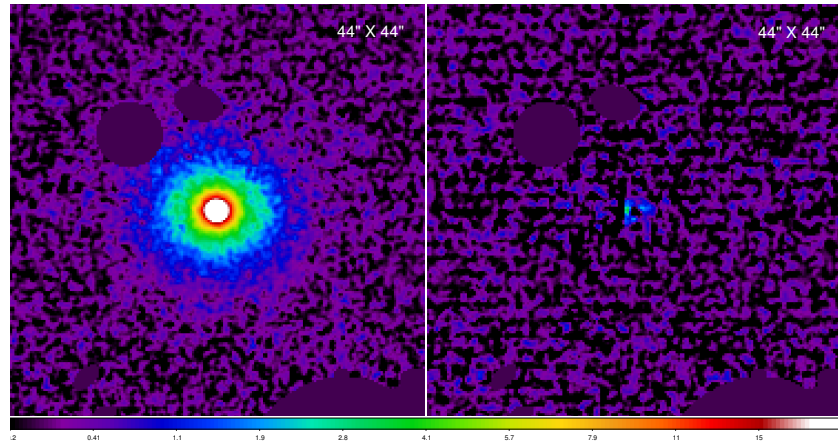


(c)

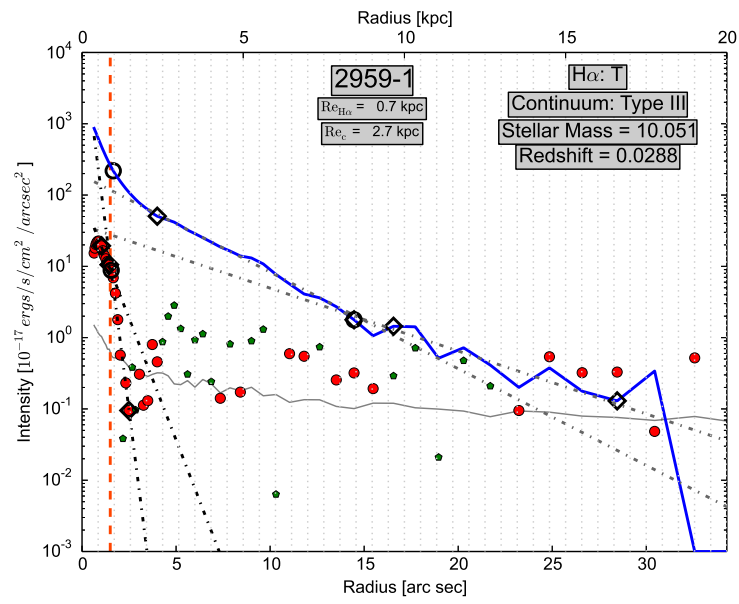


(d)

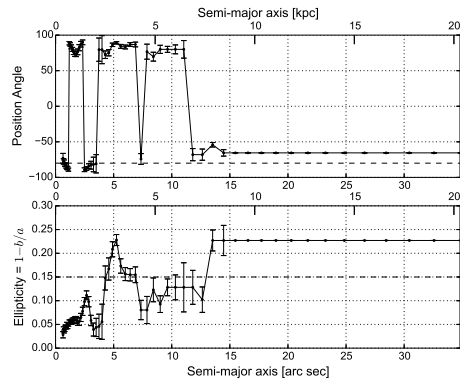




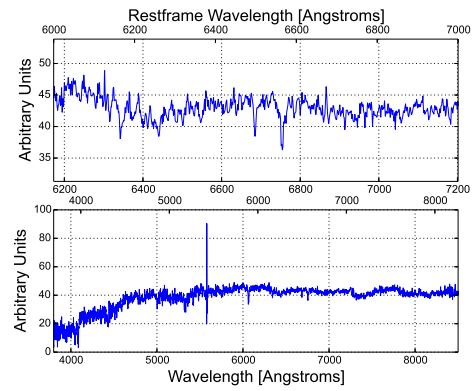
(a)



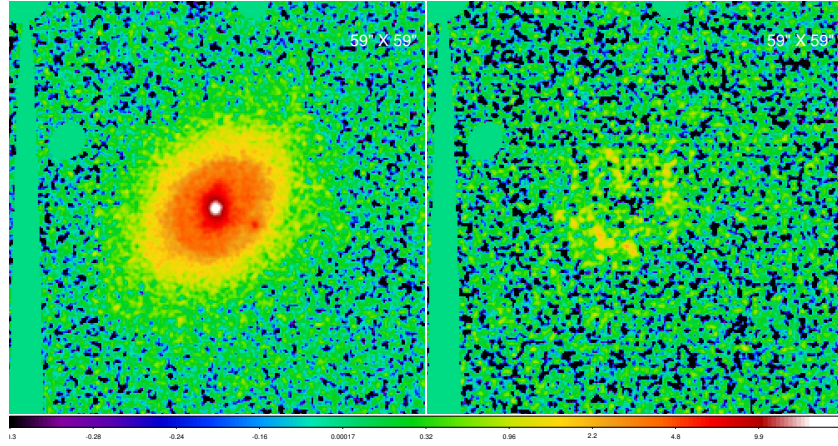
(b)



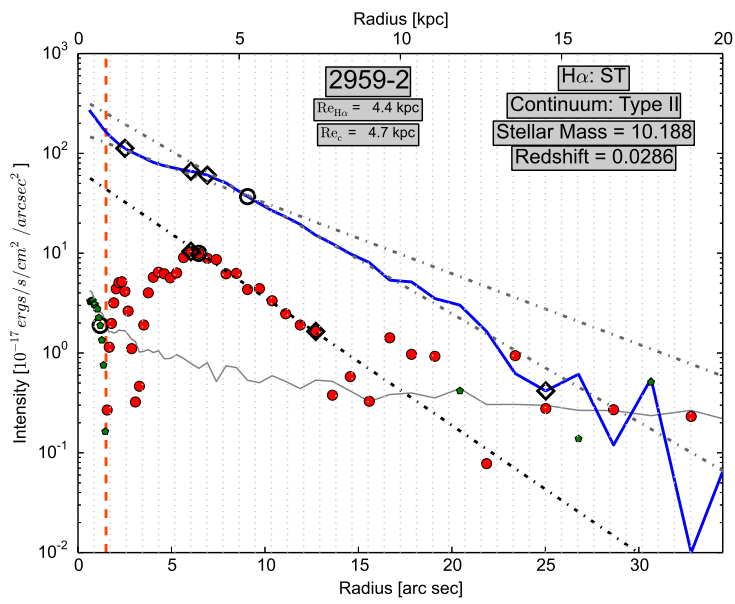
(c)



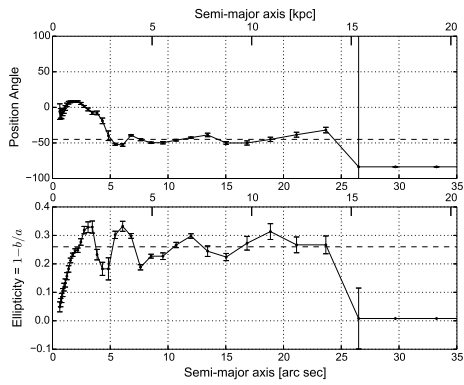
(d)



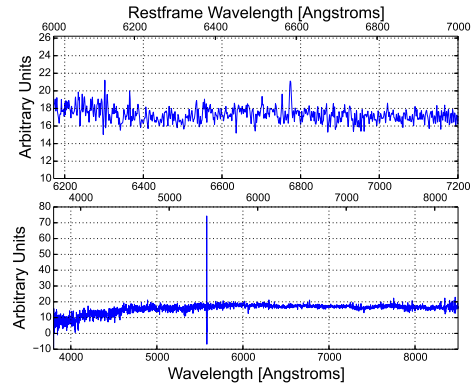
(a)



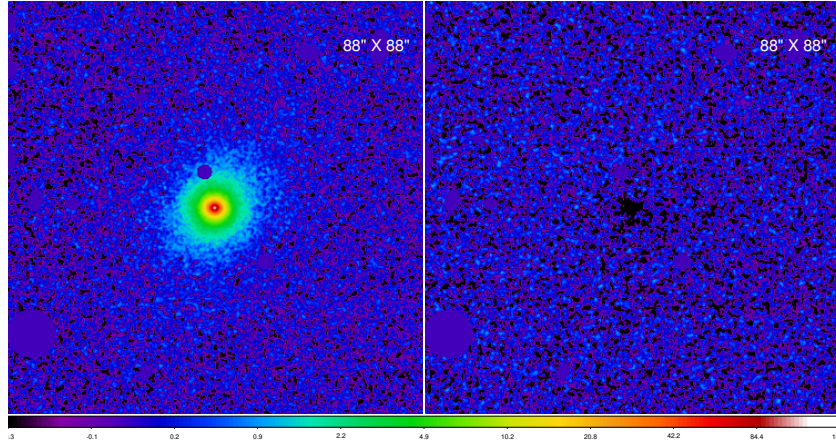
(b)



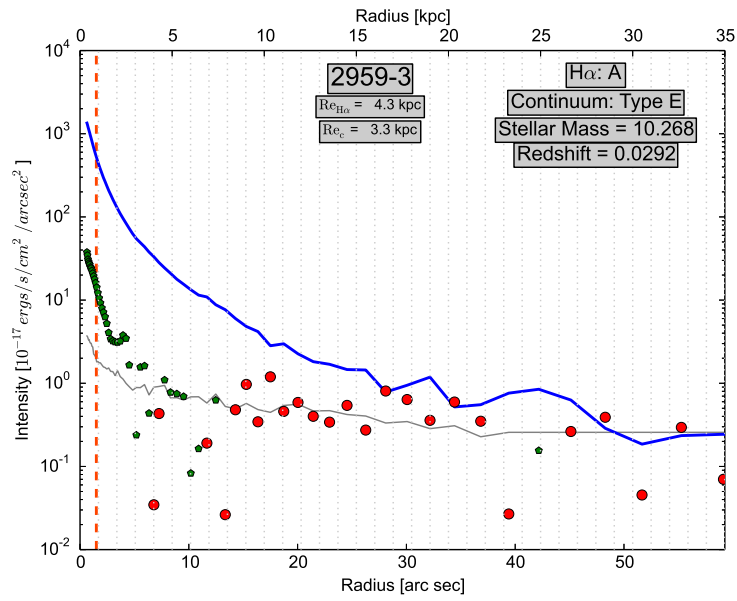
(c)



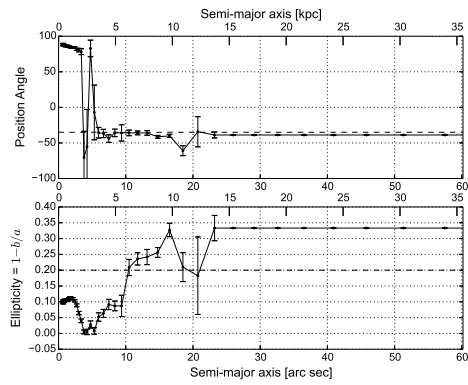
(d)



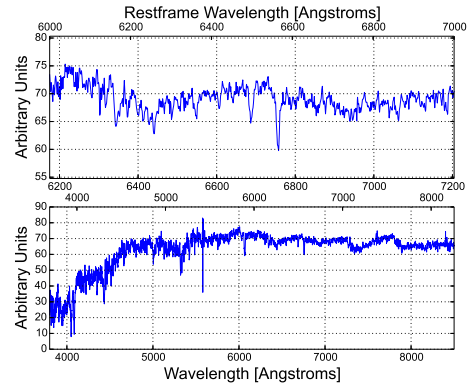
(a)



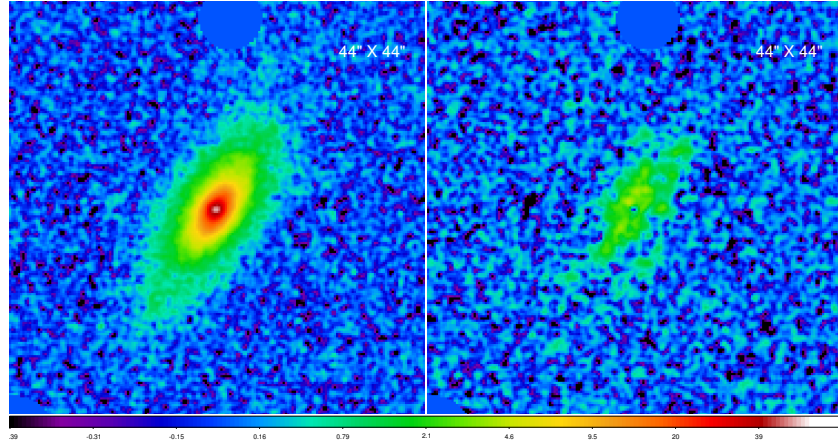
(b)



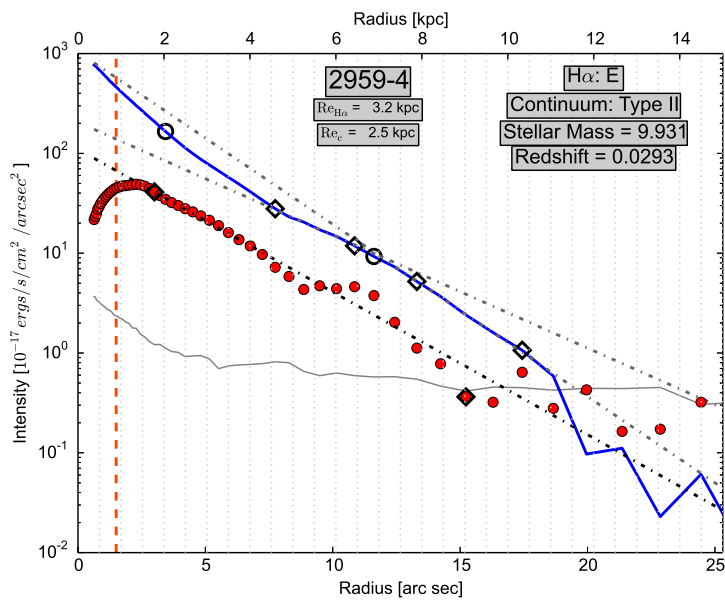
(c)



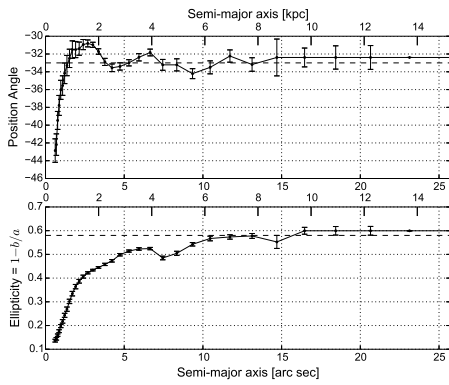
(d)



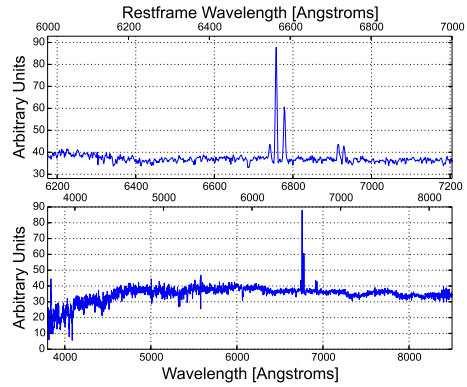
(a)



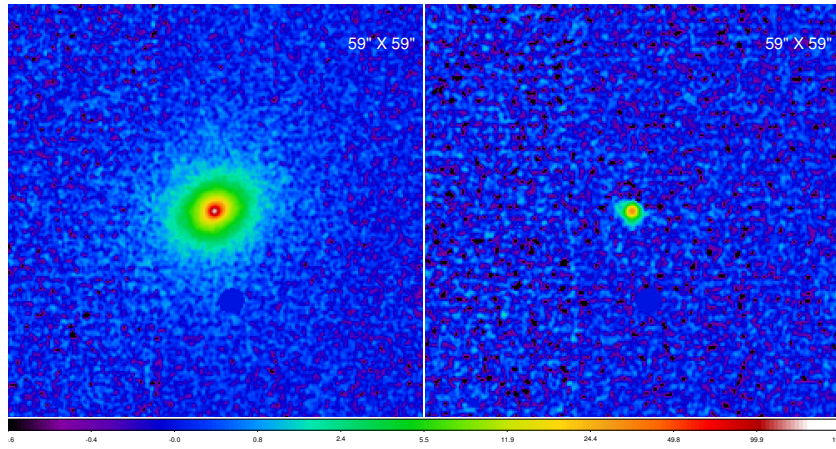
(b)



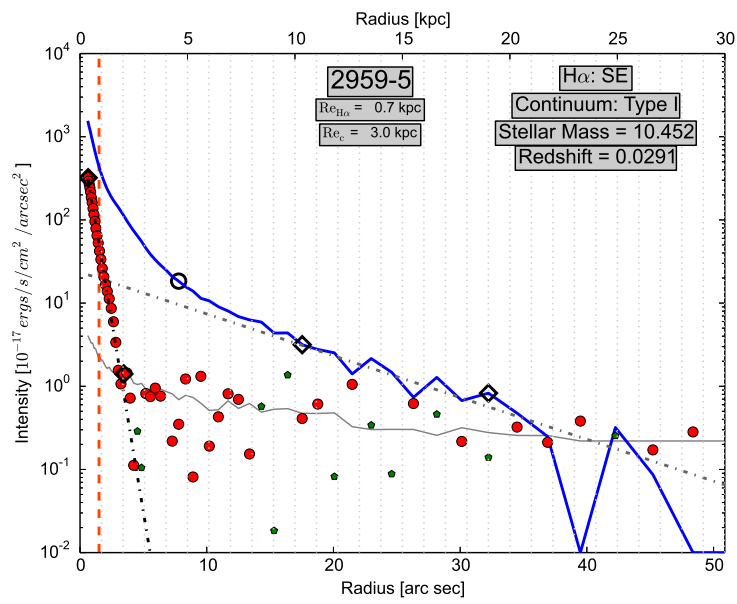
(c)



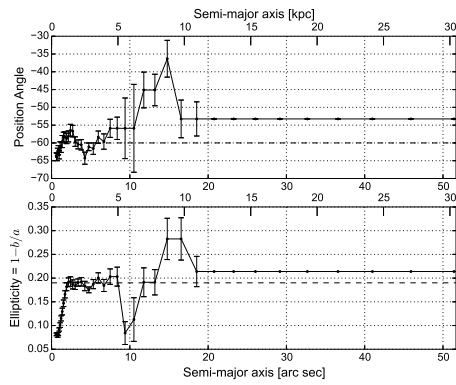
(d)



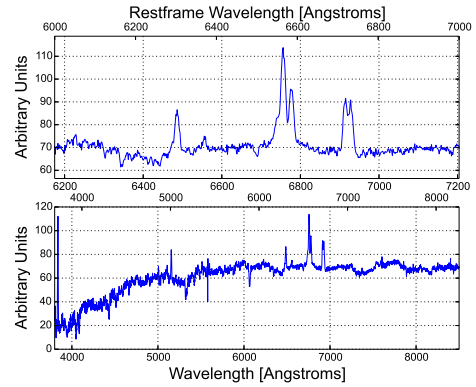
(a)



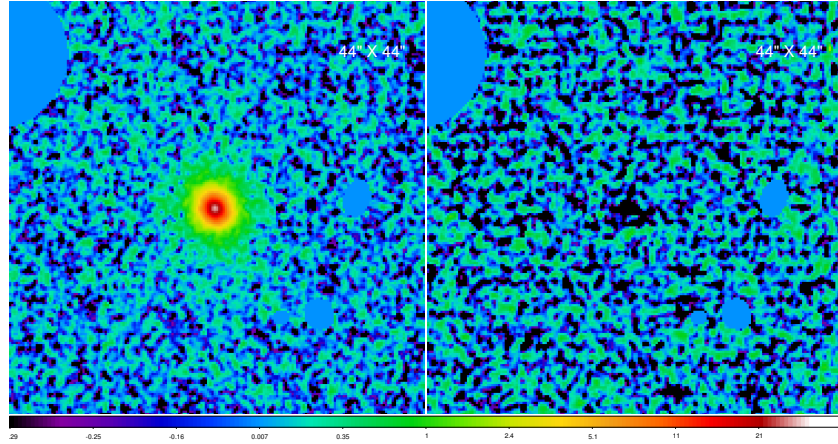
(b)



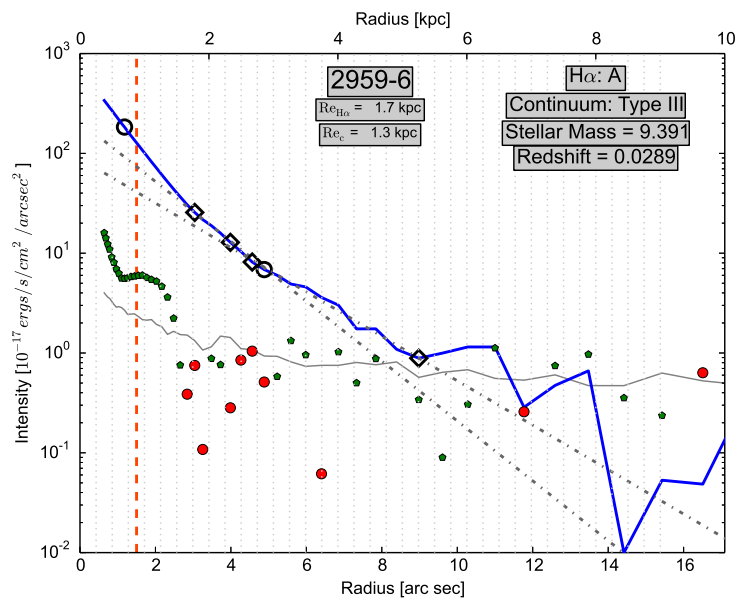
(c)



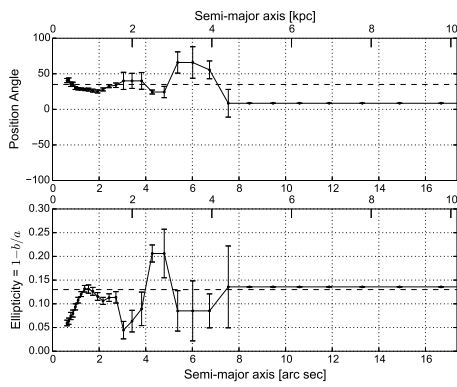
(d)



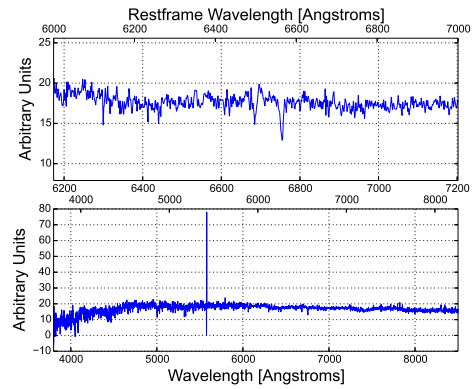
(a)



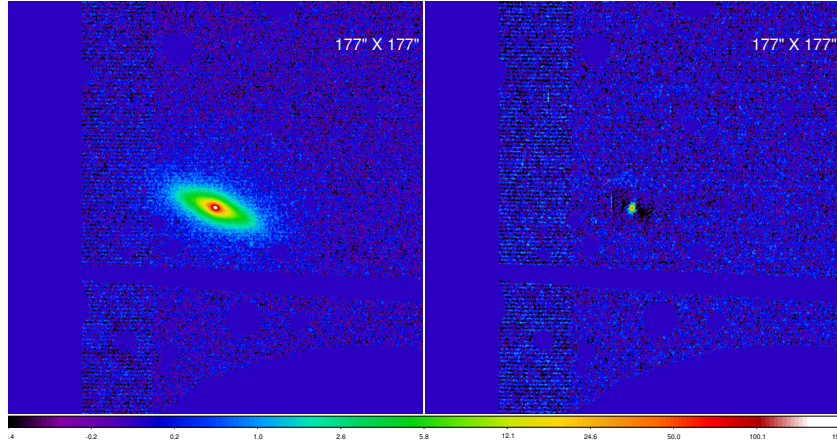
(b)



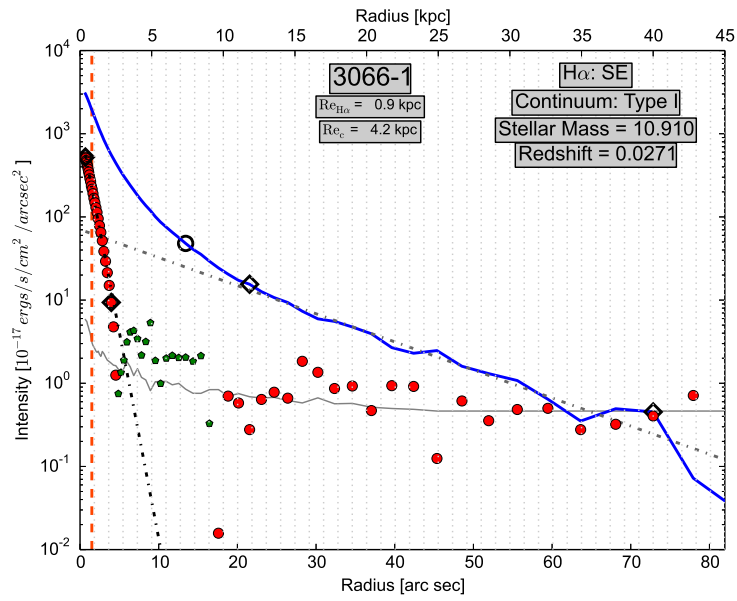
(c)



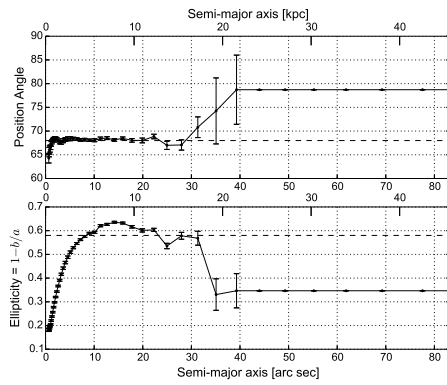
(d)



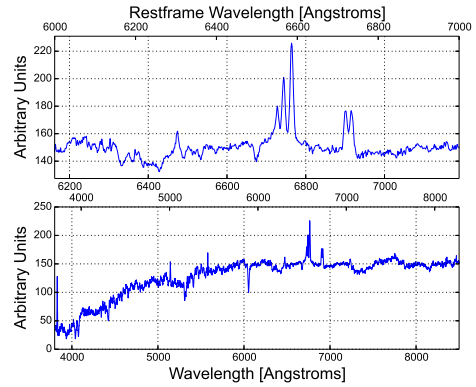
(a)



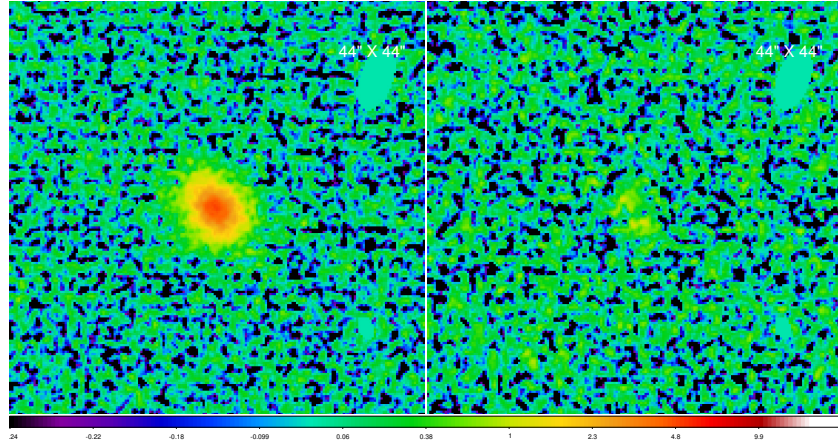
(b)



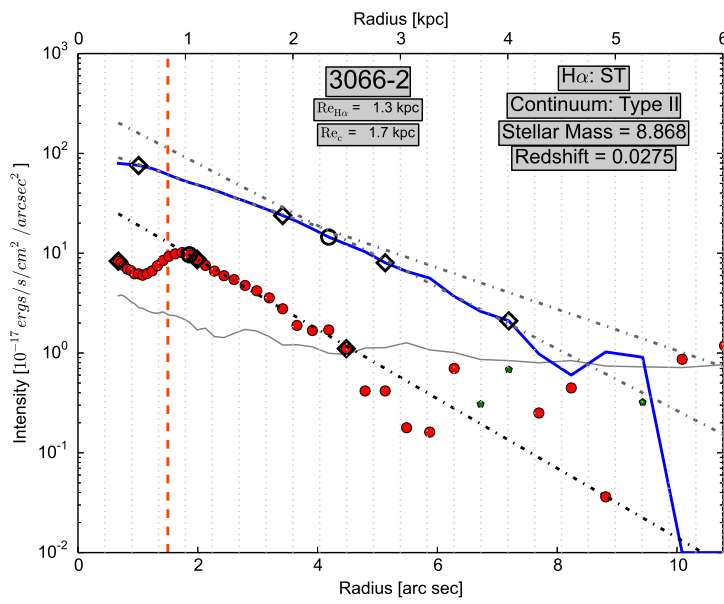
(c)



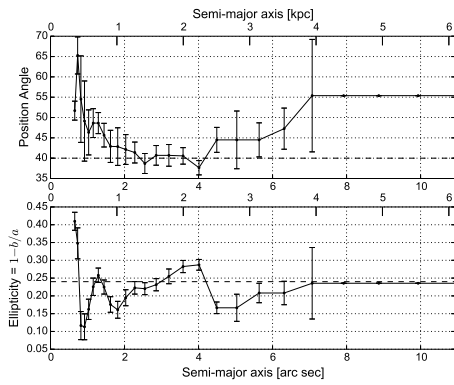
(d)



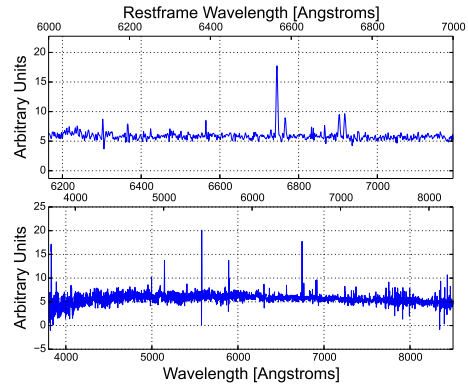
(a)



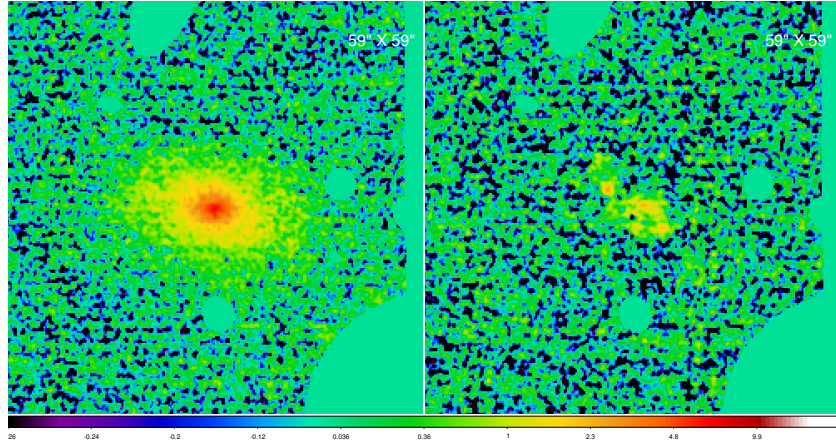
(b)



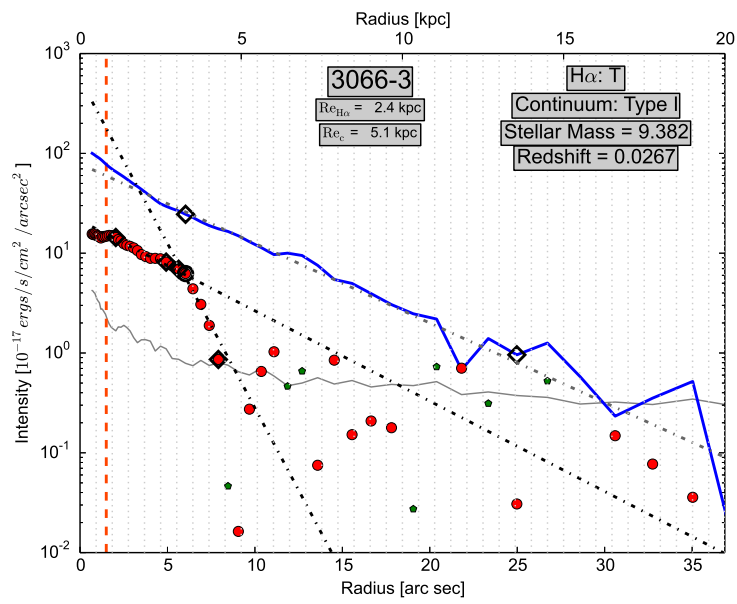
(c)



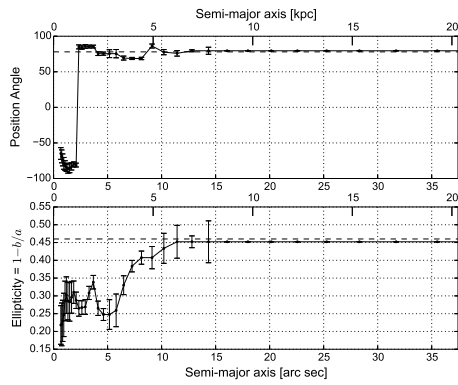
(d)



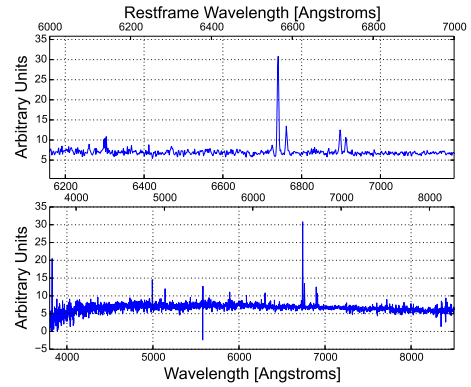
(a)



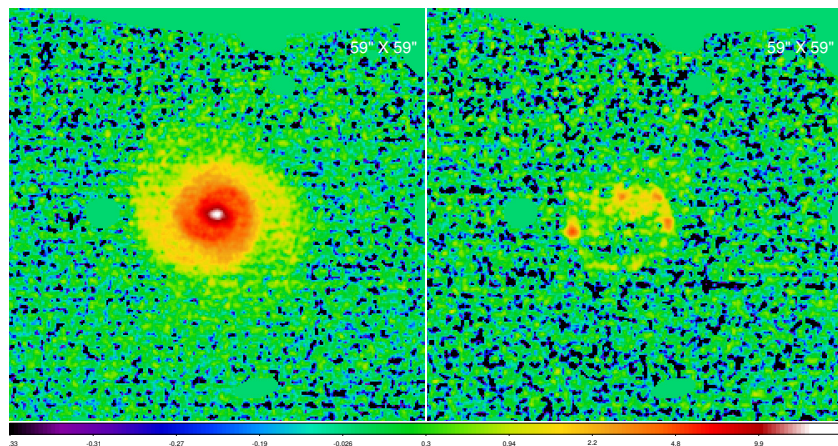
(b)



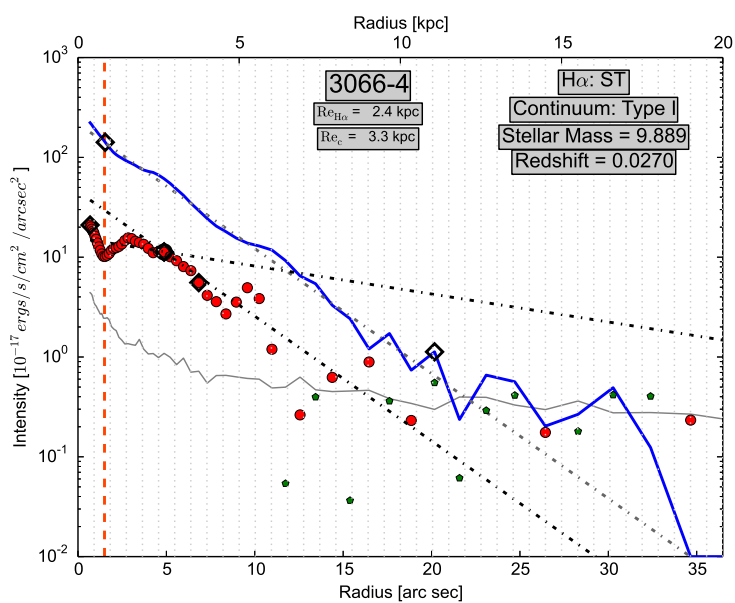
(c)



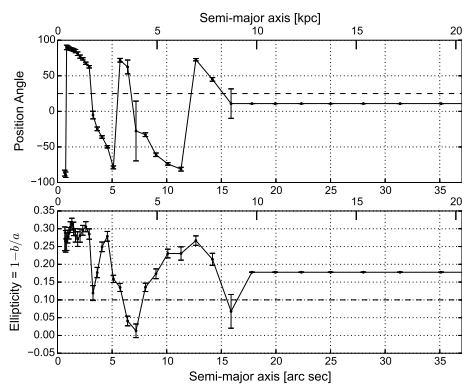
(d)



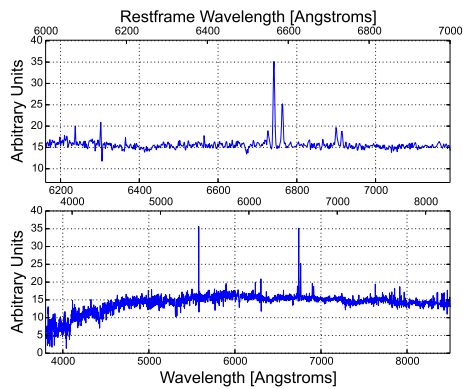
(a)



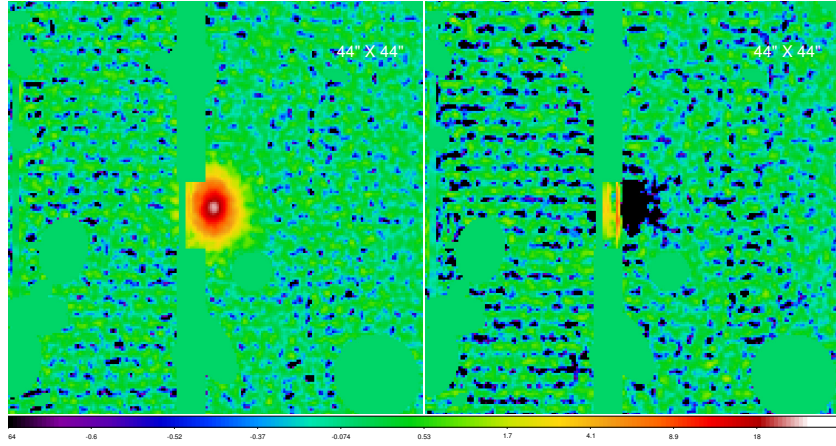
(b)



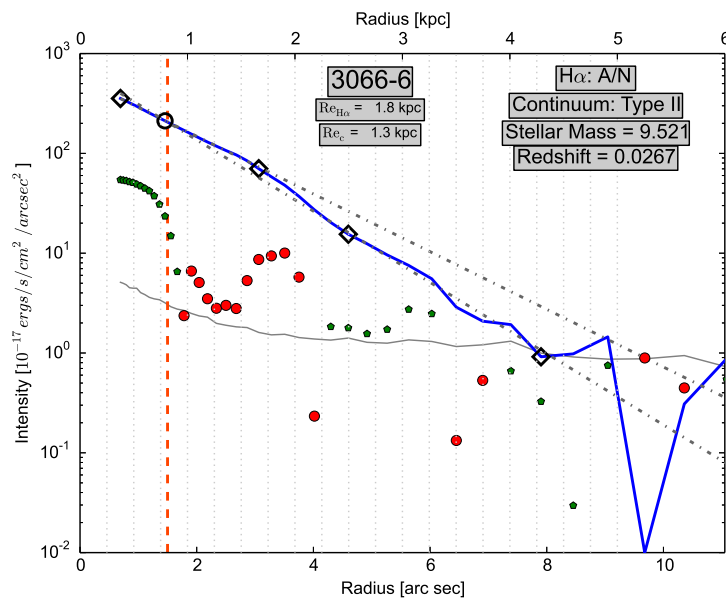
(c)



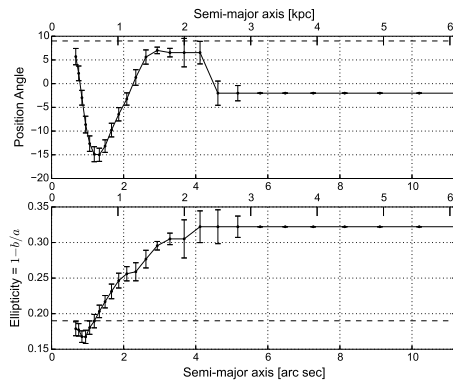
(d)



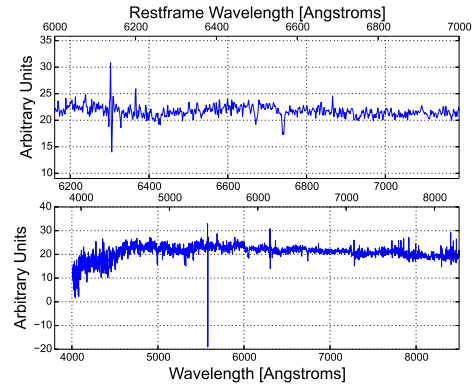
(a)



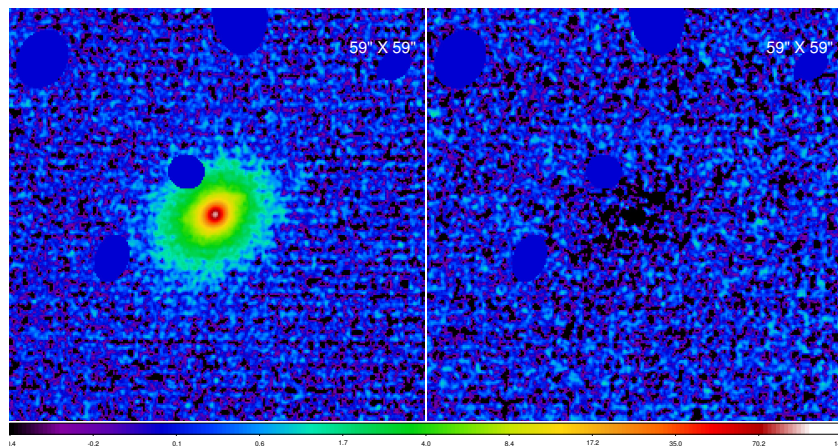
(b)



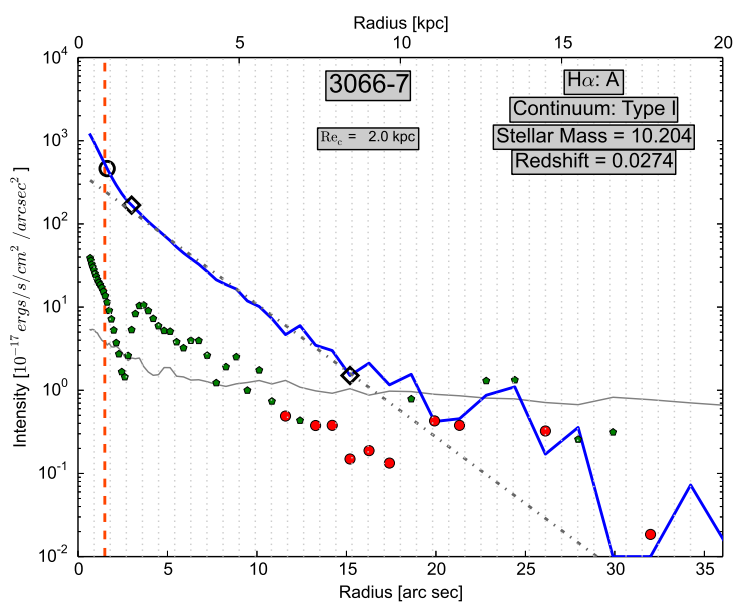
(c)



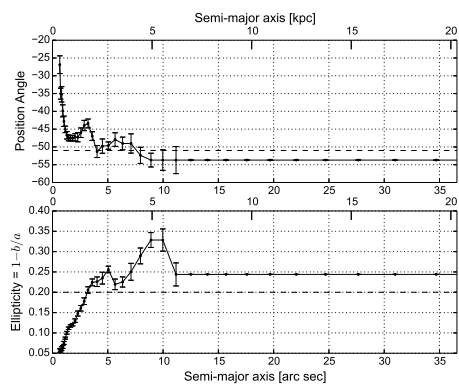
(d)



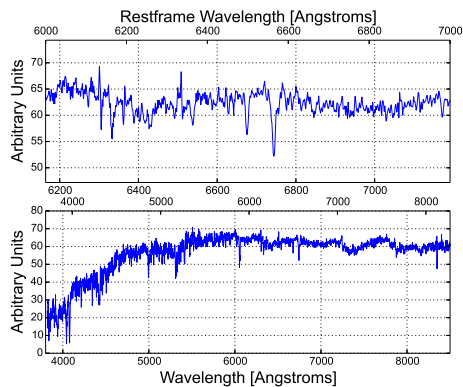
(a)



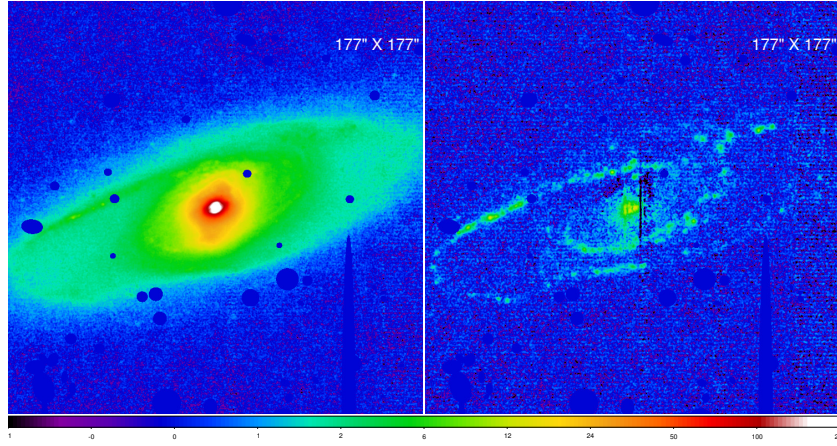
(b)



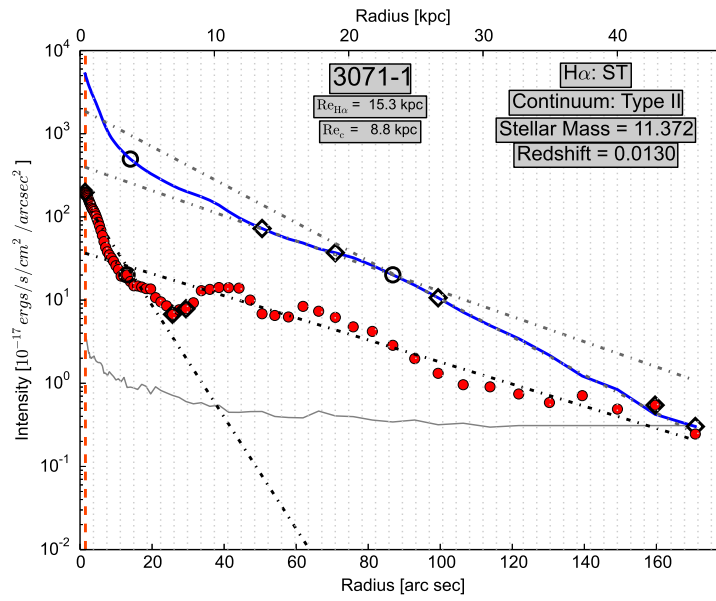
(c)



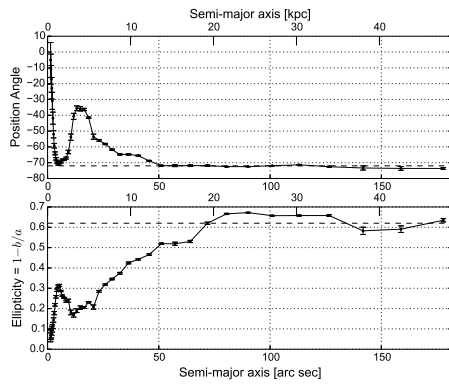
(d)



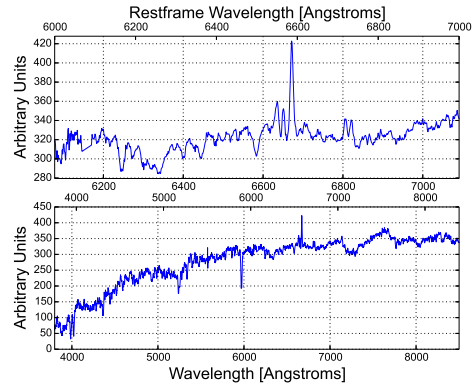
(a)



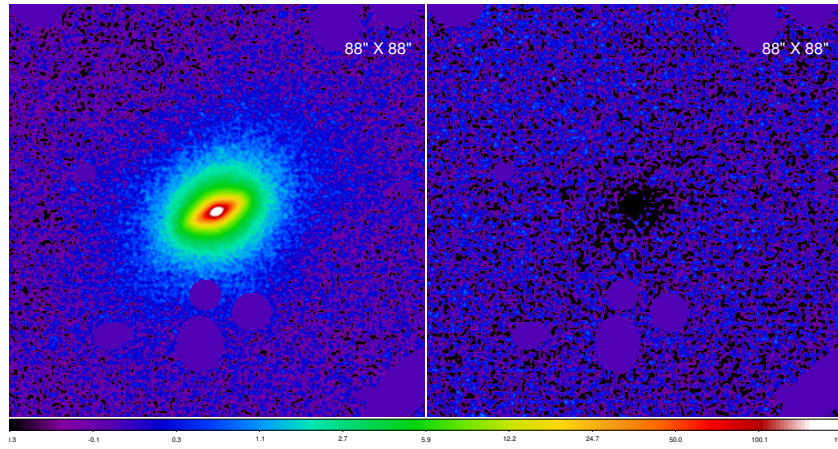
(b)



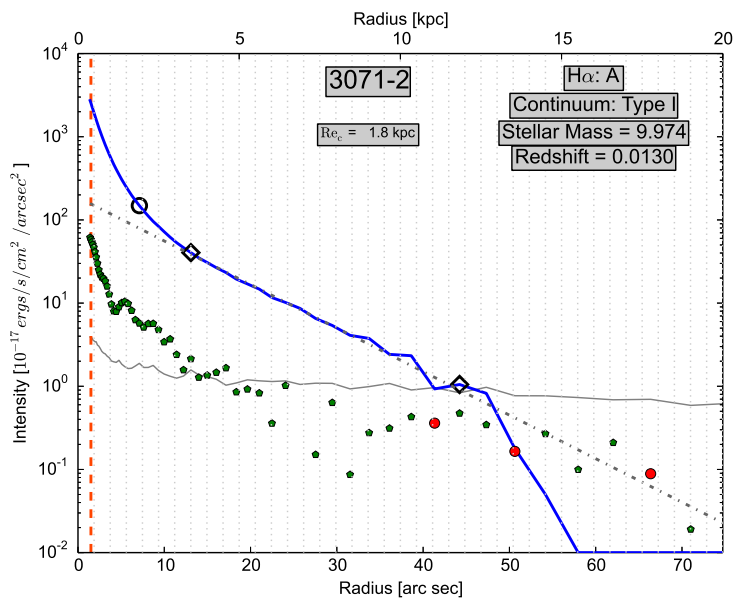
(c)



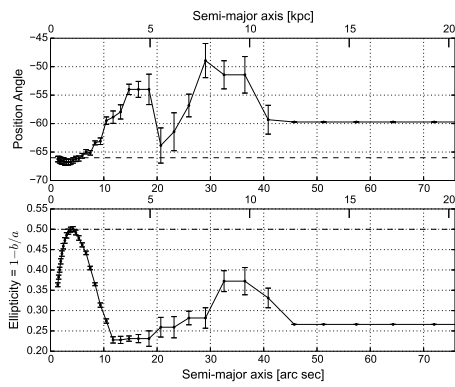
(d)



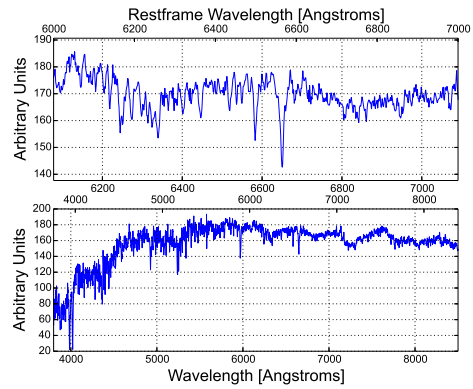
(a)



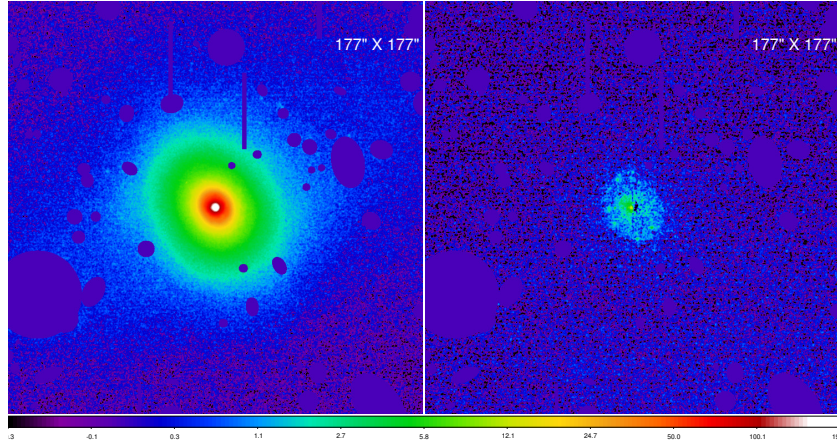
(b)



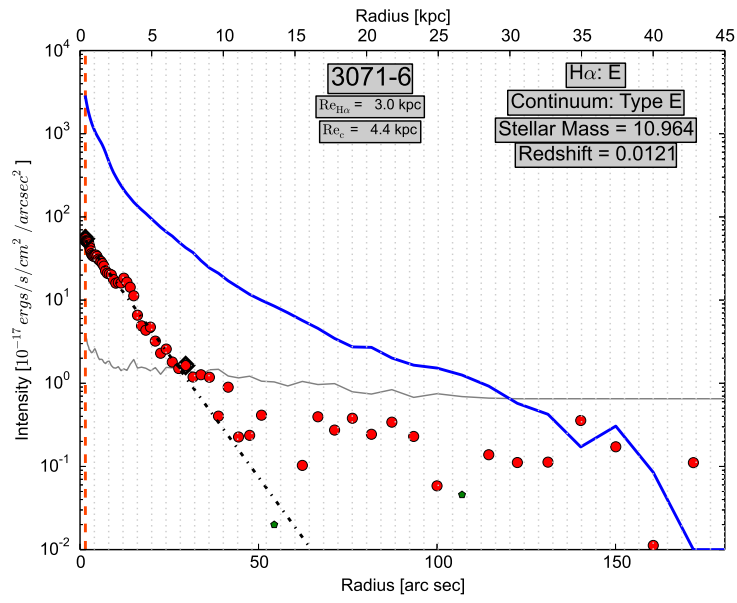
(c)



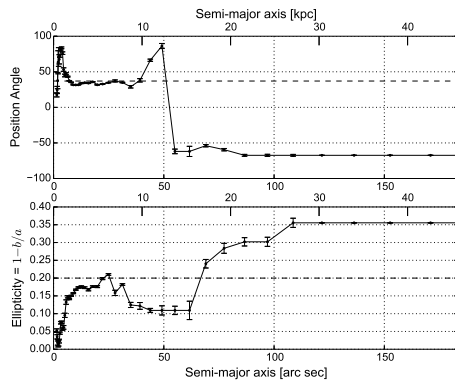
(d)



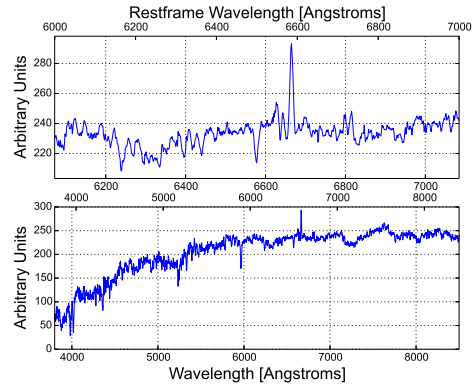
(a)



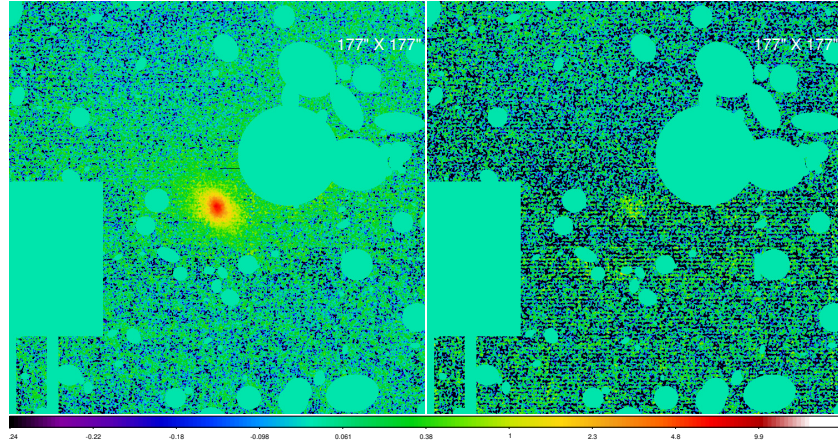
(b)



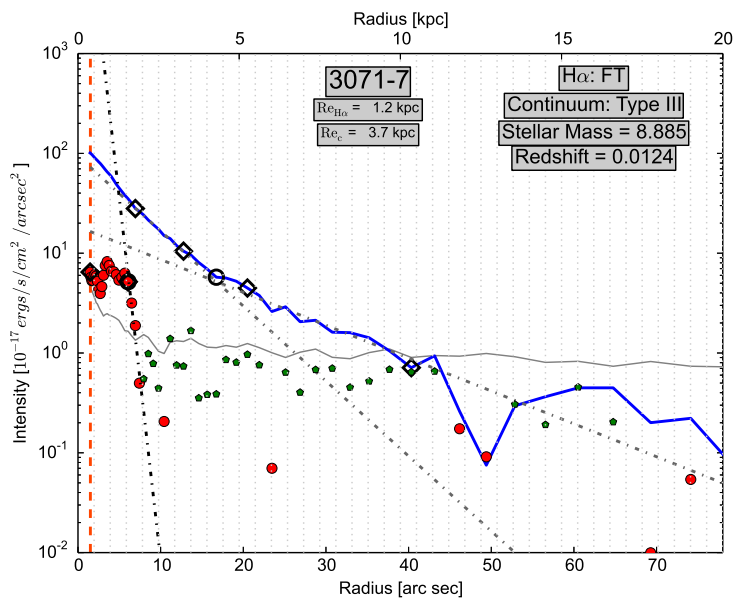
(c)



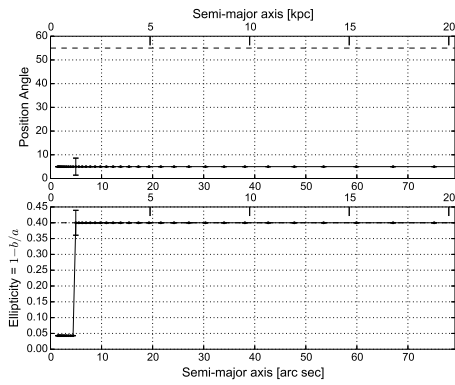
(d)



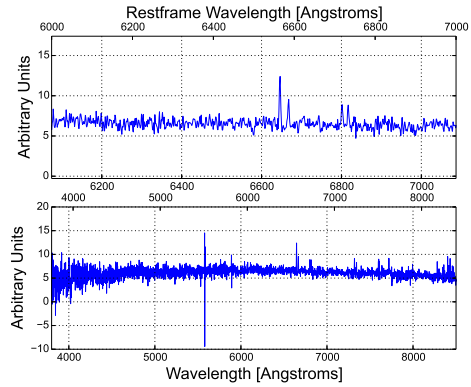
(a)



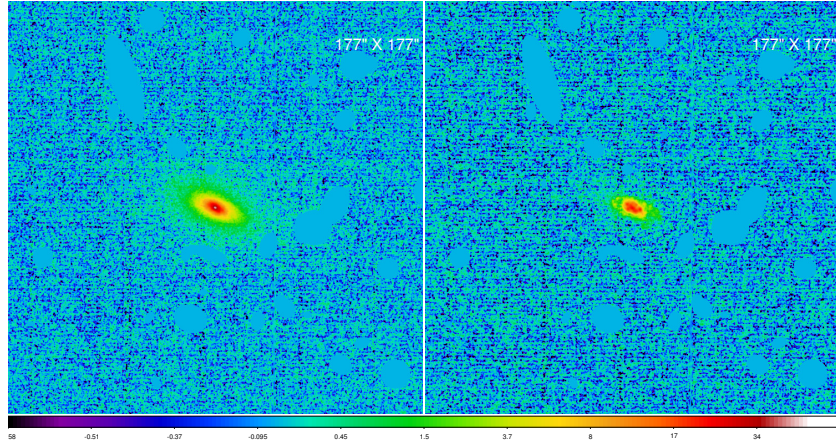
(b)



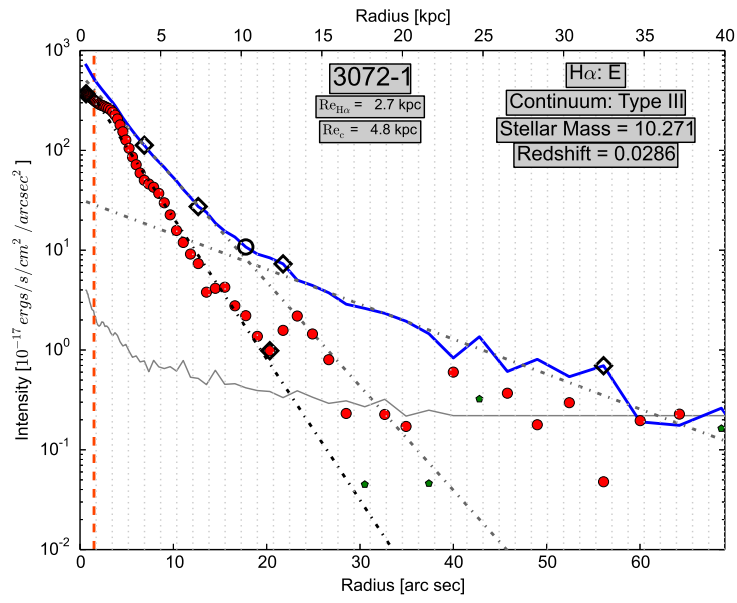
(c)



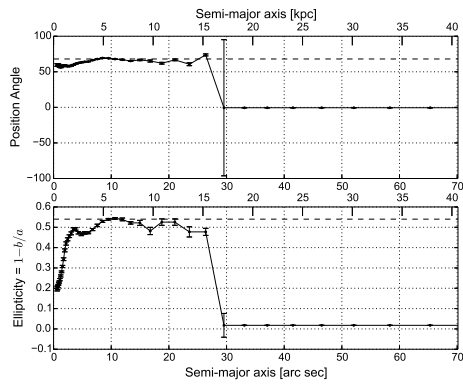
(d)



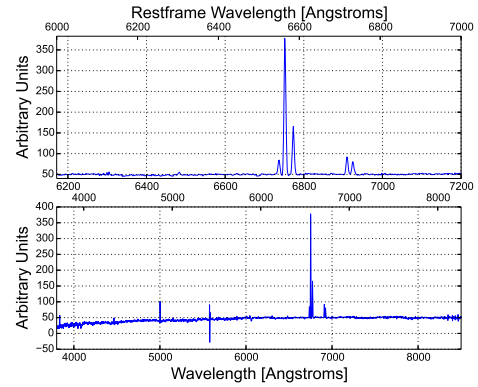
(a)



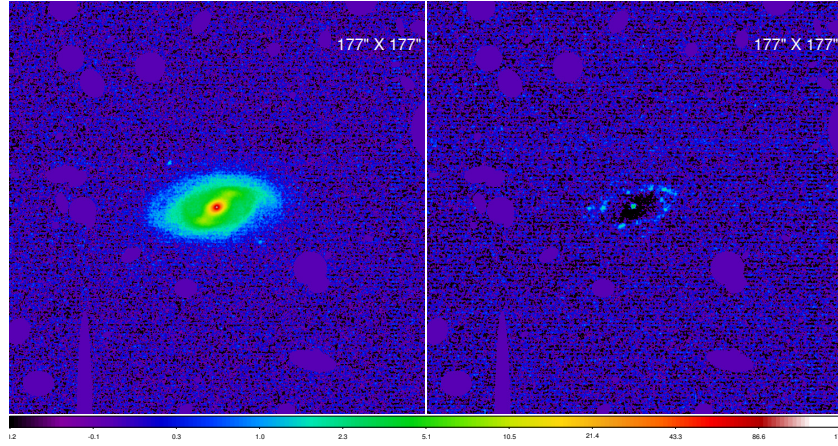
(b)



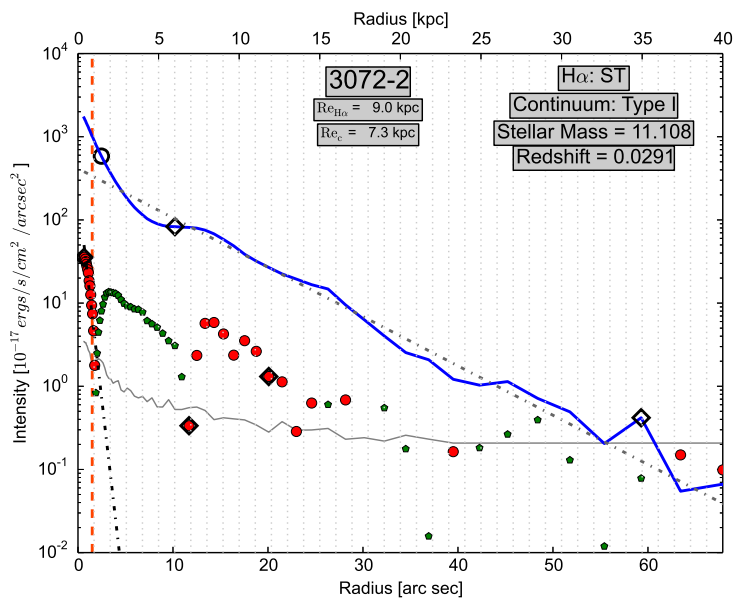
(c)



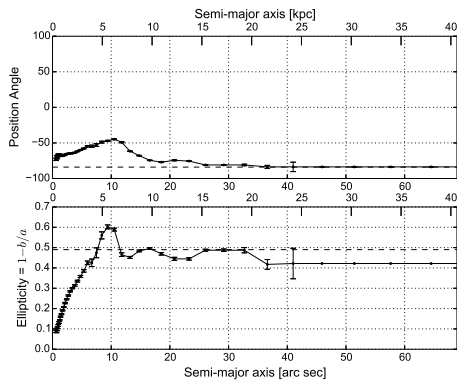
(d)



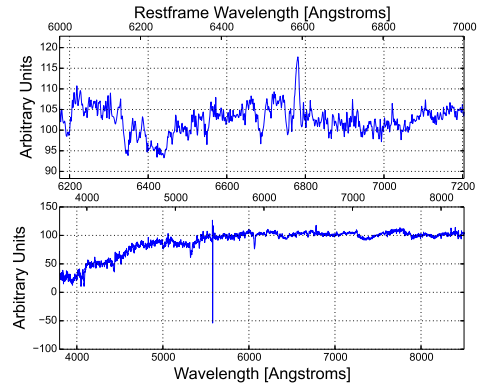
(a)



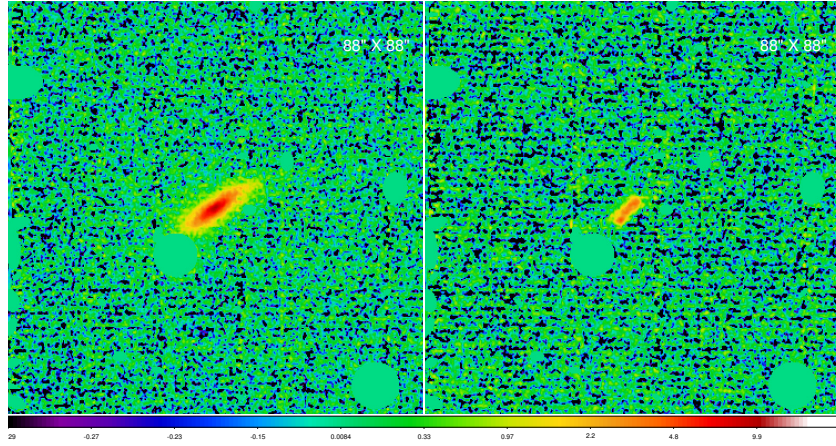
(b)



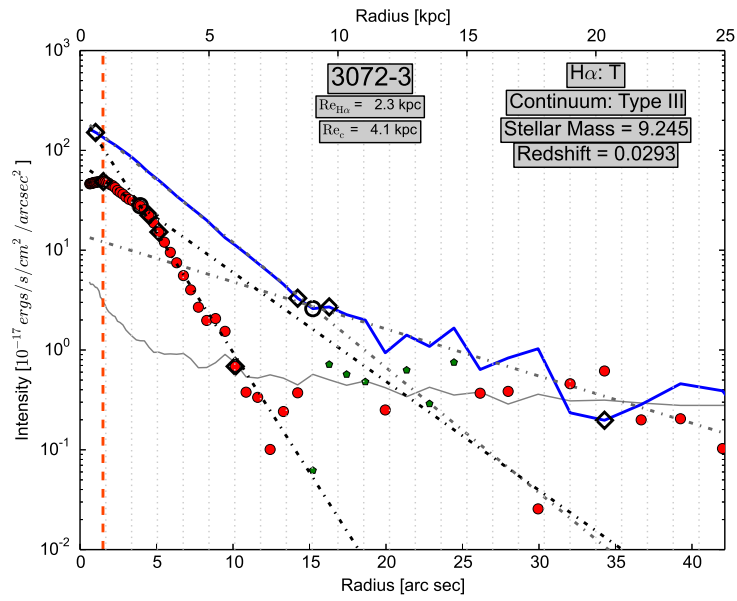
(c)



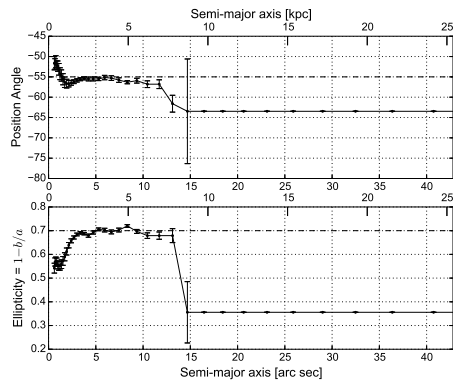
(d)



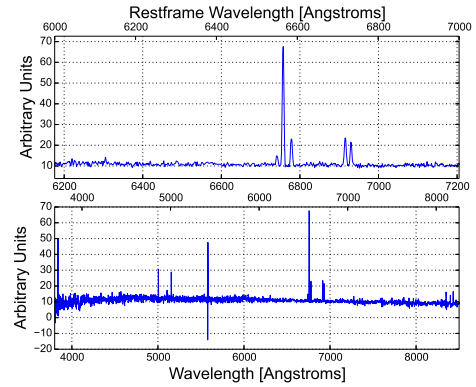
(a)



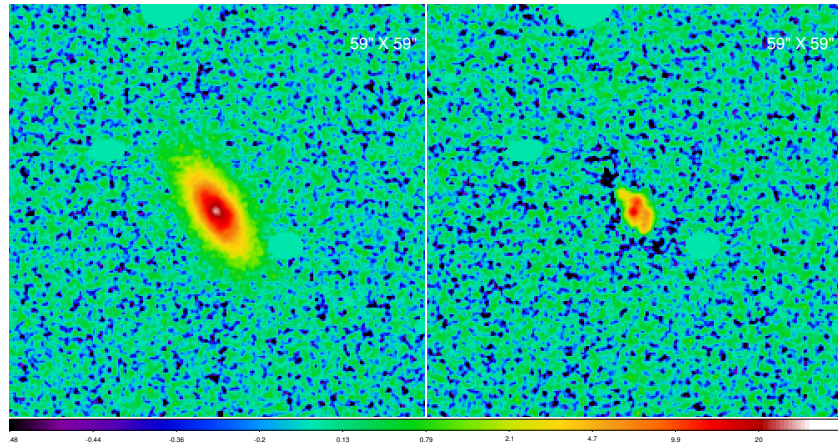
(b)



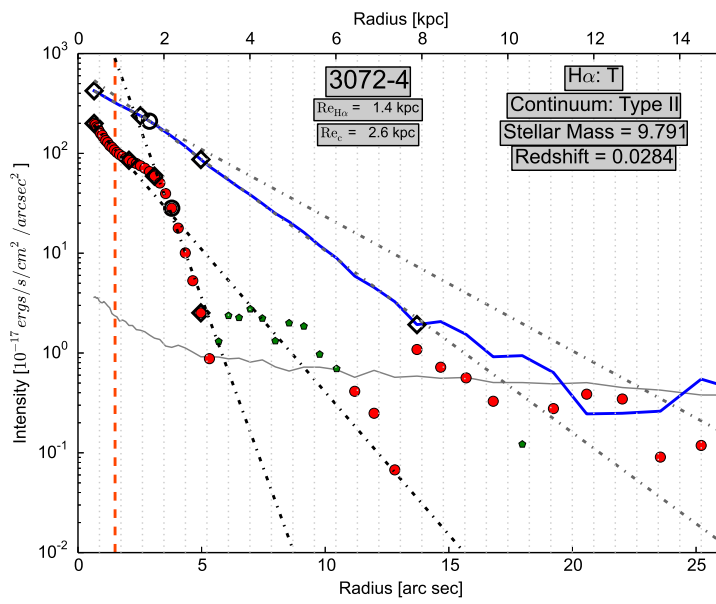
(c)



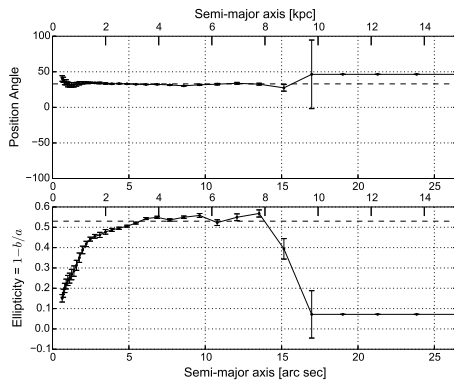
(d)



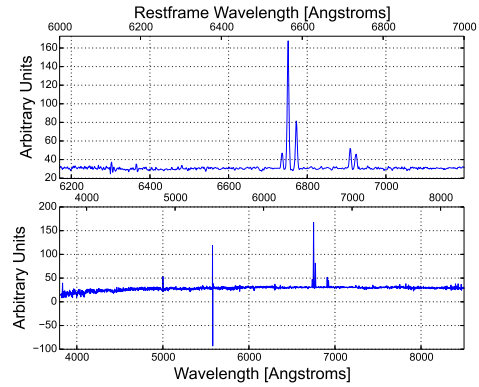
(a)



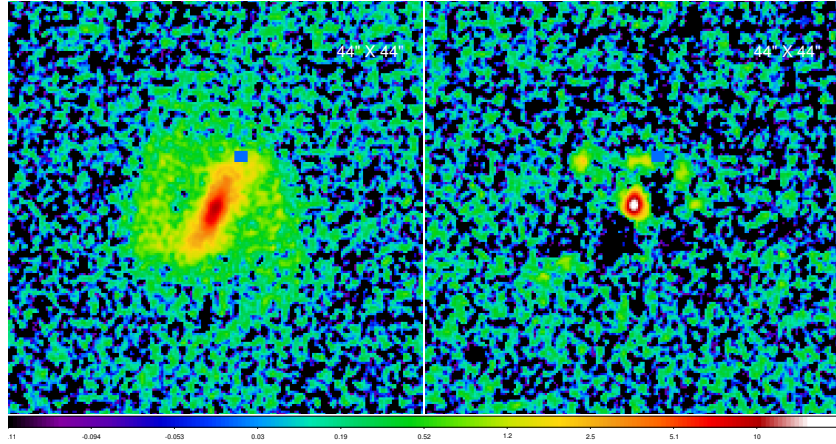
(b)



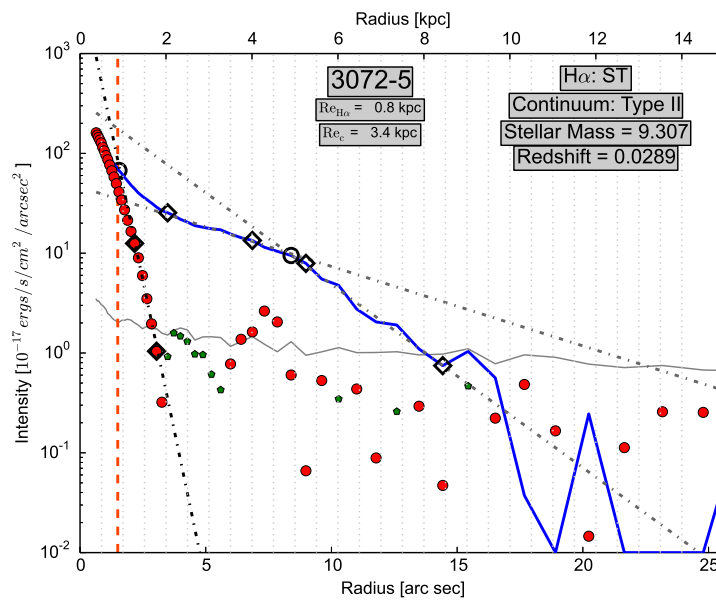
(c)



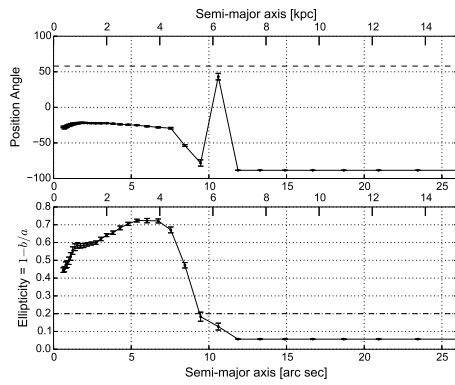
(d)



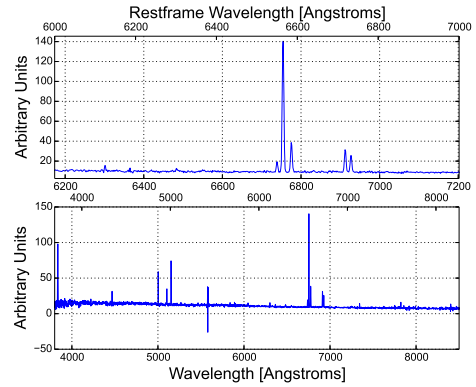
(a)



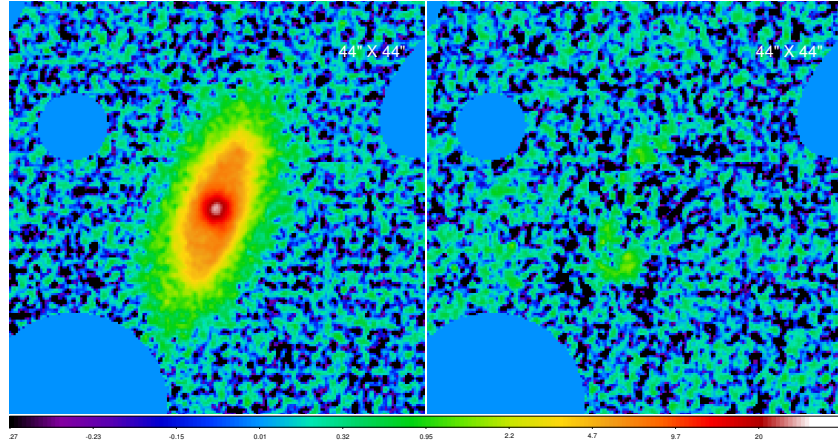
(b)



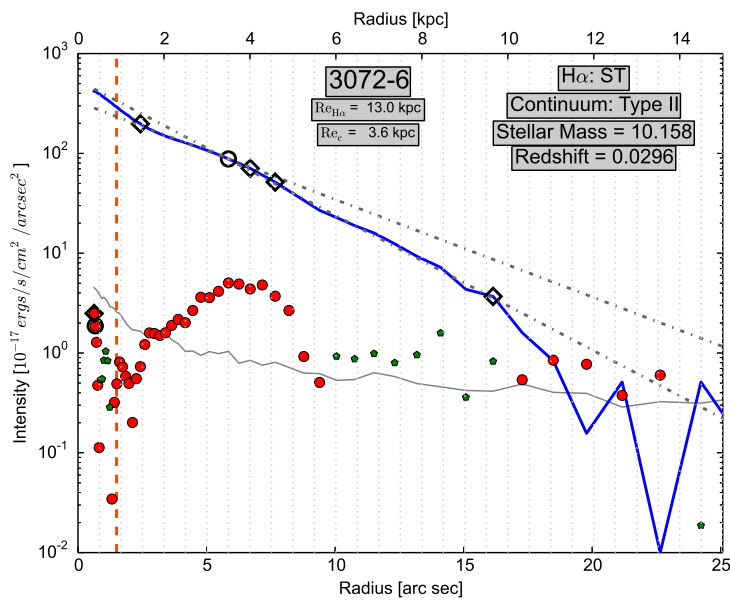
(c)



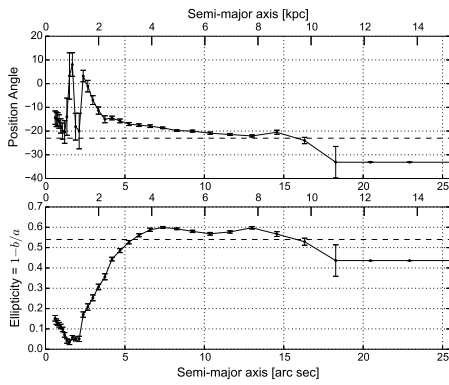
(d)



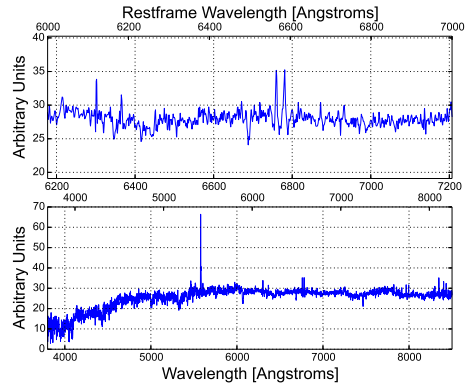
(a)



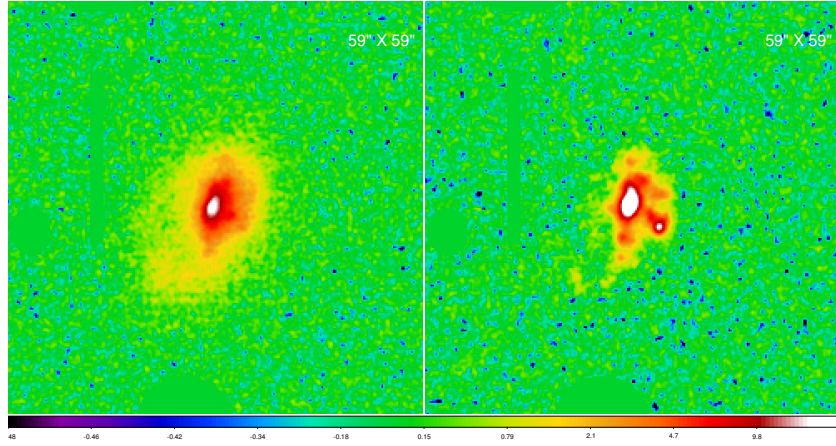
(b)



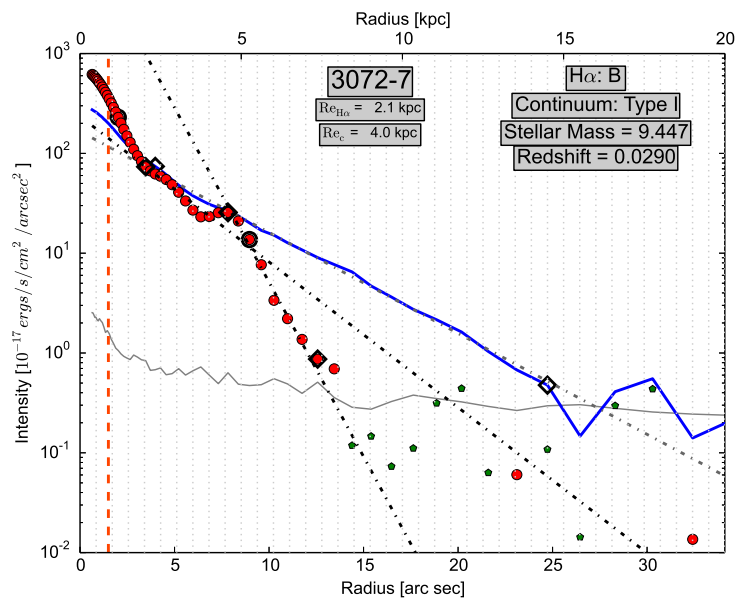
(c)



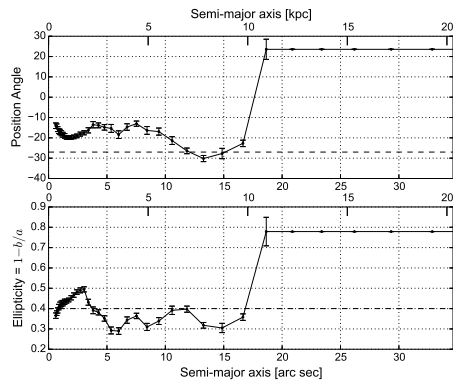
(d)



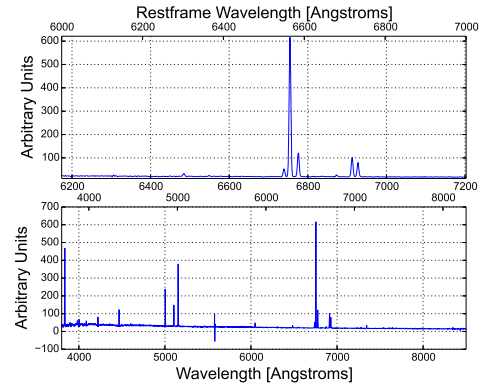
(a)



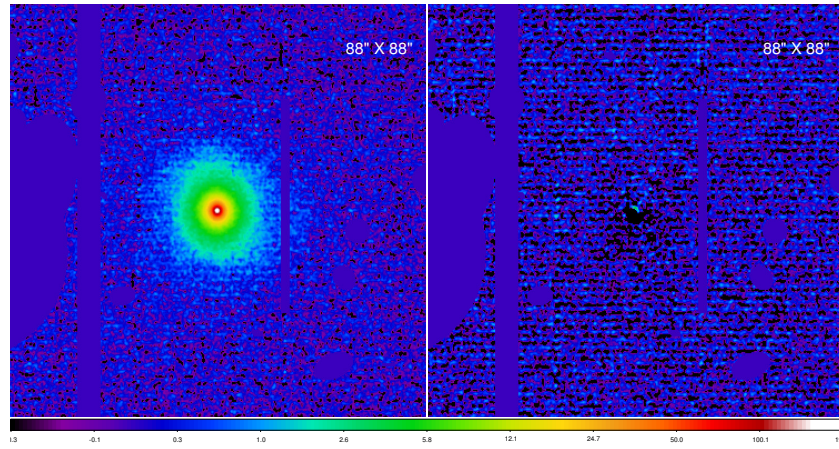
(b)



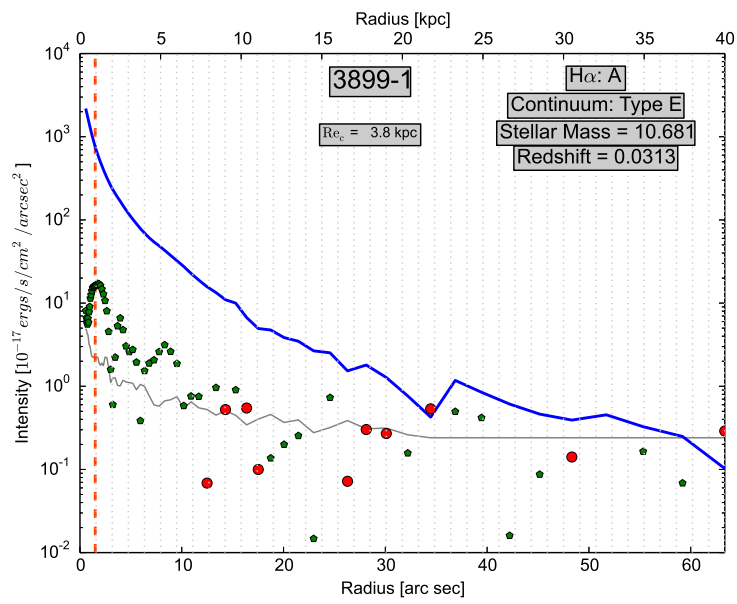
(c)



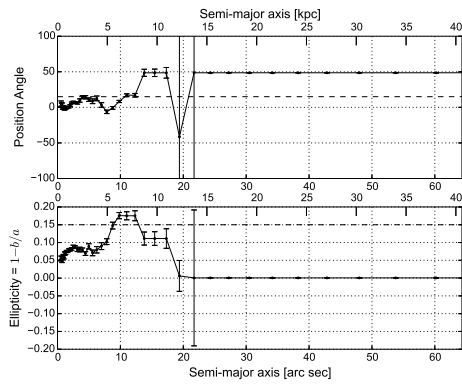
(d)



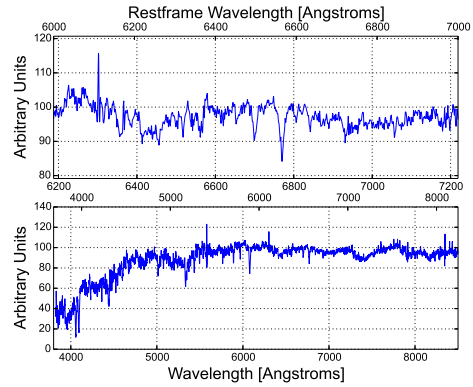
(a)



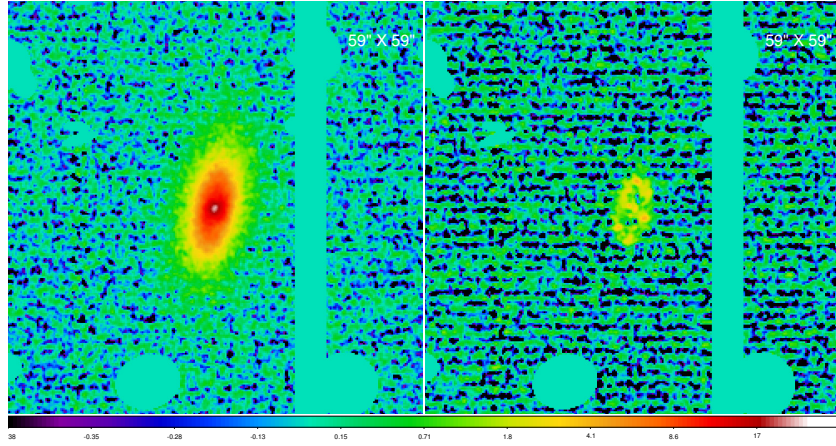
(b)



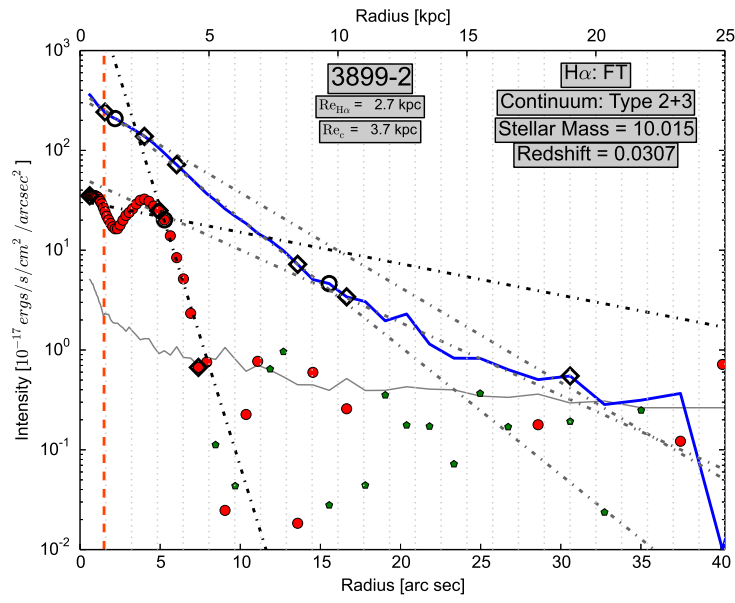
(c)



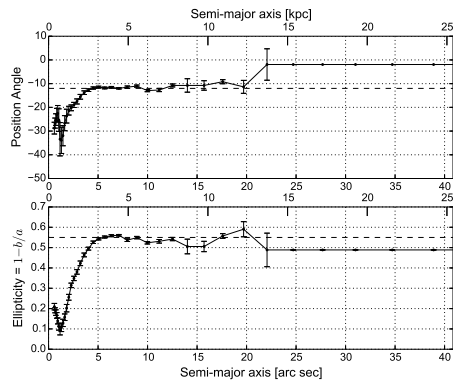
(d)



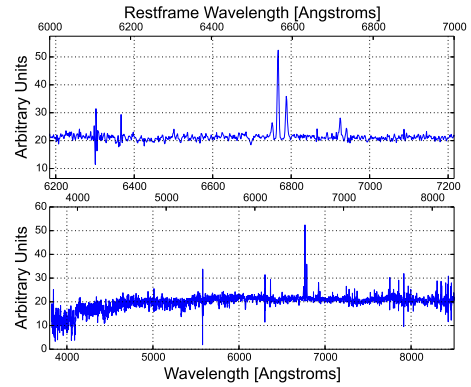
(a)



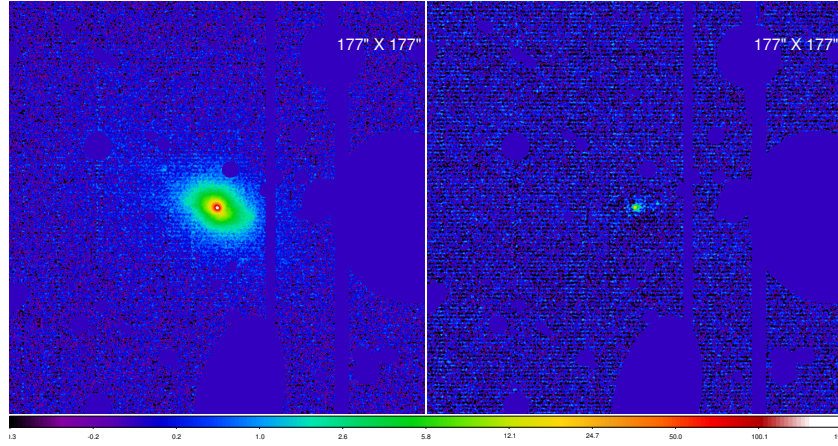
(b)



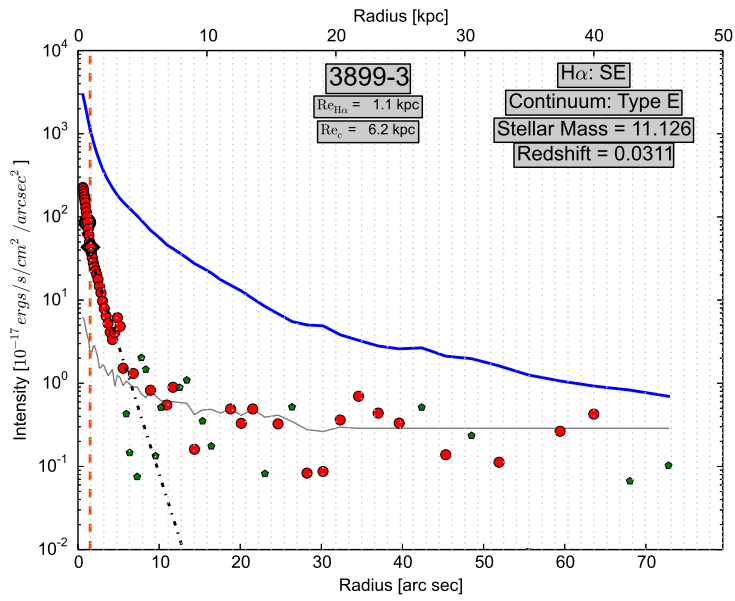
(c)



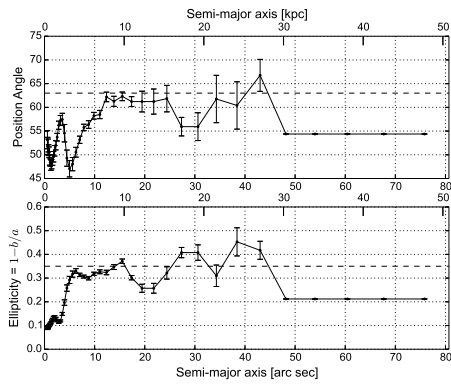
(d)



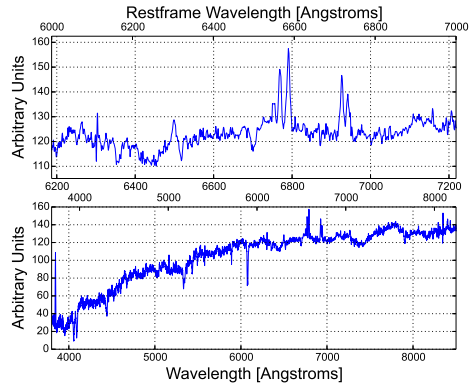
(a)



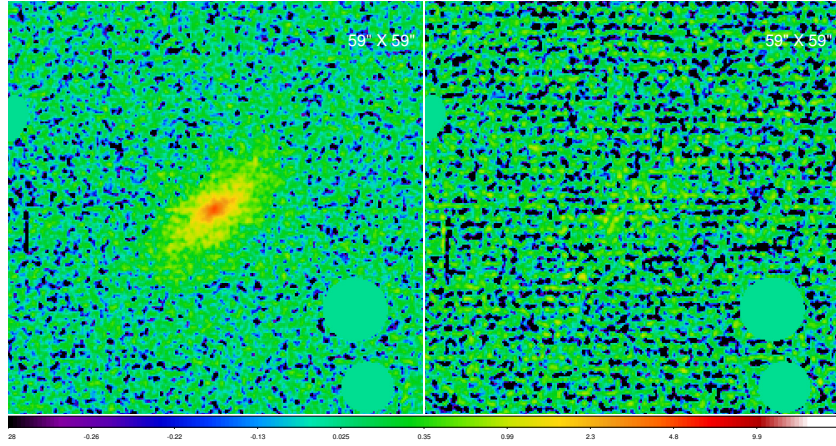
(b)



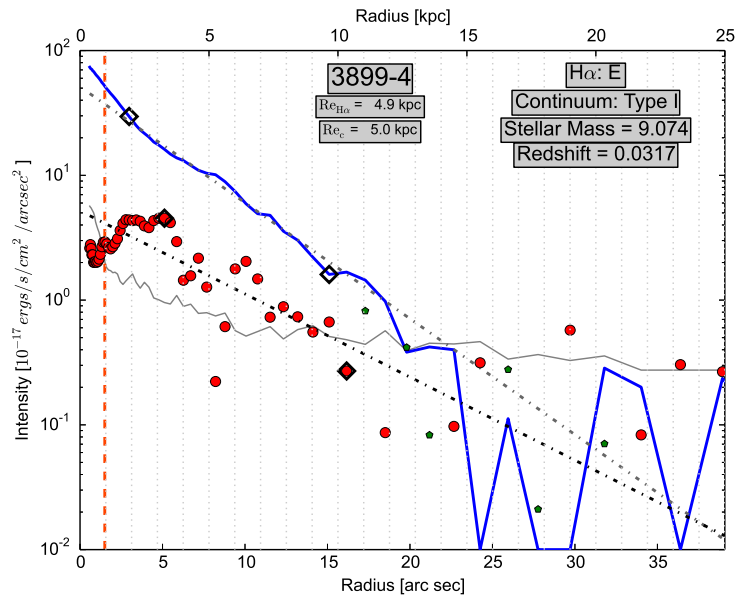
(c)



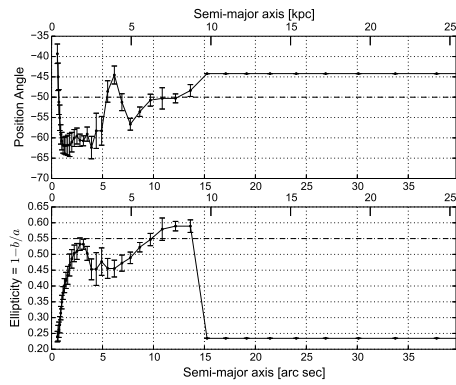
(d)



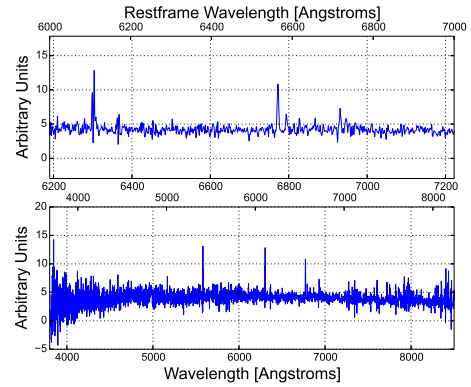
(a)



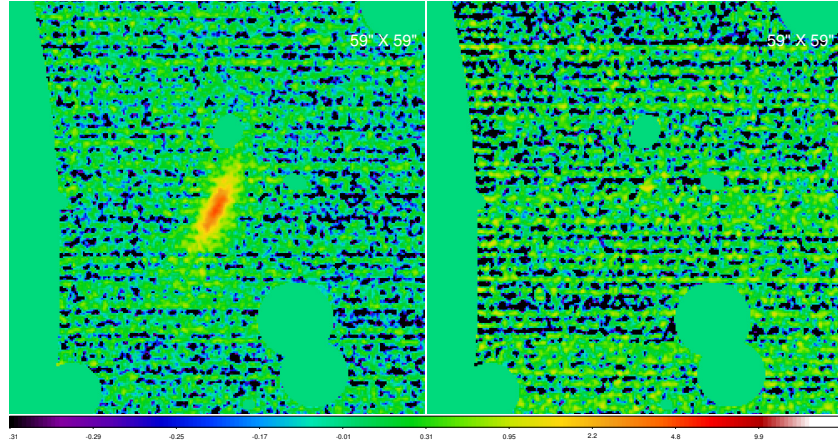
(b)



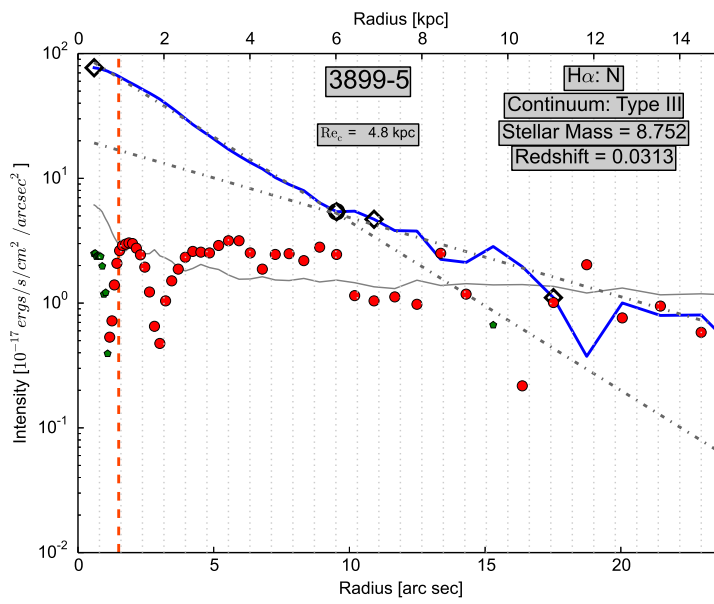
(c)



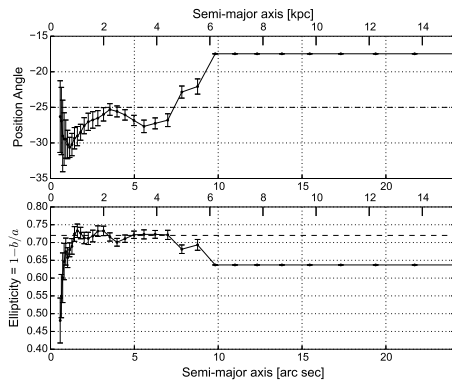
(d)



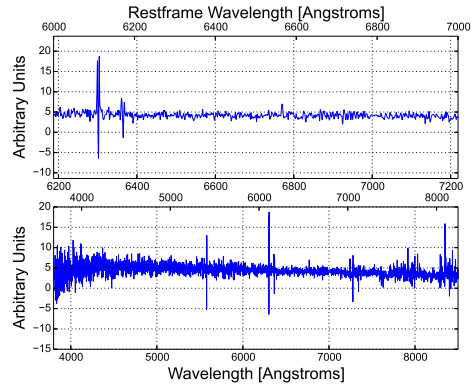
(a)



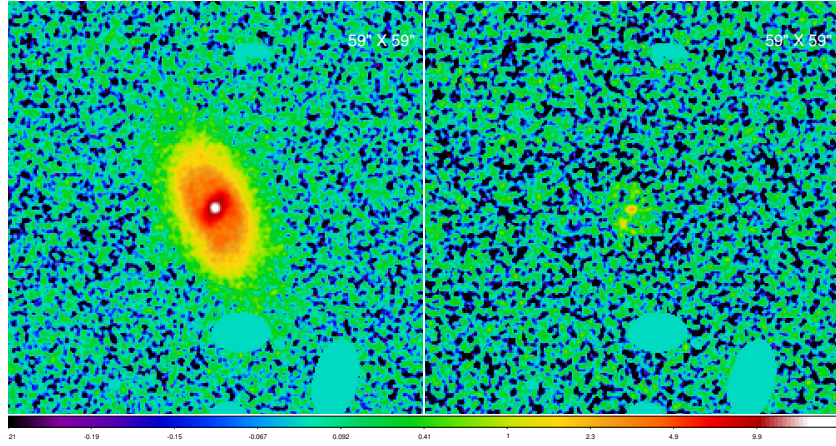
(b)



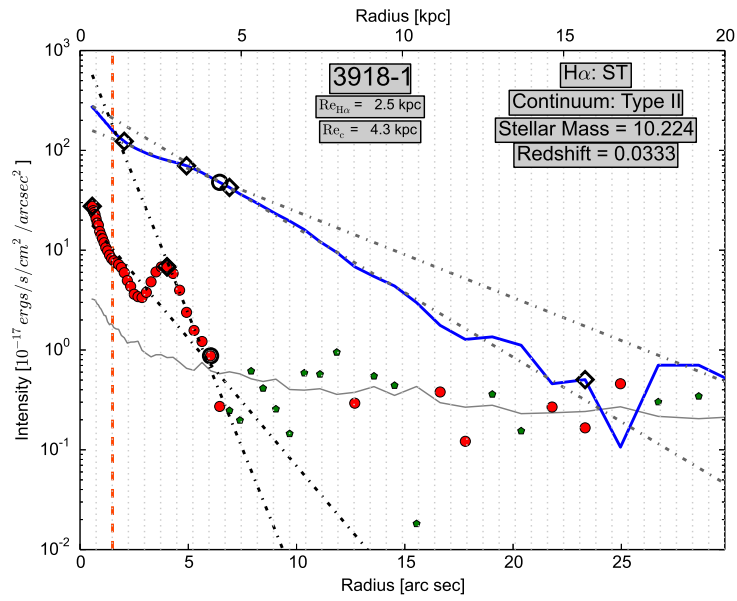
(c)



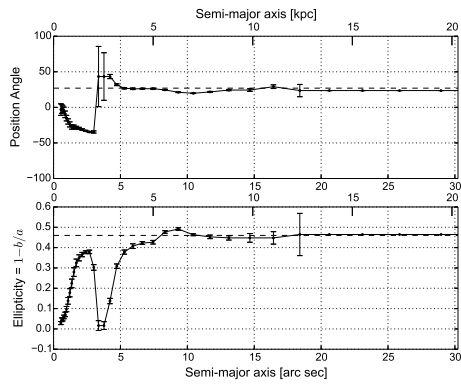
(d)



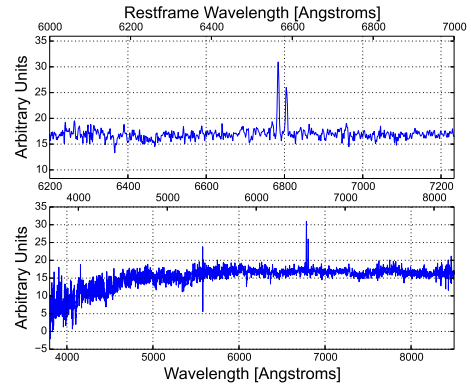
(a)



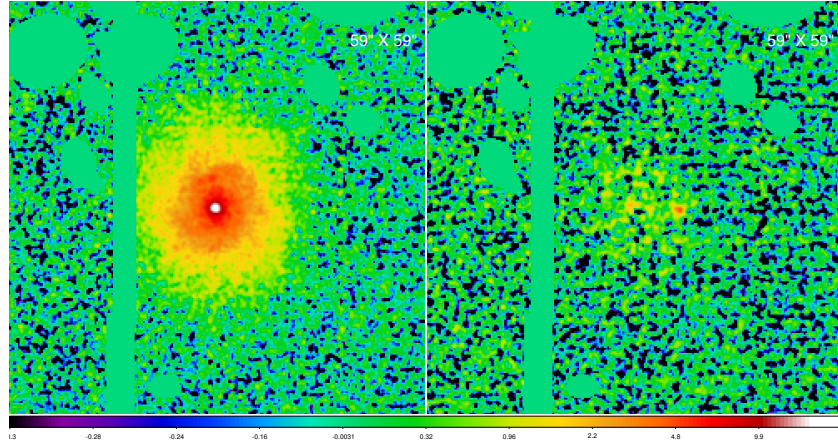
(b)



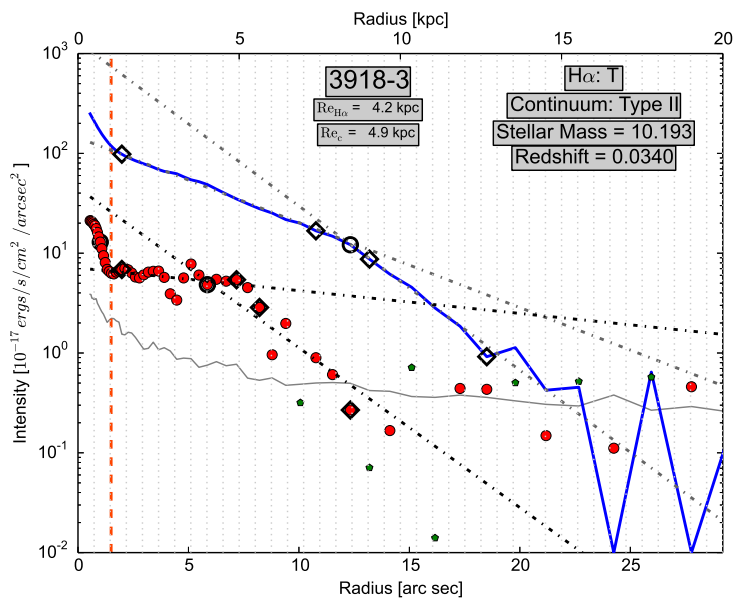
(c)



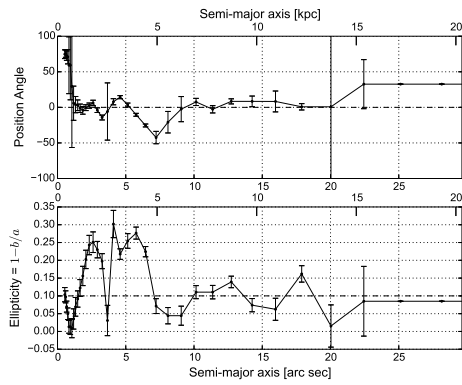
(d)



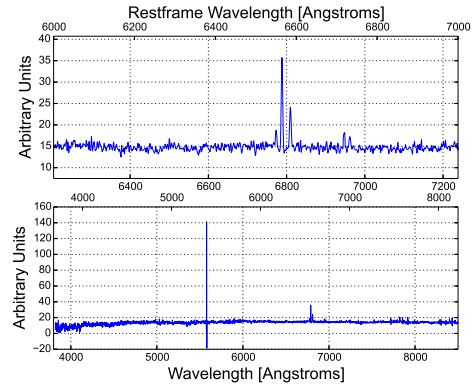
(a)



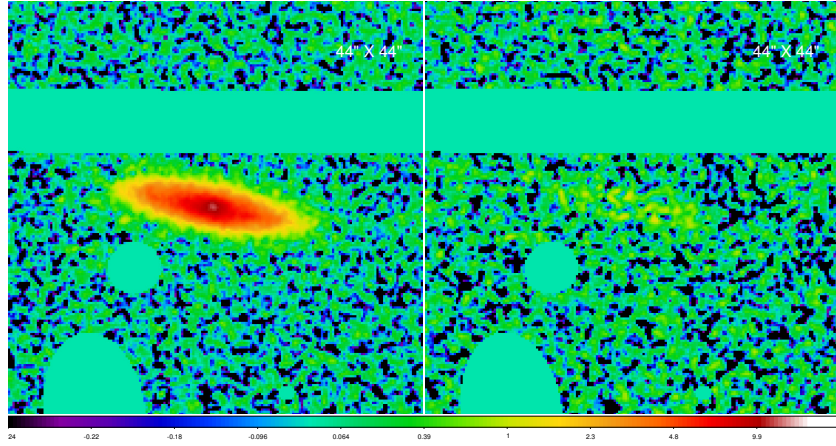
(b)



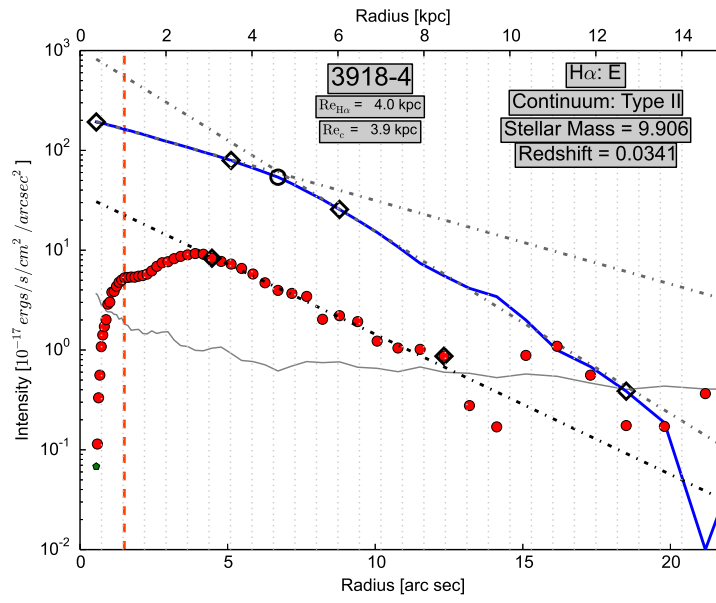
(c)



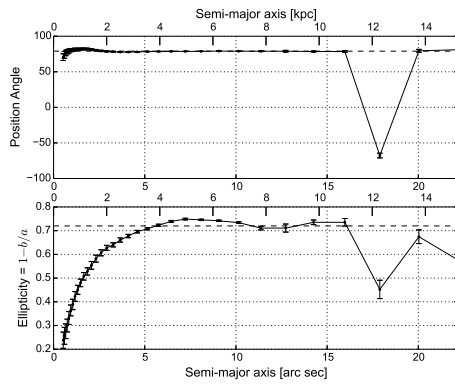
(d)



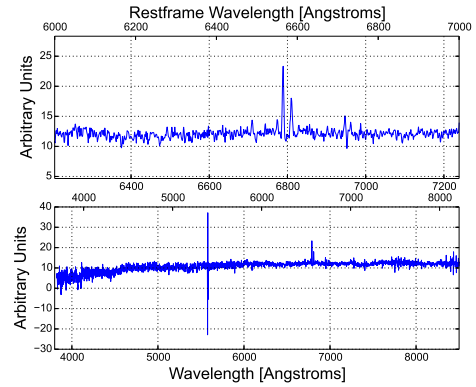
(a)



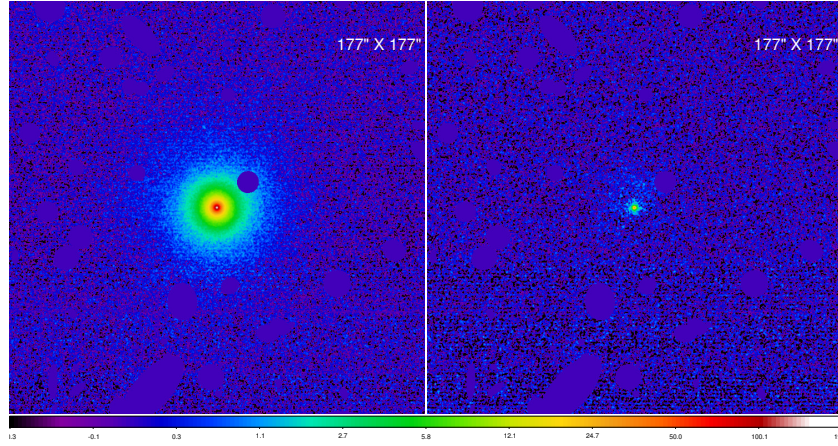
(b)



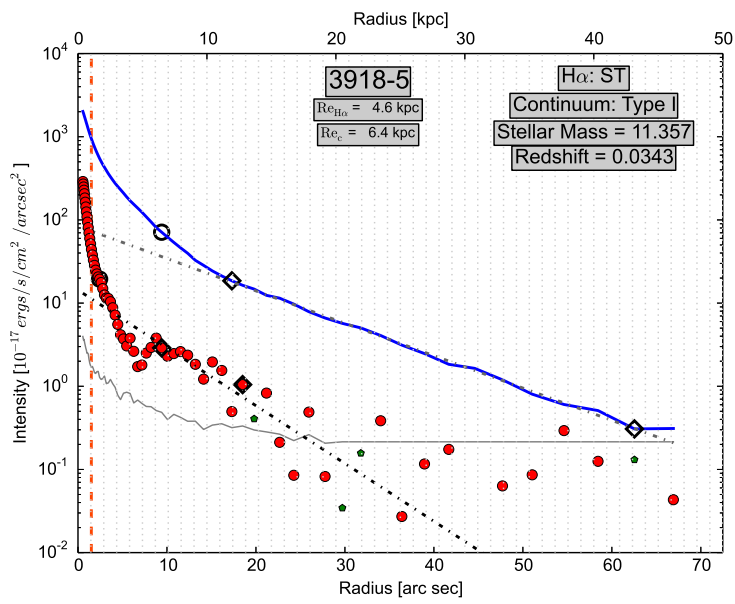
(c)



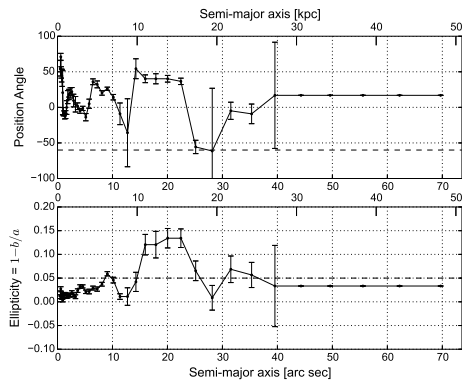
(d)



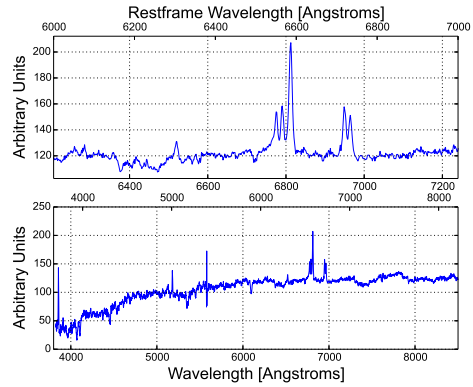
(a)



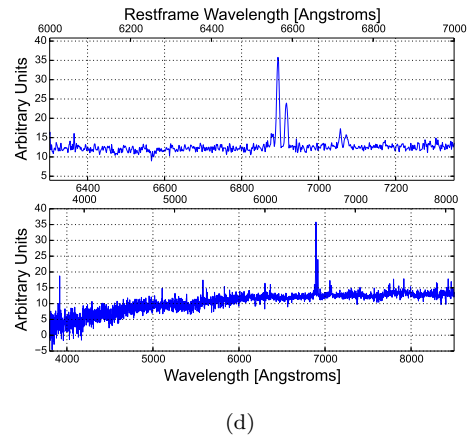
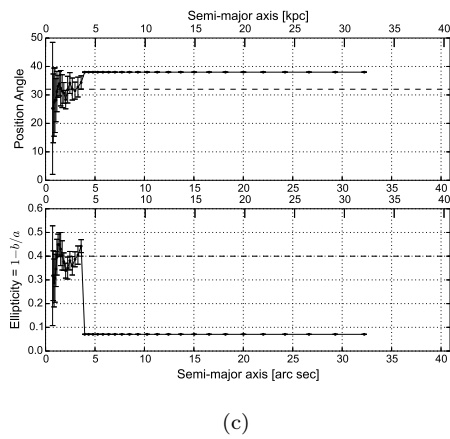
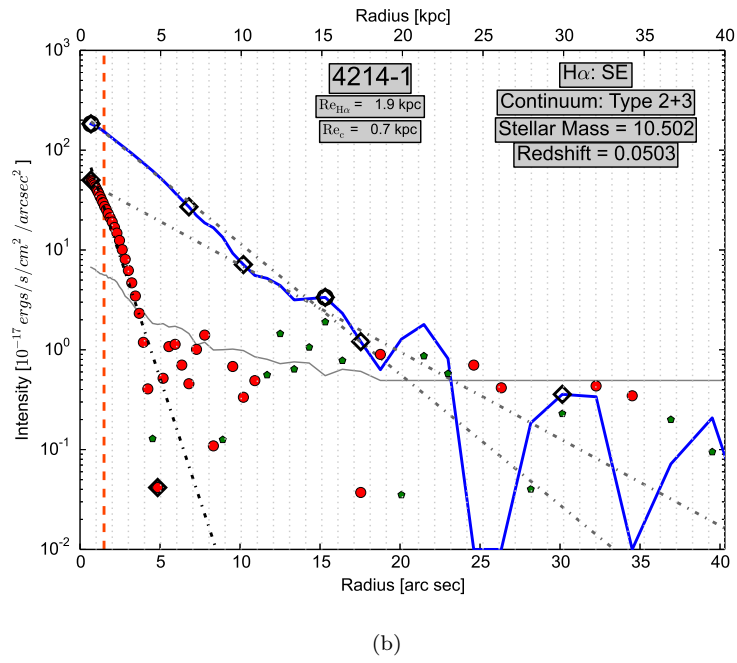
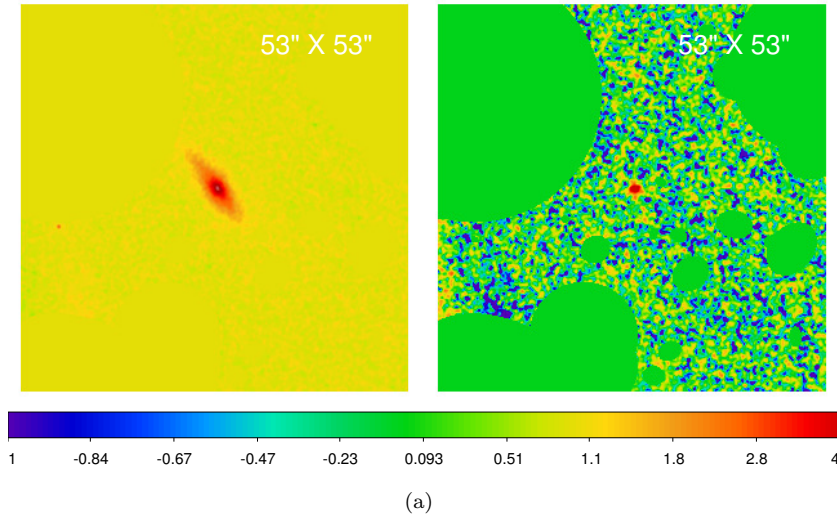
(b)

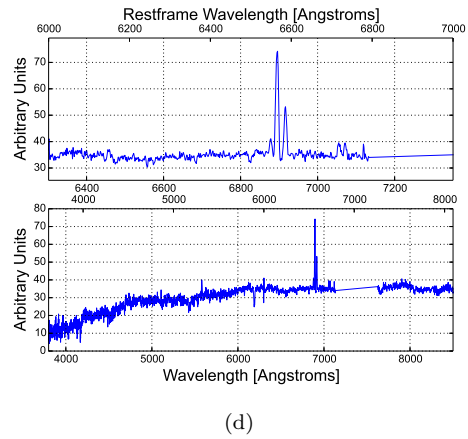
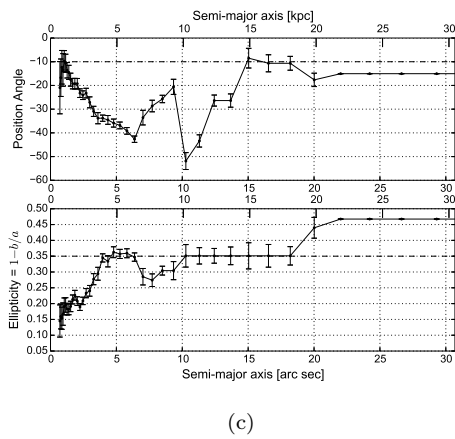
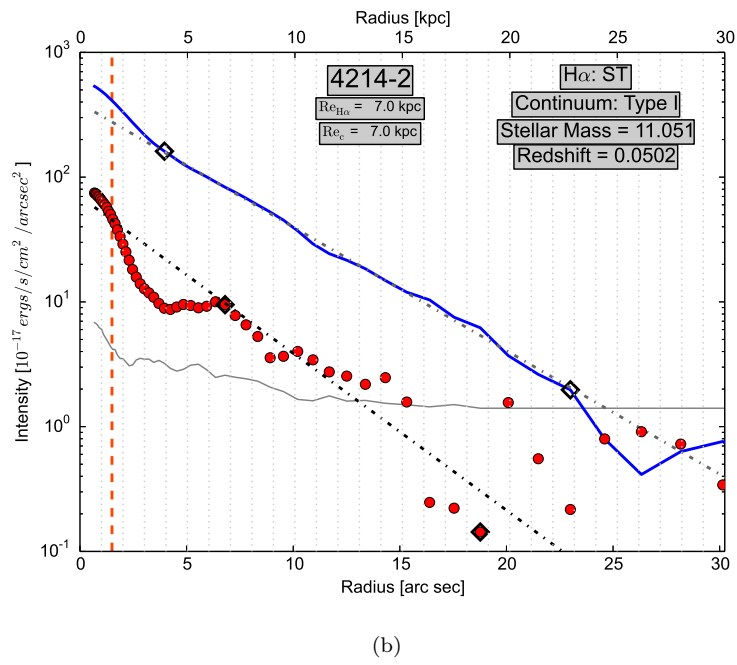
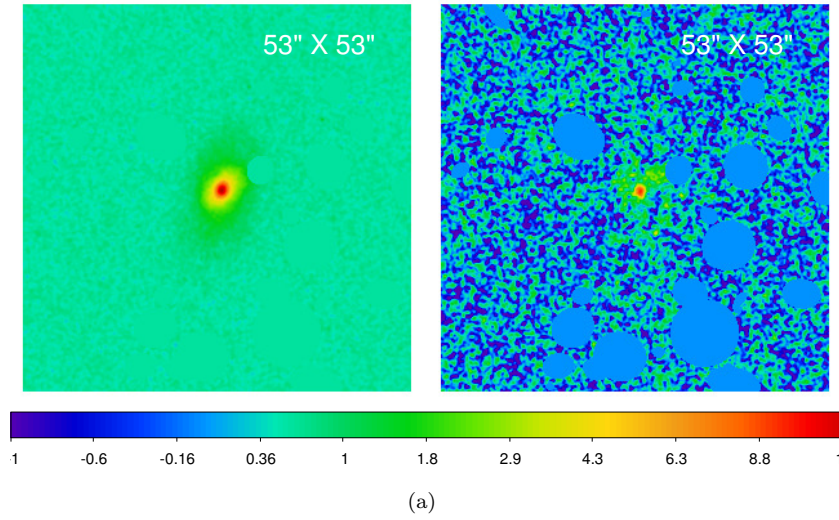


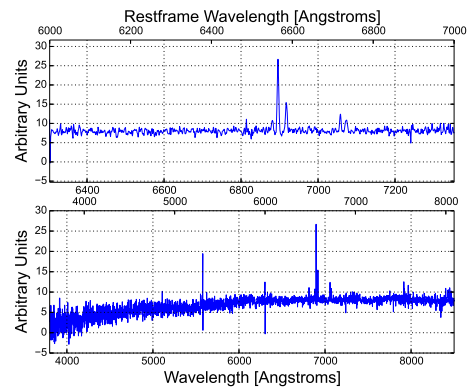
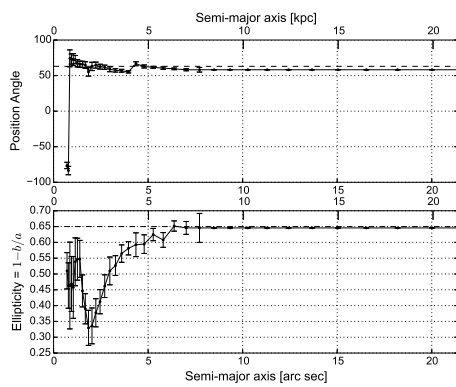
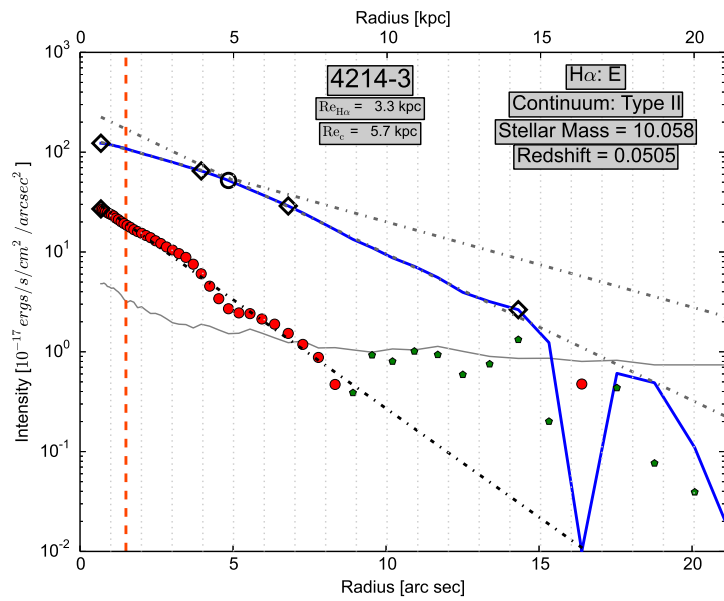
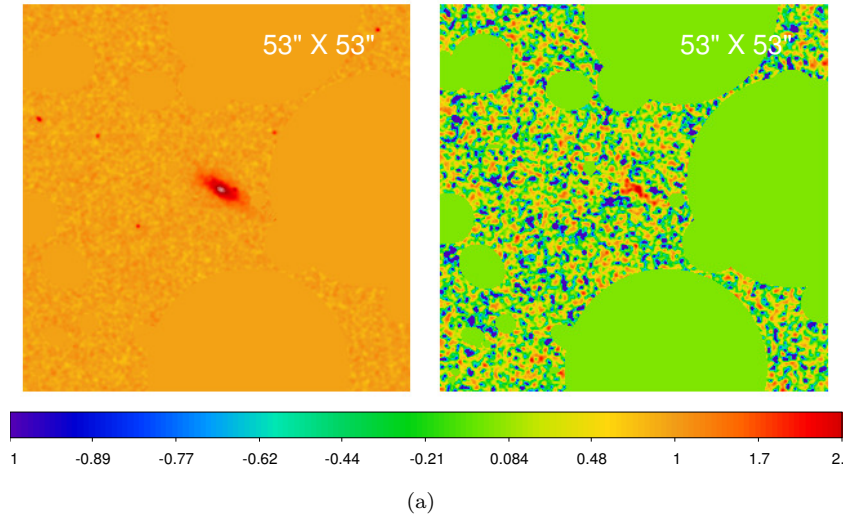
(c)

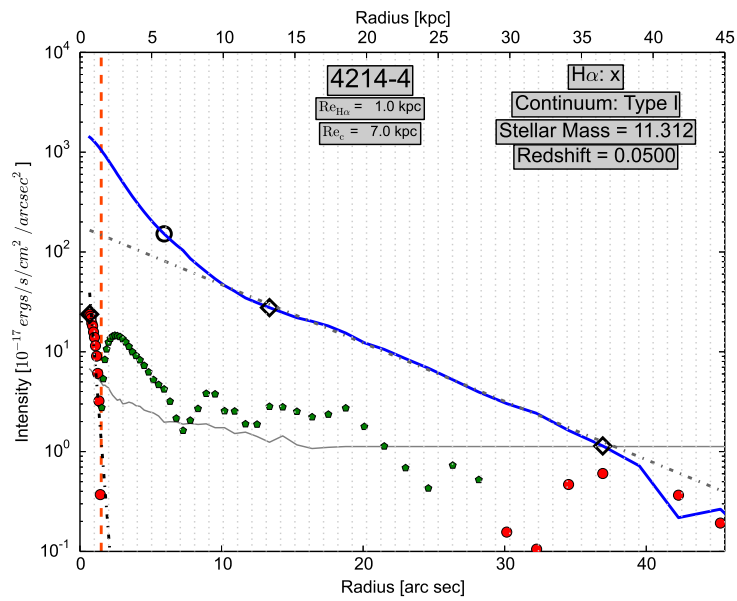
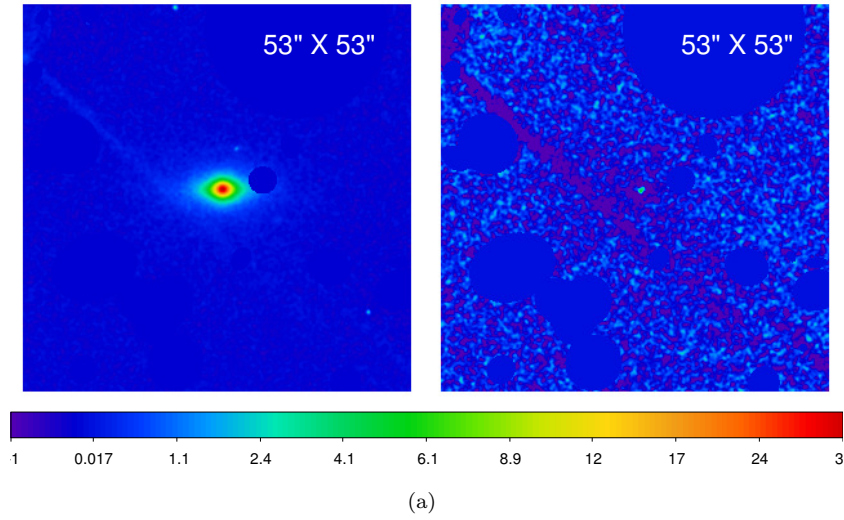


(d)

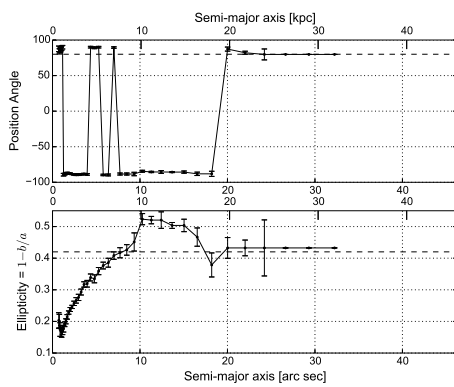




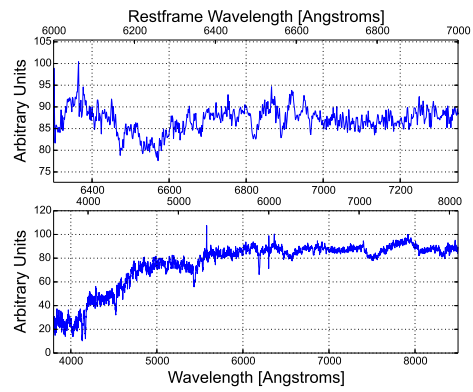




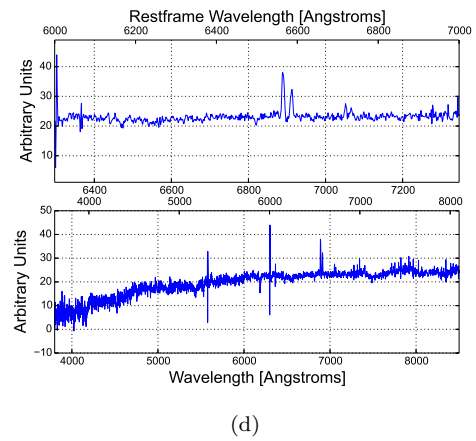
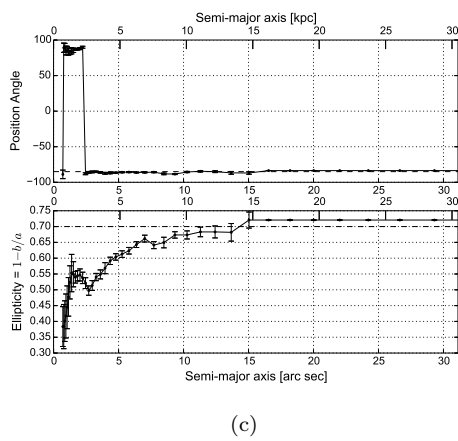
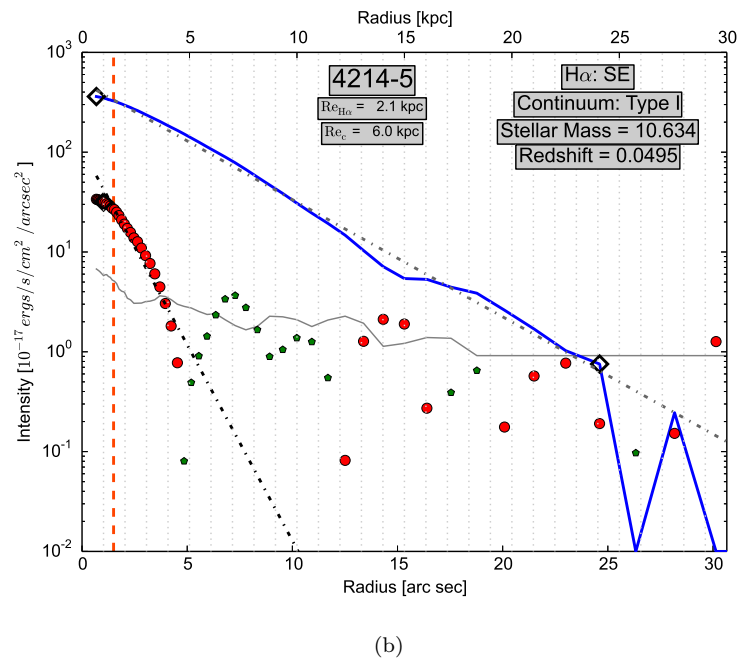
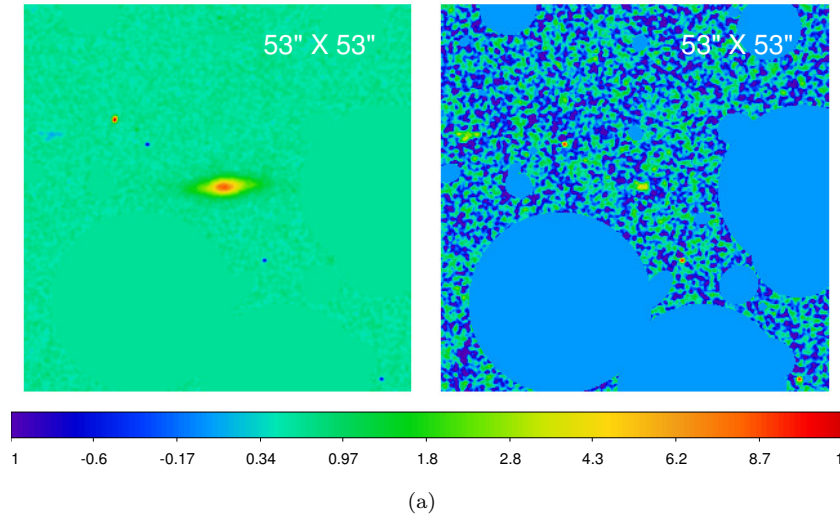
(b)

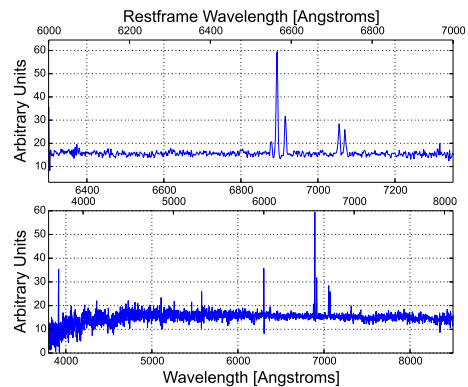
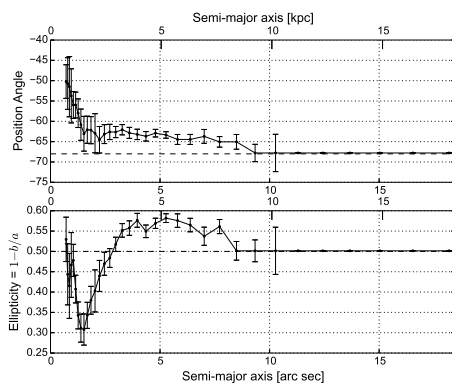
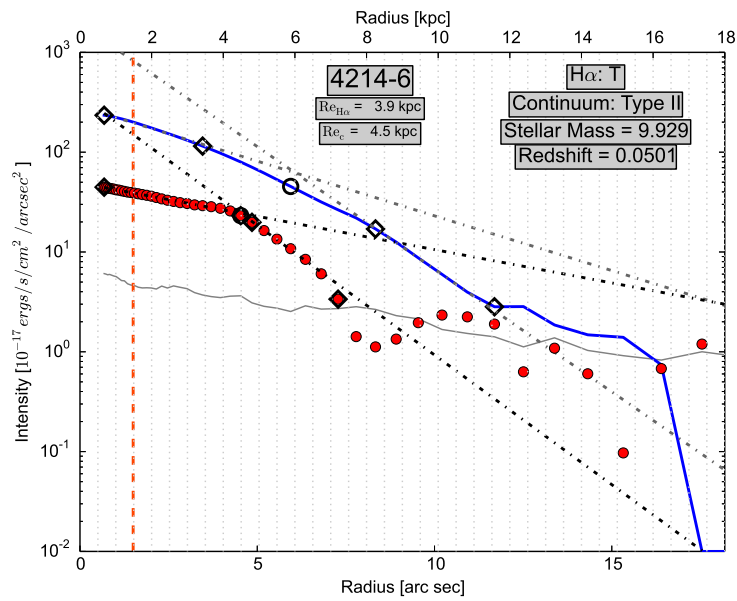
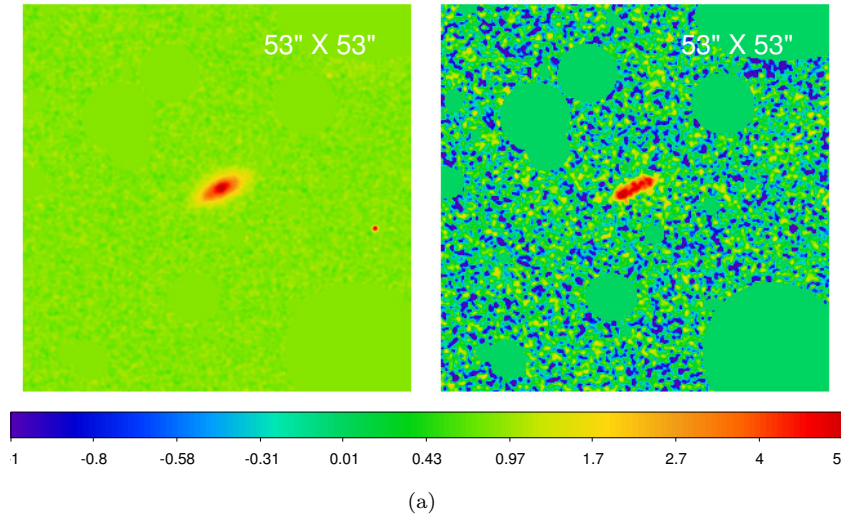


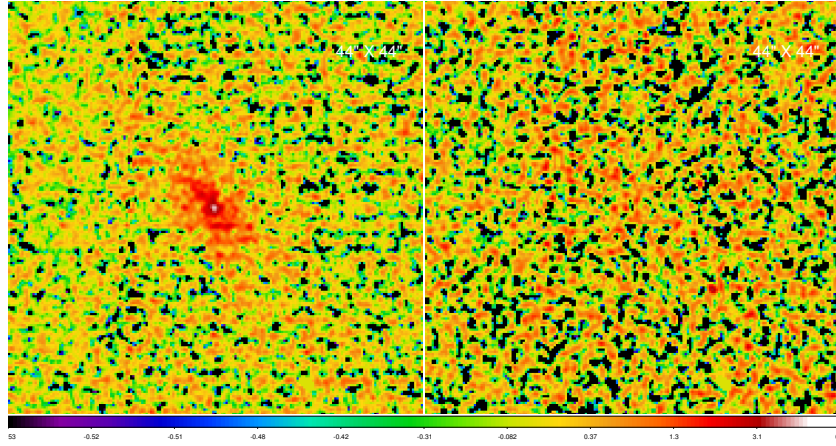
(c)



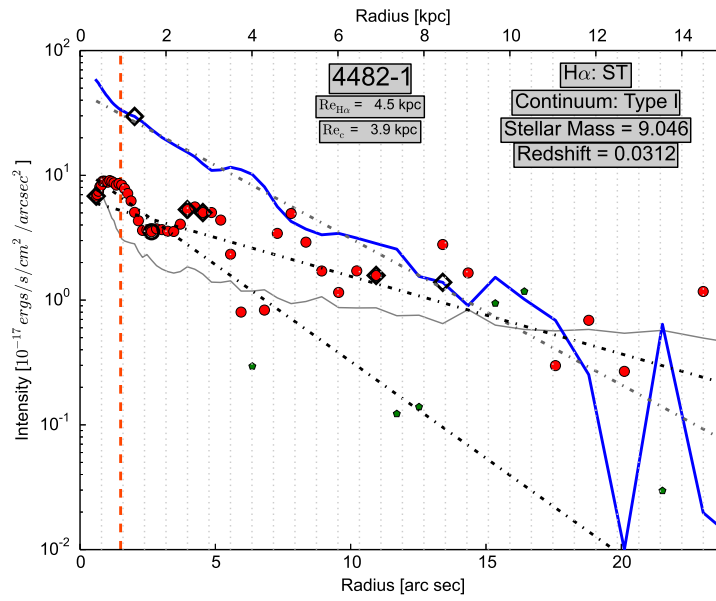
(d)



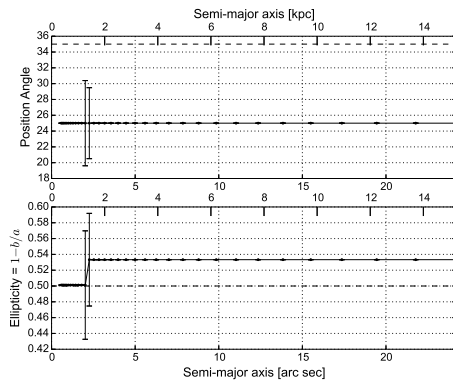




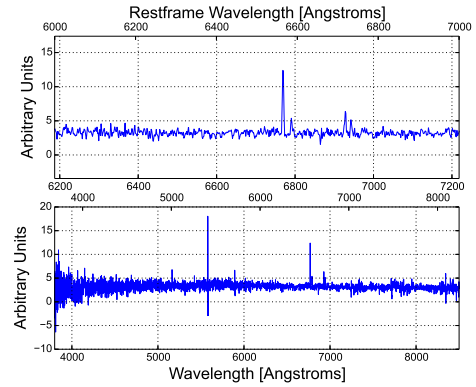
(a)



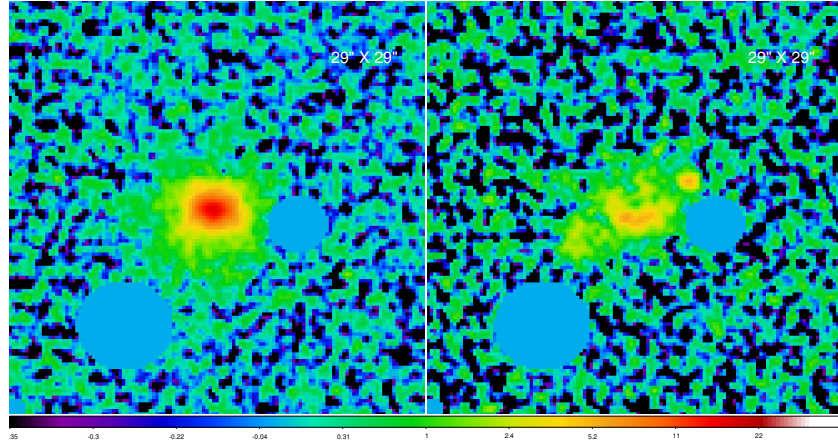
(b)



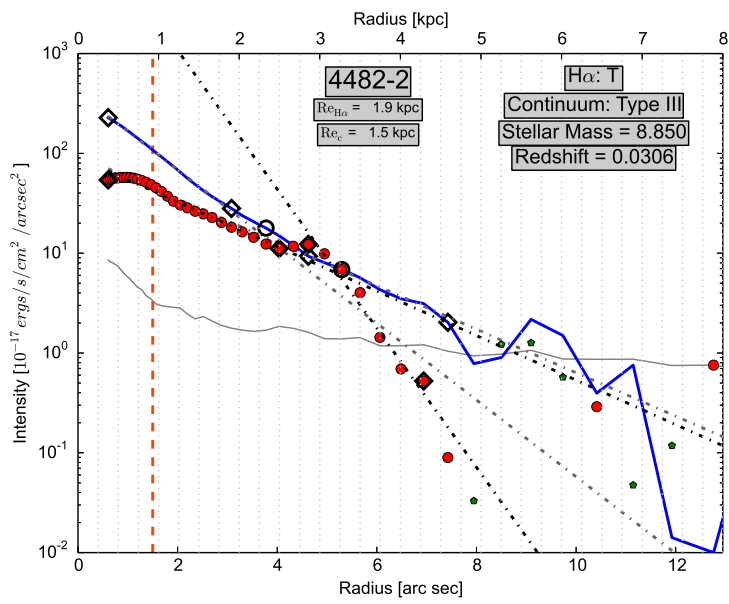
(c)



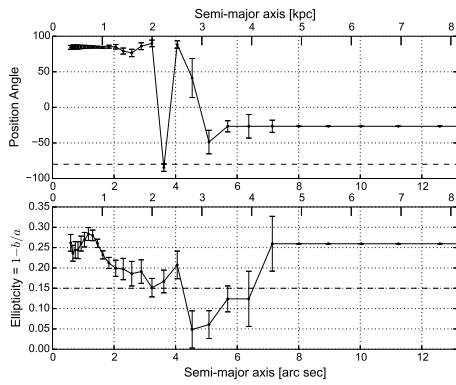
(d)



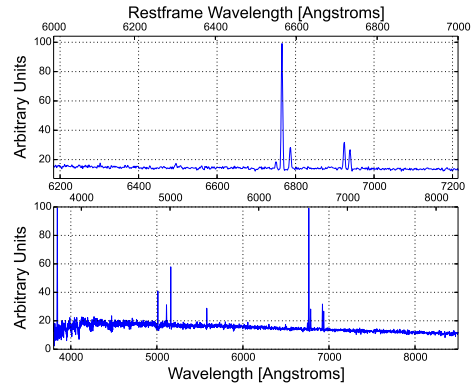
(a)



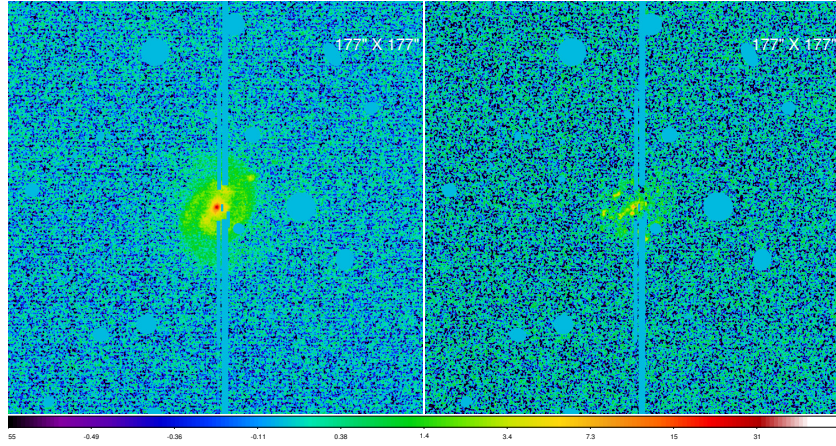
(b)



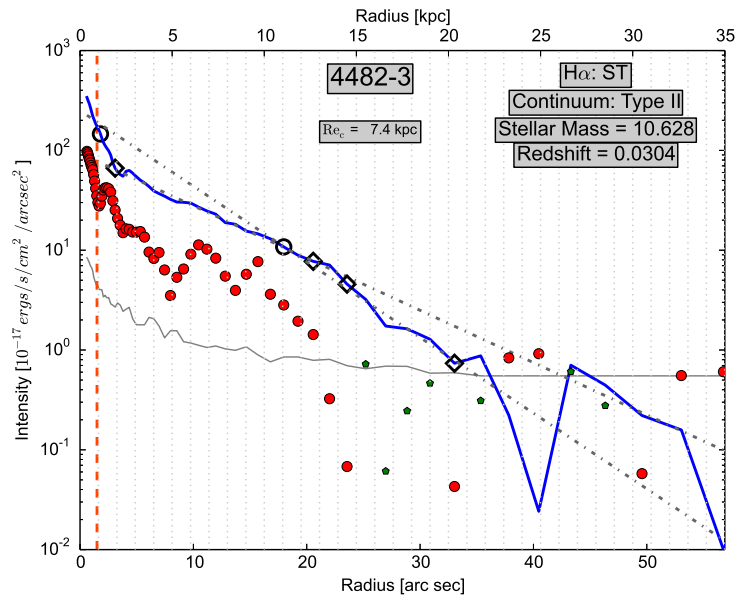
(c)



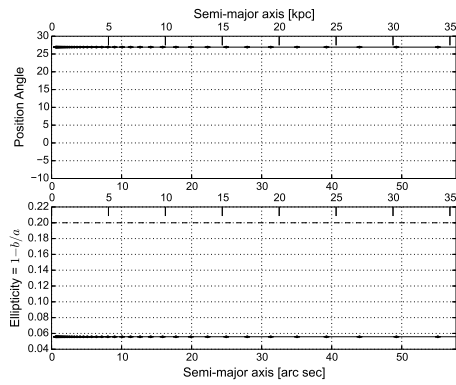
(d)



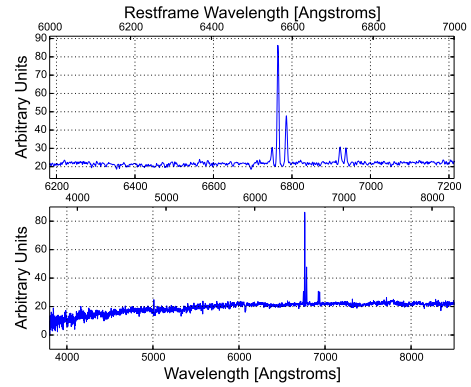
(a)



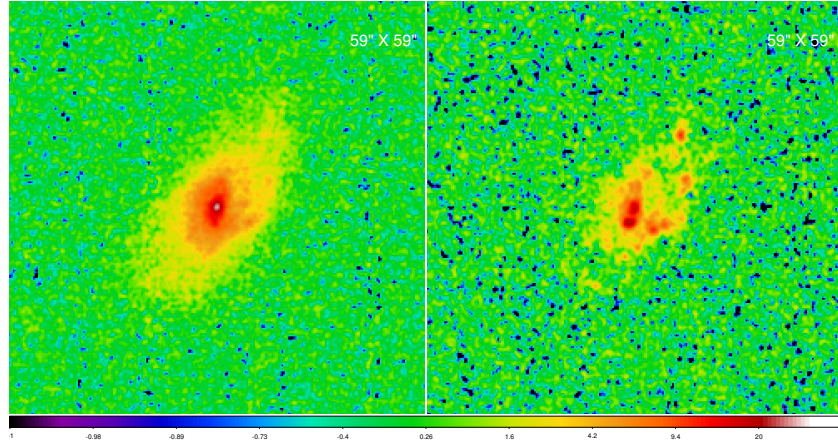
(b)



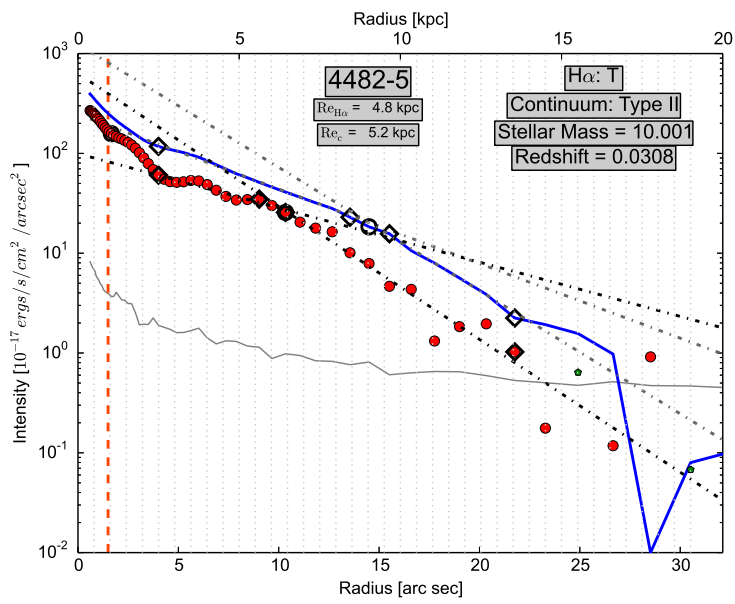
(c)



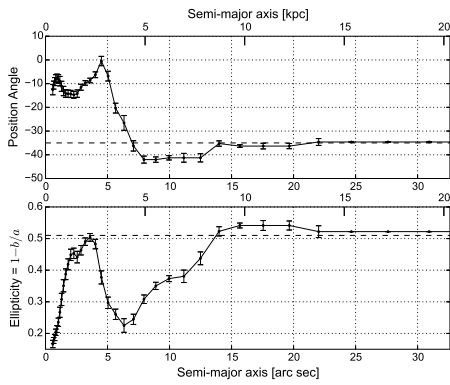
(d)



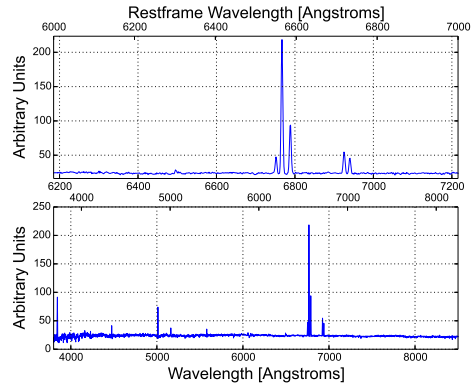
(a)



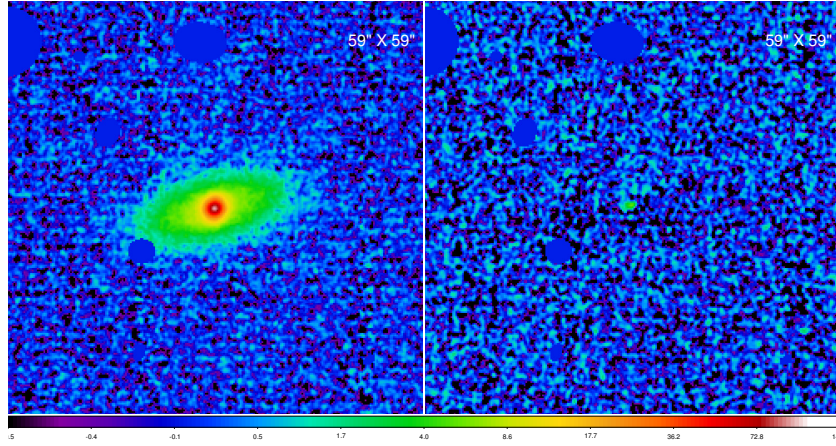
(b)



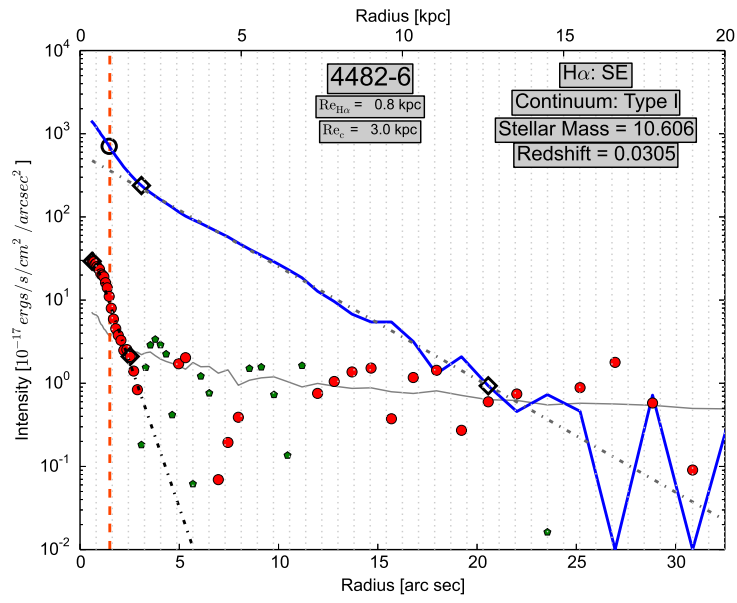
(c)



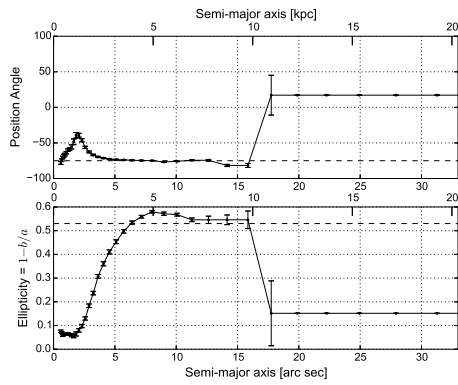
(d)



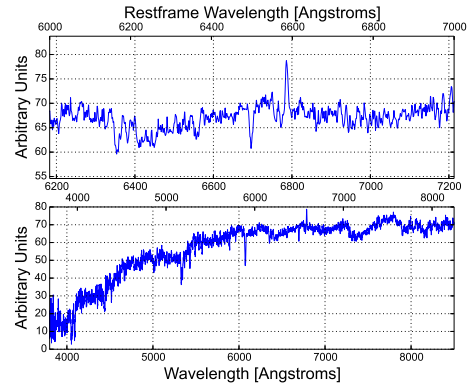
(a)



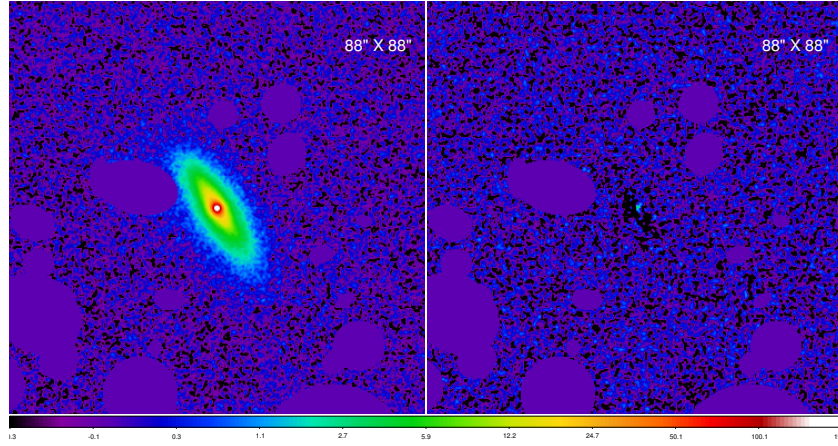
(b)



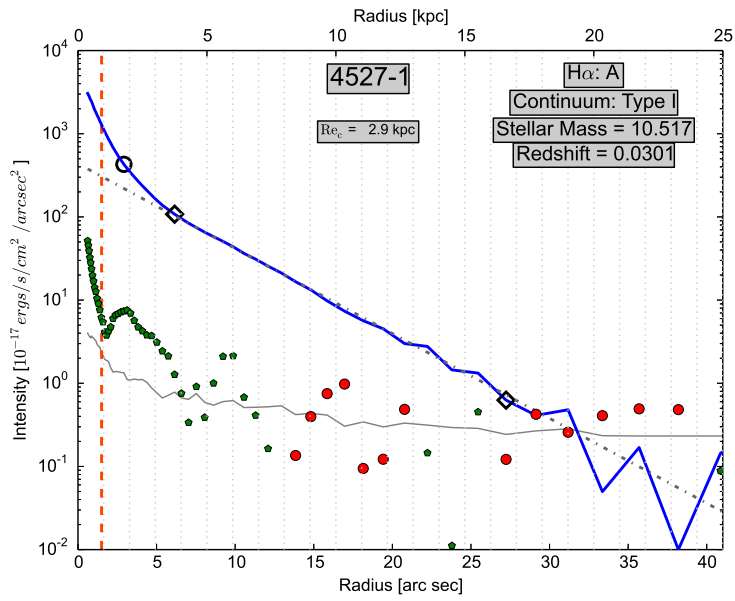
(c)



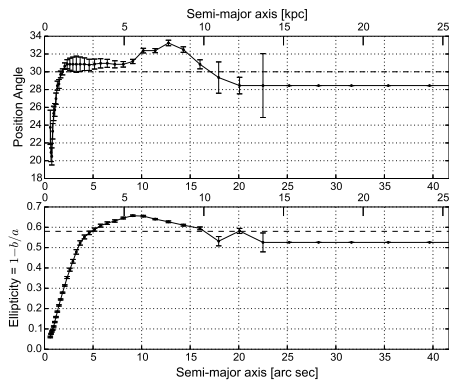
(d)



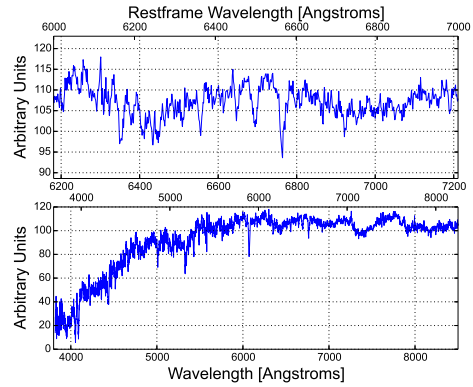
(a)



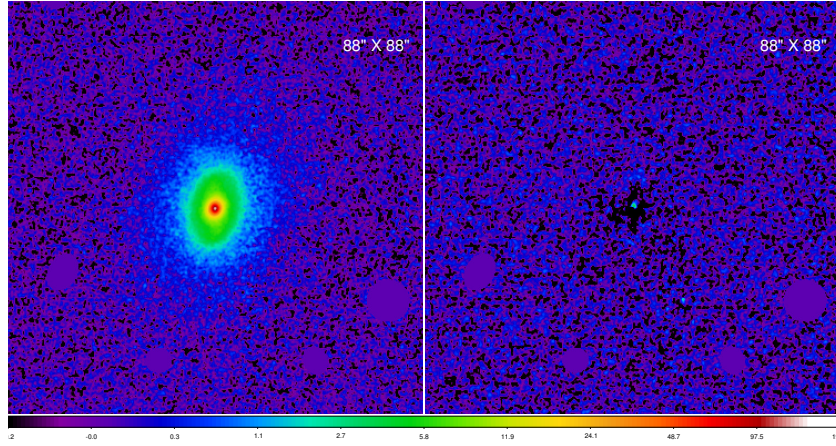
(b)



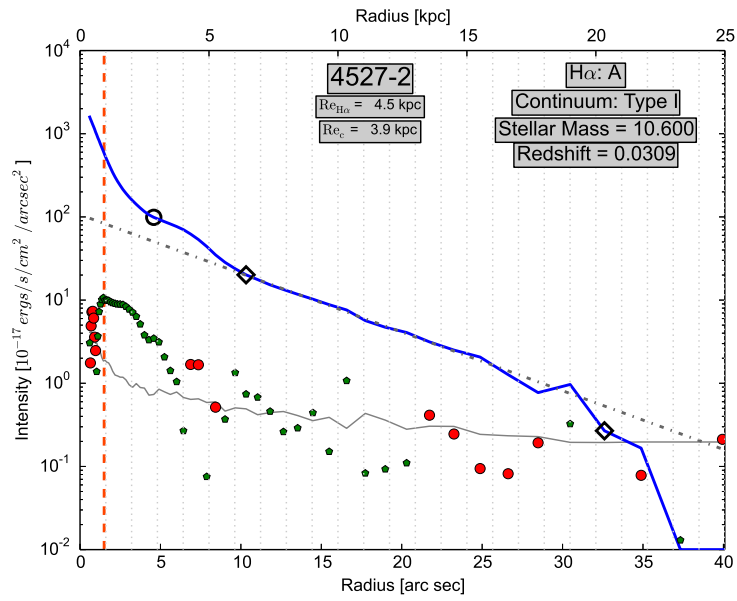
(c)



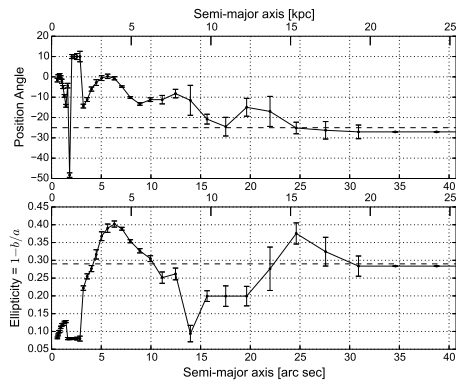
(d)



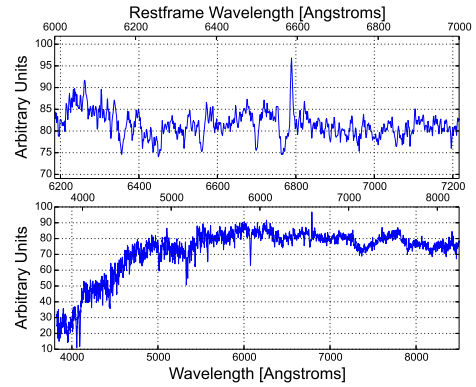
(a)



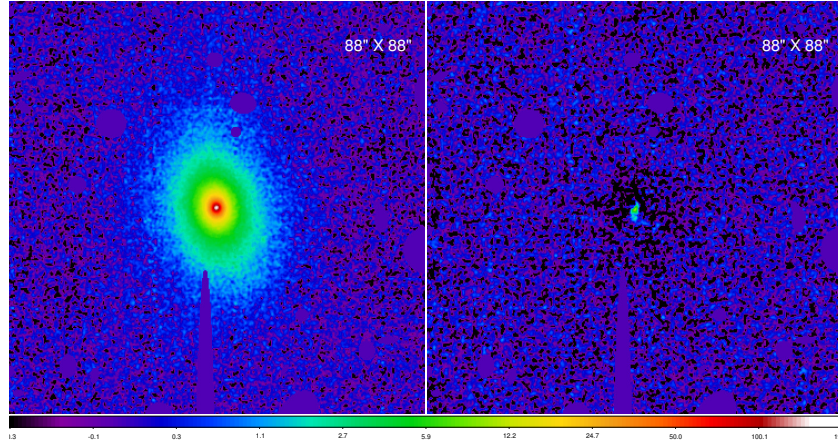
(b)



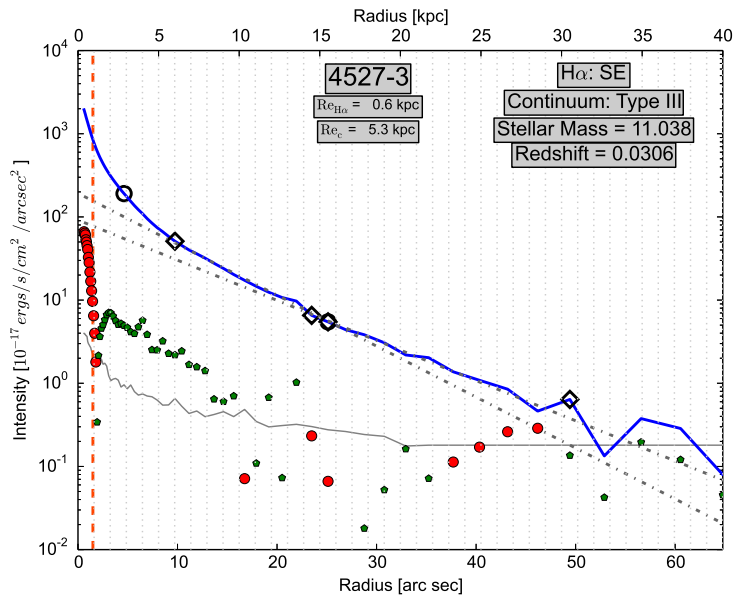
(c)



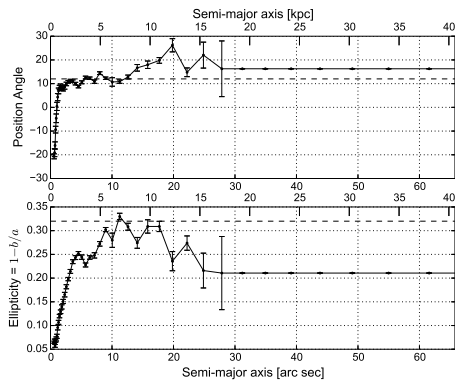
(d)



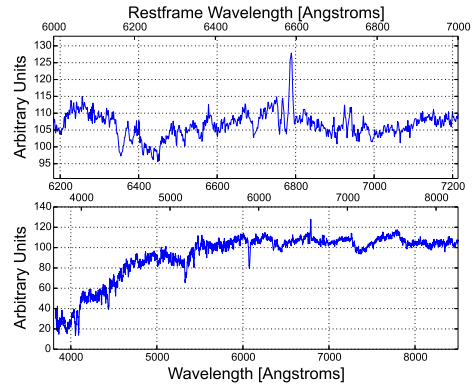
(a)



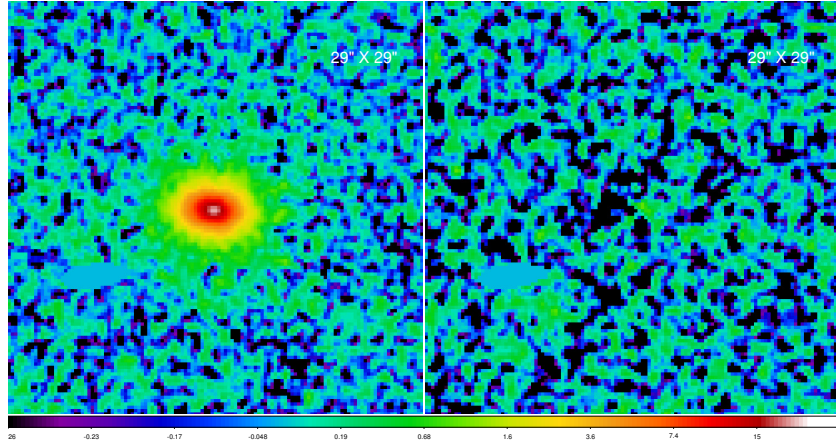
(b)



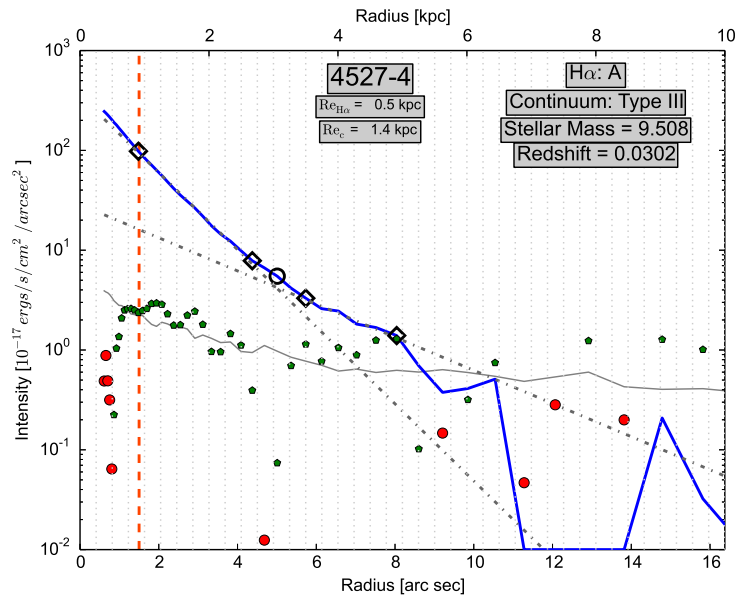
(c)



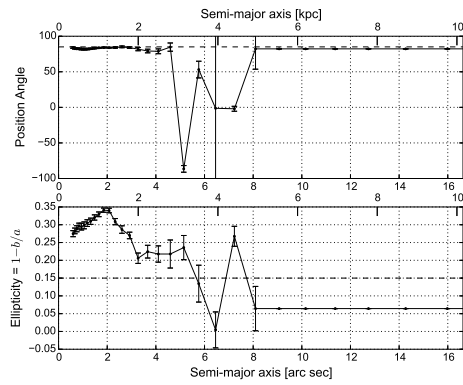
(d)



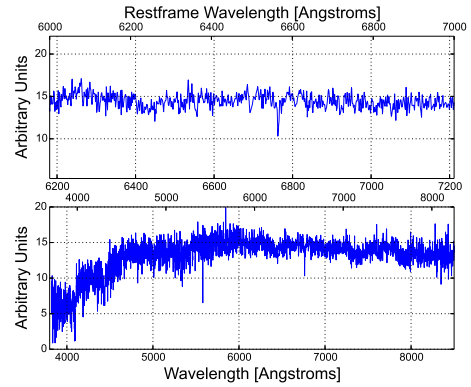
(a)



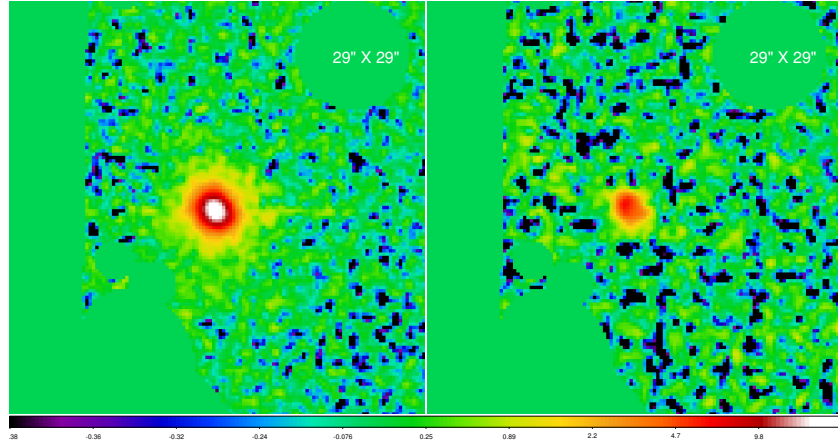
(b)



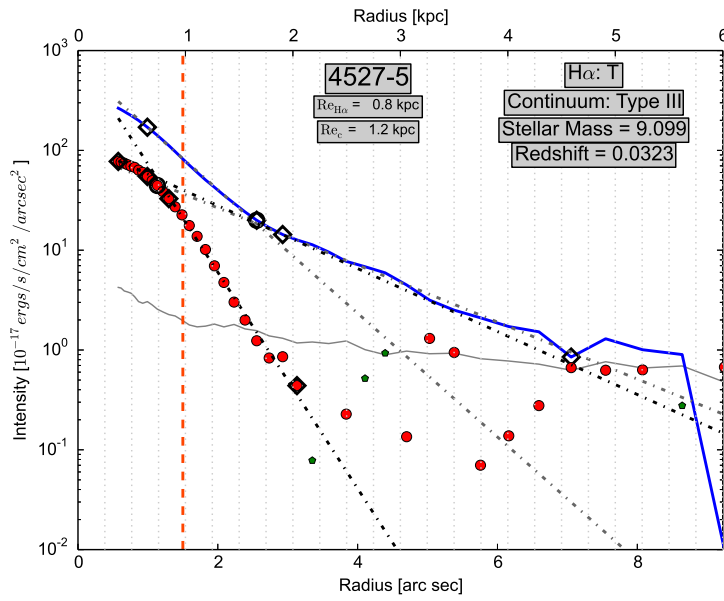
(c)



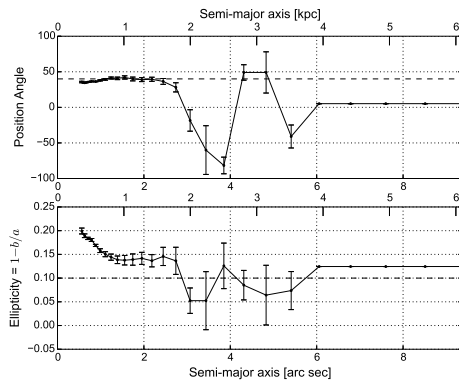
(d)



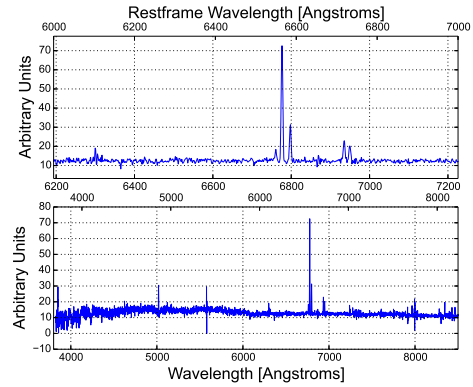
(a)



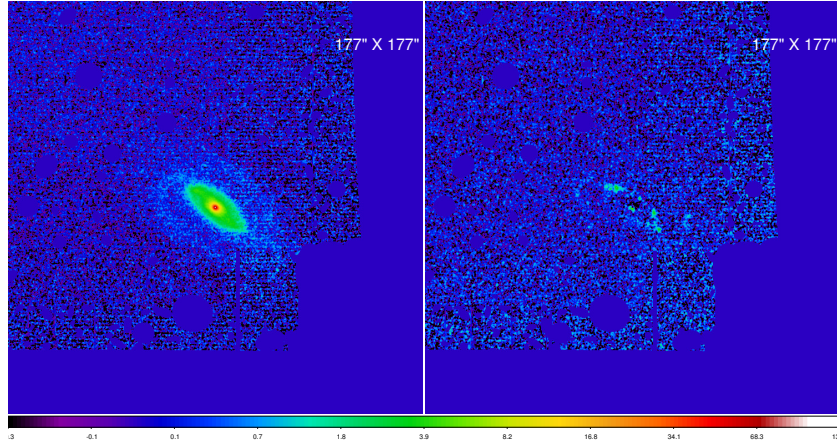
(b)



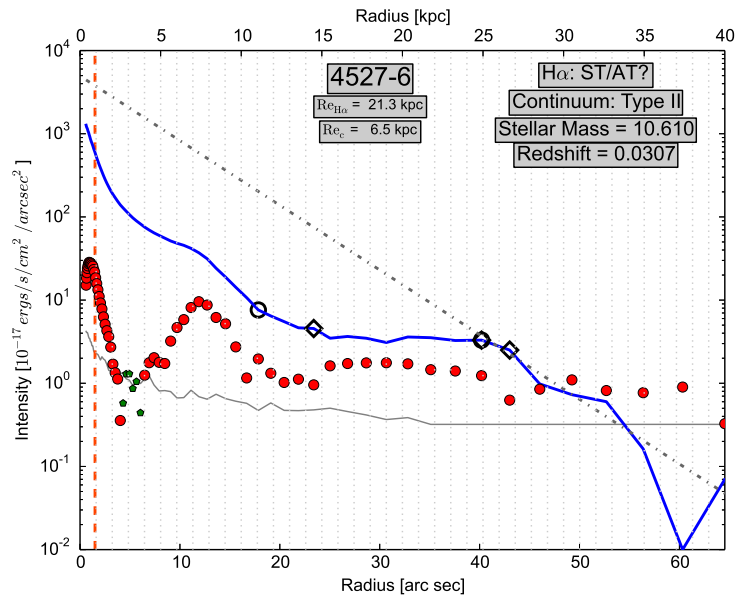
(c)



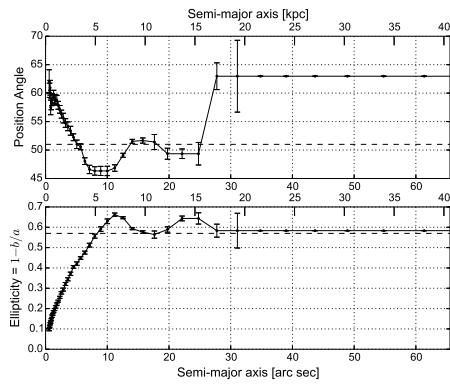
(d)



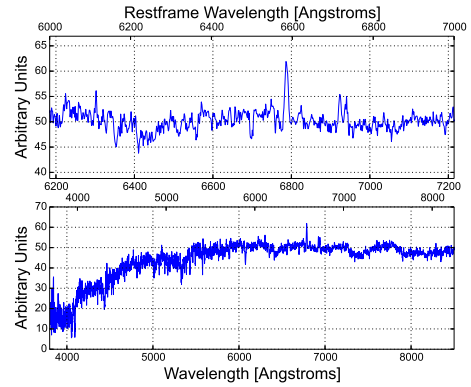
(a)



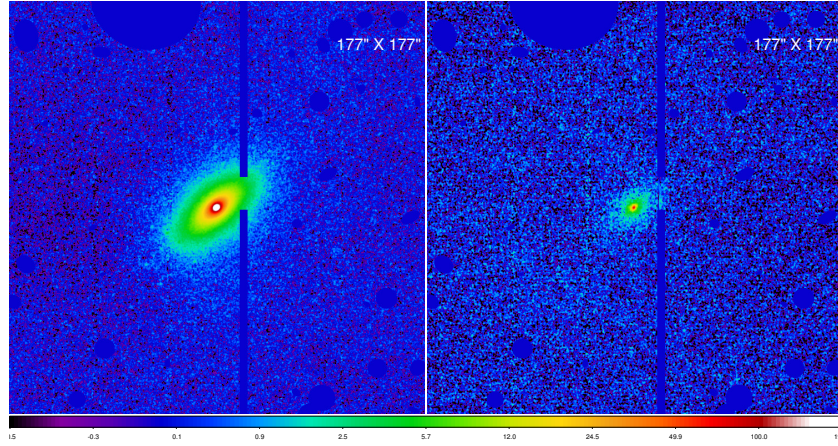
(b)



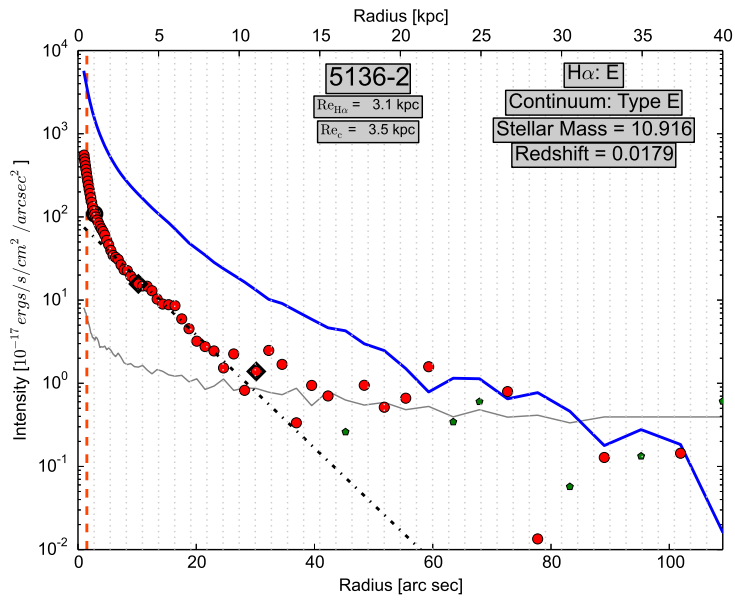
(c)



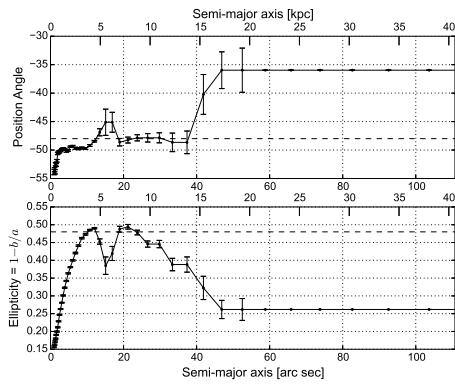
(d)



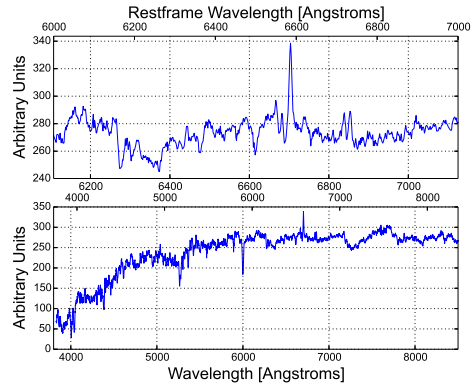
(a)



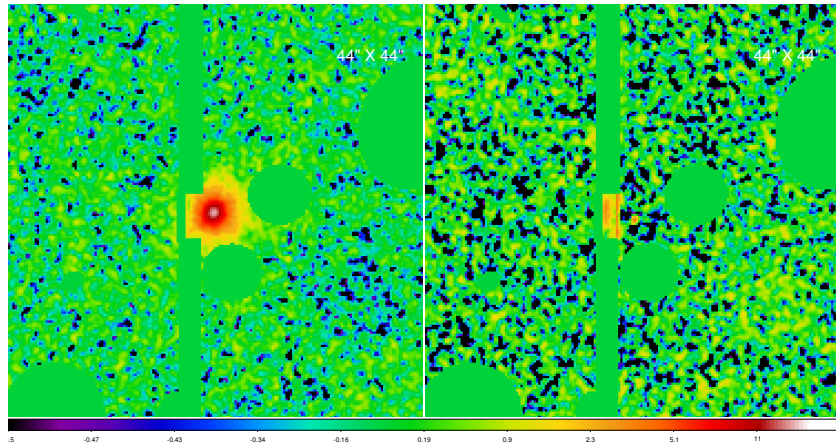
(b)



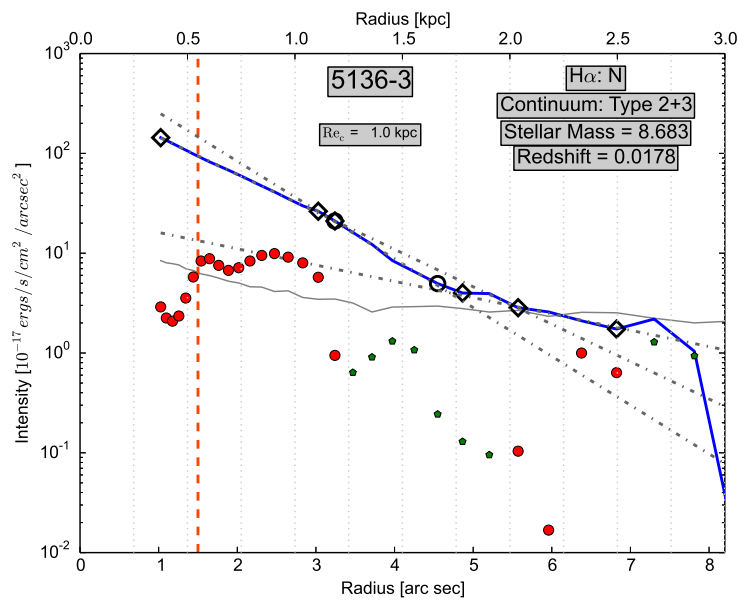
(c)



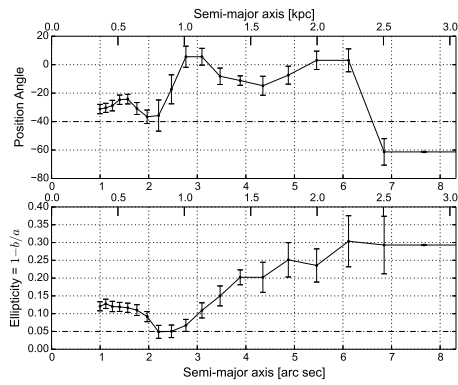
(d)



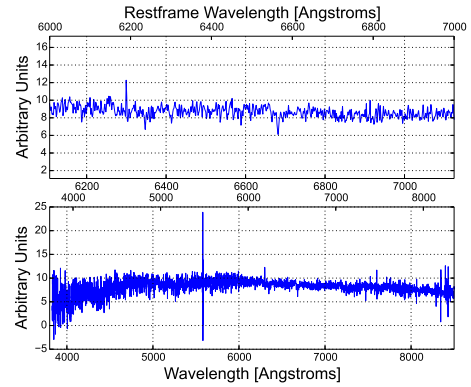
(a)



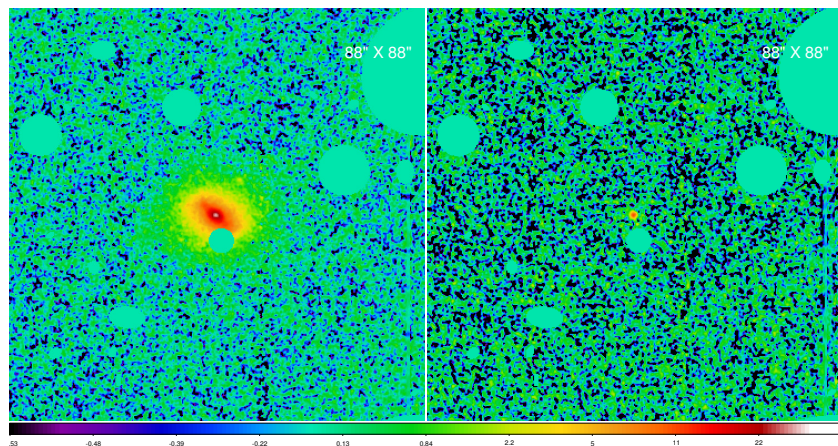
(b)



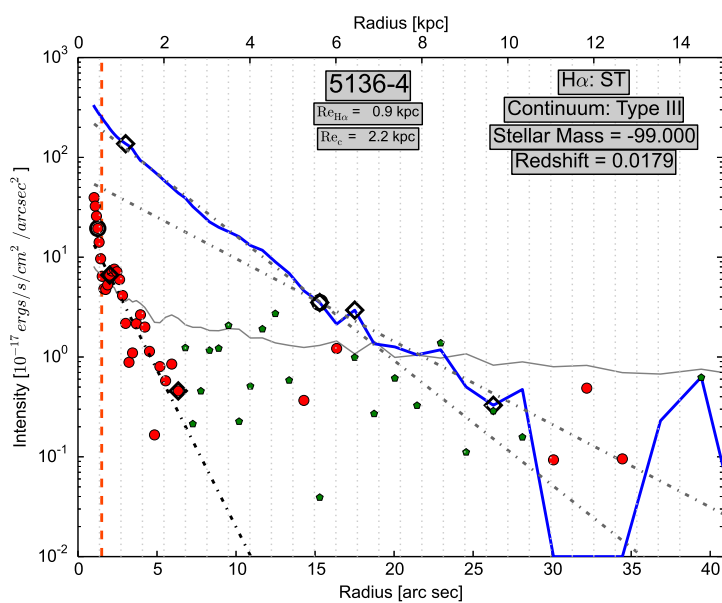
(c)



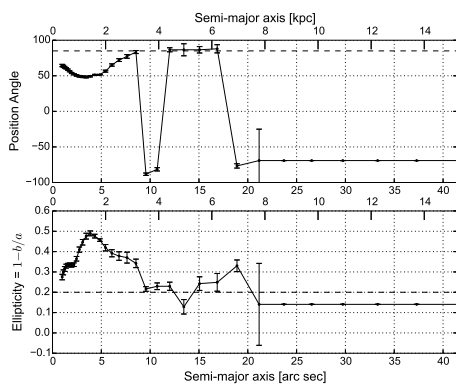
(d)



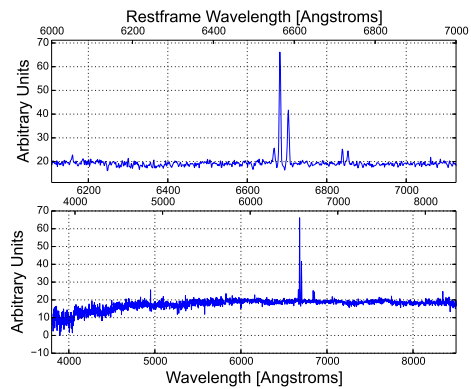
(a)



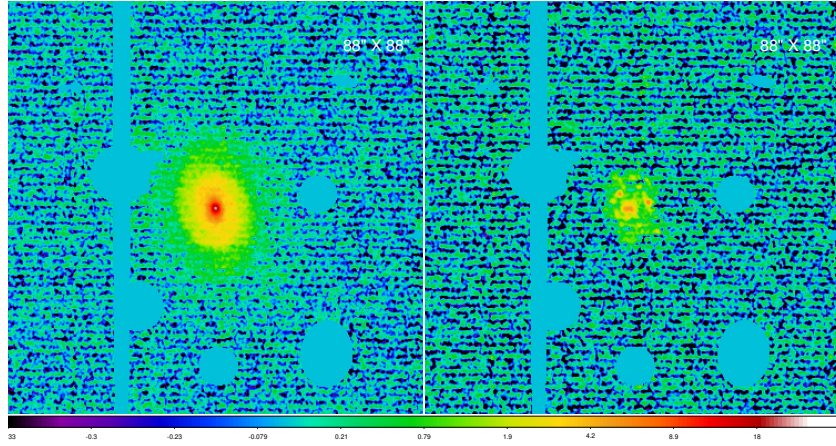
(b)



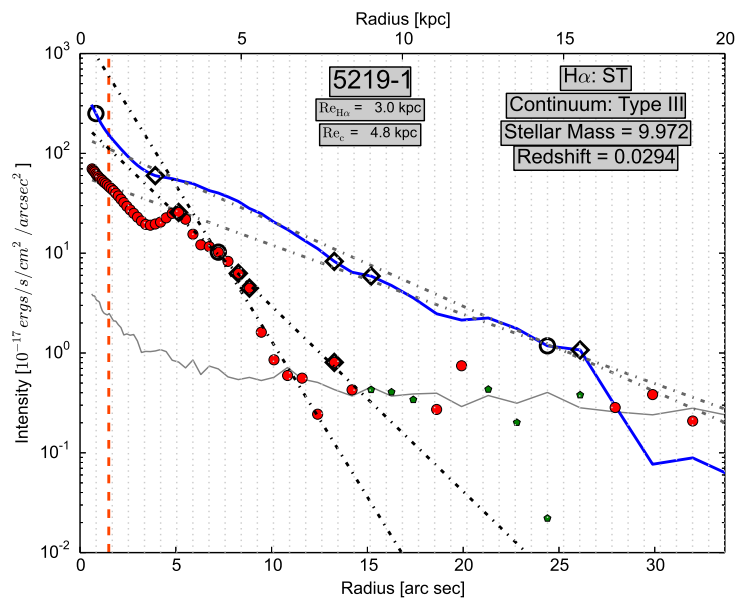
(c)



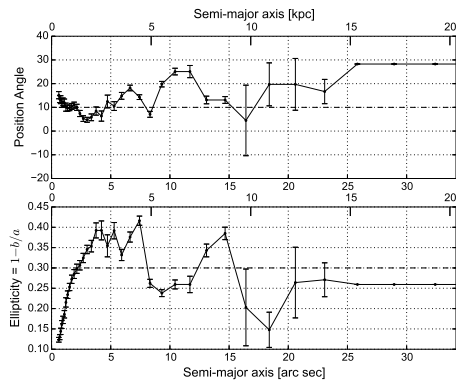
(d)



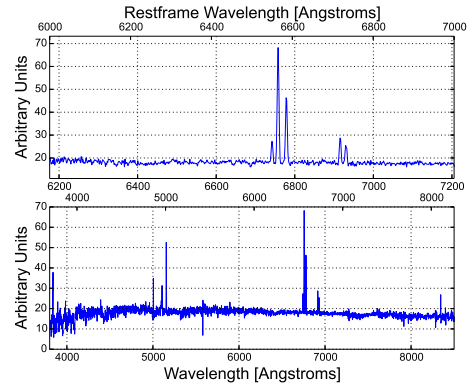
(a)



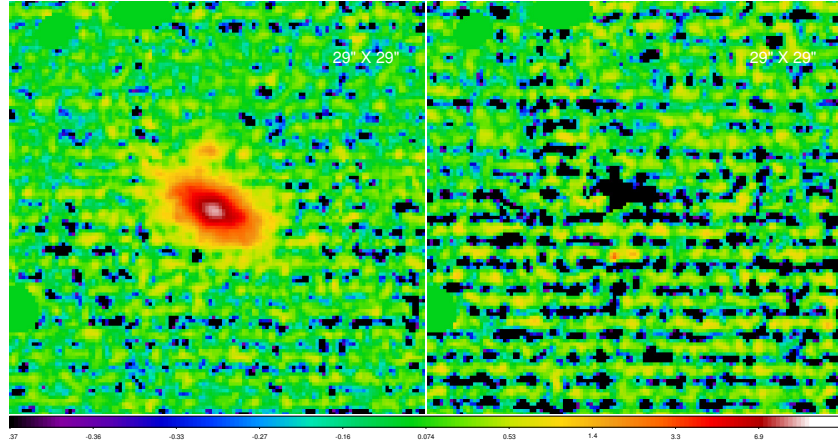
(b)



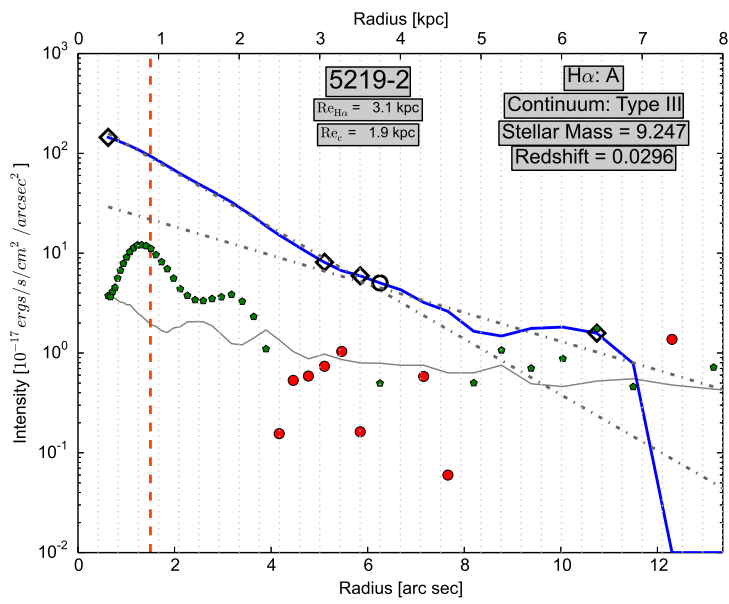
(c)



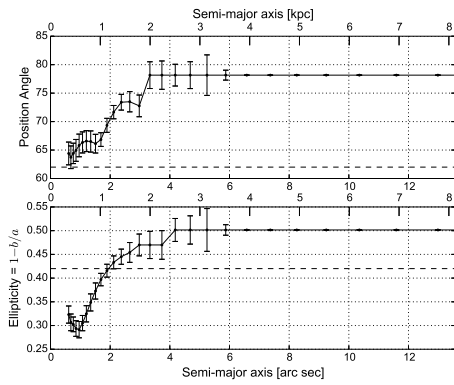
(d)



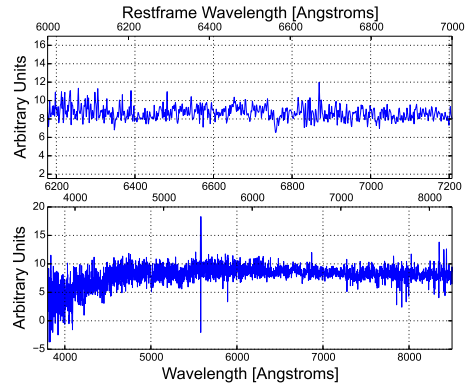
(a)



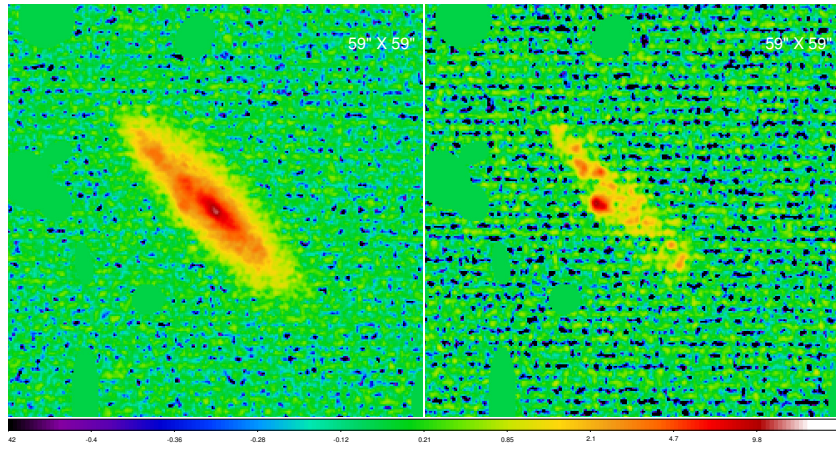
(b)



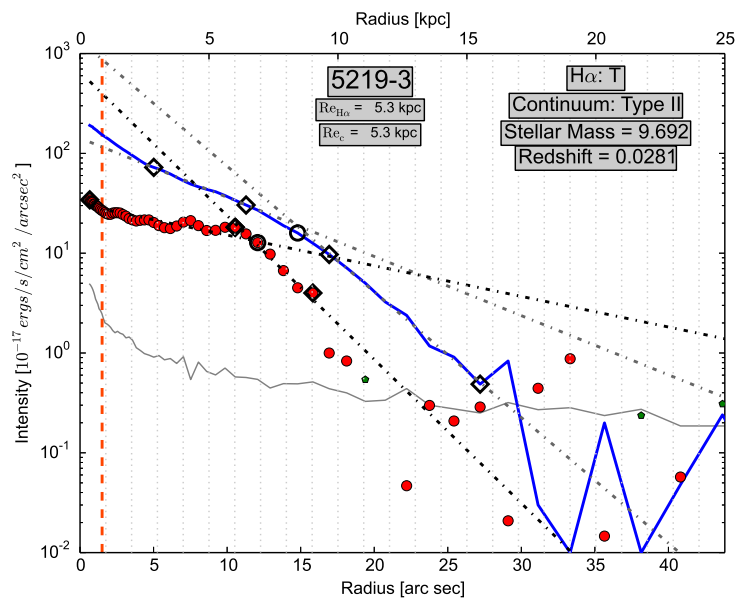
(c)



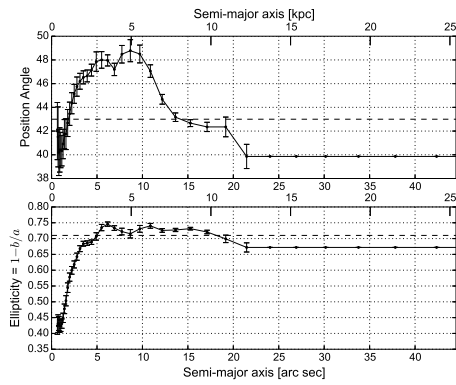
(d)



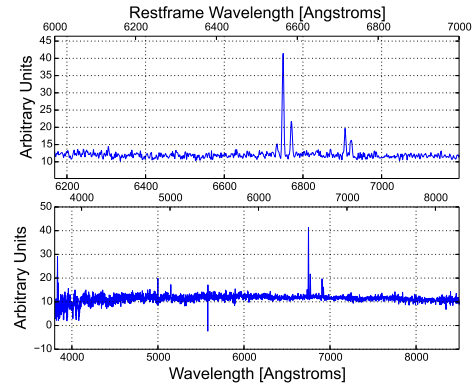
(a)



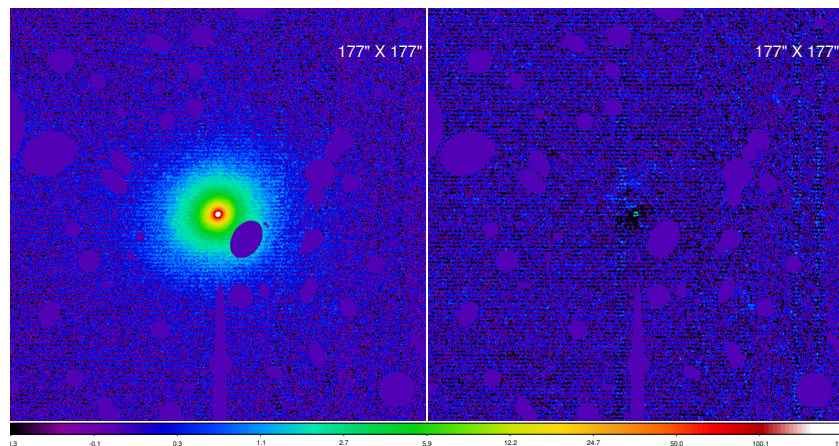
(b)



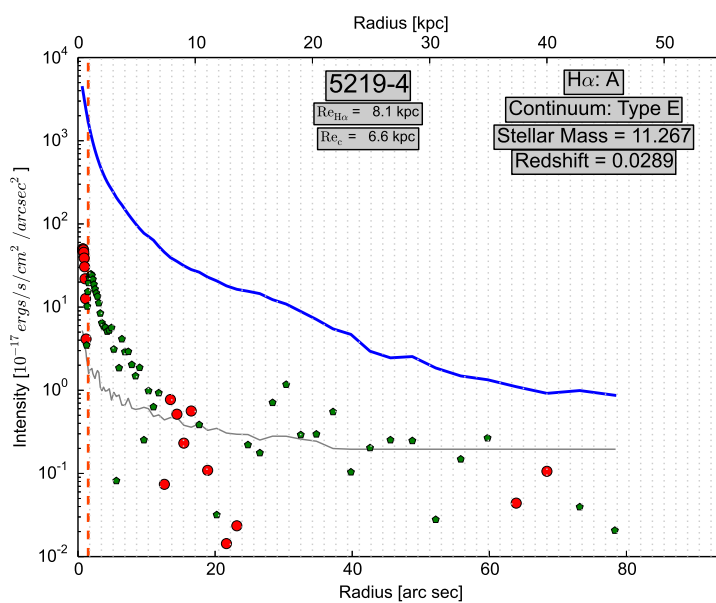
(c)



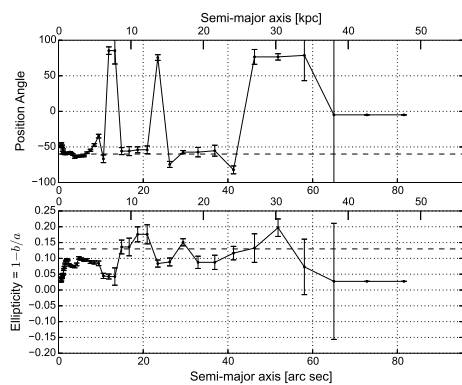
(d)



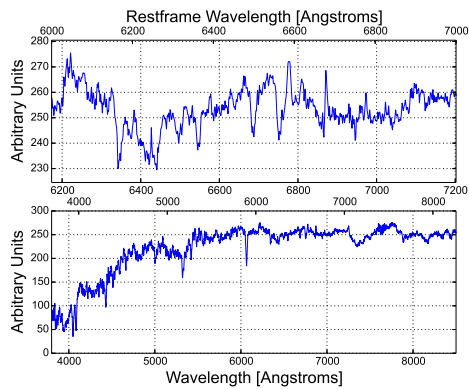
(a)



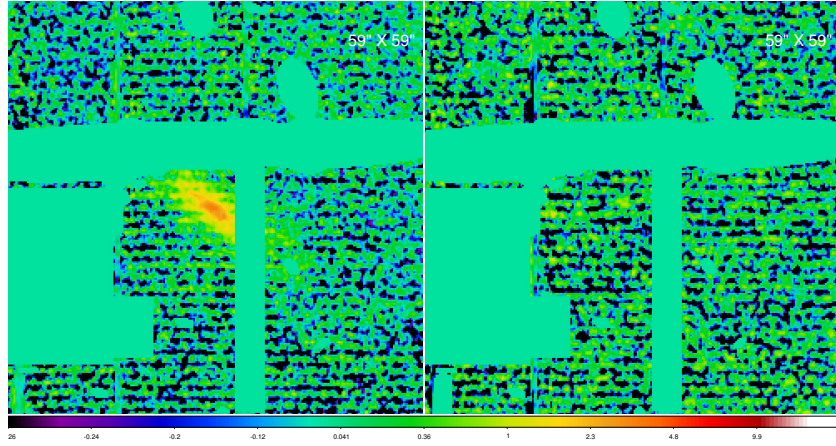
(b)



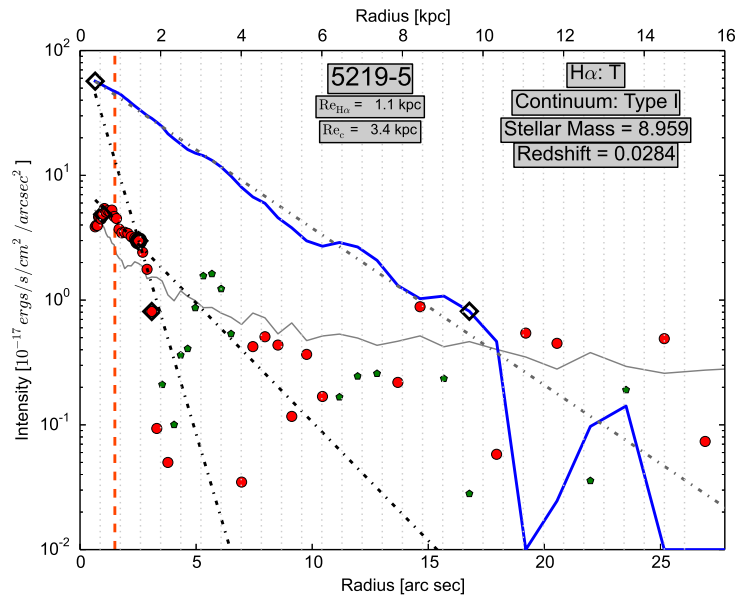
(c)



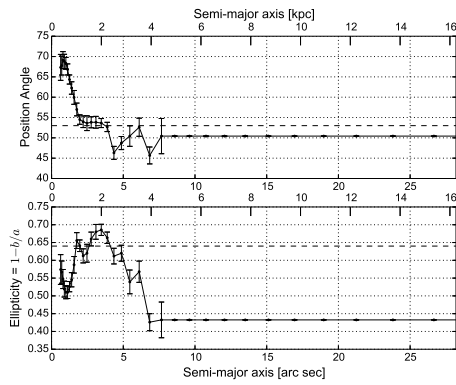
(d)



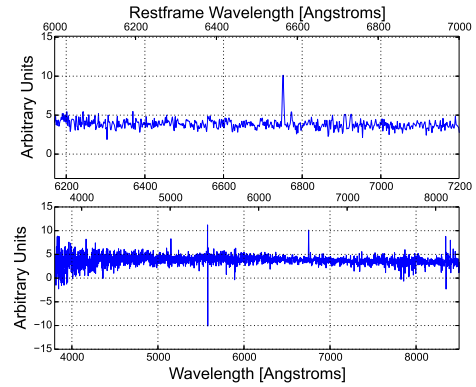
(a)



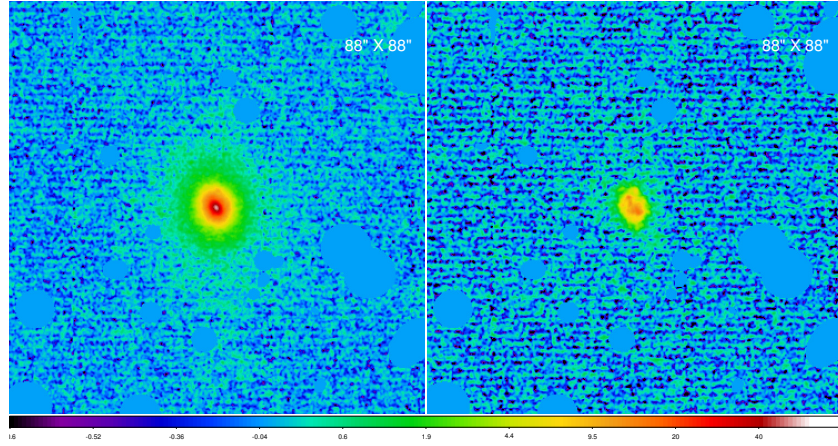
(b)



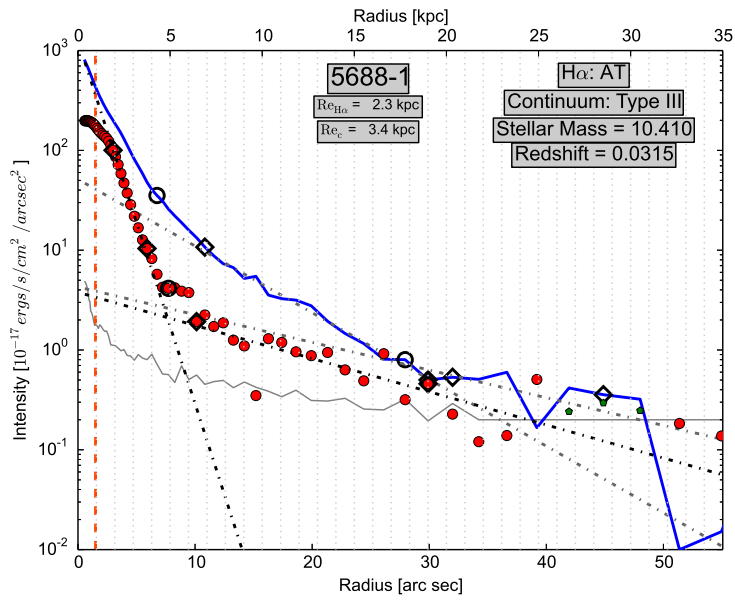
(c)



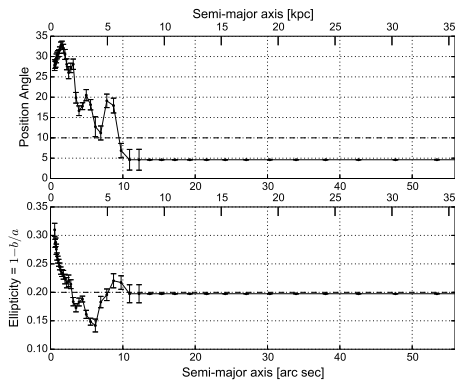
(d)



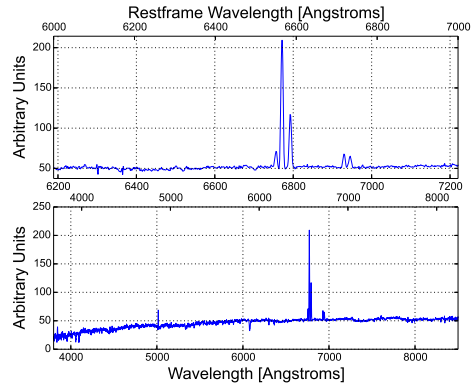
(a)



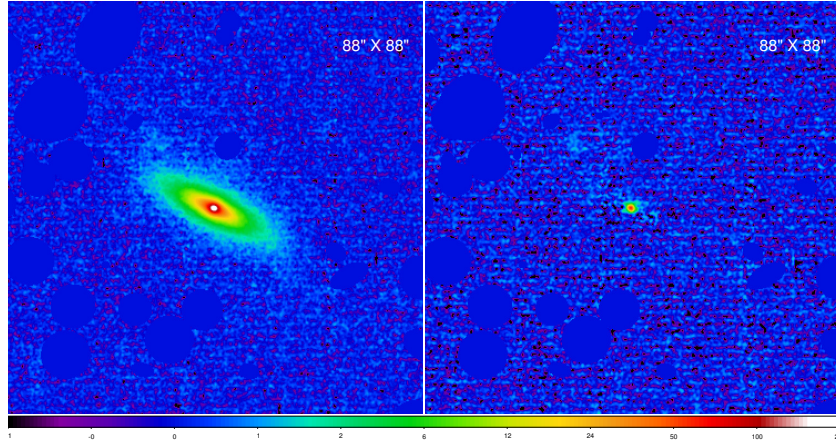
(b)



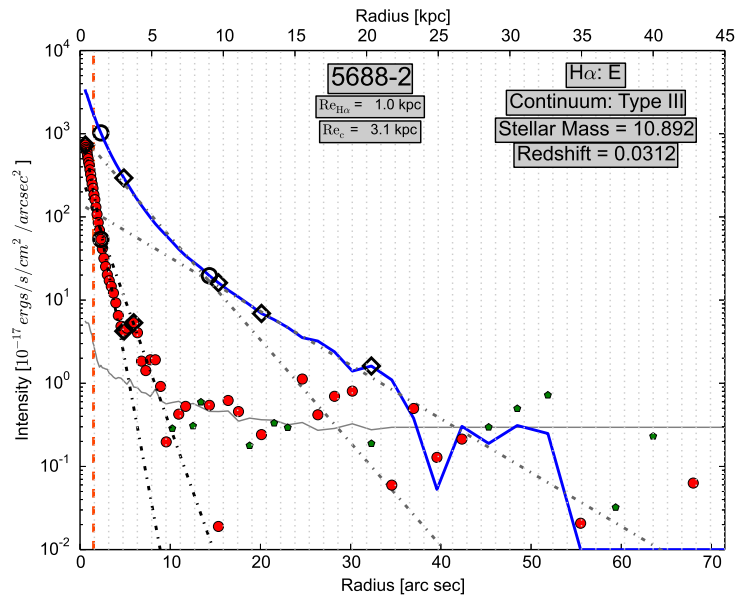
(c)



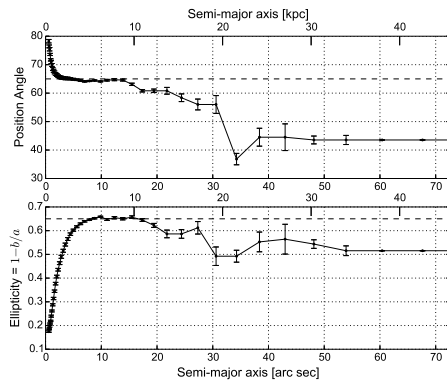
(d)



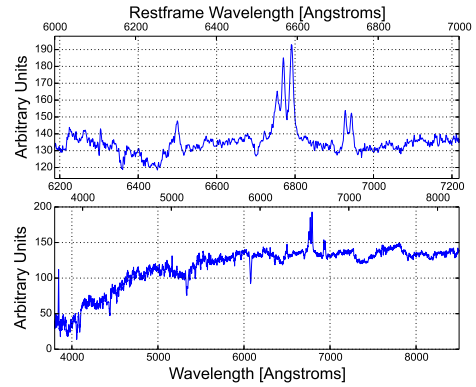
(a)



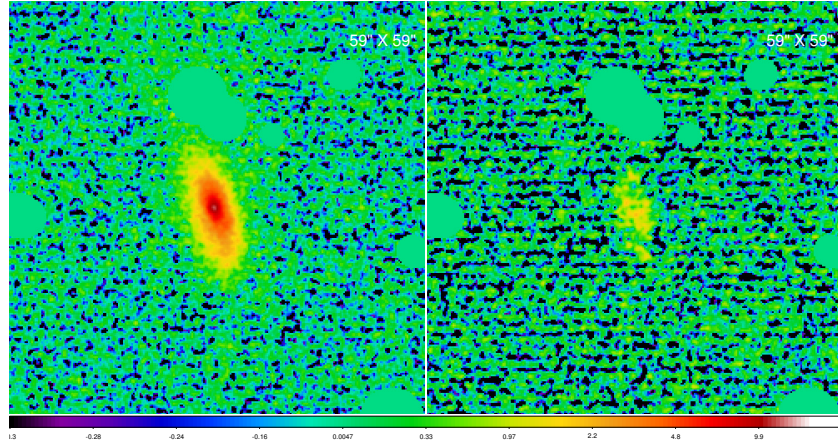
(b)



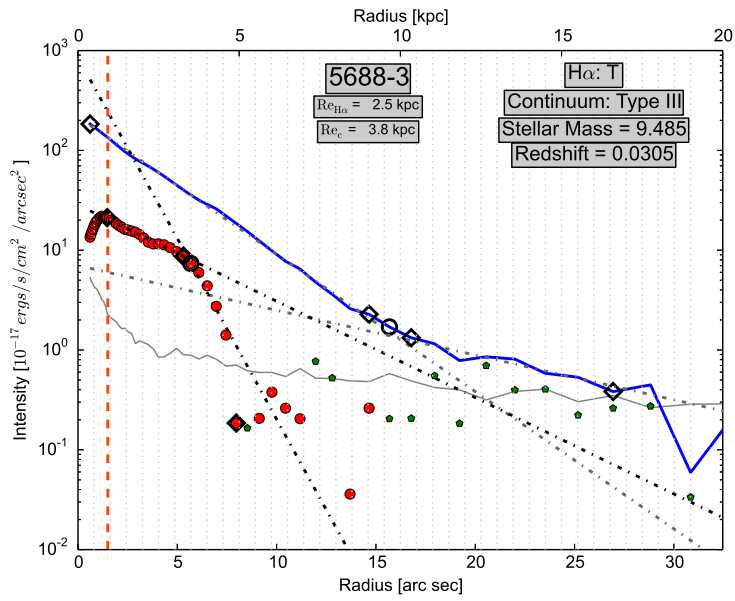
(c)



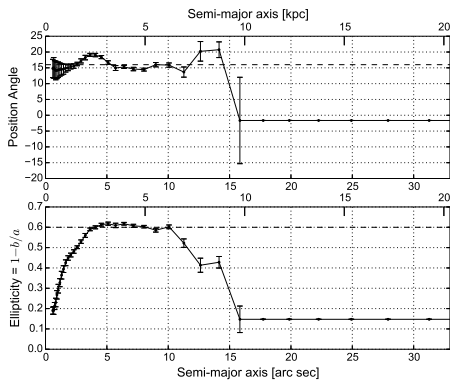
(d)



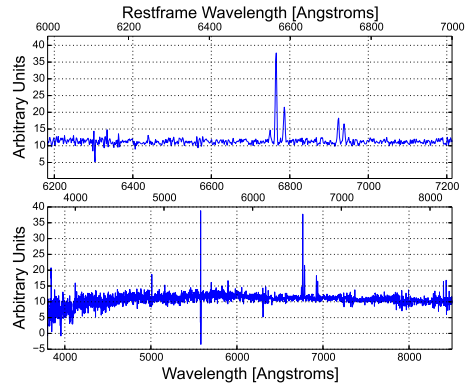
(a)



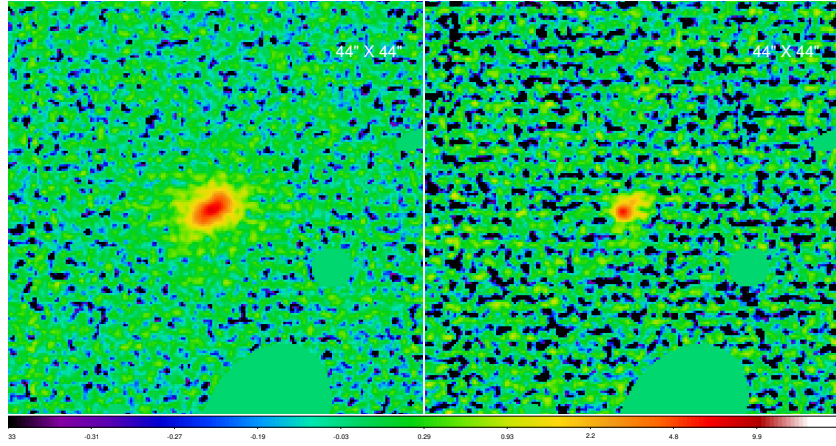
(b)



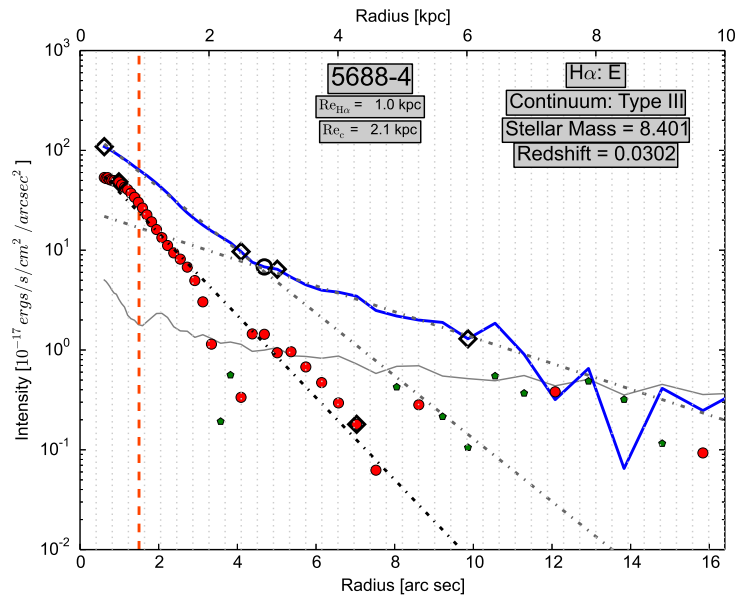
(c)



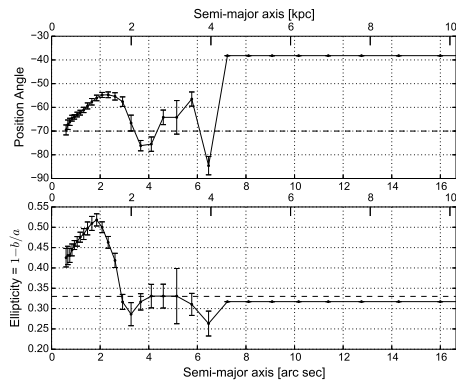
(d)



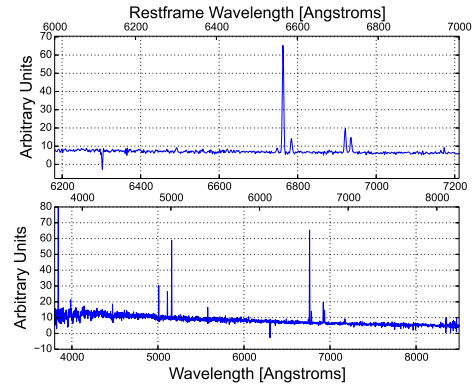
(a)



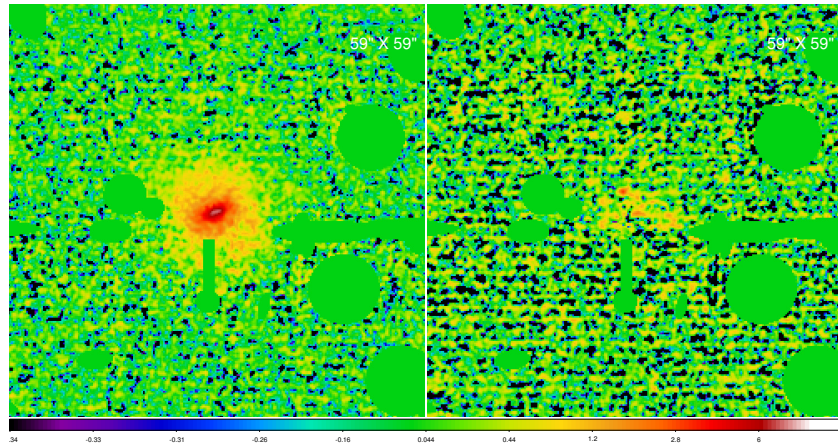
(b)



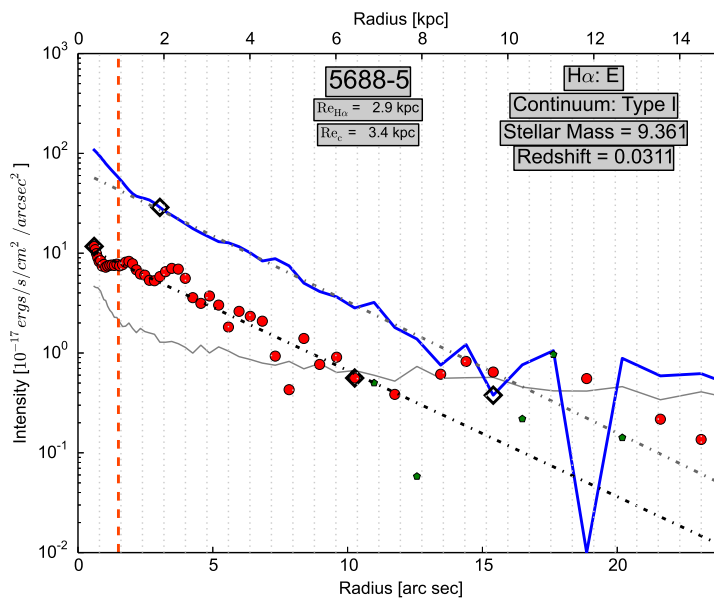
(c)



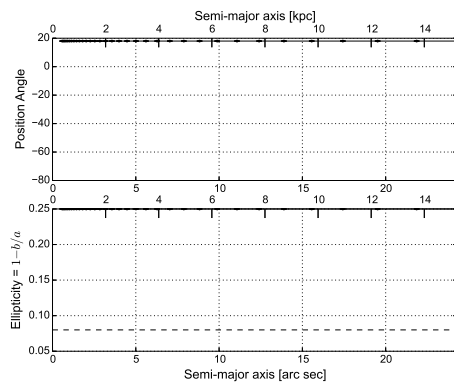
(d)



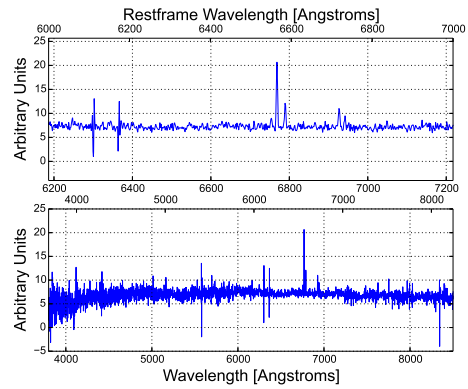
(a)



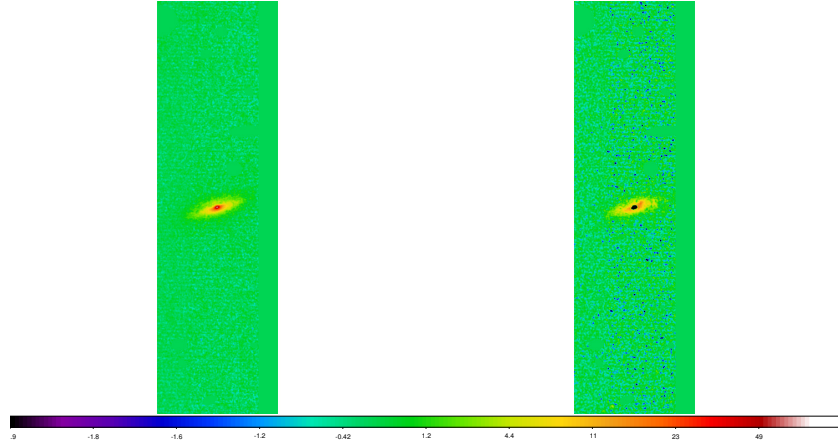
(b)



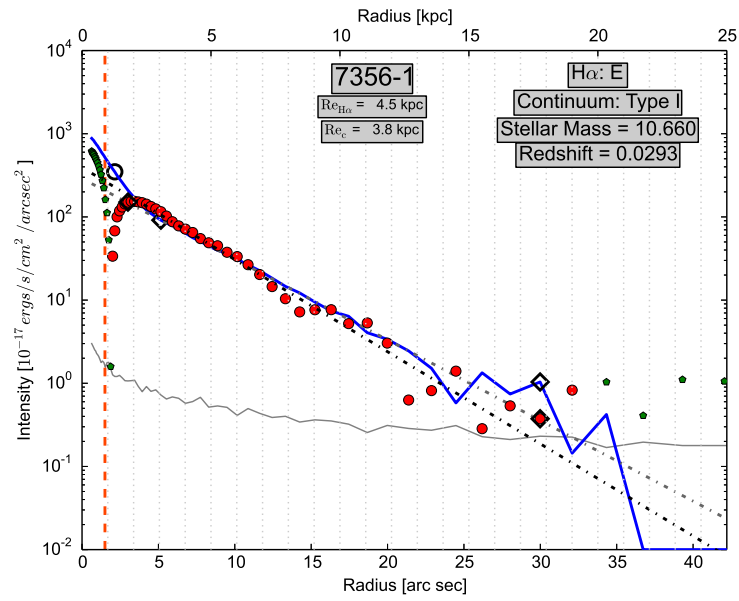
(c)



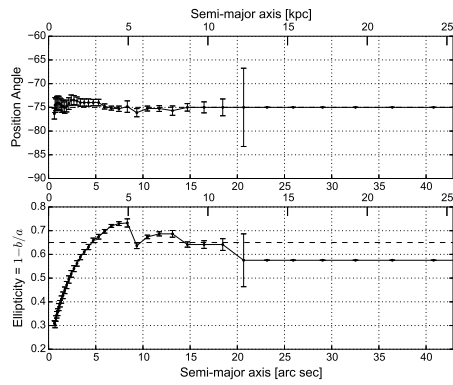
(d)



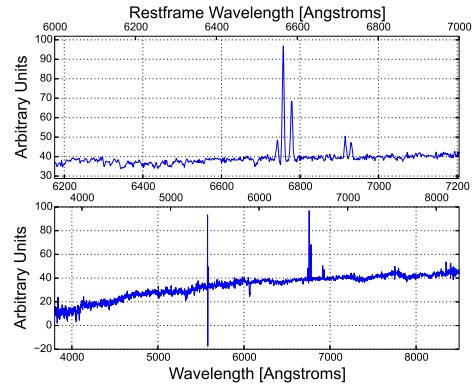
(a)



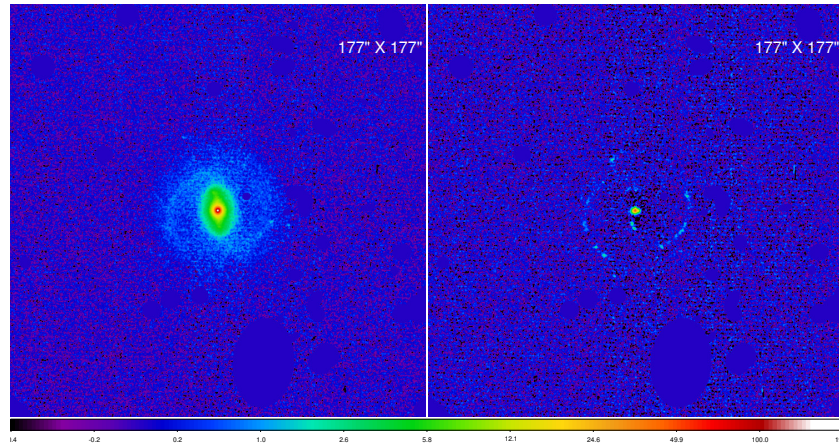
(b)



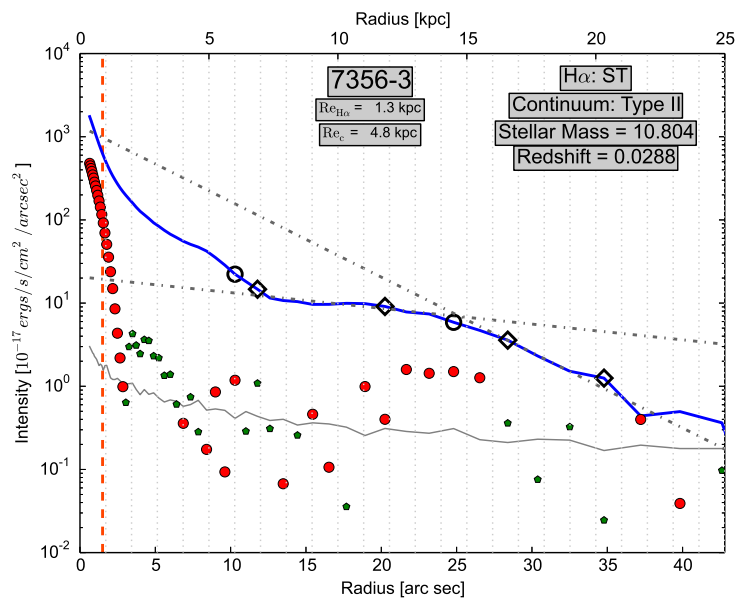
(c)



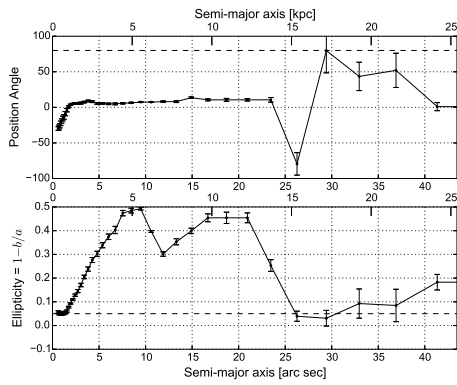
(d)



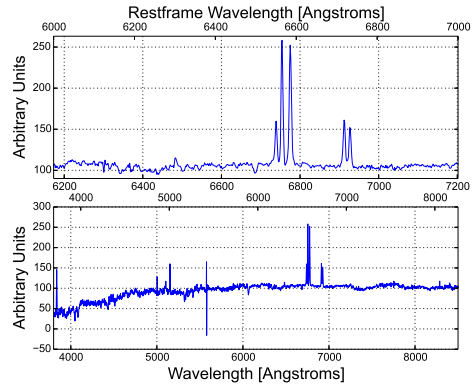
(a)



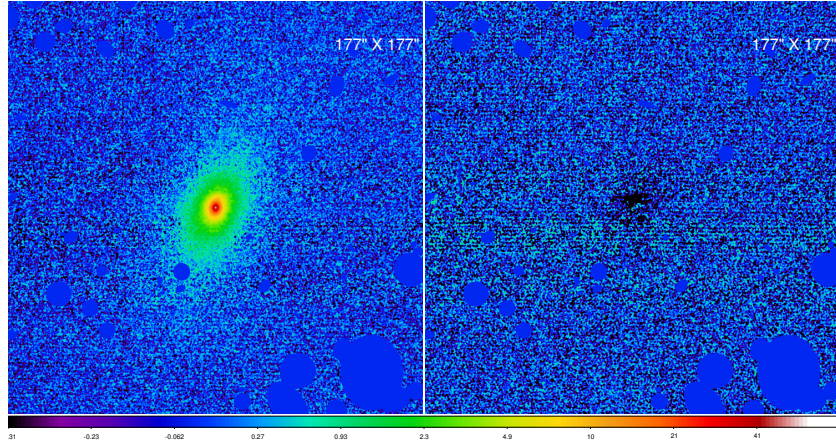
(b)



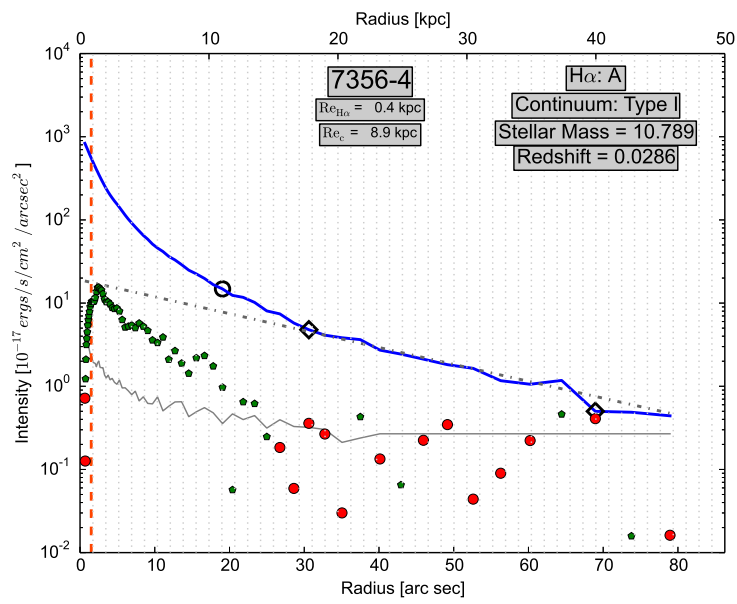
(c)



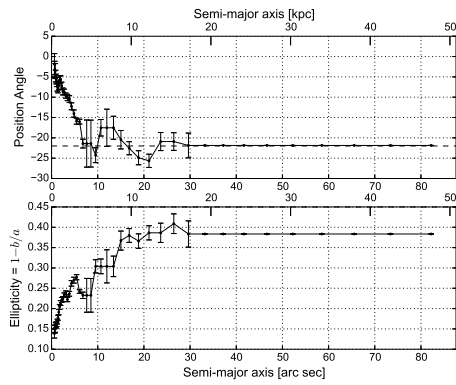
(d)



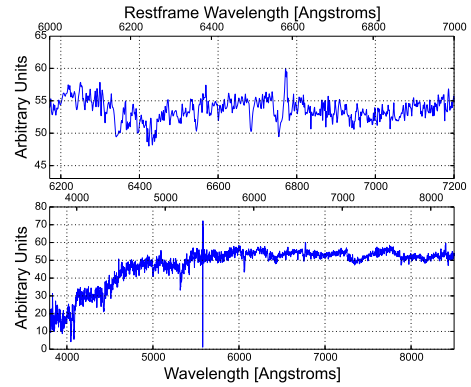
(a)



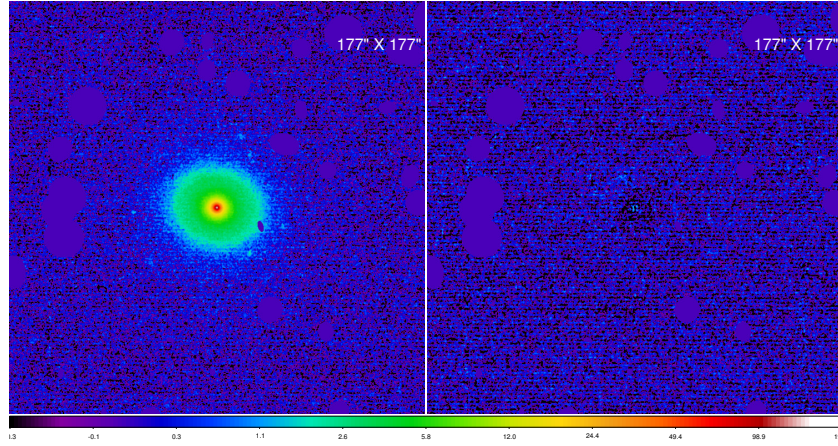
(b)



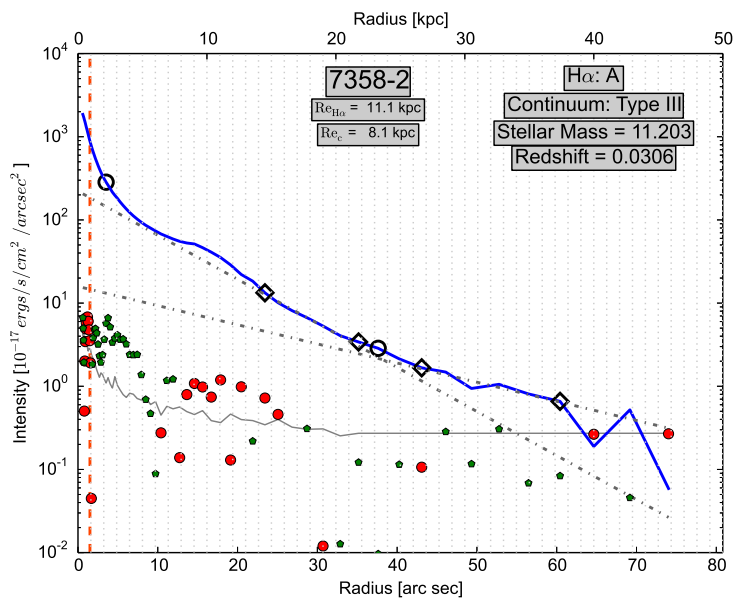
(c)



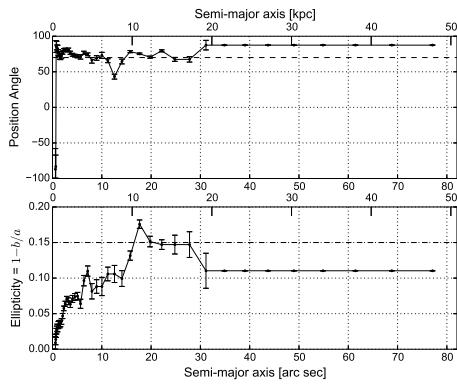
(d)



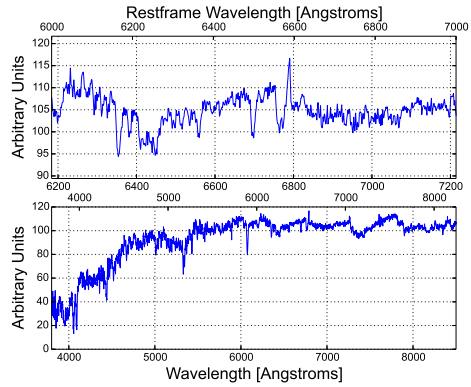
(a)



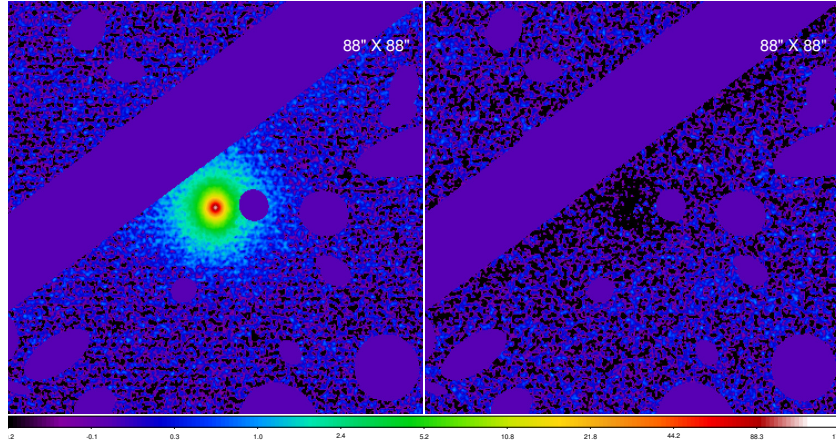
(b)



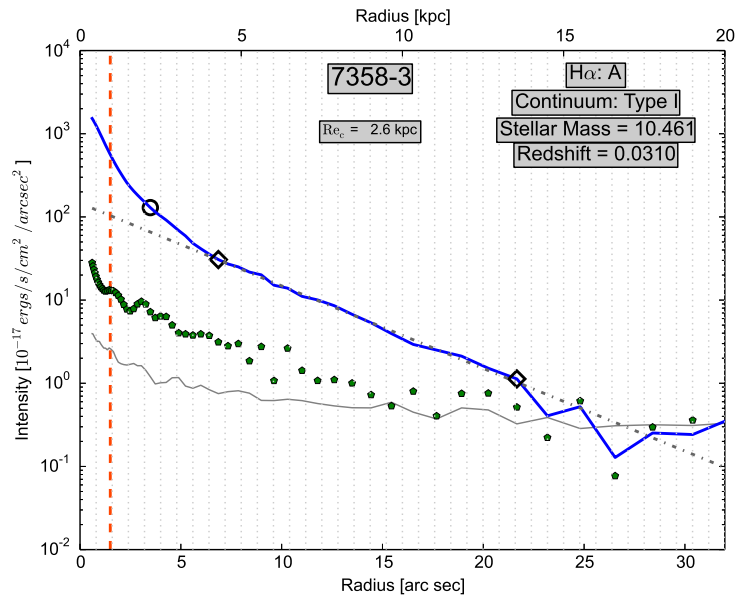
(c)



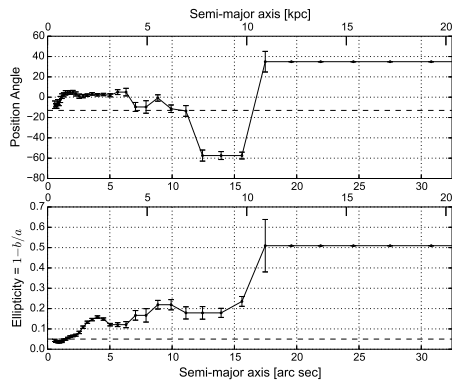
(d)



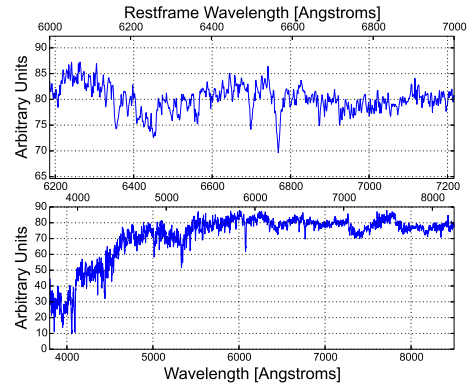
(a)



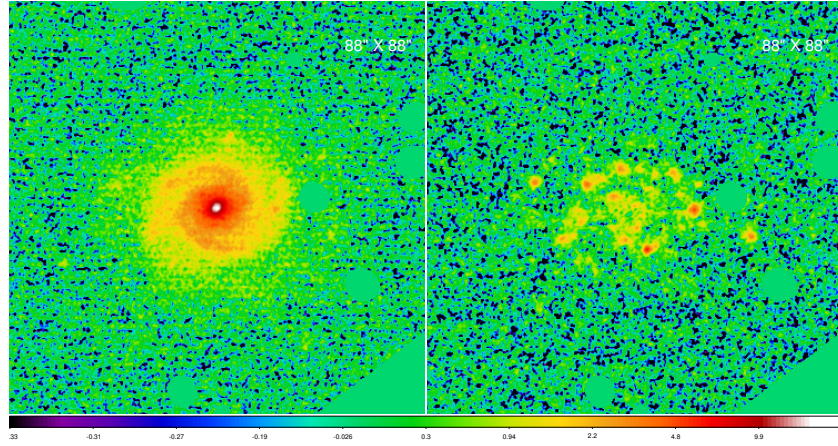
(b)



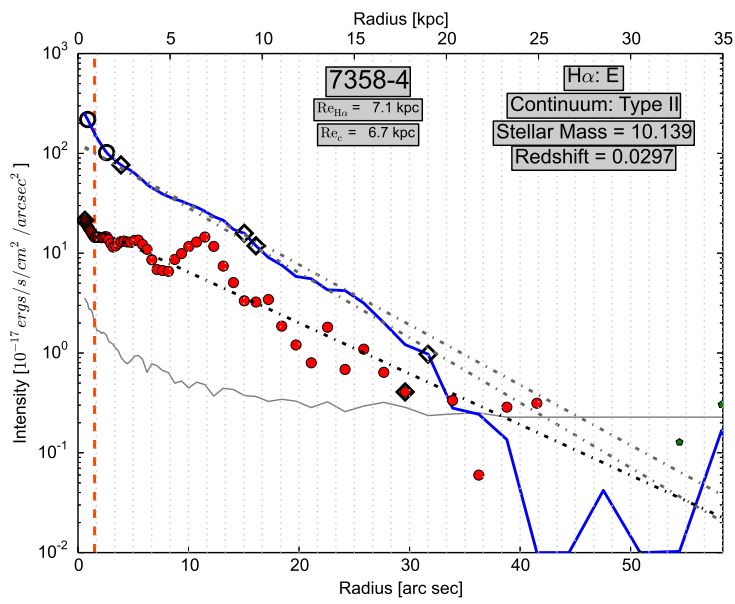
(c)



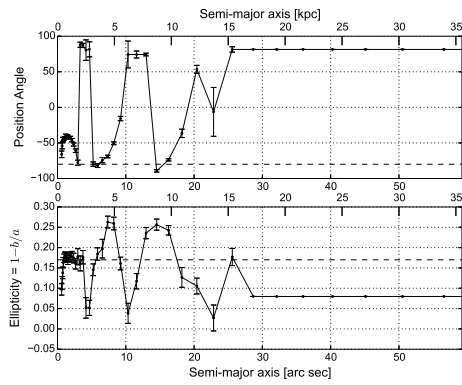
(d)



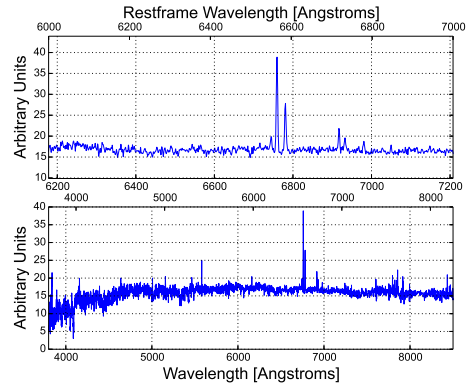
(a)



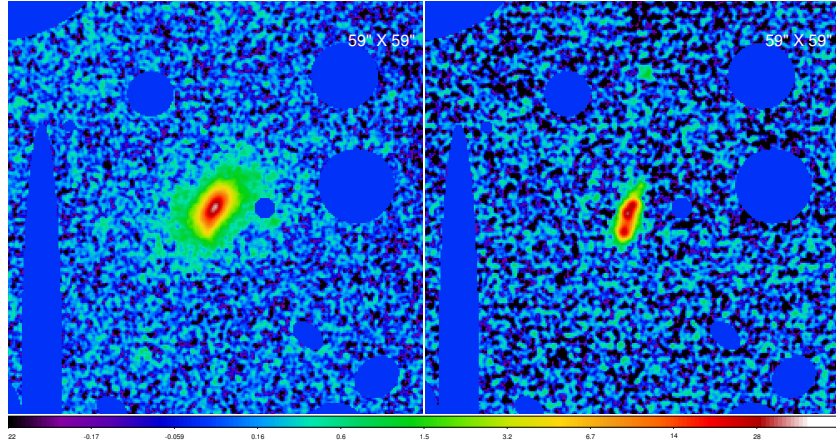
(b)



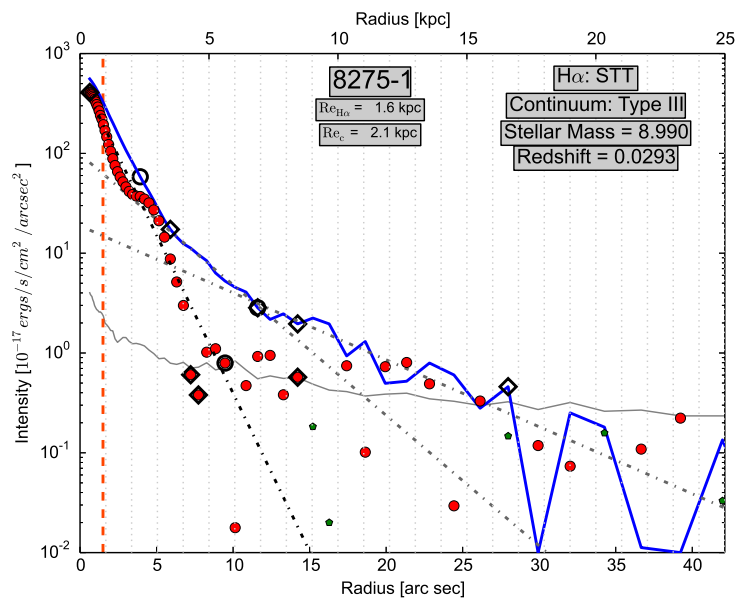
(c)



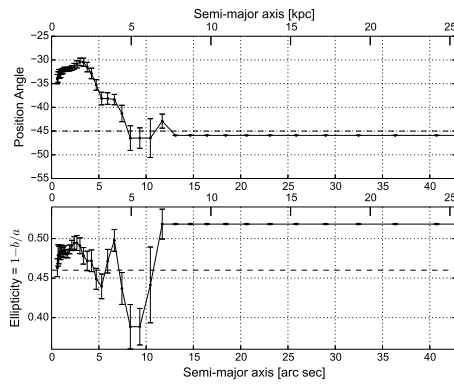
(d)



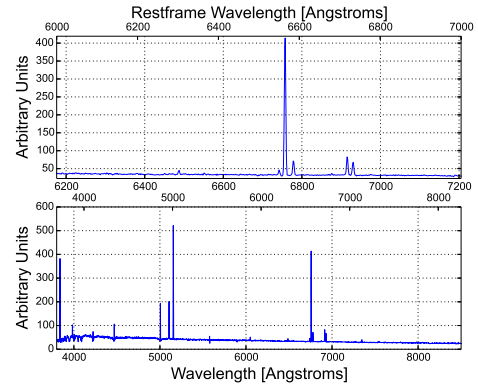
(a)



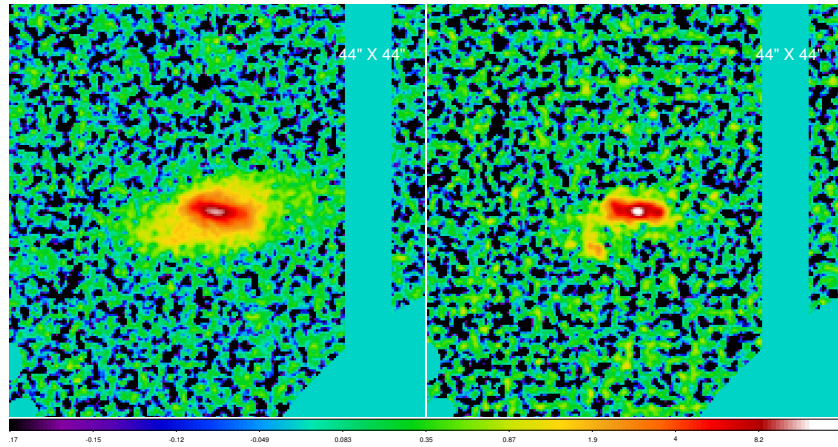
(b)



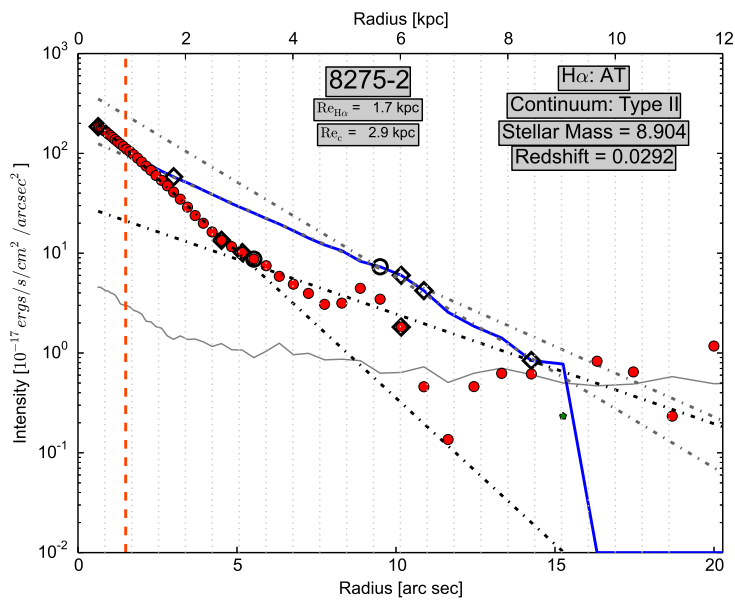
(c)



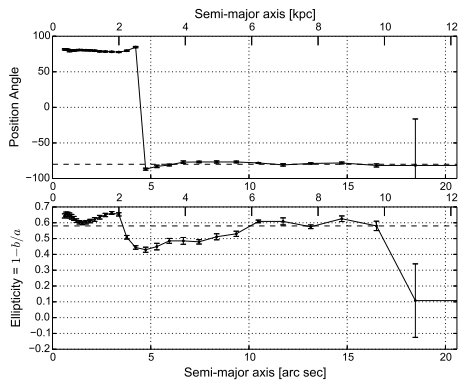
(d)



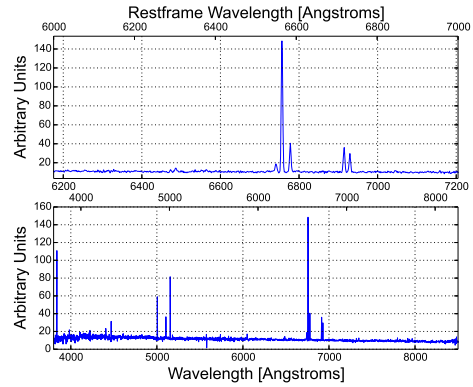
(a)



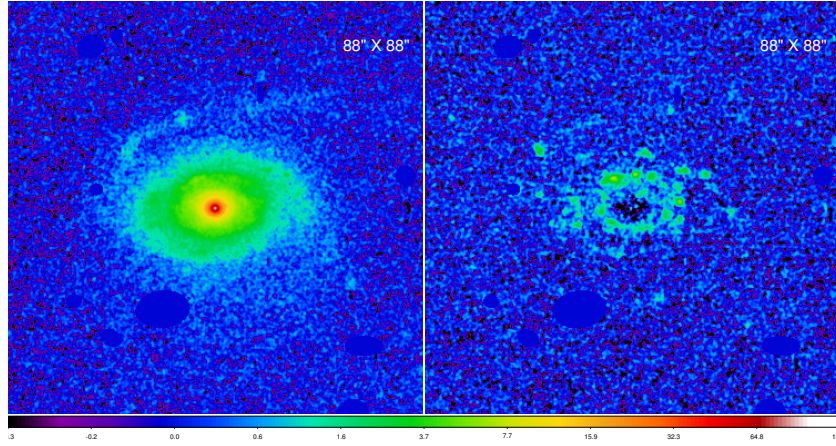
(b)



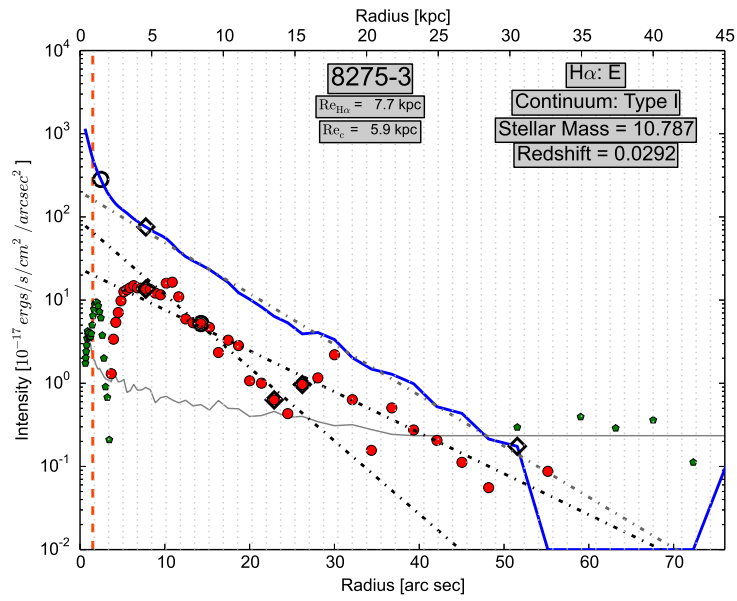
(c)



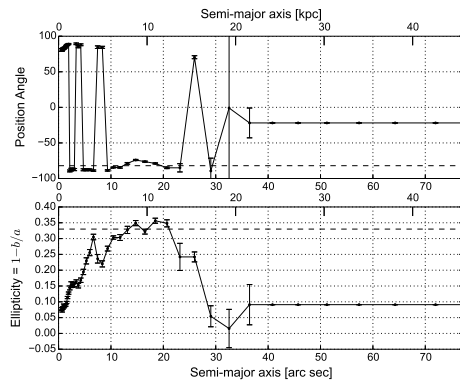
(d)



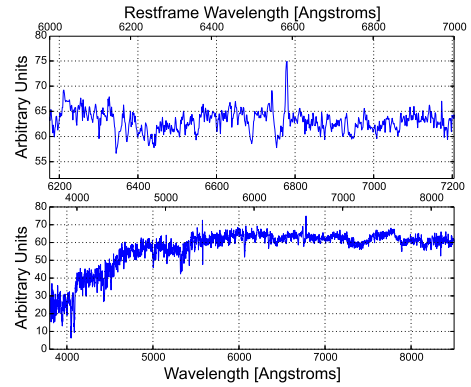
(a)



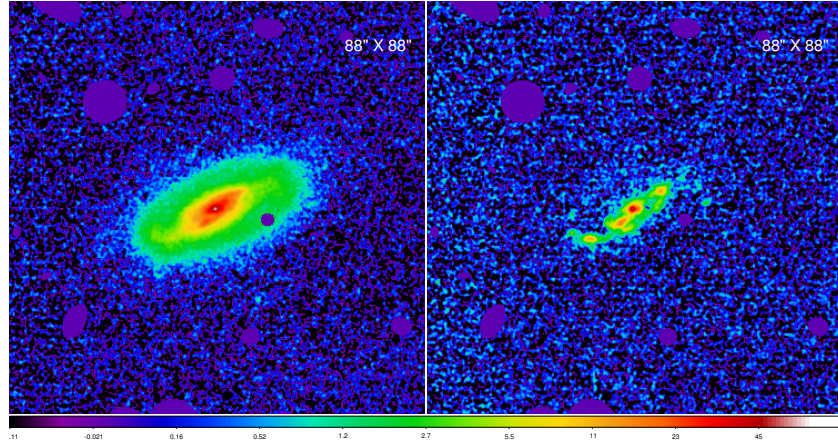
(b)



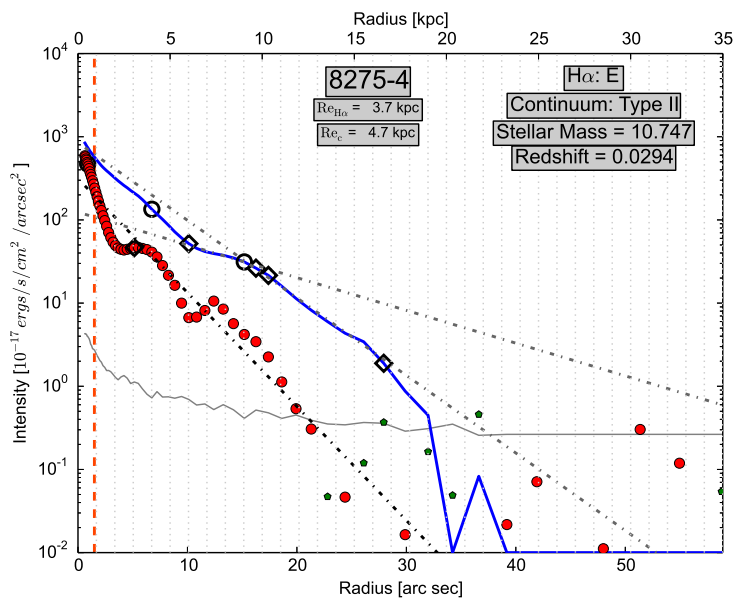
(c)



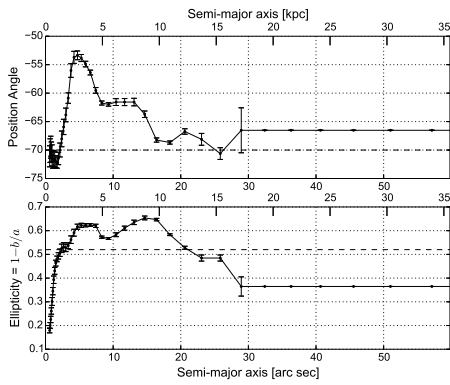
(d)



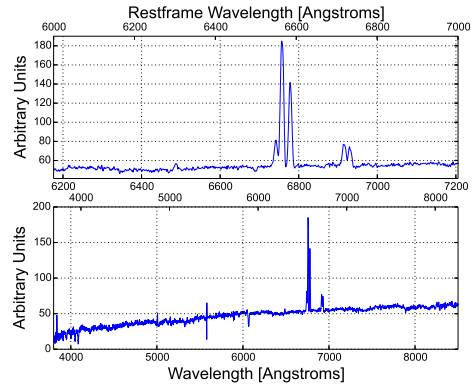
(a)



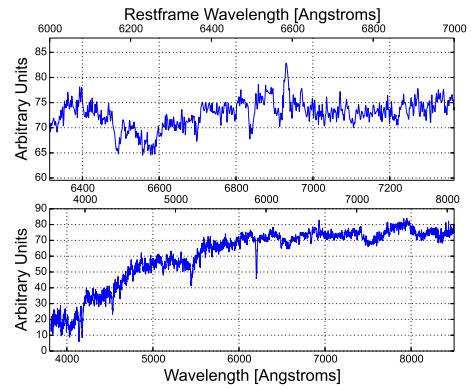
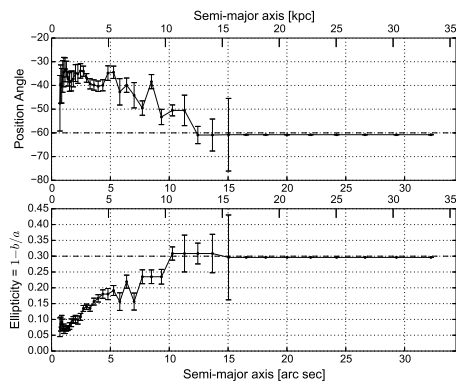
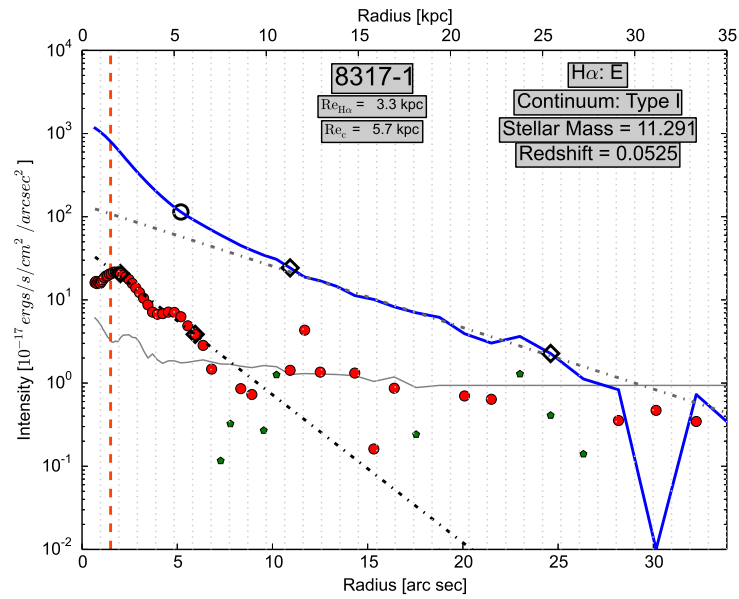
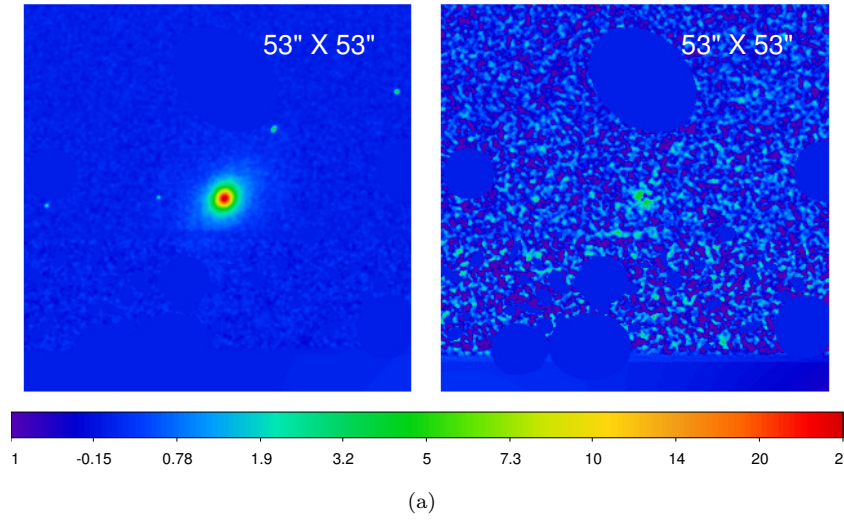
(b)

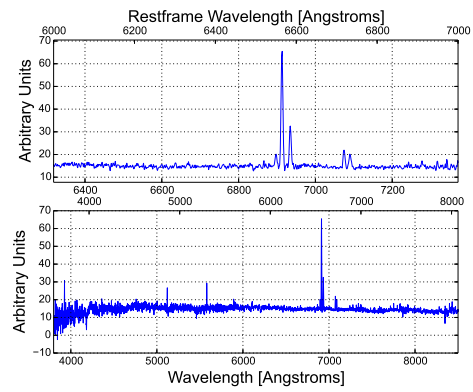
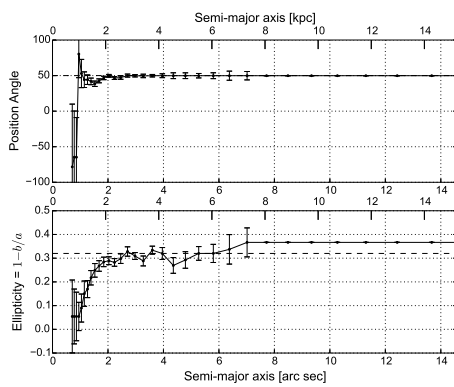
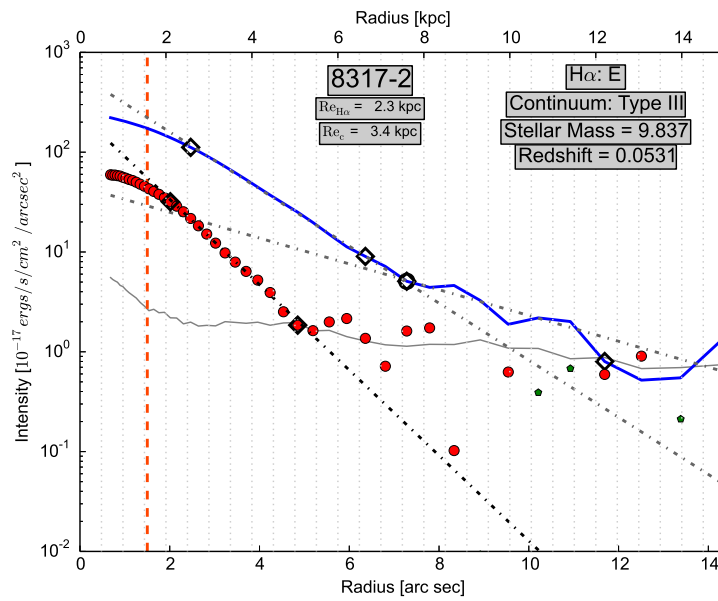
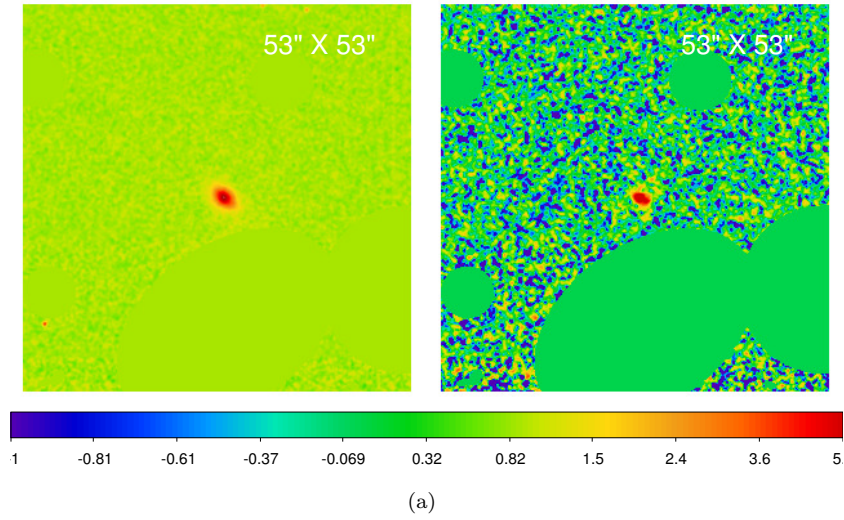


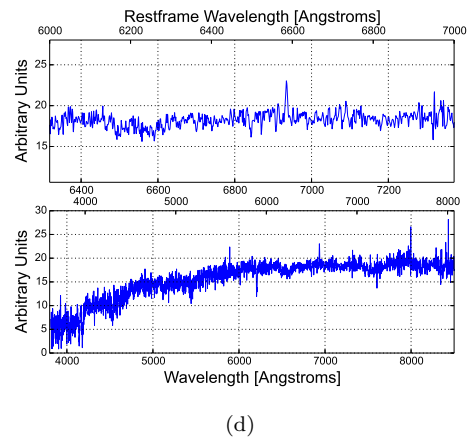
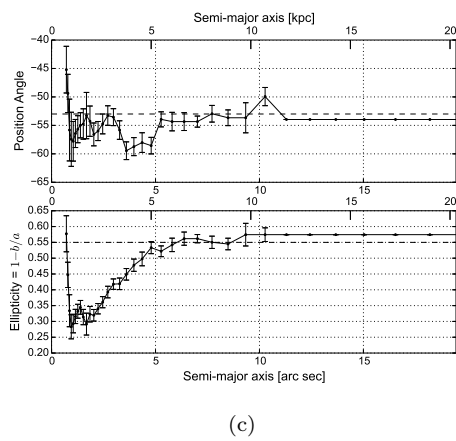
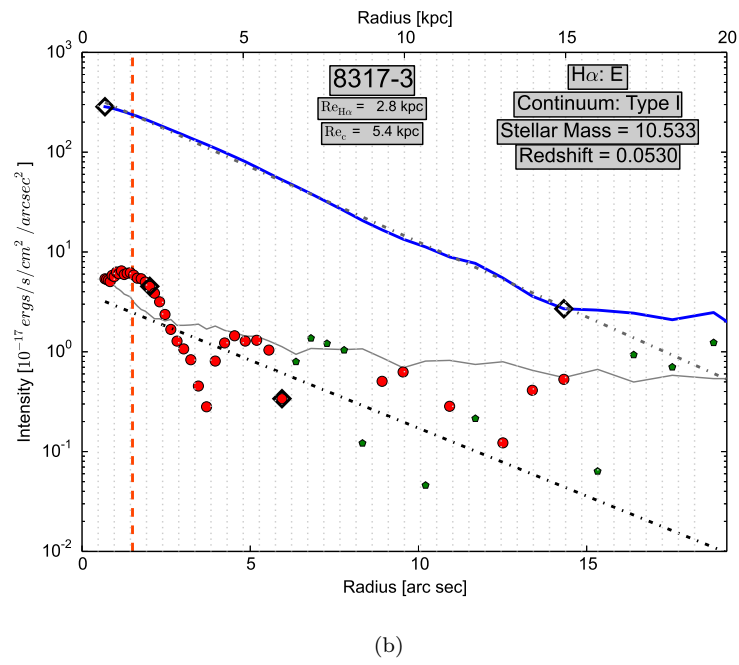
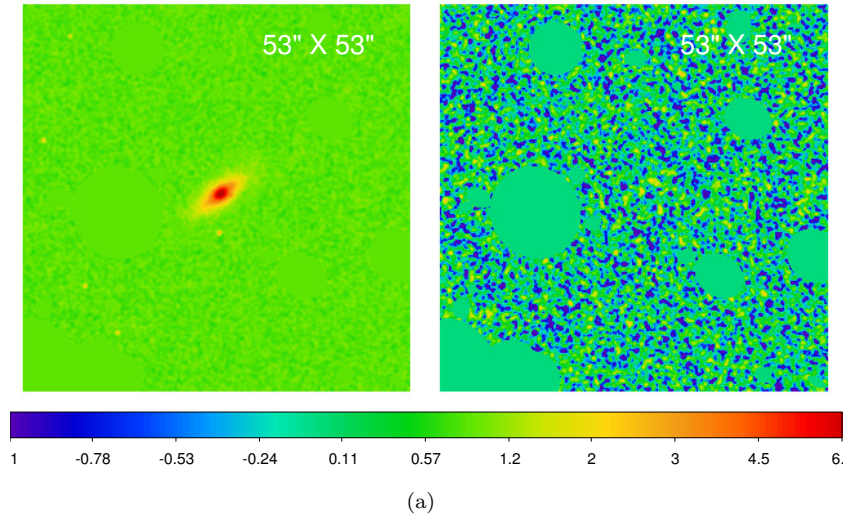
(c)

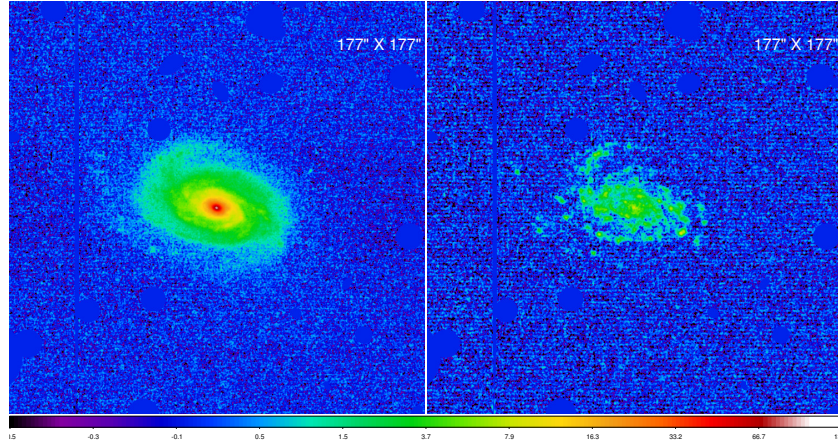


(d)

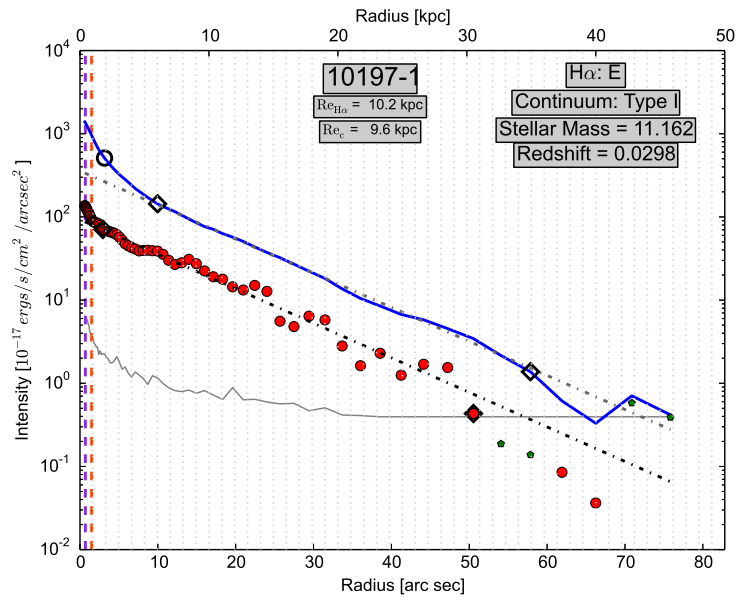




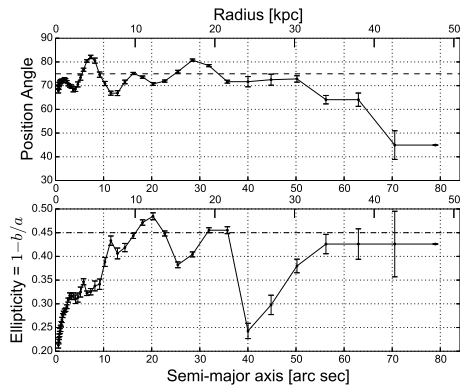




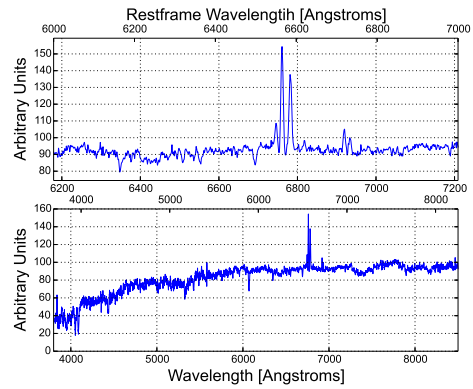
(a)



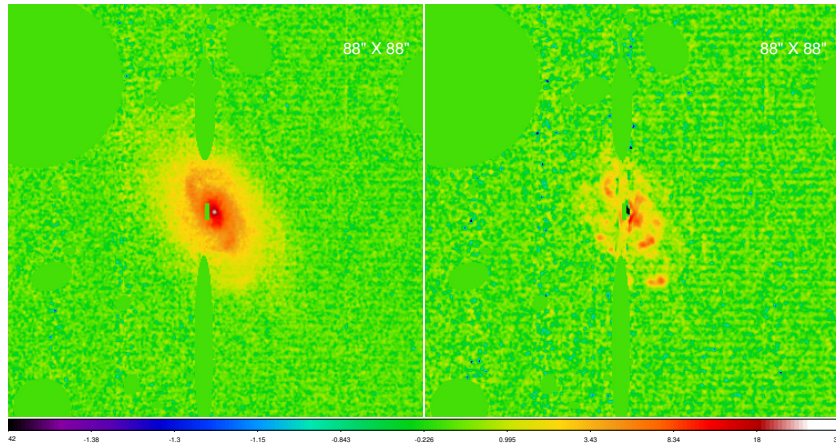
(b)



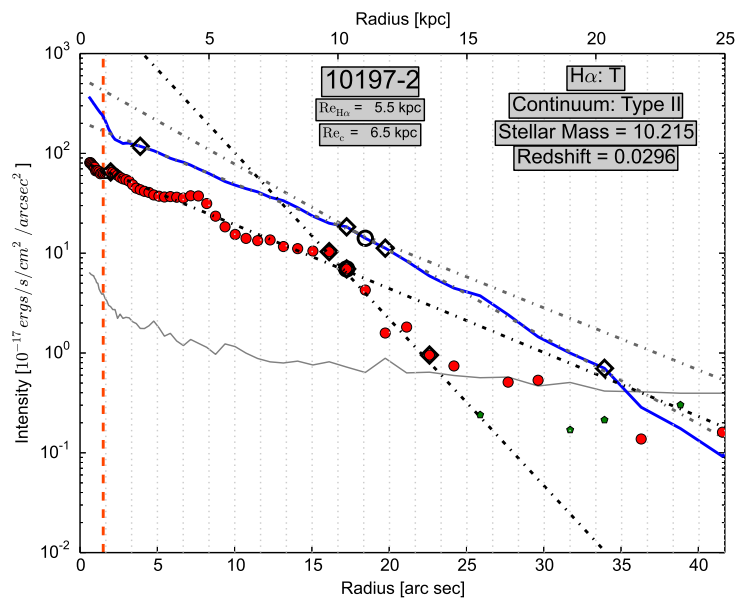
(c)



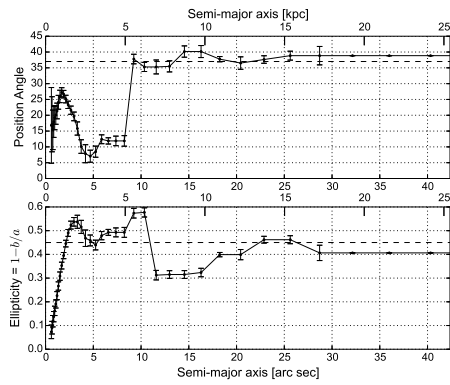
(d)



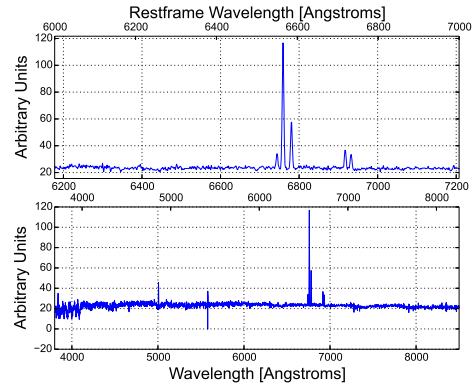
(a)



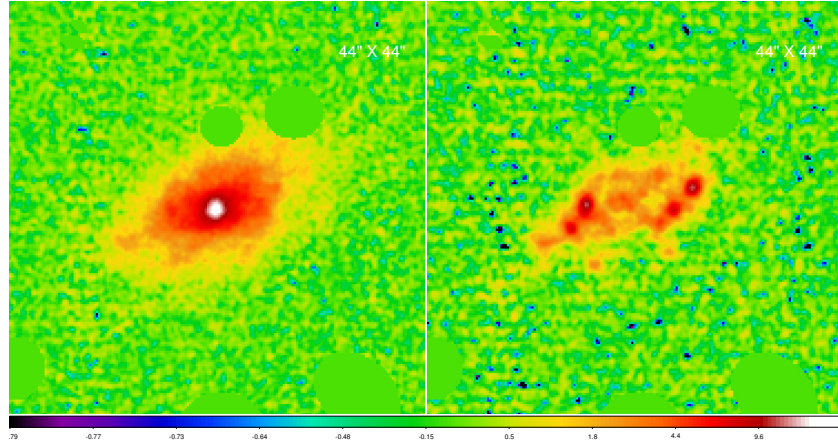
(b)



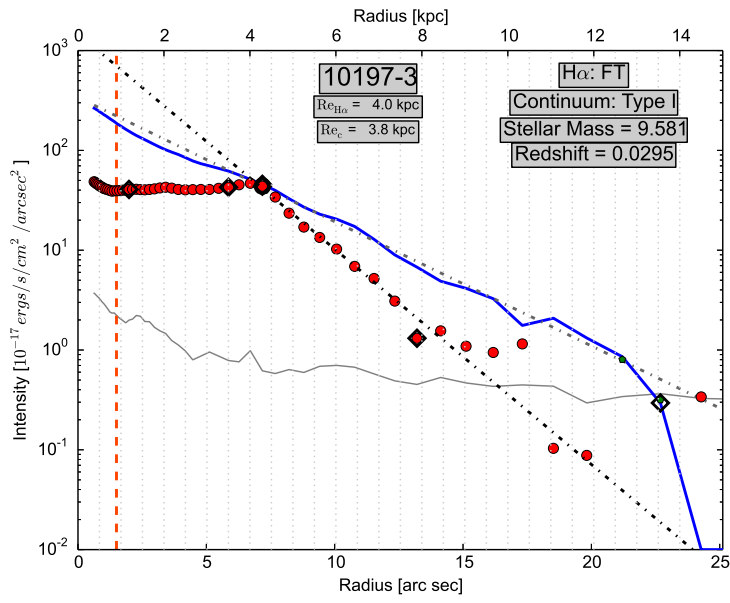
(c)



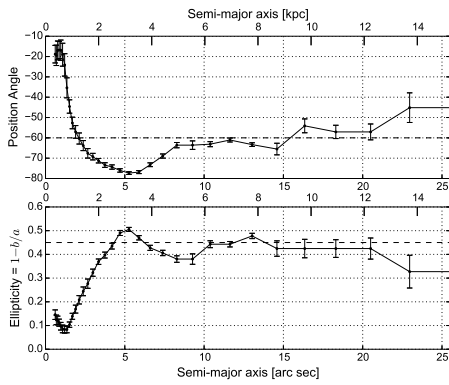
(d)



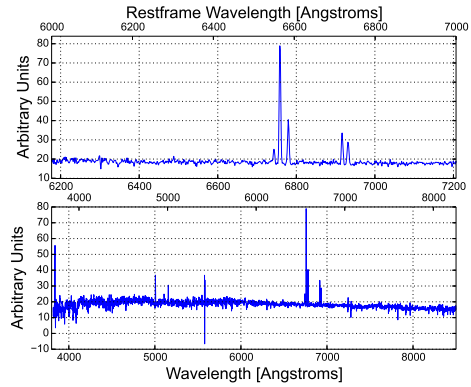
(a)



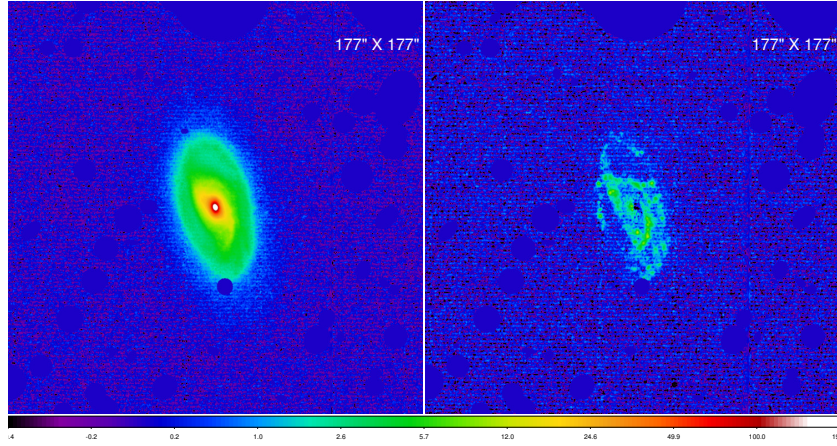
(b)



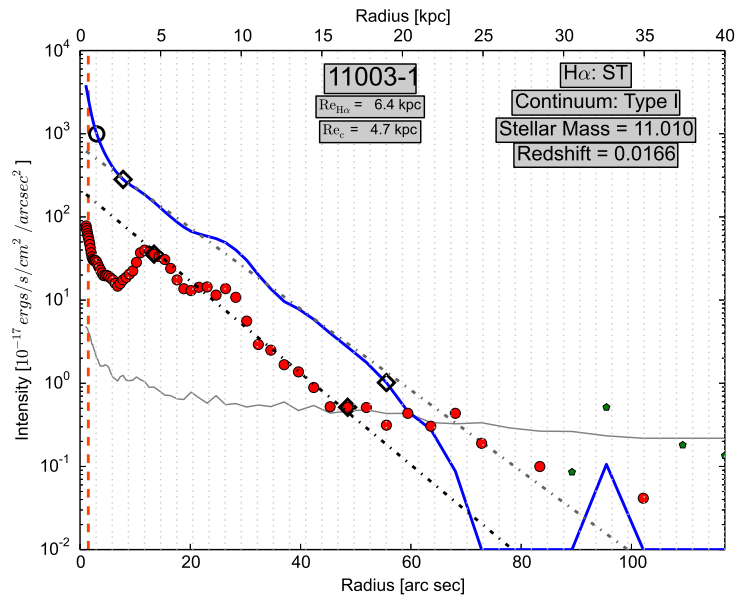
(c)



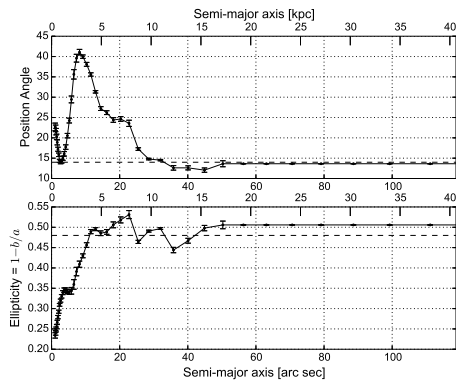
(d)



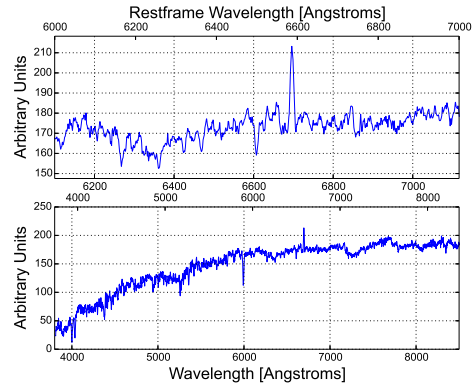
(a)



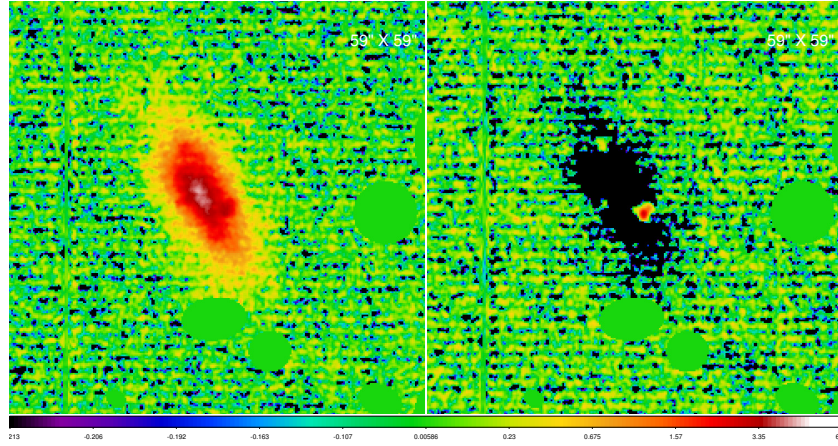
(b)



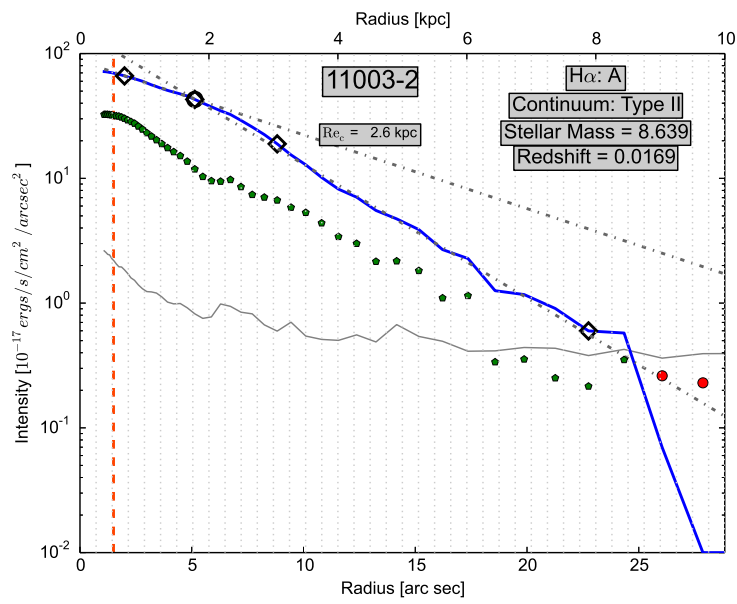
(c)



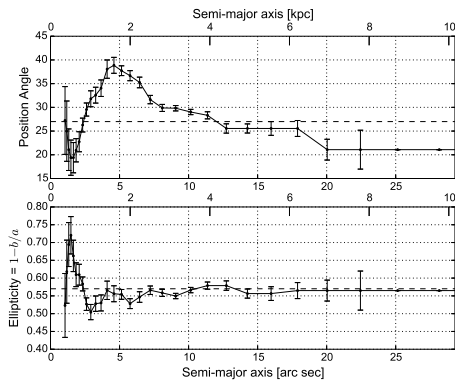
(d)



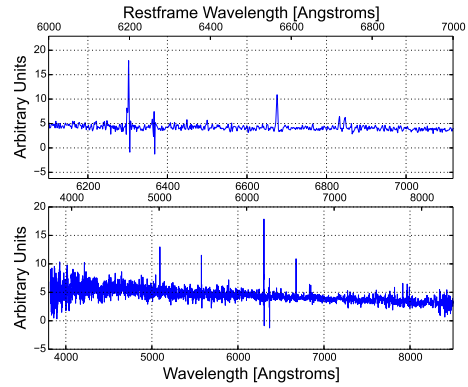
(a)



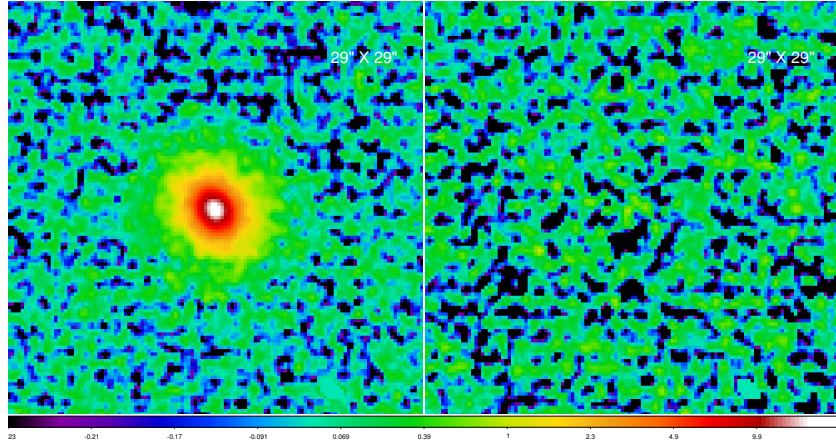
(b)



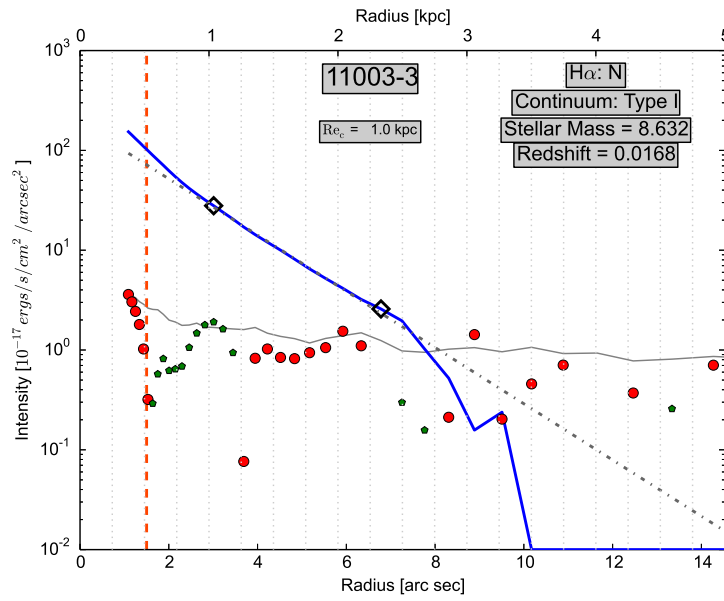
(c)



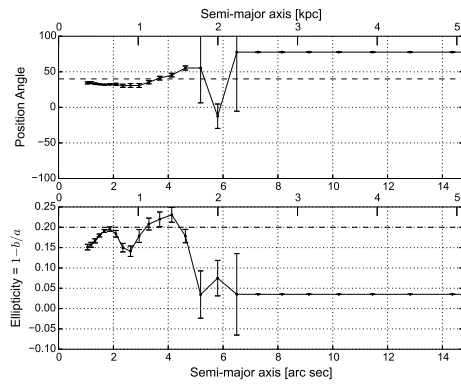
(d)



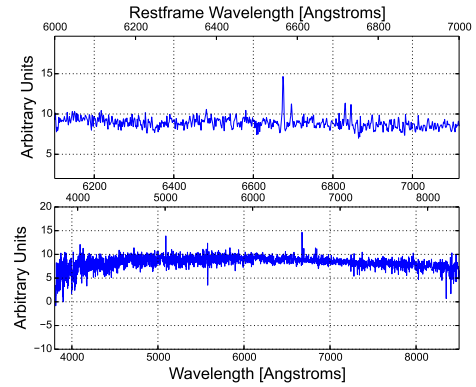
(a)



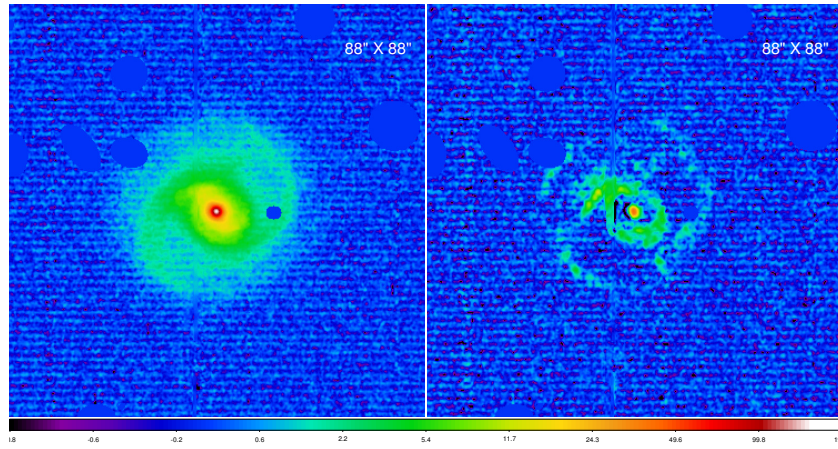
(b)



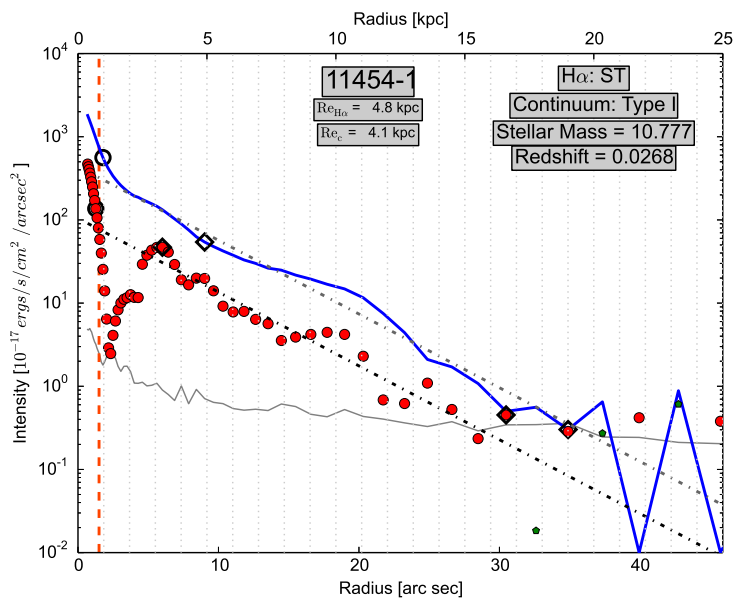
(c)



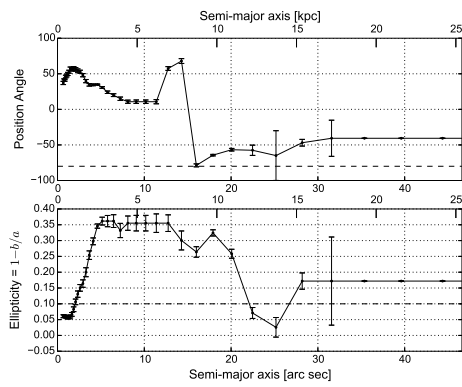
(d)



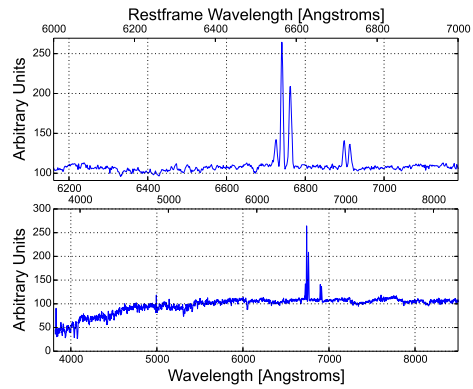
(a)



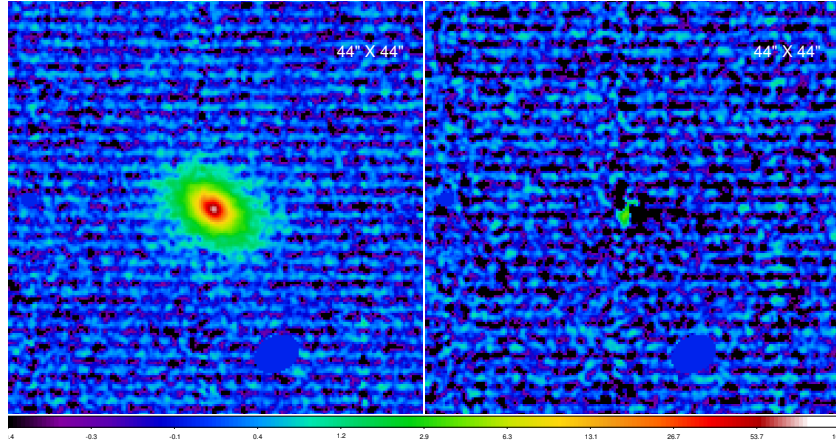
(b)



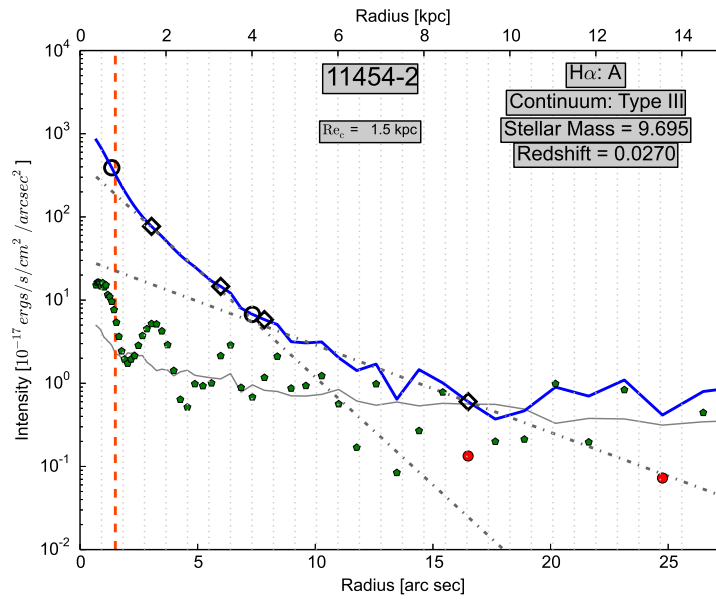
(c)



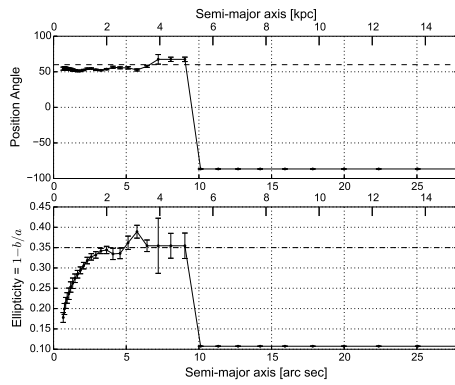
(d)



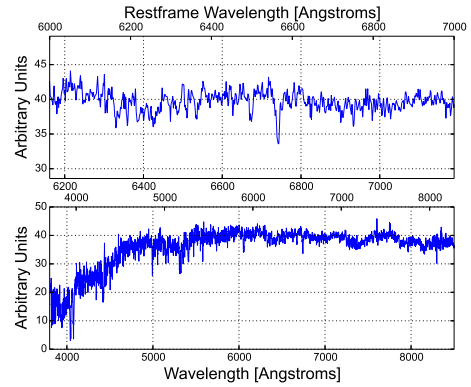
(a)



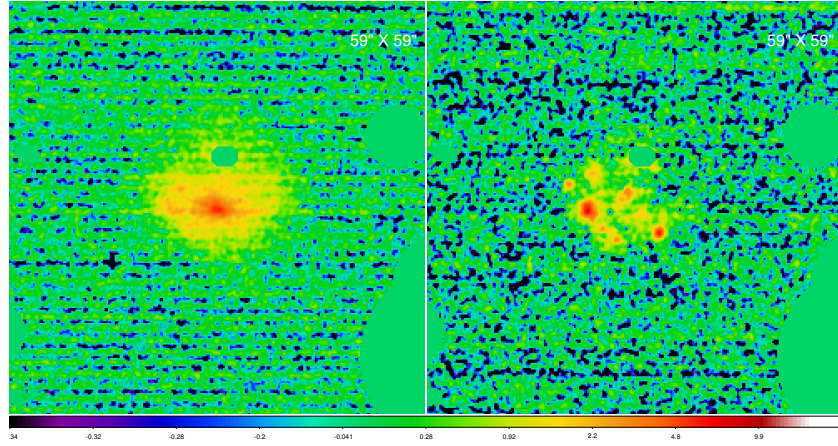
(b)



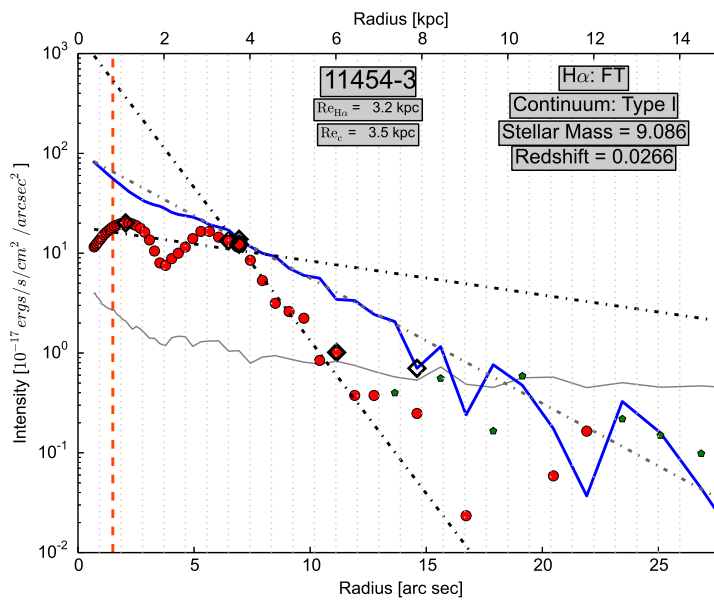
(c)



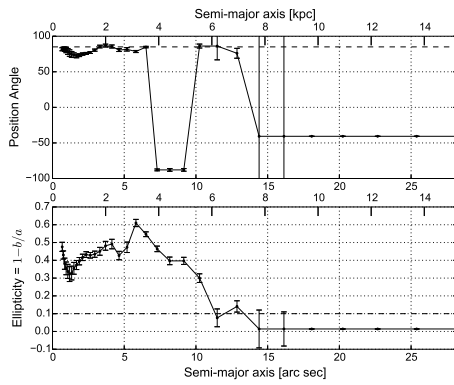
(d)



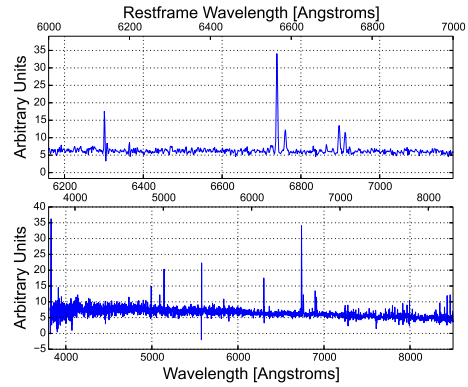
(a)



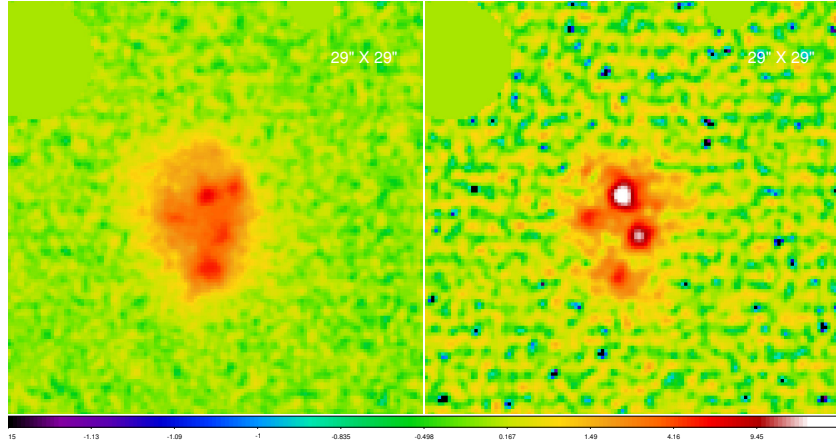
(b)



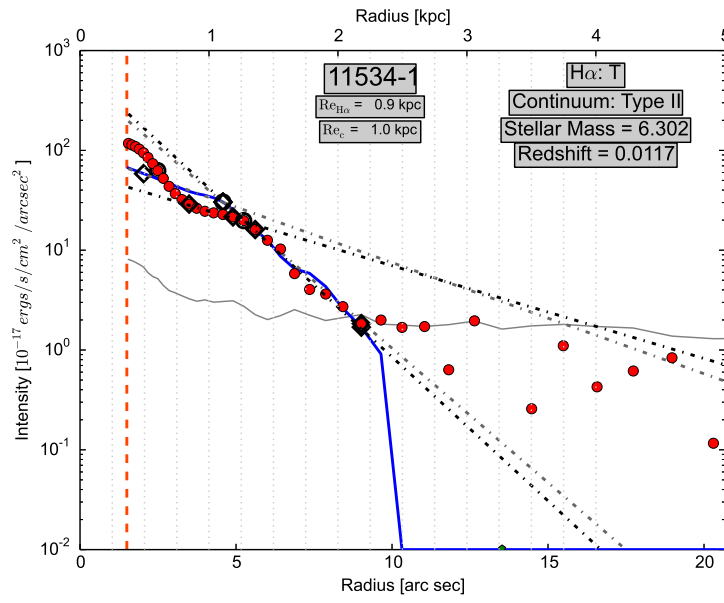
(c)



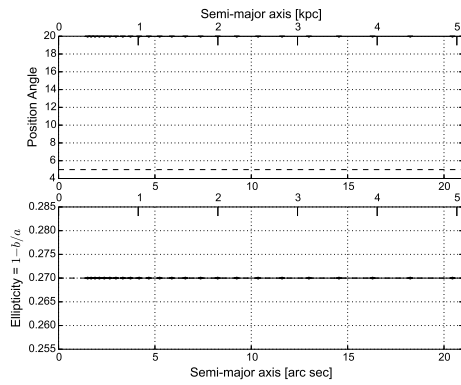
(d)



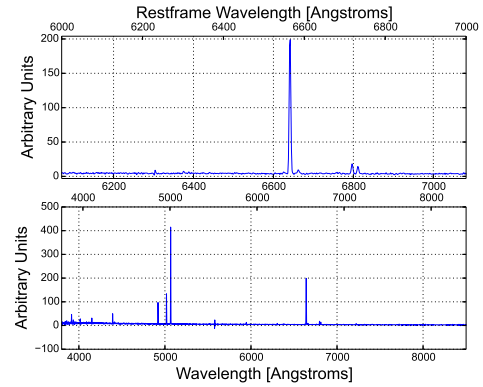
(a)



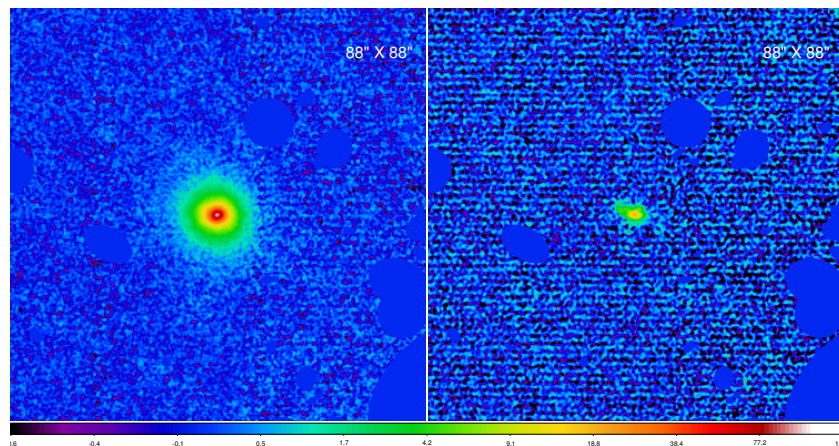
(b)



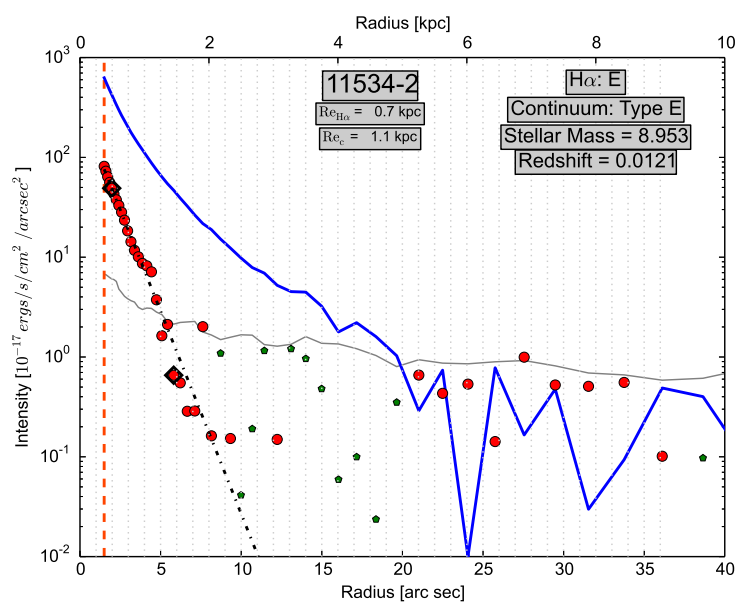
(c)



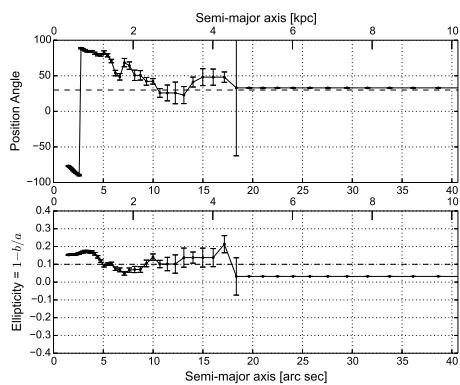
(d)



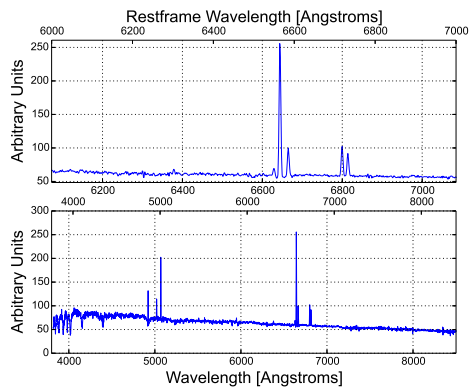
(a)



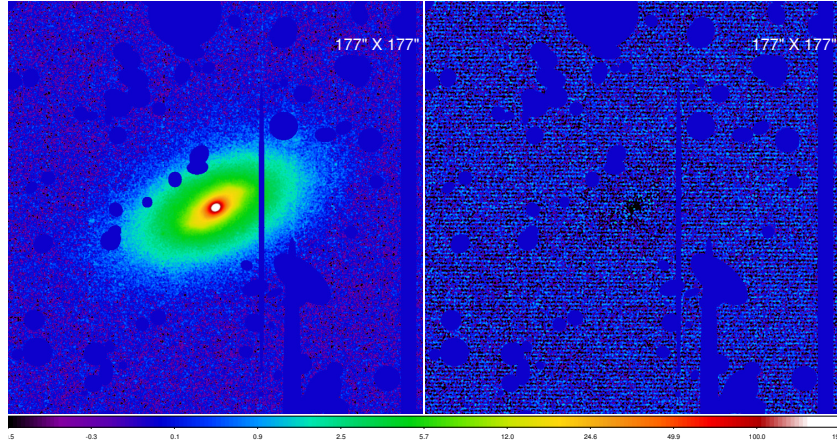
(b)



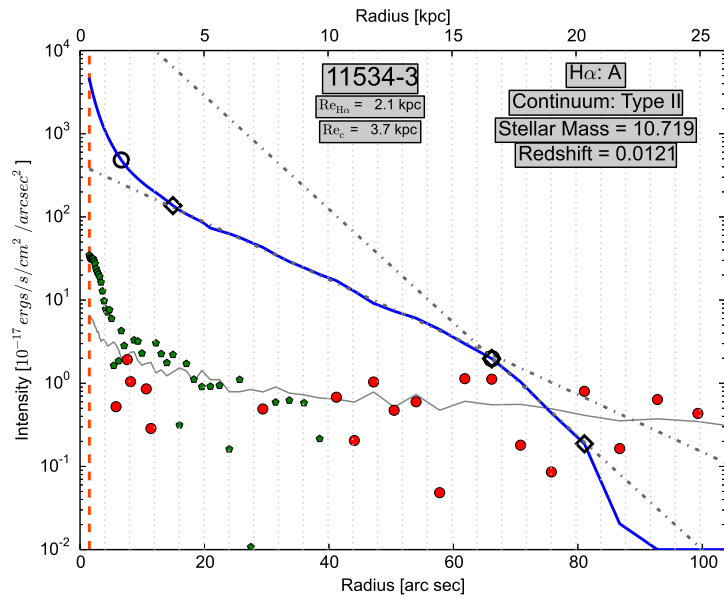
(c)



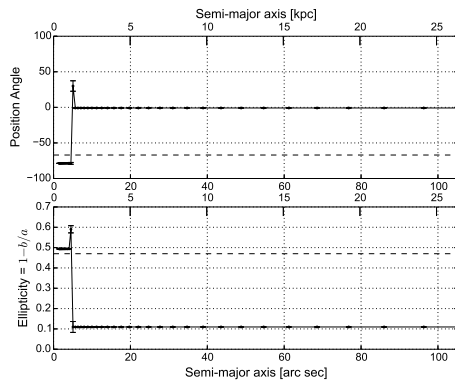
(d)



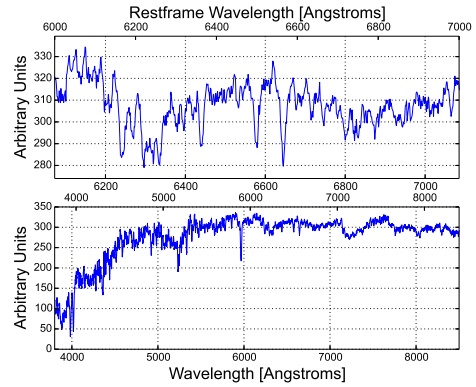
(a)



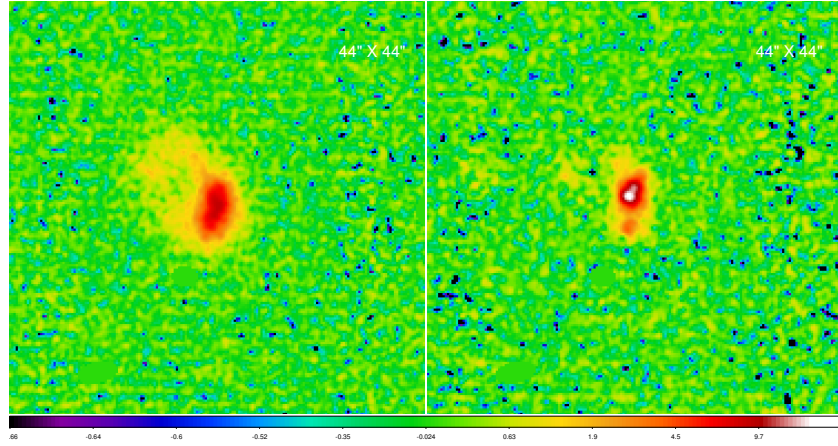
(b)



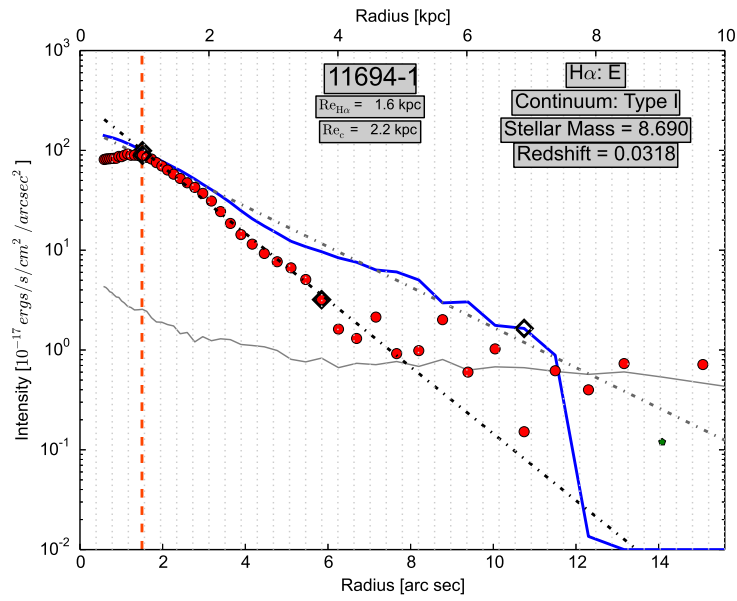
(c)



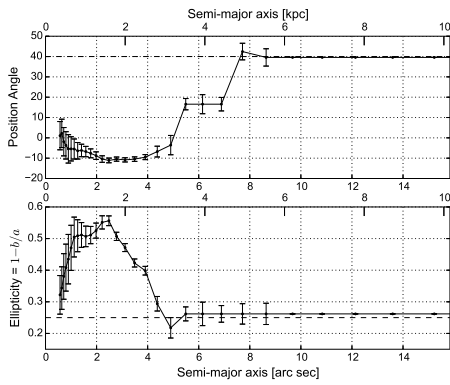
(d)



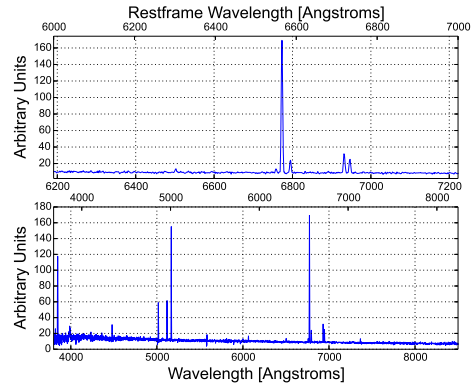
(a)



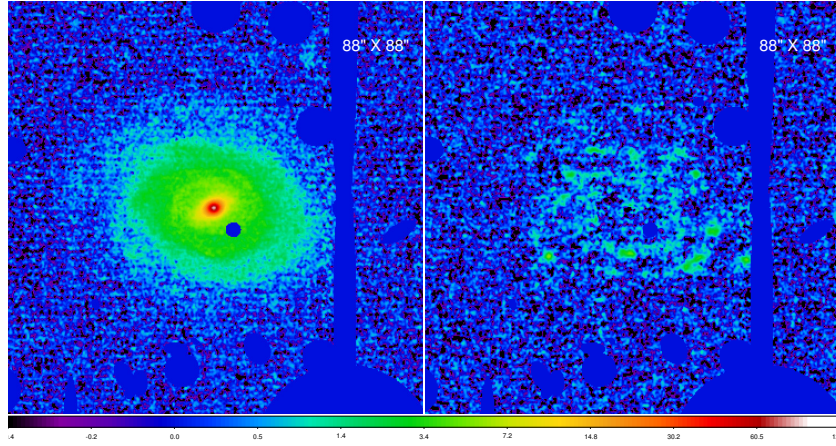
(b)



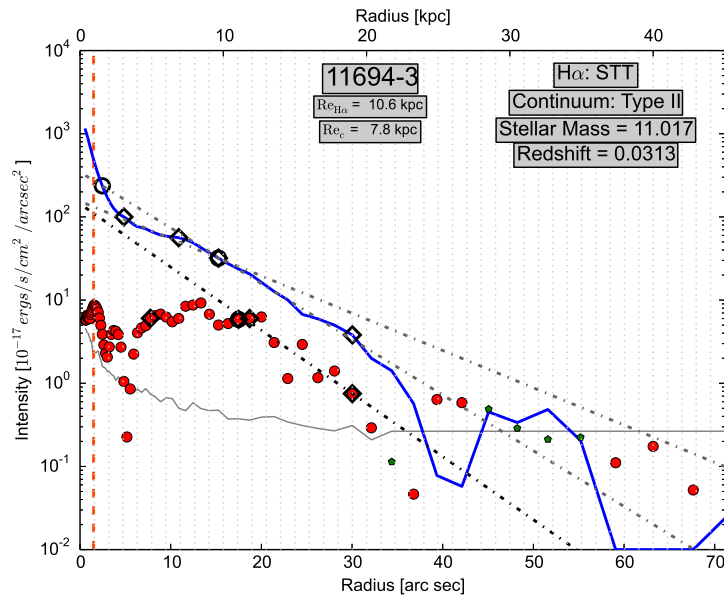
(c)



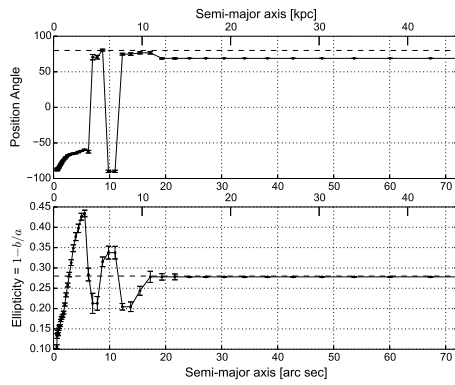
(d)



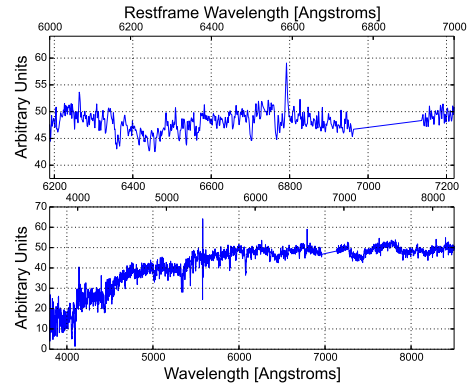
(a)



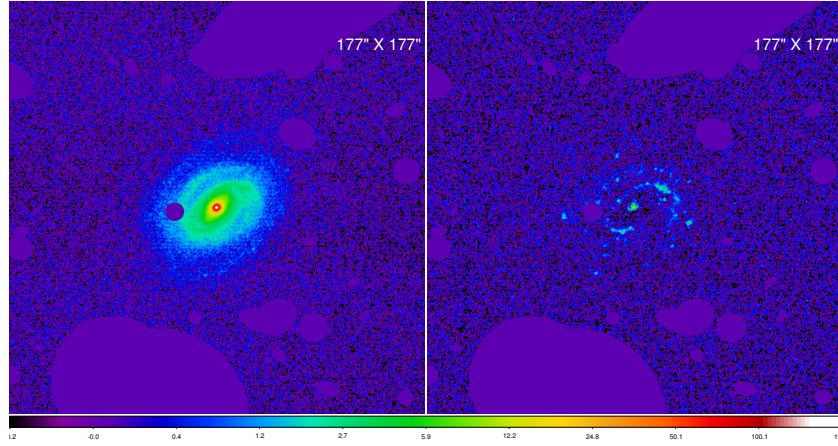
(b)



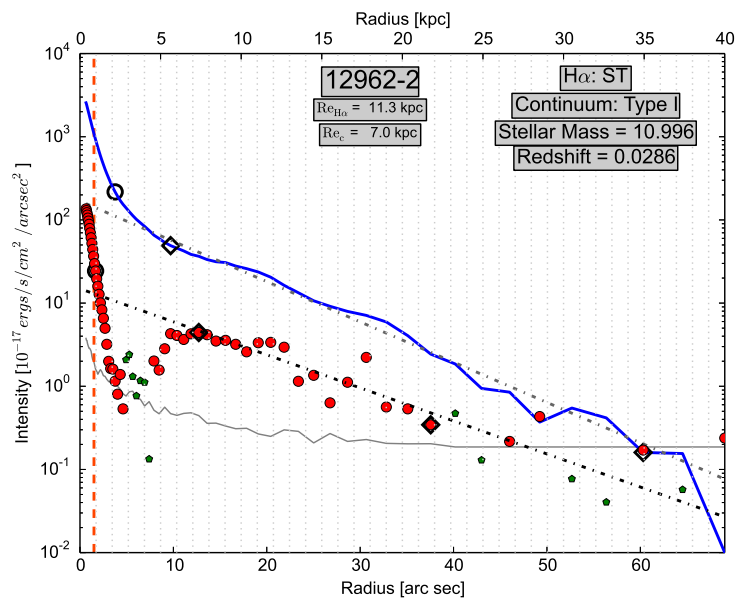
(c)



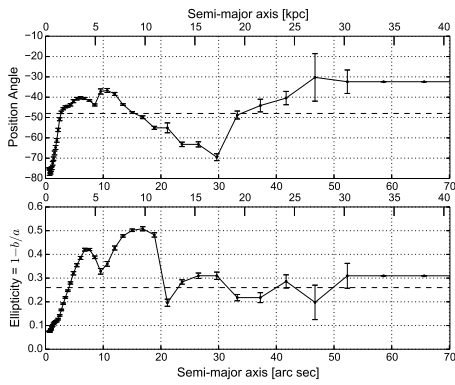
(d)



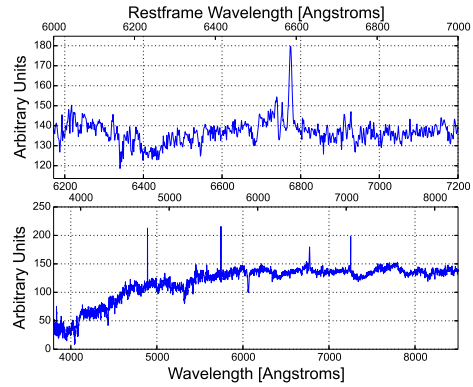
(a)



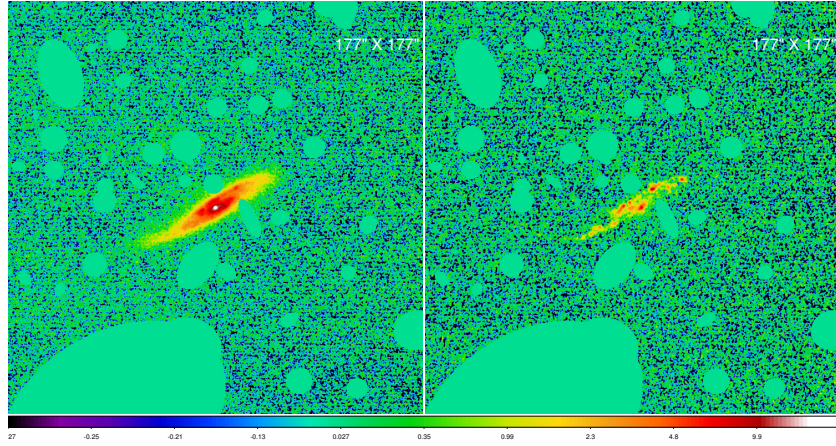
(b)



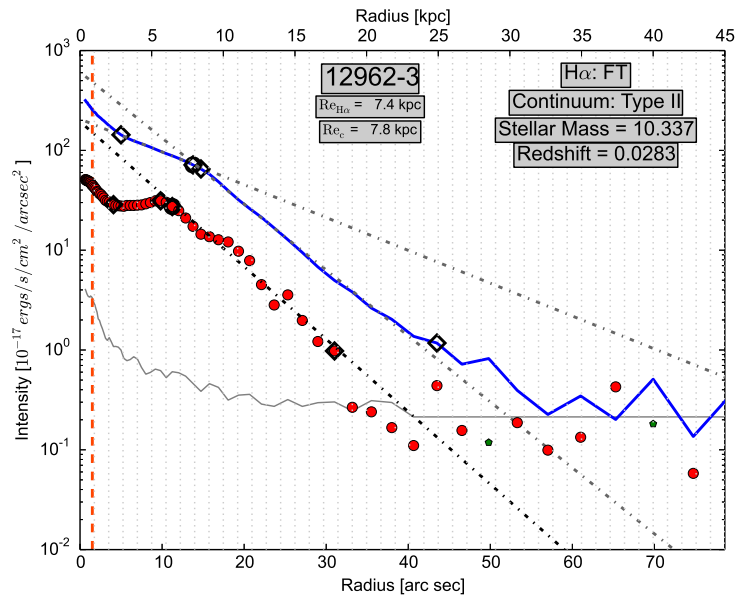
(c)



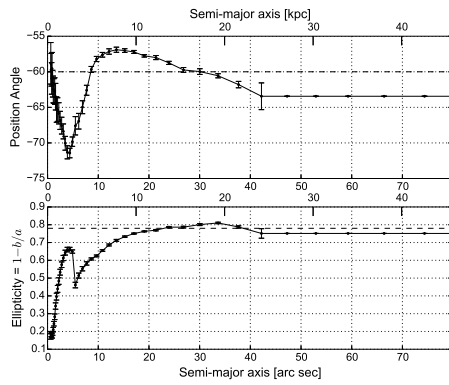
(d)



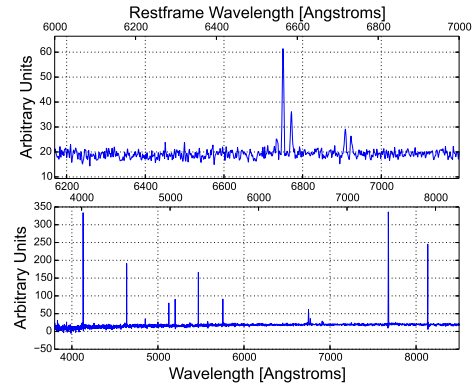
(a)



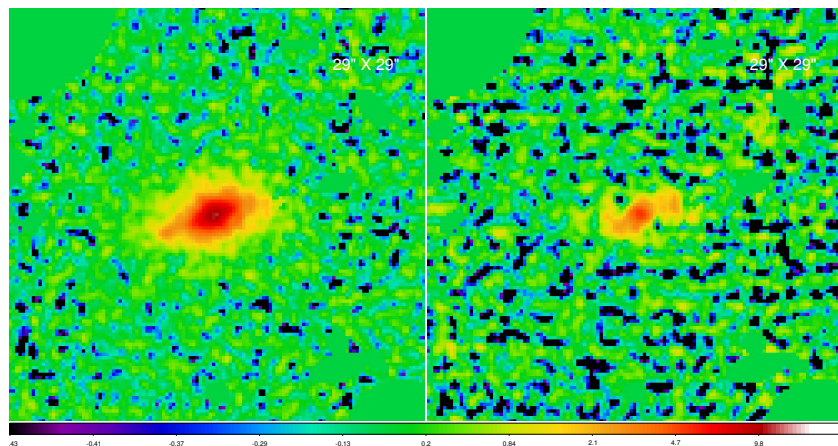
(b)



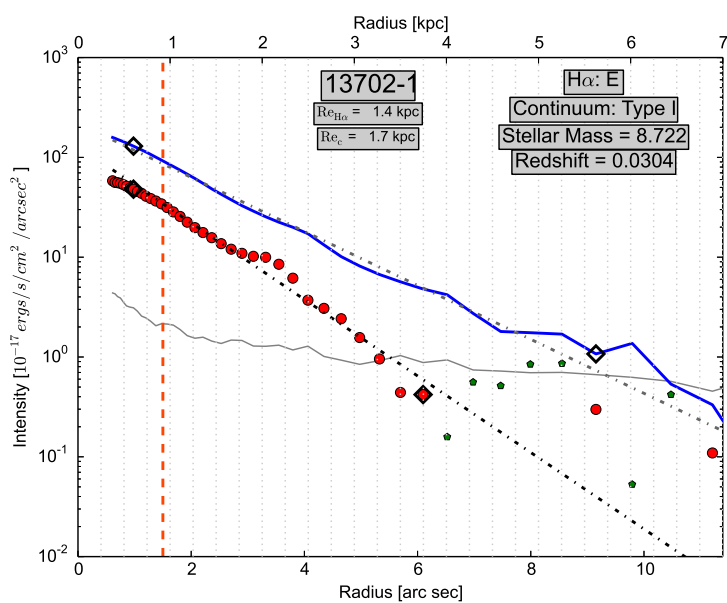
(c)



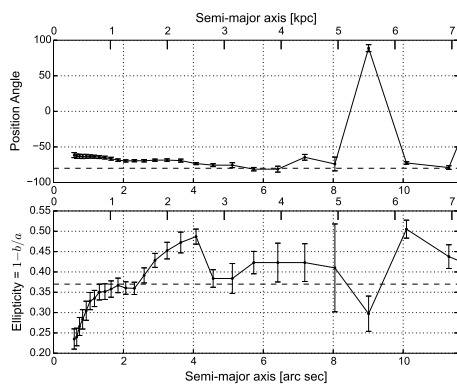
(d)



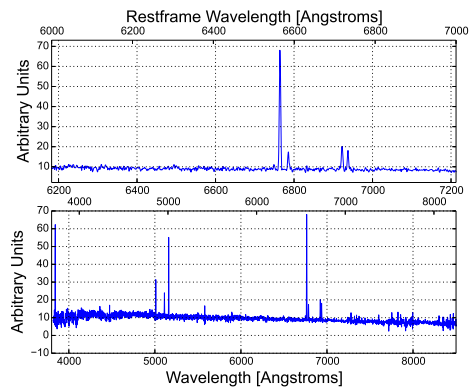
(a)



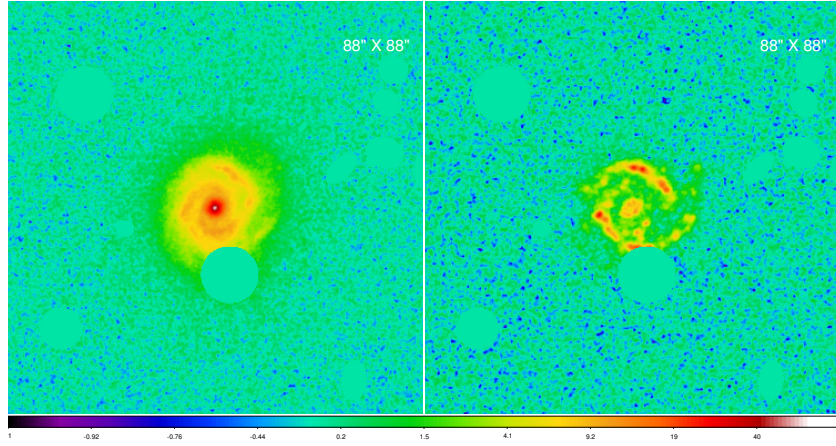
(b)



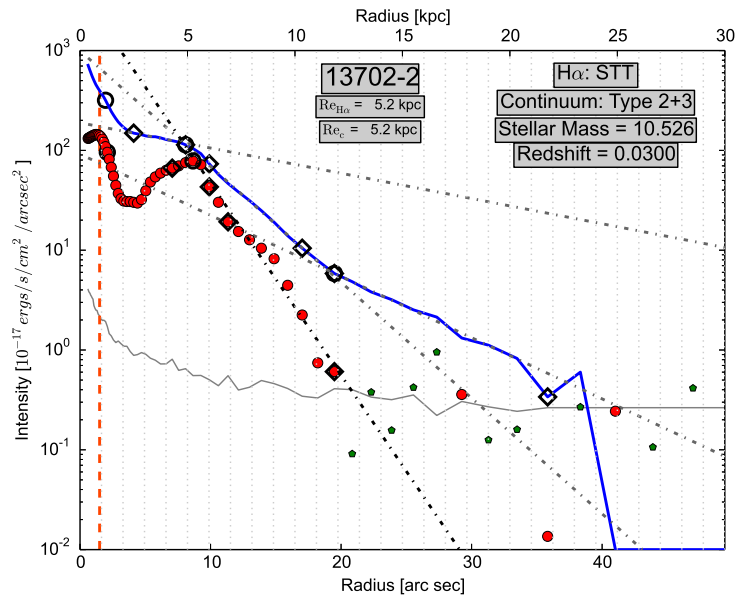
(c)



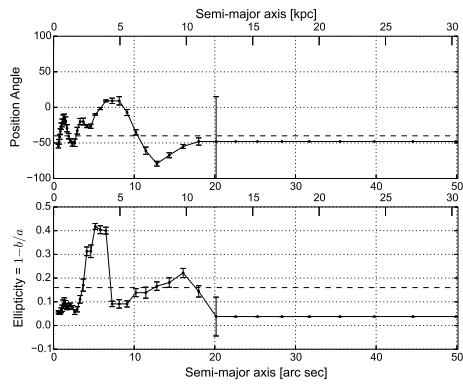
(d)



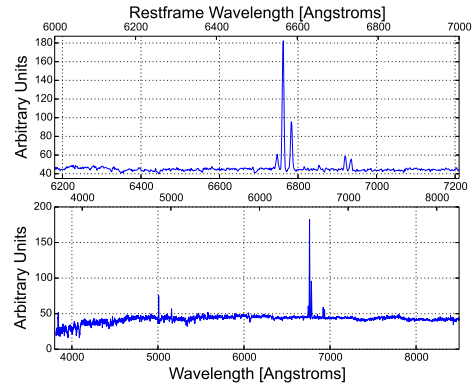
(a)



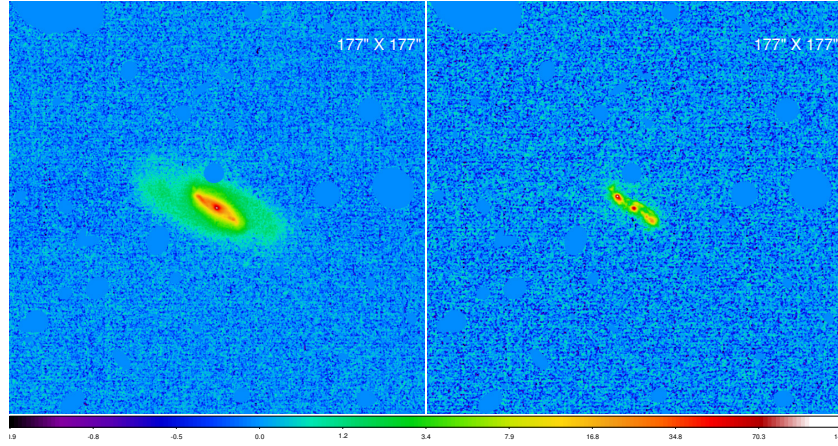
(b)



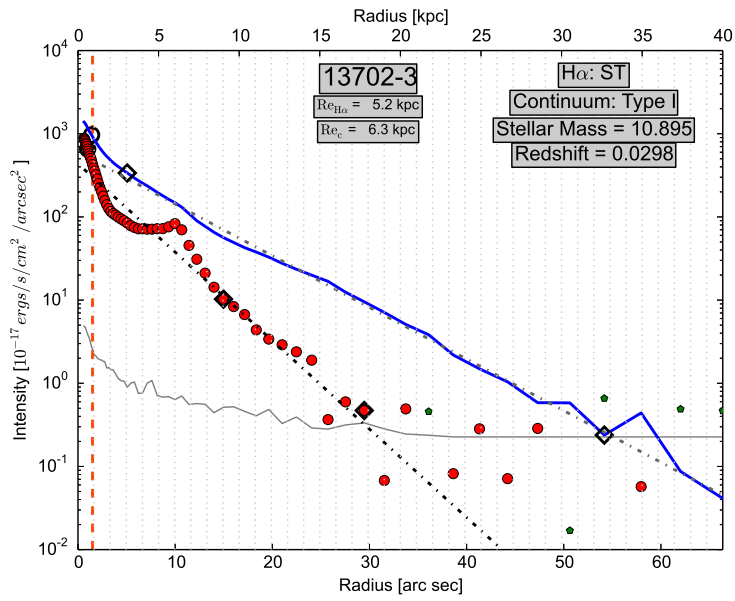
(c)



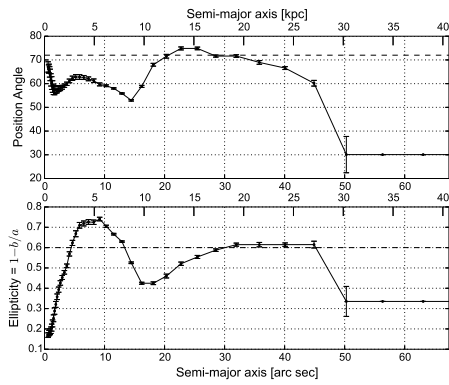
(d)



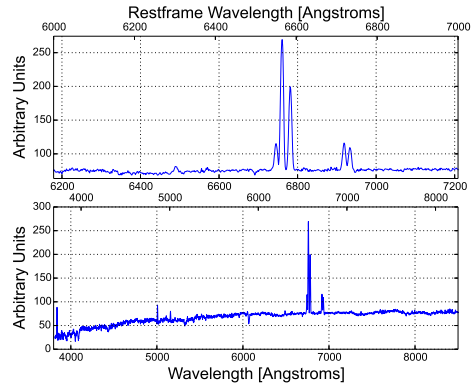
(a)



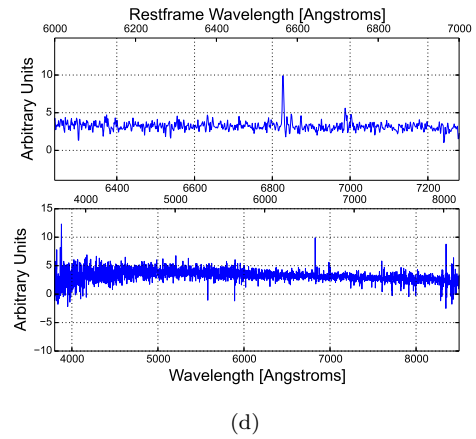
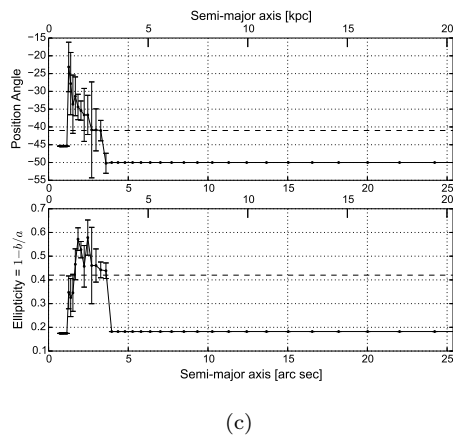
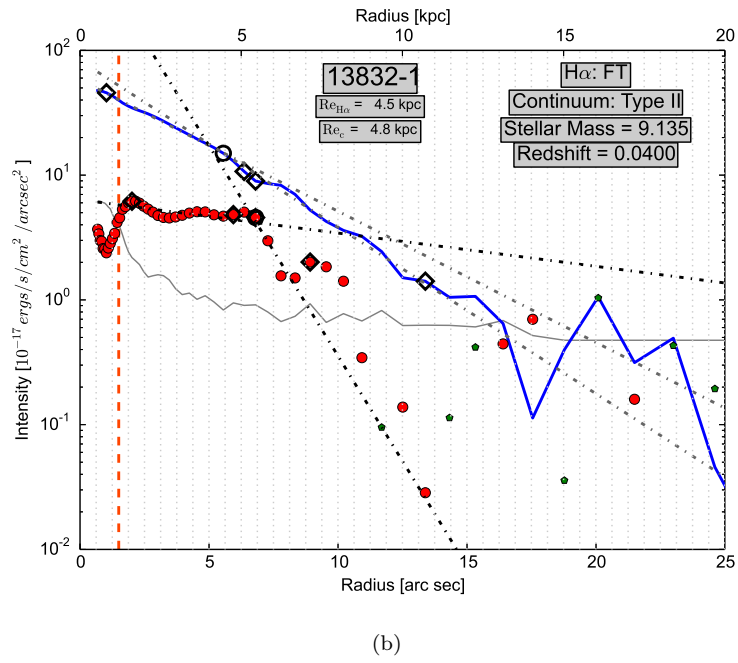
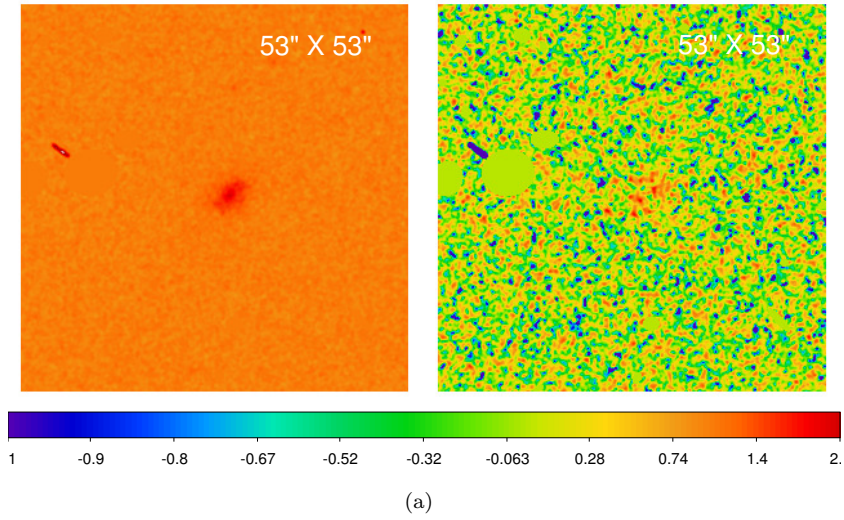
(b)

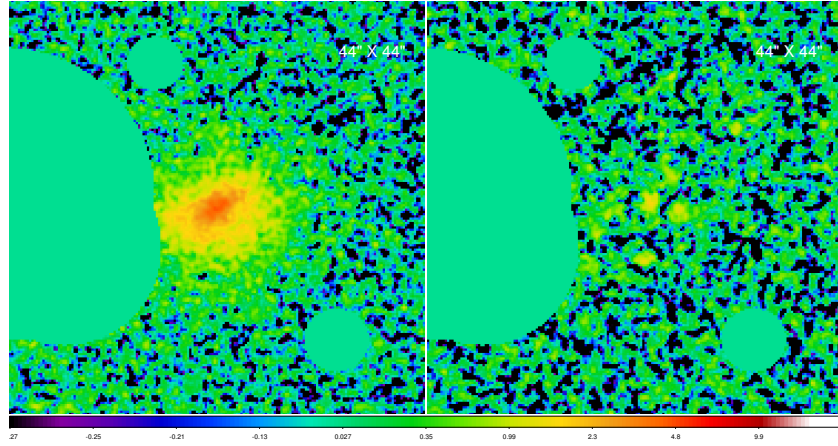


(c)

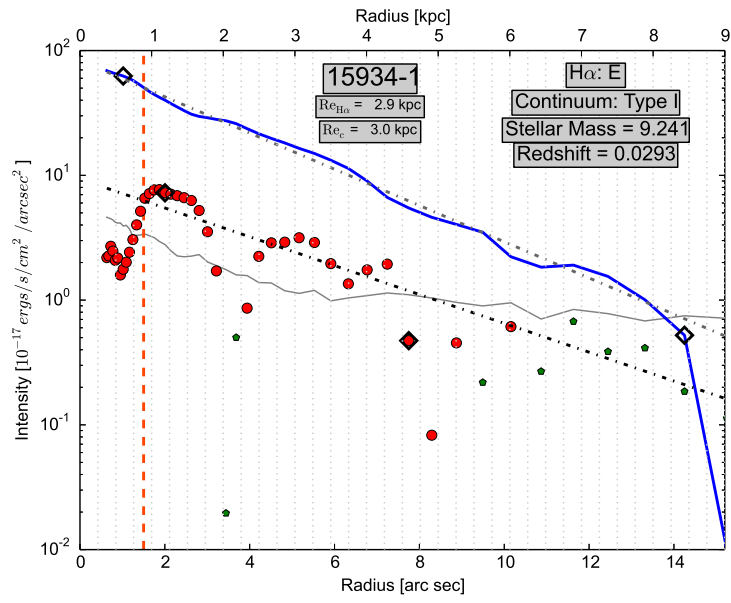


(d)

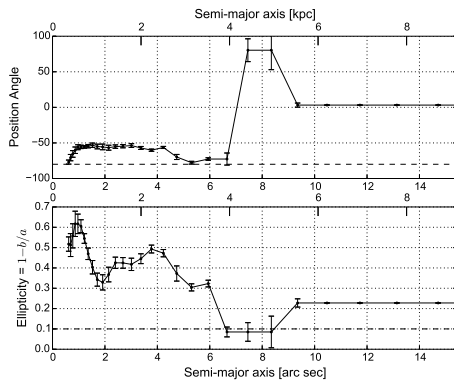




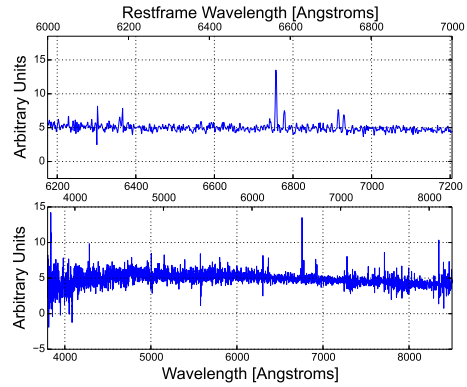
(a)



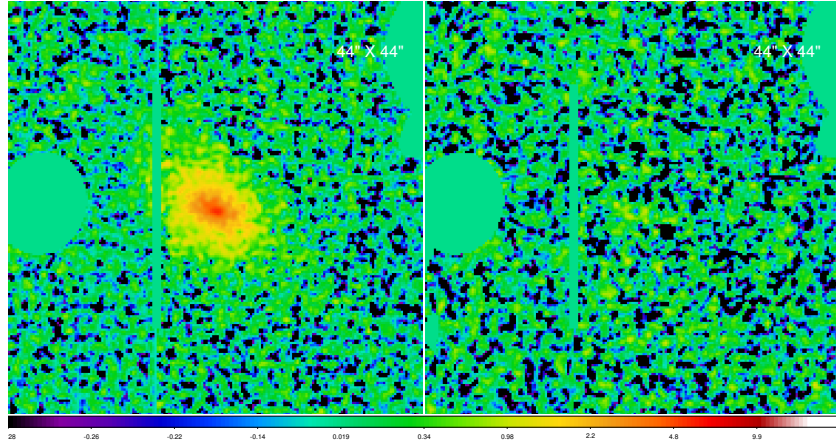
(b)



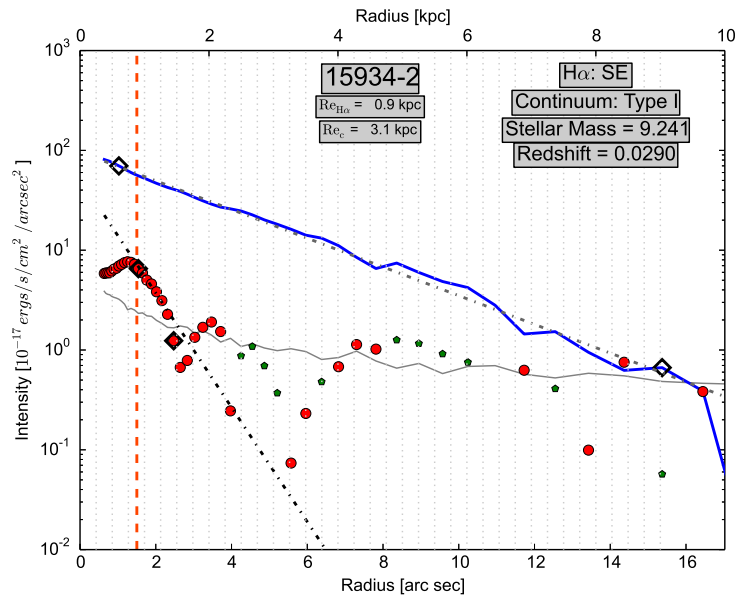
(c)



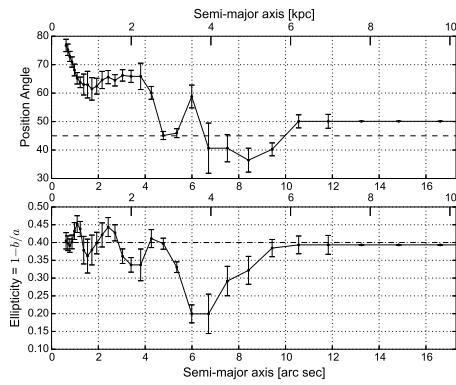
(d)



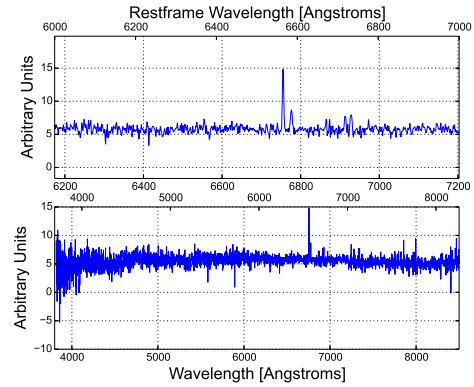
(a)



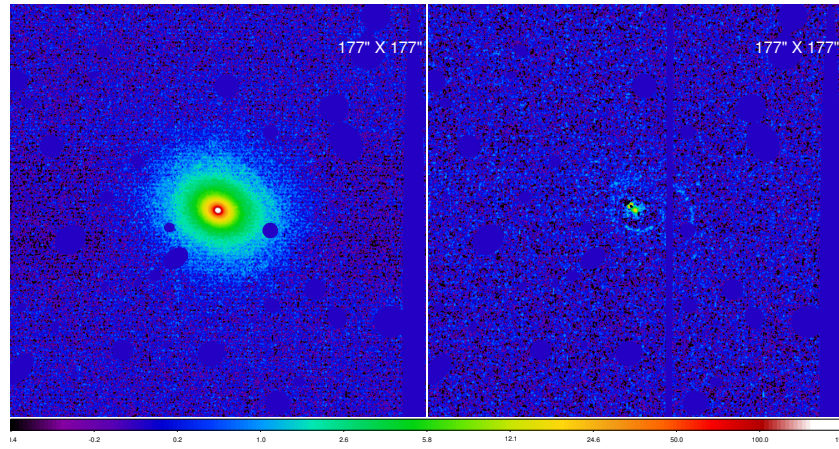
(b)



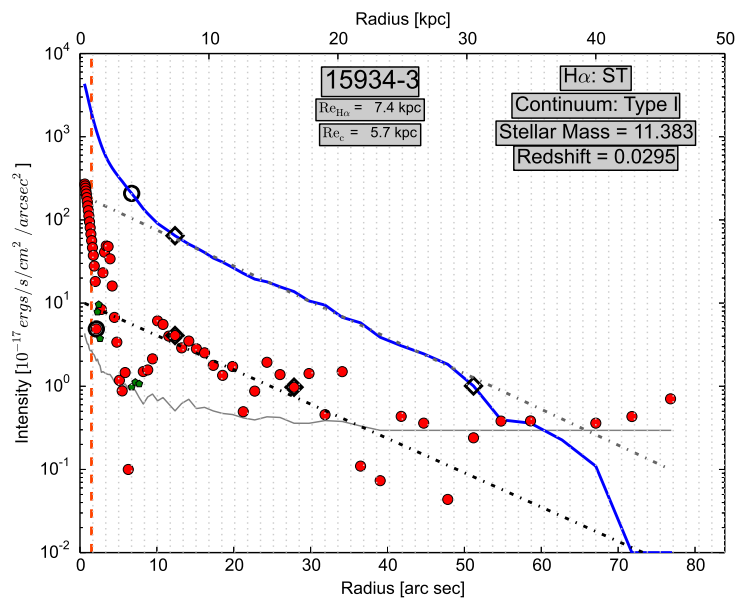
(c)



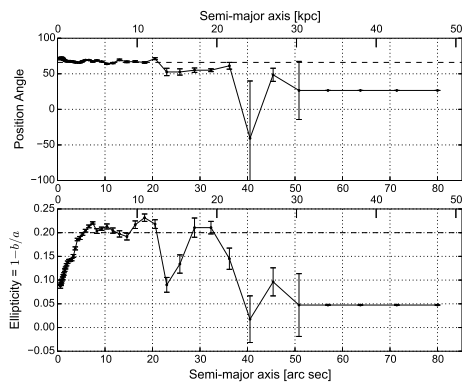
(d)



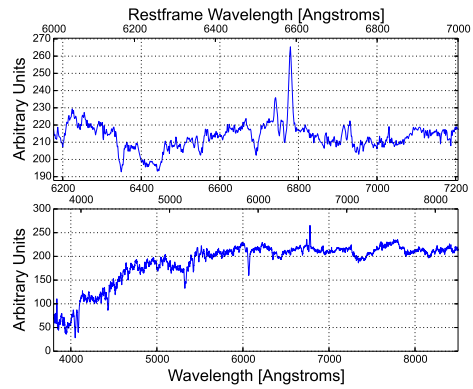
(a)



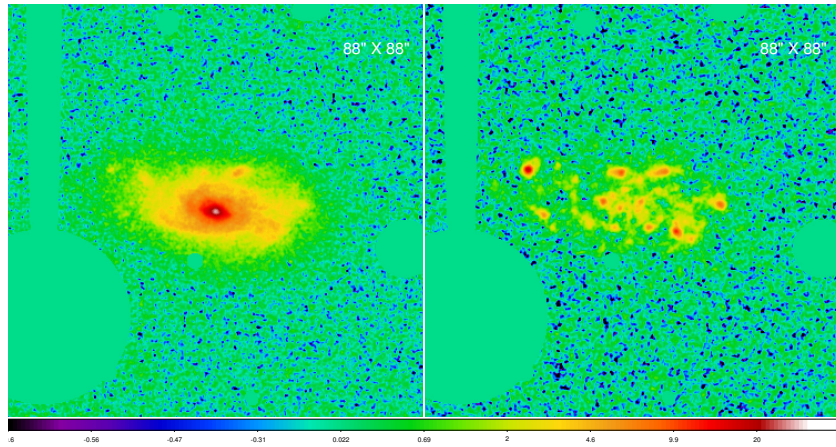
(b)



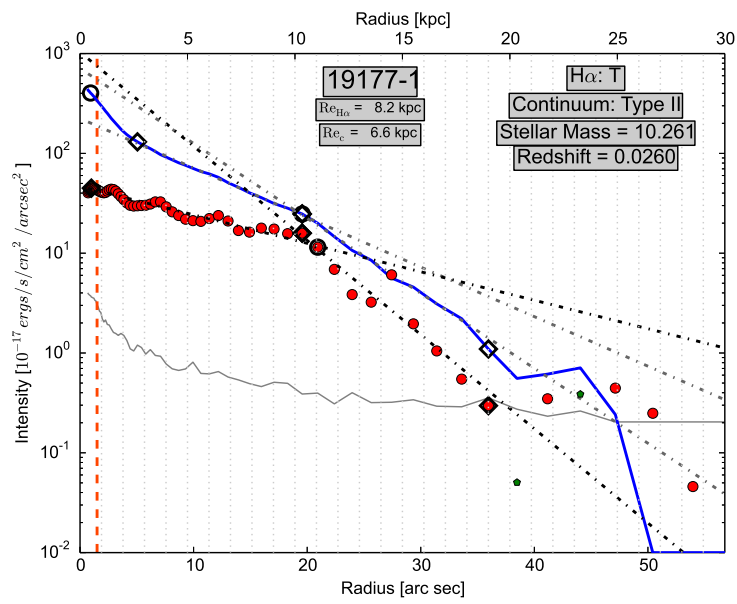
(c)



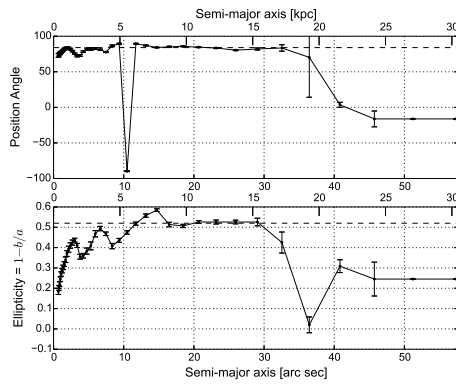
(d)



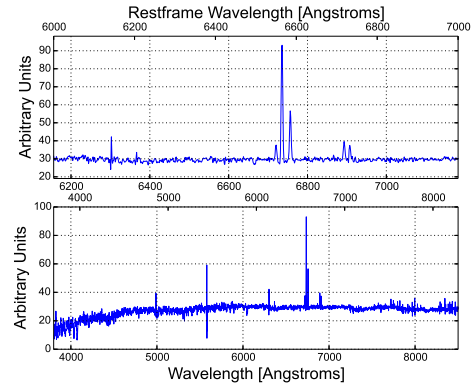
(a)



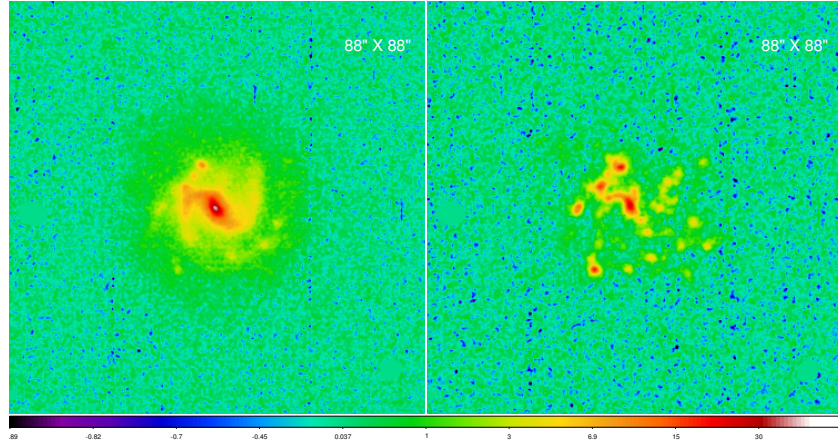
(b)



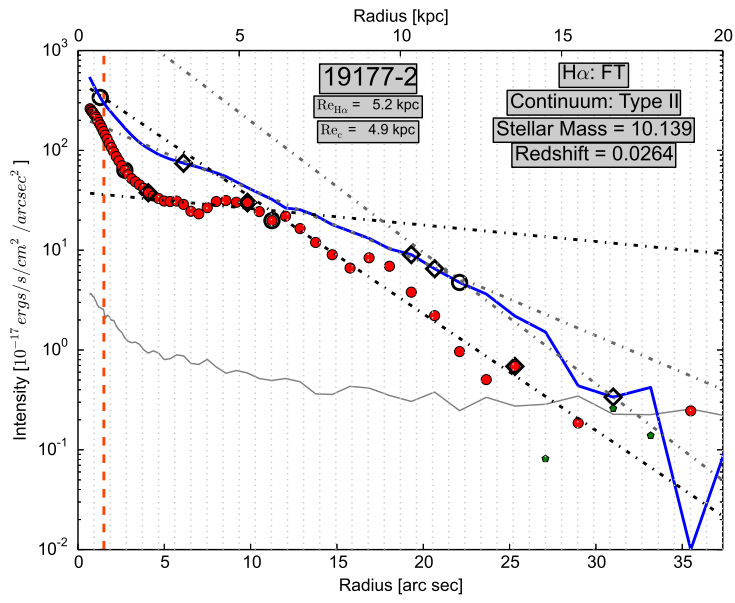
(c)



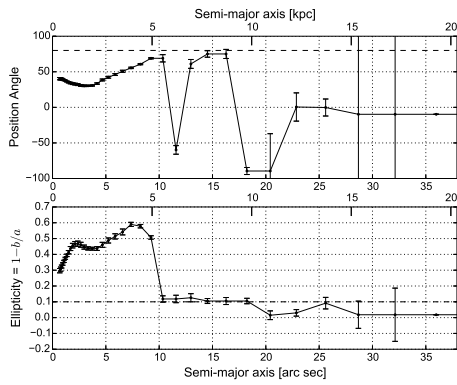
(d)



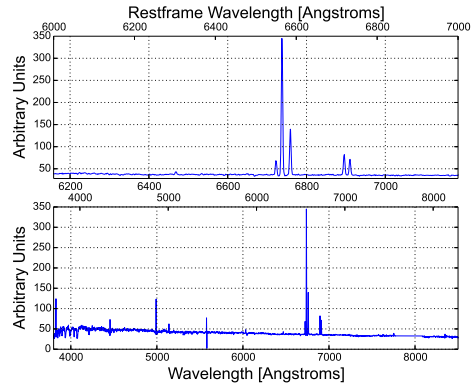
(a)



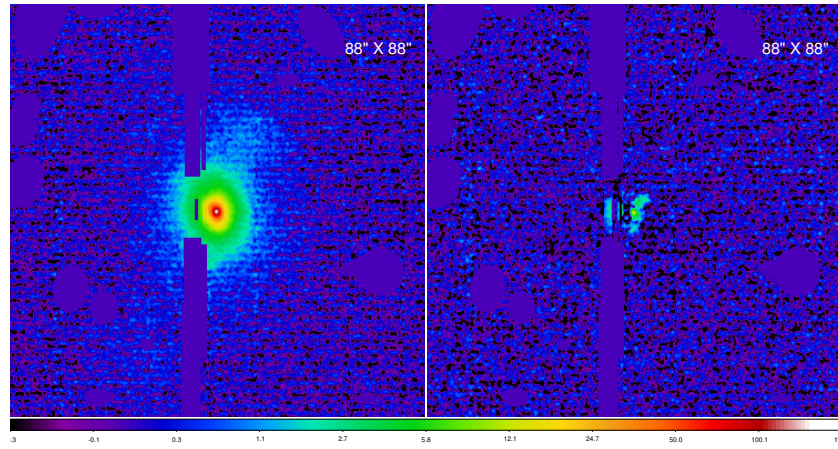
(b)



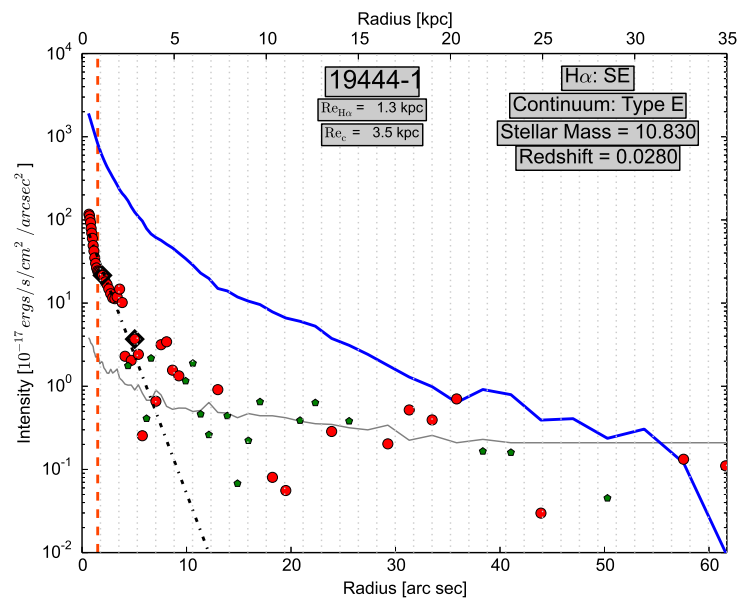
(c)



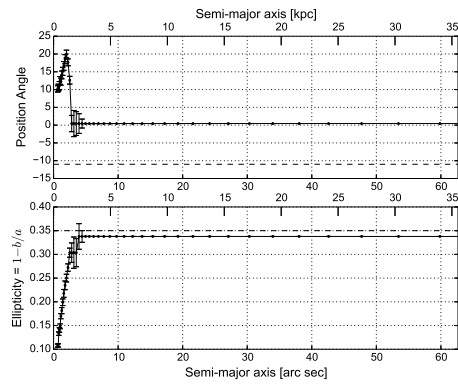
(d)



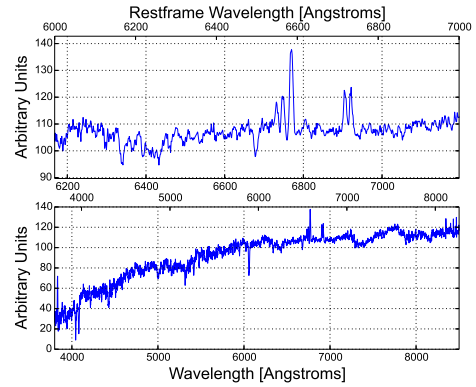
(a)



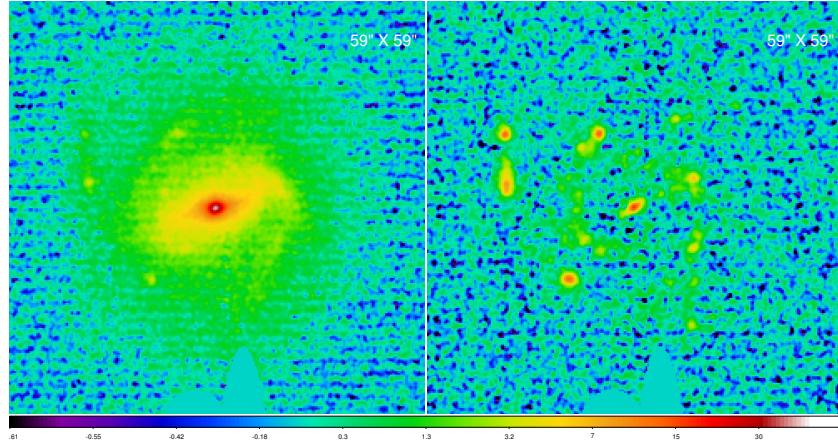
(b)



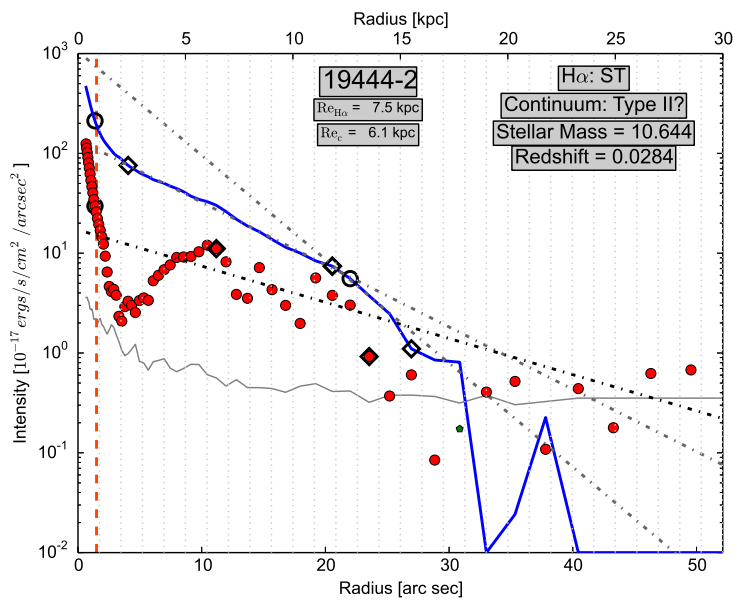
(c)



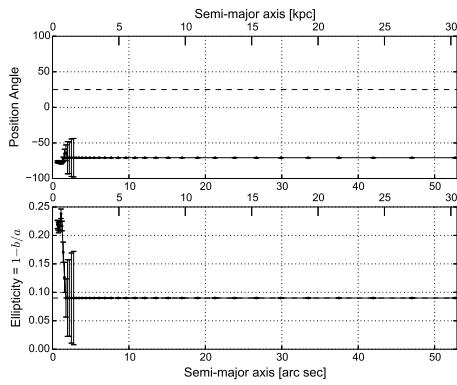
(d)



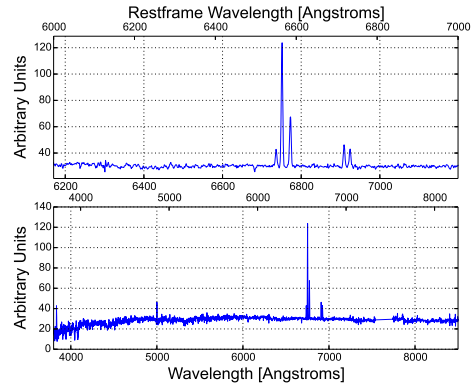
(a)



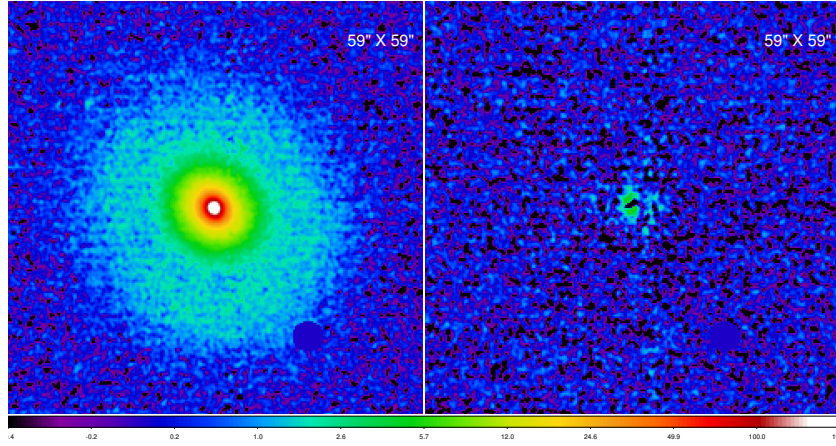
(b)



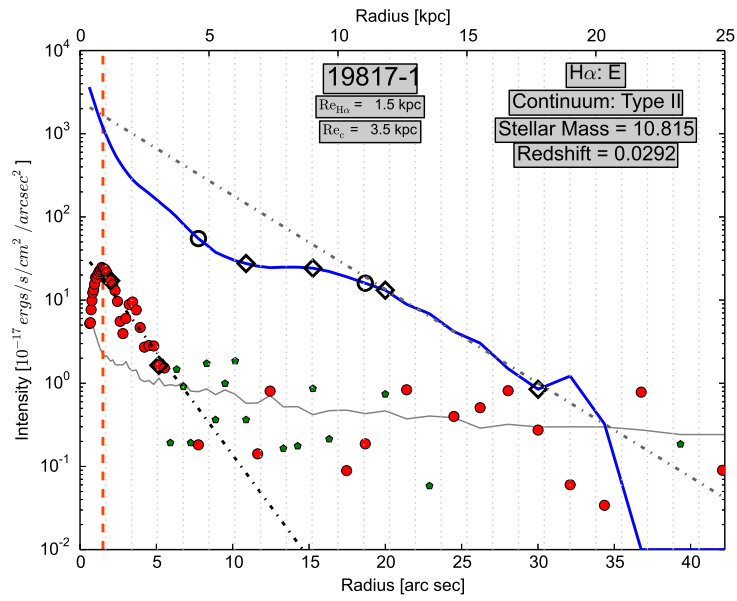
(c)



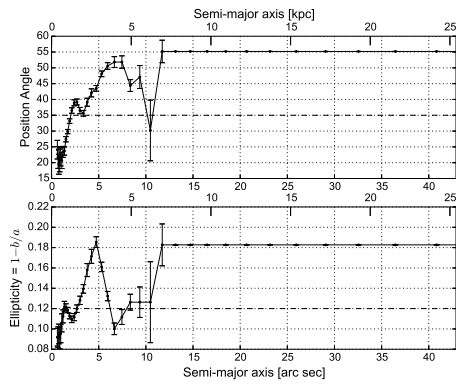
(d)



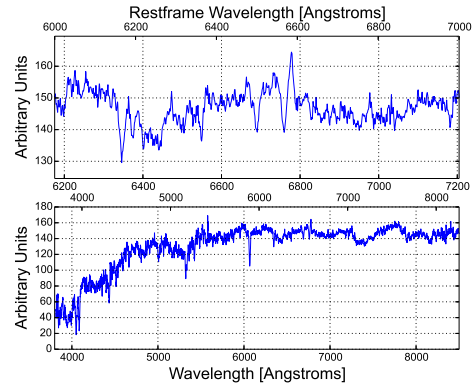
(a)



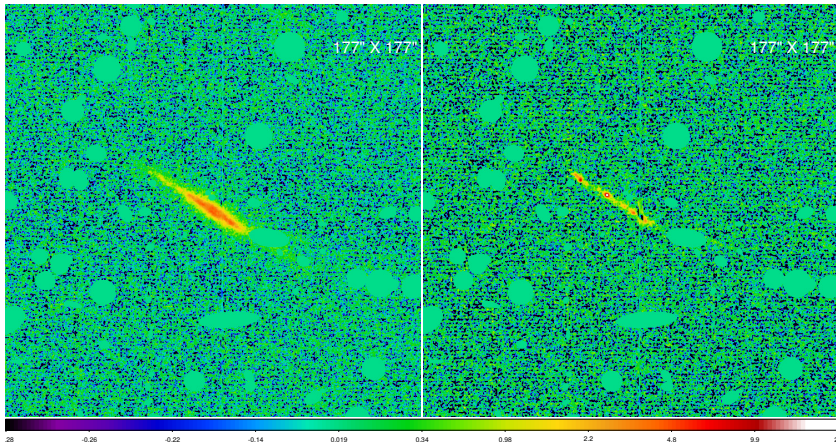
(b)



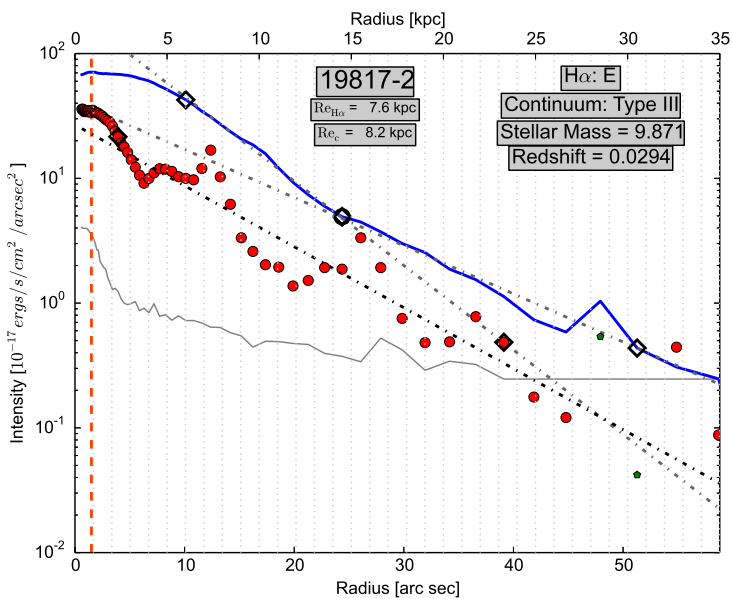
(c)



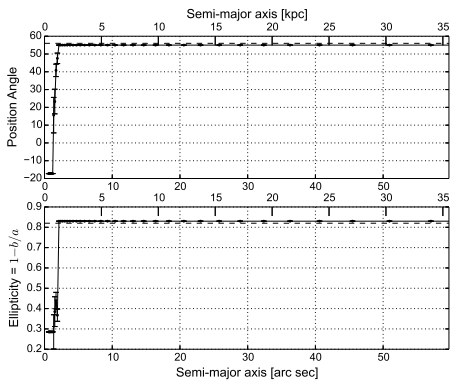
(d)



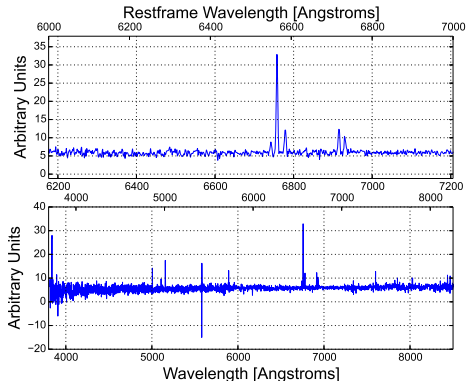
(a)



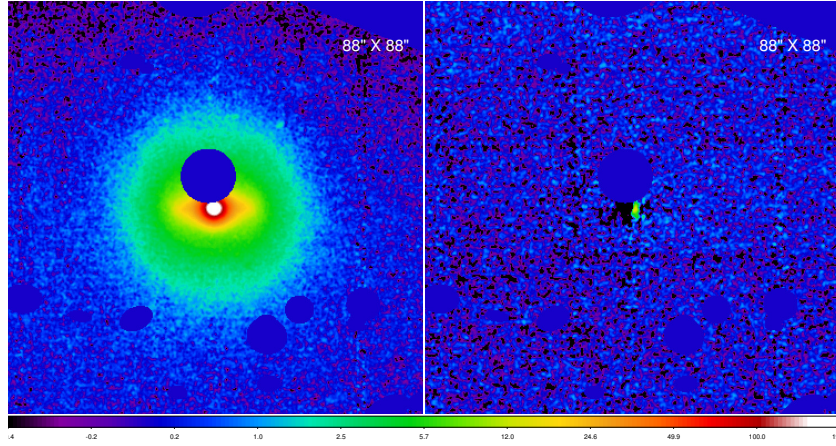
(b)



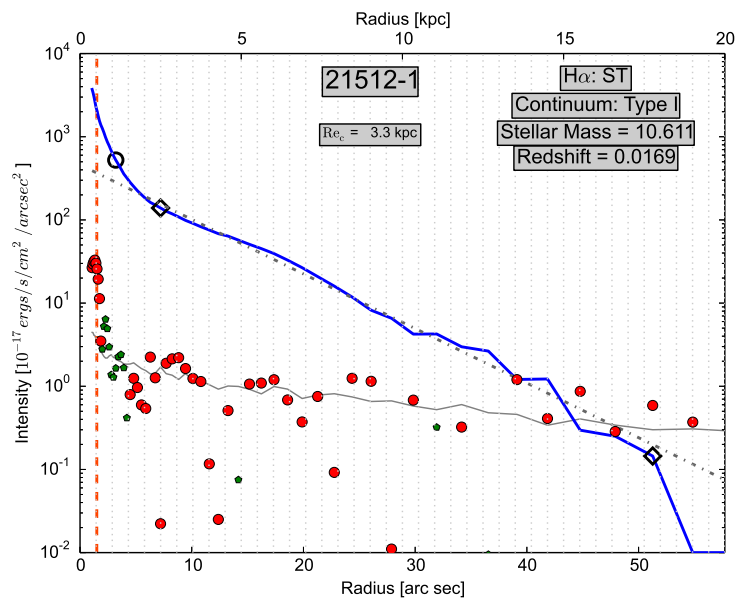
(c)



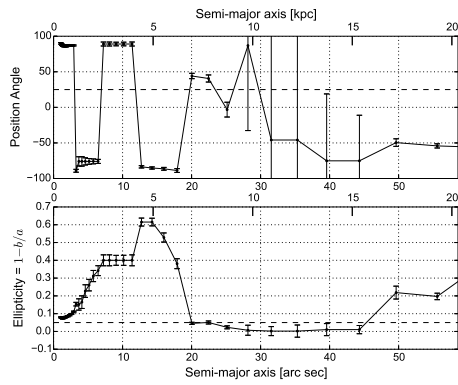
(d)



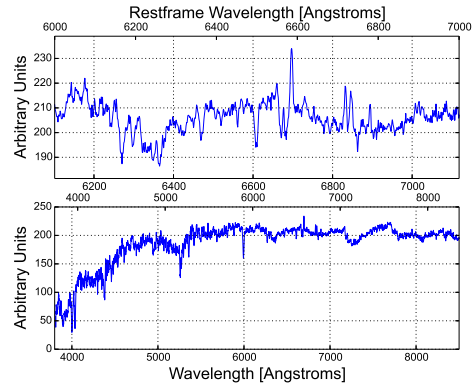
(a)



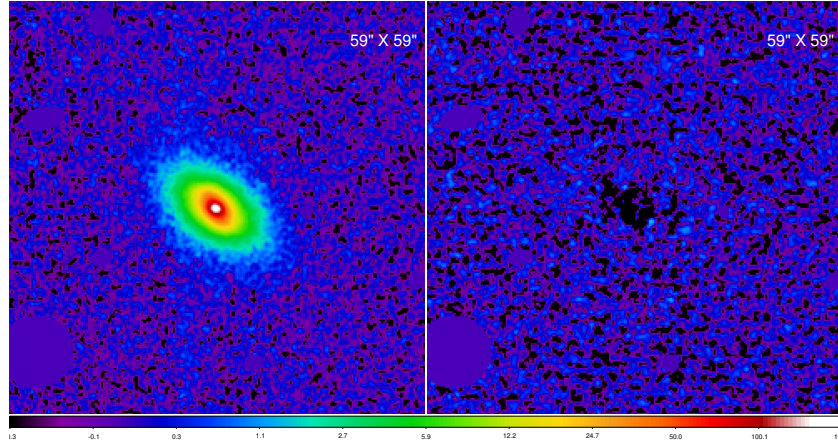
(b)



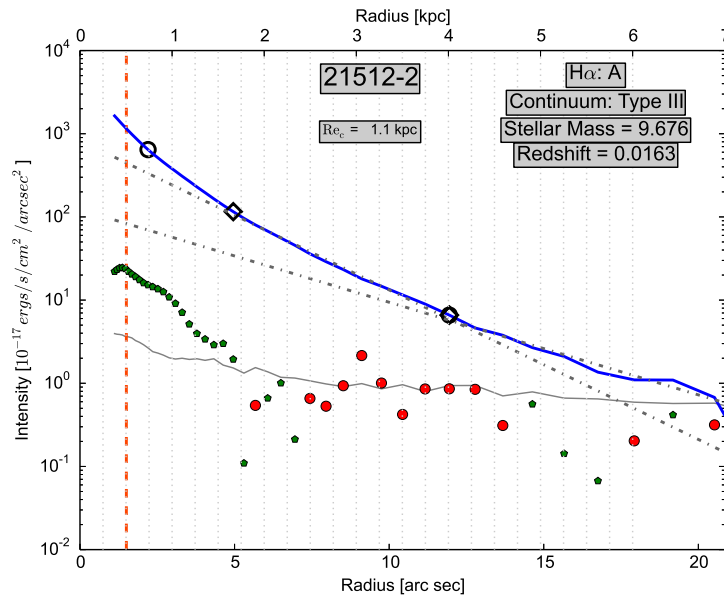
(c)



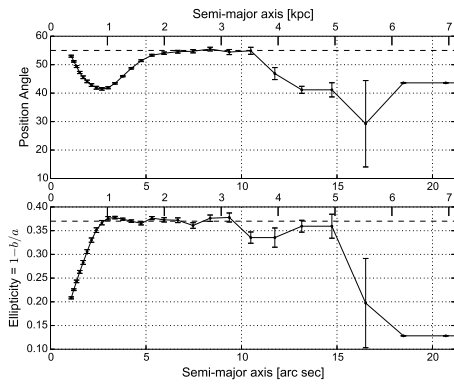
(d)



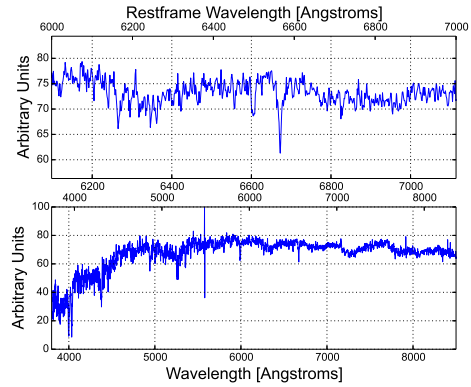
(a)



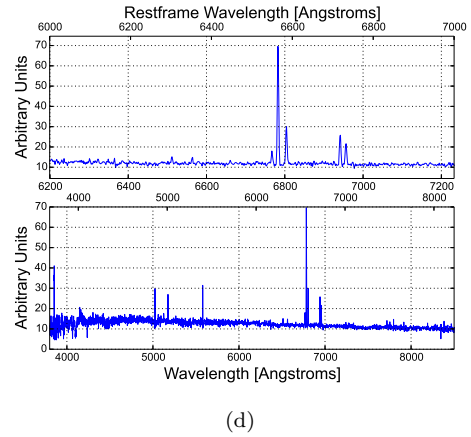
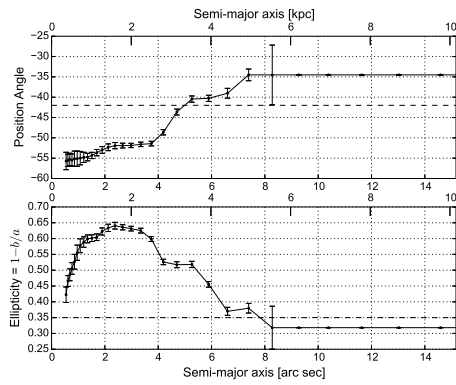
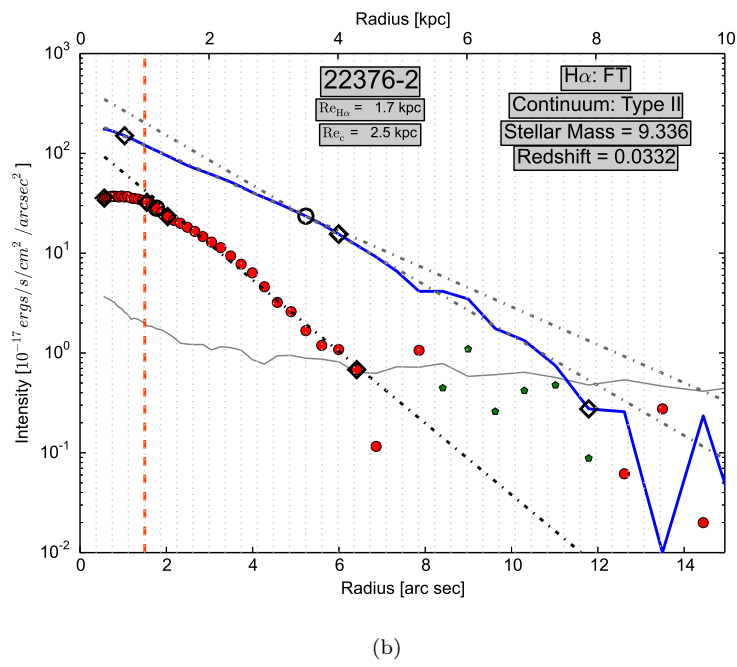
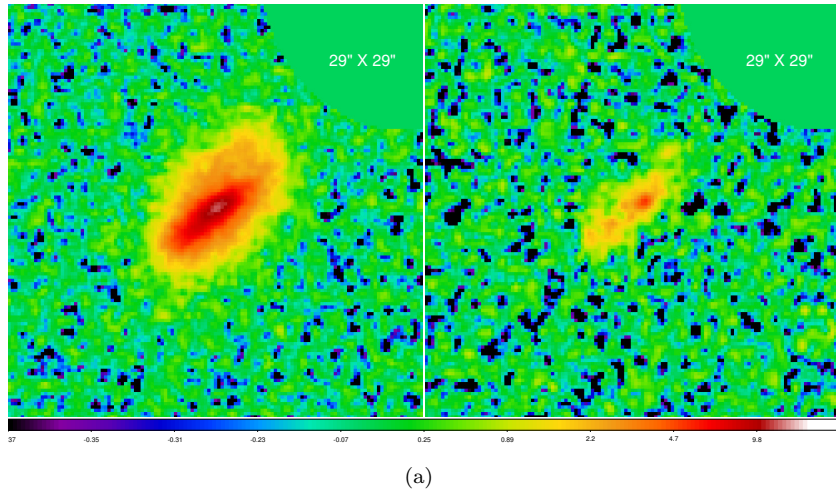
(b)

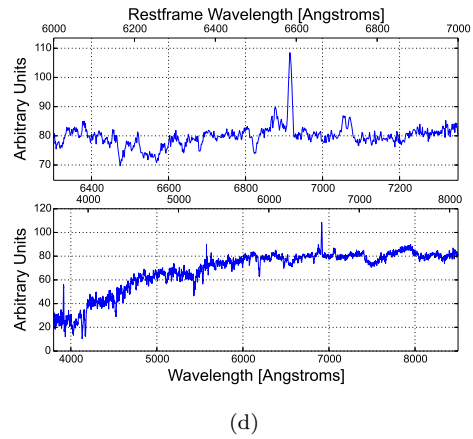
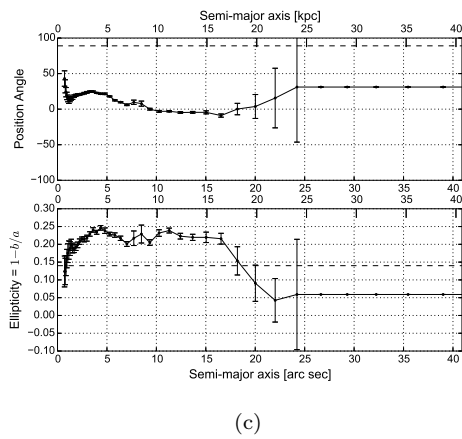
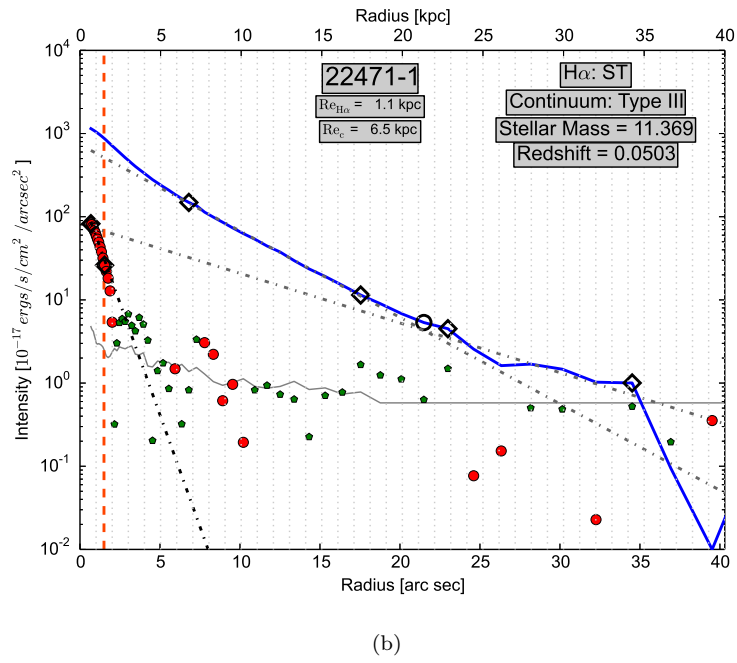
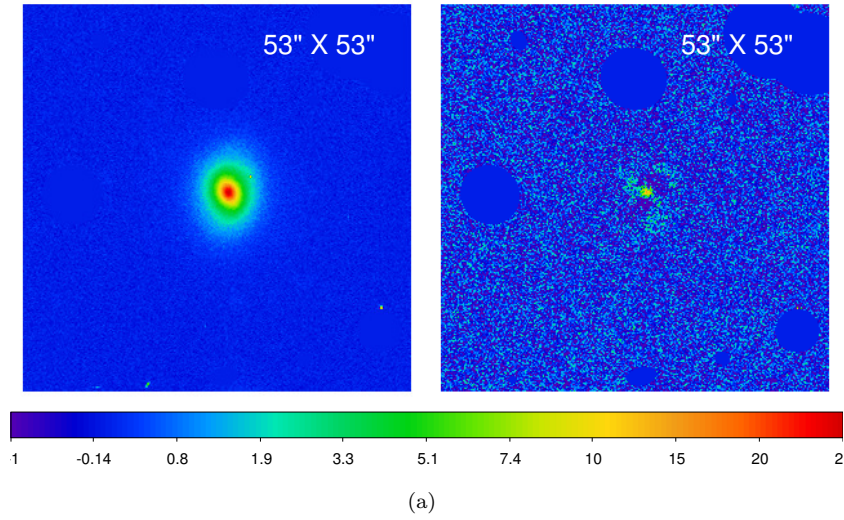


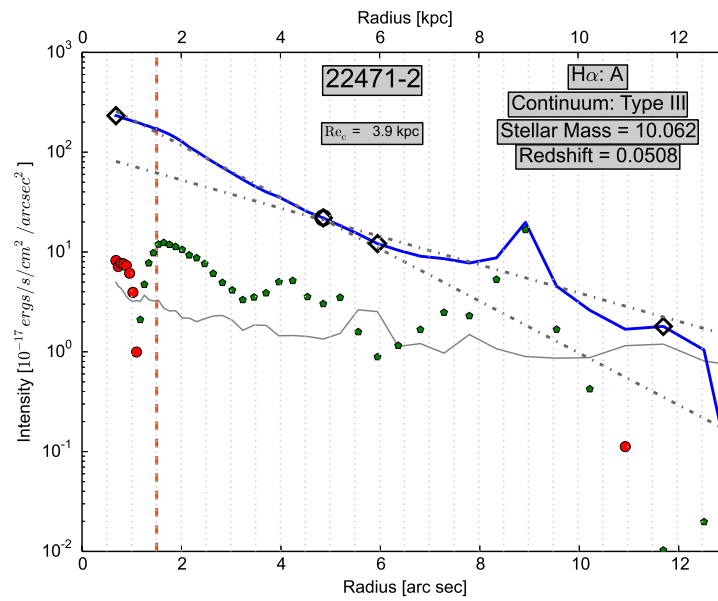
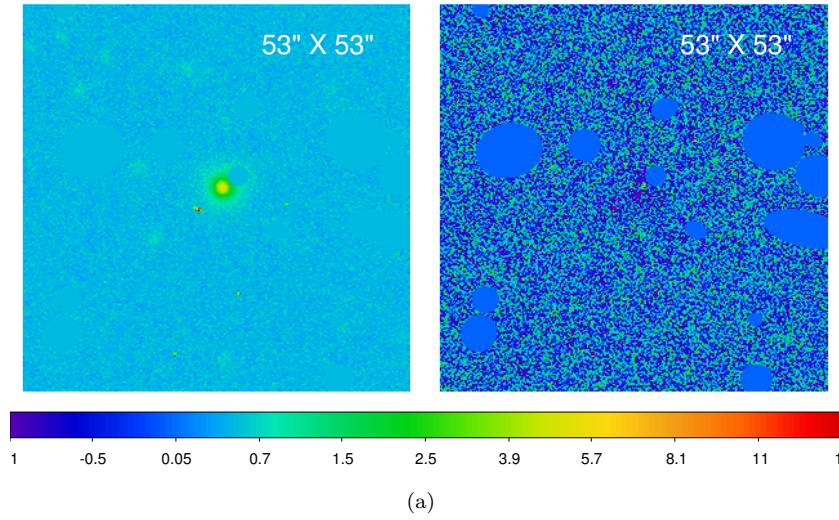
(c)



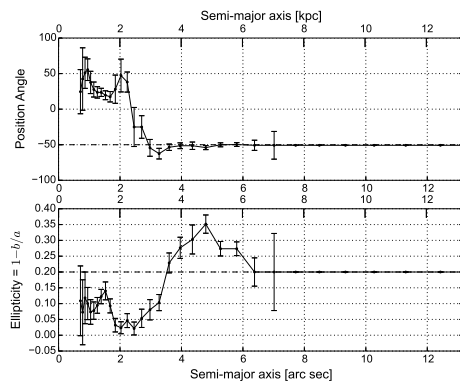
(d)



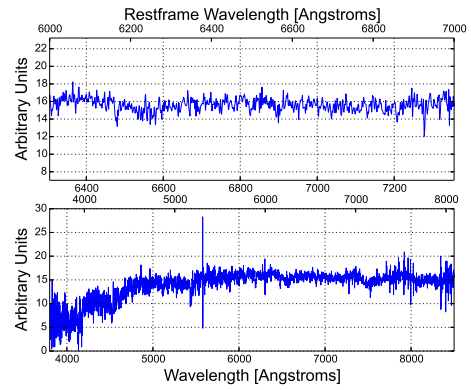




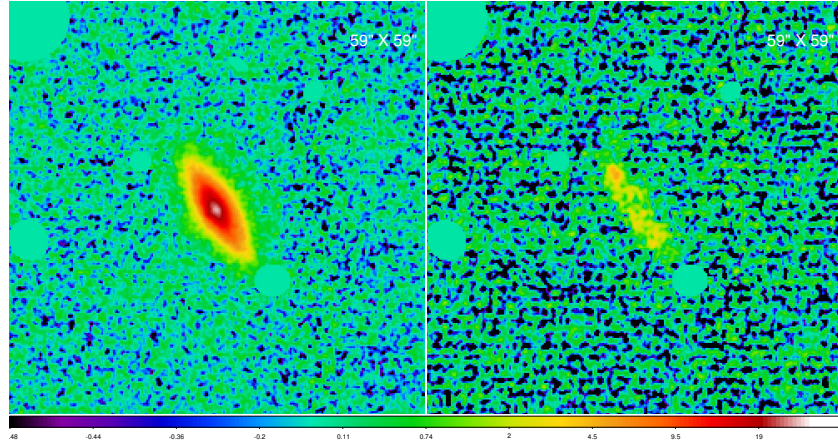
(b)



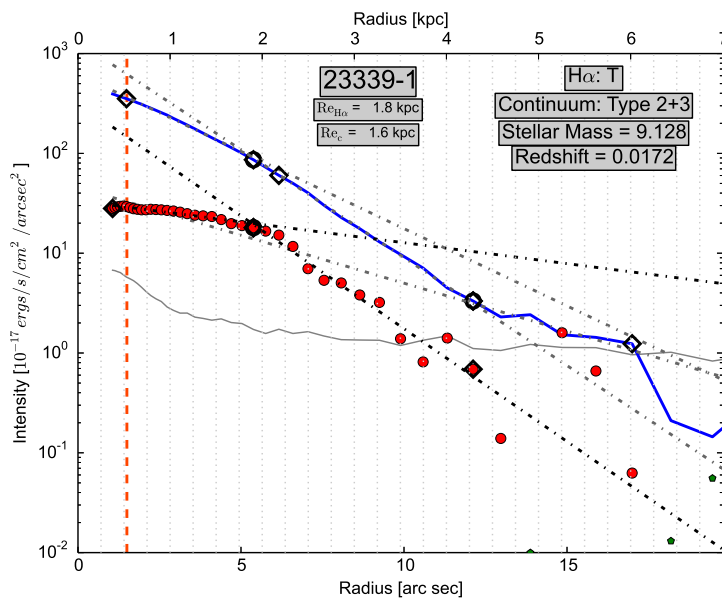
(c)



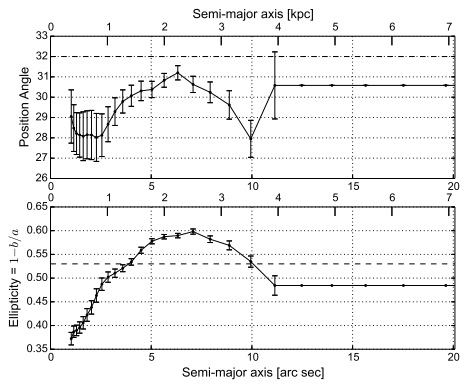
(d)



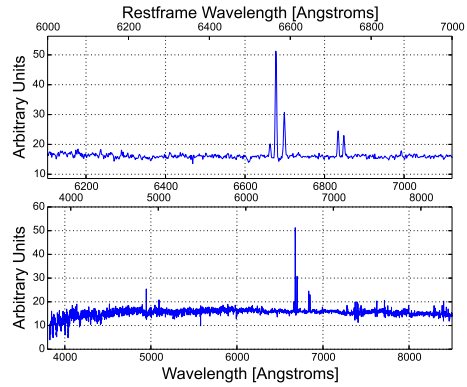
(a)



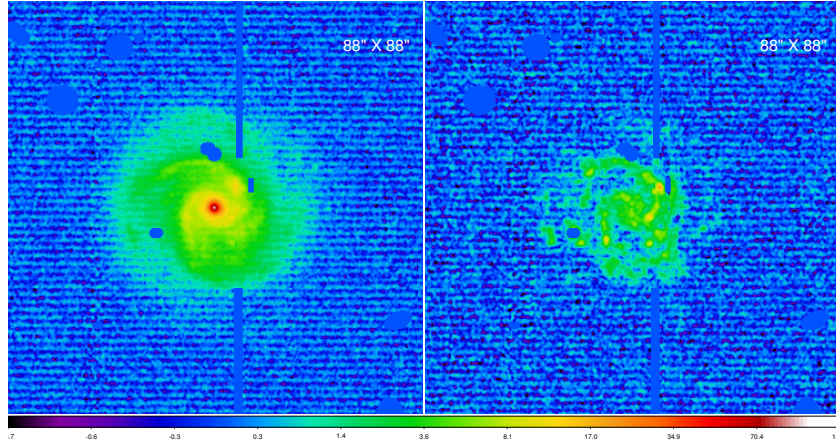
(b)



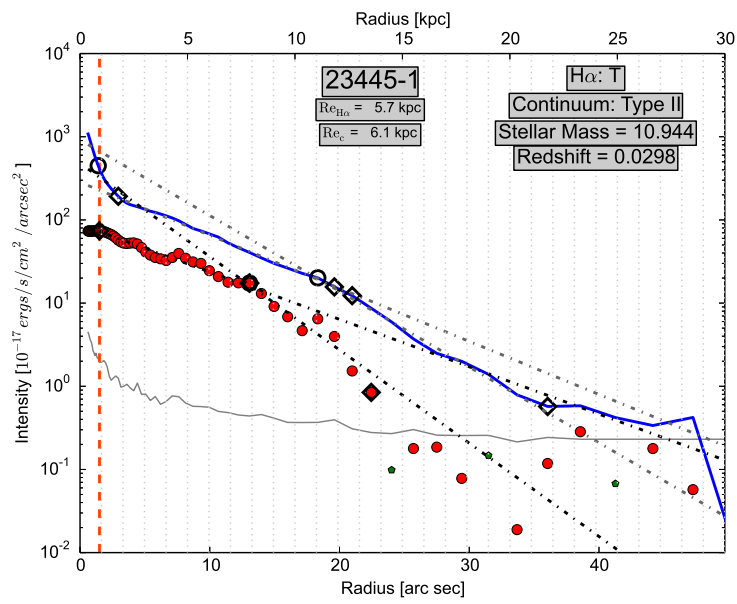
(c)



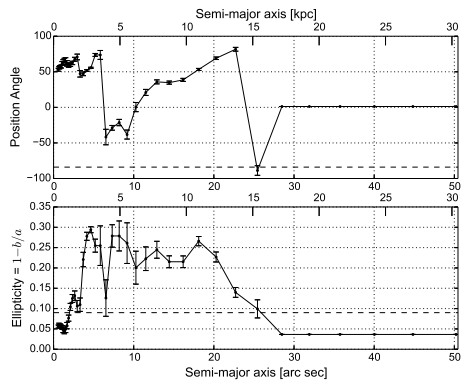
(d)



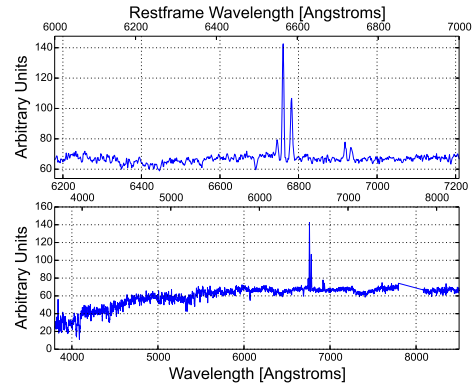
(a)



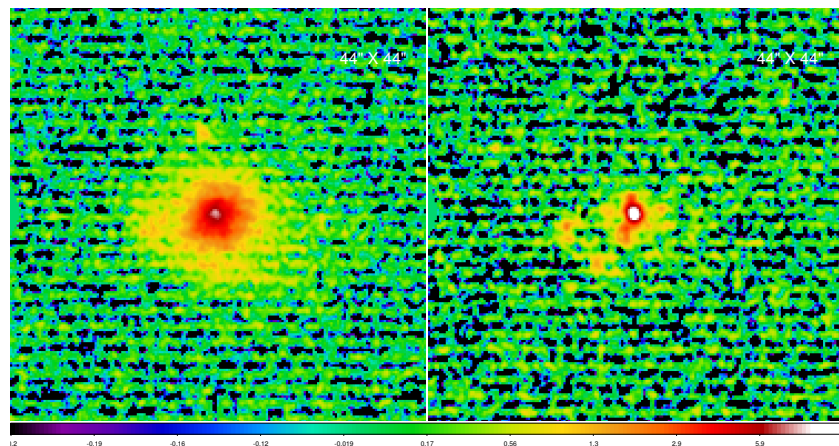
(b)



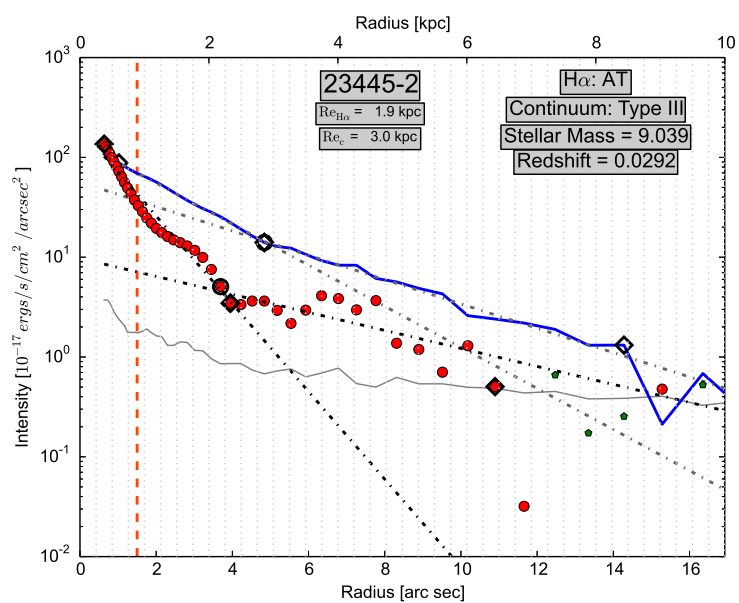
(c)



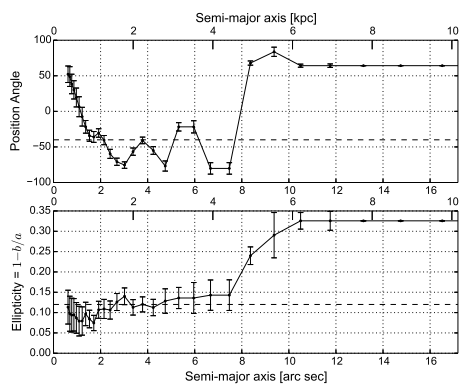
(d)



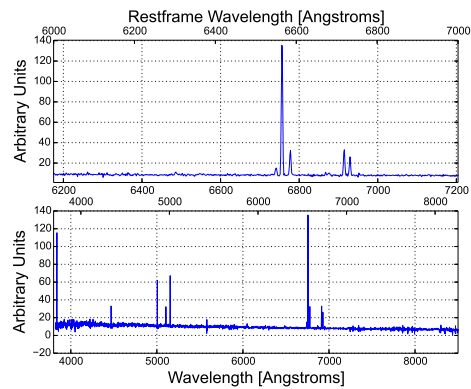
(a)



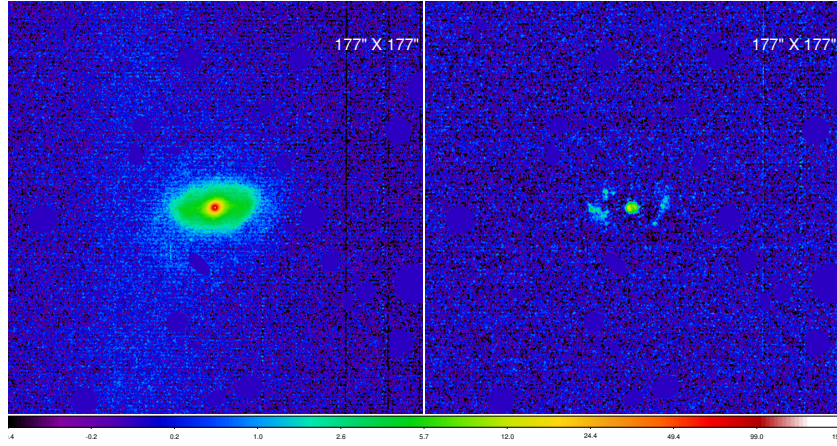
(b)



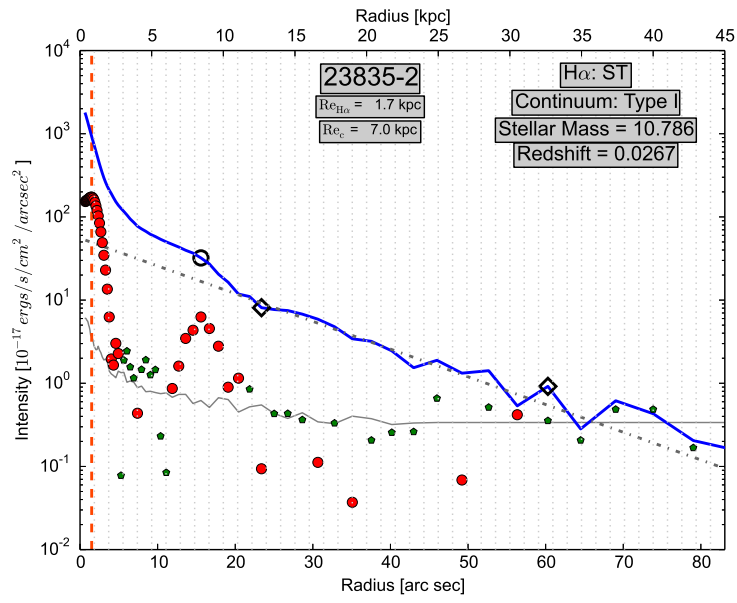
(c)



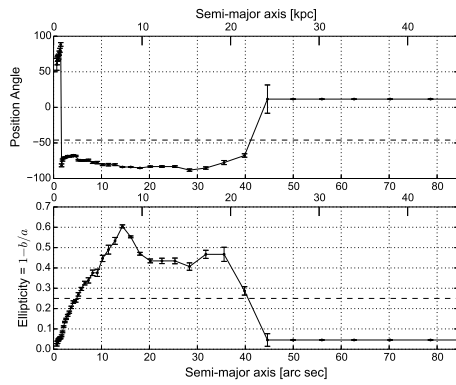
(d)



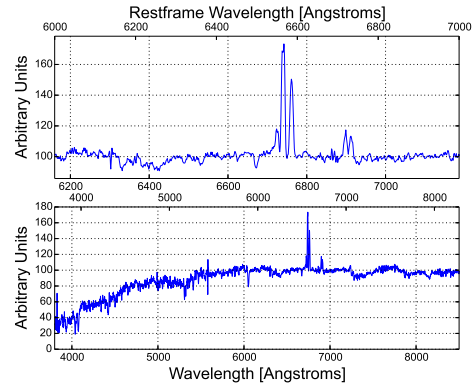
(a)



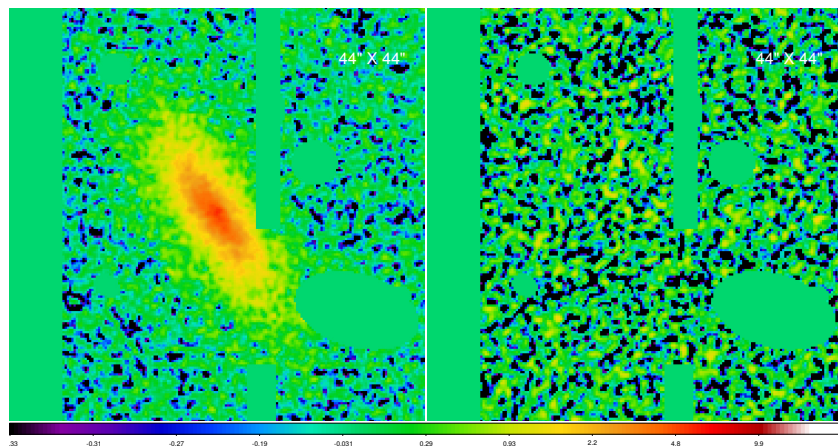
(b)



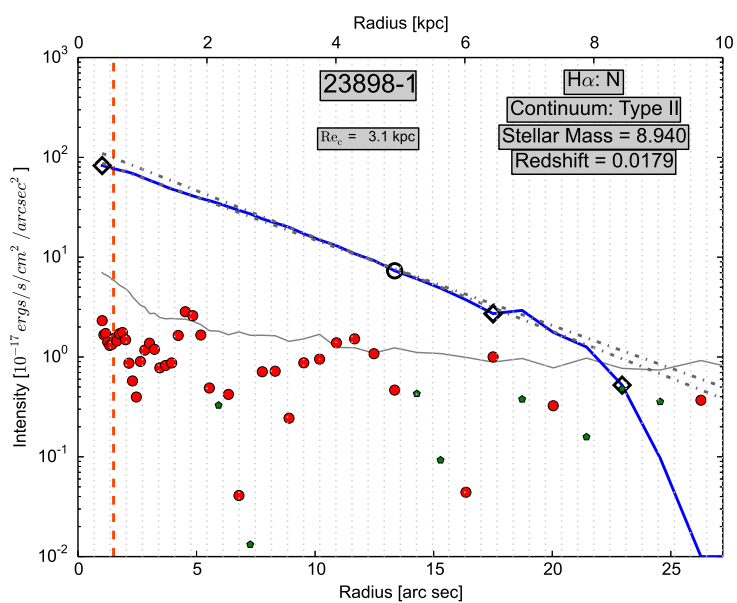
(c)



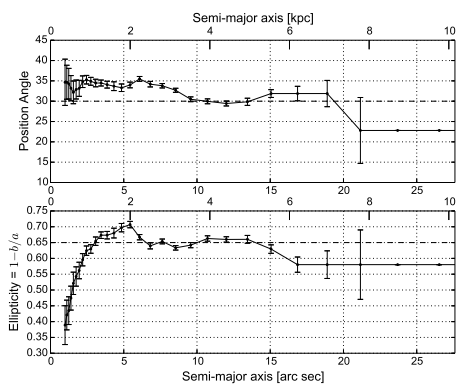
(d)



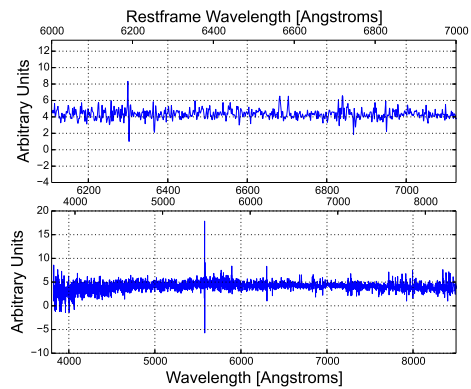
(a)



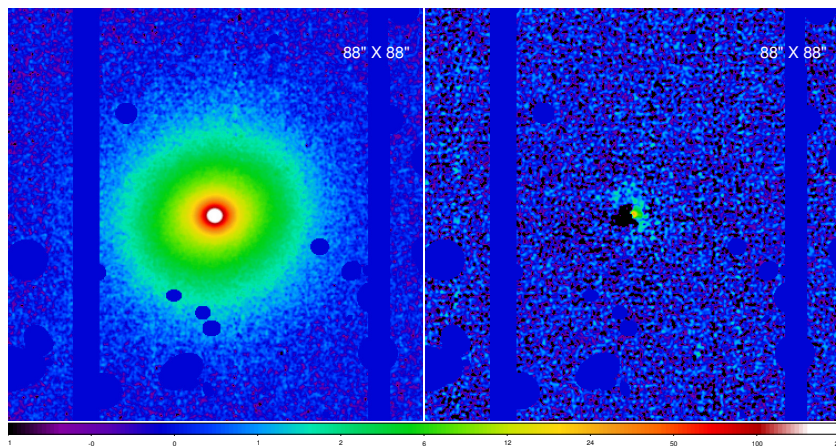
(b)



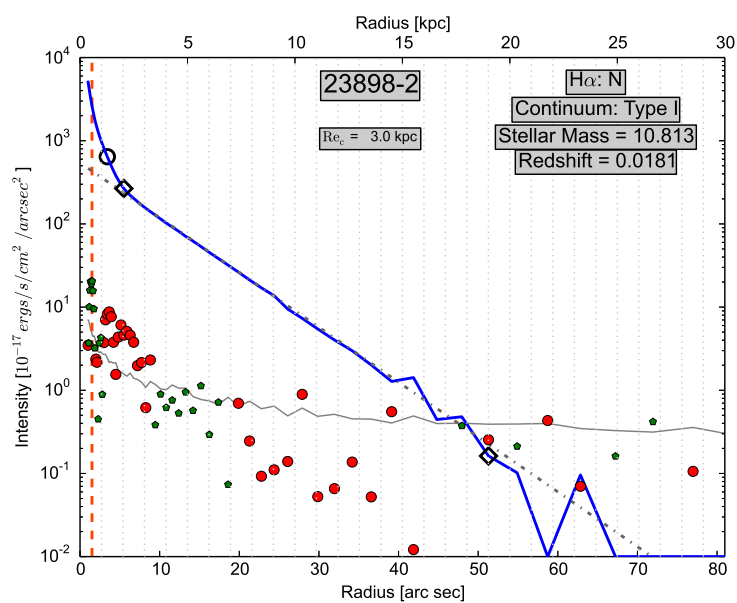
(c)



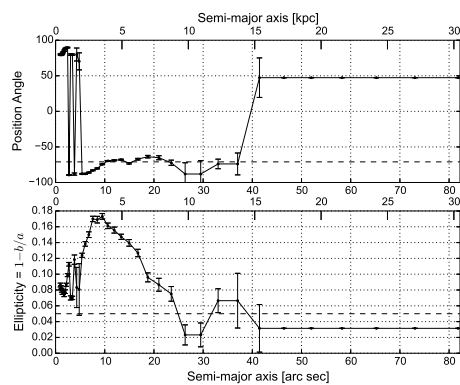
(d)



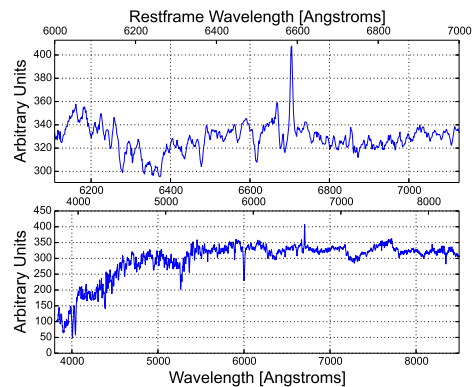
(a)



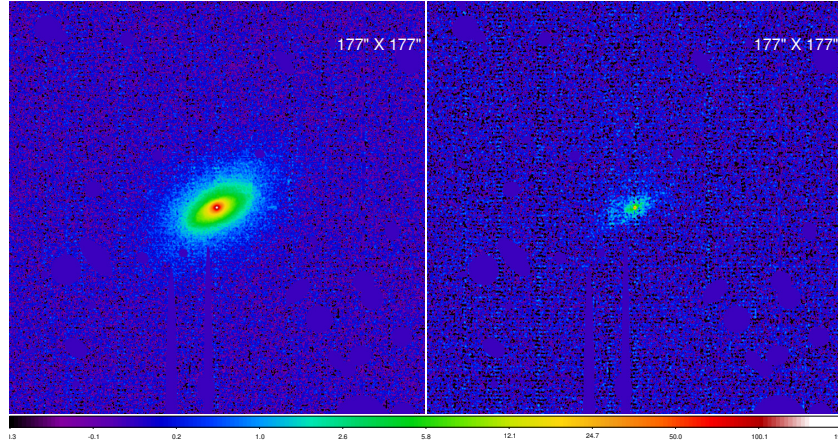
(b)



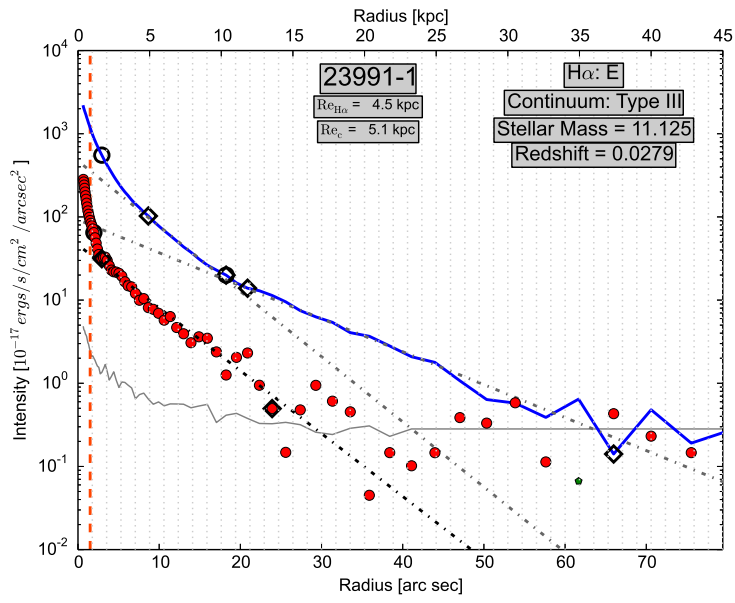
(c)



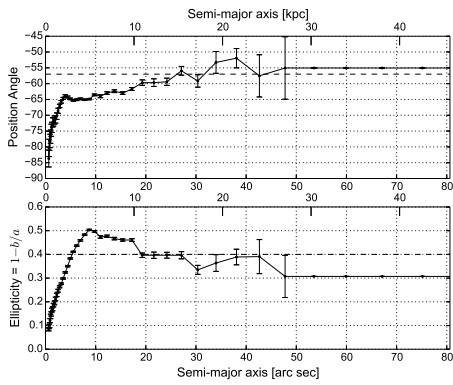
(d)



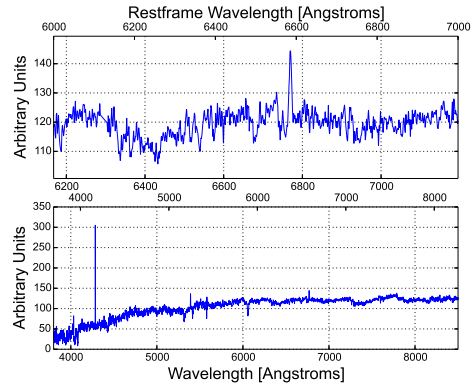
(a)



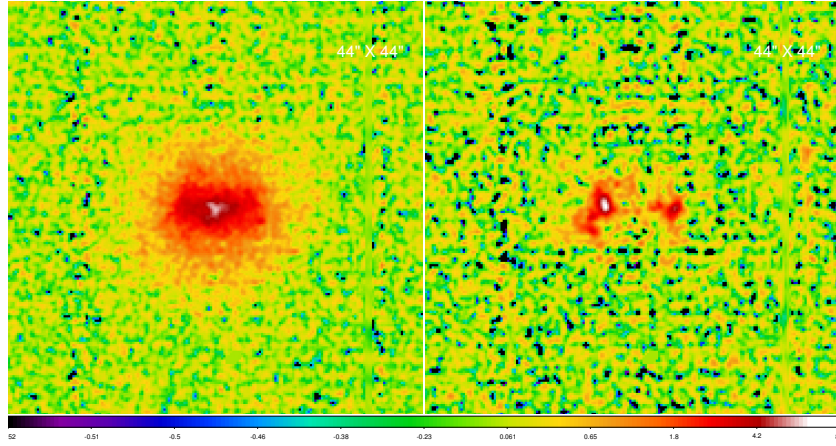
(b)



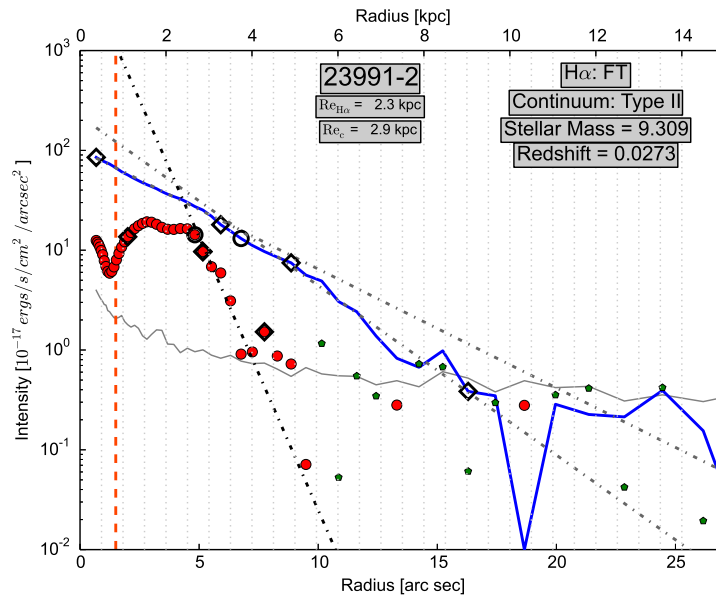
(c)



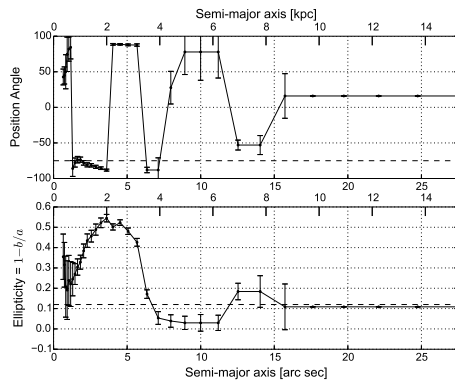
(d)



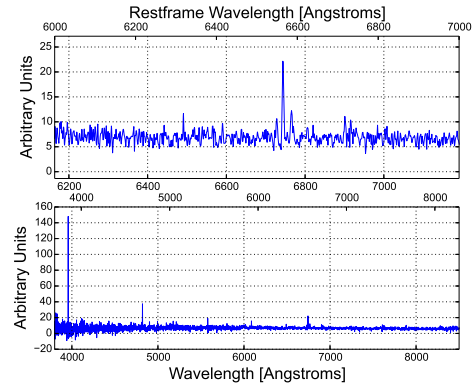
(a)



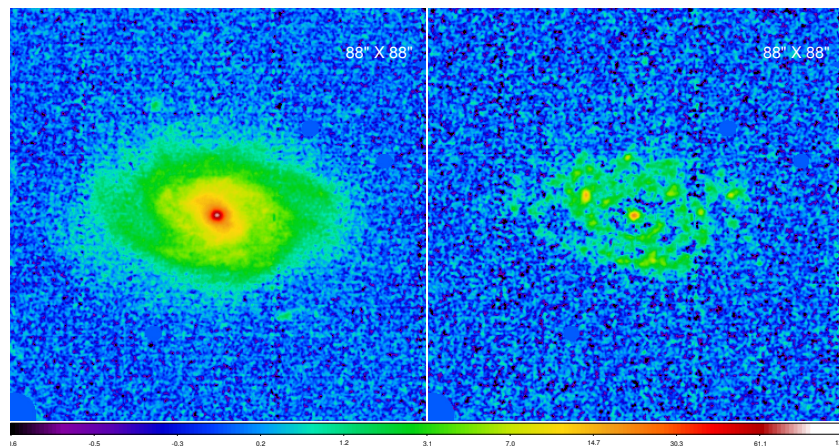
(b)



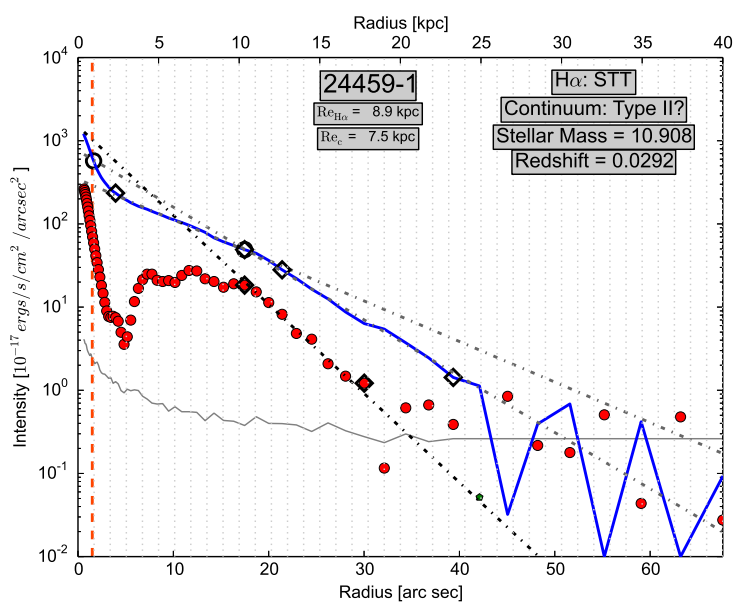
(c)



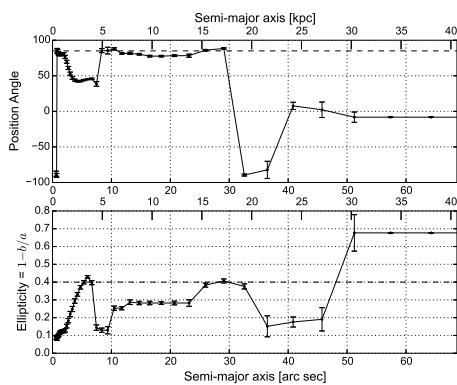
(d)



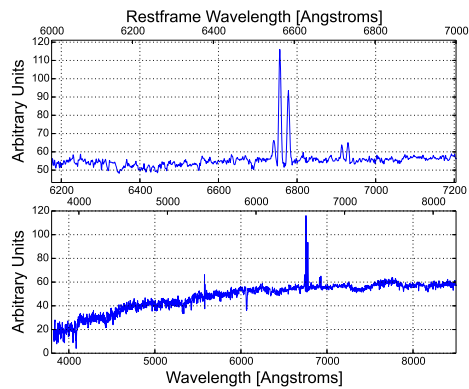
(a)



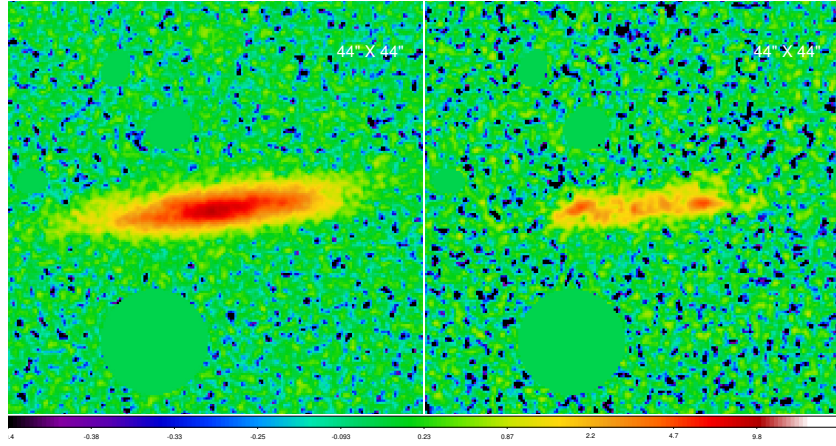
(b)



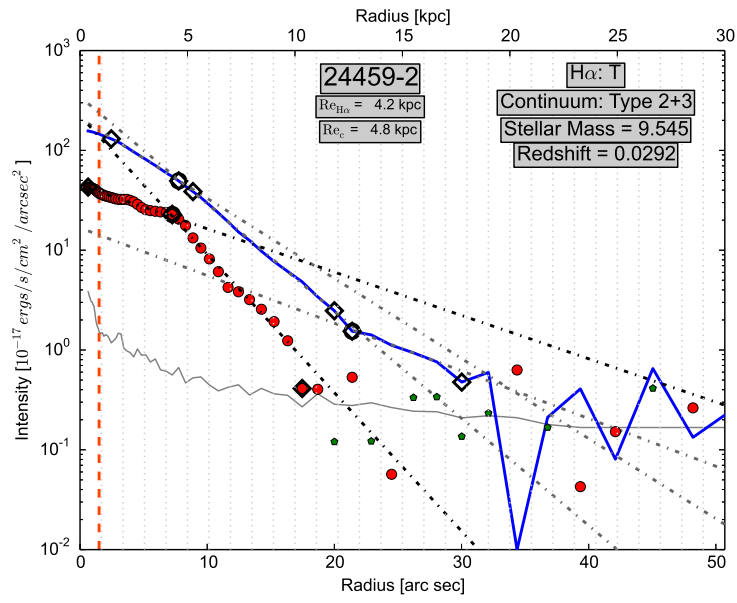
(c)



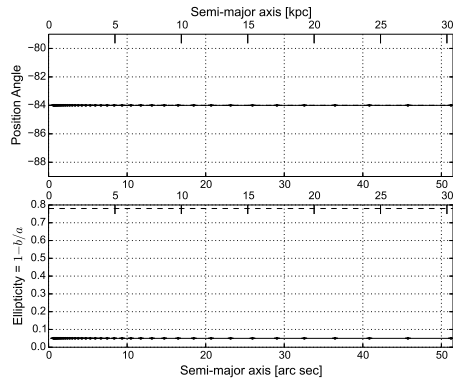
(d)



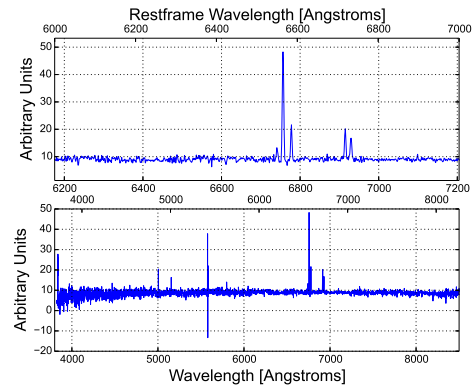
(a)



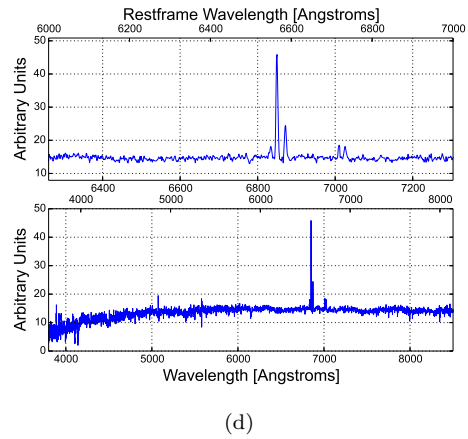
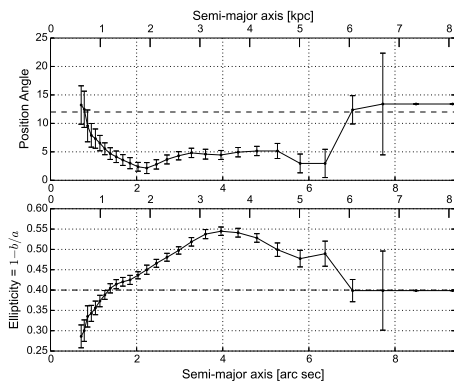
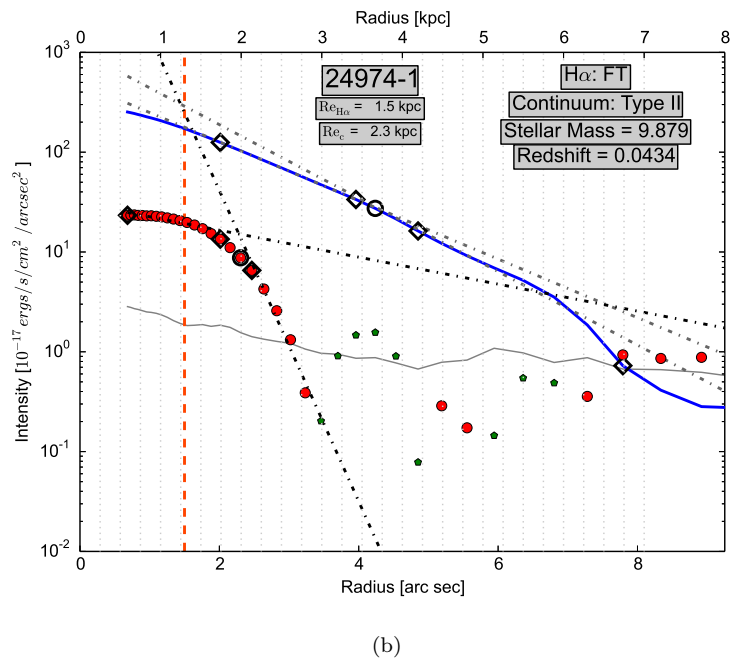
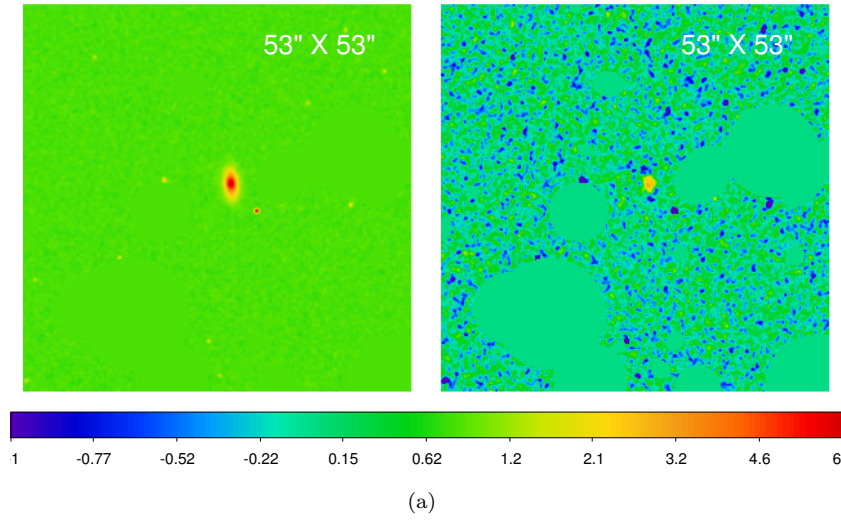
(b)

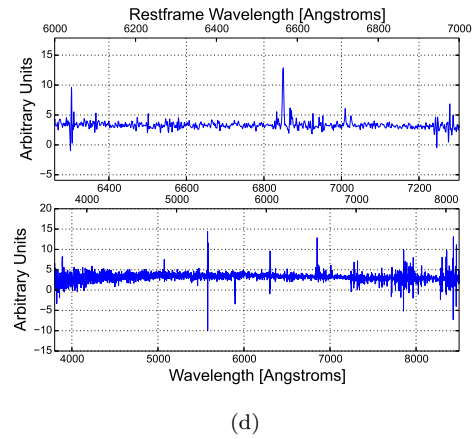
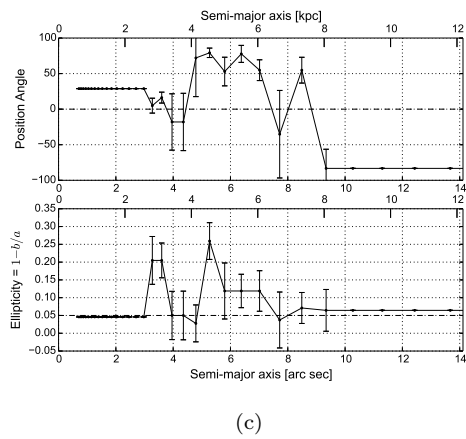
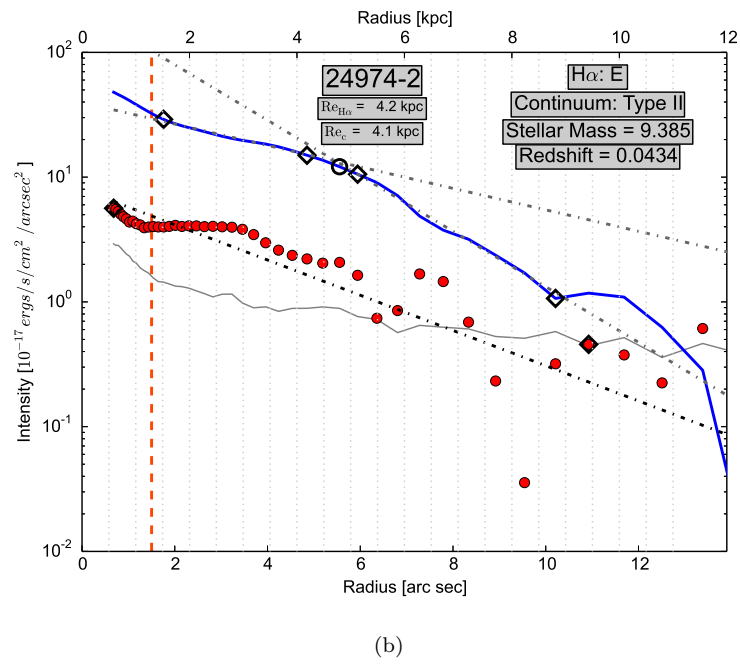
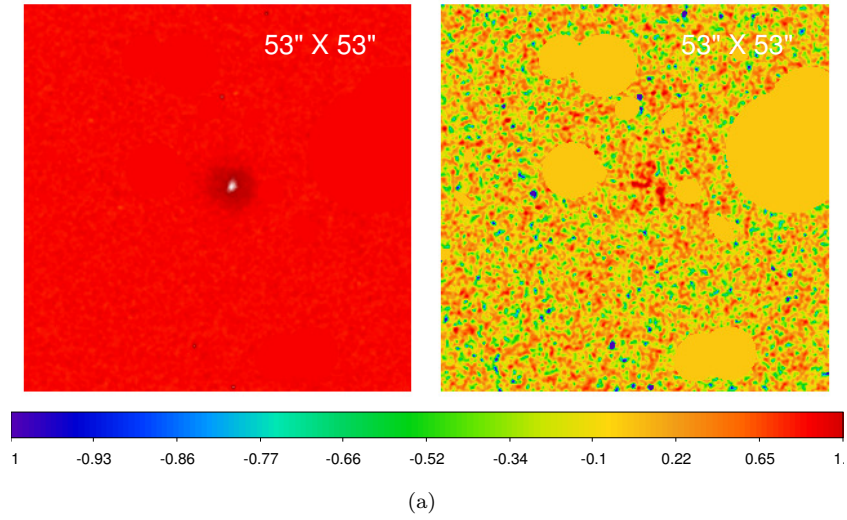


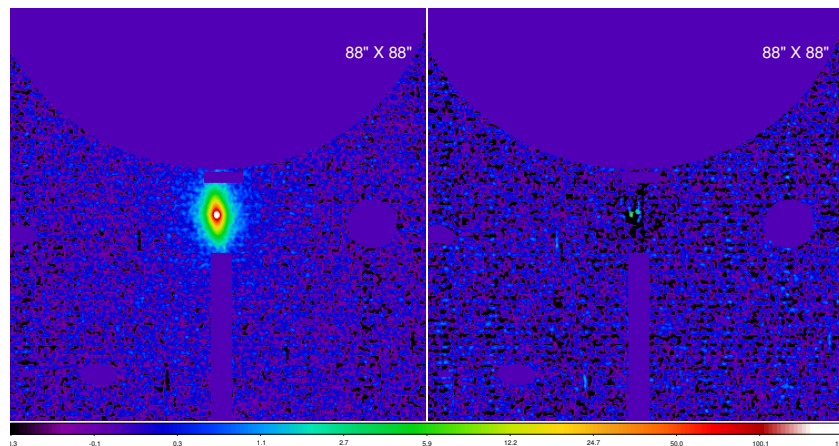
(c)



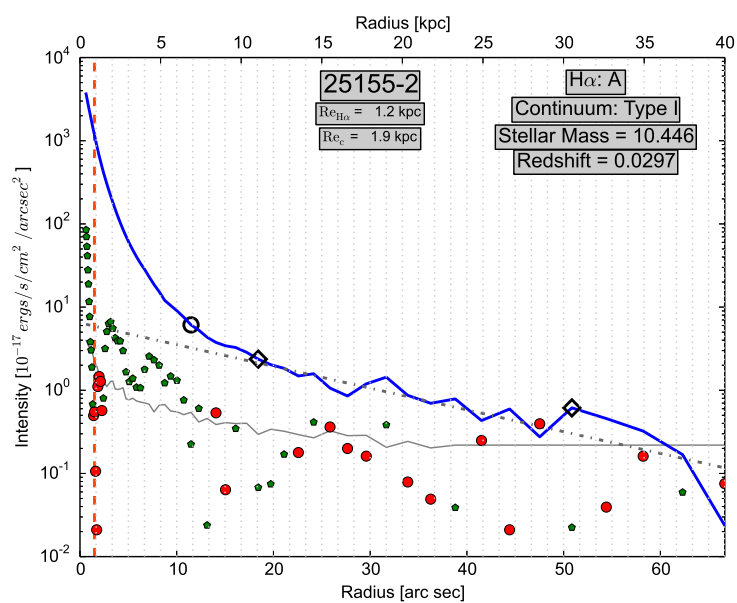
(d)



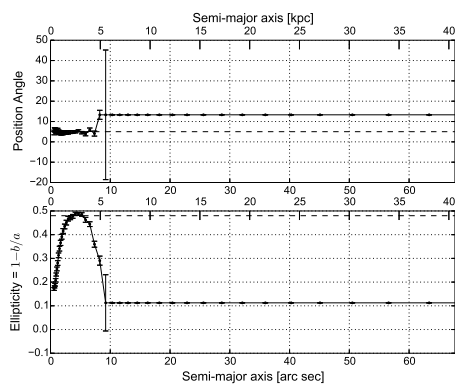




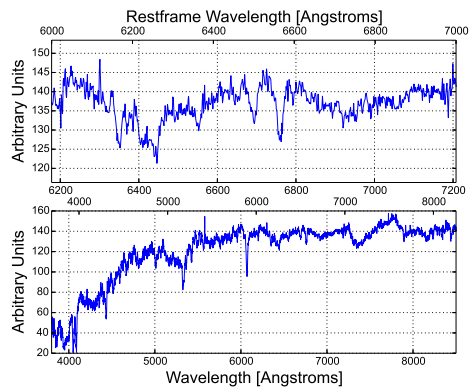
(a)



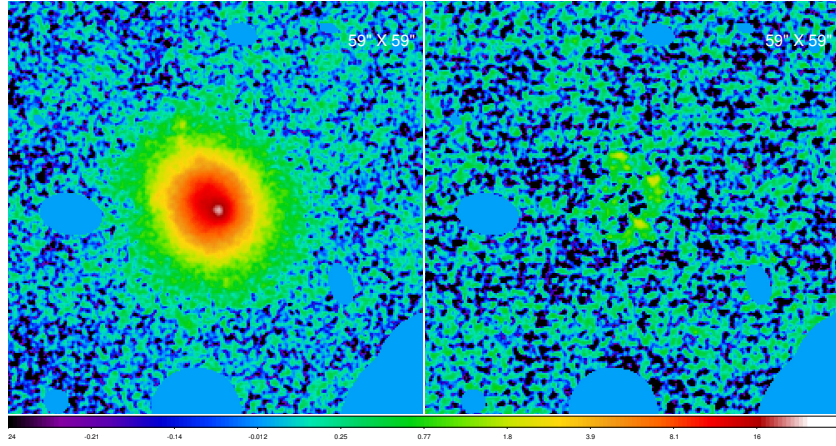
(b)



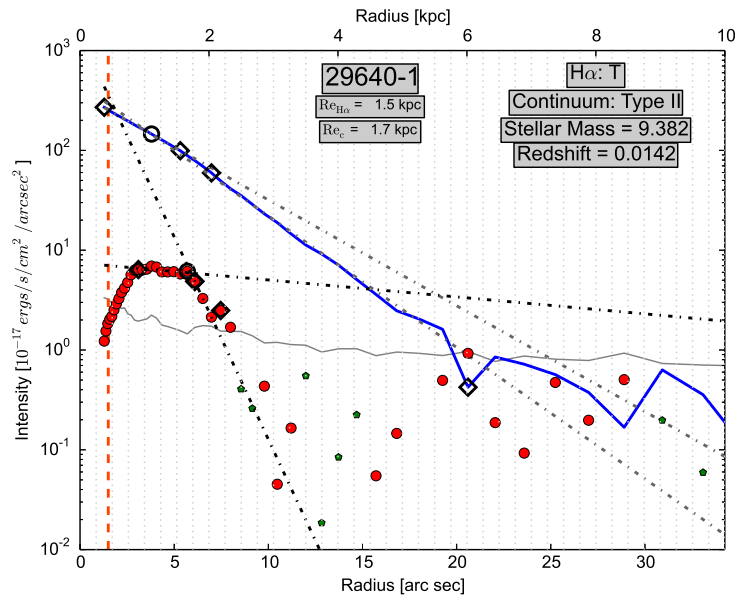
(c)



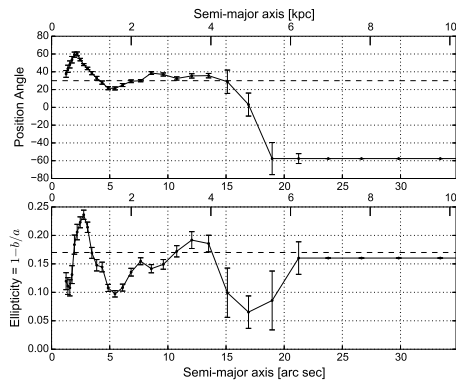
(d)



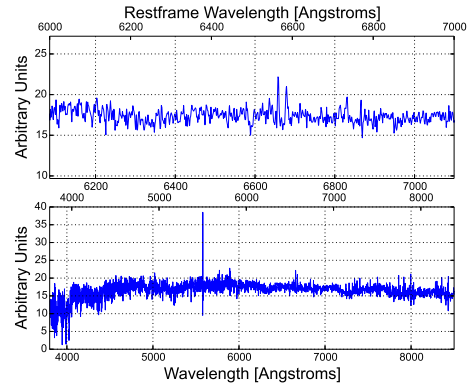
(a)



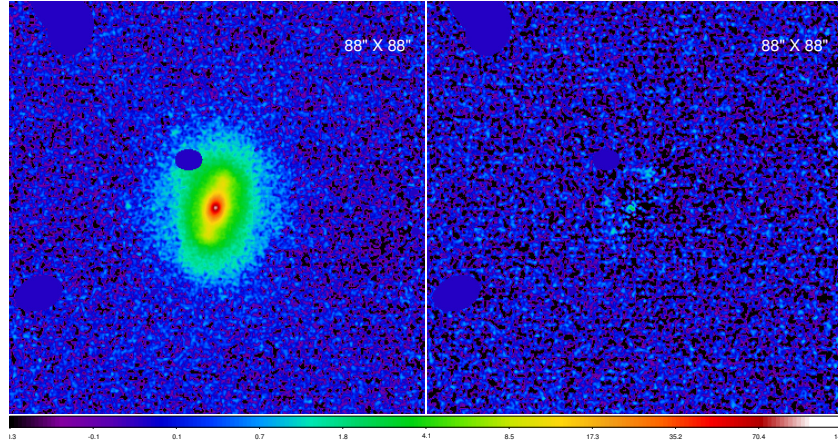
(b)



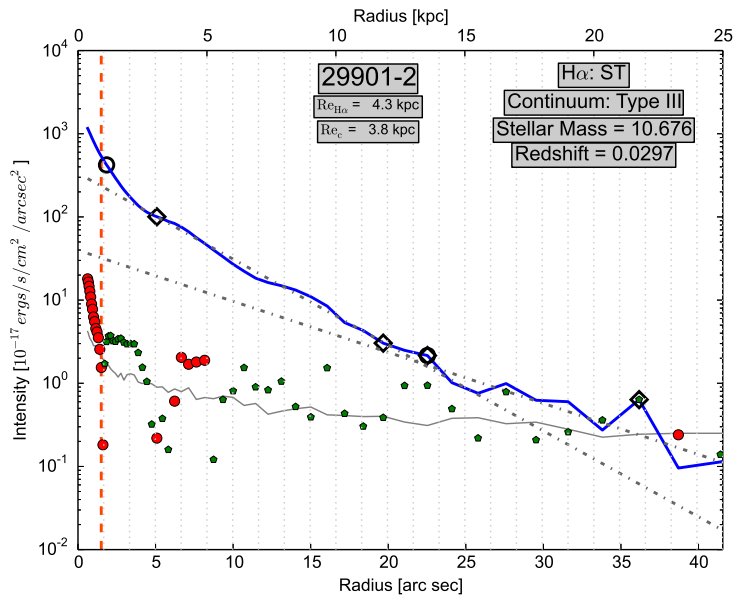
(c)



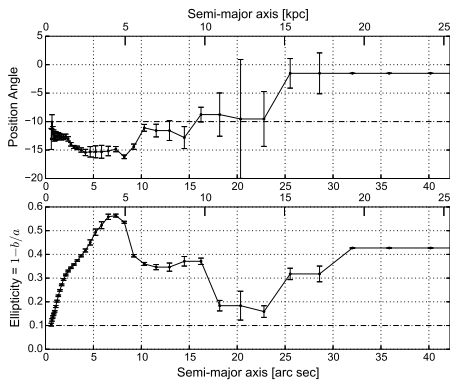
(d)



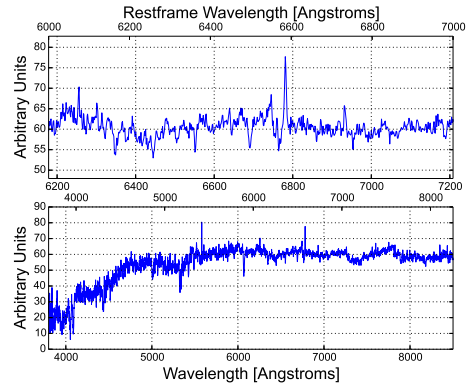
(a)



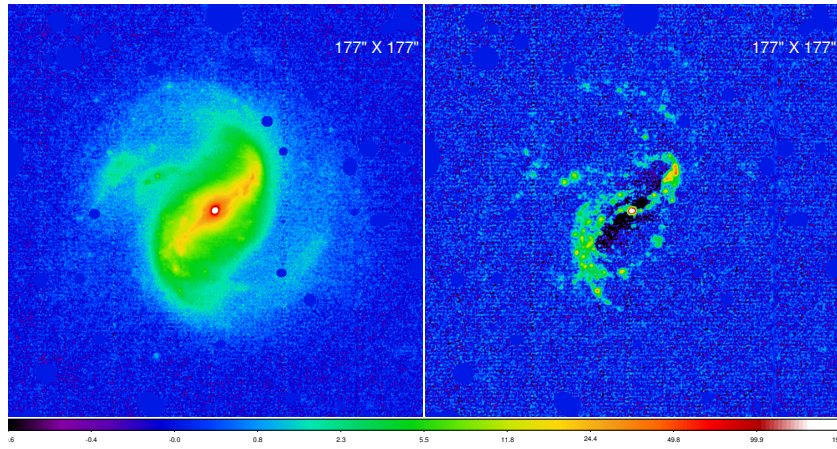
(b)



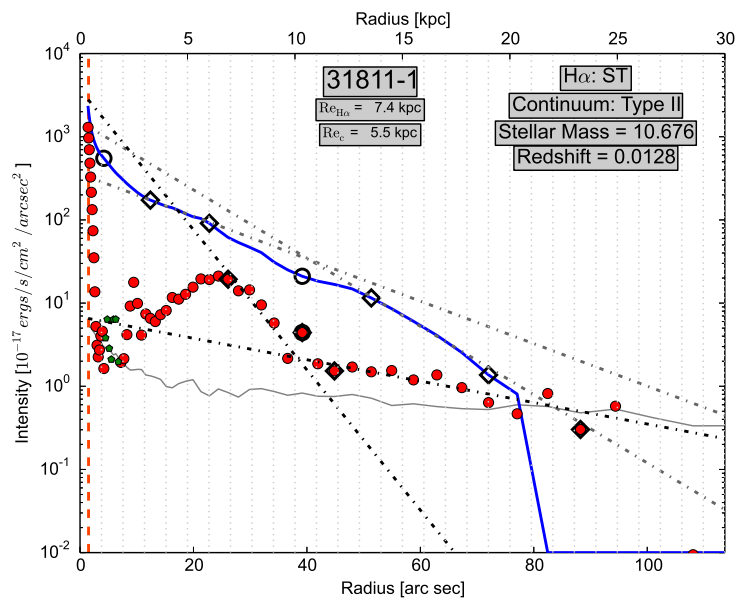
(c)



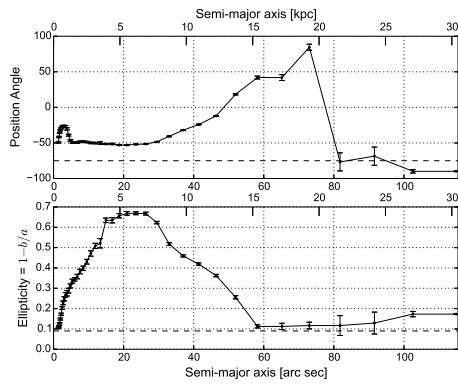
(d)



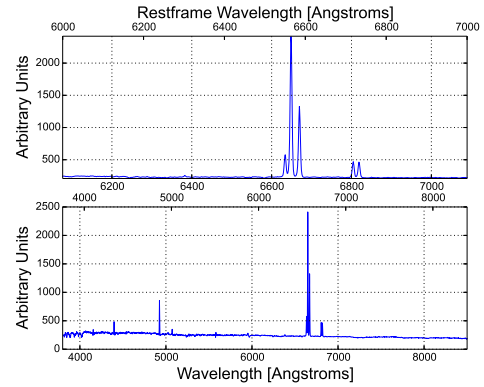
(a)



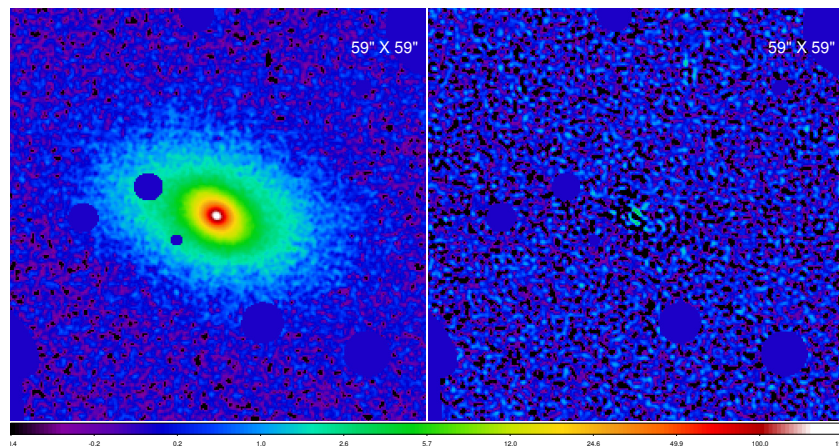
(b)



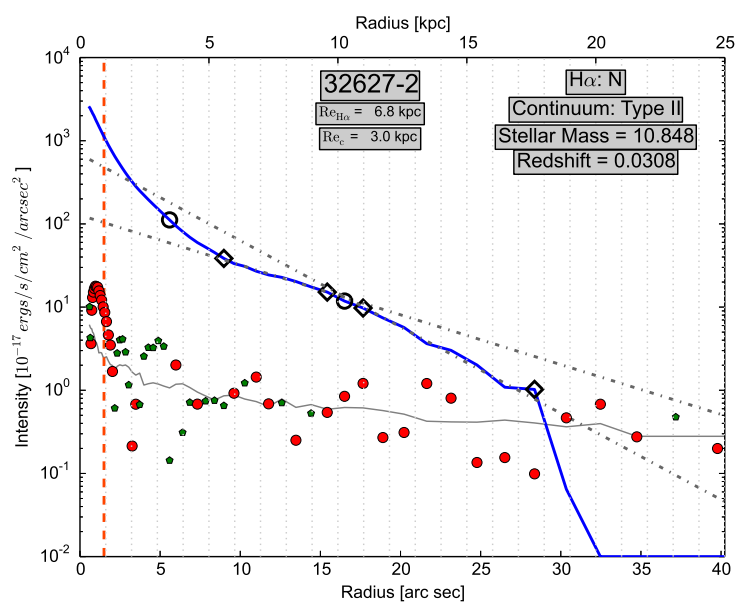
(c)



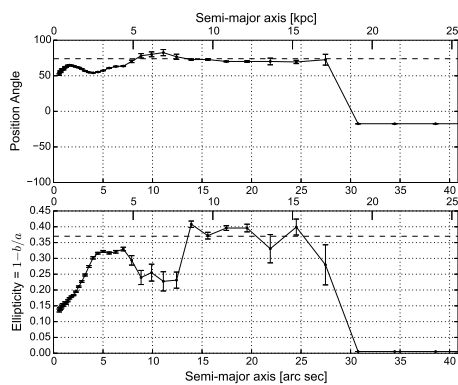
(d)



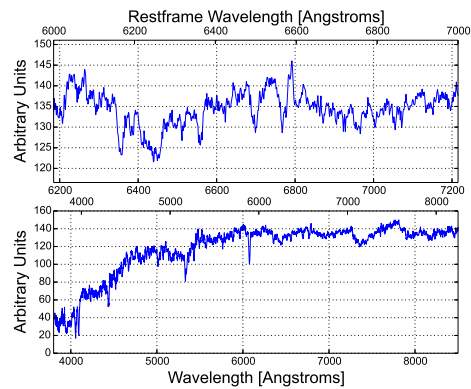
(a)



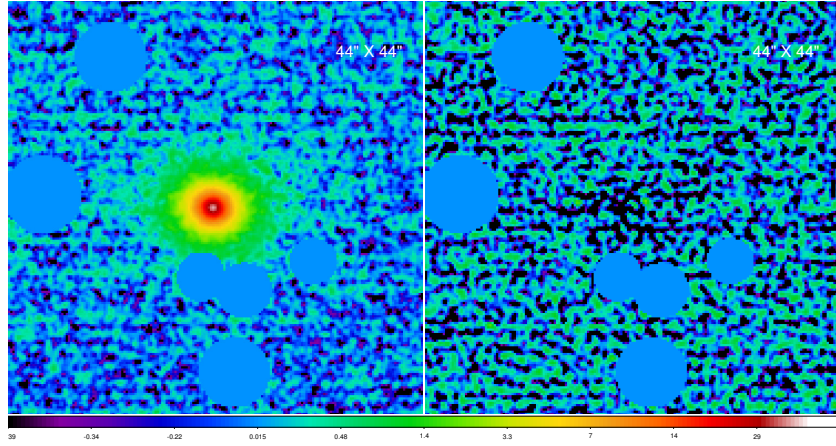
(b)



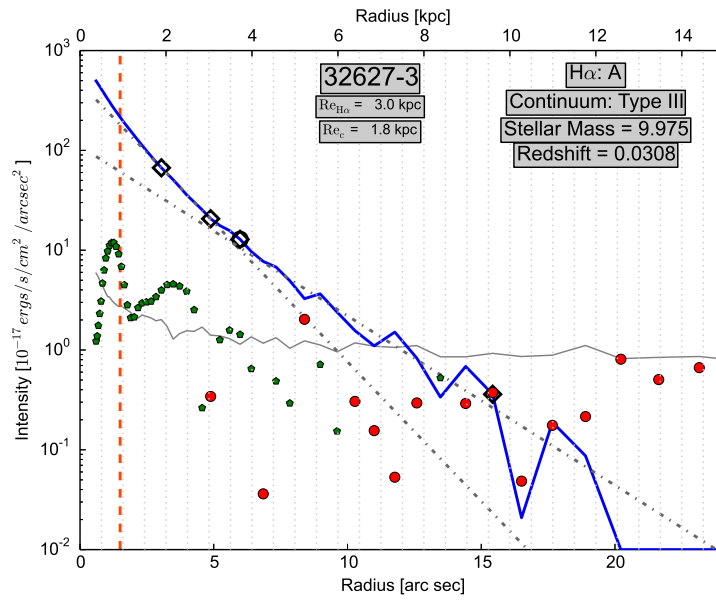
(c)



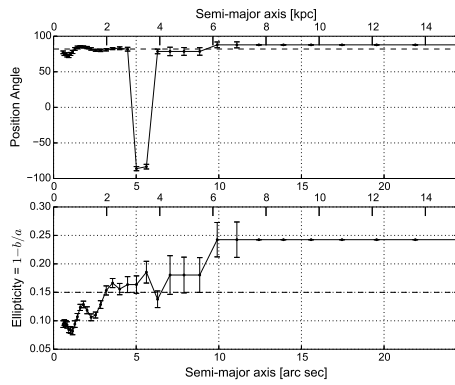
(d)



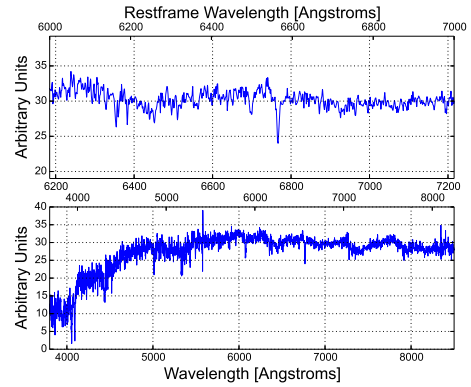
(a)



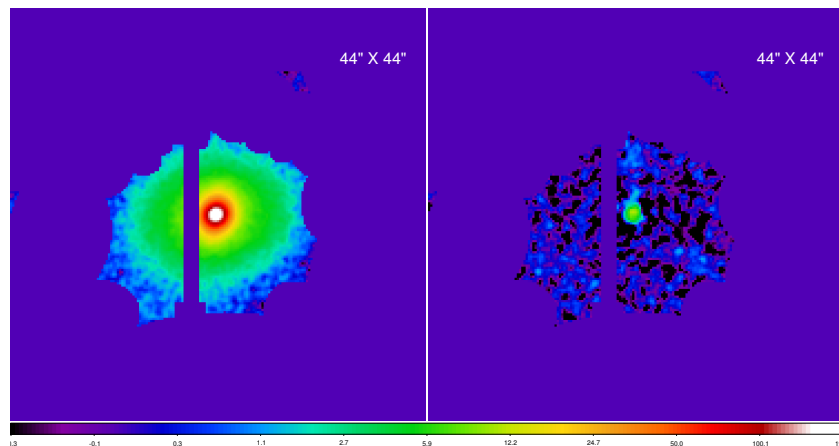
(b)



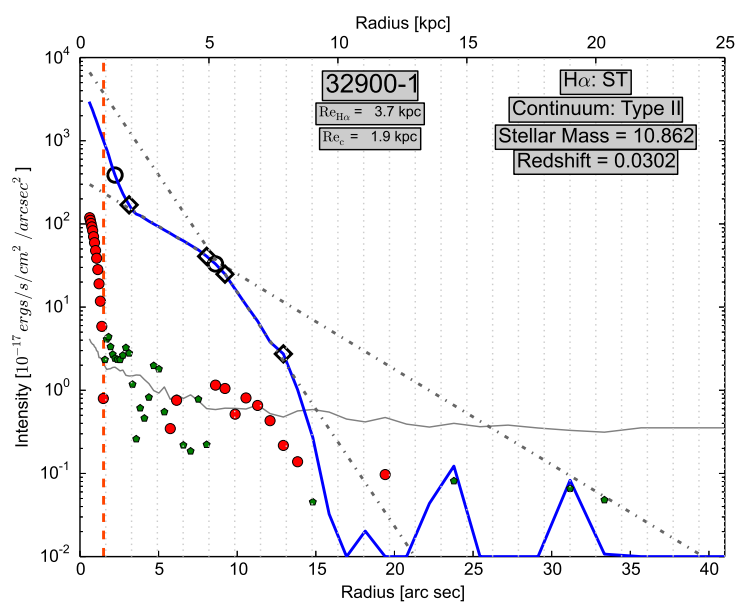
(c)



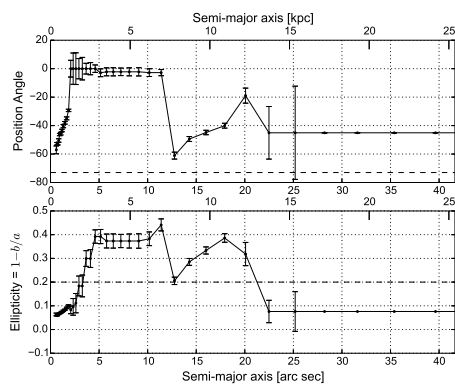
(d)



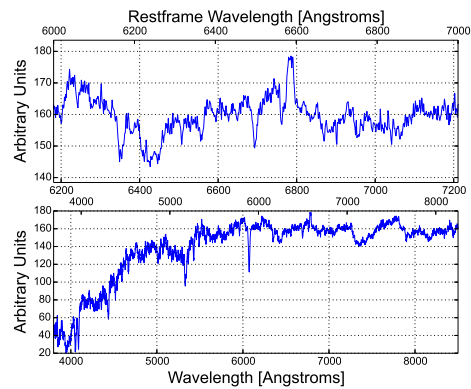
(a)



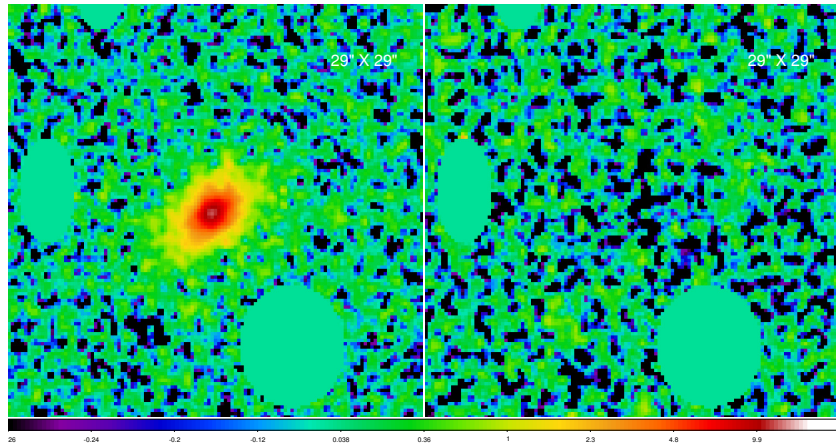
(b)



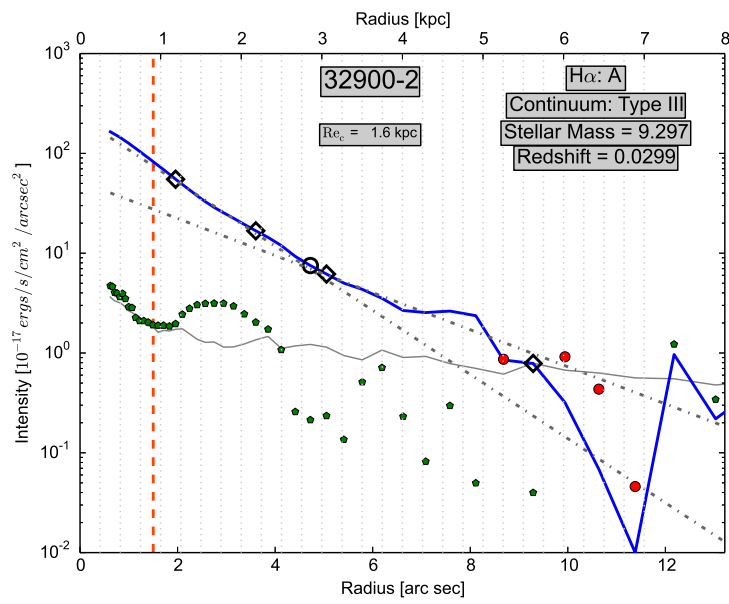
(c)



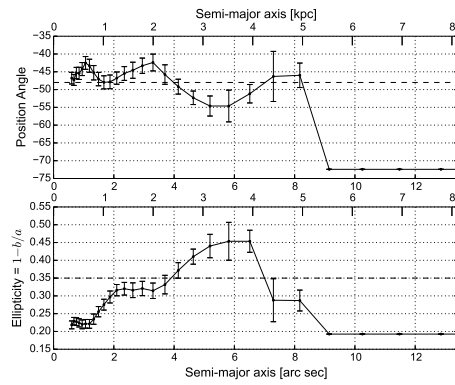
(d)



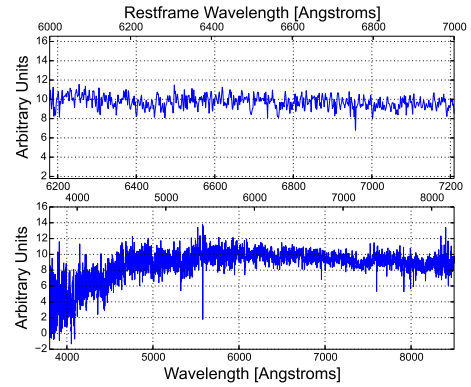
(a)



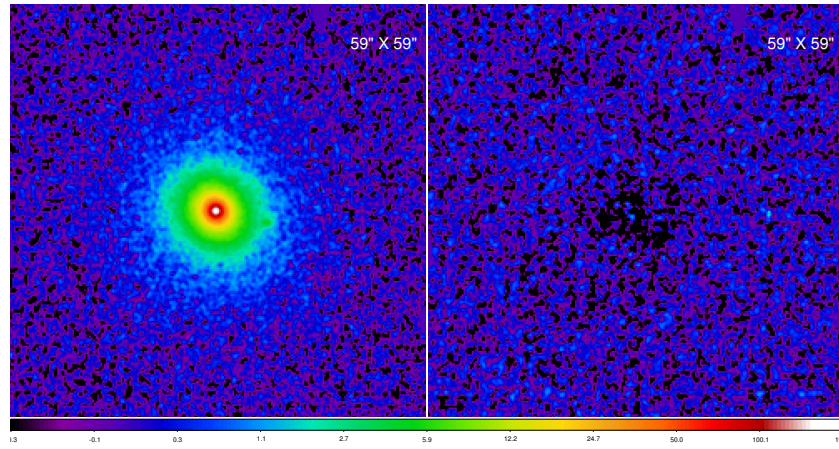
(b)



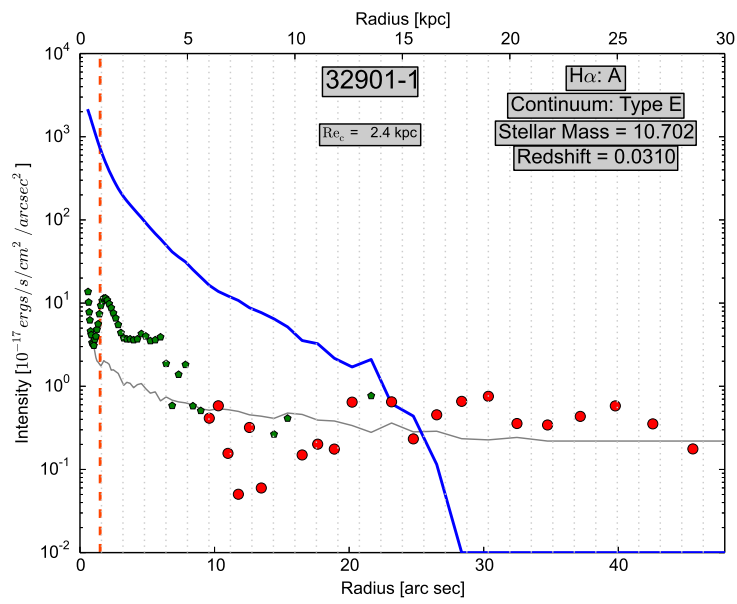
(c)



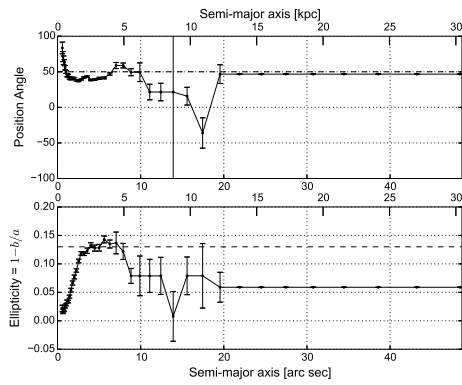
(d)



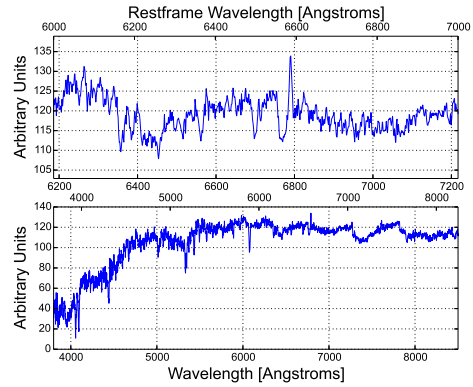
(a)



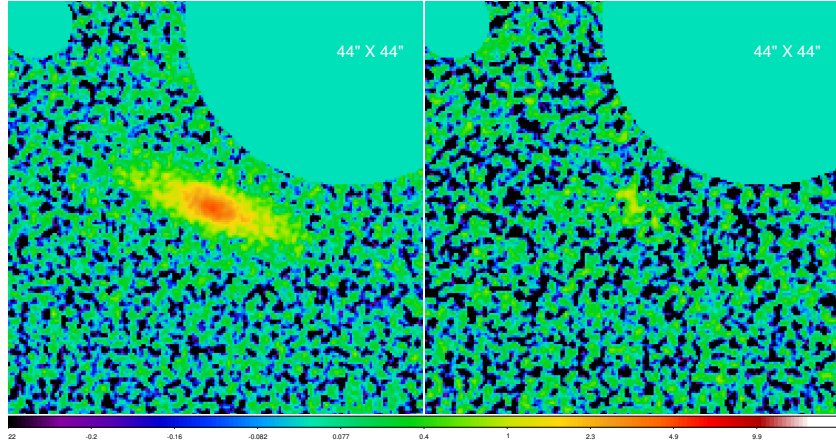
(b)



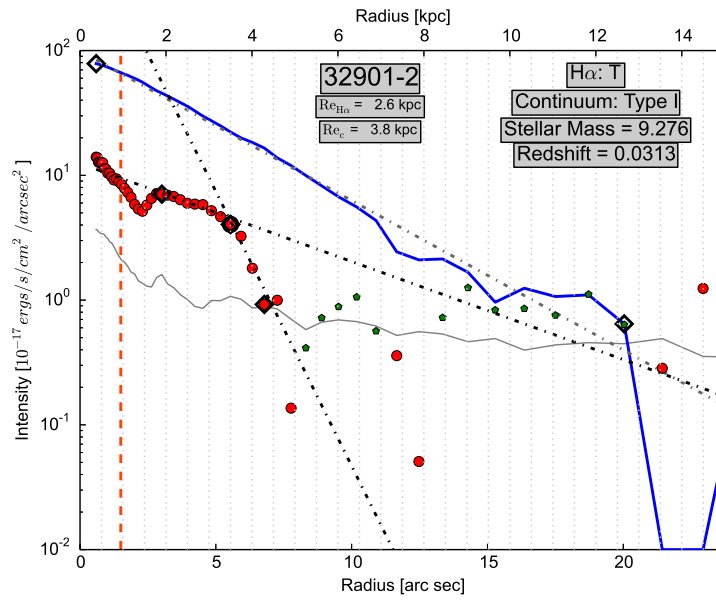
(c)



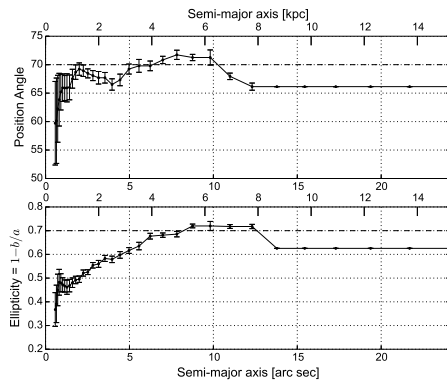
(d)



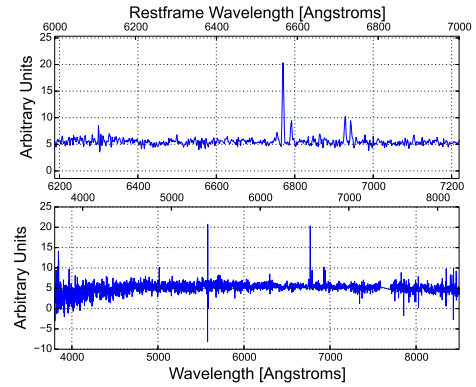
(a)



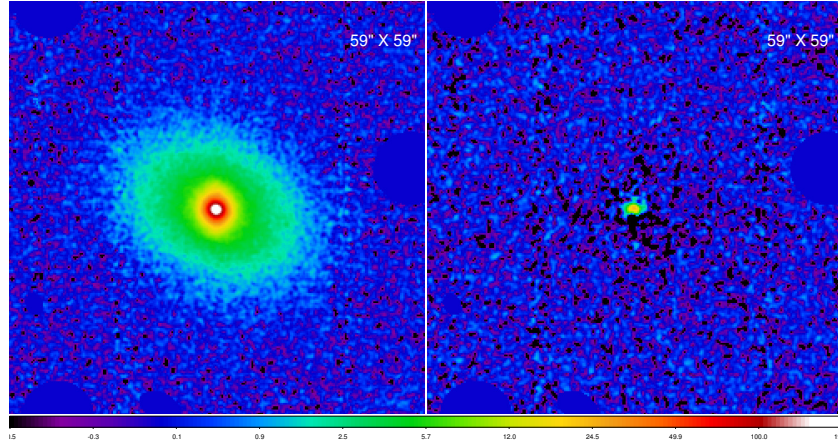
(b)



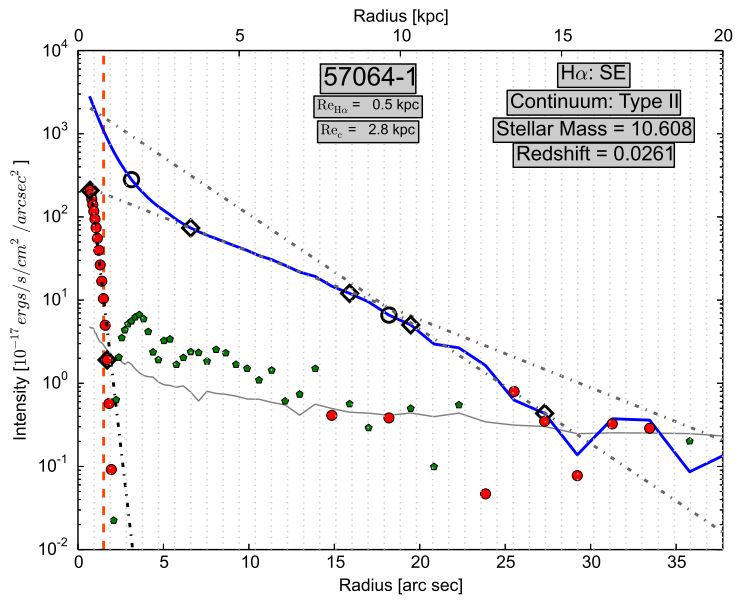
(c)



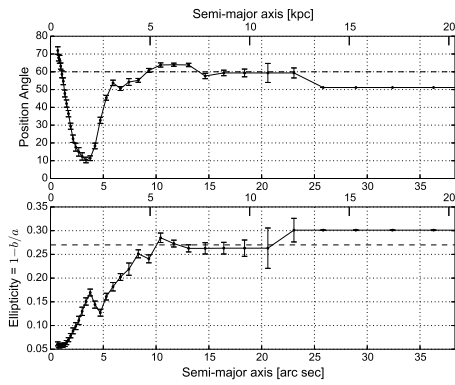
(d)



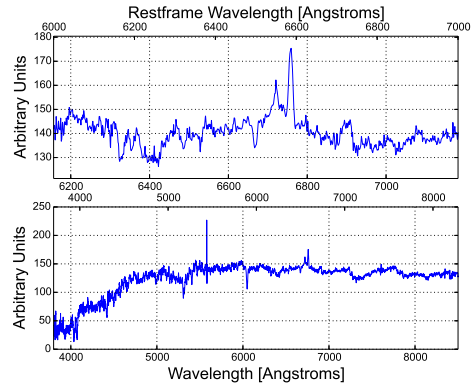
(a)



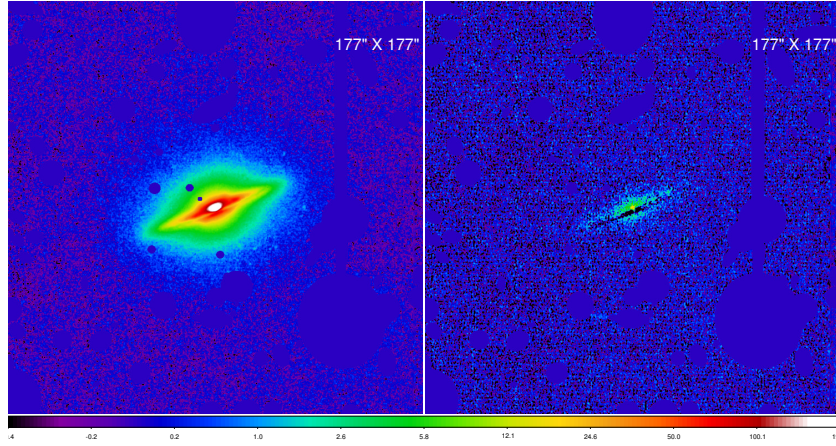
(b)



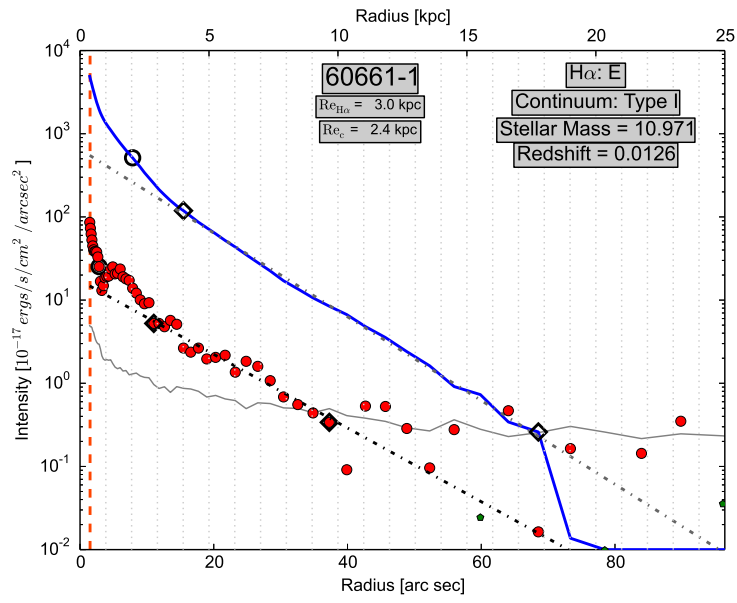
(c)



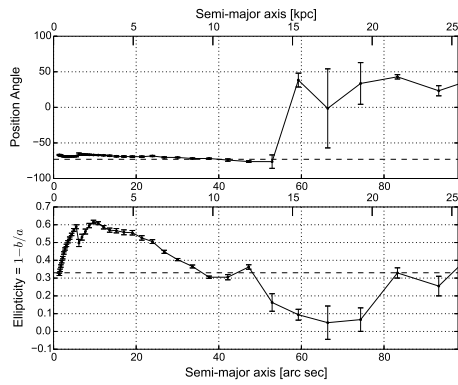
(d)



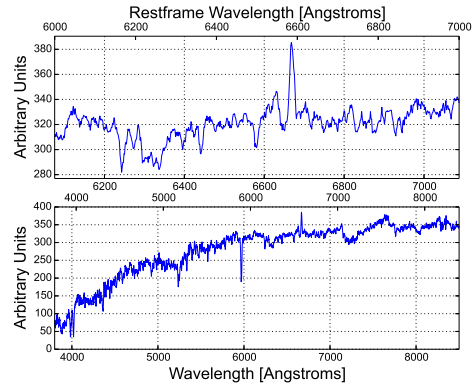
(a)



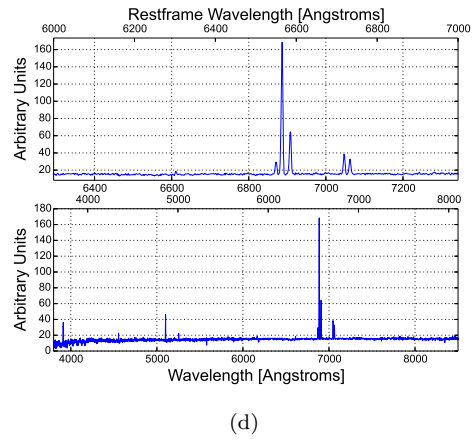
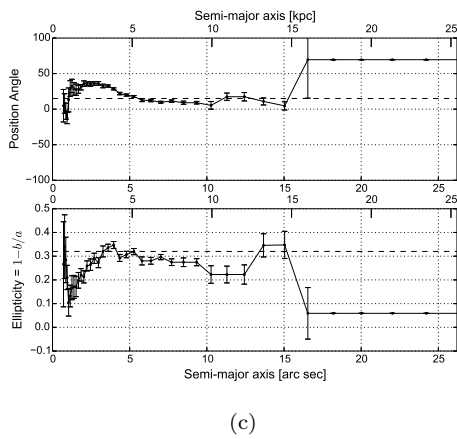
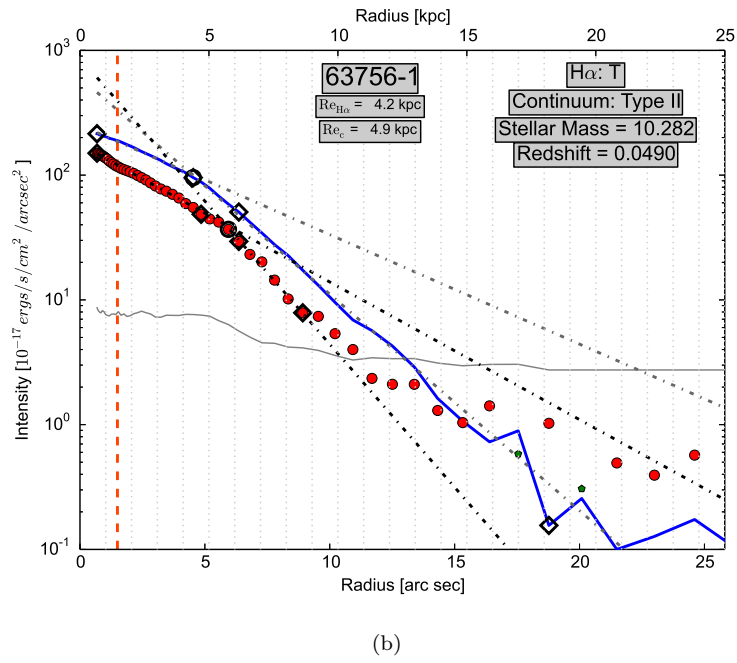
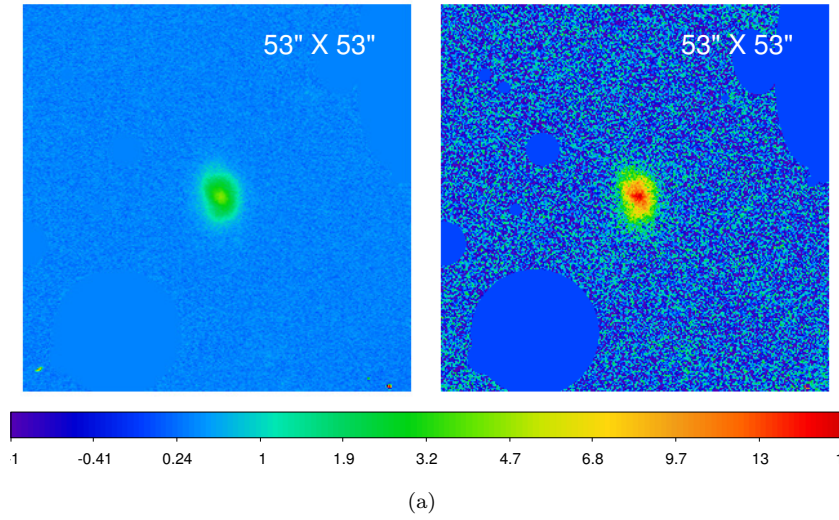
(b)

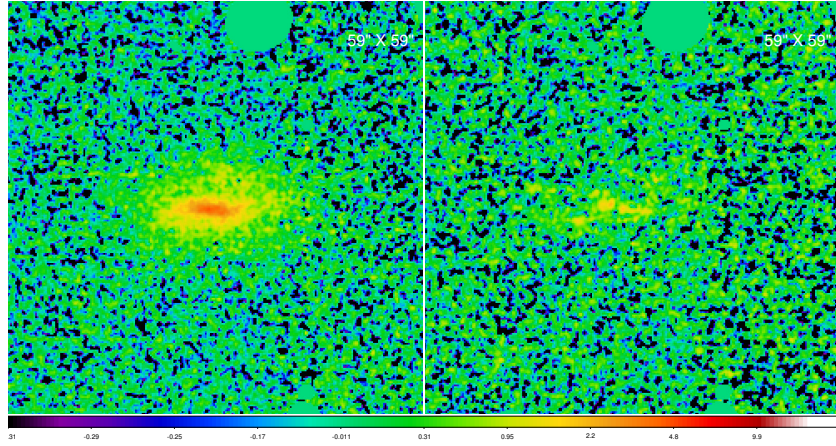


(c)

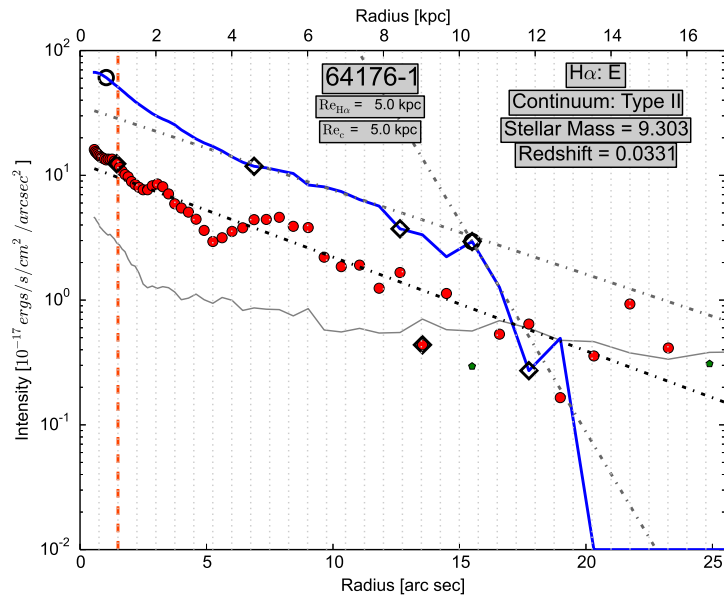


(d)

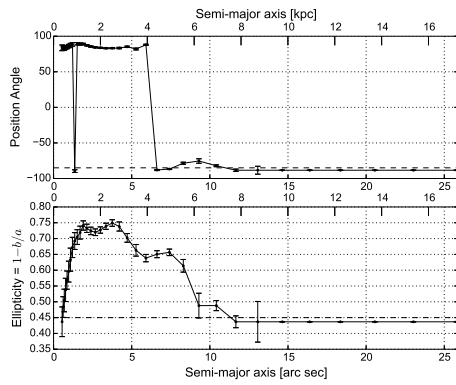




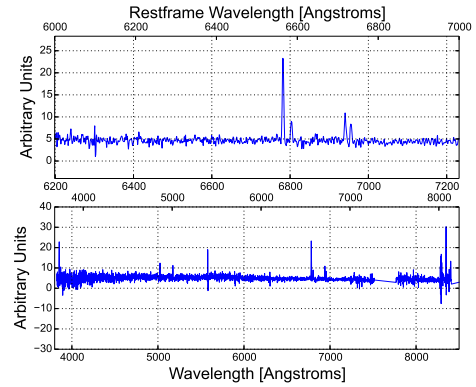
(a)



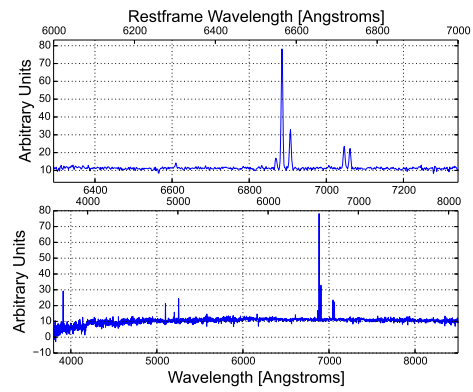
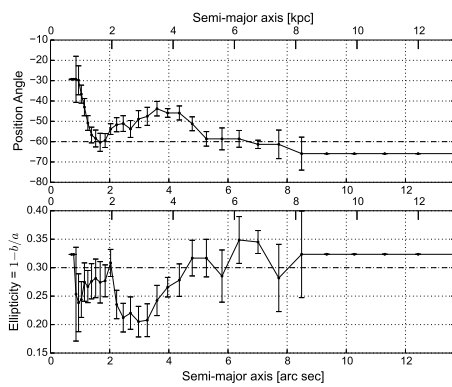
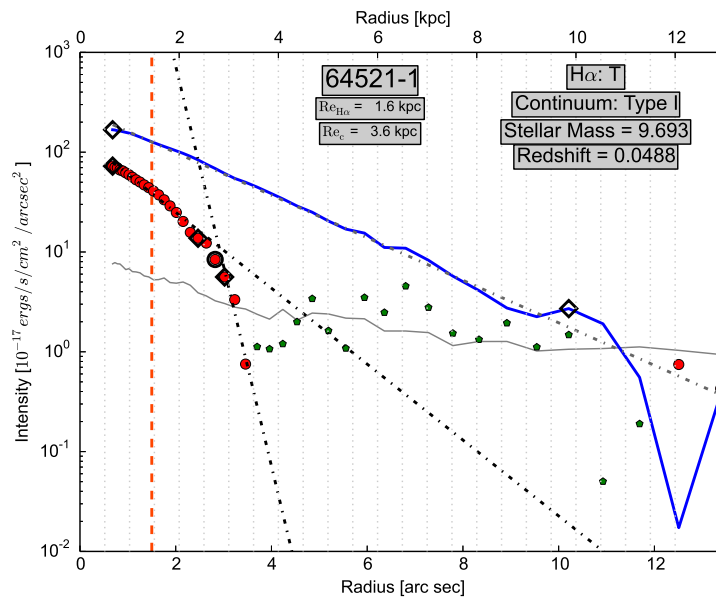
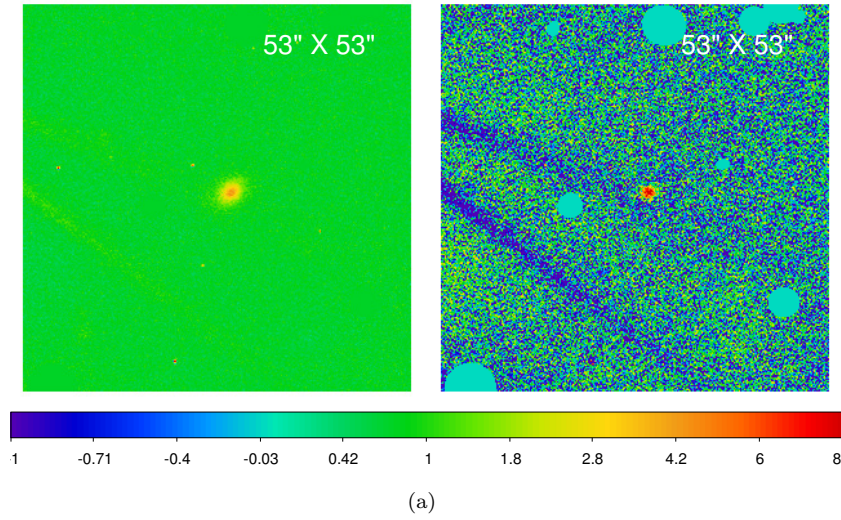
(b)

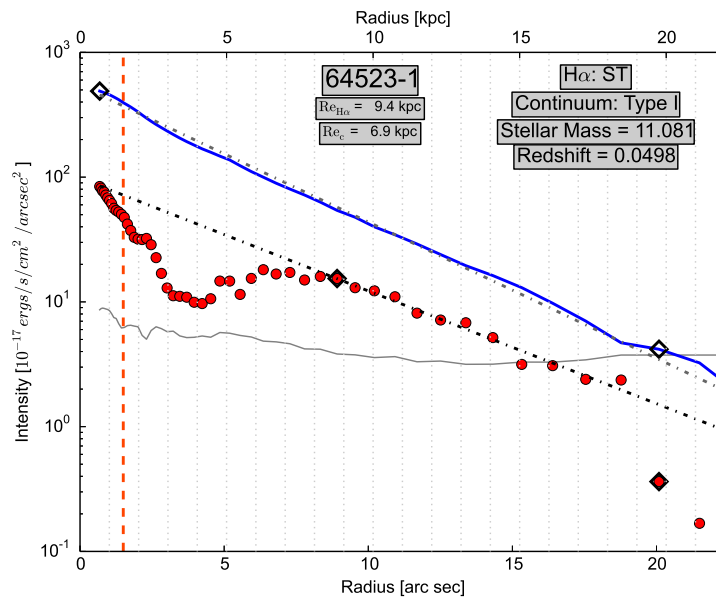
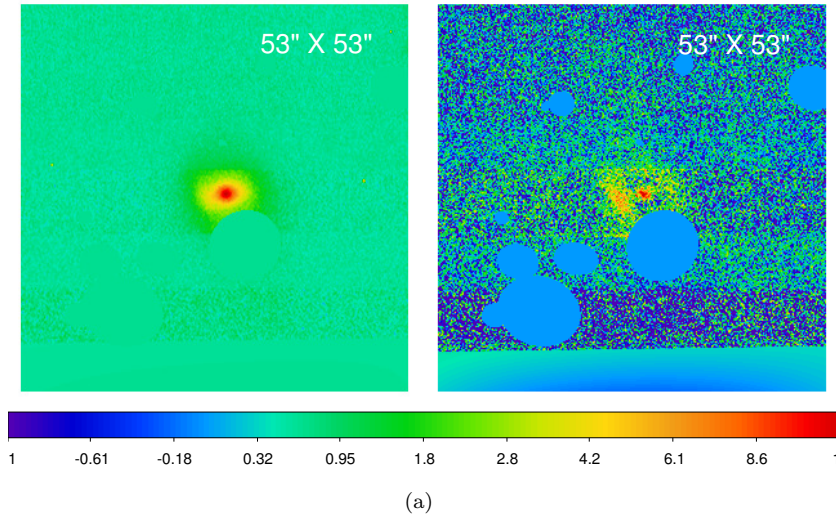


(c)

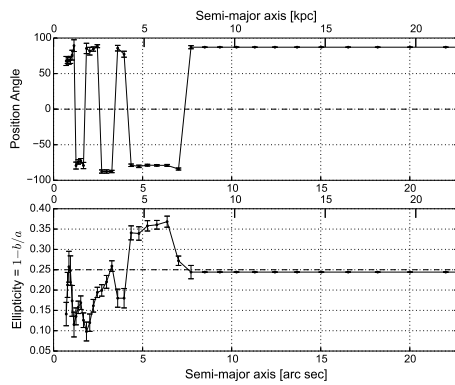


(d)

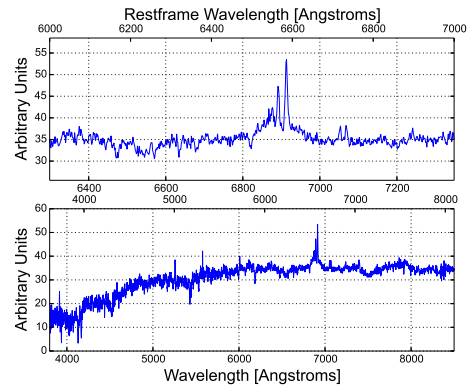




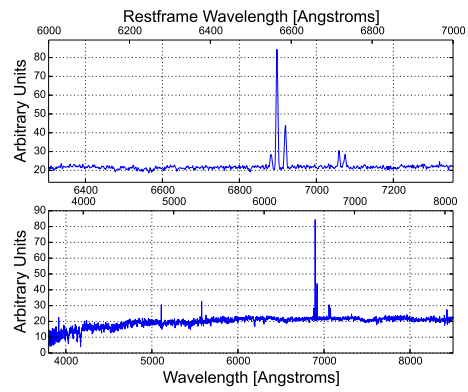
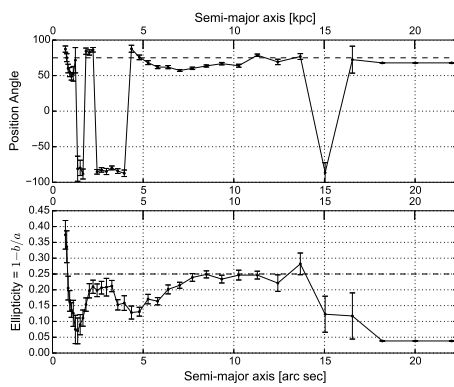
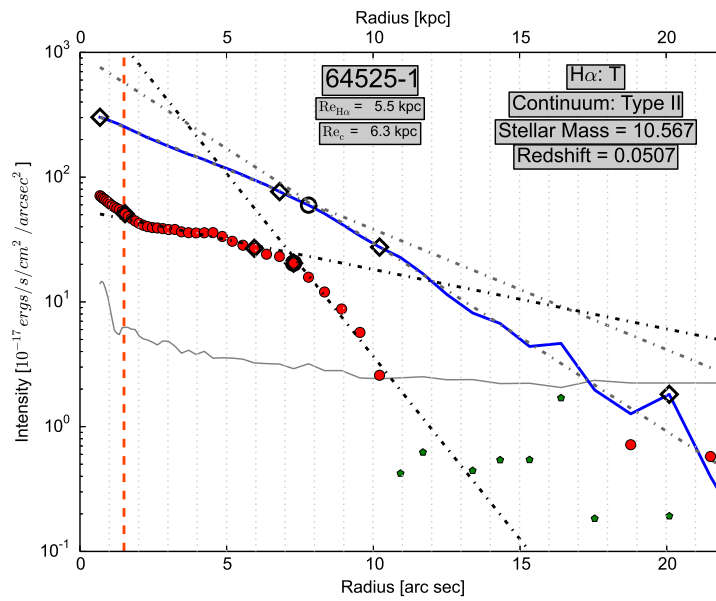
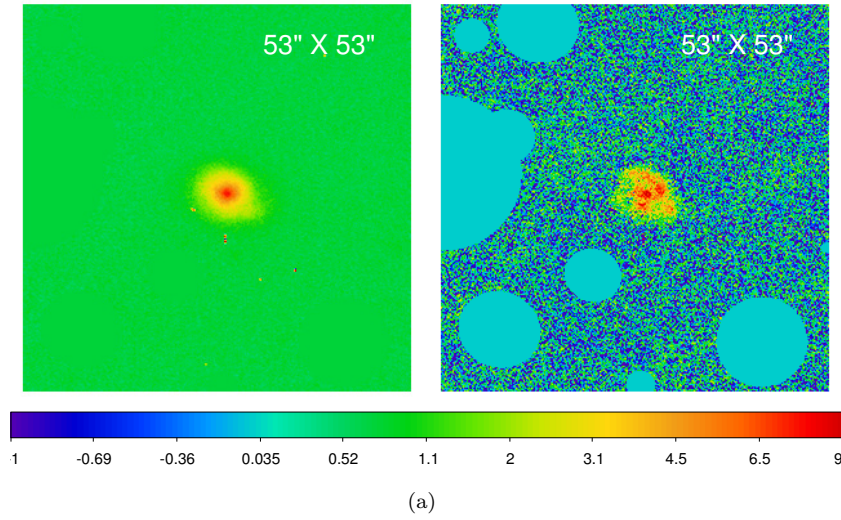
(b)

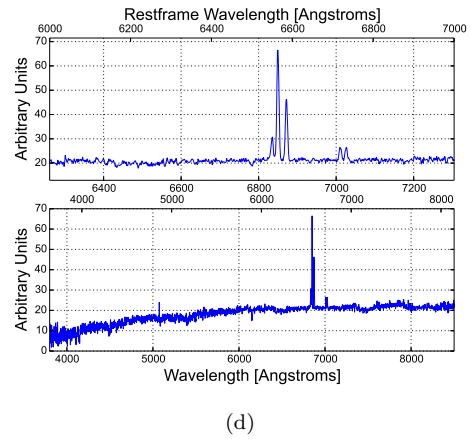
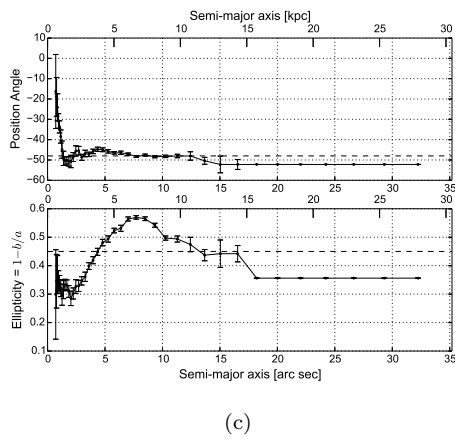
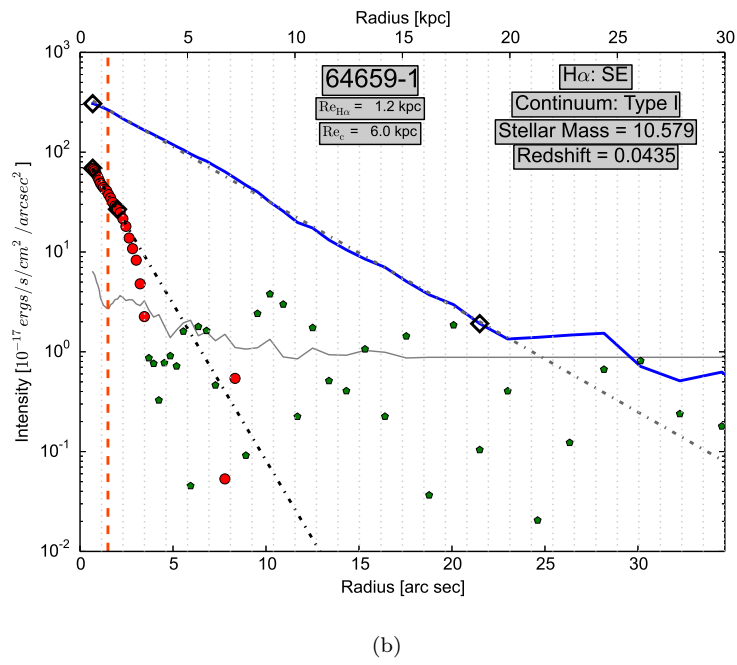
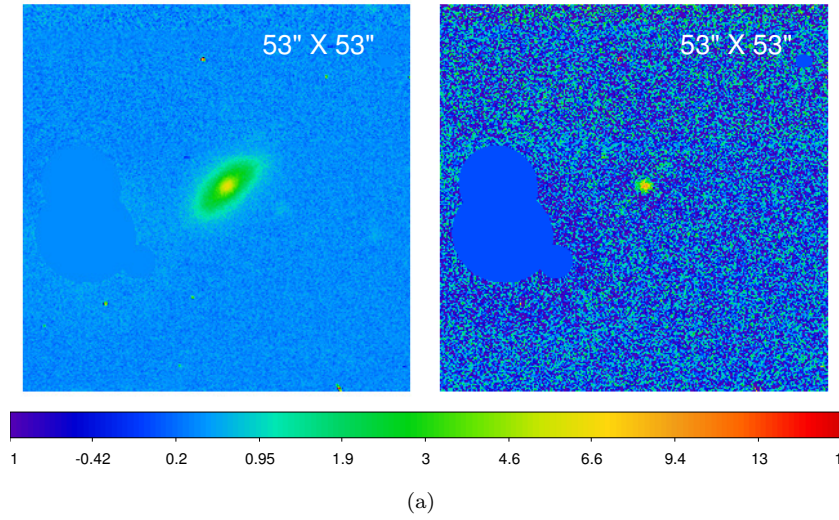


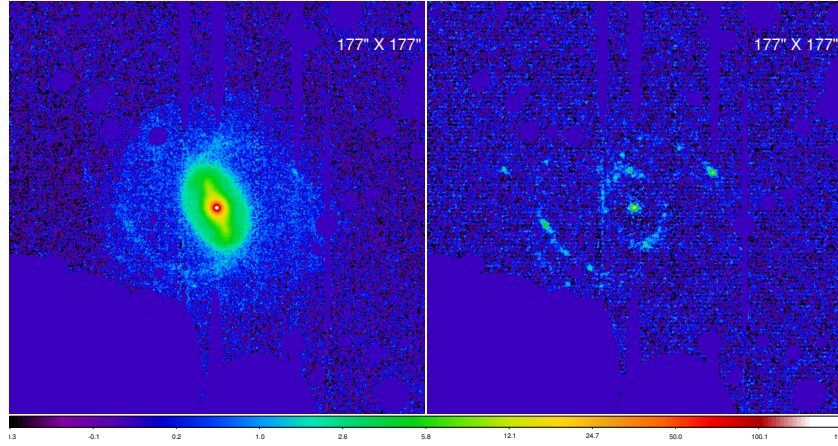
(c)



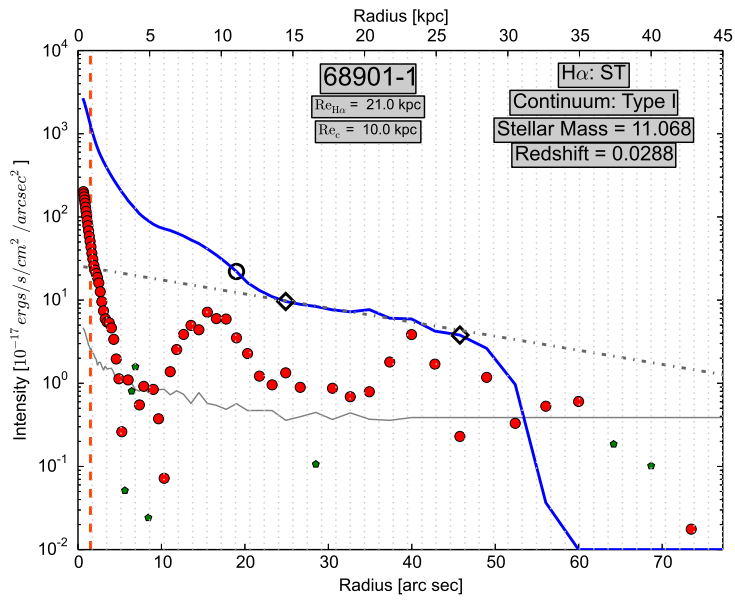
(d)



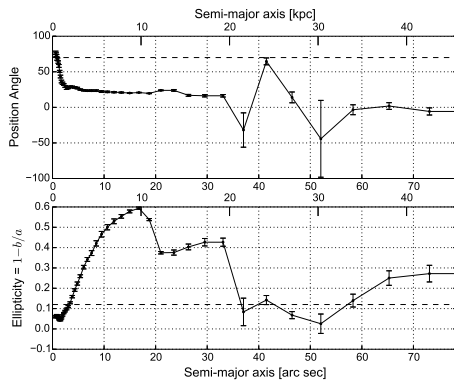




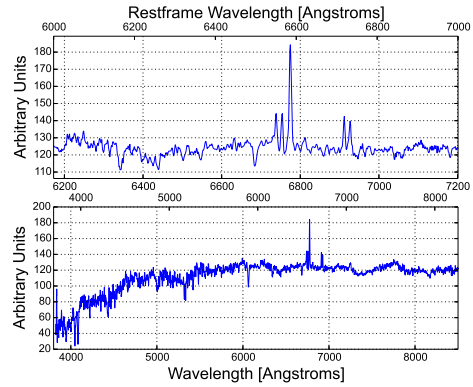
(a)



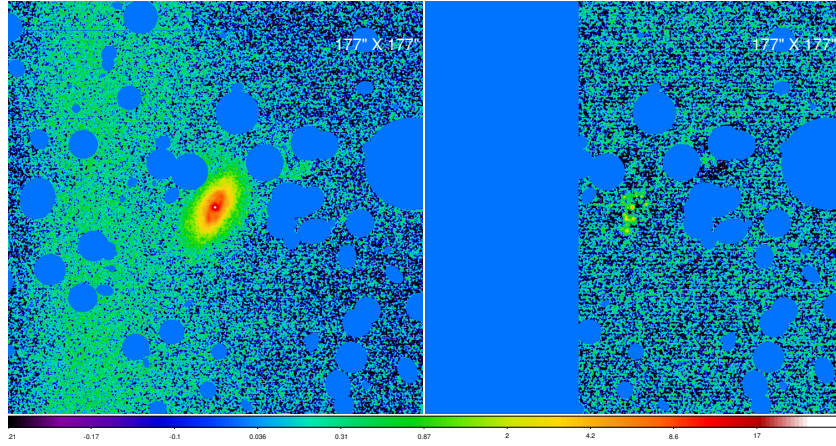
(b)



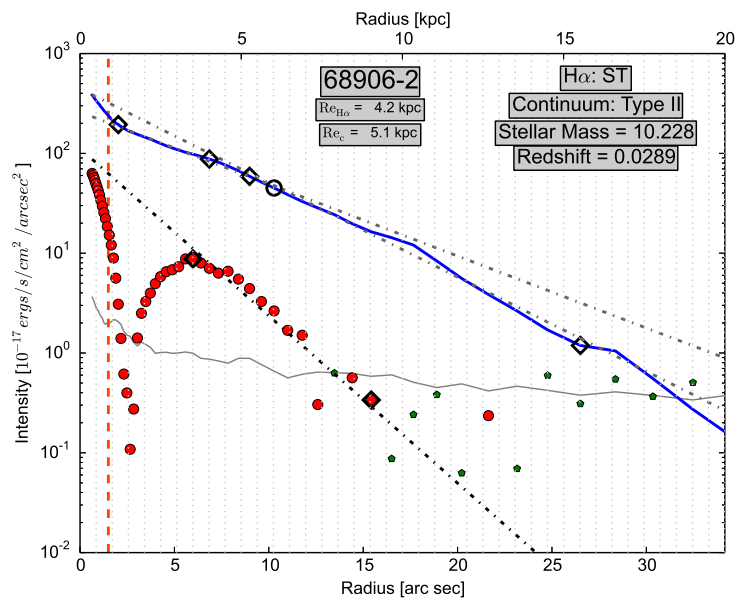
(c)



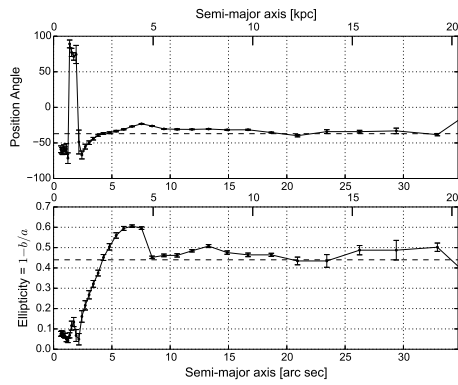
(d)



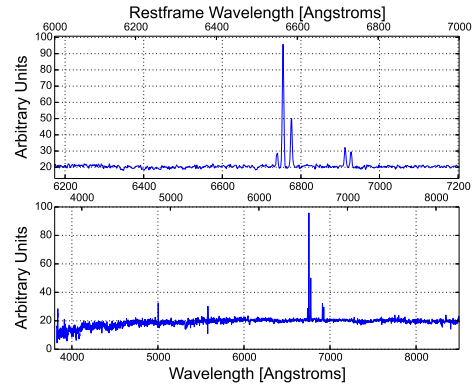
(a)



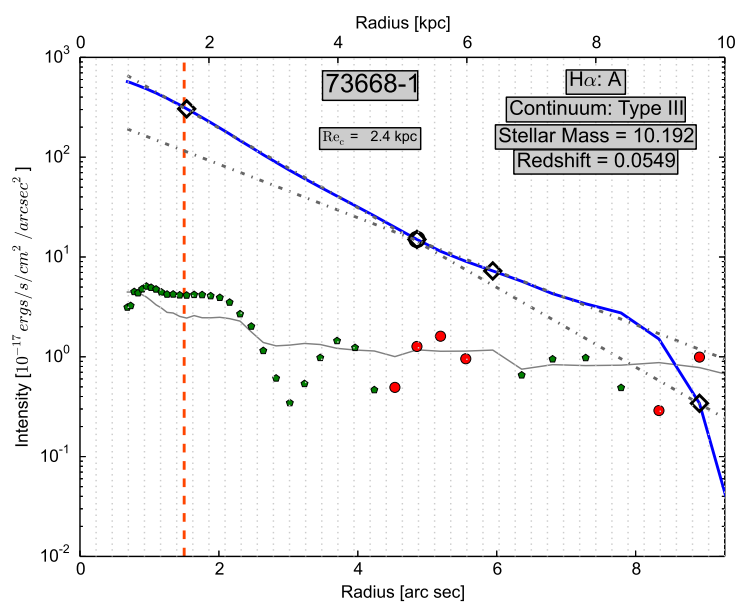
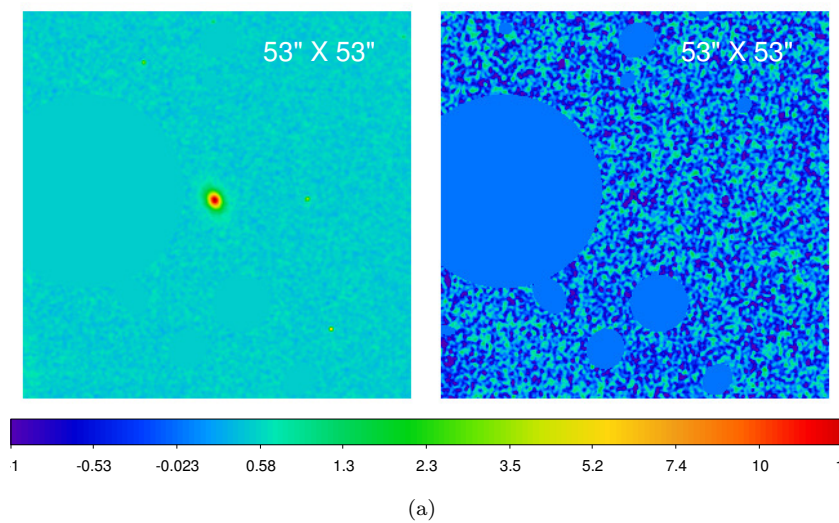
(b)



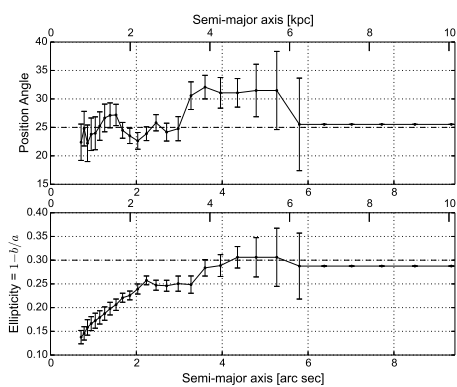
(c)



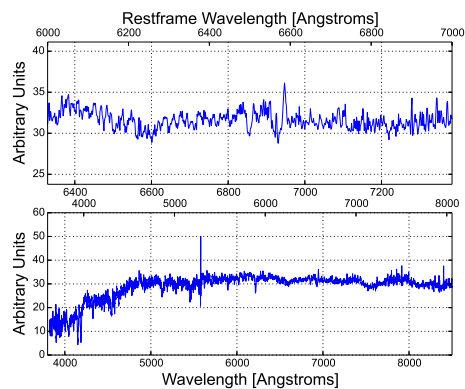
(d)



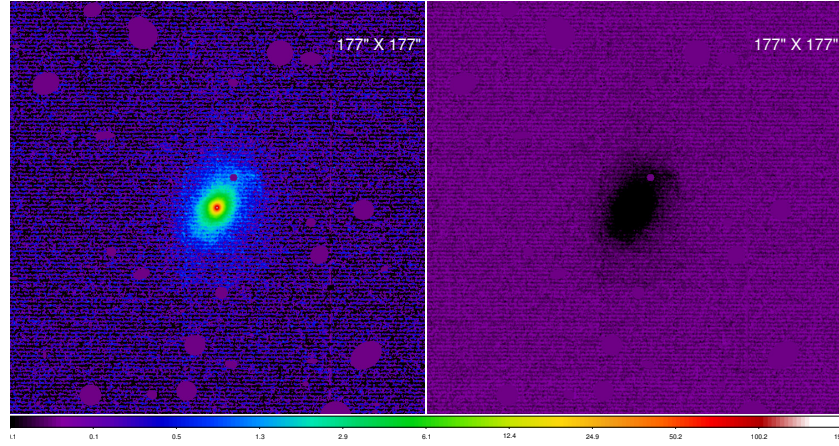
(b)



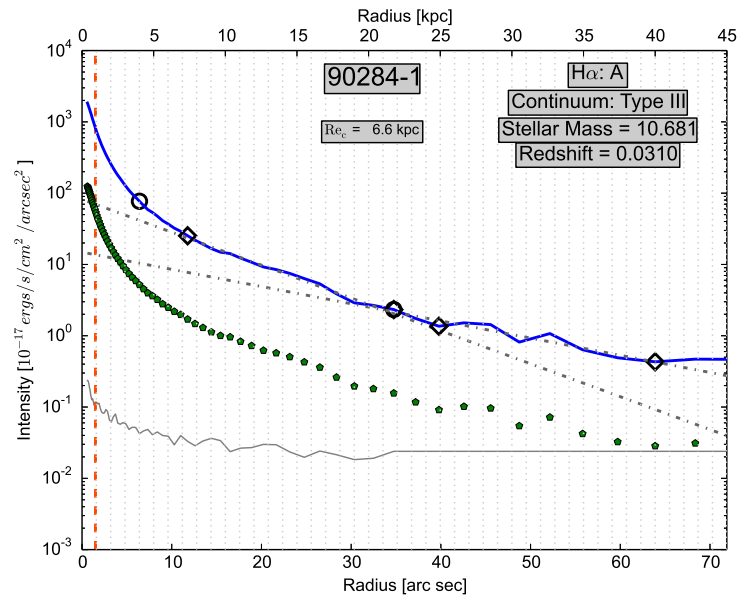
(c)



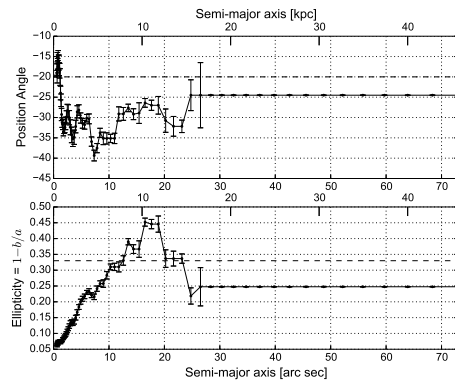
(d)



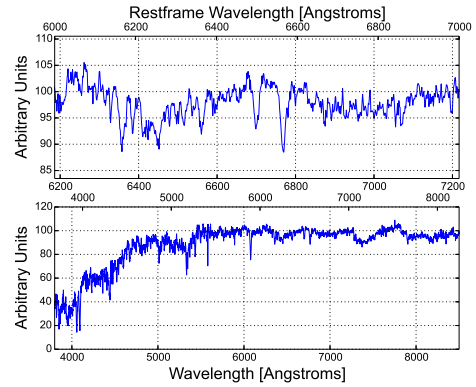
(a)



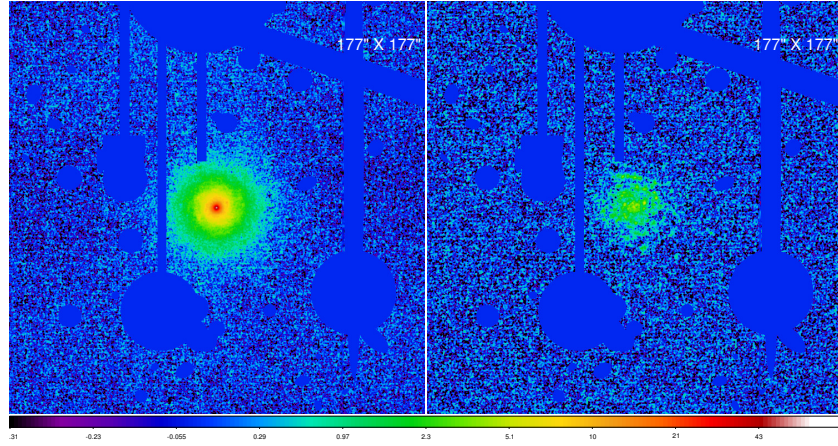
(b)



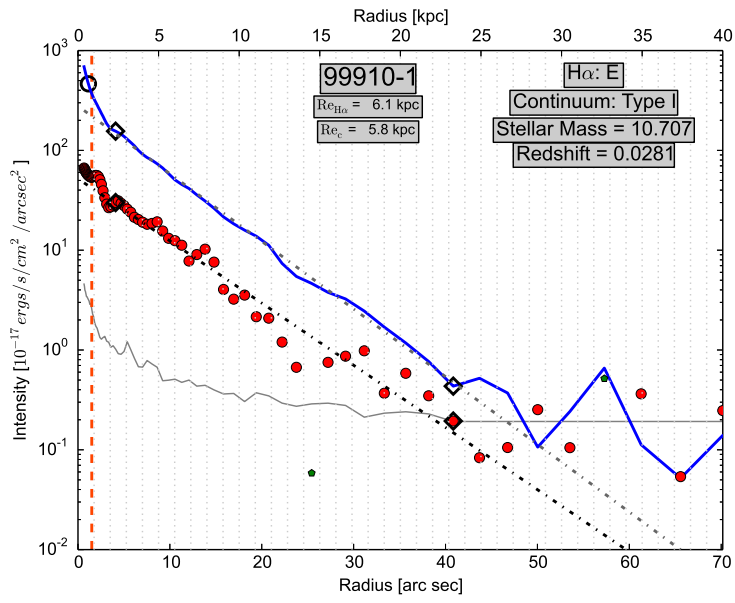
(c)



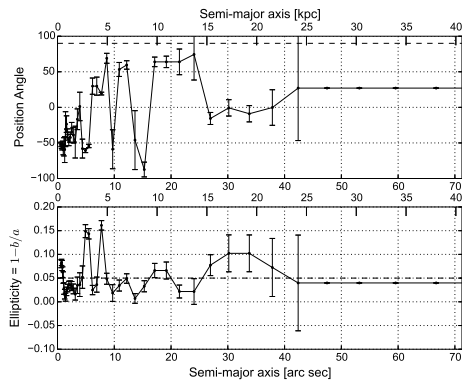
(d)



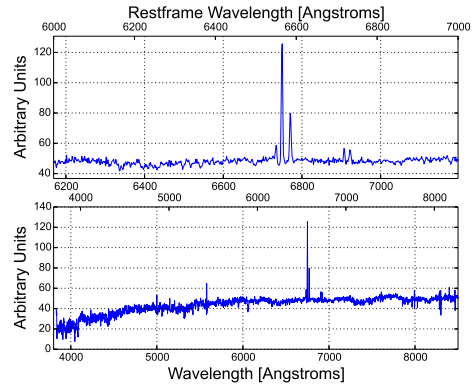
(a)



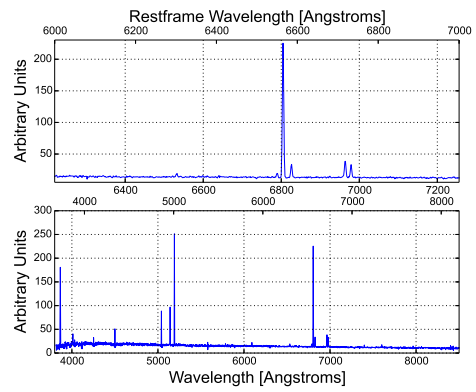
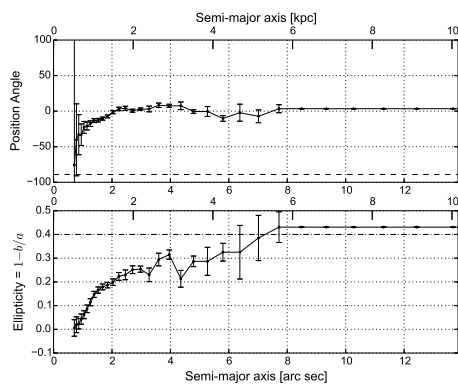
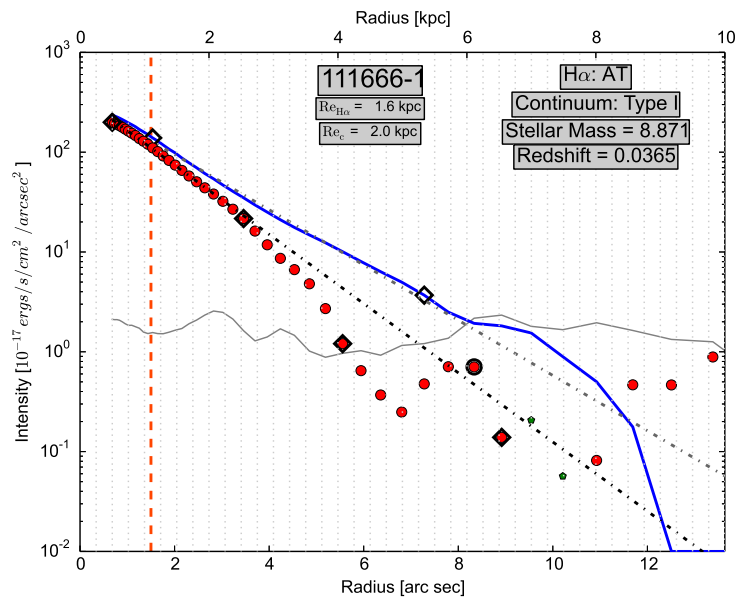
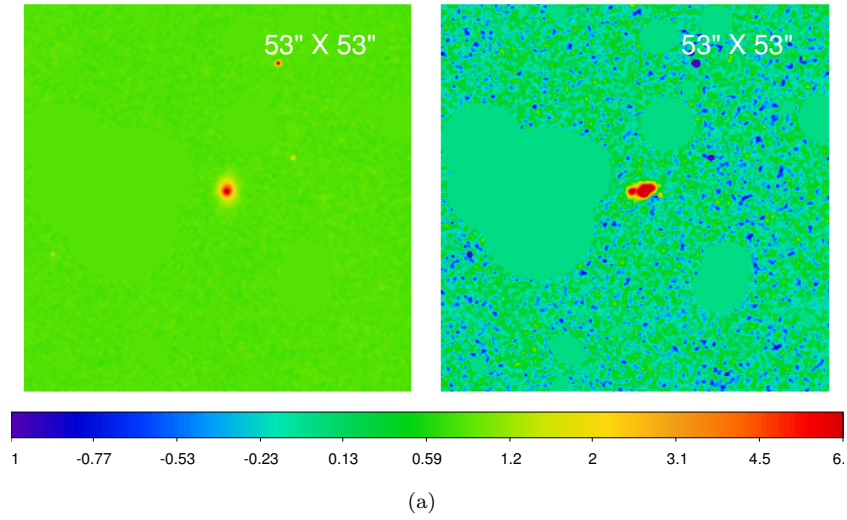
(b)

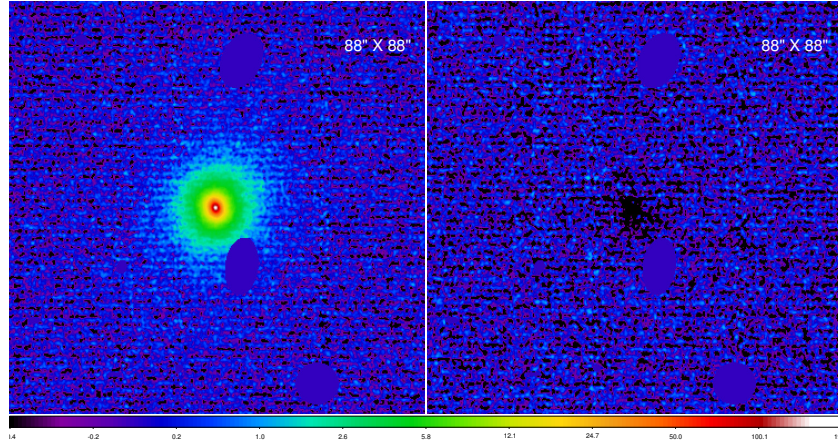


(c)

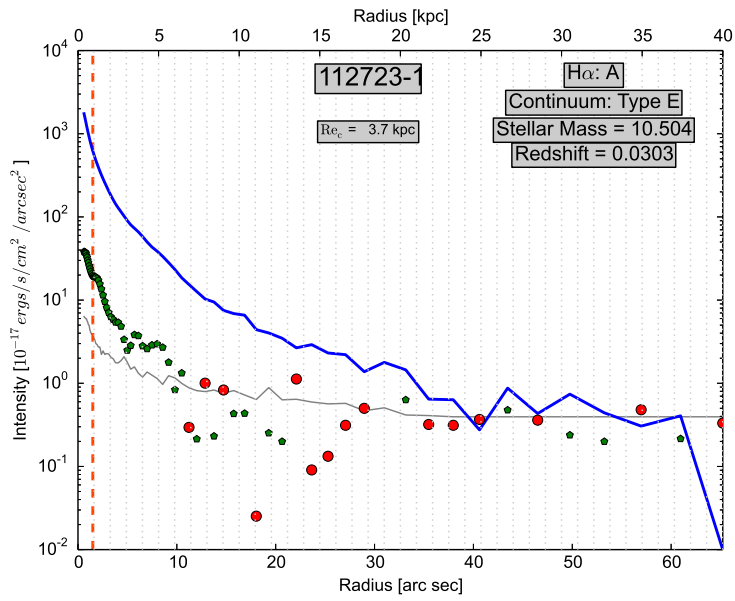


(d)

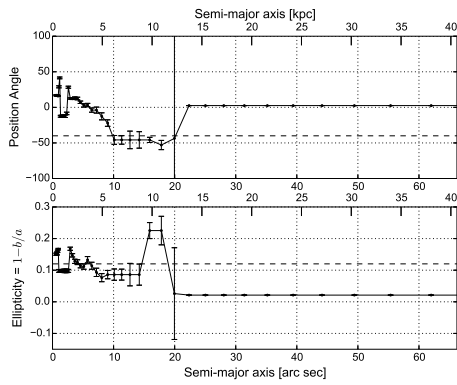




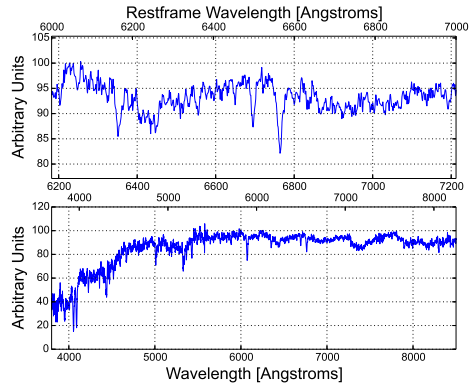
(a)



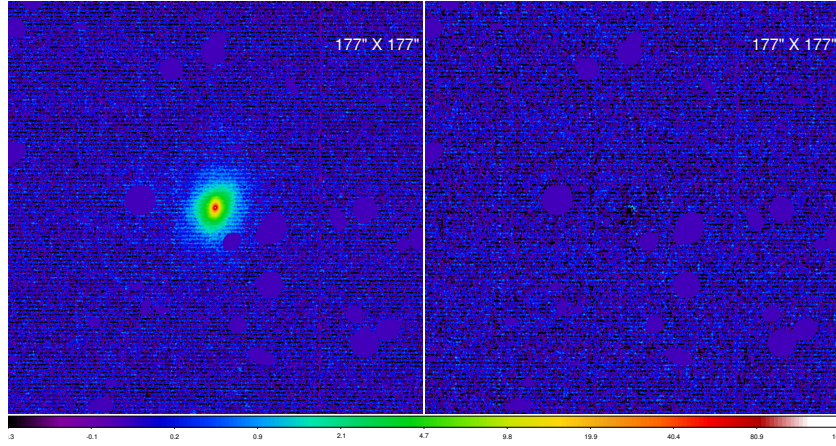
(b)



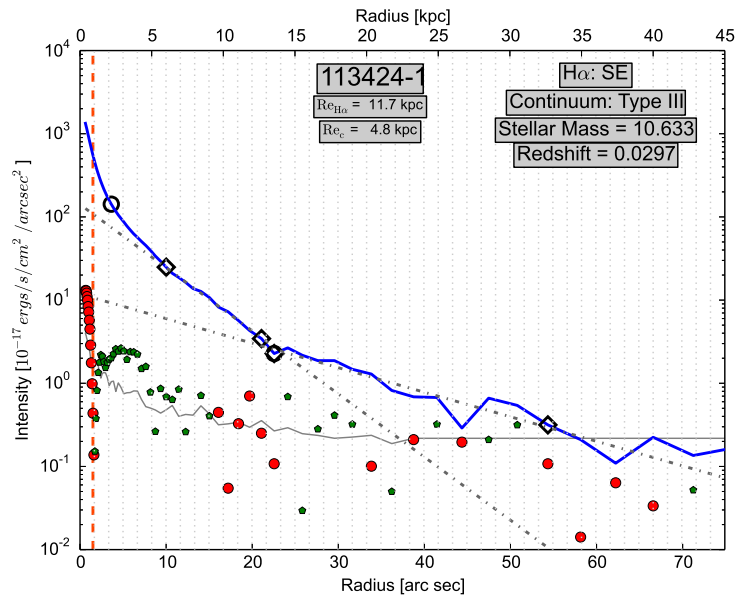
(c)



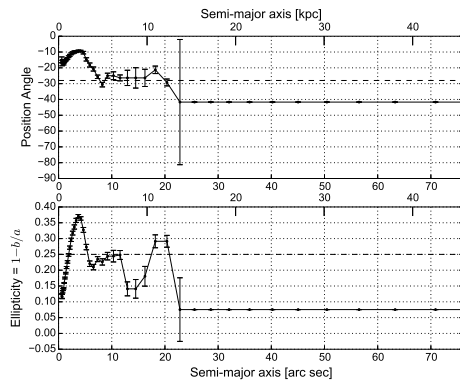
(d)



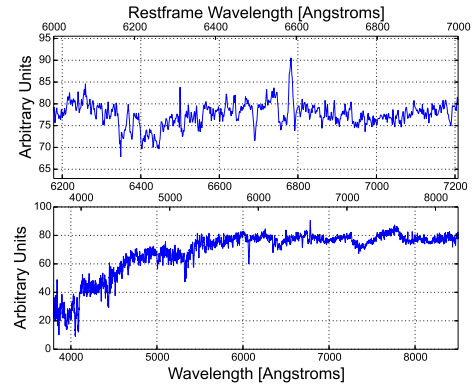
(a)



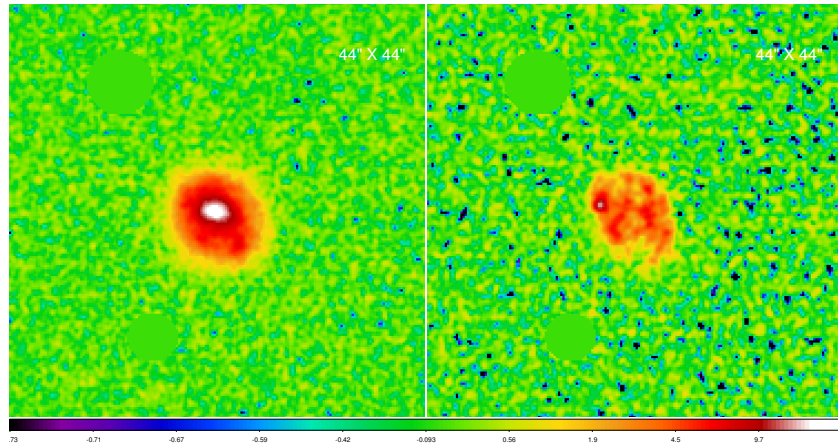
(b)



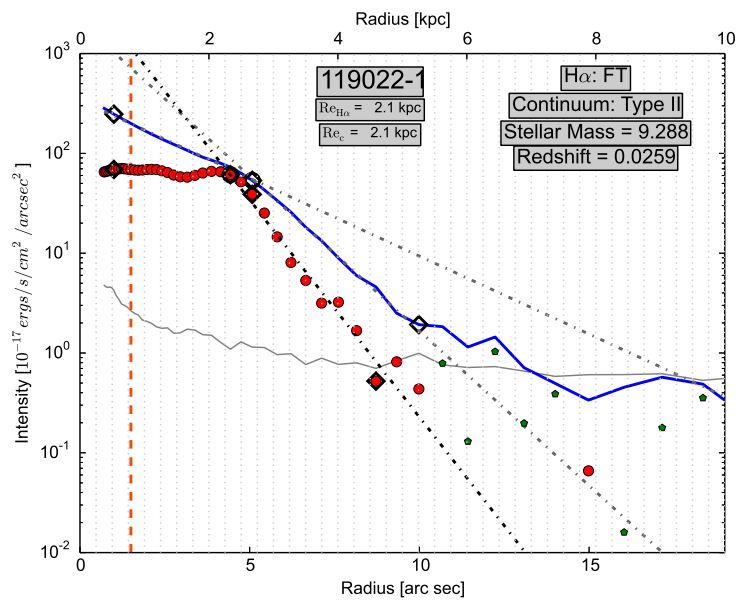
(c)



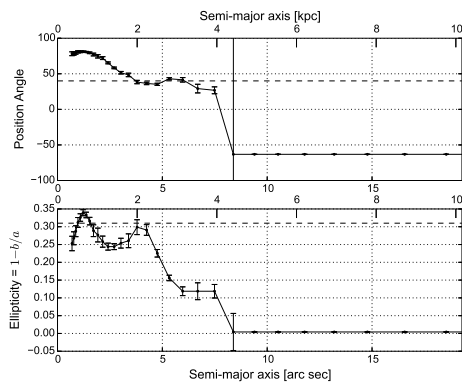
(d)



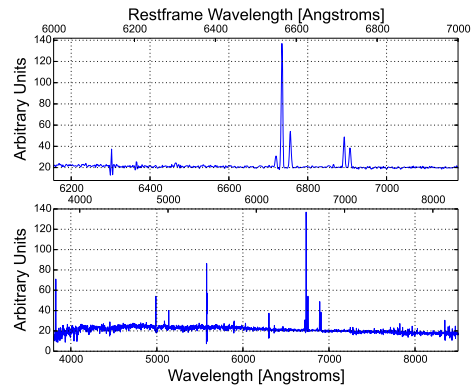
(a)



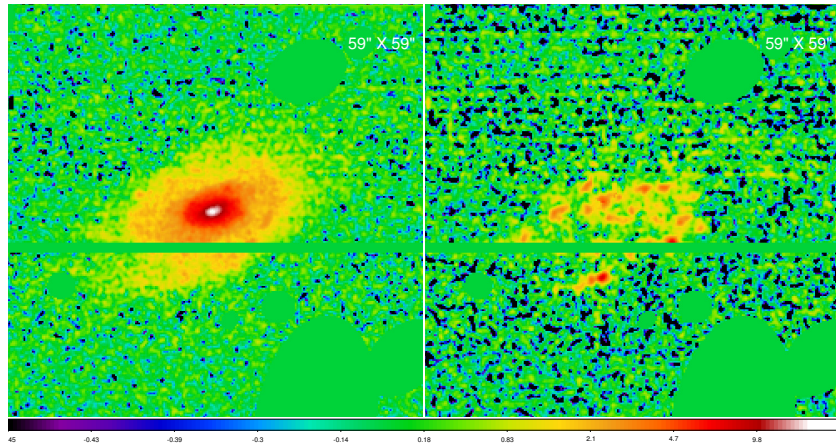
(b)



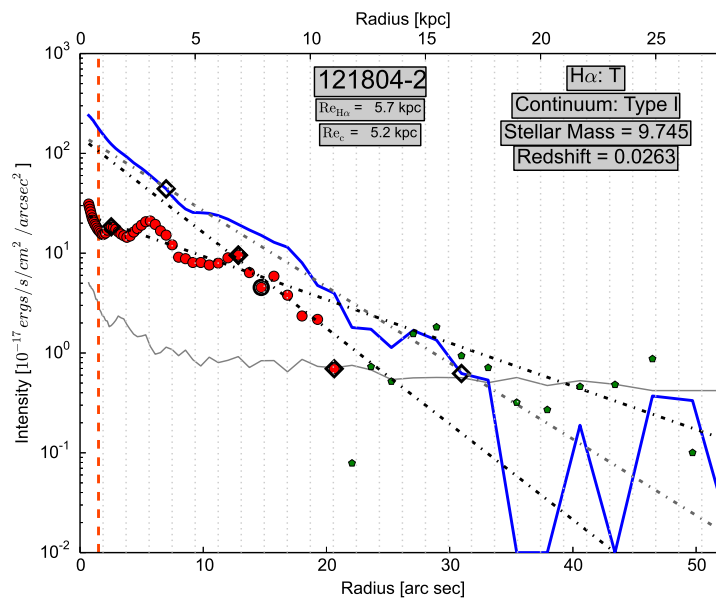
(c)



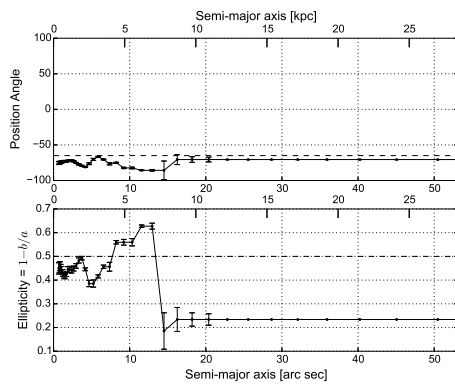
(d)



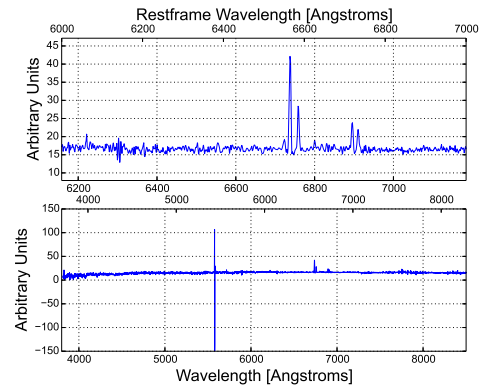
(a)



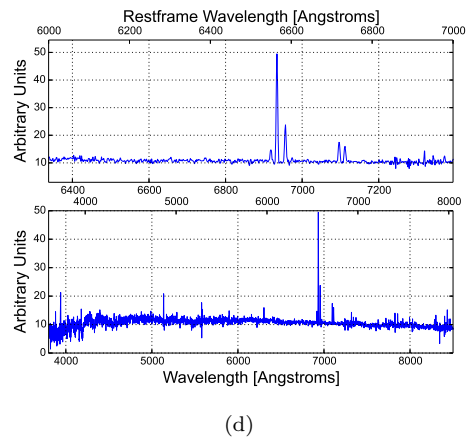
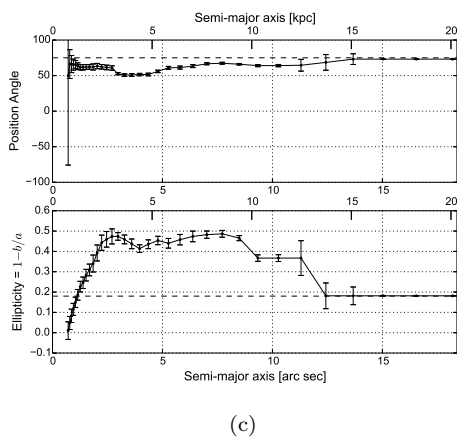
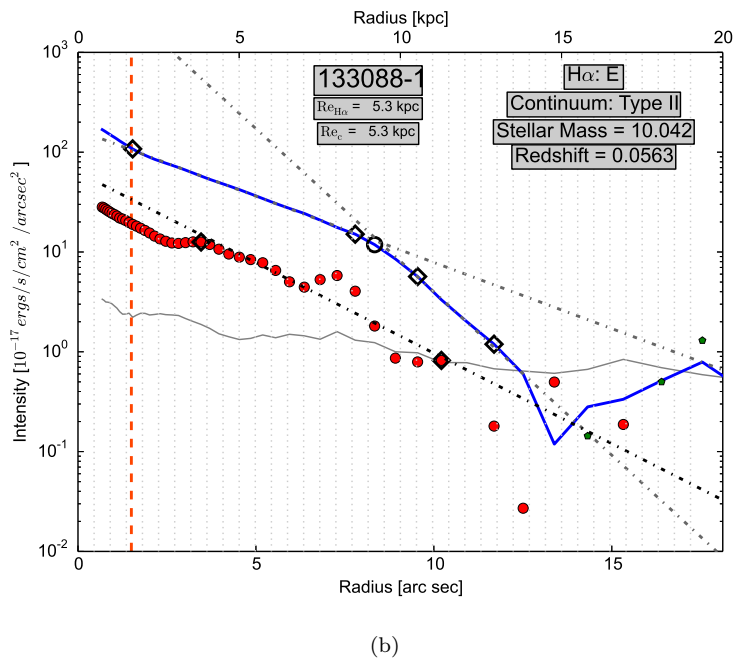
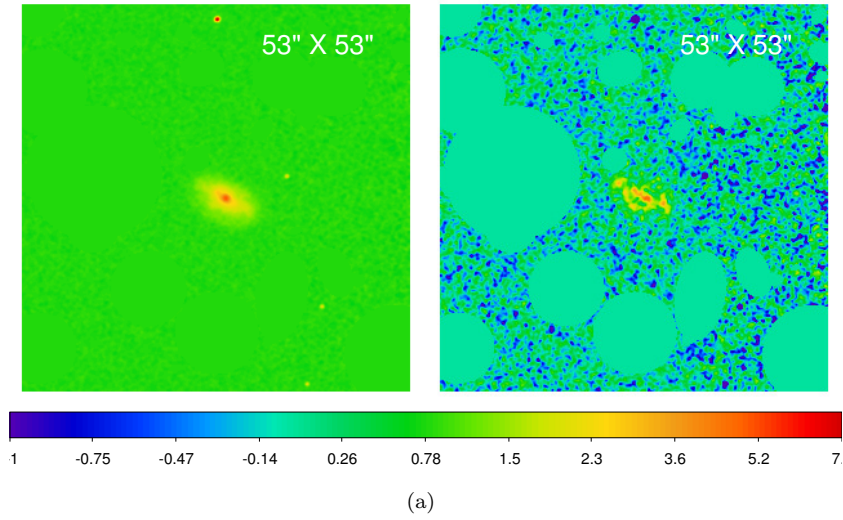
(b)

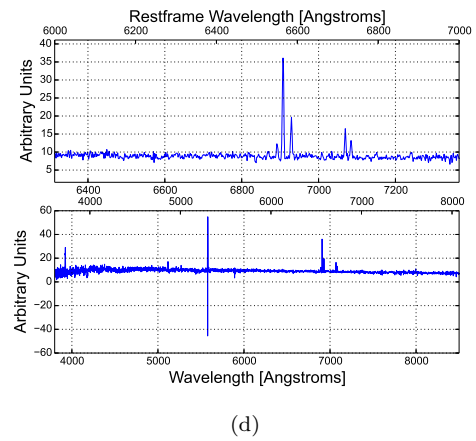
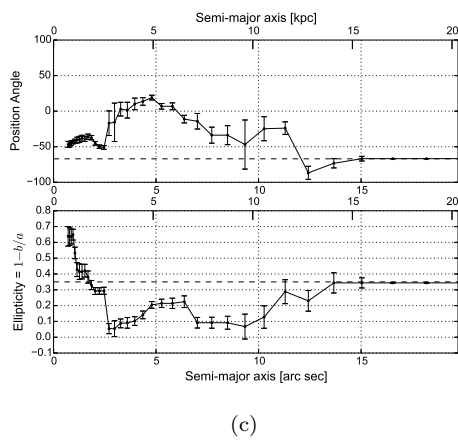
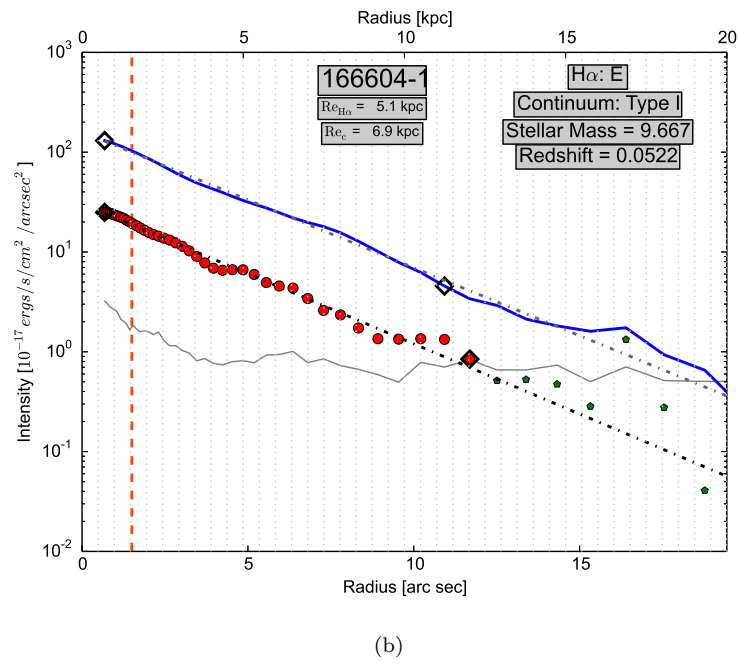
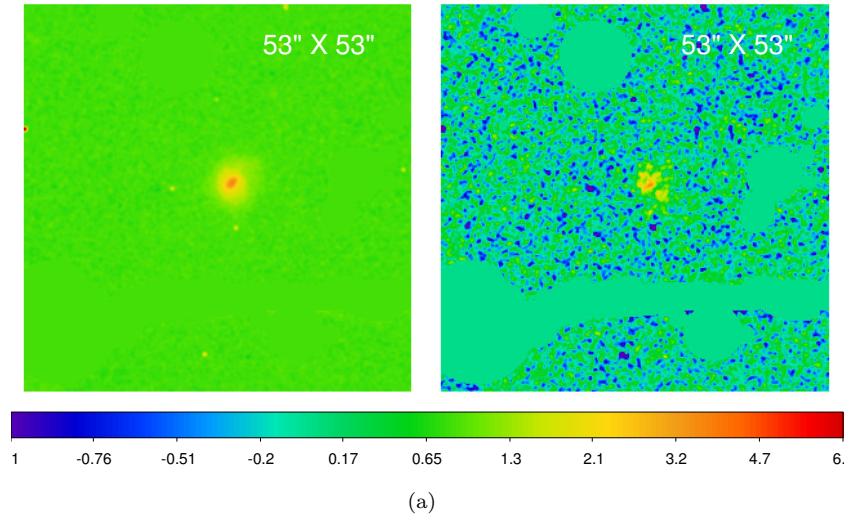


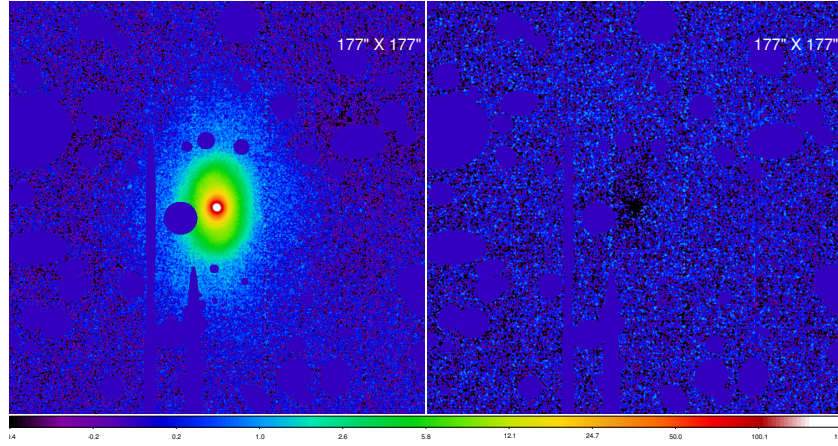
(c)



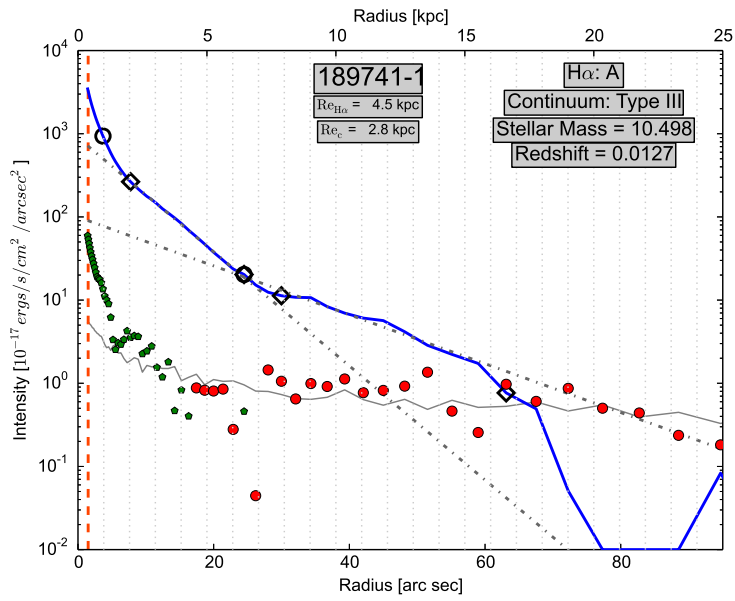
(d)



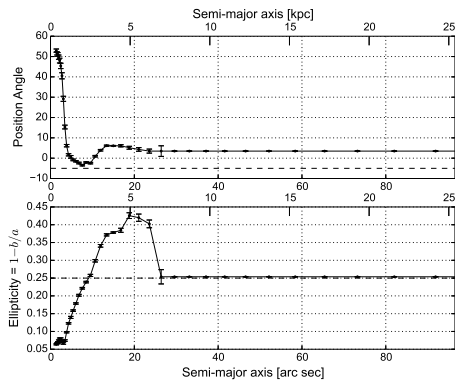




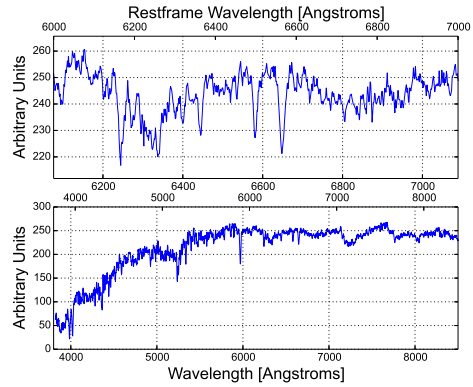
(a)



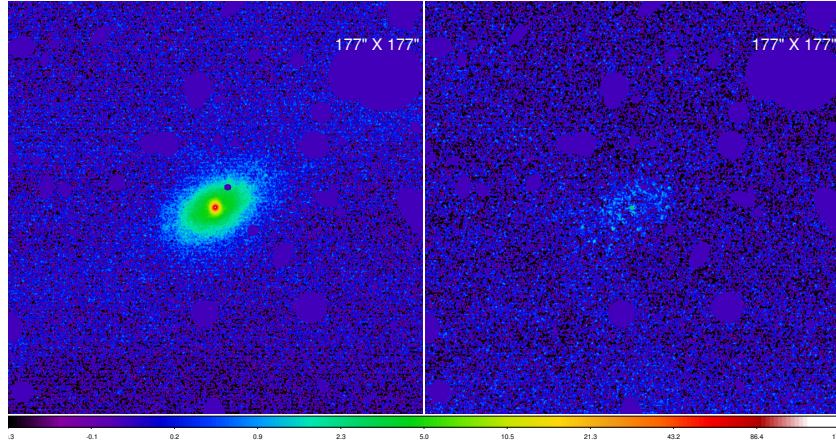
(b)



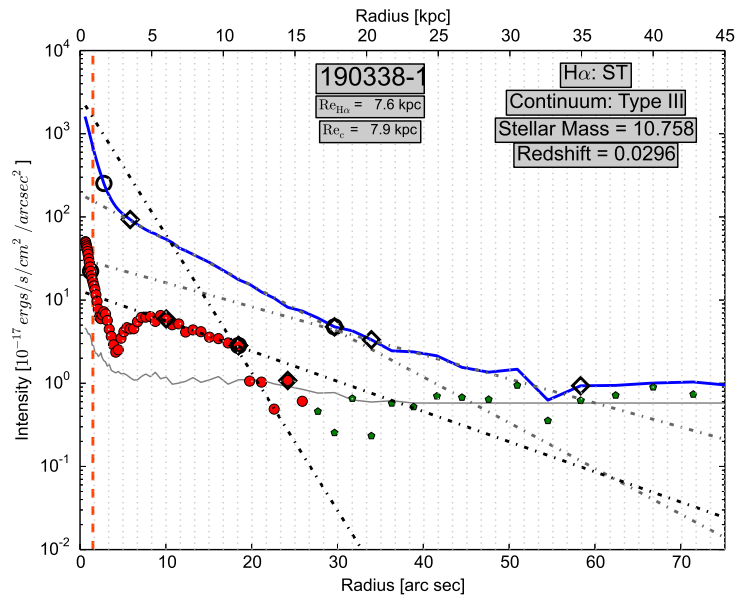
(c)



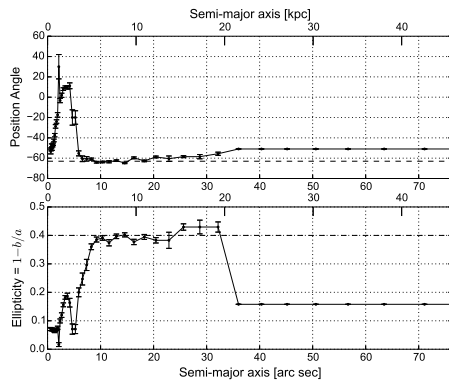
(d)



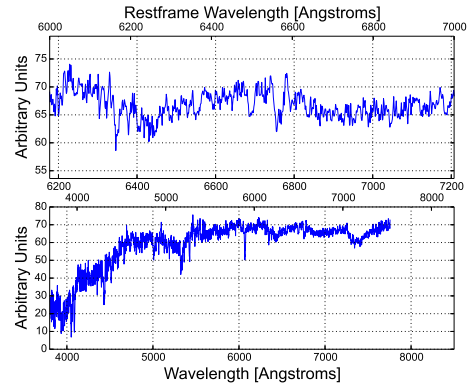
(a)



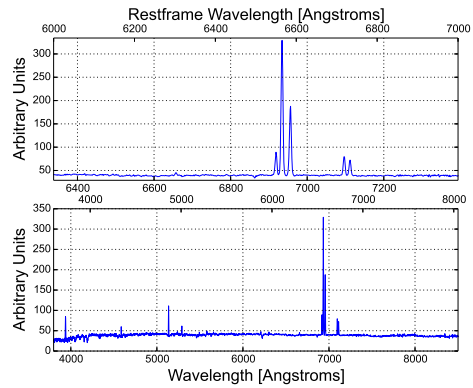
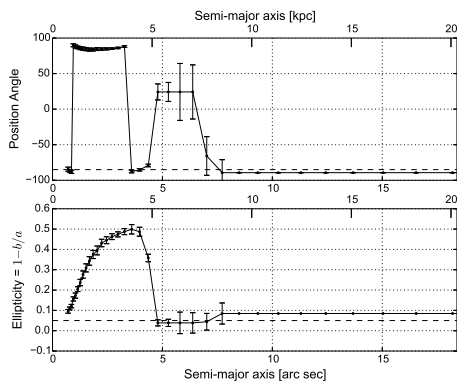
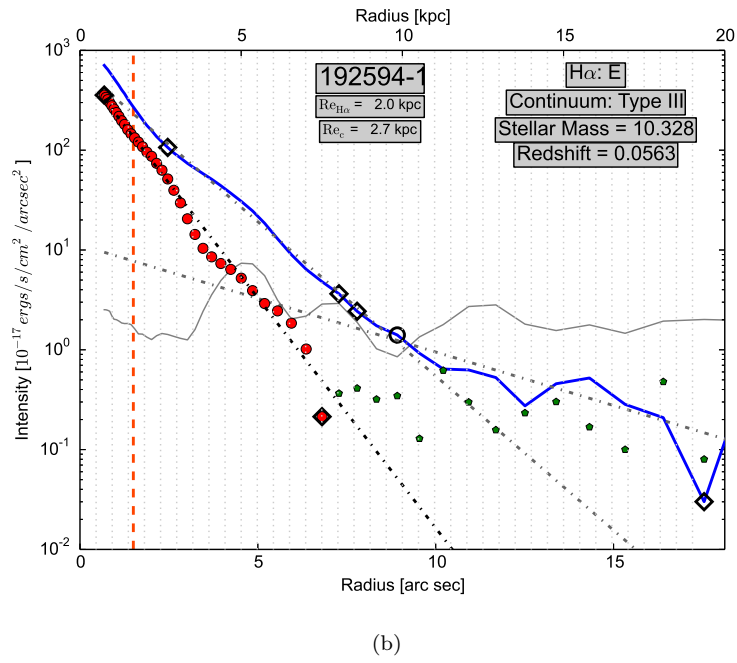
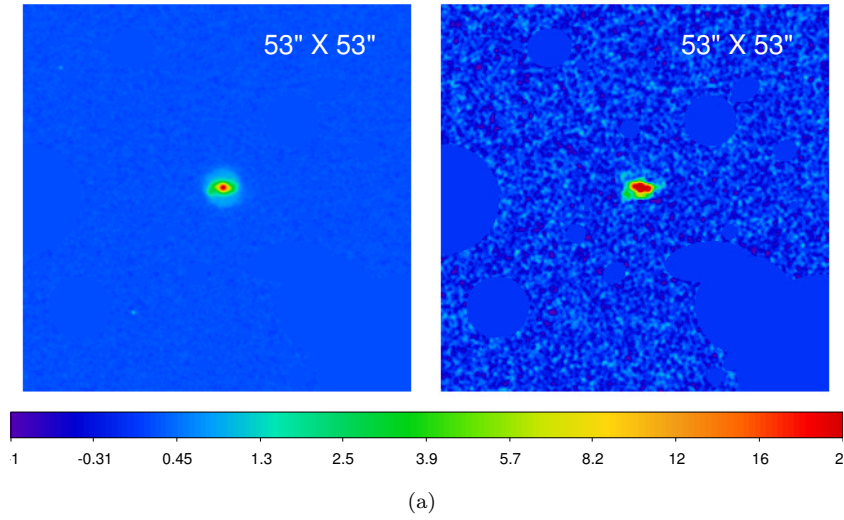
(b)

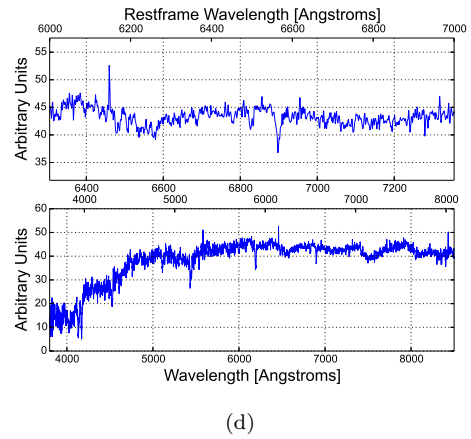
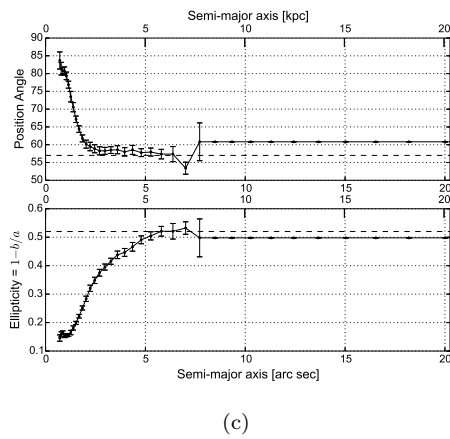
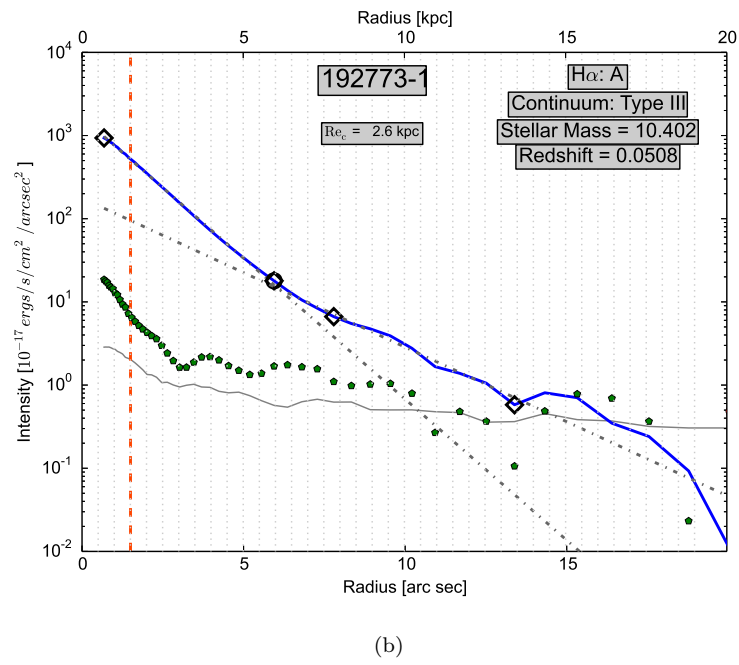
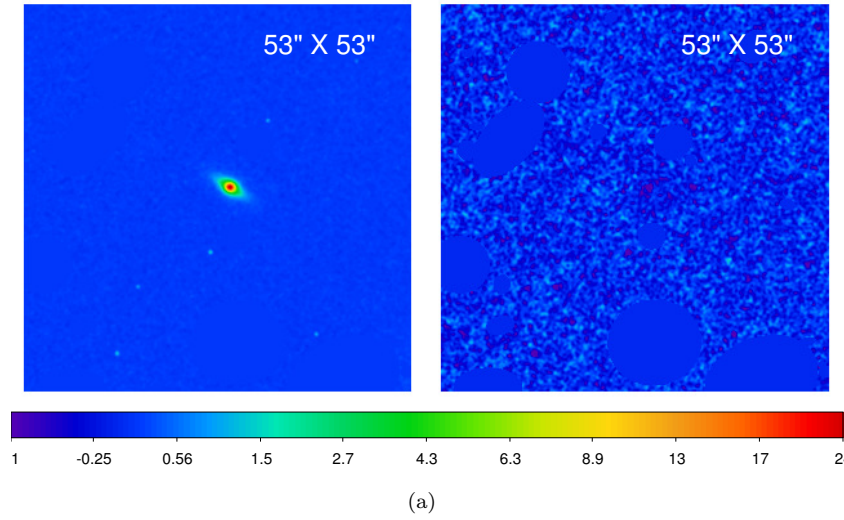


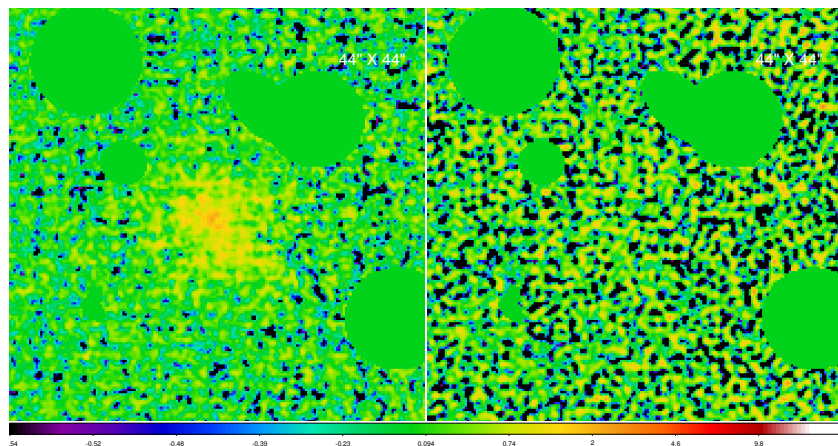
(c)



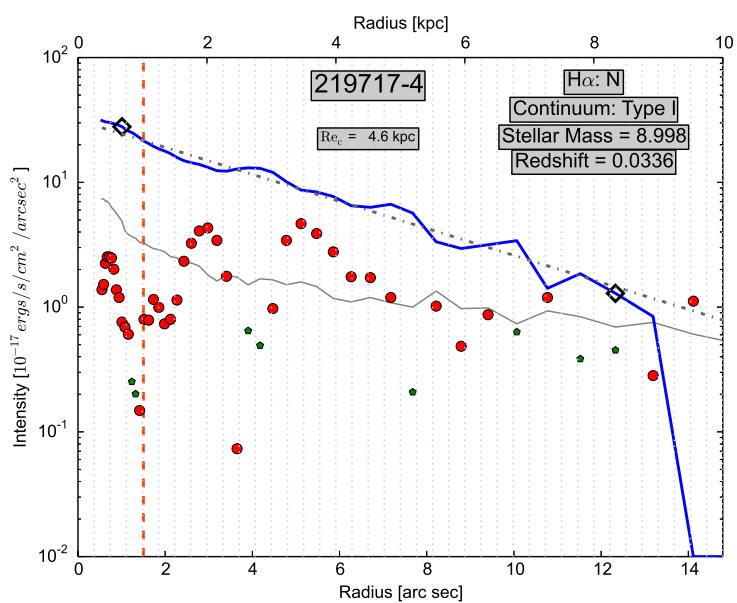
(d)



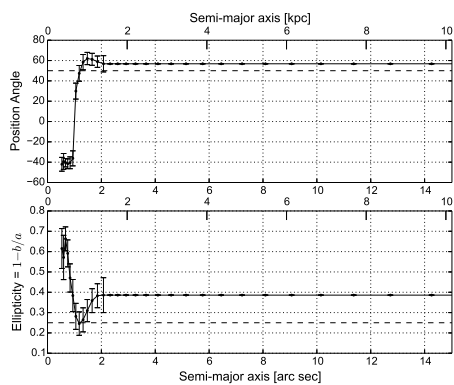




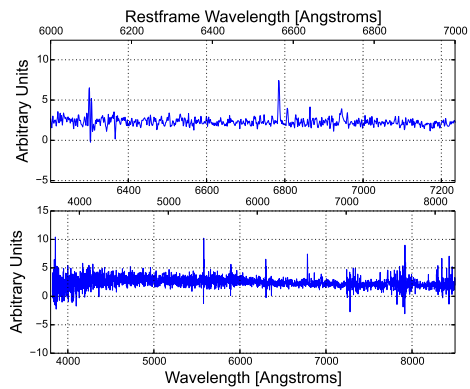
(a)



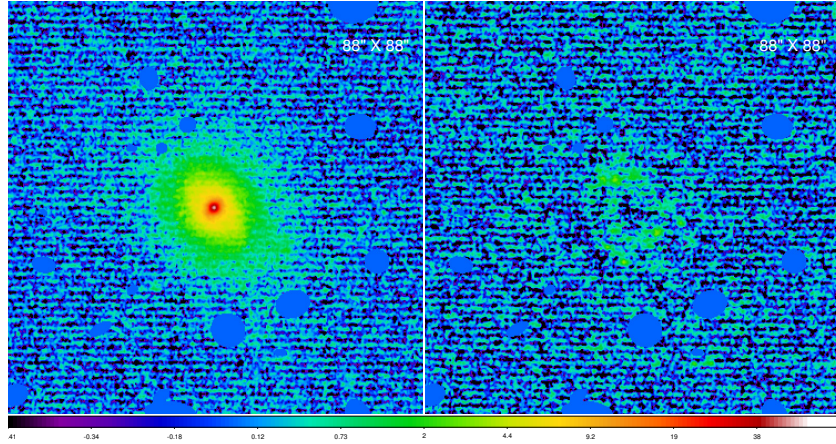
(b)



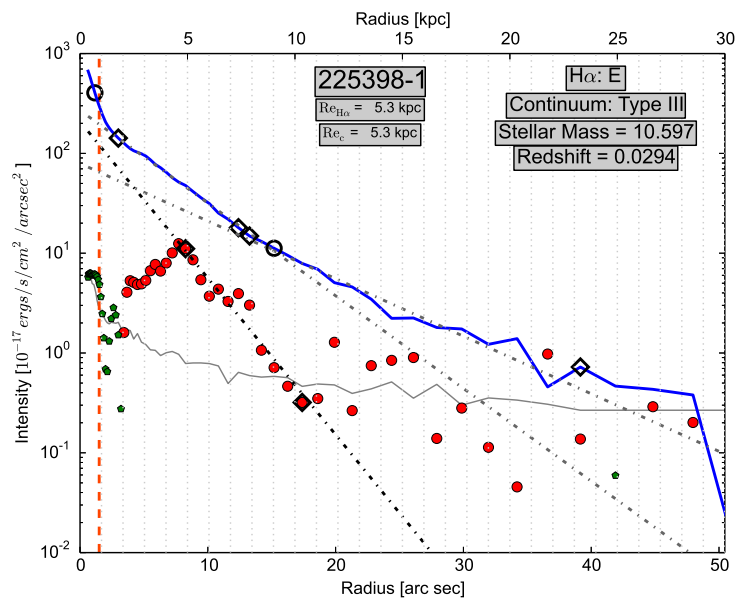
(c)



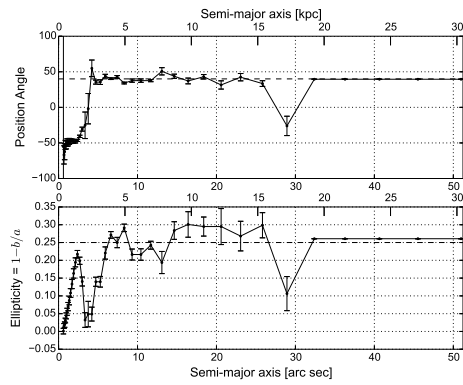
(d)



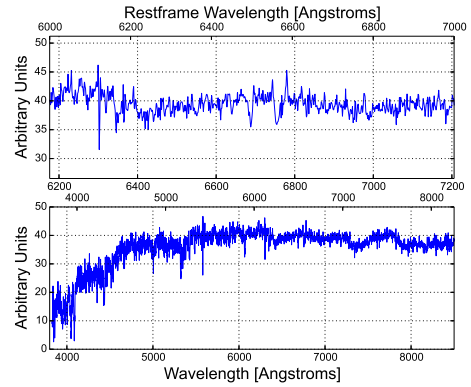
(a)



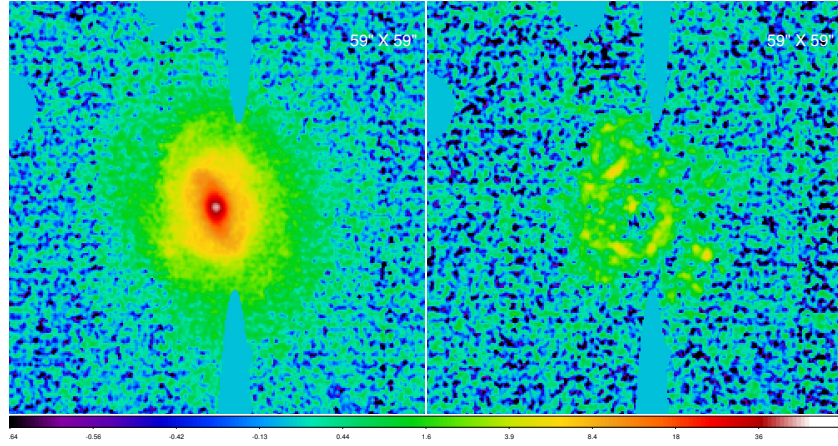
(b)



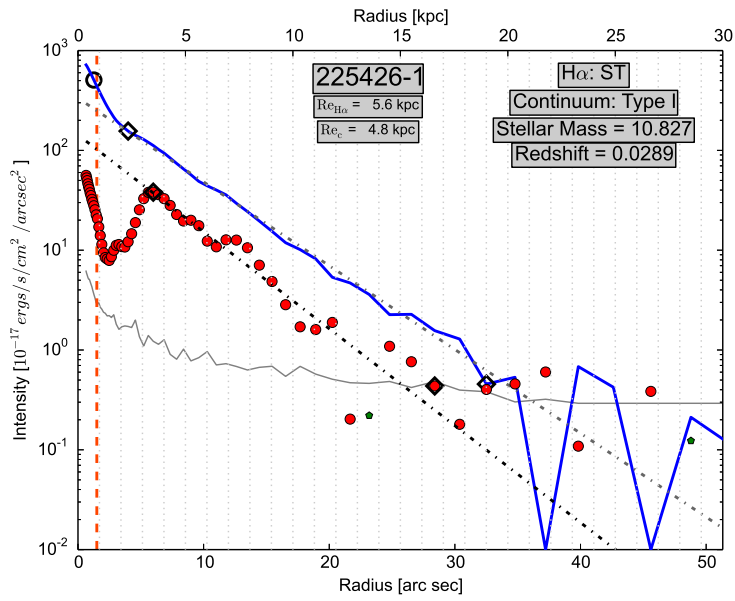
(c)



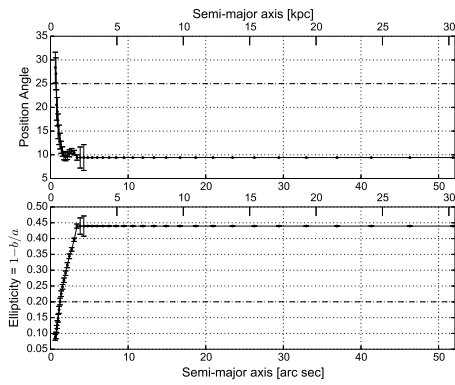
(d)



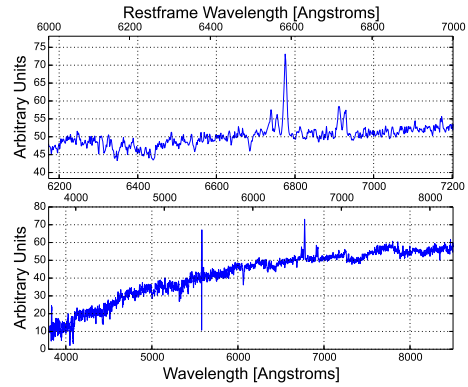
(a)



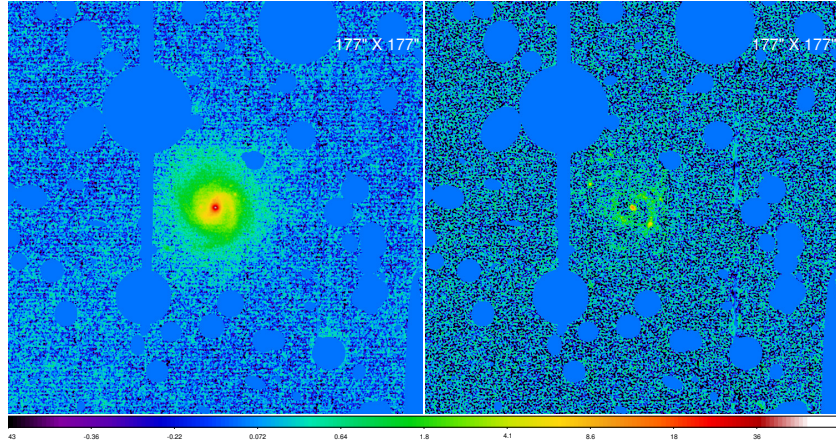
(b)



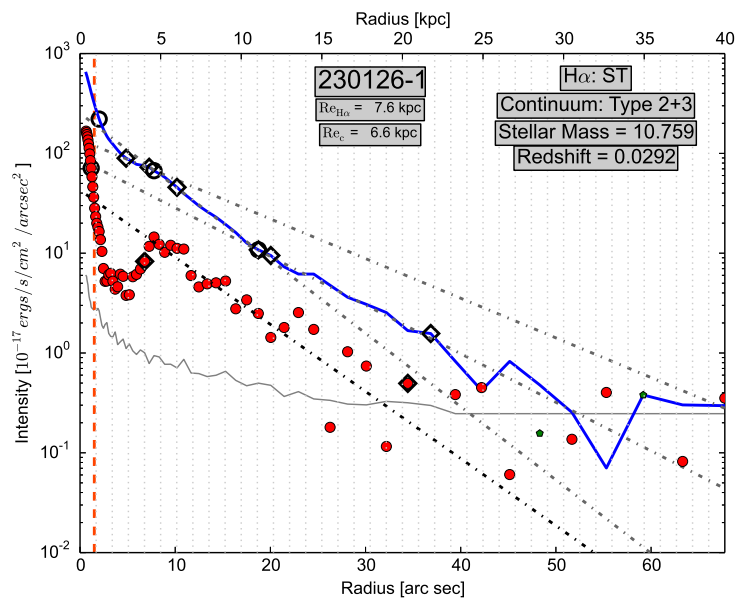
(c)



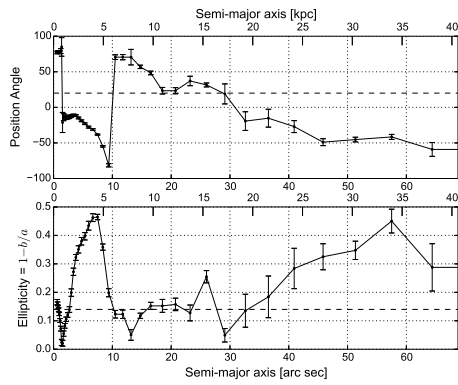
(d)



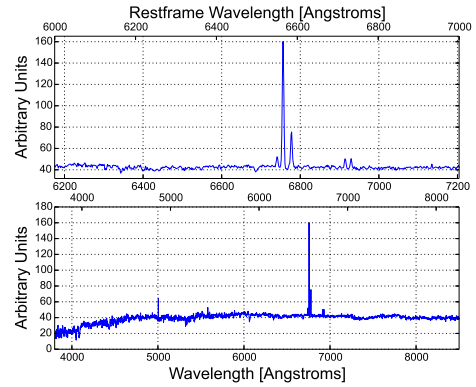
(a)



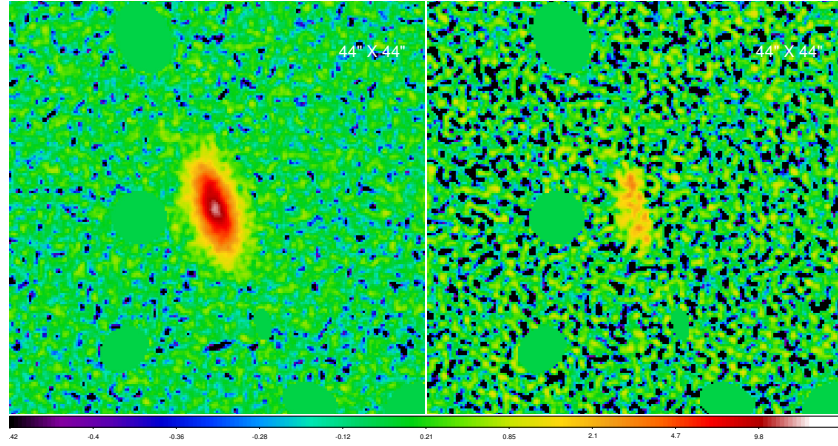
(b)



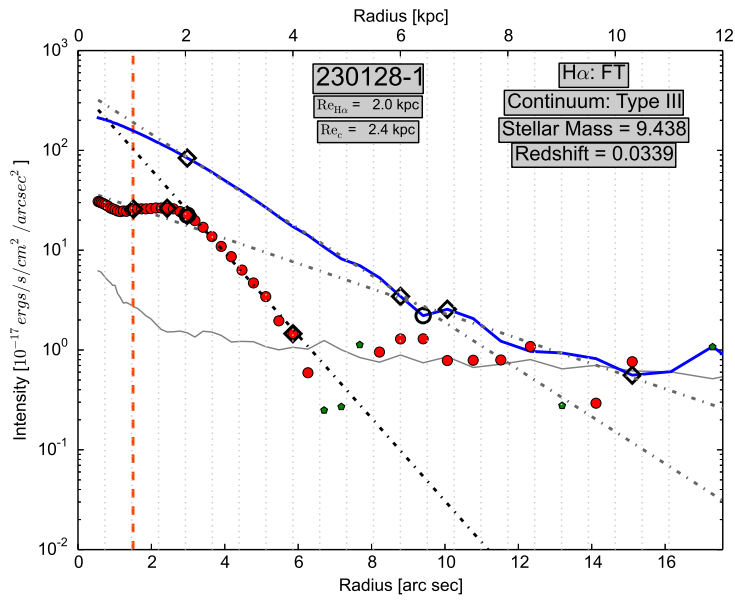
(c)



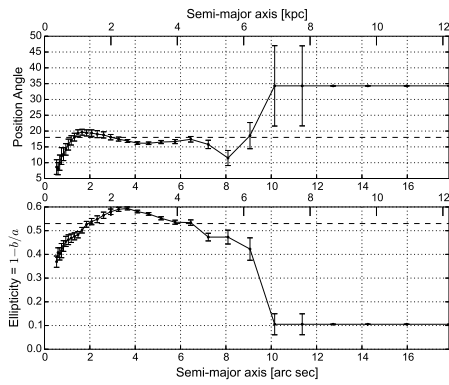
(d)



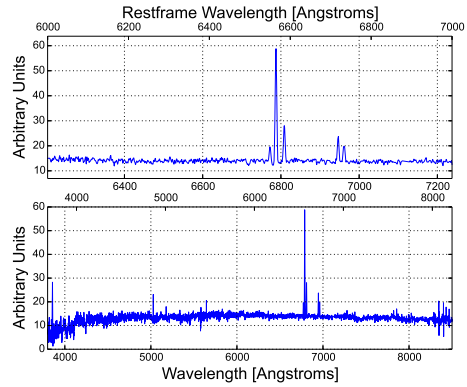
(a)



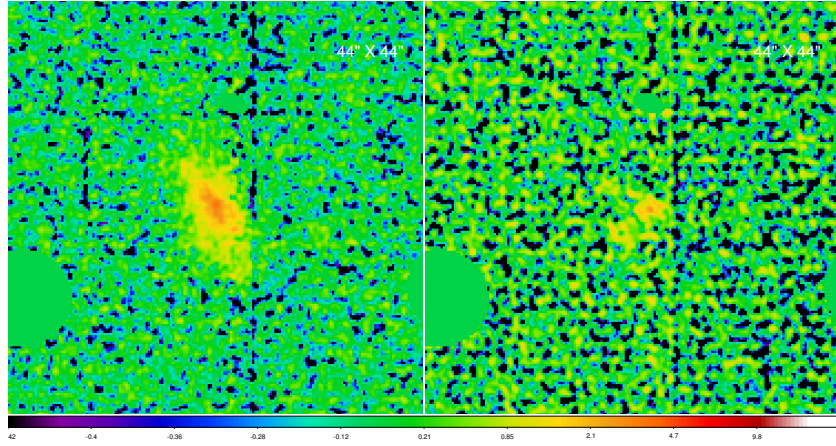
(b)



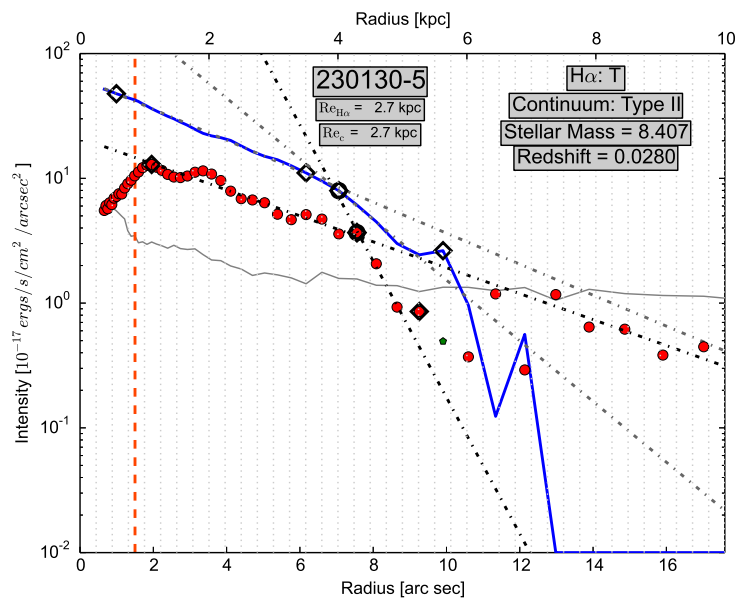
(c)



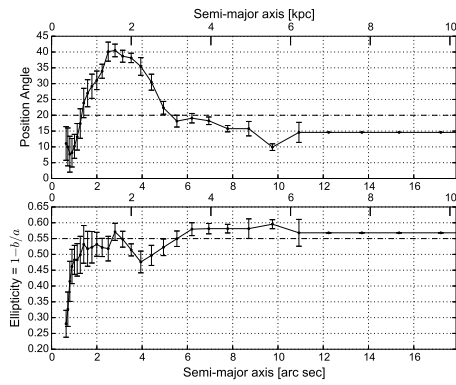
(d)



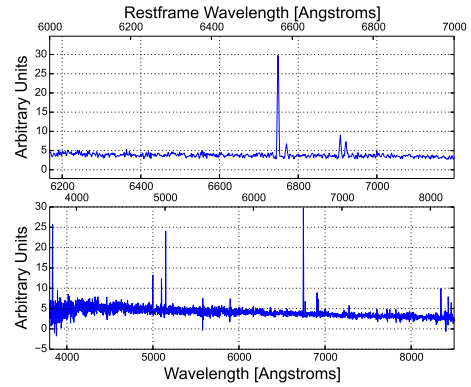
(a)



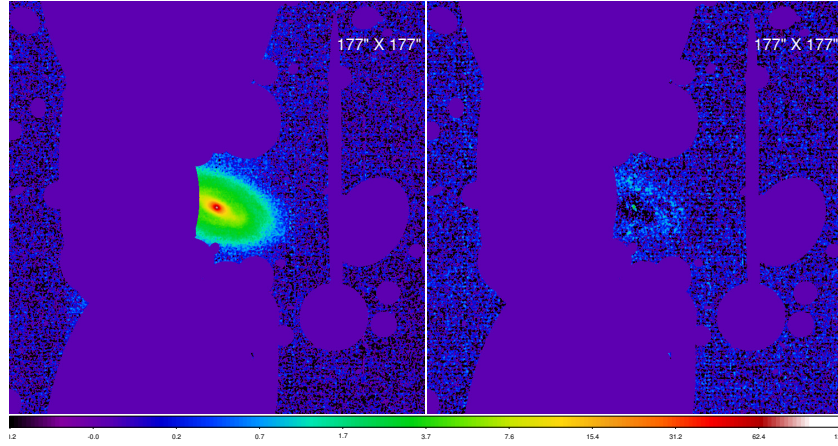
(b)



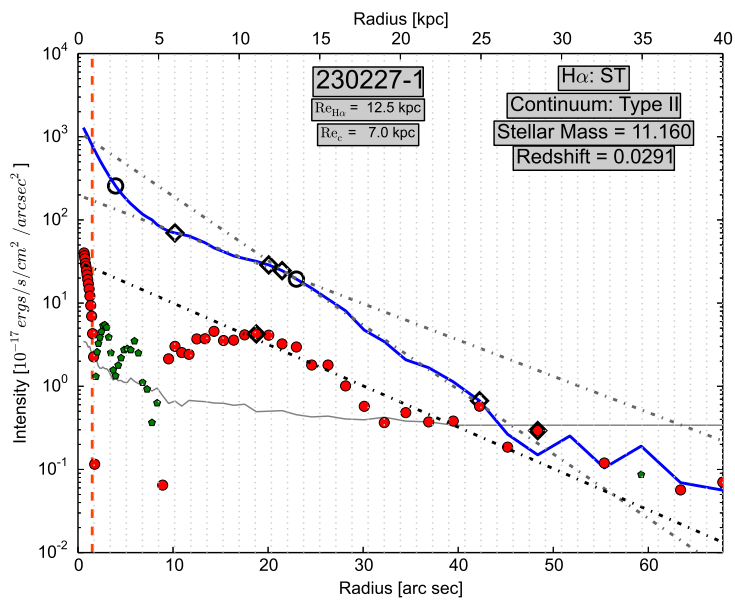
(c)



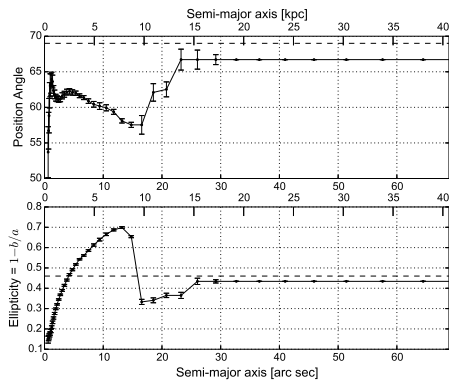
(d)



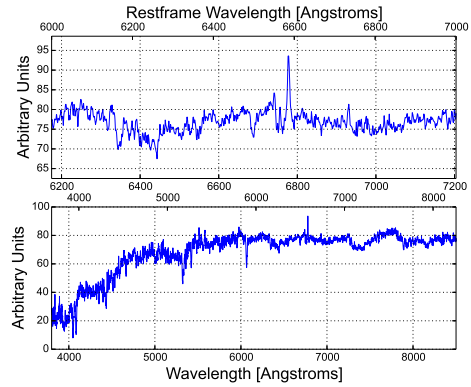
(a)



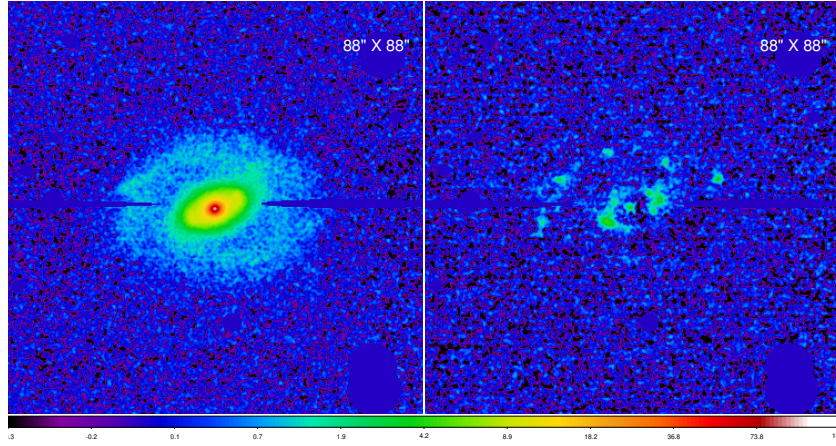
(b)



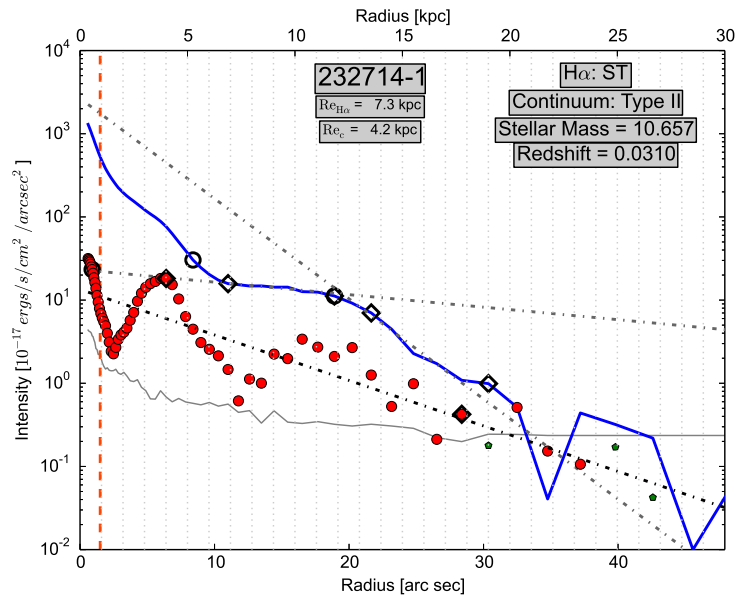
(c)



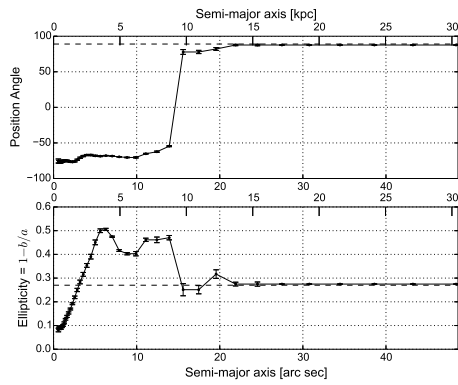
(d)



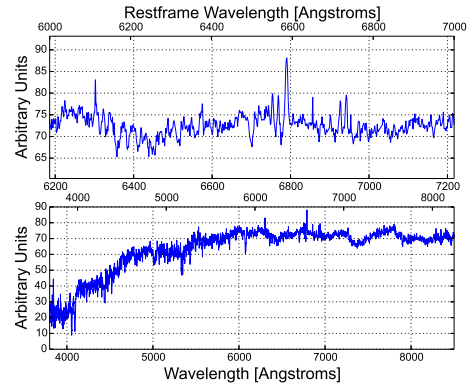
(a)



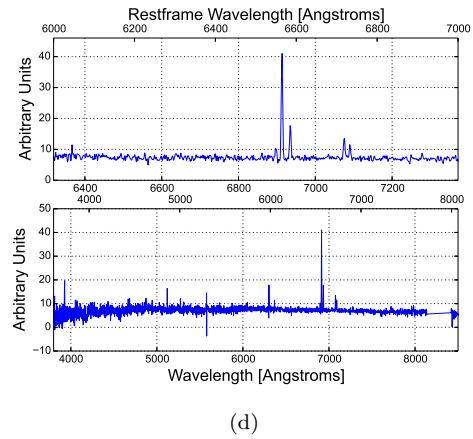
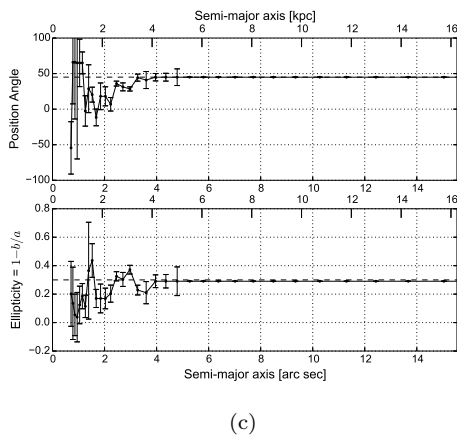
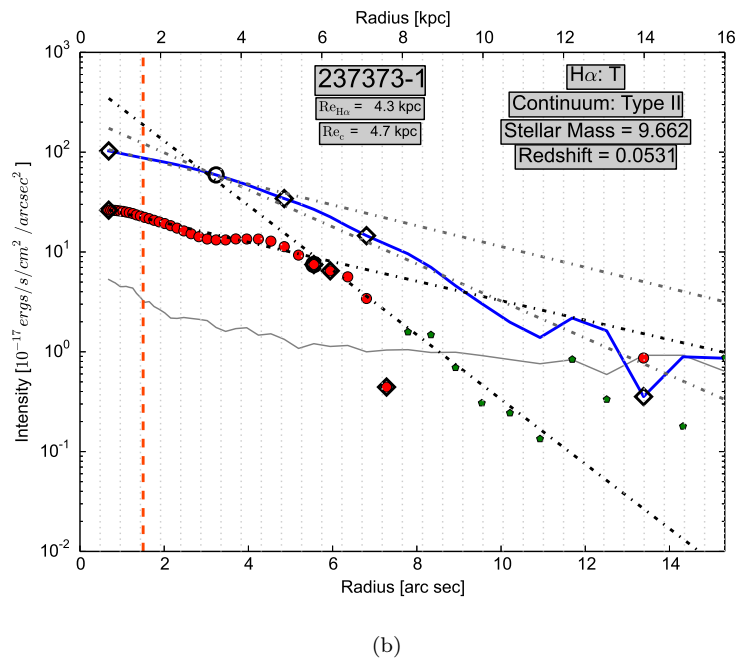
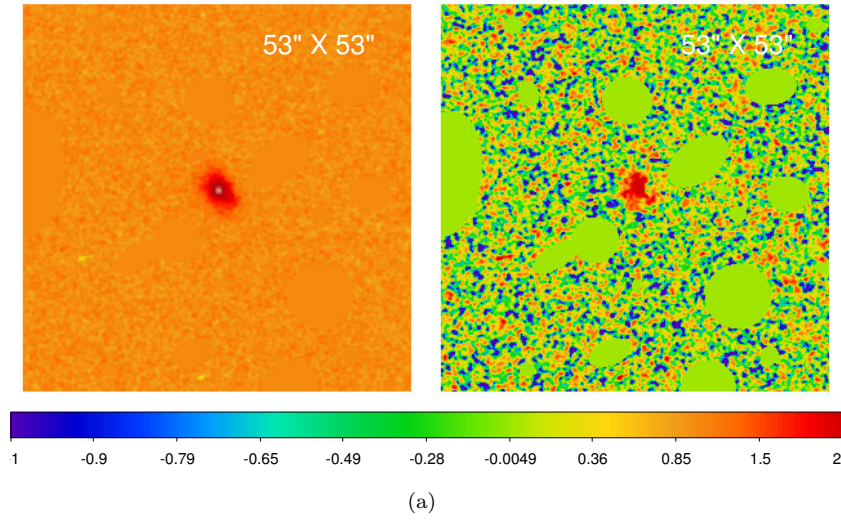
(b)

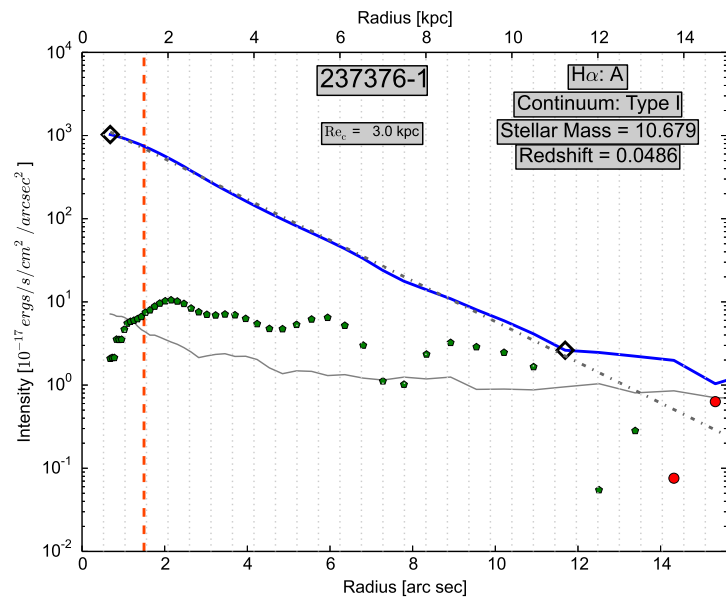
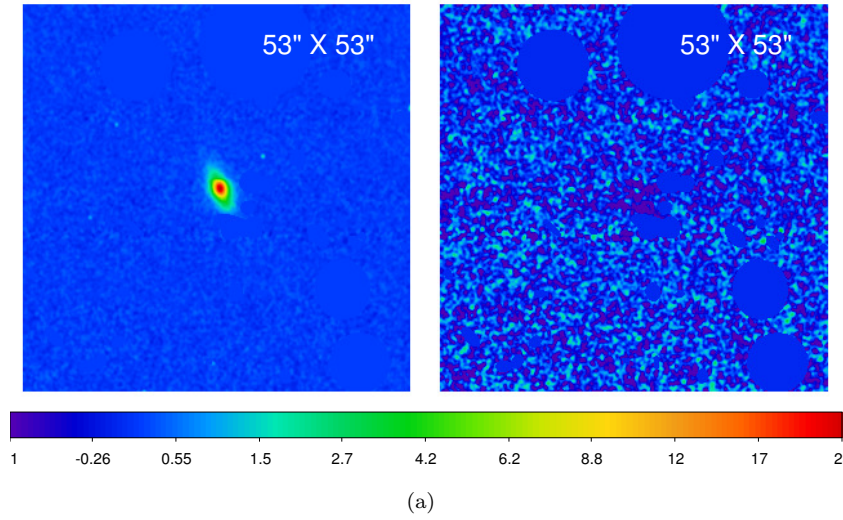


(c)

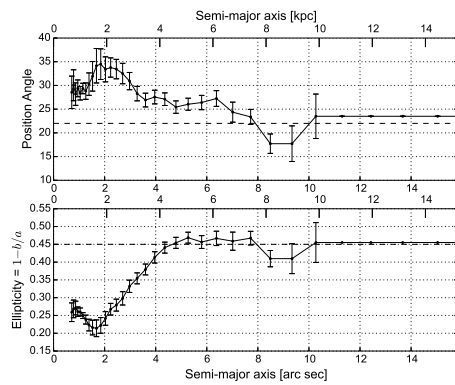


(d)

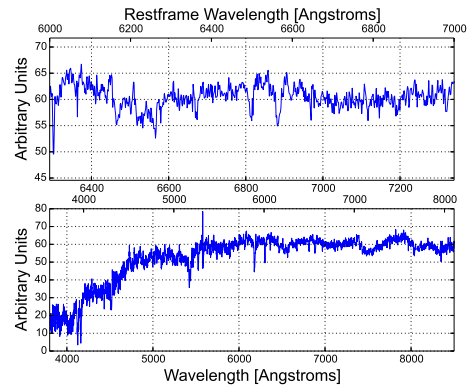




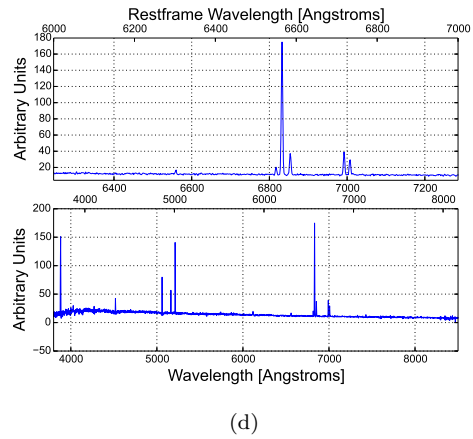
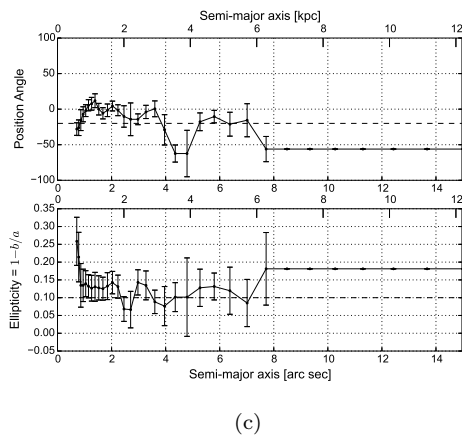
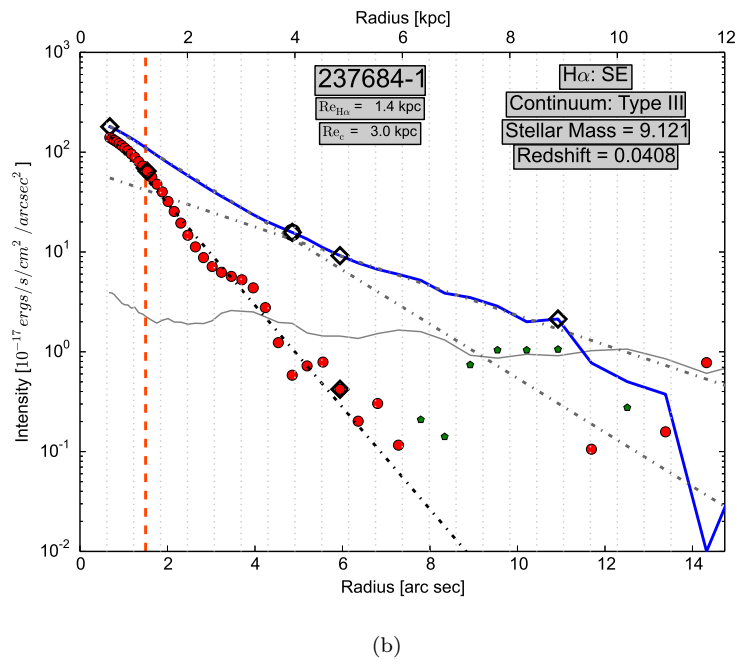
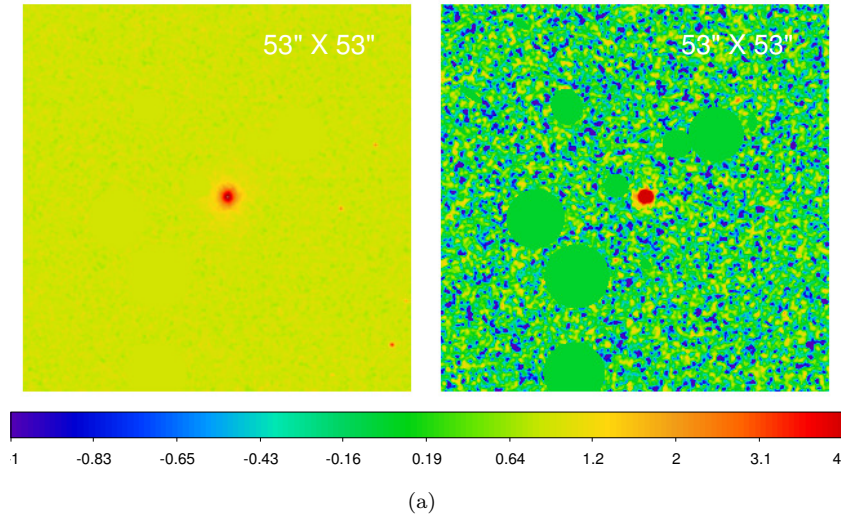
(b)

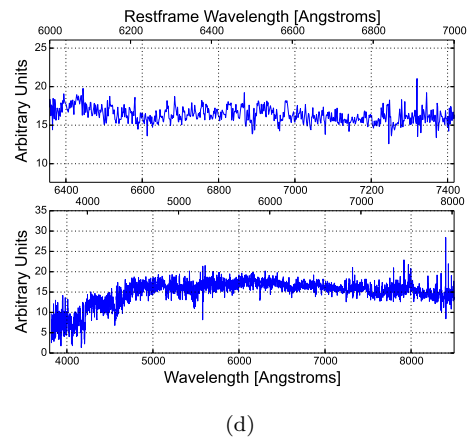
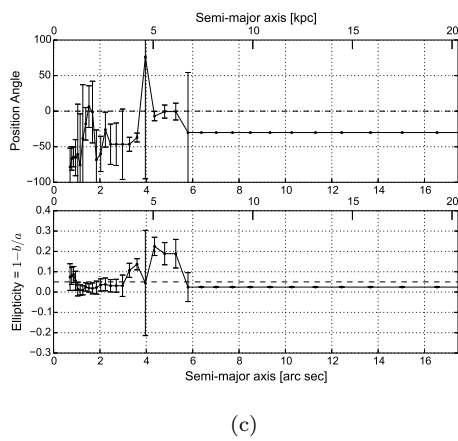
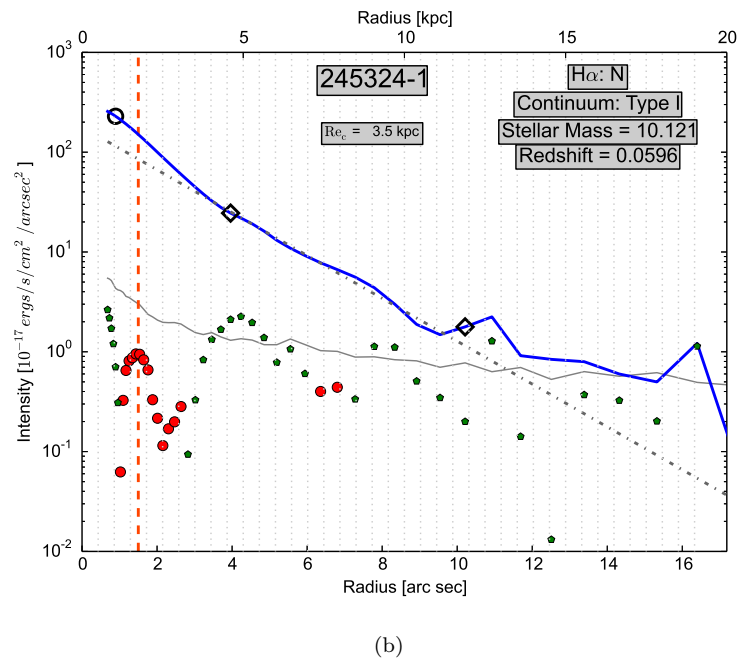
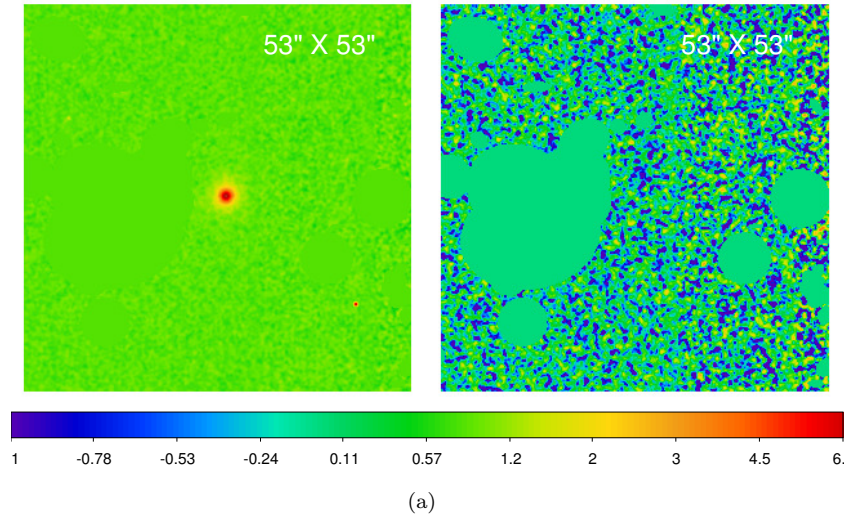


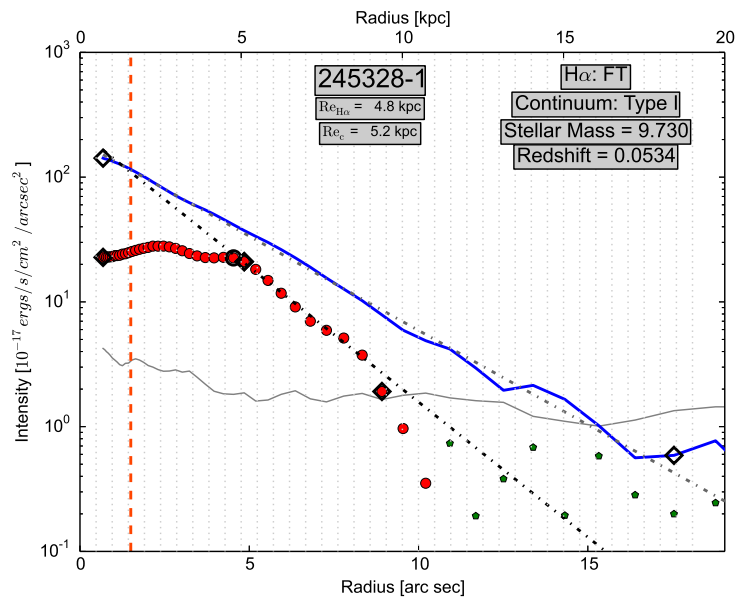
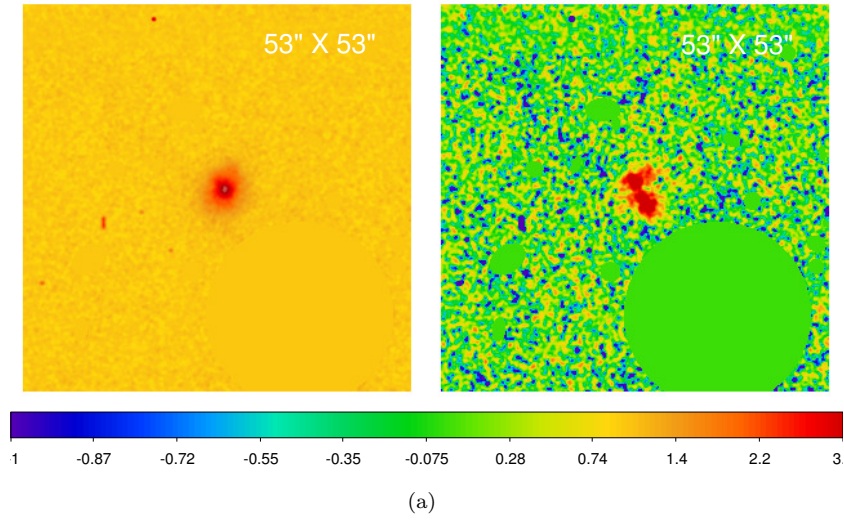
(c)



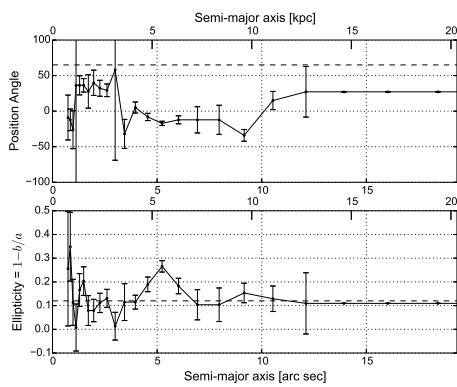
(d)



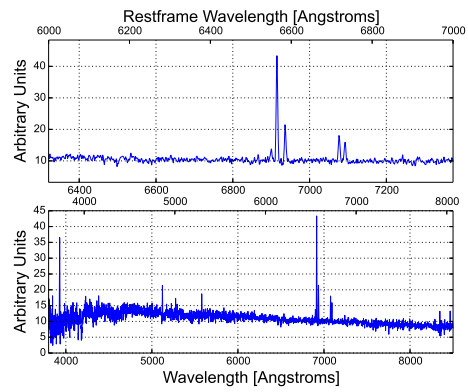




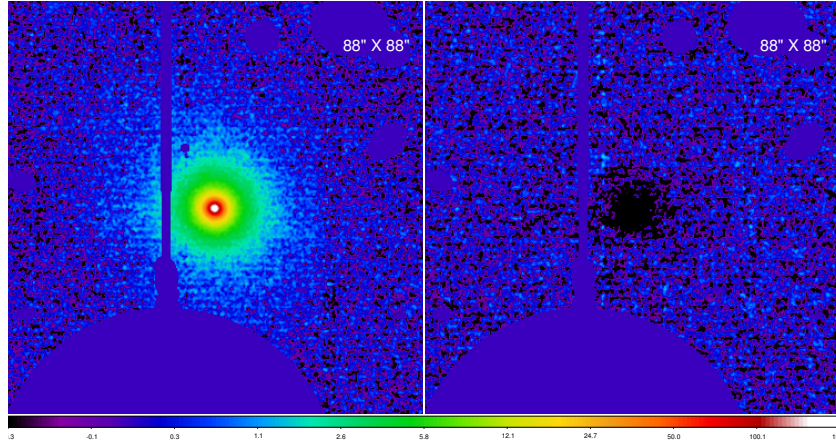
(b)



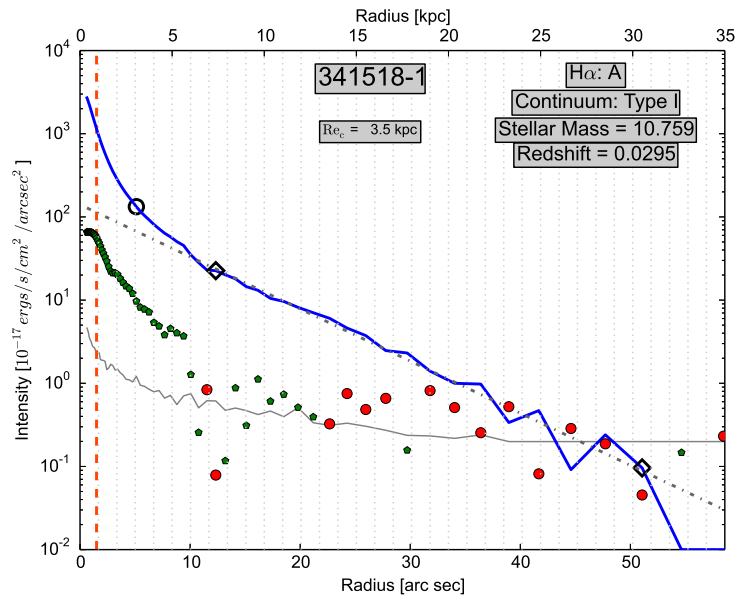
(c)



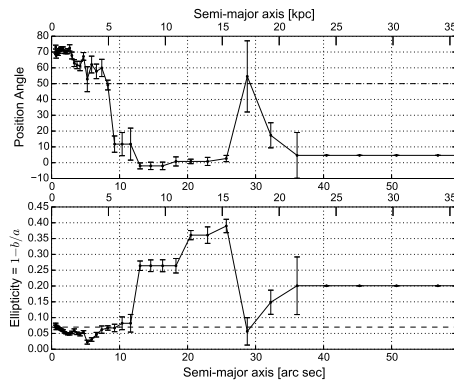
(d)



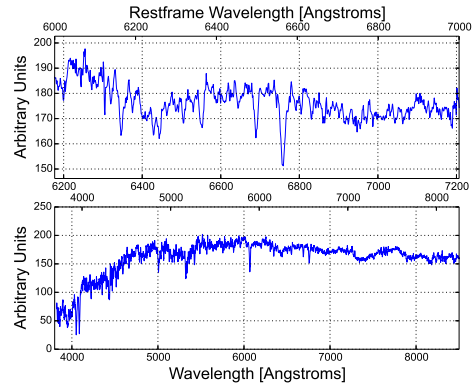
(a)



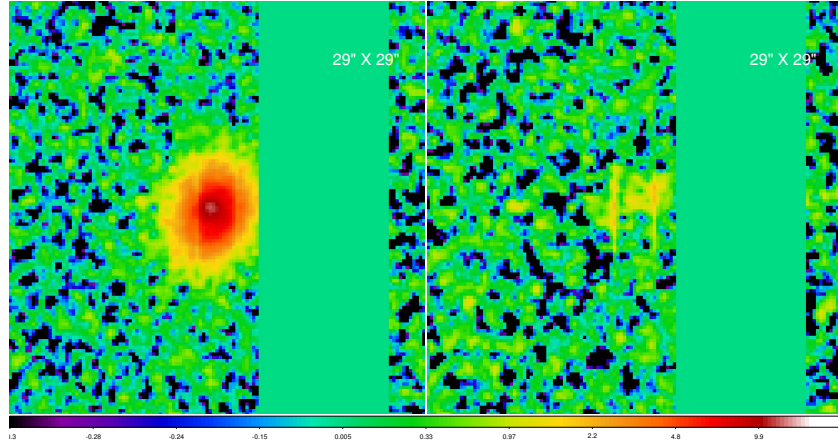
(b)



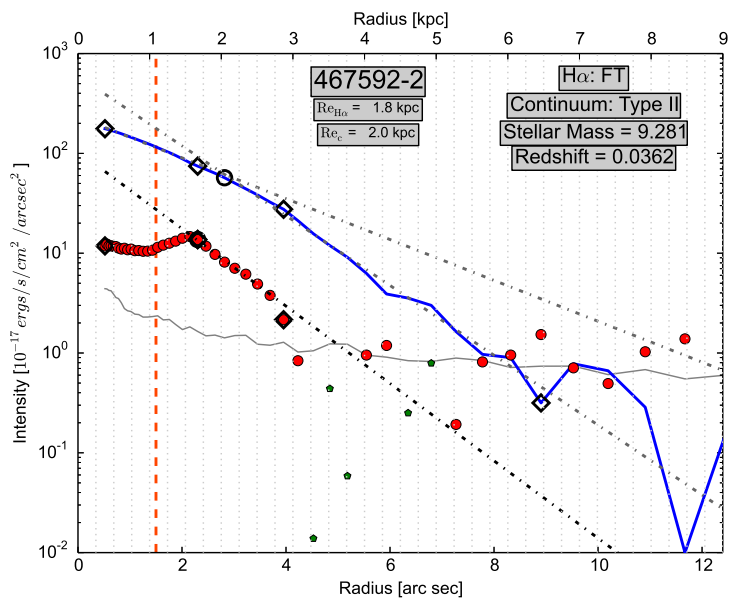
(c)



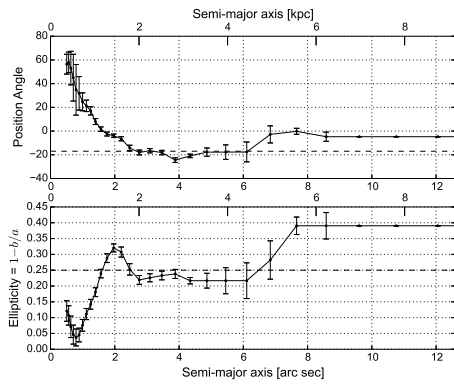
(d)



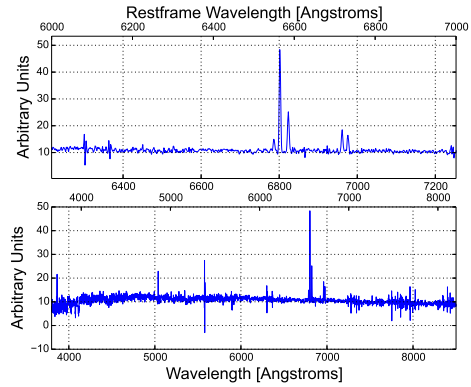
(a)



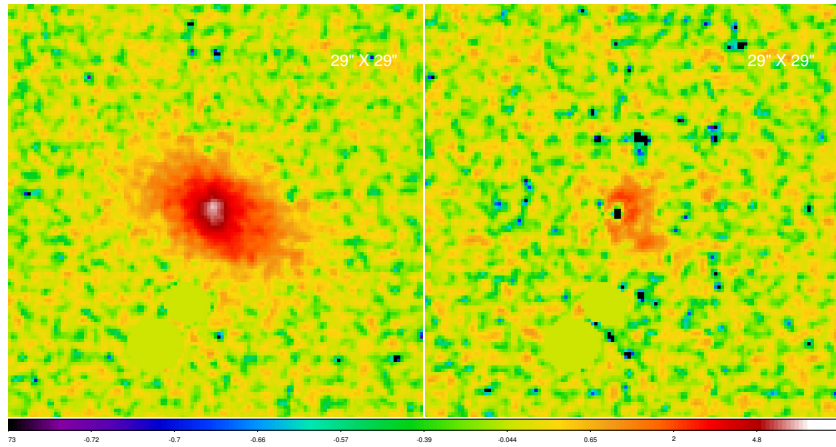
(b)



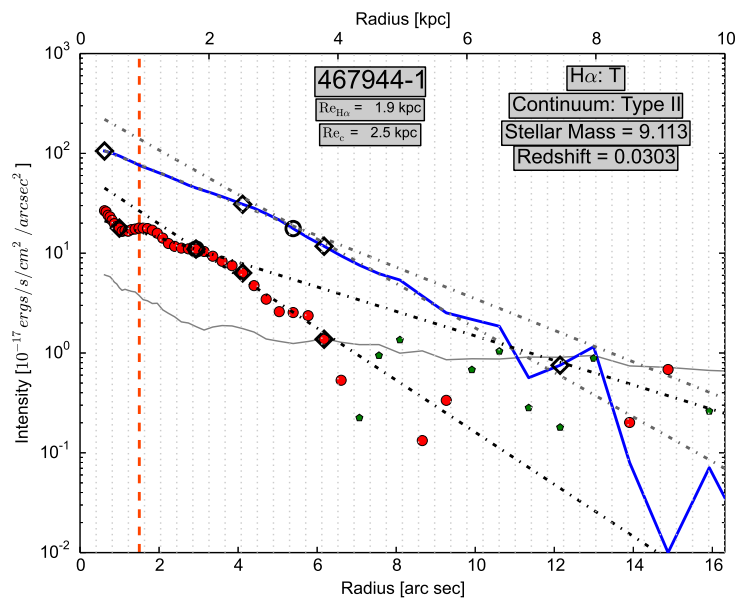
(c)



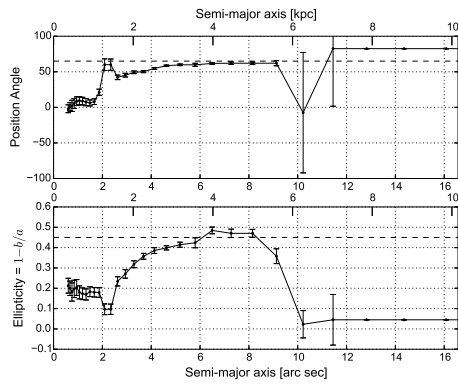
(d)



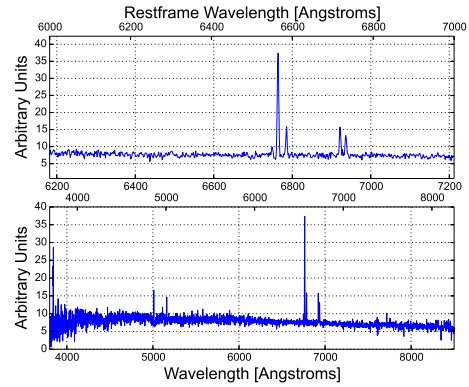
(a)



(b)



(c)



(d)

Appendix B

SDSS derived parameters

Here we include the table containing various galaxy derived parameters using SDSS spectroscopic and photometric survey data. The details of each column are given below (also see Chapter 2 section 2.1).

- **Col 1:** Group id from the [Yang et al. \(2007\)](#) catalog based on SDSS DR7 data.
- **Col 2:** Galaxy id assigned for the observed galaxy in the HAGGIS survey.
- **Col 3:** Galaxy id from New York University Value-Added Galaxy Catalog (NYU VAGC) catalog based on SDSS DR7 data. This can be used in cross-matching HAGGIS galaxies with SDSS and other surveys.
- **Col 4,5:** Positional coordinates of the galaxy in world coordinate (WCS) system in decimal degrees (J2000).
- **Col 6,7:** Weighted average of the positional coordinates in world coordinate (WCS) system in decimal degrees (J2000) of all galaxies in the respective groups derived for this work.
- **Col 8:** SDSS spectroscopic redshift of the galaxy.
- **Col 9:** : The logarithmic stellar mass of the galaxy in units of M_{\odot} computed using i -band luminosity derived from SDSS photometric observations and i -band mass to light ratio computed from SDSS derived $g-i$ color based on the prescriptions given in [Zibetti et al. \(2009\)](#) which assume a Chabrier IMF.

- **Col 10:** The estimated logarithmic halo mass of the group in units of M_{\odot} described in Yang et al. (2007). It is derived as described in Chapter 2 section 2.1.
- **Col 11:** The classification of a galaxy into central (1) or satellite (2) based on a ranking in stellar mass.

TABLE B.1: Table of derived parameters from SDSS photometric and spectroscopic data.

Group id (1)	Galaxy id (2)	NYU VAGC (3)	Galaxy RA (4)	Galaxy DEC (5)	Group RA (6)	Group DEC (7)	SDSS redshift (8)	$\log_{10}(M_*)$ (M_{\odot}) (9)	$\log_{10}(M_{\text{halo}})$ (M_{\odot}) (10)	Central/ Satellite (11)
13	13-1	1734937	13.8457	-1.2112	14.2269	-0.6660	0.0418	10.47	14.52	2
13	13-2	1734938	13.8625	-1.2231	14.2269	-0.6660	0.0435	9.77	14.52	2
13	13-3	1734939	13.8797	-1.2235	14.2269	-0.6660	0.0430	10.25	14.52	2
13	13-4	1734940	13.8846	-1.2111	14.2269	-0.6660	0.0459	10.27	14.52	2
13	13-8	1734957	13.9399	-1.0548	14.2269	-0.6660	0.0440	10.02	14.52	2
13	13-9	1734958	13.9403	-1.0843	14.2269	-0.6660	0.0423	9.88	14.52	2
13	13-11	1734960	13.9566	-1.0817	14.2269	-0.6660	0.0446	10.56	14.52	2
13	13-12	1734961	13.9631	-1.1647	14.2269	-0.6660	0.0477	11.14	14.52	2
13	13-13	1734963	13.9722	-1.1165	14.2269	-0.6660	0.0455	9.82	14.52	2
13	13-14	1734965	13.9914	-1.2399	14.2269	-0.6660	0.0446	10.22	14.52	2
13	13-15	1734966	13.9966	-1.1635	14.2269	-0.6660	0.0459	10.11	14.52	2
13	13-16	1734968	14.0169	-1.2175	14.2269	-0.6660	0.0437	9.70	14.52	2
13	13-17	1734969	14.0207	-1.1359	14.2269	-0.6660	0.0450	10.07	14.52	2
13	13-18	1734970	14.0251	-1.0571	14.2269	-0.6660	0.0432	10.29	14.52	2
13	13-19	1734978	14.0597	-1.1444	14.2269	-0.6660	0.0450	10.41	14.52	2
13	13-20	1734990	14.1280	-1.1729	14.2269	-0.6660	0.0422	10.71	14.52	2
13	13-21	1734992	14.2197	-1.1592	14.2269	-0.6660	0.0457	10.75	14.52	2
13	13-22	1734995	14.1026	-1.1429	14.2269	-0.6660	0.0430	10.69	14.52	2
13	13-23	1734997	14.1217	-1.2255	14.2269	-0.6660	0.0441	10.75	14.52	2
13	13-24	1734998	14.1222	-1.0991	14.2269	-0.6660	0.0421	9.75	14.52	2
13	13-25	1735004	14.1601	-1.1260	14.2269	-0.6660	0.0453	10.45	14.52	2
13	13-32	2091881	13.9772	-0.9207	14.2269	-0.6660	0.0450	11.54	14.52	2
13	13-34	2091883	14.0981	-0.9869	14.2269	-0.6660	0.0440	10.90	14.52	2
13	13-35	2091891	14.0473	-0.9702	14.2269	-0.6660	0.0462	9.99	14.52	2
13	13-37	2091904	14.1154	-1.0240	14.2269	-0.6660	0.0464	10.23	14.52	2
13	13-38	2091907	14.1703	-1.0345	14.2269	-0.6660	0.0443	10.69	14.52	2
13	13-40	2091912	14.2150	-1.0072	14.2269	-0.6660	0.0479	10.17	14.52	2
13	13-41	2091914	14.2332	-0.9968	14.2269	-0.6660	0.0459	10.10	14.52	2
13	13-43	2091927	14.2705	-0.9192	14.2269	-0.6660	0.0446	10.73	14.52	2
183	183-1	509387	151.2738	54.3581	151.0250	54.6380	0.0461	9.95	13.88	2
183	183-2	509388	151.3379	54.4382	151.0250	54.6380	0.0476	10.35	13.88	2
183	183-3	511476	150.3838	54.4898	151.0250	54.6380	0.0467	10.38	13.88	2
183	183-5	511487	150.6182	54.7214	151.0250	54.6380	0.0477	10.23	13.88	2
183	183-7	511490	150.8293	54.6856	151.0250	54.6380	0.0472	10.62	13.88	2
183	183-8	511491	150.7254	54.8052	151.0250	54.6380	0.0473	9.95	13.88	2
183	183-9	511494	150.8165	54.7732	151.0250	54.6380	0.0480	10.88	13.88	2
183	183-14	916913	151.0036	54.5172	151.0250	54.6380	0.0471	10.00	13.88	2
183	183-17	916916	151.0127	54.6687	151.0250	54.6380	0.0481	10.01	13.88	2
183	183-18	916917	151.1119	54.5967	151.0250	54.6380	0.0471	9.82	13.88	2
183	183-19	916918	151.0633	54.6627	151.0250	54.6380	0.0473	10.23	13.88	2
183	183-20	916919	151.1905	54.5372	151.0250	54.6380	0.0446	10.03	13.88	2
183	183-23	916925	151.2154	54.5919	151.0250	54.6380	0.0463	10.05	13.88	2
183	183-24	916926	151.2086	54.6096	151.0250	54.6380	0.0482	9.96	13.88	2
183	183-25	916927	151.2938	54.5488	151.0250	54.6380	0.0499	10.21	13.88	2
183	183-26	916928	151.2958	54.5735	151.0250	54.6380	0.0481	9.95	13.88	2
183	183-28	917561	150.7126	54.8423	151.0250	54.6380	0.0491	10.34	13.88	2
183	183-29	917562	150.7398	54.8294	151.0250	54.6380	0.0481	9.77	13.88	2
390	390-1	327346	40.8031	-8.3778	41.0741	-8.1832	0.0307	8.84	13.77	2
390	390-2	327351	41.1592	-8.3141	41.0741	-8.1832	0.0299	10.02	13.77	2
390	390-4	327356	41.2341	-8.4033	41.0741	-8.1832	0.0295	10.27	13.77	2
390	390-5	329877	40.8628	-8.1093	41.0741	-8.1832	0.0311	11.06	13.77	2
390	390-6	329879	40.7740	-8.1334	41.0741	-8.1832	0.0296	10.10	13.77	2
390	390-7	329880	40.7742	-7.9815	41.0741	-8.1832	0.0289	8.63	13.77	2
390	390-8	329887	40.9247	-8.1012	41.0741	-8.1832	0.0316	10.52	13.77	2
390	390-9	329888	41.0099	-7.9744	41.0741	-8.1832	0.0309	10.77	13.77	2
390	390-10	329889	40.8929	-8.0329	41.0741	-8.1832	0.0319	9.93	13.77	2
390	390-11	329894	41.0817	-8.0885	41.0741	-8.1832	0.0287	9.25	13.77	2
390	390-18	369885	40.7493	-8.2895	41.0741	-8.1832	0.0316	11.38	13.77	1

Group id (1)	Galaxy id (2)	NYU VAGC (3)	Galaxy RA (4)	Galaxy DEC (5)	Group RA (6)	Group DEC (7)	SDSS redshift (8)	$\log_{10}(M_*)$ (M_\odot) (9)	$\log_{10}(M_{\text{halo}})$ (M_\odot) (10)	Central/ Satellite (11)
390	390-22	369898	40.9103	-8.2610	41.0741	-8.1832	0.0303	9.06	13.77	2
390	390-23	369899	40.9414	-8.1825	41.0741	-8.1832	0.0305	10.46	13.77	2
390	390-24	369903	41.1892	-8.1642	41.0741	-8.1832	0.0300	11.06	13.77	2
596	596-1	801065	151.2728	50.1149	151.3455	50.1811	0.0500	10.70	13.69	2
596	596-2	801066	151.3339	50.0535	151.3455	50.1811	0.0502	10.85	13.69	2
596	596-3	801067	151.4305	50.0249	151.3455	50.1811	0.0494	10.53	13.69	2
596	596-4	801069	151.3379	50.1613	151.3455	50.1811	0.0511	9.68	13.69	2
596	596-5	801070	151.4671	50.0839	151.3455	50.1811	0.0507	9.70	13.69	2
596	596-6	801071	151.6125	50.1092	151.3455	50.1811	0.0504	10.51	13.69	2
596	596-7	801072	151.6106	50.1149	151.3455	50.1811	0.0504	10.37	13.69	2
596	596-8	801073	151.5697	50.2233	151.3455	50.1811	0.0507	10.41	13.69	2
596	596-10	819399	150.8796	50.0963	151.3455	50.1811	0.0502	10.34	13.69	2
596	596-11	819404	151.1989	50.2220	151.3455	50.1811	0.0511	10.95	13.69	2
596	596-12	819410	151.2994	50.1832	151.3455	50.1811	0.0505	11.50	13.69	1
596	596-13	819413	151.2470	50.2467	151.3455	50.1811	0.0493	10.72	13.69	2
596	596-14	819414	151.3153	50.1708	151.3455	50.1811	0.0506	9.90	13.69	2
596	596-15	819415	151.2844	50.2047	151.3455	50.1811	0.0496	10.27	13.69	2
596	596-17	819418	151.4244	50.1918	151.3455	50.1811	0.0512	9.78	13.69	2
596	596-18	819419	151.3966	50.2459	151.3455	50.1811	0.0495	10.24	13.69	2
596	596-19	819422	151.5337	50.2401	151.3455	50.1811	0.0509	11.19	13.69	2
596	596-20	819423	151.4661	50.3345	151.3455	50.1811	0.0495	9.52	13.69	2
596	596-21	819425	151.5337	50.3571	151.3455	50.1811	0.0509	9.83	13.69	2
607	607-1	1156943	148.8064	36.4243	149.2106	36.5097	0.0502	10.02	13.82	2
607	607-3	1156950	149.0643	36.4321	149.2106	36.5097	0.0516	10.47	13.82	2
607	607-4	1156952	149.0369	36.3514	149.2106	36.5097	0.0518	10.01	13.82	2
607	607-5	1156953	149.0379	36.3779	149.2106	36.5097	0.0518	10.10	13.82	2
607	607-6	1156954	149.0248	36.4274	149.2106	36.5097	0.0517	9.81	13.82	2
607	607-7	1156955	149.0118	36.4803	149.2106	36.5097	0.0508	10.14	13.82	2
607	607-8	1156959	149.1370	36.3892	149.2106	36.5097	0.0500	10.55	13.82	2
607	607-9	1156960	149.0822	36.4958	149.2106	36.5097	0.0504	10.89	13.82	2
607	607-10	1156962	149.1576	36.6029	149.2106	36.5097	0.0517	10.92	13.82	2
607	607-12	1156966	149.3696	36.6437	149.2106	36.5097	0.0497	11.25	13.82	2
607	607-14	1180768	149.1816	36.3601	149.2106	36.5097	0.0496	10.49	13.82	2
607	607-15	1180770	149.2718	36.3228	149.2106	36.5097	0.0514	10.16	13.82	2
607	607-17	1181754	149.3359	36.7719	149.2106	36.5097	0.0486	10.02	13.82	2
607	607-18	1181762	149.4351	36.7129	149.2106	36.5097	0.0495	11.08	13.82	2
639	639-1	447724	167.8401	4.5497	167.5965	4.8281	0.0303	9.34	13.04	2
639	639-3	449354	167.5536	4.7844	167.5965	4.8281	0.0302	10.57	13.04	2
639	639-4	449355	167.5704	4.7873	167.5965	4.8281	0.0294	9.31	13.04	2
639	639-6	449365	167.5966	4.7897	167.5965	4.8281	0.0318	10.17	13.04	2
639	639-7	449366	167.6023	4.8300	167.5965	4.8281	0.0304	10.92	13.04	1
639	639-13	458286	167.5834	4.6883	167.5965	4.8281	0.0305	10.73	13.04	2
639	639-14	458289	167.5868	4.5797	167.5965	4.8281	0.0304	9.21	13.04	2
639	639-15	458299	167.6830	4.7346	167.5965	4.8281	0.0294	9.39	13.04	2
639	639-16	458301	167.7568	4.6293	167.5965	4.8281	0.0307	8.98	13.04	2
916	916-4	290871	167.7334	3.2761	167.9154	3.1559	0.0293	9.12	13.36	2
916	916-5	290877	167.8090	3.3706	167.9154	3.1559	0.0292	8.61	13.36	2
916	916-6	290882	167.8705	3.2976	167.9154	3.1559	0.0294	8.54	13.36	2
916	916-7	290885	167.8696	3.2715	167.9154	3.1559	0.0302	10.55	13.36	2
916	916-8	290887	167.8911	3.4005	167.9154	3.1559	0.0300	8.89	13.36	2
916	916-9	429024	167.8022	3.0762	167.9154	3.1559	0.0314	10.00	13.36	2
916	916-10	429025	167.8239	3.1980	167.9154	3.1559	0.0299	10.76	13.36	2
916	916-11	429029	167.8215	3.2110	167.9154	3.1559	0.0301	10.35	13.36	2
916	916-12	429034	167.8927	3.1829	167.9154	3.1559	0.0305	9.37	13.36	2
916	916-13	429038	167.9964	3.1358	167.9154	3.1559	0.0298	11.27	13.36	1
916	916-14	429039	168.0078	3.0445	167.9154	3.1559	0.0297	10.53	13.36	2
916	916-15	429040	168.0282	3.1434	167.9154	3.1559	0.0302	10.57	13.36	2
916	916-16	429046	168.1139	3.2314	167.9154	3.1559	0.0302	9.56	13.36	2
960	960-1	1086047	137.0553	32.4999	137.2340	32.2991	0.0490	10.27	13.64	2
960	960-3	1086051	137.0879	32.4295	137.2340	32.2991	0.0499	11.04	13.64	2
960	960-4	1086053	137.2315	32.5759	137.2340	32.2991	0.0490	10.53	13.64	2
960	960-5	1153764	137.3849	32.0567	137.2340	32.2991	0.0486	10.60	13.64	2
960	960-7	1154751	137.1894	32.3899	137.2340	32.2991	0.0486	10.39	13.64	2
960	960-8	1182511	137.0923	32.1130	137.2340	32.2991	0.0497	10.19	13.64	2
960	960-10	1182516	137.1067	32.2615	137.2340	32.2991	0.0488	10.35	13.64	2
960	960-12	1182520	137.2431	32.3350	137.2340	32.2991	0.0500	9.88	13.64	2
960	960-14	1182523	137.4335	32.2243	137.2340	32.2991	0.0495	10.30	13.64	2
1084	1084-1	1155400	147.1210	34.8174	147.4106	34.7100	0.0382	10.44	13.53	2
1084	1084-3	1178619	147.2205	34.7367	147.4106	34.7100	0.0389	9.33	13.53	2
1084	1084-4	1178621	147.3807	34.6388	147.4106	34.7100	0.0388	10.17	13.53	2
1084	1084-5	1178622	147.3989	34.7331	147.4106	34.7100	0.0391	10.87	13.53	2
1084	1084-6	1178624	147.4220	34.6240	147.4106	34.7100	0.0383	9.83	13.53	2
1084	1084-8	1178631	147.4993	34.8042	147.4106	34.7100	0.0384	10.06	13.53	2
1228	1228-1	168854	176.2765	-1.6692	176.3052	-1.7102	0.0276	10.48	13.27	2
1228	1228-2	168855	176.2912	-1.7626	176.3052	-1.7102	0.0270	10.85	13.27	2

Group id (1)	Galaxy id (2)	NYU VAGC (3)	Galaxy RA (4)	Galaxy DEC (5)	Group RA (6)	Group DEC (7)	SDSS redshift (8)	$\log_{10}(M_*)$ (M_\odot) (9)	$\log_{10}(M_{\text{halo}})$ (M_\odot) (10)	Central/ Satellite (11)
1228	1228-3	168857	176.3126	-1.7028	176.3052	-1.7102	0.0277	10.66	13.27	2
1228	1228-5	168872	176.3371	-1.8128	176.3052	-1.7102	0.0267	9.73	13.27	2
1228	1228-6	168873	176.3379	-1.7230	176.3052	-1.7102	0.0281	9.67	13.27	2
1228	1228-7	168878	176.3559	-1.7377	176.3052	-1.7102	0.0285	8.89	13.27	2
1228	1228-8	168879	176.3599	-1.7323	176.3052	-1.7102	0.0275	9.39	13.27	2
1228	1228-9	176579	176.3433	-1.8767	176.3052	-1.7102	0.0270	10.60	13.27	2
1228	1228-11	177779	176.1755	-1.6143	176.3052	-1.7102	0.0291	9.42	13.27	2
1228	1228-12	177780	176.2103	-1.6013	176.3052	-1.7102	0.0284	11.11	13.27	1
1228	1228-13	177787	176.3420	-1.5652	176.3052	-1.7102	0.0283	9.46	13.27	2
1644	1644-1	1075371	143.3599	10.0114	143.4667	10.1146	0.0109	8.67	12.65	2
1644	1644-2	1075383	143.5006	10.0295	143.4667	10.1146	0.0105	9.93	12.65	2
1644	1644-3	1075387	143.6110	9.9165	143.4667	10.1146	0.0105	9.79	12.65	2
1644	1644-4	1075390	143.7085	10.0671	143.4667	10.1146	0.0112	8.06	12.65	2
1644	1644-6	1121137	143.4420	10.1525	143.4667	10.1146	0.0108	11.28	12.65	1
1644	1644-7	1121139	143.4637	10.1594	143.4667	10.1146	0.0107	8.35	12.65	2
1644	1644-8	1121142	143.5116	10.1087	143.4667	10.1146	0.0105	10.43	12.65	2
1644	1644-11	1822637	143.3896	10.3873	143.4667	10.1146	0.0103	8.26	12.65	2
1791	1791-1	150438	31.0718	13.2504	31.3879	13.2852	0.0259	9.02	13.48	2
1791	1791-2	150440	31.3328	13.2585	31.3879	13.2852	0.0270	10.57	13.48	2
1791	1791-5	150446	31.4201	13.1755	31.3879	13.2852	0.0259	9.43	13.48	2
1826	1826-1	446536	131.7477	2.5817	131.7231	2.5943	0.0277	9.32	13.05	2
1826	1826-3	446543	131.8277	2.7623	131.7231	2.5943	0.0285	10.79	13.05	2
1826	1826-4	446544	131.8811	2.6902	131.7231	2.5943	0.0287	9.95	13.05	2
1826	1826-6	454514	131.5510	2.4105	131.7231	2.5943	0.0280	9.24	13.05	2
1826	1826-7	454520	131.6832	2.5374	131.7231	2.5943	0.0281	11.13	13.05	1
1826	1826-8	454524	131.7262	2.5601	131.7231	2.5943	0.0287	10.21	13.05	2
1826	1826-9	454525	131.7135	2.5697	131.7231	2.5943	0.0296	9.17	13.05	2
1826	1826-10	454526	131.7252	2.5015	131.7231	2.5943	0.0282	9.80	13.05	2
1872	1872-1	451530	159.8174	5.4871	159.7507	5.6797	0.0284	10.22	12.62	2
1872	1872-2	906738	159.5780	5.6561	159.7507	5.6797	0.0274	8.89	12.62	2
1872	1872-3	906739	159.6189	5.6667	159.7507	5.6797	0.0275	8.93	12.62	2
1872	1872-4	906741	159.7155	5.6701	159.7507	5.6797	0.0283	10.22	12.62	2
1872	1872-5	906742	159.6426	5.5981	159.7507	5.6797	0.0280	8.70	12.62	2
1872	1872-6	906744	159.6949	5.6969	159.7507	5.6797	0.0279	10.73	12.62	1
1872	1872-7	906749	159.8620	5.5629	159.7507	5.6797	0.0285	8.50	12.62	2
1872	1872-9	924101	159.6163	5.8088	159.7507	5.6797	0.0274	9.23	12.62	2
1872	1872-10	924111	159.8738	5.7954	159.7507	5.6797	0.0278	10.04	12.62	2
1874	1874-1	910053	161.2156	6.5969	161.1252	6.6574	0.0276	11.07	12.65	1
1874	1874-6	925888	160.8525	6.3809	161.1252	6.6574	0.0276	9.35	12.65	2
1874	1874-7	928195	160.8271	6.7818	161.1252	6.6574	0.0272	9.49	12.65	2
1874	1874-8	928198	160.9607	6.7630	161.1252	6.6574	0.0275	10.15	12.65	2
1874	1874-9	928205	161.0767	6.7727	161.1252	6.6574	0.0275	10.11	12.65	2
1874	1874-10	928212	161.2569	6.6872	161.1252	6.6574	0.0271	9.05	12.65	2
2069	2069-1	162581	177.3847	-3.4762	177.4105	-3.5186	0.0270	10.06	13.14	2
2069	2069-2	162587	177.3880	-3.4346	177.4105	-3.5186	0.0267	8.57	13.14	2
2069	2069-3	162592	177.3975	-3.4882	177.4105	-3.5186	0.0274	11.04	13.14	1
2069	2069-4	162593	177.4101	-3.5082	177.4105	-3.5186	0.0287	10.18	13.14	2
2069	2069-5	162595	177.4575	-3.5177	177.4105	-3.5186	0.0267	10.68	13.14	2
2069	2069-7	171379	177.4015	-3.6275	177.4105	-3.5186	0.0280	10.22	13.14	2
2069	2069-8	171381	177.4090	-3.5691	177.4105	-3.5186	0.0273	11.04	13.14	2
2069	2069-9	171383	177.4155	-3.5297	177.4105	-3.5186	0.0276	10.55	13.14	2
2499	2499-1	151304	19.7833	14.5988	19.9870	14.5719	0.0377	10.22	13.20	2
2499	2499-2	151316	19.9265	14.5592	19.9870	14.5719	0.0372	9.58	13.20	2
2499	2499-3	151320	20.0028	14.5566	19.9870	14.5719	0.0389	9.78	13.20	2
2499	2499-4	151321	20.0504	14.5613	19.9870	14.5719	0.0378	11.58	13.20	1
2499	2499-5	151323	20.0896	14.5757	19.9870	14.5719	0.0382	9.56	13.20	2
2499	2499-6	151324	20.1043	14.5213	19.9870	14.5719	0.0381	9.63	13.20	2
2499	2499-7	381512	20.0393	14.4265	19.9870	14.5719	0.0374	9.31	13.20	2
2499	2499-8	382826	20.0088	14.7923	19.9870	14.5719	0.0374	9.06	13.20	2
2501	2501-5	184189	139.9800	0.9451	140.0067	1.0088	0.0176	10.45	12.57	2
2501	2501-6	184190	139.9987	0.9309	140.0067	1.0088	0.0173	10.06	12.57	2
2501	2501-7	184191	140.0090	1.0383	140.0067	1.0088	0.0170	11.11	12.57	1
2501	2501-8	386399	140.0651	1.2888	140.0067	1.0088	0.0175	9.98	12.57	2
2517	2517-1	449185	162.3683	4.7994	162.0822	4.9135	0.0263	10.16	12.91	2
2517	2517-2	450637	162.0731	5.0316	162.0822	4.9135	0.0265	8.74	12.91	2
2517	2517-3	460283	161.6806	4.9314	162.0822	4.9135	0.0258	9.58	12.91	2
2517	2517-5	460289	162.0485	4.9277	162.0822	4.9135	0.0259	11.32	12.91	1
2517	2517-7	460302	162.0611	4.9570	162.0822	4.9135	0.0256	9.84	12.91	2
2517	2517-8	460303	162.0811	4.9026	162.0822	4.9135	0.0262	9.70	12.91	2
2650	2650-2	1074506	149.4862	10.4325	149.5508	10.3602	0.0176	10.38	12.82	2
2650	2650-4	1074508	149.6003	10.3629	149.5508	10.3602	0.0180	10.15	12.82	2
2650	2650-5	1074515	149.7714	10.3611	149.5508	10.3602	0.0179	9.74	12.82	2
2650	2650-6	1074519	149.7483	10.3789	149.5508	10.3602	0.0184	9.00	12.82	2
2655	2655-3	1125977	138.9792	10.1325	139.0156	10.1313	0.0313	11.00	13.00	1
2655	2655-4	1125978	138.9002	10.1593	139.0156	10.1313	0.0304	9.86	13.00	2

Group id (1)	Galaxy id (2)	NYU VAGC (3)	Galaxy RA (4)	Galaxy DEC (5)	Group RA (6)	Group DEC (7)	SDSS redshift (8)	$\log_{10}(M_*)$ (M_\odot) (9)	$\log_{10}(M_{\text{halo}})$ (M_\odot) (10)	Central/ Satellite (11)
2655	2655-5	1125982	139.0922	10.2317	139.0156	10.1313	0.0308	10.73	13.00	2
2655	2655-6	1125983	138.9978	10.1649	139.0156	10.1313	0.0303	9.73	13.00	2
2655	2655-7	1125991	139.2351	10.2371	139.0156	10.1313	0.0307	9.83	13.00	2
2774	2774-1	1734976	14.0436	-1.1402	14.1394	-1.1977	0.0483	10.56	13.38	2
2774	2774-2	1734977	14.0559	-1.2384	14.1394	-1.1977	0.0486	5.44	13.38	2
2774	2774-3	1734986	14.0952	-1.2098	14.1394	-1.1977	0.0498	10.59	13.38	1
2774	2774-4	1734999	14.1251	-1.0870	14.1394	-1.1977	0.0480	10.05	13.38	2
2774	2774-5	1735008	14.2197	-1.1312	14.1394	-1.1977	0.0480	10.20	13.38	2
2774	2774-6	1735015	14.2371	-1.2119	14.1394	-1.1977	0.0500	10.90	13.38	2
2774	2774-7	1735019	14.2410	-1.1581	14.1394	-1.1977	0.0480	9.76	13.38	2
2774	2774-8	1735022	14.2672	-1.1519	14.1394	-1.1977	0.0487	9.87	13.38	2
2959	2959-1	48119	173.6599	0.1887	173.7031	0.1805	0.0288	10.05	12.36	2
2959	2959-2	48120	173.6631	0.1248	173.7031	0.1805	0.0286	10.19	12.36	2
2959	2959-3	48124	173.8470	0.0906	173.7031	0.1805	0.0292	10.27	12.36	2
2959	2959-4	69662	173.7973	-0.0300	173.7031	0.1805	0.0293	9.93	12.36	2
2959	2959-5	74717	173.5855	0.3157	173.7031	0.1805	0.0291	10.45	12.36	2
2959	2959-6	74718	173.5780	0.2941	173.7031	0.1805	0.0289	9.39	12.36	2
3066	3066-1	448313	135.6224	3.3850	135.6263	3.4041	0.0271	10.91	12.38	1
3066	3066-2	448315	135.5939	3.3911	135.6263	3.4041	0.0275	8.87	12.38	2
3066	3066-3	448318	135.6659	3.3924	135.6263	3.4041	0.0267	9.38	12.38	2
3066	3066-4	448321	135.6899	3.4118	135.6263	3.4041	0.0270	9.89	12.38	2
3066	3066-6	457147	135.7721	3.2689	135.6263	3.4041	0.0267	9.52	12.38	2
3066	3066-7	459491	135.5275	3.4977	135.6263	3.4041	0.0274	10.20	12.38	2
3071	3071-1	446587	134.3354	2.9213	134.3696	2.9678	0.0130	11.37	13.06	1
3071	3071-2	446595	134.6270	2.9255	134.3696	2.9678	0.0130	9.97	13.06	2
3071	3071-6	457075	134.3995	3.0902	134.3696	2.9678	0.0121	10.96	13.06	2
3071	3071-7	457076	134.4147	2.9876	134.3696	2.9678	0.0124	8.88	13.06	2
3072	3072-1	445921	167.6419	4.0710	167.6203	4.0626	0.0287	10.27	12.75	2
3072	3072-2	445922	167.6074	3.9866	167.6203	4.0626	0.0291	11.11	12.75	1
3072	3072-3	445926	167.6745	3.9625	167.6203	4.0626	0.0293	9.24	12.75	2
3072	3072-4	445936	167.8185	4.0118	167.6203	4.0626	0.0284	9.79	12.75	2
3072	3072-5	447717	167.5033	4.3643	167.6203	4.0626	0.0289	9.31	12.75	2
3072	3072-6	455660	167.5170	4.1473	167.6203	4.0626	0.0296	10.16	12.75	2
3072	3072-7	455661	167.6560	4.1914	167.6203	4.0626	0.0290	9.45	12.75	2
3899	3899-1	290826	166.5200	3.3196	166.5280	3.3417	0.0313	10.68	12.77	2
3899	3899-2	290829	166.5400	3.2971	166.5280	3.3417	0.0307	10.02	12.77	2
3899	3899-3	290830	166.5425	3.3207	166.5280	3.3417	0.0311	11.13	12.77	1
3899	3899-4	290834	166.6254	3.3440	166.5280	3.3417	0.0317	9.07	12.77	2
3899	3899-5	429388	166.7134	3.4319	166.5280	3.3417	0.0313	8.75	12.77	2
3918	3918-1	449177	162.1578	4.7990	162.0883	4.9227	0.0330	10.22	13.11	2
3918	3918-3	460308	162.1140	4.8255	162.0883	4.9227	0.0340	10.19	13.11	2
3918	3918-4	460313	162.2363	4.8879	162.0883	4.9227	0.0340	9.91	13.11	2
3918	3918-5	460290	162.0496	4.9986	162.0883	4.9227	0.0340	11.36	13.11	1
4214	4214-1	1144192	117.2955	20.3113	117.3431	20.3625	0.0503	10.50	13.23	2
4214	4214-2	1144193	117.3038	20.3456	117.3431	20.3625	0.0502	11.05	13.23	2
4214	4214-3	1144194	117.2816	20.3864	117.3431	20.3625	0.0505	10.06	13.23	2
4214	4214-4	1144196	117.3772	20.3598	117.3431	20.3625	0.0500	11.31	13.23	1
4214	4214-5	1144197	117.3024	20.4905	117.3431	20.3625	0.0495	10.63	13.23	2
4214	4214-6	1154183	117.4641	20.3387	117.3431	20.3625	0.0501	9.93	13.23	2
4482	4482-1	1668025	53.1014	-1.0901	53.1745	-1.1352	0.0312	9.05	12.39	2
4482	4482-2	1668028	53.1182	-1.0626	53.1745	-1.1352	0.0306	8.85	12.39	2
4482	4482-3	1668030	53.1715	-1.1836	53.1745	-1.1352	0.0305	10.63	12.39	1
4482	4482-5	1668033	53.1856	-1.0688	53.1745	-1.1352	0.0308	10.00	12.39	2
4482	4482-6	1668035	53.1857	-1.1536	53.1745	-1.1352	0.0305	10.61	12.39	2
4527	4527-1	1821473	151.9636	12.4601	152.1230	12.5312	0.0301	10.52	13.10	2
4527	4527-2	1821475	152.0574	12.4859	152.1230	12.5312	0.0309	10.60	13.10	2
4527	4527-3	1821481	152.1447	12.5555	152.1230	12.5312	0.0306	11.04	13.10	1
4527	4527-4	1821483	152.1275	12.5766	152.1230	12.5312	0.0302	9.51	13.10	2
4527	4527-5	1821485	152.1417	12.5168	152.1230	12.5312	0.0323	9.10	13.10	2
4527	4527-6	1821486	152.3267	12.6042	152.1230	12.5312	0.0307	10.61	13.10	2
5136	5136-2	330294	54.3891	-6.5205	54.3841	-6.5434	0.0179	10.92	12.31	1
5136	5136-3	330295	54.3850	-6.4872	54.3841	-6.5434	0.0178	8.68	12.31	2
5136	5136-4	330296	54.3975	-6.4959	54.3841	-6.5434	0.0179	9.61	12.31	2
5219	5219-1	450168	145.6929	4.2928	145.6140	4.2820	0.0294	9.97	12.85	2
5219	5219-2	450169	145.6704	4.3627	145.6140	4.2820	0.0296	9.25	12.85	2
5219	5219-3	459776	145.5556	4.2737	145.6140	4.2820	0.0281	9.69	12.85	2
5219	5219-4	459778	145.6040	4.2832	145.6140	4.2820	0.0289	11.27	12.85	1
5219	5219-5	459783	145.7170	4.1084	145.6140	4.2820	0.0284	8.96	12.85	2
5688	5688-1	1119352	126.7327	7.4170	126.7275	7.4797	0.0315	10.41	12.61	2
5688	5688-2	1119353	126.7276	7.4981	126.7275	7.4797	0.0312	10.89	12.61	1
5688	5688-3	1826495	126.6854	7.5049	126.7275	7.4797	0.0305	9.48	12.61	2
5688	5688-4	1826498	126.7355	7.5147	126.7275	7.4797	0.0302	8.40	12.61	2
5688	5688-5	1826499	126.7502	7.5794	126.7275	7.4797	0.0311	9.36	12.61	2
7356	7356-1	447716	167.5357	4.5329	167.6234	4.5435	0.0293	10.66	12.81	2
7356	7356-3	447720	167.6870	4.5108	167.6234	4.5435	0.0289	10.80	12.81	1

Group id (1)	Galaxy id (2)	NYU VAGC (3)	Galaxy RA (4)	Galaxy DEC (5)	Group RA (6)	Group DEC (7)	SDSS redshift (8)	$\log_{10}(M_*)$ (M_{\odot}) (9)	$\log_{10}(M_{\text{halo}})$ (M_{\odot}) (10)	Central/ Satellite (11)
7356	7356-4	458290	167.6055	4.5995	167.6234	4.5435	0.0286	10.79	12.81	2
7358	7358-2	448735	148.0030	4.1508	147.9860	4.1688	0.0306	11.20	12.98	1
7358	7358-3	459850	148.0499	4.2146	147.9860	4.1688	0.0310	10.46	12.98	2
7358	7358-4	459852	148.0344	4.2523	147.9860	4.1688	0.0297	10.14	12.98	2
8275	8275-1	1125824	133.1569	9.1402	133.2617	9.2104	0.0293	8.99	12.59	2
8275	8275-2	1125829	133.2003	9.1587	133.2617	9.2104	0.0292	8.90	12.59	2
8275	8275-3	1125831	133.2972	9.1482	133.2617	9.2104	0.0292	10.79	12.59	1
8275	8275-4	1827163	133.2377	9.3171	133.2617	9.2104	0.0294	10.75	12.59	2
8317	8317-1	1156941	148.8758	36.2861	148.8715	36.2936	0.0525	11.29	12.72	1
8317	8317-2	1156942	148.8756	36.2946	148.8715	36.2936	0.0531	9.84	12.72	2
8317	8317-3	1156945	148.9033	36.3449	148.8715	36.2936	0.0530	10.53	12.72	2
10197	10197-1	1822185	147.4611	12.6952	147.4638	12.7087	0.0299	11.16	12.76	1
10197	10197-2	1822187	147.5300	12.7461	147.4638	12.7087	0.0296	10.21	12.76	2
10197	10197-3	1822189	147.4243	12.6575	147.4638	12.7087	0.0295	9.58	12.76	2
11003	11003-1	284710	148.1236	2.1545	148.1226	2.1576	0.0166	11.01	12.33	1
11003	11003-2	284714	148.1044	2.1810	148.1226	2.1576	0.0169	8.64	12.33	2
11003	11003-3	388354	148.1118	2.2789	148.1226	2.1576	0.0168	8.63	12.33	2
11454	11454-1	288713	175.0809	3.0008	175.0953	3.0092	0.0268	10.78	12.18	1
11454	11454-2	288718	175.1244	2.9725	175.0953	3.0092	0.0270	9.70	12.18	2
11454	11454-3	429252	175.2201	3.1437	175.0953	3.0092	0.0266	9.09	12.18	2
11534	11534-1	446816	140.9280	3.3669	140.7248	3.1539	0.0117	6.30	12.03	2
11534	11534-2	454761	140.6423	3.0837	140.7248	3.1539	0.0121	8.95	12.03	2
11534	11534-3	454769	140.7292	3.1569	140.7248	3.1539	0.0121	10.72	12.03	1
11694	11694-1	476543	158.3867	-0.6859	158.4560	-0.5758	0.0318	8.69	12.38	2
11694	11694-3	64275	158.4640	-0.5614	158.4560	-0.5758	0.0313	11.02	12.38	1
12962	12962-2	906724	159.4008	5.6037	159.3742	5.6038	0.0286	11.00	12.67	1
12962	12962-3	906727	159.3881	5.6286	159.3742	5.6038	0.0283	10.34	12.67	2
13702	13702-1	1118421	148.9674	10.5038	149.0435	10.4919	0.0304	8.72	12.52	2
13702	13702-2	1118423	149.0166	10.4989	149.0435	10.4919	0.0300	10.53	12.52	2
13702	13702-3	1118425	149.0673	10.4861	149.0435	10.4919	0.0298	10.89	12.52	1
13832	13832-1	1155396	146.8893	34.8174	146.7864	34.7618	0.0400	9.13	11.83	2
15934	15934-1	1827690	135.5213	10.6324	135.2557	10.6202	0.0293	9.24	12.97	2
15934	15934-2	2490122	135.1491	10.7090	135.2557	10.6202	0.0290	9.24	12.97	2
15934	15934-3	2496938	135.2504	10.6172	135.2557	10.6202	0.0295	11.38	12.97	1
19177	19177-1	79646	171.0383	0.7006	171.0628	0.6652	0.0260	10.26	12.00	1
19177	19177-2	79647	171.0777	0.6437	171.0628	0.6652	0.0264	10.14	12.00	2
19444	19444-1	155311	57.6990	-7.0288	57.7158	-7.0463	0.0280	10.83	12.62	1
19444	19444-2	155313	57.7296	-7.0606	57.7158	-7.0463	0.0284	10.64	12.62	2
19817	19817-1	170517	186.7821	-1.3542	186.7796	-1.3789	0.0292	10.81	12.22	1
19817	19817-2	178105	186.7654	-1.5159	186.7796	-1.3789	0.0294	9.87	12.22	2
21512	21512-1	279427	189.6199	1.7543	189.6156	1.7427	0.0169	10.61	12.05	1
21512	21512-2	279428	189.5923	1.6792	189.6156	1.7427	0.0163	9.68	12.05	2
22376	22376-2	327848	56.3989	-6.6530	56.3174	-6.5886	0.0332	9.34	0.00	2
22471	22471-1	333287	55.0458	-5.9158	55.0554	-5.9117	0.0503	11.37	12.95	1
22471	22471-2	333296	55.2007	-5.8490	55.0554	-5.9117	0.0508	10.06	12.95	2
23339	23339-1	388112	140.8051	2.0602	140.8981	2.1333	0.0172	9.13	12.09	2
23445	23445-1	288474	169.0721	2.8888	169.0844	2.8828	0.0298	10.94	12.40	1
23445	23445-2	428431	169.2968	2.7796	169.0844	2.8828	0.0292	9.04	12.40	2
23835	23835-2	459512	136.0154	3.5847	136.0205	3.5758	0.0267	10.79	12.14	1
23898	23898-1	451368	142.8164	4.6260	142.9198	4.5044	0.0179	8.94	12.24	2
23898	23898-2	906269	142.9235	4.5000	142.9198	4.5044	0.0181	10.81	12.24	1
23991	23991-1	455386	158.9626	3.8913	158.9617	3.8935	0.0279	11.12	12.60	1
23991	23991-2	455397	158.9497	3.9222	158.9617	3.8935	0.0273	9.31	12.60	2
24459	24459-1	74194	159.2391	0.2297	159.2259	0.2160	0.0292	10.91	12.24	1
24459	24459-2	478400	159.0935	0.0775	159.2259	0.2160	0.0292	9.54	12.24	2
24974	24974-1	511498	151.1302	54.7523	151.1213	54.7630	0.0434	9.88	0.00	1
24974	24974-2	511502	151.1115	54.7749	151.1213	54.7630	0.0434	9.38	0.00	2
25155	25155-2	519897	168.7482	3.5871	168.7484	3.5992	0.0297	10.45	12.70	2
29640	29640-1	912552	125.5079	4.3926	125.6526	4.2776	0.0142	9.38	12.42	2
29901	29901-2	925897	161.0401	6.3696	161.0385	6.3705	0.0297	10.68	12.05	1
31811	31811-1	1040667	134.7103	6.2930	134.7105	6.2930	0.0128	10.68	12.92	1
32627	32627-2	1114372	122.0685	5.2161	122.0848	5.2287	0.0310	10.85	12.36	1
32627	32627-3	1114380	122.1648	5.2905	122.0848	5.2287	0.0310	9.97	12.36	2
32900	32900-1	1126342	150.7985	12.1267	150.8006	12.1261	0.0302	10.86	12.31	1
32900	32900-2	1126350	150.8384	12.1157	150.8006	12.1261	0.0299	9.30	12.31	2
32901	32901-1	1126344	150.8541	12.0982	150.8519	12.0985	0.0310	10.70	12.17	1
32901	32901-2	1126343	150.8220	12.1025	150.8519	12.0985	0.0313	9.28	12.17	2
57064	57064-1	60278	173.0385	-0.9426	173.0385	-0.9426	0.0261	10.61	12.05	1
60661	60661-1	78807	148.3343	0.6977	148.3342	0.6977	0.0126	10.97	12.18	1
63756	63756-1	153610	18.3324	15.4909	18.3324	15.4909	0.0490	10.28	11.77	1
64176	64176-1	156329	56.5344	-6.7094	56.5344	-6.7094	0.0331	9.30	0.00	1
64521	64521-1	158860	54.7846	-6.1520	54.7846	-6.1520	0.0488	9.69	0.00	1
64523	64523-1	158871	54.9911	-6.2042	54.9911	-6.2042	0.0498	11.08	12.57	1
64525	64525-1	158881	55.1879	-6.0895	55.1879	-6.0895	0.0507	10.57	12.02	1
64659	64659-1	160021	54.9375	-5.6424	54.9375	-5.6424	0.0435	10.58	11.91	1

Group id (1)	Galaxy id (2)	NYU VAGC (3)	Galaxy RA (4)	Galaxy DEC (5)	Group RA (6)	Group DEC (7)	SDSS redshift (8)	$\log_{10}(M_*)$ (M_\odot) (9)	$\log_{10}(M_{\text{halo}})$ (M_\odot) (10)	Central/ Satellite (11)
68901	68901-1	183973	132.1676	1.0388	132.1676	1.0388	0.0288	11.07	12.43	1
68906	68906-2	183988	132.4410	1.0105	132.4410	1.0105	0.0289	10.23	0.00	1
73668	73668-1	209549	128.2031	49.5256	128.2031	49.5256	0.0549	10.19	0.00	1
90284	90284-1	281410	151.1395	1.7877	151.1395	1.7878	0.0310	10.68	12.14	1
99910	99910-1	327856	56.6124	-6.5313	56.6124	-6.5313	0.0281	10.71	12.09	1
111666	111666-1	382811	19.9401	14.7637	19.9401	14.7637	0.0365	8.87	0.00	1
112723	112723-1	387428	151.1614	1.8896	151.1614	1.8896	0.0303	10.50	12.02	1
113424	113424-1	426709	170.4247	1.5208	170.4247	1.5208	0.0297	10.63	12.04	1
119022	119022-1	447719	167.5581	4.3775	167.5581	4.3775	0.0259	9.29	0.00	1
121804	121804-2	458304	167.8602	4.5940	167.8602	4.5940	0.0264	9.74	0.00	1
133088	133088-1	511479	150.4026	54.5831	150.4026	54.5831	0.0563	10.04	0.00	1
166604	166604-1	801538	151.4037	50.4383	151.4037	50.4383	0.0522	9.67	0.00	1
189741	189741-1	906105	135.3692	3.7206	135.3692	3.7206	0.0127	10.50	12.06	1
190338	190338-1	908240	159.5407	5.9474	159.5407	5.9474	0.0296	10.76	12.06	1
192594	192594-1	916911	151.0041	54.5732	151.0041	54.5732	0.0563	10.33	11.80	1
192773	192773-1	917572	150.7541	54.8433	150.7541	54.8433	0.0508	10.40	11.81	1
219717	219717-4	1042286	121.7716	5.2862	121.7715	5.2862	0.0340	9.00	0.00	1
225398	225398-1	1072464	132.2828	7.3731	132.2828	7.3731	0.0294	10.60	12.03	1
225426	225426-1	1072541	135.0461	7.7261	135.0460	7.7261	0.0289	10.83	12.10	1
230126	230126-1	1114369	121.9921	5.2066	121.9921	5.2067	0.0292	10.76	12.20	1
230128	230128-1	1114382	122.2213	5.2005	122.2212	5.2005	0.0340	9.44	0.00	1
230130	230130-5	1114387	122.2556	5.3091	122.2556	5.3091	0.0280	8.41	0.00	1
230227	230227-1	1114679	131.6884	6.9600	131.6884	6.9600	0.0291	11.16	12.53	1
232714	232714-1	1123981	151.2073	11.9129	151.2073	11.9129	0.0310	10.66	12.16	1
237373	237373-1	1154176	117.2730	20.1373	117.2730	20.1373	0.0531	9.66	0.00	1
237376	237376-1	1154182	117.4482	20.2515	117.4482	20.2515	0.0486	10.68	12.01	1
237684	237684-1	1155390	146.9977	34.7417	146.9977	34.7417	0.0408	9.12	0.00	1
245324	245324-1	1181738	148.7676	36.5012	148.7676	36.5012	0.0596	10.12	0.00	1
245328	245328-1	1181748	149.1813	36.6452	149.1813	36.6452	0.0534	9.73	0.00	1
341518	341518-1	1826090	129.6814	7.8066	129.6813	7.8066	0.0295	10.76	12.29	1
467592	467592-2	2488696	135.3065	10.4371	135.3065	10.4371	0.0360	9.28	0.00	1
467944	467944-1	2490124	135.1385	10.8354	135.1386	10.8354	0.0300	9.11	0.00	1

Appendix C

HAGGIS derived parameters

Here we include the table containing various galaxy derived parameters from HAGGIS data (see Chapter 4 section 4.3). The details of each column are given below.

- **Col 1:** Galaxy ID
- **Col 2:** Continuum profile type
- **Col 3,4:** Continuum break radii (kpc)
- **Col 5:** Continuum half light radius (kpc)
- **Col 6,7,8:** Continuum scale lengths in regions I, II and III of the profile (kpc)
- **Col 9:** Total integrated stellar continuum flux ($\times 10^{-17} \text{ergs sec}^{-1} \text{cm}^{-2}$)
- **Col 10:** H α profile type
- **Col 11:** H α break radius (kpc)
- **Col 12:** H α half light radius (kpc)
- **Col 13,14:** H α scale lengths in regions I and II of the profile (kpc)
- **Col 15:** Total integrated H α flux excluding any contribution from absorption ($\times 10^{-17} \text{ergs sec}^{-1} \text{cm}^{-2}$)
- **Col 16:** Logarithm of H α Luminosity (ergs sec^{-1})
- **Col 17:** Logarithm of total integrated star-formation rate ($M_{\odot} \text{yr}^{-1}$)

TABLE C.1: Table of derived parameters for continuum and H α profiles.

Galaxy ID	Continuum										H α					
	Profile Type	R _{break} (kpc)		Re (kpc)	Scale length (kpc)			Flux ($\times 10^{-17}$ $(ergs\ sec^{-1} cm^{-2})$)	Profile Type	R _{break} (kpc)	Re (kpc)	Scale length (kpc)		Flux ($\times 10^{-17}$ $(ergs\ sec^{-1} cm^{-2})$)	Log Luminosity $(ergs\ sec^{-1})$ (16)	Log SFR $(M_{\odot} yr^{-1})$ (17)
		1-2 (3)	2-3 (4)		1 (6)	2 (7)	3 (8)					1 (13)	2 (14)			
(1)	(2)	(3)	(4)	(5)	(6)	(7)	(8)	(9)	(10)	(11)	(12)	(13)	(14)	(15)	(16)	(17)
13-1	I	-	-	4.7	3.5	-	-	15062	SE	-	1.1	0.3	-	99	39.73	0.04
13-2	III	5.5	-	2.2	1.0	2.1	-	3293	A	-	8.5	-	-	2	38.11	0.00
13-3	I	-	-	3.9	2.5	-	-	6869	A	-	7.1	-	-	19	39.05	0.01
13-4	III	9.4	-	3.7	1.8	5.6	-	8598	A	-	11.9	-	-	113	39.85	0.06
13-8	II	-	-	0.6	1.5	-	-	3044	N	-	-	-	-	-	-	-
13-9	II	2.7	-	3.4	3.6	1.8	-	4925	SE	-	1.5	0.9	-	176	39.96	0.07
13-11	III	5.6	-	2.1	1.1	2.1	-	7480	A	-	9.0	-	-	18	39.03	0.01
13-12	I	-	-	4.1	3.1	-	-	18450	SE	-	1.1	0.6	-	62	39.68	0.04
13-13	I	-	-	2.6	1.4	-	-	2578	A	-	2.8	-	-	21	39.10	0.01
13-14	E	-	-	2.1	-	-	-	5210	A	-	-	-	-	0	-	-
13-15	III	6.6	-	3.0	1.5	2.6	-	4288	A	-	8.0	-	-	34	39.33	0.02
13-16	II	11.0	-	2.5	2.4	1.4	-	2706	A	-	6.7	-	-	14	38.88	0.01
13-17	III	5.3	-	3.4	1.6	2.5	-	3493	A	-	10.9	-	-	19	39.05	0.01
13-18	III	10.6	-	3.1	1.7	3.0	-	8180	A	-	12.7	-	-	10	38.79	0.00
13-19	E	-	-	3.9	-	-	-	10624	N	-	3.0	-	-	39	39.41	0.02
13-20	E	-	-	3.7	-	-	-	25213	A	-	30.0	-	-	299	40.26	0.14
13-21	I	-	-	3.4	4.1	-	-	18349	A	-	20.7	-	-	52	39.58	0.03
13-22	2+3	6.7	23.4	26.4	3.3	10.8	18.5	54407	SE	-	1.7	2.7	-	93	39.78	0.05
13-23	III	10.7	-	3.8	2.0	2.9	-	11660	A	-	-	-	-	-	-	-
13-24	III	4.2	-	2.2	1.0	1.6	-	2791	N	-	4.4	-	-	85	39.63	0.03
13-25	III	6.1	-	3.7	1.8	2.5	-	9948	A	-	15.5	-	-	22	39.16	0.01
13-32	I	-	-	9.0	8.9	-	-	84901	SE	-	2.6	1.6	-	469	40.58	0.30
13-34	E	-	-	-	-	-	-	-	A	-	-	-	-	-	-	-
13-35	II	5.0	-	2.3	1.4	0.7	-	3469	N	-	3.8	3.5	-	138	39.93	0.07
13-37	III	6.9	-	2.7	1.4	2.5	-	6857	A	-	8.4	-	-	107	39.85	0.06
13-38	E	-	-	-	-	-	-	-	A	-	-	-	-	-	-	-
13-40	III	5.7	-	2.8	1.4	2.7	-	5240	A	-	11.2	-	-	59	39.62	0.03
13-41	I	-	-	2.4	1.3	-	-	4232	A	-	8.7	-	-	29	39.27	0.01
13-43	E	-	-	-	-	-	-	-	N	-	-	-	-	-	-	-
183-1	I	-	-	2.6	1.6	-	-	3667	A	-	-	-	-	0	-	-

Galaxy ID	Continuum										H α					
	Profile Type	R _{break} (kpc)		Re (kpc)	Scale length (kpc)			Flux ($\times 10^{-17}$ ergs sec $^{-1}$ cm $^{-2}$)	Profile Type	R _{break} (kpc)	Re (kpc)	Scale length (kpc)		Flux ($\times 10^{-17}$ ergs sec $^{-1}$ cm $^{-2}$)	Log Luminosity (ergs sec $^{-1}$)	Log SFR (M_{\odot} yr $^{-1}$)
		1-2 (3)	2-3 (4)		1 (6)	2 (7)	3 (8)					1 (13)	2 (14)			
183-2	2+3	5.5	11.1	4.3	2.4	2.0	5.7	6194	SE	-	1.4	0.8	-	102	39.80	0.05
183-3	II	6.9	-	2.7	1.6	1.2	-	8355	ST	-	1.7	1.0	-	332	40.34	0.17
183-5	II	12.0	-	5.6	3.5	2.2	-	8975	ST	-	6.5	5.2	-	447	40.48	0.24
183-7	I	-	-	3.4	3.0	-	-	13391	A	-	-	-	-	-	-	-
183-8	II	6.9	-	3.3	1.8	1.3	-	6367	ST	-	3.2	1.9	-	1608	41.02	0.83
183-9	I	-	-	4.1	5.0	-	-	22457	A	-	-	-	-	-	-	-
183-14	III	-	-	0.6	0.9	-	-	2989	A	-	6.0	-	-	28	39.23	0.01
183-17	I	-	-	3.2	1.7	-	-	2875	SE	-	8.4	-	-	60	39.58	0.03
183-18	I	-	-	3.2	1.9	-	-	4298	T	2.2	2.2	1.9	1.1	599	40.57	0.29
183-19	I	-	-	2.6	2.2	-	-	6219	A	-	-	-	-	-	-	-
183-20	II	7.9	-	4.1	2.8	1.7	-	8308	E	-	3.6	2.7	-	1103	40.81	0.51
183-23	II	2.5	-	3.0	2.8	1.6	-	3136	ST	-	3.0	-	-	80	39.65	0.04
183-24	III	5.2	-	2.7	1.3	2.4	-	2777	A	-	-	-	-	0	-	-
183-25	II	7.3	-	3.2	2.0	1.4	-	5166	SE	-	1.2	0.4	-	288	40.30	0.16
183-26	III	5.2	-	2.5	1.1	2.4	-	2615	A	-	-	-	-	0	-	-
183-28	III	6.7	-	2.6	1.3	3.3	-	7144	SE	-	1.0	0.2	-	20	39.14	0.01
183-29	III	6.7	-	3.0	1.6	2.2	-	3205	ST	3.2	2.2	0.8	7.1	221	40.13	0.11
390-1	I	-	-	3.7	2.1	-	-	2055	ST	-	1.2	0.7	-	87	39.39	0.02
390-2	I	-	-	9.4	5.6	-	-	11734	ST	1.6	6.4	0.3	4.5	1714	40.73	0.42
390-4	I	-	-	5.7	3.3	-	-	14830	E	-	5.0	2.1	-	1965	40.74	0.44
390-5	E	-	-	3.7	-	-	-	61163	SE	-	1.2	0.3	-	1130	40.62	0.33
390-6	E	-	-	2.0	-	-	-	9531	A	-	-	-	-	0	-	-
390-7	III	4.5	-	6.6	1.1	4.4	-	2737	SE	-	0.6	-	-	0	37.32	0.00
390-8	I	-	-	3.5	3.3	-	-	21983	A	-	4.5	-	-	50	39.24	0.01
390-9	III	16.5	-	3.6	2.2	4.7	-	36903	ST	11.1	4.2	2.4	1.3	3831	41.13	1.07
390-10	III	5.4	-	1.6	0.9	1.5	-	6987	A	-	-	-	-	0	-	-
390-11	III	7.6	-	1.7	0.9	2.3	-	2879	T	2.3	0.9	0.5	0.3	324	39.90	0.06
390-18	I	-	-	11.5	7.7	-	-	129350	ST	-	13.8	6.3	-	23605	42.00	7.93
390-22	I	-	-	3.8	2.2	-	-	3383	ST	2.5	2.1	0.6	1.4	910	40.41	0.21
390-23	E	-	-	3.0	-	-	-	22400	N	-	1.5	-	-	15	38.69	0.00

Galaxy ID	Continuum										H α					
	Profile Type	R _{break} (kpc)		Re (kpc)	Scale length (kpc)			Flux ($\times 10^{-17}$) ($ergs\ sec^{-1} cm^{-2}$)	Profile Type	R _{break} (kpc)	Re (kpc)	Scale length (kpc)		Flux ($\times 10^{-17}$) ($ergs\ sec^{-1} cm^{-2}$)	Log Luminosity ($ergs\ sec^{-1}$)	Log SFR ($M_{\odot} yr^{-1}$)
		1-2 (3)	2-3 (4)		1 (6)	2 (7)	3 (8)					1 (13)	2 (14)			
(1)	(2)	(3)	(4)	(5)	(6)	(7)	(8)	(9)	(10)	(11)	(12)	(13)	(14)	(15)	(16)	(17)
390-24	II	26.1	-	11.2	9.5	5.9	-	72830	E	-	15.6	10.0	-	4044	41.16	1.13
596-1	E	-	-	2.9	-	-	-	14147	A	-	-	-	-	0	-	-
596-2	I	-	-	4.8	3.1	-	-	17757	SE	-	1.3	0.5	-	373	40.49	0.25
596-3	III	22.0	-	6.9	3.8	10.1	-	6588	E	-	4.0	2.4	-	795	40.78	0.48
596-4	I	-	-	2.7	1.6	-	-	2284	A	-	5.0	-	-	32	39.36	0.02
596-5	II	5.3	-	3.6	2.7	1.1	-	5241	FT	2.9	3.5	-6.7	1.6	2667	41.32	1.65
596-6	III	9.9	-	3.9	2.0	4.1	-	14435	A	-	-	-	-	0	-	-
596-7	I	-	-	2.4	1.9	-	-	6597	N	-	5.5	-	-	161	40.07	0.09
596-8	II	5.4	-	11.1	3.0	7.3	-	6008	E	-	3.7	2.8	-	205	40.16	0.11
596-10	I	-	-	2.2	1.1	-	-	5172	N	-	-	-	-	-	-	-
596-11	II	11.7	-	3.8	5.2	2.0	-	21504	SE	-	1.3	0.6	-	178	40.18	0.12
596-12	I	-	-	6.6	8.5	-	-	76409	A	-	-	-	-	-	-	-
596-13	I	-	-	3.1	3.5	-	-	8917	SE	-	1.2	0.6	-	256	40.27	0.15
596-14	III	6.7	-	2.3	1.4	4.8	-	4339	A	-	-	-	-	0	-	-
596-15	E	-	-	3.0	-	-	-	7302	A	-	8.3	-	-	3	38.37	0.00
596-17	III	6.2	-	3.1	1.5	3.6	-	2835	SE	-	1.0	0.4	-	25	39.25	0.01
596-18	III	8.3	-	2.8	1.7	4.6	-	6694	A	-	-	-	-	0	-	-
596-19	II	15.2	-	9.8	8.5	3.6	-	43407	ST	0.4	10.3	0.6	6.2	1616	41.20	1.24
596-20	II	2.7	-	2.5	2.2	1.0	-	3492	FT	2.6	2.2	3.7	0.7	1145	40.91	0.65
596-21	I	-	-	3.4	1.9	-	-	4213	FT	3.6	3.2	12.2	1.1	362	40.43	0.21
607-1	III	6.9	-	3.3	1.6	4.1	-	7133	E	-	1.8	1.0	-	662	40.69	0.38
607-3	III	9.6	-	5.7	2.2	9.6	-	12396	SE	-	1.4	0.9	-	186	40.18	0.12
607-4	2+3	4.5	7.8	3.8	2.2	1.4	5.7	4946	A	-	1.0	-	-	1	37.91	0.00
607-5	I	-	-	3.6	2.0	-	-	7273	E	-	3.0	1.7	-	643	40.71	0.40
607-6	II	3.4	-	3.4	3.3	1.6	-	4019	T	4.9	3.3	3.1	0.5	281	40.32	0.17
607-7	II	2.6	-	4.6	4.5	2.3	-	5365	SE	2.1	1.7	2.0	0.4	51	39.56	0.03
607-8	III	5.8	-	2.9	1.4	2.8	-	13857	SE	-	1.0	0.3	-	132	40.00	0.08
607-9	I	-	-	5.1	2.9	-	-	22560	ST	-	5.6	2.8	-	1451	41.09	0.97
607-10	II	14.9	-	5.5	7.0	1.6	-	36679	ST	-	10.7	6.5	-	7343	41.83	5.39
607-12	I	-	-	7.5	8.2	-	-	62140	A	-	-	-	-	-	-	-

Galaxy ID (1)	Continuum										H α						
	Profile Type (2)	R _{break} (kpc)		Re (kpc) (5)	Scale length (kpc)			Flux ($\times 10^{-17}$) ($ergs\ sec^{-1} cm^{-2}$) (9)	Profile Type (10)	R _{break} (kpc) (11)	Re (kpc) (12)	Scale length (kpc)		Flux ($\times 10^{-17}$) ($ergs\ sec^{-1} cm^{-2}$) (15)	Log Luminosity ($ergs\ sec^{-1}$) (16)	Log SFR ($M_{\odot} yr^{-1}$) (17)	
		1-2 (3)	2-3 (4)		1 (6)	2 (7)	3 (8)					1 (13)	2 (14)				
607-14	III	13.3	-	5.1	3.0	6.5	-	47485	A	-	25.7	-	-	517	40.45	0.22	
607-15	I	-	-	5.1	3.0	-	-	14003	T	5.0	4.6	4.1	2.0	2351	41.30	1.59	
607-17	I	-	-	4.1	2.4	-	-	7554	AT	7.2	3.5	1.4	-3.5	1271	40.94	0.69	
607-18	I	-	-	6.5	4.7	-	-	45980	ST	-	7.2	4.9	-	9991	41.97	7.39	
639-1	II	13.0	-	4.3	3.2	1.5	-	8218	A	-	-	-	-	0	-	-	
639-3	III	13.6	-	2.3	2.4	3.4	-	23645	A	-	-	-	-	-	-	-	
639-4	III	4.4	-	1.6	0.8	1.0	-	2546	A	-	-	-	-	-	-	-	
639-6	2+3	10.4	14.1	4.4	3.1	1.6	2.6	22742	T	9.7	3.5	2.7	0.9	7655	41.52	2.63	
639-7	II	22.8	-	8.5	6.4	4.2	-	109184	STT	26.2	7.1	3.8	1.1	33034	42.19	12.25	
639-13	III	20.7	-	3.8	2.3	7.0	-	44110	A	-	-	-	-	0	-	-	
639-14	I	-	-	2.8	1.6	-	-	2961	SE	-	0.9	0.4	-	153	39.69	0.04	
639-15	III	6.8	-	1.6	1.0	2.2	-	2730	E	-	0.8	0.4	-	404	40.09	0.10	
639-16	I	-	-	3.0	1.8	-	-	2495	T	4.7	1.9	1.2	0.8	366	40.08	0.10	
916-4	II	2.6	-	2.5	2.1	1.4	-	2374	T	1.1	1.3	2.9	0.9	323	39.96	0.07	
916-5	I	-	-	2.6	1.5	-	-	1987	T	6.6	2.7	3.3	1.1	375	40.02	0.08	
916-6	2+3	3.4	10.0	3.1	2.3	1.5	3.3	2626	T	7.1	2.8	1.9	0.7	5379	41.19	1.24	
916-7	III	18.0	-	3.9	2.5	6.8	-	29141	N	-	2.7	-	-	28	39.00	0.01	
916-8	III	6.8	-	6.4	2.1	4.2	-	2773	E	-	3.5	2.5	-	634	40.30	0.16	
916-9	III	12.4	-	3.7	1.8	5.4	-	30314	FT	7.4	3.2	2.6	0.6	7707	41.48	2.39	
916-10	I	-	-	5.7	7.0	-	-	55819	A	-	-	-	-	0	-	-	
916-11	III	15.0	-	3.5	2.1	3.0	-	10165	E	-	1.4	0.7	-	567	40.25	0.14	
916-12	II	8.0	-	3.0	2.0	1.2	-	2843	ST	3.2	1.7	-20.9	0.3	153	39.68	0.04	
916-13	III	37.8	-	9.8	8.5	15.3	-	187049	A	-	0.5	-	-	7	38.51	0.00	
916-14	I	-	-	4.0	6.8	-	-	33819	A	-	7.0	-	-	9	38.49	0.00	
916-15	III	14.4	-	2.8	2.2	3.7	-	31413	A	-	0.5	-	-	0	37.40	0.00	
916-16	III	4.5	-	2.4	1.3	1.6	-	5993	SE	-	0.8	0.4	-	257	39.91	0.06	
960-1	I	-	-	4.3	3.2	-	-	8811	SE	-	1.8	1.5	-	1145	40.94	0.69	
960-3	I	-	-	6.4	3.8	-	-	24111	ST	-	4.6	2.5	-	420	40.57	0.29	
960-4	I	-	-	4.0	2.4	-	-	13155	A	-	1.0	-	-	6	38.67	0.00	
960-5	I	-	-	5.9	3.4	-	-	24728	T	7.9	5.4	7.3	1.6	5801	41.69	3.90	

Galaxy ID	Continuum										H α					
	Profile Type	R _{break} (kpc)		Re (kpc)	Scale length (kpc)			Flux ($\times 10^{-17}$) ($ergs\ sec^{-1} cm^{-2}$)	Profile Type	R _{break} (kpc)	Re (kpc)	Scale length (kpc)		Flux ($\times 10^{-17}$) ($ergs\ sec^{-1} cm^{-2}$)	Log Luminosity ($ergs\ sec^{-1}$)	Log SFR ($M_{\odot} yr^{-1}$)
		1-2 (3)	2-3 (4)		1 (6)	2 (7)	3 (8)					1 (13)	2 (14)			
960-7	I	-	-	3.7	2.4	-	-	7196	A	-	-	-	-	-	-	-
960-8	I	-	-	2.9	3.9	-	-	7483	SE	-	1.6	0.4	-	875	40.82	0.52
960-10	I	-	-	3.5	2.0	-	-	6920	SE	-	1.3	0.6	-	329	40.37	0.18
960-12	I	-	-	2.7	1.5	-	-	2663	A	-	-	-	-	-	-	-
960-14	I	-	-	5.0	2.8	-	-	8344	FT	-7.6	6.4	2.2	2.8	1505	41.06	0.90
1084-1	II	9.6	-	6.0	5.9	2.4	-	29099	FT	8.9	6.0	-14.4	1.3	5736	41.44	2.17
1084-3	I	-	-	6.5	3.7	-	-	2550	E	-	5.4	6.8	-	227	39.95	0.07
1084-4	III	10.5	-	2.6	1.8	3.0	-	18993	SE	-	1.5	0.8	-	4190	41.29	1.52
1084-5	I	-	-	4.0	4.2	-	-	41397	A	-	11.6	-	-	70	39.55	0.03
1084-6	III	4.5	-	2.1	1.1	1.5	-	6226	A	-	-	-	-	-	-	-
1084-8	2+3	4.0	12.6	7.4	2.3	4.1	5.3	14629	N	-	9.2	-	-	85	39.54	0.03
1228-1	I	-	-	3.0	3.5	-	-	40010	A	-	-	-	-	-	-	-
1228-2	I	-	-	9.7	13.5	-	-	98409	A	-	1.9	-	-	9	38.39	0.00
1228-3	I	-	-	3.0	2.3	-	-	58345	T	5.6	1.7	1.3	0.3	1688	40.65	0.35
1228-5	I	-	-	2.1	1.2	-	-	9157	SE	-	0.5	0.2	-	34	38.85	0.01
1228-6	I	-	-	2.1	1.3	-	-	3910	A	-	-	-	-	0	-	-
1228-7	I	-	-	2.1	1.1	-	-	3272	FT	2.4	1.2	1.8	0.3	635	40.17	0.12
1228-8	I	-	-	2.5	1.7	-	-	3589	x	-	-	-	-	-	-	-
1228-9	I	-	-	3.3	2.0	-	-	36860	A	-	-	-	-	-	-	-
1228-11	I	-	-	1.6	0.9	-	-	3107	A	-	-	-	-	-	-	-
1228-12	II	34.9	-	9.6	5.8	4.1	-	98328	STT	25.2	8.7	11.1	1.5	11570	41.57	2.92
1228-13	II	4.3	-	2.3	1.6	1.1	-	9291	FT	4.5	2.4	-11.5	0.7	3407	40.93	0.67
1644-1	III	11.7	-	1.2	0.7	1.2	-	8110	SE	-	0.5	0.1	-	100	38.55	0.00
1644-2	II	16.3	-	3.0	2.2	1.5	-	86691	FT	13.6	2.8	7.5	1.0	10116	40.54	0.28
1644-3	I	-	-	2.9	1.9	-	-	47042	E	-	3.1	2.2	-	5230	40.23	0.14
1644-4	III	5.5	-	1.1	0.4	0.8	-	2390	N	-	-	-	-	-	-	-
1644-6	E	-	-	3.0	-	-	-	401965	T	64.5	4.7	5.3	3.6	92310	41.57	2.95
1644-7	I	-	-	1.6	0.9	-	-	11062	T	10.2	1.6	1.6	0.2	1914	39.82	0.05
1644-8	III	42.7	-	2.3	1.9	5.0	-	304758	A	-	-	-	-	0	-	-
1644-11	I	-	-	0.8	0.4	-	-	2309	E	-	0.6	0.2	-	222	38.84	0.01

Galaxy ID	Continuum										H α					
	Profile Type	R _{break} (kpc)		Re (kpc)	Scale length (kpc)			Flux ($\times 10^{-17}$) ($ergs\ sec^{-1} cm^{-2}$)	Profile Type	R _{break} (kpc)	Re (kpc)	Scale length (kpc)		Flux ($\times 10^{-17}$) ($ergs\ sec^{-1} cm^{-2}$)	Log Luminosity ($ergs\ sec^{-1}$)	Log SFR ($M_{\odot} yr^{-1}$)
		1-2 (3)	2-3 (4)		1 (6)	2 (7)	3 (8)					1 (13)	2 (14)			
1791-1	I	-	-	11.7	6.9	-	-	4020	E	-	7.3	13.4	-	701	40.16	0.11
1791-2	III	22.6	-	3.4	2.8	5.6	-	71593	E	-	4.9	3.1	-	6108	41.19	1.23
1791-5	I	-	-	3.6	2.1	-	-	12372	E	-	2.7	1.6	-	6090	41.11	1.02
1826-1	III	5.9	-	1.6	0.8	1.6	-	3643	x	-	0.5	-	-	4	38.08	0.00
1826-3	III	10.6	-	6.2	1.9	6.8	-	45225	ST	-	0.7	-	-	45	39.15	0.01
1826-4	III	18.1	-	9.6	3.9	8.2	-	21593	T	-	5.8	4.3	-	3348	40.99	0.78
1826-6	II	13.6	-	3.9	2.5	1.6	-	7625	E	-	3.8	1.9	-	2833	40.92	0.66
1826-7	E	-	-	3.9	-	-	-	91950	SE	-	1.1	0.5	-	998	40.53	0.27
1826-8	I	-	-	3.0	2.0	-	-	17210	SE	-	0.7	0.3	-	1416	40.64	0.35
1826-9	I	-	-	3.2	1.9	-	-	5964	T	5.8	2.1	1.4	0.6	1509	40.68	0.38
1826-10	I	-	-	3.0	1.9	-	-	11935	ST	-	1.4	0.8	-	3648	41.05	0.89
1872-1	III	9.9	-	1.9	1.0	1.7	-	23881	SE	-	1.1	0.6	-	7904	41.32	1.66
1872-2	I	-	-	2.7	1.6	-	-	4807	E	-	2.8	1.5	-	774	40.26	0.14
1872-3	II	10.3	-	3.6	3.0	1.2	-	6261	FT	5.6	3.6	108.1	1.7	2481	40.78	0.47
1872-4	III	14.2	-	3.2	1.9	3.6	-	26059	A	-	-	-	-	0	-	-
1872-5	I	-	-	3.7	2.2	-	-	2600	E	-	2.6	1.6	-	950	40.35	0.18
1872-6	II	20.3	-	7.4	4.8	4.0	-	82731	ST	15.2	7.7	17.9	2.2	7181	41.32	1.65
1872-7	III	4.1	-	1.8	0.7	1.6	-	2602	T	3.9	1.9	1.6	0.8	393	39.98	0.08
1872-9	I	-	-	3.4	2.0	-	-	5021	T	8.0	2.2	1.3	0.9	1037	40.36	0.18
1872-10	II	6.7	-	4.7	4.8	2.7	-	23748	ST	-	3.4	1.3	-	7884	41.33	1.68
1874-1	II	33.9	-	8.0	5.1	2.9	-	185760	E	-	7.6	5.1	-	51199	42.25	14.11
1874-6	I	-	-	3.3	1.8	-	-	5124	E	-	3.0	1.7	-	1159	40.42	0.21
1874-7	I	-	-	2.0	1.1	-	-	9496	E	-	2.1	1.4	-	3119	40.89	0.61
1874-8	I	-	-	4.2	2.8	-	-	52781	ST	-	3.0	1.3	-	26977	41.92	6.60
1874-9	III	10.6	-	3.1	2.1	2.8	-	19011	SE	-	1.3	0.8	-	2534	40.81	0.51
1874-10	I	-	-	3.1	1.8	-	-	2551	ST	5.2	1.9	1.5	0.4	143	39.49	0.02
2069-1	II	5.9	-	3.5	4.0	1.7	-	47418	ST	-	3.0	1.1	-	21733	41.76	4.59
2069-2	III	8.4	-	3.4	1.1	4.4	-	4067	T	3.2	1.6	2.0	0.6	490	40.03	0.08
2069-3	E	-	-	4.7	-	-	-	87899	A	-	1.0	-	-	36	39.00	0.01
2069-4	I	-	-	3.8	2.2	-	-	20428	FT	6.6	3.6	19.0	1.3	2570	40.85	0.56

Galaxy ID (1)	Continuum										H α					
	Profile Type (2)	R _{break} (kpc) 1-2 (3) 2-3 (4)		Re (kpc) (5)	Scale length (kpc) 1 (6) 2 (7) 3 (8)			Flux ($\times 10^{-17}$) ($ergs\ sec^{-1} cm^{-2}$) (9)	Profile Type (10)	R _{break} (kpc) (11)	Re (kpc) (12)	Scale length (kpc) 1 (13) 2 (14)		Flux ($\times 10^{-17}$) ($ergs\ sec^{-1} cm^{-2}$) (15)	Log Luminosity ($ergs\ sec^{-1}$) (16)	Log SFR ($M_{\odot} yr^{-1}$) (17)
2069-5	III	31.0	-	5.6	3.2	7.3	-	58643	ST	-	5.7	3.0	-	6283	41.19	1.23
2069-7	III	12.4	-	2.6	1.8	2.7	-	20963	A	-	-	-	-	0	-	-
2069-8	III	32.0	-	7.0	4.8	7.4	-	49644	E	-	5.1	2.8	-	3133	40.91	0.63
2069-9	E	-	-	2.8	-	-	-	32514	SE	-	0.5	-	-	59	39.19	0.01
2499-1	II	10.5	-	6.8	5.0	3.2	-	26497	FT	8.0	7.7	-13.6	3.6	8222	41.61	3.19
2499-2	II	8.1	-	4.3	3.2	2.0	-	12092	T	7.6	3.0	1.8	1.1	7235	41.53	2.65
2499-3	2+3	5.2	8.9	3.6	3.5	1.4	2.0	7281	T	4.9	3.1	2.9	1.1	2031	40.98	0.75
2499-4	I	-	-	8.4	7.1	-	-	76951	SE	-	0.9	0.4	-	414	40.37	0.18
2499-5	II	3.4	-	2.3	1.9	1.0	-	3100	E	-	1.6	0.7	-	443	40.27	0.15
2499-6	II	4.1	-	3.1	2.5	1.5	-	2864	T	3.7	2.4	2.3	1.1	246	40.01	0.08
2499-7	I	-	-	5.2	3.0	-	-	2762	T	4.5	2.8	2.8	1.3	236	39.97	0.07
2499-8	III	7.4	-	3.7	1.7	3.2	-	6278	T	3.2	2.1	1.7	0.8	4958	41.34	1.74
2501-5	III	27.3	-	2.4	1.9	3.4	-	139263	SE	-	0.7	0.3	-	231	39.37	0.02
2501-6	E	-	-	2.2	-	-	-	91137	A	-	-	-	-	0	-	-
2501-7	E	-	-	4.8	-	-	-	411027	A	-	-	-	-	0	-	-
2501-8	E	-	-	1.9	-	-	-	43350	A	-	-	-	-	0	-	-
2517-1	I	-	-	8.4	4.7	-	-	33847	STT	22.4	7.6	4.0	1.8	8388	41.32	1.66
2517-2	II	-26.1	-	4.0	2.7	2.6	-	2346	STT	6.3	2.5	10.3	0.3	77	39.21	0.01
2517-3	II	22.0	-	2.7	1.4	1.3	-	14762	FT	-11.1	1.5	-3.6	-341.5	184	39.56	0.03
2517-5	E	-	-	5.2	-	-	-	152666	A	-	-	-	-	0	-	-
2517-7	II	8.4	-	3.8	3.7	1.7	-	10622	FT	6.5	3.1	-8.4	14.2	437	39.95	0.07
2517-8	E	-	-	1.9	-	-	-	5756	A	-	-	-	-	0	-	-
2650-2	III	20.6	-	2.3	1.4	4.3	-	78925	A	-	-	-	-	0	-	-
2650-4	I	-	-	1.9	1.5	-	-	40028	A	-	-	-	-	-	-	-
2650-5	III	15.6	-	2.1	1.1	4.5	-	42758	T	5.8	2.1	10.9	0.7	9885	41.06	0.91
2650-6	III	10.2	-	3.3	1.1	3.5	-	6328	A	-	2.1	-	-	60	38.81	0.01
2655-3	II	22.4	-	6.4	-23.9	3.9	-	69629	STT	55.2	12.6	4.2	3.1	16363	41.89	6.11
2655-4	2+3	4.0	16.1	3.8	2.3	1.9	7.3	6840	SE	-	1.4	0.8	-	432	40.16	0.11
2655-5	II	15.4	-	2.7	3.7	1.6	-	45626	A	-	-	-	-	0	-	-
2655-6	II	8.6	-	4.2	2.4	2.3	-	11167	B	8.0	3.8	18.2	1.2	2156	40.88	0.60

Galaxy ID (1)	Continuum										H α						
	Profile Type (2)	R _{break} (kpc)		Re (kpc) (5)	Scale length (kpc)			Flux ($\times 10^{-17}$) ($ergs\ sec^{-1}\ cm^{-2}$) (9)	Profile Type (10)	R _{break} (kpc) (11)	Re (kpc) (12)	Scale length (kpc)		Flux ($\times 10^{-17}$) ($ergs\ sec^{-1}\ cm^{-2}$) (15)	Log Luminosity ($ergs\ sec^{-1}$) (16)	Log SFR ($M_{\odot} yr^{-1}$) (17)	
		1-2 (3)	2-3 (4)		1 (6)	2 (7)	3 (8)					1 (13)	2 (14)				
2655-7	2+3	4.9	9.4	3.0	3.2	1.3	1.9	14924	FT	5.1	2.7	13.5	0.5	4578	41.19	1.23	
2774-1	III	7.9	-	3.5	1.8	3.0	-	13400	A	-	-	-	-	0	-	-	
2774-2	I	-	-	3.7	2.5	-	-	5357	A	-	-	-	-	-	-	-	
2774-3	I	-	-	6.0	7.7	-	-	82741	SE	-	1.7	0.7	-	803	40.76	0.45	
2774-4	III	5.7	-	2.3	1.1	1.8	-	4079	x	-	2.7	1.8	-	123	39.93	0.07	
2774-5	II	8.4	-	3.4	2.8	2.1	-	5386	N	-	-	-	-	0	-	-	
2774-6	I	-	-	9.2	5.5	-	-	38711	SE	-	2.8	2.1	-	5451	41.76	4.59	
2774-7	III	6.1	-	2.9	1.5	2.1	-	2288	A	-	-	-	-	0	-	-	
2774-8	III	5.4	-	3.3	1.6	2.2	-	3007	N	-	-	-	-	0	-	-	
2959-1	III	14.8	-	2.7	1.9	2.9	-	12764	T	1.6	0.7	0.4	0.1	101	39.40	0.02	
2959-2	II	9.4	-	4.7	3.6	2.3	-	22264	ST	6.5	4.4	-1.4	2.0	1748	40.66	0.36	
2959-3	E	-	-	2.3	-	-	-	21064	A	-	-	-	-	0	-	-	
2959-4	II	11.8	-	2.5	2.3	1.5	-	11463	E	-	3.2	1.8	-	2395	40.82	0.52	
2959-5	I	-	-	3.0	5.1	-	-	20762	SE	-	0.7	0.3	-	823	40.33	0.17	
2959-6	III	4.8	-	1.3	0.8	1.1	-	3059	A	-	-	-	-	-	-	-	
3066-1	I	-	-	4.2	7.1	-	-	77504	SE	-	0.9	0.5	-	1892	40.76	0.46	
3066-2	II	4.1	-	1.7	1.2	0.8	-	1913	ST	1.9	1.3	-1.8	0.7	196	39.71	0.04	
3066-3	I	-	-	5.1	3.0	-	-	7660	T	5.9	2.4	2.6	0.7	714	40.25	0.14	
3066-4	I	-	-	3.3	1.9	-	-	14719	ST	4.8	2.4	8.5	1.9	1383	40.56	0.29	
3066-6	II	1.5	-	1.3	0.8	0.7	-	4964	A/N	-	1.8	-	-	190	39.64	0.03	
3066-7	I	-	-	2.0	1.5	-	-	18763	A	-	-	-	-	0	-	-	
3071-1	II	88.3	-	8.8	7.7	5.1	-	1070705	ST	12.9	15.3	1.7	8.8	94513	41.82	5.22	
3071-2	I	-	-	1.8	2.2	-	-	71930	A	-	-	-	-	-	-	-	
3071-6	E	-	-	2.9	-	-	-	395338	E	-	3.0	1.8	-	16387	40.99	0.77	
3071-7	III	16.7	-	3.7	1.5	3.4	-	15390	FT	6.0	1.2	-7.1	0.2	484	39.37	0.02	
3072-1	III	18.1	-	4.8	2.4	7.2	-	37277	E	-	2.7	1.8	-	15311	41.71	4.08	
3072-2	I	-	-	7.3	4.3	-	-	75028	ST	2.7	9.0	0.3	-4.2	1486	40.75	0.45	
3072-3	III	15.1	-	4.1	2.1	5.5	-	5432	T	3.9	2.3	2.4	1.1	1052	40.51	0.25	
3072-4	II	2.9	-	2.4	1.9	1.4	-	10920	T	3.8	1.4	0.9	0.4	1693	40.69	0.38	
3072-5	II	8.3	-	3.4	3.2	1.4	-	4644	ST	-	0.8	0.2	-	609	40.28	0.15	

Galaxy ID (1)	Continuum										H α					
	Profile Type (2)	R _{break} (kpc)		Re (kpc) (5)	Scale length (kpc)			Flux ($\times 10^{-17}$) ($ergs\ sec^{-1} cm^{-2}$) (9)	Profile Type (10)	R _{break} (kpc) (11)	Re (kpc) (12)	Scale length (kpc)		Flux ($\times 10^{-17}$) ($ergs\ sec^{-1} cm^{-2}$) (15)	Log Luminosity ($ergs\ sec^{-1}$) (16)	Log SFR ($M_{\odot} yr^{-1}$) (17)
		1-2 (3)	2-3 (4)		1 (6)	2 (7)	3 (8)					1 (13)	2 (14)			
3072-6	II	5.8	-	3.5	2.7	1.9	-	14121	ST	-	13.0	22.3	-	1077	40.53	0.27
3072-7	I	-	-	4.0	2.5	-	-	12151	B	9.0	2.1	1.7	0.7	9092	41.51	2.58
3899-1	E	-	-	3.3	-	-	-	42462	A	-	-	-	-	0	-	-
3899-2	2+3	2.2	15.6	3.7	2.8	2.1	3.7	13746	FT	5.2	2.7	8.6	0.5	1267	40.67	0.37
3899-3	E	-	-	5.2	-	-	-	67253	SE	-	1.1	0.9	-	925	40.61	0.32
3899-4	I	-	-	5.0	3.0	-	-	2736	E	-	3.5	-	-	319	40.08	0.09
3899-5	III	9.6	-	4.8	2.0	4.3	-	2007	N	-	3.6	-	-	123	39.65	0.04
3918-1	II	6.2	-	4.3	3.4	2.3	-	11106	ST	5.9	2.5	1.1	0.5	267	39.98	0.08
3918-3	II	12.1	-	4.9	3.5	1.8	-	17198	T	5.8	4.2	13.0	1.9	1255	40.71	0.41
3918-4	II	6.9	-	3.9	3.6	1.6	-	5924	E	-	4.0	2.1	-	428	40.19	0.12
3918-5	I	-	-	6.4	7.7	-	-	110607	ST	-	4.6	4.3	-	3229	41.20	1.24
4214-1	2+3	14.9	-	0.7	3.3	4.9	-	9380	SE	-	1.9	0.9	-	361	40.45	0.22
4214-2	I	-	-	7.0	4.3	-	-	30900	ST	-	7.0	3.4	-	2668	41.40	2.00
4214-3	II	4.8	-	5.7	5.1	2.9	-	4461	E	-	3.3	2.0	-	323	40.38	0.19
4214-4	I	-	-	7.0	7.3	-	-	54206	x	-	1.0	0.2	-	32	39.50	0.02
4214-5	I	-	-	6.0	3.6	-	-	13056	SE	-	2.1	1.1	-	199	40.18	0.12
4214-6	II	6.1	-	4.5	3.9	1.8	-	8194	T	4.5	3.9	6.4	1.7	1910	41.19	1.23
4482-1	I	-	-	3.9	2.3	-	-	1758	ST	2.7	4.5	1.8	4.4	504	40.44	0.22
4482-2	III	3.8	-	1.5	0.7	1.2	-	2762	T	5.2	1.9	1.2	0.4	1506	40.90	0.63
4482-3	II	18.4	-	7.4	5.1	3.5	-	28806	ST	-	6.7	-	-	7204	41.67	3.69
4482-5	II	14.4	-	5.2	3.6	2.2	-	21675	T	10.2	4.8	5.0	2.0	11916	41.87	5.80
4482-6	I	-	-	2.9	2.0	-	-	19599	SE	-	0.8	0.4	-	77	39.67	0.04
4527-1	I	-	-	2.8	2.6	-	-	30061	A	-	-	-	-	0	-	-
4527-2	I	-	-	3.9	3.8	-	-	29425	A	-	4.1	-	-	189	39.84	0.06
4527-3	III	24.8	-	5.1	4.4	5.6	-	59406	SE	-	0.6	-	-	131	39.71	0.04
4527-4	III	5.0	-	1.4	0.7	1.6	-	2353	A	-	0.4	-	-	0	36.99	0.00
4527-5	III	2.6	-	1.2	0.5	1.0	-	1882	T	1.1	0.8	0.9	0.3	341	40.06	0.09
4527-6	II	41.3	-	6.5	46.0	3.5	-	30710	ST/AT?	-	-	-	-	-	-	-
5136-2	E	-	-	2.9	-	-	-	157058	E	-	3.1	2.3	-	13404	41.27	1.47
5136-3	2+3	3.2	4.7	1.0	0.4	0.3	1.0	2055	N	-	0.4	-	-	3	37.59	0.00

Galaxy ID	Continuum										H α						
	Profile Type	R _{break} (kpc)		Re (kpc)	Scale length (kpc)			Flux ($\times 10^{-17}$) ($ergs\ sec^{-1}\ cm^{-2}$)	Profile Type	R _{break} (kpc)	Re (kpc)	Scale length (kpc)		Flux ($\times 10^{-17}$) ($ergs\ sec^{-1}\ cm^{-2}$)	Log Luminosity ($ergs\ sec^{-1}$)	Log SFR ($M_{\odot} yr^{-1}$)	
		1-2 (3)	2-3 (4)		1 (6)	2 (7)	3 (8)					1 (13)	2 (14)				
(1)	III	15.5	-	2.2	1.3	1.9	-	17919	ST	-	0.9	0.5	-	239	39.43	0.02	
5136-4	III	25.1	-	4.8	3.0	3.7	-	15874	ST	7.2	3.0	1.4	0.8	2989	40.99	0.78	
5219-1	III	6.1	-	1.9	0.9	1.8	-	2099	A	-	-	-	-	-	-	-	
5219-2	II	14.7	-	5.3	4.2	2.0	-	10389	T	11.7	5.3	8.1	1.7	3113	40.94	0.69	
5219-3	E	-	-	5.6	-	-	-	138980	A	-	0.6	-	-	83	39.50	0.02	
5219-4	I	-	-	3.4	2.0	-	-	1688	T	2.6	1.1	1.3	0.4	33	38.95	0.01	
5219-5	III	27.6	-	3.4	4.1	9.9	-	24619	AT	7.6	2.3	0.8	8.3	7826	41.46	2.25	
5688-1	III	14.2	-	3.0	2.2	4.2	-	38159	E	2.3	1.0	0.5	0.9	1620	40.78	0.47	
5688-2	III	16.1	-	3.8	1.9	6.0	-	5614	T	5.6	2.5	2.8	0.7	628	40.29	0.15	
5688-3	III	4.5	-	2.1	0.8	2.0	-	1619	E	-	1.0	0.6	-	395	40.08	0.09	
5688-4	I	-	-	3.5	2.1	-	-	4232	E	-	2.9	2.2	-	704	40.35	0.18	
5688-5	I	-	-	3.8	2.6	-	-	13755	E	-	4.3	2.4	-	11373	41.56	2.88	
7356-1	II	25.2	-	4.6	13.4	2.8	-	49217	ST	-	0.7	-	-	1657	40.78	0.48	
7356-3	I	-	-	8.8	12.4	-	-	55250	A	-	0.4	-	-	0	36.17	0.00	
7356-4	III	38.2	-	8.1	5.1	11.7	-	111070	A	-	8.4	-	-	218	39.94	0.07	
7358-2	I	-	-	2.6	2.7	-	-	26845	A	-	-	-	-	0	-	-	
7358-3	II	2.5	-	6.7	4.3	4.0	-	30247	E	-	7.1	5.1	-	7933	41.41	2.04	
7358-4	III	11.3	-	2.1	2.0	3.8	-	7673	STT	9.8	1.6	0.8	42.2	3399	41.05	0.89	
8275-1	II	9.7	-	2.9	1.8	1.3	-	3599	AT	5.4	1.7	0.9	2.3	1846	40.76	0.46	
8275-2	I	-	-	5.9	4.2	-	-	48739	E	14.7	7.7	2.9	5.2	7745	41.47	2.35	
8275-3	II	15.5	-	4.7	6.6	2.8	-	40942	E	-	3.7	1.9	-	8511	41.51	2.53	
8275-4	I	-	-	5.7	6.1	-	-	36638	E	-	3.3	2.5	-	725	40.83	0.53	
8317-1	III	7.1	-	3.4	1.6	3.5	-	5138	E	-	2.3	1.1	-	898	40.86	0.57	
8317-2	I	-	-	5.4	3.0	-	-	9627	E	-	2.8	3.3	-	146	40.07	0.09	
8317-3	I	-	-	9.6	6.4	-	-	150398	E	-	10.2	6.3	-	34478	42.15	11.08	
10197-1	II	18.0	-	6.5	4.2	3.0	-	31634	T	17.0	5.5	4.1	1.6	10839	41.57	2.91	
10197-2	I	-	-	3.8	2.1	-	-	12874	FT	7.2	4.0	-365.2	1.2	6185	41.28	1.52	
10197-3	I	-	-	4.7	3.0	-	-	202543	ST	-	6.4	2.7	-	29793	41.64	3.48	
11003-1	II	5.1	-	2.6	2.5	1.4	-	6175	A	-	-	-	-	0	-	-	
11003-2	I	-	-	1.0	0.5	-	-	2003	N	-	-	-	-	-	-	-	

Galaxy ID (1)	Continuum										H α						
	Profile Type (2)	R _{break} (kpc) (3) (4)		Re (kpc) (5)	Scale length (kpc) (6) (7) (8)			Flux ($\times 10^{-17}$) ($ergs\ sec^{-1} cm^{-2}$) (9)	Profile Type (10)	R _{break} (kpc) (11)	Re (kpc) (12)	Scale length (kpc) (13) (14)		Flux ($\times 10^{-17}$) ($ergs\ sec^{-1} cm^{-2}$) (15)	Log Luminosity ($ergs\ sec^{-1}$) (16)	Log SFR ($M_{\odot} yr^{-1}$) (17)	
		1-2 (3)	2-3 (4)		1 (6)	2 (7)	3 (8)					1 (13)	2 (14)				
11454-1	I	-	-	4.1	2.7	-	-	65297	ST	-	4.8	2.7	-	12816	41.53	2.69	
11454-2	III	7.5	-	1.5	0.9	2.3	-	6968	A	-	-	-	-	0	-	-	
11454-3	I	-	-	3.5	1.9	-	-	5712	FT	7.1	3.2	6.9	0.8	2591	40.74	0.44	
11534-1	II	4.6	-	1.0	0.9	0.4	-	3046	T	5.3	0.9	1.1	0.4	2991	40.19	0.12	
11534-2	E	-	-	0.8	-	-	-	12932	E	-	0.7	0.3	-	1137	39.76	0.05	
11534-3	II	65.2	-	3.7	3.2	1.6	-	293653	A	-	-	-	-	0	-	-	
11694-1	I	-	-	2.2	1.4	-	-	3573	E	-	1.6	0.8	-	1983	40.92	0.65	
11694-3	II	15.8	-	7.7	6.1	4.1	-	54484	STT	17.8	10.6	121.7	3.6	7695	41.57	2.95	
12962-2	I	-	-	7.0	5.2	-	-	80944	ST	-	11.3	6.3	-	6063	41.27	1.48	
12962-3	II	14.2	-	7.8	7.6	3.8	-	27820	FT	11.0	7.4	-34.5	3.4	6570	41.25	1.41	
13702-1	I	-	-	1.7	1.0	-	-	2037	E	-	1.4	0.7	-	572	40.21	0.13	
13702-2	2+3	8.0	18.9	5.2	10.4	2.3	4.3	5962	STT	8.9	5.2	-12.7	1.4	22548	41.89	6.07	
13702-3	I	-	-	6.3	4.2	-	-	76651	ST	-	5.2	2.5	-	19712	41.83	5.38	
13832-1	II	5.5	-	4.8	3.3	2.6	-	2657	FT	6.8	4.5	13.0	1.0	540	40.38	0.19	
15934-1	I	-	-	3.0	1.8	-	-	3947	E	-	2.9	2.2	-	407	40.06	0.09	
15934-2	I	-	-	3.1	1.8	-	-	3203	SE	-	0.9	0.4	-	51	39.14	0.01	
15934-3	I	-	-	5.7	6.0	-	-	155554	ST	-	7.4	6.3	-	5268	41.32	1.64	
19177-1	II	19.7	-	6.6	4.6	3.1	-	45086	T	20.4	8.2	8.0	2.4	17069	41.64	3.49	
19177-2	II	21.7	-	4.9	3.2	1.8	-	42566	FT	11.1	5.2	14.1	2.0	20334	41.75	4.47	
19444-1	E	-	-	3.2	-	-	-	37885	SE	-	1.3	0.7	-	627	40.35	0.18	
19444-2	II?	21.3	-	6.0	4.0	2.4	-	34641	ST	-	7.5	6.9	-	7978	41.50	2.49	
19817-1	II	18.1	-	3.5	22.4	2.3	-	69217	E	-	1.5	1.0	-	545	40.24	0.14	
19817-2	III	24.5	-	8.2	3.8	6.7	-	9427	E	-	7.6	5.3	-	2503	40.84	0.54	
21512-1	I	-	-	3.3	2.3	-	-	146402	ST	-	-	-	-	-	-	-	
21512-2	III	12.2	-	1.1	0.8	1.3	-	25371	A	-	-	-	-	0	-	-	
22376-2	II	5.2	-	2.5	1.5	1.2	-	4290	FT	1.8	1.7	10.6	0.8	668	40.47	0.23	
22471-1	III	21.5	-	6.5	4.1	7.2	-	79299	ST	-	1.1	0.8	-	534	40.76	0.45	
22471-2	III	4.4	-	3.8	1.7	2.7	-	6307	A	-	-	-	-	-	-	-	
23339-1	2+3	5.3	12.1	1.6	1.0	0.7	1.6	11485	T	5.3	1.8	3.7	0.7	1740	40.22	0.13	
23445-1	II	18.7	-	6.1	4.1	2.9	-	71451	T	13.3	5.7	4.6	2.3	20297	41.95	6.98	

Galaxy ID (1)	Continuum										H α						
	Profile Type (2)	R _{break} (kpc)		Re (kpc) (5)	Scale length (kpc)			Flux ($\times 10^{-17}$) ($ergs\ sec^{-1}\ cm^{-2}$) (9)	Profile Type (10)	R _{break} (kpc) (11)	Re (kpc) (12)	Scale length (kpc)		Flux ($\times 10^{-17}$) ($ergs\ sec^{-1}\ cm^{-2}$) (15)	Log Luminosity ($ergs\ sec^{-1}$) (16)	Log SFR ($M_{\odot}\ yr^{-1}$) (17)	
		1-2 (3)	2-3 (4)		1 (6)	2 (7)	3 (8)					1 (13)	2 (14)				
23445-2	III	4.8	-	3.0	1.2	2.1	-	4274	AT	3.7	1.9	0.6	2.8	1406	40.64	0.35	
23835-2	I	-	-	6.7	7.1	-	-	79476	ST	-	1.1	-	-	2919	40.90	0.63	
23898-1	II	13.1	-	3.1	1.9	1.7	-	5559	N	-	-	-	-	-	-	-	
23898-2	I	-	-	3.0	2.4	-	-	178834	N	-	-	-	-	-	-	-	
23991-1	III	18.2	-	5.1	3.1	6.2	-	81499	E	-	4.5	3.3	-	5738	41.28	1.50	
23991-2	II	6.7	-	2.9	2.0	1.4	-	5810	FT	4.9	2.3	42.7	0.4	1395	40.56	0.29	
24459-1	II?	18.0	-	7.5	5.3	3.8	-	91294	STT	-	8.9	2.4	-	18236	41.91	6.39	
24459-2	2+3	7.9	22.0	4.8	3.2	2.4	5.4	6855	T	7.3	4.2	5.9	1.9	1917	40.85	0.56	
24974-1	II	4.3	-	2.3	1.3	1.0	-	3373	FT	2.3	1.5	2.8	0.2	191	39.98	0.08	
24974-2	II	5.5	-	4.1	4.4	1.7	-	2748	E	-	4.2	2.7	-	469	40.39	0.19	
25155-2	I	-	-	1.8	10.0	-	-	22333	A	-	1.2	-	-	4	38.13	0.00	
29640-1	II	3.8	-	1.7	1.2	1.0	-	24135	T	5.9	1.5	7.5	0.3	668	39.59	0.03	
29901-2	III	22.1	-	3.8	2.5	4.3	-	39276	ST	-	4.3	-	-	198	39.80	0.05	
31811-1	II	40.5	-	5.5	4.5	2.8	-	485330	ST	38.3	7.4	1.4	8.9	69065	41.72	4.11	
32627-2	II	16.7	-	3.0	4.5	2.6	-	41460	N	-	0.8	-	-	78	39.45	0.02	
32627-3	III	5.8	-	1.8	1.0	1.6	-	6938	A	-	-	-	-	0	-	-	
32900-1	II	8.7	-	1.9	2.3	0.9	-	29326	ST	-	0.6	-	-	176	39.80	0.05	
32900-2	III	4.7	-	1.6	0.8	1.4	-	1783	A	-	-	-	-	0	-	-	
32901-1	E	-	-	2.3	-	-	-	29480	A	-	-	-	-	0	-	-	
32901-2	I	-	-	3.8	2.3	-	-	2381	T	5.5	2.6	3.5	0.6	209	39.82	0.05	
57064-1	II	18.0	-	2.8	2.8	1.7	-	44227	SE	-	0.5	0.1	-	277	39.80	0.05	
60661-1	I	-	-	2.4	2.2	-	-	319497	E	-	3.0	2.5	-	8059	40.71	0.40	
63756-1	II	4.4	-	4.9	4.8	2.4	-	13381	T	5.8	4.2	3.8	1.8	6691	41.78	4.74	
64176-1	II	15.3	-	5.0	4.3	0.9	-	3908	E	-	5.0	3.9	-	985	40.62	0.33	
64521-1	I	-	-	3.6	2.0	-	-	4631	T	2.9	1.6	1.1	0.2	512	40.56	0.29	
64523-1	I	-	-	6.9	3.9	-	-	37147	ST	-	9.4	4.7	-	7026	41.84	5.52	
64525-1	II	8.0	-	6.3	4.5	2.9	-	25864	T	7.2	5.5	9.1	1.5	5158	41.70	3.92	
64659-1	I	-	-	6.0	3.5	-	-	21683	SE	-	1.2	1.2	-	251	40.19	0.12	
68901-1	I	-	-	9.8	14.9	-	-	127689	ST	-	13.7	-	-	11040	41.58	2.99	
68906-2	II	10.5	-	5.1	3.5	2.7	-	28171	ST	-	4.2	1.5	-	1275	40.59	0.31	

Galaxy ID (1)	Continuum										H α						
	Profile Type (2)	R _{break} (kpc)		Re (kpc) (5)	Scale length (kpc)			Flux ($\times 10^{-17}$) ($ergs\ sec^{-1} cm^{-2}$) (9)	Profile Type (10)	R _{break} (kpc) (11)	Re (kpc) (12)	Scale length (kpc)		Flux ($\times 10^{-17}$) ($ergs\ sec^{-1} cm^{-2}$) (15)	Log Luminosity ($ergs\ sec^{-1}$) (16)	Log SFR ($M_{\odot} yr^{-1}$) (17)	
		1-2 (3)	2-3 (4)		1 (6)	2 (7)	3 (8)					1 (13)	2 (14)				
73668-1	III	4.8	-	2.4	1.2	1.7	-	5670	A	-	5.9	-	-	50	39.68	0.04	
90284-1	III	33.6	-	6.4	5.9	11.3	-	51209	A	-	-	-	-	0	-	-	
99910-1	I	-	-	5.8	3.7	-	-	69130	E	-	6.1	4.0	-	14681	41.78	4.75	
111666-1	I	-	-	2.0	1.2	-	-	2796	AT	8.2	1.6	0.9	11.4	1738	40.84	0.55	
112723-1	E	-	-	3.2	-	-	-	35951	A	-	-	-	-	0	-	-	
113424-1	III	23.2	-	4.7	3.4	8.8	-	34937	SE	-	0.6	-	-	23	38.89	0.01	
119022-1	II	5.1	-	2.0	1.5	0.7	-	8009	FT	4.4	2.1	11.6	0.5	4147	41.01	0.80	
121804-2	I	-	-	5.2	3.0	-	-	16503	T	14.5	5.7	5.4	2.4	4511	41.08	0.95	
133088-1	II	8.5	-	5.3	3.6	1.5	-	7418	E	-	5.3	2.6	-	1498	41.19	1.22	
166604-1	I	-	-	6.9	3.3	-	-	6655	E	-	5.1	3.2	-	1043	40.95	0.70	
189741-1	III	24.3	-	2.8	1.7	3.9	-	231060	A	-	-	-	-	0	-	-	
190338-1	III	29.8	-	7.9	4.7	9.0	-	54912	ST	18.0	7.6	7.2	1.6	3379	41.02	0.83	
192594-1	III	8.8	-	2.7	1.6	4.5	-	8185	E	-	2.0	1.0	-	2919	41.47	2.36	
192773-1	III	6.1	-	2.6	1.3	2.4	-	7818	A	-	-	-	-	-	-	-	
219717-4	I	-	-	4.6	2.7	-	-	1946	N	-	-	-	-	-	-	-	
225398-1	III	15.1	-	5.1	2.8	4.5	-	32016	E	-	5.3	1.6	-	2515	40.98	0.75	
225426-1	I	-	-	4.7	3.0	-	-	46415	ST	-	5.6	2.6	-	10892	41.73	4.23	
230126-1	2+3	7.8	18.6	6.6	6.5	3.5	5.3	50211	ST	-	7.6	3.8	-	8527	41.46	2.27	
230128-1	III	9.2	-	2.4	1.3	2.4	-	3976	FT	2.9	2.0	-18.6	0.7	605	40.35	0.18	
230130-5	II	6.8	-	2.7	2.0	1.0	-	1544	T	7.6	2.7	2.4	0.5	595	40.17	0.12	
230227-1	II	22.5	-	7.0	5.9	3.3	-	66736	ST	-	12.5	5.2	-	4663	41.25	1.41	
232714-1	II	19.5	-	4.2	18.1	2.3	-	35251	ST	-	7.3	5.0	-	4199	41.21	1.27	
237373-1	II	3.3	-	4.7	4.4	2.4	-	5218	T	5.6	4.3	4.6	1.4	1141	41.02	0.82	
237376-1	I	-	-	3.0	1.7	-	-	16410	A	-	-	-	-	-	-	-	
237684-1	III	4.9	-	3.0	1.3	2.4	-	4373	SE	-	1.4	0.7	-	1128	40.74	0.44	
245324-1	I	-	-	3.5	2.4	-	-	5016	N	-	-	-	-	-	-	-	
245328-1	I	-	-	5.2	3.0	-	-	8517	FT	4.5	4.8	-401.1	2.1	2767	41.41	2.03	
341518-1	I	-	-	3.5	4.1	-	-	68630	A	-	-	-	-	0	-	-	
467592-2	II	2.8	-	2.0	1.5	0.9	-	3179	FT	2.3	1.8	-7.7	0.8	304	40.11	0.10	
467944-1	II	5.5	-	2.5	1.7	1.2	-	2839	T	3.0	1.9	2.2	1.0	438	40.10	0.10	

Acknowledgements

Foremost, I wish to thank my Ph.D. supervisors, PD. Dr. Roberto Saglia and Dr. David Wilman, for all their scientific and personal support over the last four years. Their guidance and encouragement has been instrumental in the production of this thesis and I consider myself extremely fortunate to have benefited from their experience and expertise.

I would also like to thank Dr. Peter Erwin for his detailed and helpful discussions and for providing his expertise on various topics. My sincere thanks also goes to Dr. Leonel Gutiérrez to provide me the reduced INT data well in time and to other collaborators — Prof. John Beckman and Prof. Bodo Ziegler for meaningful discussions, and Dr. Johannes Koppenhöfer, Dr. Arno Riffeser and Dr. Jan Snigula for providing the software tools and helping me out with their expertise in data reduction. Additionally, I would like to thank all members of Optical and Interpretative Astronomy (OPINAS) group at Max Planck Institute For Extraterrestrial Physics (MPE) especially my fellow office mates — Michael, Fabrizio, Salvador and Jan — for bearing me patiently for four years.

Finally, my special thanks go to my family and friends for their valuable support during my Ph.D studies and for putting up with my high stress levels over the last few months of writing.